

Fracture Mechanics: Nineteenth Symposium

Thomas A. Cruse,
editor



STP 969

FRACTURE MECHANICS: NINETEENTH SYMPOSIUM

**Nineteenth National Symposium
on Fracture Mechanics
sponsored by
ASTM Committee E-24
on Fracture Testing and
Southwest Research Institute
San Antonio, TX, 30 June–2 July 1986**

**ASTM SPECIAL TECHNICAL PUBLICATION 969
Thomas A. Cruse, Southwest Research Institute,
editor**

**ASTM Publication Code Number (PCN)
04-969000-30**



1916 Race Street, Philadelphia, PA 19103

Library of Congress Cataloging-in-Publication Data

National Symposium on Fracture Mechanics (19th: 1986:
San Antonio, Tex.)
Fracture mechanics, nineteenth symposium.

(ASTM special technical publication; 969)

“ASTM publication code number (PCN) 04-969000-30.”

Includes bibliographies and index.

1. Fracture mechanics—Congresses. I. Cruse, Thomas A.
II. ASTM Committee E-24 on Fracture Testing. III. Southwest
Research Institute (San Antonio, Tex.). IV. Title. V. Series.
TA409.N38 1986 620.1'126 88-3320
ISBN 0-8031-0972-5

Copyright © by AMERICAN SOCIETY FOR TESTING AND MATERIALS 1988
Library of Congress Catalog Card Number: 88-3320

NOTE

The Society is not responsible, as a body,
for the statements and opinions
advanced in this publication.

Foreword

The Nineteenth National Symposium on Fracture Mechanics was held on 30 June–2 July 1986 in San Antonio, TX. ASTM Committee E-24 on Fracture Testing and the Southwest Research Institute sponsored the event. The symposium chairman was Thomas A. Cruse, Southwest Research Institute, who also served as editor of this publication.

Related ASTM Publications

Fracture Mechanics: Eighteenth Symposium, STP 945 (1987), 04-945000-30

Fracture Mechanics: Seventeenth Volume, STP 905 (1986), 04-905000-30

Fracture Mechanics: Sixteenth Symposium, STP 868 (1985), 04-868000-30

Fracture Mechanics: Fifteenth Symposium, STP 833 (1984), 04-833000-30

Case Histories Involving Fatigue and Fracture, STP 918 (1986), 04-918000-30

Elastic-Plastic Fracture Mechanics Technology, STP 896 (1986), 04-896000-30

Automated Test Methods for Fracture and Fatigue Crack Growth, STP 877 (1985), 04-877000-30

Elastic-Plastic Fracture Test Methods: The User's Experience, STP 856 (1985), 04-856000-30

A Note of Appreciation to Reviewers

The quality of the papers that appear in this publication reflects not only the obvious efforts of the authors but also the unheralded, though essential, work of the reviewers. On behalf of ASTM we acknowledge with appreciation their dedication to high professional standards and their sacrifice of time and effort.

ASTM Committee on Publications

ASTM Editorial Staff

**Helen Mahy
Janet R. Schroeder
Kathleen A. Greene
William T. Benzing**

Contents

Introduction	1
---------------------	---

THREE-DIMENSIONAL ISSUES

Measurement of Three-Dimensional Effects in Fracture Mechanics—C. WILLIAM SMITH	5
Three-Dimensional Elastic Surface Cracks—THOMAS A. CRUSE	19
Stress-Intensity Factors for Corner Cracks in Rectangular Bars— I. S. RAJU AND J. C. NEWMAN, JR.	43
Some Remarks on Three-Dimensional Fracture— EFTHYMIOS S. FOLIAS	56
Three-Dimensional Effects Affecting the Precision of Lifetime Predictions—HORST KORDISCH AND ERWIN SOMMER	73
Three Dimensions Versus Two Dimensions in Fracture Mechanics—J. L. SWEDLOW	88

COMPUTATIONAL AND ANALYTICAL ISSUES

Computation of the Amplitude of Stress Singular Terms for Cracks and Reentrant Corners—BARNA A. SZABÓ AND IVO BABUŠKA	101
Line Spring Model and Its Applications to Part-Through Crack Problems in Plates and Shells—FAZIL ERDOGAN AND BULENT AKSEL	125
Methodology for Mixed-Mode Stress-Intensity Factor Calculations—E. THOMAS MOYER	153

DAMAGE TOLERANCE AND FATIGUE

Damage Tolerance of Stiffened-Skin Structures: Prediction and Experimental Verification—HENK VLIETGER	169
--	-----

Mechanical Durability Assurance in Automotive Structures— RONALD W. LANDGRAF	220
Role of Damage Tolerance and Fatigue Crack Growth in the Power Generation Industry— LOUIS F. COFFIN	235
Structural Integrity of Rail in Railroad Track in the United States— OSCAR ORRINGER AND ROGER K. STEELE	260

ELASTOPLASTIC FRACTURE

Three-Dimensional Crack-Tip Deformation in a Plastically Deformed Three-Point Bending Specimen— XIAO-PING WU AND FU-PEN CHIANG	281
On the Application of <i>R</i>-Curves and Maximum Load Toughness to Structures— TED L. ANDERSON, J. ROBIN GORDON, AND STEVEN J. GARWOOD	291
Application of the <i>J</i> Concept to Fatigue Crack Growth in Large- Scale Yielding— YVAN LAMBERT, PATRICK SAILLARD, AND CLAUDE BATHIAS	318
Fracture Toughness of Stainless Steel Welds— WILLIAM J. MILLS	330
Use of <i>R</i>-Curves for Design in the Elastic-Plastic Fracture Mechanics Regime— CEDRIC E. TURNER AND MOHAMMAD R. ETEMAD	356
Fatigue Behavior of Axial and Pressure Cycled Butt and Girth Welds Containing Defects— BRIAN N. LEIS, DOUGLAS P. GOETZ, PAUL M. SCOTT, AND C. MICHAEL HUDSON	374
Effect of Temperature and Strain Rate on Upper Shelf Fracture Behavior of A533B Class I Pressure Vessel Steel— OUN H. JUNG AND K. LINGA MURTY	392

DYNAMIC INELASTIC FRACTURE

Using Combined Experiments and Analysis to Generate Dynamic Critical Stress Intensity Data— DANIEL V. SWENSON AND ANTHONY R. INGRAFFEA	405
--	-----

Analysis of Crack Arrest Under Elastic-Plastic Conditions— GEORGE T. HAHN, PEDRO C. BASTIAS, ARUN M. KUMAR, AND CAROL A. RUBIN	427
Ductile Crack Bifurcation and Arrest in Pressurized Pipe— ALBERT S. KOBAYASHI, A. F. EMERY, W. J. LOVE, Y.-H. CHAO, AND O. JOHANSSON	441
Dynamic Measurement of Crack-Tip Opening Displacement— WILLIAM N. SHARPE, JR., ZENON WACLAWIW, AND ANDREW S. DOUGLAS	466
Dynamic Moiré Interferometry Studies of Stress Wave and Crack- Tip Diffraction Events in 1018 Steel— JONATHAN S. EPSTEIN, VANCE A. DEASON, AND WALTER G. REUTER	482

CRACK ARREST THEORY AND APPLICATIONS: PART I

Determination of Dynamic Fracture Behavior in 4340 Steel Compact Crack Arrest Specimens Using Birefringent Coatings and Finite-Element Analysis— SHAMSUDDIN KHATRI AND DON B. BARKER	507
Approximate Methods for Analysis of Dynamic Crack Growth and Arrest— FRED NILSSON	524
Some Aspects of Performing Dynamic Measurements and Analyses on the Compact Crack Arrest Specimen for A533-B Steel— BJÖRN BRICKSTAD AND LARS DAHLBERG	532
A Cooperative Study for the Evaluation of Crack Arrest Toughness of RPV Materials in Japan— YUZURU SAKAI, GENKI YAGAWA, AND YOSHIO ANDO	547
A Method for Determining the Crack Arrest Fracture Toughness of Ferritic Materials— D. B. BARKER, R. CHONA, W. R. CORWIN, W. L. FOURNEY, G. R. IRWIN, C. W. MARSCHALL, A. R. ROSENFELD, AND E. T. WESSEL	569

CRACK ARREST THEORY AND APPLICATIONS: PART I—ANALYSIS

Experimental Evaluation of an Equation Applicable for Surface Cracks Under Tensile or Bending Loads— WALTER G. REUTER AND JONATHAN S. EPSTEIN	597
---	-----

A Three-Dimensional Weight Function Method— LESLIE BANKS-SILLS	620
--	-----

Constraint-Loss Model for the Growth of Surface Fatigue Cracks— R. H. VAN STONE, M. S. GILBERT, O. C. GOODEN, AND J. H. LAFLEN	637
--	-----

Line Spring Method of Stress-Intensity Factor Determination for Surface Cracks in Plates Under Arbitrary In-Plane Stresses— CHUANG-YEH YANG	657
--	-----

Mixed-Mode Stress-Intensity Factor Solutions for Offshore Structural Tubular Joints— H. CHONG RHEE AND MAMDOUH M. SALAMA	669
--	-----

CRACK ARREST THEORY AND APPLICATIONS: PART II

Wide-Plate Crack-Arrest Testing: Evolution of Experimental Procedures— ROLAND DEWIT, SAMUEL R. LOW III, AND RICHARD J. FIELDS	679
---	-----

Fracture Analyses of Heavy-Section Steel Technology Wide-Plate Crack-Arrest Experiments— B. RICHARD BASS, CLAUD E. PUGH, JOHN G. MERKLE, DAN J. NAUS, AND JANIS KEENEY-WALKER	691
--	-----

Comparison of Analysis and Experimental Data for a Unique Crack Arrest Specimen— DAVID J. AYRES, RAYMOND J. FABI, ROBERT Y. SCHONENBERG, AND DOUGLAS M. NORRIS	724
---	-----

Review of Pressurized-Water-Reactor-Related Thermal Shock Studies— RICHARD D. CHEVERTON, SHAFIK K. ISKANDER, AND DAVID G. BALL	752
--	-----

Pressurized Thermal Shock Experiments with Thick Vessels— ROBERT H. BRYAN, JOHN G. MERKLE, RANDY K. NANSTAD, AND GROVER C. ROBINSON	767
--	-----

CRACK ARREST THEORY AND APPLICATIONS: PART II—FATIGUE

Fatigue Crack Propagation Behavior and Damage Accumulation Relationships in an Aluminum Alloy— BRIAN P. D. O'CONNOR AND ALAN PLUMTREE	787
---	-----

Fatigue Crack Growth at High Load Ratios in the Time-Dependent Regime— THEODORE NICHOLAS AND NOEL E. ASHBAUGH	800
Threshold and Nonpropagation of Fatigue Cracks Under Service Loading— D. E. CASTRO, GUNTER MARCI, AND D. MUNZ	818
Fatigue Crack Growth Rate Properties of SA508 and SA533 Pressure Vessel Steels and Submerged-Arc Weldments in a Pressurized Water Environment— WILLIAM A. LOGSDON, PETER K. LIAW, AND JAMES A. BEGLEY	830
Fatigue Crack Growth in Aircraft Main Landing Gear Wheels— ARVIND NAGAR	868
Near-Threshold Crack Growth in Nickel-Base Superalloys— R. H. VAN STONE AND D. D. KRUEGER	883
Effect of Frequency on Fatigue Crack Growth Rate of Inconel 718 at High Temperature— TUSIT WEERASOORIYA	907

INDEXES

Author Index	927
Subject Index	929

Introduction

In the 19 years of the National Symposium on Fracture Mechanics, the field of fracture mechanics has undergone considerable maturation. Much of the maturation of this critical technology is the direct result of work accomplished by members of ASTM Committee E-24 on Fracture Testing and the supporting analysis efforts. A significant amount of that effort has been reported in ASTM Special Technical Publications, such as the current volume. The quality of the research can be seen in the importance attached to these volumes and in the expertise of the reviewers, whose work is essential to the production of these volumes.

The goal of the Nineteenth National Symposium on Fracture Mechanics, on which this publication is based, was the identification of major issues in the principle technology subdivisions of fracture mechanics: three-dimensional issues, computational and analytical issues, damage tolerance and fatigue, elastoplastic fracture, dynamic inelastic fracture, and crack arrest theory and applications. Leading developers and applications engineers contributed to these focused sessions. The quality of these sessions, and of this volume, is due to these organizers: Professors J. L. Swedlow, C. W. Smith, and G. T. Hahn; Drs. J. C. Newman and M. F. Kanninen; and Messrs. D. P. Wilhem, T. Swift, and M. Vagins.

The emphasis throughout this volume is on reduction to practice. The quality of the research effort in the field of fracture mechanics can be seen in the success that has been achieved in the past 19 years in solving so many of the critical issues of test methodology, analytical and computational modeling, nonlinear behavior, damage tolerance, nonlinear fatigue crack growth behavior, and other issues. The major new area of research is dynamic fracture, as shown by the numerous contributions contained in this volume. Of greatest importance is the very large effort sponsored by the Nuclear Regulatory Commission to develop methodologies for predicting the arrest of a running crack in materials of variable toughness conditions. There are numerous ongoing experimental and numerical tasks related to this problem, and further developments are expected in the near future.

The National Symposium on Fracture Mechanics is also an opportunity for ASTM Committee E-24 on Fracture Testing to honor its members. This year Dr. J. C. Newman, Jr., was awarded the ASTM Award of Merit for his numerous contributions to the literature and to Committee E-24.

The real success of the 19th symposium as a forum for key researchers and appliers of the art of fracture mechanics is due to the local arrangements staff. Without the key support of Cathy Dean and Beatrice Moreno at Southwest Research Institute, this symposium would not have taken place in San Antonio. I heartily thank both of them, especially Ms. Dean for her patience and endurance. I would also like to thank Steve Hudak and Dr. Mel Kanninen for their helpful advice.

Thomas A. Cruse

Southwest Research Institute, San Antonio, TX
78284; symposium chairman and editor.

Three-Dimensional Issues

Measurement of Three-Dimensional Effects in Fracture Mechanics

REFERENCE: Smith, C. W., "Measurement of Three-Dimensional Effects in Fracture Mechanics," *Fracture Mechanics: Nineteenth Symposium, ASTM STP 969*, T. A. Cruse, Ed., American Society for Testing and Materials, Philadelphia, 1988, pp. 5–18.

ABSTRACT: After citing several experimental methods used for measuring three-dimensional effects in opaque and transparent cracked bodies, an integrated optical method is focused upon for obtaining two independent estimates of fracture parameters associated with linear elastic fracture mechanics (LEFM). Results of the use of these methods to study the effect of free surfaces upon the stress singularity of cracks intersecting them are presented and a means of interpreting the results within the framework of LEFM is suggested.

KEY WORDS: stress-intensity factor, linear elastic fracture mechanics, eigen-function solutions, free-surface effects, crack/surface intersections, optical methods, fracture parameters, fracture mechanics

Nomenclature

$\sigma_{ij}; \sigma_{ij}^O$	$(i, j = n, z)$	In-plane stress components; nonsingular part of in-plane stress components
K_I		Mode I stress-intensity factor
r, θ		Polar coordinates in nz plane with origin at crack tip
a		Crack length (or half-crack length)
$\tau_{\max}; \tau_{\max}^{nz}; \tau_O$		Maximum in-plane shear stress; in nz plane; due to nonsingular part of stress field
K_{Ap}		Apparent stress-intensity factor $K_{Ap} = \tau_{\max}^{nz}(8\pi r)^{1/2}$
U_i	$(i = n, z)$	In-plane displacement components
σ		Remote uniform stress
C, D		Elastic coefficients
λ_σ		Dominant eigenvalue in stress field equations
λ_u		Dominant eigenvalue in displacement equations
$(K_\lambda)_{Ap}; K_\lambda$		Apparent; actual stress eigenfactor
$(K_{cor})_{Ap}; K_{cor}$		Apparent; actual corresponding stress-intensity factor

Although fracture toughness testing is based upon two-dimensional concepts [1], a number of effects such as "thumbnailing" of through cracks, variation in measured stress-intensity factors (SIF) and plastic zone sizes along flaw borders, and non-self-similar growth of surface flaws suggest the presence of three-dimensional effects. In fact, one such effect, the variation of crack growth resistance along a crack border and radially from the crack tip, is a major cause in the difference between the "plane strain" critical stress-intensity factor and other higher critical values.

¹ Professor, Department of Engineering Science and Mechanics, Virginia Polytechnic Institute and State University, Blacksburg, VA 24061.

Most measurement techniques in fracture mechanics yield, in fact, either thickness averaged values or surface measurements (for example, loads, crack size, crack-mouth or crack-tip opening displacements, and so forth). However, methods are available for three-dimensional measurements. We use three-dimensional here in the context of obtaining fracture parameter distributions rather than thickness averaged values.

There are several methods which are available for experimental analysis of three-dimensional fracture problems within the above context and they may be conveniently partitioned into measurement methods for opaque and transparent bodies, respectively.

Opaque Bodies—By measuring crack growth increments under fatigue loading and relating the crack growth at points along the flaw border to the SIF through a power law relationship, SIF distributions have been obtained along flaw borders in heterogeneous stress fields [2].

Transparent Bodies—Such bodies are well suited for optical methods and we shall briefly cite the major ones here:

1. Frozen stress photoelasticity—For problems involving only small-scale yielding, stress fringe patterns may be frozen into transparent bodies and slices can be removed along the flaw border, without disturbing the optical field, and analyzed photoelastically. This method has been employed, together with the near-tip equations of linear elastic fracture mechanics (LEFM), to measure SIF distributions in three-dimensional finite cracked bodies [3].

2. Scattered light photoelasticity—By making observations along directions other than the incident light direction (as normally done), stress fringe patterns due to scattering of the incident light may be obtained for planes internal to the body and converted to SIF values. Two different approaches have been used:

- (a) Isodyne photoelasticity—Using scattered light, fringes representing curves of constant intensity of normal forces (isodynes) can be measured and used to obtain SIF distributions in cracked bodies [4].

- (b) Optical slicing—By passing two parallel sheets of polarized light through a loaded photoelastic model, an optical slice of material between the planes is isolated, and the light scattered from this slice is observed normal to the light planes. By properly orienting such planes normal to the flaw border SIF distributions have been obtained [5].

3. Interferometry—These methods are based upon the interference of two rays of light. The interference may be constructive or destructive and can be controlled to maximize or eliminate light intensity. By directing incident light normal to a crack surface in a transparent model, the distribution of crack-opening displacements across the model thickness has been measured [6].

4. Integrated methods—By applying moiré gratings to slices removed from a stress frozen body near the crack tip after photoelastic analysis, and annealing the slices, a moiré analysis of the resulting deformed grating will produce near-tip displacements and the photoelastic analysis produces near-tip stresses for each slice. This allows two estimates of the SIF [7]. Moreover, the order of the near-tip stress singularity can be obtained where cracks intersect a free surface [8].

In the sequel, the integrated frozen stress-moiré interferometric method of analysis will be briefly reviewed and results obtained by applying the method to three-dimensional cracked body problems will be discussed.

The Integrated Method

An integrated optical method which has evolved over a period of some 15 years consists of six separate steps. We now briefly consider the features and limitations associated with each step.

1. A model is constructed from suitable, transparent, stress free, stress freezing material. For complex shapes, this may necessitate casting the model in sections and then gluing the sections together. After the model parts are constructed, a starter crack is produced by striking a sharp round-tipped blade held normal to the surface at the desired crack location. Care must be exercised to keep cracks to be analyzed away from glue lines. The crack will emanate dynamically from the blade tip a short distance and arrest. In the sequel, we will study cracks produced in this way and also by machining. Artificial cracks of known front shape may be machined using a vee-tipped cutter with a cutter tip angle of less than 30° .

2. The second step involves "freezing in" the stress fringes and deformation fields in a servo-controlled stress freezing oven. The model material exhibits diphase behavior. That is, at room temperature both linear elastic and viscous response to mechanical load occurs. However, when loaded above a certain temperature (called the critical temperature) the viscous effect is suppressed and virtually pure linear elastic response results. Moreover, above critical temperature the material is some 25 times more sensitive to stress fringes than at room temperature and is two orders of magnitude less stiff than at room temperature. Thus, when the loaded model is cooled to room temperature, load removal will produce negligible recovery. In addition, the model may be sliced without altering the stress fringes or deformations produced above critical temperature, and the slices can be analyzed photoelastically. Before cooling, sufficient load is applied to grow the crack to its approximate desired size as observed through an oven port (the crack size is controlled by the load distribution and body geometry), and the load is then reduced to stop crack growth. The loading scheme is monotonic.

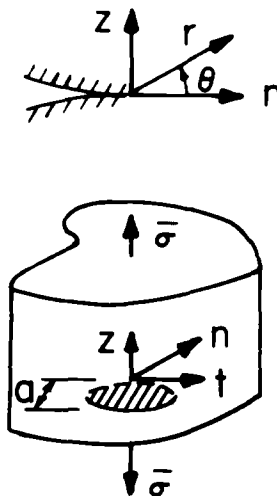


FIG. 1—General problem geometry and notation.

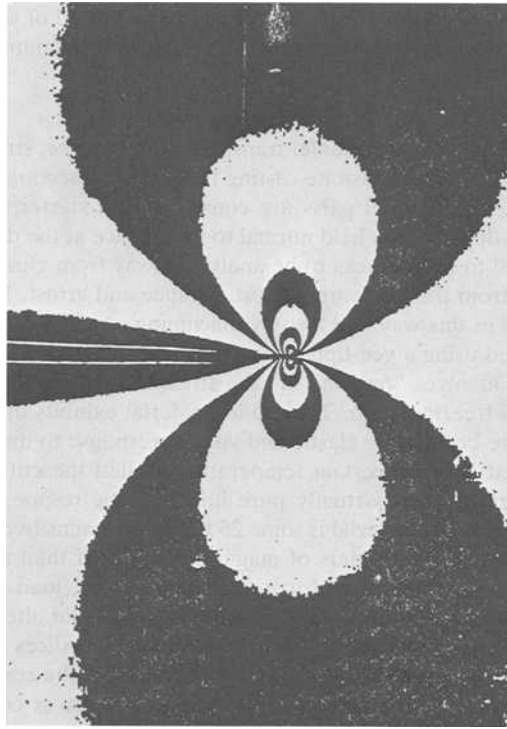


FIG. 2—Near-tip Mode I stress fringe pattern.

3. Thin slices of material are then removed, which are mutually orthogonal to the flaw border and the crack front (that is, parallel to the nz plane (Fig. 1)), and analyzed photoelastically. Only the region near the crack tip is analyzed (Fig. 2), and one order of magnitude magnification of the stress fringe pattern is employed, together with fractional fringe order measuring techniques. Due to the need to maintain small loads to control deformations above the critical temperature, the photoelastic analysis involves an optical system which permits the use of both partial mirror fringe multiplication [9] and the Tardy method [10]. The system is shown schematically in Fig. 3 and consists of a Model 051 photolastic polariscope fitted with a set of partial mirrors and a laser light source. The polariscope has a scale for measuring the rotation of the polarizer and the upper part of the system allows selection of the desired fringe multiple for viewing on a screen. Using a 10-mW Helium-Neon laser, multiple orders up to 17 have been obtained. Data are then digitized and entered into an algorithm for converting photoelastic data into "apparent" fracture parameter values. Then, using a least squares program in a microcomputer, an estimate of K_I for each slice is obtained. Normally, an algorithm based upon the near-tip LEFM stresses, which vary as the inverse square root of distance from the crack tip, is used and allows extraction of stress-intensity factor values for each slice. However, when a crack border intersects a free surface at right angles, the inverse square root order in the stress singularity is lost, and this effect may be significant in nearly incompressible materials and requires a different form of algorithm. Algorithms will be discussed in the sequel.

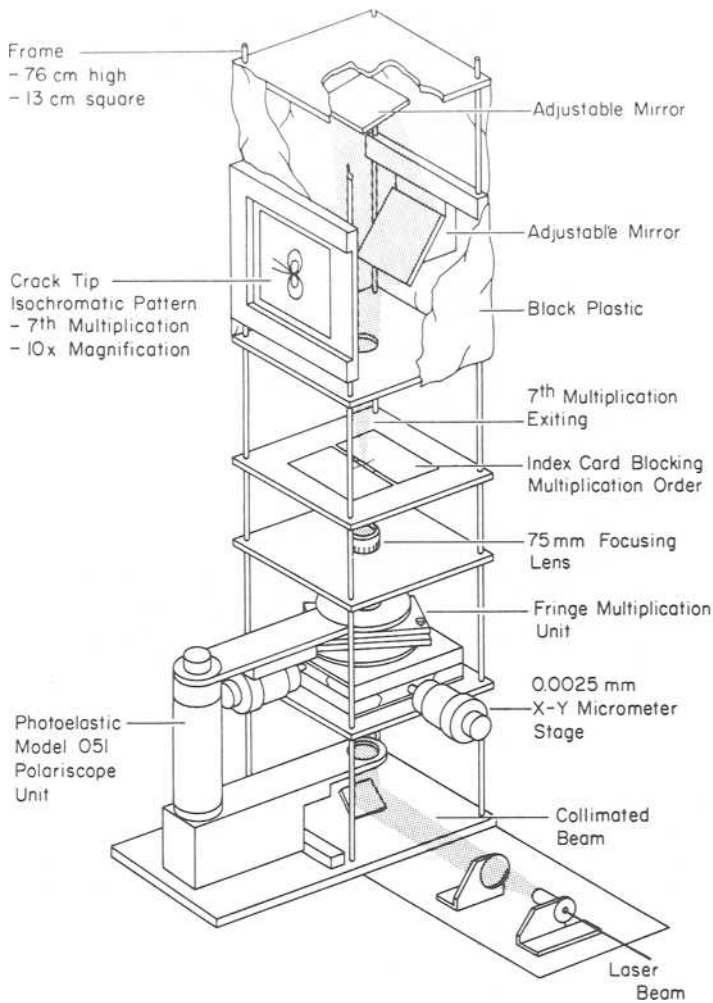
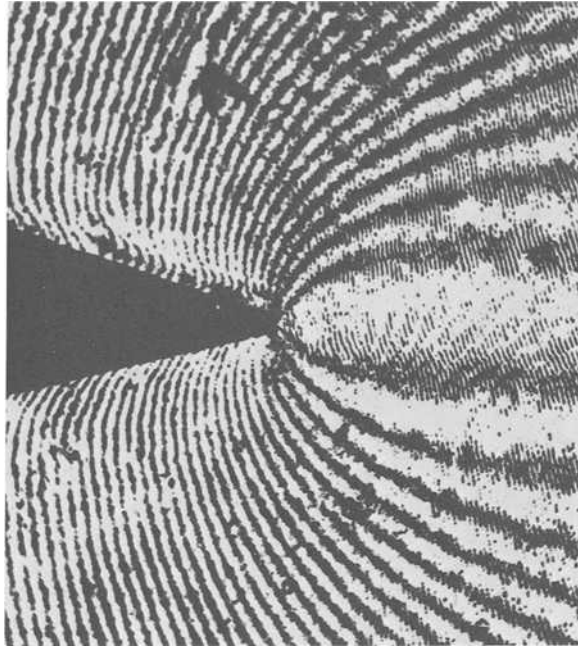



FIG. 3—Modified polariscope for determination of fractional fringe orders.

4. Silicone phase gratings are then applied to the thin, stress frozen slices. The effective frequency of these phase gratings is 1200 lines/mm. The grating replication process is described in Ref 17.

5. Slices are then annealed with the goal of reversing the deformation field that was frozen in. That is, the slices are to be returned to their undeformed state. However, this will deform the grating. By observing the deformed grating through an undeformed “virtual” grating (formed by splitting a laser and recombining its components to form walls of constructive and destructive interference) moiré fringes proportional to the in-plane displacement component normal to the crack plane (U_z in Fig. 1) are obtained (Fig. 4).

6. Displacement data must be converted into appropriate fracture parameters through a suitable algorithm.




 FIG. 4—Near-tip moiré pattern for U_z .

Algorithms

In the interest of brevity, we shall limit the present discussion to Mode I algorithms, Mode I, in fact, is the preferred mode for growing cracks under steady-state conditions [12].

In linear elastic fracture mechanics (LEFM) using the photoelastic approach, one can begin with Mode I near-tip equations (Fig. 1)

$$\sigma_{ij} = \frac{K_I}{(2\pi r)^{1/2}} f_{ij}(\theta) + \sigma_{ij}^o \quad (i, j = n, z) \quad (1)$$

where K_I is the Mode I SIF, σ_{ij}^o are the contribution of the nonsingular stresses in the measurement zone, and r, θ then are centered on the crack tip. The following expression is computed, in truncated form, along $\theta = \pi/2$.

$$\tau_{\max} = \frac{K_{Ap}}{(8\pi r)^{1/2}} = \frac{K_I}{(8\pi r)^{1/2}} + f(\sigma_{ij}^o) \quad (2)$$

where K_{Ap} is an "apparent" SIF which includes the effect of σ_{ij}^o with the singular effect in the measurement zone. By rearranging terms in Eq 2 and normalizing, we can obtain

$$\frac{K_{Ap}}{\bar{\sigma}(\pi a)^{1/2}} = \frac{K_I}{\bar{\sigma}(\pi a)^{1/2}} + \frac{(8\pi)^{1/2}}{\bar{\sigma}} f(\sigma_{ij}^o) \left(\frac{r}{a}\right)^{1/2} \quad (3)$$

where $f(\sigma_{ij}^o)$ is a constant, $\bar{\sigma}$ is the remote normal stress, and a is the crack size.

Equation 3 suggests that the normalized K_{Ap} varies linearly with the square root of the normalized distance from the crack tip $\{(r/a)^{1/2}\}$ in the singularity dominated zone.

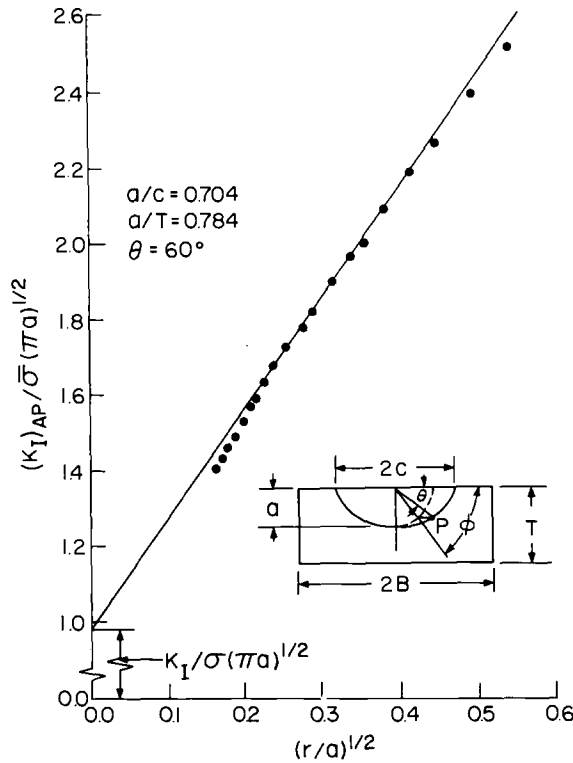


FIG. 5—Determination of normalized K_I from a slide from a stress frozen body.

Thus, by plotting the digitized raw data, $[K_{Ap}/\bar{\sigma}(\pi a)^{1/2}]$ versus $[(r/a)^{1/2}]$, the linear zone may be found. Then using a least squares fit, the line representing these data can be constructed and extrapolated across a near-tip nonlinear zone to determine the normalized $K_I[K_I/\bar{\sigma}(\pi a)^{1/2}]$ at the crack tip.

Figure 5 illustrates such a procedure for a stress frozen slice removed from a surface flaw in a flat plate under Mode I loading.

When using moiré interferometry with LEFM, the fringes are proportional to in-plane displacement and we choose to obtain U_z values (Fig. 1) from a horizontal grating (that is, parallel to the crack plane). Since we are concerned with near-tip data, we use the plane strain form of the equations for U_i whence, for $\theta = \pi/2$

$$K_{Ap} = \frac{CU_z}{r^{1/2}} \quad (4)$$

where C depends upon the elastic constants of the material [13]. Noting the similarity between Eqs 2 and 4, we can obtain K_I from moiré data by plotting the normalized K_{Ap} versus $(r/a)^{1/2}$ as before. Since, in practice, the moiré data are generated from the same stress frozen slices, from which K_I has already been determined, by annealing the slice after grating deposition, we can compare the two estimates for K_I ; such a comparison is shown in Fig. 6 for a slice from a compact bending specimen. Note that the elastic-linear zone (ELZ) from moiré data is somewhat further from the crack tip than the frozen stress ELZ. This is believed to be due to the fact that the anneal is not completely reversible at the crack tip. However, the differences in the values of K_I do not appear large. In fact, Fig. 6

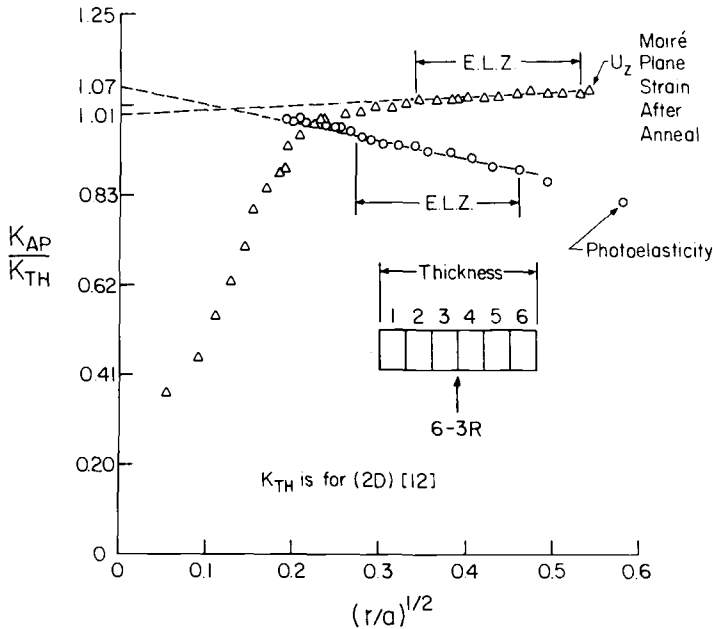


FIG. 6—Determination of normalized K_I from an annealed stress frozen slice (see also Ref 13).

shows the largest difference which we have encountered to date. We note that, while the comparisons are for the same slice, which has a thickness of about 0.5 mm, the photoelastic data are thickness averaged over the slice, but the moiré data are not. Thus, the compared data are for planes about 0.25 mm apart.

In 1977, Benthem [14] proved analytically that, when a crack intersects a free surface at right angles, the inverse square root singularity in the stresses is lost. Originally, this effect was believed to be more academic than practical, and its effect was expected to be measurable only in nearly incompressible materials. However, because of the ascending importance of such materials as rubber, plastics, and rocket propellants, a practical interest in this effect has developed. Several years ago, the author and his colleagues began to study this phenomenon [13] using the optical methods described above. In this study, it was necessary to introduce different algorithms to allow the exponent of r in the near-tip stress and displacement field equations to be unknown. Following the approach used by Benthem, the displacement algorithm along $\theta = \pi/2$ was taken as

$$U_z = Dr^{\lambda_u} \quad (5)$$

where λ_u represents the lowest eigenvalue in an eigenfunction expansion for U_z .

This leads to

$$\log U_z = \log D + \lambda_u \log r \quad (6)$$

and suggests that λ_u can be obtained from the slope of the log-log plot of U_z versus r .

For stresses, by introducing a quasi-two-dimensional stress function to represent the thick-

ness averaged stress field in a slice, we may obtain, after truncation, the approximate expression [8]

$$\tau_{\max}^{nz} = \frac{(K_\lambda)_{Ap}}{(8\pi r)^{\lambda_\sigma}} = \frac{K_\lambda f(\lambda_\sigma)}{(8\pi r)^{\lambda_\sigma}} + \tau_o \quad (7)$$

where K_λ is a stress eigenfactor (but not a SIF), λ_σ is the lowest order eigenvalue in an expansion of the stresses, and τ_o represents the approximate contribution of the nonsingular stresses in the measurement zone. Equation 6 leads to

$$\log(\tau_{\max}^{nz} - \tau_o) = \log K_\lambda f(\lambda_\sigma) - \lambda_\sigma \log(8\pi r) \quad (8)$$

so that if τ_o is known, λ_σ can be found as was done for λ_u . Also, $\lambda_\sigma = 1 - \lambda_u$.

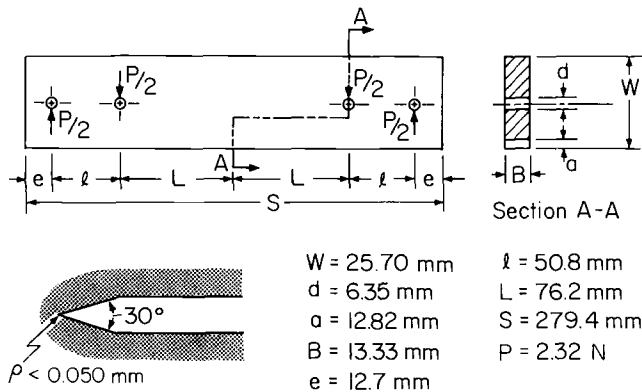
Experimental Results: A Summary

The writer and his colleagues conducted a series of experiments on compact bending specimens containing straight-front artificial cracks which intersected the specimen sides at right angles. The specimens were made from a commercially available stress freezing photoelastic material, PSM-9, with a modified hardener content. Specimen geometry is shown in Fig. 7.

The first tests were both room temperature and critical temperature tests using moiré gratings on the beam outer surface to obtain data for comparison with Benthem's results. A typical set of moiré data from the frozen stress test is shown in Fig. 8 and the results are summarized in Table 1 and compared with the results of Benthem's analysis.

It was concluded that the moiré method measured surface values quite accurately.

We then turned to an evaluation of the values of λ_u (and λ_σ) along the flaw border through the beam thickness in order to determine if a boundary layer effect was present. Most analyses require that there be no such effect. However, in our experiments, which involved the tandem application of photoelasticity and moiré interferometry, we obtained results



(drawing not to scale)

FIG. 7—Compact bending specimen geometry.

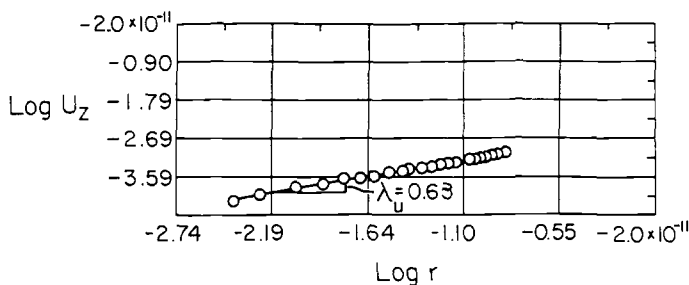


FIG. 8—Determination of λ_u from moiré data from free surface of compact bending specimen.

shown in Fig. 9. These results show a slight offset between moiré and photoelastic values of λ_σ , but the difference is not large enough to affect the observation of a definite transition zone during which λ varies from the surface value predicted by Benthem [14] (Table 1) to a value of nearly one half in the central region of the beam.

Interpretation of Results

Since most near-tip measurements on cracked bodies are made on or near free surfaces where cracks intersect them, one is led to inquire as to how results such as those obtained above should be interpreted. With LEFM firmly established within the fracture mechanics community, it would not seem inappropriate to attempt to interpret such data from high Poisson's ratio materials within the framework of LEFM. In order to achieve this, we note that, in photoelastic work, the stress fringes are proportional to the maximum in-plane

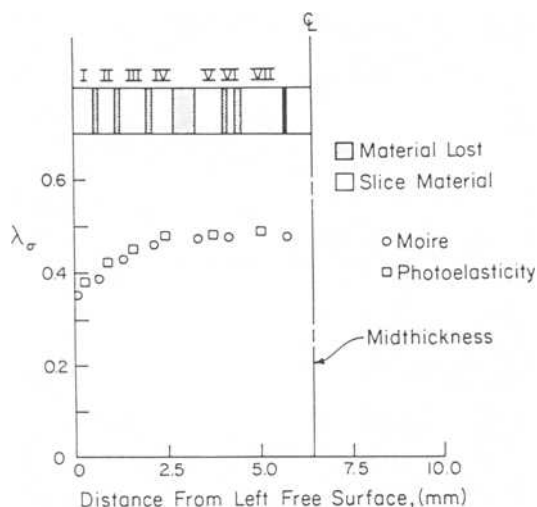


FIG. 9—Distribution of λ_σ along a straight-front crack across a compact bending specimen.

TABLE 1—Values of λ_u .

Poisson's Ratio, ν	Bentham's Analysis	Experiment
0.30	0.55	...
0.40	0.59	0.58
0.48	...	0.63
0.50	0.67	...

shearing stress, which we may then regard as the measured quantity. Then, from Eqs 2 and 7, respectively, we write

$$\tau_{\max}^{nz} = \frac{(K_{\text{cor}})_{\text{Ap}}}{r^{1/2}} = \frac{(K_\lambda)_{\text{Ap}}}{r^{\lambda_\sigma}} \quad (9)$$

or

$$(K_{\text{cor}})_{\text{Ap}} = (K_\lambda)_{\text{Ap}} r^{1/2 - \lambda_\sigma} \quad (10)$$

where K_{cor} is the SIF which corresponds to the same τ_{\max}^{nz} as the $(K_\lambda)_{\text{Ap}}$ does. Thus, we can compute $(K_{\text{cor}})_{\text{Ap}}$ values from Eq 9 and, by plotting the $(K_{\text{cor}})_{\text{Ap}}$ values versus $r^{1/2}$, a value of K_{cor} can be obtained for use in place of K_I . Such a plot from a stress frozen slice from a compact bending specimen is shown in Fig. 10.

Figure 11 shows a comparison between K_I and K_{cor} distributions for the compact bending

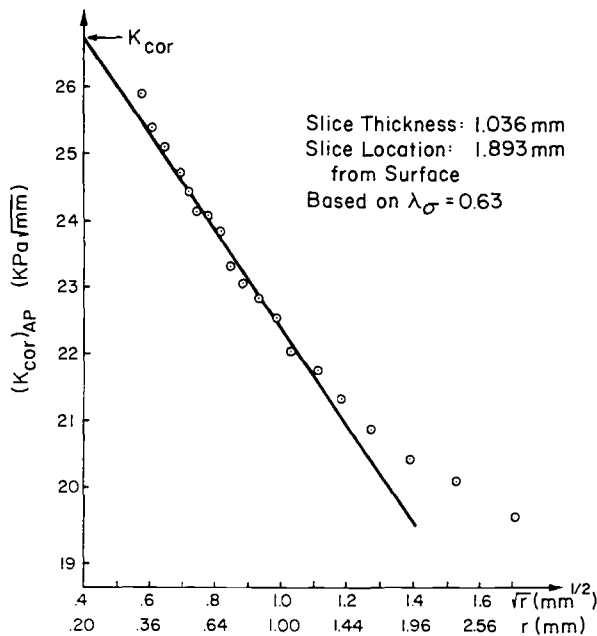


FIG. 10—Determination of K_{cor} from $(K_{\text{cor}})_{\text{Ap}}$ for a frozen slide.

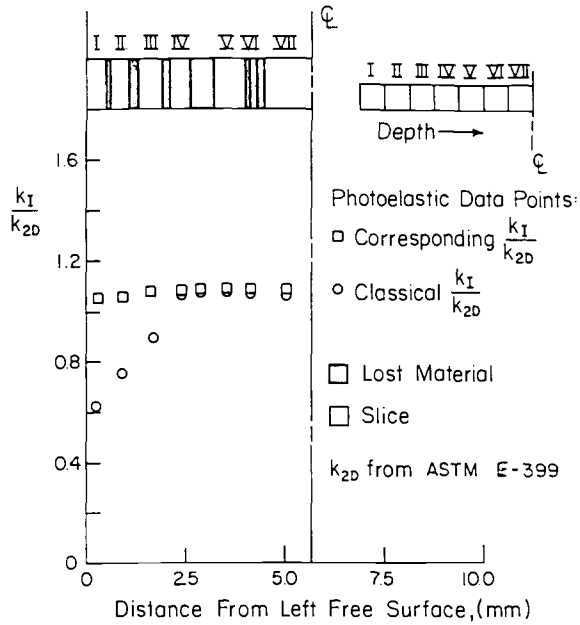


FIG. 11— K_I and K_{cor} distributions for a straight-front crack in a compact bending specimen.

problem and Fig. 12 shows similar results for the more practical geometry of a surface flaw in a finite-thickness plate. Both figures indicate the presence of a transition zone denoted by the divergence in K_{cor} and K_I over which λ_a varies from about 0.33 to 0.50. If such preliminary results are confirmed with further studies, it would seem that K_{cor} would provide a reasonable interpretation within the context of LEFM for the free-surface effect described herein.

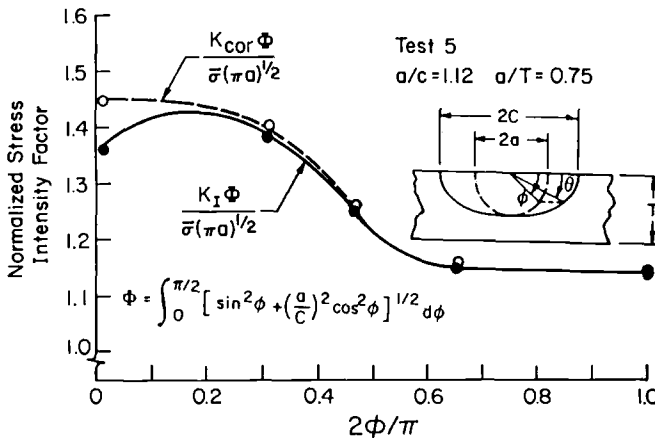


FIG. 12— K_I and K_{cor} distributions around the half-length of a surface flaw border.

Future Measurement Challenges

The present discussion has dealt with what is normally regarded as elastic or small-scale yield behavior. Measurement challenges which lie ahead in three-dimensional fracture include elastic-plastic and dynamic conditions, as well as complex elastic problems. Excellent discourses on such problems are included in this conference. In the former case, unloaded plastically deformed cracked metal specimens have been sliced metallographically normal to the crack border and the plastic crack-tip opening displacement (CTOD) distribution has been measured. The elastic CTOD from three-dimensional finite-element codes has then been added to obtain the total CTOD.² Such innovative techniques will yield further insight into three-dimensional effects in complex problems.

Acknowledgments

The author wishes to acknowledge the contributions of his colleagues, as noted by reference, and former students who contributed to this work. He is also most grateful to the National Science Foundation for support for this work under MEA 832-0252.

References

- [1] Annual Book of ASTM Standards, Vol. 03.01, Section 3, 1984.
- [2] Riedmüller, J., Sommer, E., and Kunzelmann, S., "Evaluation of Cracks in Nonhomogeneous Stress Fields," *Deutscher Verband für Materialprüfung e. v. sitzung des Arbeitskreises Bruchvorgänge*, Vol. 12, No. 10, Berlin, 1977.
- [3] Smith, C. W., "Use of Three-Dimensional Photoelasticity and Progress in Related Areas," *Experimental Techniques in Fracture Mechanics*, Monograph No. 2, Society for Experimental Stress Analysis, Iowa State University Press, Ames, IA, 1975, pp. 3-58.
- [4] Pindera, J. T. and Krasnowski, B. R., "Determination of Stress-Intensity Factors in Thin and Thick Plates Using Isodyne Photoelasticity," *Fracture Problems and Solutions in the Energy Industry*, 1981, pp. 147-156.
- [5] Desailly, R. and Lagarde, A., "Surface Crack Analysis by an Optical Slicing Method of Three-Dimensional Photoelasticity," (in French), *Proceedings, Seventh International Conference on Experimental Stress Analysis*, Cannes, France, August 1982, pp. 315-329.
- [6] Weidmann, G. W. and Doll, W., "Some Results of Optical Interference Measurements of Critical Displacements at the Crack Tip," *International Journal of Fracture*, Vol. 14, 1978, pp. R189-R193.
- [7] Smith, C. W., Post, D., and Epstein, J. S., "Measurement of Stress and Displacement Fields Near Crack Tips by Optical Methods," *Proceedings, 40th Anniversary Meeting of the Society for Experimental Stress Analysis*, Cleveland, OH, May 1983, pp. 1-6.
- [8] Smith, C. W. and Epstein, J. S., "Measurement of Three-Dimensional Effects in Cracked Bodies," *Proceedings, Fifth International Congress on Experimental Mechanics*, Montreal, Canada, May 1984, pp. 102-110.
- [9] Post, D., "Isochromatic Fringe Sharpening and Fringe Multiplication in Photoelasticity," *Proceedings of the Society for Experimental Stress Analysis*, Vol. 12, No. 2, 1955, pp. 143-156.
- [10] Tardy, M. H. L., "Methode Pratique D'examen de Mesure de la Birefringence des Verres d'Optique," *Optics Review*, Vol. 8, 1929, pp. 59-69.
- [11] Post, D., Czarnek, R., and Smith, C. W., "Patterns of U and V Displacements Around Cracks in Aluminum by Moiré Interferometry," *Proceedings, International Conference on Application of Fracture Mechanics to Materials & Structures*, G. C. Sih, E. Sommer, and W. Dahl, Eds., Martinus-Nijhoff Publishers, Amsterdam, 1984, pp. 699-708.

² Epstein, J. S. and Reuter, W. G., Idaho National Engineering Laboratory, personal communication, June 1985.

- [12] Smith, C. W. and Wiersma, S. J., "Stress Fringe Signatures for Propagating Cracks," *Journal of Engineering Fracture Mechanics*, Vol. 23, No. 1, 1986, pp. 229–236.
- [13] Smith, C. W., Post, D., and Epstein, J. S., "Measurement of Stress and Displacement Fields Near Crack Tips by Optical Methods," *Proceedings, 40th Anniversary Meeting of the Society for Experimental Stress Analysis*, Cleveland, OH, May 1983, pp. 1–6.
- [14] Benthem, J. P., "State of Stress at the Vertex of a Quarter-Infinite Crack in a Half-Space," *International Journal of Solids & Structures*, Vol. 13, 1977, pp. 479–492.

Three-Dimensional Elastic Surface Cracks

REFERENCE: Cruse, T. A., "Three-Dimensional Elastic Surface Cracks," *Fracture Mechanics: Nineteenth Symposium, ASTM STP 969*, T. A. Cruse, Ed., American Society for Testing and Materials, Philadelphia, 1988, pp. 19-42.

ABSTRACT: This paper discusses a variety of issues associated with the elastic fracture mechanics modeling of surface cracks; both analytical and experimental issues are addressed. The primary analytical focus is on the use of the boundary integral equation method for elastic fracture mechanics analysis. An advanced code is highlighted. A new formulation for three-dimensional crack-surface integral equations is presented with some new analytical results associated with the free-surface singularity. Essential agreements with the results of Benthem are obtained. Fatigue crack growth results for surface cracks in tension and bending are compared with analytical solutions. It is shown that surface cracks in tension grow essentially in accord with an elastic fracture mechanics prediction, whereas surface cracks in bending do not conform to the elastic prediction, based on surface values of the elastic stress-intensity factor. Some thoughts for further research are given.

KEY WORDS: analytical methods, computational fracture mechanics methods, elastic fracture mechanics, fatigue, life prediction, stress analysis, surface cracks, fracture mechanics

The purpose of the current paper is to review some of the computational and modeling issues associated with elastic fracture mechanics for surface cracks. The importance of the elastic problem is illustrated in Fig. 1, which shows a gas turbine disk that failed due to the growth of a surface crack from a machining defect. The problem is strictly controlled by elastic fracture mechanics. The fatigue crack growth simulation requires an estimate of the crack front behavior and some algorithm for integrating the crack size and aspect ratio as a function of load history and material properties.

The elastic fracture mechanics analysis problem for surface cracks is generally based on three-dimensional models for the stress-intensity factor distribution. Important variables include crack front curvature, local stress gradients, and, as will be shown in some detail, the nature of the crack near the material free surface. The crack growth algorithm must take these factors into account and must, in addition, account directly for the interaction of the stress-intensity factor distribution along the crack front and the crack shape changes during fatigue.

The paper is broken into two major sections. The first is concerned with efficient and accurate modeling of three-dimensional fracture mechanics problems. The principal tool favored by this author is the advanced boundary integral equation (BIE) method, sometimes referred to in a generic way as a boundary element method. Some new results obtained on an advanced three-dimensional BIE code will be compared with accepted finite-element methods (FEM) results. The primary issues will be efficiency in engineering modeling and accuracy of the solutions.

¹ Director, Department of Engineering Mechanics, Southwest Research Institute, 6220 Culebra Road, San Antonio, TX 78284.



FIG. 1—*Surface crack growing in a rotor part.*

A new, and potentially very powerful, BIE-based method for three-dimensional cracks will be reported. The method offers the opportunity to model cracks in an even more efficient manner than the current BIE method. It will form the basis of a general alternating-traction algorithm for future fracture mechanics analysis.

The second major section of the paper is concerned with the issue of modeling actual three-dimensional surface cracks. Data for two problems of surface cracks grown in fatigue will be compared to both BIE and FEM stress-intensity factor estimates. The essential feature of the tension fatigue problem is that the aspect ratio of the crack does not change markedly during fatigue growth. The second problem concerns a surface crack grown in four-point bending. In this problem the surface crack aspect ratio is a dominant variable.

Fatigue crack growth simulation for surface cracks has been portrayed by some as a closed subject. The surface crack stress-intensity factor distribution near the free surface is said by others to be known. It is hoped that the current paper will shed useful light on what is and is not known about these problems. Fatigue crack growth modeling will be shown to offer continuing challenges in terms of modeling efficiency and accuracy, as well as in the development of a realistic algorithm for surface crack growth behavior near the free surface.

Elastic Fracture Mechanics Results

Computational Modeling with the Three-Dimensional BIE Method

Figure 2 illustrates a BIE model being developed for a welded T-joint. The crack location defines a nonsymmetric geometry to be analyzed. Southwest Research Institute (SwRI) has developed a general three-dimensional BIE fracture mechanics tool based on a National Aeronautics and Space Administration (NASA) code [1]. The principal features of the modeling approach are illustrated by this example. The body is broken into subregions for modeling accuracy and efficiency [2] with a surface containing the crack itself. This modeling approach, based on multiregion modeling [3], avoids the ill-conditioning that besets direct BIE modeling of the entire geometry, with two coplanar crack surfaces [4]. The subregion approach results in improved accuracy for each subregion as well as improved matrix reduction time.

The basis of the BIE methodology is reviewed elsewhere [5–8] and will not be repeated herein. The principal feature of the fracture mechanics capability with BIE is to use a singular traction formulation for the nodes at the crack tip. This is achieved through a reprogramming of the standard eight-noded isoparametric interpolation functions for the boundary data.

The usual interpolation scheme for boundary data is to express the boundary tractions (t) and displacements (u) in terms of the finite-element method shape functions M^α , as

$$t_j(x) = M^\alpha(\xi, \eta) t_j^\alpha \quad (1a)$$

$$u_j(x) = M^\alpha(\xi, \eta) u_j^\alpha \quad (1b)$$

where t_j^α , u_j^α are nodal values. The nodal coordinates (x) are given by the same relationship. It is well established [9] that by placing the midside node for the row of boundary elements adjacent to and behind the crack at the geometric quarter point, the crack-opening displacements over that element are nearly uniformly defined by an asymptotic $\sqrt{\delta}$ (δ = distance from the crack front) behavior. If, now, the elements ahead of the crack have the shape functions modified to the form

$$t_j(x) = M^\alpha(\xi, \eta) \sqrt{\left(\frac{L}{\delta}\right)} \hat{t}_j^\alpha \quad (2)$$

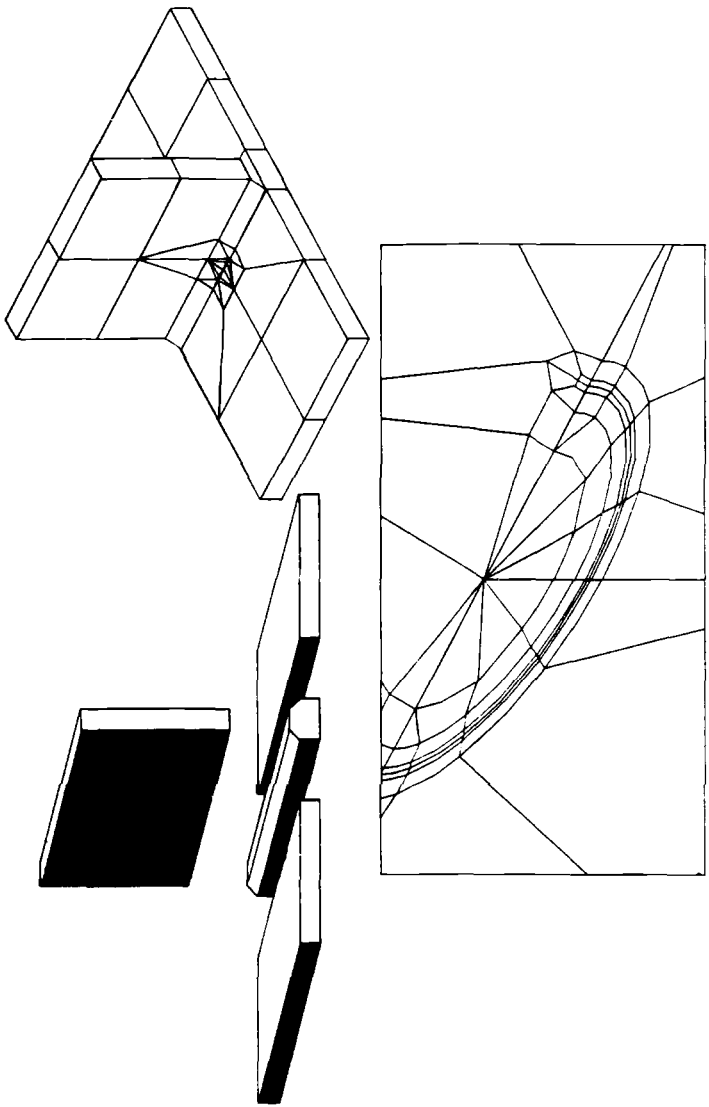


FIG. 2—A surface crack BIE model for a simulated, welded T-joint showing subregions, the overall model, and a crack-front model.

for a constant element depth of L , then the proper crack-tip traction singularity is achieved for the same quarter-point modeling. The term t_i^a is a generalized crack-front stress-intensity factor. Further, the tractions on the first element have the necessary singular, constant, and $\sqrt{\delta}$ terms that describe the continuum field in the vicinity ahead of the crack.

The advanced BIE code [called the boundary element solution technique for cracks (BEST/CRX)] directly models the traction singularity and computes the estimated stress-intensity factor from both the crack-opening displacements at the quarter point and from the modified traction variable at the actual crack tip. The second of these is used throughout the current discussion, even though both give nearly the same result.

Figure 3 shows a test problem of a buried internal circular crack subject to remote tension. The model uses 73 elements and 208 nodes; 2 h of Vax 11/780 time were required. The BIE model makes use of the geometric symmetry of the plane $X = 0$. The crack-front stress-intensity factor was computed for this mesh to be within 1% of the published results.

Figure 4 shows a center-cracked tension specimen analyzed using special three-dimensional finite-element procedures by Raju and Newman [10]. The BIE mesh for one-fourth of the geometry is shown in Fig. 5. The stress-intensity factor distribution for the BIE and FEM results are shown in Fig. 6. The BIE results are plotted with and without the traction singularity (Eq 2). The BIE (with traction singularity) and FEM results are virtually indistinguishable, except for minor differences in the free surface boundary layer. Unlike the results for the compact-tension specimen [7,11], the surface stress-intensity factor rises over the two-dimensional result before dropping at the free surface. It is judged that the modeling requirements for the mesh in Fig. 5 are a small fraction of those needed in Ref 10.

Figure 7 shows the BIE stress obtained for various values of z/a (thickness coordinate) as a function of distance from the crack tip. Unlike the much earlier BIE results [7], the current data clearly show that the square-root traction singularity is preserved up to distances

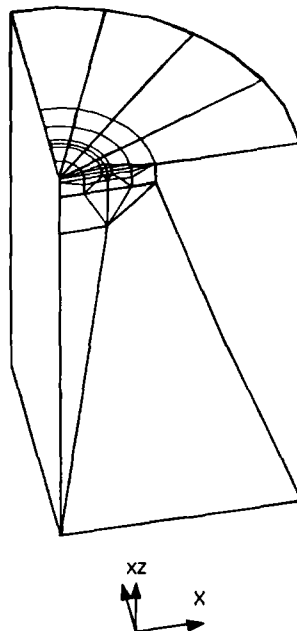
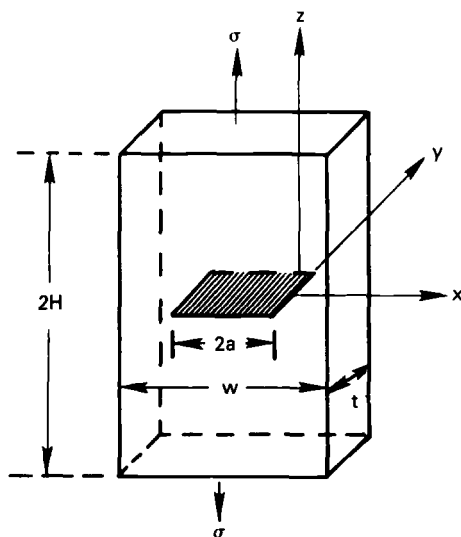


FIG. 3—Circular buried and surface crack validation model.



$$H/a = 1.75; 2a/w = 0.5$$

$$t/w = .75; \nu = 1/3$$

FIG. 4—Center-cracked test specimen.

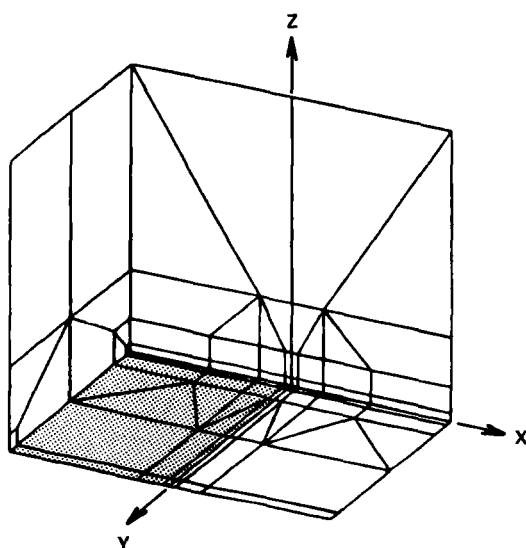


FIG. 5—BIE mesh used for the symmetric quarter of a center-cracked solid.

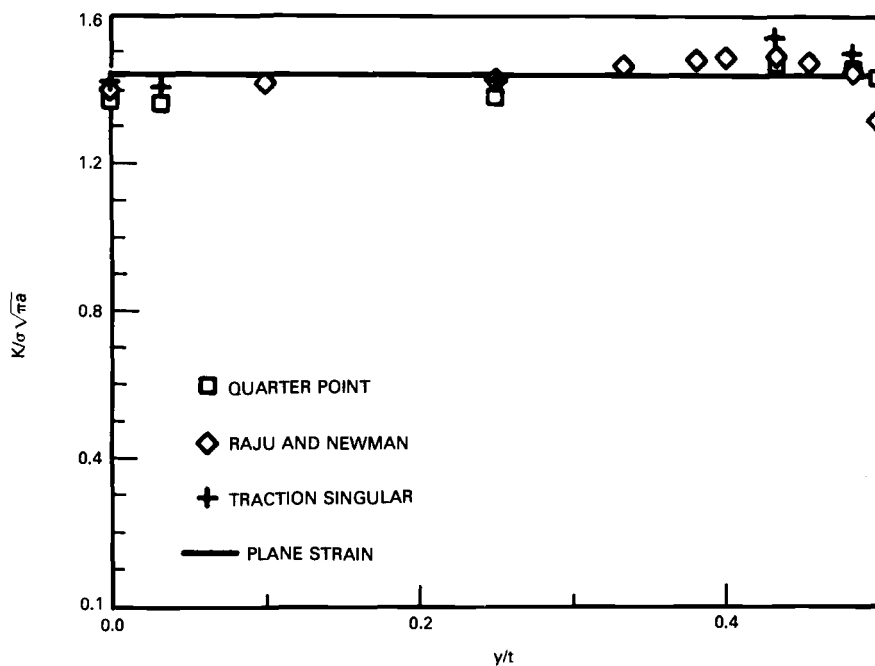


FIG. 6—Stress-intensity factor distribution through the thickness for a center-cracked solid.

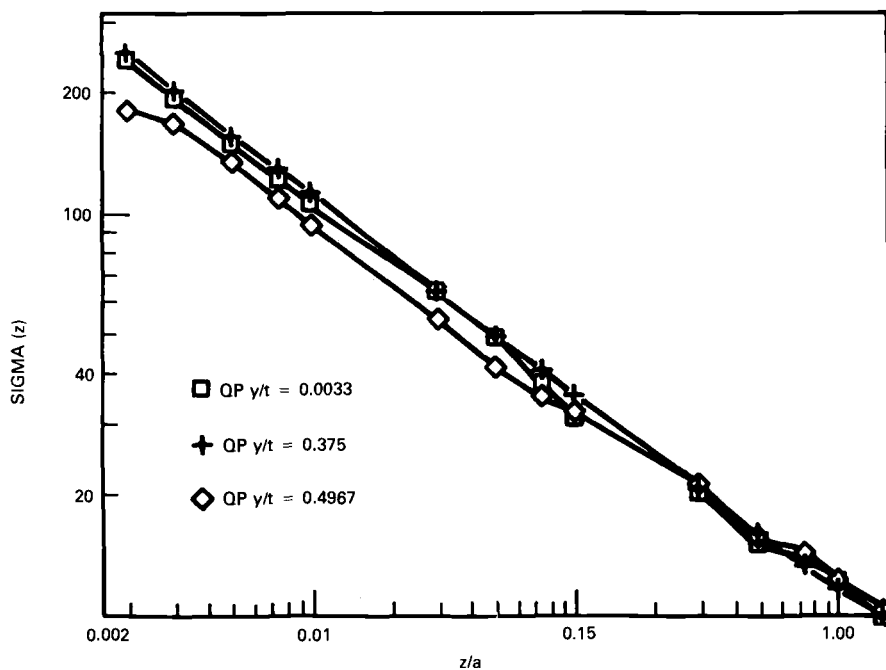


FIG. 7—Stresses near the crack tip at various thickness locations.

very close to the free surface. This is in conformity with the analytical model of Benthem [12], and will be discussed below in this report.

Figure 8 shows the crack surface mesh from Fig. 3. The actual element shapes are quadratic curves, while the computer-drawn mesh represents the higher order elements as being piecewise straight, between the nodes. Also shown in Fig. 8 are two crack-front perturbations—one with the actual crack outside the original circle, and one inside the original circle. The nodes in the row ahead of the crack front and behind it were perturbed by an equal amount, but are not shown for clarity.

The problem considers the effect of crack curvature change for equal "sized" surface cracks. Thus, crack length and depth are kept constant. Figure 9 shows the effect on K distribution of these perturbations. It is apparent that the local stress-intensity factor is strongly influenced by the local crack-front curvature. Thus, for the inner contour, the surface and buried location K values are depressed by the locally smaller curvature, and vice versa for the outer contour.

The implications of this simple study are clear for the elastic fracture mechanics model for fatigue growth of surface cracks. To use surface length and depth as the size variables, assuming an elliptical shape, will necessarily result in potentially important errors in local K estimates for real cracks. This will be shown in the discussions of fatigue crack growth data in this report.

The point to be made is that the proper shape of the crack is important in setting the stress-intensity factor near the free surface. The question is to determine how important this issue is for fatigue crack growth behavior.

Traction BIE

An additional, new BIE modeling procedure for three-dimensional cracks is briefly mentioned. The basis of the new method is the solution of the so-called traction BIE [4,14].

$$\sigma_{k3}(p) = \int_{\Gamma} U_{k\alpha}(p,Q) \Delta u_{i,\alpha}(Q) dS \quad (k,i = 1,2,3; \alpha = 1,2) \quad (3)$$

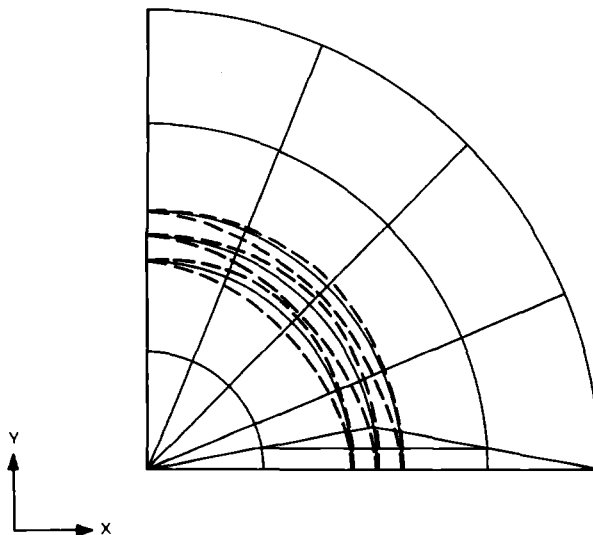


FIG. 8—Crack shape changes modeled by distorted BEM meshes.

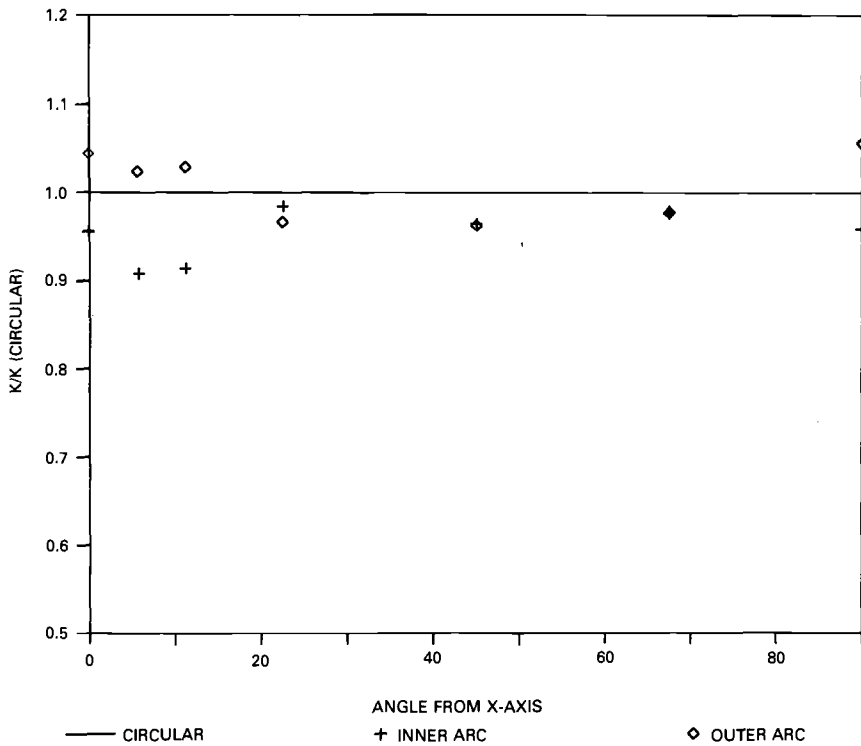


FIG. 9—Crack shape effect on normalized stress-intensity factors.

In Eq 3, the normal to the crack surface, Γ , is taken to be x_3 ; the x_1, x_2 coordinates are in the plane of the crack. The delta operator in Eq 3 refers to the relative displacement of the upper and lower crack surfaces. The kernel $U_{k\alpha}$ is derived from the standard BIE method [14,15]. The integral equation (for unknown displacement gradients) is to be solved by a numerical inversion of Eq 3 for a defined set of nodal tractions σ_{k3} .

The integral equation is strongly singular and is interpreted in the principal value sense. A variety of investigators [16–18] have used this dislocation solution method for modeling three-dimensional cracks, but the numerical results have not been completely satisfactory. All meshes used were uniform with no grading and, with the exception of Weaver [17], who solved only the rectangular crack problem, stress-intensity factor data are not developed.

The development of a solution algorithm for the integral equation (Eq 3) has not been easy, but has now been successfully achieved for graded crack meshes with excellent results for crack-tip stress-intensity factors. The details of the numerical implementation will be subsequently published [19].

Figure 10 shows the mesh used for a buried circular crack. Only the crack surface needs to be modeled to solve Eq 3. Figure 11 shows the numerical results for the validation problem of a uniform pressure load on the crack surface. One curve shows crack-opening displacements. The crack-front results are within 2% of the published value. The second result shows the pressure developed by substituting the exact displacement field into Eq 3. Some effect of mesh grading and the interpolation functions is still seen. Further development of numerical integration algorithms near the crack front is expected to bring the accuracy to within 1%.

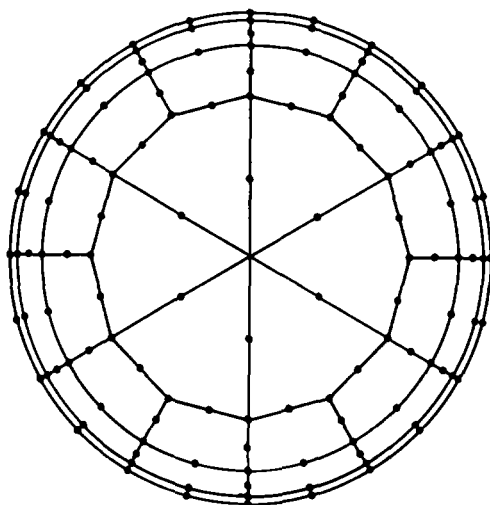


FIG. 10—Graded mesh used to validate the traction BIE solution for a buried crack.

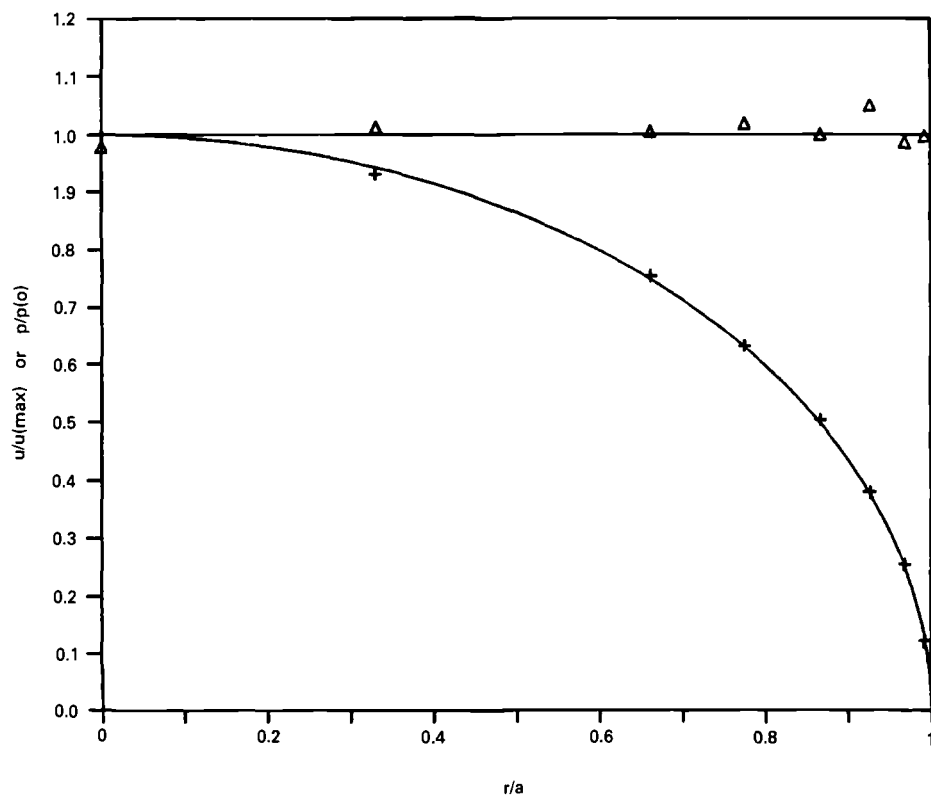


FIG. 11—Validation solution for the traction BIE.

The traction BIE fracture mechanics analysis method offers the potential to be used with an alternating stress method [20] and not be restricted to elliptical cracks as in Ref 20. Further, the integral equation can be extended to the case of cracks that are not flat. It is believed that this new algorithm offers the potential for very cost-effective and accurate three-dimensional fracture mechanics analysis in the future.

Surface Layer Stress Distribution

Considerable work has been devoted to the surface crack/free surface intersection stress singularity problem. The principal analytical work has been done by Benthem [12] and Folias [21]. In addition, Burton et al. [22] have contributed some important numerical results. The following discussion will focus on Benthem's analytical approach and conclusions.

Benthem assumed that the field equations for the surface intersection could be resolved into a form based on separation of variables, and that this form was mathematically complete. Based on his results, which represent a substantial piece of analytical work, the stress-based order of singularity is given by

$$\sigma \sim r^\lambda \quad (4)$$

where $\lambda = \lambda(\nu)$, ν = Poisson's ratio, and r is the polar distance from the free-surface intersection point as used by Benthem. The values for λ range from $-\frac{1}{2}$ for $\nu = 0$ to $-\frac{1}{3}$ for $\nu = 0.5$. In all cases, the stress singularity is weaker than the plane-strain result. Benthem [12] shows, however, that the stress in terms of crack-front distance preserves the square-root singularity of the plane-strain solution with a clear thickness-direction dependence of the stress-intensity factor.

The following is a report on some new analytical results for the stress behavior in the vicinity of the crack front/free surface intersection. The analytical results are based on the use of the BIE method for three-dimensional elastic behavior. The approach taken is to separate the solution into that part due to the crack and that part due to the free surface.

The interior stress state for the three-dimensional elastic problem is given for the crack problem by Refs 4 and 5 as

$$\sigma(p) = \int_s S u dS + \int_s D t dS + \int_\Gamma S \Delta u dS \quad (5)$$

where it is assumed that the crack surface (Γ) tractions are equal in magnitude and opposite in sense; thus only the relative crack-opening displacements (Δu) occur as crack surface variables. In Eq 5, S is the uncracked surface, Γ the crack surface, and $p(x)$ is the interior point where the stresses are to be computed.

The traction BIE formulation from Ref 4 forms the basis of a study of the three-dimensional crack-front stresses. Taking only the term for stress due to the crack itself, we obtain the result previously cited (Eq 3). The point $p(x)$ will be taken in the plane of the crack Γ , taken for now to be $x_3 = 0$, and a slight distance δ ahead of the crack front. Let x_2 be normal to the crack front, directed along the crack surface, and x_1 along the crack front. The relative crack-surface motions near the crack tip are represented asymptotically by

$$\Delta u_i = 2C_i(x_1)x_2^\lambda \quad (6)$$

where $C_i(x_1)$ is a smooth function and $\lambda > 0$.

The in-plane gradients of the relative crack surface motion are given by

$$\begin{aligned}\Delta u_{i,1} &= 2 \left(\frac{dC_i}{dx_1} \right) x_2^\lambda \\ \Delta u_{i,2} &= 2\lambda C_i(x_1) x_2^{\lambda-1}\end{aligned}\quad (7)$$

Let $p(x)$ be located at $(x_1, -\delta, 0)$ where δ is taken to be very small relative to the in-plane dimensions of the crack, and let $r(p, Q)$ be the Cartesian distance between $p(x)$ and the integration point. Then Eq 3 can be rewritten for the case of Mode I response and for $k = 3$ in the limit as $\delta \rightarrow 0$

$$\sigma_{33}(p) = \frac{\mu}{4\pi(1-\nu)} \int_{-\infty}^{\infty} d\left(\frac{x_1}{\delta}\right) \int_0^{\infty} \Delta u_{3,\alpha} \frac{r, \alpha}{\left(\frac{r}{\delta}\right)^2} d\left(\frac{x_2}{\delta}\right) \quad (8)$$

Now let $\xi = x_1/\delta$ and $\eta = x_2/\delta$ so that $(r/\delta)^2 = (1 + \eta)^2 + \xi^2$. It is easily established that the term for $\Delta u_{3,1}$ gives a zero result in Eq 8. Taking then the crack-opening term in Eq 7 with $r_{,1} = (1 + \eta)/(r/\delta)$ Eq 8 becomes

$$\sigma_{33}(p) = \frac{\mu\delta^{\lambda-1}}{4\pi(1-\nu)} \int_{-\infty}^{\infty} d\xi \int_0^{\infty} 2\lambda C_3 \eta^{\lambda-1} \frac{(1 + \eta)d\eta}{[(1 + \eta)^2 + \xi^2]^{3/2}} \quad (9)$$

In the local vicinity of δ , $C_3(\xi)$ is approximately constant so that the first integral can be evaluated

$$\sigma_{33}(p) = \frac{\mu\delta^{\lambda-1}}{4\pi(1-\nu)} (2\lambda C_3) 2 \int_0^{\infty} \frac{\eta^{\lambda-1} d\eta}{\eta + 1} \quad (10)$$

$$= \frac{\mu\lambda\delta^{\lambda-1}C_3}{1-\nu} \operatorname{cosec}[(1-\lambda)\pi] \quad (11)$$

It can be established separately, for σ_{33} to be finite and real on the crack surface, that $\lambda = 1/2$, with the result that

$$\sigma_{33}(p) = \frac{\mu}{1-\nu} \left(\frac{C_3}{2} \right) \frac{1}{\sqrt{\delta}} \quad (12)$$

In the case of the two-dimensional crack-opening displacement solution

$$C_3 = \frac{2(1-\nu)K_I}{\mu\sqrt{(2\pi)}} \quad (13)$$

From the use of Eq 13 in Eq 12, we obtain the crack-tip stress for the three-dimensional problem

$$\sigma_{33}(p) = \frac{K_I}{\sqrt{(2\pi\delta)}} \quad (14)$$

which, of course, is the same as the two-dimensional result.

Thus, it is apparent that for any interior point $p(x)$ the stress state ahead of the three-dimensional crack has a $1/\sqrt{\delta}$ singularity identical to the two-dimensional results. In fact, if the crack surface is only taken to be from zero to infinity (corresponding to $p(x)$ at the surface), then the result is still that for the two-dimensional case (Eq 14), except for a division by a factor of two. By inversion, finite crack surface stresses must lead to a square-root singular stress (strain) field ahead of the crack.

The second step is to consider the interior stresses at $p(x)$ due to removal of the two-dimensional crack-induced stresses on a surface normal to the crack front. There are two terms to be considered in the solution to Eq 4—the stresses on S due to the two-dimensional crack and the change in displacement on S as the plane-strain condition is relaxed to a stress-free state on S . Due to the BIE constraint equation for the problem on S , the singular stress terms for each of these surface variables will be the same, and we therefore only need to consider the traction loading integral in Eq 4.

The usual stress identity for an interior point $p(x)$ is given by two integrals: one of the boundary tractions t_k , and one of the boundary displacements u_k . Since both integrals will result in the same singular behavior, we shall carry only the first term and denote this as $\hat{\sigma}_{ij}(p)$

$$\frac{1}{\mu} \hat{\sigma}_{ij}(p) = \int_S \left\{ \frac{2\nu}{1-2\nu} \delta_{ij} U_{km,m} + U_{kj,i} + U_{ki,j} \right\} t_k dS \quad (15)$$

where $U_{ij}(p, Q)$ is the displacement solution to point loads at $p(x)$.

The first step in formulating the effect of the free surface on crack-tip singularity is to solve, in an asymptotic sense, Eq 15 as a half-plane subject to crack-induced traction loading. These tractions are taken to be the stress on a plane perpendicular to the crack front for the plane strain solution.

We will restrict our analysis to the case of Mode I loading. The coordinate directions relative to the crack front/free surface intersection are shown in Fig. 12.

$$\sigma_z = -\nu \cos \frac{\theta}{2} \frac{K_I}{\sqrt{(2\pi\delta)}} \quad (16)$$

where δ is the two-dimensional distance from the crack tip for the integration point (Q) and θ is the two-dimensional angle from the plane ahead of the crack.

Let $r(p, Q)$ be the distance between the interior stress evaluation point $p(x)$ and the surface integration point $Q(x)$. Also, let D be some radial distance on S from the origin that is sufficiently large to encompass the singular stress term in Eq 16. Then Eq 15 can be reduced to an integral, considering only the stress transverse to the crack:

$$\sigma_x(p) = \frac{\nu}{4\pi} \int_{-\pi}^{\pi} \int_0^D \left\{ \frac{\nu}{1-\nu} \nabla^2 r_{,33} - \frac{1}{1-\nu} r_{,311} \right\} \cos \frac{\theta}{2} \frac{K_I}{\sqrt{(2\pi\delta)}} \delta d\delta d\theta \quad (17)$$

while somewhat arduous, the θ integrations in Eq 17 can be evaluated in closed form, so that

$$\begin{aligned} \sigma_x(p) = \frac{\nu K_I}{4\pi(1-\nu)} \int_0^D \left\{ -\frac{2(1-2\nu)z}{[(\delta-\rho)^2+z^2]R} + \frac{2z\delta}{3\rho R} \frac{1}{[(\delta-\rho)^2+z^2]} \right. \\ \left. + \frac{z}{2\rho^2 R} \left(1 - \frac{R}{4\sqrt{(\delta\rho)}} \ln \left[\frac{R+2\sqrt{(\delta\rho)}}{R-2\sqrt{(\delta\rho)}} \right] \right) \right\} \sqrt{\delta} d\delta \quad (18) \end{aligned}$$

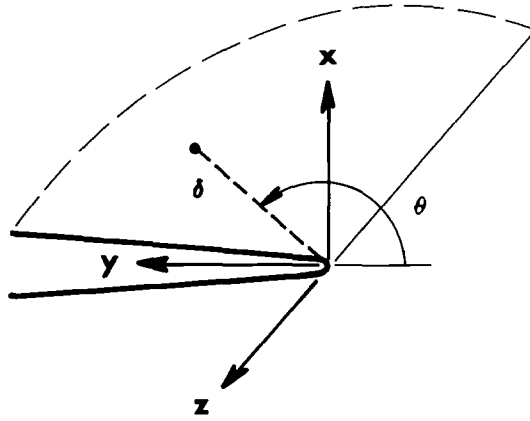


FIG. 12—Coordinates for a local crack-tip analysis.

where ρ is the two-dimensional distance from the crack tip for any $p(x)$ and $R^2 = (\delta + \rho)^2 + z^2$. The form in Eq 18 is based on $p(x)$ taken in the plane ahead of the crack. When $p(x)$ is on the virtual crack surface ($x = 0, y > 0$) the natural-log term becomes an arcsine function, but with the same asymptotic behavior as the natural log.

Equation 18 can be made nondimensional. Recognizing that some crack size parameter (L) is associated with the stress-intensity factor K_I , we take $\delta/L = \alpha$, $\rho/L = \beta$, $z/L = \gamma$

$$\sigma_x(p) \frac{\sqrt{L}}{K_I} = \frac{\nu}{4\pi(1-\nu)} \left(\frac{z}{\rho} \right) \int_0^{D/L} \left\{ -\frac{2(1-2\nu)\beta}{\zeta_1^2 \zeta_2} + \frac{2}{3} \frac{\alpha}{\zeta_1^2 \zeta_2} \right. \\ \left. - \frac{\gamma}{2\beta \zeta_2} \left(1 - \frac{\zeta_2}{4\sqrt{(\alpha\beta)}} \ln \left[\frac{\zeta_2 + 2\sqrt{(\alpha\beta)}}{\zeta_2 - 2\sqrt{(\alpha\beta)}} \right] \right) \right\} \sqrt{\alpha} d\alpha \quad (19)$$

where $\zeta_1^2 = (\alpha - \beta)^2 + \gamma^2$ and $\zeta_2^2 = (\alpha + \beta)^2 + \gamma^2$. If we now take $\rho/L \ll 1$, Eq 19 can be rewritten through expansion of the log term (up to three terms). The second and third terms in the integral can be found to cancel up to an order gamma term as follows

$$\sigma_{11}(p) \frac{\sqrt{L}}{K_I} = \frac{\nu\gamma}{4\pi(1-\nu)} \int_0^{D/L} \left\{ -\frac{2(1-2\nu)}{\zeta_1^2 \zeta_2} + \alpha 0(\gamma) \right\} \sqrt{\alpha} d\alpha \quad (20)$$

where $0(\gamma)$ is of the order of γ . It is seen that the singularity at $\rho = 0$, which shows in Eq 19, in fact cancels, leaving a regular state of stress in the half-space. The regular state of stress also exists on the actual plane of the crack; the arcsine function replaces the natural-log function for that case. It can be shown that Eq 19 goes to zero as $1/z^2$ for values of z that are large compared with D . For $\nu = 1/2$, the stress state is developed only from the $\alpha 0(\gamma)$ term in Eq 20, resulting in a stronger dependence on z .

For the case that $\rho \neq 0$, Eq 19 can be nondimensionalized in a manner that depends parametrically on z/ρ . This is directly related to one of the polar angles used by Benthem [13] emanating from the free-surface intersection point. In this form, Benthem's use of the polar coordinate decomposition is entirely supported by this analysis for the problem of freeing the tractions on the half-space.

The last step in the evaluation of the stress state, in the vicinity of the free surface, is to

have a stress-free crack surface. Since we have now established that the stresses due to the stress-free half plane are everywhere nonsingular, the solution of Eq 3 guarantees, as proven above, that the plane-strain singularity applies throughout the surface layer near the free-surface intersection point. The stress-intensity factor is obviously dependent on z . The numerical data presented show that the variation of $K_I(z)$ is quite problem specific, and not a general solution.

The Near Surface Issue

The computational data clearly show that the elastic stress-intensity factor distribution in the free surface layer is very problem specific and leaves some room for further definition. The proper question is whether or not such further definition adds anything to our ability to predict crack behavior. The next section reviews the fatigue crack growth problem in order to shed further light on the issue.

Fatigue Crack Growth Studies

Surface Crack in Tension

Figure 13 shows a surface crack fatigue specimen previously reported in Ref 23. The specimen is AMS4928 titanium with a nominal crack growth rate taken to be $da/dN = 1.43E-10(\Delta K)^{2.6}$, for ΔK in MPa \sqrt{m} and a in m . The crack was grown in simple tension with $\Delta S = 275.8$ MPa at a stress ratio of $R = 0.1$. As previously reported [23], the crack was heat tinted to define the crack depth and shape at various stages in its fatigue life. Figure 14 shows the contours that were established.

Figure 15 compares the experimentally determined value of the stress-intensity factor at the deep part of the crack front to that determined from the measured crack growth rate at the above-cited crack growth relationship. The comparison with stress-intensity factor estimates by the FEM results of Newman and Raju [13], as well as earlier BIE results of Cruse et al. [23], is excellent.

Figure 16 compares the same items but now for the surface length of the crack. The problem in comparison with surface length predictions is that the shape of the crack front near the free surface is quite unlike that of an ellipse. As noted in Ref 23, this particular crack experienced crack-front turn-back near the free surface. The titanium plate was found to have surface residual stresses that were judged in Ref 23 to probably be responsible for this effect. The best estimate of an ellipse to model the crack was taken to be one with a surface length 1.1 times that of the actual crack. This extended-length ellipse has about the right crack-front curvature, although it obviously overestimates the surface length.

Many correlations of surface crack growth [24–26] have been based on using the stress intensity some number of elliptical degrees below the free surface, a weighted stress-intensity factor, or a smoothed stress-intensity factor in order to best correlate the growth. The value of 15° has been used previously [23]; both 0° and 15° are shown in Fig. 16 for the Newman and Raju model. It is apparent that the above modeling approach correlates the surface crack growth rate during the early stages of crack growth, but not the later stages.

At this point, the only conclusion to be drawn is that the local crack shape and an understanding of free-surface residual stresses can be very important to the proper prediction of crack surface length growth, as shown in this figure. The answer to this issue is not currently available, but various interpretations have been discussed [13,24–26]. A further example of the issue is shown in the problem of surface crack growth in bending.

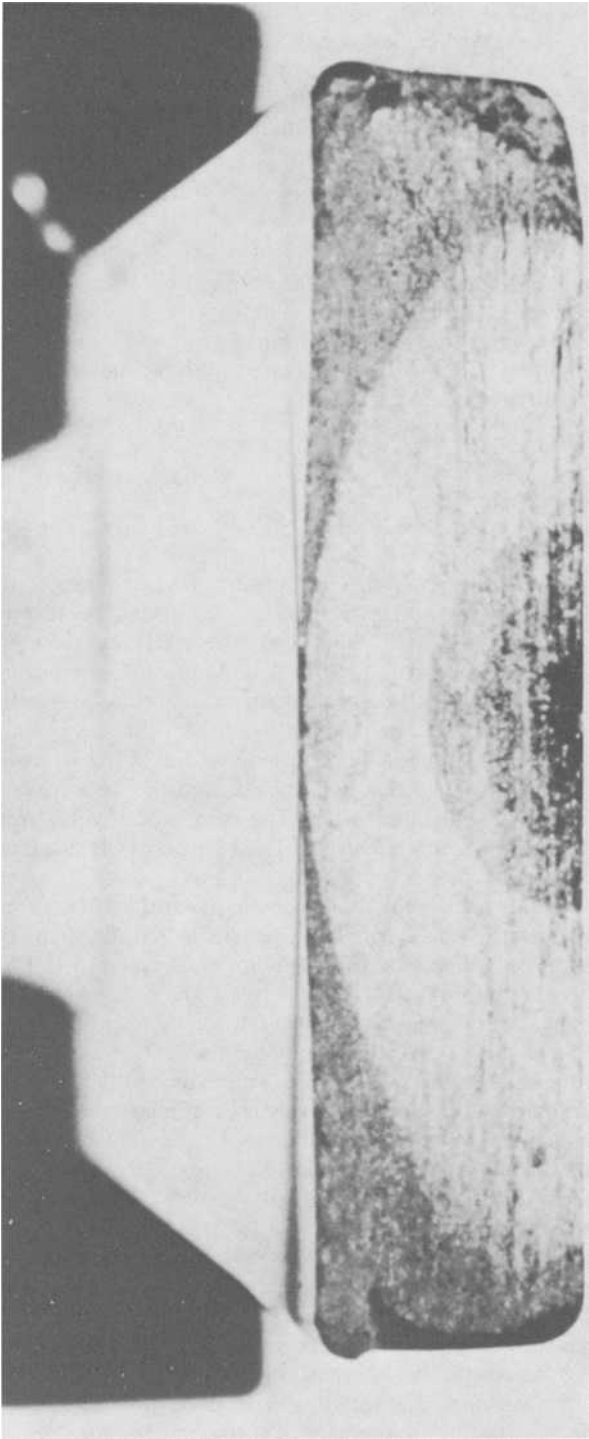


FIG. 13—Tension specimen with surface fatigue crack growth markings.

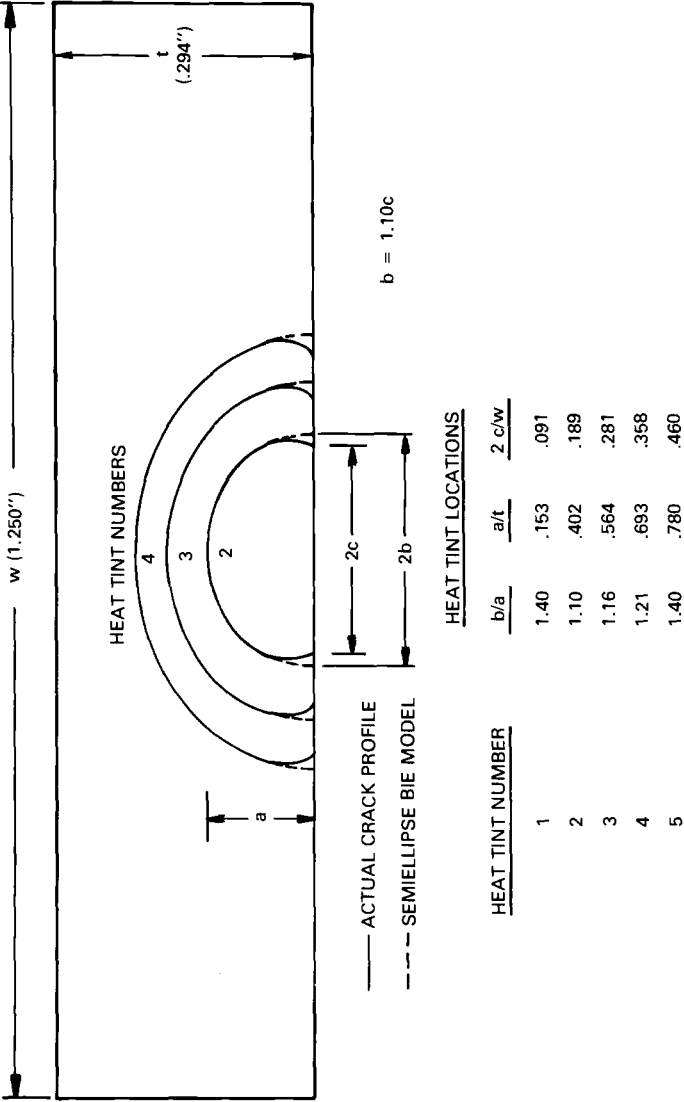


FIG. 14—Crack shapes determined for a tension specimen.

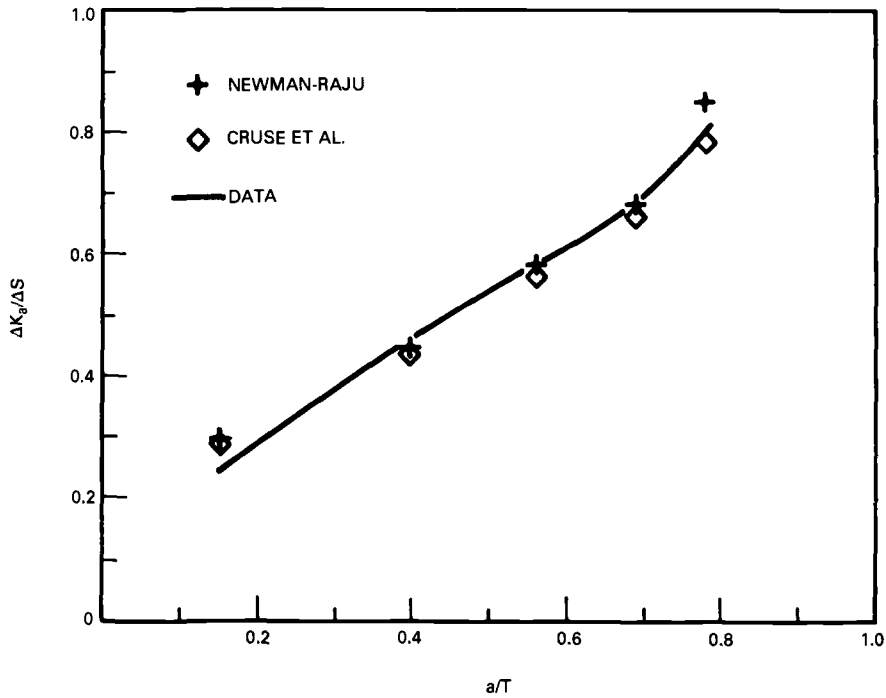


FIG. 15—Crack depth correlation.

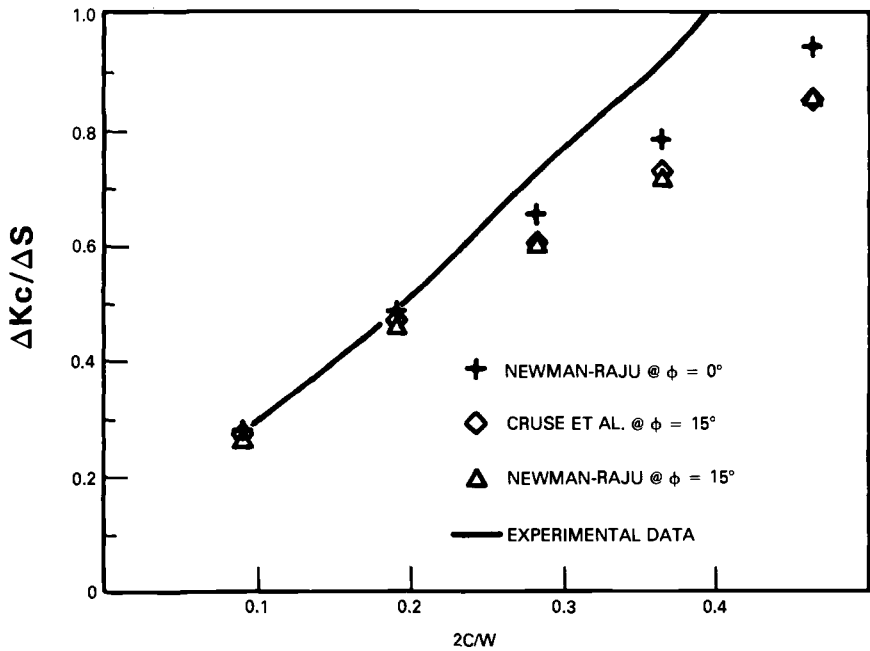


FIG. 16—Comparison of the stress-intensity factor for a surface-cracked tension specimen at a near-free-surface location.

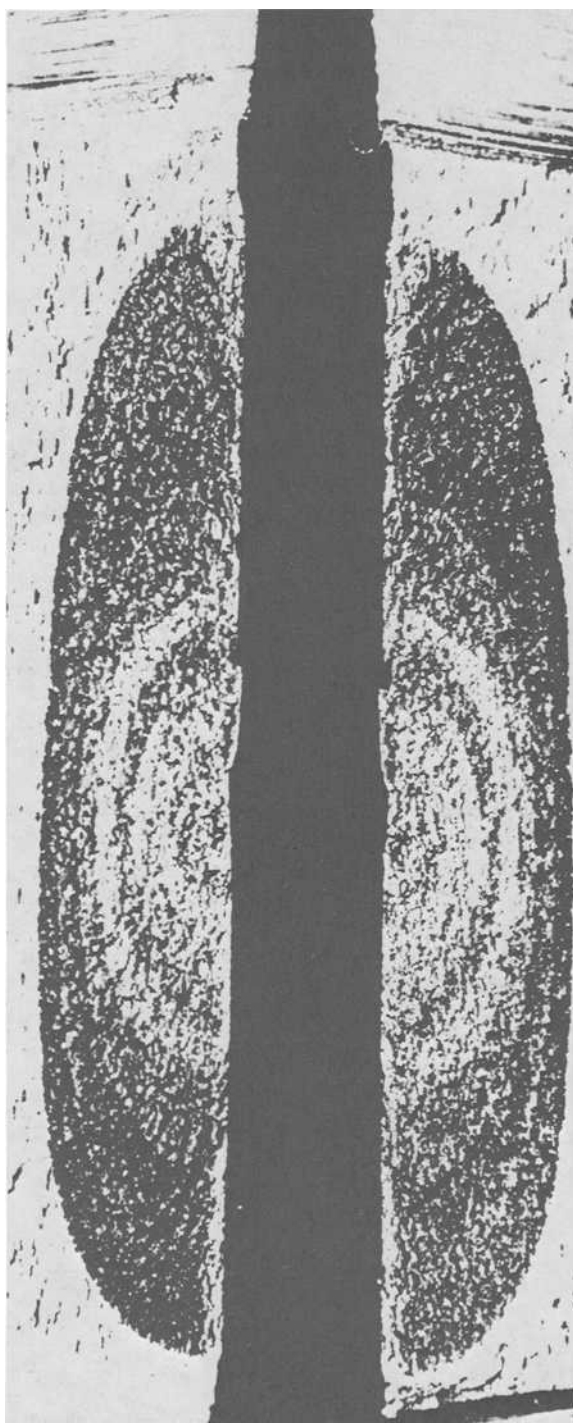


FIG. 17—Surface crack in bending.

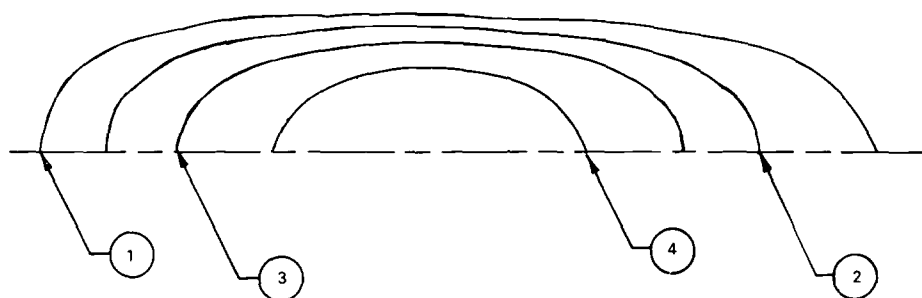


FIG. 18—Surface flaw contours.

Surface Crack in Bending

Figure 17 shows the crack growth profiles revealed by heat-tinting for a nickel-base superalloy specimen. The crack was grown in four-point bending with a surface stress range of 82.7 to 827 MPa. The baseline crack growth rate model for this material and condition was determined to be $da/dN = 1.017 \times 10^{-10} (\Delta K - 11)^{2.375}$, for ΔK in MPa \sqrt{m} , and for a stress ratio of $R = 0.1$. The plate was 0.146 m long, 0.044 m wide, and 3.05×10^{-3} m thick. The crack was induced by electron deposition machining (EDM) initiation at the center of one surface; four crack shapes are shown in Fig. 18.

Figures 19 and 20 compare some of the experimentally determined crack profiles with ellipses. It is again apparent that an ellipse with a surface length of 1.1 times the actual surface length approximates the crack-front curvature, especially as seen at the left-hand crack tip of Contour 2. To use the actual crack length results in an ellipse that underestimates the surface K value, due to smaller curvature at the surface; this underestimate becomes more important as the aspect ratio of the crack increases (the surface K reduces because of the aspect ratio).

Figure 21 compares the experimentally determined stress-intensity factor at the deep crack location to the Newman and Raju [13] prediction for various modeling aspect ratios (surface length to depth). The variations of predicted K are all within the experimental scatter of crack growth behavior for such low values of K (approaching threshold).

Figure 22 compares the surface values as before. The results are based on averaging the crack growth characteristics of the two ends of the crack. In this problem there is no crack

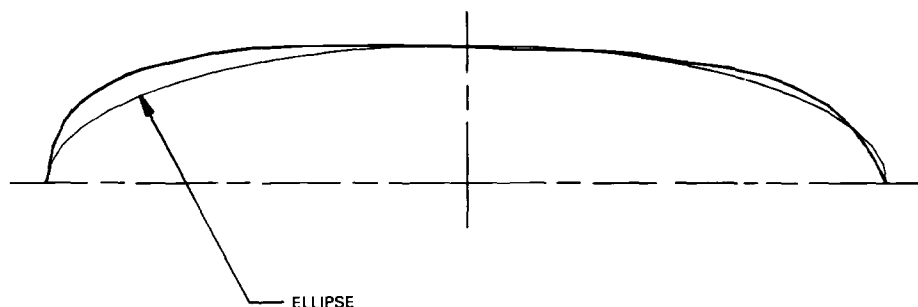


FIG. 19—Comparison of Contour No. 1 with an equal-length ellipse.

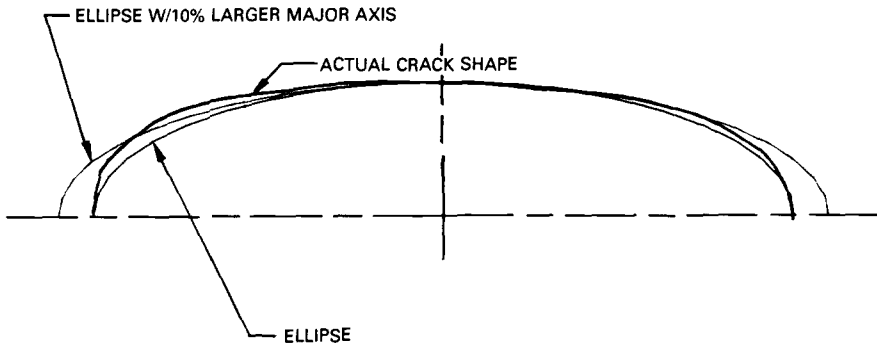


FIG. 20—Comparison of Contour No. 2 with an ellipse of equal length and an ellipse of 10% greater surface length.

front turn-back, indicating the lack of significant surface residual stresses. However, the surface stresses are approaching the yield strength of the material, a condition not unlike the actual application that led to this particular experimental study. The Newman and Raju [13] estimates are given for various elliptical angle distances from the free surface. It is apparent that the surface value consistently overpredicts the apparent surface stress-intensity factor. The values at 5° seem to provide the best comparison except at the largest crack size.

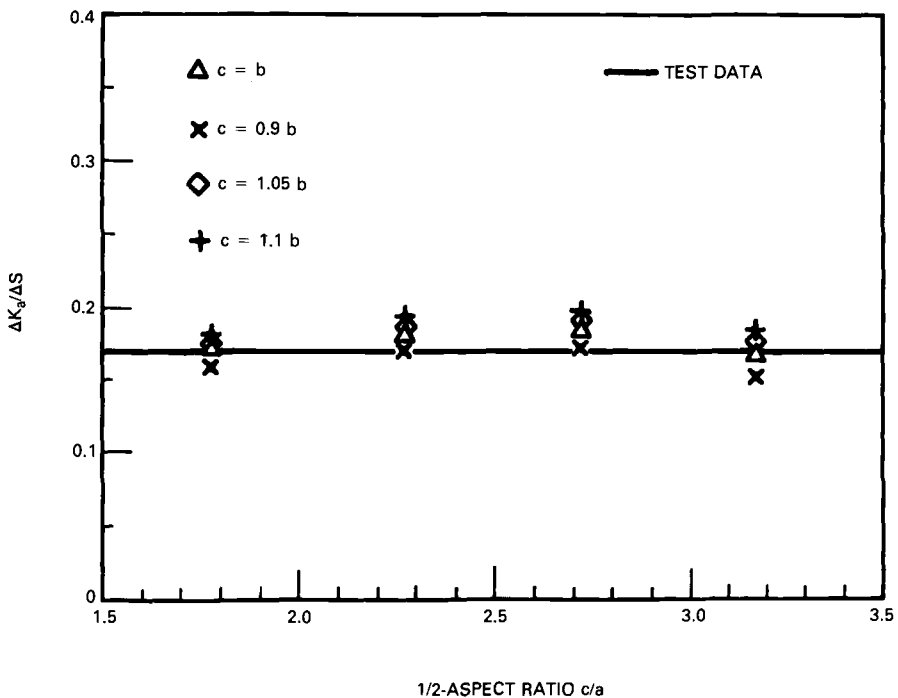


FIG. 21—Stress-intensity factor comparison for a surface-cracked bending specimen at a deep-crack location.

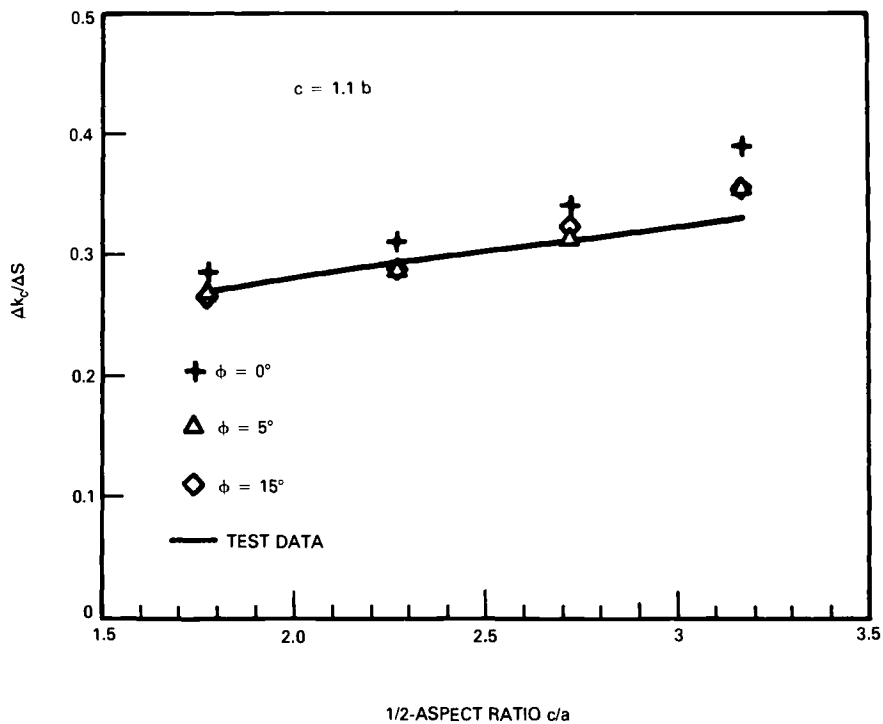


FIG. 22—Stress-intensity factor comparison for a surface-cracked bending specimen at various near-surface points.

Conclusions

The fatigue crack growth models demonstrate the significant three-dimensional problem of fatigue crack growth modeling for simple unnotched specimens with surface cracks. There is no apparent and consistent modeling algorithm for the near-surface crack length. What crack sizes should be assumed if we are to use elliptical crack models? If not ellipses, what crack shape can be used near the free surface? Is there a fatigue criterion that applies in the surface layer where the stresses are not subject to plane-strain constraint behavior? Does this criterion apply over some distance? Is local closure due to plasticity important? Should the surface crack growth behavior be governed by the stress-intensity factor some depth below the free surface where plane strain governs? How much do these issues affect fatigue crack growth lives? How important are these issues for surface crack growth in notches?

Complete answers to these questions are beyond the scope of this paper. Rather, it is hoped that these questions will illustrate that the surface crack problem still offers many interesting and challenging three-dimensional issues for continuing study. A serious program to establish a firm experimental basis for surface crack growth behavior, crack-front shape, plastic zone size and closure effects, and so forth, is clearly a continuing need in providing a proper basis for surface crack fatigue growth prediction.

Acknowledgments

The numerical work presented in this report summarizes earlier published and unpublished findings. The new analytical result for the surface crack/free surface intersection point was

the result of work supported by the U.S. Air Force Office of Scientific Research (AFOSR), Contract F49620-84-C-0048, and activity funded by the Internal Research Panel of Southwest Research Institute. (The United States Government is authorized to reproduce and distribute reprints for governmental purposes notwithstanding any copyright notation hereon.) The support and patience of both the AFOSR and SwRI are gratefully acknowledged. The author also wishes to thank Dr. Ewaryst Polch for developing the traction BIE analysis results, Dr. Sathasivam Raveendra for the numerical BEST/CRX results, and Tanya Jackson and Victor Holmes for related support.

References

- [1] Wilson, R. B., Bak, M. F., Nakazawa, S., and Banerjee, P. K., "3-D Inelastic Analysis Methods for Hot Section Components (Base Program)," First Annual Status Report, NASA Contract NAS3-23697, National Aeronautics and Space Administration, Washington, D.C., 1984.
- [2] Lachat, J. C. and Watson, J. O., "Effective Numerical Treatment of Boundary Integral Equations: A Formulation for Three-Dimensional Elastostatics," *International Journal for Numerical Methods in Engineering*, Vol. 10, 1976, pp. 991-1005.
- [3] Blandford, G. E., Ingraffea, A. R., and Liggett, J. A., "Two-Dimensional Stress Intensity Factor Computations Using the Boundary Element Method," *International Journal for Numerical Methods in Engineering*, Vol. 17, 1981, pp. 387-404.
- [4] Cruse, T. A., "Two-Dimensional BIE Fracture Mechanics Analysis," *Applied Mathematical Modelling*, Vol. 2, 1978, pp. 287-293.
- [5] Cruse, T. A., "Numerical Solutions in Three-Dimensional Elastostatics," *International Journal of Solids & Structures*, Vol. 5, 1969, pp. 1259-1274.
- [6] Cruse, T. A. and Meyers, G. J., "Three-Dimensional Fracture Mechanics Analysis," *Journal of the Structural Division, ASCE*, Vol. 103, No. ST2, 1977, pp. 309-320.
- [7] Cruse, T. A. and Van Buren, W., "Three-Dimensional Elastic Stress Analysis of a Fracture Specimen with an Edge Crack," *International Journal of Fracture Mechanics*, Vol. 7, No. 1, 1971, pp. 1-15.
- [8] Cruse, T. A., "Two- and Three-Dimensional Problems of Fracture Mechanics," *Developments in Boundary Element Methods*, Vol. 1, P. K. Banerjee and R. Butterfield, Eds., Applied Science, London, 1979, pp. 97-119.
- [9] Cruse, T. A. and Wilson, R. B., "Advanced Applications of Boundary-Integral Equation Methods," *Nuclear Engineering and Design*, Vol. 46, pp. 223-234.
- [10] Raju, I. S. and Newman, J. C., Jr., "Three-Dimensional Finite-Element Analysis of Finite-Thickness Fracture Specimens," NASA Technical Note, NASA TN D-8414, National Aeronautics and Space Administration, Washington, D.C., May 1977.
- [11] Yamamoto, Y. and Sumi, Y., "Stress-Intensity Factors for Three-Dimensional Cracks," *International Journal of Fracture*, Vol. 14, No. 1, 1978, pp. 17-38.
- [12] Benthem, J. P., "State of Stress at the Vertex of a Quarter-Infinite Crack in a Half Space," *International Journal of Solids and Structures*, Vol. 13, 1977, pp. 479-492.
- [13] Newman, J. C., Jr., and Raju, I. S., "Stress-Intensity Factors for a Wide Range of Semi-Elliptical Surface Cracks in Finite-Thickness Plates," *Engineering Fracture Mechanics*, Vol. 11, 1979, pp. 817-829.
- [14] Cruse, T. A., "Boundary-Integral Equation Method for Three-Dimensional Elastic Fracture Mechanics Analysis," Interim Scientific Report AFOSR-TR-75-0813, Air Force Office of Scientific Research, Bolling Air Force Base, Washington, DC, 1975.
- [15] Guidera, J. T. and Lardner, R. W., "Penny-Shaped Cracks," *Journal of Elasticity*, Vol. 5, No. 1, 1975, pp. 59-73.
- [16] Bui, H. D., "An Integral Equations Method for Solving the Problem of a Plane Crack of Arbitrary Shape," *Journal of Mechanics and Physics of Solids*, Vol. 25, 1977, pp. 29-39.
- [17] Weaver, J., "Three-Dimensional Crack Analysis," *International Journal of Solids & Structures*, Vol. 13, 1977, pp. 321-330.
- [18] Plutot, C. J., "Une Nouvelle Methode D'Equations Integrales Pour Certains Problemes de Fissures Planes," thesis presented at the University Pierre et Marie Curie, Paris, France, 18 Feb. 1980.
- [19] Cruse, T. A., Polch, E. Z., and Huang, C.-J., "Traction BIE Solutions for Flat Cracks," *Computational Mechanics*, Vol. 2, 1987, pp. 253-267.

- [20] Nishioka, T. and Atluri, S. N., "Analysis of Surface Flaw in Pressure Vessels by a New 3-Dimensional Alternating Method," *Journal of Pressure Vessel Technology*, Vol. 104, 1982, pp. 299-307.
- [21] Folias, E. S., "Method of Solution of a Class of Three-Dimensional Problems Under Mode-I Loading," *International Journal of Fracture*, Vol. 16, 1980, pp. 335-348.
- [22] Burton, W. S., Sinclair, G. B., Solecki, J. S., and Swedlow, J. L., "On the Implications for LEFM of the Three-Dimensional Aspects in Some Crack/Surface Intersection Problems," *International Journal of Fracture*, Vol. 25, 1984, pp. 3-32.
- [23] Cruse, T. A., Meyers, G. J., and Wilson, R. B., "Fatigue Growth of Surface Crack," *Flaw Growth and Fracture: Tenth Conference, ASTM STP 631*, American Society for Testing and Materials, Philadelphia, 1977, pp. 174-189.
- [24] Müller, H. M., Müller, S., Munz, D., and Neumann, J., "Extension of Surface Cracks During Cyclic Loading," *Proceedings, 17th National Symposium on Fracture Mechanics*, Albany, NY, 1984.
- [25] Hosseini, A. and Mahmoud, M. A., "Evaluation of Stress-Intensity Factor and Fatigue Growth of Surface Cracks in Tension Plates," *Engineering Fracture Mechanics*, Vol. 22, No. 6, 1985, pp. 957-974.
- [26] Schijve, J., "Comparison Between Empirical and Calculated Stress-Intensity Factors of Hole Edge Cracks," *Engineering Fracture Mechanics*, Vol. 22, No. 1, 1985, pp. 49-58.

Stress-Intensity Factors for Corner Cracks in Rectangular Bars

REFERENCE: Raju, I. S. and Newman, J. C., Jr., "Stress-Intensity Factors for Corner Cracks in Rectangular Bars," *Fracture Mechanics: Nineteenth Symposium, ASTM STP 969*, T. A. Cruse, Ed., American Society for Testing and Materials, Philadelphia, 1988, pp. 43-55.

ABSTRACT: This paper presents stress-intensity factors for a wide range of quarter-elliptical corner cracks in rectangular bars. Cracked configurations were subjected to remote tension, in-plane bending, or out-of-plane bending. The ratio of crack depth to crack length ranged from 0.2 to 2; the ratio of crack depth to specimen thickness ranged from 0.2 to 0.8; and the ratio of crack length to specimen width ranged from 0.04 to 0.8. The configurations analyzed varied from a square bar to a very wide plate. These particular crack configurations were chosen to cover the range of shapes and sizes that have been observed to grow in experiments conducted on rectangular bars. The stress-intensity factors were calculated by a three-dimensional finite-element method. Finite-element models employed singularity elements along the crack front and linear-strain elements elsewhere. The models had about 7000 degrees of freedom. Stress-intensity factors were calculated using a nodal-force method.

The present results were compared with other numerical results for a quarter-circular corner crack configuration. The present results along the interior of the crack generally agreed within 3% with those from the literature. Some larger differences (3 to 13%) were observed near the intersection of the crack front and the free surfaces (in the boundary-layer region). Thus, analyses were also performed to study the effect of mesh refinement in the boundary-layer region and the influence of Poisson's ratio on the distribution of stress-intensity factors.

KEY WORDS: cracks, surface cracks, crack propagation, fracture, stress analysis, materials fatigue, stress-intensity factors, finite elements, boundary-layer region, fracture mechanics

Corner cracks can occur in many structural components. These cracks can cause premature failure of landing gear of aircraft, spars, stiffeners, and other reinforcements which employ rectangular-shaped components. Accurate stress analyses of these corner crack components are needed for reliable prediction of crack-growth rates and fracture strengths. A task group of ASTM Committee E-24 on Fracture Testing has also proposed including this crack configuration in the ASTM Practice for Fracture Testing with Surface-Crack Tension Specimens [E 740-80(86)].

One of the earliest analyses of a corner crack configuration was made by Tracey [1]. He analyzed a quarter circle corner crack in a quarter-circular bar subjected to remote tension using a three-dimensional finite-element method. Tracey obtained the stress-intensity factor distribution for a shallow crack (the ratio of the crack depth to specimen radius was 0.2). Kobayashi and Enetanya [2] used the alternating method to obtain stress-intensity factors for corner cracks in three shapes (crack-depth-to-surface-half-length ratios of 0.98, 0.4, and

¹ Senior scientist, Analytical Services and Materials, Inc., Hampton, VA 23666.

² Senior scientist, Materials Division, National Aeronautics and Space Administration, Langley Research Center, Hampton, VA 23665.

0.2). These results were obtained for uniform and linearly varying crack-face pressure loadings. Pickard [3] used three-dimensional finite-element analyses to obtain stress-intensity factors for circular and elliptical cracks in rectangular bars for various values of crack-depth-to-specimen-thickness ratios. These results were obtained for uniform remote tensile loading. Newman and Raju [4,5] also used the three-dimensional finite-element method to obtain stress-intensity factors for corner cracks for a wide range of crack shapes and crack sizes in wide plates. They also presented empirical equations for stress-intensity factors obtained by curve fitting to the finite-element results and using engineering judgment. The results in Refs 4 and 5 were obtained for uniform tensile and out-of-plane bending loadings. While the results in Refs 4 and 5 are comprehensive, stress-intensity factor solutions are needed for a wide range in plate sizes (from a square bar to a wide plate). In addition to the two loadings used in Refs 4 and 5, the results for remote in-plane bending loading are also of interest.

This paper presents stress-intensity factors for a wide range of quarter-elliptical corner cracks in a rectangular bar as shown in Fig. 1. The bar was subjected to remote tension, in-plane bending, or out-of-plane bending loads. The ratio of crack depth to crack length (a/c) ranged from 0.2 to 2, the ratio of crack depth to specimen thickness (a/t) ranged from 0.2 to 0.8, and the ratio of crack length to specimen width (c/b) ranged from 0.04 to 0.8. The ratio of specimen width to thickness varied from a square bar to a very wide plate. Stress-intensity factors were calculated from a three-dimensional finite-element analysis using the nodal-force method [6-8]. The present results are compared with other numerical results from the literature for a shallow quarter-circular corner-crack configuration. Analyses were also performed to study the effect of mesh refinement and the influence of Poisson's ratio

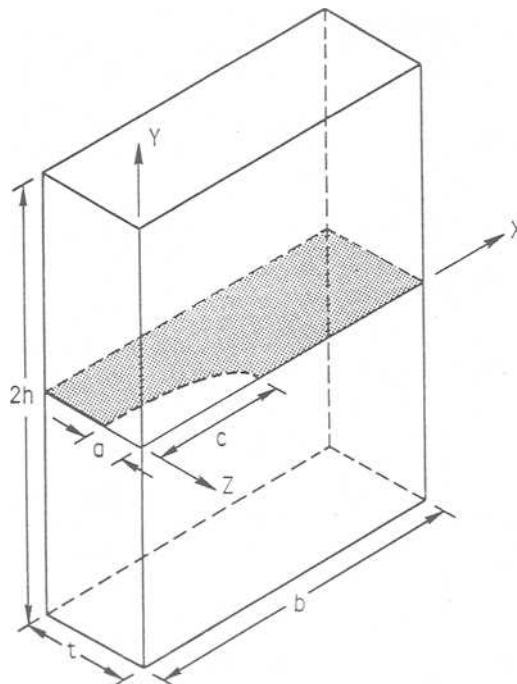


FIG. 1—Quarter-elliptical corner crack in rectangular bar.

on the distribution of stress-intensity factors in the boundary-layer region where the crack front intersects the free surface.

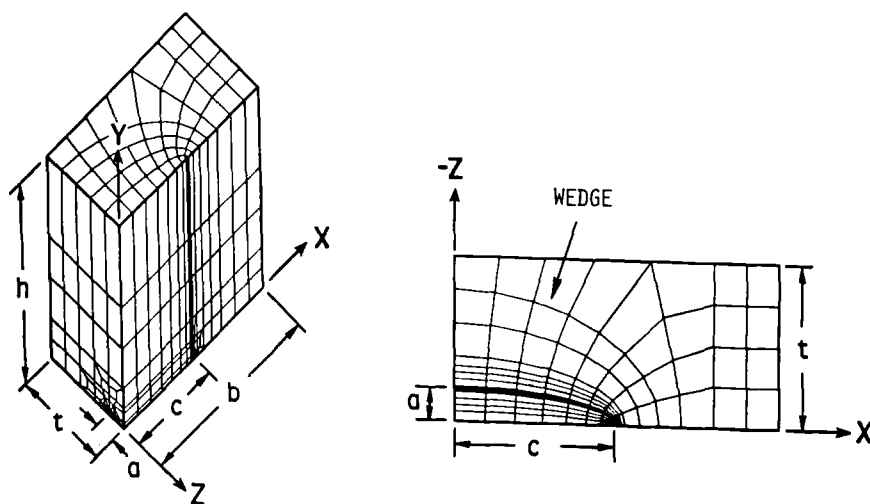
Nomenclature

- a Depth of corner crack
- b Width of bar
- c Length of corner crack
- F Stress-intensity boundary-correction factor
- h Half-length of bar
- K Stress-intensity factor (Mode I)
- Q Shape factor for elliptical crack
- S_{bx} Remote stress on outer fiber due to bending about x -axis (out-of-plane bending)
- S_{bz} Remote stress on outer fiber due to bending about z -axis (in-plane bending)
- S_t Remote uniform tensile stress
- t Thickness of bar
- x, y, z Cartesian coordinate system
- ν Poisson's ratio
- ϕ Parametric angle of ellipse

Three-Dimensional Finite-Element Analysis

A three-dimensional finite-element analysis was used to calculate the Mode I stress-intensity factor variations along the crack front for a corner crack in a bar, as shown in Fig. 1. In this analysis, Poisson's ratio, ν , was assumed to be 0.3. In the investigation of the boundary-layer effect, however, Poisson's ratio was varied from 0 to 0.45.

Figure 2 shows a typical finite-element model for a corner crack in a rectangular bar. The finite-element models employed singularity elements along the crack front and eight-noded



(a) Model of cracked bar.

(b) Mesh pattern on $Y = 0$ plane.

FIG. 2—Finite-element mesh for surface and corner crack.

hexahedral elements elsewhere. The models had about 7000 degrees of freedom. Stress-intensity factors were evaluated using a nodal-force method. Details of the formulation of these types of elements, the development of the models, and the development of the nodal-force method are given in Refs 6 through 8 and are not repeated here.

Loading

Three types of loads were applied to the finite-element models of the corner cracked bar: remote uniform tension, remote in-plane bending (bending about z -axis), and remote out-of-plane bending (bending about x -axis). The remote uniform tensile stress is S_i and the remote outer-fiber bending stresses are either S_{bx} or S_{bz} . The bending stress S_{bx} and S_{bz} are calculated at the origin of the surface crack ($x = y = z = 0$ in Fig. 1) without the crack present.

Stress-Intensity Factor

The tensile and bending loads cause only Mode I deformations. The Mode I stress-intensity factor K for any point along the corner crack front was taken to be

$$K = S_i \sqrt{\pi \frac{a}{Q}} F \left(\frac{a}{t}, \frac{a}{c}, \frac{c}{b}, \phi \right) \quad (1)$$

where the subscript i denotes tension load ($i = t$) or bending loads ($i = bx$ or bz). The half-length of the bar, h , was chosen large enough to have a negligible effect on stress-intensity factors ($h/b > 5$). Values for F , the boundary-correction factor, were calculated along the crack front for various combinations of parameters (a/t , a/c , c/b , and ϕ). The crack dimensions and parametric angle, ϕ , are defined in Fig. 3. Note that the parametric angle is measured from the x -axis for all crack shapes. The shape factor for an ellipse, Q , is given by the square of the complete elliptic integral of the second kind.

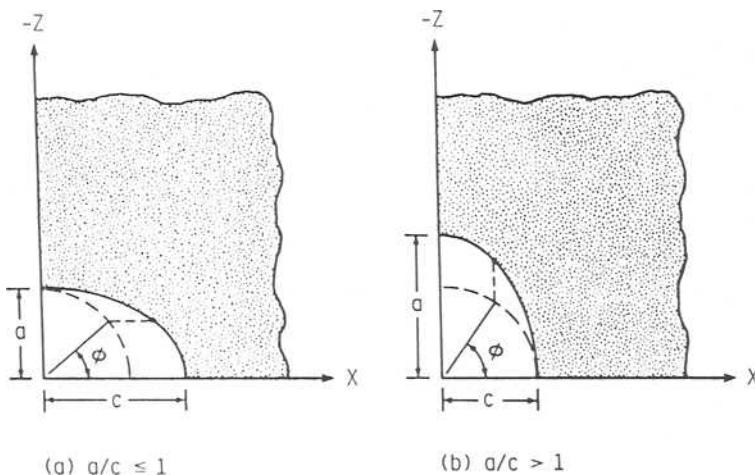


FIG. 3—Definition of parametric angle.

The empirical expressions for Q (taken from Ref 7) used in this paper are

$$Q = 1 + 1.464(a/c)^{1.65} \quad \text{for } a/c \leq 1 \quad (2a)$$

$$Q = 1 + 1.464(c/a)^{1.65} \quad \text{for } a/c > 1 \quad (2b)$$

Results and Discussion

The stress-intensity factors were obtained for corner cracks in bars subjected to the three loadings: remote uniform tension, out-of-plane bending, and in-plane bending. For these loading conditions, corner cracked bars with various crack sizes (a/t) and crack shapes (a/c) were analyzed. The range of the parameters considered included the following:

- (a) $a/t = 0.2, 0.5$, and 0.8 ;
- (b) $a/c = 0.2, 0.4, 1$, and 2 ;
- (c) $c/b = 0.04, 0.1, 0.2, 0.5$, and 0.8 ; and
- (d) $h/b \geq 5$.

For each of these combinations, stress-intensity factors were obtained along the crack front. Because of the voluminous results generated from this study, only typical results for each type of loading are presented herein. The complete results are given in Ref 9. In all the figures, the normalized stress-intensity factor, $K/(S_i\sqrt{\pi a/Q})$, is presented as a function of the parametric angle, ϕ .

Rectangular Bar

Tensile Loading—Figure 4 presents the normalized stress-intensity factors for a quarter-circular corner crack ($a/c = 1$) in a large plate ($c/b = 0.1$). Because the crack shape is symmetric about $\phi = \pi/4$, the stress-intensity factors are also almost symmetric. The stress-intensity factors are slightly larger at $\phi = 0$ than at $\phi = \pi/2$. As expected, deeper cracks (larger a/t values) produced higher normalized stress-intensity factors.

Out-of-Plane Bending—Figures 5 and 6 show the normalized stress-intensity factors for quarter-elliptic corner cracks ($a/c = 0.4$ and 0.2 , respectively) in a large plate ($c/b = 0.1$). At $\phi = 0$, deeper cracks gave higher normalized stress-intensity factors. However, at $\phi = \pi/2$, the stress-intensity factors are lower for deeper cracks. This behavior is expected because, at $\phi = \pi/2$, the crack front is in a lower stress field than that at $\phi = 0$. A comparison of Figs. 5 and 6 shows that the lower a/c ratio caused higher normalized stress-intensity factors at the maximum depth location ($\phi = \pi/2$) but caused lower normalized stress-intensity factors at the free surface ($\phi = 0$).

In-Plane Bending—Figure 7 shows the normalized stress-intensity factors for a quarter-elliptic corner crack ($a/c = 2$) in a large plate ($c/b = 0.1$). Note that, in contrast to the earlier crack shapes, this crack shape has the major axis in the thickness direction. Figure 7 shows that larger values of a/t produced larger normalized stress-intensity factors all along the crack front. There is no appreciable change in the shape of the stress-intensity factor distribution from shallow to deep cracks. Because of the large width ($c/b = 0.1$), under in-plane bending, the crack experiences a state of near uniform stress. Therefore, the stress-

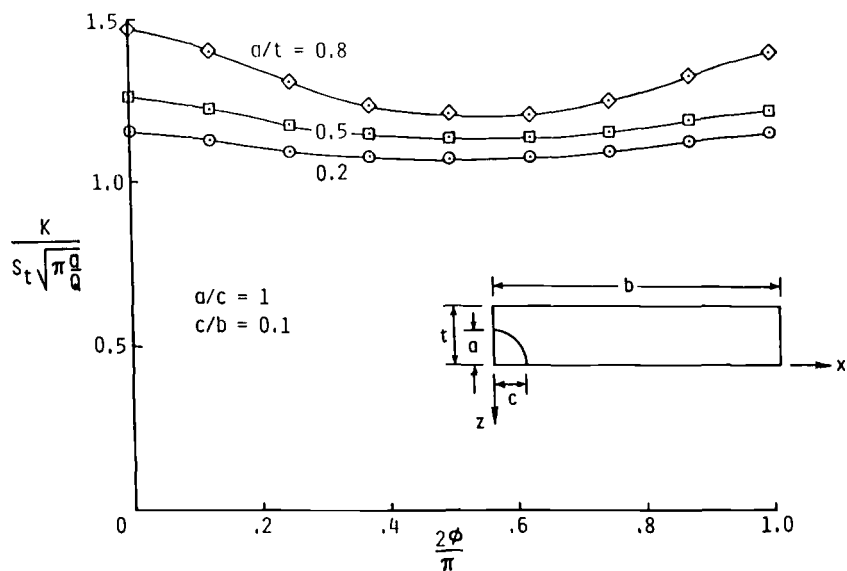


FIG. 4—Normalized stress-intensity factors for a quarter-circular corner crack subjected to remote tension.

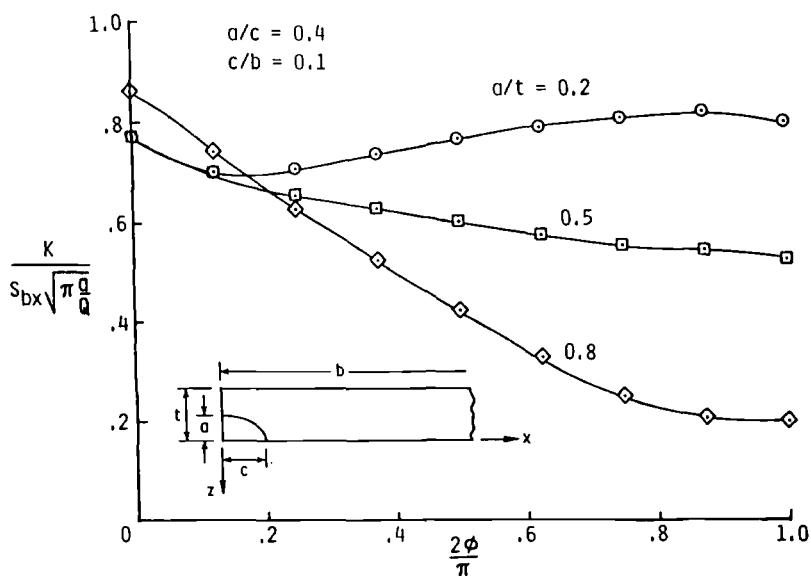


FIG. 5—Normalized stress-intensity factors for a quarter-elliptic corner crack subjected to out-of-plane bending.

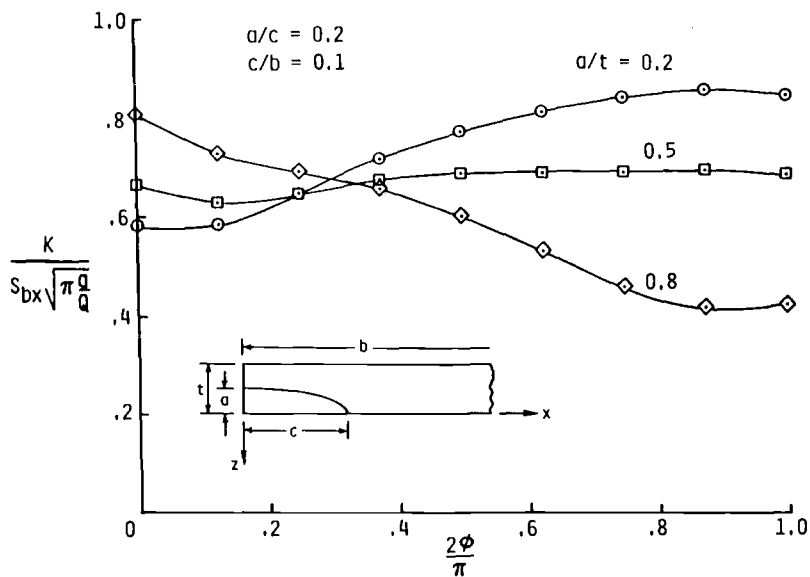


FIG. 6—Normalized stress-intensity factors for a long quarter-elliptic corner crack subjected to out-of-plane bending.

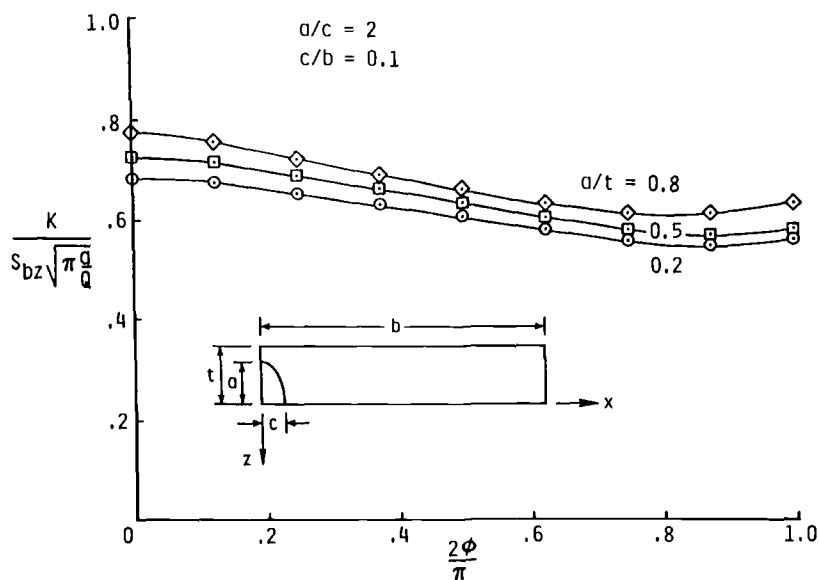


FIG. 7—Normalized stress-intensity factors for a quarter-elliptic corner crack subjected to in-plane bending.

intensity factors for this case are not vastly different from those due to a remote tensile loading. Comparison of results from Ref 4 with those in Fig. 7 confirms this observation.

Square Bar

As previously mentioned, the corner-crack specimen is being considered for inclusion in the ASTM Practice for Fracture Testing of Surface-Crack Tension Specimens [E 740-80(86)]. One of the corner-crack configurations being considered is a square bar ($b = t$). Some typical results for a square bar with a quarter-circular corner crack ($a/c = 1$ and $a/t = 0.2$) subjected to all three loadings are presented in Fig 8. In this figure the circular symbols denote the normalized stress-intensity factors due to remote tension, the square symbols denote the results due to out-of-plane bending, and the diamond symbols denote the results due to in-plane bending. As expected, the tensile loading produced higher normalized stress-intensity factors than the other loadings. Also, all the results are symmetric about $\phi = \pi/4$ because of the symmetric specimen configuration. Comparison of the results in Figs. 4 and 8 ($c/b = 0.1$ and 0.2 , respectively) show that the normalized stress-intensity factors are larger for larger c/b . The results for the out-of-plane bending can be obtained from those for in-plane bending by changing ϕ to $\pi/2 - \phi$.

Comparison with Results from the Literature

Figure 9 shows normalized stress-intensity factors calculated by several investigators for a quarter-circular corner crack in a rectangular bar ($a/t = 0.2$) subjected to remote tensile loading. The present finite-element results are shown as solid circular symbols and Eq 27 of Ref 4 is shown as the solid curve. Tracey [1] and Pickard [3] also used the finite-element method, but the width (b) and half length (h) of their model were equal to the thickness (see quarter-circular and square configurations in the insert in Fig. 9). Kobayashi and

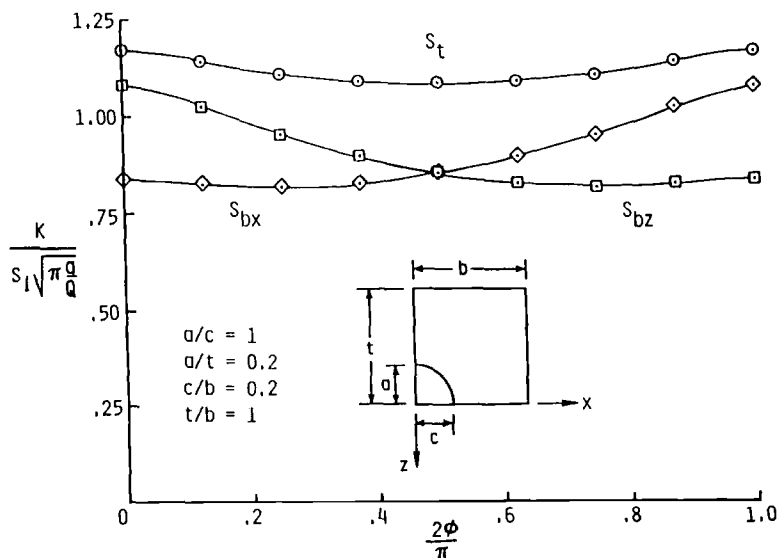


FIG. 8—Normalized stress-intensity factors for a quarter-circular corner crack in a square bar subjected to various loading.

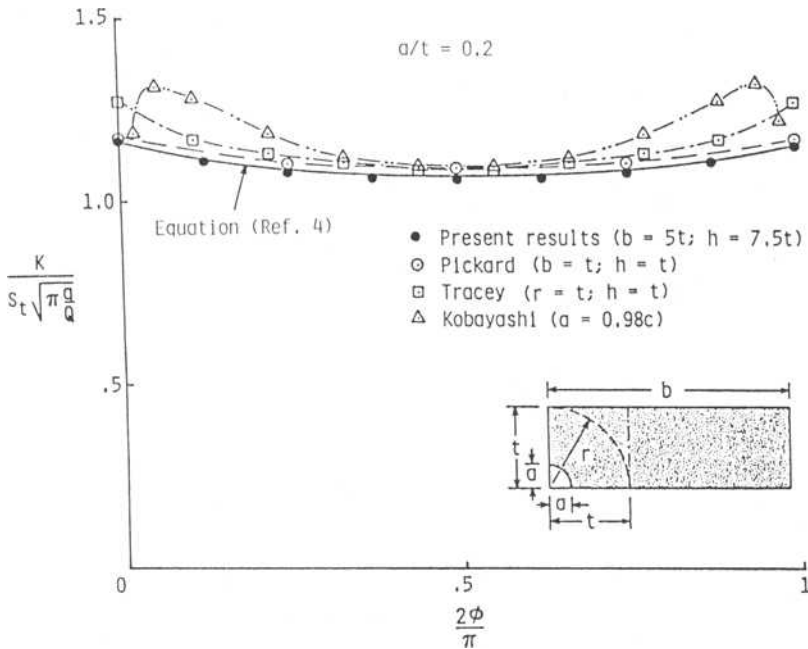


FIG. 9—Comparison of normalized stress-intensity factors for quarter-circular corner crack subjected to remote tension.

Enetanya [2] used the alternating method. Their model had an a/c ratio of 0.98 and the width (b) and half length (h) were large compared with crack length. For all values of ϕ , Pickard's results were 1 to 3% higher than the present finite-element results. Part of the difference is due to a width and length effect in Pickard's model. Near $\phi = 0$ and $\pi/2$, Tracey's and Kobayashi's results are 5 to 13% higher than the present results. All results are in good agreement (within 3%) at the midpoint ($\phi = \pi/4$).

Kobayashi's and Enetanya's results [2] show a drop in the stress-intensity factor near the ends of the crack (at $\phi = 0$ and $\pi/2$). This is believed to be due to the boundary-layer effect at the locations where the crack front intersects a free surface [10–14]. The present finite-element model with eight wedges (Fig. 2) did not show any boundary-layer effect. The boundary-layer effect is investigated in the next section by refining the finite-element model and by analyzing the configuration with several values of Poisson's ratio.

Boundary-Layer Effect on Stress-Intensity Factors

This section examines the boundary-layer effect where the crack front meets a free surface. To study this effect, a semicircular surface crack ($a/c = 1$) in a large bar ($a/t = 0.2$ and $c/b = 0.04$) was used. The surface-crack configuration was chosen because, due to symmetry, only one of the locations where the crack meets the free surface needs to be analyzed. In contrast, the corner-crack configuration would require examination at two locations. However, the boundary-layer effect is expected to be identical for the two configurations.

Effect of Mesh Refinement—Four different finite-element models with 8, 10, 14, and 16 wedges between $0 \leq \phi \leq \pi/2$ were considered. The 8-wedge model, shown in Fig. 2, has 8 equal wedges, each with a parametric angle of $\pi/16$. The other models have nonuniform

wedges and were obtained by refining the 8-wedge model near the free surface. The smallest wedge angles for the 10, 14, and 16-wedge models are $\pi/64$, $\pi/128$, and $\pi/256$, respectively. The normalized stress-intensity factors for remote tensile loading obtained from these four models are shown in Fig. 10, where the parametric angle is measured from the free surface (see insert). Except for the 8-wedge model, the maximum stress-intensity factor occurred very near the free surface (at $\phi = \pi/80$ from the free edge). At the free edge, however, the stress-intensity factor dropped rapidly. The drop-off is most pronounced for the 16-wedge model. The stress-intensity factors in the interior ($\phi > \pi/80$) showed little or no change with mesh refinement. This strongly suggests that the region $0 \leq \phi \leq \pi/80$ is a boundary-layer region, where the computed stress-intensity factors depend on the mesh refinement and, hence, may not be reliable.

Although, as shown in Fig. 10, the stress-intensity factors show larger drop-offs at $\phi = 0$ with further mesh refinement, the peak values were nearly the same as that obtained from the 8-wedge model at $\phi = 0$ (within about 1.5%). Thus, the stress-intensity factors obtained from the 8-wedge model should be interpreted as an average value near the free surface. Results from the 8-wedge models at $\phi = 0$ have been successfully used to predict crack-growth patterns and lives for several surface-crack and corner-crack configurations and materials in Ref 15.

Effect of Poisson's Ratio—Many investigators have postulated that the stress singularity where the crack front meets a free surface is different from the classical square-root singularity and is a function of Poisson's ratio, ν , of the material [10–14]. To study this, the 16-wedge model was analyzed with Poisson's ratios of 0, 0.3, and 0.45. (The limiting value of $\nu = 0.5$ was not analyzed because the three-dimensional finite-element analysis does not permit the use of this value.) Figure 11 presents the normalized stress-intensity factors obtained with these three Poisson's ratios. For $\nu = 0$, the 16-wedge model does not show any drop-off in the stress-intensity factor at the free surface. But, higher values of Poisson's ratio showed large drop-offs near the free surface. References 10 through 14 showed that

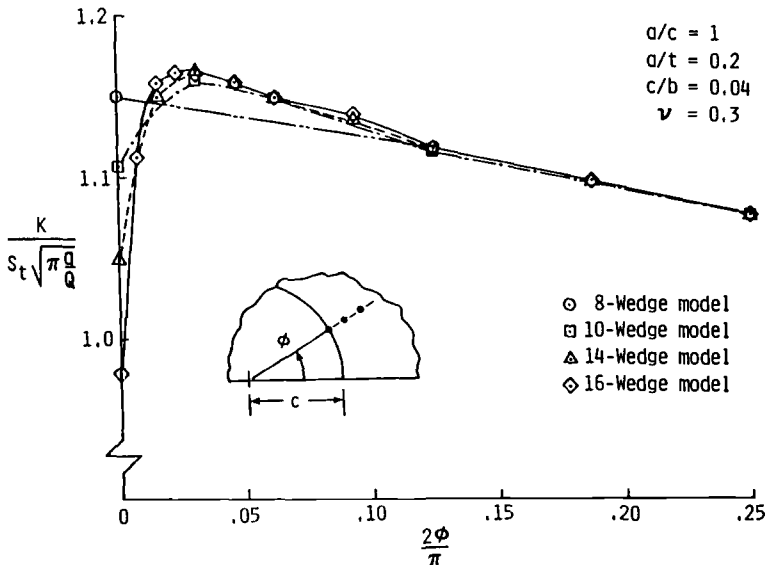


FIG. 10—Effect of mesh refinement on normalized stress-intensity factors near a free surface.

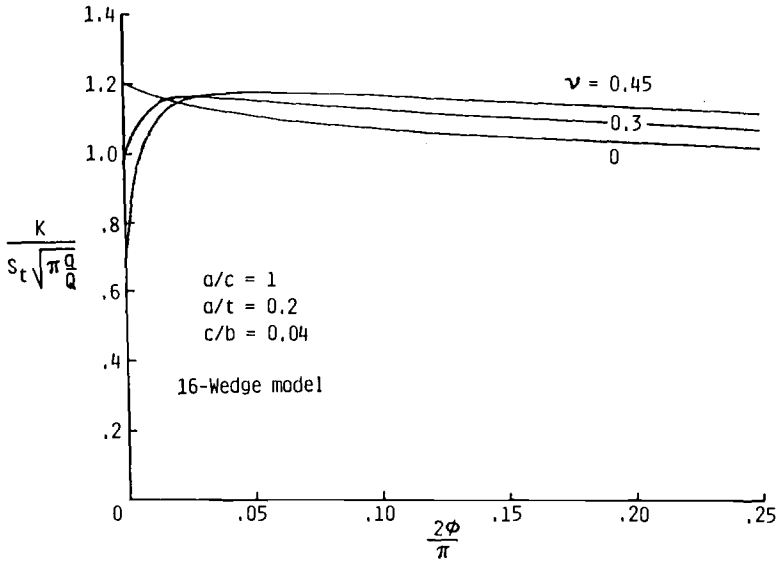


FIG. 11—Effect of Poisson's ratio on normalized stress-intensity factors.

the power of the singularity has the largest deviation from the classical square root for $\nu = 0.5$. The present results appear to agree with these findings. Away from the free surface, higher Poisson's ratios gave higher stress-intensity factors (10% difference between results for Poisson's ratios of 0 and 0.45).

Concluding Remarks

Stress-intensity factors for corner cracks in rectangular bars have been obtained by a three-dimensional finite-element analysis. The bars were subjected to remote tension, out-of-plane bending, or in-plane bending loading. A wide range of crack shapes, crack sizes, and crack-length-to-specimen-width ratios were considered. Only typical results for each type of loading are presented in this paper.

For all loadings considered, smaller width bars produced higher normalized stress-intensity factors than the larger width bars. For tensile loading, quarter-circular corner cracks gave higher stress-intensity factors near the free surfaces and lower values in the interior. The maximum normalized stress-intensity factors occurred at the free surface along the width direction for cracks with crack-depth-to-length (a/c) ratios >1 and at the free surface along the thickness direction for $a/c < 1$.

For out-of-plane bending loading, the highest value of the normalized stress-intensity factor occurred at either end of a shallow crack (low crack-depth-to-specimen-thickness (a/t) ratios); the location depended on the crack shape. However, for deep cracks the highest values occurred at the free surface in the width direction. For bars of large widths, the normalized stress-intensity factors due to in-plane bending loading are nearly the same as those due to remote tension.

Stress-intensity factors from the present analysis for shallow quarter-circular corner cracks were compared to those in the literature for remote tensile loading. The present results for stress-intensity factors in the interior agreed well (within 3%) with those obtained by other

three-dimensional finite-element and alternating methods. Some differences (3 to 13%) were observed near the two free surfaces.

A boundary-layer effect exists at locations where a crack intersects a free surface. In the small region where the crack meets the free surface, the stress-intensity factors showed a sudden drop. The region in which this drop occurred has a parametric angle of about $\pi/80$ from the free surface. Smaller mesh refinements gave larger drop-offs. The boundary-layer effect is more pronounced for materials with larger Poisson's ratios. Away from the free surface, higher Poisson's ratios gave higher stress-intensity factors (10% difference between results for Poisson's ratios of 0 and 0.45).

The stress-intensity factors given in this paper should be useful in predicting crack growth rates and fracture strengths, in designing structural components, and in establishing inspection intervals for structures subjected to cyclic loading.

Acknowledgment

This work was performed, by the first author, under Contract NAS 1-18256.

References

- [1] Tracey, D. M., "3D Elastic Singularity Element for Evaluation of K Along an Arbitrary Crack Front," *International Journal of Fracture*, Vol. 9, 1973, pp. 340-343.
- [2] Kobayashi, A. S. and Enetanya, A. N., "Stress-Intensity Factor of a Corner Crack," *Mechanics of Crack Growth, ASTM STP 590*, American Society for Testing and Materials, Philadelphia, 1976, pp. 477-495.
- [3] Pickard, A. C., "Stress-Intensity Factors for Cracks with Circular and Elliptic Crack Fronts—Determined by 3D Finite-Element Methods," PNR-90035, Rolls-Royce Limited, London, UK, May 1980.
- [4] Newman, J. C., Jr. and Raju, I. S., "Stress-Intensity Factor Equations for Cracks in Three-Dimensional Finite Bodies," *Fracture Mechanics: Fourteenth Symposium. Volume 1: Theory and Analysis, ASTM STP 791*, J. C. Lewis and G. Sines, Eds., American Society for Testing and Materials, Philadelphia, 1983, pp. I-238-I-265.
- [5] Newman, J. C., Jr. and Raju, I. S., "Stress-Intensity Factor Equations for Cracks in Three-Dimensional Finite Bodies Subjected to Tension and Bending Loads," NASA TM-85793, National Aeronautics and Space Administration, Washington, DC, April 1984.
- [6] Raju, I. S. and Newman, J. C., Jr., "Three-Dimensional Finite-Element Analysis of Finite-Thickness Fracture Specimens," NASA TN D-8414, National Aeronautics and Space Administration, Washington, DC, 1977.
- [7] Raju, I. S. and Newman, J. C., Jr., "Improved Stress-Intensity Factors for Semi-Elliptical Surface Cracks in Finite-Thickness Plates," NASA TM X-72825, National Aeronautics and Space Administration, Washington, DC, 1977.
- [8] Raju, I. S. and Newman, J. C., Jr., "Stress-Intensity Factors for a Wide Range of Semi-Elliptical Surface Cracks in Finite-Thickness Plates," *Engineering Fracture Mechanics*, Vol. 11, No. 4, 1979, pp. 817-829.
- [9] Raju, I. S. and Newman, J. C., Jr., "Finite-Element Analysis of Corner Cracks in Rectangular Bars," NASA TM-89070, National Aeronautics and Space Administration, Washington, DC, 1987.
- [10] Hartranft, R. J. and Sih, G. C., "An Approximate Three-Dimensional Theory of Plates with Application to Crack Problems," *International Journal of Engineering Science*, Vol. 8, 1970, pp. 711-729.
- [11] Benthem, J. P., "State of Stress at the Vertex of a Quarter-Infinite Crack in a Half-Space," *International Journal of Solids and Structures*, Vol. 13, 1977, pp. 479-492.
- [12] Benthem, J. P., "The Quarter-Infinite Crack in a Half-Space: Alternative and Additional Solutions," *International Journal of Solids and Structures*, Vol. 16, 1980, pp. 119-130.
- [13] Bazant, Z. P. and Estenssoro, L. F., "General Numerical Method for Three-Dimensional Singularities in Cracked or Notched Elastic Solids," *Advances in Research on the Strength and Fracture of Materials*, D. M. R. Taplin, Ed., Vol. 3a, Pergamon Press, New York, 1977, pp. 371-385.

- [14] Solecki, J. S. and Swedlow, J. L., "On the Three-Dimensional Implications of LEFM: Finite-Element Analysis of Straight and Curved Through Cracks in a Plate," *Fracture Mechanics: Sixteenth Symposium, ASTM STP 868*, American Society for Testing and Materials, Philadelphia, 1985, pp. 535-553.
- [15] Newman, J. C., Jr. and Raju, I. S., "Prediction of Fatigue Crack-Growth Patterns and Lives in Three-Dimensional Cracked Bodies," *Advances in Fracture Research, Proceedings*, 6th International Conference on Fracture (ICFG), New Delhi, India, 4-10 Dec., 1984.

Some Remarks on Three-Dimensional Fracture

REFERENCE: Folias, E. S., "Some Remarks on Three-Dimensional Fracture," *Fracture Mechanics: Nineteenth Symposium, ASTM STP 969*, T. A. Cruse, Ed., American Society for Testing and Materials, Philadelphia, 1988, pp. 56–72.

ABSTRACT: In this paper, the author presents the effect of specimen thickness on the stress concentration factor of a plate that has been weakened by a circular hole. The results compare very well with existing results on thin and very thick plates and bridge the data gap between them. Furthermore, the solution is shown to be derived from the same general solution from which the three-dimensional crack problem solution can be derived. The author also, by analogy, draws some conclusions regarding the behavior of the stress intensity factor.

KEY WORDS: thickness effect, stress concentration factor, circular hole, three-dimensional analysis, fracture, fracture mechanics

In the field of fracture mechanics it is well recognized that the role which the specimen thickness plays in the mechanism of failure is not very well understood. For example, the common experimental observation of a change from ductile failure at the edge to brittle fracture at the center of a broken sheet material has so far defied analysis. Moreover, the fracture toughness of a material is assumed to be constant. Yet failure theories in the field of fracture mechanics define two different values for fracture toughness, K_c and K_{Ic} .

Similarly, the failure of linear elastic fracture mechanics (LEFM) to predict the behavior of short cracks to the same degree of accuracy as that obtained for long crack behavior is usually attributed to one of two reasons (or possibly both). These are either that LEFM is not the appropriate analysis technique, or that other effects not normally accounted for are important and must be included.

Factors which are often neglected in LEFM analysis, but which are likely to be important in short crack conditions, fall into three categories:

- (a) surface conditions (for example, residual stresses due to machining, cold working, or chemical finishing, and applied stresses due to fretting),
- (b) three-dimensional considerations, and
- (c) plasticity considerations (for example, a yielded zone at the crack tip and also crack closure due to the wake of the yielded material).

While undoubtedly all three categories are equally important for the proper understanding of short crack growth behavior, the author believes that it is rather premature for researchers to conclude that LEFM theories do not adequately predict the behavior of short cracks and that considerations of realistic, three-dimensional, specimen geometries becomes ever more essential. Thus, an orderly theoretical attack on the three-dimensional Griffith problem can provide guidance to these and other phases of fracture research.

The most potent mathematical tool for this attack is the linear theory of infinitesimal

¹ Professor, University of Utah, Department of Civil Engineering, Salt Lake City, UT 84112.

elasticity as applied to a cracked plate of finite thickness. While it is true that this theory cannot include the nonelastic behavior of the material at the crack tip per se, it can (1) show many characteristics of the actual behavior of a cracked plate, including those due to thickness, and (2) assist us in understanding better the three-dimensional elastic-plastic analog (for example, by providing us with a proper discretized element mesh). Thus, the theory of three-dimensional linear elasticity is a logical fountainhead for detailed theoretical study, for it represents a relatively simple mathematical model.

Even so, the mathematical difficulties posed by three-dimensional problems are substantially greater than those associated with either plane stress or plane strain. As a result, there exist in the literature very few analytical papers² that deal specifically with the three-dimensional stress character at the base of a stationary crack. Simultaneously, in the last two decades, numerous attempts have been made to obtain finite element solutions by very capable researchers. Although they, too, have experienced some difficulties in the past,³ at present a consensus appears to have emerged as will be evident from the results presented in this volume. The fact, however, remains that there exists no explicit analytical solution with which numerical results can be compared. Be that as it may, the following three-dimensional elasticity problems immediately come to mind:

- (a) a plate weakened by a cylindrical hole,
- (b) a plate weakened by a through crack, and
- (c) a plate weakened by a partially through crack,

listed in the order of relative difficulty.

In this paper, the author will present some numerical results for the first problem and, by analogy, draw certain conclusions for the second problem. Moreover, the results of the first problem will be compared with two existing asymptotic solutions, one applicable to thin plates and the other applicable to very thick plates. The main purpose of this paper, however, is threefold: first, to show that the solution of the cylindrical hole problem is derivable from the same general analytical solution that the three-dimensional crack problem solution can be derived from; second, to acquire enough experience and a "feel" for the ultimate construction of an explicit analytical solution to the crack problem; and, third, to illustrate how the general solution for the equilibrium of elastic layers can be used effectively to solve a whole class of three-dimensional problems of practical interest.

Effect of Thickness

A general three-dimensional solution to Navier's equation for plates of uniform thickness, $2h$, and with plate faces free of stress has previously been constructed by the author, and the results are reported in Ref 2. Perhaps it may be appropriate here to note that the same displacement field is also recovered if one uses a double Fourier integral transform in x and y and, subsequently, a contour integration. This matter is discussed in great detail in Ref 3. Without going into the mathematical details, the general displacement field can be found in the Appendix where it has been written in a more convenient form.

By choosing appropriately the remaining five arbitrary functions, that is, H , H^* , I_1 , I_2 , and I_3 , one may now solve a whole class of three-dimensional linear elastic problems, for example, the problem of a cylindrical hole, an elliptical hole, a crack, a cylindrical inclusion,

² For a historical discussion see Ref 1.

³ See *Proceedings, Workshop on Three-Dimensional Fracture Analysis*, held at Battelle, Columbus, OH, 26–28 April 1976.

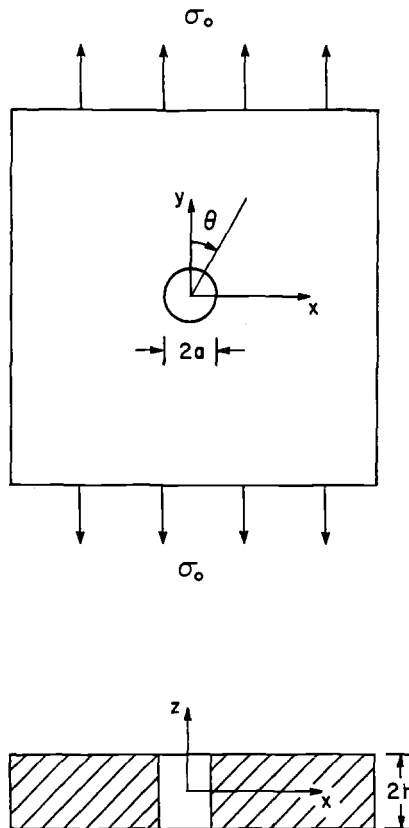


FIG. 1—Geometrical configuration of a plate weakened by a circular hole of radius a .

and so forth. In Ref 4, for example, the author uses the problem of a plate weakened by a cylindrical hole (see Fig. 1) as a vehicle to show how the general solution can be used to construct the three-dimensional stress field. The problem was ultimately reduced to the solution of three equations involving a series of complex eigenfunctions for the determination of the unknown, but constant, coefficients. These equations represent the free-of-stress boundary conditions at the surface of the hole where the θ and r dependence has now been totally eliminated.

Without going into the mathematical details, the system was solved numerically,⁴ and the stress concentration factor at $\theta = \pi/2$ and $r = a$ was computed for various radius-to-thickness ratios, a/h , and for Poisson's ratio of $\nu = 0.33$. The results are presented in Figs. 2 through 7. It may be noted that double precision was used throughout the numerical work and that a very sophisticated algorithm was used for the evaluation of the Bessel modified functions of the second kind.

The results show the stress concentration factor to be sensitive to the ratio of (a/h) and to Poisson's ratio ν . For example, for $\nu = 0.33$ and ratios of $(a/h) \geq 0.5$, it was found that the stress concentration factor attains its maximum in the middle of the plate and decreases parabolically as one approaches the free surfaces. On the other hand, for $(a/h) < 0.5$, the

⁴ It should be noted that we have also constructed the orthogonality condition of these eigenfunctions.

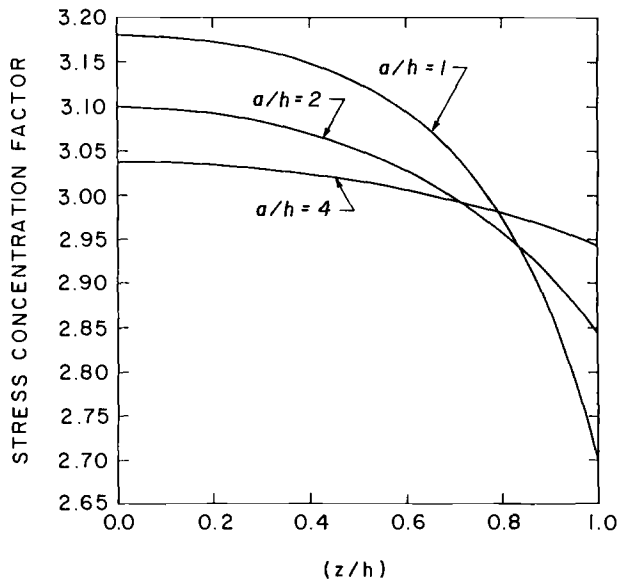


FIG. 2—Stress concentration factor across the thickness for Poisson's ratio $\nu = 0.33$ and various a/h ratios.

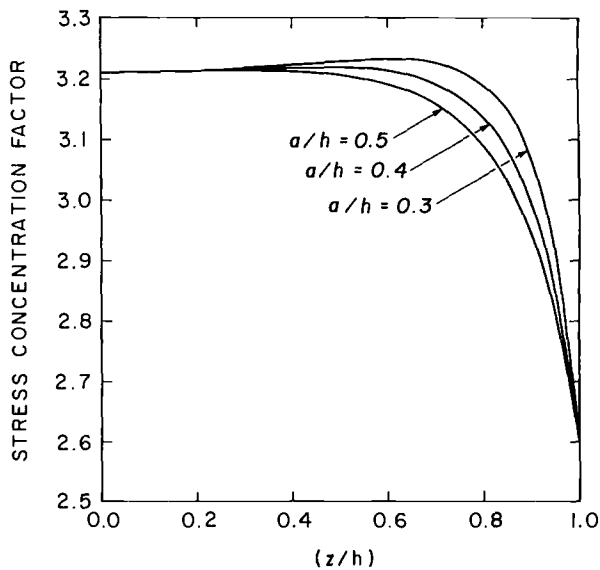


FIG. 3—Stress concentration factor across the thickness for Poisson's ratio $\nu = 0.33$ and various a/h ratios.

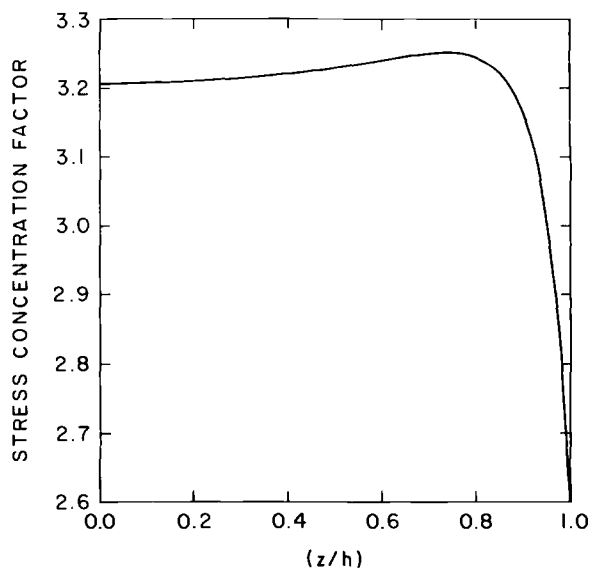


FIG. 4—Stress concentration factor across the thickness for Poisson's ratio of $\nu = 0.33$ and $a/h = 0.2$.

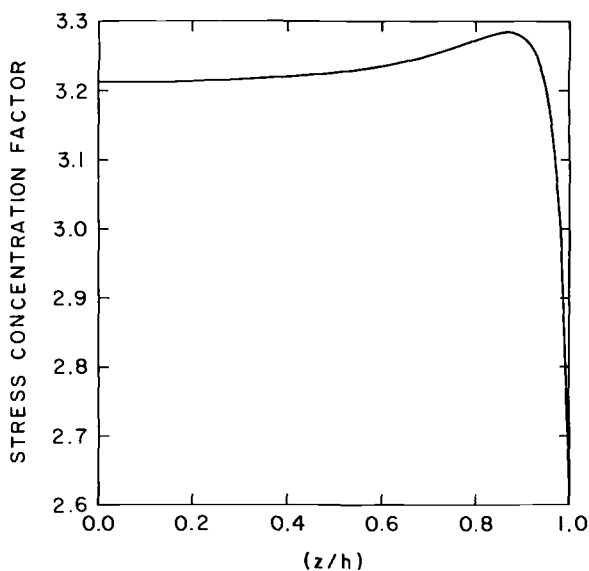


FIG. 5—Stress concentration factor across the thickness for Poisson's ratio of $\nu = 0.33$ and $a/h = 0.1$.

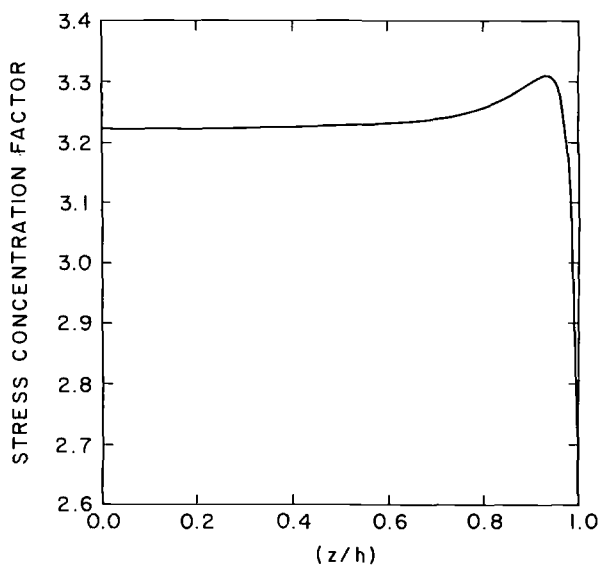


FIG. 6—Stress concentration factor across the thickness for Poisson's ratio of $\nu = 0.33$ and $a/h = 0.05$.

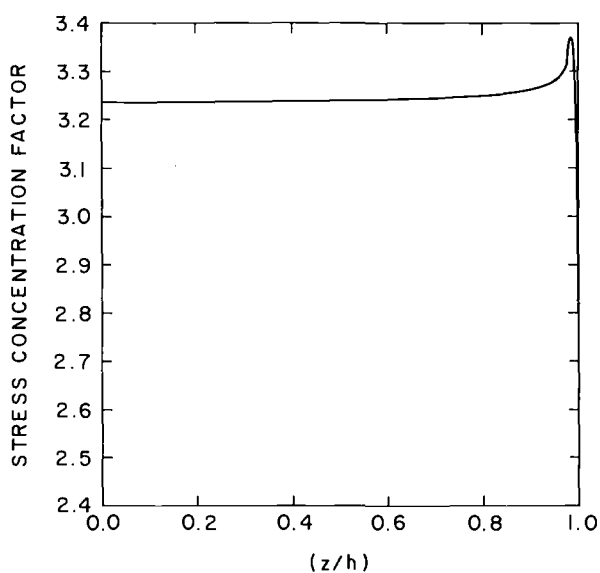


FIG. 7—Stress concentration factor across the thickness for Poisson's ratio of $\nu = 0.33$ and $a/h = 0.01$.

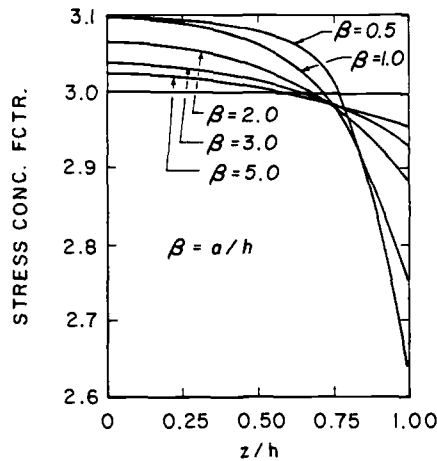


FIG. 8—Stress concentration factor across the thickness for Poisson's ratio $\nu = 0.25$ and various a/h ratios (Alblas 1957).

stress concentration factor attains its maximum close to the plate faces. Moreover, as the ratio of a/h decreases further, the following numerical trends are observed for the stress concentration factor (SCF):

- (a) the magnitude of the rise slowly increases,⁵
- (b) the maximum occurs closer and closer to the free surface so that the depth below the surface approaches the radius of the hole,
- (c) at the surface of the plate it drops rather abruptly, and
- (d) the magnitude at the surface slowly decreases.

It is appropriate at this time to compare our results with those already existing in the literature. Historically, the two-dimensional problem was first studied by Kirsch [5] in 1898 and the stress concentration factor was found to be equal to three. It was not until 1948 that Green [6] constructed a three-dimensional solution which was in an infinite series form. Unfortunately, he did not pursue the solution far enough to extract numerical results. In 1949, Sternberg and Sadowsky [7] used a modified version of the Ritz method to obtain an approximate solution to the problem. Subsequently, in 1957 Alblas [8], applying the same scheme proposed by Green, succeeded in obtaining a solution in a more convenient series from whereby he was able to perform extensive numerical calculations. His results for Poisson's ratio of $\nu = 1/4$ are shown in Fig. 8. For ratios of $(a/h) > 1$ our results are identical to those obtained by Alblas. Moreover, for the ratio of $(a/h) = 1$ the difference is minimal, as can be seen by a comparison of the results in Fig. 9. The small difference is attributed to the fact that Alblas at that time did not have access to modern computer facilities; consequently, he was forced to truncate the system to 14 roots.

Our results on the other hand, reflect the use of 300 roots. Even so, the agreement for ratios of $(a/h) \geq 1$ is remarkably good. For ratios of $(a/h) < 1$, however, more roots are needed to eliminate undesirable oscillations, and therefore he was forced to limit his calculation to ratios of $(a/h) \geq 0.5$.

⁵ The reader should be cautioned that this remark does not necessarily imply that the SCF will increase indefinitely.

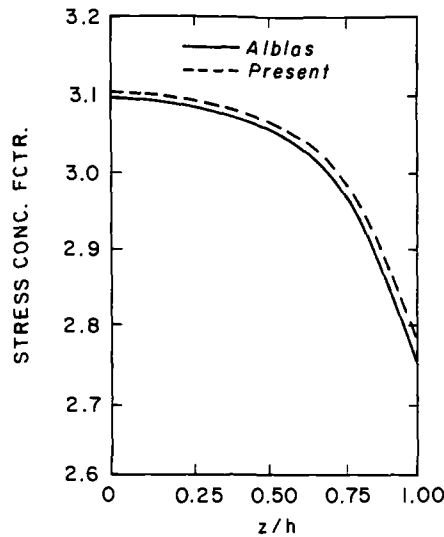


FIG. 9—Comparison of the stress concentration factor for $\nu = 0.25$ and $a/h = 1.0$.

In 1962, Reiss [9] using a perturbation analysis was able to obtain a solution which yielded “three-dimensional” corrections to those of the generalized plane stress. The results are shown in Fig. 10. Finally, in 1966 Youngdahl and Sternberg [10], recognizing the sensitivity of the SCF on the diameter-to-thickness ratio, studied the problem of a half-space with a hole in order to establish the behavior of the SCF for very thick plates. The problem was finally casted into a Fredholm integral equation of the second kind, the solution of which was finally sought numerically. Perhaps it is appropriate at this point to state an observation made by the authors of Ref 10:

the burden of the numerical analysis of the solution established was at least equal to the effort expended on its derivation.

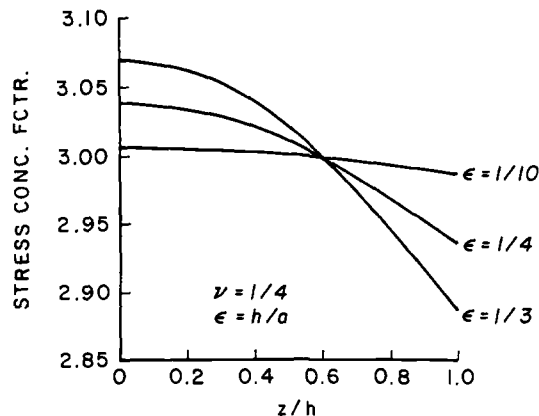


FIG. 10—Stress concentration factor across the thickness for Poisson's ratio $\nu = 0.25$ and various a/h ratios (Reiss 1963).

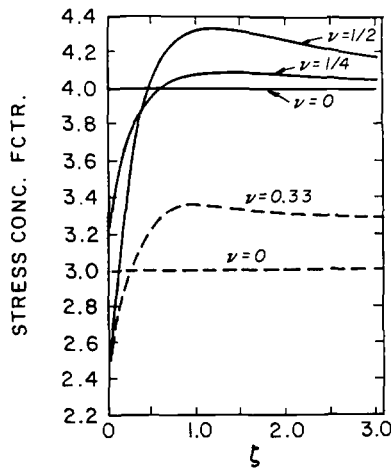


FIG. 11—Comparison of the stress concentration factor in the vicinity of the free surface with results of Ref 10.

The present author also concurs with this observation, for the nature of this problem is such that it does not lend itself to routine numerical calculations.

In any event, their results clearly show the existence of a three-dimensional stress boundary layer that emerges near the edges of the hole in the analogous problem of a plate of finite thickness, as the ratio of the diameter of the hole to the plate thickness becomes very small. Our present results substantiate the existence of such a boundary layer at the vicinity of the free surfaces. In fact, if we examine the local behavior of the rise, for example, for the ratio of $(a/h) = 0.01$, and stretch the variable by letting $\zeta = 100(1 - z/h)$, we observe (see Fig. 11) that the behavior is similar to⁶ that obtained by Youngdahl and Sternberg [10]. We also observe that the rise here is not quite as noticeable as in Fig. 7. This is due to the vertical scale, which the authors of Ref 10 used, and to the stretching of the horizontal variable z/h . In view of the findings of Ref 10, one concludes that the surface effects become dominant and that the amplitude of the characteristic rise ultimately reaches an upper bound.⁷ This matter will be investigated further in the section on stress behavior at the corner.

Finally, it is appropriate to comment on the conditions of plane stress and plane strain. For $(a/h) \rightarrow \infty$, our numerical results give precisely the value of plane stress, that is, the value of three. Similarly, for $\nu = 0$ the value of three is also recovered. This result meets our expectations, for it represents an exact solution.

In the case of plane strain, the boundary planes $z = \pm h$ are thrown to infinity, and simultaneously the boundary conditions must be relaxed by requiring that all stresses and displacements must be finite. Assuming that the radius of the hole is sufficiently large, the author suspects that the SCF at the center of the plate will begin to slowly decrease as the ratio of a/h decreases beyond the value of 0.01, until it finally reaches the value of plane strain. Such an effort, however, requires considerably more computer time than was available to us.

⁶ In Ref 10, the reader should notice that the loading is in both the x and y directions.

⁷ For $a/h = 0.01$ and $\nu = 0.33$, our numerical results show the max value of the SCF to be 3.3675. This value should be very close to the upper bound. It is interesting to note that it is $\approx 3/(1 - \nu^2)$.

Observations On Some Numerical Results

Before we attempt to interpret the physical meaning of the numerical results, particularly at the neighborhood of the intersection between the hole and the free surface, it will be appropriate for us first to examine the numerical results of a well known two-dimensional solution and then, we hope, to make some associations.

Let us consider for the sake of discussion the two curves, I and J , shown on Fig. 12. The curves have been drawn based on a number of calculated points which, for convenience, have been located on the graphs. Furthermore, let us assume that these curves represent the two local stress profiles τ_{xz} and σ_{xx} , respectively, in a body that lies to the right of the vertical axis, has the vertical axis as a boundary, and is symmetric with respect to the z -axis. The stress profiles have been calculated along the line $x = 0.05$. Given this limited information, can one draw a definite conclusion as to whether or not a stress singularity exists at the point $x = z = 0$?

An examination of the stress curves shows that, as one moves from right to left along the line $x = 0.05$, both stresses are initially zero, then rise slowly to reach a maximum, and finally decrease to zero as the value of $z = 0$ is reached. Because the stress drops as one approaches the boundary, one is tempted to conclude that there exists no stress singularity at the point $x = z = 0$. But this would be an erroneous conclusion since this particular stress field represents that of a concentrated line load P on a half space (see Fig. 13), that is

$$\tau_{xz} = -\frac{2P}{\pi r} \sin \phi \cos^2 \phi = -\frac{2P}{\pi} \frac{xz^2}{(x^2 + z^2)^2} = -PI$$

$$\sigma_{xx} = -\frac{2P}{\pi r} \cos \phi \sin^2 \phi = -\frac{2P}{\pi} \frac{x^2 z}{(x^2 + z^2)^2} = -PJ$$

$$\sigma_{zz} = -\frac{2P}{\pi r} \cos^3 \phi$$

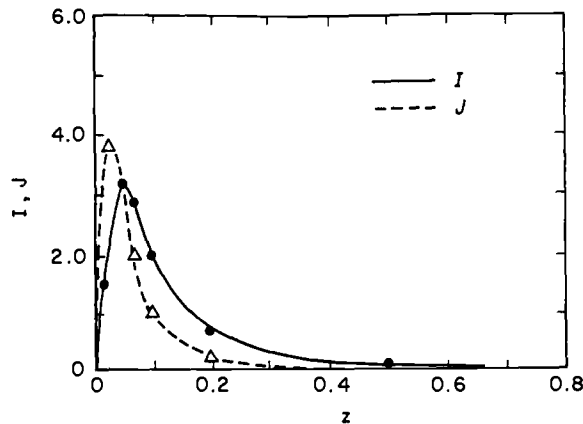


FIG. 12—The functions I and J for $x = 0.05$ and various values of z .

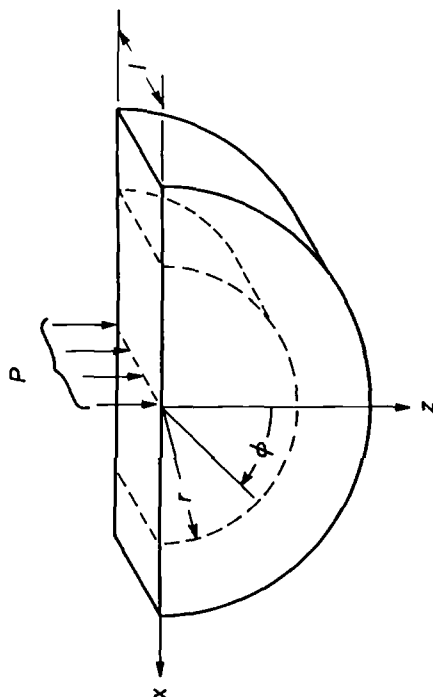


FIG. 13—Geometrical configuration.

where ϕ now represents the angle from the horizontal axis. By examining the above equations more carefully, we notice that the location of the maximum rise depends on the chosen value of x . In particular, I and J attain their maximums at $z = x$ and $z = x/\sqrt{3}$, respectively. This suggests, therefore, that as the value of x becomes smaller and smaller, the rise moves closer and closer to the x -axis while its amplitude increases simultaneously. Furthermore, it should be noted that for a given value of x , similar stress profiles are observed. In view of the above, the author makes the following observations:

1. As one approaches the free surface, the stresses exhibit a rise or a hump.
2. At the surface, the stresses decrease rather abruptly to zero.
3. As x decreases, the amplitude of the rise increases.
4. The analytical solution exhibits the presence of a stress singularity at $x = z = 0$.

Let us next look at another related problem which was studied⁸ by Filon in 1903. He discusses the case shown in Fig. 14a, where the forces P are displaced one with respect to the other. The distribution of shearing stresses over the cross section nn in this case is shown in Fig. 14b. Notice that for small values of the ratio b/c this distribution does not resemble the parabolic distribution given by the elementary theory, and that there are very large stresses at the top and bottom of the beam while the middle portion of the beam is practically free from shearing stresses. One conjectures, therefore, that close to the free surfaces there exists a boundary layer solution. Moreover, we know that at the point of application of the load there exists a stress singularity, the presence of which is not evident from the numerical

⁸ See also Timoshenko and Goodier, *Theory of Elasticity*, 3rd ed., pp. 57–58.

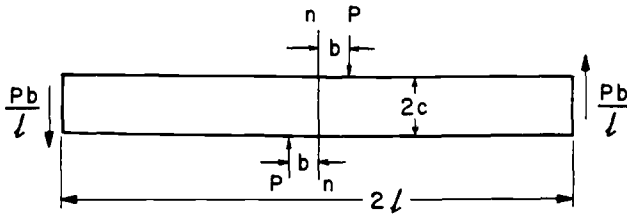


FIG. 14a—Geometrical configuration of a beam subjected to two concentrated loads.

work depicted in Fig. 14b. In fact, the numerical results show the shear stress there to vanish.

It becomes evident from this discussion that even though the numerical results show the stress profiles to vanish at the boundary, this does not necessarily exclude the possibility of a stress singularity being present at certain points of the boundary.

The Stress Behavior at the Corner

Finally it is of some academic and practical interest to examine the behavior of the stress field in the very immediate vicinity of the corner point, that is, the point where the hole meets the free surface of the plate. However, in view of our previous discussion, such information is best if it is extracted by analytical rather than numerical means. Utilizing the local coordinates of the corner point, an asymptotic analysis was carried out for the exponent α of an assumed displacement field $u_i \sim \rho^\alpha$, where $\rho \ll a$. Without going into the mathematical details, the satisfaction of all the boundary conditions of the three-dimensional stress problem

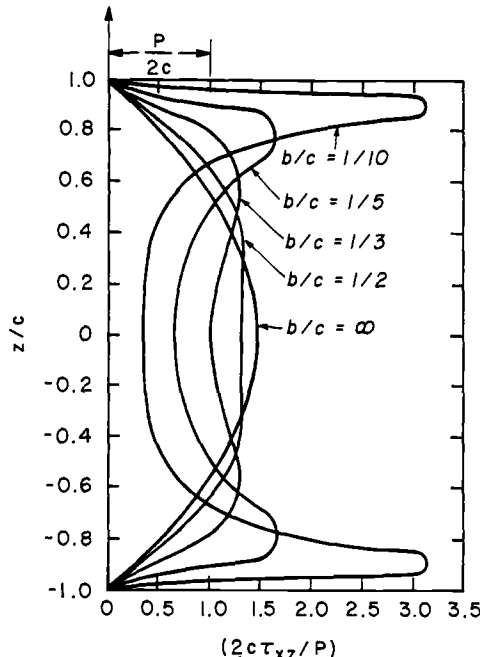


FIG. 14b—The behavior of the shear stress over the Cross Section n-n for various ratios of b/c .

lead to a characteristic equation which has an infinite number of complex roots. It is interesting to note that the first root is the same as that obtained by the Williams solution [11] for a 90° corner with free free-of-stress boundaries, that is, $\alpha = 2.739\ 59 \pm 1.119\ 02$. While this result was to be anticipated on intuitive grounds, it could not be taken for granted. The details of this asymptotic analysis will be reported in a future paper.

In view of the above, one may draw the following conclusions:

1. The solution is derivable from a general three-dimensional solution to Navier's equations.
2. The solution recovers the existing limiting results for thin plates [8,9] as well as for thick plates [10] and bridges the gap between them.
3. For ratios of $(a/h) \geq 0.5$, the maximum stress occurs in the middle plane.
4. For ratios of $(a/h) < 0.5$, the maximum stress occurs close to the free surface (approximately one radius distance away from the surface).
5. The results show the transition between thin and thick plates to occur at a ratio of $(a/h) = 0.5$.
6. As a/h becomes small, there exists in the neighborhood of the free surfaces a boundary layer solution similar to that reported in Ref 10.
7. Depending on the value of the ratio of a/h , the fatigue life of the member may be substantially shorter than that predicted by the two-dimensional elasticity theory.
8. For $\rho \ll a$, there is no stress singularity present at the corner where the hole intersects the free surface of the plate.

The Crack Problem

Inasmuch as the solution of both the hole and the crack problems can be obtained from the same general three-dimensional solution, similar trends are expected to prevail. Therefore, by analogy, one is tempted to conclude the following regarding the stress intensity factor:

1. It will be sensitive to the crack-to-thickness ratio and to Poisson's ratio, ν .
2. It will drop rather abruptly at the free surface.
3. For certain values of c/h , it will attain a maximum at the middle plane and will decrease parabolically as one approaches the free surface.
4. For the remaining values of c/h , the maximum will occur closer to the free surface (approximately half a crack size away), where a small rise will develop.
5. For relatively thick plates, the shear lip will be found to be related to the width of this rise.
6. No conclusion can be drawn from this analysis regarding the corner singularity.

Engineering fracture mechanics can deliver the methodology to compensate for the inadequacies of conventional design concepts that were based on tensile strength or yield strength. While such criteria are adequate for many engineering structures, they are insufficient when the likelihood of cracks exists. Now, after approximately three decades of development, fracture mechanics has become a useful tool in design, particularly with high-strength materials. Interestingly enough, this advancement has been based primarily on the two-dimensional solution of the Griffith crack problem. We believe that the three-dimensional solution of the Griffith crack problem will not only enable us to understand the mechanism of fracture propagation better, but it will also expand our horizons for future

research and, we hope, will contribute to the advancement of the field of fracture mechanics to higher levels of safe design against fracture.

Acknowledgment

The contents of this paper are an outgrowth of some previous work on three-dimensional fracture which was supported by the U.S. Air Force Office of Scientific Research. The author is grateful for this support.

APPENDIX

A general solution to Navier's equations for plates of uniform thickness, $2h$, and with the plate faces free of stress has already been constructed by the author and the results are reported in Ref 2. Thus, without going into the long and tedious mathematical details, the complementary displacement and stress fields may be written in the form:

The Displacement Field

$$\begin{aligned}
 u^{(c)} &= \frac{1}{m-2} \sum_{v=1}^{\infty} A_v \frac{\partial H_v}{\partial x} [2(m-1) \cos(\beta_v h) \cos(\beta_v z) \\
 &\quad + m\beta_v h \sin(\beta_v h) \cos(\beta_v z) - m\beta_v z \cos(\beta_v h) \sin(\beta_v z)] \\
 &\quad + \sum_{n=1}^{\infty} B_n \frac{\partial H_n^*}{\partial y} \cos(\alpha_n h) \cos(\alpha_n z) \\
 &\quad + I_1 - y \frac{\partial I_3}{\partial x} + \frac{1}{m+1} z^2 \frac{\partial^2 I_3}{\partial x \partial y} \\
 v^{(c)} &= \frac{1}{m-2} \sum_{v=1}^{\infty} A_v \frac{\partial H_v}{\partial y} [2(m-1) \cos(\beta_v h) \cos(\beta_v z) \\
 &\quad + m\beta_v h \sin(\beta_v h) \cos(\beta_v z) - m\beta_v z \cos(\beta_v h) \sin(\beta_v z)] \\
 &\quad - \sum_{n=1}^{\infty} B_n \frac{\partial H_n^*}{\partial x} \cos(\alpha_n h) \cos(\alpha_n z) + \frac{3m-1}{m+1} I_3 + I_2 \\
 &\quad - y \frac{\partial I_3}{\partial y} - \frac{1}{m+1} z^2 \frac{\partial^2 I_3}{\partial x^2} \\
 w^{(c)} &= \frac{1}{m-2} \sum_{v=1}^{\infty} A_v H_v \beta_v [(m-2) \cos(\beta_v h) \sin(\beta_v z) \\
 &\quad - m\beta_v h \sin(\beta_v h) \sin(\beta_v z) - m\beta_v z \cos(\beta_v h) \cos(\beta_v z)] \\
 &\quad - \frac{2}{m+1} z \frac{\partial I_3}{\partial y}
 \end{aligned}$$

The Stress Field

$$\begin{aligned}
\frac{1}{2G} \sigma_{xx}^{(c)} &= \frac{2}{m-2} \sum_{v=1}^{\infty} A_v \beta_v^2 H_v \cos(\beta_v h) \cos(\beta_v z) \\
&+ \frac{1}{m-2} \sum_{v=1}^{\infty} A_v \frac{\partial^2 H_v}{\partial x^2} [2(m-1) \cos(\beta_v h) \cos(\beta_v z) \\
&+ m\beta_v h \sin(\beta_v h) \cos(\beta_v z) - m\beta_v z \cos(\beta_v h) \sin(\beta_v z)] \\
&+ \sum_{n=1}^{\infty} B_n \frac{\partial^2 H_n^*}{\partial x \partial y} \cos(\alpha_n h) \cos(\alpha_n z) \\
&+ \frac{\partial I_1}{\partial x} - y \frac{\partial^2 I_3}{\partial x^2} + \frac{1}{m+1} z^2 \frac{\partial^3 I_3}{\partial x^2 \partial y} + \frac{2}{m+1} \frac{\partial I_3}{\partial y} \\
\frac{1}{2G} \sigma_{yy}^{(c)} &= \frac{2}{m-2} \sum_{v=1}^{\infty} \beta_v^2 A_v H_v \cos(\beta_v h) \cos(\beta_v z) \\
&- \frac{1}{m-2} \sum_{v=1}^{\infty} A_v \left[\frac{\partial^2 H_v}{\partial x^2} - \beta_v^2 H_v \right] [2(m-1) \cos(\beta_v h) \cos(\beta_v z) \\
&+ m\beta_v h \sin(\beta_v h) \cos(\beta_v z) - m\beta_v z \cos(\beta_v h) \sin(\beta_v z)] \\
&- \sum_{n=1}^{\infty} B_n \frac{\partial^2 H_n^*}{\partial x \partial y} \cos(\alpha_n h) \cos(\alpha_n z) \\
&+ \frac{2m}{m+1} \frac{\partial I_3}{\partial y} - \frac{\partial I_1}{\partial x} + y \frac{\partial^2 I_3}{\partial x^2} - \frac{1}{m+1} z^2 \frac{\partial^3 I_3}{\partial x^2 \partial y} \\
\frac{1}{2G} \sigma_{zz}^{(c)} &= \frac{m}{m-2} \sum_{v=1}^{\infty} A_v H_v \beta_v^2 [-\beta_v h \sin(\beta_v h) \cos(\beta_v z) \\
&+ \beta_v z \cos(\beta_v h) \sin(\beta_v z)] \\
\frac{1}{G} \tau_{xy}^{(c)} &= \frac{2}{m-2} \sum_{v=1}^{\infty} A_v \frac{\partial^2 H_v}{\partial x \partial y} [2(m-1) \cos(\beta_v h) \cos(\beta_v z) \\
&+ m\beta_v h \sin(\beta_v h) \cos(\beta_v z) - m\beta_v z \cos(\beta_v h) \sin(\beta_v z)] \\
&- \sum_{n=1}^{\infty} B_n \left[2 \frac{\partial^2 H_n^*}{\partial x^2} - \alpha_n^2 H_n^* \right] \cos(\alpha_n h) \cos(\alpha_n z) \\
&+ 2 \left(\frac{m-1}{m+1} \right) \frac{\partial I_3}{\partial x} + 2 \frac{\partial I_2}{\partial x} - \frac{2}{m+1} z^2 \frac{\partial^3 I_3}{\partial x^3} - 2y \frac{\partial^2 I_3}{\partial x \partial y}
\end{aligned}$$

$$\begin{aligned}
\frac{1}{G} \tau_{xz}^{(c)} = & -\frac{2m}{m-2} \sum_{\nu=1}^{\infty} A_{\nu} \frac{\partial H_{\nu}}{\partial x} \beta_{\nu} [\cos(\beta_{\nu} h) \sin(\beta_{\nu} z) \\
& + \beta_{\nu} h \sin(\beta_{\nu} h) \sin(\beta_{\nu} z) + \beta_{\nu} z \cos(\beta_{\nu} h) \cos(\beta_{\nu} z)] \\
& - \sum_{n=1}^{\infty} B_n \frac{\partial H_n^*}{\partial y} \alpha_n \cos(\alpha_n h) \sin(\alpha_n z) \\
\frac{1}{G} \tau_{yz}^{(c)} = & -\frac{2m}{m-2} \sum_{\nu=1}^{\infty} A_{\nu} \beta_{\nu} \frac{\partial H_{\nu}}{\partial y} [\cos(\beta_{\nu} h) \sin(\beta_{\nu} z) \\
& + \beta_{\nu} h \sin(\beta_{\nu} h) \sin(\beta_{\nu} z) + \beta_{\nu} z \cos(\beta_{\nu} h) \cos(\beta_{\nu} z)] \\
& + \sum_{n=1}^{\infty} B_n a_n \frac{\partial H_n^*}{\partial x} \cos(\alpha_n h) \sin(\alpha_n z)
\end{aligned}$$

where A_{ν} and B_n are functions of β_{ν} and α_n , respectively,

$$\alpha_n \equiv \frac{n\pi}{h} \quad n = 1, 2, 3, \dots,$$

β_{ν} are the roots of the transcendental equation

$$\sin(2\beta_{\nu} h) = -2(\beta_{\nu} h)$$

and the functions H_{ν} and H_n^* satisfy the reduced wave equation, that is,

$$\frac{\partial^2 H_{\nu}}{\partial x^2} + \frac{\partial^2 H_{\nu}}{\partial y^2} - \beta_{\nu}^2 H_{\nu} = 0$$

and

$$\frac{\partial^2 H_n^*}{\partial x^2} + \frac{\partial^2 H_n^*}{\partial y^2} - \alpha_n^2 H_n^* = 0$$

and I_1 , I_2 , and I_3 are two-dimensional harmonic functions such that

$$I_1 = \text{Im} \phi$$

$$I_2 = \text{Re} \phi$$

References

- [1] Folias, E. S., *International Journal of Fracture*, Vol. 16, No. 4, August 1980, pp. 335-348.
- [2] Folias, E. S., *Journal of Applied Mechanics*, Vol. 42, No. 3, September 1975, pp. 663-674.
- [3] Wilcox, C. H., "Completeness of the Eigenfunctions for Griffith Cracks in Plates of Finite Thickness," Interim Report, Department of Mathematics, University of Utah, Salt Lake City, UT, December 1978.

- [4] Folias, E. S. and Wang, J. J., "On the Three-Dimensional Stress Field Around a Circular Hole in a Plate of Arbitrary Thickness," College of Engineering Report, University of Utah, Salt Lake City, UT, January, 1985.
- [5] Kirsch, G., *Zentralblatt verein Deutscher Ingenieure*, Vol. 42, 1898, p. 797.
- [6] Green, A. E., *Transactions of the Royal Society of London, Series A*, Vol. 240.285, 1948, p. 561.
- [7] Sternberg E. and Sadowsky, M. A., *Journal of Applied Mechanics*, Vol. 16, 1949, pp. 27-38.
- [8] Alblas, J. B., "Theorie van de driedimensionle spanningstodestand in een doorboorde platt," Ph.D. dissertation, Technische Hogeschool Delft, Amsterdam, The Netherlands, 1957.
- [9] Reiss, E. L., "Extension of an Infinite Plate with a Circular Hole, *Journal of the Society for Industrial and Applied Mathematics*, Vol. 11, No. 4, 1963, p. 840.
- [10] Youngdahl, C. K. and Sternberg, E., *Journal of Applied Mechanics*, December 1966, pp. 855-865.
- [11] Williams, M. L., *Journal of Applied Mechanics*, Vol. 19, 1952, p. 526.

Three-Dimensional Effects Affecting the Precision of Lifetime Predictions

REFERENCE: Kordisch, H. and Sommer E., "Three-Dimensional Effects Affecting the Precision of Lifetime Predictions," *Fracture Mechanics: Nineteenth Symposium, ASTM STP 969*, T. A. Cruse, Ed., American Society for Testing and Materials, Philadelphia, 1988, pp. 73–87.

ABSTRACT: A series of laboratory experiments on smooth and side-grooved compact specimens, as well as plates under tension with surface flaws, has been reevaluated by means of three-dimensional elastic-plastic finite-element analyses. Particular emphasis is laid on the calculation of the local crack-tip loading parameter, J , and of the local constraint factor, q . These parameters are correlated with experimental findings concerning initiation and stable crack propagation. A first-guess correlation between q and the slope of $J(\Delta a)$ curves is established.

KEY WORDS: fracture mechanics, finite-element method, $J(\Delta a)$ curves, initiation, crack propagation, triaxiality of the stress-strain state (constraint)

The transferability of results obtained under idealized conditions (as for instance in two-dimensional specimens) to components in service is limited, especially if precise lifetime predictions are needed. Experimental and numerical investigations of three-dimensional fracture processes under increasing complexity of geometry and load parameters help to broaden the basis for a better assessment of components.

If existing defects of cracks determine the lifetime of components, one of the important problems is the precise assessment of cracks which show a strong variation of the local loading parameter, for example J , as well as a strong variation of the local fracture resistance along their contour. This variation is caused by a variety of interacting parameters. A separation of these interacting parameters needs investigation of idealized situations. Therefore, the following considerations will be based on the simplifying assumption that the local initiation and growth of cracks depends on (a) the local value of the loading parameter, for example J , and (b) the local fracture resistance, influenced by the triaxiality of the stress-strain state (constraint).

General Approach

It is assumed that J is a suitable parameter to describe the local crack initiation and the local stable crack growth. A quantitative analysis requires that, for the corresponding region of the crack contour, the degree of triaxiality can be analyzed and related to the fracture resistance.

¹ Head, Numerical Stress Analysis, and director, respectively, Fraunhofer-Institut für Werkstoffmechanik, D7800 Freiburg, Federal Republic of Germany.

Following a definition by Clausmeyer [1], the quotient of multiaxiality will be introduced as

$$q = \frac{\sigma_v}{\sigma_H} \quad (1)$$

where

$$\sigma_v = \frac{1}{\sqrt{2}} ((\sigma_1 - \sigma_2)^2 + (\sigma_3 - \sigma_1)^2 + (\sigma_2 - \sigma_3)^2)^{1/2}$$

equals equivalent stress,

$$\sigma_H = \frac{\sigma_{xx} + \sigma_{yy} + \sigma_{zz}}{3}$$

equals hydrostatic stress, and σ_1 , σ_2 , σ_3 equal the principle stresses.

Alternatively, a plane-strain constraint factor has been introduced (for example, in Ref 2)

$$t = \frac{\sigma_{xx}}{\sigma_{yy} + \sigma_{zz}} \quad (2)$$

where σ_{xx} , σ_{yy} , and σ_{zz} are stress components in x , y , and z directions (the crack front is parallel to the x direction).

An attempt is made in this study to reevaluate several postyield fracture experiments on compact specimens with and without side grooves by three dimensional elastic-plastic finite-element analyses. From the comparison of local and average J -values and constraint factors q or t with the experimental J_i and $J(\Delta a)$, a model for the correlation of the fracture resistance with constraint is derived.

At the Fraunhofer-Institut für Werkstoffmechanik (IWM) a series of experiments was performed on different steels at different temperatures using compact specimens. Two specimens (smooth and 20% side-grooved, with a side-groove radius, r , of 0.25 mm) with a thickness, B of 20 mm from the reactor-steel alloy 22Ni-Mo-37Cr tested at room temperature were selected for this study. The force-displacement curves and the $J(\Delta a)$ curves from the experiments are given in Figs. 1 and 2. From the fracture surfaces in the insert of Fig. 1, a significant tunneling effect of the smooth specimen can be seen. More details about the experiments are given in Ref 3.

In order to evaluate the loading parameter J and the constraint values mentioned above, three-dimensional elastic-plastic finite-element analyses were carried out, using the program for automatic dynamic incremental nonlinear analysis (ADINA) [4]. The finite-element model (FEM) (Fig. 3) consists of 112 (20-noded) elements built up in four layers over the half-thickness. Because of symmetry only one-quarter of the specimen is idealized. The original stress-strain curve of the material is modeled by a multilinear curve. To ensure the $1/r$ singularity in the strains, collapsed isoparametric elements with multiple independent crack tip nodes are used (with midside nodes remaining in the midside position). For the side-grooved specimen the elements adjacent to the crack plane are distorted in the thickness direction. The loading of the specimen is simulated by imposing constant displacement increments along a line representing the bolts. A total of ten displacement increments is

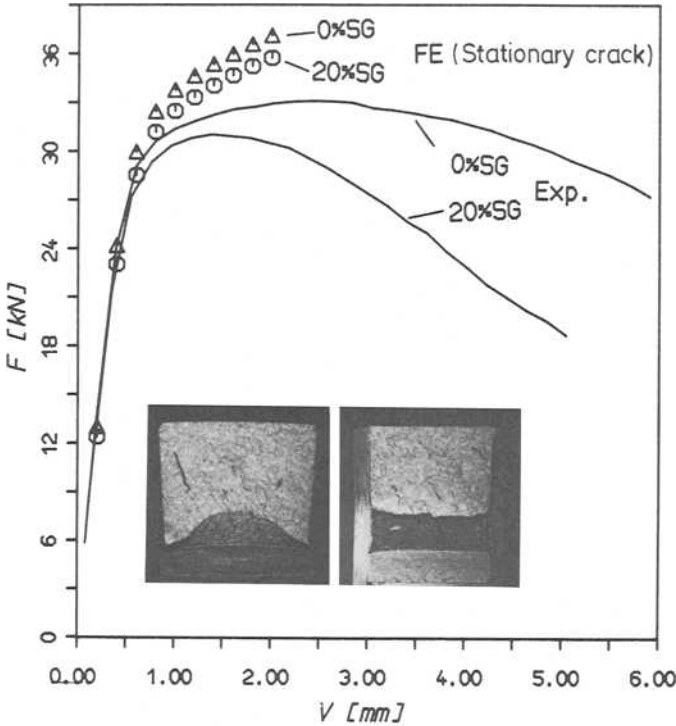


FIG. 1—Compact specimens (smooth and 20% side-grooved): load-displacement curves.

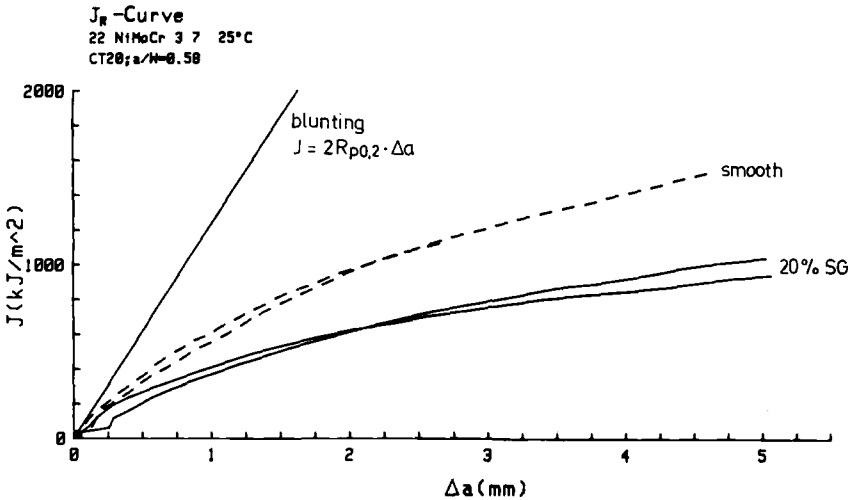


FIG. 2—Compact specimens (smooth and 20% side-grooved): $J(\Delta a)$ curves.

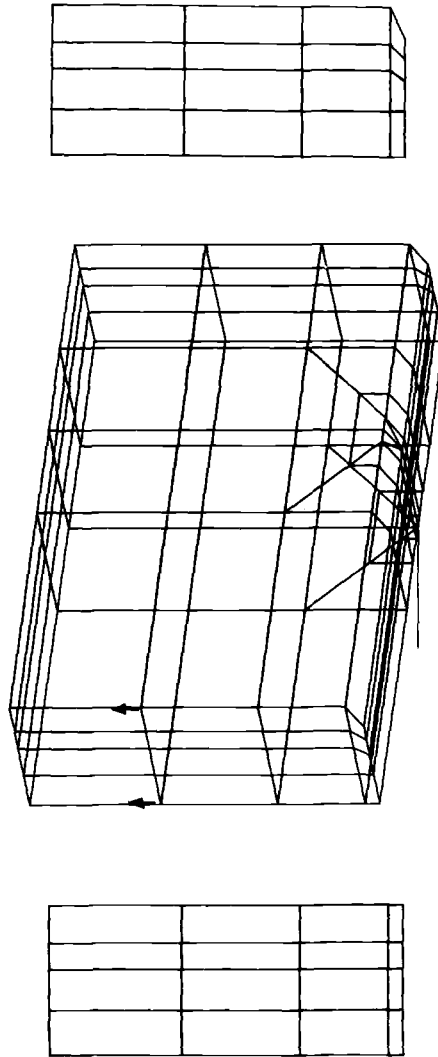


FIG. 3—Compact specimens (smooth and 20% side-grooved): three-dimensional finite-element model.

used. In Fig. 1 the calculated force-displacement results are plotted by symbols. Since stable crack growth is not simulated in this analysis the agreement between experiment and simulation is fairly good only up to initiation.

Details of the FEM Results

The local value of the loading parameter J is calculated along the three-dimensional crack front by the "virtual crack extension method" as implemented in the IWM version of ADINA [5]. Figure 4 shows the variation of J for the smooth specimen along the crack front for different load-line displacements, similar to those found in previous analyses [6]: the crack tip loading parameter J has a maximum in the center of the specimen and decreases towards the surface. The ratio of $J(\text{center})$ to $J(\text{surface})$ increases with the applied load. The respective results for the side-grooved specimen are plotted in Fig. 5. Here it is important to note that J has a more uniform distribution along the crack front with a significant rise directly at the notch. This sudden rise is not yet fully understood but may be due to the fact that at the root of the notch the virtual crack extension applied not only affects the fatigue crack but also a fictitious crack formed by the notch. These J -values at the notch are not considered for further discussion.

Similar results are reported by deLorenzi and Shih [2] with a peak at the side groove in the elastic case, but for increasing plastic deformations this peak decreases. To solve this problem completely, more effort is needed concerning the modeling of the notch.

The constraint factors q and t are calculated at the integration points near the ligament,

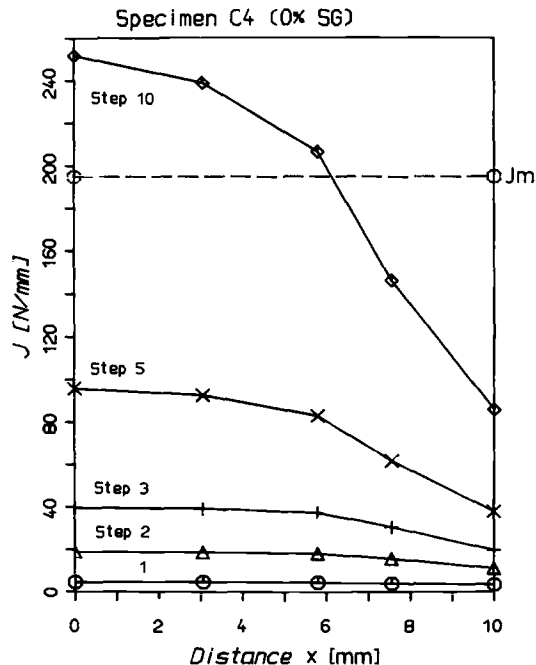


FIG. 4—Smooth specimen: variation of J along the crack front.

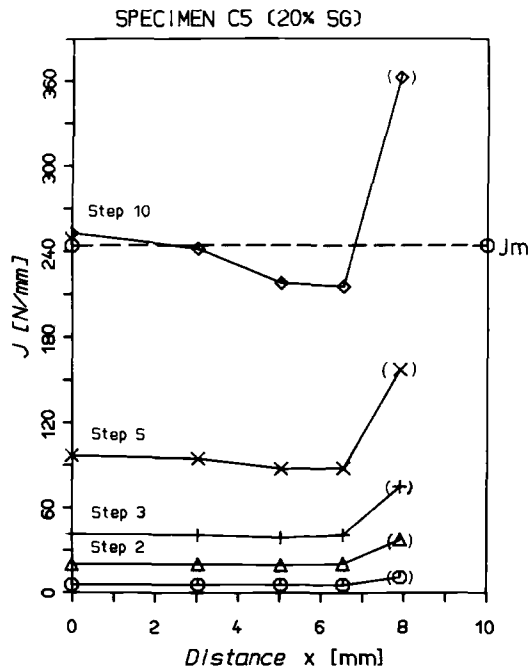


FIG. 5—Twenty percent side-grooved specimen: variation of J along the crack front.

close to the crack front. The local q -values according to Eq 2 are normalized by the plane strain q -value with

$$q_{\text{plane strain}} = \frac{3(1 - 2\nu)}{2(1 + \nu)}$$

evaluated under the assumption of $\sigma_y = \sigma_z \neq 0$ and $\sigma_x = \nu(\sigma_y + \sigma_z)$, with ν = Poisson's ratio.

During the analysis it turned out that q and t have the same evidence in defining the amount of triaxiality, but q is more sensitive than t . Therefore, the discussion is restricted on q .

Figures 6 and 7 show the variation of the q -factor along the crack front evaluated at the closest Gauss points (at $r = 0.2$ mm). The q -values are lowest in the center of the specimen—this means high triaxiality or constraint—with only little variation except for points near the surface where q rises significantly for the smooth specimen. For the side-grooved specimen, q is constant over the major part of the crack front, rises near the notch and drops down at the root of the notch. With increasing load (higher step number) q decreases, but seems to reach a limit value at about $q = 0.6$ in the center.

Interpretation and Application

For respective load levels, the maximum J at the center has about the same values for the two types of specimens. Also the constraint factor q has the same limiting value $q = 0.6$ at the center of the specimen. Of course, these constraint values depend on the distance of the evaluation point from the crack tip, see Figs. 8 and 9.

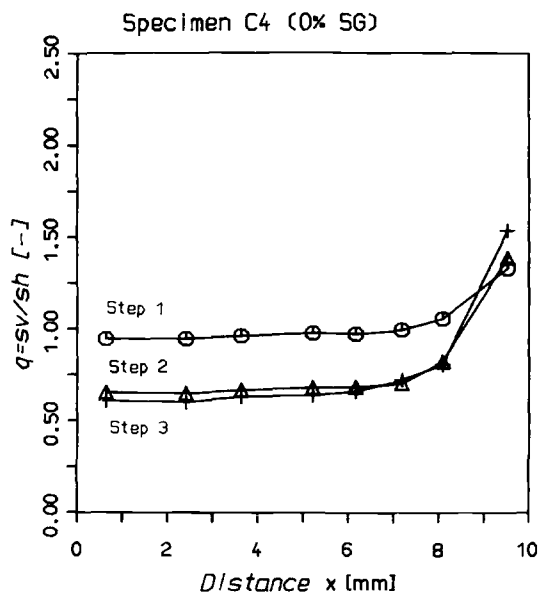


FIG. 6—Smooth specimen: variation of normalized q -values along the crack front.

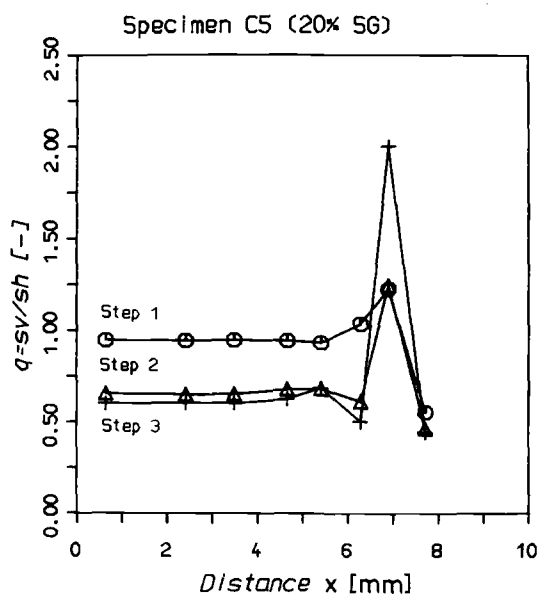


FIG. 7—Twenty percent side-grooved specimen: variation of normalized q -values along the crack front.

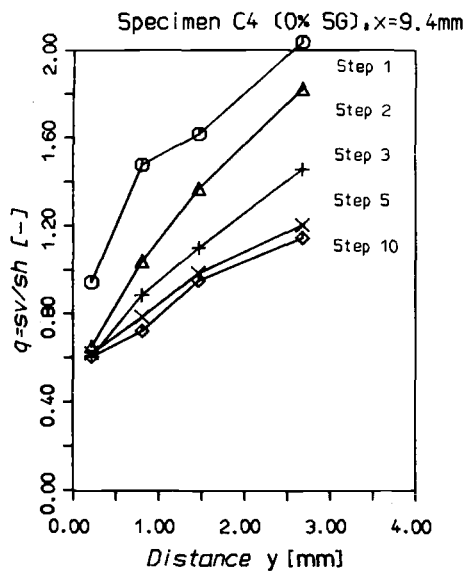


FIG. 8—Smooth specimen: normalized q -values at different distances r in the center of the specimen.

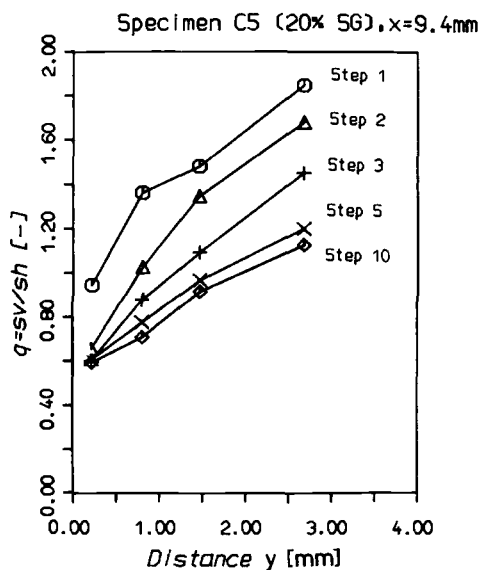


FIG. 9—Twenty percent side-grooved specimen: normalized q -values at different distances r in the center of the specimen.

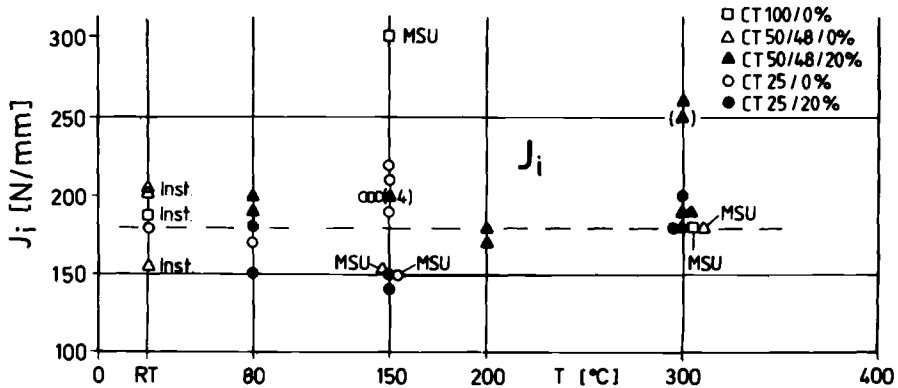


FIG. 10—Experimental results of J_i [7] for compact tension specimens of widths equal to 25, 48, 50, or 100 mm and either smooth or 20% side-grooved.

If crack initiation is considered as a local phenomenon only dependent on the local J and the local constraint, these results do not suggest any difference for the first initiation, J_i , between smooth and side-grooved compact specimens. Although a safe detection of first initiation in the experiment is extremely difficult, a systematic evaluation for a reactor steel (Fig. 10 [7]) indeed confirms this conclusion.

To apply the results of this analysis to the assessment of stable crack extension, it must be assumed that the local constraint values do not change too much after initiation. This assumption is to some degree confirmed by an additional evaluation of numerical results for a smooth specimen with crack extension from Ref 5. Figure 11 shows the variation of q along the three-dimensional crack front for the three final load steps after significant crack propagation had taken place. Again, a limiting value of $q = 0.6$ seems to prevail in the center of the specimen.

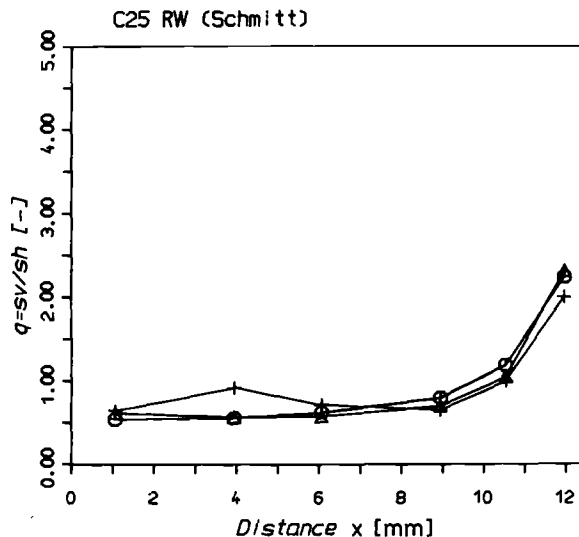


FIG. 11—Smooth compact specimen: normalized q -values along the crack front (three-dimensional calculation with simulation of stable crack growth).

In previous analyses it has been shown that the experimental evaluation of J corresponds to the average value of the local J -values obtained from numerical three-dimensional analyses

$$J_m = J_{\text{exp}} = \frac{1}{B} \int J(b)db$$

Therefore, in order to discuss experimental or numerical J - R curves it seems rational to consider average value of J across the specimen thickness.

To account for the variation of the constraint q , the same averaging procedure has also been applied for q

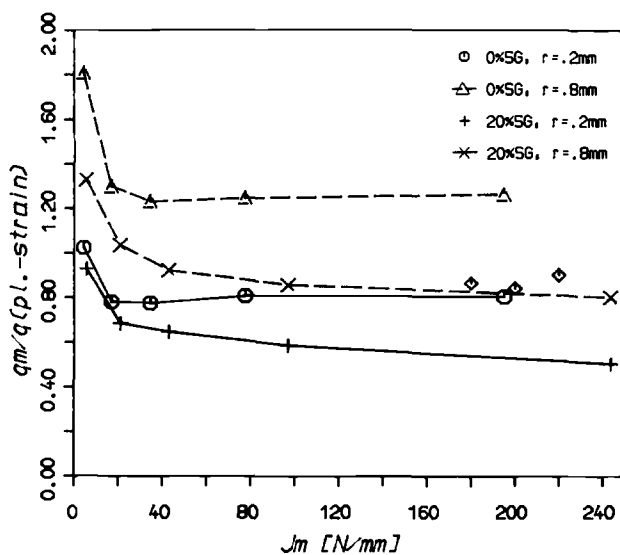
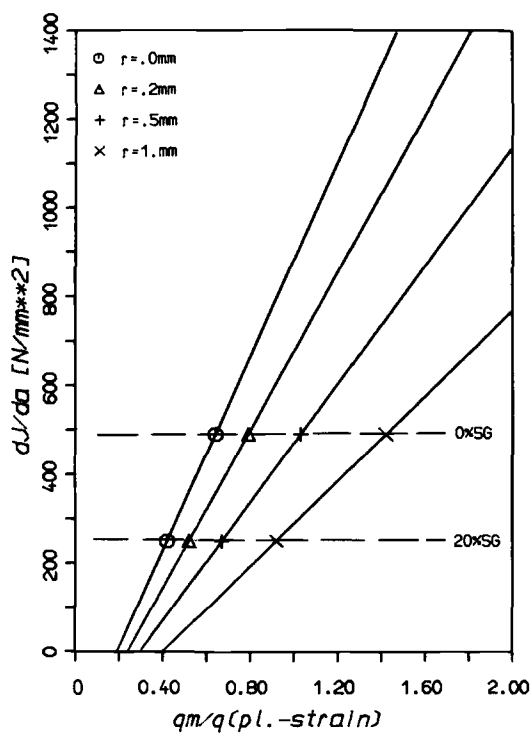
$$q_m = \frac{1}{B} \int q(b)db$$

Opposed to the local values at the center, the average values of both the J -integral and the constraint factor are different for the smooth and the side-grooved specimen. This is demonstrated in Fig. 12, where the normalized q_m evaluated at two distances from the crack front are plotted versus J_m . The smooth and the side-grooved specimens lie on clearly distinct curves. The values obtained from Ref 5 follow the general trend. This gives rise to the hope that the average q_m is a candidate parameter to explain the different slopes of the experimental $J(\Delta a)$ curves for the smooth and the side-grooved specimens, $\Delta J/\Delta a = 490 \text{ N/mm}^2$ and 250 N/mm^2 , respectively. In Fig. 13 these slopes are plotted versus q_m evaluated at different distances r from the crack front. The value for $r = 0$ has been obtained by extrapolation. For every fixed value of r , two points of slope and constraint are defined which define in a first approximation a linear relationship between $\Delta J/\Delta a$ and q_m .

Using this model, a series of fictitious $J(\Delta a)$ curves may be constructed (Fig. 14) by assuming different q_m , for example, caused by different specimen geometries. This was only done to demonstrate that a variation of q_m not larger than that encountered in the analyses of the smooth and the side-grooved specimens may explain this enormous variation of the $J(\Delta a)$ curves.

In a second step, the authors attempted to use this correlation of slope and constraint to evaluate, at least qualitatively, the development of the crack front in the two experiments. To do so it is assumed that this correlation applies to local values as well. Figure 15 gives the estimated crack extensions for two different load levels for the smooth (solid line) and the side-grooved (dashed line) specimens. For the smooth specimen the tunneling behavior is found with no initiation at the surface. For the side-grooved specimen the correlation proposes a crack propagation which is similar to that of the smooth specimen in the interior but with a distinct acceleration at the surface, even if the somewhat doubtful J -values at the root of the notch are replaced by those from the neighboring position to the inside. Surprisingly enough, this acceleration may be found on the fracture surface of the experiment (Fig. 1).

As a final application of the proposed correlation, the behavior of a part-through crack in a plate under tension [3] is reevaluated. The calculated local J -values are given in Fig. 16 and the q -values in Fig. 17. Here it is remarkable that q is significantly higher than for the compact specimens, which means that the triaxiality is lower for the part-through crack (PTC).

FIG. 12—Average q_m versus average J_m .FIG. 13—Correlation between the slopes $\Delta J/\Delta a$ and q_m based on experimental results.

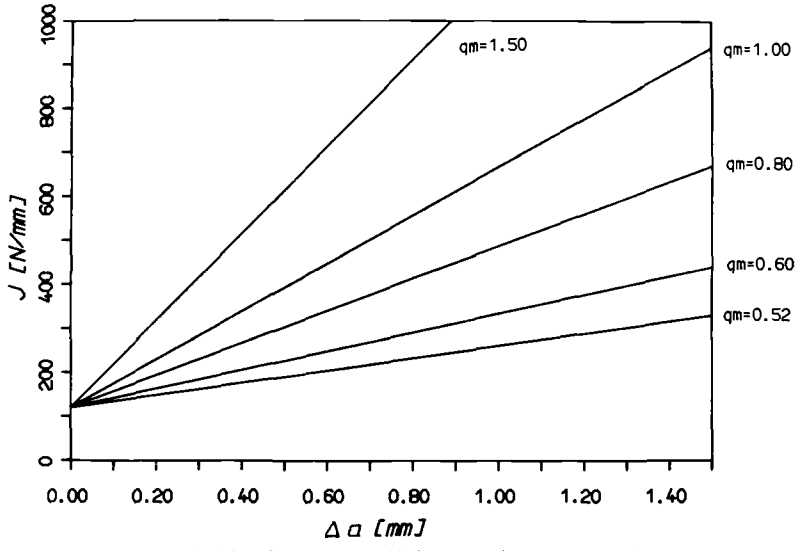


FIG. 14—Constructed $J(\Delta a)$ curves (parameter, q_m).

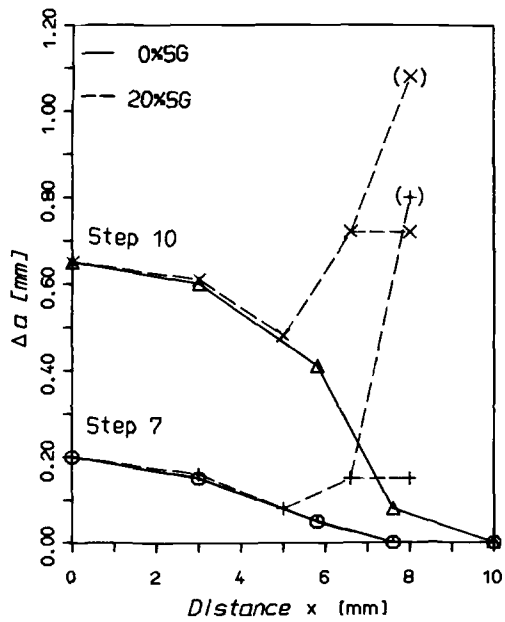


FIG. 15—Qualitative crack extension for the smooth and side-grooved specimens.

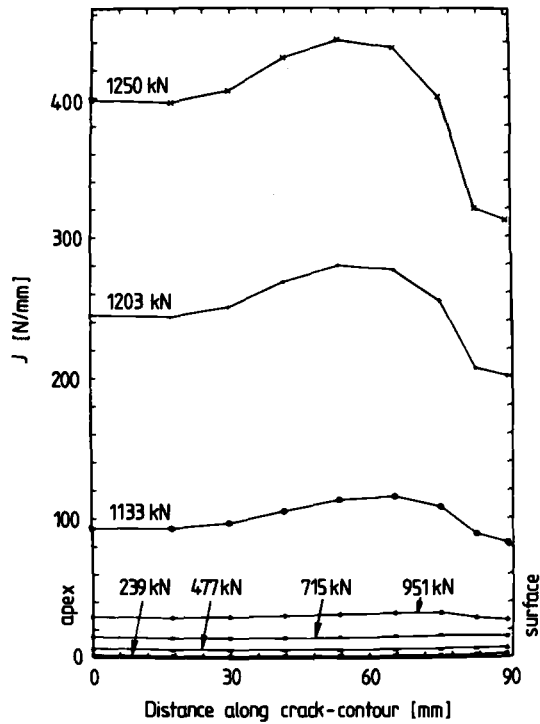


FIG. 16—Part-through crack in a plate: variation of J along the crack contour [3].

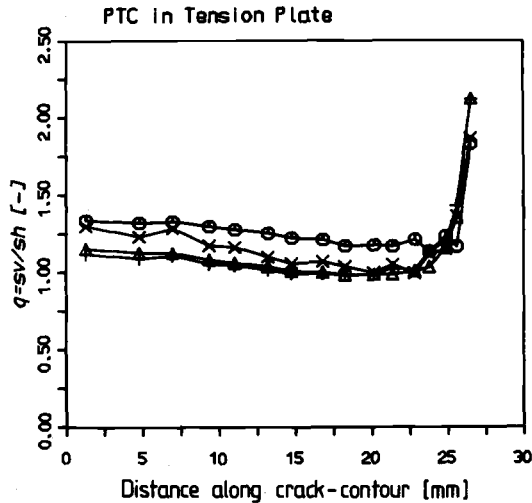


FIG. 17—Part-through crack in a plate: variation of normalized q -values along the crack contour.

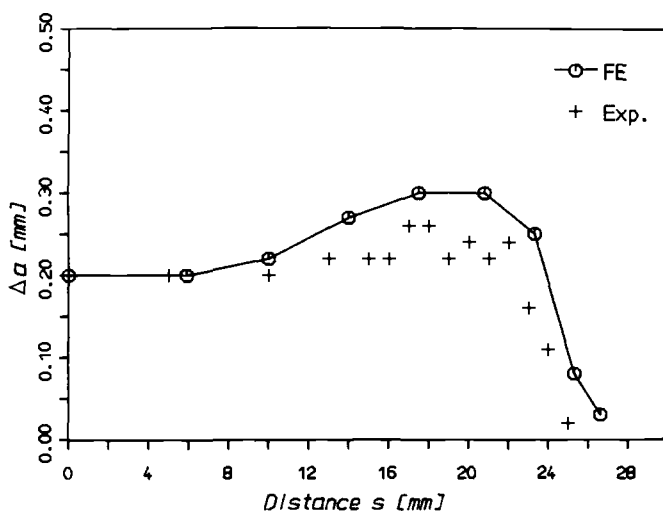
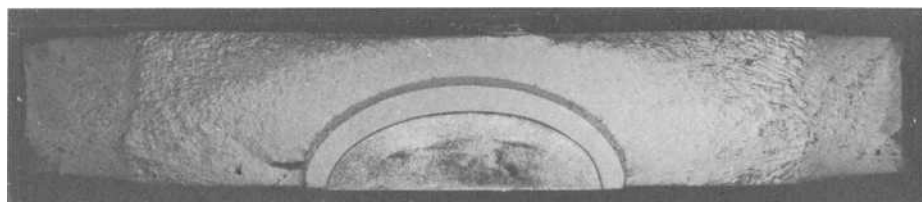


FIG. 18—Part-through crack in a plate: local crack extension along the crack contour.

The experimentally observed local crack propagation is plotted in Fig. 18 together with the prediction. The experimental values have been calibrated to match the prediction at the deepest point. The canoeing effect is obtained and the overall agreement is very good. At first glance it may seem that the same shape might have been predicted just from the variation of J alone without taking into account the constraint. That this is not so is clearly demonstrated at the surface where J alone would have led to a predicted crack growth of significant size, whereas in the experiment the crack did not initiate at the surface.

Conclusions

A combined experimental and numerical evaluation has shown that

1. The constraint factor q (the ratio between equivalent and hydrostatic stress) is a suitable parameter to characterize the local stress-strain state near the front of crack configurations analyzed in this study.
2. From the specimens analyzed a correlation could be established between the average value J_m of the loading parameter and the average value q_m of the constraint factor.
3. From this correlation not only the range of $J(\Delta a)$ curves could be explained, but also qualitative predictions of crack shape developments of compact specimens and part-through cracks in a plate could be established. To confirm the quantitative correlations found in this study, further experimental and numerical efforts are also needed. [For example, see Refs 8 and 9.]

References

- [1] Clausmeyer, H., *Konstruktion*, Vol. 20, 1968, pp. 395–401.
- [2] deLorenzi, H. G. and Shih, C. D., *International Journal of Fracture*, Vol. 21, 1983, pp. 195–220.
- [3] Hodulak, L. and Stöckl, H., "Bestimmung von J -Rißwiderstandskurven an Platten mit Oberflächenrissen," Technical Report W 11/85, Fraunhofer-Institut für Werkstoffmechanik, Freiburg, Federal Republic of Germany, September 1985.
- [4] Bathe, K. H., "ADINA, a Finite-Element Program for Automatic Dynamic Incremental Nonlinear Analysis," Report 82 448-1, Massachusetts Institute of Technology, Cambridge, MA, 1980.
- [5] Schmitt, W., "Three-Dimensional Finite-Element Simulation of Post-Yield Fracture Experiments," "Computational Fracture Mechanics—Nonlinear and 3D Problems," *International Journal of Pressure Vessels and Piping*, Vol. 85, 1984, pp. 119–131.
- [6] Schmitt, W. and Keim, E., "Numerical Aspects of Elastic-Plastic Fracture Mechanics Including 3D Applications," *Advances in Elastic-Plastic Fracture Mechanics*, L. H. Larsson Ed., Applied Science Publishers Ltd., London, 1979.
- [7] Blauel, J. G., Hodulak, L., Hollstein, T., and Voss, B., *International Journal of Pressure Vessels and Piping*, Vol. 17, 1984, pp. 139–162.
- [8] Steenkamp, P. A. J. M., in *Fracture Control of Engineering Structures, Proceedings*, Vol. 1, Sixth European Conference on Fracture, 1986, pp. 15–31.
- [9] Kienzler, R., Schmitt, W., and Sommer, E., "On the Assessment of Local Stress State Along 3D Crack Contours," EUROMECH-Kolloquium, Stuttgart, Federal Republic of Germany, 1985.

Three Dimensions Versus Two Dimensions in Fracture Mechanics

REFERENCE: Swedlow, J. L., "Three Dimensions Versus Two Dimensions in Fracture Mechanics," *Fracture Mechanics: Nineteenth Symposium, ASTM STP 969*, T. A. Cruse, Ed., American Society for Testing and Materials, Philadelphia, PA, 1988, pp. 88–98.

ABSTRACT: This study shows that modern-day fracture mechanics has strictly two-dimensional origins. Certain difficulties arise, for example, in meeting fatigue crack-front straightness requirements. Some insight into this problem is available from an analytical study of an elastic thick plate with a central crack, the M(T) specimen. The study found that modest changes in the crack-front shape have a dramatic effect on the distribution of G , the elastic energy release rate. Further examination of the internal stress distribution shows that there is no region in the vicinity of the crack front that can be credibly described as plane stress, whereas an interior region sensibly replicates plane strain. Finally, a call is issued for the development of a three-dimensional fracture mechanics.

KEY WORDS: fracture mechanics, two-dimensional fracture mechanics, three-dimensional fracture mechanics

From the very outset, the development of what has become known as linear elastic fracture mechanics (LEFM) has been based on two-dimensional technology. Consider these milestones in the theoretical basis of LEFM:

1. The fundamental paper by Inglis [1] gave us a firm analytic foundation for the stresses in the vicinity of a crack in an elastic plate. This is definitely a planar or two-dimensional analysis, and it has tempered our thinking ever since its appearance in 1913.
2. The landmark work by Griffith [2,3] established the conceptual basis for fracture mechanics and is based on Inglis's paper; it too, is limited to two-dimensional configurations.
3. Irwin's crack-healing analysis [4] served to relate the energy release rate, G , to the stress-intensity factor, K , derived from Westergaard's two-dimensional analysis [5] of the crack problem.
4. Williams's eigenseries analysis [6] of crack-tip stresses is incontrovertibly two-dimensional. This work has become the primary background for many analyses to follow, including all collocation work and finite-element work utilizing the displacement extrapolation method to extract K values.

Hence, the theoretical basis of LEFM is exclusively two-dimensional. This characteristic has limited our view of the actual problem from the earliest stages to the point where we, the technical community, are now hard-pressed to contemplate the problem in other terms.

In the same manner, the development of experimental and testing procedures has followed

¹ Professor, Department of Mechanical Engineering, Carnegie-Mellon University, Pittsburgh, PA 15213.

a two-dimensional track. The pioneering work of Brown and Srawley, as reported in two ASTM Special Technical Publications [7,8], was a series of exercises designed to demonstrate that fundamentally two-dimensional test pieces could be used as valid fracture test specimens. Central to this view is the notion that the crack front runs straight through the specimen. Even the impact testing devised by Pellini and his co-workers² [9] involved two-dimensional test specimens. Finally, when the ASTM Test Plane-Strain Fracture Toughness of Metallic Materials (E 399) emerged in 1970 as a tentative method, it was by definition two-dimensional, the culmination of all the two-dimensional technology that preceded it.

However, there has since emerged a considerable body of evidence which makes clear that the real fracture problem is three-dimensional. An early indication was given by Kaufman [10], writing on plane-strain fracture toughness testing performed by ASTM Test E 399, in which he states, "Perhaps the most frustrating of all requirements [in E 399] is that on fatigue crack-front straightness." The problem here is that, as the fatigue crack grows, it assumes a bowed or tunneled shape so that the ensuing test is sometimes invalidated. However, the engineer or technician performing the test has no way of knowing in advance that this result will be obtained or to what degree and, therefore, is obliged to incur the cost of the test anyway. When the proportion of invalid test results becomes too large, the entire prospect of fracture testing possibly becomes prohibitive. In a way, then, approaching the standardized fracture test as a two-dimensional exercise tends to nullify its benefits.³

Apparently this problem is pronounced in aluminum alloys, for ASTM Committee B-7 on Light Metals and Alloys has established the ASTM Practice for Plane-Strain Fracture Toughness Testing of Aluminum Alloys (B 645-84), as a modification to ASTM Test E 399. It may be noted that, among other modifications, Practice B 645 removes the fatigue crack-front straightness requirement in Test E 399.

Nor is the problem limited to aluminum alloys for, in a recent series of approximately 680 tests on mainly ferritic steels using compact specimens, Towers [11] found that the crack *always* tunnels to an observable degree. Of all the tests run, he observed such a level of fatigue crack-front bowing that 14% of the subsequent fracture tests would be invalidated by ASTM Test E 399.⁴ The corresponding cost of fracture testing would thus be raised by 16.3%.

Clearly there is a three-dimensional effect here. Indeed, Towers writes, "It is recommended that the formulas for calculating fracture toughness be made more appropriate to real crack-front shapes. . . ."

It is interesting to pursue this issue. One means might be a derivative of Towers's data but, regrettably, he does not report a composite of crack-front shapes. Our alternative is a sequence of elastic analyses done by Solecki [12,13] in which the following steps were taken. First, for straight crack fronts, Solecki computed the energy release rate along the crack front, using Parks's virtual crack extension method [14]. The results, for a number of values of Poisson's ratios, ν , appear in Fig. 1 in terms of the elastic energy release rate, \bar{G} , that is, G normalized on the standard two-dimensional analytical value for the same problem, albeit two dimensional. It can be seen that \bar{G} is anything but uniform across the plate thickness, achieving maxima in the range $0.7 \leq z/h \leq 0.8$, as ν varies (see Fig. 9 for definitions

² ASTM Method for Conducting Drop-Weight Test to Determine Nil-Ductility Transition Temperature of Ferritic Steels (E 208-85) and ASTM Method for Dynamic Tear Testing of Metallic Materials (E 604-83).

³ The same problem was brought to our attention by a member of the Welding Institute (J. D. Harrison, personal communication, 1976).

⁴ A similar evaluation is made in terms of British Standard BS 5447; the results, if anything, are worse in that the potential rejection rate is 17%.

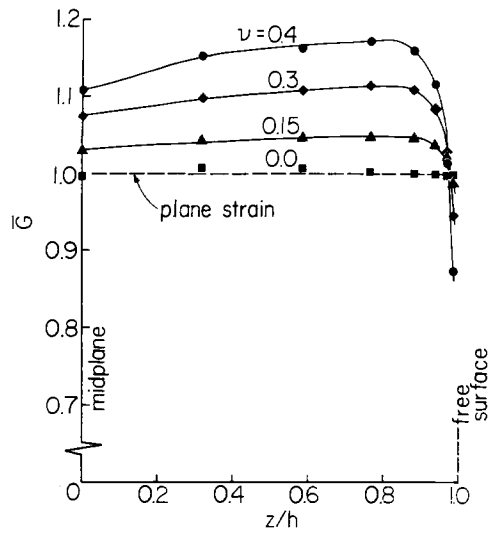


FIG. 1—Variation of the local energy release rate along the straight-crack front for $\nu = 0.0, 0.15, 0.3$, and 0.4 [12].

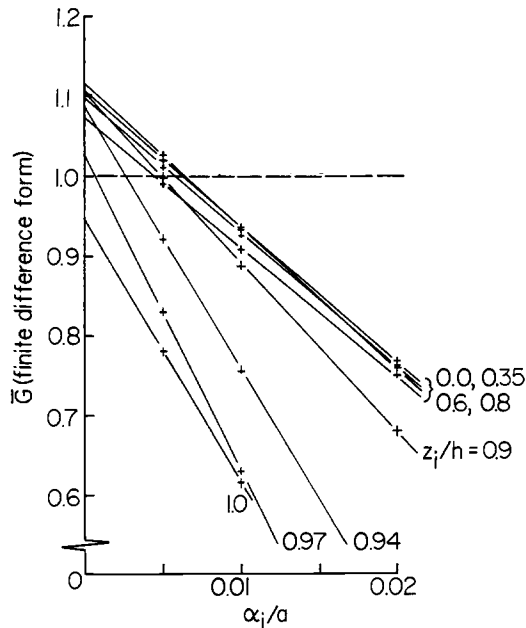


FIG. 2—Illustrated procedure for calculating G for the straight-crack geometry ($\nu = 0.3$) [12].

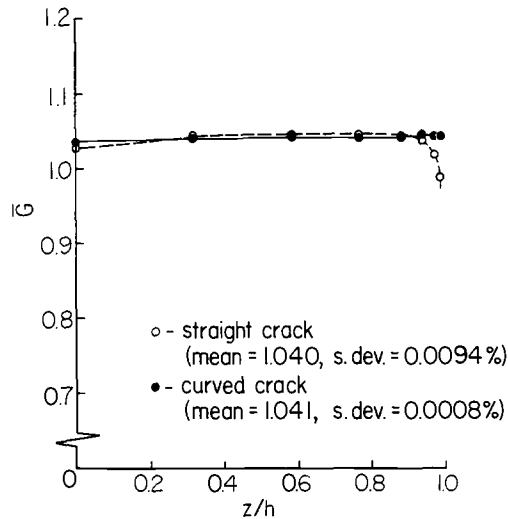


FIG. 3—Variation of the energy release rate for the straight and curved cracks ($\nu = 0.15$) [12].

of z and h). The immediate inference is that the initially straight crack front will grow in a nonuniform manner to achieve a somewhat bowed shape.

Pursuit of this inference was the next step in the analysis. It is useful in this connection to examine the procedural details whereby the data in Fig. 1 were calculated. Figure 2 shows the data from the Parks calculation, with α , representing the virtual crack extension at Node i . Two results are apparent: \bar{G} varies linearly with α at all nodes, and the variation with respect to z/h is elucidated. It follows that if the crack were extended to the position where each $\bar{G} - \alpha$ line crosses the horizontal (dashed) line in Fig. 2, one would arrive at a reasonable

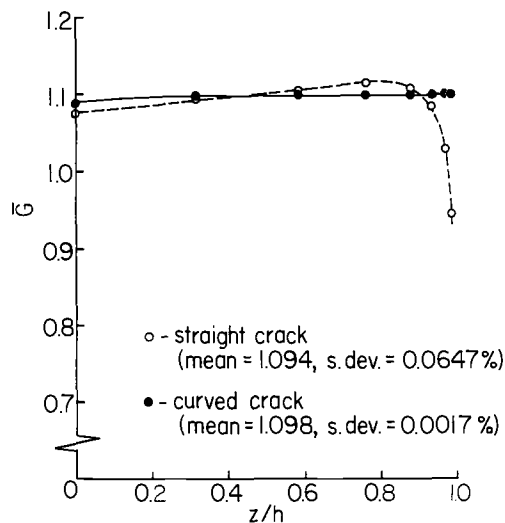


FIG. 4—Variation of the energy release rate for the straight and curved cracks ($\nu = 0.3$) [12].

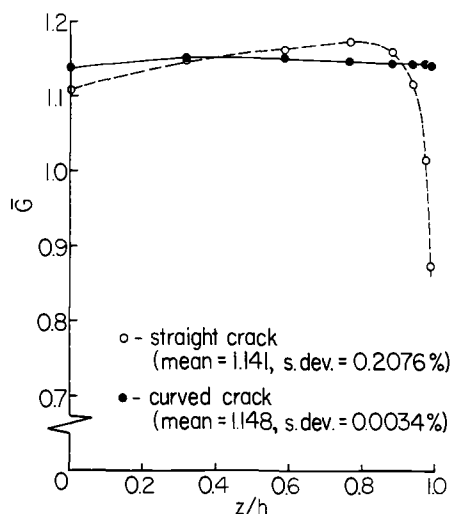


FIG. 5—Variation of the energy release rate for the straight and curved cracks ($\nu = 0.4$) [12].

estimate of a stable crack shape. In fact, Solecki followed this procedure, iterating as needed, to arrive at the \bar{G} distributions shown in Figs. 3 through 5. The crack fronts achieved the shapes shown in Fig. 6. Clearly, the crack length has not changed much, but these minor changes in shape have influenced the \bar{G} distribution to a major degree.

Certain other features are worthy of note. With such a radical change in \bar{G} , it might be expected that either the crack-opening stress or crack-opening displacement would be altered in the vicinity of the crack front. We examine each quantity in turn. In Fig. 7, we show the through-thickness variation of the crack-opening stress, σ_y , at two positions ahead of the crack front, for both straight and curved cracks, at $\nu = 0.3$. Obviously, the modest crack curvature has little influence on this stress component. However, the crack-opening displacement is strongly affected, as shown in Fig. 8. Mindful of Irwin's crack healing analysis [4], we expected one of these quantities to be affected; it was surprising to see the result. The very different shapes in Figs. 7 and 8 suggest, further, that both stress and displacement cannot be described by a common coefficient, for example, $K(z)$. Hence, it does not appear fruitful to pursue an analytic description of the near-tip stress field in terms of two-dimensional methods.

Further, we recall having raised the issue of crack-front curvature (CFC) at symposium in 1971 [15]. In that context we raised two questions of some practical interest, presuming the presence of some crack-front curvature: First, in computing K , even on the basis of planar theory, what is the correct value of the crack length to be used? Second, to what extent does CFC alter the planar value of the K just determined? Fifteen years ago, we could not answer these questions at all well; it now appears that the means to look seriously at these issues are at hand.

While we are reviewing this level of detail, it is useful to look at one further result. It is commonly thought that the stress distribution in a thick plate may be characterized by a plane-strain core, sandwiched between two thin plane-stress layers at the surfaces. Our data suggest that this sandwich construction is in serious error. As we shall see, the notion of a plane-strain core is reasonable enough; however, the surface layers are complicated, highly

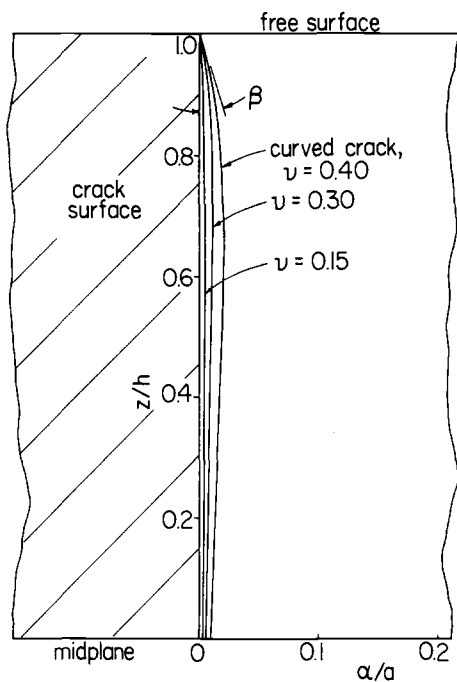


FIG. 6a—Final curved-crack profiles [12].

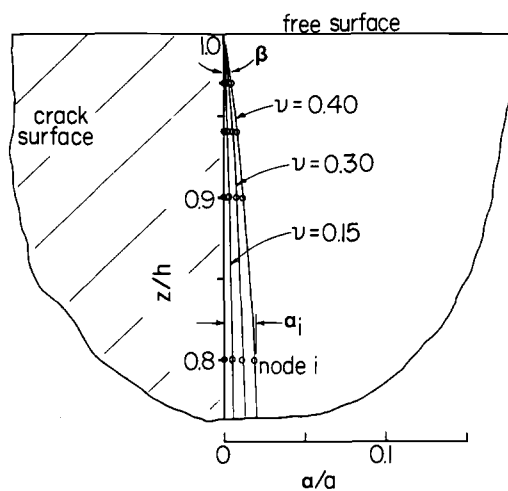


FIG. 6b—Enlargement of the final curved-crack profiles, near the free surface [12].

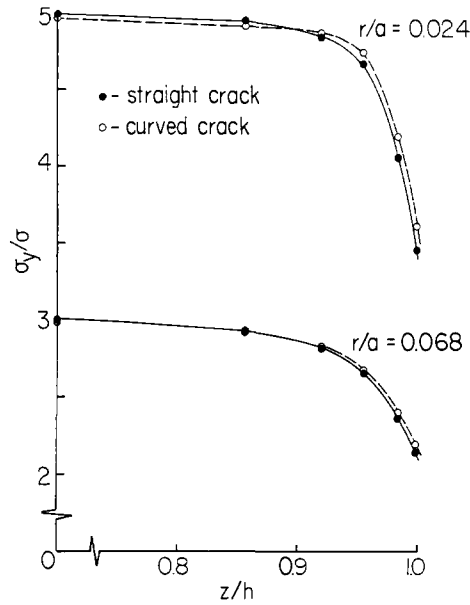


FIG. 7—Through-thickness variation of σ_y on the crack plane at two positions ahead of the straight- and curved-crack fronts ($\nu = 0.3$) [12].

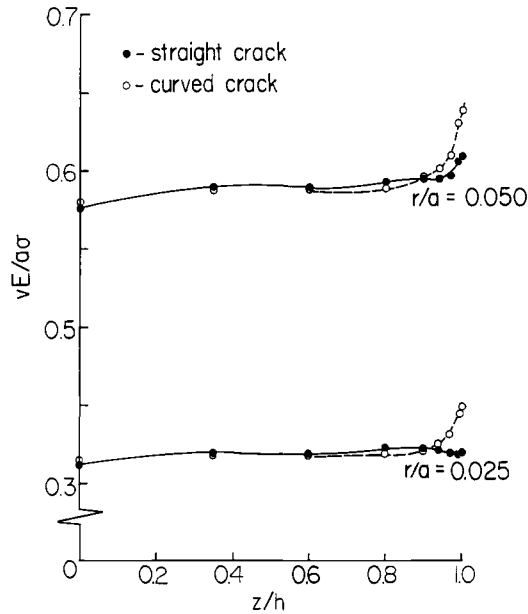


FIG. 8—Through-thickness variation of ν on the crack plane at two positions behind the straight- and curved-crack fronts ($\nu = 0.3$) [12].

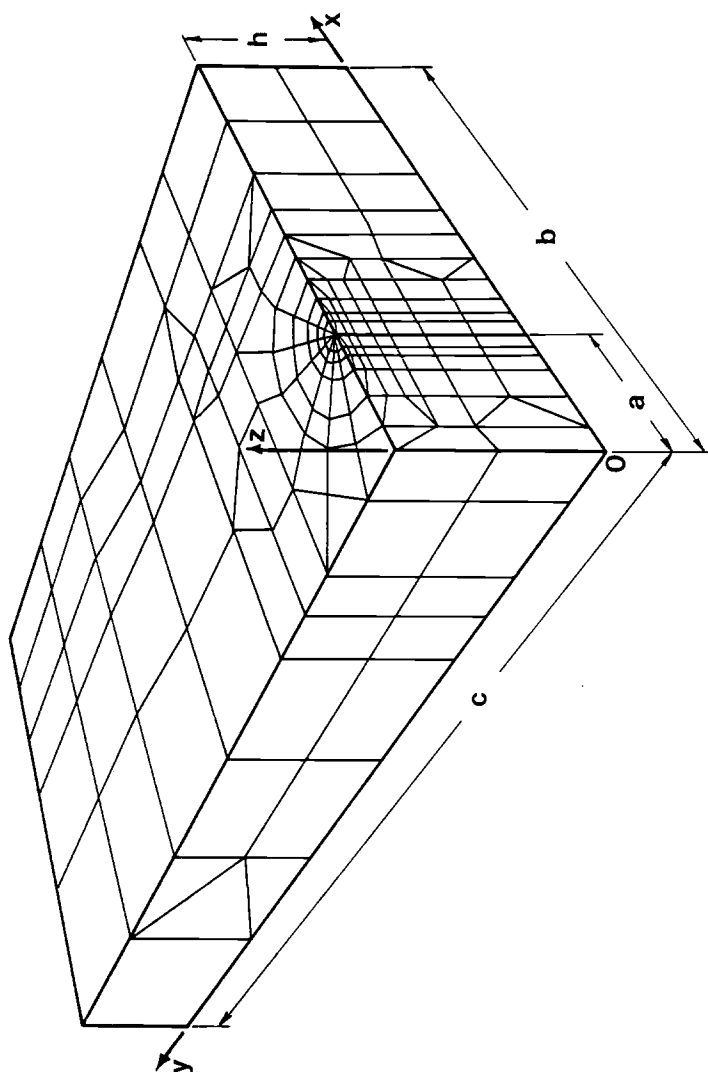


FIG. 9—Basic finite-element model (not to scale) [12].

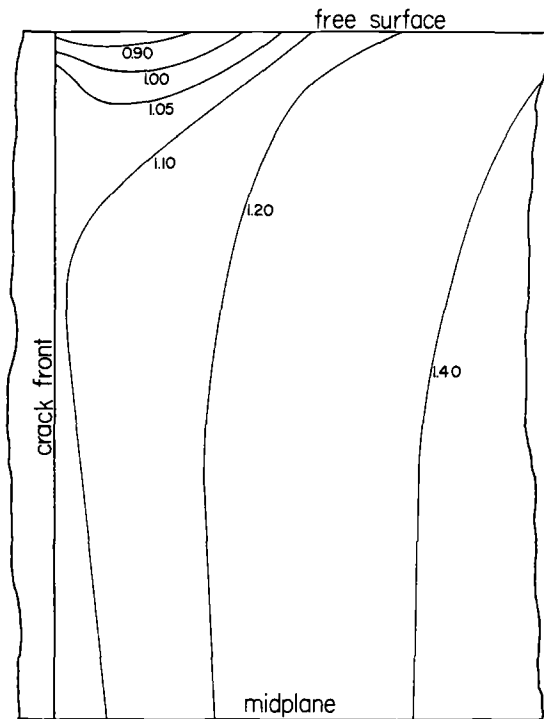


FIG. 10—Contours of $\sigma_r \sqrt{(2r)/\sigma \sqrt{a}}$ on the crack plane ahead of the crack front ($\nu = 0.3$) [12].

three-dimensional regions. For the problem treated in Ref 12, great care was taken in the modeling to extract detailed distributions of stress near the crack front, as is evident from Fig. 9.⁵ Typical results appear in Figs. 10 and 11, where we see a well-defined central core surrounded by a tortuous distribution of stress. Upon close examination of this sort of data, it was found that there is no region in the vicinity of the crack front that can be credibly described as being in a state of plane stress.

In summary, we have reviewed the two-dimensional technology base for LEFM in some detail. We then show that the physical fracture problem is in fact three-dimensional and finally, an analytical effort to describe the anatomy of the problem is reviewed. This three-dimensionality is a feature that has fascinated a number of investigators over recent years; we believe that the present data provide significant insight into the problem.

Further, we should like to suggest that the time to develop a three-dimensional fracture mechanics is now upon us. The need is evident from the difficulties encountered with crack-front straightness requirements and the expanding interest in side-grooving, otherwise two-dimensional, specimens. The baseline technology, as represented by papers in this volume, is in hand, and it is apparent to those of us who have been concerned with this problem for

⁵ The geometry is a center-cracked panel of a length $2c$, width $2b$, and thickness $2h$; the crack length is $2a$. The dimensions used are $c/a = 20$, $b/a = 10$, and $h/a = 1$. For all practical purposes, this represents an infinite plate in plane strain. Loading is in a direction perpendicular to the crack plane, at the ends of the plate. The material is linear elastic, and a small-strain theory is used. The finite-element model comprises 375 elements and 1587 degrees of freedom, most concentrated near the crack front.

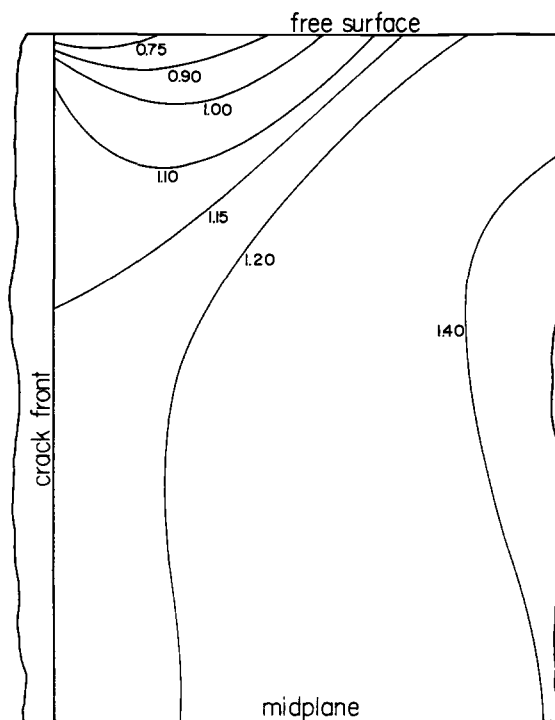


FIG. 11—Contours of $\sigma\sqrt{(2r)}/\sigma\sqrt{a}$ on the crack plane ahead of the crack front ($\nu = 0.4$) [12].

a long time that only a modest increment of effort will produce the desired result. What is needed is a clear insight into the three-dimensional mechanics of test specimens otherwise thought to be two-dimensional, plus a methodology for bridging the gap between the two. This is not now the overwhelming task it once seemed, largely because of the very recent growth of the baseline technology and the insights that have only recently been acquired and reported.

Acknowledgment

This work was performed with support by the U.S. Air Force Office of Scientific Research.

References

- [1] Inglis, C. E., *Transactions of the Institution of Naval Architects*, London, Vol. 60, 1913, pp. 219–230.
- [2] Griffith, A. A., *Philosophical Transactions of the Royal Society of London*, Vol. A221, 1921, pp. 163–198.
- [3] Griffith, A. A., *Proceedings, First International Conference on Applied Mechanics*, Delft, The Netherlands, 1924, pp. 55–63.
- [4] Irwin, G. R., *Journal of Applied Mechanics*, Vol. 24, 1957, pp. 361–364.
- [5] Westergaard, H. M., *Journal of Applied Mechanics, Transactions of the American Society of Mechanical Engineers*, Vol. 61, 1939, pp. A49–A53.
- [6] Williams, M. L., *Journal of Applied Mechanics*, Vol. 24, 1957, pp. 109–114.

- [7] *Fracture Toughness Testing and Its Applications*, ASTM STP 381, American Society for Testing and Materials, Philadelphia, 1965.
- [8] Brown, W. F., Jr., and Srawley, J. E., in *Current Status of Plane Strain Crack Toughness Testing of High Strength Metallic Materials*, ASTM STP 410, American Society for Testing and Materials, Philadelphia, 1966, pp. 1-65.
- [9] Pellini, W. S., *Principles of Structural Integrity Technology*, Office of Naval Research, Arlington, VA, 1976.
- [10] Kaufman, J. G. in *Developments in Fracture Mechanics Test Methods Standardization*, ASTM STP 632, American Society for Testing and Materials, Philadelphia, 1977, pp. 3-24.
- [11] Towers, O. L., *Journal of Testing and Evaluation*, Vol. 11, 1983, pp. 34-45.
- [12] Solecki, J. S., "Three-Dimensional Finite-Element Analysis of Straight and Curved Through Cracks in a Plate," Ph.D. thesis, Department of Mechanical Engineering, Carnegie-Mellon University, 1984.
- [13] Solecki, J. S. and Swedlow, J. L. in *Fracture Mechanics: Sixteenth Symposium*, ASTM STP 868, American Society for Testing and Materials, Philadelphia, 1985, pp. 535-553.
- [14] Parks, D. M., *International Journal of Fracture*, Vol. 10, 1974, pp. 487-502.
- [15] Swedlow, J. L. and Ritter, M. A. in *Stress Analysis and Growth of Cracks*, ASTM STP 513, American Society for Testing and Materials, Philadelphia, 1972, pp. 79-89.

Computational and Analytical Issues

Computation of the Amplitude of Stress Singular Terms for Cracks and Reentrant Corners

REFERENCE: Szabó, B. A. and Babuška, I., "Computation of the Amplitude of Stress Singular Terms for Cracks and Reentrant Corners," *Fracture Mechanics: Nineteenth Symposium, ASTM STP 969*, T. A. Cruse, Ed., American Society for Testing and Materials, Philadelphia, 1988, pp. 101–124.

ABSTRACT: The theoretical basis and performance characteristics of two new methods for the computation of the coefficients of the terms of asymptotic expansions at reentrant corners from finite-element solutions are presented. The methods, called the *contour integral method* (CIM) and the *cutoff function method* (CFM), are very efficient: the coefficients converge to their true values as fast as the strain energy, or faster.

In order to make the presentation as simple as possible, we assume that the elastic body is homogeneous and isotropic, is loaded by boundary tractions only, and, in the neighborhood of the reentrant corner, has stress-free boundaries. The methods described herein can be adapted to cases without such restrictions.

KEY WORDS: finite-element methods, p -extension, fracture mechanics, elasticity, stress-intensity factors, mixed mode, extraction methods, convergence, error estimate

Our understanding and ability to control the error of approximation in finite-element computations has advanced very substantially in the last two years. Two developments are especially important: (1) under assumptions which are generally satisfied in engineering computations, we are now able to realize *exponential* rates of convergence in any quantity of interest; and (2) by using feedback information from finite-element solutions we can ensure that the error in all quantities of interest is small. In this paper we describe two new methods for the computation of generalized stress-intensity factors in two-dimensional problems of linear elasticity and demonstrate their performance by examples.

We will restrict our attention to the displacement formulation. We denote the solution domain by Ω and the displacement vectors defined on Ω by \tilde{u} or (equivalently) $\{u\}$

$$\tilde{u} \equiv \{u\} \stackrel{\text{def}}{=} \{u_x(x, y)u_y(x, y)\} \quad (1)$$

We denote the work done on the elastic body by the stresses corresponding to \tilde{u} when the elastic body is subjected to displacements \tilde{v} by $B(\tilde{u}, \tilde{v})$, the strain energy by $U(\tilde{u})$, and the potential energy by $\Pi(\tilde{u})$. Note that $2U(\tilde{u}) = B(\tilde{u}, \tilde{u})$. We denote the set of all dis-

¹ Professor of mechanics and director, Center for Computational Mechanics, Washington University, St. Louis, MO 63130.

² Research professor, Institute for Physical Science and Technology, University of Maryland, College Park, MD 20740.

placement vector functions defined on Ω for which $U(\tilde{u}) < \infty$ by $E(\Omega)$ and associate the energy norm with this set

$$\|\tilde{u}\|_{E(\Omega)} \stackrel{\text{def}}{=} \sqrt{U(\tilde{u})} \equiv \sqrt{\frac{1}{2} B(\tilde{u}, \tilde{u})} \quad (2)$$

We denote the set of all admissible displacement functions by $\tilde{E}(\Omega)$. By definition, a displacement function \tilde{u} is admissible if it has finite strain energy and, on those boundary segments of Ω where one or both displacement components is prescribed, the components of \tilde{u} equal the prescribed displacement components values. That is

$$\tilde{E}(\Omega) \stackrel{\text{def}}{=} \{\tilde{u} | \tilde{u} \in E(\Omega); u_x(P) = \tilde{u}_x(P), P \in \partial\Omega_x^{(D)}; u_y(P) = \tilde{u}_y(P), P \in \partial\Omega_y^{(D)}\} \quad (3)$$

where \tilde{u}_x, \tilde{u}_y are prescribed displacement components and $\partial\Omega_x^{(D)} (\partial\Omega_y^{(D)})$, respectively represents those boundary segments where $u_x (u_y)$, respectively is prescribed. The exact solution of the generalized formulation of a problem of plane elasticity \tilde{u}_{EX} satisfies

$$\Pi(\tilde{u}_{EX}) = \min_{\tilde{u} \in \tilde{E}(\Omega)} \Pi(\tilde{u}) \quad (4)$$

In finite-element analysis we seek to approximate \tilde{u}_{EX} . We do this by constructing a finite-element mesh Δ on Ω . Each quadrilateral (triangular) finite element is mapped onto a standard quadrilateral (triangular) finite element by suitable mapping functions. We define sets of basis functions on the standard triangular and quadrilateral elements so that any polynomial of degree p or less defined as the standard element can be written as a linear combination of the basis function.

The polynomial basis functions defined on the standard element are mapped onto the elements of the mesh Δ and are joined to form a set of basis functions on Ω . These basis functions are continuous across interelement boundaries, but no restrictions are imposed on their derivatives across interelement boundaries. Thus the basis functions are exactly and minimally conforming. The basis functions defined on Ω are characterized by the mesh Δ , the polynomial degree p , and the mapping functions Q . The set of functions that can be expressed by linear combination of the basis function is denoted by $S^p(\Omega, \Delta, Q)$ and called finite-element space. Because the basis functions are continuous across interelement boundaries, $S^p(\Omega, \Delta, Q)$ is a subset of $E(\Omega)$. We denote the set of admissible functions in $S^p(\Omega, \Delta, Q)$ by $\tilde{S}^p(\Omega, \Delta, Q)$. The number of basis functions in $\tilde{S}^p(\Omega, \Delta, Q)$ is called the number of degrees of freedom and is denoted by N . The finite-element solution \tilde{u}_{FE} satisfies

$$\Pi(\tilde{u}_{FE}) = \min_{\tilde{u} \in \tilde{S}^p(\Omega, \Delta, Q)} \Pi(\tilde{u}) \quad (5)$$

and has the following property

$$\|\tilde{u}_{EX} - \tilde{u}_{FE}\|_{E(\Omega)} = \min_{\tilde{u} \in \tilde{S}^p(\Omega, \Delta, Q)} \|\tilde{u}_{EX} - \tilde{u}\|_{E(\Omega)} \quad (6)$$

The finite-element method selects \tilde{u}_{FE} from $\tilde{S}^p(\Omega, \Delta, Q)$ on the basis of the criterion Eq 6. We can reduce the error of approximation by mesh refinement, by an increase of the polynomial degree of elements, or by a combination of both. These are called extension processes. If the polynomial degree of elements is fixed and the error of approximation is reduced by mesh refinement, then the process is called h -extension (h refers to the size of

the elements). If the mesh is fixed and the polynomial degree of elements (p) is increased, then the process is called p -extension. We remark that neither the mesh refinement nor the distribution of polynomial degrees has to be uniform. There is a substantial improvement in performance³ and no significant increase in computational overhead, if properly designed meshes are used instead of uniform meshes. On the other hand, there is no significant improvement in performance but there is a significant increase in computational overhead, if graded p -distributions are used instead of uniform p -distributions. For this reason we will use uniform p -distributions, characterized by a single number, p . When the error of approximation is reduced so that mesh refinement is combined with increasing p , then the extension process is called h - p extension.

In the case of h - and p -extensions the rate of convergence is algebraic. That is

$$\|\tilde{u}_{EX} - \tilde{u}_{FE}\|_{E(\Omega)} \leq \frac{k}{N^\beta} \quad (7)$$

where N is the number of degrees of freedom; k and β are positive constants, independent of N but dependent on \tilde{u}_{EX} and the finite-element meshes. In the case of h - p extensions, when proper mesh refinement is used in conjunction with p -extension, the rate of convergence is exponential

$$\|\tilde{u}_{EX} - \tilde{u}_{FE}\|_{E(\Omega)} \leq \frac{k}{\exp(\gamma N^\theta)} \quad (8)$$

where k , γ , and θ are positive constants. Under certain assumptions which are generally satisfied in engineering applications $\theta \geq 1/3$.

Although it is difficult to write computer programs that automatically design meshes and assign polynomial degrees so that the rate of convergence (Eq 8) is realized for all N , very similar performance can be achieved when properly graded, fixed meshes are used in conjunction with p -extension. In this case a nearly exponential convergence rate is achieved for low N but convergence slows to an algebraic rate for high N . Clearly, the mesh should be designed so that the desired level of precision is achieved before the rate of convergence slows. Properly designed meshes are such that the sizes of elements decrease in geometric progression with a common factor of about 0.15 toward points of stress singularity. Selection of the mesh and the polynomial degree of elements depends on the accuracy one wishes to achieve. For details and examples see Refs 1 to 8.

We are now in position to outline the central point of this paper: in Ref 9 a new approach for the computation of functionals from finite-element solutions was presented. In this approach a desired functional value $\Phi(\tilde{u}_{FE})$ (for example, a stress component at a point, stress-intensity factor, and so forth) is computed from an expression which is of the form

$$\Phi(\tilde{u}_{FE}) = B(\tilde{u}_{FE}, \tilde{v}) \quad (9)$$

where \tilde{v} is a suitably chosen function, called extraction function. Methods of this type are called extraction methods. In Ref 10 it was shown that the error in the functional value computed by extraction methods can be written as

$$|\Phi(\tilde{u}_{EX}) - \Phi(\tilde{u}_{FE})| \leq \|\tilde{u}_{EX} - \tilde{u}_{FE}\|_{E(\Omega)} \|\tilde{\omega}_{EX} - \tilde{\omega}_{FE}\|_{E(\Omega)} \quad (10)$$

³ In this context "performance" means rate of change of error in energy norm with respect to the number of degrees of freedom.

where $\tilde{\omega}_{FE}$ is the finite-element solution of an auxiliary problem, the exact solution of which is $\tilde{\omega}_{EX}$. In the auxiliary problem the domain and the mesh are the same as in the original problem but the loading is computed from the extraction function \tilde{v} . The auxiliary solution serves theoretical purposes only: it is not necessary to know $\tilde{\omega}_{EX}$ or $\tilde{\omega}_{FE}$ in order to use Eq 9 for computing $\Phi(\tilde{u}_{FE})$. It is possible to select the extraction function \tilde{v} so that $\|\tilde{\omega}_{EX} - \tilde{\omega}_{FE}\|_{E(\Omega)} \rightarrow 0$ not slower than $\|\tilde{u}_{EX} - \tilde{u}_{FE}\|_{E(\Omega)} \rightarrow 0$ as $N \rightarrow \infty$ in an orderly extension process. Therefore, functional values computed by extraction methods have the same order of accuracy as the strain energy or better. Functional values computed by extraction methods exhibit superconvergence [10,11].

In this paper we describe procedures for the extraction of the amplitude of stress singular terms associated with reentrant corners in plane elasticity. We assume that the plane elastic body is homogeneous and isotropic; loaded by boundary tractions only; and, in the neighborhood of the reentrant corner, has stress-free boundaries. In Eq 3 $\tilde{u}_x = 0$, $\tilde{u}_y = 0$, however, the method described herein can be generalized to other problems such as fixed free-boundary conditions, intersection of material interfaces with external boundaries, and so forth. We demonstrate the performance of the extraction procedures on the basis of three test problems.

The Exact Solution in the Neighborhood of Reentrant Corners

In the neighborhood of reentrant corners (Fig. 1) we examine Airy stress functions of the form

$$U = U(r, \theta) = r^{\lambda+1} F(\theta) \quad (11)$$

Because U satisfies the biharmonic equation

$$\left(\frac{\partial^2}{\partial r^2} + \frac{1}{r} \frac{\partial}{\partial r} + \frac{1}{r^2} \frac{\partial^2}{\partial \theta^2} \right) \left(\frac{\partial^2}{\partial r^2} + \frac{1}{r} \frac{\partial}{\partial r} + \frac{1}{r^2} \frac{\partial^2}{\partial \theta^2} \right) U = 0 \quad (12)$$

$F(\theta)$ must satisfy

$$F'''' + 2(\lambda^2 + 1)F'' + (\lambda^2 - 1)^2 F = 0 \quad (13)$$

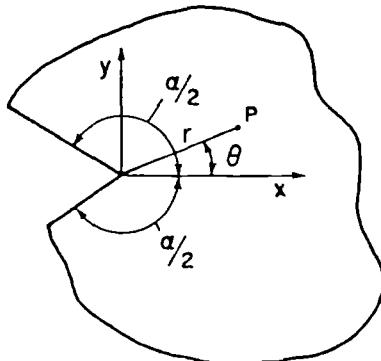


FIG. 1—Reentrant corner notation.

where the primes represent differentiation with respect to θ . The general solution of Eq 13 for $\lambda \neq 0$ and $\lambda \neq \pm 1$ is

$$F(\theta) = a_1 \cos(\lambda - 1)\theta + a_2 \cos(\lambda + 1)\theta + a_3 \sin(\lambda - 1)\theta + a_4 \sin(\lambda + 1)\theta \quad (14)$$

We need to determine λ and combinations of a_i ($i = 1, 2, 3, 4$), so that the edges that meet at the reentrant corners are stress free. From the stress function U we have

$$\sigma_\theta = \frac{\partial^2 U}{\partial r^2} = \lambda(\lambda + 1)r^{\lambda-1}F(\theta) \quad (15)$$

and

$$\tau_{r\theta} = \frac{1}{r} \frac{\partial^2 U}{\partial r \partial \theta} + \frac{1}{r^2} \frac{\partial U}{\partial \theta} = -\lambda r^{\lambda-1}F'(\theta) \quad (16)$$

Along the reentrant edges (at $\theta = \pm\alpha/2$) we have $\sigma_\theta = \tau_{r\theta} = 0$. Consequently, from Eqs 14, 15, and 16, after straightforward algebraic manipulation, we have

$$\begin{bmatrix} \cos(\lambda - 1)\frac{\alpha}{2} & \cos(\lambda + 1)\frac{\alpha}{2} & 0 & 0 \\ \Lambda \sin(\lambda - 1)\frac{\alpha}{2} & \sin(\lambda + 1)\frac{\alpha}{2} & 0 & 0 \\ 0 & 0 & \sin(\lambda - 1)\frac{\alpha}{2} & \sin(\lambda + 1)\frac{\alpha}{2} \\ 0 & 0 & \Lambda \cos(\lambda - 1)\frac{\alpha}{2} & \cos(\lambda + 1)\frac{\alpha}{2} \end{bmatrix} \begin{Bmatrix} a_1 \\ a_2 \\ a_3 \\ a_4 \end{Bmatrix} = 0 \quad (17)$$

where

$$\Lambda = \frac{1 - \lambda}{1 + \lambda} \quad (18)$$

Note that a_1, a_2 are independent of a_3, a_4 . A nontrivial solution exists only if the corresponding determinants vanish

$$\cos(\lambda - 1)\frac{\alpha}{2} \sin(\lambda + 1)\frac{\alpha}{2} - \Lambda \sin(\lambda - 1)\frac{\alpha}{2} \cos(\lambda + 1)\frac{\alpha}{2} = 0 \quad (19)$$

$$\sin(\lambda - 1)\frac{\alpha}{2} \cos(\lambda + 1)\frac{\alpha}{2} - \Lambda \cos(\lambda - 1)\frac{\alpha}{2} \sin(\lambda + 1)\frac{\alpha}{2} = 0 \quad (20)$$

which can be simplified to

$$\sin \lambda \alpha + \lambda \sin \alpha = 0 \quad (21)$$

$$\sin \lambda \alpha - \lambda \sin \alpha = 0 \quad (22)$$

See also Refs 12–16. Observe that if λ is a solution of Eq 21 or 22, then $-\lambda$ is also a solution, however, the corresponding stress field has finite strain energy only if the real part of λ is greater than zero.

Assume now that $\lambda_i^{(1)}$ ($i = 1, 2, \dots$) is a solution of Eq 21 and $\lambda_i^{(1)}$ is real and simple. Then, from Eq 17

$$a_1 \cos (\lambda_i^{(1)} - 1) \frac{\alpha}{2} + a_2 \cos (\lambda_i^{(1)} + 1) \frac{\alpha}{2} = 0 \quad (23)$$

$$a_1 \Lambda_i^{(1)} \sin (\lambda_i^{(1)} - 1) \frac{\alpha}{2} + a_2 \cos (\lambda_i^{(1)} + 1) \frac{\alpha}{2} = 0 \quad (24)$$

where $\Lambda_i^{(1)} = \frac{1 - \lambda_i^{(1)}}{1 + \lambda_i^{(1)}}$. Let us define

$$Q_i^{(1)} = \frac{a_2}{a_1} = - \frac{\cos (\lambda_i^{(1)} - 1) \frac{\alpha}{2}}{\cos (\lambda_i^{(1)} + 1) \frac{\alpha}{2}} = - \frac{\Lambda_i^{(1)} \sin (\lambda_i^{(1)} - 1) \frac{\alpha}{2}}{\sin (\lambda_i^{(1)} + 1) \frac{\alpha}{2}} \quad (25)$$

With this notation Eq 11 can be written as

$$U = r^{\lambda_i^{(1)}+1} (\cos (\lambda_i^{(1)} - 1)\theta + Q_i^{(1)} \cos (\lambda_i^{(1)} + 1)\theta) \quad (26)$$

Similarly, if $\lambda_i^{(2)}$ is a real, simple root of Eq 22, then the corresponding stress function is

$$U = r^{\lambda_i^{(2)}+1} (\sin (\lambda_i^{(2)} - 1)\theta + Q_i^{(2)} \sin (\lambda_i^{(2)} + 1)\theta) \quad (27)$$

where

$$Q_i^{(2)} = - \frac{\sin (\lambda_i^{(2)} - 1) \frac{\alpha}{2}}{\sin (\lambda_i^{(2)} + 1) \frac{\alpha}{2}} = - \frac{1 - \lambda_i^{(2)} \cos (\lambda_i^{(2)} - 1) \frac{\alpha}{2}}{1 + \lambda_i^{(2)} \cos (\lambda_i^{(2)} + 1) \frac{\alpha}{2}} \quad (28)$$

Note that Eq 26 is symmetric with respect to θ , whereas Eq 27 is antisymmetric. From Eqs 26 and 27 expressions for stress and displacement fields can be derived. These expressions are most conveniently obtained by first writing Eqs 26 and 27 in terms of the complex variable z , and then using the method of Muskhelishvili [15]. The stress and displacement fields corresponding to Eq 26 are called Mode 1 fields. The stress and displacement fields corresponding to Eq 27 are called Mode 2 fields. Specifically, the Mode 1 displacement

components, up to rigid body displacement and rotation terms, are

$$u_{xi}^{(1)} = \frac{1}{2G} r^{\lambda_i^{(1)}} [(\kappa - Q_i^{(1)}(\lambda_i^{(1)} + 1)) \cos \lambda_i^{(1)}\theta - \lambda_i^{(1)} \cos (\lambda_i^{(1)} - 2)\theta] \quad (29)$$

$$u_{yi}^{(1)} = \frac{1}{2G} r^{\lambda_i^{(1)}} [(\kappa + Q_i^{(1)}(\lambda_i^{(1)} + 1)) \sin \lambda_i^{(1)}\theta + \lambda_i^{(1)} \sin (\lambda_i^{(1)} - 2)\theta] \quad (30)$$

which can be written in the form

$$\tilde{u}_i^{(1)} \equiv \{u_i^{(1)}\} = \frac{1}{2G} r^{\lambda_i^{(1)}} \{\Psi_i^{(1)}(\theta)\} \quad (31)$$

In Eqs 29, 30, and 31 G is the modulus of rigidity, and κ depends only on Poisson's ratio. For plane strain

$$\kappa = 3 - 4\nu \quad (32)$$

and for plane stress

$$\kappa = \frac{3 - \nu}{1 + \nu} \quad (33)$$

The Mode 1 stress tensor components are

$$\begin{aligned} \sigma_{xi}^{(1)} &= \lambda_i^{(1)} r^{\lambda_i^{(1)}-1} [(2 - Q_i^{(1)}(\lambda_i^{(1)} + 1)) \\ &\quad \times \cos (\lambda_i^{(1)} - 1)\theta - (\lambda_i^{(1)} - 1) \cos (\lambda_i^{(1)} - 3)\theta] \end{aligned} \quad (34)$$

$$\begin{aligned} \sigma_{yi}^{(1)} &= \lambda_i^{(1)} r^{\lambda_i^{(1)}-1} [(2 + Q_i^{(1)}(\lambda_i^{(1)} + 1)) \\ &\quad \times \cos (\lambda_i^{(1)} - 1)\theta + (\lambda_i^{(1)} - 1) \cos (\lambda_i^{(1)} - 3)\theta] \end{aligned} \quad (35)$$

$$\tau_{xyi}^{(1)} = \lambda_i^{(1)} r^{\lambda_i^{(1)}-1} [(\lambda_i^{(1)} - 1) \sin (\lambda_i^{(1)} - 3)\theta + Q_i^{(1)}(\lambda_i^{(1)} + 1) \sin (\lambda_i^{(1)} - 1)\theta] \quad (36)$$

The Mode 2 displacement components, up to rigid body displacement and rotation terms, are

$$u_{xi}^{(2)} = \frac{1}{2G} r^{\lambda_i^{(2)}} [(\kappa - Q_i^{(2)}(\lambda_i^{(2)} + 1)) \sin \lambda_i^{(2)}\theta - \lambda_i^{(2)} \sin (\lambda_i^{(2)} - 2)\theta] \quad (37)$$

$$u_{yi}^{(2)} = -\frac{1}{2G} r^{\lambda_i^{(2)}} [(\kappa + Q_i^{(2)}(\lambda_i^{(2)} + 1)) \cos \lambda_i^{(2)}\theta + \lambda_i^{(2)} \cos (\lambda_i^{(2)} - 2)\theta] \quad (38)$$

which can be written in the form

$$\tilde{u}_i^{(2)} \equiv \{u_i^{(2)}\} = \frac{1}{2G} r^{\lambda_i^{(2)}} \{\Psi_i^{(2)}(\theta)\} \quad (39)$$

The Mode 2 stress tensor components are

$$\sigma_{xi}^{(2)} = \lambda_i^{(2)} r^{\lambda_i^{(2)}-1} [(2 - Q_i^{(2)} (\lambda_i^{(2)} + 1)) \times \sin (\lambda_i^{(2)} - 1) \theta - (\lambda_i^{(2)} - 1) \sin (\lambda_i^{(2)} - 3) \theta] \quad (40)$$

$$\sigma_{yi}^{(2)} = \lambda_i^{(2)} r^{\lambda_i^{(2)}-1} [(2 + Q_i^{(2)} (\lambda_i^{(2)} + 1)) \times \sin (\lambda_i^{(2)} - 1) \theta + (\lambda_i^{(2)} - 1) \sin (\lambda_i^{(2)} - 3) \theta] \quad (41)$$

$$\tau_{xyi}^{(2)} = -\lambda_i^{(2)} r^{\lambda_i^{(2)}-1} [(\lambda_i^{(2)} - 1) \cos (\lambda_i^{(2)} - 3) \theta + Q_i^{(2)} (\lambda_i^{(2)} + 1) \cos (\lambda_i^{(2)} - 1) \theta] \quad (42)$$

In fracture mechanics we have $\alpha = 2\pi$. In this case Eqs 21 and 22 are identical ($\sin 2\lambda\pi = 0$), and all roots are real and simple

$$\lambda_i^{(1)} = \lambda_i^{(2)} = \pm \frac{1}{2}, \pm \frac{3}{2}, \pm 2, \pm \frac{5}{2}, \dots \quad (43)$$

Assuming traction-free crack surfaces, finite strain energy, and neglecting rigid-body displacement and rotation terms, in the neighborhood of the crack tip any solution can be written in the form

$$\{u\} = \sum_{i=1}^{\infty} \frac{A_i^{(1)}}{2G} r^{\lambda_i^{(1)}} \{\Psi_i^{(1)}(\theta)\} + \sum_{i=1}^{\infty} \frac{A_i^{(2)}}{2G} r^{\lambda_i^{(2)}} \{\Psi_i^{(2)}(\theta)\} \quad (44)$$

This infinite series converges absolutely for $r < r_o$ for some $r_o > 0$. The coefficients $A_i^{(1)}$ and $A_i^{(2)}$ are called generalized stress-intensity factors. The coefficients $A_1^{(1)}$ and $A_1^{(2)}$ are related to the Mode 1 and Mode 2 stress-intensity factors, K_I and K_{II} , as follows

$$A_1^{(1)} = \frac{K_I}{\sqrt{2\pi}}, \quad A_1^{(2)} = \frac{K_{II}}{\sqrt{2\pi}} \quad (45)$$

Methods for the determination of the generalized stress-intensity factors are discussed in the following sections.

When $\alpha \neq 2\pi$, then not all roots are real, and multiple roots (both real and complex) can exist. The cases of complex roots and multiple real roots are beyond the scope of this discussion. From the point of view of engineering analysis, the vertex angles of 270, 240, 225, and 210° are of the greatest importance (in addition to the 360° already discussed). In these cases the smallest roots are real. Their values are shown in Table 1.

TABLE 1—Smallest positive roots of Eqs 21 and 22 for selected vertex angles, α .

α	$\lambda_1^{(1)}$	$\lambda_1^{(2)}$
360°	0.500 000	0.500 000
270°	0.544 484	0.908 529
240°	0.615 731	1.148 913
225°	0.673 583	1.302 086
210°	0.751 975	1.485 812

When the vertex angle is greater than 257.45° , then $\lambda_1^{(2)} > 1$ and the Mode 2 stress components are bounded. The Mode 1 stress components are unbounded when $\alpha > 180^\circ$.

Betti's Law—The Path Independent Integral $I_\Gamma(\tilde{u}, \tilde{v})$

We denote the strain tensor components, corresponding to the displacement field $\tilde{u}(x, y)$ by $\epsilon_x^{(u)}$, $\epsilon_y^{(u)}$, $\gamma_{xy}^{(u)}$. The strain-displacement relations are

$$\epsilon_x^{(u)} = \frac{\partial u_x}{\partial x}, \quad \epsilon_y^{(u)} = \frac{\partial u_y}{\partial y}, \quad \gamma_{xy}^{(u)} = \frac{\partial u_x}{\partial y} + \frac{\partial u_y}{\partial x} \quad (46)$$

Similarly, we denote the stress tensor components corresponding to displacement field $\tilde{u}(x, y)$ by $\sigma_x^{(u)}$, $\sigma_y^{(u)}$, and $\tau_{xy}^{(u)}$. The stress-strain relations are

$$\{\sigma^{(u)}\} = [E]\{\epsilon^{(u)}\} \quad (47)$$

where $\{\sigma^{(u)}\} = \{\sigma_x^{(u)} \sigma_y^{(u)} \tau_{xy}^{(u)}\}^T$; $\{\epsilon^{(u)}\} = \{\epsilon_x^{(u)} \epsilon_y^{(u)} \gamma_{xy}^{(u)}\}^T$ and $[E]$ is a symmetric, positive definite matrix, called the material stiffness matrix. We have assumed that the initial strain is zero. We shall also assume that the body forces are zero and that \tilde{u} is such that the corresponding stresses, computed from Eqs 46 and 47, satisfy the equilibrium equations with zero body forces

$$\begin{aligned} \frac{\partial \sigma_x^{(u)}}{\partial x} + \frac{\partial \tau_{xy}^{(u)}}{\partial y} &= 0 \\ \frac{\partial \tau_{xy}^{(u)}}{\partial x} + \frac{\partial \sigma_y^{(u)}}{\partial y} &= 0 \end{aligned} \quad (48)$$

We denote the direction cosines of the normal to the boundary of the plane elastic body at boundary point P by n_x , n_y . The traction vector components in terms of the stress components at point P are

$$T_x^{(u)} = \sigma_x^{(u)} n_x + \tau_{xy}^{(u)} n_y \quad (49)$$

$$T_y^{(u)} = \tau_{xy}^{(u)} n_x + \sigma_y^{(u)} n_y \quad (50)$$

Let $\tilde{v} \equiv \{v\} = \{v_x(x, y) \ v_y(x, y)\}$ be an arbitrary displacement vector field and assume that the strain energy associated with \tilde{v} is finite on Ω . Assume further that tractions are specified along the entire boundary of Ω . We denote the boundary of Ω by $\partial\Omega$. In the absence of body forces, thermal loading, and elastic constraints, the principle of virtual work states that

$$\int \int_{\Omega} \{\epsilon^{(v)}\}^T \{\sigma^{(u)}\} \, dx dy \equiv \int \int_{\Omega} \{\epsilon^{(v)}\}^T [E] \{\epsilon^{(u)}\} \, dx dy = \int_{\partial\Omega} (T_x^{(u)} v_x + T_y^{(u)} v_y) \, ds \quad (51)$$

holds for any \tilde{v} ; \tilde{v} is called virtual displacement. The strain components $\{\epsilon^{(v)}\}$ are related to \tilde{v} by Eq 46. Because $[E]$ is symmetric, Eq 51 can be written as

$$\int \int_{\Omega} ([E]\{\epsilon^{(v)}\})^T \{\epsilon^{(u)}\} \, dx dy = \int \int_{\Omega} \{\sigma^{(v)}\}^T \{\epsilon^{(u)}\} \, dx dy = \int_{\partial\Omega} (T_x^{(v)} v_x + T_y^{(v)} v_y) \, ds \quad (52)$$

which is the same as

$$\int \int_{\Omega} \left\{ \sigma_x^{(v)} \frac{\partial u_x}{\partial x} + \sigma_y^{(v)} \frac{\partial u_y}{\partial y} + \tau_{xy}^{(v)} \left(\frac{\partial u_x}{\partial y} + \frac{\partial u_y}{\partial x} \right) \right\} dx dy = \int_{\partial\Omega} (T_x^{(u)} v_x + T_y^{(u)} v_y) ds \quad (53)$$

Applying Green's lemma and using Eqs 49 and 50 we have

$$\begin{aligned} \int_{\partial\Omega} (T_x^{(u)} u_x + T_y^{(v)} u_y) ds - \int_{\partial\Omega} (T_x^{(u)} v_x + T_y^{(u)} v_y) ds \\ = \int \int_{\Omega} \left\{ \left(\frac{\partial \sigma_x^{(v)}}{\partial x} + \frac{\partial \tau_{xy}^{(v)}}{\partial y} \right) u_x + \left(\frac{\partial \tau_{xy}^{(v)}}{\partial x} + \frac{\partial \sigma_y^{(v)}}{\partial y} \right) u_y \right\} dx dy \end{aligned} \quad (54)$$

When the stresses corresponding to both \tilde{u} and \tilde{v} satisfy the equilibrium equations with the body forces equal to zero, that is Eq 48, then we have *Betti's law*

$$\int_{\partial\Omega} (T_x^{(v)} u_x + T_y^{(v)} u_y) ds = \int_{\partial\Omega} (T_x^{(u)} v_x + T_y^{(u)} v_y) ds \quad (55)$$

where the integration is counterclockwise around Ω . We denote the normal and tangential traction vector components respectively by T_n and T_t and the normal and tangential displacement vector components by u_n and u_t . Because $T_x^{(v)} u_x + T_y^{(v)} u_y = T_n^{(v)} u_n + T_t^{(v)} u_t$, and so forth, Betti's law can also be written in the following form

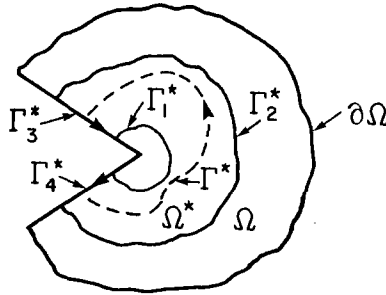
$$\int_{\partial\Omega} (T_n^{(v)} u_n + T_t^{(v)} u_t) ds = \int_{\partial\Omega} (T_n^{(u)} v_n + T_t^{(u)} v_t) ds \quad (56)$$

Let us now consider a subdomain of Ω , denoted by Ω^* , in the neighborhood of the reentrant corner. Figure 2 shows Ω^* bounded by two continuous curves, Γ_1^* and Γ_2^* , and the reentrant edges. Let $\{u\}$ and $\{v\}$ be two displacement fields, both satisfying the equilibrium equations with body forces and initial strains equal to zero, and the stress-free boundary conditions along the reentrant edges ($\sigma_\theta = \tau_\theta = 0$ at $\theta = \pm\alpha/2$). Then, according to Betti's law

$$\begin{aligned} \int_{\Gamma_1^*} (T_n^{(v)} u_n + T_t^{(v)} u_t) ds + \int_{\Gamma_2^*} (T_n^{(v)} u_n + T_t^{(v)} u_t) ds \\ = \int_{\Gamma_1^*} (T_n^{(u)} v_n + T_t^{(u)} v_t) ds + \int_{\Gamma_2^*} (T_n^{(u)} v_n + T_t^{(u)} v_t) ds \end{aligned} \quad (57)$$

We integrate around Ω^* in the counterclockwise direction. Therefore, integration along Γ_2^* is in the counterclockwise direction, while integration along Γ_1^* is in the clockwise direction with respect to the reentrant corner. Let us reverse the sense of the direction of the integral along Γ_1^* so that both contour integrals are in the counterclockwise direction with respect to the reentrant corner. We will use the symbol $\tilde{\Gamma}_1^*$ to indicate integration along Γ_1^* in the counterclockwise direction with respect to the reentrant corner. In this case we have

$$\begin{aligned} \int_{\tilde{\Gamma}_1^*} (T_n^{(u)} v_n + T_t^{(u)} v_t) ds - \int_{\tilde{\Gamma}_1^*} (T_n^{(v)} u_n + T_t^{(v)} u_t) ds \\ = \int_{\Gamma_2^*} (T_n^{(u)} v_n + T_t^{(u)} v_t) ds - \int_{\Gamma_2^*} (T_n^{(v)} u_n + T_t^{(v)} u_t) ds \end{aligned} \quad (58)$$

FIG. 2—The subdomain Ω^* .

Therefore, the integral

$$I_{\Gamma^*}(\tilde{u}, \tilde{v}) = \int_{\Gamma^*} (T_n^{(u)}v_n + T_t^{(u)}v_t) ds - \int_{\Gamma^*} (T_n^{(v)}u_n + T_t^{(v)}u_t) ds \quad (59)$$

is independent of the path Γ^* . Of course, Γ^* must begin on the reentrant edge and terminate on the other reentrant edge, as shown in Fig. 2, and the integration must be counterclockwise with respect to the reentrant corner.

When the stresses corresponding to $\{v\}$ do not satisfy the equilibrium equations and the stress-free boundary conditions along the reentrant edges, then instead of Eq 58 we have

$$\begin{aligned} \int_{\Gamma_1^*} (T_n^{(u)}v_n + T_t^{(u)}v_t) ds - \int_{\Gamma_1^*} (T_n^{(v)}u_n + T_t^{(v)}u_t) ds &= \int_{\Gamma_2^*} (T_n^{(u)}v_n + T_t^{(u)}v_t) ds \\ &- \int_{\Gamma_2^*} (T_n^{(v)}u_n + T_t^{(v)}u_t) ds - \int_{\Gamma_3^*} (T_n^{(v)}u_n + T_t^{(v)}u_t) ds - \int_{\Gamma_4^*} (T_n^{(v)}u_n + T_t^{(v)}u_t) ds \\ &+ \int \int_{\Omega^*} \left\{ \left(\frac{\partial \sigma_x^{(v)}}{\partial x} + \frac{\partial \tau_{xy}^{(v)}}{\partial y} \right) u_x + \left(\frac{\partial \tau_{xy}^{(v)}}{\partial x} + \frac{\partial \sigma_y^{(v)}}{\partial y} \right) u_y \right\} dx dy \quad (60) \end{aligned}$$

The sense of integration along Γ_3 and Γ_4 is shown in Fig. 2.

Extraction of Stress-Intensity Factors

In the following we consider only real and simple roots of Eqs 21 and 22. This is the case in linear elastic fracture mechanics. We present two algorithmic procedures for the computation of coefficients $A_i^{(m)}$ ($i = 1, 2, \dots$; $m = 1, 2$) in Eq 44. The restriction to real and simple roots is not essential, however, and all coefficients of asymptotic expansions, similar to Eq 44, can be determined by the methods described in this section.

The Contour Integral Method (CIM)

Let Γ_ρ be a circle of radius ρ centered on the crack tip, and assume that ρ is sufficiently close to the crack tip so that the exact solution $\{u_{EX}\}$ is represented by Eq 44 on Γ_ρ . The traction vector, corresponding to $\{u_{EX}\}$, can be written as

$$\{T_i^{(u_{EX})}\} = \sum_{i=1}^{\infty} \sum_{m=1}^2 A_i^{(m)} \lambda_i^{(m)} r^{\lambda_i^{(m)}-1} \{Y_i^{(m)}(\theta)\} \quad (61)$$

where $\lambda_i^{(1)} > 0$ is a real and simple root of Eq 21 and $\lambda_i^{(2)} > 0$ is a real and simple root of Eq 22.

Let $-\lambda_j^{(n)}$ be a negative root of Eq 21 or 22, and denote the corresponding displacement function by $\{v_{-j}^{(n)}\}$

$$\{v_{-j}^{(n)}\} = \frac{A_{-j}^{(n)}}{2G} r^{-\lambda_j^{(n)}} \{\Psi_{-j}^{(n)}(\theta)\} \quad (62)$$

where $A_{-j}^{(n)}$ is a constant, to be determined later. Note that $\{v_{-j}^{(n)}\}$ does not have finite strain energy on Ω and, therefore, is not an admissible displacement function on Ω . It is admissible, however, on Ω^* (Fig. 2). The traction vector on Γ_1^* , corresponding to $\{v_{-j}^{(n)}\}$, is

$$\{T_{-j}^{(v_{-j}^{(n)})}\} = -A_{-j}^{(n)} \lambda_j^{(n)} r^{-\lambda_j^{(n)}-1} \{Y_{-j}^{(n)}(\theta)\} \quad (63)$$

We now show that

$$I_{\Gamma_\rho}(\tilde{u}_{EX}, \tilde{v}_{-j}^{(n)}) = \begin{cases} A_{-i}^{(m)} A_i^{(m)} c_i^{(m)}(\alpha) & \text{if } i = j \text{ and } m = n \\ 0 & \text{otherwise} \end{cases} \quad (64)$$

where Γ_ρ is a circular arc of radius ρ centered on the reentrant corner; $c_i^{(m)}(\alpha)$ depends only on $\lambda_i^{(m)}$. The proof is straightforward. By direct evaluation from the absolutely convergent series (Eq 44), we have

$$I_{\Gamma_\rho}(\tilde{u}_{EX}, \tilde{v}_{-j}^{(n)}) = A_{-j}^{(n)} \sum_{i=1}^{\infty} \sum_{m=1}^2 A_i^{(m)} \rho^{\lambda_i^{(m)} - \lambda_j^{(n)}} C_{i,-j}^{(m,n)} \quad (n = 1, 2) \quad (65)$$

where

$$C_{i,-j}^{(m,n)} = \frac{1}{2G} \int_{-\alpha/2}^{+\alpha/2} (\lambda_i^{(m)} \{\Psi_{-j}^{(n)}(\theta)\}^T \{Y_i^{(m)}(\theta)\} + \{\lambda_j^{(n)} \Psi_i^{(m)}(\theta)\}^T \{Y_{-j}^{(n)}(\theta)\}) d\theta \quad (66)$$

Because $I_{\Gamma_\rho}(\tilde{u}_{EX}, \tilde{v}_{-j}^{(n)})$ is independent of Γ_ρ , it is independent of ρ . If $\lambda_i^{(m)} \neq \lambda_j^{(n)}$, then this is possible only if the integral expression (Eq 66) is zero. The other possibility is that $\lambda_i^{(m)} = \lambda_j^{(n)}$, but $n \neq m$. In this case, however, the integrand in Eq 66 is the sum of the dot products of symmetric and antisymmetric vector functions, therefore the integral is zero. Denoting $c_i^{(m)}(\alpha) = C_{i,-i}^{(m,m)}$, we have Eq 64 and letting $A_{-i}^{(m)} = 1/c_i^{(m)}(\alpha)$, we have from Eq 57

$$A_i^{(m)} = \int_{\Gamma_2^*} (\{v_{-i}^{(m)}\}^T \{T^{u_{EX}}\}) ds - \int_{\Gamma_2^*} (\{u_{EX}\}^T \{T^{v_{-i}^{(m)}}\}) ds \quad (67)$$

where Γ_2^* is, of course, arbitrary. The function $\{v_{-i}^{(m)}\}$ is an extraction function for $A_i^{(m)}$. Of course, we do not know $\{u_{EX}\}$ and $\{T^{u_{EX}}\}$. We therefore substitute $\{u_{FE}\}$ and $\{T^{u_{FE}}\}$ in Eq 67 for $\{u_{EX}\}$ and $\{T^{u_{EX}}\}$ to obtain an approximation to $A_i^{(m)}$. If Γ_2^* includes an external boundary where the imposed tractions are known, then the imposed tractions can be used in Eq 67. Implementation would pose some difficulties, however, and computational experience

has shown that the use of $\{T^{(u_{FE})}\}$ instead of the imposed tractions generally yields satisfactory results. Examples are presented in the next section.

The Cutoff Function Method (CFM)

Let us now assume that both contours Γ_1^* and Γ_2^* are circular arcs with radii ρ_1 and ρ_2 , respectively, $\rho_1 < \rho_2$. We define the following extraction function for $A_i^{(m)}$

$$\{w_{-i}^{(m)}\} = \phi(r)\{v_{-i}^{(m)}\} \quad (68)$$

where $\{v_{-i}^{(m)}\}$ is defined by Eq 62 and $\phi(r)$ is called the cutoff function and is defined by

$$\phi(r) = \begin{cases} 1 & r \leq \rho_1 \\ 1 - 3 \left(\frac{r - \rho_1}{\rho_2 - \rho_1} \right)^2 + 2 \left(\frac{r - \rho_1}{\rho_2 - \rho_1} \right)^3 & \rho_1 < r < \rho_2 \\ 0 & r \geq \rho_2 \end{cases} \quad (69)$$

In this case the extraction function satisfies neither the stress-free boundary conditions on the reentrant edges nor the equilibrium equations. Therefore, Eq 60 must be used for the computation of $A_i^{(m)}$, instead of Eq 58. Specifically, if we select $A_{-i}^{(m)}$ as before, that is, $A_{-i}^{(m)} = 1/c_i^{(m)}(\alpha)$, where $c_i^{(m)}(\alpha)$ is computed from Eq 66 with $\{v_{-i}^{(m)}\}$ replaced by $\{w_{-i}^{(m)}\}$, we have

$$A_i^{(m)} = \int_{\Gamma_3^*} (T_n^{(w_{-i}^{(m)})} u_n + T_t^{(w_{-i}^{(m)})} u_t) ds - \int_{\Gamma_4^*} (T_n^{(w_{-i}^{(m)})} u_n + T_t^{(w_{-i}^{(m)})} u_t) ds \\ + \int \int_{\Omega^*} \left\{ \left(\frac{\partial \sigma_x^{(w_{-i}^{(m)})}}{\partial x} + \frac{\partial \tau_{xy}^{(w_{-i}^{(m)})}}{\partial y} \right) u_x + \left(\frac{\partial \tau_{xy}^{(w_{-i}^{(m)})}}{\partial x} + \frac{\partial \sigma_y^{(w_{-i}^{(m)})}}{\partial y} \right) u_y \right\} dx dy \quad (70)$$

The contour integrals must be evaluated along the reentrant edges in the counterclockwise direction with respect to Ω^* (see Fig. 2).

The basic idea in using the cutoff function method is that we wish to localize the extraction function so that: (a) the local character of the extraction function is preserved around the reentrant corner [hence $\phi(r) = 1$ inside of the inner ring]; (b) the cutoff function is a smooth function so that the auxiliary problem corresponding to the modified extraction function $\{w_{-i}^{(m)}\}$, defined in Eq 68, can be approximated well by a finite-element solution (see Eq 10) and the discussion in the following paragraph); and (c) the extraction function multiplied by $\phi(r)$ vanishes on and outside of the outer ring, hence the stresses and tractions corresponding to $\{u_{FE}\}$ do not have to be considered. For this reason the cutoff function method is more accurate than the contour integral method. Of course, any smooth cutoff function having the basic characteristics of $\phi(r)$ could have been chosen, and the choice of cutoff function is independent of the type of reentrant corner.

Examples

The contour integral and cutoff function methods can be implemented in any finite-element computer program. However, the error in the computed data is closely related to the error

in energy norm and therefore the design of the finite element space $S^p(\Omega, \Delta, Q)$ [10,11]. Also, the cutoff function method requires the use of smooth mapping techniques. The following example problems were solved by means of a new computer program, called PROBE. PROBE implements the p -version of the finite element method, that is sequences of finite element spaces $S^p(\Omega, \Delta, Q)$ can be conveniently created by letting $p = 1, 2, \dots, 8$ while keeping the mesh, Δ , and the mappings, Q , fixed. Of course, the mesh and the mappings can be changed also. The mapping of finite elements is by the linear blending function method. Curved boundaries, such as circles, and other conical sections are represented exactly in the computation of stiffness matrices and load vectors. PROBE also permits specification of loading by FORTRAN-like expressions, hence the boundary tractions specified herein were represented exactly in the load vector computations. Twelve Gauss points are used in the computation of load vectors independently of the polynomial degree. In the case of extraction methods, 12 Gauss points are used for evaluating the contour integrals and 144 Gauss points are used for evaluating the area integrals, independent of the polynomial degree. Additional details concerning PROBE are available in Ref 17.

Other examples of the application of extraction methods, based on experimental (research) implementations, are available in Refs 18 and 19.

L-Shaped Plane Elastic Body

We consider the L-shaped plane elastic body of thickness t , shown in Fig. 3, loaded by tractions corresponding to the first symmetric and antisymmetric eigenfunctions of the asymptotic expansion of \tilde{u}_{EX} about the reentrant corner. This example is representative of plate and shell intersections and reentrant corner problems in general.

We select $\nu = 0.3$ and assume plane-strain conditions. Therefore $\kappa = 1.8$; $\lambda_1^{(1)} = 0.544\,483\,74$; $Q_1^{(1)} = 0.543\,075\,579$; $\lambda_1^{(2)} = 0.908\,529\,19$; $Q_1^{(2)} = -0.218\,923\,236$ (see Eqs 32, 21, 22, 25, and 28). We superimpose the tractions corresponding to the stress components, Eqs 34, 35, and 36 and Eqs 40, 41, and 42, along the boundaries of the L-shaped plane elastic body with the stress-intensity factors selected so that $A_1^{(1)} = A$, (A is arbitrary) and

$$A_1^{(2)} = 2Aa^{\lambda_1^{(1)} - \lambda_1^{(2)}} \quad (71)$$

where a is the dimension shown in Fig. 3. In this way the exact strain energy can be computed

$$U(\tilde{u}_{EX}) = 6.777\,769\,14 \frac{(Aa^{\lambda_1^{(1)}})^2 t}{E} \quad (72)$$

where E is the modulus of elasticity.

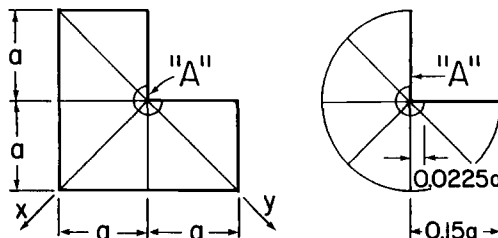


FIG. 3—Mesh design (18 elements) for a L-shaped plane elastic body.

In the contour integral method, the integration was performed along a circle of radius $0.15a$ and the finite-element solutions were computed from the elements inside the circle.

The number of degrees of freedom, the computed values of the normalized strain energy and the normalized stress-intensity factors, defined by

$$\bar{A}_1^{(1)} \stackrel{\text{def}}{=} \frac{(A_1^{(1)})_{FE}}{A} \quad \bar{A}_1^{(2)} \stackrel{\text{def}}{=} \frac{(A_1^{(2)})_{FE}}{Aa_{\lambda_1^{(1)} - \lambda_1^{(2)}}} \quad (73)$$

are listed in Table 2. Of course, $\bar{A}_1^{(1)}$ has to converge to 1 and, in view of Eq 73, $\bar{A}_1^{(2)}$ has to converge to 2.

We see from Table 2 that the stress-intensity factors computed by both methods converge strongly and obviously, although not monotonically. Greater accuracy and more nearly monotonic convergence is exhibited by the cutoff function method than the contour integral method, nevertheless both methods yield solutions that are within the range of precision normally needed in engineering computations at $p = 2$ or $p = 3$.

We have plotted the relative error in strain energy and the absolute value of the relative error in the Mode 1 and Mode 2 stress-intensity factors computed by the cutoff function method against the number of degrees of freedom on a log-log scale in Fig. 4 and on a semilog scale (the logarithms of the relative errors versus $N^{1/3}$) in Fig. 5. These choices of scale are suggested by estimates of Eqs 7 and 8, respectively. These diagrams indicate that the error in strain energy behaves differently in the range of low p values than in the range of high p values. In the range of low p values it curves downward in Fig. 4 and very nearly follows a straight-line path in Fig. 5, suggesting that the estimate in Eq 8 holds. We will refer to this as Phase 1. In the range of high p values it follows a straight-line path in Fig. 4 but has a positive, decreasing curvature in Fig. 5. We will refer to this as Phase 2. Transition from Phase 1 to Phase 2 occurs at about $p = 4$. Phase 2 is the asymptotic convergence for p -extensions: the estimate in Eq 7 holds with $\beta = 2\lambda_1^{(1)}$, in this case $\beta = 1.089$. Phase 1 is characteristic for h - p extensions.

Obviously, the rate of decrease of the error is much faster in Phase 1 than in Phase 2. We can extend Phase 1 by refining the mesh further so that the elements are graded in geometric progression toward the reentrant corner with a common factor of about 0.15. Thus the next layer of elements around the reentrant corner would have the size of 0.15^3a . In general, the mesh should be designed so that the desired level of precision is achieved in Phase 1. In this example the relative errors are less than 1% in Phase 1, therefore no further refinement was necessary.

TABLE 2—Strain energy and the normalized stress intensity factors $\bar{A}_1^{(1)}$, $\bar{A}_1^{(2)}$ computed by the contour integral method (CIM) and the cutoff function method (CFM) in the L-shaped domain.

p	N	$\frac{U(\tilde{u}_{FE})E}{(Aa^{\lambda_1^{(1)}})^2t}$	$\bar{A}_1^{(1)}$ (CIM)	$\bar{A}_1^{(1)}$ (CFM)	$\bar{A}_1^{(2)}$ (CIM)	$\bar{A}_1^{(2)}$ (CFM)
1	41	6.420 727 96	1.180 41	0.952 68	2.434 74	2.290 75
2	119	6.741 375 80	0.954 18	1.021 77	2.013 52	2.084 22
3	209	6.770 298 47	1.027 86	1.002 50	2.025 97	2.022 39
4	335	6.775 751 44	0.990 14	1.000 73	1.998 01	2.004 37
5	497	6.776 839 67	1.004 44	0.999 91	2.002 65	2.000 97
6	695	6.777 195 30	0.997 84	0.999 85	1.999 39	2.000 22
7	929	6.777 362 81	1.000 74	0.999 87	2.000 36	2.000 05
8	1 199	6.777 462 28	0.999 52	0.999 90	1.999 88	2.000 01
∞	∞	6.777 769 14	1.000 00	1.000 00	2.000 00	2.000 00

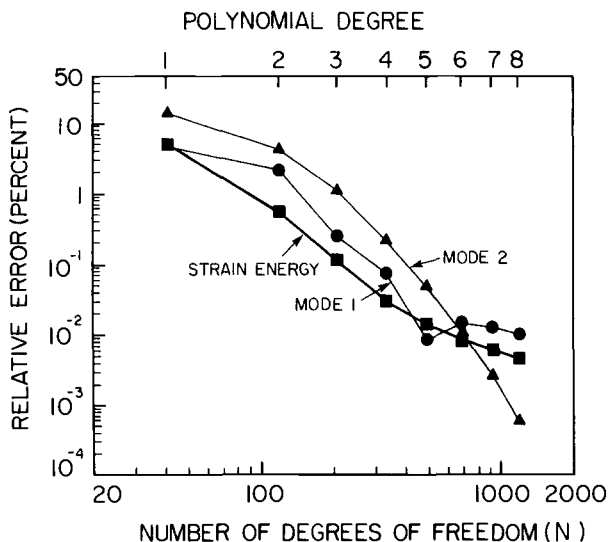


FIG. 4—Convergence of the strain energy and the Mode 1 and Mode 2 stress-intensity factors computed by the cutoff function method (log-log scale).

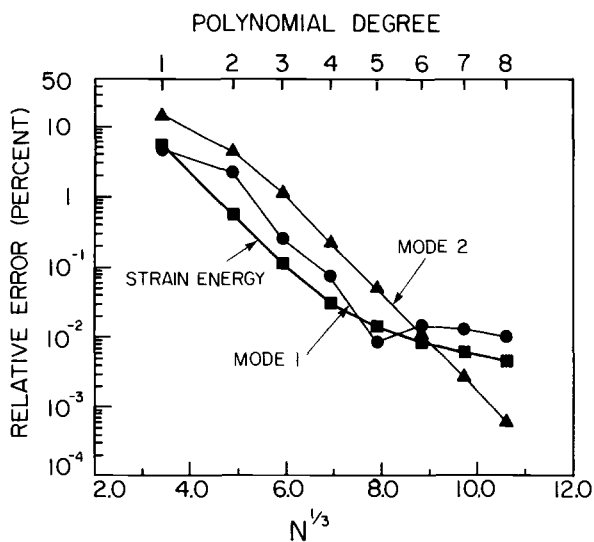


FIG. 5—Convergence of the strain energy and the Mode 1 and Mode 2 stress-intensity factors computed by the cutoff function method (semilog scale).

The convergence path of the Mode 1 stress-intensity factor follows closely that of the strain energy, whereas the path of the Mode 2 stress-intensity factor converges faster. This point is discussed in Refs 10 and 11.

Edge-Cracked Panel—Problem 1

Let us now consider the edge-cracked panel shown in Fig. 6. We assume plane-strain conditions and a Poisson's ratio of 0.3. In this case $\lambda_1^{(1)} = \lambda_1^{(2)} = 1/2$, therefore $Q_1^{(1)} = -1/3$ and $Q_1^{(2)} = 1$. Once again we denote the thickness of the panel by t . We apply tractions along Sides A, B, C, D, E, F of the edge-cracked panel shown in Fig. 6 that exactly correspond to the stresses of Mode 1 and Mode 2 stress fields. In this case, using appropriate trigonometric identities, Eqs 34, 35, and 36 and Eqs 40, 41, and 42 can be written in the following form (see, for example, Ref 20)

$$\sigma_{x1}^{(1)} = \frac{K_I}{\sqrt{2\pi r}} \cos \frac{\theta}{2} \left(1 - \sin \frac{\theta}{2} \sin \frac{3\theta}{2} \right) \quad (74)$$

$$\sigma_{y1}^{(1)} = \frac{K_I}{\sqrt{2\pi r}} \cos \frac{\theta}{2} \left(1 + \sin \frac{\theta}{2} \sin \frac{3\theta}{2} \right) \quad (75)$$

$$\tau_{xy1}^{(1)} = \frac{K_I}{\sqrt{2\pi r}} \sin \frac{\theta}{2} \cos \frac{\theta}{2} \sin \frac{3\theta}{2} \quad (76)$$

where $-\pi \leq \theta \leq \pi$. The Mode 2 stress components are

$$\sigma_{x1}^{(2)} = \frac{K_{II}}{\sqrt{2\pi r}} \sin \frac{\theta}{2} \left(2 + \cos \frac{\theta}{2} \cos \frac{3\theta}{2} \right) \quad (77)$$

$$\sigma_{y1}^{(2)} = \frac{K_{II}}{\sqrt{2\pi r}} \sin \frac{\theta}{2} \cos \frac{\theta}{2} \cos \frac{3\theta}{2} \quad (78)$$

$$\tau_{xy1}^{(2)} = \frac{K_{II}}{\sqrt{2\pi r}} \cos \frac{\theta}{2} \left(1 - \sin \frac{\theta}{2} \sin \frac{3\theta}{2} \right) \quad (79)$$

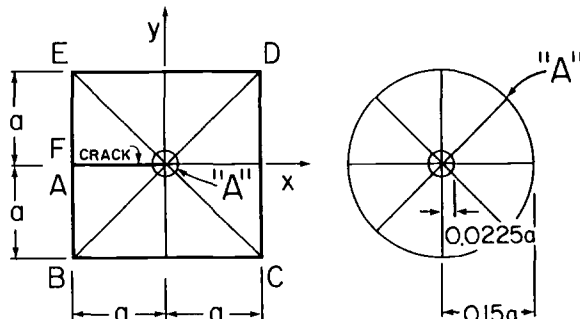


FIG. 6—Mesh design (24 elements) for edge-cracked panel problem 1.

The generalized stress-intensity factors $A_1^{(1)}$ and $A_1^{(2)}$ are related to the stress-intensity factors by Eq 45. We select $K_I = K_{II} = \sqrt{2\pi} A$ (A is arbitrary) and define the normalized stress-intensity factors $\tilde{A}_1^{(1)}$ and $\tilde{A}_1^{(2)}$ as follows

$$\tilde{A}_1^{(1)} \stackrel{\text{def}}{=} \frac{(A_1^{(1)})_{FE}}{A} \quad \tilde{A}_1^{(2)} \stackrel{\text{def}}{=} \frac{(\tilde{A}_1^{(2)})_{FE}}{A} \quad (80)$$

In this way the computed values of both $\tilde{A}_1^{(1)}$ and $\tilde{A}_1^{(2)}$ converge to 1 and therefore it is easy to monitor convergence of the stress-intensity factors. The exact strain energy is known

$$U(\tilde{u}_{EX}) = 10.541\,228\,1 \frac{A^2 a t}{E} \quad (81)$$

The number of degrees of freedom, the computed values of the normalized strain energy, and the normalized stress-intensity factors defined in Eq 80 are shown in Table 3.

We see from Table 3 that again the cutoff function method is somewhat more accurate than the contour integral method. In the case of the cutoff function method the relative error falls below 1% at $p = 3$; in the case of the contour integral method the relative error drops below 1% at $p = 5$.

The relative errors in strain energy and the absolute value of the relative error in the Mode 1 and Mode 2 stress-intensity factors, computed by the cutoff function method, are plotted against the number of degrees of freedom on a log-log scale in Fig. 7. The inverted S-curve, typical of p -convergence when strongly graded meshes are used, is clearly visible. The stress-intensity factors converge at about the same rate as the strain energy. The curves appear to enter Phase 2 at $p = 7$ or $p = 8$. The results are in agreement with the theoretical estimate given in Ref 10.

Finally, let us examine the vector length of stress-intensity factors which can be computed by the energy release rate method also known as the stiffness derivative method. Because we have selected for this test problem $K_I = K_{II} = \sqrt{2\pi} A$, we define the computed values of the normalized vector length of the stress-intensity factors as follows

$$\tilde{K} \stackrel{\text{def}}{=} \frac{1}{2\sqrt{\pi} A} (\sqrt{K_I^2 + K_{II}^2})_{FE} \quad (82)$$

TABLE 3—Values of $\tilde{A}_1^{(1)}$ and $\tilde{A}_1^{(2)}$ computed by the contour integral (CIM) and cutoff function methods (CFM).

p	N	$\frac{U(\tilde{u}_{FE})E}{A^2 a t}$	$\tilde{A}_1^{(1)}$ (CIM)	$\tilde{A}_1^{(1)}$ (CFM)	$\tilde{A}_1^{(2)}$ (CIM)	$\tilde{A}_1^{(2)}$ (CFM)
1	53	9.595 991 9	1.169 72	0.913 71	1.311 97	1.001 63
2	155	10.411 429 2	0.925 15	1.027 02	0.928 40	1.040 58
3	273	10.508 588 7	1.037 87	1.002 77	1.044 13	1.006 37
4	439	10.530 282 7	0.984 83	1.000 25	0.983 60	1.001 34
5	653	10.535 455 6	1.006 09	0.999 43	1.007 37	0.999 92
6	915	10.537 413 2	0.996 50	0.999 44	0.996 39	0.999 78
7	1 225	10.538 425 2	1.000 83	0.999 54	1.001 25	0.999 78
8	1 583	10.539 056 6	0.999 07	0.999 64	0.999 17	0.999 82
∞	∞	10.541 228 1	1.000 00	1.000 00	1.000 00	1.000 00

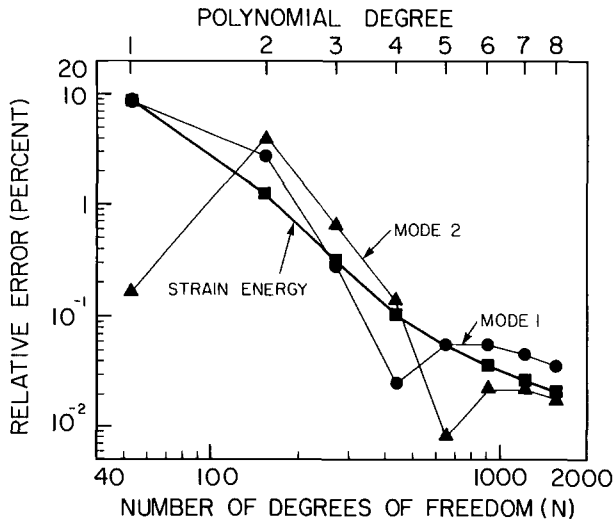


FIG. 7—Convergence of the strain energy and the Mode 1 and Mode 2 stress-intensity factors computed by the cutoff function method.

In this way \tilde{K} must converge to 1. The normalized vector length of stress-intensity factors, computed by the energy release rate method, the contour integral method, and the cutoff function method, is shown in Table 4. The three methods are seen to converge strongly. Again, the performance of the cutoff function method is seen to be the strongest.

Edge-Cracked Panel Problem 2

The two problems just discussed were constructed so that only the first symmetric and antisymmetric terms of the asymptotic expansions were nonzero. This permitted us to examine the performance of the contour integral and cutoff function methods. In practical problems no such restrictions apply and the exact solution is not known. The following test problem is more nearly representative of practical problems.

The problem definition and mesh design are shown in Fig. 8. The plane stress condition

TABLE 4—Normalized vector length of stress-intensity factors (\tilde{K}) computed by the energy release rate method (ERM), the contour integral method (CIM), and the cutoff function method (CFM).

p	ERM	CIM	CFM
1	1.065 76	1.242 88	0.958 68
2	1.022 37	0.926 78	1.033 82
3	0.999 26	1.041 00	1.004 57
4	0.996 63	0.984 21	1.000 80
5	0.996 58	1.006 73	0.999 67
6	0.997 33	0.996 44	0.999 61
7	0.997 95	1.001 04	0.999 66
8	0.998 40	0.999 12	0.999 73
∞	1.000 00	1.000 00	1.000 00

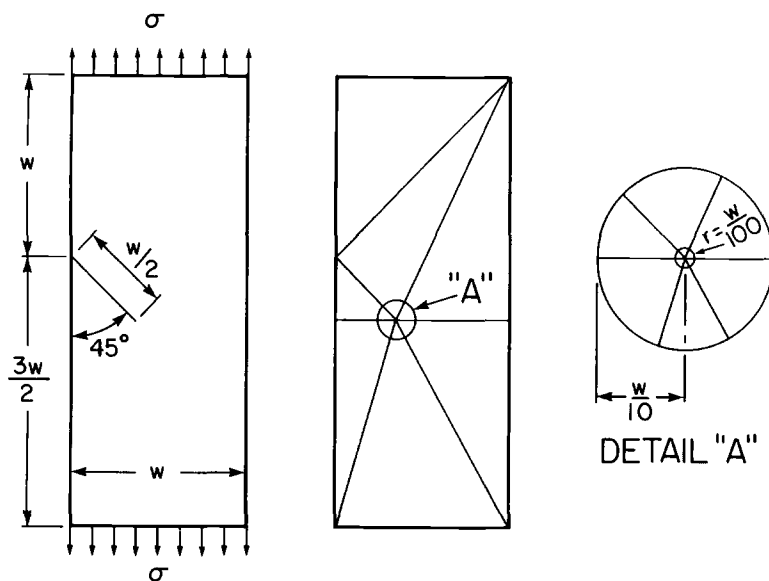


FIG. 8—Mesh design for edge-cracked panel problem 2.

and a Poisson's ratio of 0.3 are assumed. Solutions were obtained by the virtual crack-extension method, the contour integral method, and the cutoff function method. We normalize the stress-intensity factors K_I and K_{II} and their vector length K as follows

$$\begin{aligned}\bar{K}_I &\stackrel{\text{def}}{=} \frac{K_I}{\sigma\sqrt{2\pi w}} \\ \bar{K}_{II} &\stackrel{\text{def}}{=} \frac{K_{II}}{\sigma\sqrt{2\pi w}} \\ \bar{K} &\stackrel{\text{def}}{=} \frac{\sqrt{K_I^2 + K_{II}^2}}{\sigma\sqrt{w}}\end{aligned}\tag{83}$$

TABLE 5—Normalized strain energy and vector length of stress-intensity factors computed by the energy release rate method.

p	N	$\frac{U(\bar{u}_{FE})E}{\sigma^2 w}$	\bar{K}
1	43	1.484 994 7	1.439
2	125	1.616 222 7	1.605
3	221	1.659 348 1	1.587
4	355	1.694 054 3	1.656
5	527	1.701 074 9	1.666
6	737	1.703 029 6	1.671
7	985	1.703 535 7	1.673
8	1 271	1.703 722 3	1.674

TABLE 6—Normalized stress-intensity factors and their vector length computed by the contour integral (CIM) and cutoff function methods (CFM).

p	N	\tilde{K}_I (CIM)	\tilde{K}_I (CFM)	\tilde{K}_{II} (CIM)	\tilde{K}_{II} (CFM)	\tilde{K} (CIM)	\tilde{K} (CFM)
1	43	0.541 27	0.422 59	−0.374 80	−0.290 05	1.650	1.285
2	125	0.497 08	0.555 88	−0.255 78	−0.282 92	1.401	1.563
3	221	0.589 09	0.561 61	−0.289 51	−0.270 74	1.645	1.563
4	355	0.578 64	0.592 32	−0.283 19	−0.290 22	1.615	1.653
5	527	0.605 58	0.598 25	−0.293 98	−0.290 12	1.687	1.667
6	737	0.596 72	0.600 43	−0.288 97	−0.290 97	1.662	1.672
7	985	0.603 13	0.601 19	−0.291 96	−0.290 91	1.680	1.674
8	1 271	0.600 32	0.601 32	−0.290 42	−0.290 95	1.672	1.674

The results are shown in Tables 5 and 6. This problem was solved by Sha and Yang [21] using the virtual crack-extension method and by Andersson [22] using a technique similar to that proposed by Rybicki and Kanninen [23]. The results presented here agree very closely with the results given in Refs 21 and 22.

The results indicate that the computed values converge strongly. Our ability to go beyond the level of precision we actually need at a small marginal cost is very important from the point of quality control: there are no other means for ensuring the quality of computed data in practical computations where the exact solution is generally not known.

Finally, we note that the contour integral and cutoff function methods require substantially fewer CPU cycles than the virtual crack-extension method. In the case of this example, five elements have vertices on the crack tip. Therefore, using the central difference formula for evaluating the rate of change of the potential energy with respect to the crack length, we needed to recompute the stiffness matrices of five elements twice. At $p = 8$ the virtual crack-extension method required 13.5 times the central processing unit time required by the contour integral method, the cutoff function method required $10.5 \times$ the CPU time. Also, the contour integral and cutoff function methods yield the Mode 1 and Mode 2 stress-intensity factors separately, whereas the virtual crack-extension method does not.

Summary and Conclusions

We have described two methods for the computation of the amplitudes of the first symmetric and antisymmetric terms of the asymptotic expansions of the solution at reentrant corners with stress-free boundaries. This class of problems is very important from the practical point of view because it includes the problems of linear-elastic fracture mechanics, and in many cases the sites of failure initiation are reentrant corners.

The limiting assumptions of this paper were adopted in order to keep the presentation as simple as possible. The extraction methods described here are not intrinsically limited to the class of problems considered here, but implementation for the general case is somewhat more difficult. For example, we have considered real and simple roots of Eqs 21 and 22 only. If the vertex angle is 360° , then all roots are real and simple and the procedures presented here can be applied directly to computing any number of coefficients of the asymptotic expansion. If the vertex angle is arbitrary and the amplitudes of several terms of the asymptotic expansion are of interest, then the implementation must account for multiple real roots and complex roots as well. Complications also arise when the material properties change, such as along the edge of a composite panel. In such cases, determination

of the eigenvalues and eigenfunctions is more difficult than in the case discussed here. (See, for example, Ref 24.) These difficulties notwithstanding, implementation of procedures for the computation of the asymptotic expansion of stress singular terms is feasible. We have demonstrated that the amplitudes computed by the contour integral and cutoff function methods converge to their true values at about the same rate as the strain energy, or faster. Thus, the amplitudes can be computed accurately and inexpensively by these methods.

The accuracy depends on the design of the finite-element mesh and the choice of polynomial degree. In general, the mesh should be designed and the polynomial degree chosen so that the desired level of accuracy is reached just before transition occurs from Phase 1 to Phase 2 in the p -extension process. Procedures for correct mesh design and proper selection of p are discussed in Refs 7 and 25.

P -extensions can be implemented, and in fact have been implemented in PROBE, so that, once the solution for $p = p_0$ is available, the solutions for $p < p_0$ can be obtained very inexpensively. This is because stiffness matrices and load vectors have hierarchic structure [17]. Consequently the marginal cost associated with obtaining stress-intensity factors for $p < p_0$ is very small. This is not the case when the h -version of the finite element method is used.

Development of theories for the prediction of failure in metallic and nonmetallic materials is a problem of very obvious practical importance. Several failure theories have been proposed, each requiring computation of some parameters of the elastic stress field (see, for example Refs 26 through 31). In linear elastic fracture mechanics, the amplitude of the first symmetric term of the asymptotic expansion of the solution about the crack tip has been correlated with crack extension through laboratory experiments. It is conceivable that much like crack extension, failure initiation (for example, the formation of cracks at weldments and reentrant corners, the onset of delamination in composite materials, and so forth) can be correlated with the amplitudes of the terms of asymptotic expansions also. In fact, linear elasticity cannot be useful for predicting failure initiation events unless parameters of the elastic solution can be consistently correlated with occurrences of such events. Certain parameters can be computed only by extraction methods. Others can be computed directly from the finite-element solution [32]. We have shown that accurate and inexpensive determination of the amplitudes of asymptotic expansions in the neighborhood of reentrant corners is possible.

Acknowledgments

The writers wish to thank the U.S. Air Force Office of Scientific Research and the Office of Naval Research for having provided partial support for this investigation through research Grants AFOSR 82-0315 and ONR-N-00014-85-K-0169, respectively. The writers also wish to thank Noetic Technologies Corporation of St. Louis, Missouri for having provided computer facilities through a collaborative research agreement with Washington University.

References

- [1] Babuška, I. and Szabó, B., "On the Rates of Convergence of the Finite Element Method," *International Journal for Numerical Methods in Engineering*, Vol. 18, 1982, pp. 323-341.
- [2] Babuška, I., Gui, W., and Szabó, B. A., "Performance of the h , p , and h - p Versions of the Finite Element Method," *Research in Structures and Dynamics*, R. J. Hayduk and A. K. Noor, Eds. NASA Conference Publication 2335, National Aeronautics and Space Administration, Washington, DC, 1984, pp. 73-93.

- [3] Gui, W., "The h - p Version of the Finite Element Method for the One-Dimensional Problem," doctoral dissertation, University of Maryland, College Park, MD, 1985.
- [4] Guo, B. and Babuška, I., "The h - p Version of the Finite Element Method: Part I—Basic Approximation Results. Part II—General Results and Applications," *Computational Mechanics*, Springer-Verlag, New York, 1986.
- [5] Szabó, B., "Estimation and Control of Error Based on P -Convergence," *Accuracy Estimates and Adaptive Refinements in Finite Element Computations*, I. Babuška, J. Gago, E. R. de A. Oliveira, and O. C. Zienkiewicz, Eds., Wiley, New York, 1986, pp. 61–78.
- [6] Szabó, B. A., "Implementation of a Finite Element Software System with H - and P -Extension Capabilities," *Finite Elements in Analysis and Design*, Vol. 2, 1986, pp. 177–194.
- [7] Szabó, B. A., "Mesh Design for the p -Version of the Finite Element Method," *Computer Methods in Applied Mechanics and Engineering*, Vol. 55, 1986, pp. 181–197.
- [8] Babuška, I. and Suri, M., "The Optimal Convergence Rate of the p -Version of the Finite Element Method," Technical Note BN-1045, Laboratory for Numerical Analysis, Institute for Physical Science and Technology, University of Maryland, College Park, MD, October 1985.
- [9] Babuška, I. and Miller, A., "The Post-Processing Approach in the Finite Element Method: Part 1—Calculation of Displacements, Stresses, and Other Higher Derivatives of the Displacements," *International Journal for Numerical Methods in Engineering*, Vol. 20, 1984, pp. 1085–1109.
- [10] Babuška, I. and Miller, A., "The Post-Processing Approach in the Finite Element Method: Part 2—The Calculation of Stress Intensity Factors," *International Journal for Numerical Methods in Engineering*, Vol. 20, 1984, pp. 1111–1129.
- [11] Babuška, I. and Miller, A., "The Post-Processing Approach in the Finite Element Method: Part 3—A-Posteriori Error Estimates and Adaptive Mesh Selection," *International Journal for Numerical Methods in Engineering*, Vol. 20, 1984, pp. 2311–2324.
- [12] Karp, S. N. and Karal, F. C., "The Elastic-Field Behavior in the Neighborhood of a Crack of Arbitrary Angle," *Communications on Pure and Applied Mathematics*, Vol. XV, 1962, pp. 413–421.
- [13] Kondratiev, V. A., "Boundary Problems for Elliptic Equations in Domains with Conical or Angular Points," *Transactions of the Moscow Mathematical Society*, Vol. 16, 1967, pp. 227–313.
- [14] Melzer, H. and Rannacher, R., "Spannungskonzentrationen in Eckpunkten der Kirchhoffschen Platte," *Bauingenieur*, Vol. 55, 1980, pp. 181–184.
- [15] Muskhelishvili, N. I., "Some Basic Problems of the Mathematical Theory of Elasticity," P. Noordhoff Ltd., Groningen, Holland, 1953.
- [16] Williams, M. L., "Stress Singularities Resulting from Various Boundary Conditions in Angular Corners of Plates in Extension," *Journal of Applied Mechanics*, 1952, pp. 526–528.
- [17] Szabó, B. A., *PROBE: Theoretical Manual*, Noetic Technologies Corp., St. Louis, MO, 1985.
- [18] Izadpanah, K., "Computation of the Stress Components in the P -Version of the Finite Element Method," doctoral dissertation, Washington University, St. Louis, MO, 1984.
- [19] Vasilopoulos, D., "Treatment of Geometric Singularities with the P -Version of the Finite Element Method," doctoral dissertation, Washington University, St. Louis, MO, 1984.
- [20] Paris, P. C. and Sih, G. C., "Stress Analysis of Cracks," *Fracture Toughness Testing and Its Application*, ASTM STP 381, American Society for Testing and Materials, Philadelphia, 1970, pp. 30–81.
- [21] Sha, G. T. and Yang, C-T., "Weight Function Calculations for Mixed-Mode Fracture Problems with the Virtual Crack Extension Technique," *Engineering Fracture Mechanics*, Vol. 21, 1985, pp. 1119–1149.
- [22] Andersson, B., Memorandum FFAP-H-736, The Aeronautical Research Institute of Sweden, Bromma, Sweden, 19 March, 1985.
- [23] Rybicki, E. F. and Kanninen, M. F., "A Finite Element Calculation of Stress Intensity Factors by a Modified Crack Closure Integral," *Engineering Fracture Mechanics*, Vol. 9, 1977, pp. 931–938.
- [24] Dempsey, J. P. and Sinclair, G. B., "On the Singular Behavior at the Vertex of a Bi-Material Wedge," *Journal of Elasticity*, Vol. 11, 1981, pp. 317–327.
- [25] Babuška, I. and Rank, M., "An Expert System-like Feedback Approach in the h - p Version of the Finite Element Method," Technical Note, Laboratory for Numerical Analysis, Institute for Physical Science and Technology, University of Maryland, College Park, MD, April 1986.
- [26] Whitney, J. M. and Nuismer, R. J., "Stress Fracture Criteria for Laminated Composites Containing Stress Concentrations," *Journal of Composite Materials*, Vol. 8, 1974, pp. 253–265.
- [27] Nuismer, R. J. and Whitney, J. M., "Uniaxial Failure of Composite Laminates Containing Stress Concentrations," in *Fracture Mechanics of Composites*, ASTM STP 593, American Society for Testing Materials, Philadelphia, 1975, p. 117.

- [28] Potter, R. T., "On the Mechanism of Tensile Fracture in Notched Fibre Reinforced Plastics," *Proceedings of the Royal Society*, A361, 1978, pp. 325-341.
- [29] Nuismer, R. J. and J. D. Labor, "Applications of Average Stress Failure Criterion: Part I—Tension," *Journal of Composite Materials*, Vol. 12, 1978, p. 238.
- [30] Nuismer, R. J., "Applications of Average Stress Failure Criterion: Part II—Compression," *Journal of Composite Materials*, Vol. 13, 1979, pp. 49-60.
- [31] Mikulas, M. M., "Failure Prediction Techniques for Compression Loaded Laminates with Holes," NASA Conference Publication 2142, National Aeronautics and Space Administration, Washington, DC, 1980.
- [32] Szabó, B. A., "Computation of Stress Field Parameters in Areas of Steep Stress Gradients," *Communications in Applied Numerical Methods*, Vol. 2, 1986, pp. 133-137.

Line Spring Model and Its Applications to Part-Through Crack Problems in Plates and Shells

REFERENCE: Erdogan, F. and Aksel, B., "Line Spring Model and Its Applications to Part-Through Crack Problems in Plates and Shells," *Fracture Mechanics: Nineteenth Symposium, ASTM STP 969*, T. A. Cruse, Ed., American Society for Testing and Materials, Philadelphia, 1988, pp. 125–152.

ABSTRACT: This paper, after giving a general description of the line spring model, covers the problem of the interaction of multiple internal and surface cracks in plates and shells. The shape functions for various related crack geometries obtained from the plane strain solution and the results of some multiple crack problems are presented. The problems considered include coplanar surface cracks on the same or opposite sides of a plate; nonsymmetrically located coplanar internal elliptic cracks; and, in a very limited way, the surface and corner cracks in a plate of finite width and a surface crack in a cylindrical shell with fixed end.

KEY WORDS: stress intensity factor, line spring model, surface crack, internal crack, three-dimensional crack problem, part-through crack, cracks in plates, cracks in shells, fracture mechanics

The analysis of a part-through crack in a component that may locally be represented by a "plate" or a "shell" is certainly one of the important problems in fracture mechanics. The general problem is one of a three-dimensional crack in a solid with bounded geometry where there is a strong interaction between the stress field disturbed by the crack and the bounding surfaces of the medium. Even under the assumption of linear elasticity, a neat analytical treatment of the problem seems to be intractable. The existing solutions, therefore, rely very heavily on the techniques of computational mechanics. In this respect, the standard technique has been that of three-dimensional finite element analysis (see, for example, Refs 1 through 5 for some of the typical contributions). Other numerical techniques used have been the boundary integral equation method [6] and the alternating method (see, for example, the article by Shah and Kobayashi in Ref 7). The finite element and the alternating methods have also been combined in a new hybrid technique to treat three-dimensional elliptic crack problems [8,9].

If one is dealing with a relatively thin-walled structure containing a part-through crack in a plane perpendicular to the bounding surfaces of the medium, the three-dimensional crack problem can be made analytically tractable under two important approximating assumptions. The first is the representation of the structure by a "plate" or a "shell" and the second is the treatment of the part-through crack by a "line spring model." Through the use of a plate or a shell theory, the coordinate in the thickness direction is suppressed and the basically three-dimensional elasticity problem is rendered two-dimensional. Modeling of the crack

¹ Professor of mechanics and graduate student, respectively, Lehigh University, Bethlehem, PA 18015.

by a line spring, on the other hand, not only lends itself to plate or shell treatment, but also preserves the basic plane strain character of the stress field along the crack front (everywhere except near the ends). In a relatively thin-walled structure containing a part-through crack, the net ligament in the plane of the crack would generally have a constraining effect on the crack opening displacements. The physical concept underlying the line spring model, which was first proposed in Ref 10, consists of approximating the three-dimensional crack problem by a coupled membrane-bending problem through reducing the net ligament stresses to the neutral axis of the plate or the shell as an (unknown) membrane load N and bending moment M . In the resulting problem, the crack surface displacements are also represented by two lumped quantities, namely, the crack opening displacement δ and the crack surface rotation θ measured at the neutral surface. The unknowns N , M , δ , and θ are now functions of a single variable, x_1 , the coordinate along the crack in the neutral surface (Fig. 1). The

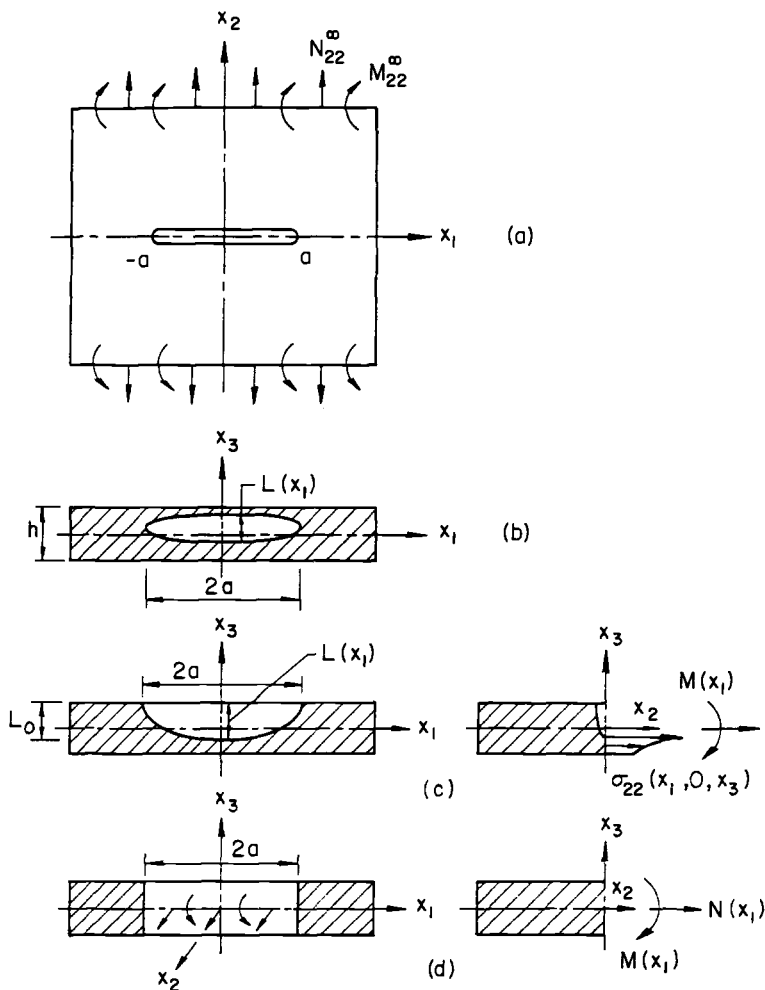


FIG. 1—Notation for internal and surface cracks.

complementary pairs of functions (N, M) and (δ, θ) defined along the crack are not independent and are assumed to be related through the corresponding plane strain problem for the cracked strip. The functions (N, M) or (δ, θ) are determined from the related mixed boundary value problem for the plate or the shell with a through crack in which N and M are treated as unknown crack surface loads. After determining N and M , the stress intensity factor at a given location, x_1 , along the crack is calculated from the corresponding two-dimensional elasticity solution of the cracked strip lying in a plane perpendicular to x_1 (Figs. 1c, 2, and 3).

In the original model, the classical plate bending theory was used and the problem was formulated with N and M as the unknown functions (Ref 10, see also Rice's article in Ref 7). In the application of the model the main problem is the solution of a plate or a shell containing a through crack and subjected to membrane or bending loads. On the other hand, to have an asymptotic solution around the crack tips in a plate under bending which is compatible with the elasticity results, the necessity of using a higher order plate bending theory such as that of Reissner [11,12] has now been well established [13-15]. Unlike the classical theory (in which one can use one less boundary condition than needed through the Kirchhoff assumption), the transverse shear theories of plates and shells can accommodate all the stress and moment resultants (or their displacement complements) on the crack surfaces separately, that is, one can specify three boundary conditions in plates and five in shells. The consequence of this is that the transverse shear theories give asymptotic results that are identical to those obtained from plane strain and antiplane shear elasticity solutions of the crack problems [16,17], whereas not only is the angular distribution of the stresses given by the classical plate and shell theories different from the elasticity results but, for skew-symmetric problems, even the powers of singularity (in the transverse shear stress) are not in agreement [16]. One may note that compatibility of the asymptotic solutions obtained from the transverse shear theories with the elasticity solutions is not restricted to

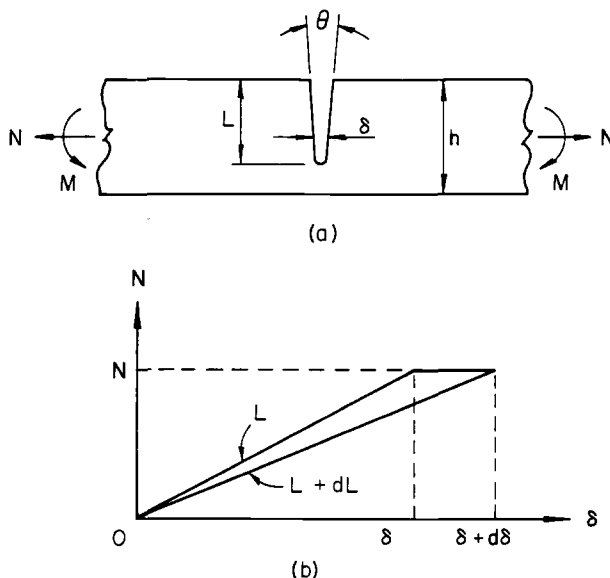


FIG. 2—The corresponding plane strain problem.

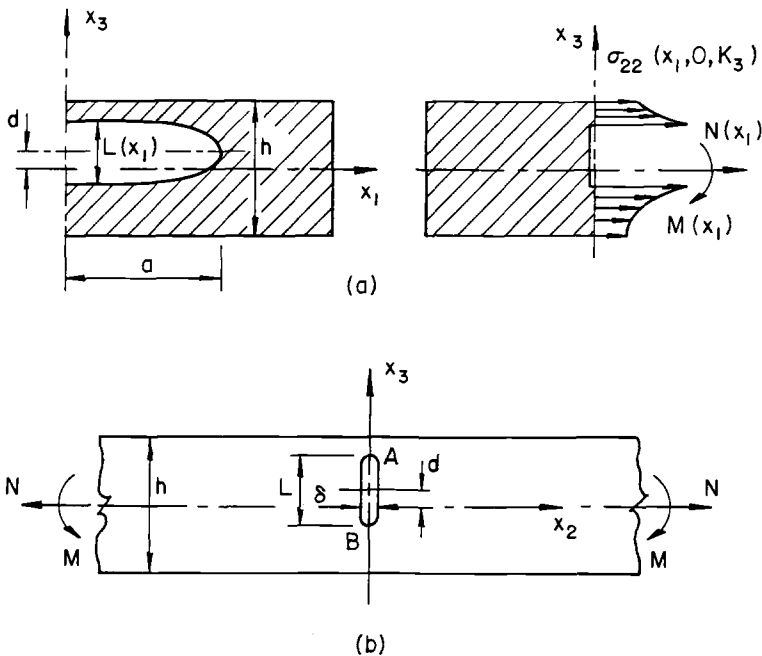


FIG. 3—Notation for an internal part-through crack.

crack problems. As shown in a recent study [18], the agreement is valid for general wedge-shaped plates of an arbitrary angle.

An additional change introduced into the line spring model as presented in this paper is the use of the "displacements" (δ, θ) rather than the stress and moment resultants (N, M) as the unknown functions in the integral equations. This is simply a matter of convenience, as δ and θ turn out to be more natural unknowns in formulating the problem.

In recent years there seems to be a renewed interest in the applications of the line spring model. The main reasons for this is that the model is very simple to apply, is highly flexible with regard to the crack profile, and, as will be shown in this paper, can be routinely extended to treat multiple crack problems of varying geometries. Some recent applications of the model to a variety of plate and shell problems may be found in Refs 19 through 27.

In this paper the line spring model is generalized to cover multiple coplanar cracks of arbitrary orientations, including internal as well as surface cracks, and the related stress intensity shape functions are given. The model is applied to plate and shell problems by using Reissner's transverse shear theory, and the results of some typical examples are discussed.

Description of the Line Spring Model

Let us first consider the problem of a surface crack in a plate or a shell under Mode I loading condition (Fig. 1). Referred to as the local coordinate system, it will be assumed that u_1 , u_2 , and u_3 are the displacement components; β_1 , β_2 are the rotations of the normal to the neutral surface (in the x_1x_3 and x_2x_3 planes, respectively), and N_{ij} , M_{ij} , and V_i ($i, j = 1, 2$) are the membrane, bending, and transverse shear resultants, respectively. Let N_{22}^∞ and

M_{22}^{∞} be external loads applied to the structure away from the crack region (Fig. 1) and define

$$\begin{aligned}\sigma_{\infty} &= \frac{N_{22}}{h} \\ m_{\infty} &= \frac{6M_{22}^{\infty}}{h^2}\end{aligned}\quad (1)$$

Similarly, let N and M represent membrane and bending resultants statically equivalent to the net ligament stress $\sigma_{22}(x_1, 0, x_3)$ (Fig. 1c) and define

$$\begin{aligned}\sigma(x_1) &= \frac{N(x_1, 0)}{h} \\ m(x_1) &= \frac{6M(x_1, 0)}{h^2}\end{aligned}\quad (2)$$

Defining now the unknown functions

$$\begin{aligned}f_1(x_1) &= \frac{\partial}{\partial x_1} \beta_2(x_1, +0) \\ f_2(x_1) &= \frac{\partial}{\partial x_1} u_2(x_1, +0)\end{aligned}\quad (3)$$

and referring to, for example, Refs 24 and 17 for details, the through crack problem for the structure under the applied loads of Eqs 1 and 2 may be expressed as

$$\sum_1^2 \int_{-a}^a k_{ij}(x_1, t) f_j(t) dt = g_i(x_1), \quad -a < x_1 < a, \quad i = 1, 2 \quad (4)$$

$$\int_{-a}^a f_j(t) dt = 0, \quad j = 1, 2 \quad (5)$$

where

$$\begin{aligned}g_1(x_1) &= \frac{-m_{\infty} + m(x_1)}{6E} \\ g_2(x_1) &= \frac{-\sigma_{\infty} + \sigma(x_1)}{E}\end{aligned}\quad (6)$$

In shells, the integral equations (Eq 4) are coupled (that is, k_{12} and k_{21} are not zero), whereas in plates, bending-membrane coupling would be through the input functions m and σ only. Note that m and σ tend to close the crack surfaces while the external loads m_{∞} and σ_{∞} tend to open them.

The first approximating assumption made in developing the line spring model is that the crack is a through crack and the constraint caused by the net ligament stress, $\sigma_{22}(x_1, 0, x_3)$, which tends to prevent the crack from opening and rotating, may be accounted for by applying the membrane and bending resultants N and M on the crack surfaces. The second

major assumption states that the stress intensity factor along the crack front at a location x_1 may be approximated by the corresponding plane strain value obtained from a strip that contains a part-through crack of length $L(x_1)$ and is subjected to uniform tension $N(x_1)$ and bending $M(x_1)$ away from the crack region (Figs. 1 and 2). The main problem in the development of the model is expressing the functions N and M in terms of the unknown functions f_1 and f_2 and it is the second assumption which makes this possible.

To obtain N and M in terms of f_1 and f_2 we now express the energy available for fracture in two alternate forms. First, we note that at a location, x_1 , along the crack front, by using the crack closure concept, the energy available for fracture may be expressed as

$$\mathfrak{G} = \frac{\partial}{\partial L} (U - V) = \frac{1 - \nu^2}{E} K_1^2 \quad (7)$$

where $L(x_1)$ is the crack size, K_1 is the stress intensity factor, U is the work done by the external loads, V is the strain energy, and E and ν are the elastic constants. From the solution of the plane elasticity problem, the stress intensity factor for an edge crack shown in Fig. 2 is obtained as follows

$$K_1 = \sqrt{h} [\sigma g_i(s) + m g_b(s)] \quad (8)$$

where $s = L/h$ and σ and m are given by Eq 2. For analytical convenience the shape functions g_i and g_b may be expressed as

$$\begin{aligned} g_i(s) &= \sqrt{\pi s} \sum_{i=0}^6 b_i s^{2i} \\ g_b(s) &= \sqrt{\pi s} \sum_{i=0}^6 c_i s^i \end{aligned} \quad (9)$$

The calculated values² of K_1 [28,29] and the coefficients b_i and c_i obtained from a least square curve fit are given in Table 1.

Referring to Fig. 2, we now let $d\delta$ and $d\theta$ be the changes in the "load line displacements" δ and θ (corresponding to "loads" N and M) as the crack length goes from L to $L + dL$ under "fixed load" conditions. From Fig. 2b it then follows that

$$dU = Nd\delta + Md\theta \quad (10)$$

$$dV = \frac{1}{2} [N(\delta + d\delta) + M(\theta + d\theta)] - \frac{1}{2} (N\delta + M\theta) = \frac{1}{2} (Nd\delta + Md\theta) \quad (11)$$

giving the energy available for crack growth dL as

$$d(U - V) = \frac{1}{2} (Nd\delta + Md\theta) \quad (12)$$

² The values of K , shown in Table 1, are from Ref 28 and are considered to be accurate.

TABLE 1—The stress intensity factors and the coefficients b_i and c_i of the shape functions $g_i(s)$ and $g_b(s)$ in a strip containing an edge crack of length L and subjected to uniform tensile stress N/h and bending moment M (see Eqs 8 and 9 and Fig. 2).

$\frac{L}{h}$	Tension, $\frac{K_I}{\left(\frac{N}{h}\right)\sqrt{\pi L}}$	Bending, $\frac{K_I}{\left(\frac{6M}{h^2}\right)\sqrt{\pi L}}$	b_i	c_i	i
$\rightarrow 0$	1.121 522 26	1.121 522 26	1.121 5	1.120 2	0
10^{-5}	1.121 522	1.121 5	6.520 0	-1.887 2	1
10^{-3}	1.121 531	1.120 2	-12.387 7	18.014 3	2
0.1	1.189 2	1.047 2	89.055 4	-87.385 1	3
0.2	1.367 3	1.055 3	-188.608 0	241.912 4	4
0.3	1.659 9	1.124 1	207.387 0	-319.940 2	5
0.4	2.111 4	1.260 6	-32.052 4	168.010 5	6
0.5	2.824 6	1.497 2			
0.6	4.033 2	1.914 0			
0.7	6.354 9	2.725 2			
0.8	11.955	4.676 4			
0.85	18.628	6.981 7			
0.9	34.633	12.462			
0.95	99.14	34.31			

Observing that for constant N and M and varying L

$$\begin{aligned} d\delta &= \frac{\partial \delta}{\partial L} dL \\ d\theta &= \frac{\partial \theta}{\partial L} dL \end{aligned} \quad (13)$$

from Eqs 12, 13, and 7 we obtain

$$\frac{\partial}{\partial L} (U - V) = \mathfrak{G} = \frac{1}{2} \left(N \frac{\partial \delta}{\partial L} + M \frac{\partial \theta}{\partial L} \right) = \frac{1 - \nu^2}{E} K_I^2 \quad (14)$$

If we now define the matrices

$$\begin{aligned} \tau &= (\tau_i) = \begin{bmatrix} m \\ \sigma \end{bmatrix} \\ \omega &= (\omega_i) = \begin{bmatrix} h\theta/6 \\ \delta \end{bmatrix} \\ G(s) &= g_{ij} = \begin{bmatrix} g_b^2 & g_b g_i \\ g_b g_i & g_i^2 \end{bmatrix} \end{aligned} \quad (15)$$

substituting from Eqs 2 and 8 into Eq 14 we obtain

$$\mathfrak{G} = \left(\frac{1 - \nu^2}{E} h \right) \tau^T G \tau = \left(\frac{h}{2} \right) \tau^T \frac{\partial \omega}{\partial L} \quad (16)$$

giving

$$\frac{\partial \omega}{\partial L} = \frac{2(1 - \nu^2)}{E} G\tau \quad (17)$$

Note that G is a function and τ is independent of the variable L and $\omega = 0$ for $L = 0$. Thus, from Eq 17 it is seen that

$$\omega = \frac{2(1 - \nu^2)}{E} \left(\int_0^L G dL \right) \tau \quad (18)$$

Referring to Eq 3, Eq 5, and Fig. 2, if we observe that

$$\begin{aligned} \delta &= 2u_2(x_1, 0) = 2 \int_{-a}^{x_1} f_2(t) dt \\ \theta &= 2\beta_2(x_1, 0) = 2 \int_{-a}^{x_1} f_1(t) dt \end{aligned} \quad (19)$$

Eq 18 gives the desired relationship between the pairs of complementary quantities (m, σ) and (f_1, f_2) which may be expressed as

$$\tau = \begin{bmatrix} m \\ \sigma \end{bmatrix} = \frac{E}{1 - \nu^2} \left(\int_0^L G dL \right)^{-1} \begin{bmatrix} \frac{h}{6} \int_{-a}^{x_1} f_1(t) dt \\ \int_{-a}^{x_1} f_2(t) dt \end{bmatrix} \quad (20)$$

It should also be observed that since the crack depth $L(x_1)$ is a known function of x_1 , the coefficient matrix C defined by

$$C = (c_{ij}(x_1)) = \frac{1}{1 - \nu^2} \left(\int_0^L G dL \right)^{-1} \quad (21)$$

would also consist of known functions $c_{ij}(x_1)$ of x_1 .

Substituting now from Eqs 20 and 21 into Eq 4 and rearranging, we obtain

$$\begin{aligned} \int_{-a}^a [k_{11}(x_1, t) f_1(t) + k_{12}(x_1, t) f_2(t)] dt - \frac{h}{36} c_{11}(x_1) \int_{-a}^{x_1} f_1(t) dt - \frac{1}{6} c_{12}(x_1) \int_{-a}^{x_1} f_2(t) dt \\ = -\frac{m_x}{6E}, \quad -a < x_1 < a \end{aligned} \quad (22a)$$

$$\begin{aligned} \int_{-a}^a [k_{21}(x_1, t) f_1(t) + k_{22}(x_1, t) f_2(t)] dt - \frac{h}{6} c_{21}(x_1) \int_{-a}^{x_1} f_1(t) dt - c_{22}(x_1) \int_{-a}^{x_1} f_2(t) dt \\ = -\frac{\sigma_x}{E}, \quad -a < x_1 < a \end{aligned} \quad (22b)$$

After solving Eq 22 for f_1 and f_2 , the stress intensity factor $K_I(x)$ may be obtained from Eqs 20 and 8.

If the plate or the shell contains collinear surface cracks in the x_1x_3 plane along $a_k < x_1 < b_k$, ($k = 1, \dots, n$), the integral equations in Eq 8 remain essentially unchanged and the problem can be solved by defining the unknown functions f_1 and f_2 given by Eq 3 for each crack separately.

Internal and Multiple Cracks

The line spring model described in the previous section can be applied to any coplanar part-through crack problem provided that, on any cross-section parallel to the x_2x_3 plane, there is only one net ligament and one crack, if any (Figs. 1c and 2). The model can also be extended to apply to part-through cracks involving more than one net ligament, as in internal cracks (Fig. 3), or more than one crack, as in coplanar surface cracks on both sides of the plate or the shell. Here the major difficulty lies in the fact that in such cases usually there is more than one stress intensity factor that must be expressed in terms of more than one dimensionless variable. Thus, aside from the generalization of the basic concept, the problem reduces to sufficiently accurate parametrization of the stress intensity factors.

Consider, for example, the nonsymmetric crack geometry shown in Fig. 3. The integral equations for the corresponding through crack problem is again given by Eq 8. The difference between the two problems is in expressing the resultants $\sigma(x_1)$ and $m(x_1)$ in terms of the unknown functions f_1 and f_2 defined by Eq 3. At each cross section we note that there are two dimensionless length parameters, $L(x_1)/h$ and $d(x_1)/h$. The problem can be simplified considerably, however, if we restrict the discussion to cracks which are symmetric with respect to the $x_3 = d$ plane (Fig. 3). Thus, defining the plane internal crack by

$$-a < x_1 < a, \quad x_2 = 0, \quad d - \frac{L(x_1)}{2} < x_3 < d + \frac{L(x_1)}{2} \quad (23)$$

in the discussion that follows it will be assumed that d is independent of x_1 . Referring to Fig. 3b, if K_A and K_B are the stress intensity factors at the crack tips A and B obtained from the plane elasticity solution, for an increase, dL , in the crack length the energy increment available for fracture (as determined from crack closure) may be expressed as

$$d(U - V) = \frac{1 - \nu^2}{E} \left[K_A^2 \frac{dL}{2} + K_B^2 \frac{dL}{2} \right] \quad (24)$$

or

$$\mathcal{G} = \frac{\partial}{\partial L} (U - V) = \frac{1 - \nu^2}{2E} (K_A^2 + K_B^2) \quad (25)$$

We now note that as long as there is only one variable L representing the crack size, the argument leading to the expression of \mathcal{G} in terms of (N, M) and (δ, θ) will remain unchanged (see Eqs 10 to 14) and from Eqs 14 and 25 it follows that

$$\frac{1}{2} \left(N \frac{\partial \delta}{\partial L} + M \frac{\partial \theta}{\partial L} \right) = \frac{1 - \nu^2}{2E} (K_A^2 + K_B^2) \quad (26)$$

The solution of the plane elasticity problem shown in Fig. 3b is available in Ref 29, and K_A and K_B can be expressed in terms of certain shape functions as follows

$$K_A = \sqrt{h} [\sigma g_{At}(s) + m g_{Ab}(s)] \quad (27)$$

$$K_B = \sqrt{h} [\sigma g_{Bt}(s) + m g_{Bb}(s)]$$

where $s = L/h$, $\sigma = N/h$, and $m = 6M/h^2$.

The shape functions are, in turn, expressed by

$$g_{At}(s) = \sqrt{\pi s} \sum_{i=0}^n b_{Ai} s^{2i} \quad (28a)$$

$$g_{Ab}(s) = \sqrt{\pi s} \sum_o^n c_{Ai} s^i \quad (28b)$$

$$g_{Bt}(s) = \sqrt{\pi s} \sum_o^n b_{Bi} s^{2i} \quad (28c)$$

$$g_{Bb}(s) = \sqrt{\pi s} \sum_o^n c_{Bi} s^i \quad (28d)$$

where for a given d the coefficients are obtained from Ref 29 by using a least square curve fit [30].

For $d = 0$, $K_A = K_B$ in tension and $K_A = -K_B$ in bending and the corresponding membrane and bending stress intensity factors as well as the coefficients b_i and c_i are given in Table 2 [30]. In the case of a nonsymmetrically located internal crack, for six different values of d/h the coefficients of the shape functions as defined by Eq 28 are shown in Table 3 [30].

By examining Eqs 14 through 22, it may be seen from the derivation given that the only difference between the models representing the surface crack and the internal crack will be in the matrix $G(s)$ defined by Eq 15 for the edge crack. In particular, for the internal crack

TABLE 2—The stress intensity factors and the coefficients of shape functions in a strip with a symmetric internal crack ($d = 0$, Fig. 3b) under tension and bending (see Eqs 27 and 28).

$\frac{L}{h}$	Tension, $\frac{K_A}{\sigma \sqrt{\frac{\pi L}{2}}}$	Bending, $\frac{K_A}{m \sqrt{\frac{\pi L}{2}}}$	$b_{Ai} = b_{Bi}$	$c_{Ai} = -c_{Bi}$	i
0.05	1.0002	0.0250	0.7071	0.1013	0
0.1	1.0060	0.0500	0.4325	-0.4629	1
0.2	1.0246	0.1001	-0.1091	15.0622	2
0.3	1.0577	0.1505	7.3711	-143.7384	3
0.4	1.1094	0.2023	-57.7894	807.2449	4
0.5	1.1867	0.2573	271.1551	-2844.8525	5
0.6	1.3033	0.3197	-744.4204	6468.9152	6
0.7	1.4884	0.3986	1183.9529	-9477.5512	7
0.8	1.8169	0.5186	-1001.4920	8638.7826	8
0.9	2.585	0.7776	347.9786	-4455.2167	9
0.95	4.252	1.1421	...	5959.4888	10

problem Eq 20 will remain valid provided the matrix G is evaluated from

$$G(s) = \frac{1}{2} \begin{bmatrix} g_{Ab}^2 + g_{Bb}^2 & g_{Ab}g_{Ai} + g_{Bb}g_{Bi} \\ g_{Ab}g_{Ai} + g_{Bb}g_{Bi} & g_{Ai}^2 + g_{Bi}^2 \end{bmatrix} \quad (29)$$

which follows from Eqs 26 to 28 and Eq 16.

Another special case is that of two coplanar surface cracks symmetrically located on opposite sides of the plate (Fig. 4). Going through the argument step by step one may easily show that, except for the shape functions, this case is identical to the internal crack problem with $d = 0$ (Fig. 3). If the plate is under membrane loading only, because of symmetry no bending would take place and there is no need for the bending components of the shape functions, g_{Ab} , g_{Bb} . For the corresponding symmetric edge cracks of depths $L/2$, the stress intensity factors and the coefficients b_i for the membrane shape function are given in Table 4 [30].

For more general crack geometries the problem can be rather complicated. Consider, for example, the nonsymmetric case of the surface crack problem shown in Fig. 4. Let the two cracks be defined by reasonably smooth arbitrary functions, $L_1(x_1)$ and $L_2(x_1)$, and again designate the crack tips at an $x_1 = \text{constant}$ plane by A and B (corresponding to cracks L_1 and L_2 , respectively). The energy available for incremental crack growths dL_1 and dL_2 may again be expressed in the following alternate forms

$$d(U - V) = \frac{1 - \nu^2}{E} [K_A^2 dL_1 + K_B^2 dL_2] \quad (30)$$

$$d(U - V) = \frac{1}{2} \left[\left(N \frac{\partial \delta}{\partial L_1} + M \frac{\partial \theta}{\partial L_1} \right) dL_1 + \left(N \frac{\partial \delta}{\partial L_2} + M \frac{\partial \theta}{\partial L_2} \right) dL_2 \right] \quad (31)$$

If we now define the matrices as in Eq 15, replacing G by G_A and G_B (where the shape functions as defined in Eq 27 would be functions of the variables $s_1 = L_1/h$ and $s_2 = L_2/h$) from Eqs 30 and 31, it can be shown that

$$\frac{\partial \omega}{\partial L_1} dL_1 + \frac{\partial \omega}{\partial L_2} dL_2 = d\omega = \frac{2(1 - \nu^2)}{E} (G_A dL_1 + G_B dL_2) \tau \quad (32)$$

Again by observing that $\omega = 0$ for $L_1 = 0 = L_2$ and $L_1 = L_1(x_1)$, $L_2 = L_2(x_1)$, from Eq 32 we find

$$\omega(x_1) = \frac{2(1 - \nu^2)}{E} \left(\int_0^{L_1} G_A dL_1 + \int_0^{L_2} G_B dL_2 \right) \tau \quad (33)$$

From Eq 33 and Eqs 18 to 21 it then follows that the integral equations of Eq 22 are still valid provided the matrix C defined by Eq 21 is replaced by

$$C = (c_{ij}(x_1)) = \frac{1}{2(1 - \nu^2)} \left(\int_0^{L_1} G_A dL_1 + \int_0^{L_2} G_B dL_2 \right)^{-1} \quad (34)$$

Of course the main difficulty in problems such as the one described above is that they require a complete two-way parametrization of the stress intensity factors or the determi-

TABLE 3—Coefficients of the shape functions in a strip with an asymmetric internal crack under tension and bending; $d \neq 0$, see Eqs 27 and 28 and Fig. 3b.

$\frac{d}{h}$	i	b_{Ai}	b_{Bi}	c_{Ai}	c_{Bi}
0.05	0	0.707 1	0.707 1	0.070 8	0.070 7
	1	0.459 7	0.434 7	-0.062 3	-0.370 1
	2	0.767 1	-0.091 5	13.122 9	0.565 4
	3	0.155 2	2.697 3	-166.428 0	-6.642 3
	4	-9.301 7	-14.119 5	1 145.821 7	45.718 9
	5	97.317 2	54.965 3	-4 762.091 4	-189.951 5
	6	-413.967 3	-135.343 2	12 511.515 2	498.846 3
	7	936.471 9	205.305 1	-20 927.001 9	-834.570 4
	8	-1 078.232 2	-173.348 0	21 613.936 2	862.167 2
	9	504.055 5	62.884 7	-12 568.026 8	-501.435 4
0.1	10			3 148.487 9	125.586 9
	0	0.707 1	0.707 2	0.141 5	0.141 4
	1	0.549 8	0.504 3	-0.173 4	-0.387 1
	2	1.523 5	-0.577 9	18.743 4	1.293 6
	3	-2.239 5	7.648 0	-266.771 3	-17.071 5
	4	-5.284 4	-52.879 3	2 066.469 2	132.028 2
	5	226.026 7	257.207 4	-9 661.521 8	-617.302 3
	6	-1 423.288 7	-799.741 0	28 556.276 4	1 826.319 1
	7	4 348.144 6	1 530.831 4	-53 734.121 6	-3 441.979 7
	8	-6 553.554 0	-1 634.024 0	62 435.934 0	4 007.664 2
0.15	9	3 959.211 6	749.067 3	-40 844.236 4	-2 628.664 2
	10			11 511.591 2	743.334 3
	0	0.707 1	0.707 2	0.212 2	0.212 1
	1	0.702 8	0.637 6	-0.292 9	-0.404 2
	2	2.765 3	-1.233 1	26.323 9	2.249 4
	3	-7.203 6	19.005 7	-427.255 8	-33.675 7
	4	9.138 4	-173.840 7	3 782.959 1	297.499 0
	5	667.495 4	1 108.941 0	-20 214.125 0	-1 590.110 9
	6	-6 105.723 3	-4 517.101 9	68 285.534 4	5 378.604 9
	7	25 260.284 7	11 317.346 9	-146 859.586 6	-11 588.221 7
0.20	8	-50 586.095 4	-15 802.548 5	195 038.234 1	15 425.169 9
	9	40 325.838 8	9 475.748 0	-145 833.622 8	-11 566.828 8
	10			46 980.524 3	3 740.353 8
	0	0.707 1	0.707 2	0.282 9	0.282 8
	1	0.939 4	0.853 4	-0.410 5	-0.419 2
	2	5.018 6	-2.251 8	36.367 5	3.452 4
	3	-19.634 5	47.261 0	-686.992 4	-59.384 8
	4	76.148 9	-589.373 6	7 097.174 5	611.719 4
	5	2 376.877 0	5 125.543 2	-44 245.103 7	-3 814.774 3
	6	-32 402.066 3	-28 413.718 1	174 386.673 3	15 058.001 9
0.25	7	187 563.307 3	96 818.066 4	-437 594.166 1	-37 860.229 0
	8	-517 758.746 5	-183 743.914 1	678 087.650 6	58 816.951 4
	9	566 112.648 2	149 736.514 1	-591 607.763 4	-51 479.621 7
	10			222 394.827 7	19 433.745 6
	0	0.707 1	0.707 1	0.353 6	0.353 6
	1	1.304 1	1.191 8	-0.524 6	-0.428 4
	2	9.651 0	-4.179 3	50.258 9	4.859 2
	3	-57.816 3	129.735 8	-1 136.102 7	-97.655 8
	4	450.776 1	-2 325.355 1	14 085.024 5	1 206.521 0
	5	10 351.862 1	29 069.605 3	-105 370.017 3	-9 029.916 2
0.25	6	-227 973.919 3	-231 101.001 1	498 386.147 5	42 788.338 9
	7	1 960 136.608 0	1 128 028.354 1	-1 500 844.130 5	-129 153.305 2
	8	-7 899 243.558 3	-3 063 223.022 5	2 791 092.049 7	240 895.977 5
	9	12 538 854.755 0	3 568 834.509 7	-2 922 538.277 9	253 169.587 3
	10			1 318 591.941 6	114 779.296 5

TABLE 3—Continued.

$\frac{d}{h}$	i	b_{Ai}	b_{Bi}	c_{Ai}	c_{Bi}
0.30	0	0.707 1	0.707 1	0.424 4	0.424 3
	1	1.902 7	1.748 0	-0.655 3	-0.432 1
	2	20.863 6	-8.908 7	72.317 9	6.640 3
	3	-197.889 5	440.710 3	-2 037.155 3	-160.042 9
	4	2 675.151 3	-12 390.966 8	31 569.750 5	2 468.774 7
	5	71 601.388 0	241 718.267 7	-295 202.511 5	-23 090.848 6
	6	-2 639 273.531 4	-2 989 605.665 9	1 745 346.790 8	136 788.415 9
	7	35 994 016.151 1	22 618 755.130 6	-6 570 139.705 2	-516 213.407 4
	8	-227 958 779.215 5	-94 950 523.975 7	15 273 818.230 2	1 203 928.202 6
	9	567 162 515.860 4	170 542 044.257 8	-19 993 047.660 4	-1 582 260.061 4
	10			11 276 922.905 3	897 240.798 3

nation of the shape functions $g_{\alpha\beta} [\alpha = (A, B), \beta = (t, b)]$ as functions of two variables $s_1 = L_1/h$ and $s_2 = L_2/h$.

Applications and Some Results

In order to apply the line spring model to coplanar multiple cracks, the integral equations need to be cast in a more convenient form. First we note that for the case of through cracks in plates and shells, derivation of the integral equations for colinear multiple cracks is no more difficult than for a single crack. In fact, if no symmetry with respect to the coordinate x_1 is required (Fig. 1), the expressions of the kernels for the two cases are identical. If, for

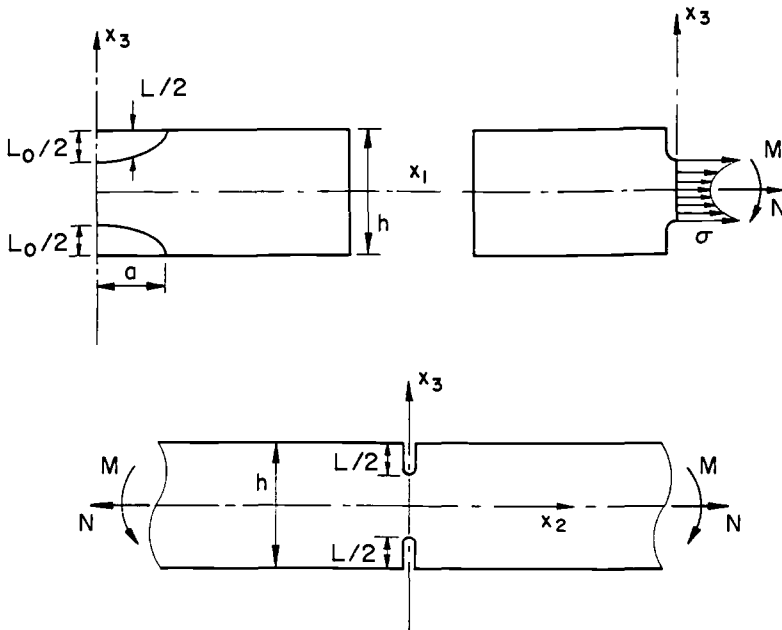


FIG. 4—Geometry and notation for two coplanar semielliptic surface cracks on opposite sides of the plate.

TABLE 4—The stress intensity factor and the coefficients of the shape function for a strip with two collinear symmetric edge cracks of depths $L/2$ under tension σ .

$\frac{L}{h}$	$\frac{K_I}{\sigma \sqrt{\frac{\pi L}{2}}}$	b_i	i
0.0001	1.1221	0.7934	0
0.1	1.1231	0.0775	1
0.2	1.1254	-0.7542	2
0.3	1.1292	7.5825	3
0.4	1.1370	-12.1712	4
0.5	1.1546	-186.5011	5
0.6	1.2117	1236.2858	6
0.7	1.3254	-3043.6190	7
0.8	1.5393	3350.3456	8
0.9	2.0836	-1374.8426	9

example, the structure contains P through cracks in the x_1x_3 plane along $a_p < x_1 < b_p$, $p = 1, 2, \dots, P$, the integral equations for a plate or a shallow shell (replacing Eqs 4 and 5) may be expressed as

$$\sum_{p=1}^P \int_{a_p}^{b_p} \sum_1^2 k_{ij}(x_1, t) f_j(t) dt = g_i(x_1), \quad x_1 \in \sum_1^P (a_p, b_p) \quad (35)$$

$$\int_{a_p}^{b_p} f_j(t) dt = 0, \quad j = 1, 2, p = 1, \dots, P \quad (36)$$

where the functions g_i again represent the crack surface loads and in the case of part-through cracks, the definitions given by Eqs 3, 6, 1, and 2 are still valid. We note that there are really $2P$ unknown functions in the problem, namely f_1 and f_2 on each one of the P cracks. Thus, for the purpose of solving the integral equations, Eq 35 can be written in a more convenient form by defining

$$f_i(x_1) = f_{ip}(x_1) \quad a_p < x_1 < b_p, \quad p = 1, \dots, P, \quad i = 1, 2 \quad (37)$$

$$m(x_1) = m_p(x_1) \quad a_p < x_1 < b_p, \quad p = 1, \dots, P \quad (38)$$

$$\sigma(x_1) = \sigma_p(x_1) \quad a_p < x_1 < b_p, \quad p = 1, \dots, P \quad (39)$$

We also observe that for each crack the net ligament resultants m and σ are related to f_1 and f_2 through equations such as Eqs 20 and 21 where the matrices G and C are dependent on the local (two dimensional) crack geometry and C is a function of x_1 . This means that by using Eq 21, Eq 20 may be replaced by

$$\tau_p = \begin{bmatrix} m_p \\ \sigma_p \end{bmatrix} = EC^p(x_1) \begin{bmatrix} \frac{h}{6} \int_{a_p}^{x_1} f_{1p}(t) dt \\ \int_{a_p}^{x_1} f_{2p}(t) dt \end{bmatrix} \quad a_p < x_1 < b_p, \quad p = 1, \dots, P \quad (40)$$

If we now express the integral equations for each interval (a_p, b_p) separately, from Eqs 35 to 40 and Eq 6 we obtain

$$\sum_{p=1}^P \int_{a_p}^{b_p} \sum_{j=1}^2 k_{1j}(x_1, t) f_{jp}(t) dt - \frac{h}{36} c_{11}'(x_1) \int_{a_r}^{x_1} f_{1r}(t) dt - \frac{1}{6} c_{12}'(x_1) \int_{a_r}^{x_1} f_{2r}(t) dt = -\frac{m_\infty}{6E} \quad a_r < x_1 < b_r, r = 1, \dots, P \quad (41)$$

$$\sum_{p=1}^P \int_{a_p}^{b_p} \sum_{j=1}^2 k_{2j}(x_1, t) f_{jp}(t) dt - \frac{h}{6} c_{21}'(x_1) \int_{a_r}^{x_1} f_{1r}(t) dt - c_{22}'(x_1) \int_{a_r}^{x_1} f_{2r}(t) dt = -\frac{\sigma_\infty}{E} \quad a_r < x_1 < b_r, r = 1, \dots, P \quad (42)$$

$$\int_{a_r}^{b_r} f_{ir}(t) dt = 0, \quad i = 1, 2, r = 1, 2, \dots, P \quad (43)$$

where the functions $c_{ij}'(x_1)$ are determined from Eq 21 or 34 by using the geometry and the shape functions for the r th crack.

It is seen that once the kernels k_{ij} corresponding to the through cracks are determined and the part-through crack profiles $L_r(x_1)$ (or L_{r1} and L_{r2}) are specified, the integral Eqs 41 and 42 (subject to conditions of Eq 43) may be solved for $f_{jr}(t)$ and Eqs 40 and 8 or 27 would then give the stress intensity factors as functions of x_1 . The kernels k_{ij} for various plates and shells containing through cracks may be found in Refs 21, 22, and 24 through 26. For example, if we use a length parameter a^* (usually a half-crack length) to normalize the dimensions, coordinates, and other quantities as

$$\begin{aligned} \frac{x_1}{a^*} &= x \\ \frac{u_2}{a^*} &= v \\ \frac{a_p}{a^*} &= a'_p \\ \frac{b_p}{a^*} &= b'_p \end{aligned} \quad (44)$$

and define

$$\begin{aligned} \frac{\partial}{\partial x} \beta_2(x, +0) &= \phi_1(x) \\ \frac{\partial}{\partial x} v(x, +0) &= \phi_2(x) \end{aligned} \quad (45)$$

The integral equations (Eq 35) for an infinite plate may be expressed as [31]

$$\frac{h}{24\pi a^*} \sum_1^P \int_{a'_p}^{b'_p} \left\{ \frac{3+\nu}{1+\nu} \frac{1}{\xi-x} - \frac{4h^2}{5(a^*)^2(1+\nu)} \frac{1}{(\xi-x)^3} + \frac{4}{1+\nu} \frac{1}{\xi-x} K_2(\gamma|\xi-x|) \right\} \phi_1(\xi) d\xi = -\frac{m_z}{6E} + \frac{m(x)}{6E}, \quad x \in \sum_1^P (a'_p, b'_p) \quad (46)$$

$$\frac{1}{\pi} \sum_1^P \int_{a'_p}^{b'_p} \frac{\phi_2(\xi)}{\xi-x} d\xi = \frac{2}{E} [-\sigma_\infty + \sigma(x)], \quad x \in \sum_1^P (a'_p, b'_p) \quad (47)$$

where $\gamma = 10(a^*)^2/h^2$.

To give an idea of the applications of the line spring model some sample results are shown in Tables 5 through 10 and in Figs. 6 through 13. Table 5 gives the normalized stress intensity factor at the deepest penetration points of two coplanar semielliptic surface cracks symmetrically located on opposite sides of an infinite plate under uniform tension $\sigma_o = N/h$ (Fig. 4). The table also shows the corresponding plane strain result, which is the limiting value of the stress intensity factor as the crack length $2a$ tends to infinity. In this, as well as in other examples discussed in this section, the crack border in the x_1x_3 plane is assumed to be defined (Fig. 1) by

$$L(x_1) = L_o \sqrt{1 - \frac{x_1^2}{a^2}} \quad (48)$$

where a is the half crack length.

The results for the two semielliptic coplanar surface cracks of the same dimensions and located on the same side of an infinite plate are given in Tables 6 and 7. Table 6 shows the maximum value of the normalized stress intensity factor for the plate under uniform tension σ_o in a direction perpendicular to the plane of the crack. The notation used in these tables regarding the dimensions is the same as in Fig. 5a with $d = h/2$. The stress intensity factor for the same plate under bending is given in Table 7. The tables also show the stress intensity factors for the single surface crack, which are the limiting values of the two crack results for $b \rightarrow \infty$. In the two-crack problem considered, the distribution of stress intensity factor $K(x_1)$ along the crack border (or as a function of x_1) is somewhat skewed and the maximum K occurs at a value of x_1 that is somewhat less than $b + a$ [24].

Figure 6 shows the normalized stress-intensity factor in a plate containing a symmetrically located internal elliptic crack ($d = 0$, Fig. 3) at the points where the minor axis intersects the crack border. The results are given for a plate under uniform tension perpendicular to the plane of the crack. In this, as well as in the symmetric surface crack problem considered in Table 5, there is no bending and hence the solution by the line spring method is extremely simple. The figure also shows the finite element results from Ref 3. Disregarding some small values of a/L_o for which the line spring model is not really suitable, it may be noted that the agreement between the two results is fairly good.

Some sample results for an eccentrically located internal elliptic crack are shown in Figs. 7 through 10. In these figures the values K_A and K_B correspond to the points at the midsection of the ellipse (see insert in Fig. 7). Figures 7 and 8 show the normalized stress intensity factors in a plate under uniform tension σ_o for a fixed value of $a/L_o = 4$ and varying values of d/h and L_o/h . Figures 9 and 10 show the tension results for $d/h = 0.15$ and varying values of L_o/h and a/L_o .

TABLE 5—Normalized stress intensity factor K/K_0 calculated at the midsection of two opposite planar elliptic surface cracks in a plate under uniform tension σ_0 , $K_0 = \sigma_0\sqrt{\pi L_0/2}$ (Fig. 4).

$\frac{L_0}{h}$	$\frac{a}{L_0}$						Plane Strain
	1.0	2.0	3.0	4.0	10.0	100.0	
0.1	1.060	1.089	1.099	1.104	1.113	1.119	1.123
0.2	1.009	1.062	1.081	1.091	1.109	1.121	1.125
0.3	0.966	1.028	1.065	1.079	1.106	1.124	1.129
0.4	0.929	1.019	1.053	1.072	1.108	1.131	1.137
0.5	0.902	1.008	1.050	1.073	1.118	1.148	1.155
0.6	0.902	1.038	1.080	1.108	1.165	1.203	1.212
0.7	0.929	1.082	1.149	1.186	1.262	1.315	1.325
0.8	0.997	1.195	1.284	1.336	1.445	1.524	1.539

TABLE 6—Maximum normalized stress intensity factor K/K_0 for two planar elliptic surface cracks in a plate under uniform tension σ_0 , $K_0 = \sigma_0\sqrt{\pi L_0}$ (Fig. 5a, $d = h/2$).

$\frac{L_0}{h}$	$\frac{a}{L_0}$	$\frac{b}{a}$				Single Crack
		0.1	1.0	4.0	20.0	
0.1	2	0.996	0.986	0.982	0.981	0.981
	4	1.072	1.065	1.062	1.062	1.062
	10	1.127	1.122	1.121	1.120	1.120
0.2	2	0.979	0.959	0.951	0.949	0.949
	4	1.107	1.090	1.084	1.082	1.082
	10	1.221	1.210	1.207	1.206	1.206
0.3	2	1.007	0.975	0.963	0.961	0.961
	4	1.189	1.160	1.151	1.149	1.149
	10	1.382	1.364	1.359	1.358	1.358
0.4	2	1.051	1.006	0.991	0.989	0.989
	4	1.299	1.255	1.243	1.240	1.240
	10	1.600	1.571	1.563	1.562	1.562
0.5	2	1.106	1.048	1.032	1.030	1.030
	4	1.430	1.370	1.354	1.352	1.352
	10	1.879	1.836	1.824	1.822	1.821
0.6	2	1.230	1.096	1.080	1.077	1.077
	4	1.568	1.491	1.472	1.469	1.469
	10	2.208	2.141	2.124	2.121	2.121
0.7	2	1.370	1.120	1.100	1.097	1.097
	4	1.694	1.575	1.553	1.550	1.550
	10	2.532	2.434	2.409	2.405	2.405

TABLE 7—Maximum normalized stress intensity factor K/K_0 for two planar elliptic surface cracks in a plate under uniform bending M , $K_0 = \sigma_0 \sqrt{\pi L_0}$, $\sigma_0 = 6M/h^2$ (Fig. 5a, $d = h/2$).

$\frac{L_0}{h}$	$\frac{a}{L_0}$	$\frac{b}{a}$				Single Crack
		0.1	1.0	4.0	20.0	
0.1	2	0.874	0.864	0.861	0.860	0.860
	4	0.943	0.936	0.934	0.933	0.933
	10	0.992	0.988	0.987	0.986	0.986
0.2	2	0.766	0.728	0.719	0.718	0.718
	4	0.847	0.830	0.825	0.824	0.824
	10	0.940	0.930	0.927	0.927	0.927
0.3	2	0.751	0.665	0.651	0.650	0.650
	4	0.803	0.755	0.745	0.744	0.744
	10	0.915	0.900	0.896	0.896	0.895
0.4	2	0.792	0.677	0.659	0.658	0.656
	4	0.801	0.726	0.713	0.711	0.711
	10	0.923	0.902	0.896	0.895	0.895
0.5	2	0.826	0.684	0.663	0.661	0.659
	4	0.834	0.719	0.703	0.701	0.700
	10	0.950	0.910	0.902	0.901	0.901
0.6	2	0.855	0.686	0.662	0.660	0.659
	4	0.909	0.743	0.724	0.722	0.721
	10	0.995	0.925	0.912	0.910	0.910
0.7	2	0.874	0.683	0.658	0.655	0.654
	4	0.989	0.784	0.761	0.759	0.757
	10	1.064	0.956	0.939	0.937	0.936

The normalized stress intensity factor for two symmetrically located identical coplanar internal elliptic cracks in a plate under uniform tension is given in Table 8 ($d = 0$, Fig. 5a). The table shows the results at the midsection of the ellipses. The result for the limiting case of a single crack is also given in the table.

The results for three identical cracks shown in Fig. 5b are given in Table 9. In this case, K_A and K_B also refer to the points of intersection of the minor axes of ellipses with the crack border (Fig. 5b). Since $d \neq 0$ K_A and K_B are not equal. One may observe that the stress intensity factors for the middle crack are only slightly higher than that for the two end cracks. If one may make a general observation regarding the interaction between multiple cracks, it would be that for the same crack lengths and distances in the x_1 direction, the interaction for the part-through cracks is much weaker than the interaction between through cracks.

An example for the distribution of the stress intensity factors along the crack border is given in Table 10. More extensive results on the interaction of multiple part-through cracks of various geometries in an infinite plate may be found in Ref 30.

Some results for a plate of finite width are shown in Figs. 11 and 12. Figure 11 shows the distribution of the normalized stress intensity factors for a symmetrically located surface crack having a semielliptic or a rectangular profile. The normalizing stress intensity factors

TABLE 8—Normalized stress intensity factor K/K_0 , calculated at the midsection of symmetrically located ($d = 0$) two identical planar internal elliptic cracks in a plate under uniform tension σ_0 , $K_0 = \sigma_0\sqrt{\pi L_0/2}$ (Fig. 5a).

$\frac{L_0}{h}$	$\frac{a}{L_0}$	$\frac{b}{a}$				Single Crack
		0.1	1.0	4.0	20.0	
0.1	2	0.977	0.976	0.976	0.976	0.976
	4	0.987	0.987	0.987	0.986	0.987
	10	0.994	0.993	0.993	0.993	0.993
0.2	2	0.975	0.972	0.971	0.971	0.971
	4	0.995	0.994	0.993	0.993	0.993
	10	1.008	1.007	1.007	1.007	1.007
0.3	2	0.980	0.980	0.979	0.979	0.979
	4	1.015	1.013	1.012	1.012	1.012
	10	1.035	1.034	1.034	1.034	1.034
0.4	2	1.007	1.002	1.000	1.000	1.000
	4	1.051	1.048	1.047	1.047	1.047
	10	1.080	1.078	1.078	1.078	1.078
0.5	2	1.046	1.039	1.037	1.036	1.036
	4	1.106	1.102	1.101	1.101	1.101
	10	1.147	1.145	1.145	1.145	1.145
0.6	2	1.108	1.098	1.095	1.095	1.095
	4	1.190	1.185	1.183	1.183	1.183
	10	1.248	1.246	1.245	1.245	1.245
0.7	2	1.205	1.192	1.188	1.187	1.187
	4	1.321	1.313	1.311	1.310	1.310
	10	1.407	1.404	1.403	1.403	1.403
0.8	2	1.367	1.348	1.342	1.341	1.341
	4	1.541	1.529	1.526	1.525	1.525
	10	1.681	1.676	1.674	1.674	1.674
0.9	2	1.703	1.672	1.662	1.661	1.661
	4	2.007	1.988	1.982	1.981	1.981
	10	2.285	2.275	2.272	2.272	...

shown in these figures are the corresponding plane strain values for an edge-cracked strip and are defined by (see Eqs 8 and 9)

$$K_{to} = \frac{N_{22}^{\infty}}{h} \sqrt{h} g_t(s_o)$$

$$K_{bo} = \frac{6M_{22}^{\infty}}{h^2} \sqrt{h} g_b(s_o) \quad (49)$$

$$s_o = \frac{L_o}{h}$$

TABLE 9—Normalized stress intensity factors K_A/K_0 and K_B/K_0 calculated at the midsection of three identical planar internal elliptic cracks in a plate under uniform tension σ_0 ,

$$K_0 = \sigma_0 \sqrt{\pi L_0/2}.$$

				$\frac{b}{a}$				
				0.1	1.0	4.0	20.0	
THE MIDDLE CRACK								
$\frac{K_A}{K_o}$	0.1	0.1	2	0.983	0.981	0.979	0.979	
			4	0.994	0.992	0.992	0.991	
		0.2	2	0.985	0.980	0.977	0.976	
			4	1.007	1.004	1.002	1.001	
	0.3	2	1.006	0.997	0.991	0.989		
		4	1.040	1.035	1.032	1.031		
	0.2	0.1	2	0.981	0.978	0.976	0.975	
			4	0.995	0.994	0.992	0.992	
		0.2	2	0.993	0.986	0.981	0.979	
			4	1.023	1.018	1.015	1.014	
	0.3	0.1	2	0.983	0.979	0.976	0.975	
			4	1.003	1.001	0.999	0.998	
	$\frac{K_B}{K_o}$	0.1	0.1	2	0.983	0.981	0.979	0.979
				4	0.994	0.992	0.991	0.991
			0.2	2	0.984	0.980	0.977	0.976
				4	1.003	1.001	0.999	0.999
		0.3	2	0.997	0.990	0.986	0.984	
			4	1.026	1.022	1.020	1.019	
0.2		0.1	2	0.981	0.978	0.976	0.975	
			4	0.994	0.993	0.992	0.991	
		0.2	2	0.987	0.981	0.977	0.976	
			4	1.012	1.009	1.006	1.005	
0.3		0.1	2	0.981	0.977	0.975	0.974	
			4	0.999	0.997	0.996	0.995	
THE OUTER CRACKS								
$\frac{K_A}{K_o}$	0.1	0.1	2	0.982	0.980	0.979	0.979	
			4	0.993	0.992	0.991	0.991	
		0.2	2	0.982	0.978	0.976	0.976	
			4	1.005	1.003	1.002	1.001	
	0.3	2	0.999	0.994	0.991	0.989		
		4	1.037	1.034	1.032	1.031		
	0.2	0.1	2	0.979	0.977	0.976	0.975	
			4	0.994	0.993	0.992	0.992	
		0.2	2	0.988	0.983	0.980	0.979	
			4	1.019	1.016	1.014	1.014	
	0.3	0.1	2	0.980	0.978	0.976	0.975	
			4	1.001	1.000	0.999	0.998	

TABLE 9—Continued.

	d	$\frac{L_o}{h}$	$\frac{a}{L_o}$	$\frac{b}{a}$			
				0.1	1.0	4.0	20.0
$\frac{K_B}{K_o}$	0.1	0.1	2	0.982	0.980	0.979	0.979
			4	0.993	0.992	0.991	0.991
		0.2	2	0.981	0.978	0.976	0.976
			4	1.002	1.000	0.999	0.999
	0.2	0.3	2	0.992	0.988	0.985	0.984
			4	1.023	1.021	1.020	1.019
		0.1	2	0.979	0.978	0.976	0.975
			4	0.993	0.992	0.991	0.991
	0.3	0.2	2	0.983	0.979	0.977	0.976
			4	1.010	1.007	1.006	1.005
		0.1	2	0.978	0.976	0.974	0.974
			4	0.998	0.996	0.995	0.995

Figure 12 shows an example for the corner cracks. More extensive results for multiple cracks in a plate of finite width obtained by using the line spring model and a comparison with some of the finite element solutions may be found in Ref 24.

Aside from some additional rather complicated Fredholm kernels in the integral equations for shells, from the viewpoint of applications of the line spring model, the problems in shells and plates are identical. The results for various crack and shell geometries obtained by using a transverse shear theory of shallow shells are given in Refs 22, 23, 25, and 26. Figure 13 shows an example for a pressurized cylindrical shell with a fixed end containing a semielliptic axial surface crack. The problem may simulate a rigid end plate or a relatively heavy flange. It is apparent that the effect of shell curvature on the stress intensity factors can be very significant.

TABLE 10—Normalized stress intensity factors on the crack front for an internal elliptic crack in a plate under uniform membrane load $N_{22} = h\sigma_o$ and bending moment $M_{22} = h^2\sigma_b/h$ with $d/h = 0.20$, $L_o/h = 0.45$, $a/L_o = 4$, $K = \sigma_o\sqrt{\pi L_o/2}$ or $K_o = \sigma_b\sqrt{\pi L_o/2}$ (see Fig. 3).

$\frac{x_1}{a}$	$\left(\frac{K_A}{K_o}\right)_N$	$\left(\frac{K_B}{K_o}\right)_N$	$\left(\frac{K_B}{K_o}\right)_M$	$\left(\frac{K_B}{K_o}\right)_M$
0.90	0.723	0.707	0.357	0.218
0.80	0.865	0.831	0.454	0.229
0.70	0.974	0.916	0.531	0.233
0.60	1.065	0.980	0.595	0.233
0.50	1.143	1.028	0.649	0.233
0.40	1.211	1.068	0.697	0.233
0.30	1.266	1.096	0.735	0.233
0.20	1.307	1.116	0.763	0.233
0.10	1.333	1.128	0.781	0.233
0.00	1.342	1.132	0.787	0.232

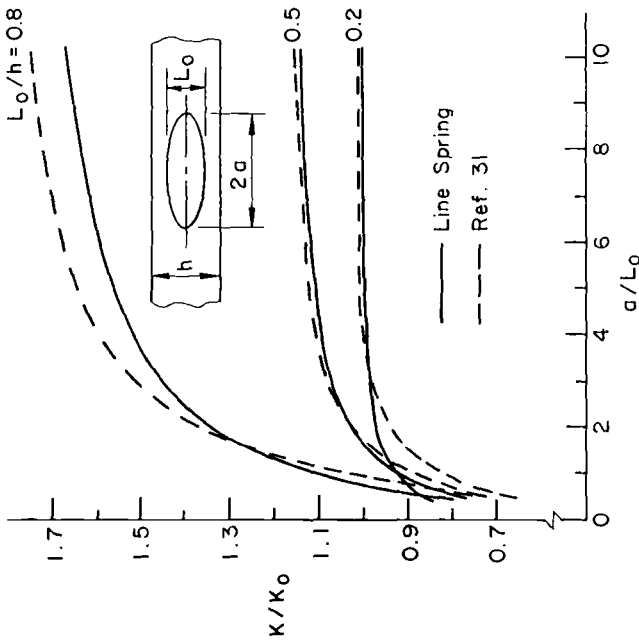


FIG. 6—Normalized stress intensity factor for a symmetrically located internal elliptic crack ($d = 0$, Fig. 3) in a plate under uniform tension perpendicular to the crack plane; $K_0 = \sigma_0 \sqrt{\pi L_0/2}$.

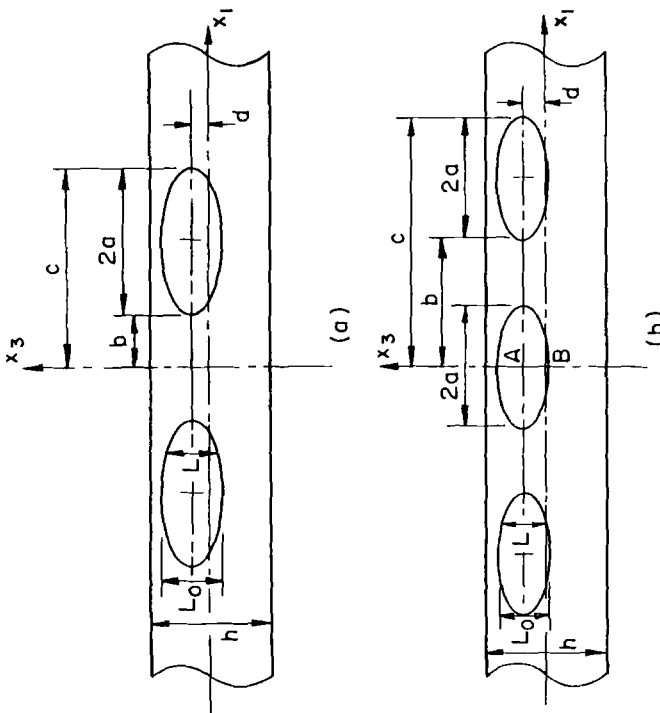


FIG. 5—Geometry and notation for coplanar internal elliptic cracks.

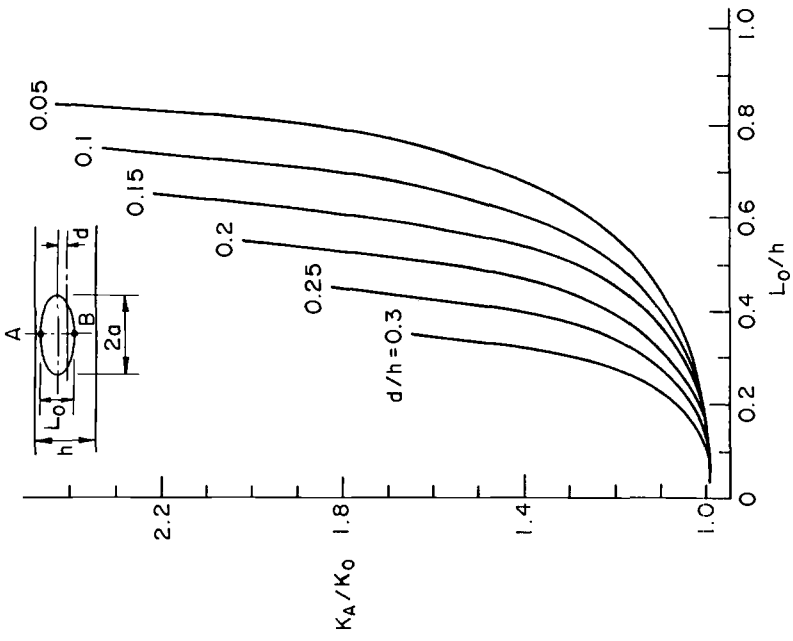


FIG. 7—Normalized stress intensity factor at the midsection of an eccentrically located internal elliptic crack in a plate under uniform tension σ_0 ; $a/L_0 = 4$; $K_0 = \sigma_0 \sqrt{\pi L_0/2}$; Subscript A refers to the smaller net ligament.

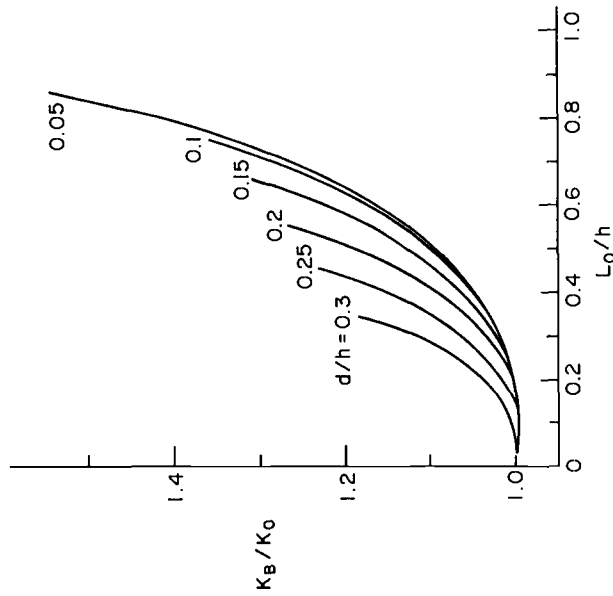


FIG. 8—Same conditions as in Fig. 7; Subscript B refers to the greater net ligament.

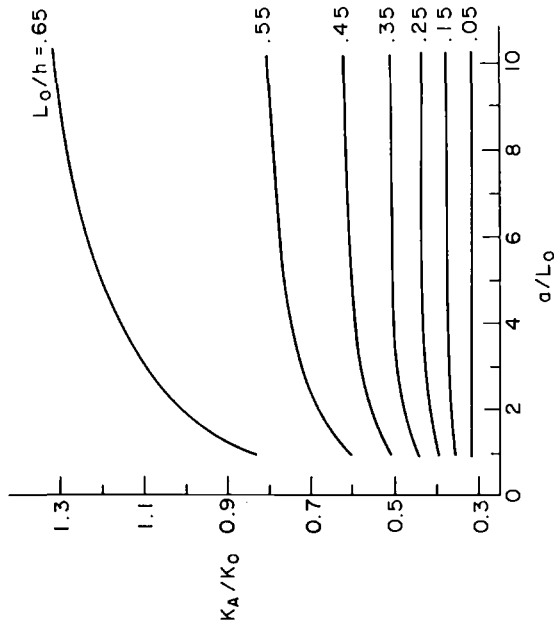


FIG. 10—Stress intensity factor for the greater net ligament, using the conditions in Fig. 9.

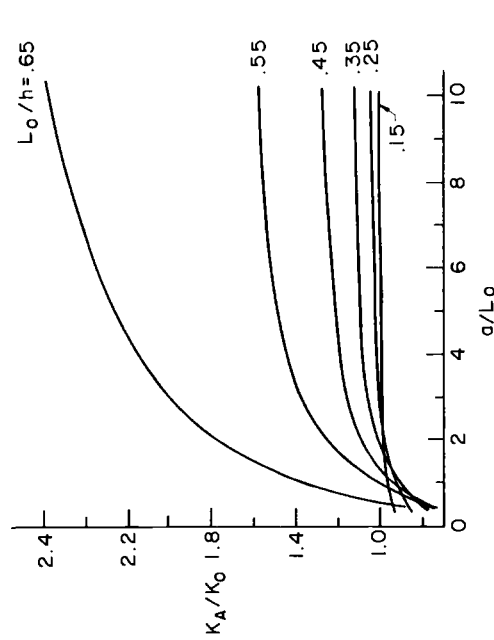


FIG. 9—Normalized stress intensity factor at the midsection of an eccentrically located internal elliptic crack in a plate under tension σ_0 ; $d/h = 0.15$; $K_0 = \sigma_0\sqrt{\pi L_0/2}$; see the insert in Fig. 7.

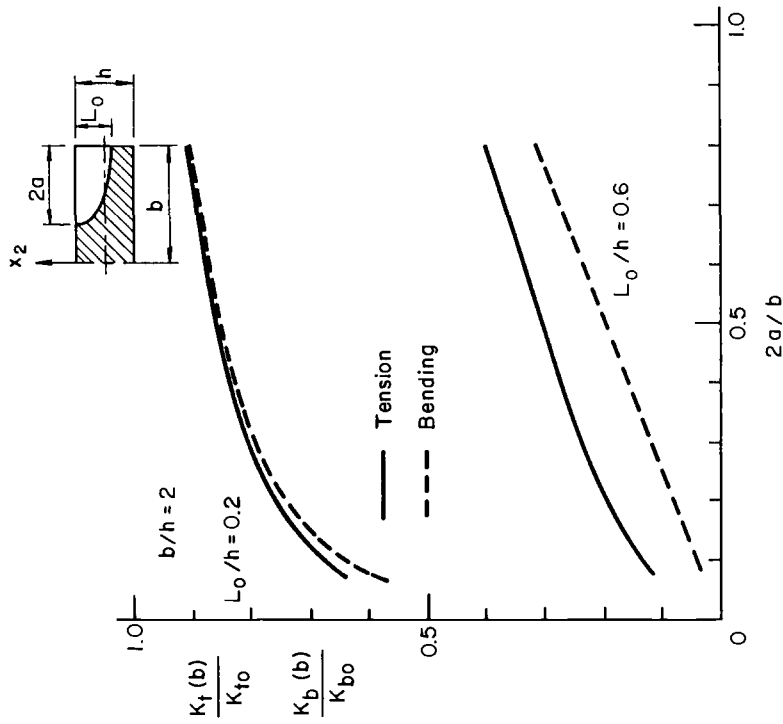


FIG. 12—Stress intensity factor at the maximum penetration point of elliptic corner cracks in a plate of finite width under tension and bending.

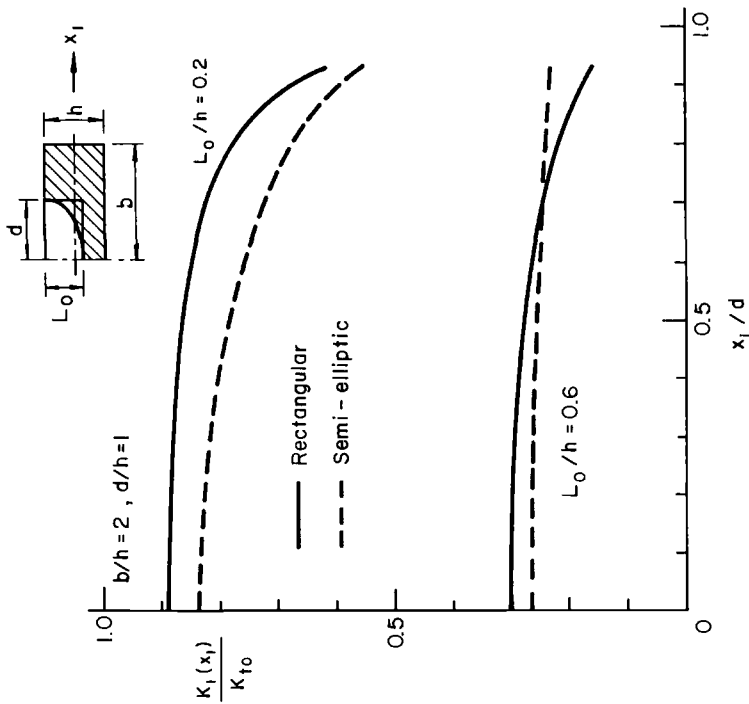


FIG. 11—Distribution of the normalized stress intensity factor along the front of a semielliptic and a rectangular surface crack in a plate of finite width under uniform tension perpendicular to the crack plane.

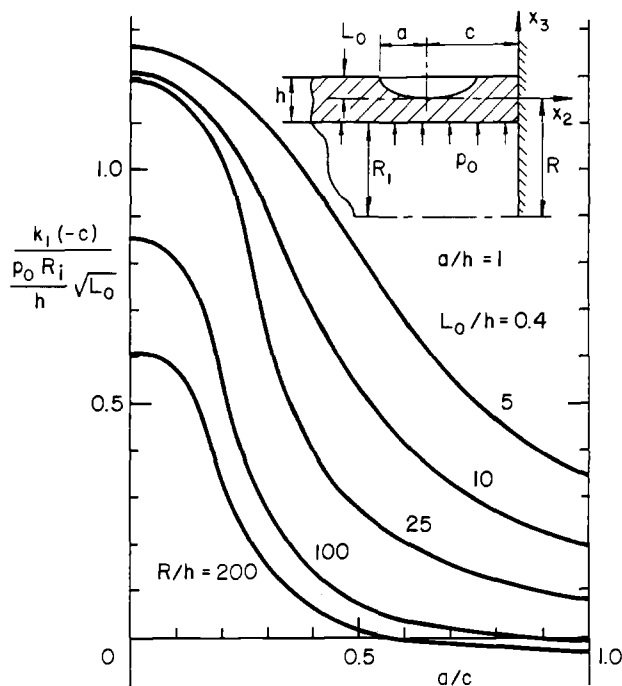


FIG. 13—Stress intensity factor at the midsection of a semi-elliptical axial surface crack in a pressurized cylinder with a fixed end ($\nu = 0.3$, $a/h = 1$, $L_o/h = 0.4$).

Conclusions

In reviewing the results one may conclude that, despite its simplicity and when carefully and judiciously applied, the line spring model may give very useful results for some three-dimensional part-through crack problems that are otherwise analytically intractable. The method is naturally suited to account for plastic deformations in certain approximate ways. The questions currently being studied concern the extension of the model to mixed-mode problems where, unlike the Mode I case, Modes II and III are always coupled. It should also be emphasized that the model has some inherent limitations. For example, the model is not suited to treat problems with a relatively low crack length to wall thickness ratio $2a/h$ (see Fig. 1). The condition $(2a/h) > 1$ may be used as a practical limit in applications. Also the model is not expected to give reliable results near and at the ends of the crack, $x_1 = \pm a$, and at locations along the crack front where the crack depth $L(x_1)$ has a steep variation in x_1 (Fig. 1).

Acknowledgments

The work reported in this paper was supported by NASA-Langley under Grant NGR 39007011 and by National Science Foundation under Grant MEA-8414477.

References

- [1] Raju, I. S. and Newman, J. C., Jr., "Stress Intensity Factors for a Wide Range of Semi-Elliptical Surface Cracks in Finite Thickness Plates," *Journal of Engineering Fracture Mechanics*, Vol. 11, 1979, pp. 817-829.

- [2] Newman, J. C., Jr. and Raju, I. S. "Stress Intensity Factors for Internal Surface Cracks in Cylindrical Pressure Vessels," NASA Technical Memorandum 88073, July 1979; see also *Journal of Pressure Vessel Technology*, Vol. 102, 1980, pp. 342-346.
- [3] Newman, J. C., Jr. and Raju, I. S. "Stress Intensity Factor Equations for Surface Cracks in Three-Dimensional Finite Bodies," *Fracture Mechanics: Fourteenth Symposium, ASTM STP 791*, American Society for Testing and Materials, Philadelphia, 1983.
- [4] McGowan, J. J. and Raymond, M. "Stress Intensity Factor Solutions for Internal Longitudinal Semi-Elliptic Surface Flaws in a Cylinder Under Arbitrary Loading," *Fracture Mechanics: Eleventh Conference, ASTM STP 677*, American Society for Testing and Materials, Philadelphia, 1979.
- [5] Atluri, S. N. and Kathiresan, K., "3-D Analysis of Surface Flaws in Thick-Walled Reactor Pressure Vessels Using Displacement-Hybrid Finite Element Method," *Nuclear Engineering and Design*, Vol. 51, 1980, pp. 163-176.
- [6] Heliot, J., Labbens, R. C., and Pellissier-Tanon, A. "Semi-Elliptic Cracks in the Meridional Plane of a Cylinder Subjected to Stress Gradients," *Fracture Mechanics: Eleventh Conference, ASTM STP 677*, American Society for Testing and Materials, Philadelphia, 1979.
- [7] *The Surface Crack: Physical Problems and Computational Solutions*, J. L. Swedlow, Ed. American Society of Mechanical Engineering, New York, 1972.
- [8] Nishioka, T. and Atluri, S. N. "Analytical Solution for Embedded Elliptical Cracks and Finite Element Alternating Method for Elliptical Surface Cracks Subjected to Arbitrary Loadings," *Engineering Fracture Mechanics*, Vol. 17, 1983, pp. 247-268.
- [9] Nishioka, T. and Atluri, S. N. "Analysis of Surface Flaws in Pressure Vessels by a New 3-D Alternating Method," *Journal of Pressure Vessel Technology*, Vol. 104, 1982, pp. 299-307.
- [10] Rice, J. R. and Levy, N. "The Part-Through Surface Crack in an Elastic Plate," *Journal of Applied Mechanics*, Vol. 39, 1972, pp. 185-194.
- [11] Reissner, E. "On Bending of Elastic Plates," *Quarterly of Applied Mathematics*, Vol. 5, 1947, p. 55.
- [12] Reissner, E. and Wan, F. Y. M. "On the Equations of Linear Shallow Shell Theory," *Studies in Applied Mathematics*, Vol. 48, 1969, p. 132.
- [13] Knowles, J. K. and Wang, N. M. "On the Bending of an Elastic Plate Containing a Crack," *Journal of Mathematics and Physics*, Vol. 39, 1960, p. 223.
- [14] Wang, N. M. "Effects of Plate Thickness on the Bending of an Elastic Plate Containing a Crack," *Journal of Mathematics and Physics*, Vol. 47, 1968, p. 371.
- [15] Hartranft, R. J. and Sih, G. C. "Effect of Plate Thickness on the Bending Stress Distribution Around Through Cracks," *Journal of Mathematics and Physics*, Vol. 47, 1968, p. 276.
- [16] Delale, F. and Erdogan, F. "The Effect of Transverse Shear in a Cracked Plate under Skewsymmetric Loading," *Journal of Applied Mechanics*, Vol. 46, 1979, pp. 618-624.
- [17] Delale, F. and Erdogan, F. "Transverse Shear Effect in a Circumferentially Cracked Cylindrical Shell," *Quarterly of Applied Mathematics*, Vol. 37, 1979, p. 239.
- [18] Burton, W. S. and Sinclair, G. B. "On the Singularities in Reissner's Theory for Bending of Elastic Plates," *Journal of Applied Mechanics*, Vol. 53, 1986, pp. 220-222.
- [19] Parks, D. M. "The Inelastic Line Spring: Estimates of Elastic-plastic Fracture Parameters for Surface Cracked Plates and Shells," Paper 80-C2/PVP-109, American Society of Mechanical Engineers, 1980.
- [20] Parks, D. M. "Inelastic Analysis of Surface Flaws Using the Line Spring Model," *Proceedings, Fifth International Conference on Fracture*, Cannes, France, 1981.
- [21] Delale, F. and Erdogan, F. "Line Spring Model for Surface Cracks in a Reissner Plate," *International Journal of Engineering Science*, Vol. 19, 1981, p. 1331.
- [22] Delale, F. and Erdogan, F. "Application of the Line Spring Model to a Cylindrical Shell Containing a Circumferential or an Axial Part-Through Crack," *Journal of Applied Mechanics*, Vol. 49, 1982, p. 97.
- [23] Erdogan, F. and Ezzat, H. "Fracture of Pipelines Containing a Circumferential Crack," *Welding Research Council Bulletin* 288, 1983.
- [24] Erdogan, F. and Boduroglu, H. "Surface Cracks in a Plate of Finite Width Under Extension or Bending," *Theoretical and Applied Fracture Mechanics*, Vol. 2, 1984, pp. 197-216.
- [25] Erdogan, F. and Yahsi, O. S. "A Cylindrical Shell with a Stress-Free End Which Contains an Axial Part-Through or Through Crack," *International Journal of Engineering Science*, Vol. 23, 1985, pp. 1215-1237.
- [26] Yahsi, O. S. and Erdogan, F. "A Pressurized Cylindrical Shell with a Fixed End Which Contains an Axial Part-Through or Through Crack," *International Journal of Fracture*, Vol. 28, 1975, pp. 161-187.
- [27] Alabi, J. A. and Sanders, J. L., Jr. "Circumferential Part-Through Cracks in Cylindrical Shells Under Tension," *Journal of Applied Mechanics*, Vol. 52, 1985, pp. 478-479.

- [28] Kaya, A. C. and Erdogan, F. "On the Solution of Integral Equations with Strongly Singular Kernels," *Quarterly of Applied Mathematics*, Vol. 45, No. 1, 1987, pp. 105-122.
- [29] Kaya, A. C. and Erdogan, F. "Stress Intensity Factors and COD in an Orthotropic Strip," *International Journal of Fracture*, Vol. 16, 1980, pp. 171.
- [30] Aksel, B. and Erdogan, F. "Interaction of Part-Through Cracks in a Flat Plate," Project Report NASA-Langley, NGR 39007011, National Aeronautics and Space Administration, Langley, VA, April 1985.
- [31] Boduroglu, H. and Erdogan, F. "Internal and Edge Cracks in a Plate of Finite Width Under Bending," *Journal of Applied Mechanics*, Vol. 50, 1983, pp. 621-629.

Methodology for Mixed-Mode Stress-Intensity Factor Calculations

REFERENCE: Moyer, E. T., "Methodology for Mixed-Mode Stress-Intensity Factor Calculations," *Fracture Mechanics: Nineteenth Symposium, ASTM STP 969*, T. A. Cruse, Ed., American Society for Testing and Materials, Philadelphia, 1988, pp. 153-166.

ABSTRACT: A method is presented for the calculation of mixed-mode stress-intensity factors for three dimensional crack fronts. The method uses the nodal forces for the calculation. The strength of this approach is the accuracy of nodal force calculations and the avoidance of the assumption of plane strain. The methodology is described for general crack fronts. The special case of a straight crack front is presented in detail. An example problem is solved with a reference solution. The results of the present method agree to within 3% of the reference value.

KEY WORDS: three-dimensional stress-intensity factors, curved crack front, finite-element method, fracture mechanics, mixed-mode fracture

It has long been accepted that, in the analysis of real-world failures of engineering components, one often finds evidence of multiple failure modes and mechanisms. The field of fracture mechanics has attempted over the last 25 to 30 years to provide a theoretical formalism from which to predict and prevent failures of in-service components. While much progress has been made, many open questions still remain.

For theoretical convenience, fracture problems are usually divided into two broad categories: brittle fracture problems (characterized by essentially elastic deformation prior to a sudden and catastrophic failure) and ductile fracture problems (characterized by the presence of significant plastic deformation and stable crack growth prior to catastrophic failure). These areas are typically subdivided further into those problems which can be approximately modeled with a two-dimensional geometry (either in a state of plane stress, plane strain, or axial symmetry) and those which are irreducibly three dimensional. The final subdivision usually separates those problems which are predominantly governed by a single fracture mode (either tensile/compressive mode, Mode I; in-plane shear, Mode II; or out-of-plane shear, Mode III). All of these problems have received much attention in the past; however, problems involving irreducible three-dimensionality, extreme ductility, or multiple fracture modes are still open problems. Research has been done in each of these areas; however, no definitive approaches or theoretical methodologies have emerged to accurately and consistently solve these problems.

The purpose of this work is to address the problem of calculating the stress-intensity factors for an arbitrary three-dimensional crack front under combined mode loading. All

¹ Associate professor of engineering, School of Engineering and Applied Science, The George Washington University, Washington, DC 20052.

failure theories used in the solution of brittle fracture problems depend on the accurate knowledge of the stress-intensity factors along the crack front.

Computationally, the accurate calculation of stress-intensity factors for two-dimensional geometries under arbitrary loading has become commonplace. Many techniques are available which (when used properly) guarantee an accurate prediction. Unfortunately, the two-dimensional techniques all require the assumption of a state of plane stress, plane strain, or axial symmetry ahead of the crack front. Their extension to three-dimensional problems is, therefore, dubious.

Fully three-dimensional problems have received much research for the case of Mode I loading. Early work [1,2] assumed a state of plane strain ahead of the crack front in the calculation of stress-intensity factors. Later work, however, demonstrated that this assumption gave poor results for problems with curved crack fronts (especially near the intersection of the crack front and a free surface) [3,4]. The nodal-force approach (used in Refs 3 and 4) has the unique feature of not requiring the assumption of plane strain ahead of the crack front. It has been well tested and established as an accurate approach for Mode I problems. Unfortunately, the formulation was only developed for Mode I problems. An excellent review of three-dimensional Mode I problem solution methodology can be found in Ref 5.

In this paper, a nodal-force approach will be presented for arbitrary crack fronts in three dimensions under general loading (all three fracture modes can exist). The method will then be specialized to the case of straight crack fronts with combined Mode I and Mode II loading. An example problem is then solved in three dimensions. By constraining the free surfaces appropriately, a state of plane strain can be induced through the thickness of the specimen. The solution is then generated, demonstrating the consistency of the method.

Prior to this work, few studies have been performed to analyze combined-mode three-dimensional problems. Two techniques, however, have been suggested and used in the literature. One such technique, the virtual crack extension method, has been proposed recently [2]. It suffers, however, from the assumptions of plane strain ahead of the crack front and the sensitivity of the direction of crack extension. The results presented in Ref 2 indicate that the virtual crack extension is sensitive to the decoupling and modeling of the shear failure mode. The resolution of this difficulty is problem dependent. In addition, the amount of virtual extension influences the prediction, making the solution of unknown problems difficult. The other approach suggested in the literature uses elements whose shape functions explicitly contain the asymptotic displacement fields for a plane-strain crack [6]. The formulation is a displacement formulation, however, and assumes plane strain in the enriched element. To date, only the formulation has been presented. No mixed-mode example problems have been solved using this technique (at least none appear in the open literature).

Formulation of the Force Approach for Stress-Intensity Factor Calculations

Consider a planar crack with a generally curved front in an infinite solid, as shown in Fig. 1. The only restriction to the crack will be that the crack must lie in a single plane (this assumption could be relaxed, but the algebraic complexity would increase significantly). The plane defined by the crack faces is designated by P . Consider the P plane shown in Fig. 2 with a rectangular Cartesian coordinate system (n,t) defined at Point B in the P plane. The n direction is normal to the crack front and the t direction is tangent to the crack front. Let the z coordinate designate the binormal direction for the crack front (that is, the direction in a right-hand sense). Consider a small area A in this coordinate system as shown. Near

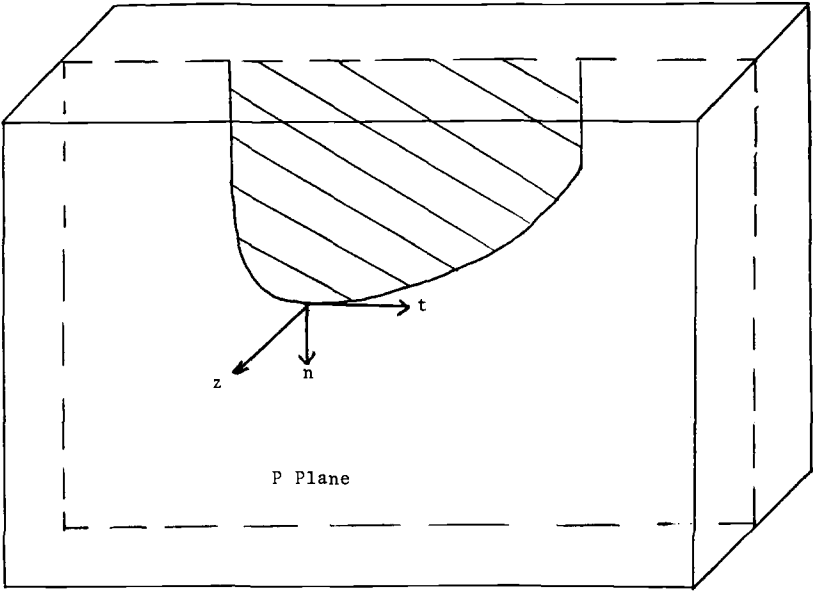


FIG. 1—General three-dimensional plane crack geometry.

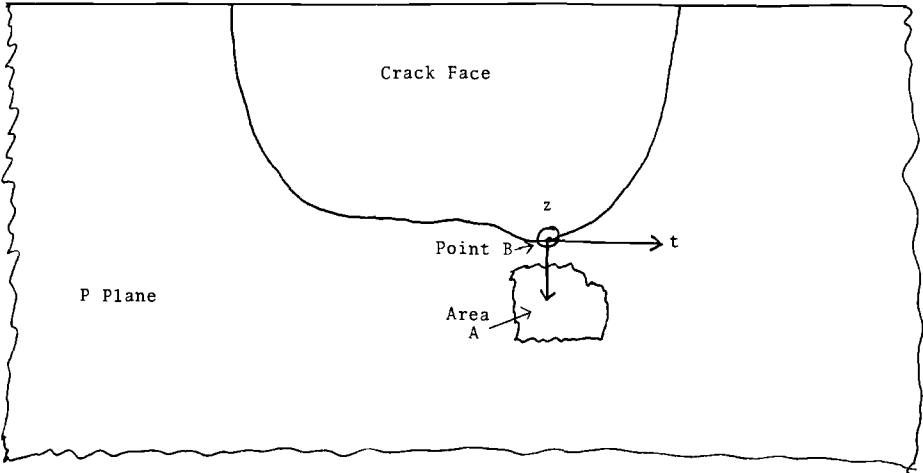


FIG. 2—Geometry of P plane.

the crack front the stress components active in the P plane can be written as follows²

$$\sigma_{zz} = \frac{k_1(t)}{4\sqrt{2}r} \left[5 \cos \left(\frac{\theta}{2} \right) - \cos \left(\frac{5\theta}{2} \right) \right] - \frac{k_2(t)}{4\sqrt{2}r} \left[\sin \left(\frac{\theta}{2} \right) - \sin \left(\frac{5\theta}{2} \right) \right] \quad (1a)$$

$$\sigma_{zt} = \frac{k_3(t)}{\sqrt{2}r} \cos \left(\frac{\theta}{2} \right) \quad (1b)$$

$$\sigma_{zn} = -\frac{k_1(t)}{4\sqrt{2}r} \left[\sin \left(\frac{\theta}{2} \right) - \sin \left(\frac{5\theta}{2} \right) \right] + \frac{k_2(t)}{4\sqrt{2}r} \left[3 \cos \left(\frac{\theta}{2} \right) + \cos \left(\frac{5\theta}{2} \right) \right] \quad (1c)$$

where $k_1(t)$, $k_2(t)$, $k_3(t)$ vary, along the crack front.

These stresses are the general asymptotic solution to the full three-dimensional elasticity formulation for an isotropic material [7]. No assumption of plane stress, plane strain, or axial symmetry has been made.

It is possible to use the stresses predicted from a finite-element analysis together with Eq 1 to find the three stress-intensity factors operative at the point B . This approach, however, suffers from many problems: first, the stresses from a displacement formulation finite-element analysis are not as accurate as the forces or displacements, and second, the stress (theoretically) should approach infinity as the crack front is approached. These problems dictate choosing a different approach.

If Eq 1 is integrated over the area A , the resulting forces can be written in the form

$$\begin{aligned} F_z &= \int_A \sigma_{zz} dA \\ F_t &= \int_A \sigma_{zt} dA \\ F_n &= \int_A \sigma_{zn} dA \end{aligned} \quad (2)$$

or

$$\begin{aligned} F_z &= H_1 k_1 + H_2 k_2 \\ F_t &= H_3 k_3 \\ F_n &= H_4 k_1 + H_5 k_2 \end{aligned} \quad (3)$$

where k_1 , k_2 , and k_3 are the values of the stress-intensity factors at point B . If the net forces on the area A are calculated from a finite-element analysis, the three stress-intensity factors could be solved for directly. It should be noted that the functions H_1 , H_2 , H_3 , H_4 , and H_5 are known from the geometric integrations.

In the derivation of Eq 3, a critical assumption was made. Referring to Fig. 2, it is assumed that the area A was close enough to the crack front and sufficiently small that the variation

² Note that the mathematical definition of stress-intensity factors (k_1 , k_2 , k_3) has been employed. They are related to the "engineering" stress-intensity factors by $K_1 = \sqrt{\pi} k_1$, $K_2 = \sqrt{\pi} k_2$, and $K_3 = \sqrt{\pi} k_3$.

of the stress field in area A can be characterized solely by the stress-intensity factor at the point B . In practice, this appears to be a reasonable assumption if the width of the area A (along the t direction) is small relative to the stress-intensity factor variation along the arc length of the crack. At worst, this assumption will predict a stress-intensity factor level which is an average value of the stress-intensity factor along the crack front in the neighborhood of the point B .

The method outlined above can be implemented numerically in a number of ways. From a theoretical view, no single computational scheme has merit over another if consistent assumptions and approximations are used. In the next section, a simple approach for straight crack fronts will be presented and numerical solutions for an example problem will be demonstrated.

A major problem occurs if the crack intersects a free surface. No analytical solution has been generated on the free surface which intersects with a crack. It has been shown, however, that this problem only affects the solution in a thin boundary layer region near the free surface [8]. For Mode I problems, this has also been demonstrated computationally. No attempt is made in this work to address the free surface problem. The numerical boundary layer approach investigation in Ref 9 can be employed for computational purposes, and the results should be accurate outside the boundary layer.

An important point to be emphasized is that the asymptotic solutions employed are the general solutions to Navier's equations in three dimensions. No assumption of plane stress or plane strain has been made. It can be shown that the stress potentials leading to this solution approach plane strain in the limit as the crack front is approached. The asymptotic limit of this result, however, is far more restrictive than that of Eq 3. For Mode I problems, Raju and Newman [3,4] have demonstrated the error which can be incurred when the assumption of plane strain is made for three-dimensional cracks. The procedure developed in this paper is, therefore, expected to yield accurate results for a wide range of problems.

Computational Procedure for a Straight Crack Front

Consider a straight crack front, as shown in Fig. 3. The area F is the crack face and the area G is part of the solid material. The surface S represents the free surface which intersects the crack. Consider a small area, A , ahead of the crack with dimensions XL by ZL . The total force on the area can be written as (see Appendix)

$$\begin{aligned} F_y &= k_1 \cdot (ZL)\sqrt{2XL} \\ F_x &= k_2 \cdot (ZL)\sqrt{2XL} \\ F_z &= k_3 \cdot (ZL)\sqrt{2XL} \end{aligned} \quad (4)$$

If the body is subdivided into a finite-element grid, the net force acting on A can be computed from the nodal forces. These results can then be used with Eq 4 to find the stress-intensity factors as a function of Z . The results will provide an average measure of the stress-intensity factor over the length ZL .

The approach outlined above suffers only from the assumption that the asymptotic solution is complete. This assumption is not true, however, for most problems. Only in the limit as XL is small relative to all other dimensions would this be true. To compensate for this problem, the concept of an effective stress-intensity factor is introduced. Let the stress be defined as in Eq 1; however, let the stress-intensity factors be functions of the area of

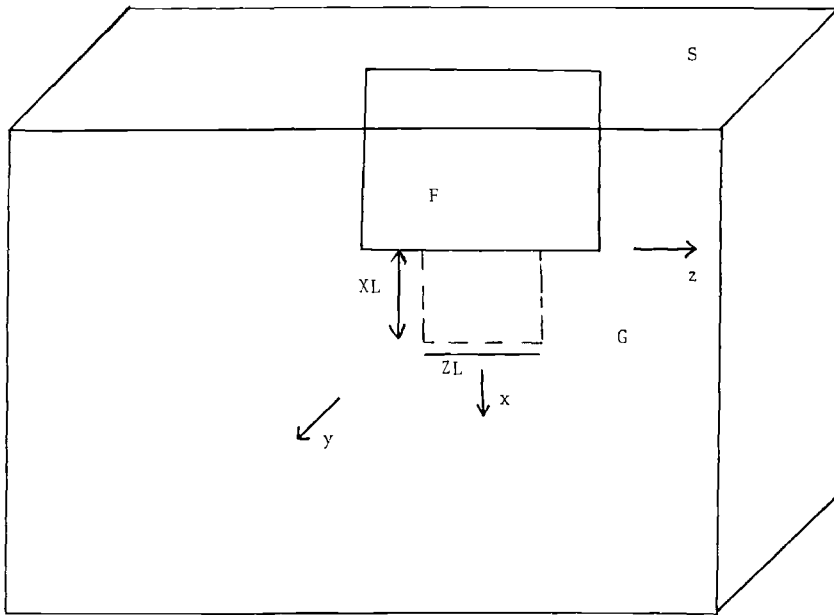


FIG. 3—Geometry for straight crack front.

integration. In the plane crack problem, they are functions of XL only. To find the true stress-intensity factor, the results are linearly extrapolated to $XL = 0$. These extrapolated examples are the true values. This approach has been very successful in problems solved by the nodal force method subjected to Mode I loading only.

Example Problem

Consider the two-dimensional geometry and loading shown in Fig. 4 with the reference stress-intensity factors. Figure 5 shows the equivalent three-dimensional geometry with face constraints to enforce plane strain. This problem is discretized with the grid shown in Fig. 6a to c. The band of pie-shaped elements surrounding the crack front are 15-node quadratic elements with midpoints at the quarter point to induce the $1/\sqrt{r}$ stress behavior [10]. The remaining elements in the grid are all 20-node isoparametric quadratic elements with midside nodes at the midpoints of the arcs of the respective sides. Since the problem is constrained to plane-strain behavior, all elements through the thickness have equal dimensions. If a free surface problem were considered, the boundary layer approach would have been employed.

The solution was generated using the code described in Ref 9. It is a standard elastic solution. The program was modified to provide the nodal forces on arbitrary free-body cuts provided the cuts corresponded to element boundaries. In this problem, the stress-intensity factor is constant through the thickness; therefore, the only area dimension of importance is XL . The results predicted force variation through the thickness of less than 0.01% (using double precision calculations) and, therefore, was ignored. The area considered in the analysis is shown in Fig. 7. The midside node forces from the nodes which lie on the area edge are assumed to contribute half their total force to the area. This assumption is consistent with the finite-element formulation. From the nodal forces, the effective stress-intensity factors, \bar{k}_1 and \bar{k}_2 , are plotted as a function of XL in Fig. 8. As expected, they are very linear and the extrapolated values were calculated using least squares linear regression. The

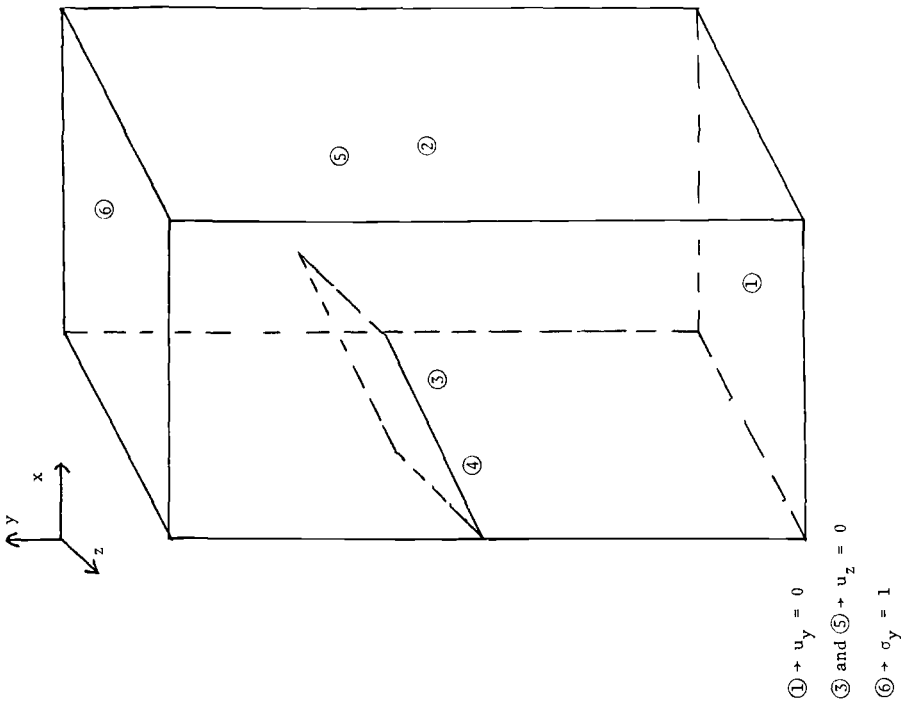


FIG. 5—Equivalent three-dimensional problem.

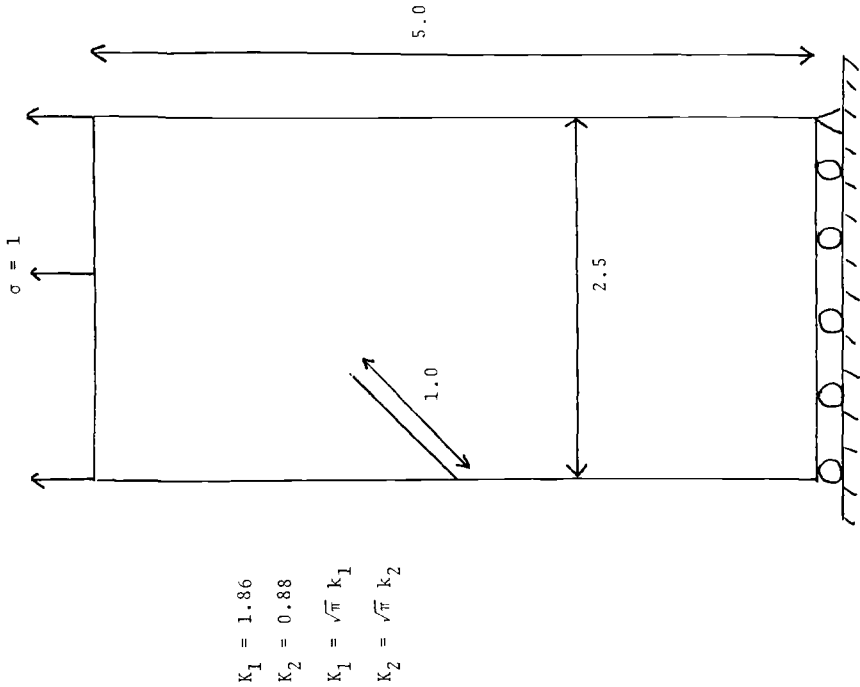


FIG. 4—Mixed-mode reference problem in plane strain.

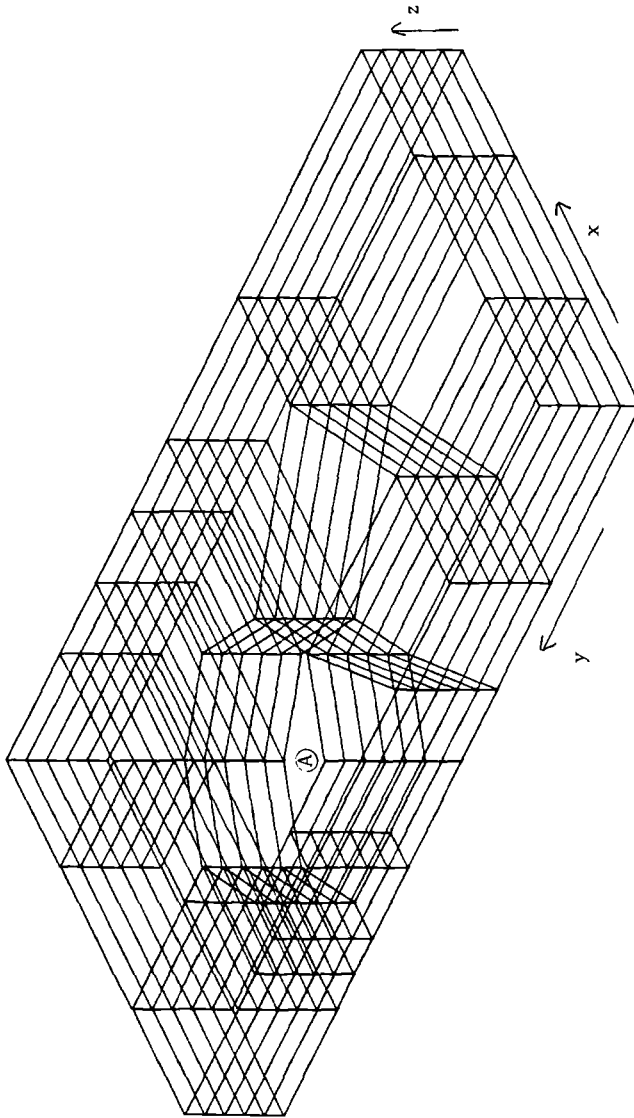


FIG. 6a—Finite-element idealization.

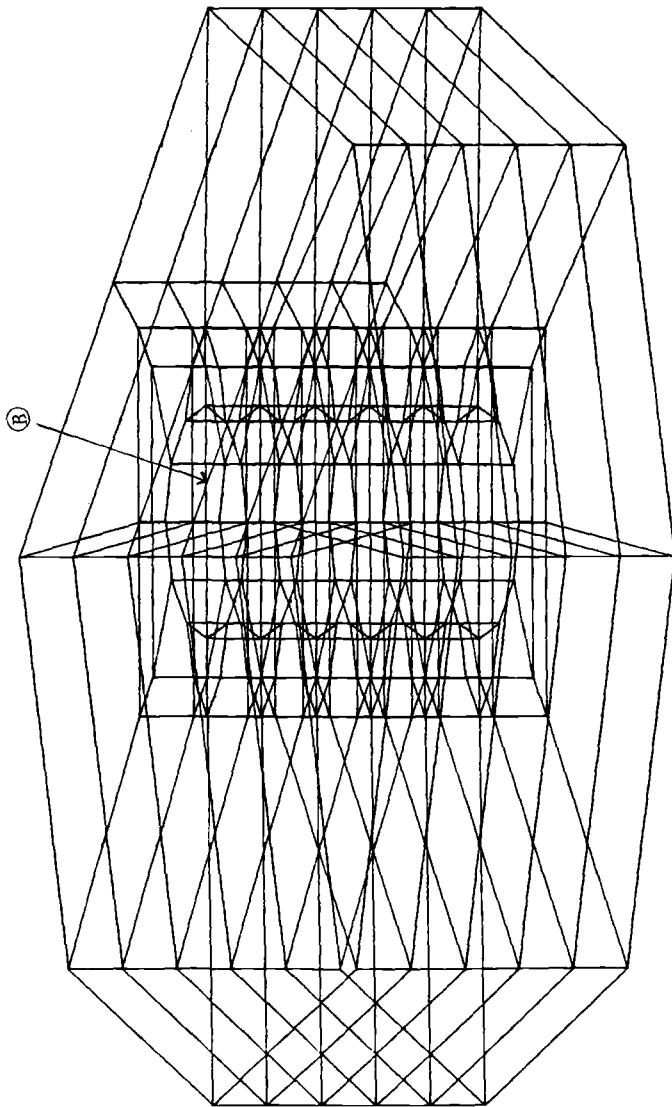


FIG. 6b—Blowup of section A of the finite-element idealization.

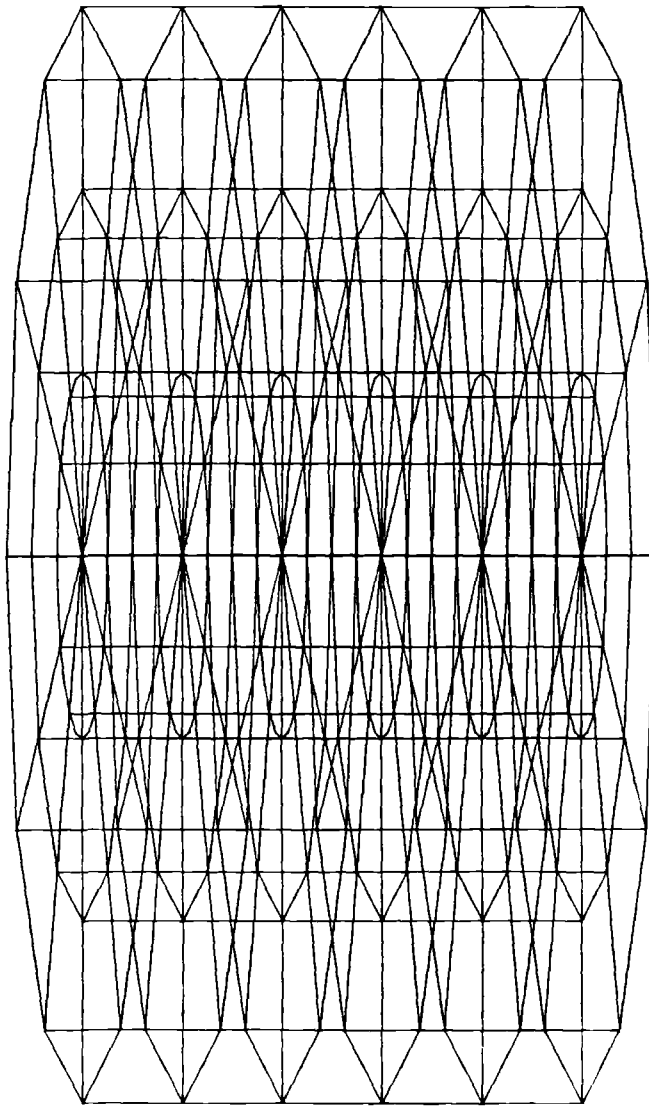


FIG. 6c—Blowup of section B of the finite-element idealization.

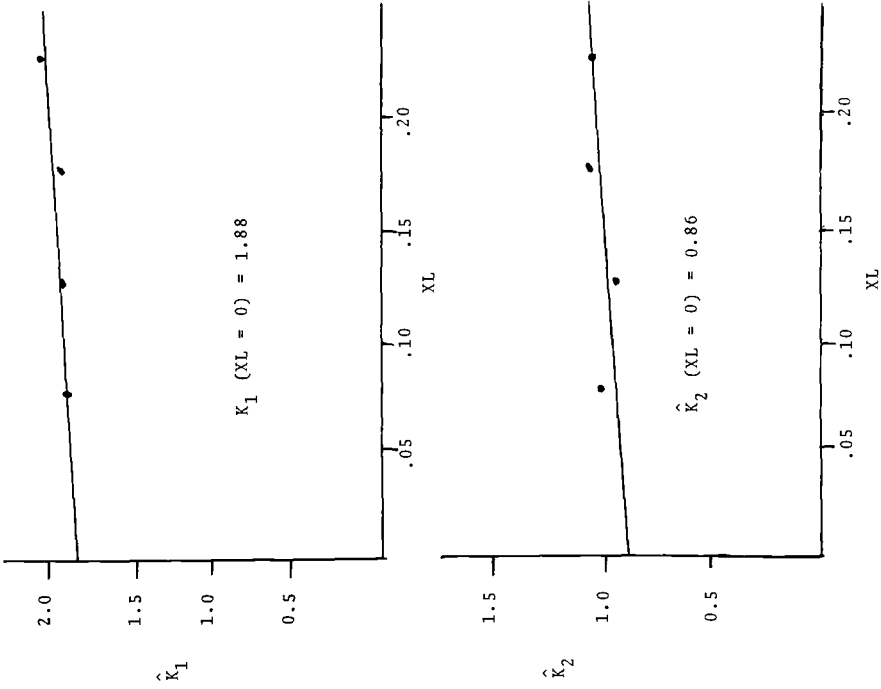


FIG. 8—Resultant stress-intensity factors.

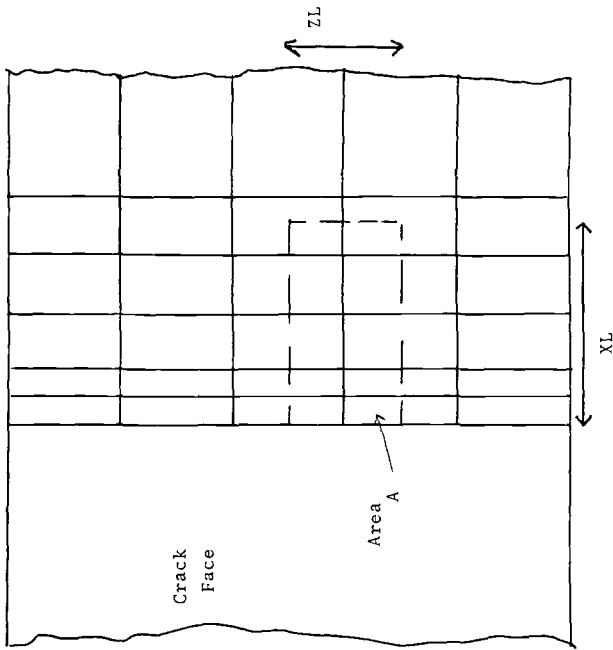


FIG. 7—P plane for the example problem.

extrapolated results are within 3% of the reference values and well within the idealization errors. This example should demonstrate the accuracy of the approach and the ease of application.

Concluding Remarks

A nodal-force method for the determination of mixed-mode stress-intensity factors in three dimensions has been presented in this work. A reference plane-strain problem has been solved in three dimensions and the results agree well with the known solution. The method presented, however, is totally general and should accurately predict stress-intensity factors for a wide range of problems.

The key features of this technique are the use of the general three-dimensional stress fields based only on an asymptotic expansion. No assumption of plane strain needs to be invoked. In addition, the nodal forces are used in the calculation. Nodal forces are the most accurate quantity (along with nodal displacements) in a displacement formulation finite-element analysis. The procedure presented, therefore, will predict stress-intensity factors as accurately as the idealization permits.

Further research is needed on this topic. The range in which plane strain is an accurate assumption needs to be delineated numerically. In addition, the sensitivity of the method to crack curvature needs to be studied (much the same way as it has for Mode I problems). While the algebraic manipulations for curved crack fronts are more involved than for the straight crack front, the extension of this method to arbitrary crack fronts is simply an exercise in algebra. No new assumptions or restrictions need be invoked.

Acknowledgments

The author would like to acknowledge support for this research from the Department of the Navy, Office of Naval Research under Contract No. N00014-84-K-0027.

APPENDIX

Derivation for a Straight Crack

Referring to Fig. 3, the stresses operative on the area A are

$$\begin{aligned}\sigma_{yy} &= \frac{k_{1(z)}}{\sqrt{2x}} \\ \sigma_{yx} &= \frac{k_{2(z)}}{\sqrt{2x}} \\ \sigma_{yx} &= \frac{k_{3(z)}}{\sqrt{2x}}\end{aligned}\tag{5}$$

These can be integrated to give the net force on the face

$$\begin{aligned}
 F_y &= \int_{z_1}^{z_2} \int_0^{XL} \frac{k_1(z)}{\sqrt{2x}} dx dz = \sqrt{2XL} \int_{z_1}^{z_2} k_1(z) dz \\
 F_x &= \int_{z_1}^{z_2} \int_0^{XL} \frac{k_2(z)}{\sqrt{2x}} dx dz = \sqrt{2XL} \int_{z_1}^{z_2} k_2(z) dz \\
 F_z &= \int_{z_1}^{z_2} \int_0^{XL} \frac{k_3(z)}{\sqrt{2x}} dx dz = \sqrt{2XL} \int_{z_1}^{z_2} k_3(z) dz
 \end{aligned} \tag{6}$$

Introducing the average stress-intensity factor over the length ZL (denoted by the symbol \hat{k})

$$\begin{aligned}
 \hat{k}_1 \cdot (ZL) &= \int_{z_1}^{z_2} k_1(z) dz \\
 \hat{k}_2 \cdot (ZL) &= \int_{z_1}^{z_2} k_2(z) dz \\
 \hat{k}_3 \cdot (ZL) &= \int_{z_1}^{z_2} k_3(z) dz
 \end{aligned} \tag{7}$$

• → Nodes Used In Calculation Of Area Force

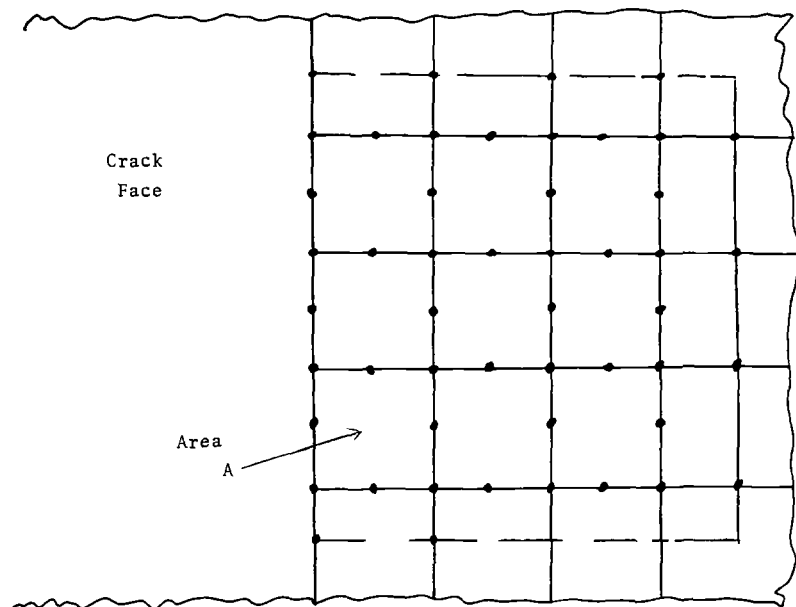


FIG. 9—Enlarged typical P plane for a straight crack front.

The resultant force becomes

$$\begin{aligned}F_y &= k_1 \cdot (ZL)\sqrt{2XL} \\F_x &= k_2 \cdot (ZL)\sqrt{2XL} \\F_z &= k_3 \cdot (ZL)\sqrt{2XL}\end{aligned}\tag{8}$$

A typical finite-element grid segment on the face A is shown in Fig. 9. In practice, the best results are found if the edges of the integration area, A , are parallel to element edges and cut through the midside nodes as shown in the figure. The midside node forces are then assumed to contribute 50% of their value to the area A (this is entirely consistent if the midside nodes lie on the midpoint of the element edge and the edges are straight). If this convention is adhered to, no ambiguities arise with the method.

References

- [1] Hilton, P. D. and Kiefer, B. V., Pressure Vessels and Piping Division Conference, American Society of Mechanical Engineers, San Francisco, June 1979.
- [2] Sha, G. T. and Yang, C. T., *Journal of Engineering Fracture Mechanics*, Vol. 21, No. 6, 1985, pp. 1119.
- [3] Raju, I. S. and Newman, J. C., Jr., *Journal of Engineering Fracture Mechanics*, Vol. 11, 1979, p. 817.
- [4] Raju, I. S. and Newman, J. C., Jr., "Three-Dimensional Finite-Element Analysis of Finite Thickness Fracture Specimens," NASA TN D-8414, National Aeronautics and Space Administration Washington, DC, 1977.
- [5] Raju, I. S. and Newman, J. C., Jr., in "Special Issue on Fracture Mechanics," *Journal of The Aeronautical Society of India*, Vol. 1, 1984.
- [6] Hilton, A. D. and Pierce, D. C., "APES3D—Documentation and Theoretical Manual," NSRDC Report, Contract No. N00167-81-C-0260, Case No. 87058, Naval Ship Research and Development Center, 1983.
- [7] Sih, G. C., *International Journal of Fracture Mechanics*, Vol. 7, 1971, p. 39.
- [8] Hartranft, R. J. and Sih, G. C., *Journal of Mathematics and Mechanics*, Vol. 19, 1969, p. 123.
- [9] Moyer, E. T., Jr., *Proceedings*, International Conference on Application of Fracture Mechanics to Materials and Structures, Freiburg, West Germany, June 1983.
- [10] Barsoum, R. S., *International Journal of Numerical Methods of Engineering*, Vol. 10, 1976, pp. 25–37.

Damage Tolerance and Fatigue

Damage Tolerance of Stiffened-Skin Structures: Prediction and Experimental Verification

REFERENCE: Vlieger, H., "Damage Tolerance of Stiffened-Skin Structures: Prediction and Experimental Verification," *Fracture Mechanics: Nineteenth Symposium, ASTM STP 969*, T. A. Cruse, Ed., American Society for Testing and Materials, Philadelphia, 1988, pp. 169–219.

ABSTRACT: Some consequences of application of current damage tolerance airworthiness requirements for transport aircraft are discussed in terms of designing stiffened-skin structures for safety under all operational load conditions. Compliance with these requirements can be shown by analysis supported by test evidence. To provide the designer with analytical tools to demonstrate that his design meets the required residual strength and crack propagation properties, a number of computer routines were developed by the National Aerospace Laboratory. The principles underlying the calculation procedures used in these computer programs are discussed. An approach incorporated in the computer programs to predict the residual strength of stiffened panels with a skin of a ductile material (such as 2024 alloy) is included. Applications of these programs to some practical stiffened-skin structures are presented together with analysis-test correlations.

KEY WORDS: damage tolerance, cracked stiffened-skin structure, residual strength, ductile material, variable-amplitude crack propagation, fracture mechanics, crack closure, crack growth model, crack opening

The stiffened panel configuration built up of sheet and stringers is very commonly used in aircraft primary structures, for example, in wing, empennage, and fuselage skin panels. Despite all precautions, any of the elements composing this built-up structure may contain defects or cracks, even in the new product as delivered to the customer, or cracks may arise during operational use of the aircraft. Cracks will reduce the stiffness and the load carrying capacity of the stiffened structure and, because any element in built-up structures is essential for the functioning of the structure as a whole, the possibility of cracking must be taken into account early in the design stage.

To guarantee safe operation of the aircraft despite the presence of cracks in primary structural elements, airworthiness authorities have developed criteria with which the designer must comply in order to get his design certified. Since 1956 it has been common practice for the authorities to demand that a designer show that his design will meet the "fail-safe" requirements when cracks arise during the operational life of the aircraft. More recent developments in the airworthiness regulations (effective since 1974) replaced these fail-safe requirements with those of "damage tolerance." The military authorities took the lead in specifying the latter design philosophy [1]. The current civil airworthiness regulations, with

¹ Senior research engineer, Structures and Materials Div., National Aerospace Laboratory (NLR), 1059 CM Amsterdam, The Netherlands.

regard to fatigue, corrosion, or accidental damage, are more or less derived from the military specifications.

According to the current damage tolerance (fail-safe) airworthiness requirements for transport aircraft in the United States (see Ref 2), the designer of a new aircraft has to show that, throughout the operational life of the aircraft, fatigue, corrosion, or accidental damage will not lead to catastrophic failure due either to high, occasionally occurring (residual strength) loads or to lower, much more regularly occurring (fatigue) loads. Compliance with these requirements may be shown by analysis supported by test evidence and (if available) by service experience. Some consequences of application of these current damage tolerance requirements in the design of stiffened-skin structures for safety under all operational load conditions will be discussed in more detail in this paper.

Apparently, during the design stage, the designer must have analytical tools already available to demonstrate that his design has the residual strength (in terms of load) and crack propagation (in terms of life) properties to comply with the airworthiness requirements. Of course, in this context, it is preferable to have analytical techniques that enable the designer to optimize his design in view of the possible consequences of failure of any of the structural elements. To provide the designer with such tools a number of computer routines were developed by the National Aerospace Laboratory (NLR).

Regarding the prediction of the residual strength of stiffened-skin structures, two computer programs are available now, namely, the ARREST and BOND programs. The computer program CORPUS has been developed to predict the growth rates of fatigue cracks in structural components subjected to flight simulation loading conditions. In this paper the principles underlying the calculation procedures used in these computer programs will be discussed. Further, the paper will present applications of these programs to some practical stiffened-skin configurations together with analysis-test correlations.

Application of Current Airworthiness Regulations to Stiffened-Skin Structures

Review of Current Airworthiness Regulations

The structural failures in a number of U.S. Air Force aircraft in the late 1960s and early 1970s, owing to the presence of minute flaws in almost-new aircraft, caused the Air Force to adopt a new design philosophy, namely, damage tolerance design [1]. This philosophy goes one step further than the traditional fail-safe philosophy in that it includes the assumption of the existence of undetected flaws, already built-in at each critical location of the structure simultaneously during the initial construction of the aircraft. These flaws are assumed either to occur from deficiencies in the materials or to be introduced during the manufacture and assembly of the aircraft. The sizes of the initial flaws to be assumed by the designer at the various critical locations for his crack growth analysis depend on the design category (slow crack growth or fail-safe) and structural configuration (holes or cutouts, locations other than holes, or splices between load path elements). Reference 1 contains a specification of the initial flaw sizes to be assumed for the different design categories and structural configurations. Guidelines to assist the designer in complying with the intent of the military specifications are compiled in Ref 3.

Adoption of the damage tolerance approach by the U.S. Air Force also influenced the views of the civil airworthiness authorities concerning the hitherto applicable fatigue and fail-safe requirements for commercial aircraft. In the United States in 1978 the Federal Aviation Administration (FAA) issued an amendment to Paragraph 571 of Federal Aviation Regulation (FAR) 25 [2], thereby introducing damage tolerance criteria for commercial aircraft. The new requirements were accompanied by an advisory circular [4] that outlined

an acceptable means of compliance with the new regulations. The philosophy of Refs 2 and 4 is slightly different from that applying to military aircraft. An outline of the main differences is given in Ref 5.

In Europe, at the same time, a set of Joint Airworthiness Requirements, JAR 25.571, was issued relating to damage tolerance and fatigue evaluation of aircraft structures [6]. This requirement, which is similar to the civil regulations in the United States, is also accompanied by an advisory circular containing guidance material [7].

In this section of the paper, the author outlined what the current airworthiness requirements are with regard to fatigue and fail-safety and how they arose from the older requirements owing to modified views on the design of safe structures. Those readers who are interested in historical reviews and arguments underlying the successive developments in the airworthiness requirements are referred to Refs 8 through 10. Examples of application of damage tolerance requirements to recent aircraft designs can be found in Ref 11.

Consequences of Compliance with Damage Tolerance Requirements

Here we will briefly discuss what compliance with the current damage tolerance requirements means to the designer of an aircraft structure, paying particular attention to stiffened-skin structures. In doing so, the requirements set by the FAA [2,4,5] will be taken as guidelines.

The actions that have to be taken to meet the new FAR 25.571 damage tolerance regulations are compiled in Fig. 1 [12], together with relevant assumptions and requisites, and compared with those of the traditional fail-safe requirements. It is shown in this figure that the application of the damage tolerance philosophy depends upon three essential elements: a residual strength analysis, a crack propagation analysis, and (on the basis of results gained from these analyses) the establishment of an inspection and maintenance program. The analyses may be based on fracture mechanics methodologies. However, sufficient testing on small coupons and large components must be performed to ensure that the analysis methods are not unconservative.

One of the striking differences between the old and new regulations is that under the new regulations initial damage has to be assumed to be already present at multiple sites in the structure of the new aircraft. These cracks are assumed to propagate independently during the operational use of the aircraft. When one load path in a multiple load path structure fails after crack growth, then the analysis of crack growth acceleration in the intact component or components, owing to the load transferred from the failed to the intact elements, has to be allowed for.

The consequences of applying these requirements with regard to the residual strength and crack growth analyses is illustrated in Fig. 2 for multiple load path structures consisting of skin and stiffeners, each containing an initial damage, a_i . The upper half of this figure shows the residual strength diagram, and the lower half shows the crack growth curves. Two situations are depicted, namely, a stiffened panel with a skin crack only (Condition I, dashed-and-dotted curves) and the same panel configuration with both elements cracked initially (Condition II, solid curves). It has to be noted here that, in constructing the diagrams of Fig. 2, any local effect of stiffeners being present ahead of the tip of the advancing crack on the course of the curves (see further on in this paper) is ignored for reasons of simplicity. According to the requirements, the undamaged structure must be able to carry the ultimate load. In the cracked condition, the structure with an undetected crack must have a limit-load capability (see upper half of Fig. 2). Allowing for the latter capability and accounting for the decrease of the residual strength with increasing crack size, the "maximum tolerable crack size," a_{tol} , for the panel with a skin crack only will be given by a_{tol_1} in Fig. 2. Assuming



ACTIONS TO BE TAKEN	PHILOSOPHIES	
	FAIL-SAFE OLD FAR 25.571 (PRE-1978)	DAMAGE TOLERANT NEW FAR 25.571 (POST-1978)
RESIDUAL STRENGTH ANALYSIS	 <ul style="list-style-type: none"> ● single element or obvious partial failure ● residual strength level equal to 80% limit load with an additional 15% dynamic factor 	 <ul style="list-style-type: none"> ● multiple active cracks one of which is readily detectable ● residual strength level equal to 100% limit load. No dynamic effects to be allowed for
CRACK GROWTH ANALYSIS	<ul style="list-style-type: none"> ● no analysis required 	<ul style="list-style-type: none"> ● extensive analysis required for typical loading and environmental spectra expected in service
ESTABLISHMENT OF INSPECTION AND MAINTENANCE PROGRAMME	<ul style="list-style-type: none"> ● based on past service history ● not taken into account for type certificate 	<ul style="list-style-type: none"> ● related to structural damage characteristics and past service history ● taken into account for type certificate

FIG. 1—Comparison of old and new FAR requirements. The essential part of this figure is taken from Ref 12.

that, in the panel with skin and stiffener cracked simultaneously, the cracks in both elements will grow and the stiffener, after a certain amount of crack growth in the skin, will fail (specifically, at a total skin crack length of $2a_f$), and assuming further that the panel under these circumstances will still have limit-load capability, then the effect of stiffener crack growth and ultimate failure on a_{tol} is illustrated in the residual strength diagram of Fig. 2. The residual strength decreases below the limit-load value at a_{tol} .

The lower half of Fig. 2 illustrates the effect of the presence of a crack in the stiffener and ultimate stiffener failure on the crack propagation curve of the skin. The dashed-and-dotted curve relates to the situation when only the skin is cracked. When a crack is also present in the stiffener the propagation rate of the skin crack will increase slightly. A progressive increase of the growth rate will occur after the stiffener has failed. The increments of crack growth due to both effects are indicated in Fig. 2 by Δa_2 and Δa_3 , respectively. It is assumed that the panel is only externally inspectable and that a certain amount of skin crack growth must have occurred before the crack can be discovered during inspection. This crack size is called the "minimum detectable crack size," a_{det} , and depends on the accessibility of the cracked area and the inspection technique applied. In Fig. 2 the value of a_{det} for a panel with a failed stiffener (a_{detf}) is taken to be slightly smaller than that for a panel with an intact stiffener (a_{deti}) because in the former case the crack is pulled open during flight by the failed stiffener and discovery during ground inspection may be easier (because of fuel leakage through the lower wing skin). The time interval between crack growth from a_{det} and a_{tol} is available for the crack to be detected and repaired. This period is denoted in Fig. 2

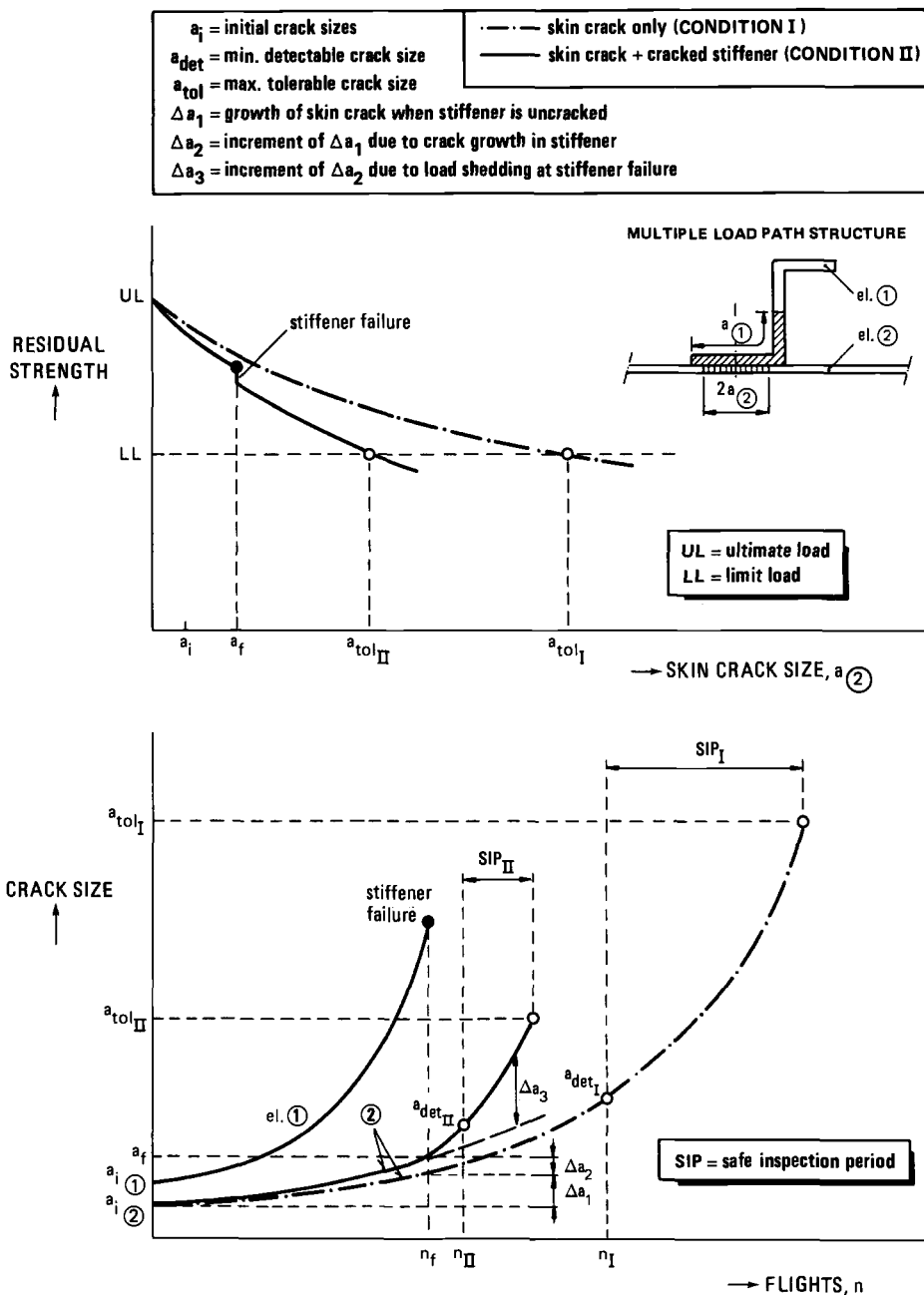


FIG. 2—Residual strength and crack propagation diagrams (schematic) to be used in damage tolerance analysis.

as the "safe inspection period" (SIP). It is evident that the SIP is reduced owing to the requirement of multiple site damage. For safe operation there should be at least two inspections in the SIP to prevent a crack of the minimum detectable size (which can barely escape attention during an inspection) growing to a_{tol} before the next inspection can be made. For economical reasons the inspection intervals during the operational life of the aircraft must cover an acceptable number of flights. If the analyses shown in Fig. 2 reveal that the frequency of inspection is too high to be economically feasible for the operator of the aircraft, then the designer has the following options (see Fig. 2):

- (a) selection of another skin material with better residual strength (to increase a_{tol}) or crack propagation properties (to lengthen SIP), or selection of another stiffener material with better crack propagation properties (to postpone stiffener failure);
- (b) redesigning (for example, better detail design or a reduction of stress level) to slow down crack growth, or selection of another design configuration (for example, application of crack arrest straps) to increase the residual strength;
- (c) requiring a more sophisticated inspection technique so that smaller cracks can be detected (decrease of a_{det}); and
- (d) selection of another degree of inspectability (see below).

Optional Structural Design Categories

In Fig. 2 it is illustrated how, on the basis of residual strength and crack growth analyses, the SIP is determined for a multiple load path stiffened-skin structure that can only be inspected externally. Figure 3 gives a review of various options of stiffened-skin structures, all meeting the FAA damage tolerance requirements, together with their inspectabilities and crack propagation diagrams. In constructing the latter diagrams it is assumed that failure of one of the composing elements will not impair the limit-load capability of the structure. In the diagrams the SIPs are indicated. All structural configurations considered in Fig. 3 relate to wing lower skin panels.

According to FAR regulations two categories of structures are distinguished, namely, "fatigue (safe-life) structures" and "damage tolerant (fail-safe) structures." Single load path integrally stiffened-skin panels can fall in either category depending on the relative values of a_{det} and a_{tol} (see Fig. 3). For example, if such a panel configuration is machined from a very brittle material, then the tolerable crack size at limit load will be so small that cracks cannot be detected prior to fracture instability. This implies that cracks cannot be tolerated at all or, in other words, that the structure falls into the safe-life category. Machining this panel configuration from a ductile material can make it damage tolerant provided partial damage can be shown to be obvious before it becomes critical. Because of this requirement, application of a single load path damage tolerant structure is allowed but not encouraged by the FAA. To obtain a safe inspection interval, division of the SIP by a factor of three is recommended by the FAA for this design category [13]. This design category is designated in the military specifications [1] as a "slow crack growth structure."

Crack growth diagrams for multiple load path structures can take several forms depending on structural design (for example, skin with separate stiffeners or skin consisting of a number of integrally stiffened planks) and inspectability (only externally inspectable or inspectable at partial or complete failure of a load path) (see Fig. 3). In the crack growth diagrams of Fig. 3 the SIPs for the various multiple load path designs are indicated. To obtain a safe inspection interval, division of the SIPs by a factor of two is recommended by the FAA [13]. It is shown in Fig. 3 that for a multiple load path structure consisting of a skin with separate stiffeners (riveted or bonded) the length of the SIP depends on the degree of

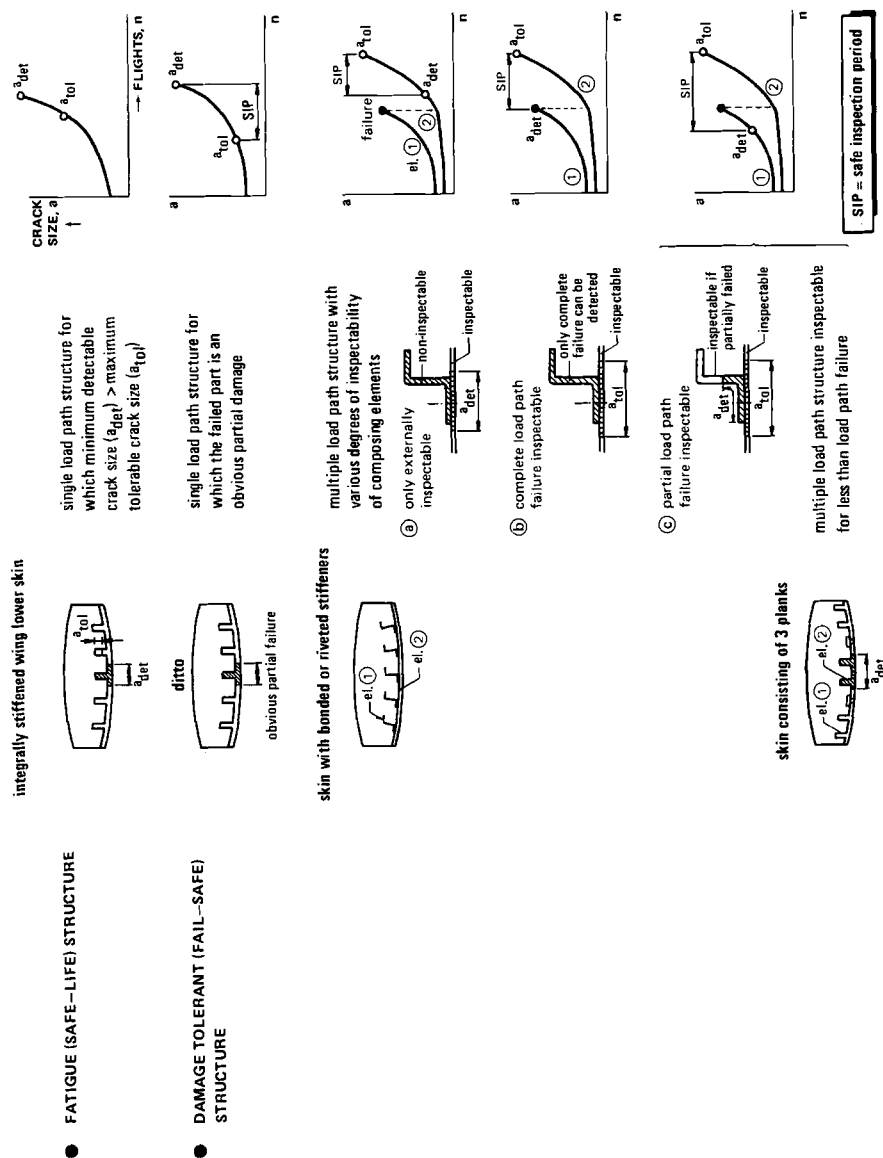


FIG. 3—Structural design categories and associated safe inspection periods (SIPs) for stiffened-skin structures according to FAA damage tolerance requirements [2,4,5].

inspectability. For a certain panel geometry the “only externally inspectable” option yields the shortest SIP or, in other words, the largest a_{det} implying that a relatively unsophisticated inspection technique will be sufficient to find this crack during frequent inspections, which, however, are undesirable economically. Be that as it may, another advantage of this inspectability option is that inspection of the internal stiffener, which may require access into the wing fuel tank or removal of the internal fuselage lining, will not be necessary.

Establishment of Inspection Programs

It has been shown in Figs. 2 and 3 how, on the basis of residual strength and crack propagation diagrams corresponding to a certain structural configuration, a safe inspection period can be found for a specified degree of inspectability. This is performed by defining a minimum detectable crack size, a_{det} (depending on inspection technique to be used), and determining the maximum tolerable crack size, a_{tol} , from the limit-load capability of the structure as found from a residual strength analysis. By dividing this SIP by a factor of two or three, depending on whether it concerns a multiple or a single load path structure, the inspection frequency can be found. Which a_{det} and inspection frequency are acceptable will result from a cost trade-off between the sophistication of the inspection technique to be applied and the hours acceptable for grounding of the aircraft. Since the operators are the people who have to decide on the alternative they prefer in this respect, they should be involved in this trade-off between inspection method and frequency of inspection.

A point that has not been discussed so far is that, apart from the inspection interval to be determined from the SIP (in the literature this interval is known as the “repeat inspection interval”), there should be defined another inspection interval, namely, the time to the first inspection (known in the literature as the “threshold inspection interval”). This time should be based on the time the inspection target takes to appear and be detectable or, alternatively, on the time it takes to fail a primary load path completely; that is, on the interval n_{II} or n_f in Fig. 2, respectively. A means of establishing the threshold inspection interval cannot be found in any of the regulatory documents for the design of new aircraft. In Ref 13 it is suggested that the U.S. Air Force criteria be adopted to establish this threshold for inspecting fatigue critical items. These criteria are summarized in Ref 13 (Fig. 44 of that reference), together with criteria recommended for repeat inspection intervals.

Analytical Verification of Damage Tolerance

It has been shown that to comply with the current damage tolerant (fail-safe) airworthiness requirements for civil transport aircraft, the designer of a new aircraft has to perform comprehensive residual strength and crack growth analyses. In the first place, these analyses are required to demonstrate that the structure, despite the presence of cracks, will be able to carry limit load and will have a sufficiently long life. It is also essential during the design stage of a damage tolerance design that inspection and maintenance programs be established to ensure safe operational use of the aircraft. It was shown previously that such programs can also be derived from residual strength and crack growth analyses. Consequently, during the design process of a new aircraft, there will be a continuous trade-off between structural design (that is, the choice of design category, panel geometry and dimensions, detail design, choice of materials, and so forth) and inspection and maintenance requirements (that is, the inspectability of the structure, repair procedures, inspection frequency, inspection techniques, and so forth). Of course, to enable the designer during this trade-off process to optimize his design with regard to the various aims that have to be met, the availability of analytical tools is desirable. The authorities accept the application of analytical calculation

procedures to demonstrate damage tolerance provided there is sufficient test evidence to show that the analytical methods are conservative. To provide the designer with such tools a number of computer routines were developed by the NLR. The programs ARREST and BOND enable prediction of the residual strength of a stiffened panel, including its crack arrest properties. The ARREST program applies to riveted stiffeners and the BOND program to adhesively bonded stiffeners. The program CORPUS (computation of retarded propagation under spectrum loading) has been developed to predict the growth rates of fatigue cracks in structural components subjected to flight simulation loading conditions.

In the following sections, a brief description of these programs will be given. Furthermore, application of these programs to some practical stiffened-skin configurations will be presented, together with analysis and test verification.

Residual Strength Programs ARREST and BOND

The computer program ARREST is well-documented [14], while a description of the BOND program is being prepared [15]. Therefore, a brief description of the approach underlying the calculation procedures applied in these programs will suffice here. To facilitate understanding of the incorporation of these procedures in the computer programs, the information flow through the programs during the calculation procedure will be illustrated by a flow diagram (see Fig. 4). Because the architecture and capabilities of ARREST and BOND are very similar, the principles of both programs will be discussed simultaneously, denoting the rivets and bonding connections by attachments in general. Wherever typical differences apply they will be indicated in the text.

After the description of the calculation procedures applied in the computer programs, we will discuss which panel configurations can be handled with these programs.

Finally, results of applications of these programs to some practical stiffened-skin configurations will be presented, together with analysis and test correlations.

Brief Description of Calculation Procedure

To translate the behavior of a cracked stiffened-skin structures with increasing external load in a reliable way into a computational model, including the possibly decreasing stiffness of stiffeners and attachments (rivets or bonding layers) owing to yielding of the stiffener and attachment materials, it is of paramount importance to treat the interaction of the cracked sheet and stiffeners appropriately. When the interaction forces of sheet and stiffeners are known, then, as far as the sheet is concerned, fracture mechanics principles can be used to predict the behavior of the cracked sheet as a function of crack size. The stiffeners will obey the conventional strength laws of the stiffener material. Possible failure of the sheet-stiffener attachments due to local overloads is ruled out.

Calculation of Sheet-Stiffener Interaction Forces—The approach underlying the calculation procedure applied in the computer programs is based on the sheet-stiffener interaction occurring in the cracked region. This interaction is illustrated in Fig. 5 for a cracked panel with intact stiffeners by breaking down the panel into its composing elements (see the upper half of Fig. 5) and considering the loading of the cracked sheet as a superposition of three load cases (see lower half of Fig. 5). The sheet-stiffener interaction forces, F_{ik} , are determined analytically by assuming sheet-stiffener displacement compatibility at the various attachment locations. To satisfy this compatibility, the displacement components in sheet and stiffeners owing to both the external stresses and the interaction forces are determined (see displacements v_{SH} and v_{ST} in Fig. 5). Further, when connecting the corresponding points of sheet

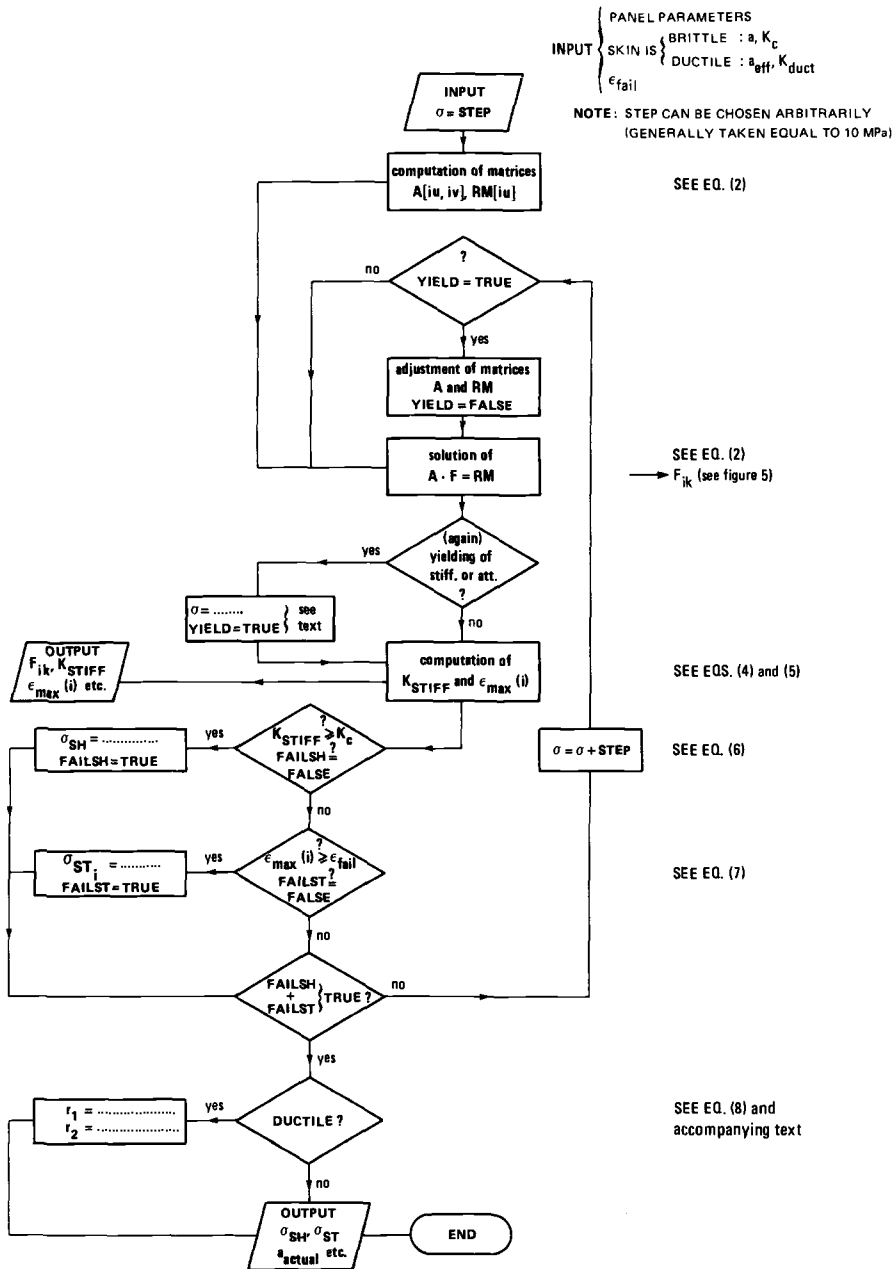


FIG. 4—Simplified flow diagram of calculation procedure applied in the ARREST and BOND programs.

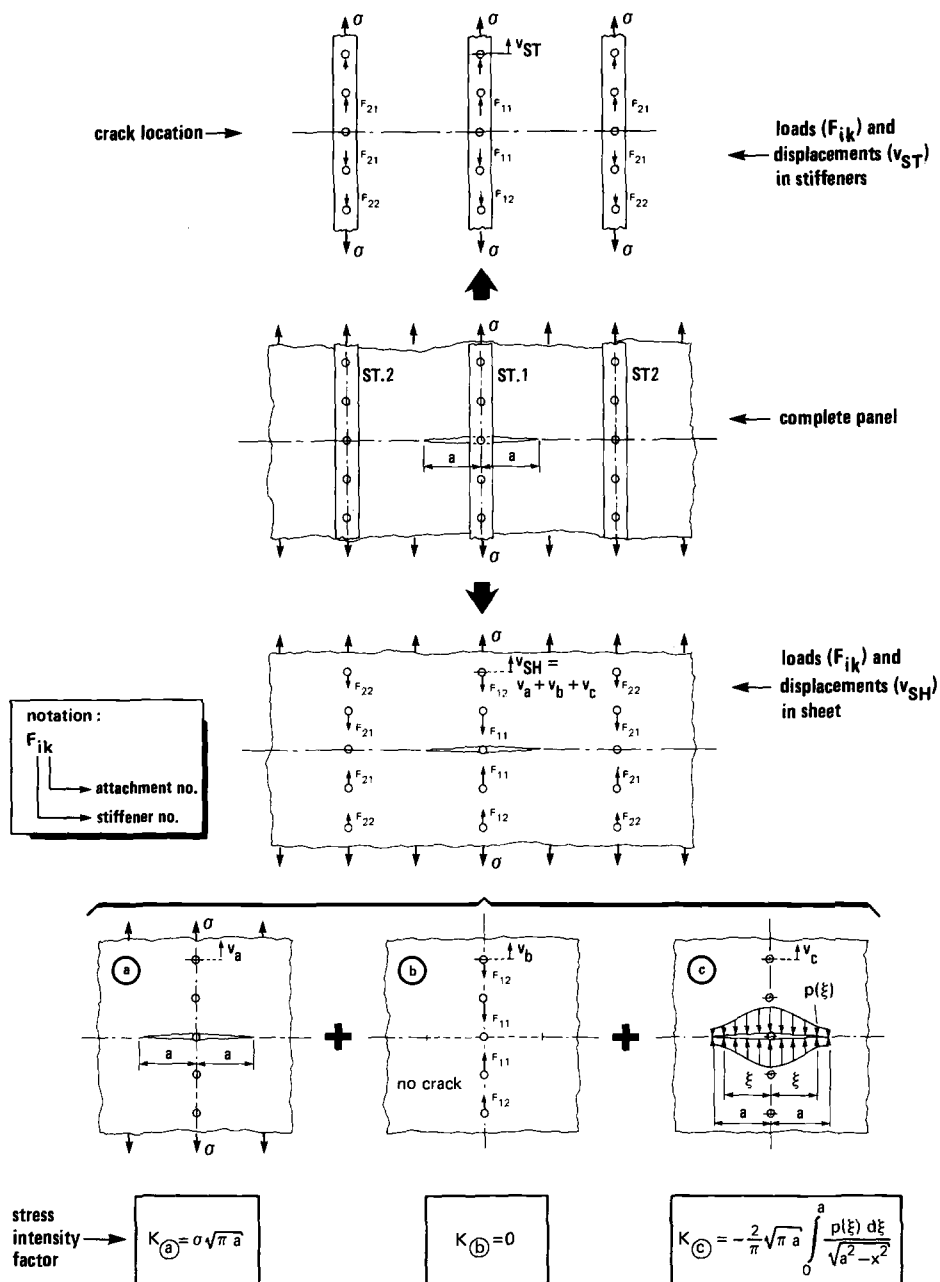


FIG. 5—Interaction forces (F_{ik}) and displacements (v) in a stiffened panel with a central crack and intact stiffeners.

and stiffeners, the shear deformation of the attachment material owing to the interaction forces is accounted for. Consequently, the total displacement compatibility equation for determining the interaction forces will read

$$v_{SH} = v_{ST} + v_{ATT} \quad (1)$$

where the subscripts *SH*, *ST*, and *ATT* refer to sheet, stiffener, and sheet-stiffener attachment, respectively. Substituting in Eq 1 the contributions of the various displacement components corresponding to the different load cases shown in Fig. 5 results in a set of equations containing the unknown interaction forces F_{ik} . In contracted matrix notation this set of equations will be given by

$$A[iu,iv] \cdot F[iv] = RM[iu] \quad (2)$$

where *A* represents a square coefficient matrix with dimensions *iu* by *iv* and the matrices *F* and *RM* are vectors with *iv* elements. The matrix *A* and the vector *RM* are functions of the panel characteristics (that is, the panel geometry and dimensions and the material properties of panel components) and the crack size. The vector *F* represents the sheet-stiffener interaction forces (F_{ik} in Fig. 5). In the computer programs the Matrices *A* and *RM*, which are associated with a certain stiffened panel configuration, are generated and the set of equations in the *iv* unknown F_{ik} values is solved.

Calculation of Crack Tip Stress-Intensity Factor—In linear-elastic fracture mechanics it is usually assumed that the stress condition at the crack tip is governed by the stress-intensity factor, *K*. It is common practice in fracture mechanics to employ this parameter to characterize the crack propagation and fracture instability properties of a structure.

For an unstiffened panel with a central crack of a length $2a$, loaded remote from the crack by a stress, σ , the stress-intensity factor is defined by

$$K = \sigma\sqrt{\pi a} \quad (3)$$

It has to be noted here that, in fact, Eq 3 should contain a correction factor for finite width. However, since cracks in aircraft skins are generally limited to a small fraction of the panel width, this correction factor will be close to unity and, therefore, in this paper will be ignored in the expressions for the stress-intensity factor.

In a stiffened-skin structure with a skin crack, the value of the stress-intensity factor will differ from that in an unstiffened sheet. The effect of the stiffeners on *K* is illustrated at the bottom of Fig. 5. It is shown there that in the stiffened panel the stress-intensity factor will be given by

$$K_{STIFF} = \sigma\sqrt{\pi a} \left\{ 1 - \frac{2}{\pi\sigma} \int_{x=0}^a \frac{p(\xi)d\xi}{\sqrt{a^2 - x^2}} \right\} = C(a) \cdot \sigma\sqrt{\pi a} \quad (4)$$

where the term $\sigma\sqrt{\pi a}$ represents the value of *K* in the unstiffened panel (see Sketch (a) in Fig. 5), and *C(a)* represents the term between accolades in Eq 4. (The other terms are explained in Fig. 5.) The stress distribution $p(\xi)$ is equal in magnitude, but of opposite sign to the stresses caused by the interaction forces along the crack segment in the uncracked sheet of Sketch (b) in Fig. 5. This stress distribution serves to provide the necessary stress-free crack surface. The value of the parameter *C(a)* in Eq 4 reflects the effectiveness of the stiffeners in reducing the crack-tip stress intensity.

It should be noticed that the contribution of $p(\xi)$ to $C(a)$ will have a negative sign when it concerns intact stiffeners (see Fig. 5 and Eq 4). On the other hand a broken stiffener will yield a positive contribution to $C(a)$.

Calculation of Maximum Strain in Stiffeners—Due to the load transfer from the cracked sheet to the stiffeners (or the other way around when it concerns a broken stiffener) the strains in the stiffeners vary in panel length direction (see the upper half of Fig. 5). In the case of an eccentric stiffener, the strain also varies over the stiffener cross section. The maximum stiffener strain in a certain stiffener (i) will be given by

$$\epsilon_{\max}(i) = \frac{\sigma}{E} + \frac{\sum_{k=1}^n F_{ik}}{EA_{ST}(i)} \left(1 + \left(\frac{e}{\rho} \right)^2 \right) = \frac{\sigma}{E} \left\{ 1 + \frac{\sum_{k=1}^n F_{ik}}{\sigma A_{ST}(i)} \left(1 + \left(\frac{e}{\rho} \right)^2 \right) \right\} = L_i(a) \frac{\sigma}{E} \quad (5)$$

where F_{ik} represents the k th attachment load of the i th stiffener, n is the number of connecting elements at either side of the crack line, $L_i(a)$ represents the term between accolades in Eq 5, and σ , A_{ST} , and E are the panel end-stress, the stiffener cross-sectional area, and the Young's modulus of its material, respectively. The parameters e and ρ represent the stiffener eccentricity and its radius of gyration. The value of the parameter $L_i(a)$ in Eq 5 again reflects the effectiveness of the stiffeners.

Calculation of Stress Levels that Determine Sheet and Stiffener Failure—Assuming that fracture instability in the sheet of a stiffened-skin structure will occur when its stress intensity, K_{STIFF} , attains a critical value, a relation between the stress level of the stiffened panel at which fracture instability occurs, σ_{SH} , and the crack length can be found from Eq 4.

When the skin of the stiffened panel consists of a brittle material it is assumed that fracture instability in the stiffened sheet occurs when K_{STIFF} exceeds the plane-stress fracture toughness, K_c , of the unstiffened sheet material.

However, in the case of ductile skin material (for example, 2024 alloy) a large amount of plasticity takes place at the crack tips. This means that, in the unstiffened sheet, yielding across the entire net section will generally occur before the stress-intensity factor, based on the actual crack length, can attain its critical value. This implies that with materials similar to 2024 the stress-intensity factor approach cannot simply be used as a failure criterion. In the Appendix to this paper an approach is presented that allows a representative “ductile” stress-intensity factor, K_{duct} , to be applied. This stress-intensity factor is related to an “effective” crack length, a_{eff} . In the Appendix it is shown how K_{duct} can be determined as a function of a_{eff} . In applying this approach to the stiffened panel the calculations have to be carried out for a chosen value of the effective crack length. To find the actual crack size at which fracture instability occurs, a correction for crack-tip plasticity in the stiffened sheet is carried out afterwards. This procedure will be discussed in a separate section.

When the critical value of K_{STIFF} (that is, either K_c or K_{duct}) is known as a function of crack size, then the relation between σ_{SH} and the actual or effective crack length can be found from Eq 4 to be equal to

$$\text{for brittle material: } \sigma_{SH}(a) = \frac{K_c}{C(a)\sqrt{\pi a}} \quad (6a)$$

$$\text{for ductile material: } \sigma_{SH}(a_{eff}) = \frac{K_{duct}}{C(a_{eff})\sqrt{\pi a_{eff}}} \quad (6b)$$

Regarding stiffener failure, it is assumed that this will occur when the value of ϵ_{\max} in the stiffener becomes equal to the failure strain of the stiffener material, ϵ_{fail} . Thus, the relation between the end stress at which the critical stiffener fails, σ_{ST} , and the crack length can be found from Eq 5 to be equal to

$$\sigma_{ST_i}(a) = \frac{E \cdot \epsilon_{\text{fail}}}{L_i(a)} \quad (7)$$

It has to be noticed here that in the case where the skin consists of a ductile material, just as with the calculation of σ_{SH} , the value of σ_{ST_i} is calculated for a chosen a_{eff} value. The actual crack size corresponding to σ_{ST_i} is then found by applying a crack-tip plasticity correction afterwards.

By plotting σ_{SH} and σ_{ST_i} as a function of crack size, a complete residual strength diagram of the stiffened panel configuration will be obtained (see Ref 16). The relative locations of the sheet and stiffener failure curves in this diagram will determine the failure mode of the stiffened panel. On the basis of its failure mode, the panel can be classified as a skin- or stiffener-critical configuration. Further, on the basis of such a diagram the crack arrest properties of the panel can be predicted. The classification of panel configurations on the basis of their failure modes and the possible crack arrest properties of each configuration are illustrated in Fig. 6.

In this figure the instability curves of the skin and the failure curves of the critical stiffener are given schematically as σ_{SH} and σ_{ST} , respectively, versus the crack length, a . The way the panel configurations under (a), (b), and (c) in Fig. 6 fail as a function of the panel stress, σ , is explained for each configuration separately (see also the legend given at the top of Fig. 6). Concerning the classification used in Fig. 6, it will be obvious that Configurations (a) and (c) are skin- and stiffener-critical, respectively, because panel failure clearly will start here as a result of failure of these structural elements. Strictly speaking, however, on that basis, Configuration (b) would have to be characterized as a skin/stiffener-critical configuration because the failure mode here depends on the stress level (with respect to σ_s) at which unstable crack growth in the skin occurs (see the text accompanying this configuration in Fig. 6). However, because it is recommended that a structure be designed so that stresses in excess of σ_s will never occur (in view of fail-safety, see Ref 16), Configuration (b) in Fig. 6 has also been classified as a stiffener-critical configuration.

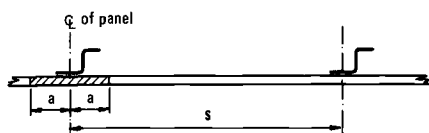
The stress levels denoted in the diagrams of Fig. 6 by σ_T and σ_S have a special meaning. If fracture instability of a skin crack occurs at any stress below these stress levels, then the unstably growing crack will be arrested at the adjacent stiffeners (see the crack growth histories of the crack lengths labelled ② in Fig. 6). Thus, the stiffened panel will "fail" safely when the design stress level is chosen equal to or lower than σ_T or σ_S . For that reason these stress levels are the so-called fail-safe stress levels, σ_{FS} . (In previous papers published by this author, for example Ref 16, this particular stress level is denoted by $\bar{\sigma}$.)

Incorporation of Plasticity of Stiffeners and Attachments (see Fig. 4)—It was previously shown in this paper that the matrices A and RM of Eq 2, which correspond to a certain stiffened panel configuration, are generated in the computer programs and, further, that the set of equations in the unknown interaction forces (see Eq 2) is solved in these programs. In assembling the matrices A and RM , the stiffness parameters of all panel components are initially taken to be elastic. All these calculations are carried out for a chosen value of the crack length (that is, a or a_{eff}). Further, the panel end-stress level is taken to be sufficiently low (generally σ is taken to be equal to 10 MPa) to be sure that no plastic deformation of stiffeners and attachments occurs.

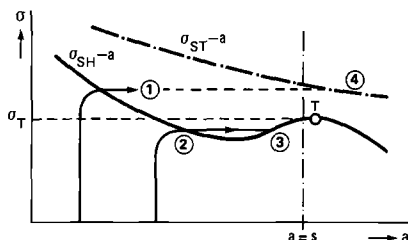
$\sigma_{SH}-a$ and $\sigma_{ST}-a$ represent the stiffened sheet instability curve and the failure curve of the critical stiffener as given by equations (6) and (7) in text, respectively

- ① fracture instability in skin without crack arrest
- ② ditto, with crack arrest
- ③ crack arrest

- ④ stiffener failure
- T panel failure, after crack arrest, due to skin failure
- S ditto, due to stiffener failure

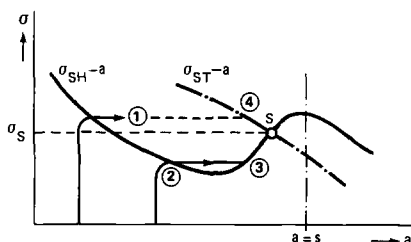


(a) skin-critical configuration with crack arrest capabilities



Failure of this panel configuration will always occur due to fracture instability of the skin. If instability occurs at $\sigma > \sigma_T$ then the panel will fail without crack arrest. If instability occurs at $\sigma < \sigma_T$ then, after crack arrest, the panel ultimately will fail at σ_T .

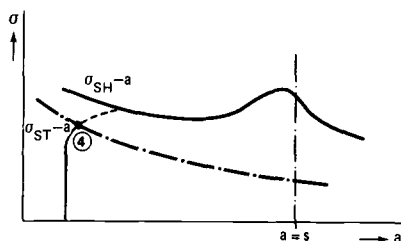
(b) stiffener-critical configuration with crack arrest capabilities



Failure of this panel configuration may commence either by fracture instability of the skin or by stiffener failure. If instability occurs at $\sigma > \sigma_S$ then the panel will fail without crack arrest. If instability occurs at $\sigma < \sigma_S$ then, after crack arrest, the panel ultimately will fail due to stiffener failure.

(c) stiffener-critical configuration.

Crack arrest capabilities not to be predicted from this diagram, but from diagram dictated by new situation with failed stiffener



Independent of stress level, in this panel configuration failure of a stiffener always occurs before the skin fracture toughness will be fully exhausted. The subsequent failure mode will depend on relative location of other σ_{SH} and σ_{ST} -curves, namely those being applicable to the new situation.

FIG. 6—Classification of critical panel configurations as imposed by the relative locations of the failure curves of sheet and critical stiffener.

When the interaction forces are known the parameters $C(a)$ and $L(a)$ (see Eqs 4 and 5, respectively) can be determined. When $C(a)$ and $L(a)$ are known by means of Eqs 6 and 7, the stress levels at which sheet and critical stiffener would fail can be found. Hence, in this way, at the end of each calculation run, for the crack length chosen, a total of two points in the stress versus crack length plot can be obtained. However, such a procedure applies only provided that the behavior of stiffeners and attachments remains elastic until the failure levels of sheet and stiffeners are attained. In general this will not be the case. Therefore, in the computer programs, after the first (elastic) calculation step the panel end stress is increased stepwise. The step size can be chosen arbitrarily. After each step it is determined whether any stiffener or attachment started to yield in the last calculation step. If so, the end stress is decreased to the stress level at which this yielding occurred, and the K_{STIFF} and $\epsilon_{max}(i)$ values corresponding to that stress level are determined (see Eqs 4 and 5). Then the stiffness of the yielding element (that is, stiffener or attachment) is adapted in the matrices A and RM , and the calculation process is continued. The calculations are terminated when both K_{STIFF} and $\epsilon_{max}(i)$ have reached critical values. By performing such a calculation procedure for a range of crack lengths, the complete failure curves of sheet and critical stiffener can be obtained.

Applicability of the Presented Calculation Procedure—It should be noted here that, in the presented calculation procedure, the crack length chosen during each calculation run is kept constant with increasing panel stress until ultimate panel failure. Actually, with increasing panel stress, some stable crack growth will generally occur prior to fracture instability in the sheet. This implies that, when assuming that fracture instability in test and calculation occurs at the same critical crack size, the crack length in the test during the greater part of the stress range up to unstable crack growth will be smaller than that assumed in the calculation; consequently, the stress levels at fracture instability, as obtained from test and calculation, in general, will be slightly different.

The presented calculation procedure (that is, plotting of σ_{SH} and σ_{ST} in a stress versus crack length diagram and neglecting stable crack growth with increasing panel end stress) generally will be appropriate when prediction of the residual strength properties of a stiffened panel during the design process is under discussion (knowledge of the crack arrest properties and the fail-safe stress level are then of primary importance). However, apparently such a calculation procedure will not suffice to predict the behavior of a cracked stiffened panel with increasing end stress (that is, the crack growth history in a residual strength test). In such a case, application of the so-called crack growth resistance (or R -curve) approach to the computer output data is preferable. The principles of that approach are discussed comprehensively in an earlier publication [16] and, therefore, will not be repeated here. An application of the latter procedure to an actual structure will be presented later on in this paper.

Calculation of Crack-Tip Plasticity Correction—It was previously shown that when the skin of a stiffened panel is of a ductile material (for example, 2024 alloy) the procedure for determining σ_{SH} and σ_{ST} (see Eqs 6 and 7) cannot simply be applied to the actual crack size owing to the large amount of plasticity at the crack tip. The application of fracture mechanics principles adapted in such cases is illustrated in Fig. 7. The actual stress distribution present in the net section of the stiffened sheet with an actual (visible) crack length, $2a$, and a crack-tip plastic zone size equal to d is considered to be equivalent to an elastic stress distribution $\sigma_e(x)$ in the same sheet but with a larger crack size, namely an effective crack length

$$a_{eff} = a + r_1 \quad (8)$$

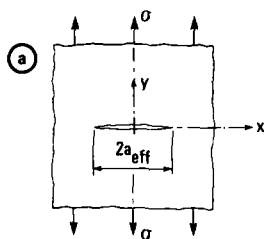
the stress distribution in the net section of a cracked sheet ($y = 0$) is given by

$$\sigma_y(x) = \operatorname{Re}(Z(z)), \text{ with } z = x + iy$$

where $Z(z)$ is the stress function of Westergaard (Ref. 17)

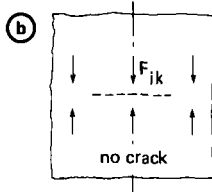
in the literature stress functions for various load cases can be found (e.g. Ref. 18)

APPLIED TO CRACKED SHEET OF THE STIFFENED PANEL, CONTAINING A CRACK OF LENGTH $2a_{\text{eff}}$, IT FOLLOWS THAT (see lower half of figure 5)

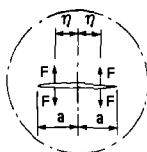


$$Z(z) = \frac{\sigma \cdot z}{\sqrt{z^2 - a_{\text{eff}}^2}}$$

$$\text{or: } \sigma_{y(a)}(x) = \frac{\sigma \cdot x}{\sqrt{x^2 - a_{\text{eff}}^2}}$$



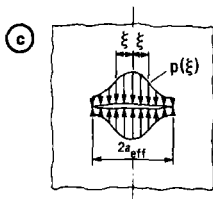
$$\sigma_{y(b)}(x) = -p(\xi) \text{ due to } F_{ik} \text{ for } x \geq a_{\text{eff}} \text{ (see (c))}$$



for this load case in the literature can be found:

$$Z(z) = \frac{2}{\pi} \frac{Fz}{(z^2 - \eta^2)} \sqrt{\frac{a^2 - \eta^2}{z^2 - a^2}}$$

where F = force per unit thickness



with F being equal to $p(\xi) d\xi$ it follows that

$$\sigma_{y(c)}(x) = -\frac{2}{\pi} \frac{x}{\sqrt{x^2 - a_{\text{eff}}^2}} \int_{\xi=0}^{\xi=a_{\text{eff}}} \frac{p(\xi) d\xi}{x^2 - \xi^2} \sqrt{a_{\text{eff}}^2 - \xi^2}$$

NOTE: expressions for $p(\xi)$ can be found in e.g. Ref. 19

$$\sigma_y(x) = \sigma_{y(a)}(x) + \sigma_{y(b)}(x) + \sigma_{y(c)}(x)$$

FIG. 8—Derivation of stress distribution in the net section ($\sigma_y(x)$) of a stiffened panel containing a crack length $2a_{\text{eff}}$.

in the case of intact stiffeners the load cases (b) and (c) of Fig. 8 will yield a negative contribution to $\sigma_y(x)$, which implies that the plastic zone size in the stiffened panel will be smaller than that in the unstiffened sheet.

In the computer programs the unknown plastic zone parameter r_2 for an assumed (input) value of a_{eff} is first determined from Condition ii in Fig. 7 by means of a "regula falsi" procedure. When r_2 is known, the value of r_1 can be found simply by integrating the stress distribution $\sigma_y(x)$ according to Condition i in Fig. 7. It must be noted here that, in the computer programs, this procedure for determining the crack-tip plasticity correction is carried out only for the stress levels at which the sheet and critical stiffener fail (σ_{SH} and σ_{ST_i} , respectively).

Optional Stiffened-Panel Configurations

The ARREST and BOND computer programs are written for stiffened panels with a central skin crack running in a direction perpendicular to the longitudinal stiffeners. Symmetry with respect to both panel centerlines is assumed for the panel. The panel contains $(M - 1)$ stiffeners at either side of the panel longitudinal centerline. The value of M can be chosen arbitrarily. The presence of a central stiffener is optional. If this stiffener is present it can be taken to be intact or broken. Absence of the central stiffener allows configurations with a crack extending between two stiffeners. The relative stiffener spacings can be chosen arbitrarily.

Each stiffener consists of L parallel elements. For riveted stiffeners $L = 1$; for bonded stiffeners L can be chosen arbitrarily. The interconnection of the parallel elements of a stiffener is optional: it can be either fully loose or connected in an infinitely stiff way. Each parallel element of a stiffener (lengthwise) contains N elements at either side of the line of the crack, each of the elements being connected to the skin by means of its own attachment, which implies that each stiffener is connected to the skin by means of a total of $2 \cdot L \cdot N$ attachments. The flexibility of the attachments is accounted for. The number of attachments and the element dimensions can be chosen arbitrarily (the latter option is mainly of interest for bonded stiffeners). Consequently, the dimensions of the stiffener elements can be adjusted to the expected stress gradients in the stiffeners. With bonded stiffeners the sheet-stiffener bonding layers are idealized in the same way as the stiffeners. The interconnections of sheet and stiffeners are then in the element centers. The shear stresses in the bonding layer elements are assumed to be constant per element (both in length and width directions). The shear stresses integrated over each element will yield the sheet-stiffener interaction forces acting on that element. For riveted panels there are two options for crack location with regard to the nearest rivets: the crack line passes either through rivet holes or midway between two rivets. Configurations with either eccentric stiffeners or strip stiffeners can be handled. Mixed configurations are also allowable, that is, both types of stiffener incorporated in one panel. With eccentric stiffeners the stiffener bending is accounted for.

Application of Programs to Actual Structures

Using the ARREST and BOND programs, residual strength calculations were carried out on cracked panels with riveted and bonded stiffeners. The rivets used were 4.8-mm DD rivets with protruding head at a spacing of 20 mm. The bonding material was Redux. The skin consisted of 2024-T3 alloy and the stiffeners were of 7075-T6 alloy, both of clad material. All panels were 300 mm wide and contained five stiffeners (one stiffener at the panel centerline and two at either side) at a spacing of 60 mm. Stiffener configurations with and without eccentricities were considered. More details about the stiffener design are presented

in Table 1. The panels contained central skin cracks, extending symmetrically with respect to the panel centerline, in combination with either an intact or sawcut central stiffener.

In Figs. 9 through 13a [20] the results of the calculations are plotted in residual strength diagrams (panel end stress, σ , versus effective and actual crack sizes, a_{eff} and a , respectively). In these diagrams, test results are also plotted to allow experimental verification of the calculated results. In Fig. 13c the calculation results of Fig. 13a are also plotted according to the R -curve approach (curves for $\sigma = \text{a constant}$ in a K versus a_{eff} plot) to allow for stable crack growth with increasing panel stress.

It must be noted that the calculations presented in Figs. 9 through 13a are all carried out for (selected) a_{eff} values. The actual (visible) crack length, a , is derived from a_{eff} by means of the plasticity correction parameter, r_1 , where $a = a_{\text{eff}} - r_1$. The procedure applied in determining r_1 for a certain a_{eff} value and stress level has been discussed previously.

Panels with Riveted Stiffeners—Figures 9 and 10 show the calculated and test results for panel configurations with Z stiffeners. With the panels of Fig. 9 only the skin is cracked, whereas with those of Fig. 10 the central stiffener is sawcut as well.

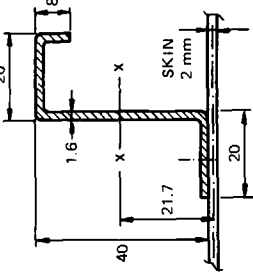
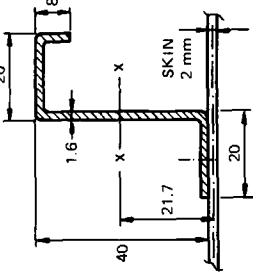
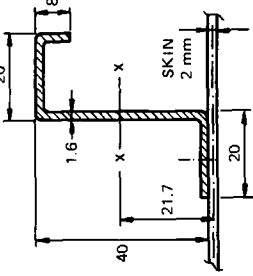
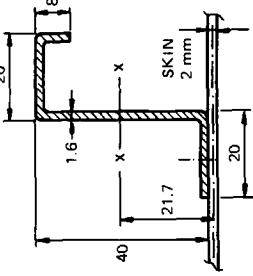
In generating the calculated curves, calculations are carried out for selected a_{eff} values. For each a_{eff} value, the failure stresses of sheet (σ_{SH}) and critical stiffener (σ_{ST}) are found by means of Eqs 6 and 7, respectively. Corrections for plasticity to find the corresponding actual crack sizes, a , at the failure stress levels are indicated in the residual strength diagrams by means of arrows representing the calculated r_1 values (see the example in the diagram of Fig. 9 for $a_{\text{eff}} = 40$ mm and also the sketch in this figure). The required σ_{SH} versus a relation is found then by smoothing curves through the arrow points. The $\sigma_{SH}(a)$ curves obtained are indicated by a solid line. The dashed-and-dotted curves represent the failure curves of the critical stiffeners as a function of the effective crack size. Plasticity corrections cannot be carried out for the points of these curves because the corresponding stress levels are so high that Condition ii in Fig. 7 cannot be met anymore. Point A in Fig. 7 in this case will be located beyond the panel edge (or $a_{\text{eff}} + r_2 > W/2$, where W represents the total panel width).

From the plotted curves in Figs. 9 and 10 it can be concluded that the present panel configurations are to be classified as skin critical (see Fig. 6). From the shape of the $\sigma_{SH}(a)$ curves the predicted fail-safe stress levels, σ_{FS} , have been determined (see for example, Ref 16). The quantitative values of σ_{FS} are compiled in Table 1. Apparently, for this panel configuration, failure of the central stiffener will reduce its fail-safe strength by approximately 20%.

In Figs. 9 and 10 the results of residual strength tests are also recorded (panel end stresses as a function of visible crack sizes). The stress levels at which final failure of the test panels occurred are indicated in the diagrams by solid points.

Although the behavior of the panels during the tests is clear from their crack growth histories, a few comments are in order. Specimens 4 and 5 in Fig. 9 both showed unstable crack growth followed by distinct crack arrest in rivet holes. However, crack arrest in Specimen 4 was immediately followed by total panel failure, whereas with Specimen 5, the panel load could be further increased after crack arrest until ultimate panel failure without showing any further crack growth from the rivet holes. One of the panels in Fig. 10 (Specimen 6) showed continuous stable crack growth until the crack ran into the rivet holes of the adjacent stiffeners. Thereafter, during a slight increase of the panel load, one crack tip remained arrested in the rivet hole, whereas the other tip grew further in a stable way until ultimate panel failure (only the crack growth history of the latter tip is shown in Fig. 10). The other panel (Specimen 7) showed fracture instability followed by crack arrest in the rivet holes. Thereafter, with increasing external load, both crack tips initially remained

TABLE 1—Characteristics of panel configurations considered in analysis-test verification.

CALCULATION EXAMPLE No.	MATERIAL		CONFIGURATION AND STIFFENER DIMENSIONS (mm)	CONDITION OF CENTRAL STIFFENER	PREDICTED FAIL-SAFE STRESS, σ_{FS} (MPa)	CALCULATED AND TEST RESULTS IN FIGURE
	SHEET	STIFFENERS				
1			<div>$A_{ST} = 123 \text{ mm}^2$ $I_{X-X} = 28600 \text{ mm}^4$ </div>	INTACT	303	9
2			<div></div>	SAWCUT	239	10
3			<div></div>	INTACT	SEE TEXT	11
4			<div></div>	SAWCUT	327	12
5			DITTO AS WITH RIVETED PANELS	INTACT	330	13

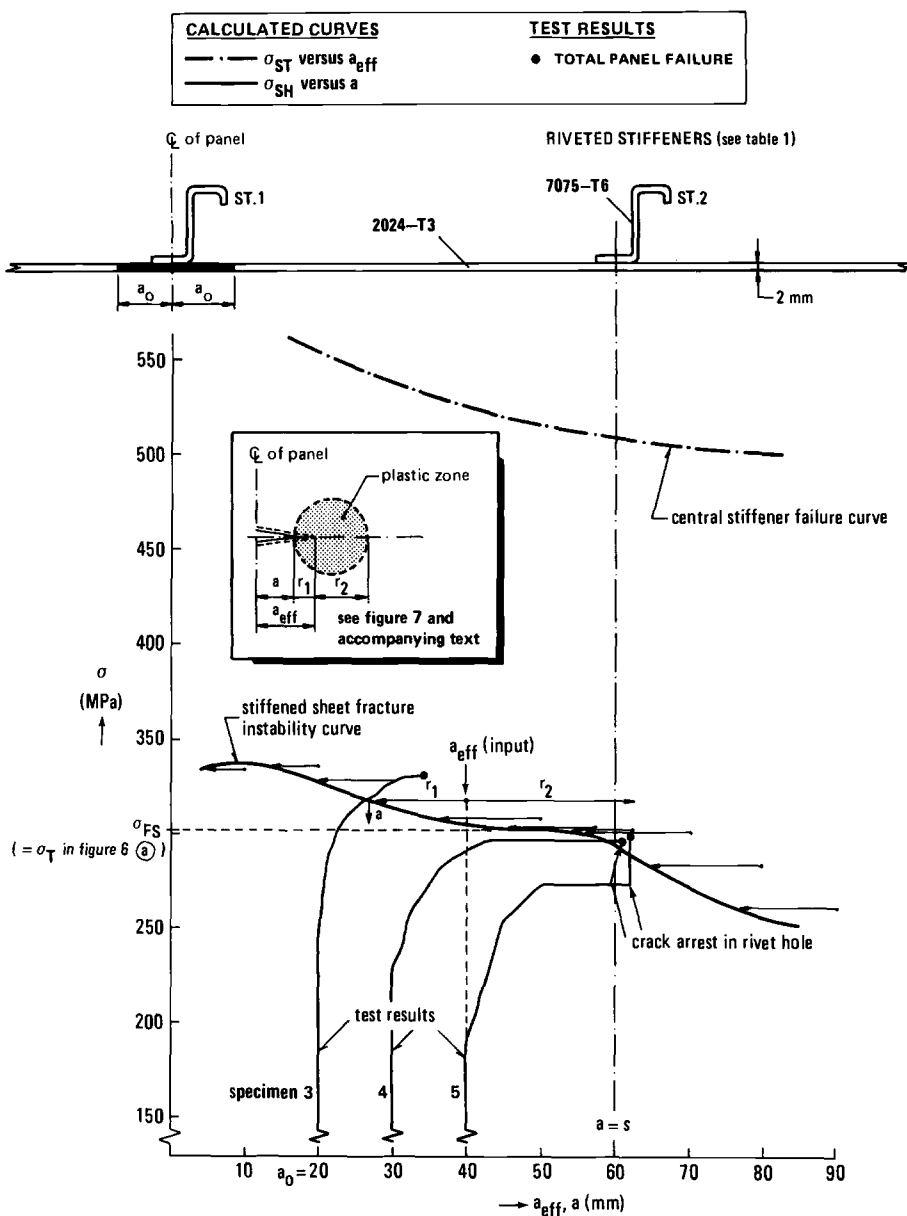


FIG. 9—Calculation example No. 1 (see Table 1): predicted residual strength diagram (obtained with ARREST) and a comparison with test results for a panel configuration with five intact 7075-T6 Z stiffeners and a 2024-T3 skin.

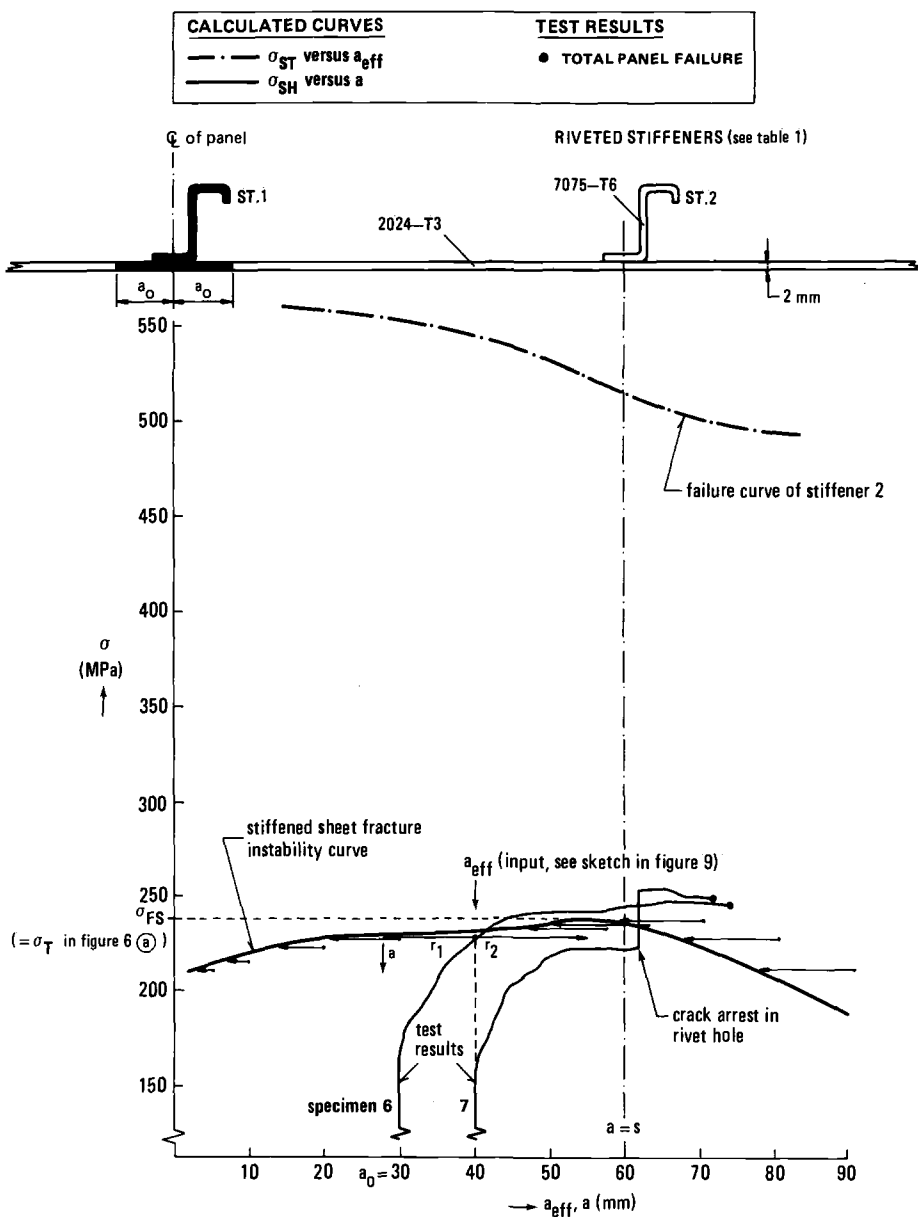


FIG. 10—Calculation example No. 2 (see Table 1): predicted residual strength diagram (obtained with ARREST) and a comparison with test results for a panel configuration with five 7075-T6 Z stiffeners (broken central stiffener) and a 2024-T3 skin.

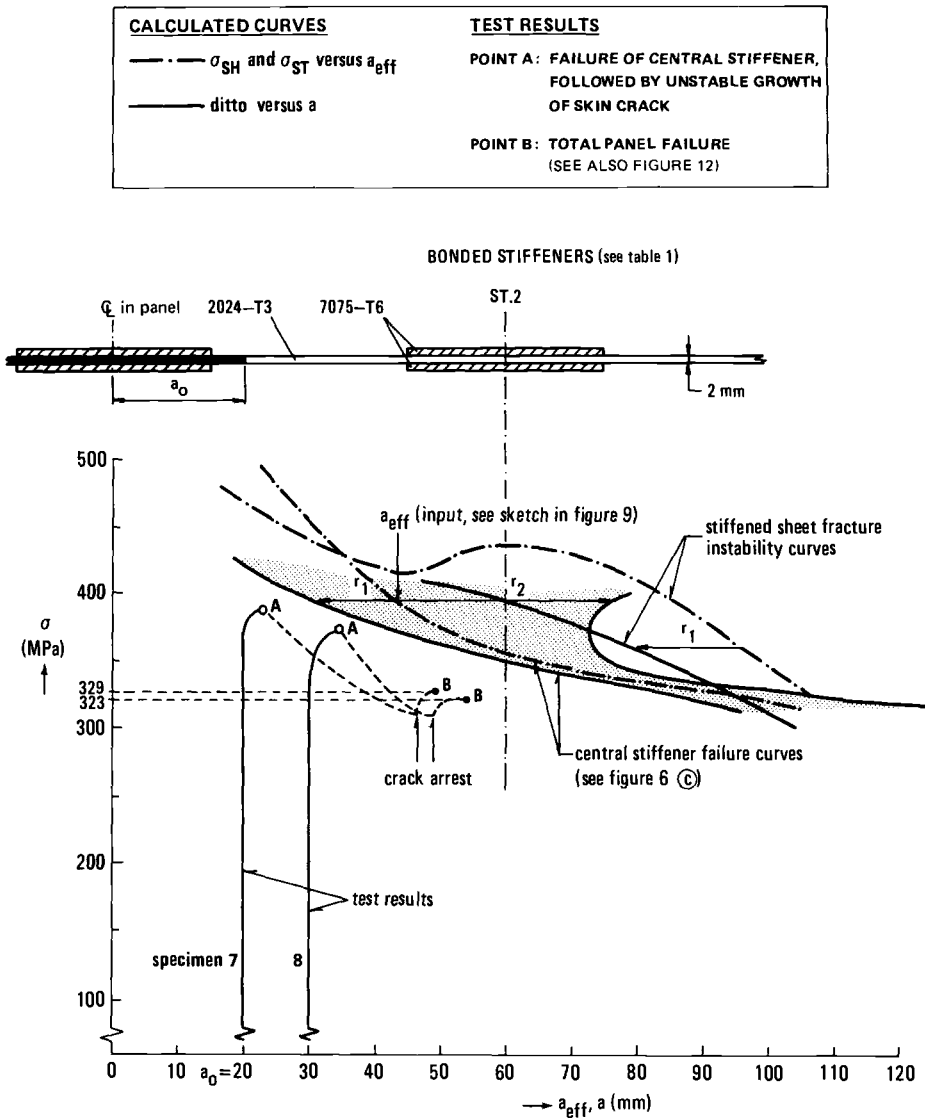


FIG. 11—Calculation example No. 3 (see Table 1): predicted residual strength diagram (obtained with BOND) and a comparison with test results for a panel configuration with five intact 7075-T6 strip stiffeners and a 2024-T3 skin (from Ref 20).

arrested in the rivet holes. However, after a certain amount of load increase, one crack tip started to grow again from the rivet hole (the other tip remained arrested) and extended in a stable way until ultimate panel failure.

It can be concluded from the results in Figs. 9 and 10 that the behavior of the test panels after unstable crack growth (that is, crack arrest or immediate total panel failure) is in good agreement with the behavior to be expected on the basis of the predicted fail-safe stress levels, σ_{FS} . Apparently, design stress levels chosen equal to or lower than the predicted σ_{FS}

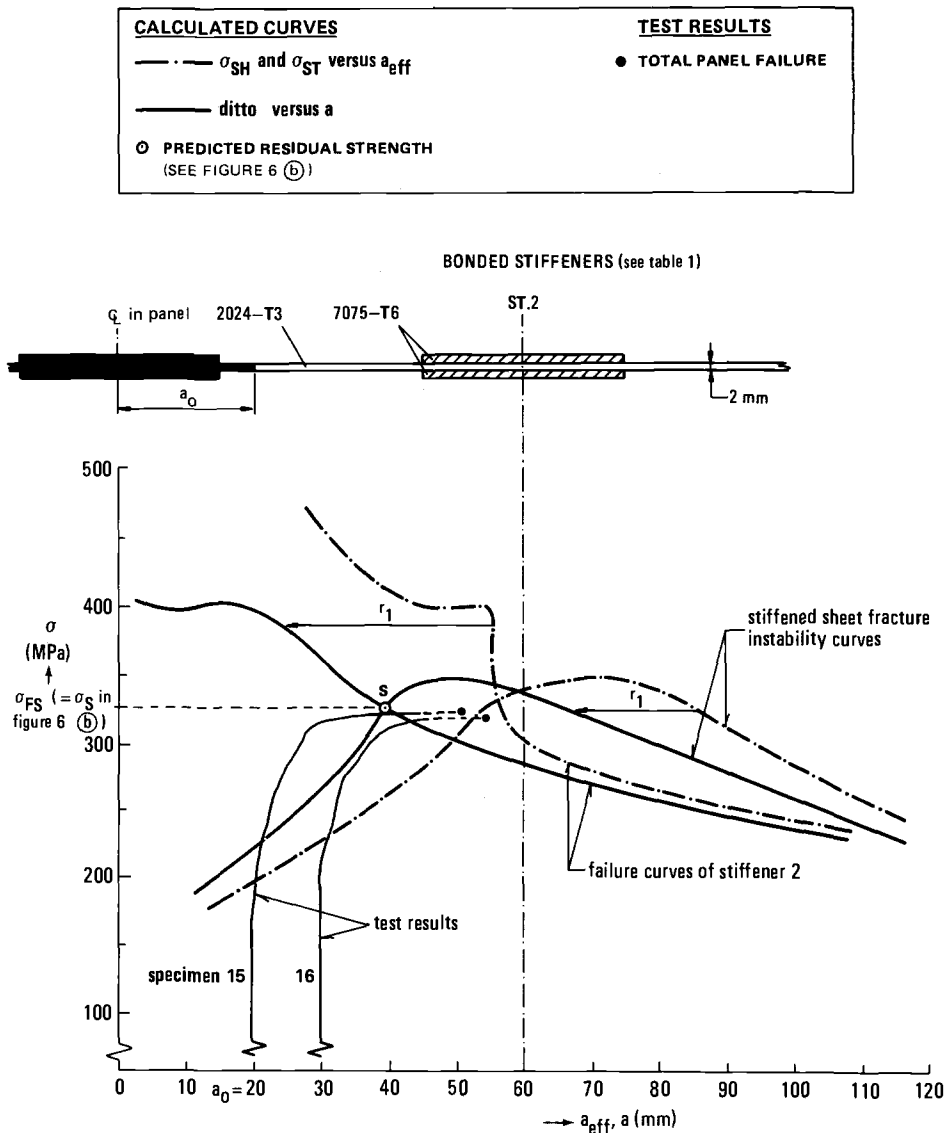


FIG. 12—Calculation example No. 4 (see Table 1): predicted residual strength diagram (obtained with BOND) and a comparison with test results for a panel configuration with five 7075-T6 strip stiffeners (broken central stiffener) and a 2024-T3 skin (from Ref 20).

values will warrant a fail-safe design for skin cracks that are smaller than, or at most equal to, a two-bay crack.

Panels with Bonded Stiffeners—Figures 11 and 12 show the calculated and test results for panel configurations with strip stiffeners. The strips are bonded to either side of the skin to prevent eccentricity. With the panels in Fig. 11 only the skin is cracked, whereas with those presented in Fig. 12 the central stiffener is sawcut as well. Figure 13a shows calculated and test results for panel configurations provided with Z stiffeners but otherwise similar to

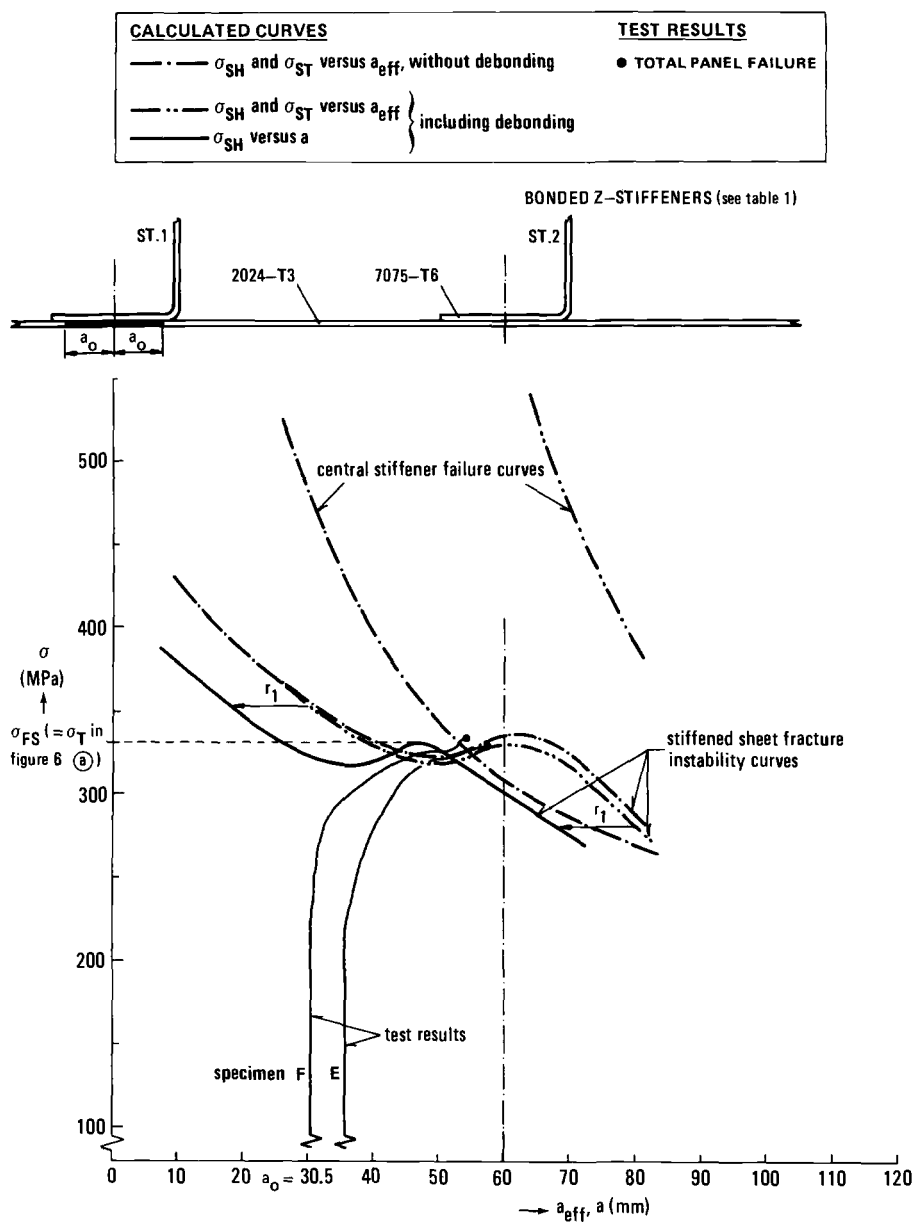


FIG. 13a—Calculation example No. 5 (see Table 1): predicted residual strength diagram (obtained with BOND) and a comparison with test results for a panel configuration with five intact 7075-T6 Z stiffeners and a 2024-T3 skin.

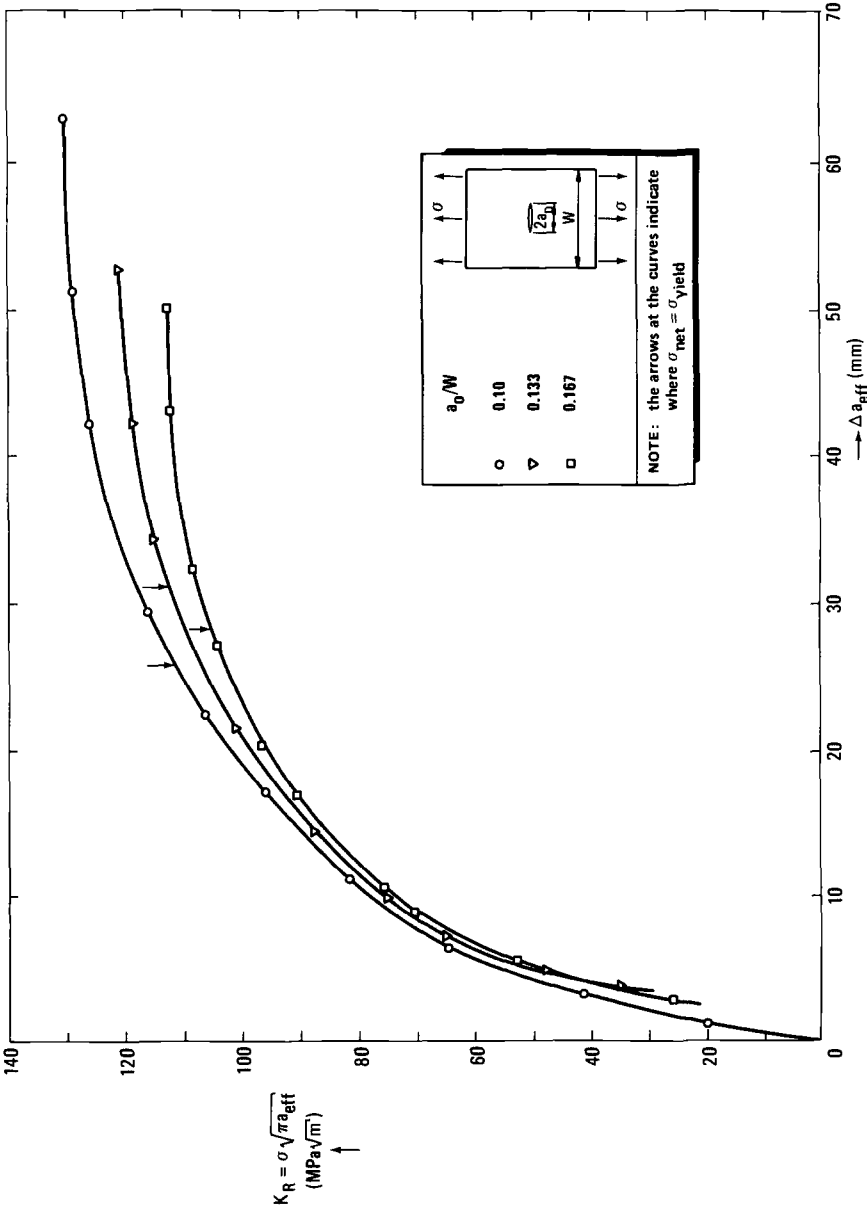


FIG. 13b—R-curves for skin material of test panels (2024-T3 clad, 2-mm thick, $W = 300$ mm).

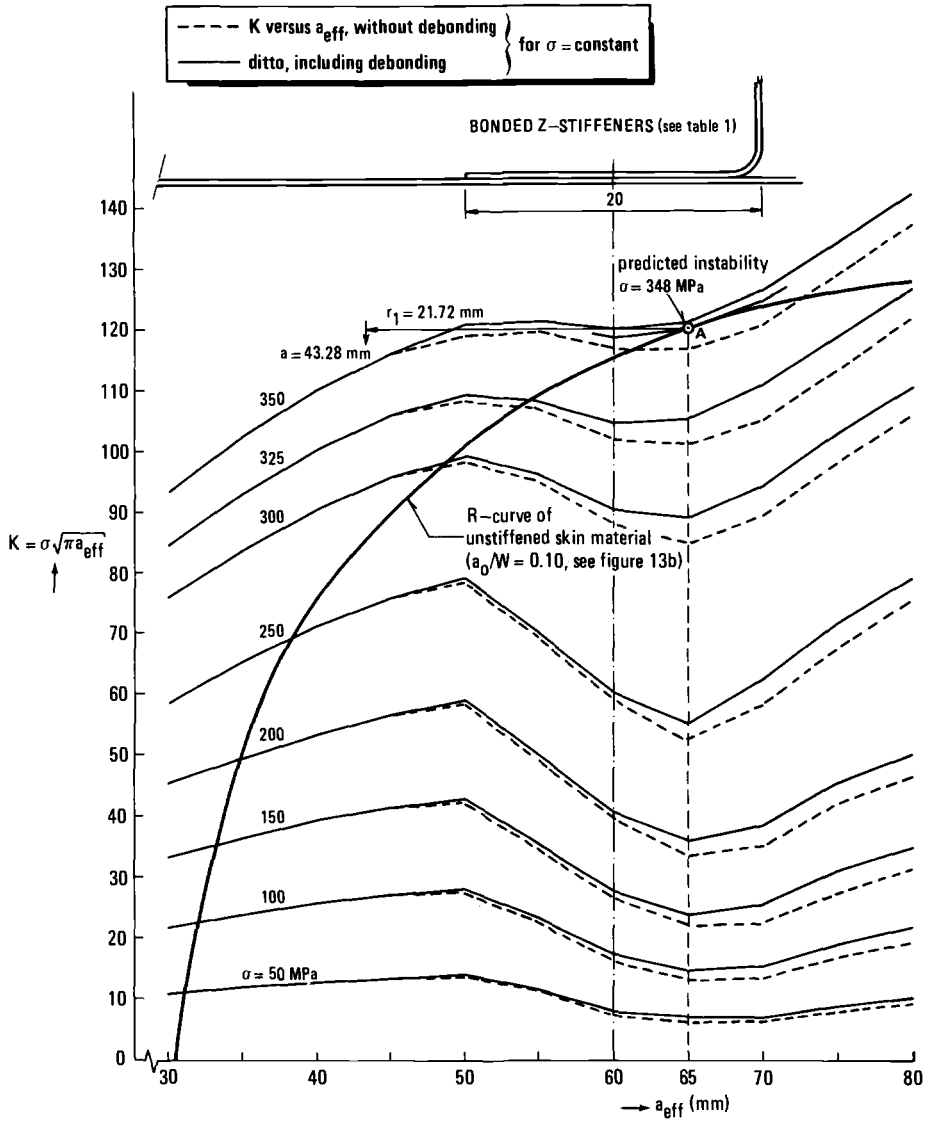




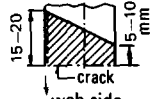


FIG. 13c—Plot of K versus a_{eff} for constant σ -levels as obtained with BOND.

	CALCULATED WITH BOND			AMOUNT OF DEBONDING IN SKIN-STIFFENER BONDING LAYER	
	a_{eff} (mm)	r_1 (mm)	a_{actual} (mm)	central stiffener	adjacent stiffener
FOUND IN CALCULATIONS	35	2.50	32.50	none	
	40	6.18	33.82		none
	45	8.79	36.21		
	50	10.92	39.08		
	55	13.66	41.34		none
	60	17.93	42.07	ditto	
	65	21.72	43.28	ditto	
FOUND IN TEST	—	—	~50		none

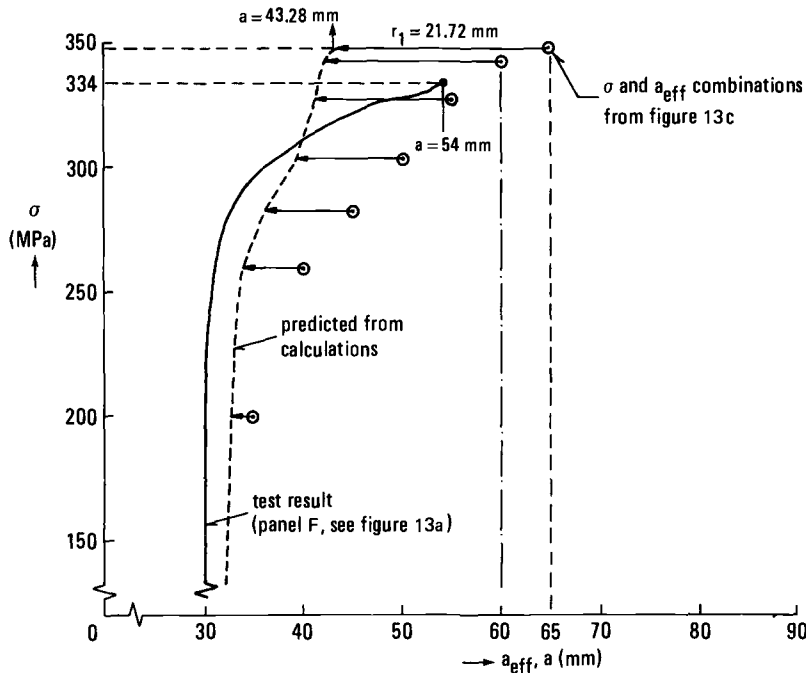


FIG. 13d—Comparison of stable crack growth history and the amount of debonding found in a test with results obtained from R-curve calculations (see Fig. 13c).

those shown in Fig. 11. The cross-sectional areas of the Z stiffeners are approximately equal to those of the strip stiffeners (see Table 1). All calculation results shown in Figs. 11 through 13a are for selected a_{eff} values. Generation of the failure curves of sheet and stiffeners from these results occurred in the same way as was described for the riveted panels, with the exception that now the results, both for the effective and actual crack sizes, are presented in the form of curves.

In Figs. 11 through 13a, the results of the residual strength tests are also recorded (panel end stresses as a function of visible crack sizes). The stress levels at which final failure of the test panels occurred are indicated in the diagrams by solid points.

Considering the results presented in Fig. 11, it can be concluded from the relative position of the calculated failure curves of sheet and stiffeners as a function of the actual crack size (curves drawn solid) that the panels are stiffener critical (see Configuration © in Fig. 6). This predicted behavior is in agreement with the test results, although the calculation results are slightly unconservative. In the tests, failure of the central stiffener occurred at stress levels given by Points A. This stiffener failure would have induced total panel failure if the testing machine had been able to maintain this stress level (there was a sudden elongation of the panel owing to the unstably growing skin crack associated with failure of the central stiffener).

Concerning the calculated curves presented in Fig. 11, it has to be remarked that after failure of the central stiffener a new situation has arisen, which implies that these curves will not be valid any longer. Instead, failure curves related to the configuration with a broken central stiffener will now apply. Curves corresponding to that situation are presented in Fig. 12. Indeed, comparing the stress levels at which ultimate failure of the panels in Fig. 11 occurs (see Points B) with those given by the intersection of the failure curves in Fig. 12, Point S (see also Table 1), the results of tests and calculations appear to compare very well.

By way of illustration, in Fig. 11 the size of the plastic zone ($r_1 + r_2$, see the sketch in Fig. 9) found from the calculated $\sigma_{ST}(a_{\text{eff}})$ curve is indicated as a function of crack size and stress level. Apparently, the plastic zone size has a minimum value when the crack tip is just at the outer edge of Stiffener 2.

On the basis of the calculated failure curves of sheet and stiffeners drawn in Fig. 12 as a function of visible crack size (curves drawn solid), it is to be expected that this panel configuration is stiffener critical (see Configuration ⑥ in Fig. 6). Consequently, for stress levels below σ_{FS} , Stiffener 2 would fail before the skin toughness is fully exhausted (as dictated by the top of the calculated skin instability curve). Failure of Stiffener 2 would thus entail total panel failure, because after failure of this stiffener the calculated sheet curve will not be valid any longer, since this curve applies to a panel configuration with a failed central stiffener only. The predicted failure stress of the panels in Fig. 12 compares very well with those found in the tests, although it could not be observed from the tests whether panel failure was indeed induced by failure of Stiffener 2.

Figure 13a shows the residual strength diagram for the panel configuration shown in Fig. 11, but now with eccentric stiffeners. Comparing the results of Fig. 13a with those presented in Fig. 11, it can be concluded (on the basis of both calculated and test results) that the behavior of the panels with eccentric stiffeners differs in a number of respects from that of panels with strip stiffeners. First, contrary to the panels with strip stiffeners, the panels with Z stiffeners showed debonding of the skin-stiffener bonding layers. This debonding was found both in tests and in calculations. Second, the crack growth histories of both panel configurations were completely different (compare the test records in Figs. 11 and 13a).

In Fig. 13a calculated failure curves of sheet and stiffeners are presented with and without accounting for debonding, related to the effective crack size. When debonding is not accounted for, these curves (drawn dashed and single dotted) intersect and yield a stiffener-

critical configuration (see Configuration (b) in Fig. 6). However, allowing for debonding (see the curves drawn dashed and double dotted) shifts the skin curve only slightly downwards, whereas the stiffener curve almost leaves the diagram, resulting in a skin-critical configuration (see Configuration (a) in Fig. 6). Correcting the latter skin curve for crack-tip plasticity ultimately yields the solidly drawn curve in Fig. 13a. Apparently the σ_{FS} level derived from this curve compares very well with the failure stresses of the test panels. However, it could not be observed from the tests whether panel failure was indeed induced by skin failure.

It was discussed previously that when plotting the calculation results presented in Fig. 9 through 13a, the effect of possibly occurring stable crack growth with increasing panel stress is not accounted for. This aspect can be allowed for by applying the *R*-curve approach to the stiffened panel calculations (see Ref 16). This is illustrated in Fig. 13c for Specimen F of Fig. 13a, having an initial crack size, a_0 , of 30.5 mm. The required *R*-curve of the unstiffened skin material was determined experimentally according to the recommendations of Ref 21. Figure 13b shows the *R*-curves obtained from three a_0/W ratios. These curves were obtained by increasing the loads on the specimens under displacement control. The crack opening was measured during these tests as a function of the external panel load by means of a clip gage mounted in the center of the crack. By using a compliance calibration curve [21] from these clip gage measurements, the effective crack size was found as a function of the panel stress. The experimental results were plotted as $K_R (= \sigma\sqrt{\pi a_{eff}})$ versus a_{eff} (see Fig. 13b).

Using the *R*-curve plotted in Fig. 13b for $a_0 = 30.5$ mm, together with the calculation results already presented in Fig. 13a but now plotted as $K (= \sigma\sqrt{\pi a_{eff}})$ versus a_{eff} for a number of constant σ levels, the curves presented in Fig. 13c are obtained. The calculation results are plotted with and without allowance for debonding. Fracture instability in the stiffened panel will occur at that stress level and the effective crack size for which the constant- σ curve is tangent to the *R*-curve [16]. This is shown in Fig. 13c by Point A. By correcting at that stress level for crack-tip plasticity, the actual crack size at skin fracture instability will be found. By carrying out such a procedure for a number of combinations of stress and effective crack size, as dictated by the shape of the *R*-curve in Fig. 13c, the instantaneous actual crack size as a function of increasing panel stress can be obtained. This result is plotted in Fig. 13d together with the crack growth history found in a test. The amount of debonding found in the calculations and during the test (in the test only one debond check was carried out just before panel failure) is also presented in Fig. 13d. The predicted crack growth history in Fig. 13d compares reasonably well with that found in the test, except for the final part where the predicted crack growth falls behind. This slower crack growth corresponds to the lesser amount of debonding found in the calculations in comparison with the test (see the table in Fig. 13d).

Crack Growth Program Corpus

In the analysis of fatigue crack growth it is common practice to relate the crack growth rate, da/dn , to the stress-intensity range in a load cycle, ΔK . Such a relation will depend on the value of the stress ratio, R , which is equal to the ratio of the minimum and the maximum stress in a load cycle, or $R = \sigma_{min}/\sigma_{max}$. Several crack growth laws were proposed in the past to account for the effect of R . Using these laws, crack growth rates can be predicted rather accurately for some simple crack configurations in specimens subjected to constant-amplitude loading. However, for more complex loading sequences, such as flight simulation loading, the results are conservative by a factor of three to ten, or more. Nowadays, it is known that these disappointing experiences were a result of ignoring plastic

deformation in the region of the crack. Elber showed [22] that fatigue cracks in sheets of aluminum alloy close before all tensile load is removed. He attributed this observation to residual compressive stresses which exist in the plastic zones in front of and in the wake of the crack. Elber assumed that the crack propagates only when it is fully open and he suggested relating the crack propagation rate to an "effective" stress-intensity factor range, ΔK_{eff} , which relates to the stress range in a cycle for which the crack is fully open.

At the NLR the computer program CORPUS has been developed based on an approximate description of the crack-opening behavior. The crack growth model underlying the CORPUS program is sufficiently realistic to account for the magnitudes and sequence of loads, the growth of fatigue cracks through peak load plastic zones, and the influence of underloads. A full description of the model has been given by De Koning [23]. For the sake of completeness the description of the crack growth model given in that reference will be repeated briefly here.

Description of the Crack Growth Model

The model used in CORPUS is based on a cycle-by-cycle analysis of crack growth, that is

$$a = a_0 + \sum_i \Delta a_i \quad (10)$$

where Δa_i represents the amount of growth associated with the stress increment $\Delta \sigma^i = \sigma^{i+1} - \sigma^i$ (see Fig. 14). It is assumed that crack growth occurs only in the upward part of the load cycles. However, although it is assumed that the crack will not grow during the downward part of the load cycle, in the analysis of deformations near the crack tip, this part of the load cycle plays an important role, as will be shown below. During crack growth the principles of fracture mechanics are adopted and crack growth is related to the variation of the effective stress-intensity factor ΔK_{eff}^i . The foregoing assumptions can be written as

$$\begin{aligned} \Delta a_i &= f(\Delta K_{\text{eff}}^i) & \text{if } \Delta \sigma^i > 0 \\ \Delta a_i &= 0 & \text{if } \Delta \sigma^i \leq 0 \end{aligned} \quad (11)$$

where $\Delta K_{\text{eff}}^i = \Delta \sigma_{\text{eff}}^i \sqrt{\pi a}$. In this expression the effective stress range $\Delta \sigma_{\text{eff}}^i$ is that portion of the upward part of the cycle for which the crack is open (see Fig. 14). It is evident from Fig. 14 that in the present model the crack-opening stress, σ_{op} , governs the effective part of the stress range and consequently the amount of crack growth in a cycle. To determine the crack-opening stress, a model for crack opening must be formulated. Because plastic deformation near the crack tip (both in front of the crack tip and in the wake of the growing crack) plays a dominant role in crack closure and opening, the present crack-opening model is based on these plasticity effects.

It is shown in Ref 23 that the plastic deformation in front of the crack tip, owing to a single peak load-underload excursion, tends to reduce σ_{op} (see Fig. 15a). When the crack propagates through the overload plastic zone, the permanent deformation due to the previous peak load-underload excursion is left in the wake of the growing crack and forms a ridge that results in an increase of σ_{op} (see Fig. 15b). In the model, crack growth retardation effects are based on the crack-opening stress associated with the height of the ridge and also on the plastic zone size existing at the time the ridge under consideration was created.

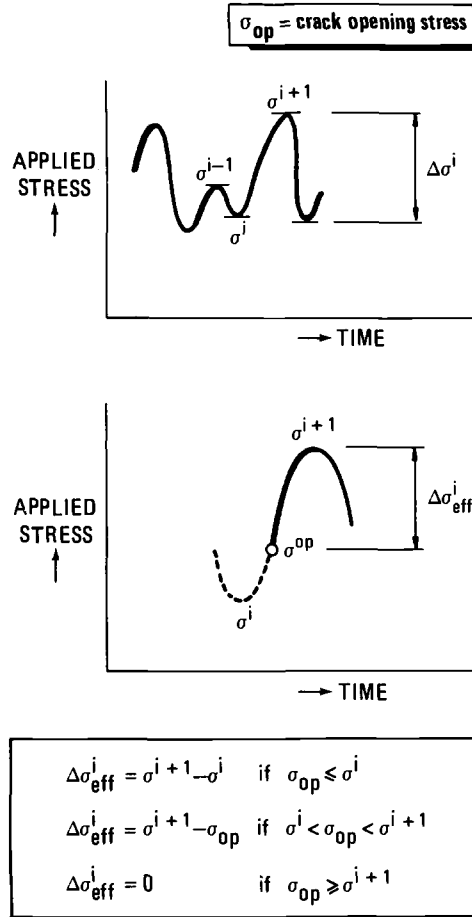


FIG. 14—Assumptions made in the crack growth model for CORPUS.

Finite-element calculations [24] and experimental techniques [25] have shown that the σ_{op} occurring due to a certain peak load-underload excursion is roughly constant while the crack propagates through the plastic zone. After the crack tip has intersected the primary plastic zone boundary (see Fig. 15a) the opening stress level decreases more sharply (see Fig. 16). In the model the ridge-opening behavior sketched in Fig. 16 is approximated by using a “delay” switch. The switch is set *on* after application of the peak load and set *off* if the crack has grown through the peak-load plastic zone. In this way the opening stress is switched from zero to a positive value, σ_{op}^n , if a peak stress σ_{max}^n of level n is applied. Further, it is assumed that the *level* of the opening stress σ_{op} depends on the stress σ_{max}^n applied to create the ridge and on the minimum stress σ_{min}^n experienced by the ridge afterwards. Therefore (see Fig. 16)

$$\begin{aligned} \sigma_{op}^n &= g(\sigma_{max}^n, \sigma_{min}^n) & \text{if } a^n < a < a^n + D^n \\ \sigma_{op}^n &= 0 & \text{if } a > a^n + D^n \end{aligned} \quad (12)$$

where g is the ridge-opening function. Since crack closure and crack opening depend on the plastic deformation behavior of the material, the function g will in principle be different for different materials. With regard to the functional behavior of σ_{op}^n the following observations can be made.

1. The height of the ridge increases with the stress level, σ_{max}^n , that created the ridge. The same is true for the opening stress, σ_{op}^n .
2. When a σ_{min}^n is encountered that is of a lower level than that met before, the ridge is flattened further and consequently opens at a lower stress, that is, σ_{op}^n decreases with σ_{min}^n .

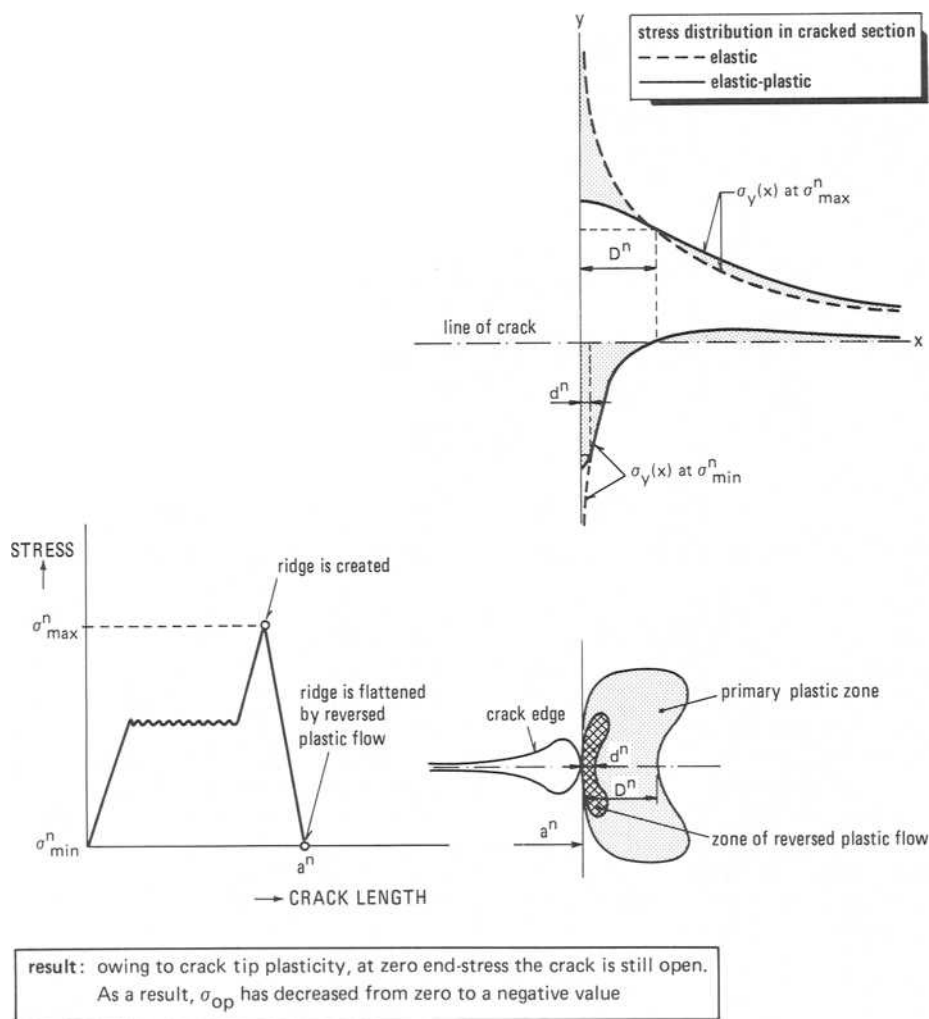
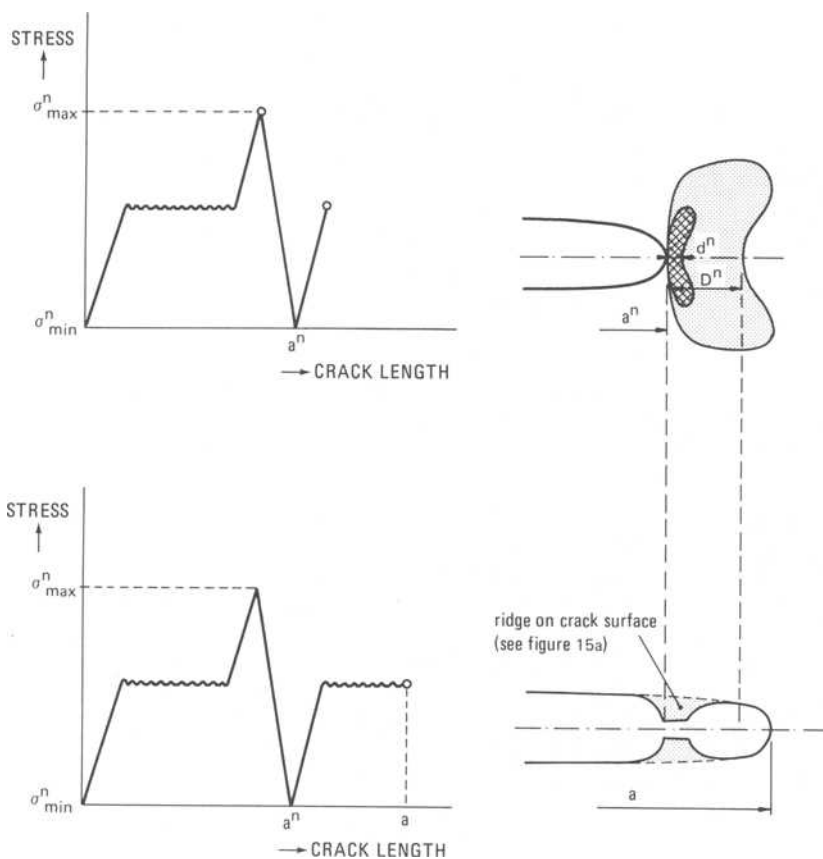


FIG. 15a—Effect of plastic deformation in front of the crack tip.



result: plastic deformation left in the wake of the crack forms a ridge and tends to decrease the crack opening displacement. In other words σ_{op} has increased

FIG. 15b—Effect of plastic deformation when the crack propagates through the plastic zone.

In the original version of the model, an empirical expression for the function g was derived with a form similar to Elber's function [22]. In the current version, the function g is calculated using the "strip-yield" model [26]. It was stated previously that in the model it is assumed that the delay effects, apart from the crack-opening stress, depend on the plastic zone size present at the time the ridge was created. Clearly, the procedure used to estimate the plastic zone size has an effect on the accuracy of the predicted crack growth retardations. It is known that the size of the plastic zone strongly depends on the state of stress near the crack tip. Two extreme situations are the states of plane strain and plane stress. In general, near the front of a through-crack in sheet material, both conditions are present simultaneously (provided the sheet thickness is large enough). Thus, there is plane strain in the middle of the sheet and more or less plane stress near the free surfaces. Fatigue cracks in sheet always start under plane strain conditions. With an increasing amount of crack growth, transition to the plane stress situation occurs. The effect of the plane-strain/plane-stress condition on

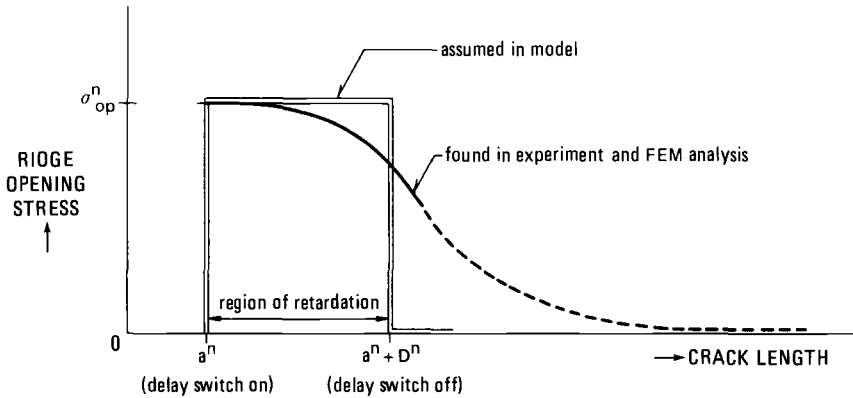


FIG. 16—Ridge-opening behavior, as found in experiments and calculations, compared with the assumption made in the model for CORPUS.

the plastic zone size and the transition from plane strain to plane stress with increasing crack size is incorporated in the model.

So far, the considerations were restricted to the opening behavior observed after application of a single peak load-underload excursion. Variable amplitude loading can be considered as a sequence of such excursions. In general, the number of load levels in the spectrum is limited. Application of the present model implies that one delay switch per load level is introduced. Each switch n accounts for the opening behavior of one set of ridges created by application of that particular load level. The crack is assumed to be closed as long as one or more of the ridges are in contact with their counterparts on the opposite crack surface. The crack is opened if all ridges have lost contact. The ridge that last lost contact determines the crack-opening stress, σ_{op} , that is,

$$\sigma_{op} = \max(\sigma_{op}^n) \quad (13)$$

where σ_{op}^n is the opening stress level at which ridge n breaks contact. This crack-opening behavior is illustrated in Fig. 17.

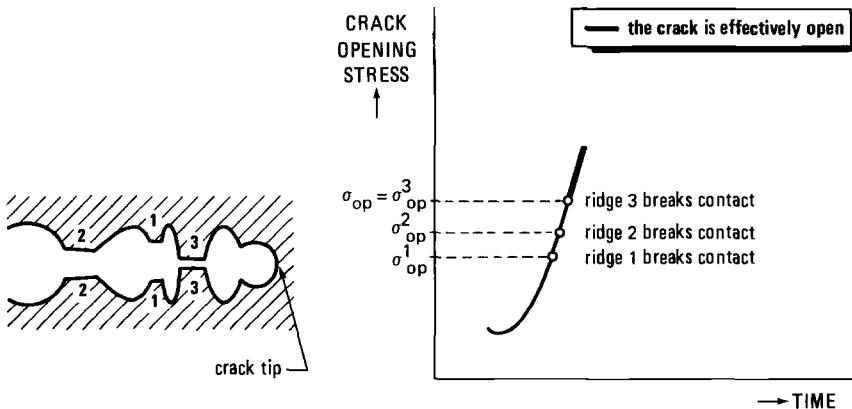


FIG. 17—The opening behavior of a crack tip in the case of three significant ridges on the crack surface.

Functioning of the Crack-Opening Model in CORPUS

How the basic features of the crack-opening model are incorporated in CORPUS will now be explained using Fig. 18. In Fig. 18, Graph *a* shows a load sequence schematically depicting crack growth only during upward load excursions. The first load excursion to σ_{\max}^1 and σ_{\min}^1 (Graph *b*) will eventually result in flattened ridges on the fracture surface. However, CORPUS assumes that the effect of the ridges on crack-opening stress occurs immediately during the next load excursion. The opening stress, σ_{op}^1 , for this second load excursion is indicated in Graph *b*.

During the second load excursion, crack growth commences at σ_{op}^1 and stops at σ_{\max}^2 (Graph *c*, Fig. 18). The ridges to be formed by σ_{\max}^2 (and flattened by σ_{\min}^2) will be smaller than the ridges formed by σ_{\max}^1 and will therefore have a lower opening stress, σ_{op}^2 , as shown in Graph *d*.

The modeling of load interaction effects is illustrated by the next load excursion. Here the third upward load excursion to σ_{\max}^3 is assumed to be effective for crack growth only above the larger of σ_{op}^1 and σ_{op}^2 (Graph *e*, Fig. 18). In terms of fracture surface ridges this is equivalent to the assumption that the crack is effectively open at all locations behind the crack tip; that is, the ridges that are the last to lose contact determine the opening stress at which crack growth commences.

Unloading from σ_{\max}^3 results in a minimum stress, σ_{\min}^3 , below the previous ones (Graph *f*, Fig. 18). This means not only that the ridges due to σ_{\max}^3 will be flattened, but also that the ridges due to σ_{\max}^1 and σ_{\max}^2 will be flattened further. Thus both σ_{op}^1 and σ_{op}^2 will be reduced, as shown in Graph *f*. Consequently, during the next upward load excursion to σ_{\max}^4 , crack growth commences at the lowered value of σ_{op}^1 (see Graph *g*, Fig. 18).

The load excursion to σ_{\max}^4 and σ_{\min}^4 illustrates another feature of CORPUS. This load excursion results in an opening stress, σ_{op}^4 , higher than all previous ones, the effects of which are then lost. The value σ_{op}^4 becomes the opening stress governing further crack growth, as shown in Fig. 18, Graph *h*. Apart from the peak load-underload effects on the crack-opening stress, as illustrated in Fig. 18, Graphs *b* through *h*, the CORPUS model assumes that the effect of each peak load and its associated opening stress are also lost once the fatigue crack has grown through the plastic zone caused by the peak load.

Comparison of Results Obtained with CORPUS with Those from Other Methods

The demand for damage tolerance design tools has stimulated in the past the development of fatigue crack propagation methods and models. The various methods and models now available differ in complexity and accuracy. Therefore, GARTEUR (Group of Aeronautical Research and Technology in Europe) proposed a collaborative program by the end of 1979 to check methods and models in use or under development in the four GARTEUR countries (France, Federal Republic of Germany, United Kingdom, and the Netherlands) with a well-defined set of fatigue test data. The scope of the program would be limited to predictions under variable amplitude flight simulation loading applied to a widely used aluminum alloy sheet material. The participants in this program were DFVLR, Fokker, NLR, ONERA, RAE, MBB-VFW, and Delft University of Technology. The crack propagation prediction methods used by these institutes and companies ranged from simple linear damage accumulation methods to advanced cycle-by-cycle prediction models based on the crack closure phenomenon. Each participant was requested to prepare a report that described in detail the method or model used, together with the predictions made. The required set of test data was provided by the NLR and was obtained from F-27 spectrum flight simulation tests. These tests were carried out on centrally cracked 160-mm-wide, 2-mm-thick aluminum alloy

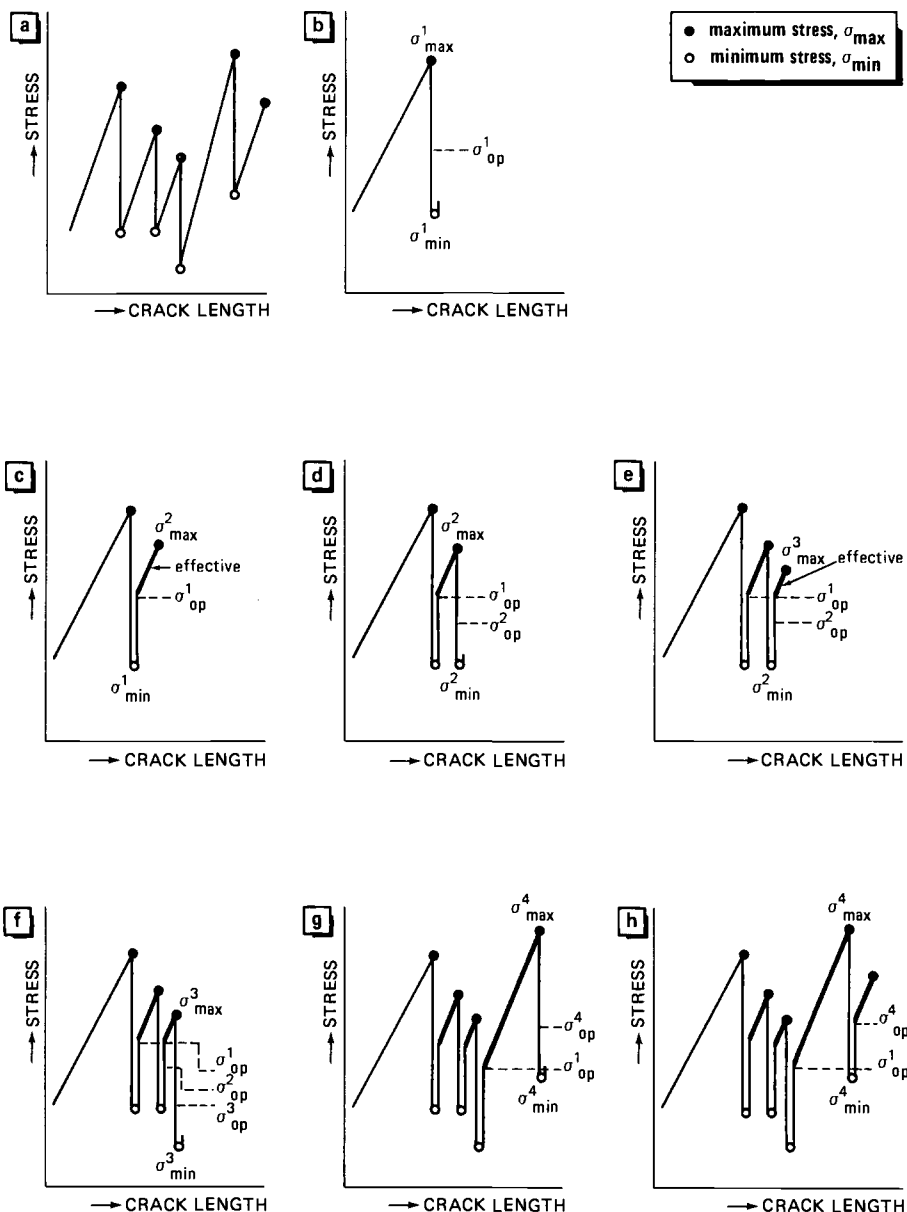


FIG. 18—Crack-opening behavior modeled in CORPUS.

2024-T3 Alclad material. The results of this collaborative program are compiled in Ref 27. This reference also provides a brief description of the methods and models used by the various participants. Table 2 gives an overview of the various combinations of gust severity and ground load levels that were considered in the test and prediction program. Because most crack propagation methods and models require adjustment to the type of loading and material used, the normal gust severity/normal ground load level (labelled NN in Table 2)

TABLE 2—Program overview of gust severity/ground load level combinations considered in the GARTEUR program [27].

material : 2024-T3, 2 mm, Alclad specimen : centre cracked sheet spectrum : F-27 flight simulation			
GROUND LOAD LEVEL \ GUST SEVERITY	LIGHT	NORMAL	SEVERE
LIGHT	LL	NL	SL
NORMAL	LN	NN	SN
SEVERE	LS	NS	SS

xy test results which may be used for adjustment of model

xy crack propagation and crack propagation life to be predicted with model

allowed such an adjustment. The adjusted models were then to be used to predict the crack propagation for four gust severity/ground load level variations (labelled LL, LS, SL, and SS in Table 2). The remaining four combinations in Table 2 were optional. Figure 19 shows the results obtained with this program for the LL, LS, SL, and SS combinations. Both the predicted and test results are presented in this figure. Evidently the predictions range all the way from very conservative to rather accurate and then to unconservative. The models developed by Delft University of Technology (see Ref 27), ONERA, and NLR give results that can be classified from good to very good. The models used by these three institutes are all based on the crack closure concept.

Application of CORPUS to a Stiffened Panel Configuration

In the preceding section, an evaluation of CORPUS was given on the basis of predicted and test results obtained for unstiffened 2024-T3 alloy center-cracked specimens. An evaluation of the model when applied to the prediction of crack growth in the skin of a stiffened panel subjected to flight simulation loading will be the next step.

The geometry and dimensions of the stiffened panel configuration used for that purpose are given at the top of Fig. 20. The lower half of this figure presents the calculated stress-intensity factor of that panel configuration as a function of the skin crack size. Two stiffener idealizations were used to obtain these results, each being representative of the relative position of one of the two crack tips with regard to the nearest stiffener. The results of Fig. 20 were obtained with the BOND program. It can be concluded from the $K(a)$ curves in Fig. 20 that for the assumed stiffener idealization, the orientation of the stiffener with respect to the crack tip does not have much effect on the crack-tip stress intensity. This conclusion is confirmed by observations from the crack growth behavior of both crack tips during a test on a similar panel configuration (see below).

To evaluate the applied stiffener idealization, the results of Fig. 20, which apply to the right-hand crack tip (Idealization ①), were used together with a plot of da/dn versus ΔK (for $R = \sigma_{\min}/\sigma_{\max} = 0.625$) obtained from constant-amplitude fatigue crack growth tests

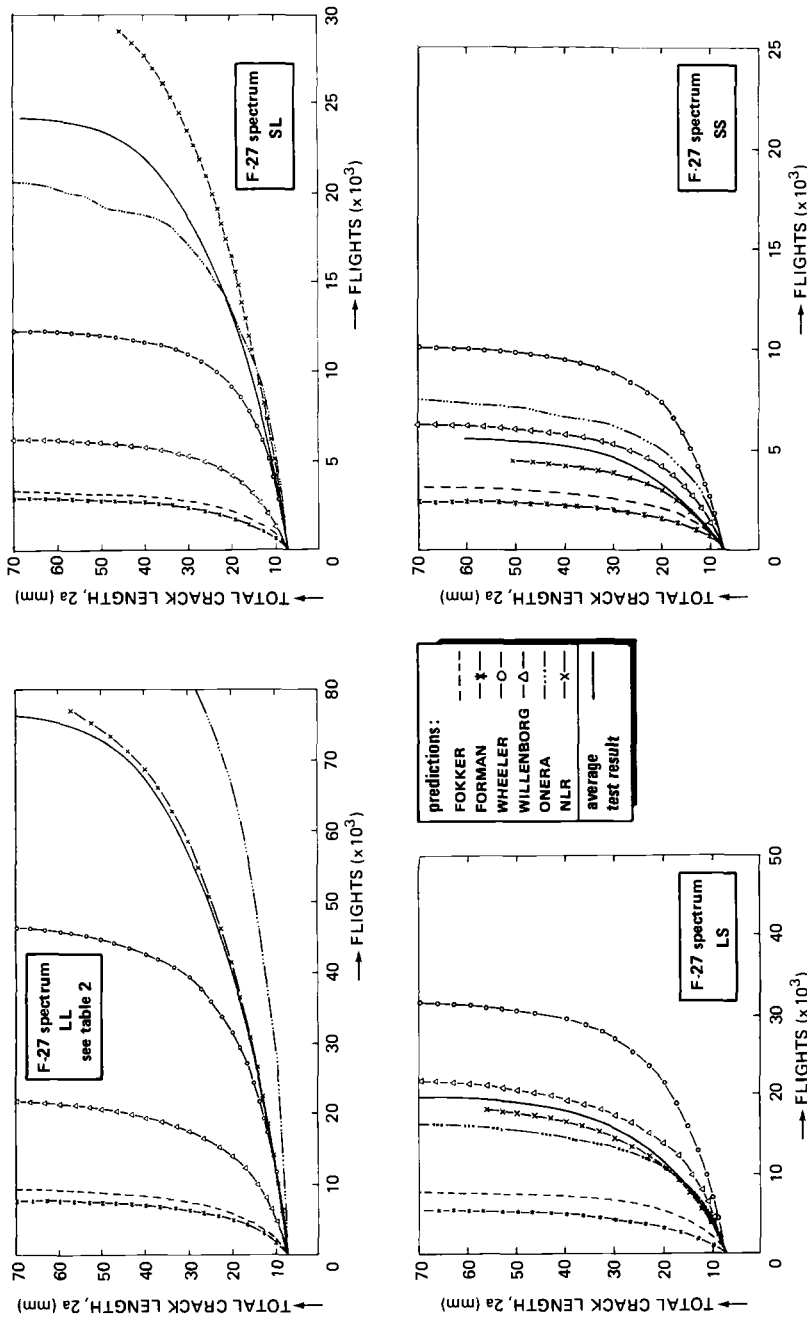


FIG. 19—Comparison of predictions obtained with various crack propagation models with test results for four combinations of gust severity and ground load level [27].

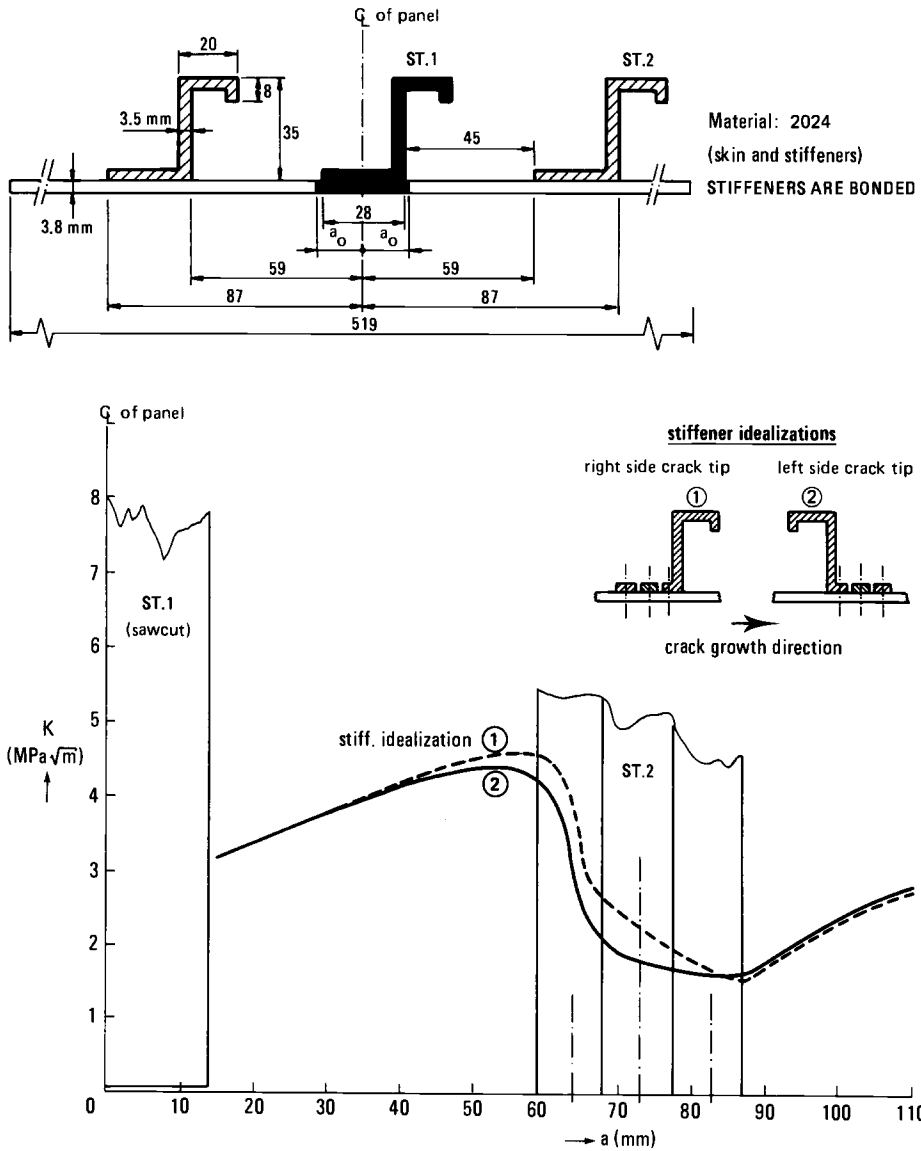


FIG. 20—Calculated (with BOND) stress-intensity factor as a function of crack size for a panel configuration with seven Z stiffeners.

on the unstiffened skin material. By means of an integration procedure from these data, a plot of the crack size, a , versus the number of load cycles, n , was determined. This result is given in Fig. 21, together with a plot found from a constant-amplitude test performed on the stiffened panel (the data referring to the right-hand crack tip have also been plotted here, although the difference in crack growth behavior of both crack tips was negligible). Comparing the calculated and test results in Fig. 21, the applied stiffener idealization appears to yield slightly unconservative results. The deviation between test and analysis for larger crack sizes ($a > 65$ mm) presumably was caused by crack initiation in the skin flange of the

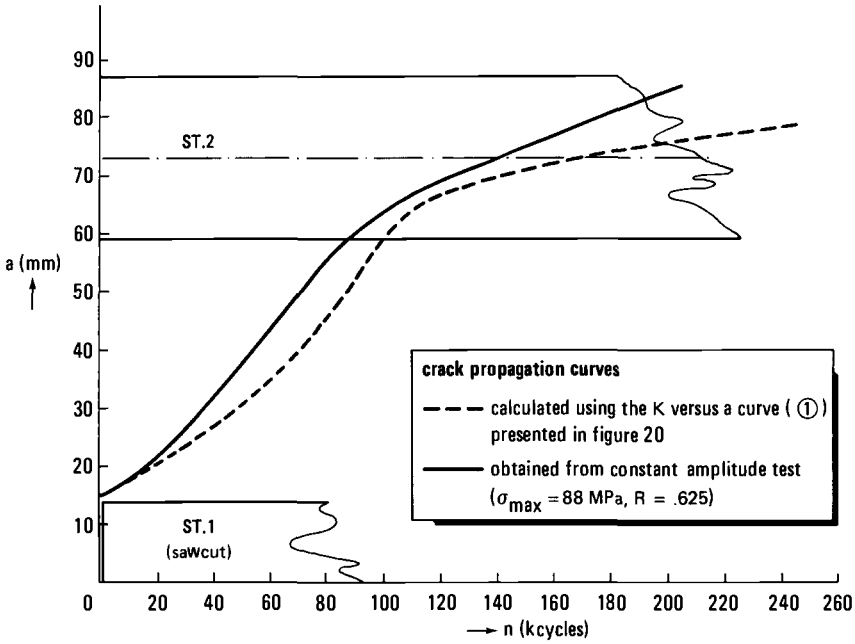


FIG. 21—Comparison of a calculated crack propagation curve with the result obtained from a constant-amplitude test for the panel configuration shown in Fig. 20.

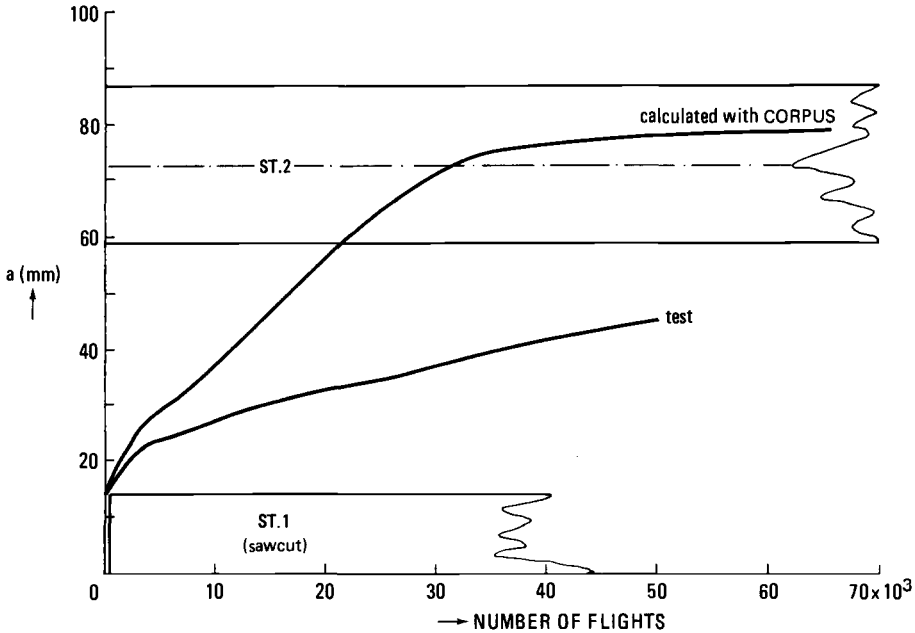


FIG. 22—Comparison of a calculated crack growth curve (by CORPUS) with the test result using a flight-simulation spectrum applied to the wing lower skin of a modern transport aircraft. The results apply to the panel configuration shown in Fig. 20.

stiffener bridging this crack tip. (At least, this is thought to be so because after the test it was discovered that the skin flange of this stiffener was almost completely severed).

To calculate the crack propagation curve of the stiffened panel configuration under flight-simulation loading, the calculated $K(a)$ curve relating to stiffener Idealization ① in Fig. 20 was used as input to the CORPUS program. The predicted crack propagation curve is shown in Fig. 22, together with the curve obtained from a test on this panel configuration. Evidently the first part of the predicted curve compares very well with the test result. Later on (after the plane strain/plane stress transition) the predicted and experimental curves deviate progressively, resulting ultimately in a prediction of crack propagation life that is too conservative by a factor of approximately 3.5.

Summary and Conclusions

To comply with the current damage tolerance (fail-safe) airworthiness requirements for civil transport aircraft, the designer of a new aircraft has to show that fatigue, corrosion, or accidental damage occurring within the operational life of the aircraft will not lead to catastrophic failure as a result of either high, occasionally occurring (residual strength) loads or lower, much more regularly occurring (fatigue) loads. The airworthiness authorities accept application of analytical calculation procedures to demonstrate damage tolerance provided there is sufficient test evidence to show that the analysis methods are conservative. To provide the designer with such tools, a number of computer routines were developed by the NLR. The programs ARREST and BOND enable the prediction of residual strength of a stiffened panel, including its crack arrest properties. The ARREST program applies to riveted stiffeners, and the BOND program to adhesively bonded stiffeners. The CORPUS program has been developed to predict the growth rates of fatigue cracks in structural components subjected to flight simulation loading conditions.

The principles underlying the calculation procedures used in these computer programs are discussed in this paper. An approach incorporated in the computer programs to predict the residual strength of stiffened panels with a skin of a ductile material (such as 2024 alloy) is included. Applications of the programs to some practical stiffened-skin structures are presented together with analysis-test correlations. In their standard format, the residual strength programs yield a complete residual strength diagram (that is, panel end stress versus crack size) containing failure curves of skin and critical stiffener. On the basis of the relative positions of these curves, the residual strength characteristics of the panel can be predicted, including its crack arrest properties. Another important aspect of such a diagram is that a fail-safe stress level, σ_{FS} , can be found from it. Choosing the design stress level equal to or lower than this σ_{FS} will yield a design for which fracture instability, if it occurs, will always be arrested. It has to be noted that in constructing the residual strength diagram, the possible occurrence of stable crack growth in the skin before fracture instability is not accounted for. Based on the results obtained from residual strength calculations on stiffened panels with a 2024 alloy skin, it can be concluded that the predicted panel behavior on the basis of the calculated σ_{FS} compares very well with the experimental results (see Figs. 9 through 13a). Additional calculations, using the *R*-curve approach to allow for stable crack growth in the skin, showed reasonable agreement with experimental observations (see Fig. 13d).

Comparing several institutes' crack growth predictions with test data for unstiffened 2024-T3 alloy center-cracked specimens subjected to flight simulation loading showed that the CORPUS results were excellent (see Fig. 19). Application of CORPUS to predict the crack propagation properties of a stiffened panel under flight-simulation loading resulted in

an overly conservative prediction of the crack propagation life by a factor of approximately 3.5 (see Fig. 22).

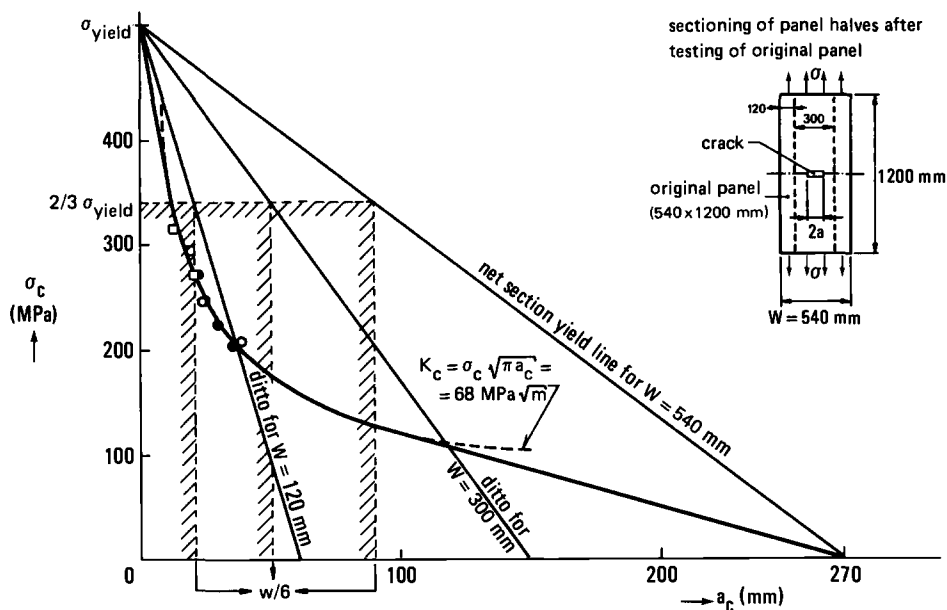
APPENDIX

Residual Strength of Unstiffened Skin Material

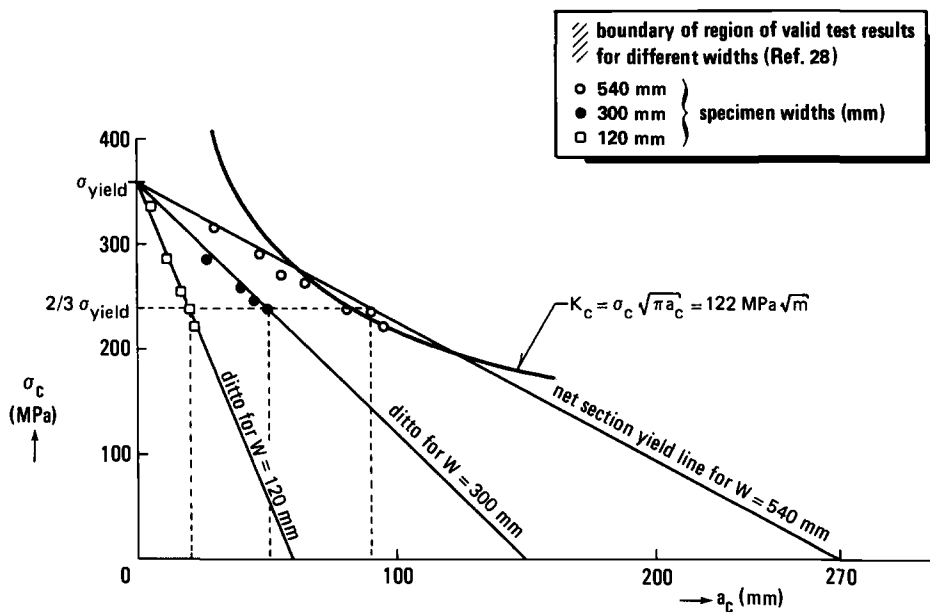
To be able to predict the residual strength properties of a stiffened panel configuration, it is essential in the calculation procedure applied in the computer programs ARREST and BOND that the residual strength properties of the unstiffened skin be known as a function of crack size. It is assumed then that these properties are characterized by the value of the stress-intensity factor, K . How the required K versus crack length relation can be obtained from tests carried out on the unstiffened panels is discussed in this Appendix. In particular it is discussed how the approach will function when it concerns ductile skin materials like 2024-T3 alloy, which in fact do not simply obey elastic fracture mechanics principles.

Residual Strength of Brittle Materials

Residual strength tests on unstiffened panels have shown that for brittle materials, and for panels of a given thickness and size with an intermediate range of crack lengths, sheet failure can be represented by a constant value of the stress-intensity factor, namely, $K_c = \sigma_c \sqrt{\pi a_c}$, where σ_c and a_c are the failure values of the panel end stress and half-crack length, respectively. This is illustrated in Fig. 23a, which shows results of residual strength tests on unstiffened panels of 2-mm-thick 7075-T6 clad material of different widths. Panels of different widths were taken to investigate whether the obtained test results deliver valid K_c values (that is, values independent of panel geometry). To be sure that the panels were identical in all other respects, the following test procedure was applied (see sketch in Fig. 23a). First, residual strength tests were carried out on 540-mm-wide panels. After these tests, a number of specimen halves were used to prepare specimens of 300- and 120-mm width by sawcutting the halves of the failed specimens lengthwise. The results of all the residual strength tests (failure values of stresses and crack lengths) are plotted in Fig. 23a. Apparently, all the test results are located on a single K_c curve ($K_c = \sigma_c \sqrt{\pi a_c} = 68 \text{ MPa } \sqrt{m}$) independent of panel widths. Also shown in this figure are straight lines representing the lines for net section yielding of the respective panel widths: at all points on these lines the average net stresses of the uncracked ligament of the specimens are just equal to the yield stress, σ_{yield} , of the material. Apparently, all test data are well below the respective net section yield lines, this being a requirement to be met when desiring valid K_c values. In the present test program, no failure data were found for crack sizes either small or large compared with the panel widths, W . Feddersen has shown [28] that for such crack lengths the constant- K_c curve will overestimate the actual residual strength of the panel. Feddersen proposed that the residual strength properties for small and large a/W ratios can be obtained by drawing two linear tangents to the K_c curve as shown in Fig. 23a. One tangent is drawn from the point $\sigma = \sigma_{\text{yield}}$ on the vertical axis; the other tangent is drawn from the point $a = W/2$ on the horizontal axis. Assuming the approach proposed by Feddersen, the residual strength, as a function of crack size for the 540-mm-wide 7075-T6 specimens, will be given by the heavily drawn curve in Fig. 23a. Apparently, for crack lengths corresponding to the hyperbolic part of this curve, the fracture toughness, $K_c = \sigma_c \sqrt{\pi a_c}$, will be constant and equal to $68 \text{ MPa } \sqrt{m}$. For crack sizes corresponding to the tangents to the hyperbolic curve, K_c will be lower than $68 \text{ MPa } \sqrt{m}$ and vary as a function of crack size.



a) 7075-T6 sheet of 2 mm thickness ($\sigma_{\text{yield}} = 510 \text{ MPa}$)



b) 2024-T3 sheet of 2 mm thickness ($\sigma_{\text{yield}} = 357 \text{ MPa}$)

FIG. 23—Results of residual strength tests (failure data) on unstiffened panels of different widths for a brittle and a ductile aluminum alloy.

Residual Strength of Ductile Materials

So far, it was assumed that the skin of the stiffened panel consisted of a relatively brittle material, implying that the plane-stress fracture toughness, K_{Ic} , can be taken as a criterion for fracture instability of the cracked sheet. However, this approach does not apply when the stiffened panel contains a skin of ductile material (such as 2024 alloy). This is shown in Fig. 23b, which presents results of residual strength tests (failure data) of unstiffened panels of 2-mm-thick 2024-T3 clad material of different widths. To be sure that the specimens only differed in width and were identical in all other respects, the same test procedure as applied with the 7075-T6 specimens was used (see also sketch in Fig. 23a). Apparently, in the case of the much more ductile 2024-T3 material (in contrast with 7075-T6, see Fig. 23a) for panels having widths of 300 mm and smaller, no data points meet the validity requirements set by Feddersen [28]. This implies that the K_{Ic} curve based on the actual (or visible) crack length in this case, in fact, is reduced to one point: the two points of tangency of the tangents to the K_{Ic} curve coincide and the two tangents are on the net section yield line. Regarding the 540-mm-wide panels, two data points indeed meet the validity requirements of Feddersen but, because these points are fairly close to the net section yield line, even for this width the validity of the drawn K_{Ic} curve of $122 \text{ MPa} \sqrt{m}$ is questionable. The different behavior of the 2024-T3 material compared with that of 7075-T6 alloy (shown in Fig. 23a) is due to the large amount of plasticity taking place at the crack tips in ductile materials. This apparently means that yielding across the entire net section will occur before the stress-intensity factor, based on the actual crack length, can attain its critical value. The foregoing implies that with ductile materials the stress-intensity factor approach cannot simply be used as a failure criterion. Therefore, an approach is presented here that allows a representative “ductile” stress-intensity factor to be applied for the prediction of residual strength of stiffened panels with a skin of ductile material.

The principles of the approach are illustrated in Fig. 24. It was shown by the test data in Fig. 23b that cracked sheets of 2024-T3 material fail when the *average* stress across the net section becomes equal to σ_{yield} (see Sketch (a) in Fig. 24). However, it is plausible that with increasing panel load, due to strain hardening properties of the material, the stresses in the region closest to the crack tip will become slightly larger than σ_{yield} . This would imply that at ultimate panel failure the plastic zone does not extend across the entire panel net section, but remains limited to a region at the crack tip. The size of the plastic zone would be determined then by the condition that the stress in the net section, on an average, is equal to σ_{yield} . This is illustrated in Sketch (b) of Fig. 24, in which the maximum stress at the crack tip is taken to be equal to σ^* , which has to obey the condition

$$\sigma_{\text{yield}} < \sigma^* < \sigma_{\text{ult}} \quad (14)$$

where σ_{yield} is the 0.2% offset yield strength and σ_{ult} is the ultimate tensile strength of the material. The condition of average net section stress being equal to σ_{yield} provides the equality of Areas A_1 and A_2 in Sketch (b) of Fig. 24. Assuming that the stress distribution in the region ahead of the plastic zone remains elastic, then the amount of plasticity at the crack tip can be accounted for by enlarging the actual crack size, a , by an amount r_1 , so that the actual elastic-plastic stress distribution across the net section, corresponding to a half-crack length (a), is imagined to be equivalent to an elastic distribution that would arise from an effective half-crack length, a_{eff} , being present in a perfectly elastic material. This is illustrated in Sketch (c) of Fig. 24, where the stress across the entire plastic zone is assumed to be uniform and equal to

$$\bar{\sigma} \cong \sigma^* = f_{SH} \cdot \sigma_{\text{yield}} \quad (15)$$

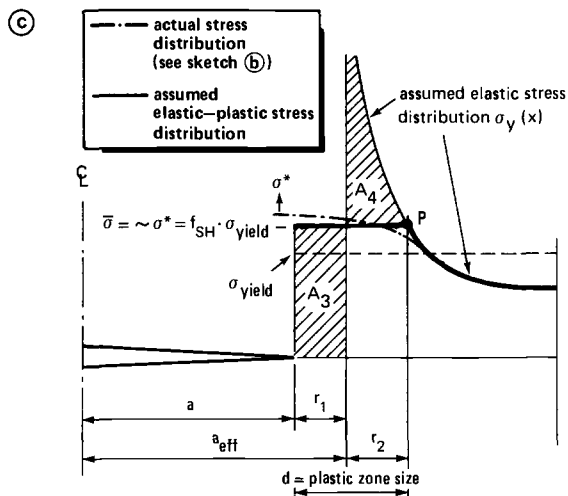
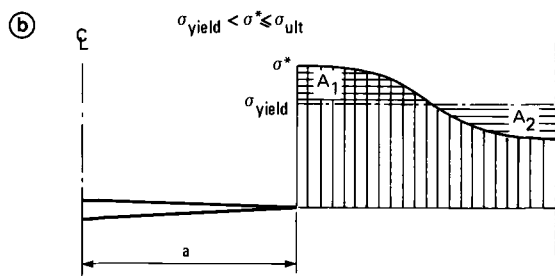
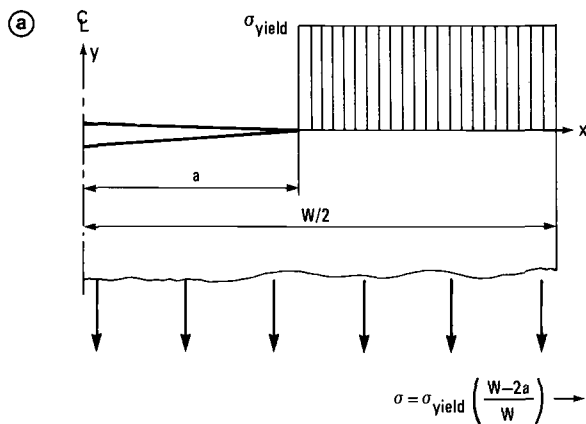


FIG. 24—Approach applied to ductile materials (see also Fig. 23b).

where f_{SH} represents a magnification factor due to strain hardening effects. The foregoing implies that

$$a_{eff} = a + r_1 \quad (16)$$

The size of a_{eff} and the plastic zone size, $d = r_1 + r_2$ (see Sketch © in Fig. 24), at the moments of fracture instability (that is, σ and a are related by the equation of the net section yield line) can now be evaluated from the equality of Areas A_3 and A_4 and the continuity of the elastic and the plastic stress distribution in Point P (Fig. 24). The values of r_1 and r_2 follow from the following conditions (see Sketch © of Fig. 24)

$$(i) \quad A_3 = A_4 \rightarrow \bar{\sigma}(r_1 + r_2) = \int_{x=a+r_1}^{x=a+r_1+r_2} \sigma_y(x) dx$$

$$(ii) \quad \text{continuity in Point P} \rightarrow \sigma_y(x) = \bar{\sigma} \quad (17)$$

$$\text{for } x = a + r_1 + r_2$$

$$(iii) \quad \text{net section yielding} \rightarrow \sigma = \sigma_{yield} \left(1 - \frac{2a}{W} \right)$$

To solve r_1 and r_2 from the conditions in Eq 17 the elastic stress distribution in the net section, $\sigma_y(x)$, has to be known. The solution of r_1 and r_2 from Eq 17 is given in Ref 14,

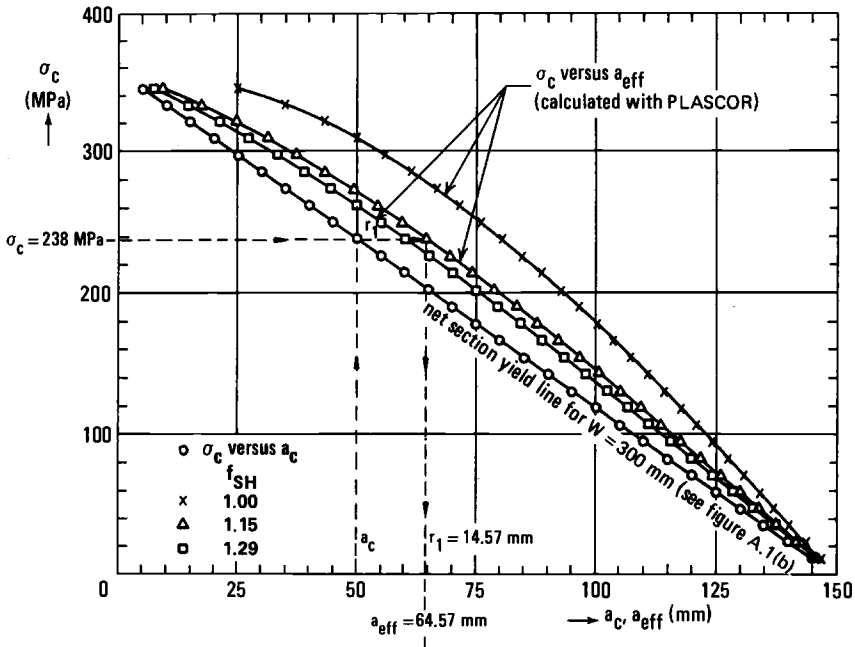


FIG. 25a—Relation between σ_c and a_{eff} for different f_{SH} values, as obtained with PLASCOR for points of the net section yield line.

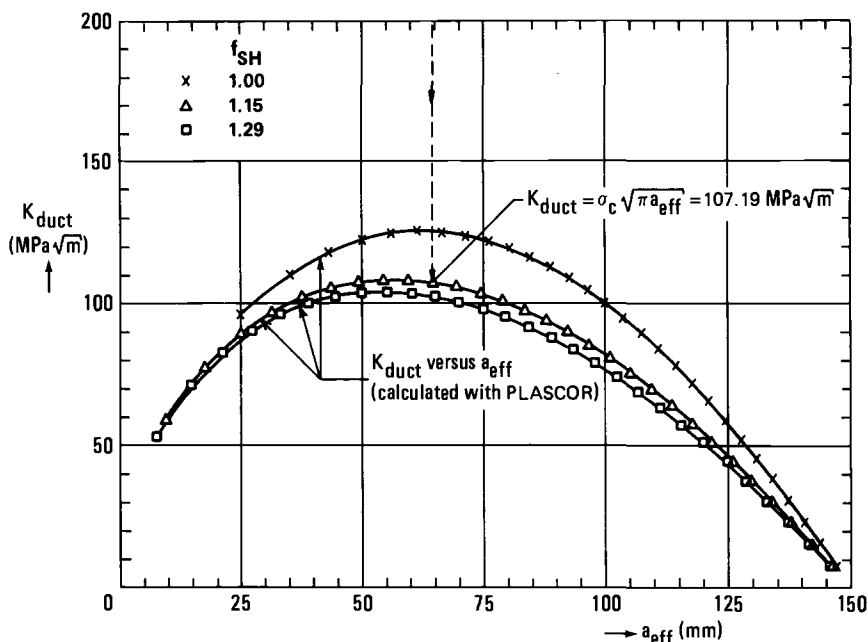


FIG. 25b— K_{duct} as a function of a_{eff} for different values of f_{SH} , as obtained from results in Fig. 25a.

using the stress function of Westergaard [17] for a periodic array of collinear cracks of length $2(a + r_1)$ to determine $\sigma_y(x)$. The distance between the crack centers is taken to be equal to W (to account for the finite panel size, W).

By following the previous approach, fracture instability in ductile materials can now be assumed to be characterized by a fictitious value of the stress-intensity factor, namely

$$K_{duct} = \sigma_c \sqrt{\pi a_{eff}} \quad (18)$$

where σ_c represents the failure stress and a_{eff} is the effective crack length as given by Eq 16, in which the actual crack length, a , has to be taken to be equal to the critical crack length, a_c .

It has to be remarked here that K_{duct} will not be a constant (as was the case with K_c for a certain range of crack lengths; see Fig. 23a) but will depend on crack size for the whole range of crack lengths. To find K_{duct} as a function of the effective crack size, the calculation of r_1 from Eq 17 has to be carried out for a whole range of points of the net section yield line. To perform such calculations the computer program PLASCOR was prepared. (Reference 14 contains a listing of this program.) In this program the unknown r_1 is solved from Eq 17 by means of the "regula falsi" procedure. Using PLASCOR, values of K_{duct} were calculated as a function of the effective crack size for points of the net section yield line of the 2024-T3 material, as given in Fig. 23b, for a panel width of 300 mm. These calculations were carried out for a number of f_{SH} values. Based on the static properties of this material (see Ref 14) f_{SH} will range between 1.0 (that is, yielding across the entire net section) and $\sigma_{ult} \div \sigma_{yield} = 460/357 = 1.29$ (see Eq 15 and Sketch © in Fig. 24). The results of these calculations are plotted in Figs. 25a and b.

References

- [1] "Airplane Damage Tolerance Requirements," MIL-A-83444, Air Force Aeronautical Systems Division, Wright-Patterson Air Force Base, OH, July 1974.
- [2] "Damage Tolerance and Fatigue Evaluation of Structure," FAA Regulations Part 25-571, including Amendment 45, Federal Aviation Administration, Washington, DC, 1978.
- [3] Wood, H. A. and Engle, R. M., Jr., *USAF Damage Tolerant Design Handbook: Guidelines for the Analysis and Design of Damage Tolerant Aircraft*, AFFDL-TR-79-3021, Air Force Flight Dynamics Laboratory, Wright-Patterson Air Force Base, OH, March 1979.
- [4] "Damage Tolerance and Fatigue Evaluation of Structure," FAA Advisory Circular AC 25-571-1, Federal Aviation Administration, Washington, DC, 1978.
- [5] Swift, T., "Application of Damage Tolerance Technology to Type Certification," SAE Technical Paper 811062, Society of Automotive Engineers, Warrendale, PA, 1981.
- [6] European Joint Airworthiness Requirements, "Damage Tolerance and Fatigue Evaluation of Structure," JAR 25-571, Civil Aviation Authority, London, UK, 1974.
- [7] European Joint Airworthiness Requirements, "Damage Tolerance and Fatigue Evaluation of Structure," *Acceptable Means of Compliance*, ACJ 25-571, Civil Aviation Authority, London, UK, 1980.
- [8] Heath, W. G., "The Changing Scene of Structural Airworthiness," Paper No. 792, presented at the 14th International Aeronautical Conference, Paris, France, 1979.
- [9] Hilaire, G. and Odorico, J., "The Damage Tolerance Design Philosophy," *L'Aeronautique et l'Astronautique*, No. 106, 1984.
- [10] Thompson, J., "Trends in Structural Qualification of Civil Transport Aircraft," *Metal Progress*, April 1984.
- [11] "Durability and Damage Tolerance in Aircraft Design" in *Proceedings*, 13th Symposium of the International Committee on Aeronautical Fatigue, A. Salvetti and G. Cavallini, Eds., Pisa, Italy, 22-24 May 1985.
- [12] Goranson, U. G. and Rogers, J. T., "Elements of Damage Tolerance Verification," paper presented to the Twelfth ICAF Symposium, International Committee on Aeronautical Fatigue, Toulouse, France, 1983.
- [13] Swift, T., "Verification of Methods for Damage Tolerance Evaluation of Aircraft Structures to FAA Requirements," paper presented to the Twelfth ICAF Symposium, International Committee on Aeronautical Fatigue, Toulouse, France, 1983.
- [14] Vlieger, H. and Sanderse, A., "User's Manual of ARREST, a Computer Routine to Predict the Residual Strength of Cracked Panels with Riveted Stiffeners," NLR Report TR 84134 U, National Aerospace Laboratory, Amsterdam, The Netherlands, October 1984.
- [15] Vlieger, H. and Sanderse, A., "User's Manual of BOND, a Computer Routine to Predict the Residual Strength of Cracked Panels with Bonded Stiffeners," NLR Report, National Aerospace Laboratory, Amsterdam, The Netherlands, in press.
- [16] Vlieger, H., "Built-up Structures," *Practical Applications of Fracture Mechanics*, AGARDograph No. 257 H. Liebowitz, Ed., North Atlantic Treaty Organization, London, UK, 1980, Chapter 3.
- [17] Westergaard, H. M., "Bearing Pressures and Cracks," *Journal of Applied Mechanics*, Vol. 6, 1939, pp. A49-A53.
- [18] Irwin, G. R., "Analysis of Stresses and Strains Near the End of a Crack Traversing a Plate," *Journal of Applied Mechanics*, Vol. 24, 1957, pp. 361-364.
- [19] Love, A. E. H., "A Treatise on the Mathematical Theory of Elasticity," New York, Dove, 4th ed. 1944, p. 209.
- [20] Vlieger, H., "Residual Strength of Bonded Stiffened Panels: Prediction and Experimental Verification," NLR Report TR 83066 U, National Aerospace Laboratory, Amsterdam, The Netherlands, May 1983.
- [21] Wheeler, C., Estabrook, J. N., Rooke, D. P., Schwalbe, K. H., Setz, W., and de Koning, A. U., "Recommendations for the Measurement of R-curves using Center-Cracked Panels," *Journal of Strain Analysis*, Vol. 17, No. 4, 1982.
- [22] Elber, W. in *Damage Tolerance in Aircraft Structures*, ASTM STP 486, American Society for Testing and Materials, Philadelphia, 1971, pp. 230-242.
- [23] de Koning, A. U., "A Simple Crack Closure Model for Prediction of Fatigue Crack Growth Rates Under Variable Amplitude Loading," *Fracture Mechanics: 13th Conference*, ASTM STP 743, American Society for Testing and Materials, Philadelphia, 1980, pp. 63-85.
- [24] de Koning, A. U. in *Proceedings*, Fourth International Conference on Fracture, Vol. 3, Waterloo, Canada, 1977, pp. 25-31.

- [25] Schijve, J. in *Fatigue Crack Growth Under Spectrum Loads*, ASTM STP 595, American Society for Testing and Materials, Philadelphia, 1976, pp. 3–23.
- [26] de Koning, A. U. and Liefting, G., “Criteria for Determination of Significant Load Cycles in Variable Amplitude Load Sequences,” paper presented to the ASTM Symposium on Fatigue Crack Closure, Charleston, SC, May 1986.
- [27] van der Linden, H. H., “A Check of Crack Propagation Prediction Models Against Test Results Generated Under Transport Aircraft Flight Simulation Loading,” NLR Report TR 84005, National Aerospace Laboratory, Amsterdam, The Netherlands, 1984.
- [28] Feddersen, C. C. in *Damage Tolerance in Aircraft Structures*, ASTM STP 486, American Society for Testing and Materials, Philadelphia, 1971, pp. 50–78.

Mechanical Durability Assurance in Automotive Structures

REFERENCE: Landgraf, R. W., "Mechanical Durability Assurance in Automotive Structures," *Fracture Mechanics: Nineteenth Symposium, ASTM STP 969*, T. A. Cruse, Ed., American Society for Testing and Materials, Philadelphia, 1988, pp. 220–234.

ABSTRACT: Approaches for assuring the mechanical durability of ground vehicle structures are reviewed in the context of continuing developments in computer-aided engineering tools. Examples involving service data acquisition, vehicle loads analysis, component stress analysis, damage analysis, and fatigue life prediction are presented to illustrate the impact of new technologies on vehicle design. Finally, some current problem areas and prospects for the development and implementation of improved design strategies are discussed.

KEY WORDS: materials, fatigue, life prediction, structural durability, data acquisition, computer simulation, material properties, fracture mechanics

The revolutionary changes occurring in the automotive industry are a matter of record. The rapid shift towards lighter, more efficient, and durable structures has created major challenges for design engineers. Examples include the substitution of a wide variety of stronger and lighter materials throughout vehicles, the use of new structural design concepts resulting in more optimized designs, and an ever-accelerating product cycle time. These pressures have resulted in a major trend to reliance on a broad array of computer-based design tools that allow engineers to quickly consider a wider range of design and performance criteria and alternatives than was previously possible. These include (a) computer-aided drafting (CAD), (b) full-scale structural modeling for vehicle dynamics and durability studies, (c) finite-element analysis of components and subsystems, (d) extensive computer data banks for material properties and service usage information, (e) sophisticated laboratory simulation systems for structural evaluation and development, and (f) new life-prediction routines for assessing product durability at various stages throughout the design cycle [1].

Considerable progress has been made in applying these new design tools to the special problems of the ground vehicle industry. Designers increasingly rely on structural modeling early in the design sequence to perform sensitivity analyses leading to structural optimization and to consider material and processing trade-offs leading to optimized manufacturing strategies. These exercises are often based on fatigue life calculations in which damage is assessed for particularly severe service usage profiles as a means of evaluating probable structural integrity. While the ultimate test of any product remains the successful completion of a carefully planned full-vehicle durability test on a proving ground, increased effort is being put into laboratory simulations of structural performance to identify potential problem areas quickly and correct them before getting to the costly and time-consuming proving ground tests.

¹ Research staff member, Ford Motor Co., Dearborn, MI 48121.

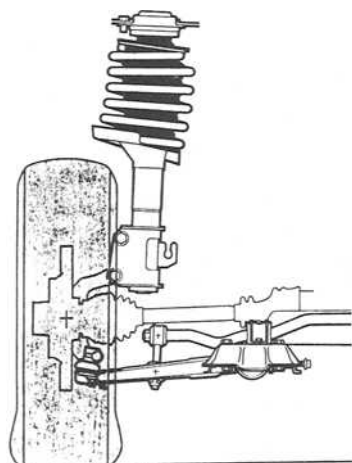
It is the plan of this paper to (a) develop a perspective of mechanical durability assurance strategies used in ground vehicle design, (b) assess the status and impact of the implementation of new methodology, and (c) identify key problem areas and future prospects for the development of improved strategies. This paper covers an appraisal of the special problems and constraints that dictate a rather different approach to design than that employed in other industries; an analysis of, and experience with, the trend toward greater use of analytical design studies in product development; and suggestions for assuring speedier implementation of developing technology in the industrial sector.

Durability Design

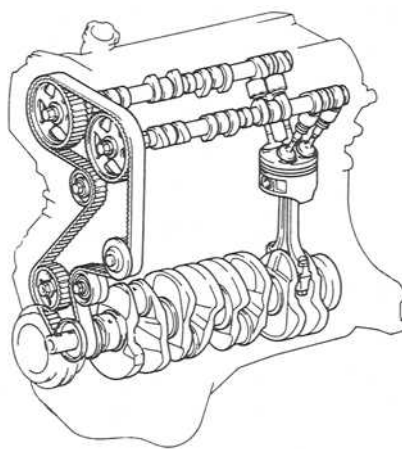
In Fig. 1, the key fatigue critical components of two major automotive systems, a front suspension and an engine, are shown. Suspension components entail a wide range of materials and processes including formed and welded sheet metal, high-performance forgings and castings, and heat-treated and surface-processed steels. Further, suspension systems are subjected to extremely variable service loadings under a variety of usage patterns.

Engine components likewise involve a range of cast, forged, and heat-treated members. To achieve greater power plant efficiencies, it is important to keep the weight of reciprocating components at a minimum. A great deal of activity is currently directed at substituting lighter weight, higher performance materials, such as aluminum and titanium alloys, ceramics, and metal-matrix composites—utilizing advanced processing technologies—for more traditional engine materials.

The automotive engineer, because of the nature and use of the product, faces some unique challenges. First, automobiles are a high-volume item and must be amenable to mass production techniques and manufacturing feasibility and cost are major considerations. The nature of the structure tends to be nonredundant, single-load path configurations of relatively thin sections. The industry does not enjoy the advantage of periodic inspections as does the aerospace industry. Finally, automobiles are subjected to an extremely wide variation in



Suspension



Engine

FIG. 1—Examples of fatigue critical components in automotive systems.

usage patterns brought about by driver-to-driver variation and differences in driving conditions between regions and countries. This latter issue takes on increased significance in light of the emerging “world car” concept.

All of these issues require the designer to take a somewhat different view of mechanical durability. Emphasis is primarily on crack initiation and early growth. Classical fracture mechanics analyses have yet to find wide application for the thin (plane stress) sections and lower strength materials normally used; they have been applied, however, to cast materials and welded joints. Further, probabilistic design strategies must be employed with a view towards anticipating the “worst scenario” service case as a design objective.

As indicated in Fig. 2, a number of activities and specialties are involved in assuring the mechanical durability of a vehicle. These involve the application of both experimental and analytical techniques that rely heavily on computers as tools for accomplishing specific tasks and as communication links between related activities. Early in the design process road-load information is developed either from previous vehicles or by using surrogate vehicles run on specific durability routes. Full vehicle computer models are then employed to determine load paths through the structure and, hence, the design loads for subsystems and

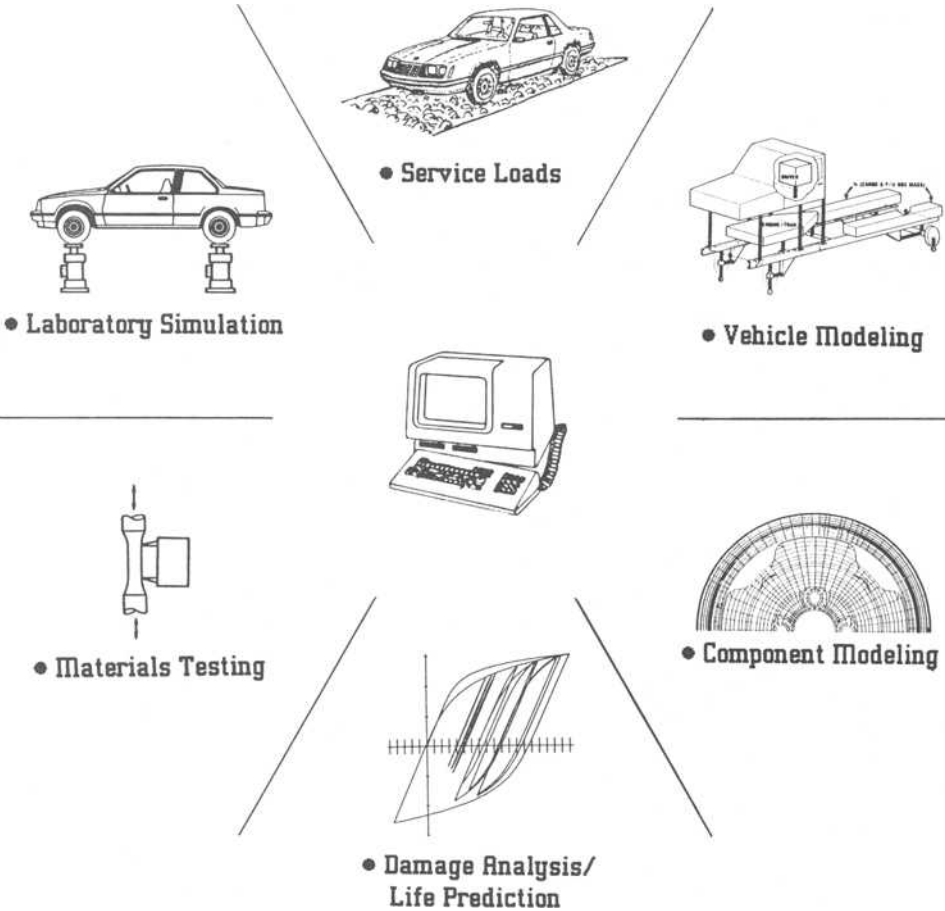


FIG. 2—Durability assurance technologies and activities.

individual components [2]. Laboratory road-load simulation systems are also finding increasing use in full vehicle analysis [3]. Finite-element modeling then provides indications of highly stressed areas in a component and establishes relations between applied loads and local stresses—a “component calibration.” At this point fatigue calculations can be made, using material property data and historical service usage profiles, to obtain early indications of probable structural integrity.

The accuracy, and hence utility, of any fatigue analysis is highly dependent on the nature and quality of input information. Thus the acquisition and manipulation of the appropriate loads, stress analysis, and material property data into suitable formats is crucial to successful fatigue analysis. Fortunately, a variety of new tools and techniques are becoming available to assist in this important task. The next section provides an overview of current trends in generating the input information for durability studies.

Durability Analysis—Input Information

Service Data Acquisition and Analysis

Road-load data, acquired under a variety of service usage conditions, provide a major input in establishing durability design and performance objectives. Figure 3 provides an overview of field-data gathering. Traditionally, service history data has been recorded on FM tape for post-processing on a central computer facility. Alternatives to this approach are provided by two recently developed devices shown at the center and bottom of the figure. The center device is a microprocessor-based digital recorder that can operate unattended on a vehicle for periods of several weeks [4]. A series of plug-in modules allows data to be summarized in various ways. At the bottom of the figure is a 16-channel data acquisition device that, in reality, is a portable computer capable of making life estimates in the field [5].

Both of these devices offer considerable data analysis flexibility. Shown on the right of Fig. 3 are examples of some available outputs including digitized peak-valley sequences and history summarizations based either on level crossing or rainflow cycle counting algorithms. The expanded use of this new generation of recorder promises to provide a greatly improved documentation of vehicle usage profiles.

Vehicle Analysis

A prime purpose for gathering road-load information is to develop the load paths and levels through critical parts of the structure so that individual components can be properly sized. Some of the complexities associated with such analyses are indicated in Fig. 4 where the three-force vectors, measured by a wheel-force transducer as the vehicle negotiates a rectangular chuckhole, are displayed on a time base. It is immediately apparent that the peak forces in each direction occur at different times, thus necessitating a detailed time increment analysis to determine the forces acting at other points in the structure, for example, the ball joints.

Computer models are becoming available to handle these rather complex structural dynamics calculations. Shown in Fig. 5 is a simplified version of a vehicle model that, when “driven” over a road profile at specified speeds, determines the load levels at critical points throughout the structure [6]. As an example, the torque levels on the front stabilizer bar during a portion of a durability circuit are shown at the bottom of the figure. Note the excellent agreement between the predictions and subsequent measurements.

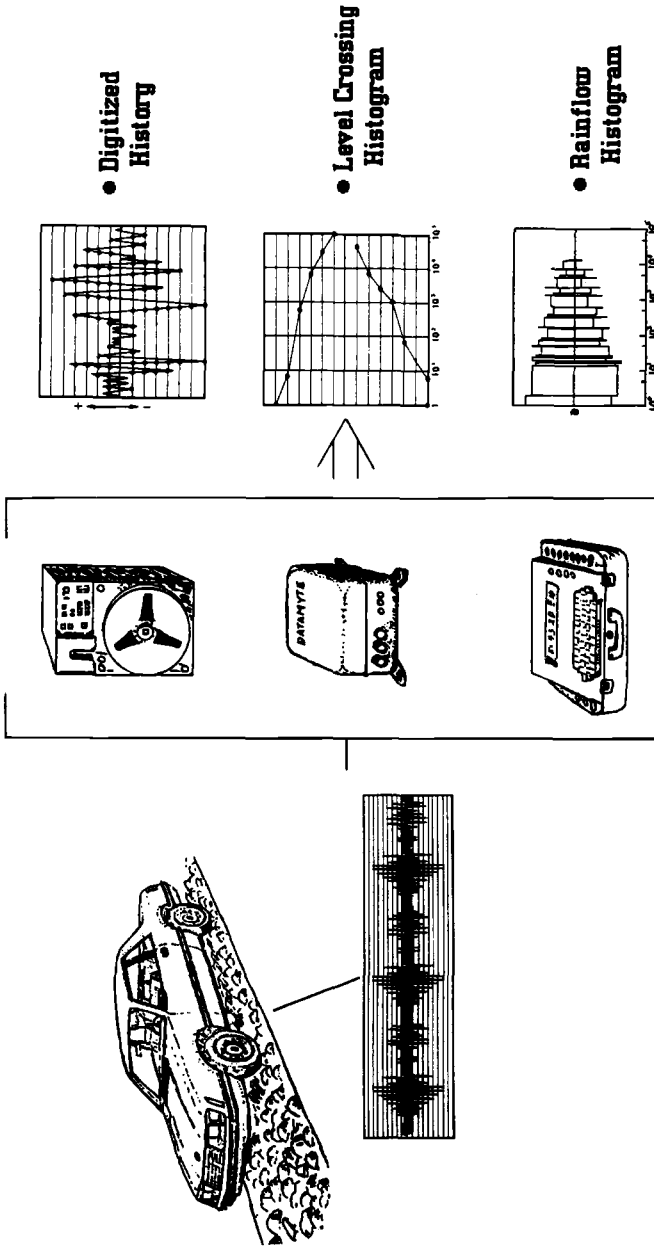


FIG. 3—Techniques for acquiring and analyzing service history data.

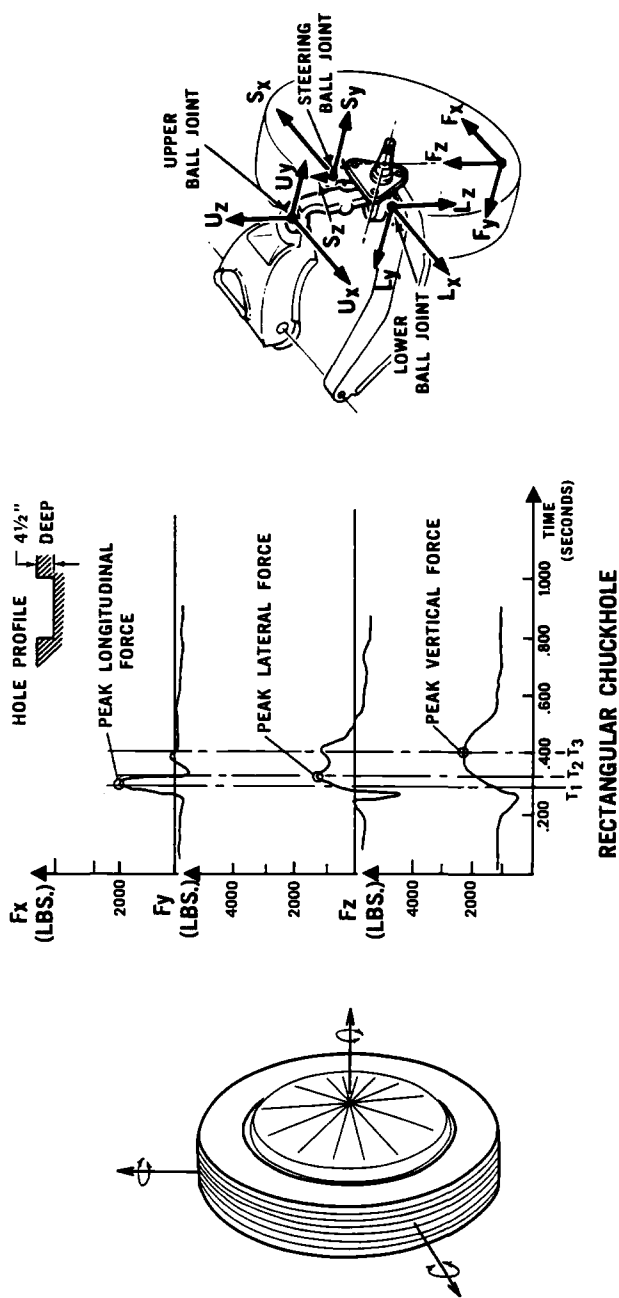


FIG. 4—Example of wheel-force transducer measurements.

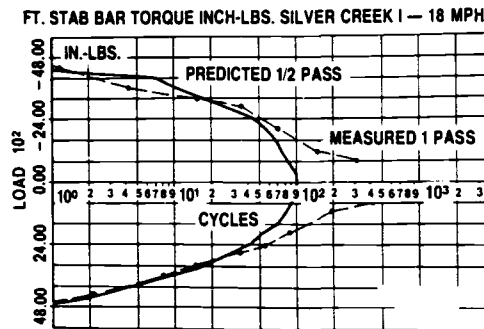
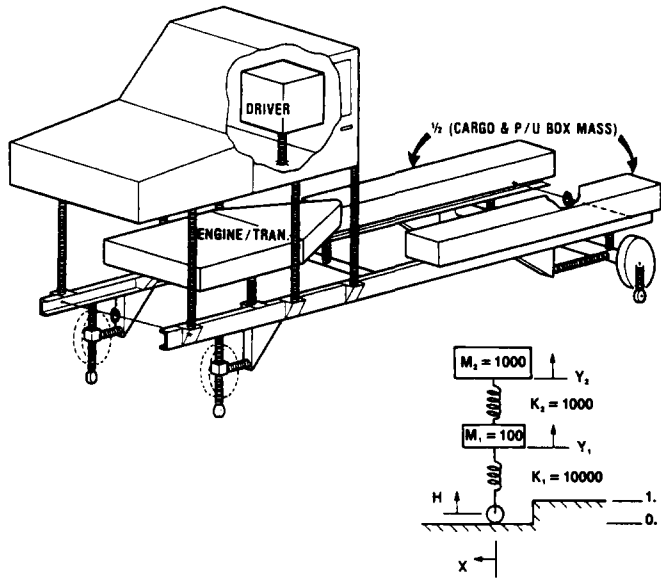


FIG. 5—Full-vehicle dynamics model for obtaining service loads [6].

Component Analysis

Once the loads experienced by individual components have been determined, stress (strain) analysis techniques are employed to identify potential failure sites and to provide inputs to damage-analysis routines. Finite-element modeling, as shown for an automotive wheel assembly in Fig. 6, is a particularly powerful technique for early design studies. Three high-stress areas, with the associated stress excursions during one wheel revolution, are indicated in the figure. Component sizing and material selection exercises can be carried out using this information. When prototype hardware becomes available, such studies assist strain gage placement for experimental verification of component performance.

Material Properties

Materials information plays a key role in any durability analysis and has evolved over the past century from simple life diagrams, defining safe ranges of operating stress, to detailed

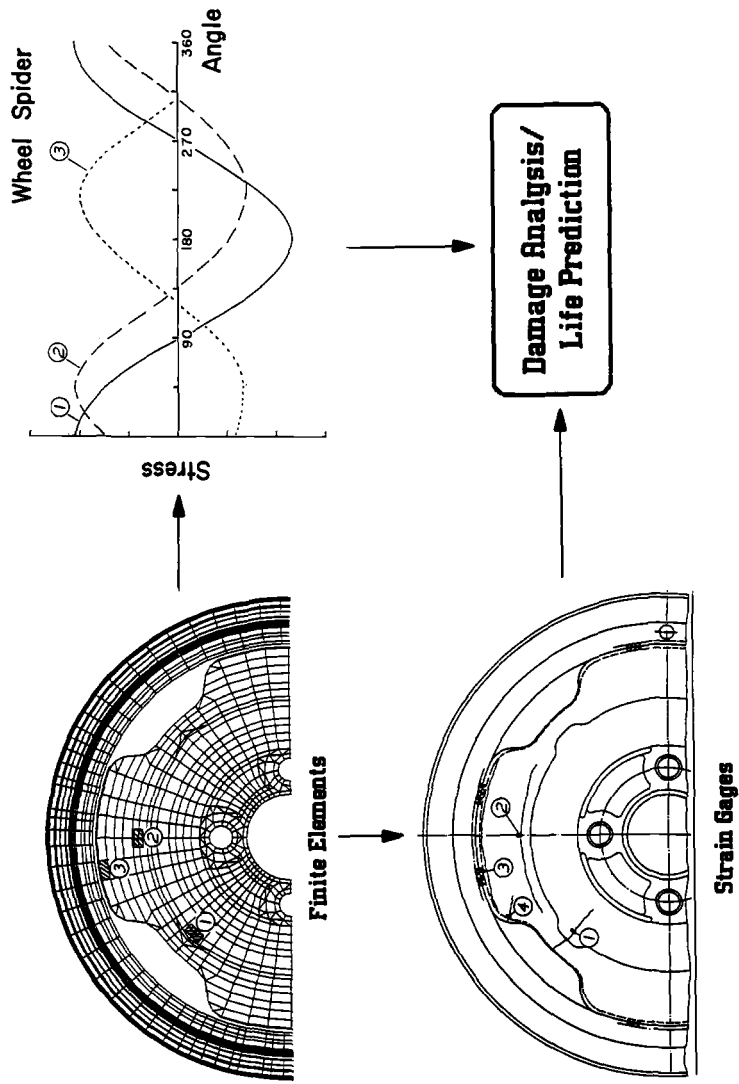


FIG. 6—Component analysis using finite elements and strain gages.

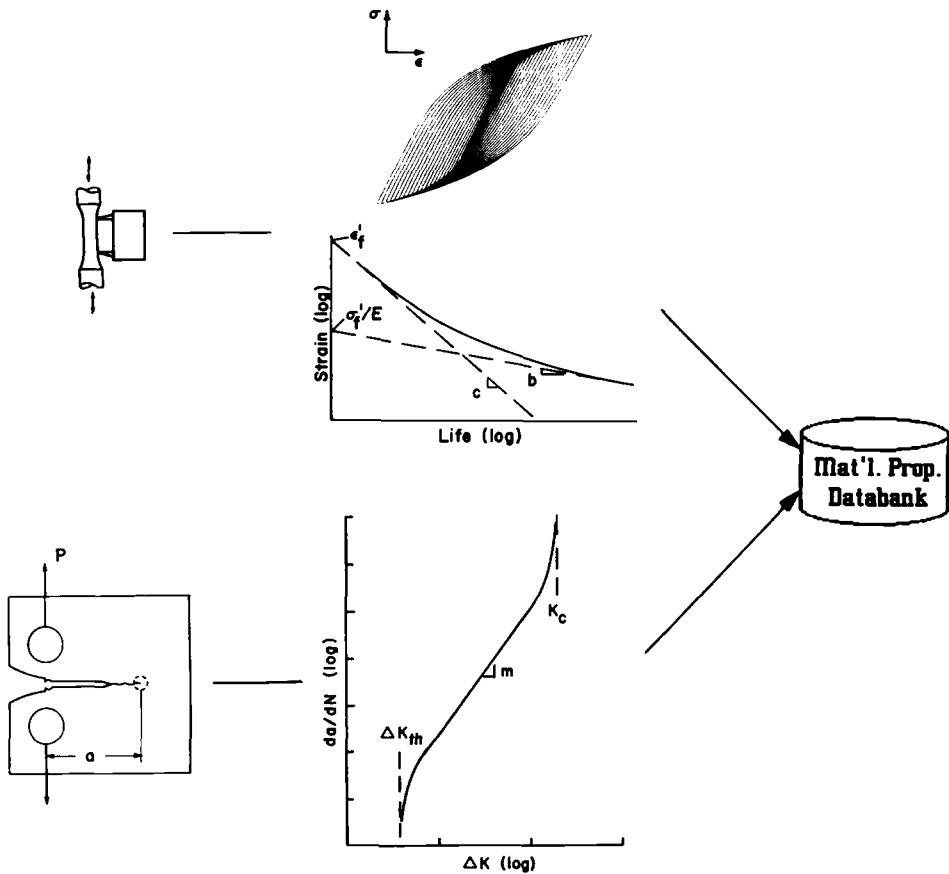


FIG. 7—Materials information for use in fatigue analysis.

portrayals of a material's resistance to fatigue crack initiation and propagation, as well as complete cyclic constitutive relations for use in structural analysis. As indicated in Fig. 7, modern materials characterization methods include strain cycling of smooth specimens to obtain cyclic deformation curves and life curves for damage analysis, and cycling of pre-cracked specimens to obtain crack growth rates as a function of stress-intensity range. Standard procedures for generating these data are contained in the ASTM Recommended Practice for Constant Amplitude Low-Cycle Fatigue Testing (E 606-80) and ASTM Test for Constant-Load-Amplitude Fatigue Crack Growth Rates Above 10^{-8} m/Cycle (E 647-86).

The lack of availability of materials data and properties in readily accessible data bases remains a serious problem and continues to restrict the widespread use of the newer life prediction methodologies. This area is currently receiving attention, and efforts are under way to develop large, central repositories of material property information [7,8].

Damage Analysis and Life Prediction

Armed with the necessary input information outlined in the previous section, a designer can perform a fatigue analysis using available life prediction methodologies. The flow chart in Fig. 8 indicates the major steps in a typical analysis. Using component load and stress

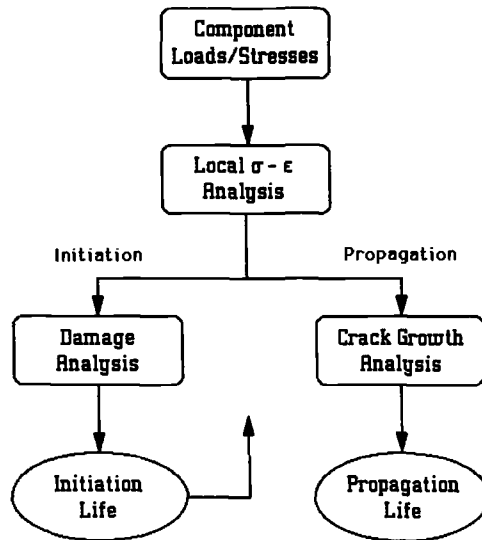


FIG. 8—Steps in performing a fatigue analysis.

information, a local stress-strain analysis is performed at potential failure locations, damage is determined for each event in a history, and an initiation life is projected. For propagation life, the local stress-strain analysis is used to determine stress-intensity factors for subsequent crack-growth analysis.

Some of the features of a general purpose fatigue analysis program, developed for ground vehicle applications, are shown in Fig. 9 [9]. Using a set of interactive modules, a designer can set up a problem by defining the component geometry, material, and loading history. The material properties and service histories are available from on-line data banks. The program then performs a local stress-strain analysis and a damage analysis using strain cycling

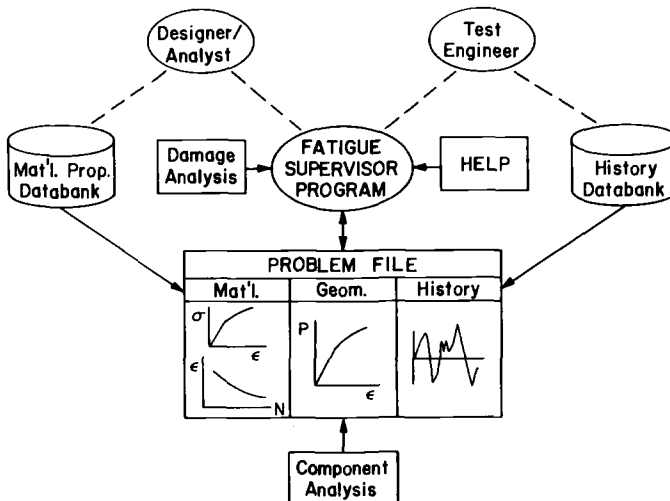


FIG. 9—Features of a general purpose fatigue analysis program.

fatigue data to provide an indication of when a crack is likely to form at a critical location. A crack-growth analysis routine is also available.

A more detailed portrayal of the damage analysis of a notched member is given in Fig. 10 [10]. The local stress-strain response at the notch root is first determined. Individual events in a history are then identified, based on the occurrence of closed hysteresis loops for which a strain range and a maximum stress can be determined. A parameter based on these values is then used in conjunction with the appropriate material life curve to determine damage, which is summed linearly to obtain an initiation life prediction. Crack-growth predictions are based on stress-intensity factors, determined from the local stress-strain analysis, used in conjunction with material crack growth curves.

A variety of tabular and graphical outputs are available to assist the designer in interpreting the results of a particular analysis. Examples of some of the graphical outputs are shown in Fig. 11. To the right of the figure is the local stress-strain response of this component as it undergoes the service history portrayed in the range-mean-occurrence plot in the lower left. Above this history is a plot indicating the percent of total damage associated with each strain level.

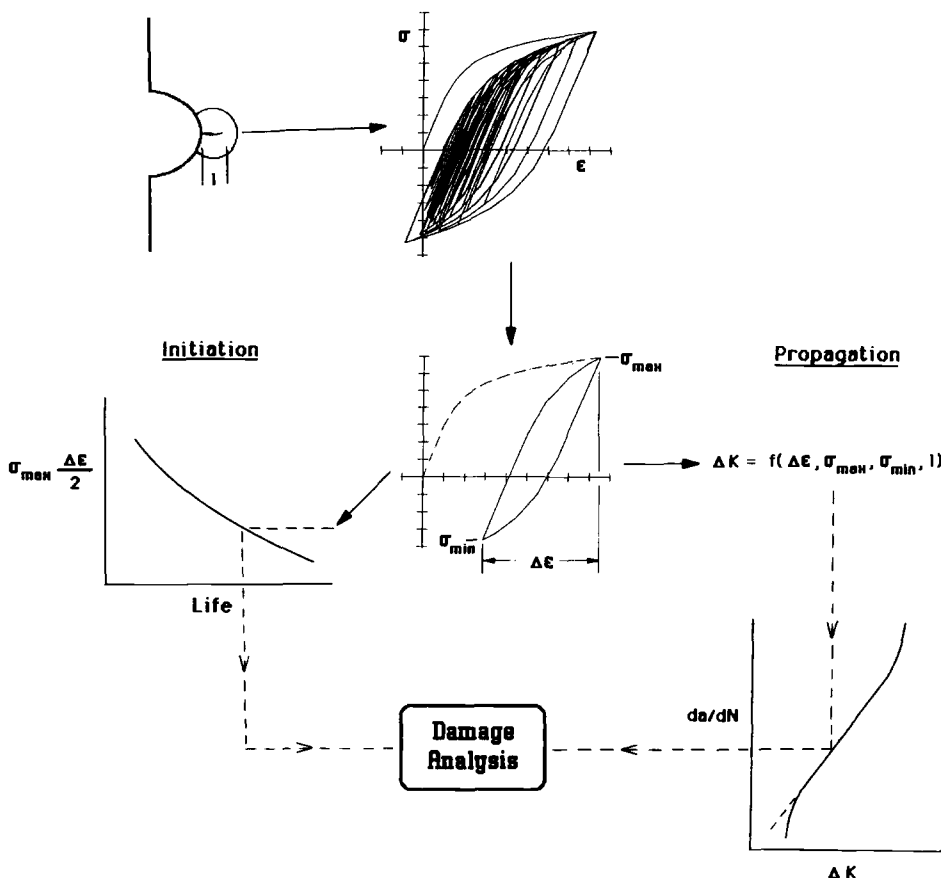


FIG. 10—Details of local stress-strain and damage analysis.

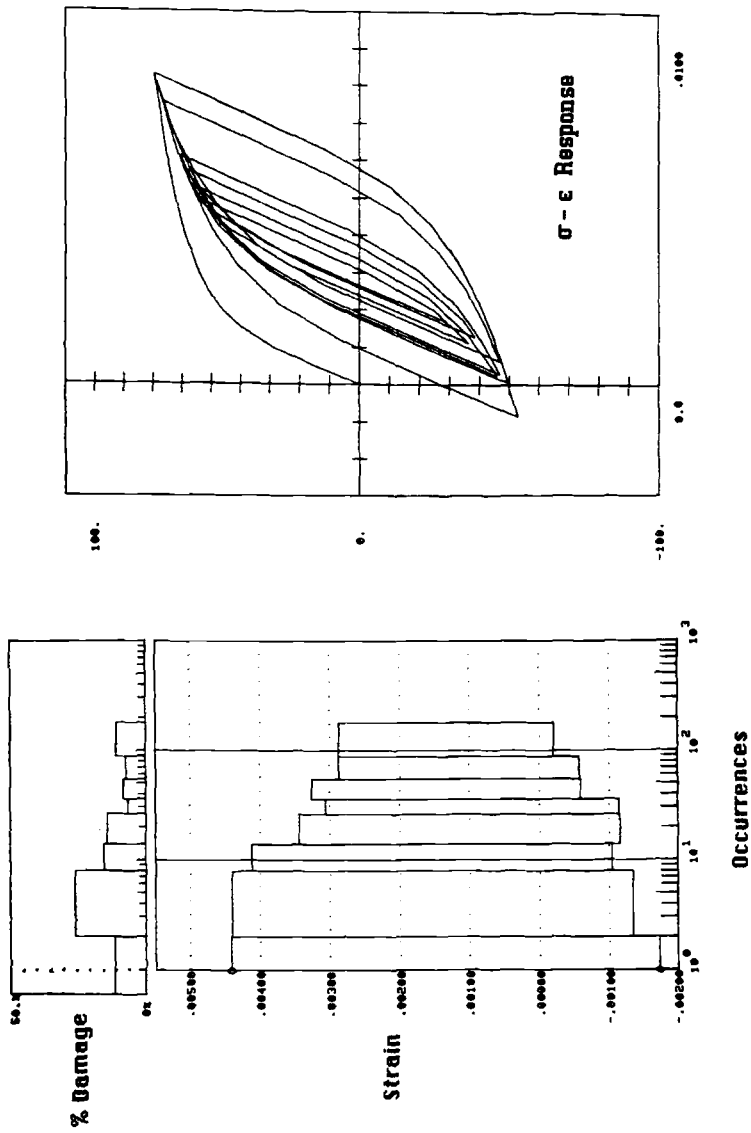


FIG. 11—Graphical outputs from a fatigue analysis.

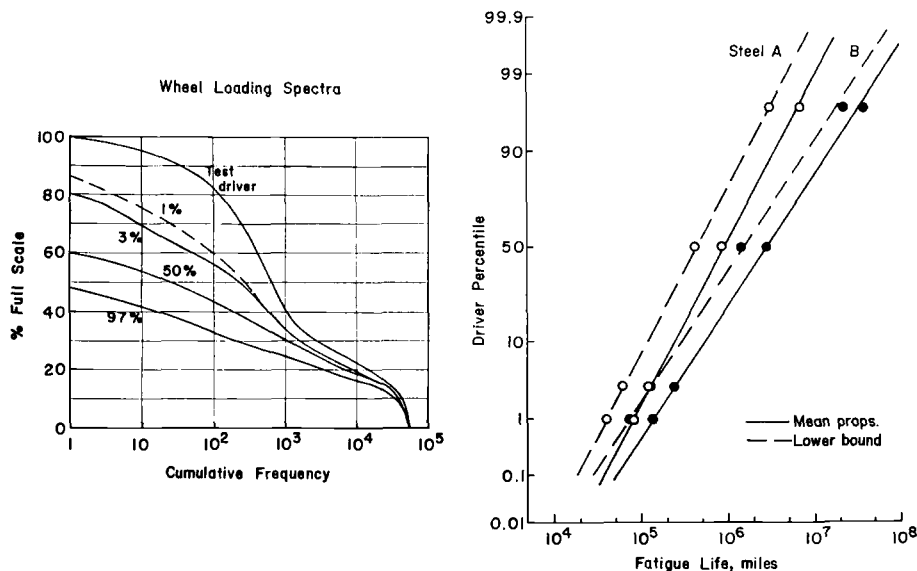


FIG. 12—Results of the fatigue analysis of a wheel assembly [9].

Calculations of this type are useful, in conjunction with finite-element results, early in the design evolution of a component as well as at later stages when service data from instrumented prototype hardware is available. Such fatigue analysis routines have been successfully employed in a number of product development programs and are finding increased application in new vehicle programs with a view to accelerating the development cycle by minimizing the number of prototype builds. Some typical durability analysis applications include:

- (a) initial component sizing,
- (b) design optimization/trade-offs,
- (c) material/process selection,
- (d) durability route/customer correlation,
- (e) laboratory simulation testing, and
- (f) problem solving/performance upgrade.

A final example of component fatigue analysis, using an automotive wheel assembly, is shown in Fig. 12 [9]. Here usage spectra obtained with a cross section of customers are displayed as bending-moment/frequency-of-occurrence distributions for various percentile drivers. Wheel bending moments have here been normalized to the levels obtained by a professional driver (100%). These usage profiles were combined with finite-element results relating applied moment to local wheel stresses to obtain life estimates for different percentile drivers. Results of this analysis, plotted on probability scales on the right, provide indications of the expected service performance of this component. Two steels are compared using both the mean and lower bound properties. Such calculations provide a convenient way to incorporate both material and usage variability in design analysis.

Future Trends and Needs

It is clear that the continuing development of a wide variety of computer-based design, analysis, and testing aids is having a major impact on automotive product development. A

major emerging trend for the next decade is the integration of these separate computer tools into powerful engineering work-station environments in which a designer, or design team, will have ready access to the complete spectrum of analysis capabilities.

In applying these technologies, a great deal of coordination and interaction is required between the various activities and specialties involved in durability assurance to achieve maximum benefits. The finite element analyst, for example, requires reliable material and load information to perform a component stress analysis. Damage analysis routines require material, structural analysis, and service loads information as inputs. And the development of realistic laboratory simulation tests requires detailed portrayals of service history experience.

The problem, then, reduces largely to one of information management. While this is certainly not a trivial task, modern computers provide all the capabilities necessary for insuring that appropriate information is available at each stage of product design. It is particularly important that logical frameworks for this task be established now since continuing technical developments and a rapidly expanding information base will only complicate matters later.

With the integration of engineering design aids into computer networks, the development of more systematic design philosophies can be anticipated. For example, decision path guidelines, to assist engineers in choosing and applying appropriate tools at particular points in design evolution, are becoming available. In this regard, the computer also becomes a natural repository for all information and experience attained in a design exercise. This provides a growing technical data base that should aid greatly in refining and optimizing future designs in a minimum of time.

The most pressing need now is for the packaging of currently available technology in the form of easily used computer routines that can be included in large libraries of design aids—that is, getting into the designer's hands what we already know. The Fatigue Supervisor Program, outlined in Fig. 9, is a first attempt to provide ground vehicle engineers with the latest developments in material and structural fatigue methodology in an interactive, self-instructive package. Results to date have been encouraging: a number of engineering groups are using the routines for problem solving with little or no assistance.

It has further become evident that such a program, in addition to analysis capabilities, provides unique educational opportunities; it can serve as an effective teaching tool for engineers, or students, with limited experience in fatigue analysis. By having to carefully define the various problem solution components, the user gains an appreciation for the nature of fatigue calculations. Further, the variety of graphical outputs available provides useful portrayals of the physical realities of a particular problem and also serves to alert the engineer to the sensitivity of fatigue calculations to relatively minor variations in input data. These features help to insure against the indiscriminate use of such a tool as a "black box" device.

In the longer term, a number of further developments and refinements leading to improved predictive capabilities can be envisioned. Examples include:

- (a) improved crack growth models incorporating plasticity and spectrum loading effects,
- (b) extensive crack growth data bases for automotive materials,
- (c) libraries of stress-intensity solutions for use with finite-element analyses,
- (d) improved methods for handling the multiaxial stress-strain fields commonly encountered in structures,
- (e) development of damage and failure criteria for advanced materials such as ceramics and composite systems, and
- (f) improved methods for predicting the durability of welds and adhesively bonded joints.

As this technology becomes available, it can easily be incorporated within current computer routines, thus greatly extending analysis capabilities.

References

- [1] Landgraf, R. W. and Conle, A., "Trends in Assuring the Mechanical Durability of Automotive Structures," *Proceedings*, 20th Fisita Congress, P-143, Society of Automotive Engineers, Warrendale, PA, 1984, pp. 4.124-4.130.
- [2] Bickerstaff, D. J., Birchmeier, J. E., and Tighe, W. R., "Overview of Design Approaches for Optimizing Fatigue Performance of Suspension Systems," *Proceedings*, SAE Fatigue Conference, P-109, Society of Automotive Engineers, Warrendale, PA, 1982, pp. 1-10.
- [3] White, K. J., "The Road Simulator—A Practical Laboratory Approach," *Prediction and Simulation of In-Service Conditions*, IMechE Conference Publication 1985-5, Institute of Mechanical Engineers, London, 1985, pp. 69-80.
- [4] Socie, D. F., Shifflet, G., and Berns, H., *International Journal of Fatigue*, Vol. 1, No. 2, April 1979, pp. 103-111.
- [5] Schaefer, R. A., *Transactions of the Society of Automotive Engineers*, Vol. 91, Section 3, 1983, pp. 2761-2771.
- [6] Birchmeier, J. E., "Computer Simulation of Nonlinear Vehicle Response to Generalized Road Inputs at Ford Light Truck," *Proceedings*, Fifth International Conference on Vehicular Structural Mechanics, P-144, Society of Automotive Engineers, Warrendale, PA, 1984, pp. 161-176.
- [7] Kaufman, J. G., *Standardization News*, Vol. 14, No. 2, 1986, pp. 28-33.
- [8] Landgraf, R. W. and Conle, F. A., "Material Property Data: A Ground Vehicle Perspective," *Materials Properties Data—Applications and Access*, MPD-Vol. 1/PVP-Vol. 111 (Book No. G00345), American Society of Mechanical Engineers, New York, 1986.
- [9] Conle, A. and Landgraf, R. W., "A Fatigue Analysis Program for Ground Vehicle Components," *Proceedings*, SEECO '83 International Conference on Digital Techniques in Fatigue, Society of Environmental Engineers, London, 1983, pp. 1-28.
- [10] Conle, A., Oxland, T. R., and Topper, T. H., "Computer-Based Prediction of Cyclic Deformation and Fatigue Behavior," *Low-Cycle Fatigue—Directions for the Future*, ASTM STP 942, American Society for Testing and Materials, Philadelphia, 1987.

Louis F. Coffin¹

Role of Damage Tolerance and Fatigue Crack Growth in the Power Generation Industry

REFERENCE: Coffin, L. F., "Role of Damage Tolerance and Fatigue Crack Growth in the Power Generation Industry," *Fracture Mechanics: Nineteenth Symposium, ASTM STP 969*, T. A. Cruse, Ed., American Society for Testing and Materials, Philadelphia, 1988, pp. 235–259.

ABSTRACT: The problem of intergranular stress-corrosion cracking (IGSCC) in boiling water reactor (BWR) piping is discussed and the body of work undertaken in the author's laboratory to solve that problem is described. Particular attention is given to the development of electrical potential crack monitoring techniques and their application to surface crack growth, particularly under conditions approaching those found in service. The important role of water chemistry and its control is described in this context.

The concept and description of sensors to monitor *in situ* the degree of damage containment from intergranular stress-corrosion cracking is then described, with reference to use in piping components and other types of monitoring.

Finally, a concept for the life management of structures is described where damage processes are identified and monitored *in situ* using appropriate sensors to measure the damage rate continuously. In conjunction with damage monitoring, an applicable life prediction model is used to forecast the future damage state and to assist in the decision process for appropriate required actions to optimize plant operation.

KEY WORDS: fatigue, fatigue crack growth, life prediction, fracture mechanics

Requirements for the performance of structural materials in the power generation industry are very broad. They must include consideration of (a) very large components, such as steam turbine and generator rotors and turbine shells; (b) high temperatures, such as those encountered in first-stage gas turbine buckets; (c) high stresses, such as those in generator retaining rings; (d) severe and cyclic thermal stresses due to rapid temperature variations, for example, from repeated shutdowns and start-ups in peak load of gas and steam turbine-generator equipment or the diurnal cycle in solar energy plants; (e) environmental concerns, such as those introduced by neutron irradiation or oxygen-containing high-temperature water, or both, in nuclear power plants or hot combustion product environments in gas turbines; and (f) many other design or material demands.

The design conditions are further defined by long life since most power generation systems require sizeable capital investment and lifetimes of up to 40 years are needed for reasonable investment costs. Reliability is important since unplanned outages can be extremely costly. For example, a large (1200-MW) nuclear plant is estimated to generate some 1×10^6 dollars worth of power per day and repairs or replacement should be scheduled to coincide with

¹ Research staff member, Corporate Research and Development, General Electric Co., Schenectady, NY 12301, currently retired.

refueling or other planned outages. The cost of forced plant outages due to corrosion-induced service failures in the United States is currently estimated as over one billion dollars per year [1]. An additional factor in the case of nuclear power plants is the close scrutiny by the Nuclear Regulatory Commission for safety-related concerns in the original design and service performance. Hence, concepts in the design and materials selection process, as well as in operation, which can result in both improved reliability and life prediction methodology are extremely important.

There would appear to be a natural affinity between the power generation field and the discipline of fracture mechanics, as evidenced by the large expenditure of research and development funds from this segment of industry, public utilities, and government in fracture mechanics related work. In particular, the role of the Electric Power Research Institute in supporting research in many areas of fracture mechanics, including the present study, is noted.

Many topics in the area of damage tolerance and fatigue crack growth could be addressed which bear on the power generation industry. To bring the subject into reasonable focus for a presentation such as this, the author will cover some selected subjects with which he has been closely associated and which could be reasonably construed to be representative of the subject being addressed here. These include:

- (a) description of a technique for service-simulated surface crack growth monitoring in specimens and components,
- (b) application to the behavior of nuclear structural materials in service-simulated and alternate water chemistry environments,
- (c) application to service-simulated components, and
- (d) application to damage monitors and life assessment in power generation systems.

Description of a Problem

During the mid-1970s and continuing to the present, there have been numerous examples of stress-corrosion cracking in nuclear power plant piping. While these have occurred predominantly in boiling water reactor (BWR) piping [2,3], cracking has also occurred in carbon steel piping in pressurized water reactor (PWR) systems.

In the case of intergranular stress-corrosion cracking (IGSCC) in BWR piping, the location of the cracks in the piping was always the same. They developed in welded Type 304 stainless steel in the heat-affected zone and were always intergranular (Fig. 1). Their cause has been the subject of intensive research. Today the phenomenon and its solution are well understood. Basically the cracking occurs because of a combination of three factors: weld sensitization of the stainless steel, high local stress caused by a combination of weld residual stress and loading, and exposure to coolant water containing sufficient dissolved oxygen. Sensitization is a metallurgical phenomenon involving a selective reduction of the available soluble chromium content in the grain boundary regions of the stainless steel as a result of the formation and precipitation of chromium carbide. Normally, stainless steel is used in the solution-treated state [rapid cooling from 1100°C (2012°F)] in which carbon is retained in solution. Further, the grain boundary chromium content is maintained so as to provide protection against selective oxidation. High temperature is necessary to cause the sensitization reaction; this reaction can come about in welding, in furnace heating, or wherever temperatures of 550 to 800°C (1022 to 1472°F) are reached [4].

In addition to sensitization, tensile stress and oxygenated water are necessary ingredients to cause IGSCC. The tensile stress must be sufficient to provide creep deformation either

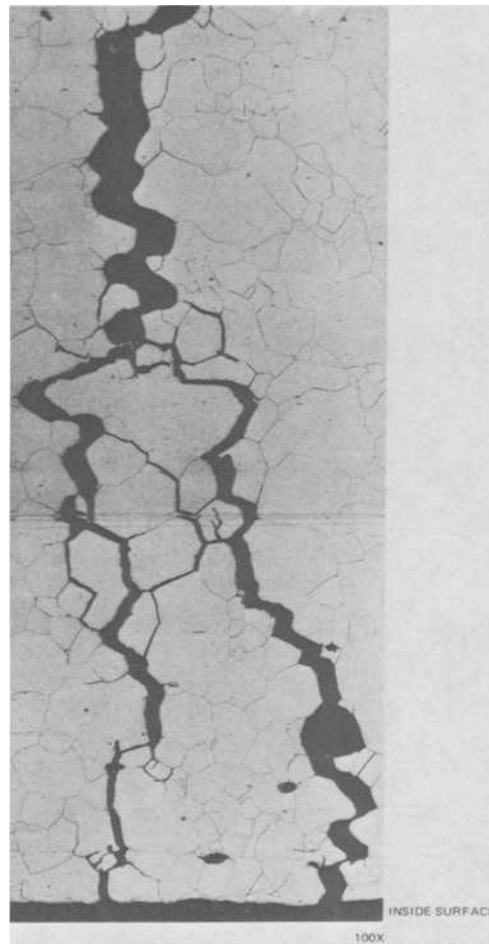
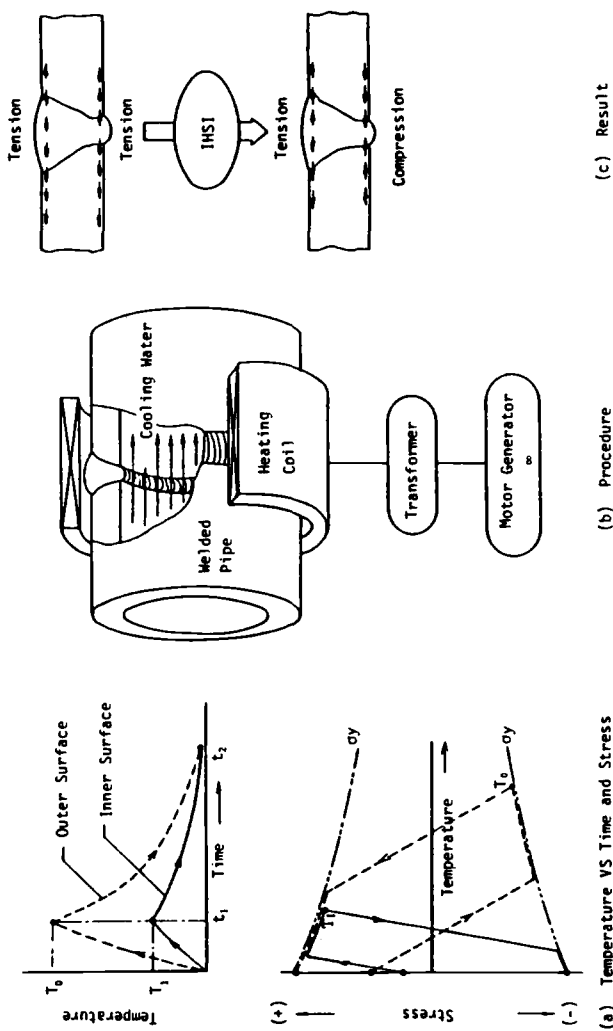


FIG. 1—*Metallographic section of a cracked pipe in the heat-affected zone—Dresden Two Loop [3].*

in bulk or locally, as at the crack tip, to cause continued rupture of passivated surface films. Piping applied stresses, together with weld residual stresses, provide the source of stress. The oxygen level in the water must be sufficient to cause oxidation of the chromium-depleted iron at the grain boundary, weakening the boundary and causing intergranular cracking. Oxygenated water is inherent in operating BWRs. These three ingredients are present in almost every BWR plant with welded Type 304 stainless steel pipe in service today.

The problem was identified early as a non-safety issue [3]. The identified cracking process can be categorized as one of subcritical crack growth, and the bulk material remains undamaged. Type 304 stainless steel is a tough ductile material whose fracture toughness is maintained in the uncracked remaining elements. Thus, the process of leak-before-break can exist so that no sudden fracture will occur. Rather, leakage of a pipe develops and gives adequate warning for an orderly control of the problems during plant operation.



(a) Temperature VS Time and Stress (b) Procedure (c) Result (d) Result
FIG. 2—Schematic of induction heating stress improvement method [5].

Remedies for IGSCC

Remedies for the IGSCC problem have evolved from the very first plant occurrence of the weld cracking. The list is now very large. Essentially, they break down into three distinct categories:

- (a) residual stress improvement,
- (b) alternate materials, and
- (c) hydrogen water chemistry.

The intent of the residual stress approach is to introduce a compressive axial and circumferential residual stress on the inside diameter (ID) surface of the pipe so as to prevent initiation and growth of intergranular cracks. Several procedures have been introduced, including induction heating stress improvement (IHSI), heat sink welding (HSW), last-pass heat sink welding (LPHSW), and weld overlay. In IHSI, the pipe is induction heated from the outside in the weld region, while cold water flows through the pipe producing severe thermal stresses (Fig. 2). When the pipe cools, compressive residual stresses remain on the ID surface. HSW is similar, except that heat is applied by the welding process. In LPHSW, cooling of the ID is applied only during the last welding pass on the outside. Finally, in weld overlay, a heavy overlay of a nonsensitizable stainless steel is applied to the outside diameter (OD) in the weld region to provide residual stress protection with a sufficient thickness of nonsensitized material to provide strength to the pipe. This process differs from the others in that it is applied following detection of weld cracks.

Several materials have been proposed as substitutes for weld-sensitized 304 stainless steel to reduce the tendency towards sensitization by inhibiting formation of chromium carbide during welding. One material is a very low carbon Type 304 stainless steel, 304 L, another is Type 316 NG, a very low carbon form of Type 316 stainless steel (2% molybdenum and a nickel content in excess of that in Type 304) with high nitrogen to replace the low carbon content for strength purposes. Other alloys have also been proposed. Solution-treated Type 304 stainless steel also shows improved resistance to IGSCC.

Finally, an attack on the problem has been directed to control the dissolved oxygen level in the coolant water by the addition of small amounts of hydrogen. Normally the oxygen level in the water during plant operation runs at about 200 ppb oxygen. Additions of hydrogen of the order of 150 ppb hydrogen can lower the oxygen level sufficiently to completely arrest crack growth. This effect will be discussed in more detail later. Suffice it to say here that this fairly simple modification in plant water chemistry can have a significant effect on IGSCC throughout the plant. Its benefit is directed not only to weld-sensitized Type 304 stainless steel but also to other plant materials which have shown some environmentally accelerated cracking in BWR water.

The general topic of remedies for IGSCC has been summarized in Electric Power Research Institute (EPRI) workshop proceedings [5].

Monitoring for Stress-Corrosion Cracking in the Laboratory

Since the first evidence of cracking of sensitized 304 stainless steel in oxygenated water, the problem has been intensively studied in the laboratory using autoclaves and appropriate water chemistry. Early techniques include U-bend and clamped bars, low-cycle fatigue [6], and constant extension rate tests [7]. To evaluate IGSCC in welded pipe, General Electric's Nuclear Energy Business Operation has employed a multiple-station Pipe Test Laboratory [8] where 102-mm (4-in.) and 254-mm (10-in.) welded pipes can be axially loaded and cycled

under reactor-simulated water conditions. Here various materials, welding conditions, and remedies have been evaluated in advance of plant modifications for their anticipated improvements in life.

Only fairly recently have studies of IGSCC involved crack growth measurement techniques. Early work by Hale and associates undertook such measurements in simulated water environments using compact-type (CT) specimens with a series of capillary holes in the uncracked ligament so that as the crack grew, hole by hole, the crack depth could be measured by the pressure change as each hole was exposed [9]. More recently, use of linear voltage differential transformers (LVDT) [10–13] on CT specimen geometries have led to improved crack growth information. However, these tests are difficult to interpret directly when evaluating component behavior because of differences in geometry and stress conditions. For this reason a study of the behavior of surface cracks in otherwise uniformly stressed specimen geometries is more representative of the actual situation in service components.

Surface Crack Testing Methods

Surface cracks have their origin at the surface of a specimen or component usually at some flaw or other defect, and grow in both the thickness and width direction, in a “thumb-nail” or “fan-shaped” manner. They represent natural crack growth in service components. Hence, the growth of this form of crack in a uniaxially loaded specimen has been selected for investigation at our laboratory. Results can then be compared with those obtained from other test configurations, such as the CT specimen geometry.

In addition to the particular crack size and shape, other testing conditions have been selected to bring the investigation as close as possible to the conditions encountered in actual service of nuclear components in high-temperature water environments. These include cyclic trapezoidal loading, where the stress levels employed approach or occasionally exceed the yield strength of the material, following the design approach of the American Society of Mechanical Engineers (ASME) Boiler and Pressure Vessel Code, Section III, for secondary stresses and for low-cycle fatigue. Other matching conditions include cyclic periods, with hold times approaching those in service applications, stress gradients reflecting those found in full size pipes or pressure vessels, and temperatures and environments typical of boiling water reactors in operation.

The specimen chosen in our work is a rectangular bar having a small thumbnail defect introduced on a side face and subjected to uniaxial cyclic or static tensile loading. Appropriate loads, frequencies, and waveforms are applied. Temperature, pressure, and water chemistry are established by use of an autoclave and a water chemistry control system. In order to study crack growth, a measurement method is required which is compatible with the test conditions used, has the necessary sensitivity and accuracy, and is responsive to static as well as cyclic crack growth. Central to this investigation is the application of a crack growth monitoring technique known as the reversing d-c electrical potential method. The method, shown schematically in Fig. 3 was developed at General Electric's Corporate Research and Development Center in recent years [14–17].

Figure 4 can be used to illustrate the capability of the system to monitor surface crack growth. A defect 0.64 mm (0.025 in.) deep by 2.54 mm (0.100 in.) long was introduced at the midpoint of a specimen of SA333 Gr6 carbon steel by electrical discharge machining (EDM). Six pairs of active potential probes were attached to the specimen surface in such a way that each straddled the defect or the plane in which the crack was expected to propagate (upper left of Fig. 4). The specimen was subjected to uniaxial cyclic loading for over 10 000 cycles while enclosed in an autoclave containing 288°C (550°F) water with 0.2 ppm oxygen.

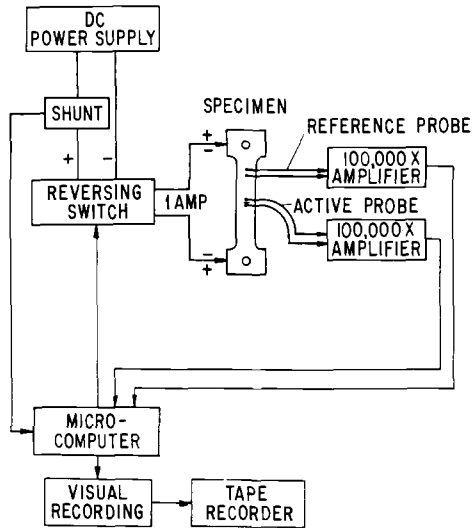


FIG. 3—Block diagram of components used for a microprocessor-controlled reversing d-c potential crack growth measurement system [17].

The output from each of the probe pairs is shown in the upper right portion of Fig. 4. Probe pairs No. 3 and 4 show a steady increase in potential from the outset of cycling. Probes No. 2 and 5 show little increase through the first 6000 cycles, but respond when the crack has propagated to a point close to a line connecting the two probes. The similarity of the response of these two probes indicates that the crack growth is nearly symmetrical. Probes No. 1 and 6 showed only a minimal response to growth of the crack since they were still beyond the extent of the crack at the termination of the test. Data from the six probe pairs, normalized with respect to similar readings taken from a reference probe pair located away from the crack, are used to calculate, cycle by cycle, the dimensions of the ellipse, which describes the shape of the crack at all points during the test [15,17]. These results are plotted in the lower portion of Fig. 4. In this plot the upper and lower curves are the calculated length and depth of the crack, respectively. The intermediate, dotted curve is the square root of the area of the cracked surface. It will be noted that the aspect ratio, defined as the crack depth divided by the width, changed from 0.25 at the outset of growth to 0.49 at the termination of cycling. The fractured surface of this specimen is shown in Fig. 5. The calculated "best fitting ellipse" is shown in white. The excellence of the fit is obvious. It is also clear from this photo that the shape of the crack changed during growth. Testing of a large number of specimens of different sizes but similar cross-sectional shapes has shown that semicircular defects tend to retain their shape as they grow, and shallower defects approach a semicircular shape as they increase in size.

While a complete description of crack growth requires readings from several probe pairs and off-line calculation of the crack dimensions, crack depth can be approximated by noting the potential change at one probe position and assuming that the crack does not change shape during growth. As earlier indicated, this is a very good approximation when the starting defect is semicircular. Hence, in evaluating the effect of various parameters such as water chemistry, temperature, R value, and cycle frequency, all growth rate measurements were based on readings from the probe pair that straddled a semicircular defect at its midlength. Data are obtained from all active probe pairs, but only the data from the central

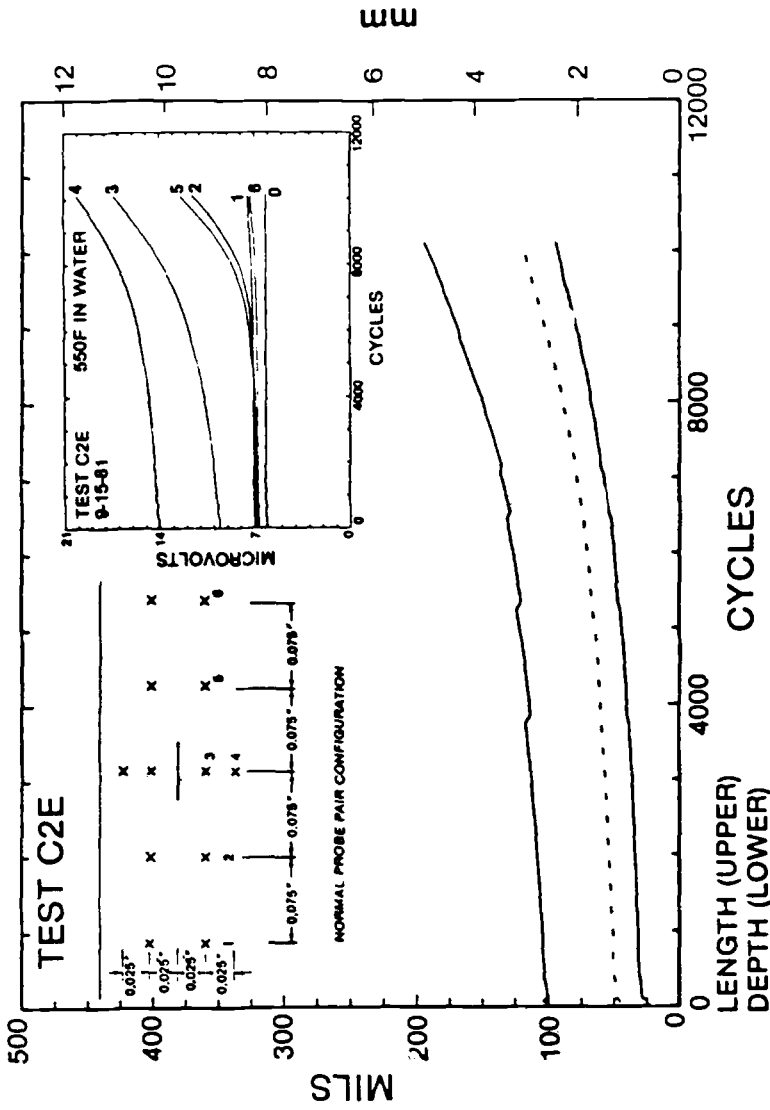


FIG. 4—Probe positions, potential readings, and calculated crack dimensions attained in testing of surface-defected Specimen C2E [17]. The dashed line is the square root of the area.

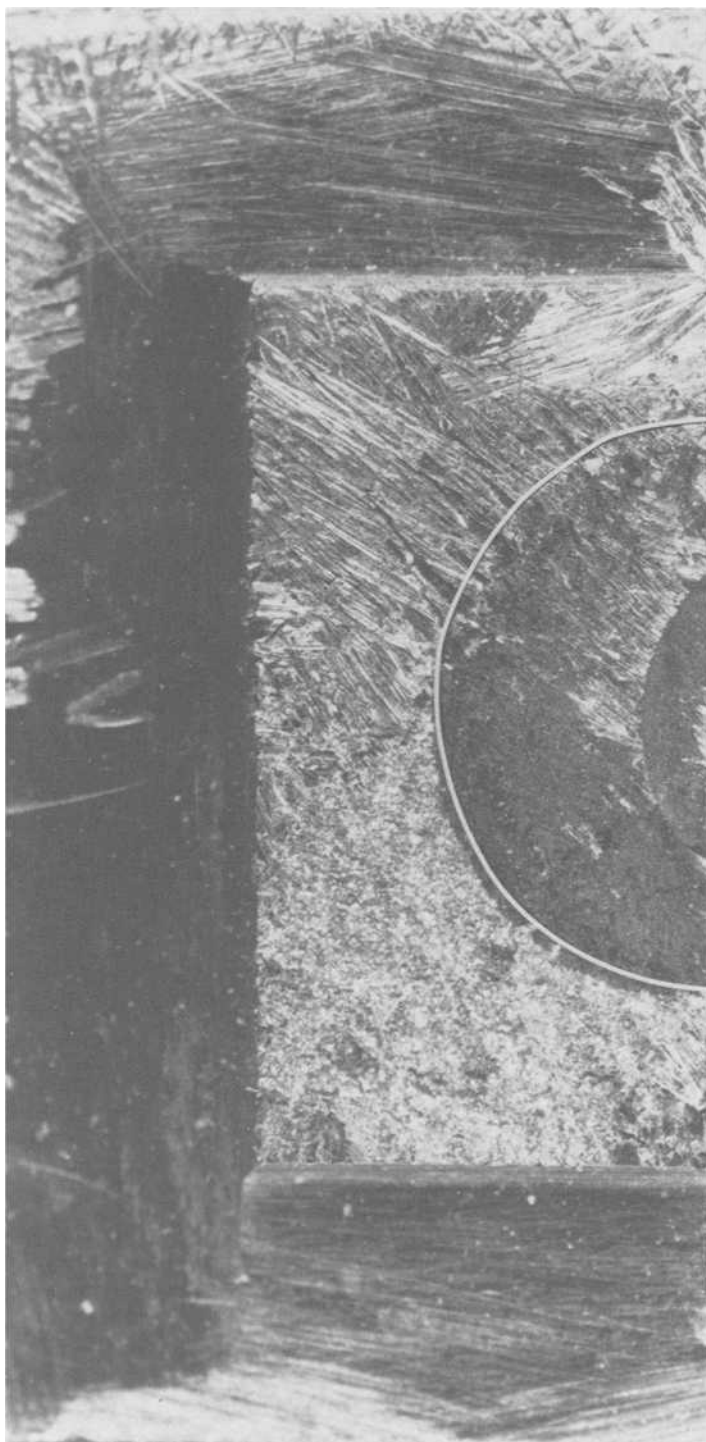


FIG. 5—Fractured surface of Specimen C2E showing agreement of the "best fitting ellipse" with the crack front [20].

probe pair were used to calculate the crack depth. This depth was then used to calculate the load required to maintain a constant value of K_{\max} and K_{\min} . Values for K are calculated after Rooke and Cartwright's [18] analysis which was done for plates of finite thickness and infinite width and modified for finite widths after Newman and Raju [19].

Environmental Surface Crack Growth Test Results

A large amount of environmental surface crack growth testing has been performed in our laboratory using the techniques just described [20], and the specimen geometries are shown in Fig. 6. The materials investigated include a piping steel, SA333 Grade 6 carbon steel, SA533 B-1 pressure vessel steel, and Type 304 stainless steel. Environments include air and oxygenated water at temperatures ranging from 149°C (300°F) to 288°C (550°F) at pressures of 10.3 MPa (1500 psi). Values for R varied from 0.1 to 0.9.

Results will first be reported for ferritic materials, specifically the carbon steel piping material and the pressure vessel steel. Figure 7, for example, compares the cyclic crack growth response of the carbon steel in air at room temperature with a CT (compact type) specimen of the same material, using K_{eff} as defined. Figure 8 shows the cyclic crack growth response of six surface-defected specimens of this material with that of a CT geometry at 288°C (550°F) in 0.2 ppm oxygen water and a 10-min hold period. For the condition where the stress-intensity factors overlap, there is little difference in crack growth response for the two geometries. The peaking behavior of the CT geometry seen is not unusual for this material, environment, and frequency [13]. Note also the crack growth information provided in the ASME Boiler and Pressure Vessel Code, Section XI [21].

A feature of the measured surface crack growth response is the very steep rise in cyclic crack growth with increasing ΔK . It should also be pointed out that, because the radii of starting defects in the specimens employed were of the order of 1.27 to 3.81 mm (0.05 to 0.15 in.), maximum net section stresses as high as 379 MPa (55 ksi) were employed to achieve adequate stress-intensity factors for cyclic crack growth. Use of the linear elastic fracture mechanics parameter K was justified since cyclic load displacement response was essentially elastic once the desired net section stress was obtained.

Another feature of load cycled tests with small surface defects, high net section stress, and severe environment is the occurrence of mixed cyclic and time-dependent crack growth. This is seen in Fig. 9. Here 8 ppm of oxygen water was used with the testing conditions as indicated. Note that the bulk of the crack growth was largely time-dependent growth during the hold time, while a much smaller increment of growth developed during the unloading and reloading process. When this test was repeated in air only cyclic dependent growth occurred, indicating the strong coupling between the environment and the deformation process, be it monotonic (creep) or cyclic. In all cases cracking was transgranular.

The steepness of the da/dN versus ΔK response for carbon steel illustrated in Fig. 8 and the observed shift in this response with temperature provides an explanation for another observation, shown in Fig. 10, of a marked transition in crack depth versus cycles. This transition is found between 191°C (375°F) and 232°C (450°F) for the R -value, wave form, and frequency indicated. Because of the steepness of the crack growth response, a small shift of these curves with temperature can lead to a large cyclic crack growth change with temperature at the same value of ΔK . The alloy steel studied also shows changes in growth rate with temperature but no sharp transition in a versus N . The mechanistic cause for the effect in carbon steel has not been sorted out but may be associated with changes in the nature of the oxide film formed at the crack tip with changing temperature.

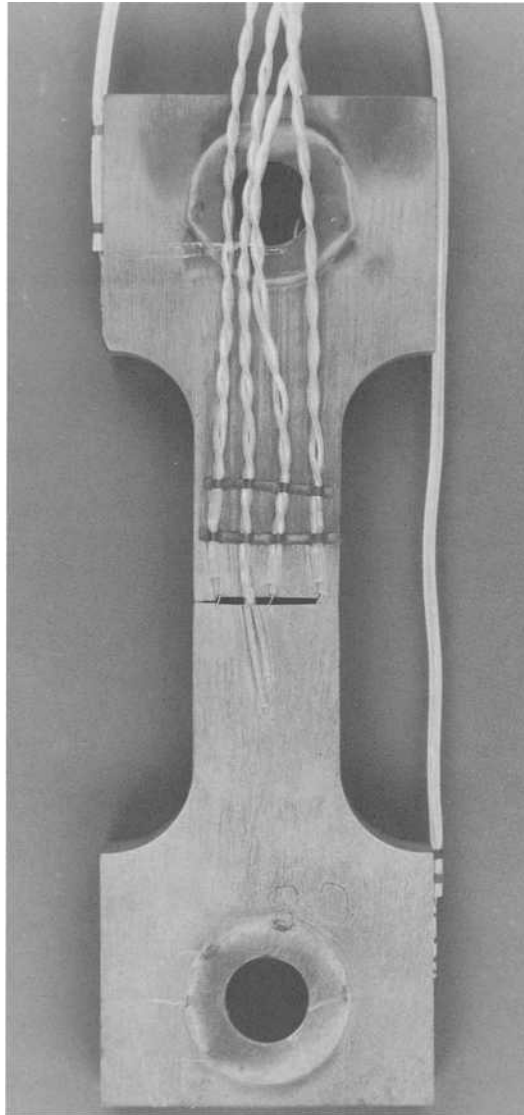


FIG. 6—Typical surface-defected specimen.

Environmental Crack Growth Behavior of Sensitized 304 Stainless Steel

Oxygen Water Chemistry

Several investigators have examined the effect of heat treatment and test conditions on the resulting mode of fracture of compact-type (CT) specimens of Type 304 stainless steel under cyclic loads [10–12,22]. Their work suggests that an environmentally controlled frequency effect is present in Type 304 stainless steel so that the cyclic crack growth rate

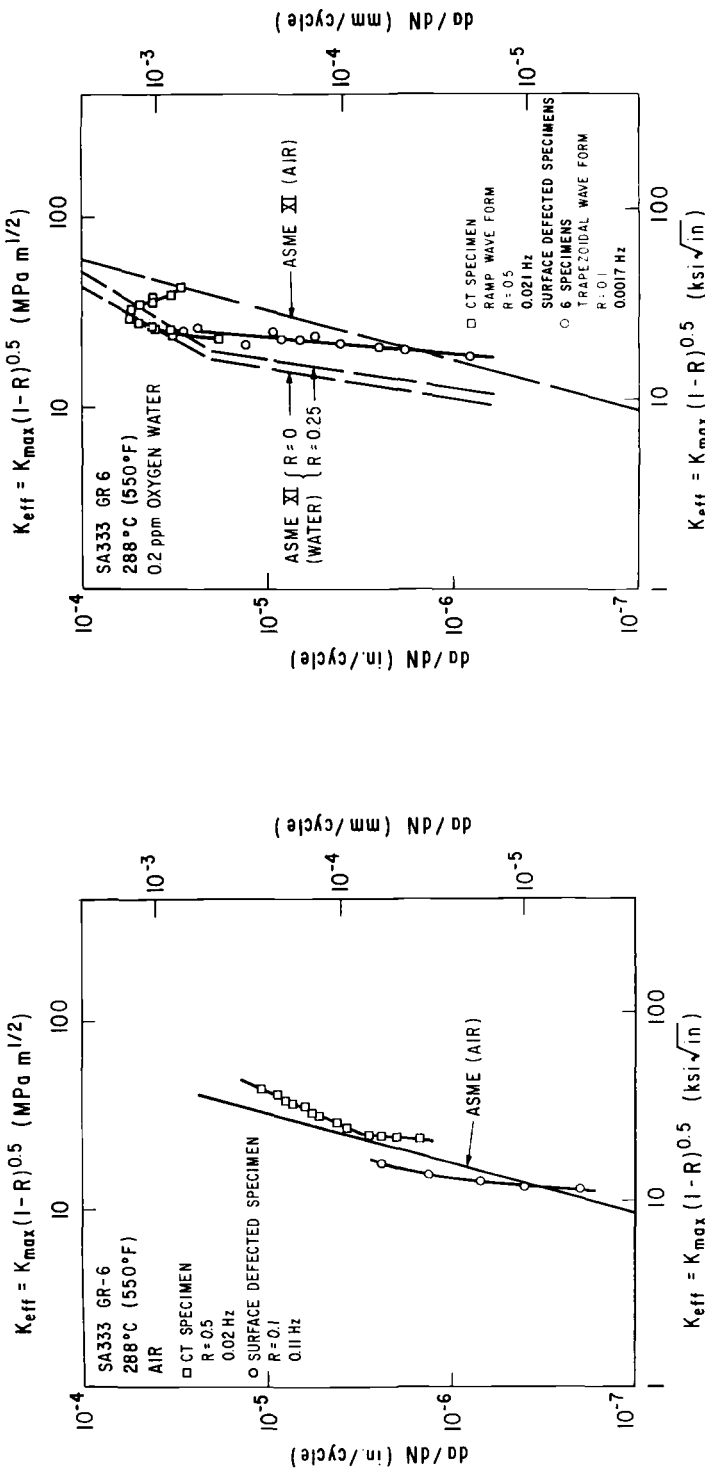


FIG. 7—Crack growth rates for surface-defected and CT specimens of SA333 Gr6 carbon steel when tested in 288°C (550°F) air [20].

FIG. 8—Crack growth rates for six surface-defected specimens and one CT specimen of SA333 Gr6 carbon steel when tested in 0.2 ppm oxygen water at 288°C (550°F) [20].

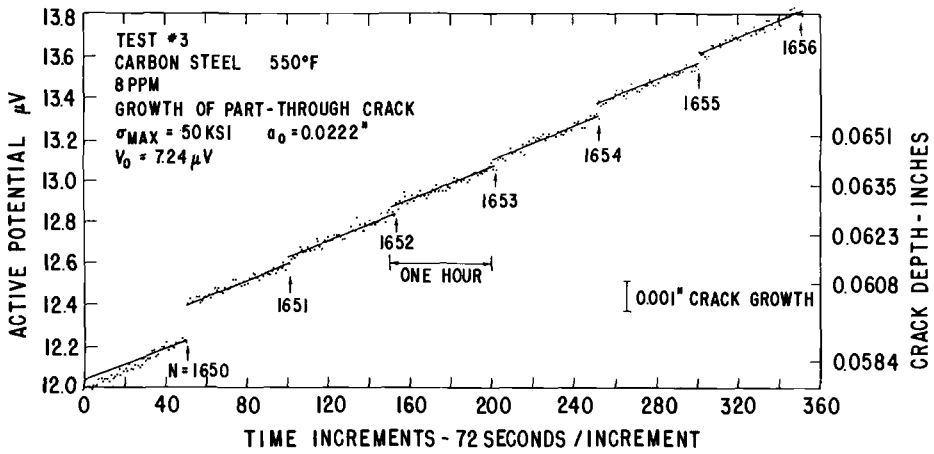


FIG. 9—Crack growth of carbon steel surface-defected specimen subjected to cyclic loading in 8 ppm oxygen water [15].

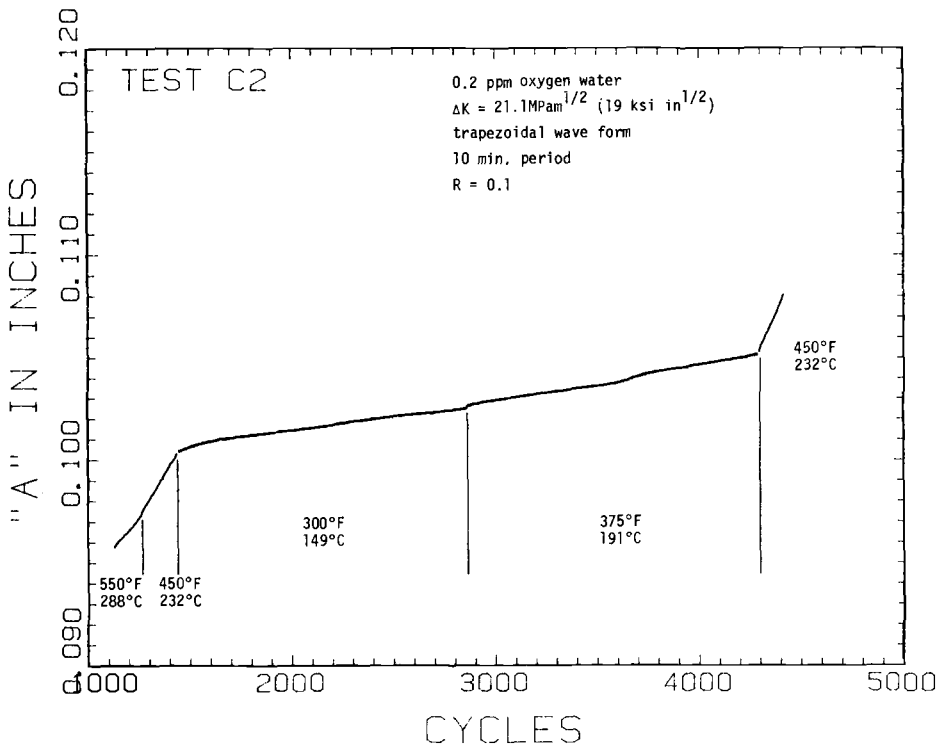


FIG. 10—Comparison of crack growth rates in SA333 Gr6 surface-defected Specimen C2 in 0.2 ppm oxygen water as a function of temperature (1 in. = 25.4 mm).

increases with decreasing frequency. Depending on the degree of sensitization, the oxygen level in the water, the stress-intensity factor, and crack depth, when the crack growth rate has decreased to the order of 1.4×10^{-10} to 7×10^{-10} m/s (2×10^{-5} to 1×10^{-4} in./h), the cracking mode can change from transgranular to intergranular and the cracking velocity appears to level off to a constant value. This would suggest that the intergranular crack growth mode is controlled largely by the time necessary for the corrosion processes to penetrate the grain boundaries at the crack tip and to weaken and sever the grain boundary bonds. This is a very slow process, so that, for most cyclic loading tests, the more conventional transgranular fatigue crack growth process is preferred, unless the frequency is adequately low to permit the alternate slow velocity intergranular process to occur. It is only when

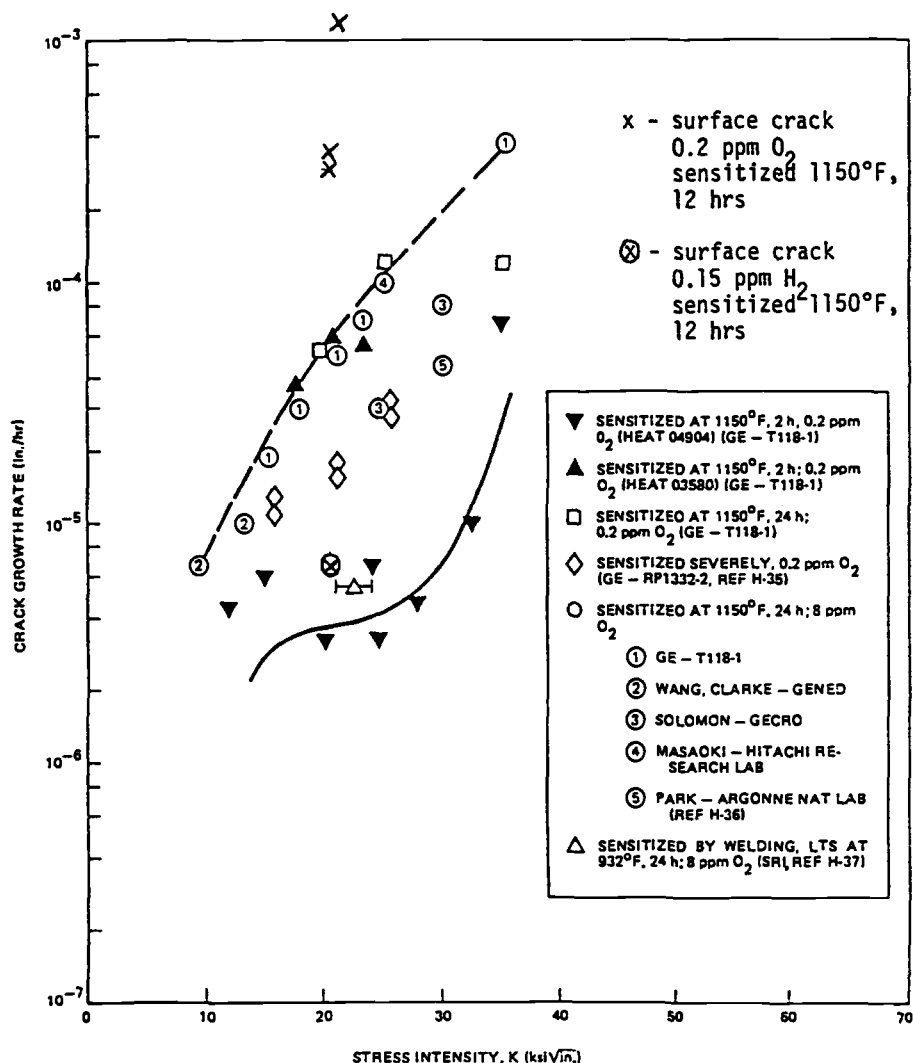


FIG. 11—Constant-load crack growth data in oxygenated high-temperature water [11]. The upper bound and average IGSCC curves used to evaluate crack growth are displayed.

these conditions are reached that contributing factors such as materials and heat-treatment response or the effect of different water chemistries can be evaluated.

Other supportive evidence to show that IGSCC in sensitized 304 stainless steel is a time-dependent process is seen in Fig. 11 from the work of Horn, Kass, and Ranganath [23]. This figure summarizes the work of several investigations on static load crack growth in CT specimens in various oxygenated water chemistries. Not only is there a K dependence, but there is also considerable scatter from heat to heat, probably associated with differing degrees of sensitization.

For the reasons indicated earlier, in our work the approach was to investigate the environmental surface crack growth behavior in sensitized Type 304 stainless steel. Significant differences are found for static and cyclic tests when compared with CT tests. In static surface crack tests with nominal stresses of 275 MPa (40 ksi) and elastically calculated stress-intensity factors of $23 \text{ MPa m}^{1/2}$ ($21 \text{ ksi in.}^{1/2}$), crack velocities of $300 \times 10^{-4} \text{ mm/h}$ ($1130 \times 10^{-5} \text{ in./h}$) are obtained in 200 ppb of oxygen water. These velocities are substantially above those found in Fig. 11 (7.5×10^{-5} to $1.5 \times 10^{-3} \text{ mm/h}$ (3×10^{-6} to $6 \times 10^{-5} \text{ in./h}$)) for the same stress-intensity factors when CT geometries are employed. These results show the effect of creep due to the high net section stress in surface defected geometries not encountered in CT geometries.

Hydrogen Water Chemistry

As indicated above, water chemistry modification involving the additions of small amounts of hydrogen to reactor coolant has been shown to be beneficial in controlled IGSCC [24]. Supporting tests have been conducted in our laboratory to demonstrate the effectiveness of this remedy, using techniques described above. The work here focused largely on furnace-sensitized 304 stainless steel.

Additions of 150 ppb of hydrogen to 200 ppb of oxygen water reduces the oxygen level to nearly zero and can have profound effects on both static and cyclic crack growth. Note in Fig. 12 the crack growth behavior for statically loaded surface-defected specimen geometries when the water chemistry is so altered. These results are summarized in Table 1 and show that hydrogen water chemistry reduces the crack velocity to near zero, despite the high net section stress of these geometries.

Figure 13 describes the results for cyclic crack growth tests. The crack velocity results are recorded in Table 2 for the several cyclic periods employed for each water chemistry. The solid line in Fig. 13 represents the time-independent response for the imposed ΔK of the test. Its position is obtained by assuming that all growth during cycling at a frequency of 1 cpm in a hydrogen-containing water environment is time independent. This appears to be justified by examination of the other data obtained in cycling in hydrogen-containing water. It will be noted in Table 2 that the amount of growth per cycle is nearly equal for cyclic rates ranging from 1 to 0.001 cpm. Consequently, all data for tests in hydrogen water fall on this time-independent curve.

Also Fig. 13 shows that, when cycling is done in oxygen-containing water, the crack growth rate is greatly influenced by the cyclic frequency. When a period of 1 min is employed, the growth rate in oxygen-containing water is only slightly greater than that observed in hydrogen-containing water, indicating little or no time dependence in either environment. As the period is increased, the divergence in behavior in the two environments increases until, in the oxygen-containing water, the time-dependent growth dominates and the effect of cyclic growth becomes insignificant. At these long periods the growth rate approaches the rate noted in constant load tests, and the fracture mode becomes intergranular.

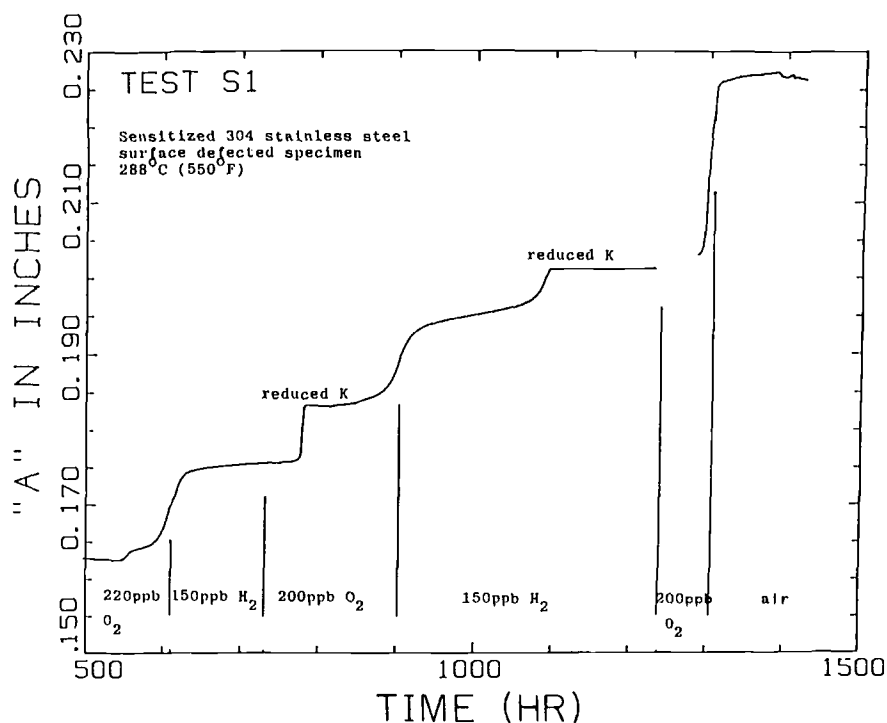


FIG. 12—Dependence of crack growth in statically loaded, surface-defected, sensitized 304 stainless steel Specimen S1 on the changing water chemistry and stress intensity.

Applications to Crack Growth Monitoring of Piping Components

There are a variety of reasons for developing methods for measuring crack growth in simulated or actual plant components including (1) improved confirmation of the ability to predict performance from test specimen information, (2) application of information to current plant operations, (3) confirmation that remedies introduced for IGSCC control are, in fact, functioning, and (4) application of information to life prediction and life extension.

The techniques described earlier have been so applied [25]. Desirably in piping appli-

TABLE 1—Comparison of crack growth rates of sensitized Type 304 stainless steel under constant load in water containing oxygen or hydrogen.

Time, h	K, MPa m ^{1/2}	Gas Content of Water, ppb	da/dt	
			mm × 10 ⁻⁴ /h	in. × 10 ⁻⁶ /h
610	22.2	oxygen 200	81	320
731	22.8	hydrogen 150	1.5	6
780	23.3	oxygen 200	300	1180
900	21.6	oxygen 200	88	345
1093	22.4	hydrogen 150	66 ^a	260 ^a
1150	20.9	hydrogen 150	0.25	1
1300	22.5	oxygen 200	272	1070

^a May be creep crack growth, $\sigma_{net} > 50.5$ MPa (46 ksi).

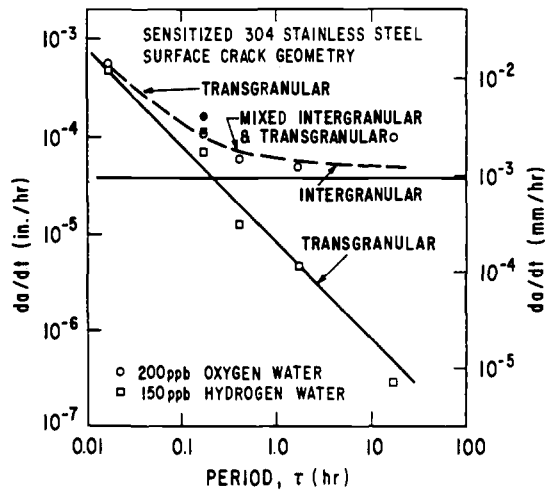


FIG. 13—Effect of frequency on the crack growth rate of a surface-defected specimen of sensitized 304 stainless steel tested in oxygen- and hydrogen-containing water at 288°C (550°F).

cations, current and probe attachments must be located on the OD of the pipe in the vicinity of the growing ID crack. Sensitivity and resolution of data as well as ID crack shape are key questions. Calculations were made from electrical potential solutions for pipe walls containing elliptical ID cracks, external potential probes, and current sources and sinks, assuming that the potential test data can be resolved to 0.1%. For a crack which had grown to 10% of the wall thickness, if that crack were nearly circumferential, its depth could be determined to within 2.3% of its actual depth. On the other hand, if the crack were semi-circular, its depth could be found to within 190%. The uncertainty in this later case reduced to 22% when the semicircular crack had grown to 20% of the weld. Figure 14 shows a more complete solution of this problem.

Reference 25 describes experiments on 102-mm (4-in.)-diameter OD by 8.64-mm (0.34-in.) wall thickness furnace-sensitized 304 stainless steel pipes with two internal circumferentially oriented electrical discharge machining defects, each 1.27 mm (0.05 in.) thick; one defect was semicircular in shape and the other was an arc of a circle of 25.4 mm (1 in.) radius. Loading was axial and cyclic with a 10-min-hold trapezoidal waveform. The water chemistry was 200 ppb oxygen or 150 ppb hydrogen water at 288°C (550°F) and 8.8-MPa (1275-psi) pressure. Calculated stress-intensity factors for the largest defect were $K_{\max} = 16.8 \text{ MPa in.}^{1/2}$ (15.4 ksi in.^{1/2}) and $K_{\min} = 4.3 \text{ MPa in.}^{1/2}$ (3.9 ksi in.^{1/2}).

Current attachments were located on the OD of the pipe remotely and close to the defect where, according to calculation, a reasonably uniform current distribution could be assumed near the defect. Three pairs of potential probes were attached about 2.54 mm (0.1 in.) axially from the crack plane, one pair at the midposition of the crack, the others 12.7 mm (0.5 in.) away, on both the ID and OD of the pipe.

Details of the data gathering and printout procedures and testing techniques are given elsewhere [25]. Figures 15 and 16 show the crack growth results, presented in terms of area versus loading cycles rather than depth versus loading cycles. Data reduction was performed as in Fig. 4. These results are also summarized in Table 3. Prediction of crack growth from internal and external probes was in close agreement, and the prediction versus the actual crack area was within 8%. The sensitivity is adequate, as can be seen in Fig. 14, noting that the starting crack depth to wall thickness ratio is 0.147 and the starting aspect ratio is 0.05.

TABLE 2—Effect of frequency on crack growth rates of sensitized Type 304 stainless steel of 200 ppb oxygen water and 150 ppb hydrogen water on a surface-defected specimen. Crack growth rate when $K = 15.3 \text{ MPa m}$.

Specimen	Cycle Period, min	da/dN , $\text{mm} \times 10^{-4}/\text{cycle}$		da/dt , $\text{mm} \times 10^{-4}/\text{h}$		Crack Depth, mm	Net Stress, MPa
		200 ppb oxygen	150 ppb hydrogen	200 ppb oxygen	150 ppb hydrogen		
S-2	1	2.4	2.1	142	123	5.38 to 5.97	234 to 242
S-2	10	4.7	2.9	28	18	6.15 to 6.60	245 to 256
S-2	30 ^a	20.0	5.6	40	11	6.60 to 6.91	256 to 268
S-2	100	22.0	2.1	13	1.2	5.97 to 6.15	242 to 245
S-2	1000 ^a	indefinite	13.0	...	0.8	6.91 to 7.54	268 to 332
S-3	30	8	1.7	16	3.4	4.70 to 4.81	238 to 239
S-3	1000	427	1.1	25	0.07	4.81 to 5.10	239 to 240

^a Data for 30 and 1000-min cycles of Specimen S-2 are inaccurate because of the great depth of the crack, which resulted in very high net section stress to give the desired K .

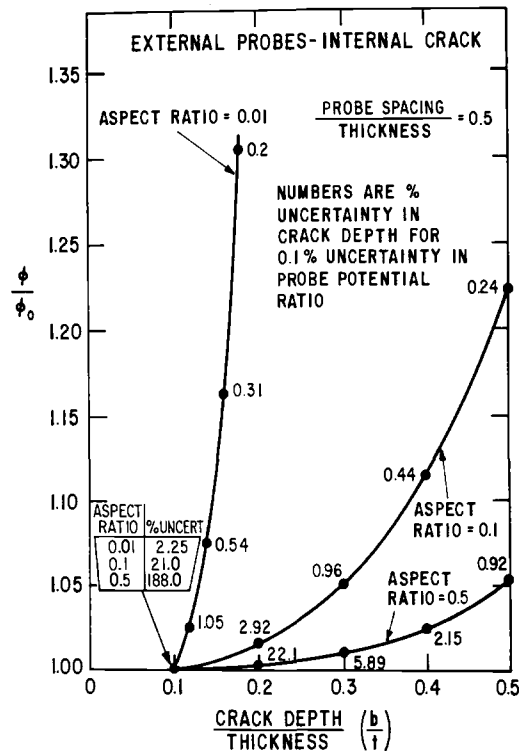


FIG. 14—Relationship between uncertainty in the crack depth growth prediction and uncertainty in the probe potential readings for cracks with three aspect ratios.

As seen in Table 3, the crack growth rates were in good agreement with surface-defected laboratory tests when adjusted for stress-intensity factor differences. Little difference in growth rates was noted between the oxygen and hydrogen water chemistries (Fig. 13). This is to be expected for the 10-min-hold testing of this experiment.

Steps are now under way to extend this approach to the in-plant verification of IGSCC remedies.

Other Monitoring Techniques

A second form of monitor consists of a wedge-loaded double-cantilever beam (DCB) specimen that can be used in an on-line, *in situ* manner. Its crack growth can be monitored by electrical potential probes mounted at discreet locations on the sensor. Its use is primarily to determine, for the material and the stress-intensity factor level (K) of interest, the instantaneous and accumulated crack growth rate at a particular location of concern. The device can be located in various positions in piping or in the reactor core to determine such effects as long-term damage to specific materials and heat treatments in reactor water, effects of impurities inadvertently introduced into the coolant, and effects of neutron irradiation when coupled with stress corrosion. Plans are under way to investigate the use of such a monitor and to determine specific stress-corrosion effects in an operating BWR.

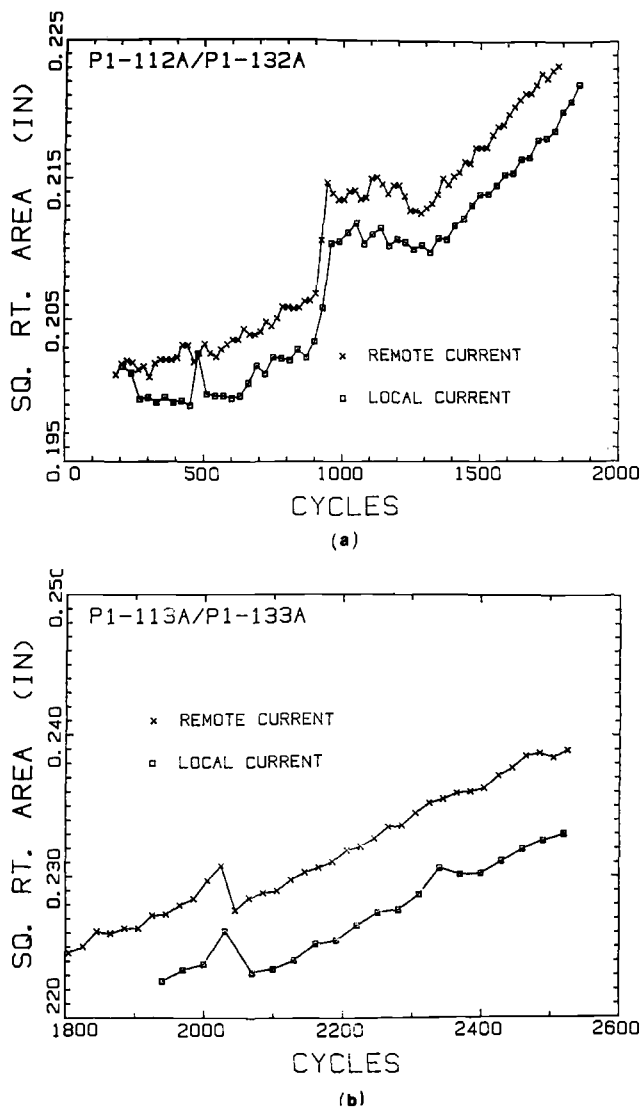


FIG. 15—Comparison of the crack dimensions predicted by potential probes on the inside and outside surface of a pipe.

Depending on the nature of the damage, other monitor types are possible. Relative to stress-corrosion cracking it is very useful to know something of the water chemistry throughout the plant. Several kinds of measurements can be made to give more insight into the nature of environmental damage. These include dissolved hydrogen and oxygen concentrations, resistivity of the water, pH of the water, and the corrosion potential of the material-environment system relative to a reference electrode. Reference 26 describes a system used in our own laboratory autoclave work, and this is one method for monitoring the corrosion potential in high-temperature aqueous environments.

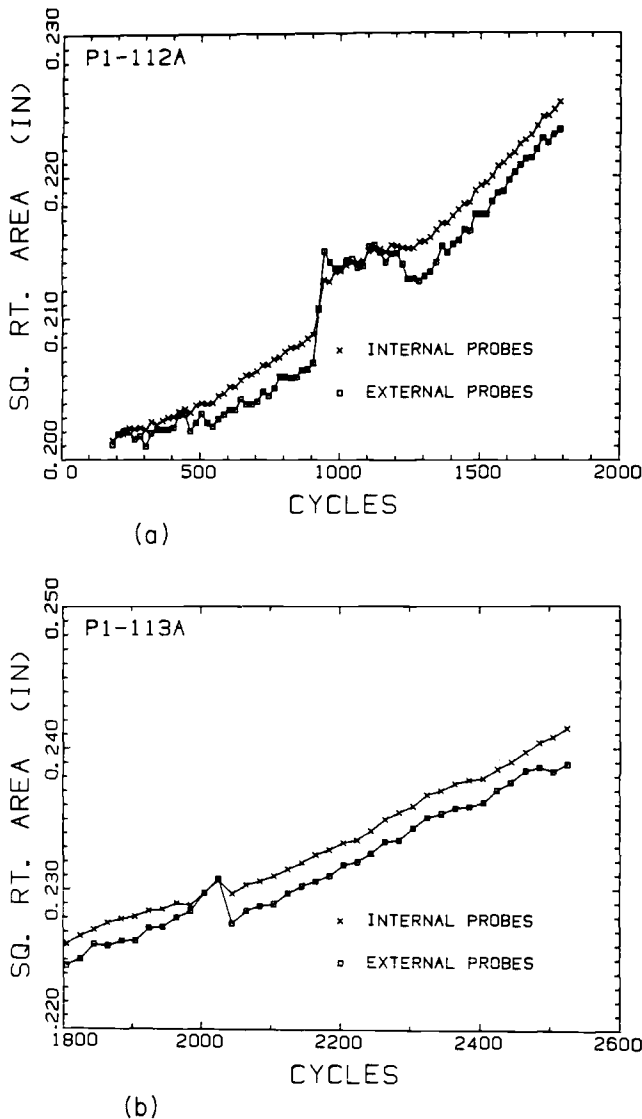


FIG. 16—Comparison of predictions of crack growth using remote and local current sources and sinks with outside surface potential probes in (a) 200 ppb oxygen water and (b) 150 ppb hydrogen water [25].

Modeling IGSCC

A significant effort has been under way at our laboratory in recent years to develop a quantitative model for IGSCC, based on appropriate underlying mechanisms believed to be operative. This model is in an advanced state of development, to the point that it can be combined with experimental monitoring techniques for applications to life prediction and life extension (see below) [25]. The model assumes the slip dissolution/film rupture mech-

TABLE 3—Comparison of crack growth rates in pipe and specimen testing.

Environment	Test	K_{\max} , MPa m ^{1/2}	$K_{\text{eff}} = \frac{K_{\max}}{(1-R)^{0.5}}$, MPa m ^{1/2}	da/dN , mm/cycle
200 ppb oxygen at 288°C	Specimen S2	16.8	15.9	4.7×10^{-4}
	pipe	19.0 ^a	16.5 ^a	6.9×10^{-4}
150 ppb hydrogen water at 288°C	Specimen S2	16.8	15.9	2.9×10^{-4}
	pipe	19 to 20.4 ^a	16.5 to 17.7 ^a	4.8×10^{-4}

^a These values are probably low for reasons discussed in the text.

anisms of environmentally assisted crack propagation to be operative [27]. Crack advance is assumed to be dependent on the oxidation processes which occur on a bare surface created by rupture of a surface oxide film at the crack tip. The propagation rate is related electrochemically to the oxidation rate on the bare surface and the frequency of the repeated oxide rupture process at the crack tip. The oxidation rate is determined by the material and environmental conditions in the region of the crack tip, while the oxide rupture periodicity is a function of the strain rate in the matrix near the crack tip and the crack-tip oxide fracture strain. An average crack-propagation velocity rate, \bar{V}' , can be expressed as

$$\bar{V}' = A \dot{\epsilon}_{cr}^n \quad (1)$$

where A and n are material and environment dependent constants, and $\dot{\epsilon}_{cr}$ is the crack-tip strain rate. This expression can also be formulated more conveniently in terms of stress, stress-intensity factor, frequency, and so forth, depending on loading conditions.

Work has focused on the quantification of the parameters of this model, including definitions of the crack tip environment, bare surface oxidation rates, and so forth, so that the terms A , n , and $\dot{\epsilon}_{cr}$ could be independently defined. Current work is aimed at a statistical validation of the approach over a wide range of combinations of environments, material, and stress conditions.

Future Directions—Smart Monitors

When treating IGSCC or other component life limiting problems, the plant operator needs information regarding the state of damage of critical components in his plant, the degree to which corrective remedies are effective in controlling this damage, and an assessment of the remaining life of each component so that repairs could be properly planned or life extended beyond the original design life. A useful way to obtain this information is by a "smart" monitor. Smartness in this sense is defined as "interpretation of the indicated information which, in conjunction with a broad knowledge base, allows intelligent decisions to be made regarding operations so as to improve performance and extend life."

Assuming that a crack growth monitor or monitors have been located in the plant at critical locations, smartness involves making judgments about the significance of the information. Is the information as expected? What can be said about other cracks with the same water chemistry but at different K levels? What about crack growth for other water chemistries and other K levels? What about variations in temperature, materials, and so forth?

For the monitor to be smart it must have access to a predictive model of crack growth behavior that is sufficiently broad to encompass the range of variables involved in the application (for example, temperature, material, environment, loading, and corrosion potential). Using the current crack size given by the monitor and an assumed or known crack size in the component, the predictive model and the other parameters given about the smart monitor could determine the following:

- (a) the monitor and component crack depth at some later time assuming no change in operating conditions;
- (b) the monitor and or component crack depth at some later time for some known change in loading, temperature, and environment (water chemistry) with time; and
- (c) the monitor and component crack depth at some later time assuming the material to be of another composition, but subject to the same conditions of load, temperature, and environments as in (b).

Because the monitor crack depth is known as time proceeds, the predictive crack growth of the monitor and component can be continually updated. In fact, there may be learning from the differences between the measured and predictive monitor information so as to improve the predictive capability of the model.

A model for stress-corrosion crack growth in sensitized stainless steel developed by F. P. Ford and his associates at our laboratory has been described earlier in this paper. The approach is to consider crack velocity as the result of the crack-tip strain rate and material dissolution by crack-tip chemical processes. Such a model when appropriately expanded to encompass the engineering requirements for crack growth prediction becomes important input to the smart monitor.

A logic diagram for the smart monitor concept is shown in Fig. 17. Information from the monitor's sensor determines if damage is occurring (that is, is time dependent) or if stress corrosion cracking is taking place. If there is no damage, the monitor will be queried again at a later time. If damage is found, the amount of damage so calculated is used in the damage model built into the logic of the system. This is equivalent to saying that the information gathered from the sensor is used to determine the disposable constants in the model to develop a relationship of crack depth as the dependent variable with time, material, loads, temperature, and environment as independent variables. Having this relationship, alternative actions may be examined relative to plant operations. The monitor can be queried as to when to shut down for repairs, when to introduce water chemistry changes, or for

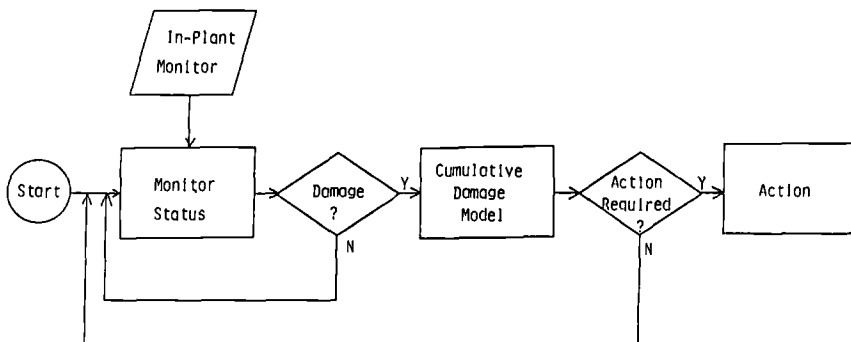


FIG. 17—"Smart" monitor life prediction logic.

how long the plant can be operated beyond its design life. From this information gathered by the monitor, decisions can be taken by the plant operator to bring about the appropriate response.

Summary

In this paper the problem of IGSCC in BWR piping has been discussed and the body of work undertaken in the author's laboratory to solve that problem described. Particular attention is given to the development of electrical potential crack monitoring techniques and their application to surface crack growth, particularly under conditions approaching those found in service. The important role of water chemistry and its control is described in this context.

The concept and description of sensors to monitor *in situ* the degree of damage from intergranular stress-corrosion cracking is then described, with reference to using piping components and other monitor types.

Finally, a concept for the life management of structures is described where damage processes are identified and monitored *in situ* using appropriate sensors to measure the damage rate continuously. In conjunction with damage monitoring, an applicable life prediction model is used to forecast the future damage state and to assist in the decision process for appropriate required actions to optimize plant operation.

Acknowledgments

During the development of the techniques and concepts described in this paper the author has had the support and counsel of many people. From General Electric's Corporate Research and Development, the advice and help of M. G. Benz and T. A. Prater is acknowledged. From General Electric's Nuclear Energy Business Operation, the help of D. Weinstein is noted. From the Electric Power Research Institute, the strong support by R. L. Jones and J. D. Gilman of this work is appreciated.

References

- [1] Jones, R. L. and Gilman, J. D., "Corrosion Cracking in Water Reactor Environments—Mechanical Viewpoint," *Proceedings*, Second International Symposium on Environmental Degradation of Materials in Nuclear Power Systems-Water Reactors, Monterey, CA, September 1985, American Nuclear Society, 1986.
- [2] Fox, M., "An Overview of Intergranular Stress-Corrosion Cracking in BWR's," *Proceedings*, Seminar on Countermeasures for Pipe Cracking in BWR's, Report WS-79-174, Vol. 1, Paper No. 1, Electric Power Research Institute, Palo Alto, CA, May 1980.
- [3] Klepfer, H. H., et al., "Investigation of the Cause of Cracking in Austenitic Stainless Steel Piping," Report NEDO 21000-1, Class 1, General Electric Co., Schenectady, NY, July 1975.
- [4] Bain, E. C., Aborn, R. H., and Rutherford, J. J. B., "The Nature and Prevention of Intergranular Corrosion in Austenitic Stainless Steels," *Transactions of the American Steel Heat Treating Society*, Vol. 21, 1933, pp. 481-531.
- [5] Danko, J. C. and Smith, R. E., *Proceedings*, Seminar on Countermeasures for Pipe Cracking in BWR's, Report WS-79-174, Vol. 1-4, Electric Power Research Institute, Palo Alto, CA, May 1980.
- [6] Hale, D. A., et al., "Low-Cycle Fatigue Evaluation of Primary Piping Materials in a BWR Environment," Report GEAP 20244 for the U.S. Nuclear Regulatory Commission, General Electric Co., Schenectady, NY, September 1977.
- [7] Solomon, H. D., Povich, M. J., and Devine, T. M., "Slow Strain Rate Testing in High-Temperature Water," *Stress Corrosion Cracking—The Slow Strain Rate Technique*, ASTM STP 665, American Society for Testing and Materials, Philadelphia, 1979, pp. 132-149.

- [8] Hughes, N., "Qualification of Solution Heat Treatment, Corrosion Resistant Cladding, and Heat Sink Welding," *Proceedings*, Seminar on Countermeasures for Pipe Cracking in BWR's, Report WS-79-174, Vol. 1, Paper 17, Electric Power Research Institute, Palo Alto, CA, May 1980.
- [9] Hale, D. A., et al., "Reactor Primary Coolant Pipe Rupture Study," Progress Report No. 34, General Electric Co. Report GEAP-10207-34 prepared for the U.S. Nuclear Regulatory Commission, General Electric Co., Schenectady, NY, February 1976.
- [10] Jewitt, C. W., "Environmental Crack Growth in Alternate Pipe Alloys," Internal Report EM 79-04, General Electric Co. Nuclear Energy Business Operation, Schenectady, NY, January 1979.
- [11] Henry, M. F., "Fatigue Crack Propagation in Austenitic Stainless Steel in High Purity Water at 288°C," Corporate Research and Development Report MOR-79-169, General Electric Co., Schenectady, NY, December 1979.
- [12] Kawakubo, T., Hishida, M., Amano, K., and Katsuta, M., "Crack Growth Behavior of Type 304 Stainless Steel in Oxygenated 290°C Pure Water Under Low-Frequency Cyclic Loading," *Corrosion—NACE*, Vol. 36, No. 11, 1980, pp. 638–647.
- [13] Prater, T. A. and Coffin, L. F., "Crack Growth Studies in a Carbon Steel in Oxygenated High Pressure Water at Elevated Temperatures," *Micro and Macro Mechanisms of Crack Growth*, American Institute of Mechanical Engineers, New York, NY, 1982.
- [14] Catlin, W. R., Morgan, H. M., Lord, D. C., and Coffin, L. F., "A Method for Monitoring Crack Growth from Flaws in Piping and Other Components," *Proceedings*, Seminar on Countermeasures for Pipe Cracking in BWR's, Report EPRI WS-79-174, Vol. 2, Electric Power Research Institute, Palo Alto, CA, May 1980.
- [15] Prater, T. A. and Coffin, L. F., "Part-Through and Compact Tension Corrosion Fatigue Crack Growth Behavior of Carbon Steel in High-Temperature Water," *Proceedings*, Second International Conference on Environmental Degradation of Engineering Materials, Virginia Polytechnic Institute, Blacksburg, VA, September 1981, pp. 59–72.
- [16] Prater, T. A., Catlin, W. R., and Coffin, L. F., "Surface Crack Growth in High-Temperature Water," *Proceedings*, International Symposium on Environmental Degradation of Materials in Nuclear Power Systems—Water Reactors, National Association of Corrosion Engineers, Houston, TX, 22–25 Aug. 1983, pp. 746–762.
- [17] Catlin, W. R., Lord, D. C., Prater, T. A., and Coffin, L. F., "The Reversing dc Electrical Potential Method," *Automated Test Methods for Fracture and Fatigue Crack Growth*, ASTM STP 877, American Society of Testing and Materials, Philadelphia, 1985.
- [18] Rooke, D. P. and Cartwright, D. J., *Compendium of Stress-Intensity Factors*, Her Majesty's Printing Office, Hillingdon Press, London, 1976.
- [19] Newman, J. C. and Raju, I. S., "Analysis of Surface Crack in Finite Plates Under Tension or Bending Loads," NASA Technical Paper 1578, NASA Scientific and Technical Information Branch, National Aeronautics and Space Administration, Washington, D.C. December 1979.
- [20] Prater, T. A., Catlin, W. R., and Coffin, L. F., "Surface Crack Growth Behavior of Structural Metals in High Temperature Water Environments," *Journal of Engineering Materials and Technology*, *Transactions of the American Society of Mechanical Engineers* Vol. 108, 1986, pp. 2–9.
- [21] "Rules for In-Service Inspection of Nuclear Power Plant Components," ASME Boiler and Pressure Vessel Code, Section XI, American Society of Mechanical Engineers, New York, NY, 1980.
- [22] Hale, D. A., et al., *The Growth and Stability of Stress Corrosion Cracks in Large Diameter BWR Piping*, Vol. 2, EPRI NP-2472, Electric Power Research Institute, Palo Alto, CA, July 1982, Appendix H.
- [23] Horn, R. M., "Evaluation of Crack Growth in Oxygenated High-Temperature Water Using Full Size Pipe Tests," *Journal of Engineering Materials and Technology*, *Transactions of the American Society of Mechanical Engineers*, Vol. 108, 1986, pp. 50–56.
- [24] "Supply Options and Safety Issues for Hydrogen Use in the Control of Intergranular Stress-Corrosion Cracking in Boiling Water Reactors," EPRI NP-3282 Final Report, Electric Power Research Institute, Palo Alto, CA, November 1983.
- [25] Prater, T. A., Catlin, W. R., and Coffin, L. F., "Application of the Reversing dc Electrical Potential Technique to Monitoring Crack Growth in Pipes," International Atomic Energy Agency, Specialist Meeting on Subcritical Crack Growth, Sendai, Japan, 15–17 May, 1985.
- [26] Niedrach, L. W. and Stoddard, W. H., "Monitoring of pH and Corrosion Potentials in High Temperature Aqueous Environments," *Corrosion 84—NACE*, Vol. 41, National Association of Corrosion Engineers, Boston, MA, 1985, pp. 45–51.
- [27] Ford, F. P., Andresen, P. L., Taylor, D. F., and Caramihas-Foust, C. A., "Prediction and Control of Stress-Corrosion Cracking in the Sensitized Steel-Water System," Paper 352, *Corrosion 84—NACE*, National Association of Corrosion Engineers, Boston, March 1985.

Structural Integrity of Rail in Railroad Track in the United States

REFERENCE: Orringer, O. and Steele, R. K., "Structural Integrity of Rail in Railroad Track in the United States," *Fracture Mechanics: Nineteenth Symposium, ASTM STP 969*, T. A. Cruse, Ed., American Society for Testing and Materials, Philadelphia, 1988, pp. 260–278.

ABSTRACT: The resistance of rail to fatigue crack propagation and fracture are discussed. Preliminary results of crack growth calculations are presented to illustrate the correlation of an elementary crack growth model with a full-scale experiment. The possible effects of current trends in railroad operations on safe crack growth life and damage tolerance of rail are noted.

KEY WORDS: crack growth, fracture, nondestructive inspection, rail, steel alloys, structural integrity, fracture mechanics

Rail is unique among primary load-carrying structures because it is nonredundant, is repeatedly stressed above its initial yield strength by normal service loads, and operates consistently below its ductility transition temperature. The ability of rail to survive these conditions economically results from its unique crack growth environment and from railroad strategies for periodic inspection. Study of rail from a fracture mechanics perspective started about ten years ago and continues today [1–4].

Modern rail is a hot-rolled ferritic steel of eutectoid (0.8% carbon) or near-eutectoid composition and pearlitic microstructure. The standard composition is alloyed with silicon and manganese. Many different "premium-alloy" rails have been developed over the past 60 years by increasing the alloy content or by adding other elements such as chromium, columbium, molybdenum, and vanadium. Rail steel alloy development has reflected a trend toward better strength and hardness to resist permanent deformation and wear. Parallel development of rail section designs (Fig. 1) has reflected a trend toward heavier sections for better bending and torsional stiffness to bear increasing axle loads. One result of this history is that railroad tracks contain a wide variety of rail types, weights, and ages.

The history of rail development and use also reflects episodes of product defects and fatigue flaws that can grow and fracture under service loads. For a century the railroads kept rail defects under control by means of visual inspections. Increasing traffic, speeds, and loads led to increased occurrence of fatigue cracks, however, and in the 1930s the railroads began to supplement visual inspection with continuous rail testing by trained specialists. The first rail test organization was the Sperry Rail Service, which used a fleet of self-propelled rail-bound cars to find rail defects by means of magnetic induction testing. Sperry continues to provide inspection services today, as do other independent companies, and some of the larger railroads also operate their own inspection fleets.

¹ Mechanical engineer, U.S. Department of Transportation, Transportation Systems Center, Cambridge, MA 02142.

² Assistant director, Metallurgy, Association of American Railroads Research and Technical Center, Chicago, IL 60616.

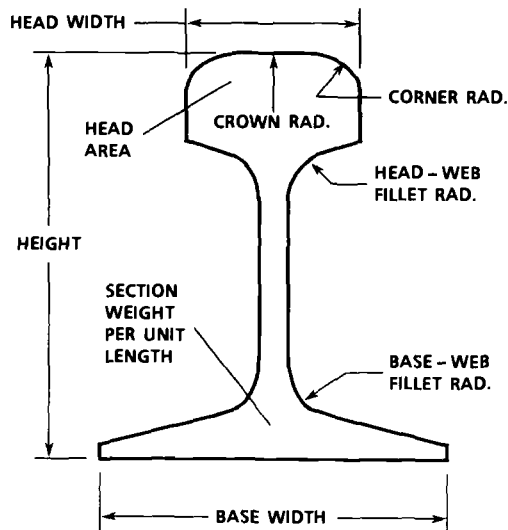


FIG. 1—Rail section design parameters.

Rail testing has become the primary method for controlling rail defects, and testing technology has kept pace with rail development and railroad operations. Ultrasonic testing equipment was introduced in the 1960s and 1970s; the consequent reduction in operating power requirements made it possible to mount these detection systems in light trucks specially equipped with hydraulically deployable wheelsets for running on the rails. These "hi-rail" vehicles travel on roads between inspection sites, enabling the railroads to maintain flexible testing schedules. The schedules now in use have evolved from each railroad's aggregate experience with its own track, environment, defect occurrences, maintenance practices, and train operations.

The near future will probably bring an increasing rate of change in railroad characteristics that can affect the fatigue performance of rail. The following are examples of major changes, several already well under way. Traffic densities have increased dramatically in the last ten years, approaching 91 million gross metric tons (100 million gross tons) annually on some lines; much of this traffic is in the form of fully loaded hundred-car [120 gross metric tons (132 gross tons) per car] unit trains. Premium alloy rail has been laid on 5 to 10% of the main-line track mileage, principally on curves where there is the most need to control wear. Older bolted-joint rail in main-line track is being replaced with continuous welded rail (CWR), which is subject to thermal stress, at the rate of about 8000 km (5000 miles) per year. These trends are expected to continue. Within the last two to three years, significant numbers of double-stack container cars have been placed in unit train service. A double-stack container car consists of five articulated platforms (Fig. 2) with as yet unknown dynamic behavior and with the potential for overloading [5]. The railroads are currently considering the idea of increasing the maximum standard freight car axle load permitted for interchange service. The available experience with such heavy cars in non-interchange service suggests a change in rail fatigue performance [6]. Individual railroads are also considering the extension of rail lubrication from curves to entire lengths of main-line track in order to save fuel and reduce wheel and rail wear. Experiments performed at the U.S. Transportation Test Center (TTC) in Pueblo, Colorado, have demonstrated these benefits but have also shown that fatigue crack nucleation may replace wear as the primary life-limiting factor on

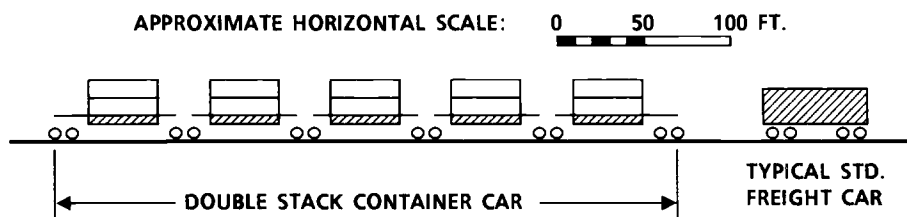


FIG. 2—Double-stack container car and standard freight car (1 ft = 0.3048 m).

lubricated rail [2]. The foregoing trends suggest that the further evolution of rail testing schedules should take advantage of fracture mechanics to assist the projection of past experience to the future.

Rail Defect Behavior in Existing Track

The behavior of rail defects in existing track has been the subject of several studies supported by cooperating railroads. The first studies addressed the taxonomy and occurrence characteristics of the defect population. Later studies have emphasized the service stress environment and fatigue crack growth characteristics.

The 14 different types of rail defect listed in the federal track safety standards [7] include service-induced permanent deformation, unclassified breaks, and rolling mill defects (some of which behave like sharp cracks), as well as fatigue cracks. The growth rates of the crack type defects depend, in general, on the defect location and orientation. Studies of field defect reports [3] have shown that the three types of fatigue cracks illustrated in Fig. 3 comprise 70 to 95% of the defect population in rail that is well into its service life. Recently a Weibull model for crack nucleation based on field defect statistics [2] was combined with an economic model for rail replacement to study the effect of the crack occurrence rate on the rail inspection interval [8]. The results of this study suggest that a good strategy is to compensate for increased crack occurrence in older rail by decreasing the inspection interval. Individual railroads have evolved this type of strategy empirically, but general guidelines have so far proved difficult to formulate.

The fatigue crack growth studies are intended to define safe crack growth intervals [4]. Of the three major defect types shown in Fig. 3, the detail fracture has been the most

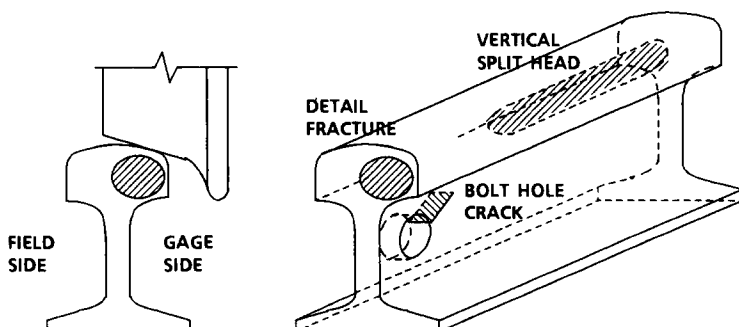


FIG. 3—Most frequently occurring rail defects.

extensively studied, and realistic life estimates for this type are now possible. Crack growth behavior is not yet well understood for bolt hole cracks or vertical split heads.

Detail Fractures

Detail fractures originate in the gage side of the rail head as branch cracks from regions of horizontal shelling (Fig. 4). The shell is a fatigue crack usually originating from an isolated inclusion but which does not pose the risk of rail failure, and shells are not classified as defects for safety purposes. A propagating detail fracture begins to be ultrasonically detectable when it covers about 10% of the railhead cross-section area and can be detected with virtual certainty at 30% of the head area. The size at which a detail fracture can break the rail varies from 10% of the head area in extreme circumstances to 80% of the head area for normal operations on tangent track. Breaks usually give immediate warning by interrupting the track signal circuit. Breaks that occur under a train pose the risk of derailment, however, particularly on the outside rail in curved track. Detail fractures presently comprise about 25% of typical rail defect populations but can account for as much as 75% in CWR track. The detail fracture is thus expected to become the dominant rail defect as the percentage of CWR increases.

Shells and detail fractures have been extensively studied because of their effects on railroad economics as well as safety. These studies have included attempts to predict nucleation life for the originating shells [9–11], stress [12] and stability [13] models that attempt to explain the branching phenomenon, and early fracture mechanics estimates for crack growth life [14]. The early life estimates suggested that detail fracture growth rates would be strongly sensitive to small changes of residual stress in the railhead; these stresses have been measured [12], and work is now in progress to develop a method for predicting the rail residual stress field [15].

The results of four-point bending static tests of rails containing detail fractures (Fig. 5) have suggested that these defects can be modelled as penny cracks [4]. With the exception of one data point believed to be the result of a load calibration error, the measured strengths were correlated with a calculation based on the Sneddon formula for the stress-intensity factor of a circular penny crack in an infinite medium [16]. The strength was calculated from the bending stress corresponding to a point 25.4 mm (1 in.) below the top of the rail, the approximate height of the centers of typical medium to large size detail fractures. This value was taken as an equivalent uniform remote tensile stress for substitution in the Sneddon formula. The two trend lines in Fig. 5 correspond to the published values of 38.5 and 27.5 MPa $\sqrt{\text{m}}$ (35 and 25 ksi $\sqrt{\text{in.}}$) for the static and dynamic fracture toughness of rail steel [17]. The model tends to follow the test data for small and medium size detail fractures; the scatter in the test data is believed to reflect variations of residual stress not accounted for in the calculation. For the larger sizes exceeding 50% of the railhead area, some of the data points fall well below the trend lines. This is not unexpected, since large detail fractures often break out on the gage face and running surface of the rail. Such defects should behave more like corner cracks than embedded penny cracks, with consequent increase in the stress-intensity factor and decrease in static strength for the given crack size.

Fatigue crack growth behavior was investigated by installing several rails containing detail fractures in a tangent section of test track at the TTC, where the defects were subjected to typical heavy haul train loads. At the time of the experiment, the test train reversed direction at intervals of approximately 0.91 million gross metric tons (1 million gross tons). This unique operation created a pattern of ridges on the test defect crack growth surfaces, facilitating the reconstruction of crack size as a function of tonnage. These results were recently reported together with a summary of the applicable load, stress, and temperature

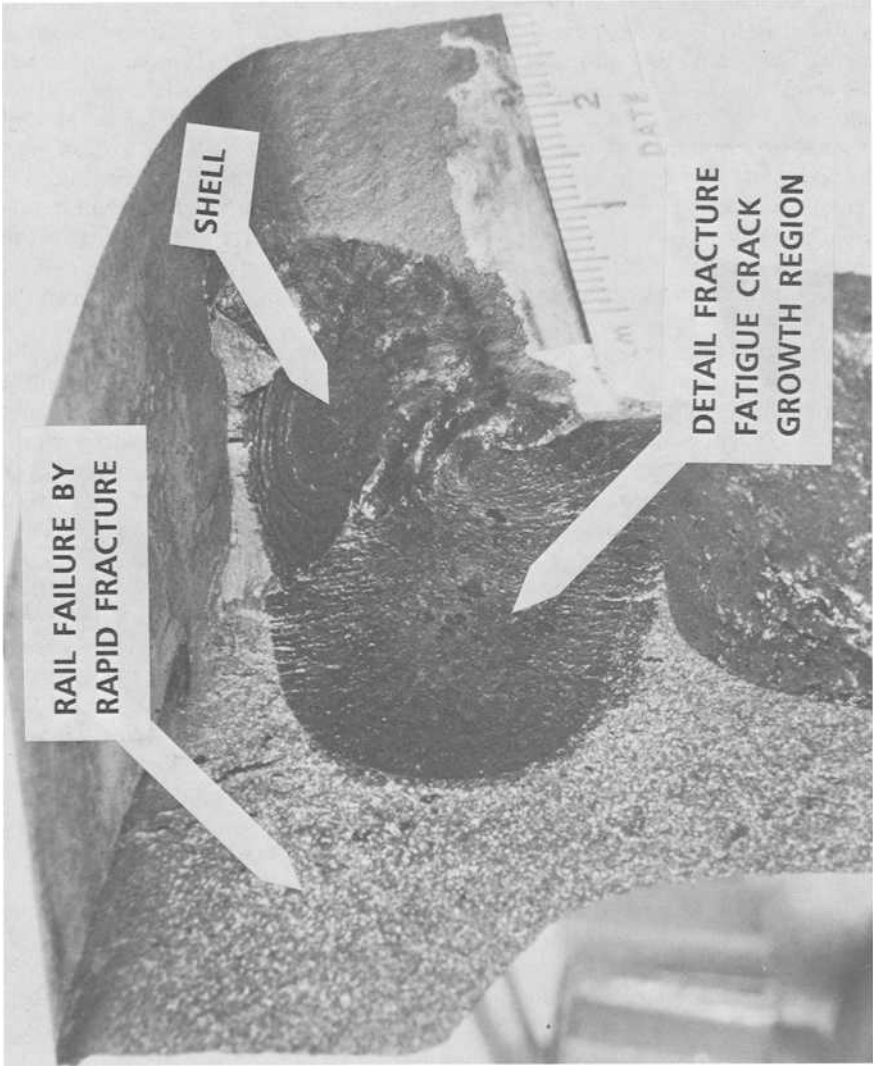


FIG. 4—Rail cut away to show shell origin of detail fracture.

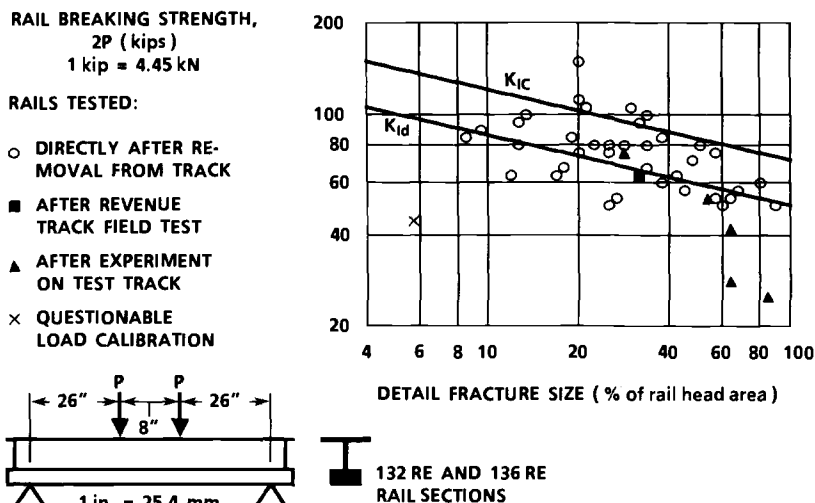


FIG. 5—Comparison of theoretical and experimental rail breaking strength.

descriptions [18]. The environment summary for one rail (test rail No. 1) included measurements of residual stress, and the flaw in this rail grew from 12 to 80% of the head area during the test. Test rail No. 1 thus provides a good data base for evaluation of crack growth models.

Further experimental work was also pursued in the laboratory to investigate the effects of load sequence on crack growth in rail steel. The reason for concern about possible sequence effects can be shown by consideration of the schematic stress cycle pattern shown in Fig. 6.

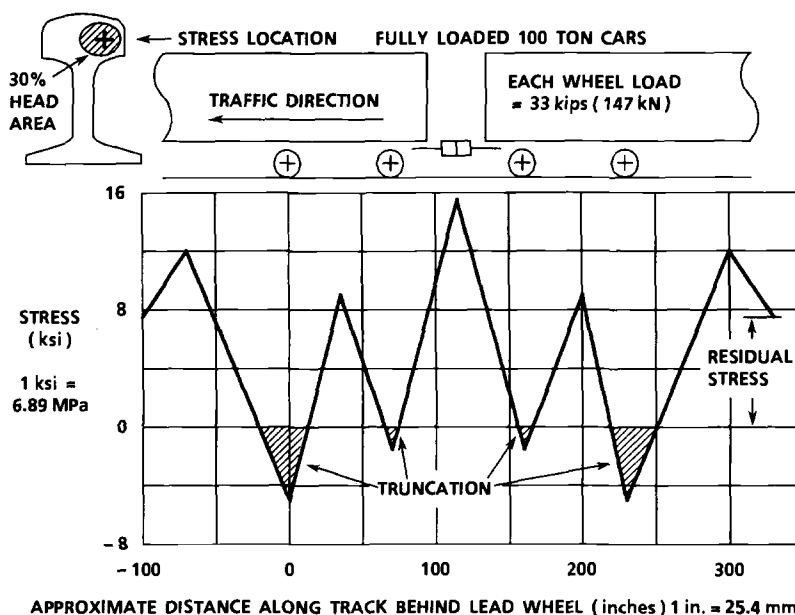


FIG. 6—Representative stress cycle pattern for rail head (1 ton = 0.91 metric tons).

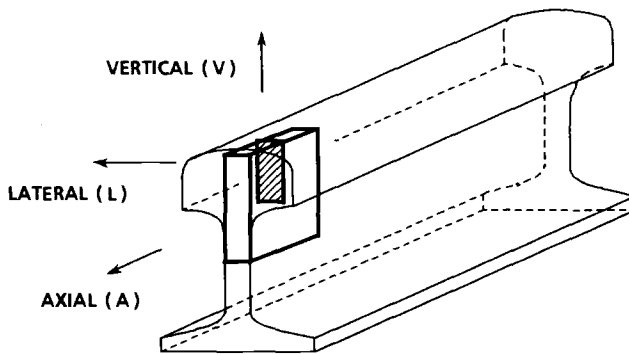


FIG. 7—Axial-vertical orientation of railhead-web CT specimen.

This pattern illustrates the minimum-maximum sequence for a group of four wheels under two adjacent heavy freight cars. Reading the graph from left to right gives the sequence at a fixed rail cross section as the cars travel from right to left. The cycles are biased by a 51.7-MPa (7.5-ksi) mean stress, which represents the average tensile residual stress that would be relieved by a detail fracture covering 30% of the railhead area. One can argue, based on superposition, that the mean relieved stress is equivalent to a mean remote tensile stress as far as the Sneddon formula is concerned. This approach cannot account for stress redistribution that may occur in the actual rail, but the approximation can be useful for engineering estimates if it is properly validated.

The conventional practice for calculating crack growth life for stress spectra like the Fig. 6 pattern is to assume crack closure for the compressive stresses; that is, some of the stress ranges are reduced by truncating the shaded areas. However, the spectrum might actually affect rail steel by creating a tensile or compressive crack opening stress (retardation or acceleration, respectively). Laboratory experiments were consequently performed in accordance with the ASTM Test for Plane-Strain Fracture Toughness of Metallic Materials (E 399-83) on compact tension (CT) specimens machined from rails in the orientation shown in Fig. 7. These specimens were subjected to a typical heavy haul train stress spectrum augmented by 103 MPa (15 ksi) to represent residual and thermal stress, and the stress-to-load conversion factor was changed at the end of each block to simulate the environment of an embedded penny crack [19].

The results of these tests appeared to match the rail No. 1 field test over part of its crack growth regime, and a preliminary comparison with a conventionally truncated calculation suggested a mild acceleration effect. Therefore, crack growth models that do not account for load sequence ought to predict somewhat longer life than was measured in the field test if conventionally truncated and equal or somewhat shorter life if not truncated.

The penny-crack model mentioned earlier was applied to the rail No. 1 test data, with the stress spectrum truncated as shown in Fig. 6. The material crack growth rate was modeled as a power law in the stress-intensity factor range with a sharp threshold cutoff and a nonlinear stress ratio effect [18] to match the results of constant-amplitude tests with rail steel CT specimens of the Fig. 7 orientation [20].³ The application accounted only for vertical loads because the lateral loads that freight car wheels exert on tangent track are generally too small to pose any risk of derailment.

³ Ref 18 incorrectly associates the stress ratio effect with tests *in vacuo*. The effect was actually reported [20] for tests in moist air.

As can be seen in Fig. 8, this first attempt to correlate a fracture mechanics model with test rail No. 1 test data was not successful. The failure spurred a thorough reexamination of the test environment summaries, the material crack growth rate parameters, and the penny-crack model itself. No obvious errors were found, nor could the acceleration effect that had been measured [19] but not included in the model be invoked to account for more than a small part of the discrepancy.

A better result was obtained by including the effect of lateral loads on the stress environment. Assuming a ratio of lateral to vertical load (L/V) equal to 0.05 produced a crack growth curve that tended to follow the rail No. 1 test up to a flaw size of about 40% of the railhead area (Fig. 9). Although such small lateral loads do not affect derailment limits, they do induce enough lateral bending to increase the severity of the cyclic stress environment and reduce crack growth life. Taking $L/V = 0.05$ in the crack growth model is logical, since freight car wheels are manufactured with a 1:20 taper on the tread (Fig. 10); that is, they tend to operate at or near $L/V = 0.05$ when contacting rail on tangent track. The penny-crack model had thus exposed an error of omission in the assumptions about the service environment.

The remaining discrepancy at the larger flaw sizes was resolved by substituting a quarter-circular corner crack for the penny crack. Figure 11 illustrates two cases in which the change is made at different flaw sizes: one at 40% and one at 50% of the head area. The second case would be consistent with the static test results (Fig. 5), but the first agrees better with the rail No. 1 test results. The model in which the change is delayed to 50% of the head area could probably be made consistent with the rail No. 1 test by incorporating stress-sequence-dependent acceleration in the rate equation.

Making the transition at 40% of the head area without the complications of history dependence is a convenient approximation. This form of the model is now being tested against other available data and will eventually be applied to the estimation of safe crack growth life in revenue service situations.

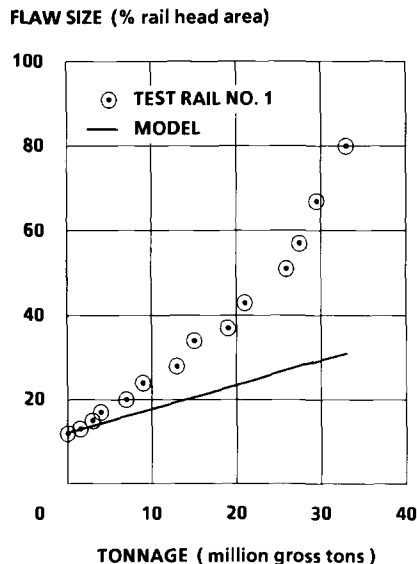


FIG. 8—First comparison of penny-crack model prediction with measured crack growth for test rail No. 1 (1 ton = 0.91 metric tons).

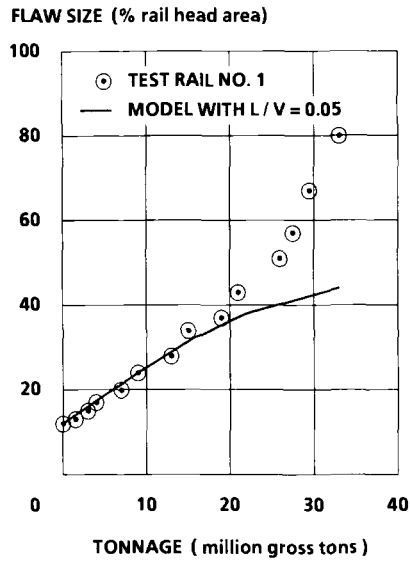


FIG. 9—Comparison with lateral loads included in the model (1 ton = 0.91 metric tons).

For example, the model can be applied to investigate the effect of track curvature as follows. Since the vehicle wheelsets are unable to maintain pure rolling motion while negotiating curves, each wheelset exerts lateral creepage forces on the rails. For the outside rail in a curve, tests and dynamic model simulations have shown that L/V for the lead wheelset of each truck can be from four to ten times the tangent track value, while L/V for the trailing wheelset tends to remain at the tangent track value [21]. Figure 12 illustrates the effect of assuming that the rail No. 1 defect was tested in 3° and 5° curves instead of

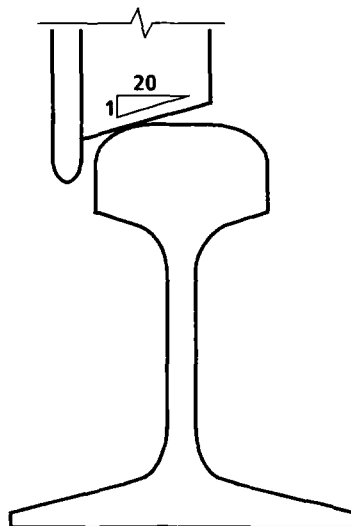


FIG. 10— Freight car wheel taper.

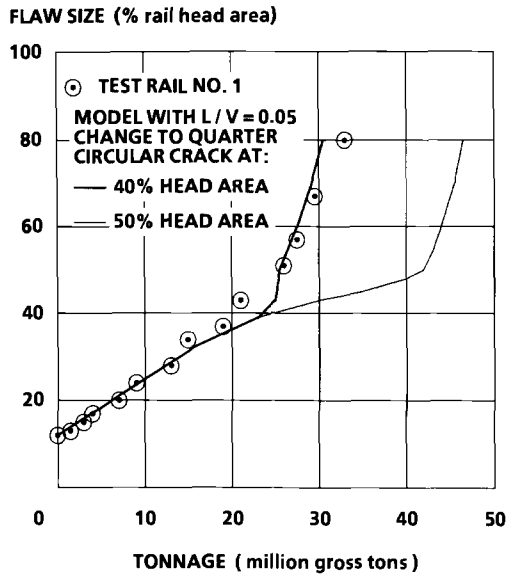


FIG. 11—Results with lateral load and change of crack configuration (1 ton = 0.91 metric tons).

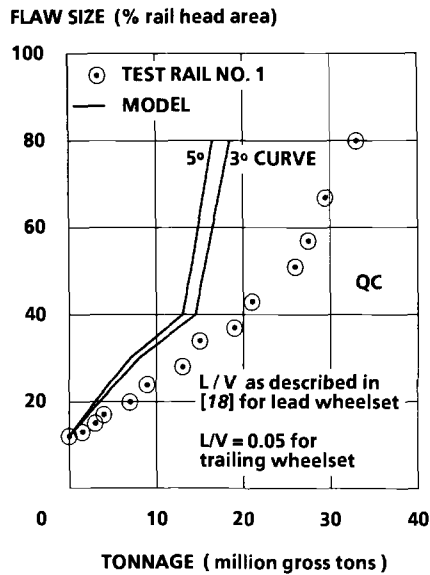


FIG. 12—Behavior predicted for defects in a curved track (1 ton = 0.91 metric tons).

tangent track, following the method outlined in Ref 18 for the prescription of L/V . The predicted trend agrees with field observations, which suggest that detail fractures in 5° curves can grow from 10 to 80% of the railhead area in half the tonnage required in tangent track or less [18].

Bolt Hole Cracks

Bolt hole cracks originate in rail joints at the corner between the rail web surface and the bolt hole inside diameter (ID). Bolt hole crack nucleation is believed to result from fretting fatigue when the bolt shank bears against the hole ID in a loose joint. Bolt hole cracks generally grow on planes at approximately $\pm 45^\circ$ from the vertical until the crack front approaches the railhead or base (Fig. 13). A propagating bolt hole crack may separate a short length of the railhead. Wheel loads can eject the broken piece without interrupting the track signals, and the loss of running surface can cause a derailment. Bolt hole cracks presently account for about half the rail defects in older jointed track, but their incidence is expected to decline as older track is rerailed with CWR. The bolt hole crack will not disappear, however, because CWR must still be jointed at the ends of track signal blocks.

The transition from corner to through crack typically occurs at about 15-mm (0.6-in.) length, that is, about when the bolt hole crack penetrates the rail web thickness. This is also the size at which ultrasonic test equipment begins to be effective in detecting bolt hole cracks. Upward planar propagation generally continues until the crack length reaches 38 to 51 mm (1.5 to 2 in.). At this point the increased thickness of the head-web fillet reduces the live stresses, and the crack growth rate decreases. If still undetected, a bolt hole crack may undulate slowly between the fillet and web or it may turn upward through the railhead and quickly break out to the running surface. Because of the uncertainty, a bolt hole crack is considered to have attained critical length when it reaches the head-web fillet.

The alternating transverse shear due to bending experienced by a rail web during a wheel passage is equivalent to alternating tension and compression on the $\pm 45^\circ$ bolt-hole-crack growth planes. The stress concentrating effect of the hole and the prying effect of the joint bar contact loads, Q , also contribute to the crack driving stress. A recent laboratory experiment simulated bolt hole crack growth with fixtures designed to supply the contact loads, Q , and the results were correlated with the stress-intensity factor for a circular hole with a radial crack in a wide plate [22]. This study showed that the stress-intensity factor was nearly independent of the crack length between detectable and critical size, suggesting that first-passage statistics of extreme wheel loads should be considered in the determination of the safe life for bolt hole cracks.

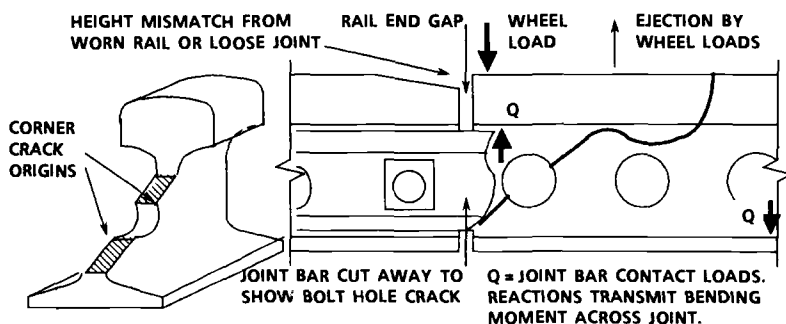


FIG. 13—Bolt hole crack behavior.

A calculation based on the test results and a simplified spectrum of maximum static freight car wheel loads gave a life of about 9.1 million gross metric tons (MGMT) [10 million gross tons (MGT)] for growing a bolt hole crack from detectable to critical size. One would expect shorter lives in track, where bolt hole cracks are subjected to the dynamic effects of wheels traversing rail end gaps and height mismatches, the eccentricity of wheel-rail contact, and lateral loads. In a 1985 field test at the TTC, however, ten rails with bolt hole cracks subjected to 22.7 MGMT (25 MGT) with tight joints and 22.7 MGMT (25 MGT) with loose joints showed no evidence of crack growth during the test. The fact that these rails had been previously removed from other track locations and reassembled with different joint hardware is suspected to have caused the lack of crack growth, but there is as yet no physical explanation for the anomalous behavior. Other field tests now in progress at the TTC are providing data on the growth of undisturbed bolt hole cracks and on typical dynamic load and stress environments as functions of rail end gap, height mismatch, and train speed.

Vertical Split Heads

Vertical split heads occur in the center or the gage side of the rail head and appear to originate from inclusion stringers. Rail test equipment can sometimes detect vertical split heads as short as 51 mm (2 in.), but the general relation between crack length and detection probability is not known. Critical crack length is also difficult to define. Vertical split heads as long as several feet have been found in rails that supported traffic without incident, while some flaws as short as 152 mm (6 in.) have broken off the gage side of the rail head and caused derailments. Vertical split heads comprise about 25% of the rail defects in typical populations, but clean steelmaking practices in new rail may reduce the incidence.

Little is known at present about the crack growth behavior of vertical split heads. Fractographic studies have been performed [23], but there are as yet no field test results from which growth rates can be determined. The fractographic studies suggest that the length of the stringer colony determines the length of the vertical split head, that lengthwise crack growth consists of sporadic cleavage jumps, and that fatigue crack growth commences during the cleavage phase. Figure 14 schematically illustrates the fatigue progression: a nonplanar propagation in the rail cross section.

The crack surface curvature suggests propagation normal to the principal in-plane tensile residual stress in the railhead. Values of 207 to 276 MPa (30 to 40 ksi) have been measured for this stress [12]. Live in-plane compressive stresses from wheel-rail contact may complete the fatigue cycle for the upper crack front, but the lower crack front lies well below the

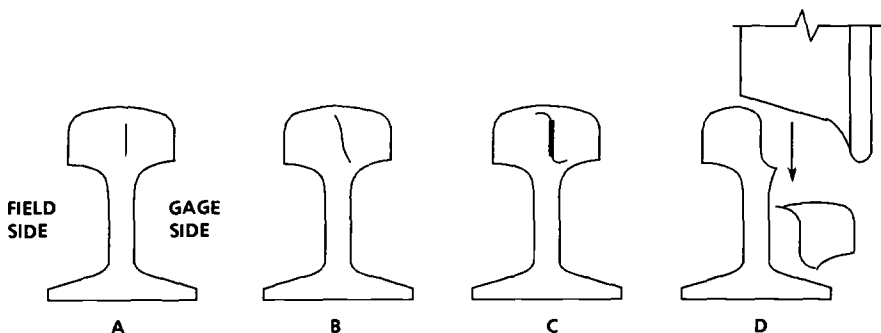


FIG. 14—Vertical split-head progression: (a) defect originates at inclusion stringers; (b) crack front deviates from the vertical plane; (c) the original defect opens; and (d) the rail fails.

zone of significant contact stress. It appears that the live stress on the lower crack front may be Mode II shear associated with transfer of the wheel load from the railhead to the web. As yet no attempt has been made to construct a fracture mechanics model of the vertical split head.

Effects of Modern Rail-Making Practices

Modern rail-making practice seeks to improve wear resistance and tighten geometrical tolerances. Wear resistance is often obtained via premium alloy chemistry, which increases strength as well as hardness. This can lead to fracture-sensitive rail in some cases. Another aspect of alloy chemistry, the control of inclusions, is also beginning to be examined for its effect on rail economic life.

Residual Stress and Fracture Resistance

The residual stresses discussed earlier result from the cold work of wheel contact loads and are concentrated in the railhead. Rails may also acquire residual stress from straightening just after manufacture. The different radiative efficiencies of the head and base cause a rail to cool nonuniformly after hot rolling, while the material is changing phase from austenite to pearlite. The associated volume and strength changes camber the rail, and cold work is needed to reduce the camber.

In the United States, older bolted-joint rail was visually inspected, and only rails having excessive camber were straightened. The straightening was done in a three-point arbor press with vertical bending loads applied at two or three discrete manually set locations. The straightening stresses were thus confined to localized regions in a small percentage of the older rail population. Tighter camber tolerances for CWR subsequently led to automated roller straightening, which has been adopted worldwide and is applied to the entire production run. Each rail is engaged in a series of rollers that apply several cycles of vertical bending cold work uniformly to the entire rail, except for 0.5 to 0.75 m (18 to 30 in.) at each end (Fig. 15).

Measurements have shown that the roller-straightening residual stress field extends throughout the rail cross section [24,25]. This field characteristically includes a parabolic axial stress in the vertical center plane and compressive vertical stress at the web surfaces. The web surface stress is believed to be balanced by internal tension, but the distribution through the web thickness is difficult to measure. Figure 16 illustrates the roller-straightening stress field and compares it with the axial component of the service-induced residual stresses.

Residual stress from roller straightening was found to have been a contributing factor in

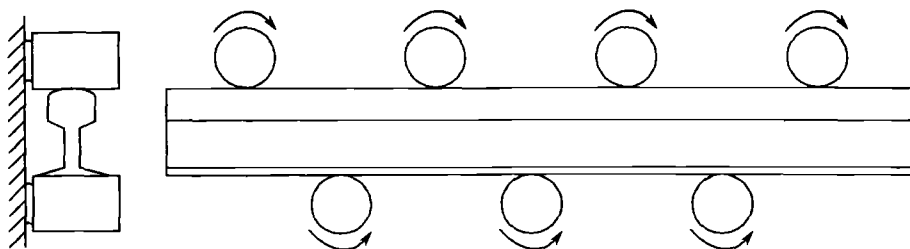


FIG. 15—Roller straightening of a rail.

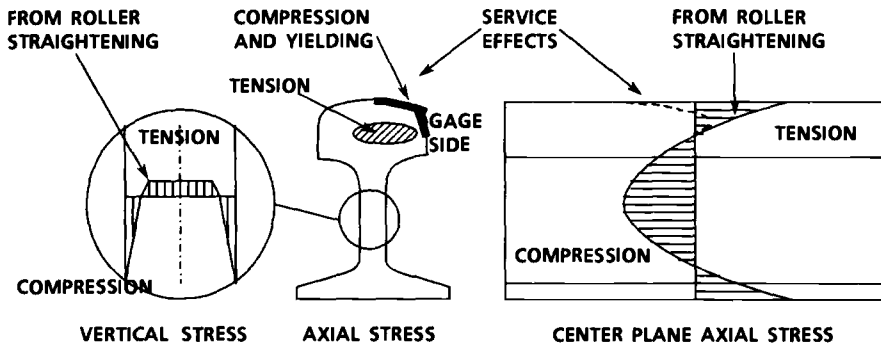


FIG. 16—Some features of rail residual stress fields.

an unusual rail failure involved in a 1983 accident in Texas that resulted in 4 deaths and 24 serious injuries [26]. The immediate cause of the failure was a quench crack left in the rail end by improper flame cutting of the rail to make a temporary repair of an unrelated defect. The rail failed under an Amtrak train; the failure was a rapid fracture through approximately 10 m (33 ft) of the rail web with several branch cracks to the head and base. The rail in question was a premium-alloy rail with less than one month of service before the accident. The unusual length of the rapid fracture was attributed to a combination of high roller-straightening residual stress and low material fracture toughness. European tests on new rails of several compositions later showed that roller-straightening residual stress levels and fracture sensitivity do tend to increase with rail strength and hardness [27]. Work now in progress in the United States is aimed at the development of a specification that can be applied to qualify production heats of rail for resistance to this type of web fracture [28]. Specimen tests for fracture arrest toughness (K_{Ia}) have not revealed any significant differences between standard and premium-alloy rail steel compositions. However, the results of static CT specimen tests performed in accordance with ASTM Test E 399-83 have shown that rails sensitive to web fracture tend to have lower K_Q values and less difference between K_Q and K_{max} than other alloys [29]; Fig. 17 summarizes these results.

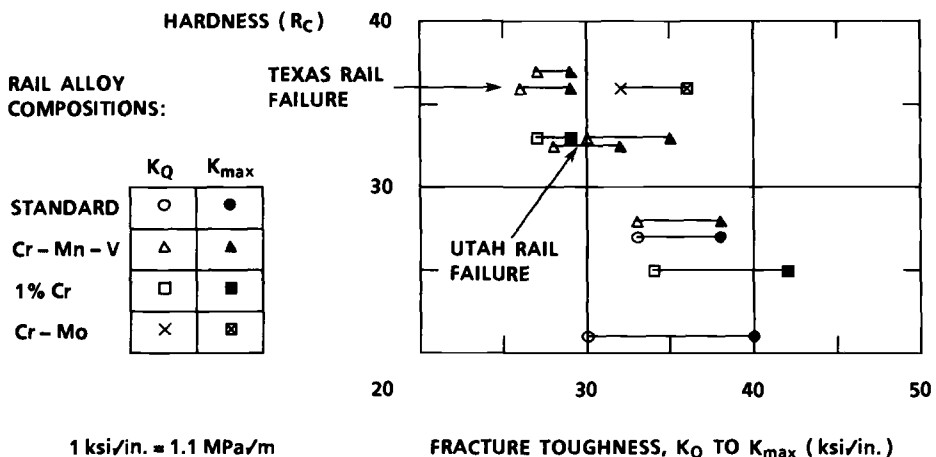


FIG. 17—Rail fracture resistance versus hardness.

Clean Steel Practice

Rail makers in the United States are now adopting clean steel practice in response to foreign competition. Aluminum deoxidizer is added earlier in the steelmaking process, and argon stirring with a flux of high calcium and fluoride content is used to remove manganese sulfide and aluminate impurities from the heat. Clean steel practice has the potential to increase the economic life of rail.

Rail economic life is currently limited by dry wear, the dry condition being the most prevalent on revenue tracks in the United States. Rail lubrication, which is presently confined to the tighter curves on most tracks, is now being actively considered for general application to reduce fuel costs as well as to increase rail wear life. For example, field tests at the TTC have shown that older standard composition (Rockwell-C hardness 25) rail in a 5° curve subjected to fully loaded 91-metric-ton (100-ton) capacity traffic reaches its head wear condemning limit at about 73 to 91 MGMT (80 to 100 MGT) in the dry condition, but will last from 455 to over 910 MGMT (500 to over 1000 MGT) when lubricated [2]. Similar benefits are envisioned for less tightly curved track, tangent track, and lighter traffic.

The extent to which such benefits can be realized depends on the crack nucleation life, which is expected to become the limiting factor if widespread lubrication is adopted. Figure 18 illustrates the problem by comparing crack nucleation data for light traffic [2] with heavy traffic data and with current practices for rail defect inspection. Each line on the plot corresponds to one section of track for which detailed records were kept on crack occurrence versus cumulative tonnage after installation of new rail. The two shaded regions reflect the range of railroad engineers' practices and perceptions with respect to testing rail for defects. The lower left region encompasses normal conditions, in the sense that current rail test schedules are able to keep pace with the rates of defect occurrence in these tracks. The upper right region represents combinations of accumulated tonnage and defect rate that motivate decisions to rereil those sections of track on which rereiling has not been previously dictated by wear.

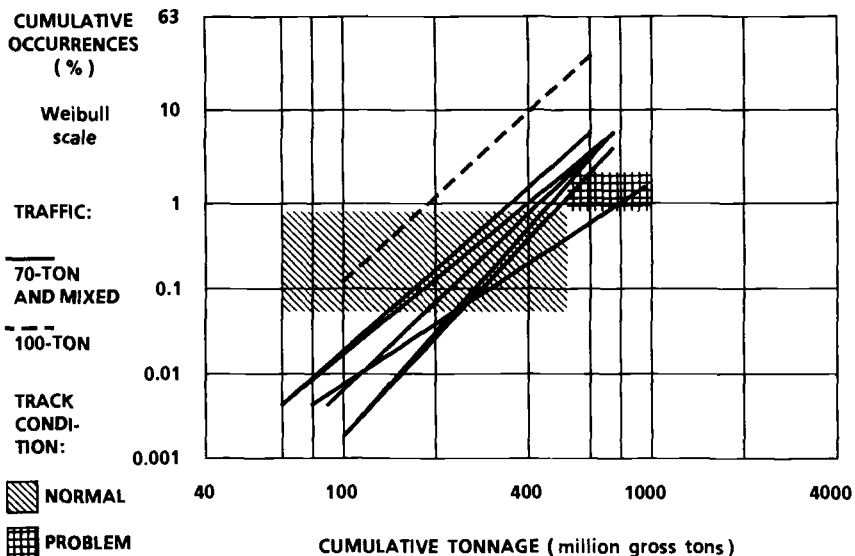


FIG. 18—Weibull plot of rail fatigue crack nucleations (1 ton = 0.91 metric tons).

The practices and perceptions of the railroads are apparently well adjusted to the effects of the type of traffic that has prevailed on the freight network in the United States from the 1950s to the present. Hence, crack nucleation is not perceived as a life-limiting factor if rail wear life increases. Railroad operations are expected to become increasingly dominated by fully loaded 91-metric-ton (100-ton) capacity traffic in the near future, however, and the available data for this case suggests that fatigue may quickly replace wear as the economic limit on rail life.

The crack nucleation data shown in Fig. 18 are for older rail that was made without clean steel practice. Laboratory tests have demonstrated an increase by a factor of two to three in the first percentile fatigue life of clean versus conventional rail steel [30], suggesting that clean steel practice can reap the benefits offered by lubrication. The fatigue life results in these tests were also correlated with increased yield and tensile strength, however, which suggests that the connection with clean steel practice might be fortuitous.

There is as yet too little field experience to demonstrate the fatigue performance of clean steel rails. Nevertheless, one should expect some improvement in the crack occurrence statistics—in particular, a declining incidence of shells and vertical split heads accompanying the decline of inclusion content. Conversely, clean steel practice is not expected to have any direct effect on crack growth rates.

Effects of Increased Wheel Loads

The idea of increasing the maximum freight car load allowed for interchange service is appealing because of the obvious gain in productivity. At the current 91-metric-ton (100-ton) capacity, a 110-car unit train can haul 10 000 metric tons (11 000 tons) of coal with six locomotives pulling about 14 545 gross metric tons (16 000 gross tons) and a crew of four. If the capacity is increased to 114 metric tons (125 tons), the same number of locomotives and crew can haul 12 500 metric tons (13 750 tons) of coal at about 17 300 gross metric tons (19 000 gross tons) over many existing routes. The price that must be paid is an increase of static freight car wheel load from the present maximum of 147 to 178 kN (33 to 40 kips).

Freight car designers compensate for increased wheel load by increasing the wheel diameter. For example, the newer 91-metric-ton (100-ton) capacity cars in the present fleet run on 0.91-m (36-in.) diameter wheels, whereas the older 64-metric-ton (70-ton) cars are equipped with 0.84-m (33-in.) wheels. Wheel diameter adjustment is generally based on elastic calculations of stress in accordance with the Hertz model for contact between two circular cylinders at right angles [31]. The interpretation of this model for wheel-rail contact (Fig. 19) is a use-

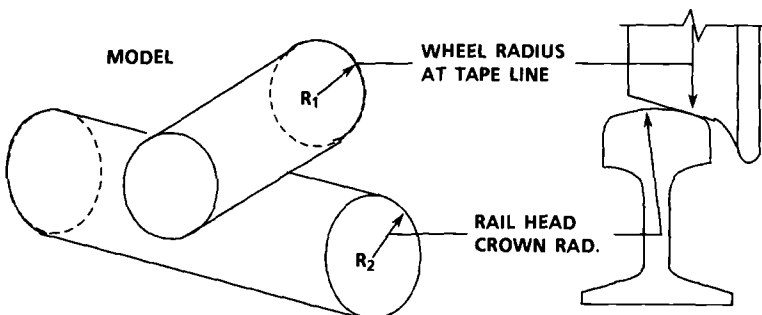


FIG. 19—Railroad engineering interpretation of the Hertz contact model.

ful approximation for design calculations. However, the Hertzian contact stresses are well above the yield strength of rail steel in a shallow layer near the running surface and are thus not a reliable guide to long-term rail performance.

Cyclic plastic flow in the running layer creates the service-induced residual stress field that affects the nucleation and growth of shells, detail fractures, and vertical split heads. Few measurements of this stress field are available [4,12,18], and methods for prediction are only beginning to be developed [15]. Prediction capabilities are also inherently hostage to the artifacts of contact stress models. For example, a recent study shows that predictions of shell nucleation life are dominated by the contact stress when the crossed-cylinder model is used and that the results are sensitive to the artifact of the design crown radius, which does not reflect the plastically deformed crown radius of a rail in service [11].

The experimental data, which pertain to light traffic with some admixture of 91-metric-ton (100-ton) traffic, suggest that heavy (132 RE and 136 RE) rail might attain a shakedown state between about 70 and 270 MGMT (80 and 300 MGT). The shakedown condition is difficult to confirm by experiment, but one of the goals of the current research on analytical methods [15] is to predict the existence or absence of shakedown states. We hope that such analysis can ultimately be used to assess the effects of increased wheel loads on existing rail.

A recent field survey and test program suggest that the effects of plastic deformation in the running layer cannot be predicted by the simpler design approaches [6]. This study examined a line that had carried 114-metric-ton (125-ton) coal cars overloaded to 118 metric tons (130 tons) in captive service. The cars were equipped with 0.97-m (38-in.)-diameter wheels, and the static wheel load was about 184 kN (41.4 kips) in the overload condition. The line was rerailed with 119 RE rail (a medium section) just before the start of this service. The study revealed that plastic deformation of the inside rail on some curves with excess superelevation had proceeded to the point of severe lateral flow and shear tearing about 16 mm ($\frac{3}{8}$ in.) below the running surface after 55 MGMT (60 MGT). Comparative study of the same rail section carrying interchange traffic suggested that about 270 MGMT (300 MGT) would be required to create similar conditions under 91-metric-ton (100-ton) traffic.

While the line studied in this case reflects an extreme condition, the results of the study raise two important questions: will rail that shakes down under present interchange loads also shake down under increased wheel loads, and what effect will increased residual stresses have on the safe crack growth life? While an increase in the residual stress level will not affect the live stress ranges, it changes the stress ratio and may change the crack opening stress. For cracks that break open to the atmosphere while still growing in fatigue, there is also some evidence to suggest that the rate of growth depends on the stress ratio [20].

Concluding Remarks

The practical application of fracture mechanics to problems in rail structural integrity poses many interesting challenges. None of the important types of rail fatigue crack satisfies the fundamental self-similar growth condition required by the theory of linear elastic fracture mechanics, yet models based on this theory must be applied to have any hope of bringing fracture mechanics to bear on railroad engineering practice.

In this light it is astonishing that the Sneddon penny crack appears to provide a good basis for modeling detail fractures, which are located close to free boundaries at the running surface and gage face of the rail. Some of the surprise disappears upon examination of supporting data, namely, the existence of large compressive residual stresses in the boundary regions and the observed tendency of the flaw to grow most rapidly on the interior segment of the crack front. Other fortuitous circumstances may facilitate the application of a linear

fracture mechanics model to bolt hole crack growth, but the prospect for vertical split heads is less hopeful.

Any simplified model is subject to misleading artifacts. The available models for live contact stress have been identified as artifact producers for the wheel-rail contact problem. Such artifacts have already affected estimates of crack nucleation life and will no doubt similarly affect crack growth life calculations for vertical split heads.

Inaccurate environment description complicates the job of fitting a simplified model to a real crack growth problem. In the case of the detail fracture, early estimates of the environment approximated the residual and live stresses. The approximations attained the status of received truth for a time, while the research emphasized refinements of the penny crack model. Later comparison of the assumptions with field data revealed first-order errors in the environment description, whereas the model refinement was addressing second-order effects. This example illustrates a weakness that engineers should guard against: the tendency to concentrate on the easy modeling aspect of a problem while neglecting the difficult aspect of data acquisition.

Even a well-calibrated fracture mechanics model is not the total answer to the question of safe crack growth life because service environments generally defy simple deterministic description. The question has many possible answers in the case of the detail fracture. The field test results per se establish a safe life for detail fractures growing in well-maintained tangent track loaded by well-maintained cars in relatively mild weather. Enough is now known about variations in service environments to identify other important situations for which the safe life may be quite different: for example, bolted-joint track versus CWR (different thermal stress), CWR in mountain territories and regions of severe midcontinent climate (extreme thermal stress), curved track (high lateral loads from lead wheels), and interchange vehicle maintenance (extreme dynamic loads from out-of-round wheels). The choice of safe crack growth lives to be used as bases for inspection intervals must ultimately depend on the judgement of risk as much as fracture mechanics calculation of narrowly defined performance measures.

References

- [1] *Rail Steels—Developments, Processing, and Use*, ASTM STP 644, D. H. Stone and G. G. Knupp, Eds., American Society for Testing and Materials, Philadelphia, 1978.
- [2] Steele, R. K. and Reiff, R. P., "Rail: Its Behavior in Relationship to Total System Wear," Paper No. 82-HH-24, *Proceedings*, Second International Heavy Haul Railway Conference, Colorado Springs, CO, 1982.
- [3] Orringer, O. and Bush, M. W., "Applying Modern Fracture Mechanics to Improve the Control of Rail Fatigue Defects in Track," *American Railway Engineering Association Bulletin* 689, Vol. 84, 1983, pp. 19–53.
- [4] Orringer, O., Morris, J. M., and Steele, R. K., "Applied Research on Rail Fatigue and Fracture in the United States," *Theoretical and Applied Fracture Mechanics*, Vol. 1, No. 1, 1984, pp. 23–49.
- [5] Cerny, L. T., "Choosing Freight Cars Which Maximize Profit (Considerations Involved in 79,000 lb. Axle Loads and Double Stack Container Trains)," *American Railway Engineering Association Bulletin* 703, Vol. 86, 1985, pp. 412–415.
- [6] Magee, G. M., "Rail Fractures on the Field Side of the Low Rail on Curves Under Heavy Axle Loads," Report No. R-546, Association of American Railroads Research and Technical Center, Chicago, IL, January 1985.
- [7] *Code of Federal Regulations*, Title 49, Transportation, Part 213.113, "Defective rails," 1982.
- [8] Davis, D. D., et al., "The Economic Consequences of Rail Integrity," *Proceedings*, Third International Heavy Haul Railway Conference, Vancouver, BC, Canada, 1986.
- [9] Abbott, R. A. and Zaremski, A. M., "On the Prediction of the Fatigue Life of Rails," *American Railway Engineering Association Bulletin* 661, Vol. 79, 1978, pp. 191–202.

- [10] Perlman, A. B., et al., "Rail Flaw Growth Investigations," *American Railway Engineering Association Bulletin* 688, Vol. 83, 1982, pp. 536–550.
- [11] Jeong, D. Y., et al., "Beam Theory Predictions of Shell Nucleation Life," *Proceedings*, Second International Symposium on Contact Mechanics and Wear of Rail/Wheel Systems, University of Rhode Island, Kingston, RI, 1986.
- [12] Rice, R. C., Rungta, R., and Scott, P. M., "Post-Service Rail Defect Analysis," Battelle-Columbus Laboratories, Columbus, OH, Fourth Technical Report, Contract DOT-TSC-1708, June 1984.
- [13] Keer, L. M., Farris, T. N., and Steele, R. K., "On Some Aspects of Fatigue Crack Growth in Rails Induced by Wheel-Rail Contact Loading," *Proceedings*, Second International Symposium on Contact Mechanics and Wear of Rail/Wheel Systems, University of Rhode Island, Kingston, RI, 1986.
- [14] Besuner, P. M., "Fracture Mechanics Analysis of Rails with Shell-Initiated Transverse Cracks," *Rail Steels—Developments, Processing, and Use*, D. H. Stone and G. G. Knupp, Eds., *ASTM STP 644*, American Society for Testing and Materials, Philadelphia, 1978, pp. 303–328.
- [15] Orkisz, J., et al., "Recent Progress in the Development of a Rail Residual Stress Calculation Method," *Proceedings*, Second International Symposium on Contact Mechanics and Wear of Rail/Wheel Systems, University of Rhode Island, Kingston, RI, 1986.
- [16] Sneddon, I. N., "The Distribution of Stress in the Neighborhood of a Crack in an Elastic Solid," *Proceedings of the Royal Society, Series A*, Vol. 187, 1946, p. 229.
- [17] Barsom, J. M. and Imhoff, E. J., Jr., "Fatigue and Fracture Behavior of Carbon Steel Rails," *Rail Steels—Developments, Processing, and Use*, D. H. Stone and G. G. Knupp, Eds., *ASTM STP 644*, American Society for Testing and Materials, Philadelphia, 1978, pp. 387–413.
- [18] Orringer, O., Morris, J. M., and Jeong, D. Y., "Detail Fracture Growth in Rails: Test Results," *Theoretical and Applied Fracture Mechanics*, Vol. 5, No. 2, 1986, pp. 63–95.
- [19] Journet, B. G. and Pelloux, R. M., "A Methodology for Studying Fatigue Crack Propagation Under Spectrum Loading: Application to Rail Steels," *Theoretical and Applied Fracture Mechanics*, Vol. 8, No. 2, 1987, pp. 117–124.
- [20] Scutti, J. J., Pelloux, R. M., and Fuquen-Moleno, R., "Fatigue Behavior of a Rail Steel," *Fatigue of Engineering Materials and Structures*, Vol. 7, No. 2, 1984, pp. 121–135.
- [21] Weinstock, H., "Vehicle Track Interaction Studies for Development of Track Performance Specifications," *Proceedings*, British Rail/Association of American Railroads Vehicle Track Interaction Symposium, Princeton, NJ, 1984.
- [22] Mayville, R. A., Hilton, P. D., and Pierce, D. C., "An Analytical and Experimental Study of Fatigue Crack Growth from Rail End Bolt Holes," Interim Report on Contract DTRS-57-80-C-00136, Arthur D. Little, Inc., Cambridge, MA, February 1984.
- [23] Mayville, R. A., "Metallurgical and Fracture Surface Analysis of Vertical Split Head Defects," Interim Report on Contract DTRS-57-80-C-00136, Arthur D. Little, Inc., Cambridge, MA, May 1985.
- [24] Konyukhov, A. D., Reikhardt, V. A., and Kaportsev, V. N., "Comparison of Two Methods for Assessing Residual Stresses in Rails," *Zavodskaya Laboratoriya*, Vol. 39, No. 1, 1973, pp. 87–89.
- [25] Deroche, R. Y., et al., "Stress Releasing and Straightening of Rail by Stretching," Paper No. 82-HH-17, *Proceedings*, Second International Heavy Haul Railway Conference, Colorado Springs, CO, 1982.
- [26] John, R. R., et al., "Task Force Report—Rail Failure Evaluation," U.S. Department of Transportation, Transportation Systems Center, Cambridge, MA, May 1984.
- [27] Gence, M., et al., "Possibilities of Improving the Service Characteristics of Rails by Metallurgical Means: Report No. 1—Factors Influencing the Fracture Resistance of Rails in the Unused Condition," D156 Committee, Office for Research and Experiments of the International Union of Railways, Utrecht, The Netherlands, October 1984.
- [28] Orringer, O. and Tong, P., "Investigation of Catastrophic Failure of a Premium-Alloy Railroad Rail," *Fracture Problems in the Transportation Industry*, P. Tong and O. Orringer, Eds., American Society of Civil Engineers, New York, 1985, pp. 62–79.
- [29] Jones, D. J. and Rice, R. C., "Determination of K_{Ic} Fracture Toughness for Alloy Rail Steel," Final Report to Department of Transportation, Transportation Systems Center, Battelle-Columbus Laboratories, Columbus, OH, November 1985.
- [30] Fowler, G. J., "Fatigue Crack Initiation and Propagation in Pearlitic Rail Steels," PhD thesis, School of Engineering and Applied Science, University of California, Los Angeles, CA, 1976.
- [31] Roark, R. J. and Young, W. C., *Formulas for Stress and Strain*, 5th ed., McGraw-Hill, New York, 1975, p. 517.

Elastoplastic Fracture

Three-Dimensional Crack-Tip Deformation in a Plastically Deformed Three-Point Bending Specimen

REFERENCE: Wu, X.-P. and Chiang, F.-P., "Three-Dimensional Crack-Tip Deformation in a Plastically Deformed Three-Point Bending Specimen," *Fracture Mechanics: Nineteenth Symposium, ASTM STP 969*, T. A. Cruse, Ed., American Society for Testing and Materials, Philadelphia, 1988, pp. 281-290.

ABSTRACT: A new technique of holospeckle interferometry using twin-plate recording has been developed in which three-dimensional crack-tip deformation within an area of 1 mm² can be mapped in detail. The resulting fringe has a sensitivity of 0 to 3 μm for out-of-plane displacement and 1.3 μm for in-plane displacement. The difficulty due to a difference in sensitivity between the hologram and specklegram techniques is eliminated by judiciously pairing the front (or back) plate of one holospecklegram with the back (or front) plate of another at different stages of loading. The technique was applied to a notched three-point-bending aluminum specimen under large-scale yielding. A three-dimensional crack-tip deformation field was obtained, and strain contours were plotted. This shows that the region directly above the crack experiences a relatively small amount of strain.

KEY WORDS: three-dimensional crack-tip deformation, elastic-plastic fracture, holography, speckle photography, sandwich holospecklegram, fracture mechanics

A clear understanding of the nature of crack-tip strain or of a displacement field is essential in establishing a proper criterion for crack initiation and growth. The problem is a complicated one, especially when the material is elastic-plastic and large-scale yielding is involved. Many analytical and numerical attempts [1-3] have been made to explain crack-tip deformation. The solved problems are treated in the condition of either plane stress [1,2], plane strain [1,2], or three-dimensional deformation [3]. The results depend on the assumptions made, and they are not all in agreement.

Experimentally, it is not easy to quantify the three-dimensional nature of crack-tip deformation, especially when plastic strain is involved. First of all, the photoelastic technique [4] is obviously not applicable because it assumes that the material behaves elastically and the birefringence obtained is aggregated through the thickness. The photoplasticity technique, on the other hand, is still immersed in the controversy of the precise nature of the relationship between birefringence and stress (or strain). The caustics method [5] is essentially a single-parameter technique wherein the three-dimensional information is lost. The in-plane moiré method [6], while very effective, yields no information on the out-of-plane displacement, and the shadow moiré method, which gives out-of-plane displacement, loses the in-plane information. Recent attempts [7] of combining both the in-plane and

¹ Visiting scholar from the Department of Mechanics, University of Science and Technology of China, Hefai, Anhui Province, China.

² Professor of mechanical engineering and director, Laboratory for Experimental Mechanics Research, State University of New York at Stony Brook, NY 11794.

shadow (or projection) moiré methods together have shown some promise, but so far the approaches are only effective in mapping the relatively far-field or global deformation of a cracked specimen. Holographic and classical interferometries have been applied to measuring the out-of-plane displacement surrounding a crack [8], whereas speckle photography has been employed in determining the in-plane displacement field [9].

In this paper, the authors introduce a novel technique called "sandwich holospeckle interferometry," in which both the in-plane and out-of-plane displacement fields can be recorded in a single recording. This technique can be applied to an area as small as 1 mm² at a crack tip, with a sensitivity of 0.3 and 1.3 μm for out-of-plane and in-plane displacement fields, respectively. We applied this technique to the measurement of three-dimensional crack-tip deformation of a notched three-point bending aluminum specimen under large-scale yielding.

Sandwich Holospeckle Interferometry

The method of speckle photography is essentially a technique for measuring in-plane displacement, whereas the method of holographic interferometry is most effective when applied to the measurement of out-of-plane displacement. A number of approaches have been developed to combine the two methods. Adams and Maddux [10] suggested a scheme to integrate the techniques of image holography and speckle photography. Boone [11] introduced a technique that combined reflection holography and objective laser speckle methods. Chiang and Li [12] developed the so-called holospeckle interferometry technique, in which they used the property of polarization to separate the in-plane and out-of-plane displacement fields in a single hologram-specklegram recording.

A common drawback of all these approaches is the fact that once the experimental parameters are selected, the resulting fringe pattern is fixed for a given loading configuration and the specimen geometry. However, in general, the two methods have a sensitivity difference exceeding one order of magnitude. Furthermore, a large difference usually exists in the magnitudes of the in-plane and out-of-plane displacements for a given problem. Thus, often one finds that the combination of speckle photography and holographic interferometry results in too many fringes in one method and too few in the other. This difficulty is largely eliminated by the sandwich holospeckle technique described below.

The experimental setup of the new technique and the geometry of the specimen used are as shown in Fig. 1. The laser beam is split into two by a partial mirror. One beam is collimated to impinge directly upon an assembly of two photographic plates sandwiched in such a way that their emulsion sides are against each other. The other beam goes through a microscope objective to illuminate normally a small region at the crack tip of the specimen. The reflected beam is collected by the same microscope objective and forms the image of the specimen at the emulsion plane of the twin-plate holospecklegram. Loading is applied in steps and for each loading a single-exposure holospecklegram is made. After processing the front (or back) plate of the holospecklegram can be paired with the back (or front) plate of any other holospecklegram to yield a sandwich holospecklegram. Since the two methods have different sensitivities, one can select the pairing judiciously so as to yield the proper number of fringes. For example, the pairing of the front (or back) plate of the holospecklegram from Loading P_i with the back (or front) plate of the holospecklegram from Loading P_j results in an equivalent double-exposure holospecklegram for Loading $P_i - P_j$.

Such a sandwich holospecklegram can be reconstructed either in hologram mode or in specklegram mode. In the former, since both the illumination and observation directions

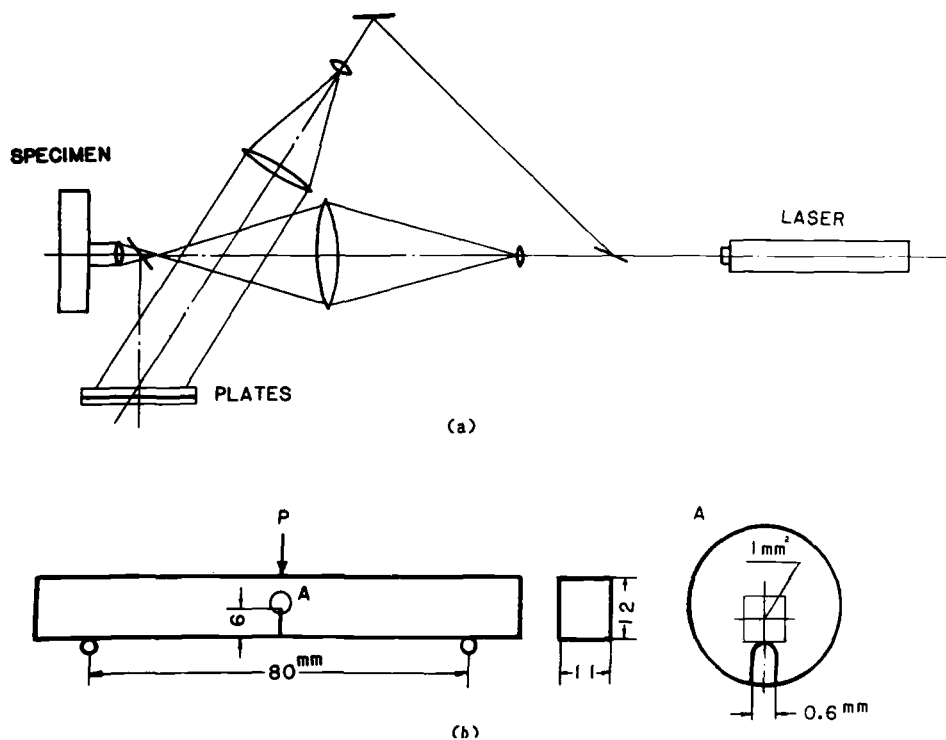


FIG. 1—(a) Optical setup of the sandwich holospeckle interferometry; (b) geometry of the specimen; (c) analyzed crack-tip region.

are normal to the specimen surface, the governing equation of holographic interferometry is simply

$$w = \frac{n\lambda}{2} \quad (1)$$

where w is the out-of-plane displacement, n the order of bright fringes, and λ the wavelength. For a helium-neon laser, $\lambda = 0.6328 \mu\text{m}$, the fringe sensitivity is then $0.31 \mu\text{m}/\text{fringe}$.

When reconstructed in the specklegram mode, the sensitivity is determined by the smallest speckle size given by the following equation

$$\Sigma = \lambda F \left(1 + \frac{1}{M} \right) \quad (2)$$

where λ is again the wavelength, F the f -number of the recording system, and M the magnification factor. In the experiments performed, the magnification was ten (or more) and the f -number was 0.25, resulting in a sensitivity of $1.3 \mu\text{m}$. The sensitivity in speckle photography can be increased if mismatch (or carrier) fringes are introduced.

In the present study, speckle displacement results from both in-plane displacement and

tilt (slope change) of the specimen surface, and the governing equations are

$$\begin{aligned}\frac{U}{M} &= u - 2\rho \left(\frac{\partial w}{\partial x} \right) \\ \frac{V}{M} &= v - 2\rho \left(\frac{\partial w}{\partial y} \right)\end{aligned}\quad (3)$$

where U and V are the recorded speckle displacements; u and v are the in-plane displacements of the specimen surface along the x and y axes, respectively; $\partial w/\partial x$ and $\partial w/\partial y$ are the local slopes; and ρ is the defocused distance due to thickness change.

Experiment and Results

The problem we selected to study using this technique was a three-point bending specimen made of H-1100 aluminum, whose dimensions are shown in Fig. 1. A single-edge notch of 0.6-mm width was made using the electric discharge machining (EDM) process, which would not create initial stress at the notch tip. The surface of the specimen was polished by 5- μm -sized aluminum oxide powder.

Twin-plate holospecklegrams were taken at different stages of incremental loading controlled by central deflection of the beam, each step being an increase of 0.0254 mm central deflection until a total of 29 steps was reached. At that stage, extensive plastic yielding throughout the remaining ligament of the beam had resulted, and a butterfly-shaped dimple at the crack tip was easily observable.

Holographic fringes were obtained by pairing the front and back plates of holospecklegrams from two adjacent loadings (for example, from P_i to P_{i+1}), whereas speckle fringes were generated by pairing the front and back plates six to eight loading steps apart. This was necessitated by the order-of-magnitude difference in sensitivity between these two methods. A typical holographic fringe pattern (each fringe representing a thickness variation of 0.31 μm) is shown in Fig. 2a. This particular result was from the difference between loading steps P_{24} and P_{26} . Essentially the same fringe pattern was obtained between any two adjacent loads. An elevation map drawn using the information from many fringe patterns is shown in Fig. 2b. Although we only analyzed a region of 1 mm^2 , the butterfly shape of the crack-tip deformation is clearly evident. Isothetic fringes, each representing a contour of vertical displacement near the crack tip obtained from sandwich specklegrams paired from Steps 9 and 15, 15 and 23, and 23 and 29, were obtained by the process of whole-field filtering [13]; these are shown in Fig. 3. While these patterns gave an overall view of the in-plane displacement field, more accurate data were obtained by the process of pointwise filtering [13] by pointing a narrow laser beam at the sandwich specklegram, as shown in Fig. 4. The resulting diffraction halo contained a series of fringes, the so-called Young's fringes, depicting the local displacement vector. Typical Young's fringe patterns at different points from a sandwich specklegram are shown in Fig. 5. The governing equations that relate the fringe parameters to the speckle displacement are

$$\begin{aligned}U &= \left(\frac{\lambda L}{s} \right) \sin \theta \\ V &= \left(\frac{\lambda L}{s} \right) \cos \theta\end{aligned}\quad (4)$$

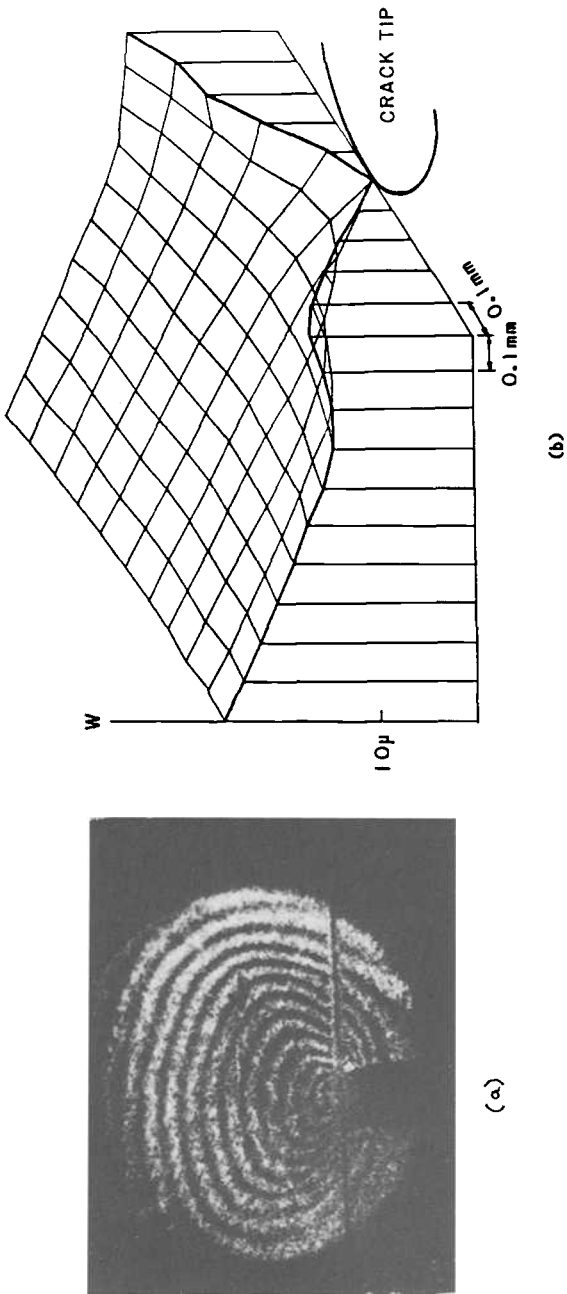


FIG. 2—Typical result of out-of-plane crack-tip deformation between two loadings: (a) holographic fringe representing the contour of the thickness variation; (b) elevation map drawn from the total information from the Step 9 and Step 29 pairing.

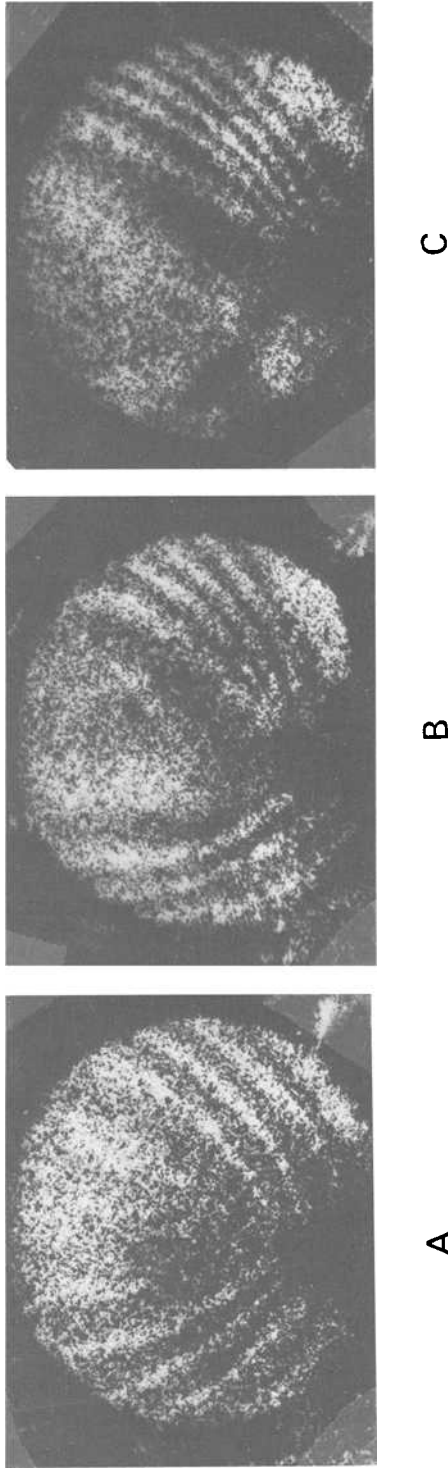


FIG. 3—Isothetic fringe pattern representing vertical displacement contours for the following loading step pairs: (a) 9 and 15, (b) 9 and 23, (c) 23 and 29.

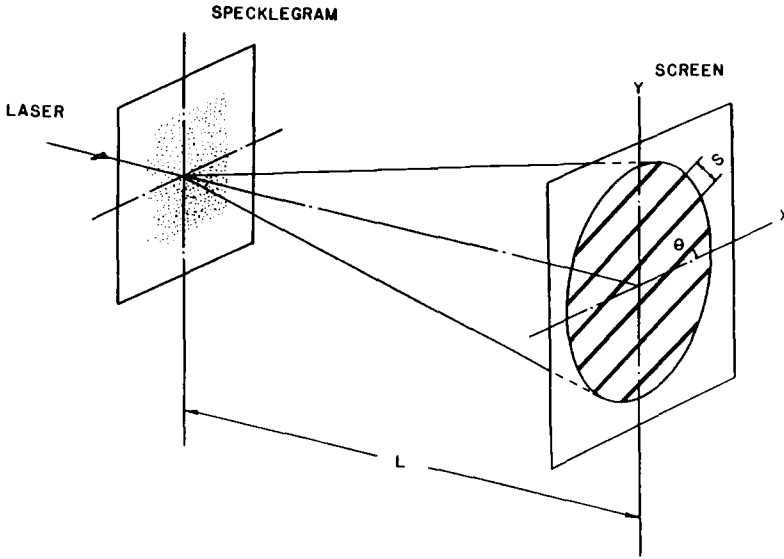


FIG. 4—Point-by-point filtering to generate Young's fringe pattern from the specklegram.

where L is the distance between the specklegram and the screen used to receive the diffraction pattern, s the spacing between two adjacent Young's fringes, and θ is the angle between the fringe and the x axis.

Each sandwich specklegram was analyzed by taking the in-plane displacement information from an array of 11 by 11 points spaced 0.1 mm apart in a 1-mm² region near the crack tip (see Fig. 1c). Speckle displacement information obtained from Young's fringes and Eq 4, together with the out-of-plane displacement information obtained from holography (used for calculating $\partial w/\partial x$ and $\partial w/\partial y$), was substituted into Eq 3 to yield the in-plane displacement within the region. Since large strain was involved, the following relations were used for the calculation of strain

$$\begin{aligned}\epsilon_{xx} &= \sqrt{1 + 2 \left(\frac{\partial u}{\partial x} \right) + \left(\frac{\partial u}{\partial x} \right)^2 + \left(\frac{\partial v}{\partial x} \right)^2 + \left(\frac{\partial w}{\partial x} \right)^2} - 1 \\ \epsilon_{yy} &= \sqrt{1 + 2 \left(\frac{\partial v}{\partial y} \right) + \left(\frac{\partial u}{\partial y} \right)^2 + \left(\frac{\partial v}{\partial y} \right)^2 + \left(\frac{\partial w}{\partial y} \right)^2} - 1 \\ \epsilon_{xy} &= \frac{1}{2} \arcsin \frac{\left(\frac{\partial u}{\partial y} \right) + \left(\frac{\partial v}{\partial x} \right) + \left(\frac{\partial u}{\partial x} \right) \left(\frac{\partial u}{\partial y} \right) + \left(\frac{\partial v}{\partial x} \right) \left(\frac{\partial v}{\partial y} \right) + \left(\frac{\partial w}{\partial x} \right) \left(\frac{\partial w}{\partial y} \right)}{(1 + \epsilon_{xx})(1 + \epsilon_{yy})}\end{aligned}\quad (5)$$

Strain contours for two stages of loading were obtained and plotted as shown in Fig. 6. It is interesting to note that a large region directly above the crack experienced very little strain. The highly strained regions were on the two sides.

Plane-strain elastic-plastic analyses by Hilton and Hutchinson [14] and by Shih [15] have shown that the material directly ahead of the crack tip deforms elastically. In the experiments of Hundy [16], notched mild steel specimens of various configurations were loaded plastically

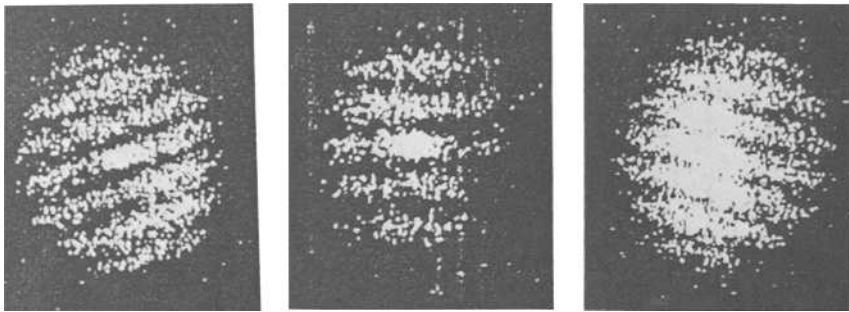


FIG. 5—Typical Young's fringe patterns at different points near the crack tip from a sandwich specklegram.

in bending and then sectioned. Interior sections under the condition of plane strain were etched to show the plastic deformation zones. Invariably an elastic region ahead of the crack tip was present. Interestingly, this is essentially what we observed using strain calculations based on surface three-dimensional deformation data. Obviously, surface deformation at a crack tip is neither plane stress nor plane strain. The authors hope that, through detailed mapping of deformation fields such as the one presented in this paper, a more realistic three-dimensional model of fracture can be constructed.

Conclusions and Discussion

We have developed a new experimental technique that is capable of mapping the three-dimensional deformation field in a region only 1 mm^2 at the crack tip. This is achieved by combining the best features of holographic interferometry, which is most suitable for measuring out-of-plane displacement, and laser speckle photography, which is most suitable for in-plane displacement. This method is different from all the other holospeckle techniques in that we introduce a twin-plate sandwich system to record the holospecklegram. During the loading, a series of the twin holospecklegrams is made. They are paired using the front (or back) plate of one sandwich at one loading stage and the back (or front) plate of another sandwich at another loading stage. In this technique the problem of a sensitivity difference exceeding one order of magnitude between the two methods is eliminated by judiciously choosing the elements of the sandwich holospecklegram.

In the current experimental arrangement, which used a microscope objective, the authors were able to achieve a sensitivity of $0.31 \text{ } \mu\text{m/fringe}$ for holography and $1.3 \text{ } \mu\text{m/fringe}$ for speckle photography. We applied this technique to the study of crack-tip deformation of a three-point bending specimen made of aluminum. While the results were from surface deformation only, they had the same features as plane-strain elastic-plastic calculations [14,15] and experiments [16].

It should be noted that, when the pairing of the plates is performed, it is inevitable that there will be some relative rigid body movement between them; but this has no effect on the calculation of strain.

Acknowledgment

The authors would like to acknowledge gratefully the financial support provided by the Office of Naval Research through Contract No. N0001482K0566 (Solid Mechanics Division,

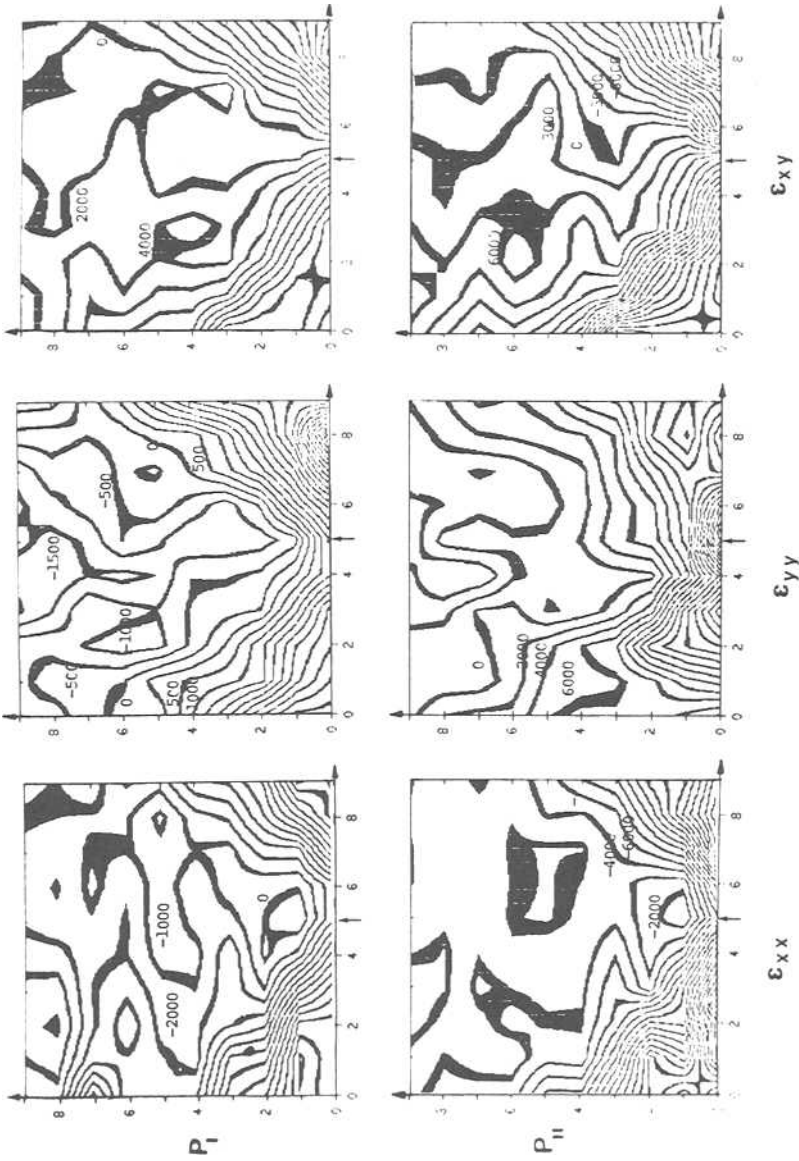


FIG. 6—Strain contours (in μ strain) within a region of 1 mm^2 (linear dimension in 10^{-1} mm) at the crack tip. The arrow indicates the position of the crack tip.

under scientific officer Dr. Y. Rajapakse) and by the National Science Foundation through Solid Mechanics Program Grant No. MEA8403912.

References

- [1] Hutchinson, J. W., "Singular Behavior at the End of a Tensile Crack in a Hardening Material," *Journal of Mechanics and Physics of Solids*, Vol. 16, 1968, pp. 13-29.
- [2] Rice, J. R. and Rosengren, G. F., "Plane Strain Deformation Near a Crack Tip in a Power-Law Hardening Material," *Journal of Mechanics and Physics of Solids*, Vol. 16, 1968, pp. 1-12.
- [3] Bakker, A., "On the Numerical Evaluation of J in Three Dimensions," *Application of Fracture Mechanics to Materials and Structures*, G. C. Sih, Ed., Martinus Nijhoff, The Hague, The Netherlands, 1984, pp. 657-671.
- [4] Smith, C. W., "Use of Photoelasticity in Fracture Mechanics," *Mechanics of Fracture*, Vol. 7, G. C. Sih, Ed., Martinus-Nijhoff, The Hague, The Netherlands, 1981, pp. 163-188.
- [5] Theocaris, P. S., "Local Yielding Around a Crack Tip in Plexiglas," *Journal of Applied Mechanics*, Vol. 37, 1970, pp. 409-415.
- [6] Post, D., "Patterns of U and V Displacement Around Cracks in Aluminum by Moiré Interferometry," *Application of Fracture Mechanics to Materials and Structures*, G. C. Sih, Ed., Martinus-Nijhoff, The Hague, The Netherlands, 1984, pp. 699-708.
- [7] Chiang, F. P. and Williams, R., "Simultaneous Determination of U, V, and W of Fracture Specimen," *Journal of Engineering Fracture Mechanics*, Vol. 22, No. 5, 1985, pp. 731-735.
- [8] Dudderer, T. D. and O'Regan, R., "Measurement of the Strain Field Near a Crack Tip in Polymethylmethacrylate by Holographic Interferometry," *Experimental Mechanics*, Vol. 11, 1971, pp. 49-56.
- [9] Evans, W. T. and Luxmoore, A. R., "Measurement of In-Plane Displacements Around a Crack Tip by a Laser Speckle Method," *Engineering Fracture Mechanics*, Vol. 6, 1974, pp. 735-738.
- [10] Adams, F. D. and Maddux, G. E., "Synthesis of Holographic Interferometry and Speckle Photography to Measure 3-D Displacements," TM-73-126-FBR, Air Force Flight Dynamics Laboratory, Wright-Patterson Air Force Base, OH, 1973.
- [11] Boone, P. M., "Use of Reflection Holograms in Holographic Interferometry and Speckle Correlation Measurement of Surface Displacements," *Optica Acta*, Vol. 22, 1975, pp. 579-589.
- [12] Chiang, F. P. and Li, Q. B., "Holospeckle Interferometry," *Proceedings, Fifth International Congress on Experimental Mechanics*, Montreal, Canada, 10-15 June, 1984.
- [13] Chiang, F. P., "A Family of 2D and 3D Experimental Stress Analysis Technique Using Laser Speckles," *Solid Mechanics Archives*, Vol. 3, No. 1, 1978, pp. 1-32.
- [14] Hilton, P. D. and Hutchinson, J. W., "Plastic Intensity Factors for Cracked Plates," *Journal of Engineering Fracture Mechanics*, Vol. 3, 1971, pp. 435-451.
- [15] Shih, C. F., "Small Scale Yielding Analysis of Mixed Mode Plane Strain Crack Problems," AFOSR Technique Report 73-1692, Air Force Office of Scientific Research, Wright-Patterson Air Force Base, OH, 1973.
- [16] Hundy, B. B., "Plane Plasticity," *Metallurgia*, Vol. 4a, 1954, pp. 109-118.

On the Application of *R*-Curves and Maximum Load Toughness to Structures

REFERENCE: Anderson, T. L., Gordon, J. R., and Garwood, S. J., "On the Application of *R*-Curves and Maximum Load Toughness to Structures," *Fracture Mechanics: Nineteenth Symposium ASTM STP 969*, T. A. Cruse, Ed., American Society for Testing and Materials, Philadelphia, 1988, pp. 291–317.

ABSTRACT: An approximate procedure is presented which allows a ductile fracture analysis to be performed with a single fracture toughness value measured at maximum load in a small-scale test. This maximum load toughness value is used to predict an *R*-curve which is then used to predict maximum stress and crack extension. Predictions from this approach are compared with experimental data from 20 wide-plate specimens made from various ductile materials. A limited number of these specimens are also analyzed using experimental *R*-curves in order to investigate the effect of the assumed shape of the *R*-curve on predictions. In addition, an analysis is presented which allows one to determine the critical tearing modulus required for a structure to exhibit collapse controlled failure. Potential applications of these analyses are discussed.

KEY WORDS: crack-tip opening displacement, ductile fracture, elastic-plastic fracture, *J*-integral, *R*-curves, structural analysis, weldments, wide-plate tests, fracture mechanics

Fracture in ductile materials usually occurs by slow, stable crack growth. As the crack advances during plastic deformation, a point is eventually reached where the strain hardening of the material cannot keep pace with the loss of load carrying capacity because of crack growth. If the structure is load controlled, an instability will occur at this point. In a displacement controlled structure, a maximum load plateau will occur, followed by a decrease in load with further crack growth. (Instability can also occur in displacement control if the structure contains sufficient elastic energy.) If a structure behaves in a linear elastic manner, a maximum load or instability point will result from an increase in compliance, caused by crack growth.

There are a number of ways to analyze ductile fracture in test specimens and structures. One of the most common approaches involves comparing the driving force for crack growth with the material's resistance to crack growth. A fracture toughness parameter such as the *J*-integral, crack extension force (*G*), or crack-tip opening displacement (CTOD) is plotted against crack length for both driving force and crack growth resistance. The maximum load is predicted at the point of tangency between the driving force and resistance (*R*) curve. Alternatively, the slopes of the driving force and *R*-curves at various points can be used to compute the applied and material tearing moduli, respectively. The two tearing modulus curves are then plotted against a fracture toughness parameter (usually *J*) and the intersection of the two curves is taken as the maximum load point. Procedures for performing analyses using either method are described in detail in Ref 1.

¹ Assistant professor, Mechanical Engineering Department, Texas A & M University, College Station, TX 77843

² Senior research engineer and department head, respectively, Fracture Department, The Welding Institute, Abington Hall, Abington, Cambridge, England CB1 6AL

The analyses described above are somewhat complicated and time-consuming. Moreover, a material R -curve must be obtained experimentally in order to perform these analyses. Recently, simplified ductile fracture analyses have been proposed [2,3] whereby the value of CTOD at maximum load (in a small-scale test) is inserted into a design equation such as the CTOD design curve [2,3] or a modified strip yield equation [3] in order to estimate the maximum stress or allowable flaw size. This procedure based on maximum load CTOD (δ_m) does not provide a means for estimating crack growth; nor does it consider the strong geometry dependence of δ_m [4]. In most cases, this simplified method gives predictions that are slightly conservative. However, one must apply a separate plastic collapse check when using the CTOD design curve. Otherwise, gross overestimates of maximum stress will result in some cases [3].

A procedure is described below which combines the advantages of complex [1] and simplified [2,3] ductile fracture analyses. The proposed analysis utilizes maximum load toughness from a small-scale test. Thus, there is no need to determine an R -curve experimentally when using this procedure. In addition, this approach considers crack growth as well as the geometry dependence of δ_m . Predictions from this procedure are compared with wide-plate test data for a variety of materials and configurations.

Background

The J estimation procedure [1] published by the Electric Power Research Institute (EPRI) assumes that materials obey a Ramberg-Osgood stress-strain relationship

$$\frac{\epsilon}{\epsilon_o} = \frac{\sigma}{\sigma_o} + \alpha \left(\frac{\sigma}{\sigma_o} \right)^n \quad (1)$$

where σ is the applied stress, ϵ is the total strain at σ , σ_o is a reference value of stress (usually yield strength), $\epsilon_o = \sigma_o/E$ (E = Young's modulus), and α and n are material constants. The EPRI J estimation procedure states that the total applied J is the sum of three terms: the elastic J ($= G$), a first order plastic zone correction, and a fully plastic J given by

$$J_{FP} = \alpha \sigma_o \epsilon_o b h_1 \left(\frac{P}{P_o} \right)^{n+1} \quad (2)$$

where b is ligament length, h_1 is a plastic geometry correction constant, P is applied load, and P_o is the load when the net section stress $= \sigma_o$.

Ainsworth [5] observed that the actual stress-strain behavior of many materials (for example, austenitic stainless steel) differs considerably from Eq 1 and that significant errors in J can result from using the EPRI procedure on these materials. Consequently, Ainsworth [5] modified the J estimation equations to remove the power law dependence of the flow behavior. He defined a reference stress as follows.

$$\sigma_{ref} = \left(\frac{P}{P_o} \right) \sigma_o \quad (3)$$

The reference strain, ϵ_{ref} , was defined as the total strain on the uniaxial stress-strain curve corresponding to σ_{ref} . Inserting these definitions for σ_{ref} and ϵ_{ref} into Eq 2 results in

$$J_{FP} = \sigma_{ref} b h_1 \left(\epsilon_{ref} - \frac{\sigma_{ref}}{E} \right) \quad (4)$$

This relationship is a more general form of Eq 2. Equation 4 is identical to Eq 2 for materials that exhibit Ramberg-Osgood flow behavior. For other materials, Eq 4 can be used in conjunction with the actual stress-strain curve to obtain a graphical solution. Alternatively, a more appropriate stress-strain law, such as a polynomial fit, can be substituted into Eq 4.

Ainsworth [5] also made an approximation to eliminate h_1 and express J_{FP} in terms of the stress intensity factor, K

$$J_{FP} = \frac{\mu K^2}{E} \left(\frac{E\epsilon_{ref}}{\sigma_{ref}} - 1 \right) \quad (5)$$

where $\mu = 0.75$ for plane stress and $\mu = 1.0$ for plane strain. The above equation eliminates the need for a fully plastic finite element analysis, which is required to determine the h_1 factor in Eqs 2 and 4. Recent investigations [6,7] indicate that Ainsworth's approximation does not adversely affect the accuracy of the analysis. In fact, Eq 5 is actually more accurate than Eq 2 for many materials because Eq 5 does not rely on a Ramberg-Osgood approximation of the flow behavior.

Recently, Anderson [7] modified the Ainsworth [5] equations to obtain a CTOD estimation procedure. The total CTOD is given by

$$\delta = \frac{\mu K^2}{\sigma_{YS} E} \left[\frac{Y_e^2 a_e}{m_{el} Y^2 a} + \frac{1}{m_{FP}} \left(\frac{E\epsilon_{ref}}{\sigma_{ref}} - 1 \right) \right] \quad (6)$$

where a is the crack size, a_e is the effective crack size with a plastic zone correction, and Y_e and Y are the stress intensity correction factors for a_e and a , respectively. The constants m_{el} and m_{FP} relate elastic and plastic components of J and CTOD. Typical values of m_{el} and m_{FP} range from 1.0 to 2.0 [8]. Predictions of applied CTOD in wide-plate specimens agreed very well with experimental results.

Equation 6 has been further modified to include residual stress and stress concentration effects [9]. This modified equation has been incorporated into a proposed procedure for elastic-plastic analysis of brittle fracture. In the present study, where ductile fracture was analyzed, residual stresses and stress concentration effects were ignored.

If it is assumed that $m_{el} = m_{FP} = \mu = 1.0$, Eq 6 can be simplified somewhat. (This also makes the equation slightly conservative.) In addition, the plastic zone correction is negligible at most stress levels [10]. Thus, a simplified version of Eq 6 is given by

$$\delta = \frac{K^2 \epsilon_{ref}}{\sigma_{YS} \sigma_{ref}} \quad (7)$$

Similarly, the simplified equation for J is given by

$$J = \frac{K^2 \epsilon_{ref}}{\sigma_{ref}} = \frac{K^2}{E_s} \quad (8)$$

where E_s is the secant modulus. Note that Eq 8 reduces to the linear elastic solution ($J = G$) at small strains.

The relatively simple form of Eqs 7 and 8 has proved to be quite useful in the present investigation. These equations can be used to derive a closed-form solution for ductile fracture in structures, as described below.

Proposed Ductile Fracture Analysis

The basic approach to the ductile fracture analysis presented below is illustrated in Fig. 1. The dashed lines in Fig. 1a represent applied CTOD versus load for stationary cracks in a structure or test specimen. The R -curve (Fig. 1b) can be used to determine the CTOD-stress curve for a growing crack. The maximum load, crack growth at maximum load, and δ_m can be determined from this plot. This approach is essentially identical with the driving force/ R -curve method [1]; the only difference is in the way the driving force is plotted.

At the maximum load plateau illustrated in Fig. 1, $dP = 0$. It is possible to solve for this point analytically using Eq 7. For example, by solving the appropriate differential equation for a single edge notched bend (SENB) specimen at maximum load, it can be shown that

$$\frac{d\delta}{da} = \frac{2\delta_m(n+1)}{W - a_m} \quad (9)$$

where W is the specimen width and a_m is the crack length at maximum load. Equation 9 is derived in the Appendix. A simple power law hardening model was assumed for this derivation, hence the dependence on the hardening exponent, n . Equation 9 can also be expressed in terms of J

$$\frac{dJ}{da} = \frac{2J_{\max}(n+1)}{W - a_m} \quad (10)$$

where J_{\max} is the value of J at maximum load.

Equations 9 and 10 make it possible to estimate tearing modulus from maximum load toughness. It is also possible to predict the entire R -curve if certain assumptions are made. For example, if the R -curve is assumed to follow a simple power law

$$\delta = \beta \Delta a^k \quad (11)$$

the constant β can be determined by differentiating the above equation and substituting

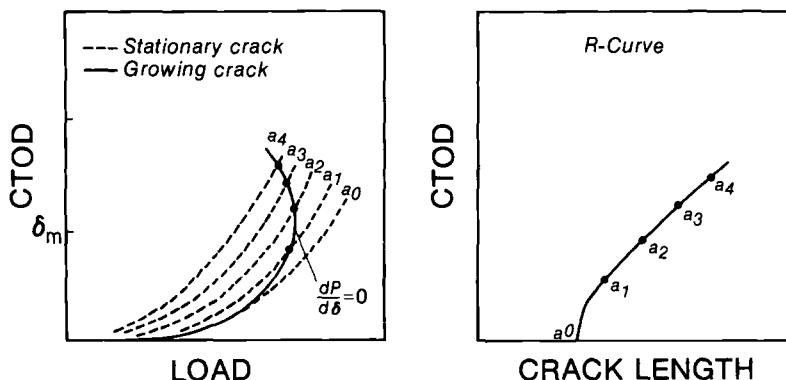


FIG. 1—Schematic ductile fracture analysis. The material's R -curve is used in conjunction with curves for various stationary cracks to derive a stress-CTOD curve for a growing crack.

into Eq 9

$$\beta = \delta_m \left[\frac{2(n+1) \left(1 + \frac{k}{n+1} \right)}{k(W - a_o)} \right]^k \quad (12)$$

where a_o is the initial crack length. Thus, if a k value is assumed for the material, the *R*-curve can be predicted from maximum load toughness. In the present study *R*-curves were predicted assuming linear ($k = 1.0$) and parabolic ($k = 0.5$) behavior.

Once an *R*-curve has been predicted for a material, it can be used to analyze the ductile fracture behavior of a structure. Analyses for several structural configurations are presented below.

CCT Geometry

A similar analysis to the one given in the Appendix can be performed on a center cracked tension (CCT) configuration to determine the relationship between the slope of the *R*-curve, the maximum load toughness, and specimen dimensions

$$\frac{d\delta}{da} = \frac{2\delta_m^*(n+1)}{W - 2a_m} \quad (13)$$

where W is the width of the panel, a_m is the half crack length at maximum load, and δ_m^* is the CTOD at maximum load in the CCT panel. (The asterisk has been added to distinguish maximum load toughness in structural configurations from δ_m in a small-scale test.)

Equations 11 to 13 can be used to solve for the crack extension at maximum load

$$\Delta a_m = \frac{k(W - a_o)}{2(n+1) \left(1 + \frac{k}{n+1} \right)} \quad (14)$$

where a_o is the initial half crack length. The δ_m^* for the CCT plate can then be obtained by substituting Δa_m into Eq 11. (Recall that the coefficient β was computed from a small-scale test and an assumed k value.) The crack length at maximum load is given by

$$2a_m = 2a_o + 2\Delta a_m \quad (15)$$

The stress at maximum load can be determined by solving Eq 7 for stress and inserting δ_m^* and a_m . Assuming power law hardening (Eq A7, appendix), the maximum stress (or collapse stress) for a CCT panel is given by

$$\sigma_c = L\sigma_{ys} \left(\frac{1 - 2a_m}{W} \right) \left[\frac{\delta_m^*}{L^2 Y^2 \pi a_m \alpha \epsilon_{ys} \left(\frac{1 - 2a_m}{W} \right)^2} \right]^{1/n+1} \quad (16)$$

where L is a constraint factor; $L = 1.0$ for plane stress and $L = 1.15$ for plane strain [11]. The linear-elastic fracture mechanics (LEFM) shape factor, Y , is a finite width correction

for a CCT panel. It must be emphasized that δ_m^* is not equal to the maximum load toughness in a small-scale test; rather it is the predicted CTOD at the maximum load point in the structure. This analysis is designed to take into account the strong geometry dependence of maximum load toughness.

SENT Geometry

The analysis of a single edge notched tension (SENT) or edge cracked configuration is very similar to the CCT panel. For a SENT panel with the ends restrained against bending, the slope of the R -curve at maximum load is given by

$$\frac{d\delta}{da} = \frac{\delta_m(n+1)}{B-a_m} \quad (17)$$

where B is the plate thickness. Equation 17, as well as other equations in this section, assume an infinitely long surface crack. In order to analyze a through-thickness edge crack, the thickness should be replaced with the plate width, W , in all equations. The crack extension at maximum load in a SENT panel is given by

$$\Delta a_m = \frac{k(B-a_o)}{(n+1)\left(1 + \frac{k}{n+1}\right)} \quad (18)$$

and the total crack length is

$$a_m = a_o + \Delta a_m \quad (19)$$

The δ_m^* for this geometry is determined from Eq 11 as before. The predicted maximum stress is obtained by solving Eq 7 for a SENT geometry

$$\sigma_c = L\sigma_{ys}\left(\frac{1-a_m}{B}\right) \left[\frac{\delta_m^*}{L^2 Y^2 \pi a_m \alpha e_{ys} \left(\frac{1-a_m}{B}\right)^2} \right]^{1/n+1} \quad (20)$$

Surface Crack (SESNT)

The analyses presented above involve one-dimensional crack growth. However, when analyzing a structure containing a semielliptical surface crack of length $2c$ and depth a , one must consider crack growth in both the a and c directions. Consequently, the ductile fracture analysis presented below for a semielliptical surface notched tension (SESNT) panel is somewhat more complicated than the CCT and SENT analyses.

The critical R -curve slope for a SESNT panel is given by

$$\frac{d\delta}{da} = \frac{\pi(c_m + \theta a_m)\delta_m^*(n+1)}{2BW - \pi c_m a_m} \quad (21)$$

where

$$\theta = \frac{dc}{da} \quad (22)$$

A θ value must be assumed based on the anticipated crack growth behavior. The crack extension in the thickness direction at maximum load is given by

$$\Delta a_m = \frac{k[2BW - \pi(c_o + \theta\Delta a_m)(a_o + \Delta a_m)]}{\pi(n+1)[c_o + \theta(a_o + 2\Delta a_m)]} \quad (23)$$

Since Δa_m appears in several places in the above equation, an iterative procedure is required to solve for crack extension. The crack dimensions at maximum load are determined as follows

$$a_m = a_o + \Delta a_m \quad (24)$$

$$c_m = c_o + \theta\Delta a_m \quad (25)$$

The δ_m^* value corresponding to Δa_m of crack extension can then be determined from Eq 11. Finally, the maximum stress can be computed from

$$\sigma_c = L\sigma_{ys} \left(1 - \frac{\pi c_m a_m}{2BW}\right) \left[\frac{\delta_m^*}{L^2 Y^2 \pi a_m \alpha \epsilon_{ys} \left(1 - \frac{\pi a_m c_m}{2BW}\right)^2} \right]^{1/n+1} \quad (26)$$

The derivations of Eqs 21 to 26 are given in the Appendix.

In the present study, the stress intensity correction factor (Y) for the SESNT configuration was obtained from Ref 12, where the severity of a surface flaw is expressed in terms of an equivalent through-thickness flaw. For a given surface crack, the half length of the equivalent through-thickness crack, \bar{a} , is defined by the following relationship

$$\bar{a} = Y_I^2 a \quad (27)$$

where Y_I is the stress intensity correction factor for a surface crack in an infinitely wide plate. The overall correction factor is then obtained by multiplying Y_I by a finite width correction [13]

$$Y^2 = Y_I^2 \sec \left(\frac{\pi c}{W} \right) \quad (28)$$

Comparison with Experiment

The analyses described above were used to predict maximum stress and crack extension in a series of wide-plate specimens. These predictions were compared to measured values in the wide-plate tests. The details of this comparison are presented below.

TABLE 1—*Tensile properties of three wide-plate materials.*

Material	Nominal Thickness, mm	Yield Strength, MPa	Tensile Strength, MPa	Power Law Coefficients ^a	
				α	n
A533B steel	110	461 ^b	600 ^b	3.32	9.68
API 5LX56 steel	13	438	584	2.10	9.82
316 stainless steel	50	250	580	5.55	4.19

^a Defined in Eq 45.^b Measured at +70°C.

Test Materials

Experimental data were obtained for a variety of materials including a 110-mm-thick plate of ASTM A533 Grade B steel, a 50-mm-thick plate of 316 stainless steel, and a 13-mm-thick plate of API 5LX56 steel. Small-scale and wide-plate tests were performed on these materials during three separate research programs. The results of these tests were published collectively in Ref 3.

The tensile properties of these three materials are given in Table 1. The tensile axis of each specimen was oriented parallel to the tensile axis in the wide plates. Power law expressions (Eq 45 in Appendix) were fitted to the stress-strain curves in order to predict wide plate results.

In addition to the materials mentioned above, wide-plate and small-scale tests have recently been performed on three 10-mm-thick welded aluminum plates. The tensile properties of these weldments are listed in Table 2. The weld metal tensile results were obtained from rectangular strips extracted perpendicular to the welding axis. In each test, strain gages were attached to the weld metal in order to determine its flow behavior in the transverse direction.

Table 3 gives the maximum load toughness (δ_m) for each of the materials studied. The notch orientations listed in this table are defined in Fig. 2. The test temperatures given (room temperature except for the A533 B material) are equivalent to the wide-plate test temperature. These temperatures were adequate to guarantee upper shelf behavior in the two ferritic steels. Three CTOD tests were performed for each material and orientation.

TABLE 2—*Tensile properties of aluminum weldments.*

Specimen No.	Parent Plate	Electrode	Weld Metal ^a		Parent Plate ^b	
			Yield Strength, MPa	Tensile Strength, MPa	Yield Strength, N/mm ²	Tensile Strength, N/mm ²
W12 ^c	5456-H116	5556	144	308 ^d	228	317
W14 ^e	6061-T651	5356	121	212	276	310
W16 ^e	6061-T651	4043	123	216	276	310

^a Power law coefficients.^b Estimated from material specification.^c $\alpha = 3.17$, $n = 3.37$.^d Failed under rising load deflection curve.^e $\alpha = 3.29$, $n = 3.58$.

TABLE 3—Maximum load CTOD in SENB specimens.

Material	Notch Orientation ^a	Specimen Dimensions, B by W, mm	Temperature, °C ^b	δ_m , mm
A533 B	L-T	55 by 110	+70	2.1
	L-S	55 by 110	+70	2.0
API 5LX56	T-L	26 by 13	+22	0.11
	T-S	13 by 13	+22	0.25
316 stainless steel	T-L	50 by 100	+20	2.55
Aluminum				
W12	T-L ^c	10 by 20	+20	0.18
W14	T-L ^c	10 by 20	+20	0.22
W16	T-L ^c	10 by 20	+20	0.09

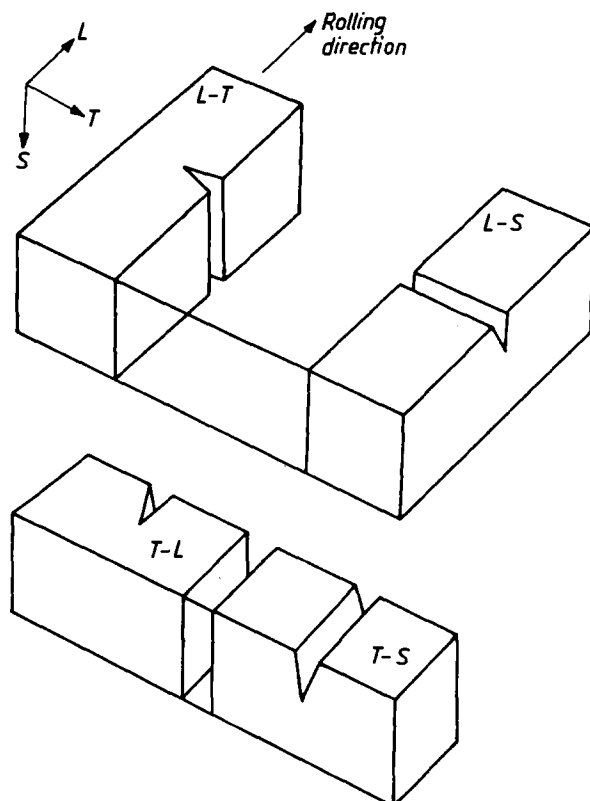
^a Defined in Fig. 2.^b Small-scale CTOD tests and wide-plate tests were performed at the same temperature for a given material.^c With respect to the welding axis.

FIG. 2—Orientation of SENB and wide plate specimens.

TABLE 4a—Configuration of CCT wide-plate specimens.

Material	Specimen Identification	Notch Orientation	Plate Width, W , mm	Plate Thickness, B , mm	Initial Half Crack Length, a_o , mm
A533 B	1008	L-T	487	113	102
	1042	L-T	491	110	128
	1043	L-T	486	112	65.6
API 5LX56	1178	T-L	898	13.0	43.0
	1179	T-L	892	13.0	133
316 stainless steel	WP3	T-L	477	51.1	31.0
	WP4	T-L	480	51.1	37.9
Aluminum weld	W12	T-L ^a	752	10.2	29.7
	W14	T-L ^a	751	10.7	27.4
	W16	T-L ^a	750	10.4	29.0

^a With respect to the welding axis.

The δ_m values in Table 3 represent the minimum of three results. However, δ_m values in the materials studied exhibited a minimal amount of scatter.

Wide-Plate Tests

A total of 20 wide-plate tests were analyzed in this investigation. This data set included a wide range of materials, thicknesses, and configurations. Table 4a lists the dimensions and notch orientation of the CCT panels analyzed. The configurations of the SENT and SESNT panels are given in Tables 4b and 4c, respectively. All SENT plates were notched perpendicular to the plate surface.

Each wide-plate specimen contained a machined notch. All plates were fatigue precracked prior to testing.

The wide-plate tests were conducted in displacement control. The panels were instrumented with clip gages, strain gages, and linear transducers. In some tests, the plate was fully unloaded at various points and then reloaded. This produced a crack marking effect which allowed crack extension to be determined at various points on the load-displacement curve.

Predictions Using δ_m

The maximum load CTOD values from small-scale tests were used to predict R -curves for the materials listed in Table 1. These R -curves were then used to predict the maximum

TABLE 4b—Configuration of SENT wide-plate specimens.

Material	Specimen Identification	Notch Orientation	Plate Width, W , mm	Plate Thickness, B , mm	Initial Crack Depth, a_o , mm
A533 B	1009	L-S	508	110	37.4
	1045	L-S	509	110	33.0
	1044	L-S	508	109	51.1
API 5LX56	1180	T-S	885	13.0	2.1
	1181	T-S	885	13.0	4.6

TABLE 4c—Configuration of SESNT wide-plate specimens.

Material	Specimen Identification	Notch Orientation	Plate Width, <i>W</i> , mm	Plate Thickness, <i>B</i> , mm	Initial Crack Depth, <i>a</i> _o , mm	Initial Crack Length, 2 <i>c</i> _o , mm
A533 B	1006	L-S	508	110	22.8	152
	1007	L-S	510	113	38.7	240
	1046	L-S	508	113	56.2	328
API 5LX56	1176	T-S	858	13.0	2.7	42
	1177	T-S	899	13.0	4.8	90

stress and crack extension in wide-plate specimens. Predictions were made assuming a linear *R*-curve ($k = 1.0$) and a parabolic *R*-curve ($k = 0.5$).

Tables 5a, 5b, and 5c list predicted and experimental data for CCT, SENT, and SESNT panels, respectively. Figure 3 is a plot of safety factor on maximum stress for various materials and configurations. Predictions were conservative in most cases, with the parabolic *R*-curve predictions giving a slightly higher degree of conservatism than predictions based on a linear *R*-curve.

The assumed θ values (Eq 11) for the SESNT panels were based on the relative toughness of the material in the *c* and *a* directions. According to Table 3, the A533 B steel has approximately the same toughness in both directions. Thus θ was assumed to equal 1.0 for this material. However, CTOD tests on API 5LX56 steel specimens in the L – T orientation resulted in lower toughness than in specimens notched from the surface. Therefore, it is likely that a semielliptical surface crack would grow faster in the *c* direction. Equation 9 can be used to estimate relative crack growth rates in the *c* and *a* directions

$$\theta = \frac{dc/d\delta}{d\delta/da} = \frac{W - a_m}{\delta_m} \bigg|_{L-T} \times \frac{\delta_m}{W - a_m} \bigg|_{L-S} \quad (29)$$

For the API 5LX56 steel, $\theta = 4.5$. Additional calculations were performed to determine the effect of θ on the predicted maximum stress. It was found that σ_c is relatively insensitive to the assumed θ , although using a high θ value results in slightly more conservative predictions.

The scatter in Fig. 3 is greater for the SENT geometry. The largest errors were obtained for SENT panels with the deepest cracks. For example, predictions for a A533 B SENT plate with $a_o/B = 0.47$ resulted in a safety factor of 0.91 for a linear *R*-curve and a safety factor of 1.41 when a parabolic *R*-curve was assumed. Other wide-plate geometries were not nearly so sensitive to the assumed shape of the *R*-curve. This wide variability in predictions for SENT wide plates is probably due to the short ligament lengths in these specimens which result in a steep driving force curve, which in turn caused the predicted maximum load point to be highly sensitive to variations in the *R*-curve.

Most of the scatter in Fig. 3 can be attributed to variations in properties for a given material. This effect is evident in the Type 316 stainless steel, where Specimen WP3 failed at a lower load than Specimen WP4 despite the fact that Specimen WP3 had a shorter initial crack. Taking into account the net cross-sectional area in these two specimens, there appears to be a 9% variation in flow properties between the two plates.

Figure 4 is a plot of predicted and experimental crack extension at maximum load. Apparently, predicted crack extension is highly sensitive to the assumed *R*-curve shape. The parabolic *R*-curve usually resulted in better predictions. In many cases the actual crack

TABLE 5a—Summary of predictions for CCT wide-plate specimens using maximum load toughness.

		Experimental Data			Predicted Data		
Material	Specimen Identification	Maximum Stress σ_c , MPa	Crack Extension at σ_c , mm	Assumed k Value	Predicted Maximum Stress, MPa	Safety Factor	Predicted Crack Extension, mm
A533 B	1008	366	7.0	1.0	342	1.07	12
				0.5	332	1.10	4.8
	1042	281	7.0	1.0	278	1.01	9.7
	1043	455	7.0	0.5	272	1.03	4.4
				1.0	439	1.04	15
				0.5	424	1.07	5.3
API 5LX56	1179	403	17	1.0	431	0.94	34
				0.5	385	1.04	18
	1179	316	18	1.0	313	1.01	26
				0.5	283	1.12	14
316 stainless steel	WP3	311	14	1.0	358	0.87	34
				0.5	337	0.92	18
	WP4	337	13	1.0	342	1.01	33
				0.5	320	1.05	18

TABLE 5b—Summary of predictions for SENT wide-plate specimens using maximum load toughness.

Material	Specimen Identification	Experimental Data			Predicted Data		
		Maximum Stress σ_c , MPa	Crack Extension at σ_c , mm	Assumed k Value	Predicted Maximum Stress, MPa	Safety Factor	Predicted Crack Extension, mm
A533 B	1009	394	8.0	1.0	377	1.04	6.3
				0.5	351	1.12	3.3
	1045	425	7.5	1.0	406	1.05	6.6
				0.5	390	1.09	3.4
API 5LX56	1044	329	6.5	1.0	361	0.91	4.9
				0.5	234	1.41	2.6
	1180	414	^a	1.0	430	0.96	0.92
				0.5	395	1.05	0.49
	1181	351	^a	1.0	299	1.17	0.70
				0.5	275	1.28	0.38

^a Not measured.

TABLE 5c—Summary of predictions for SESNT wide-plate specimens using maximum load toughness.

Experimental Data			Predicted Data				
Material	Specimen Identification	Maximum Stress σ_c , MPa	Crack Extension at σ_c , mm	Assumed k Value	Predicted Maximum Stress, MPa	Safety Factor	Predicted Crack Extension, mm ^a
A533 B	1006	609	9.0	1.0	579	1.05	21
	1007	503	11	0.5	574	1.06	13
				1.0	489	1.03	15
API 5LX56	1046	415	9.0	0.5	490	1.03	8.1
				1.0	387	1.07	10
	1176	483	b	0.5	394	1.05	5.4
				1.0	488	0.99	6.6
	1177	451	b	0.5	440	1.10	4.5
				1.0	451	1.00	5.4
				0.5	404	1.12	3.4

^a Measured in the thickness direction. It is assumed that $\theta = 1.0$ for A533 B and 4.5 for API 5LX56.^b Not measured.

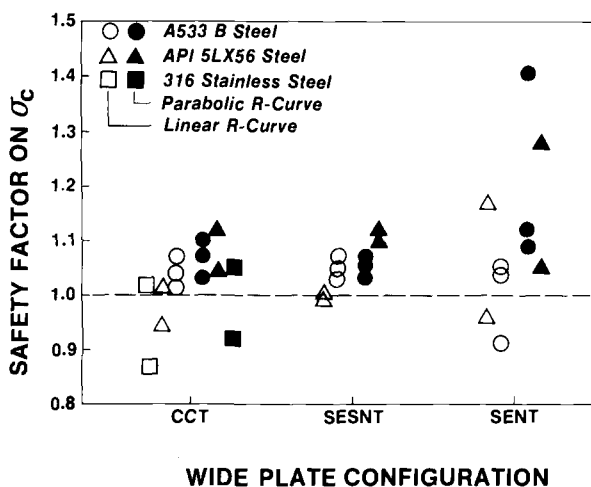


FIG. 3—Safety factor on maximum remote stress for predictions based on maximum load toughness.

extension lies between the predicted values for the two assumed *R*-curves. This implies that $0.5 \leq k \leq 1.0$ for the materials studied.

Predictions with Experimental *R*-Curves

It would be instructive to compare predictions based on experimental *R*-curves with predictions based on *R*-curves which have been estimated from maximum load toughness. This comparison was made for 316 stainless steel.

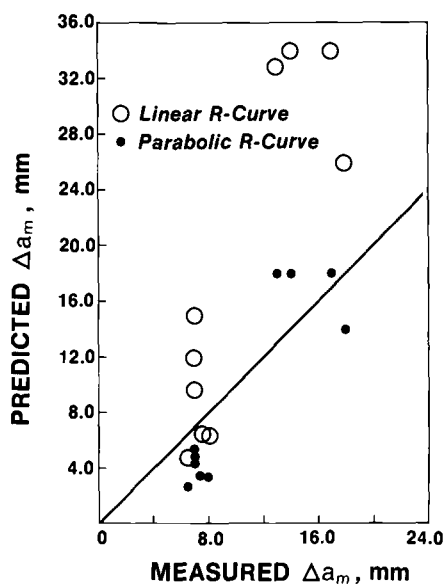


FIG. 4—Predicted and experimental crack extension at maximum stress. Predictions were based on δ_m .

The various R -curves used in the analysis of the 316 stainless steel wide plates are plotted in Fig. 5. Experimental curves for SENB specimens and CCT wide plates are included in this plot. The SENB curve was determined with six 50 by 100-mm specimens deformed to various displacements. The CCT curve was determined from the test record for Specimen WP4. The crack extension was determined by the unloading method of crack marking as described above. The applied CTOD was determined from the clip gage displacement

$$\delta = \frac{K^2}{2\sigma_{ys}E} + V_p \quad (30)$$

where V_p is the plastic component of clip gage displacement. The assumption that the plastic component of CTOD = V_p requires that the specimen maintain a constant crack opening angle (COA) in the plastic range.

Figure 5 indicates that the CCT R -curve is much steeper than the SENB R -curve. The R -curves predicted from δ_m lie between the two experimental curves at most CTOD values.

Driving force curves were computed using Eq 7 and assuming power-law hardening. The maximum stress and crack size were determined by plotting the driving force and R -curves on the same plot and determining the point of tangency. The results of this analysis are summarized in Table 6. The predictions based on δ_m are included for comparison. (It should be noted that if the maximum load conditions are determined graphically using the R -curves predicted from δ_m , one will obtain the same results as would be obtained by solving for σ_c and Δa_m algebraically using Eqs 11 to 16. However, the algebraic method is much less tedious.) For both wide plates, the highest stress was predicted by using the CCT R -curve and the lowest stress was predicted from the SENB R -curve. This is consistent with the relative position of the curves in Fig. 5. The variation in predicted maximum stress that results from using different R -curves (13% in this case) is comparable to the scatter in material flow properties ($\sim 9\%$, as discussed above). Thus, unless the material flow properties are known to a high degree of accuracy, the use of an "accurate" R -curve will not necessarily result in a more accurate prediction of maximum stress than if an approximate R -curve based on δ_m were used. However, the use of an experimental R -curve does seem to improve the crack extension predictions.

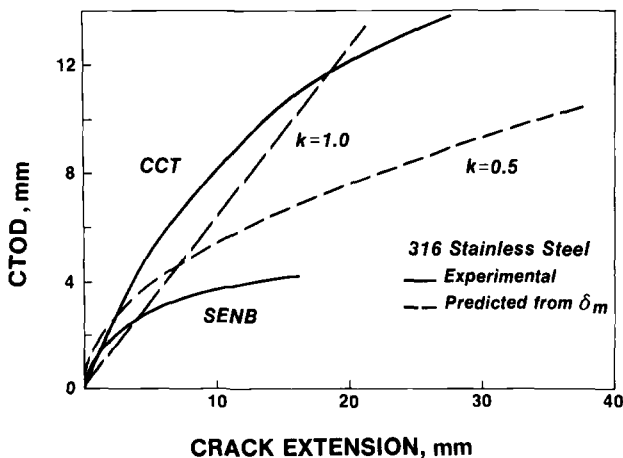


FIG. 5—Predicted and experimental R -curves for 316 stainless steel.

TABLE 6—Predictions for 316 stainless steel wide-plates using experimental and predicted *R*-curves.

Specimen Identification	Experimental Data		Predicted Data			
	Maximum Stress, MPa	Crack Extension at σ_c , mm	Assumed <i>R</i> -curve	Predicted Maximum Stress, MPa	Safety Factor	Predicted Crack Extension, mm
WP3	311	14	experimental-SENB	320	0.97	11
			experimental-CCT	368	0.85	13
			predicted $k = 1.0$	358	0.87	34
			predicted $k = 0.5$	337	0.92	18
WP4	337	13	experimental-SENB	307	1.10	12
			experimental-CCT	349	0.97	13
			predicted $k = 1.0$	342	0.99	33
			predicted $k = 0.5$	320	1.05	18

Analysis of Aluminum Weldments

The uncertainty in material flow properties is particularly pronounced in weldments. While it is relatively simple to determine tensile properties of weld metal and parent metal separately, the flow behavior at a welded joint may be quite complex if the weld metal undermatches or overmatches the yield strength of the parent plate. This behavior is demonstrated in the analyses of the three welded aluminum wide-plate specimens (see Tables 2 and 4a).

The aluminum weldments were analyzed using maximum load toughness and Eqs 11 to 16. In addition, a "best estimate" analysis was performed in an attempt to separate inherent errors in the simplified analysis from errors arising from the unusual flow behavior of the weldments.

The best estimate analysis was based on Eq 6 and the actual R -curves for the wide plates, which are plotted in Fig. 6. It was assumed that the behavior of the wide plates would be close to plane stress since the nominal thickness was 10 mm. Thus, $\mu = 0.75$ and $m_d = 1.0$ in Eq 6; m_{FP} was assumed to equal 1.3. The reference stress and strain at various loads were determined by fitting third-order polynomials to the stress-strain curves for the three weld metals

$$\epsilon = C_1\sigma^3 + C_2\sigma^2 + C_3\sigma + C_4 \quad (31)$$

These polynomial fits were made in order to allow driving force curves to be determined by computer. The maximum load conditions were determined graphically as with the 316 stainless steel.

Table 7 summarizes the predictions for the aluminum weldments. In all cases, the predictions of maximum stress lie below the experimental values. As indicated in Table 2, the parent metal is stronger than the weld metal in all three weldments. As discussed previously, the weld metal tensile properties were obtained with rectangular strips transverse to the welds with strain gages attached to the weld metal. Thus, the constraining effects of the parent metal on the weld metal flow properties were at least partially taken into account. However, additional constraint effects may be introduced in welded wide plates which contain cracks. At net section yield in a wide-plate specimen, 45° shear bands which extend from the crack to the edges of the plate would have to propagate through the parent metal. In a narrow strip, plastic flow would be confined primarily to the weld metal. Thus, the

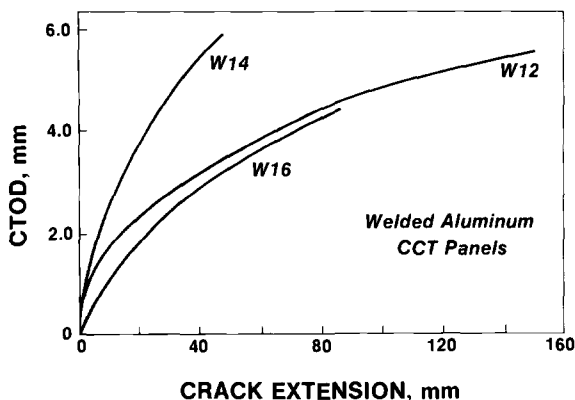


FIG. 6—Experimental R -curves for welded aluminum CCT panels.

TABLE 7—Predictions for welded aluminum wide-plate specimens.

Specimen Identification	Maximum Stress, MPa	Crack Extension at σ_c , mm	Analysis Method	Predicted Maximum Stress, MPa	Safety Factor	Predicted Crack Extension, mm
W12	200	20	$\delta_m, k = 1.0$	185	1.08	65
			$\delta_m, k = 0.5$	132	1.52	36
			best estimate	176	1.14	14
W14	181	30	$\delta_m, k = 1.0$	168	1.08	63
			$\delta_m, k = 0.5$	122	1.48	34
			best estimate	137	1.32	21
W16	154	40	$\delta_m, k = 1.0$	137	1.12	62
			$\delta_m, k = 0.5$	99.4	1.55	34
			best estimate	146	1.05	24

effective yield strength of a welded aluminum wide plate would be higher than in a narrow strip. The collapse stresses in the aluminum weldments were underestimated because the driving force curves were based on the flow properties of narrow tensile strips.

The Critical Tearing Modulus Concept

According to Eqs 16, 20, and 26, maximum stress is proportional to $(\delta_m^*)^{1/n+1}$. Thus the maximum stress is insensitive to toughness for low and medium work-hardening materials, as long as there is sufficient toughness to reach a condition of large-scale yielding prior to failure. In the fully plastic region, failure is controlled by the flow properties of the material. The failure stress in this region can be estimated from a simple limit load calculation. An analysis is presented below which is designed to estimate the required toughness to guarantee fully plastic behavior in a structure.

Consider a CCT panel. Rearranging Eq 16 to solve for maximum load CTOD leads to

$$\delta_m^* = L^2 Y^2 \pi a_m \alpha e_{ys} \left(\frac{1 - 2a_m}{W} \right)^2 \left(\frac{\sigma_n}{\sigma_{ys}} \right)^{n+1} \quad (32)$$

where σ_n is the effective net section stress at maximum load, given by

$$\sigma_n = \frac{\sigma_c}{L \left(\frac{1 - 2a_m}{W} \right)} \quad (33)$$

Equation 30 can be used to determine the required CTOD value for failure at a given σ_n/σ_{ys} ratio. However, this information alone would be of limited value because δ_m^* is highly geometry dependent. A δ_m value from a small-scale test specimen is usually much lower than the maximum load CTOD in a large structure or wide-plate specimen. A more convenient method for expressing the required toughness would be in terms of tearing modulus. By substituting Eq 13 into Eq 32, one can solve for the slope of the R -curve at maximum load

$$\frac{d\delta}{da} = 2(n + 1) L^2 Y^2 \frac{\pi a_m}{W} \left(\frac{1 - 2a_m}{W} \right) \alpha e_{ys} \left(\frac{\sigma_n}{\sigma_{ys}} \right)^{n+1} \quad (34)$$

Tearing modulus is a dimensionless parameter that is related to the slope of the $J - R$ curve. Recall from Eq 7 and 8 that J and CTOD are assumed to be related in the following way in the analyses presented in this article.

$$J = \sigma_{ys} \delta \quad (35)$$

Thus, the critical tearing modulus at maximum load is given by

$$T_c = \frac{dJ}{da} \frac{E}{\sigma_{ys}^2} = 2(n + 1) L^2 Y^2 \frac{\pi a_m}{W} \left(\frac{1 - 2a_m}{W} \right) \alpha \left(\frac{\sigma_n}{\sigma_{ys}} \right)^{n+1} \quad (36)$$

Figure 7 is a plot of critical tearing modulus versus $2a_m/W$ for σ_n/σ_{ys} ratios of 1.0 and 1.1. For this example, it was assumed that $n = 10$ and $\alpha = 2$. If the tearing modulus for a material with these assumed hardening characteristics lies above the solid line in Fig. 7, the

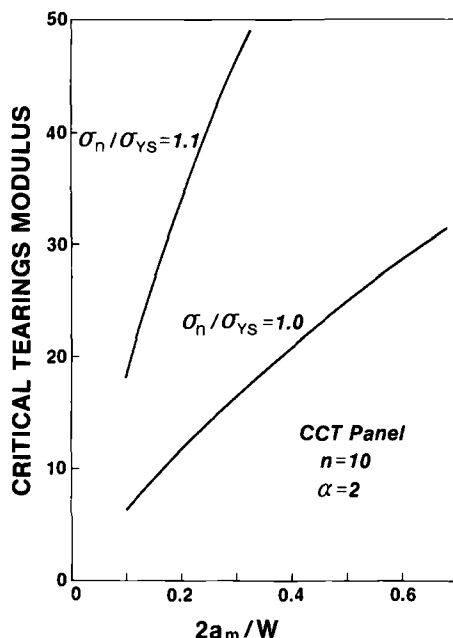


FIG. 7—Critical tearing modulus for fracture controlled failure in CCT wide plates.

structure will experience net section yielding prior to failure. Stated another way, the curves in Fig. 7 can be viewed as boundaries between collapse controlled failure and fracture controlled failure. Thus, if a material has adequate toughness to guarantee collapse controlled failure, one can avoid failure simply by ensuring that the net section stresses do not exceed σ_{YS} or $1.1 \sigma_{YS}$, depending on which curve is applicable. Note that if the crack size is relatively small, an extremely low tearing modulus ($T < \sim 10$) would be necessary for a structure to fail prior to net section yield. These results are consistent with those of Smith [14], who used a strip-yield analysis to show that for materials with $T > 10$, the failure load in a structure will be governed primarily by the net cross section rather than by the fracture properties of the material.

The critical toughness for collapse controlled failure can also be expressed in terms of maximum load CTOD in a small-scale test. By combining Eqs 11, 12, and 17, the relationship between maximum load CTOD values in small-scale and large-scale configurations can be determined

$$\delta_m^* = \delta_m \left(\frac{W - a_o}{b} \right)^k \quad (37)$$

where b is the ligament length in the small scale (SENB) specimen, $(W - 2a_o)$ is the total ligament length in the CCT panel, and δ_m^* and δ_m are the maximum load toughness values in the large-scale and small-scale configurations, respectively. Substituting the above relationship into Eq 32 gives

$$\delta_m = \left(\frac{b}{W - 2a_o} \right)^k L^2 Y^2 \pi a_m \alpha e_{YS} \left(\frac{1 - 2a_m}{W} \right)^2 \left(\frac{\sigma_n}{\sigma_{YS}} \right)^{n+1} \quad (38)$$

A small k value in the above equation will result in a large required toughness in a small-scale test. Thus, if k is assumed to equal 0.5, a conservative (high) estimate of required toughness for collapse controlled failure will be obtained for most materials.

Discussion

A method has been presented which allows a complete ductile fracture assessment to be performed without obtaining an R -curve experimentally. This approach is based on the assumption that a material's stress-strain curve and R -curve both follow simple power laws. In the present study, R -curves were predicted using maximum load CTOD values from small-scale tests. This procedure can also be applied to J values at maximum load. In addition, the procedure described in this article can be applied to an experimentally determined R -curve which is fitted to a power law expression. The advantage of applying this approach to an experimental R -curve is that maximum stress and crack extension could be determined algebraically rather than from a graphical analysis.

Figure 3 indicates that this approach tends to overestimate maximum stress. Mean safety factors on σ_c and standard deviations are listed in Table 8 for the three parent materials tested. When k is assumed to equal 0.5, the predicted stress is slightly lower than is obtained when a linear R -curve is assumed. With the exception of the SENT data, the standard deviations are relatively small. The variation in safety factor for the CCT and SESNT geometries is probably due primarily to material variability. As discussed above, the predictions for SENT panels were highly sensitive to the assumed R -curve, because the driving force curves are very steep when the ligament is small. Therefore, the SENT predictions are more widely scattered.

The use of a linear R -curve usually resulted in significant overestimates of crack extension at maximum load. A parabolic R -curve generally gave much better predictions of crack growth.

When experimental R -curves were used to analyze ductile failure in 316 stainless steel wide plates (see Table 6), the predicted maximum stresses varied only slightly from the values obtained from the estimated linear and parabolic R -curves. This indicates that maximum stress is not highly sensitive to the assumed R -curve in this material. A low work-hardening material would exhibit even less sensitivity to the R -curve. However, the results in Table 6 showed that predicted crack extension is a strong function of the assumed R -curve. Both experimental R -curves yielded good predictions of crack growth. However, the

TABLE 8—Summary of safety factors for predictions based on maximum load toughness.

Data Set	Average Safety Factor on Predicted σ_c	Standard Deviation
CCT, ^a $k = 1.0$	0.99	0.07
CCT, ^a $k = 10.5$	1.05	0.06
SESNT, $k = 1.0$	1.03	0.03
SESNT, $k = 0.5$	1.07	0.04
SENT, $k = 1.0$	1.03	0.10
SENT, $k = 0.5$	1.19	0.15
Overall, ^a $k = 1.0$	1.01	0.07
Overall, ^a $k = 0.5$	1.10	0.11

^a Does not include aluminum weldment predictions.

good agreement obtained by using the SENB *R*-curve may be fortuitous because this curve bears little resemblance to the actual *R*-curve for the CCT panel (see Fig. 5).

The predictions for the aluminum weldments were all well below the experimental maximum stress values. This was probably due to the fact that the driving force calculations were based on the weld metal yield strength, which was significantly overmatched by the parent material. Further work is necessary to improve understanding of the flow behavior of weldments before accurate fracture analyses can be performed.

It is noteworthy that the predicted stresses in Table 7 are more sensitive to the assumed *R*-curve than was the case for other materials. This is probably due to the higher strain hardening rates in the aluminum welds.

An analysis was presented which estimates the critical tearing modulus for fracture controlled failure in a CCT panel. This, analysis, with slight modifications, can also be applied to other configurations. The results of the analysis on the CCT geometry imply that only materials with fairly low toughness are likely to experience a ductile instability below net section yield. Materials such as high-strength steels on the upper shelf and high-strength aluminum alloys may fall into this category. Tougher materials, such as austenitic stainless steel, will fail at stresses well above yield. Thus, if a structure made from a tough material contains a crack, a simple limit load analysis can be applied to ensure that net section stresses do not exceed yield or flow stress, whichever is appropriate.

Although the above discussion implies that a fully ductile tearing analysis is unnecessary for many applications, there are instances where it is desirable to know the critical conditions for failure at high plastic strains. For example, the nuclear power industry frequently uses a ductile fracture analysis [1] to predict structural behavior in the event of an overload due to an accident. Also, a number of structures such as pipes and pressure vessels are sometimes proof tested beyond yield. The advantage of a detailed ductile tearing analysis is that it allows failure stress and crack extension to be predicted fairly accurately. However, this information may not be required for structures where the applied stresses are low and the toughness is high.

Thus, in structural situations involving ductile materials where it is not practical or desirable to obtain an *R*-curve experimentally, a CTOD test, in which a δ_m value is measured, would provide enough information to assess the risk of ductile fracture in the structure. If the toughness is adequate to guarantee collapse controlled failure, the designer could avoid failure simply by taking account of net section stresses. Alternatively, a more detailed assessment to predict maximum stress and crack extension could be performed using the small-scale δ_m value and the analyses developed in this article. A parabolic *R*-curve ($k = 0.5$) should be assumed in order to give a slightly conservative prediction of maximum stress and a reasonable estimate of crack extension.

When applying this approach, one should perform several CTOD (or *J*) tests on a given material in order to assess material variability. A lower bound δ_m value could be used to obtain a conservative estimate of failure stress. Alternatively, if a critical or best-estimate analysis is required, an average δ_m value might be more appropriate.

Conclusions

1. Relatively accurate ductile fracture analyses can be performed, using a parabolic *R*-curve estimated from maximum load toughness.
2. If a power law is fitted to an experimentally determined *R*-curve, the proposed analyses can be used to solve for maximum stress and crack extension algebraically.
3. Predicted values of stress are usually not sensitive to the assumed *R*-curve. In contrast, predicted crack extension values are strongly influenced by the shape of the *R*-curve.

4. Significant errors in a ductile fracture analysis can arise if material flow properties are not accurately determined. Consequently, accurate analyses of weldments are difficult, particularly when the weld metal significantly overmatches or undermatches the yield strength of the parent plate.

5. Analyses of center cracked geometries indicate that structures made from materials with a high tearing modulus (that is, $T > 10$) will fail at a net section stress above yield, as long as the flaw is small compared to the plate width.

APPENDIX

Selected Derivations of Ductile Instability Equations

SENB Specimens

As indicated in Fig. 1, $dP = 0$ at maximum load. This represents the point at which the rate of strain hardening is balanced by the loss of load carrying capacity due to crack growth. In a bend specimen where $\text{span} = 4W$, the load at net section yield is given by

$$P_Y = \frac{L\sigma_{YS}(W - a)^2 B}{4W} \quad (39)$$

where L is a constraint factor. The load at any point on the load-displacement curve can be written in terms of reference stress (Eq 3)

$$P = \frac{L\sigma_{ref}(W - a)^2 B}{4W} \quad (40)$$

At maximum load,

$$dP = 0 = \sigma_{ref}d(W - a)^2 + (W - a)^2 d\sigma_{ref} \quad (41)$$

assuming that L , B , and W remain constant.

$$\frac{d}{da}(W - a)^2 = -2(W - a) \quad (42)$$

Thus, at maximum load

$$2\sigma_{ref}(W - a_m)da = \left. \frac{\partial \sigma_{ref}}{\partial \delta} \right|_a d\delta(W - a_m)^2 \quad (43)$$

Rearranging gives

$$\frac{d\delta}{da} = \left. \frac{\partial \delta}{\partial \sigma_{ref}} \right|_a \frac{2\sigma_{ref}}{W - a_m} \quad (44)$$

The right side of Eq 44 can be solved by differentiating Eq 7 with respect to σ_{ref} . In order to solve this equation in closed form, a simple power law relationship between ϵ_{ref} and σ_{ref}

was assumed

$$\frac{\epsilon_{\text{ref}}}{\epsilon_{\text{YS}}} = \alpha \left(\frac{\sigma_{\text{ref}}}{\sigma_{\text{YS}}} \right)^n \quad (45)$$

Substituting the above relationship into Eq 7 gives

$$\delta = \alpha e_{\text{YS}} K^2 \frac{\sigma_{\text{ref}}^{n-1}}{\sigma_{\text{YS}}^{n+1}} \quad (46)$$

For a bend specimen, stress intensity is given by

$$K = \frac{PY}{BW^{1/2}} \quad (47)$$

Substituting Eqs 40 and 47 into Eq 46 gives

$$\delta = \frac{\alpha e_{\text{YS}} L^2 Y^2 (W - a)^4}{16 W^3} \left(\frac{\sigma_{\text{ref}}}{\sigma_{\text{YS}}} \right)^{n+1} \quad (48)$$

Differentiating with respect to σ_{ref} results in

$$\begin{aligned} \left. \frac{\partial \delta}{\partial \sigma_{\text{ref}}} \right|_a &= \frac{(n + 1) \alpha e_{\text{YS}} L^2 Y^2 (W - a)^4}{16 W^3} \frac{\sigma_{\text{ref}}^n}{\sigma_{\text{YS}}^{n+1}} \\ &= \frac{\delta(n + 1)}{\sigma_{\text{ref}}} \end{aligned} \quad (49)$$

Substituting Eq 49 into Eq 44 gives the conditions at maximum load

$$\frac{d\delta}{da} = \frac{2\delta_m(n + 1)}{W - a_m} \quad (50)$$

SESNT Panel

Consider a plate with a semielliptical surface crack $2c$ long and a deep. The load at a given point on the load displacement curve is given by

$$P = L\sigma_{\text{ref}} \left(BW - \frac{\pi ca}{2} \right) \quad (51)$$

At maximum load

$$dP = 0 = \sigma_{\text{ref}} d \left(BW - \frac{\pi ca}{2} \right) + d\sigma_{\text{ref}} \left(BW - \frac{\pi ca}{2} \right) \quad (52)$$

$$\frac{d}{da} \left(BW - \frac{\pi ca}{2} \right) = -\frac{\pi c}{2} - \frac{\pi a}{2} \frac{dc}{da} = -\frac{\pi}{2} (c + \theta a) \quad (53)$$

where $\theta = dc/da$.

Substituting Eq 53 into Eq 54 results in

$$\sigma_{\text{ref}} \frac{\pi}{2} (c + \theta a) da = \frac{\partial \sigma_{\text{ref}}}{\partial \delta} \bigg|_a \left(BW - \frac{\pi c a}{2} \right) d\delta \quad (54)$$

Rearranging gives

$$\frac{d\delta}{da} = \frac{\partial \delta}{\partial \sigma_{\text{ref}}} \bigg|_a \frac{\sigma_{\text{ref}} \pi (c + \theta a)}{2BW - \pi c a} \quad (55)$$

Equation 46 is also applicable to the SESNT configuration. The stress intensity factor for this geometry is given by

$$\begin{aligned} K &= Y\sigma\sqrt{\pi a} \\ &= YL\sigma_{\text{ref}} \left(1 - \frac{\pi c a}{2BW} \right) \sqrt{\pi a} \end{aligned} \quad (56)$$

Substituting into Eq 46 gives

$$\delta = L^2 Y^2 \pi a \alpha e_Y \left(1 - \frac{\pi c a}{2BW} \right)^2 \left(\frac{\sigma_{\text{ref}}}{\sigma_{\text{YS}}} \right)^{n+1} \quad (57)$$

Differentiating Eq 59 with respect to σ_{ref} leads to

$$\frac{\partial \sigma_{\text{ref}}}{\partial \delta} \bigg|_a = \frac{\delta(n+1)}{\sigma_{\text{ref}}} \quad (58)$$

which is the same result as was obtained for the SENB configuration (Eq 49). The slope of the R -curve at maximum load is therefore given by

$$\frac{d\delta}{da} = \frac{\pi(c_m + \theta a_m) \delta_m^{*(n+1)}}{2BW - \pi c_m a_m} \quad (59)$$

The maximum load CTOD is related to crack growth at maximum load by

$$\delta_m^* = \beta \Delta a_m^k \quad (60)$$

Differentiating the above expression gives

$$\frac{d\delta}{da} = k\beta \Delta a_m^{k-1} \quad (61)$$

The initial and final crack dimensions are related as follows

$$a_m = a_o + \Delta a_m \quad (62)$$

$$c_m = c_o + \theta \Delta a_m \quad (63)$$

Combining Eqs 59 and 63 and solving for Δa_m gives

$$\Delta a_m = \frac{k[2BW - \pi(c_o + \theta\Delta a_m)(a_o + \Delta a_m)]}{\pi(n+1)C_o + \theta(a_o + 2\Delta a_m)} \quad (64)$$

An iterative calculation must be performed to determine Δa_m .

The maximum remote stress can be obtained by rearranging Eq 57 and setting $\delta = \delta_m^*$, $a = a_m$, and $c = c_m$

$$\sigma_c = L\sigma_{ys} \left(1 - \frac{\pi c_m a_m}{2BW} \right) \left[\frac{\delta_m^*}{L^2 Y^2 \pi a_m \alpha e_{ys} \left(1 - \frac{\pi a_m c_m}{2BW} \right)^2} \right]^{1/n+1} \quad (65)$$

References

- [1] Kumar, V., German, M. D., and Shih, C. F., "An Engineering Approach for Elastic-Plastic Fracture Analysis," EPRI Report NP 1931, Electric Power Research Institute, Palo Alto, CA, July 1981.
- [2] Towers, O. L. and Garwood, S. J., "The Use of Maximum Load Toughness for Ductile Fracture Assessments," Welding Institute Report No. 157/1981, The Welding Institute, Cambridge, England, September 1981.
- [3] Garwood, S. J., "A Crack Tip Opening Displacement (CTOD) Method for the Analysis of Ductile Materials," *Fracture Mechanics: Eighteenth Symposium, ASTM STP 945*, American Society for Testing and Materials, Philadelphia, 1988.
- [4] Towers, O. L. and Garwood, S. J., "The Geometry Dependence and Significance of Maximum Load Toughness Values," *Proceedings*, Third European Conference on Fracture, London, England, September 1980.
- [5] Ainsworth, R. A., "The Assessment of Defects in Structures of Strain Hardening Materials," *Engineering Fracture Mechanics*, Vol. 19, 1984, p. 633.
- [6] Akhurst, K. N. and Milne, I., "Failure Assessment Diagrams and J Estimates; Validation for an Austenitic Steel," *Application of Fracture Mechanics to Materials and Structures*, Martinus Nijhoff Publishers, Dordrecht, The Netherlands, 1984, p. 401.
- [7] Anderson, T. L., "Elastic-Plastic Fracture Assessments Based on CTOD," Welding Institute Report 276/1985, The Welding Institute, Cambridge, England, June 1985.
- [8] Anderson, T. L., "A Comparison of J and CTOD as Fracture Toughness Parameters," *Fracture Mechanics: Eighteenth Symposium, ASTM STP 945*, American Society for Testing and Materials, Philadelphia, 1988.
- [9] Anderson, T. L., Leggatt, R. H., and Garwood, S. J., "The Use of CTOD Methods in Fitness for Purpose Analysis," *Proceedings*, Workshop on CTOD Methodology, Geestacht, West Germany, April 1985.
- [10] Dowling, N. E., "J-Integral Estimates for Cracks in Infinite Bodies," *Engineering Fracture Mechanics*, in press.
- [11] Chell, G. G., "Elastic-Plastic Fracture Mechanics," *Developments in Fracture Mechanics*, Applied Science Publishers, London, 1979, p. 67.
- [12] PD6493, "Guidance on Some Methods for the Derivation of Acceptance Levels for Defects in Fusion Welded Joints," British Standards Institution, London, March 1980.
- [13] Hertzberg, R. W., in *Deformation and Fracture Mechanics of Engineering Materials*, Wiley, New York, 1983.
- [14] Smith, E., "Unstable Crack Growth in a Component Subject to Constant Applied Loads: The Interaction Between Plasticity and Geometrical Effects," *International Journal of Pressure Vessels and Piping*, Vol. 15, 1984, p. 307.

Application of the J Concept to Fatigue Crack Growth in Large-Scale Yielding

REFERENCE: Lambert, Y., Saillard, P., and Bathias, C., “Application of the J Concept to Fatigue Crack Growth in Large-Scale Yielding,” *Fracture Mechanics: Nineteenth Symposium, ASTM STP 969*, T. A. Cruse, Ed., American Society for Testing and Materials, Philadelphia, 1988, pp. 318–329.

ABSTRACT: Fatigue crack propagation tests were performed on compact tension specimens of AISI 316 steel, in the elastic-plastic and plastic regions. The parameter ΔJ was chosen to characterize propagation. Results show that there is a Paris law type correlation between propagation rate and ΔJ . An effect on propagation rate, which is attributed to the $R = P_{\min}/P_{\max}$ ratio, has been noted.

A numerical verification of the applicability of the ΔJ concept was determined by use of a theoretical equation. These results were compared with experimental results.

KEY WORDS: low-cycle fatigue, fatigue crack growth rate, J integral, ΔJ integral, R -ratio effect, numerical calculation, Eisenberg model, fracture mechanics

In large structures and welded parts it is advisable and more realistic to assume the presence of a defect, and then determine how fast it grows. However, expressions based on linear elastic fracture mechanics become inaccurate in applications that involve gross plasticity before fracture. In conjunction with the “leak before break” concept, exhaustive fatigue crack propagation analysis has required study of deep cracks, for which the ligament between the crack tip and opposite wall can be in the plastic range. In this case an elastic-plastic analysis is necessary when the crack grows in a yielded zone. For this case, it appears that the most suitable approach is based on the variation of ΔJ , an extension of the J integral, during a stress cycle.

In this study, fatigue crack propagation is characterized in a structure made of stainless steel AISI 316 in a medium developing from confined to generalized plasticity. The objective is to correlate the crack growth rate da/dN with the ΔJ integral using a Paris law extension:

$$\frac{da}{dN} = C(\Delta J)^n$$

where C and n are intrinsic parameters of the material.

This study is presented in two parts:

1. Experiments were performed to determine the laws governing fatigue propagation and to demonstrate the conservation of contained yielding and da/dN with a constant ΔJ level and increasing values of a/w .

¹ Research engineers and professor, respectively, Université de Compiègne, Groupe Mécanique, 60206 Compiègne, France.

² Framatome, Centre de Calcul, 71380 Saint Marcel, France.

The ΔJ integral is an extension of the J integral under cyclic stress. In the same availability domain as J , the ΔJ integral between two loading states, l and m , can be expressed by

$$\Delta J_{l,m} = \int \left[\Delta W_{l,m} n_1 - \Delta \vec{t}_{l,m} \frac{\partial}{\partial x_1} (\Delta \vec{U}_{l,m}) \right] ds \quad (2)$$

where $\Delta W_{l,m}$, $\Delta t_{l,m}$, and $\Delta U_{l,m}$ are the variations of W , t , and U between the two states l and m .

This formula was presented by Landes and developed by Tanaka [2] in the elastic and elastoplastic domain with a physical interpretation using the Dugdale model.

The ΔJ , calculated between two states, uses the fact that J varies during cyclic stress but is not equal to the variation. It may be written as

$$\Delta J_{l,m} \neq J_m - J_l$$

To show this, it is adequate to develop Eq 2, which yields

$$\Delta J_{l,m} = J_m - J_l - \int_{\Gamma} \left\{ (\sigma_{ij})_l [(\epsilon_{ij})_m - (\epsilon_{ij})_l] n_1 - \left(\vec{t}_m \frac{\partial U_l}{\partial x_1} \right) + \vec{t}_l \frac{\partial U_m}{\partial x_1} \right\} ds \quad (3)$$

where σ_{ij} and ϵ_{ij} are stress and strain components with corresponding states.

After numerical simulation we try to calculate ΔJ with Eq 2. For experimental studies, the stress and strain fields at the crack tip are not known, so we must use a simpler formula to calculate ΔJ .

Experimental Approach

Several methods have been proposed to determine ΔJ ; the methods are based on the strain energy density [3,4,5], the loading envelope curve [6], the crack opening displacement (COD) [7,8], and the load-displacement curve [9,10,11]. The last approach was selected since the theoretical basis appears to be the best and permits easier processing of empirical data. Since ΔJ was shown to be identical to an energy rate definition similar to the original integral definition of J , ΔJ is given by

$$\Delta J = -\frac{1}{B} \left(\frac{d(\Delta U)}{da} \right) \quad (4)$$

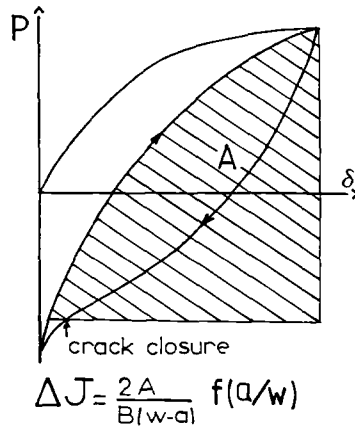
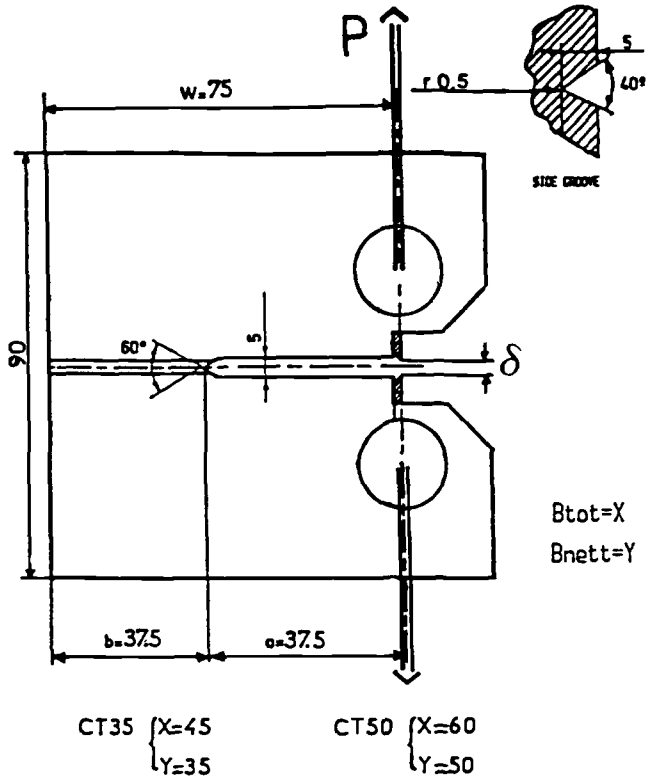
where ΔU is the potential energy treated by deformation theory, B is the specimen thickness, and a is the crack length; ΔU is given by

$$\Delta U = \int \Delta P d\delta \quad (5)$$

where ΔP is the loading amplitude and δ is the displacement. Equations 4 and 5 together give the well known formula

$$\Delta J = \frac{2A}{Bb} \quad (6)$$

where A is the area under the load-displacement curve and b is the remaining ligament (Fig. 2). Moreover, Landes [12] who studied fatigue crack propagation in the compact tension


 FIG. 2—Experimental measurement of ΔJ on the CT specimens.

(CT) specimen, showed that Eq 6 with a correct coefficient gives the best results [13]. Therefore, ΔJ will be expressed by

$$\Delta J = \frac{2A}{Bb} \left(\frac{1 + \alpha}{1 + \alpha^2} \right) \quad (7)$$

where

$$\alpha = \frac{\left[2 \left(\frac{a}{w} \right)^2 + 2 \right]^{1/2} - \left(1 + \frac{a}{w} \right)}{1 - \frac{a}{w}}$$

The ΔJ concept will be applied to analyze experimental and numerical results. Tests give the load-displacement evolution, from which a first-value ΔJ_1 may be deduced using Eq 7.

From numerical simulation, two types of information are obtained:

1. The load-displacement variation, as does the tests, gives a new value for ΔJ_2 (Eq 7), and
2. Stress and displacement fields in the structure can therefore be applied to a theoretical relation (Eq 2) to obtain the value ΔJ_3 .

This method allows us to validate the measuring technique for ΔJ , by comparing ΔJ_3 to ΔJ_2 and ΔJ_1 , for two tests performed at two different ΔJ levels.

Experimental Study

Material

The material studied is an AISI 316 stainless steel for which the chemical and mechanical properties are presented in Tables 1 and 2, respectively. The specimens were side-grooved compact tension (CT) specimens of two different thicknesses, 35 and 50 mm between the grooves. Figure 2 gives the dimensions.

Procedure

Tests were performed at ambient temperature on a Mayes servo-hydraulic fatigue machine. An opening transducer is used in the loading axis. This transducer both measured and controlled the opening. Two methods of control were used: one involved keeping ΔJ constant and the second increased ΔJ . In both cases ΔJ was calculated from the load-displacement curve. Displacement was controlled to maintain a constant ΔJ or to increase it. Crack length was measured by the electrical potential method. Optical measurements proved unsuitable because of the presence of side grooves.

TABLE 1—Chemical composition in percent by weight of AISI 316 stainless steel.

C	Ni	Cr	Mn	CU	Si	Mo	Co	P	N
0.028	12.22	17.48	1.72	0.21	0.47	2.34	0.12	0.034	0.072

TABLE 2—Mechanical properties of AISI 316 stainless steel.

0.2% Yield Strength, MPa	Ultimate Strength, MPa	Reduction in Area, %
294	590	56

Loading of the specimen was carried out in three steps:

1. Precracking to initiate the crack elastically.
2. Cracking under displacement control to reach the threshold of excessive deformation, where the elastic deformation is equal to the plastic deformation. This limit is reached after a few cycles by location on the stabilized p versus δ plot of the specimens. The threshold is determined experimentally and by the Electric Power Research Institute (EPRI) equation [14].
3. Crack propagation at constant or increasing ΔJ .

Results and Discussion

Initially tests at constant ΔJ were examined in order to verify the one-to-one relationship between da/dN and ΔJ . Subsequently, certain test conditions were varied, such as the number of cycles, crack size, and specimen geometry. Finally, the continuous variation of da/dN as a function of J was measured in the range of crack propagation rates of 5.10^{-2} and 0.5 mm/cycle.

Constant ΔJ Test— ΔJ Measurement—This type of test produces confinement effects. The points obtained at constant ΔJ are plotted in Fig. 3. It may be noted that for a given ΔJ the propagation rate is not constant but decreases slightly during the test. It seems, therefore, that the stress and strain state at the crack tip is virtually reproducible, from one cycle to another. The slight decrease is due to two phenomena:

- (a) The modification of the stress and strain fields at the crack tip at each closure.
- (b) The variation of R ratio during cycling.

A study of hysteresis curves shows that, parallel with the change in closure effects, the factor $R = P_{\min}/P_{\max}$ decreases in an acyclic manner. A potential correction formula based on the R ratio is envisaged to give another parameter $(\Delta J)_{\text{eff}}$. The literature on this subject [15] shows that the governing parameter in fatigue crack propagation must take into account the effect of R ratio. In the case of stainless steels, the following formula was used

$$(\Delta J)_{\text{eff}} = \frac{\Delta J}{\left(1 - \frac{R}{2}\right)^2}$$

Taking into account the effect of ratio R in tests with constant ΔJ , one obtains different values of $(\Delta J)_{\text{eff}}$, which could explain the differences in crack propagation rates (Fig. 3). However, it should be noted that the scatter in da/dN measurements (Fig. 4) is of the same magnitude as the scatter band for measurements of the $(da/dN) - \Delta J$ evolution presented below.

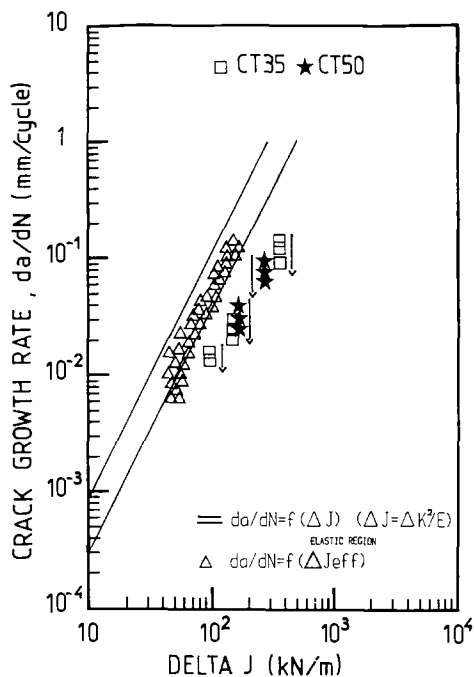


FIG. 3—Fatigue crack growth behavior at constant ΔJ and R ratio dependence.

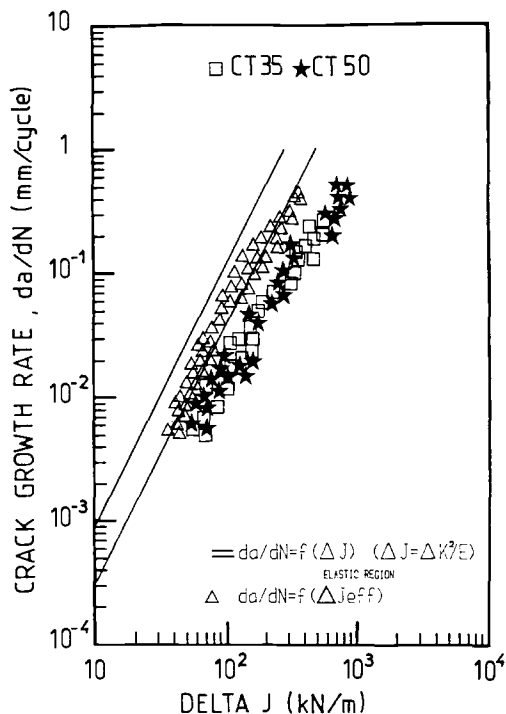


FIG. 4—Fatigue crack growth behavior at increasing ΔJ and R ratio dependence.

Propagation Rate Measurement—The crack propagation curve (propagation rate as a function of the ΔJ parameter) in Fig. 4 shows a linear relationship for a logarithmic plot of these two parameters. The crack propagation results may be analyzed by a Paris law of the form

$$\frac{da}{dN} = C(\Delta J)^n$$

where $c = 1.4151 \times 10^{-5}$ and $n = 1.55$.

The linear relationship between ΔJ and the crack propagation rate demonstrates that the ΔJ parameter characterizes cracking from the elastic to plastic range. The exponent value is in agreement with results obtained by Kaisand and Mowbray [8], Rie et al. [16], and Dowling [4]; their values were 1.6, 1.5, and 1.56, respectively. Vardar [17] obtained 1.77 for Type 1020 steel. Comparison was performed between our results and the extrapolation of the dispersion range from $da/dN = f(\Delta J)$ results, obtained in the confined region. Moreover, Fig. 4 shows a better representation of experimental results as a function of $(\Delta J)_{\text{eff}}$.

Numerical Simulation

Calculation Assumptions

The calculations are based on the following assumptions:

- (a) the crack length remains constant,
- (b) the structure is in plane strain,
- (c) a crack closure is simulated numerically, and
- (d) the material behavior is elastoplastic.

After a calculation of assumed plane strain conditions, the lateral notches may be taken into account by introducing the effective thickness of the specimen [18].

For moderate levels of plasticity

$$B_{\text{eff}_1} = \sqrt{B_{\text{total}} \cdot B_{\text{net}}}$$

where B_{total} and B_{net} are the total thickness and the thickness between side notch tips, respectively.

For high levels of plasticity

$$B_{\text{eff}_2} = \sqrt{B_{\text{total}} \cdot B_{\text{net}}} \left[1 - \left(\frac{B_{\text{total}} - B_{\text{net}}}{B_{\text{total}}} \right)^2 \right]$$

Calculation Models—Determination of Parameters

Two types of calculation models are used here: a model of cyclic plasticity proposed by Eisenberg [19] and a more classic plasticity model, implemented using the Titus system [20].

Cyclic Plasticity Model—The Eisenberg model simulates the cyclic strengthening of the materials. The behavior of the structure is calculated successively for each cycle. A simplified version of the model was preferred as it enabled a stabilized cycle to be obtained from the

first load increase and the required number of parameters to be reduced to:

- (a) the elastic limit,
- (b) the strain hardening coefficients for the initial loading, and
- (c) the strain hardening coefficients for the stabilized cycle.

These parameters are determined from a preliminary series of tests on tensile specimens in fatigue, performed at different strain amplitudes. Figure 5 shows that for these specimens the calculated results agree well with test results.

The model will be referred to as Model A.

Cinematic Plasticity Model—It is also of interest to use a simpler model; a cinematic plasticity model, associated with a strain hardening law for the material given by the cyclic law (linked to the maxima of the stabilized cycles obtained experimentally).

This model will be referred to as Model B.

Results and Discussion

The results obtained from Models A and B were compared with one another and with the experimental results for the P versus δ curve. Two loading levels, corresponding to different ΔJ values were modelled. Level I corresponds to a displacement of 1.15 mm and Level II to a displacement of 1.6 mm.

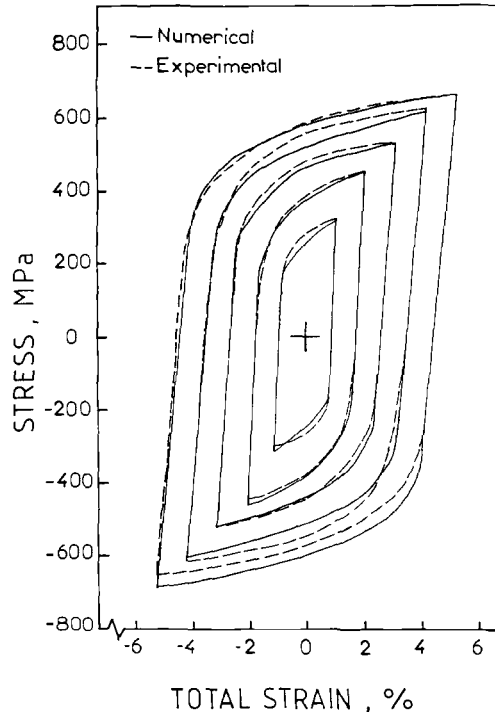


FIG. 5—Stress-strain comparison between the experimental and calculated results using the Eisenberg model.

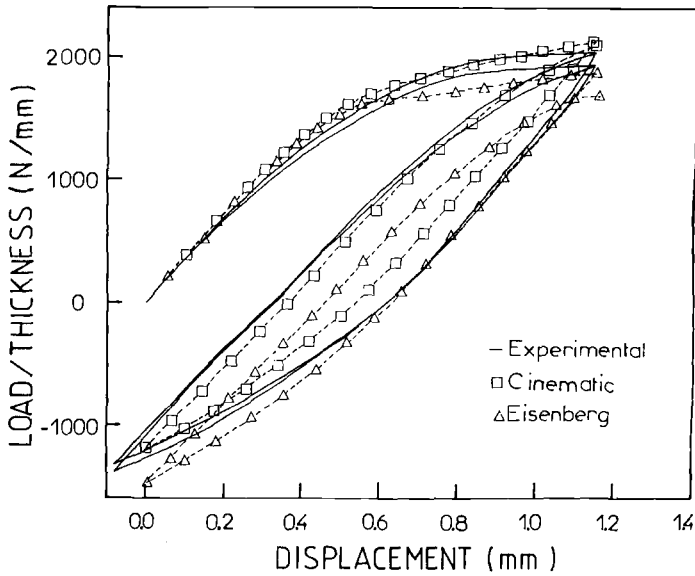


FIG. 6—Load displacement curves from the Eisenberg and kinematic plasticity models compared with the experimental results at Level I.

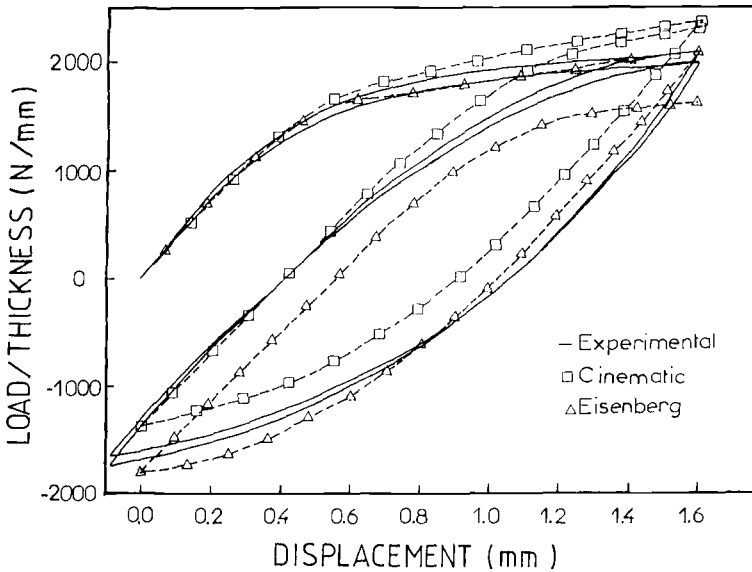


FIG. 7—Load displacement curves from the Eisenberg and kinematic plasticity models compared with the experimental results at Level II.

TABLE 3—Comparison of ΔJ values for Level I.

	Model A		Model B		Experimental, Empirical, ΔJ_1 , kN/m	
	Theoretical, ΔJ_3 , kN/m	Empirical, ΔJ_2 , kN/m	Theoretical, ΔJ_3 , kN/m	Empirical, ΔJ_2 , kN/m	min	max
ΔJ	146.29	147.6	149.84	150.5	146.35	153.95

Load Displacement Curve—For Models A and B, the P versus δ curve for Level I was compared with an experimental “envelope” of two curves (Fig. 6). The experimental curve is referred to the two effective thicknesses previously defined. For Level I, Models A and B were used to compare the results obtained.

The P versus δ curve for Level II was also compared with an experimental envelope of two curves as explained above (Fig. 7).

It should be noted that Model B more closely represents the minimum load, whereas Model A is closer to the maximum load. It can also be noted that the experimental P versus δ curve becomes slightly negative. This is due to inertia in the control system and the relocation of the transducer on the knife edges during large openings.

Calculation of ΔJ —For Levels I and II, a calculation of $\Delta J_{\text{theoretical}}$ was performed, using Eq 2, on nine contours that were concentric around the crack tip. The calculations for Models A and B were compared with the results given by the empirical Eq 7 applied to the numerical cycles, and with the experimental results interpreted by Eq 7 where B is replaced by B_{eff} . Results are shown in Table 3 for Level I and in Table 4 for Level II.

It is apparent that the scatter of ΔJ_1 values covers the numerical results, and that a comparison of ΔJ_2 and ΔJ_3 reveals a difference of the order of 1%. This comparison formally validates the experimental technique used to measure ΔJ (Eq 7).

Toughness Measurement—In this study the level at which ductile tearing begins, a level usually characterized by J_{IC} , is approximately 1500 kN/m. For the cycles at Level II the J integral at maximum loading is of the order of 190 kN/m, about seven times less than J_{IC} . Ductile tearing can thus not take place during the first cycle. However, on the fracture surfaces, microvoids and perhaps cuplike fractures are observed. The cavities appear as a result of the fatigue tearing interaction, which for large strains causes shearing of the walls of microvoids during propagation.

TABLE 4—Comparison of ΔJ values for Level II.

	Model A		Model B		Experimental, Empirical, ΔJ_1 , kN/m	
	Theoretical, ΔJ_3 , kN/m	Empirical, ΔJ_2 , kN/m	Theoretical, ΔJ_3 , kN/m	Empirical, ΔJ_2 , kN/m	min	max
ΔJ	247.8	253.3	258.53	261.3	252.95	266.1

Conclusions

The correlation between the crack propagation rate and the parameter J is conservative with respect to the material characteristics curves. The crack propagation rate can be correlated successfully with the parameter ΔJ or ΔJ_{eff} , which integrates the effect of the R ratio if more accuracy is required.

Certain tests have been simulated numerically and the ΔJ integral has been calculated, as defined by Tanaka. The experimental method of measuring ΔJ has thus been validated. A very close agreement has been shown between the empirical and numerical results.

A calculation method has been introduced which may now be applied to industrial structures for the case of generalized plasticity.

Acknowledgments

We wish to thank M. Devaux, M. Dubois, and M. Mottet from Framatome for their helpful suggestions.

References

- [1] Rice, J. R. in *Fracture—An Advanced Treatise*, Vol. II, *Mathematical Fundamentals*, Academic Press, New York, 1968, pp. 191–311.
- [2] Tanaka, K., *International Journal of Fracture*, Vol. 22, 1983, pp. 91–104.
- [3] Dowling, N. E. in *Cyclic Stress-Strain and Plastic Deformation Aspects of Fatigue Crack Growth*, ASTM STP 637, American Society for Testing and Materials, Philadelphia, 1977, pp. 97–121.
- [4] Kaisand, L. R. and Mowbray, D. F., *Journal of Testing and Evaluation*, Vol. 7, No. 5, 1979, pp. 270–280.
- [5] Liu, Y. Y. and Lin, F. S., *International Journal of Fatigue*, Vol. 6, No. 1, 1984, pp. 31–36.
- [6] Landes, J. D. and McCabe, D. E., "Load History Effects on the J_R Curve," Scientific Paper 81-107, Westinghouse R and D, Pittsburgh, PA, 1981.
- [7] Tomkins, B., Summer, G., and Wareing, J., *Proceedings*, International Symposium LCF Strength And Elastic-Plastic Behavior of Materials, Stuttgart, West Germany, 1979, p. 495.
- [8] Wang, S.-Z., and Yang, Z., *Engineering Fracture Mechanics*, Vol. 18, No. 5, 1983, pp. 895–902.
- [9] Dowling, N. E. and Begley, J. A. in *Mechanics of Crack Growth*, ASTM STP 590, American Society for Testing and Materials, Philadelphia 1976, pp. 82–103.
- [10] Dowling, N. E. in *Cracks and Fracture Ninth Conference*, ASTM STP 601, American Society for Testing and Materials, Philadelphia 1974, pp. 19–32.
- [11] Clarke, G. A. and Landes, J. D., *Journal of Testing and Evaluation*, Vol. 7, No. 5, 1979, pp. 262–269.
- [12] Landes, J. D., Walkers, H., and Clarke, G. A. in *Elastic-Plastic Fracture*, ASTM STP 668, American Society for Testing and Materials, Philadelphia, 1979, pp. 266–287.
- [13] Clarke, G. A. and Landes, J. D., "Evaluation of the J Integral for the Compact Specimen," *Journal of Testing and Evaluation*, Vol. 7, No. 5, 1979, pp. 264–269.
- [14] "An Engineering Approach for Elastic-Plastic Fracture Analysis," EPRI Report, Electric Power Research Institute, Palo Alto, CA.
- [15] Bernard, J. L. and Slama, G. S., *Nuclear Technology*, Vol. 59, 1982, pp. 136–147.
- [16] Rie, K. T., Schuber, R., and Kohler, N., in *Proceedings*, Fifth European Conference on Fracture, 1984, pp. 469–479.
- [17] Vardar, O., *Journal of Engineering Material and Technology*, Vol. 104, 1982, pp. 192–199.
- [18] Devaux, J. C., Dubois, D., and Mottet, G., "3D Elastoplastic Analysis of 2 CT 50 Fracture Specimens," *Proceedings*, Tendances Actuelle en calcul des structures, Bastia, France, 6–8 Nov. 1985, pp. 613–629.
- [19] Eisenberg, M. A., "Generalization of Plastic Flow Theory with Application to Cyclic Hardening and Softening Phenomena," *Journal of Engineering Material and Technology*, 1976, pp. 221–228.
- [20] "System Titus: Comportement élastoplastique des structures en grandes déformations," *Comportement élastoplastique des structures en fatigue oligocyclique*, Framatome, Chalon sur Soane, France.

Fracture Toughness of Stainless Steel Welds

REFERENCE: Mills, W. J., "Fracture Toughness of Stainless Steel Welds," *Fracture Mechanics: Nineteenth Symposium, ASTM STP 969*, T. A. Cruse, Ed., American Society for Testing and Materials, Philadelphia, 1988, pp. 330-355.

ABSTRACT: The effects of temperature, composition, and weld-process variations on the fracture toughness behavior for Types 308 and 16-8-2 stainless steel (SS) welds were examined using the multiple-specimen *J*-resistance-curve procedure. Fracture characteristics were found to be dependent on temperature and weld process, but not on filler material. Gas-tungsten-arc (GTA) welds exhibited the highest fracture toughness, a shielded-metal-arc (SMA) weld exhibited an intermediate toughness, and submerged-arc (SA) welds yielded the lowest toughness. Minimum expected fracture properties were defined from lower bound fracture toughness and tearing modulus values generated here and in previous studies.

Fractographic examination revealed that microvoid coalescence was the operative fracture mechanism for all welds. Second-phase particles of manganese silicide were found to be detrimental to ductile fracture behavior because they separated from the matrix during the initial stages of plastic straining. In SA welds, the high density of inclusions resulting from silicon pickup from the flux promoted premature dimple rupture. The weld produced by the SMA process contained substantially less manganese silicide, while GTA welds contained no silicide inclusions. Delta ferrite particles, present in all welds, were substantially more resistant to local failure than the silicide phase. In welds containing little or no manganese silicide, delta ferrite particles initiated microvoid coalescence, but only after extensive plastic straining.

KEY WORDS: fracture of materials, fracture toughness, *J*-integral, elevated temperature tests, fractography, stainless steel welds, fracture mechanics

Austenitic stainless steel alloys are used extensively in the welded construction of permanent structures in liquid-metal reactors. These components are typically manufactured and inspected in accordance with the American Society of Mechanical Engineers (ASME) Boiler and Pressure Vessel Code, which assures the absence of defects that could jeopardize the structural integrity of a reactor. Nevertheless, the significance of crack-like defects (either actual or hypothetical) must be evaluated to quantify structural integrity margins in support of licensing, safety assessments, and inspection requirements. Recent advances in elastic-plastic fracture mechanics enable reasonably accurate predictions of failure conditions for flawed stainless steel components to be made [1-6].

Previous studies [7-13] of the ductile fracture toughness behavior for stainless steel (SS) welds at 24 to 538°C reveal considerable variability in J_c initiation toughness.² This wide range of J_c values also persists at cryogenic temperatures [14-17]. These test results, however, were obtained using many different specimen geometries and test procedures, and the data were not analyzed using the same criterion. Therefore, some of the variability may result

¹ Fellow engineer, Westinghouse Hanford Co., Richland, WA 99352.

² Initiation toughness values are termed J_c rather than J_{Ic} because they do not strictly meet the requirements of the ASTM Test for J_{Ic} , a Measure of Fracture Toughness (E 813-81).

directly from different test procedures and analyses. Most results were generated prior to the development of the ASTM Test for J_{Ic} , a Measure of Fracture Toughness (E 813-81). Moreover, the ASTM test procedures and size requirements are not generally applicable to high-ductility, high-toughness materials, such as austenitic stainless steels.

The objective of the current investigation was to evaluate the effects of temperature, composition, and weld-process variations on the fracture toughness response for three Type 308 SS welds and two Type 16-8-2 SS welds, using consistent J -resistance, J_R , curve test procedures. Three different weld processes were studied, including shielded-metal-arc (SMA), submerged-arc (SA), and gas-tungsten-arc (GTA) processes. Metallographic and fractographic examinations were performed to relate key microstructural features to fracture toughness properties.

Experimental Procedure

Material

Chemical analyses, ferrite numbers, heat numbers, and welding processes for the test materials are given in Table 1. Cross-sectional profiles of the welds are shown in Figs. 1 and 2. The tensile properties (Table 2) were consistent with those reported previously for stainless steel welds [18].

All welds exhibited a duplex austenite-ferrite microstructure with residual delta ferrite located at the cores of primary and secondary dendritic branches (Figs. 3 through 5). Four types of ferrite phase morphologies were observed, including vermicular [19], lacy [20], lathy [19] or acicular [20], and globular [20]. Table 3 provides a summary of the microstructural features for each weld. The vermicular morphology was the most common in all welds, and it was generally accompanied by limited amounts of lacy structure. Acicular ferrite was only observed in the crown region of the 16-8-2 SA weld. This type of structure is usually found in weld metals with equivalent chromium-to-nickel (Cr_{eq}/Ni_{eq})³ ratios greater than 2 [20]. The present results are consistent with this trend since the 16-8-2 SA weld had a Cr_{eq}/Ni_{eq} ratio of 2.07. All other welds exhibited Cr_{eq}/Ni_{eq} ratios between 1.69 and 1.83.

Thermal excursions produced by subsequent weld passes caused the residual ferrite to spheroidize. This was particularly evident in the high-heat-input SA welds, where the ferrite network began to break down into a globular morphology in localized regions (Fig. 4c). Globular ferrite was observed in the intermediate-heat-input SMA weld, but it was confined to partially remelted zones between adjacent weld passes. No evidence of ferrite globules was detected in the low-heat-input GTA welds. Some ferrite coarsening was observed in the partially remelted zones, but the heat input was insufficient to induce major shape instabilities.

Figure 4 revealed a high density of spherical manganese silicide particles (identified by energy-dispersive X-ray analysis of thin foil specimens) distributed throughout the austenitic matrix in the two SA welds. A few coarse silicide particles were also found in the SMA weld, but almost none were observed in the GTA welds. The GTA welds contained a few small aluminum-rich particles (probably alumina) in the interdendritic regions, but they did not influence the overall fracture properties. High silicon contents, and therefore high silicide densities, are generic to SA welds because of silicon pickup from the flux. The two SA welds contained the highest silicon content (1.0 and 1.03%), the SMA weld had an intermediate silicon content (0.61 to 0.79%), and the GTA welds contained the least silicon (0.29 and 0.40%).

³ $Cr_{eq} = Cr + Mo + 1.5 Si + 0.5 Nb$; $Ni_{eq} = Ni + 30 C + 0.5 Mn$.

TABLE 1—Chemical composition of the test materials.

Material	Heat or Welding Process	Heat Number	Element, weight %													Ferrite Number
			C	Mn	P	S	Si	Cr	Ni	Co	Ti	Nb + Ta	Cu	Mo		
308 SS weld	SMA-A	...	0.07	1.94	0.010	0.015	0.79	20.35	9.72	0.08	...	0.04	0.21	0.22	6.8	
	SMA-B	...	0.07	1.99	0.010	0.010	0.61	20.20	9.46	0.08	...	0.03	0.14	0.18	7.7	
	SMA-C	...	0.07	1.95	0.010	0.015	0.62	20.30	9.82	0.08	...	0.04	0.21	0.21	6.4	
	GTA	Y24120308	0.04	1.77	0.023	0.014	0.40	20.21	9.60	9.9	
	SA	D3418R304L	0.03	2.30	0.010	0.009	1.03	19.41	9.51	0.08	...	0.01	0.26	0.21	10.7	
16-8-2 SS weld	GTA	Y2367R16-8-2	0.045	1.25	0.024	0.013	0.29	16.36	8.62	1.67	5.7	
	SA	D4494T16-8-2	0.047	1.95	0.020	0.006	1.0	16.1	6.98	...	0.017	0.05	0.16	1.91	9.0	

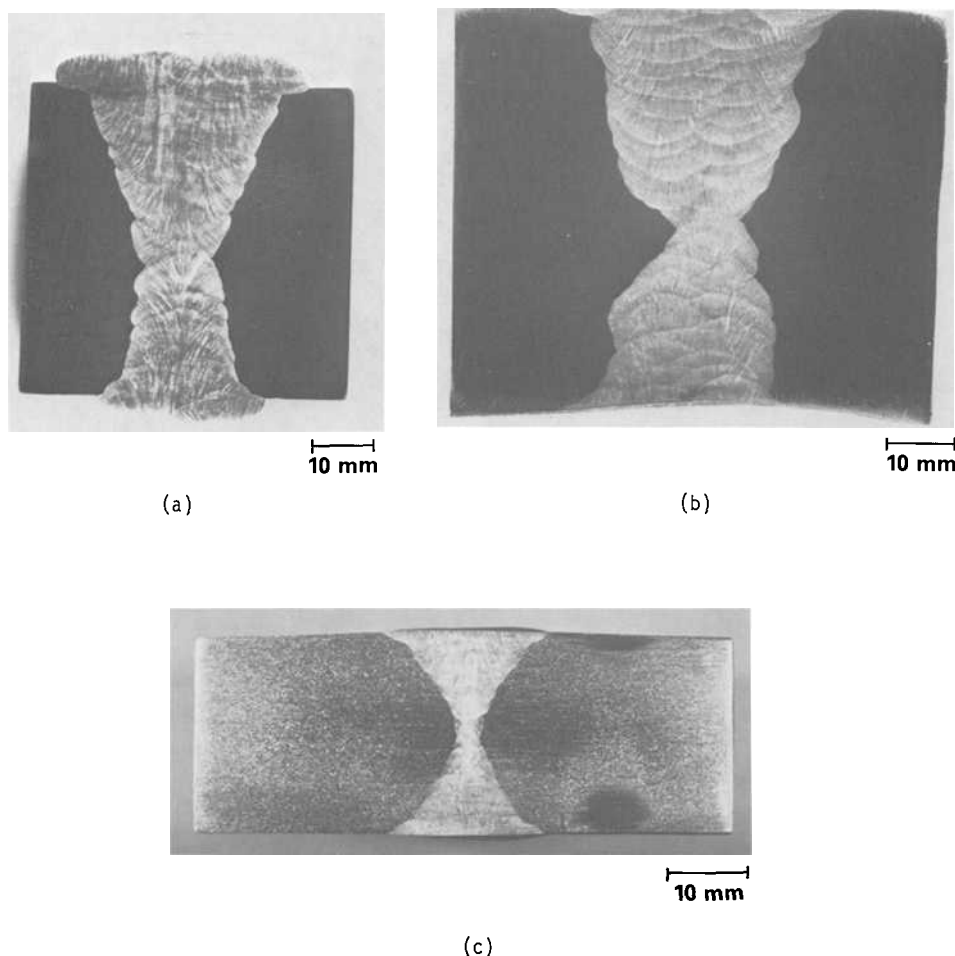
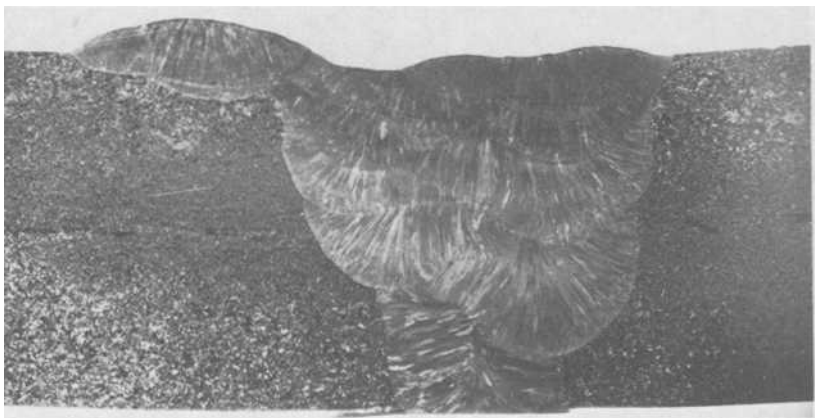


FIG. 1—Cross-sectional profiles of stainless steel welds: (a) 308 SS SA weld, (b) 308 SS SMA weld, (c) 308 SS GTA weld.

Fracture Toughness Testing

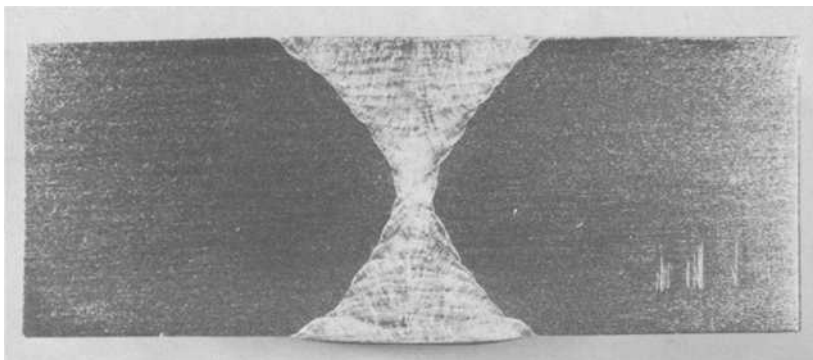
Fracture tests were performed on deeply precracked (at a maximum stress-intensity factor of approximately $25 \text{ MPa}\sqrt{\text{m}}$) compact specimens with a width of 50.8 mm. Specimen thicknesses were 25.4 mm for the SMA weld, 22.9 mm for SA welds, and 11.4 mm for GTA welds. Notches were centered in the weld deposit and oriented parallel to the welding direction.

Specimens machined from double-V welds exhibited extremely uneven precracks, because fatigue cracks did not propagate along the midthickness plane (that is, weld root region). This behavior resulted from the presence of extremely high compressive residual stresses in the center of the double-V welds. To solve this problem, specimens taken from double-V welds were sectioned through the midthickness (that is, weld root region) to relieve the severe residual stress distribution. In addition, the precracking stress ratio ($R = \text{minimum load}/\text{maximum load}$) was increased to approximately 0.4 to minimize the effects of any



10 mm

(a)



10 mm

(b)

FIG. 2—Cross-sectional profiles of stainless steel welds: (a) 16-8-2 SS SA weld, (b) 16-8-2 SS GTA weld.

remaining residual stresses. These procedures resulted in uniform fatigue precracks for double-V weld specimens. No problems were encountered during precracking of specimens taken from single-V welds.

Specimens were tested on an electrohydraulic closed-loop machine in stroke control (stroke rate of 0.5 mm/min). Displacements were measured on the load-line by a high-temperature linear variable differential transformer (LVDT) displacement monitoring tech-

TABLE 2—Summary of tensile properties.

Materials	Heat or Welding Process	Test Temperature, °C	Yield Strength, MPa	Ultimate Strength, MPa	Uniform Elongation, %	Total Elongation, %	Reduction In Area, %	Strain Hardening ^a		No. of Specimens
								Coefficient, α	Exponent, n	
308 SS Weld	SMA	24	455	634	38	44	48	15.2	3.5	4
		427	323	472	21	24	58	7.1	4.7	5
	GTA	538	303	412	19	24	52	4.8	6.5	4
		427	278	477	20	23	54	4.9	4.8	4
16-8-2 SS Weld	SA	538	268	401	15	19	47	2.7	6.4	1
		24	408	627	37	41	58	5.3	3.4	2
	GTA	427	344	474	20	24	59	6.2	6.2	3
		538	290	384	18	23	54	6.4	5.8	6
	SA	24	360	668	49	54	74	8.5	3.3	2
		427	265	510	25	29	51	7.1	3.3	1
	GTA	482	281	489	19	23	46	3.4	4.3	4
		538	263	455	21	25	55	5.5	4.2	4
SA	24	391	627	44	45	40	12.9	3.2	1	
	427	297	476	21	25	49	8.0	4.0	2	
	538	321	439	12	17	54	3.4	6.6	2	

^a Ramberg-Osgood strain-hardening law: $\frac{\epsilon}{\epsilon_{ys}} = \frac{\sigma}{\sigma_{ys}} + \alpha \left(\frac{\sigma}{\sigma_{ys}} \right)^n$; $\sigma_{ys} = E\epsilon_{ys}$.

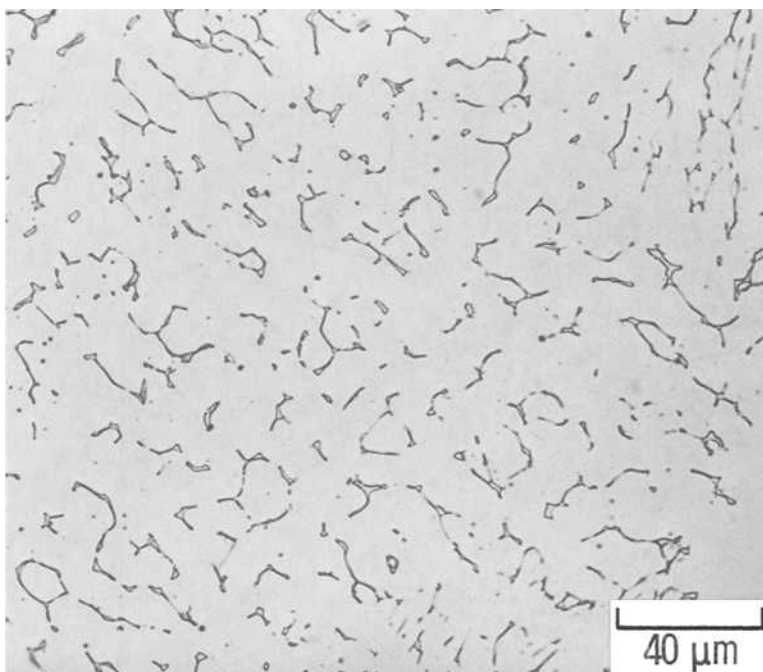


FIG. 3—Duplex austenitic-ferritic microstructure for 308 SS SMA weld. Note the typical vermicular-ferrite morphology coupled with a few spherical manganese silicide particles located in the interdendritic regions.

nique [21]. During each test the load-line displacement was recorded continuously on an X-Y recorder as a function of load.

The fracture toughness behavior was determined by the multiple-specimen J_R -curve technique. Analysis procedures differed slightly from those described in the ASTM Test for J_{Ic} , a Measure of Fracture Toughness (E 813-81) because the ASTM procedures and size requirements are generally not applicable to stainless steel alloys. Specifically, compact specimens were loaded to various displacements, producing different amounts of crack extension, Δa , and then unloaded. After unloading, each specimen was heat tinted to discolor the crack growth region and subsequently broken open so that the amount of crack extension could be measured. The value of J for each specimen was determined from the load versus load-line displacement curve by the following equation

$$J = \frac{2A}{Bb} \frac{(1 + \alpha)}{(1 + \alpha^2)} \quad (1)$$

where

A = area under load versus the load-line displacement curve,

b = unbroken ligament size,

$\alpha = [(2a/b)^2 + 2(2a/b) + 2]^{1/2} - (2a/b + 1)$,

a = crack length, and

B = specimen thickness.

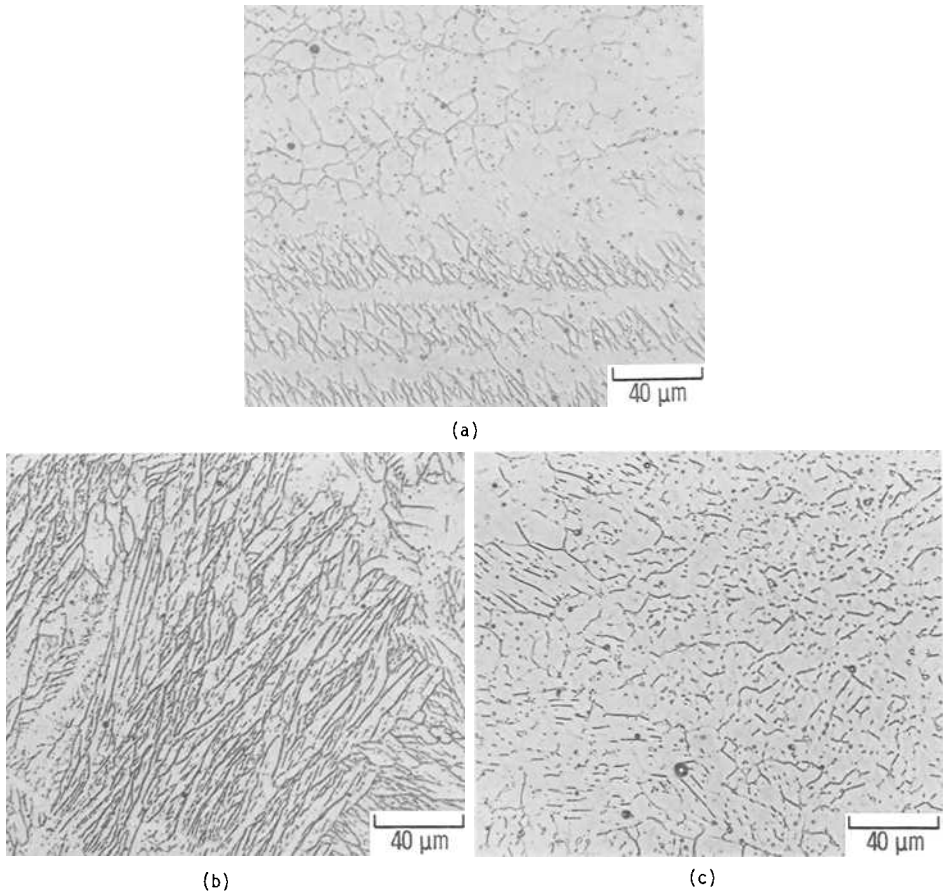


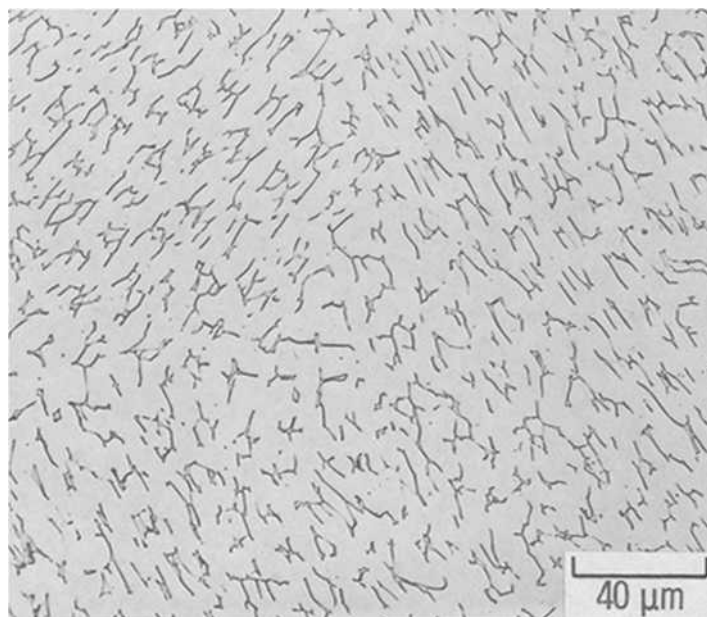
FIG. 4—Typical microstructures for SA welds. Note the high density of manganese silicide inclusions within the austenitic matrix regardless of the predominant ferrite structure: (a) 308 SS, combination of vermicular and lacy morphologies, (b) 16-8-2 SS, acicular structure, and (c) vermicular structure that started to break down because of the high heat input during SA welding.

The J_R -curve was obtained by fitting a least-squares regression line through crack extension data points falling between the 0.15 and 1.5-mm exclusion lines, in accordance with ASTM Test E 813-81. Data points falling outside the exclusion limits were denoted by a vertical slash. The initiation J_c value was then taken to be that value where the linear regression line

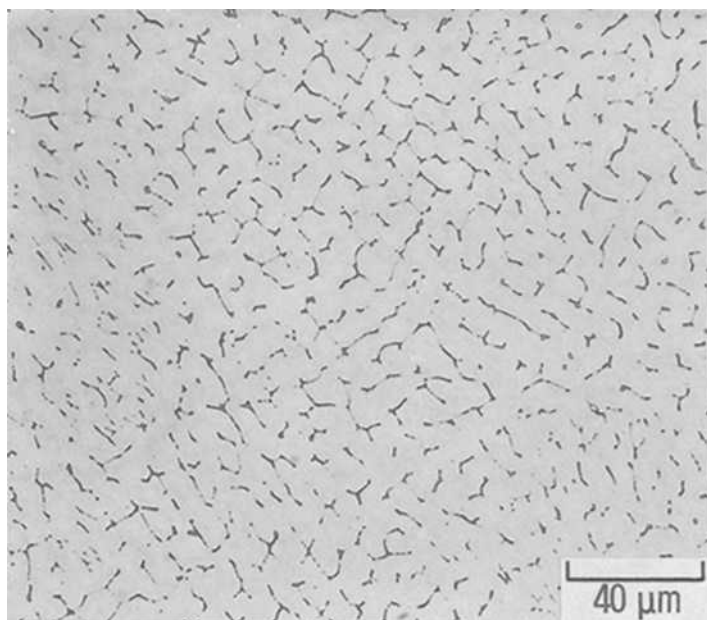
$$J = J_o + \frac{dJ_R}{da} (\Delta a) \quad (2)$$

where J_o and dJ_R/da are regression constants, intersected the stretch zone line for low-strength, high-strain-hardening materials [22]

$$J = 4\sigma_f(\Delta a) \quad (3)$$



(a)



(b)

FIG. 5—Typical vermicular ferrite morphology in the GTA welds. Note the absence of coarse globular particles from the matrix: (a) 308 SS GTA weld, (b) 16-8-2 SS GTA weld.

TABLE 3—Summary of delta ferrite morphology.

Material	Welding Process	Vermicular	Lacy	Acicular	Globular	Comments
308 SS	SMA	yes	yes	no	yes	primarily vermicular with some evidence of lacy morphology; coarse globular ferrite confined to partially remelted regions between weld passes
	SA	yes	yes	no	yes	primarily vermicular with considerable evidence of lacy structure in some regions; globular morphology in localized areas
	GTA	yes	yes	no	no	primarily vermicular; isolated islands of lacy morphology
16-8-2 SS	SA	yes	yes	yes	yes	extensive vermicular, lacy, and acicular morphologies; acicular ferrite dominant in vicinity of weld crown; globular ferrite in some regions
	GTA	yes	yes	no	no	primarily vermicular; isolated islands of lacy ferrite

where

σ_f = flow strength = $1/2(\sigma_{ys} + \sigma_{us})$,
 σ_{ys} = 0.2% offset yield strength, and
 σ_{us} = ultimate tensile strength.

The variance of J_c and dJ_R/da (S_1^2 and S_2^2 , respectively) were determined from statistical analysis of the J_R curve data using the following equations

$$S_1^2 = S^2 \left(\frac{1}{n} + \frac{\left[\left(\frac{J_c}{4\sigma_f} \right) - \bar{a} \right]^2}{\sum_{i=1}^n (\Delta a_i - \bar{a})^2} \right) \quad (4)$$

and

$$S_2^2 = \frac{S^2}{\sum_{i=1}^n (\Delta a_i - \bar{a})^2} \quad (5)$$

where

n = number of data pairs being analyzed,
 \bar{a} = mean value of Δa , and
 S^2 = sample estimate of the variance of J , given by

$$S^2 = \frac{\sum_{i=1}^n \left[J_i - J_o - \frac{dJ_R}{da} (\Delta a_i) \right]^2}{n - 2}$$

Values of $J_c \pm S_1$ and $dJ_R/da \pm S_2$ are reported for each J_R curve.

Values of the tearing modulus were computed from the following equation [23]

$$T = \frac{dJ_R}{da} \frac{E}{\sigma_f^2} \quad (6)$$

where E is the elastic modulus. Hutchinson and Paris [24] proposed the following criterion for J -controlled crack growth in fully yielded specimens

$$\omega = \frac{b}{J} \frac{dJ}{da} \gg 1 \quad (7)$$

Precise delineations on the amount of crack growth allowed prior to the loss of J -dominance on the tearing response are not presently available, but preliminary work by Kumar, et al. [1] suggests that ω should be greater than ten for a bending type of specimens. In the present study, minimum ω values ranged from six to ten, demonstrating that J -controlled crack growth dominates a major portion of each J_R curve. At very high Δa values, J -dominance may be lost so that the J_R curve becomes geometry-dependent. However, due to the high triaxial constraint in compact specimens, the resulting J_R curve provides a lower-bound response that underestimates the tearing resistance and point-of-fracture instability.

Fractographic Examination

Fracture surface morphologies were characterized by direct fractographic examination of a scanning electron microscope (SEM) operated at an accelerating potential of 25 kV. To relate fracture surface appearance to key microstructural features, selected areas of fracture surfaces were electropolished [in 25 g of chromic oxide (CrO_3), 7 mL of water, and 130 mL of acetic acid] so that the fracture surface topography and underlying microstructure could be studied simultaneously [25].

Results and Discussion

Fracture Toughness Behavior

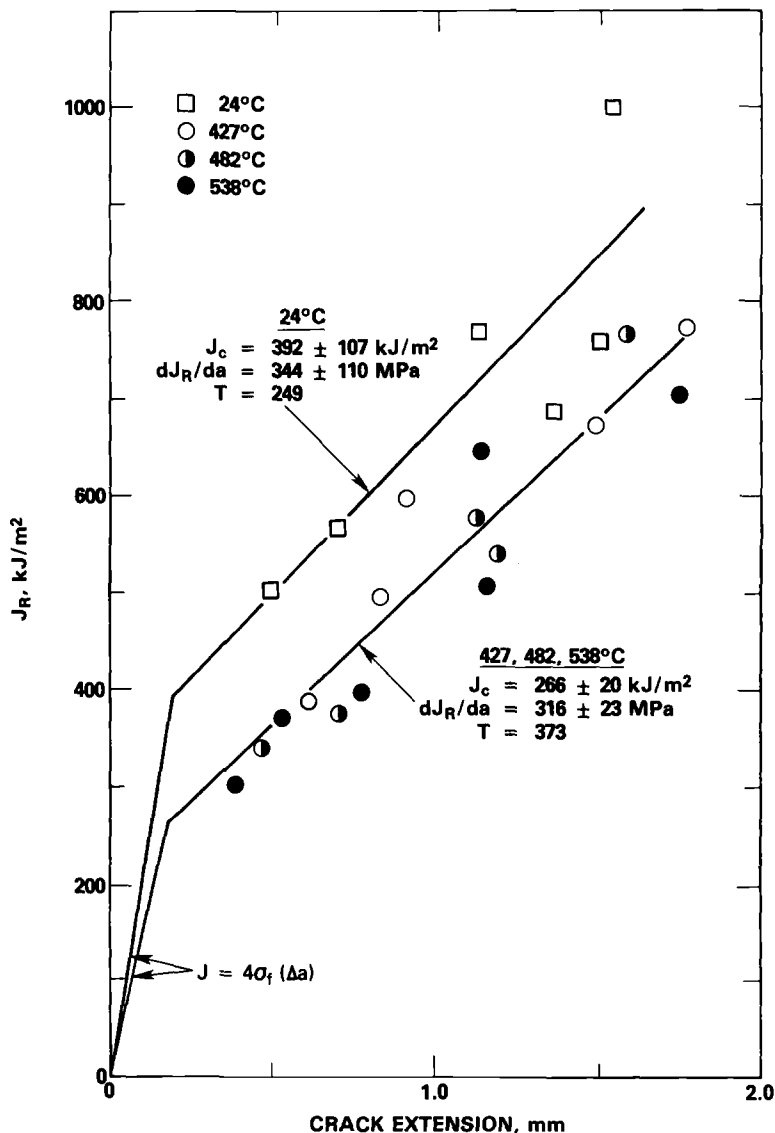
The J_R curves for the two 16-8-2 SS and three 308 SS welds are shown in Figs. 6 through 10. The trends exhibited by the 16-8-2 SS GTA weld (Fig. 6) are representative of those observed in all welds. At 427 to 538°C, the fracture toughness response was independent of temperature, so data obtained in this temperature regime were regressed together into a single J_R curve. The room temperature toughness for the two SA welds and the 16-8-2 GTA weld were found to be significantly higher than their elevated temperature counterparts. Values of dJ_R/da were unaffected by temperature, but the tearing modulus increased by approximately 50% at elevated temperatures because of a significant reduction in flow strength.

The similar responses for the 308 and 16-8-2 SS welds, when manufactured using the same welding process, indicated that the fracture properties for SS welds were insensitive to filler material. Because composition had no effect on fracture toughness behavior, data for the 308 SS and 16-8-2 SS welds manufactured using a common weld process were combined into a single J_R -curve regression. In each case where the data sets were pooled (that is, GTA welds at 427 to 538°C, SA welds at 427 to 538°C, and SA welds at 24°C), the resulting J_R curves adequately represented the individual data sets.

Welding process was found to have a dramatic effect on fracture toughness. GTA welds exhibited the highest fracture resistance, with $J_c = 392$ and 266 kJ/m^2 and $T = 249$ and 373 at room and elevated temperatures, respectively. These toughness levels were consistent with the lower range of J_c values displayed by SS base metals of 150 to 1500 kJ/m^2 [5, 7–9, 26–34]. Welds manufactured using the SA process possessed the lowest J_c (198 kJ/m^2 at 24°C and 76 kJ/m^2 at 427 to 538°C), while SMA welds displayed an intermediate J_c value of 154 kJ/m^2 . Although initiation toughness values for SA and SMA welds were relatively low, their high tearing moduli ($T = 107$ to 167 for SA welds and $T = 310$ for the SMA weld) demonstrated that these welds were very resistant to unstable fracture.

Extensive scatter was exhibited by one of three SMA weldments (Weldment B) tested at 427°C , as shown in Fig. 10. The three weldments were manufactured using the same filler material, and their chemistries were almost identical (Table 1). Hence, the increased scatter was attributed to the variability associated with a manual welding process. The scatter displayed by Weldment B was so large it masked any systematic weld-to-weld variability in J_c behavior. Weldment A exhibited relatively little scatter, and the single data point for Weldment C at 427°C agreed with the overall response for Weldment A. At 538°C , only Weldment C was examined, and it displayed very little scatter.

The $J_c \pm 2S_1$ and $dJ_R/da \pm 2S_2$ values obtained in this study are compared with previous results from the literature in Figs. 11 and 12. Variances for the 16-8-2 SS GTA weld at room temperature were uncharacteristically large because of the limited data base. The variances in J_c and dJ_R/da at elevated temperatures, which were established using a much larger data base, were expected to represent a more accurate measure of the true variance at 24°C .

FIG. 6— J_R curves for 16-8-2 SS GTA weld.

Note that S_1 and S_2 values for the SA weld at 24°C and 427 to 538°C were almost identical, demonstrating that the variance in fracture toughness was not significantly affected by temperature. For purposes of consistency, elevated temperature S_1 and S_2 limits for the GTA weld were applied to the room temperature J_c and dJ_R/da values in Figs. 11 and 12.

Figure 11 reveals that the range of J_c values obtained in this study agreed reasonably well with a compilation of results from the literature. Moreover, the ordering of fracture toughness levels for the various weld processes—SA welds exhibiting the lowest J_c values, SMA welds possessing intermediate J_c values, and GTA welds having the highest J_c levels—was apparent in both the present and previous results. Similar ordering was also reported for

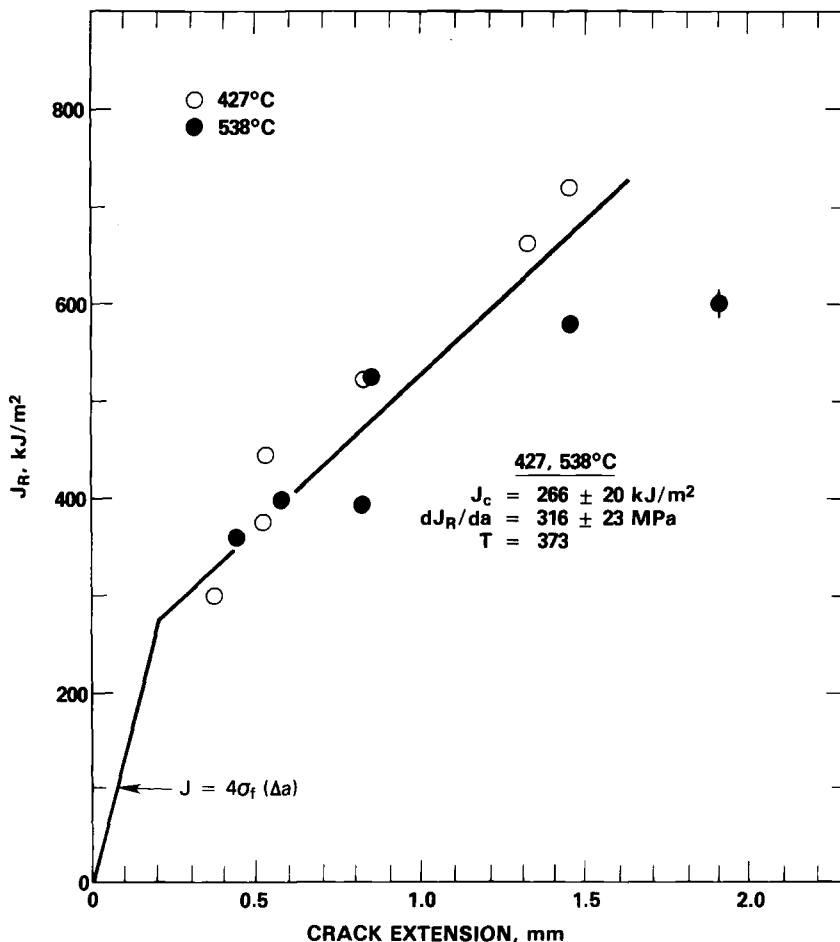


FIG. 7— J_R curve for 308 SS GTA weld. The data point with a vertical slash was not included in the J_R -curve least-squares regression because it fell outside the 1.5-mm maximum exclusion limit.

SS welds at 4K [17]. The large scatter displayed by the SMA welds caused its $2S_1$ limits to overlap with those for the GTA and SA welds. This scatter was comparable to the variability displayed by SMA welds at cryogenic temperatures, where K_{Ic} values ranged from 94 to 223 MPa \sqrt{m} (corresponding to J_c values of 43 to 241 kJ/m²).

Variability in dJ_R/da values for materials examined here was substantially less than that compiled from previous studies (Fig. 12). The extensive scatter in J_R -curve slopes obtained from the literature is attributed, at least in part, to the sensitivity of the tearing resistance to different testing procedures. This behavior contrasts with the J_c response, which was relatively insensitive to testing and analysis procedures. Previous studies [5,35–37] demonstrated that J_R curves with markedly different slopes, because of variations in testing procedures and specimen geometries, tend to extrapolate to a common J_c value.

The fracture resistance for GTA welds is sufficiently high to preclude rapid fracture in most engineering structures. To initiate tearing in these materials, components must be strained well into the plastic regime. Although J_c values for the SMA and SA welds are

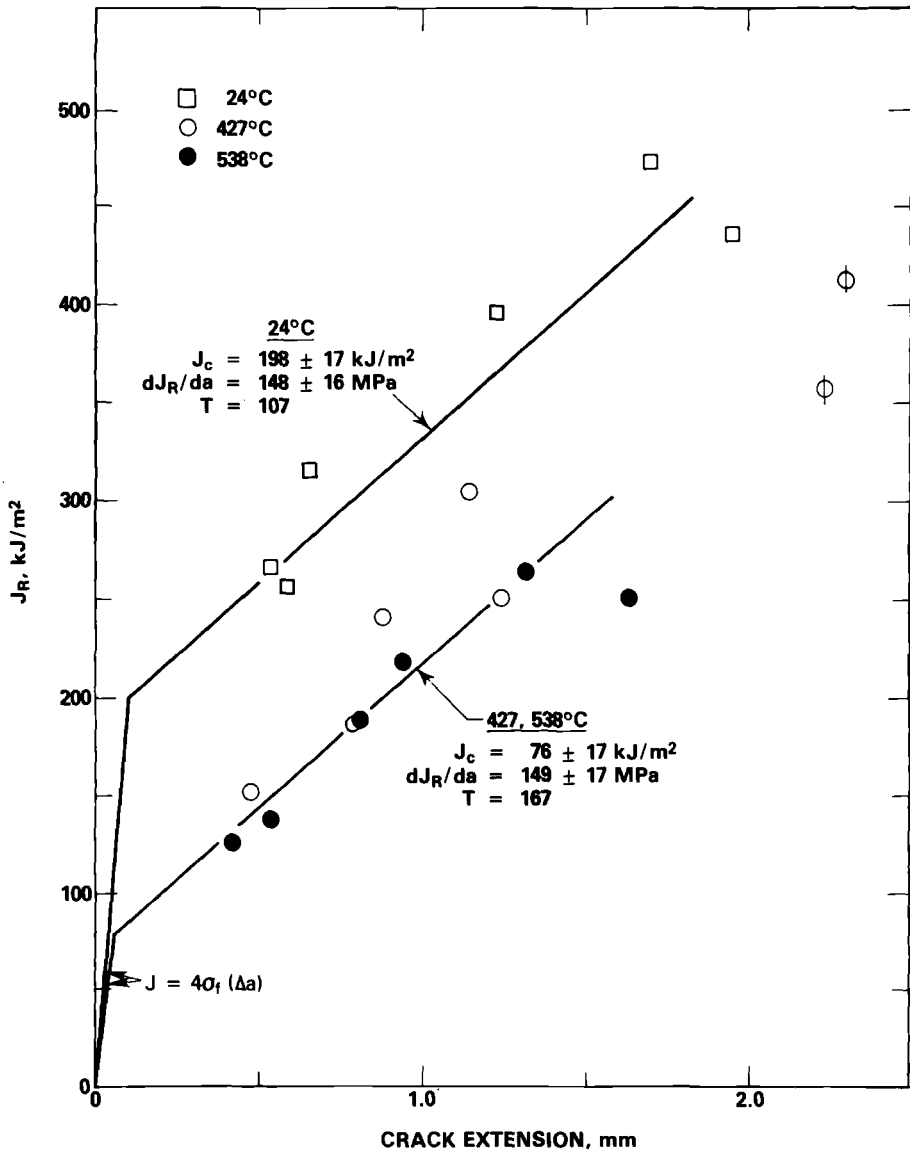


FIG. 8— J_R curves for 16-8-2 SS SA weld. Data points with a vertical slash were excluded from the J_R -curve regression.

relatively low, their high tearing moduli demonstrate that tearing instabilities are unlikely except after extensive plastic deformation. Consequently, standard design analysis procedures, such as ASME Code stress and strain limits, generally provide adequate protection against premature failure, and sophisticated elastic-plastic fracture mechanics evaluations are not routinely required. Only in special cases, such as quantifying design margins for critical components containing either real or hypothetical defects, might ductile fracture mechanics analyses be used.

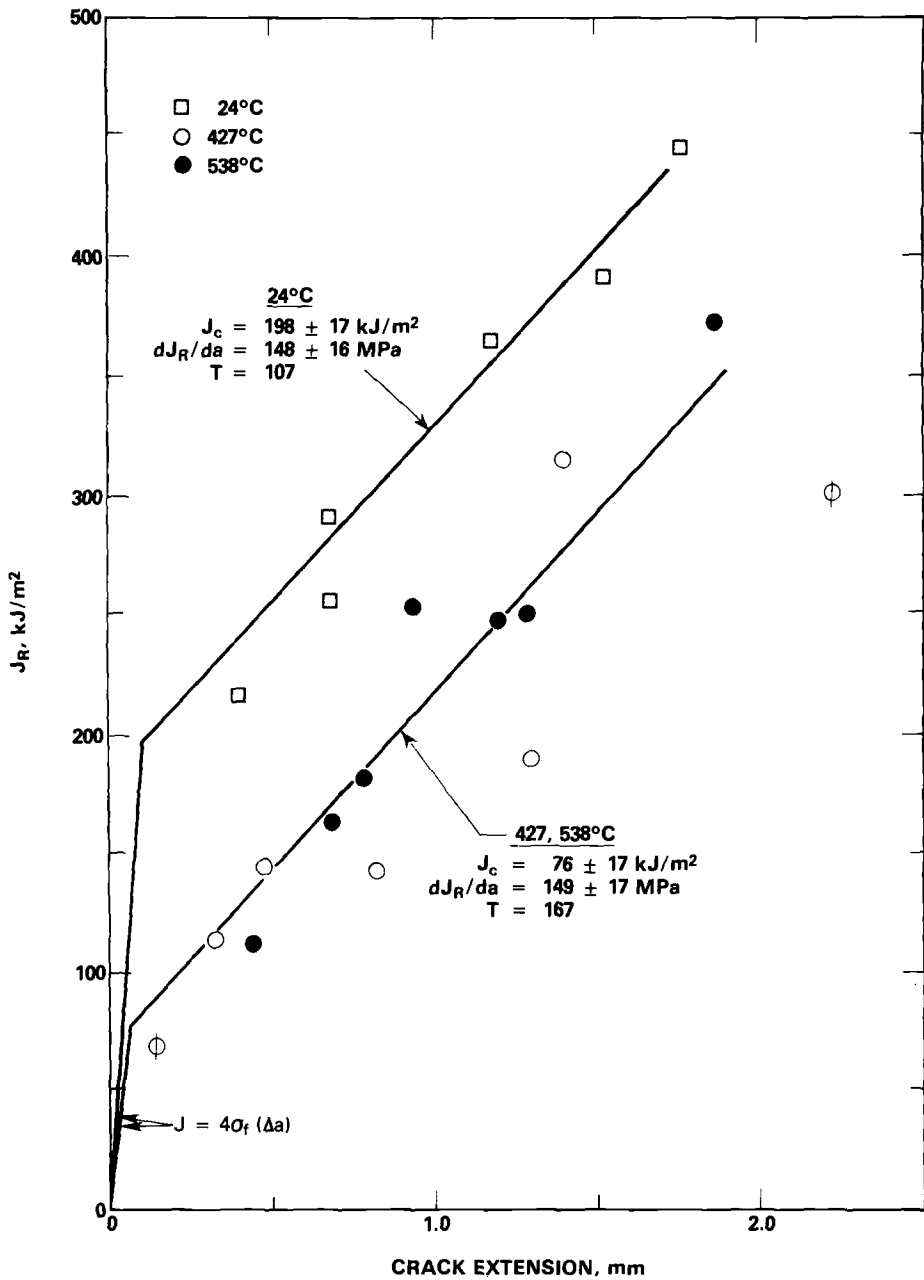


FIG. 9— J_R curves for 308 SS SA weld. Data points with a vertical slash were not included in the J_R -curve regression.

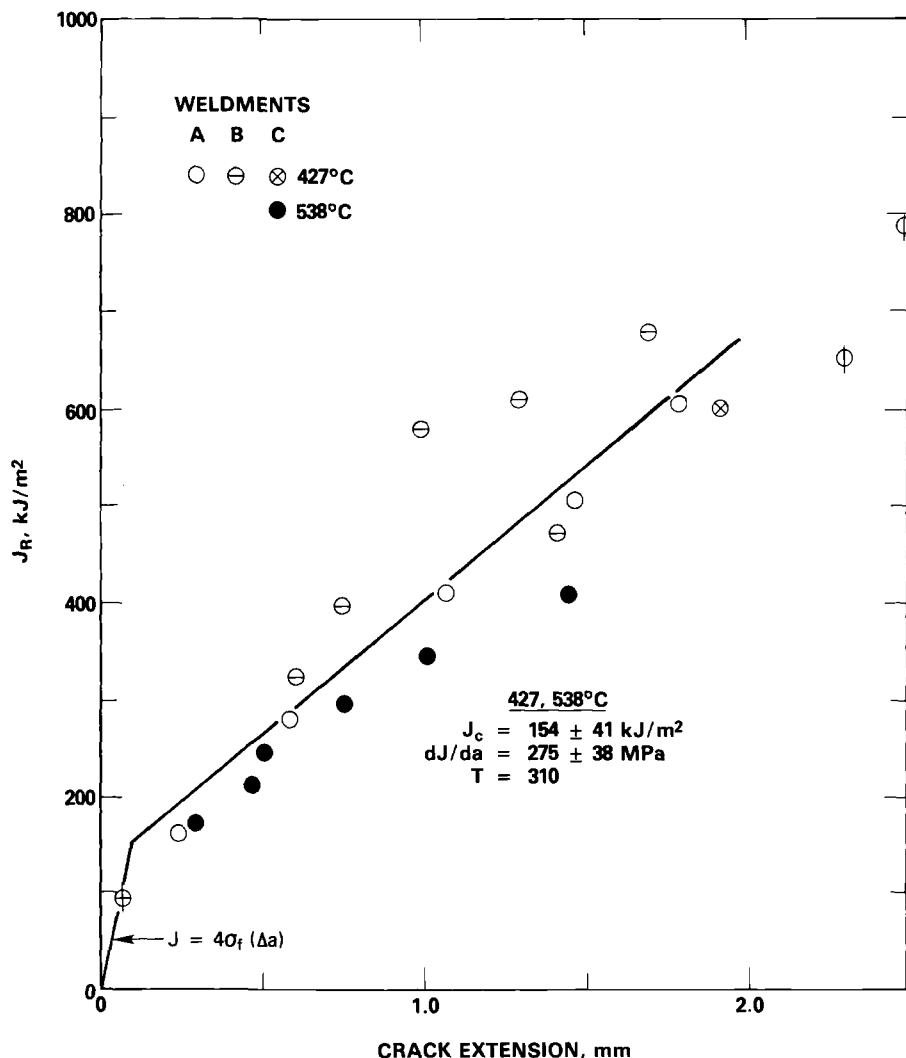


FIG. 10— J_R curve for 308 SS SMA weld. Data points with a vertical slash were excluded from the J_R -curve regression.

The results in Figs. 11 and 12 were used to establish minimum expected J_c and dJ_R/da values for use in fracture mechanics assessments. The extremely large variability among the welds makes it difficult to account for lot-to-lot differences except by a simple lower-bound approach. Minimum expected J_c values, given in Table 4, correspond to the lower bounds for all data represented in Fig. 11. To account for variability in cases where the results were particularly sparse, the lower-bound $2S_1$ limits for data generated in this study were used to determine minimum expected properties. Lower-bound dJ_R/da values, based on all data generated here and in previous studies, are also reported in Table 4. Since the J_R -curve slope was insensitive to temperature, a single lower-bound dJ_R/da value was adopted for each weld process.

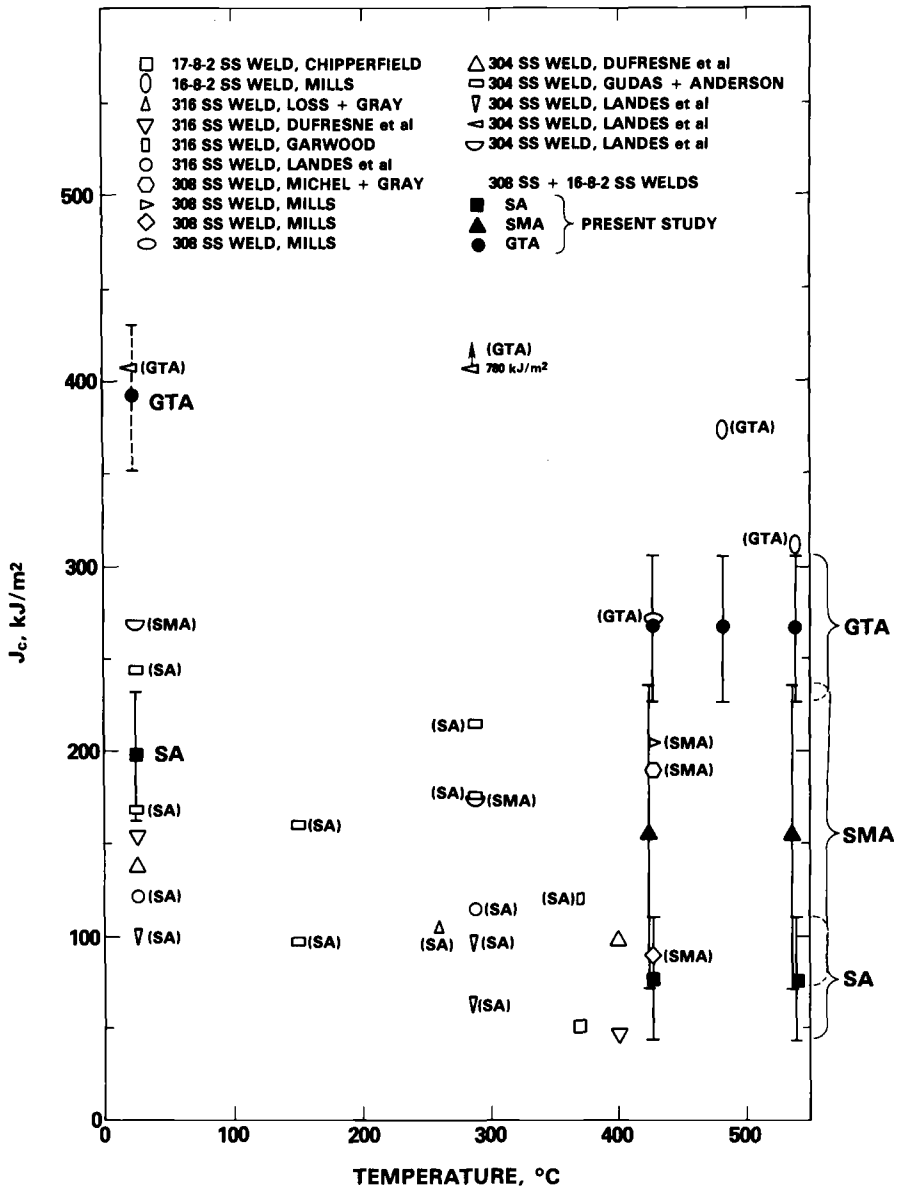


FIG. 11—Comparison of present J_c results with values reported in the literature.

Fracture Mechanisms

Figures 13 through 15 show that the welds failed exclusively via a dimple rupture mechanism. Microvoid nucleation sites included both manganese silicide and delta ferrite particles. In the SA welds, every dimple was initiated by decohesion of a silicide inclusion from the matrix. Metallographic profiles of the crack-tip region (Fig. 16) illustrate microvoids that nucleated at the spherical inclusions. Note that the delta ferrite structure at the crack tip remained intact, even though microvoids nucleated on both sides of it. This demonstrated

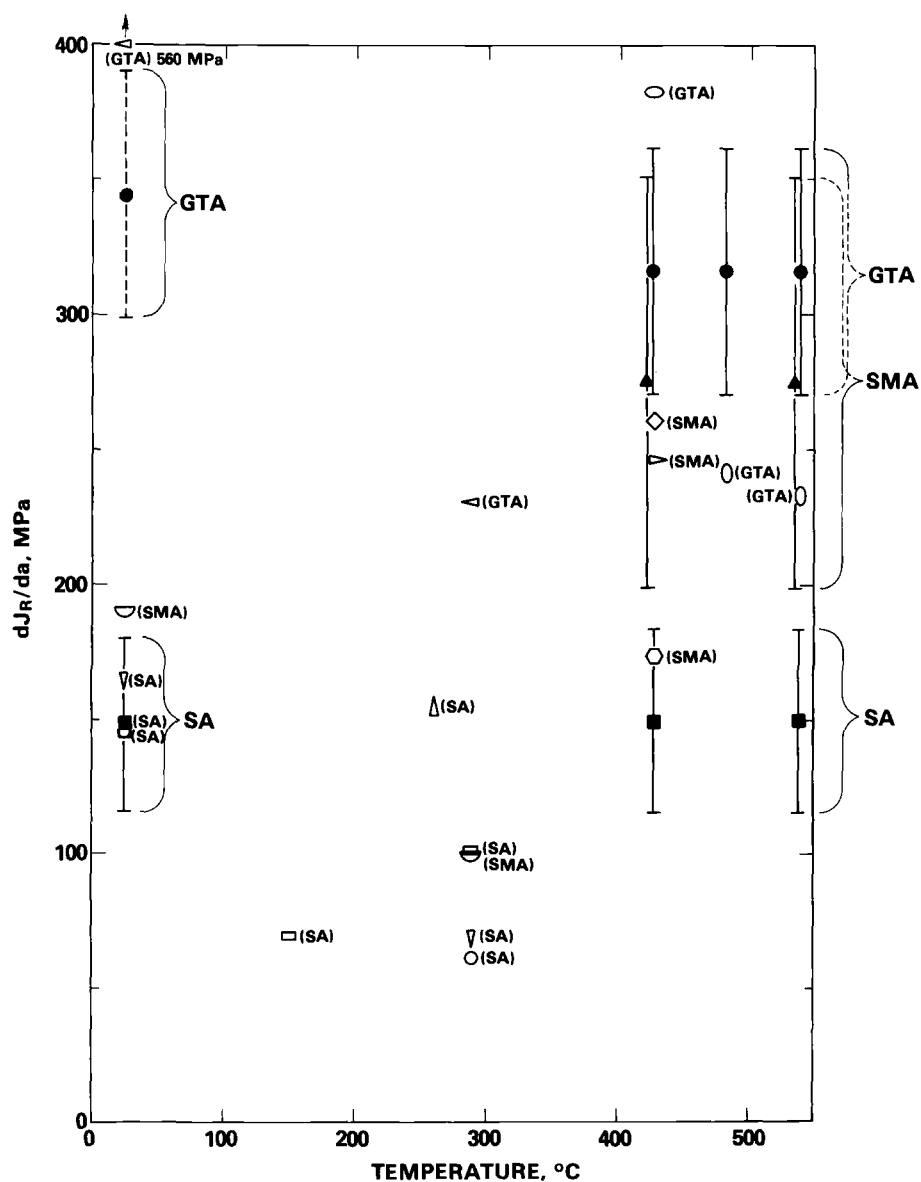


FIG. 12—Comparison of present dJ_R/da results with values reported in the literature. The symbols are consistent with Fig. 11.

TABLE 4—Minimum expected fracture toughness values based on lower-bound approach.

Material	Welding Process	Temperature, °C	Lower-Bound J_c , kJ/m ²	Lower-Bound dJ_R/da , MPa
308 SS + 16-8-2 SS welds	SA, SMA ^a (all)	24	100	60
308 SS + 16-8-2 SS welds	GTA	24	350	230
308 SS + 16-8-2 SS welds	SA (all)	427 to 538	40	60
308 SS + 16-8-2 SS welds	SMA	427 to 538	70	100
308 SS + 16-8-2 SS welds	GTA	427 to 538	230	230

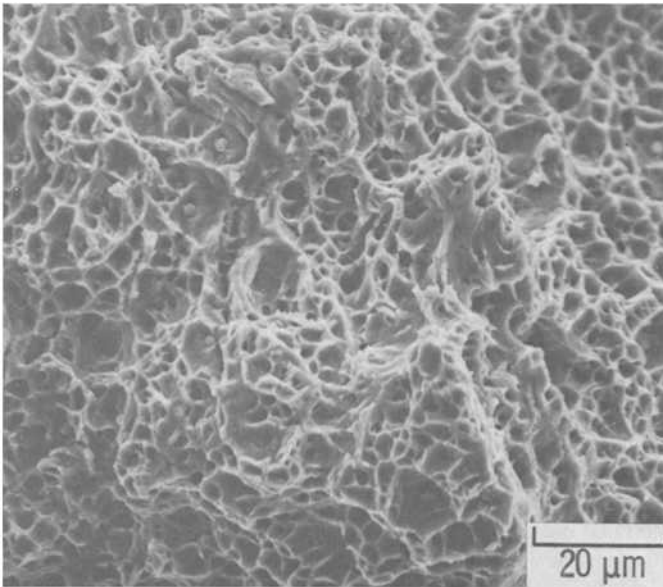
^a Due to the paucity of data for SMA welds at 24°C, a common lower-bound value applies to both SA and SMA welds.

that the residual ferrite was far more resistant to local failure than the silicide phase. In the SA weld, rupture of the delta ferrite occurred during the final stages of microvoid coalescence; hence, this phase did not significantly influence the overall fracture characteristics. The metallographic-fractographic interface in Fig. 14c illustrates that the delta ferrite phase was often located along the dimple cusps, whereas the silicide particles were always located at the bottom of microvoids.

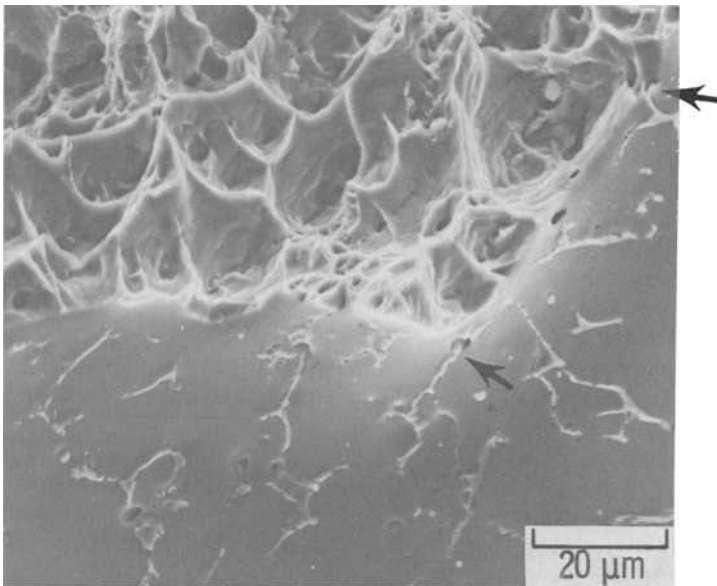
Dimples in the GTA welds were nucleated exclusively by localized failure or decohesion of the ferrite phase. The individual particles responsible for microvoid nucleation were particularly difficult to distinguish because extensive deformation in the surrounding matrix masked them. Nevertheless, the metallographic-fractographic profile shows that the residual ferrite network was responsible for nucleation of microvoids in GTA welds. In the SMA weld, a few dimples were initiated by spherical silicide inclusions, but the majority were nucleated by ferrite particles.

The overall fracture properties for SS welds were controlled by the second phase morphology. The delta phase accommodated some plastic deformation, so it was very resistant to fracture or decohesion from the matrix. By sharp contrast, the hard manganese silicide inclusions in the SA and SMA welds resisted deformation and high secondary stresses built up at the particle-matrix interface. These high local stresses caused the particles to decohere from the matrix early in the straining process, which resulted in a premature advance of the crack front. The particularly high density of inclusions in the SA weld accounts for its inferior fracture resistance. In the GTA matrix, plastic straining was allowed to continue until the delta ferrite eventually initiated microvoid coalescence. This additional plastic straining resulted in much higher J_c and T values.

Ferrite morphology and content was found to have relatively little influence on the overall fracture properties at room and elevated temperatures because this phase possessed modest plastic deformation capabilities. However, the deformation characteristics of the ferrite can be altered dramatically by testing at low temperatures or by thermally aging. Under these conditions, ferrite morphology may influence the weld fracture resistance. Delta ferrite exhibits a ductile-to-brittle transition temperature response, so its plastic straining capacity at low temperatures is essentially nil. The diminished fracture resistance results in a premature failure of this phase, thereby enhancing its role in controlling the overall fracture properties. Indeed, Charpy and J_c test results [14,38] have demonstrated that ferrite content and coarseness can adversely affect the fracture resistance of SS welds at -197 and -269°C . A similar phenomenon may also occur in welds subjected to long-term thermal aging at temperatures below 500°C . In this temperature regime, the delta ferrite is susceptible to embrittlement [39], which causes a substantial reduction in its plastic deformation capacity. The fracture resistance of the aged ferrite phase may be degraded to the point where it



(a)



(b)

FIG. 13—SEM fractographs for 308 SMA weld: (a) representative dimple rupture morphology, (b) metallographic-fractographic profile illustrating that dimples were initiated by decohesion of the silicide particles, decohesion of delta ferrite particles (see arrows) and local rupture of delta ferrite.

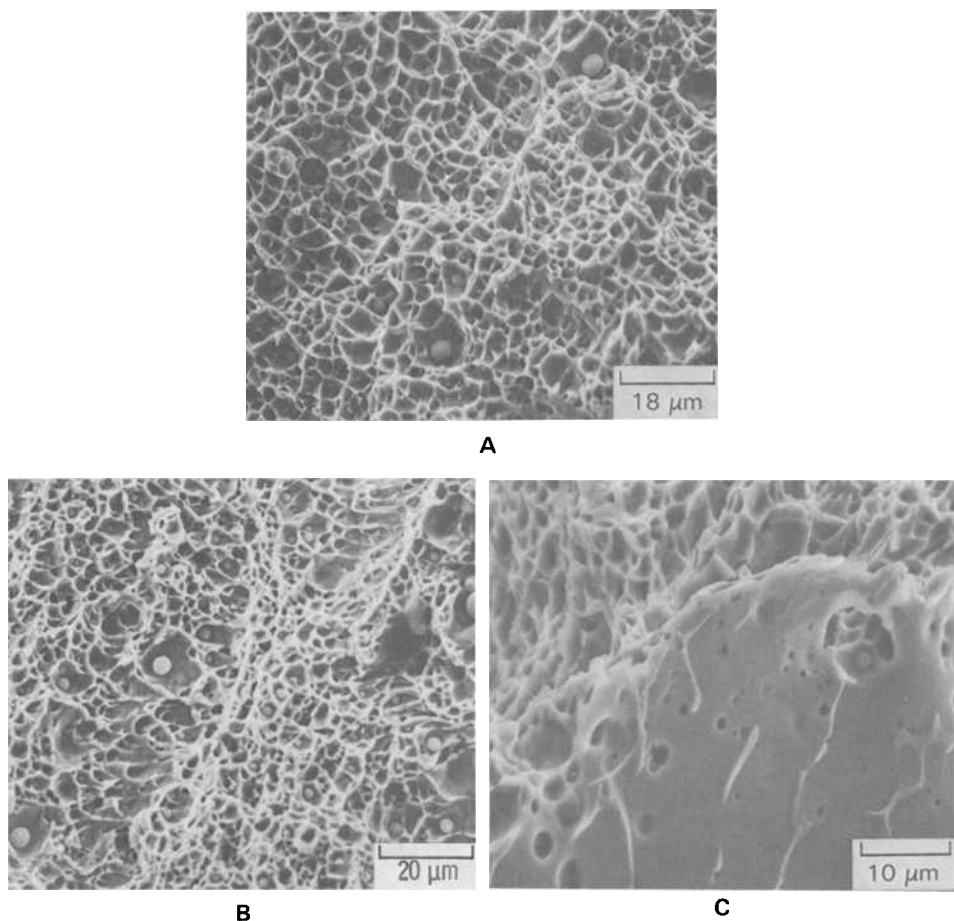


FIG. 14—SEM fractographs for SA welds: (a) 308 SS typical fracture surface appearance showing that microvoids were nucleated exclusively at silicide inclusions; (b) 16-8-2 SS microvoid coalescence nucleated by decohesion of spherical silicide particles from the matrix; (c) 308 SS metallographic-fractographic interface. Note that delta ferrite particles are often found along the dimple cusps, rather than at the bottom of the microvoids.

dominates the overall fracture properties. At aging temperatures above 500°C, the ferrite phase transformation products, carbides and sigma phase, are likely to control fracture properties. A test program designed to evaluate long-term thermal aging effects on the fracture toughness of SS welds is in progress.

Conclusions

The elastic-plastic fracture toughness response for three 308 SS welds and two 16-8-2 welds was characterized at 24, 427, and 538°C. Test results were compared with previously reported fracture properties to evaluate the effects of temperature, composition, and weld process variations. In addition, metallographic and fractographic examinations were per-

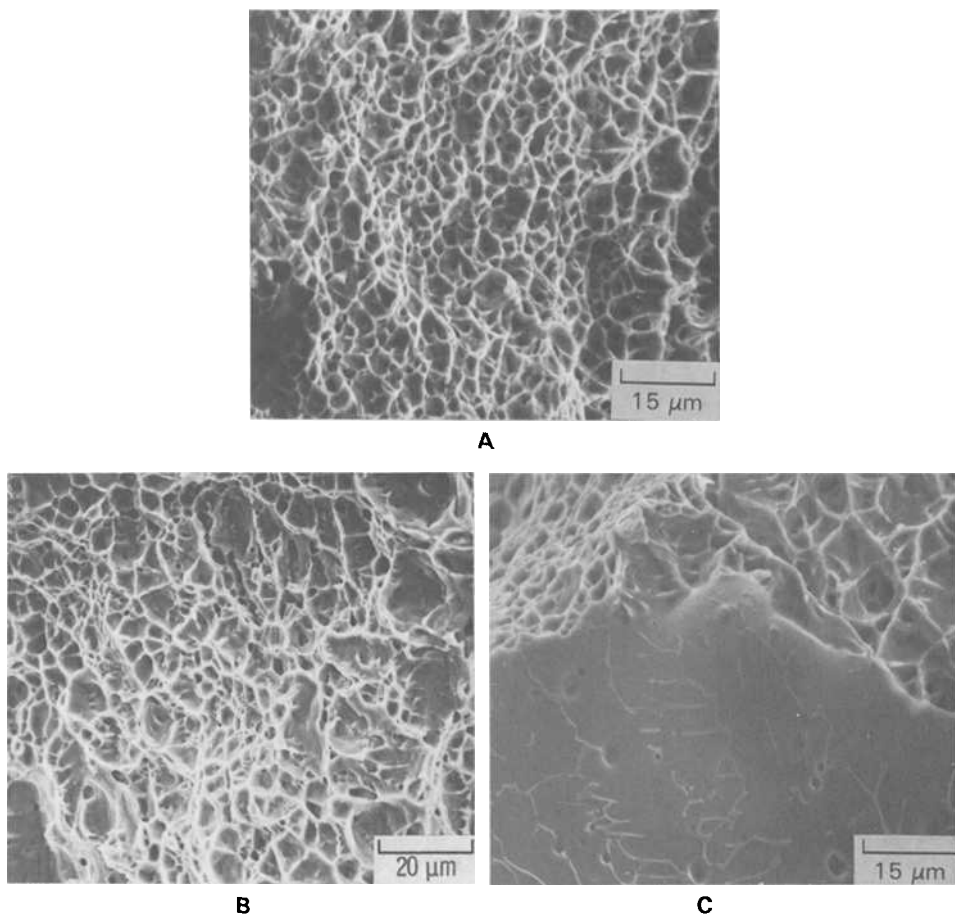


FIG. 15—SEM fractographs for GTA welds: (a) 308 SS microvoid coalescence, (b) 16-8-2 SS microvoid coalescence, (c) metallographic-fractographic profile showing that the residual ferrite network served as microvoid nucleation sites.

formed to correlate key microstructural features and operative fracture mechanisms to macroscopic properties. The results are summarized here:

1. The fracture toughness was dependent on the test temperature and welding process, but it was insensitive to filler material (that is, 308 SS versus 16-8-2 SS). GTA welds consistently yielded the highest fracture resistance ($J_c = 266 \text{ kJ/m}^2$ and $T = 373$ at elevated temperatures), the SMA weld displayed intermediate fracture properties ($J_c = 154 \text{ kJ/m}^2$ and $T = 310$), and SA welds had the lowest toughness ($J_c = 76 \text{ kJ/m}^2$ and $T = 167$). Room temperature J_c levels were 50 to 150% higher than elevated temperature values, but the tearing resistance (dJ_R/da) was independent of test temperature. The large variability in J_c fracture toughness observed in the study was comparable to that compiled from previous investigations.

2. The high tearing moduli exhibited by all welds revealed that tearing instabilities are unlikely, except after gross plastic deformation. However, the relatively low initiation tough-

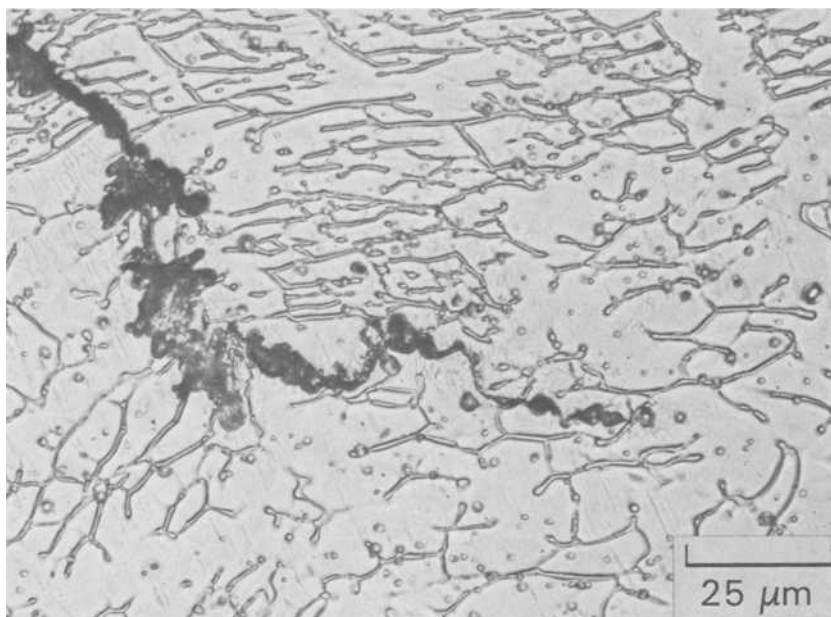


FIG. 16—Metallographic profile of crack tip region in a 16-8-2 SS SA weld specimen. Note that silicide inclusions initiated microvoids ahead of the advancing crack front; however, the delta ferrite particle between the two microvoids ahead of the crack tip remained intact.

nesses displayed by SA and SMA welds suggests that fracture control, via elastic-plastic fracture mechanics evaluations, should be considered for critical components containing these types of weldments.

3. Minimum expected toughness levels for use in fracture mechanics evaluations were established based on a lower-bound approach. Lower-bound J_c values for SA, SMA, and GTA welds at 427 to 538°C were 40, 70, and 230 kJ/m², respectively. At 24°C, the minimum expected J_c levels were 100 kJ/m² for SA and SMA welds and 350 kJ/m² for GTA welds.

4. Second phase particles of manganese silicide were found to be detrimental to the ductile fracture behavior for welds. These particles separated from the matrix during the initial stages of plastic deformation and caused a premature advance of the crack. The high density of silicide inclusions in SA welds, due to silicon pickup from the flux, was therefore responsible for the inferior fracture properties displayed by this welding process.

5. The absence of silicide particles from GTA welds accounted for its excellent fracture resistance. Delta ferrite particles served as microvoid nucleation sites in GTA welds, but this second phase was more resistant to local failure than the silicide inclusions. The SMA weld contained a relatively low density of inclusions, thereby accounting for its intermediate fracture properties.

Acknowledgements

This paper is based on work performed under U.S. Department of Energy Contract DE-AC06-76FF02170 with Westinghouse Hanford Company, a subsidiary of Westinghouse Electric Corporation.

The author wishes to acknowledge L. E. Thomas and B. Mastel for performing electron metallographic and fractographic examinations. Appreciation is also extended to L. D. Blackburn and L. A. James for their enlightening discussions. The careful experimental work of W. D. Themar is greatly appreciated.

References

- [1] Kumar, V., German, M. D., and Shih, C. F., "An Engineering Approach for Elastic-Plastic Fracture Analysis," EPRI NP-1931, General Electric Company, Schenectady, NY, 1981.
- [2] German, M. D. and Kumar, V., "Elastic-Plastic Analysis of Crack Opening; Stable Growth and Instability Behavior in Flawed 304 SS Piping," in *Aspects of Fracture Mechanics in Pressure Vessels and Piping*, ASME PVP, Vol. 58, American Society of Mechanical Engineers, New York, 1982, pp. 109-141.
- [3] Tada, H., Paris, P. C., and Gamble, R. M., "A Stability Analysis of Circumferential Cracks for Reactor Piping Systems," *Fracture Mechanics: Twelfth Conference, ASTM STP 700*, American Society for Testing and Materials, Philadelphia, 1980, pp. 296-313.
- [4] Zahoor, A. and Kanninen, M. F., "A Plastic Fracture Mechanics Prediction of Fracture Instability in a Circumferentially Cracked Pipe in Bending—Part I: *J*-Integral Analysis," *Journal of Pressure Vessel Technology*, Vol. 103, 1981, pp. 352-358.
- [5] Wilkowski, G. M., Zahoor, A., and Kanninen, N. F., "A Plastic Fracture Mechanics Prediction of Fracture Instability in a Circumferentially Cracked Pipe in Bending—Part II: Experimental Verification on a Type 304 Stainless Steel Pipe," *Journal of Pressure Vessel Technology*, Vol. 103, 1981, pp. 359-365.
- [6] Norris, D. M., Marston, T. V., and Tagart, S. W., Jr., "Acceptance Criteria for Circumferential Flaws in Stainless Steel Piping," *Aspects of Fracture Mechanics in Pressure Vessels and Piping*, ASME PVP, Vol. 58, American Society of Mechanical Engineers, New York, 1982, pp. 185-199.
- [7] Chipperfield, C. G., "A Toughness and Defect Size Assessment of Welded Stainless Steel Components," *Institution of Mechanical Engineers*, 1978, pp. 145-159.
- [8] Loss, F. J. and Gray, R. A., Jr., "Toughness of Irradiated Type 316 Forging and Weld Metal Using the *J*-Integral," NRL Memorandum Report 2875, Naval Research Laboratory, Washington, DC, July 1974, pp. 23-30.
- [9] Dufresne, J., Henry, B., and Larsson, H., "Fracture Toughness of Irradiated AISI 304 and 316L Stainless Steel," *Effect of Radiation on Structural Materials*, ASTM STP 683, American Society for Testing and Materials, Philadelphia, 1979, pp. 511-528.
- [10] Garwood, S. J., "Fracture Toughness of Stainless Steel Weldments of Elevated Temperatures," *Fracture Mechanics: Fifteenth Symposium*, ASTM STP 833, American Society for Testing and Materials, Philadelphia, 1979, pp. 333-359.
- [11] Michel, D. J. and Gray, R. A., "Effects of Irradiation on the Fracture Toughness of FBR Structural Materials," NRL Memorandum Report 4997, Naval Research Laboratory, Washington, DC, 1982.
- [12] Gudas, J. P. and Anderson, D. R., "*J_{IC}*-*R* Curve Characteristics of Piping Material and Welds," *Proceedings, Ninth Water Reactor Safety Research Information Meeting*, NUREG/CP0024, U.S. Nuclear Regulatory Commission, Washington, DC, 1982.
- [13] Landes, J. D., McCabe, D. E., and Ernst, H. A., "Elastic-Plastic Methodology to Establish *R* Curves and Instability Criteria," Eighth Semiannual Report, EPRI Contract No. RP1238, Westinghouse R & D Center, Pittsburgh, PA, July 1984.
- [14] Read, D. T., McHenry, H. I., Steinmeyer, P. A., and Thomas, R. D., Jr., "Metallurgical Factors Affecting the Toughness of 316L SMA Weldments at Cryogenic Temperatures," *Welding Research Supplement*, 1980, pp. 104s-113s.
- [15] McHenry, H. I., "Properties of Austenitic Stainless Steel at Cryogenic Temperatures," *Materials Studies for Magnetic Fusion Energy Applications at Low Temperatures—IV*, NBSIR 83-1690, National Bureau of Standards, Boulder, CO, 1983, pp. 127-155.
- [16] Whipple, T. A., McHenry, H. I., and Read, D. T., "Fracture Behavior of Ferrite-Free Stainless Steel Welds in Liquid Helium," *Welding Research Supplement*, 1981, pp. 72s-78s.
- [17] Goodwin, G. M., "Fracture Toughness of Austenitic Stainless Steel Weld Metal at 4K," Report No. ORNL/TM-9172, Oak Ridge National Laboratory, Oak Ridge, TN, 1984.
- [18] Ward, A. L. and Blackburn, L. D., "Elevated Temperature Tensile Properties of Weld-Deposited Austenitic Stainless Steels," *Journal of Engineering Materials and Technology*, Vol. 98, 1976, pp. 213-220.

- [19] Takalo, T., Suutala, N., and Moisio, T., "Influence of Ferrite Content on Its Morphology in Some Austenitic Weld Metals," *Metallurgical Transactions*, Vol. 7A, 1976, pp. 1591-1592.
- [20] David, S. A., "Ferrite Morphology and Variations in Ferrite Content in Austenitics Stainless Steel Welds," *Welding Journal*, Vol. 60, 1981, pp. 64s-71s.
- [21] Mills, W. J., James, L. A., and Williams, J. A., "A Technique for Measuring Load-Line Displacements of Compact Ductile Fracture Toughness Specimens at Elevated Temperatures," *Journal of Testing and Evaluation*, Vol. 5, 1977, pp. 446-451.
- [22] Mills, W. J., "On the Relationship Between Stretch Zone Formation and the J -Integral for High Strain-Hardening Materials," *Journal of Testing and Evaluation*, Vol. 9, 1981, pp. 56-62.
- [23] Paris, P. C., Tada, H., Zahoor, A., and Ernst, H., "The Theory of Instability of the Tearing Mode for Elastic-Plastic Crack Growth," *Elastic-Plastic Fracture, ASTM STP 668*, American Society for Testing and Materials, Philadelphia, 1979, pp. 5-36.
- [24] Hutchinson, J. W. and Paris, P. C., "Stability Analysis of J -Controlled Crack Growth," *Elastic-Plastic Fracture, ASTM STP 668*, American Society for Testing and Materials, Philadelphia, 1979, pp. 37-64.
- [25] Chesnutt, J. C. and Spurling, R. A., "Fracture Topography Microstructure Correlations in the SEM," *Metallurgical Transactions*, Vol. 8A, 1977, pp. 216-218.
- [26] Chipperfield, C. G., "A Method for Determining Dynamic J_q and J_i Values and Its Application to Ductile Steels," *International Conference on Dynamic Fracture Toughness*, The Welding Institute/The American Society for Metals, London, 5-7 July 1976.
- [27] Bamford, W. H. and Begley, J. A., "Techniques for Evaluating the Flow Tolerance of Reactor Coolant Piping," ASME Paper 76-PVP-48, American Society of Mechanical Engineers, New York, 1976.
- [28] Tobler, R. L., "Fracture of Structural Alloys at Temperatures Approaching Absolute Zero," *Proceedings*, Fourth International Conference on Fracture, Waterloo, Ontario, Canada, 1977, pp. 279-285.
- [29] Landes, J. D., "Size and Geometry Effects on Elastic-Plastic Fracture Characterizations," *Proceedings of the U.S. Nuclear Regulatory Commission CSNI Specialists Meeting on Plastic Tearing Instability*, NUREG/CP-0010, U.S. Nuclear Regulatory Commission, Washington, DC, 1979, pp. 194-225.
- [30] Chipperfield, C. G., "Detection and Toughness Characterization of Ductile Crack Initiation in 316 Stainless Steel," *International Journal of Fracture*, Vol. 12, 1976, pp. 873-886.
- [31] Begley, J. A. and Sheinker, A. A., "Crack Propagation Testing for LMFBR Piping—Phase 1 Final Report," WARD-HT-3045-17, Westinghouse Advanced Reactors Division, Madison, PA, 1976.
- [32] Mills, W. J., "Effect of Specimen Size on the Fracture Toughness of Type 304 Stainless Steel—Interim Report," HEDL-TME 81-52, Westinghouse Hanford Co., Richland, WA, 1982.
- [33] Balladon, P., Heritier, J., and Rabbe, P., "The Influence of Microstructure on the Ductile Rupture Mechanisms of a 316L Steel at Room and Elevated Temperatures," *Fracture Mechanics: Fourteenth Symposium, ASTM STP 791*, American Society for Testing and Materials, Philadelphia, 1983, pp. II-496-II-513.
- [34] Wilkowski, G. M., Wambaugh, J. O., and Prabhat, K., "Single Specimen J -Resistance Curve Evaluations Using the d -c Electric Potential Method and a Computerized Data Acquisition System," *Fracture Mechanics: Fifteenth Symposium, ASTM STP 833*, American Society for Testing and Materials, Philadelphia, 1984.
- [35] Gudas, J. P. and Vassilaros, M. G., "Degraded Pipe Experimental Program," *Proceedings*, Tenth Water Reactor Safety Research Information Meeting, NUREG/CP-0041, Vol. 4, U.S. Nuclear Regulatory Commission, Washington, DC, 1982, pp. 119-146.
- [36] Gudas, J. P., Davis, D. A., Vassilaros, M. G., and Sutton, G. E., "Compact Specimen Geometry and Elastic Compliance Test Method Effects on the J -Integral R -Curve," *Proceedings*, Tenth Water Reactor Safety Research Information Meeting, NUREG/CP-0041, Vol. 4, U.S. Nuclear Regulatory Commission, Washington, DC, 1982, pp. 99-118.
- [37] Mills, W. J., "Fracture Toughness Behavior of 2¼ Cr-1Mo Steel Plate and Weldment," *Nuclear Technology*, Vol. 64, 1984, pp. 175-185.
- [38] Siewert, T. A., "Predicting the Cryogenic Toughness of SMA Austenitic Stainless Steel Weld Deposit," paper presented at the 66th Annual AWS Convention, Las Vegas, NV, 30 April 1985.
- [39] Trautwein, A. and Gysel, W., "Influence of Long-Term Aging of CF8 and CF8M Cast Steel at Temperatures Between 300 and 500°C on Impact Toughness and Structural Properties," *Stainless Steel Castings, ASTM STP 756*, American Society for Testing and Materials, Philadelphia, 1982, pp. 165-189.

Use of *R*-Curves for Design in the Elastic-Plastic Fracture Mechanics Regime

REFERENCE: Turner, C. E. and Etemad, M. R., "Use of *R*-Curves for Design in the Elastic-Plastic Fracture Mechanics Regime," *Fracture Mechanics: Nineteenth Symposium, ASTM STP 969*, T. A. Cruse, Ed., American Society for Testing and Materials, Philadelphia, 1988, pp. 356–373.

ABSTRACT: Prediction of initiation and maximum pressure was made for two geometrically similar pressure vessels with a fivefold difference in size for two choices of steel. The vessels were supposed to contain a semielliptical axial defect in the outer surface of the cylindrical section and were subjected to internal pressure. Discussion is offered on the choice of data from plane-sided or side-grooved pieces and on the definition and geometric variability of the *R*-curves. Use of a normalized *R*-curve to allow transfer of data from a sample to the structure, beyond *J*-controlled growth, is examined and a comparison is made of all these cases. For these examples, the main effect of the choice of toughness data is on the extent of stable growth prior to maximum load.

KEY WORDS: fracture mechanics, crack propagation, *J*-integral, mechanical properties, *R*-curves, elastic-plastic fracture mechanics, fracture-safe engineering design

Fracture-safe engineering design and assessment of safety of structures requires information about material toughness and the loading conditions. The description of toughness may be by a critical value or, if it is both feasible and desirable to pass beyond initiation, by a resistance curve (*R*-curve) of increasing toughness versus crack growth, using terms such as the elastic stress-intensity factor, *K*, the closely related *J*-contour integral, or the crack-opening displacement (COD). This paper is concerned only with problems where stable growth exists in the regime of elastic-plastic fracture mechanics (EPFM) in the absence of cleavage. The main contenders for the assessment of severity of loading in the EPFM regime are the (a) COD, (b) R-6, (c) EnJ, and (d) Electric Power Research Institute (EPRI) methods. A description of all of these with some comparative studies is given in Ref 1. Among the four, the COD method [2] is most complete, offering a package for all issues involved with the assessment of defects, including interpretation of nondestructive examination (NDE) records, fatigue, and several aspects of fracture. As presently formulated, however, the COD method does not include the use of *R*-curves, except in the limited sense of helping to define a value for initiation toughness, although allowing the use of maximum load COD in the test piece, which may exceed the value at initiation. The method is not discussed further here, although it is noted that it is being updated to give a fracture assessment diagram (FAD) similar in style to R-6 that will permit the use of a COD *R*-curve for assessment of maximum load. The R-6, EnJ, and EPRI methods are, however, adapted to the use of *R*-curves for the prediction of maximum load in a structure that contains a crack-like defect, and are, therefore, the methods that are followed here. If one

¹ Professor of materials in mechanical engineering and postdoctoral research assistant, respectively, Mechanical Engineering Department, Imperial College, London, U.K.

wishes to use one of these other methods closely, then source references such as Ref 3 for EPRI, Ref 4 for R-6, and Refs 1, 5, and 6 for the less well-documented EnJ must be referred to. If the actual instability, which for other than the constant load case will occur at some point after maximum load, is of interest, then the dJ/da tangency method [3], the similar T concept [7], or the rather different energy rate I method [8] can be used. Some comparative studies of these methods have been given in Refs 1 and 9 and in Footnote 2 below. For the present purpose of discussing *R*-curves, the prediction of maximum load is quite adequate, and it is hardly necessary to distinguish between the many points of detail by which the several methods differ, so the R-6 method will be followed, though not necessarily in a rigorous manner.

The R-6 method had its origin in the two criteria of linear elastic fracture mechanics (LEFM) and plastic collapse, with the \ln secant term from the Dugdale model [10] used to interpolate between the two bounding conditions. Despite this apparent relation to COD concepts, the interpretation now used for the interpolation and its recent extension [11] is in terms of J . The resulting FAD is expressed as

$$K_r = S_r \left[\left(\frac{8}{\pi^2} \right) \ln \sec \left(\frac{S_r \pi}{2} \right) \right]^{-1/2}$$

for $K_r = K_{lc}/K$ and $S_r = Q_c/Q$, where Q is the load and the suffix c denotes collapse. Reference must be made to fuller accounts of the method for more exact definitions of these terms, but, in brief, residual and other secondary stresses are entered only on the ordinate, K_r , because they do not affect the abscissa of collapse. Hardening is allowed for by use of a flow stress averaged from yield and tensile strengths, or in Ref 11 by introducing a "tail" to the FAD for cases of high hardening.

Rising Toughness and Crack Growth

For assessing behavior after crack initiation, the R-6, EnJ, and EPRI methods make use of *R*-curves expressed in terms of J . The main purpose of this paper is to point out some of the consequences of changes that have been expressed recently in definition and interpretation of *R*-curve data beyond J -controlled growth. The authors well appreciate that these changes are not yet widely accepted, let alone recognized in standard procedures. The changes in question are the choice of a suitable definition for a J -like term, after initiation, and the choice of an appropriate axis to represent crack growth. The former was discussed at length in Ref 12 and, more specifically, in relation to rising or drooping *R*-curves [13]. The choice of abscissa has been noted in Ref 14 and then discussed in Refs 15 and 16, where it was shown that for some data a unique (that is, geometry-independent) *R*-curve was obtained if the crack extension axis was normalized to $\Delta a/c$, where c was the size factor that inhibited the continued growth of plasticity. In some cases the term c is the thickness, B , the ligament size, b , or an inherent material size factor, r_{mp} , the maximum size of a plane stress shear lip for that material. A large amount of further bending and compact test piece data from the literature is analyzed in this way in Ref 17. Some data are noted where normalization does not seem necessary, including a J -controlled regime for small amounts of growth in suitable cases. In yet further cases, particularly where shear-lip effects dominate, it is necessary to scale the J ordinate by the factors that dominate the size of the regions of plastic work. In Ref 17 some 20 or so references were cited covering about 50 different

² Etemad, M. R. and Turner, C. E. "Unstable Crack Growth of Variable Span Bending Pieces of HY130," internal report, Mechanical Engineering Department, Imperial College, London, U.K.

material-geometry combinations for bending and compact-tension pieces, but only brief attention was given to side-grooved data. A further note on side-grooved data is in preparation³ and the particular aspects relevant to the present paper are detailed later in the paper.

The root cause of the effects, as hinted in Ref 17, is the interplay between the size-dependent scaling rules for EPFM and the conventional geometrical similarity rules of plasticity, as related by the formula

$$J = \frac{\eta A}{Bb}$$

where A is the area under the load-displacement diagram, η is a geometry dependent term, and $\eta = 2$ for deep notch bending and ~ 2.2 for compact pieces. The precise manner in which that relationship is used after initiation affects the value of J and the shape of the R -curve [13] but not the scaling trends under discussion here.

Measurement of work has a direct relation to the J -integral prior to initiation for cases where the deformation is self-similar [12,18]. However, it is also widely used for postinitiation data, including that analyzed in Ref 17. Moreover if R -curves are to be applied to real structures either before or after initiation, a relevance to any geometry is implied, whether or not the deformation is self-similar. A description of the reason for and consequence of the geometric effects that are found for R -curves derived for bend tests has been offered in some detail in Ref 19, in terms of conventional arguments of engineering plasticity. In brief, the implication is that the toughness being measured by the R -curves reflects the amount of work dissipated, normalized by η/Bb . At and just after initiation that argument does not conflict with the conventional interpretation of J as a characterizing parameter. After initiation it is consistent with the J_o interpretation

$$J_o = J + dJ = \eta \frac{(A + dA)}{Bb}$$

It may also be noted that the more recently proposed J_m [20] is rather similar in value to J_o and there is again no conflict. If a definition of J after initiation is used in which the ligament is updated, then the same convention must be used in scaling one R -curve to another. If the increment of work, dU , is corrected to give an increment in internal energy, such as for J , [21] or J_{TPT} (where TPT is the "three parameter technique" given in Ref 22), the scaling is not affected in principle because the corrections are functions of the same terms as is dU . A lack of clarity or of clear-cut scaling does, however, arise with any definition of J when the R -curve is reflecting a combination of deformation modes, such as tearing and shear-lip formation with neither component dominating. This is not surprising since the crack passes from a two-dimensional configuration prior to or perhaps just after initiation, through a truly three-dimensional shape in the early stages of growth, to a quasi-two-dimensional state again, if the size of the component and the amount of growth is sufficient to allow a steady-state growth behavior to be reached.

Whether or not those arguments are accepted, in the opinion of the present writers the basis of the case that an abscissa of Δa is not adequate beyond J -controlled growth is sufficiently well established by analysis of already published experimental data in Ref 17 to warrant examination of the implications of the changes on the application of R -curve meth-

³ Etemad, M. R. and Turner, C. E., to be submitted to the *International Journal of Pressure Vessels and Piping*.

ods. Both plane-sided and side-grooved data are referred to here since, for a typical part-through wall defect, it is not clear whether the contribution of shear lips to the toughness is relevant. A second feature arising from the analysis of Ref 19 with little direct experimental evidence, is the suggestion that the extent of J -controlled growth is a function of the degree of plasticity. The commonly accepted value of $0.06 b$ was found in Ref 23 for the extent within which J contour values remained path independent with appreciable plasticity. In Ref 19 it is found that the bound on J -controlled growth with full plasticity may be appreciably more. It is inferred that as the problem degenerates to LEFM the extent of J control will reduce to $0.02 b$ for the just valid plane strain limit and to even less for brittle behavior well within LEFM. The authors accept that these two statements are not reflecting the contour meaning of J beyond initiation but rather the work dissipation, which is the physical quantity being measured. The basis of the bounding statement in Ref 19 is outlined in the Appendix.

Some R-Curve Data

Plane-Sided Pieces

In the first instance, attention is focused on plane-sided (that is, non-side-grooved) pieces. Side-grooved data are discussed later. Both will be used in the example application that follows. Data are shown in Fig. 1a and b for HY130, representative of a high-strength structural steel of moderate toughness, and in Fig. 2 for A533B steel, representative of a moderate strength steel of high toughness. For the HY130 data in Fig. 1a and b [14,15] there is a lower curve, Curve 1, from pieces $W = B = 50$ mm and an upper curve, Curve 2, from pieces $4W = B = 50$ mm. Other cases were shown in Ref 14. The two curves were normalized to a single curve using $\Delta a/b$ for the abscissa (Fig. 1b). Also shown on Fig. 1, are dotted curves, using a different definition of J , that are used later to illustrate the effect of definition of the ordinate. Data for A533B steel [24] in sizes $B = W = 10, 20, 40$, and 100 mm, also plane sided, are shown in Fig. 2. They give a unique curve and do not require normalization since the pieces are in the regime $B, b \ll r_{mp}$ in which (see Ref 17) it is argued that the effect of thickness and ligament cancel out for the geometrically similar cases.

Side-Grooved Pieces

Turning to side-grooved data, two behaviors were noted [17]. The first is side-grooved HY130 data from Ref 25 (Fig. 3), which do not require normalization. The A533B data from the same source do require normalization, using $\Delta a/b$ (Fig. 4a, b). Other data, notably from Refs 26 and 27 are examined (see Footnote 3), but the geometric scaling effects being sought are obscured by the material variability and the range of geometric variables included in those studies.

The authors now suggest that the distinction between the substantially nonscaling behavior of HY130 (Fig. 3) and the scaling behavior of A533B (Fig. 4) is that the depth of the side grooves used [25] is adequate to remove the surface plane-stress region for HY130 but not for A533B. The basis for that statement is a comparison of the actual depth of each side groove, with the size of the LEFM plastic zone in plane strain at initiation, that is

$$r_{ie} = \left(\frac{1}{6\pi} \right) \left(\frac{J_i E'}{\sigma_y \sigma_{fl}} \right)$$

For HY130, r_{ie} is about 1.5 mm; for A533B it is about 10 mm. In Ref 25 the thicknesses are from 12.5 to 51 mm for both materials and the depth of each groove is nominally 0.1

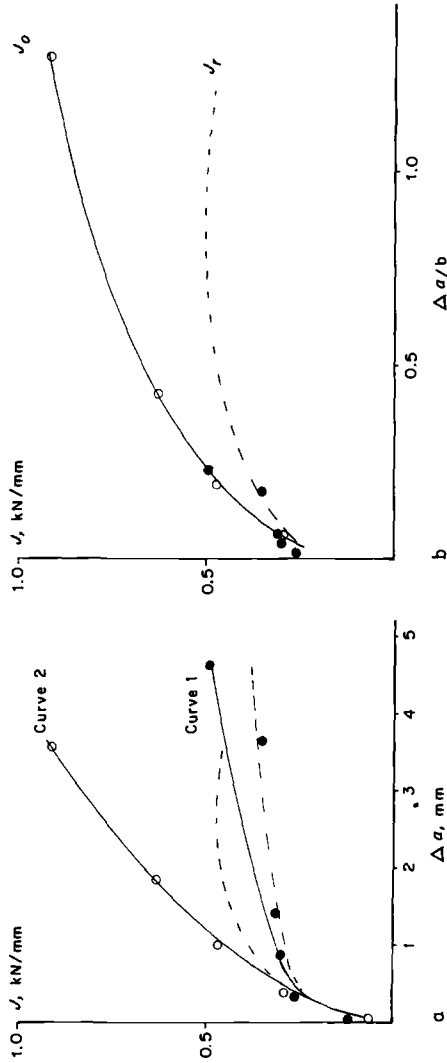


FIG. 1—R-Curves for HY130 from Ref 16 single edge notch bend (SENB) specimen (TL crack, $a/W = 0.5$, $S = 4W$, and $B = 50$ mm): (a) Curve 2 for $B = 4W$ (symbol \circ) and Curve 1 for $W = B$ (symbol \bullet); solid curves J_0 and dotted curves J_1 (symbols not shown); (b) corresponding normalization.

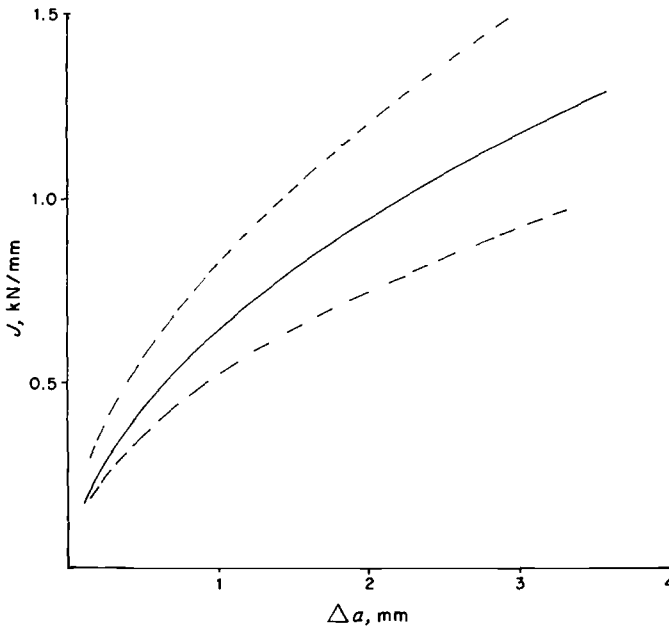


FIG. 2—R-Curves for A533B from Ref 24: compact tension (CT) samples; solid curves for 10, 20, 40, and 100-mm samples; dotted lines are 95% confidence limits.

or $0.15 B$ for HY130, from 1.05 to 5.15 mm, according to the actual thickness, and for A533B, from 1.3 to 5.05 mm. Apart from the thinnest pieces of HY130, where the depth of each groove is less than r_{te} by 0.45 mm, all the HY130 pieces are grooved to satisfy the above suggestion and give R-curves that do not need to be scaled, whereas all the A533B pieces have grooves too shallow to satisfy the suggestion and give R-curves that do need to be scaled because they retain a significant amount of a surface region of plane stress. All

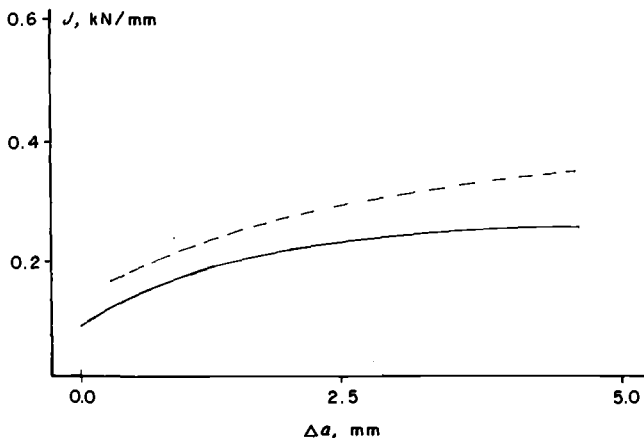


FIG. 3—R-Curves for side-grooved HY130 from Ref 25: CT samples, solid curve for $B_n = 40$ mm, dotted curve for $B_n = 16$ mm, other thicknesses in between.

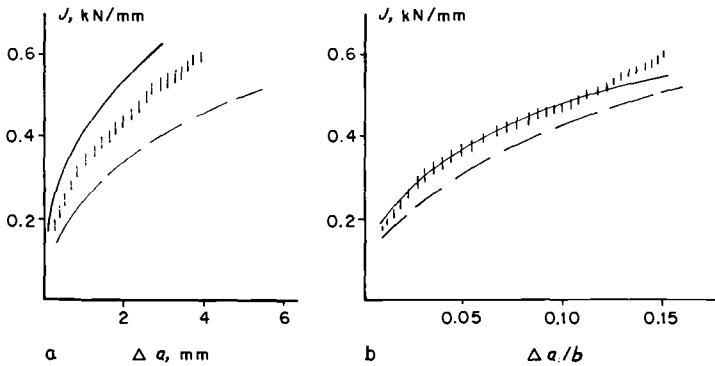


FIG. 4—R-Curves for side-grooved A533B from Ref 25: CT samples, solid curve for $b = 13$ mm, dotted curve for $b = 32$ mm, and shaded area for data with $b = 18$ to 23 mm.

the pieces satisfy another requirement seen as $B_n/B = >\sim 0.5$, below which yield cannot spread to the full thickness above and below the grooves unless the reduced thickness work hardens vigorously. An analysis supporting the general argument that the form of an R -curve is governed by the features that control the dissipation of plastic work is given in Ref 19, but the picture for the behavior of side-grooved pieces is clearly less secure than that for plane-sided pieces until more data for a range of pieces with suitably different geometric features are available.

It must also be noted that despite the emphasis here on geometric effects, one of the most important considerations—whether or not there is a difference between tensile and bend-type results (including compact-tension pieces as a bending-type stress state)—is beyond the scope of the present work, although results of very recent crack infiltration studies [28] promise more light on that aspect. The effect of absolute thickness on constraint, and hence on initiation and the R curve, is also examined in Ref 28, where the important distinction is made between constraint sufficient to cause flat fracture and that designated as “full” plane strain. Probable loss of constraint in some shallow notch configurations is also outside the scope of these remarks.

An Application

The Vessel

The implication on the use of R -curve data is now examined by way of an example. It is supposed that a pressure vessel containing a semielliptical axial defect in the outer surface of its cylindrical section is subjected to internal pressure. It is necessary to find the pressure required to cause crack initiation and then the maximum pressure that the vessel can sustain, together with the amount of tearing at that point. Two cases are examined to illustrate these points. These vessels are geometrically similar with a mean radius to thickness ratio, R/t , of 25, but with two values for absolute size, $t = 50$ mm and $t = 250$ mm. Note that t is used for vessel thickness and B for test piece thickness. In each case there is the same crack ellipticity, $a/2c = 0.133$. The absolute size of the defect will of course be different for the two cases.

Each vessel is then examined for the two materials described by Figs. 1 through 4 for initiation of crack growth, and then the conditions for maximum pressure are predicted according to both the conventional presentation, based on Abscissa Δa , and the appropriate normalized abscissa.

R-Curve Data

As already remarked, the *R*-curve data are taken for HY130 and A533B from bend or compact pieces. The tension data are not considered here. Since this example is a paper rather than real case study, for the purpose of bringing out certain implications of the behavior of *R*-curves, there is no question of whether or not either material would be an appropriate choice of steel type for some unspecified real application of a vessel of the dimensions used. Recall that the scaling under discussion relates to behavior beyond *J*-controlled growth, so that, provided the usual restrictions on the size of the test piece are observed, the value of initiation toughness and of the initial slope of the *R*-curve are taken as material properties. These remarks are taken to apply to side-grooved data in a lower bound sense, if the above conditions for the size of side grooves are also observed. The extent of *J*-controlled growth, now also seen (see Appendix) as a function of the degree of plasticity, will not affect the estimates of load made for a given *R*-curve but will have implications on the choice of *R*-curve from among several for different geometric sizes or proportions.

The first question is the choice of the appropriate size of test piece from which to take toughness data for use beyond *J*-controlled growth. For a more extensive *R*-curve, the width of the test piece, *W*, should presumably reflect the thickness of the vessel wall, *t*, since the test piece is a two dimensional idealization through the midsection of the actual defect. For the present example this dimension should therefore be either 50 or 250 mm, unless either the *R*-curve is independent of width or a normalization procedure is used as advocated here. The original crack penetration/thickness ratio for the vessel, $a/t = 0.5$, suits the HY130 data of Fig. 1, although the A533B data of Fig. 2 are for rather greater ratios. Since the crack will be constrained in the hoop sense, a plane-strain test condition is required. For both materials there is a choice of data from either plane-sided or side-grooved pieces. For HY130, a thickness such as $B = 50$ mm seems more than adequate to produce predominantly flat fracture and is readily testable so that data from non-side-grooved pieces of that thickness are accepted, although, because of the size of the maximum possible radius, r_{mp} , of the plastic zone, it is unlikely that "full" plane strain is attained. The data in Fig. 1*a*, Curve 1, are carried forward on the argument that the shear lip contribution is small enough to be neglected for a part-through crack application and the width of the test piece for Curve 1 is more relevant to the thickness of the vessel wall than that for Curve 2. This latter restriction is not necessary when the normalized form is used. Note that the proportions of the piece used for Curve 2 ($B \gg b$) are also relevant to the vessel configuration, with its hoop restraint implying a large "thickness" in the conventional *z* sense, but the absolute dimensions for Curve 2 are much smaller than those for the vessel. The side-grooved curve (Fig. 3), is also used on the grounds that it is equally applicable to a part-through crack case. For A533B the thickness for plane strain would be very large and not readily testable, so side-grooved data are used, as given in Fig. 4. The full thickness data (Fig. 2), with appreciable shear lips, are rejected as being unreasonable for a part-through thickness crack problem.

As has been seen, the side-grooved data for HY130 are a function of Δa and do not require scaling, whereas the side-grooved data for A533B are not a single function of Δa and do, therefore, require scaling by the ligament size, *b*. This difference greatly affects the use of the data in the example when taken beyond *J*-controlled growth. It is also apparent that the HY130 side-grooved data pass directly from *J* control to the ω small regime, where ω is the familiar term $(b/J)(dJ/da)$ from Ref 30. That this is not a peculiarity of HY130 can be seen in Ref 29, where a piece of A533B tested in bending with $B = 500$ mm, $W = 90$ mm also passed from *J* control directly to the ω small regime, the curve scaling [17] with a related case, $B = 45$ mm, $W = 90$ mm, as expected. A further question is whether bend or compact-tension data, as shown here, are truly representative of the actual tensile hoop

stress loading or at least represent a lower bound behavior for it. Data for a semielliptical part-through crack in a plate of thickness $t = 110$ mm have been presented in Refs 30 and 31. These data fell predominantly between the various bend cases for the same direction of growth, being below a bend case of smaller thickness but above the bend data for (approximately) $B = W = t$ with $a/W = a/t = 0.5$, except in the near-initiation regime where the part-through crack gave the lowest curve of all. These results may be further unresolved geometric effects, a consequence of the method of analysis used or the result of material variability and are not resolved here.

General Information Required

For the R-6 method the value of the LEFM shape factor, Y , is required. This can be obtained from the American Society of Mechanical Engineers (ASME) Boiler and Pressure Vessel Code, Section XI (1979), or from several well-known handbooks. The former source is used here, and results extrapolated where necessary. The values used are shown in Fig. 5. An estimate of K is taken in the form used in the ASME code

$$K = \left[\sigma_m M_m \left(\frac{\pi}{Q} \right)^{1/2} + \sigma_b M_b \left(\frac{\pi}{Q} \right)^{1/2} \right] (a)^{1/2}$$

For the form used in the EnJ method, K is written

$$K = Y(\sigma_m + \sigma_b)(a)^{1/2}$$

so that Y depends on the values of M_m , M_b , Q , and the ratio of σ to σ_Y . In this problem the value of σ_b is of course zero. The applied stress, σ , is $\sigma_m = PR/t$. The values of yield

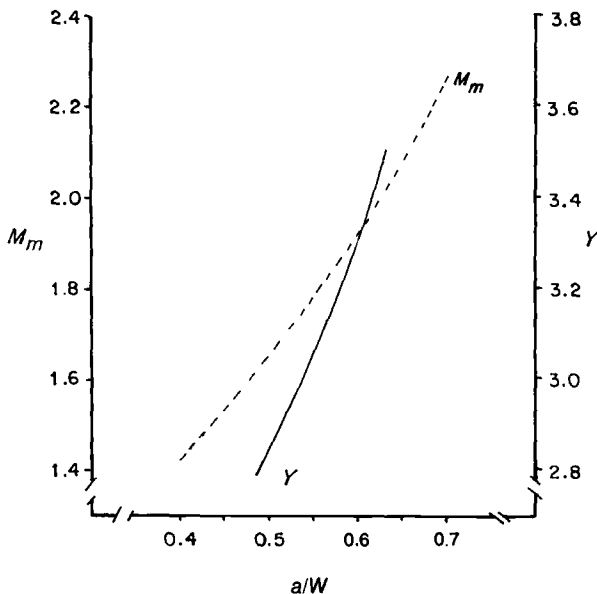


FIG. 5—General information required for K analysis.

TABLE 1—Material properties for two steels.

Material	σ_y , kN/mm ²	σ_{fl} , kN/mm ²	J_i , kN/mm	E , kN/mm ²
HY130	0.9	0.93	0.1–0.2	205
A533B	0.38	0.45	0.1–0.2	205

stress σ_y , flow stress, σ_{fl} , initiation toughness, J_i , and modulus, E , used here are shown in Table 1.

Solution for Initiation

Choice of blunting line or treatment of data where the value for initiation differs from one result to another is not entered into. For Method R-6 a value of K_{Ic} is required. This is taken as $(EJ_i)^{1/2}$, where J_i is the value used for initiation, irrespective of whether that value is strictly J_{Ic} . The terms $K_r = K_{Ic}/K$ and $S_r = Q_c/Q$ are then evaluated. The value for S_r is taken from Ref 4 as

$$S_r = \left[\frac{\frac{t}{a} - \frac{1}{m}}{\frac{t}{a} - 1} \right] \frac{Pr}{\sigma_{fl}}$$

where $m = (1 + 0.263 c^2/Rt)^{1/2}$, with $m = 1.0184$ given here for the initial crack size. An arbitrary value can be used for the pressure, P , to establish a point A (Fig. 6). Extension of OA to intersect the FAD boundary gives a value to K_r and hence using the K_{Ic} value, to

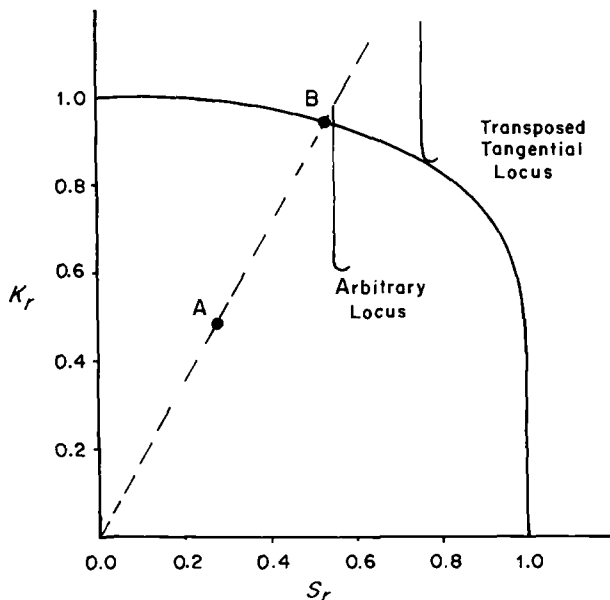


FIG. 6—Failure assessment diagram (FAD): the actual data are from Curve 2 of Fig. 1a.

TABLE 2—Results for initiation.

Material	J_i used, kN/mm	P_i for Vessel $t = 50$ mm, MPa	P_i for Vessel $t = 250$ mm, MPa
HY130	0.2	18.8	8.9
A533B	0.1	12.0	5.9

K and P . If the value of P used to establish the point A were an actual operating pressure, then the ratio OB/OA (see Fig. 6) gives a factor of safety against initiation.

All the calculations are repeated using the data for A533B. The results are given in Tables 1, 2, and 3.

Solution for Maximum Pressure

To evaluate maximum pressure and the corresponding crack length, the terms K , and S , in the R-6 method are updated both for the value of toughness, using an R -curve, and for the value of crack penetration and the corresponding shape factor, Y . On the FAD of R-6 a locus of different amounts of crack growth at a constant pressure is drawn. If an arbitrary pressure is used as in the calculation for initiation, then the locus falls away to regions on the FAD with lower values of K , but higher S . If this locus is then transposed to be tangential to the FAD, the point of tangency corresponds to the maximum pressure and the associated values of J and crack growth. It is assumed that the crack ellipticity remains constant during growth, although an alternative assumption can be made equally well if thought to be more appropriate. The procedure is shown in Fig. 6 for Curve 2 of Fig. 1a with the arbitrary locus set at $P = 20$ MPa.

The key point now arises as to which presentation of the R -curve data shall be used. As a first case the vessel with $t = 50$ mm is used with HY130 data taken from the test pieces $B = W = 50$ mm (Fig. 1, Curve 1). Since this value of W matches the vessel thickness, t , which it is supposed to model, there is no need to question the abscissa, since the actual

TABLE 3—Results for maximum pressure.

R-Curve Data	Vessel $t = 50$ mm		Vessel $t = 250$ mm	
	P_{max} , MPa	Δa at P_{max} , mm	P_{max} , MPa	Δa at P_{max} , mm
HY130				
Normalized	20	2	10	25
Direct				
Curve 1, J_o	20.5	2	>12	>7
Curve 2, J_o	28	4	>18	>7
Curve 1, J_r	20	2
Curve 2, J_r	23	2
Side-grooved	10	2
A533B, all side-grooved				
Normalized	16.5	4	10	18
Direct (Fig. 4)				
$b = 13$ mm	17	3	13	4
$b = 32$ mm	16	4	11	6

crack growth in the vessel is reproduced full-scale in the test piece. However, use of the solid line curve in Fig. 1, Curve 1 (denoting J_o), or the dotted curve (denoting J_r), or the side-grooved curve (Fig. 3), all taken as functions of absolute growth, Δa , give different predictions. This one calculation is representative of all the cases, independent of which method is used. Use of drooping R -curve data would of course give a lower prediction of maximum pressure, and use of other definitions of J would give results more or less extreme according to the rise of the R -curve in relation to Curve 1, taken here as the reference curve. Note that the effect of definition of J is much more extreme for Curve 2, where $\Delta a/b$ values are much larger (see Fig. 7).

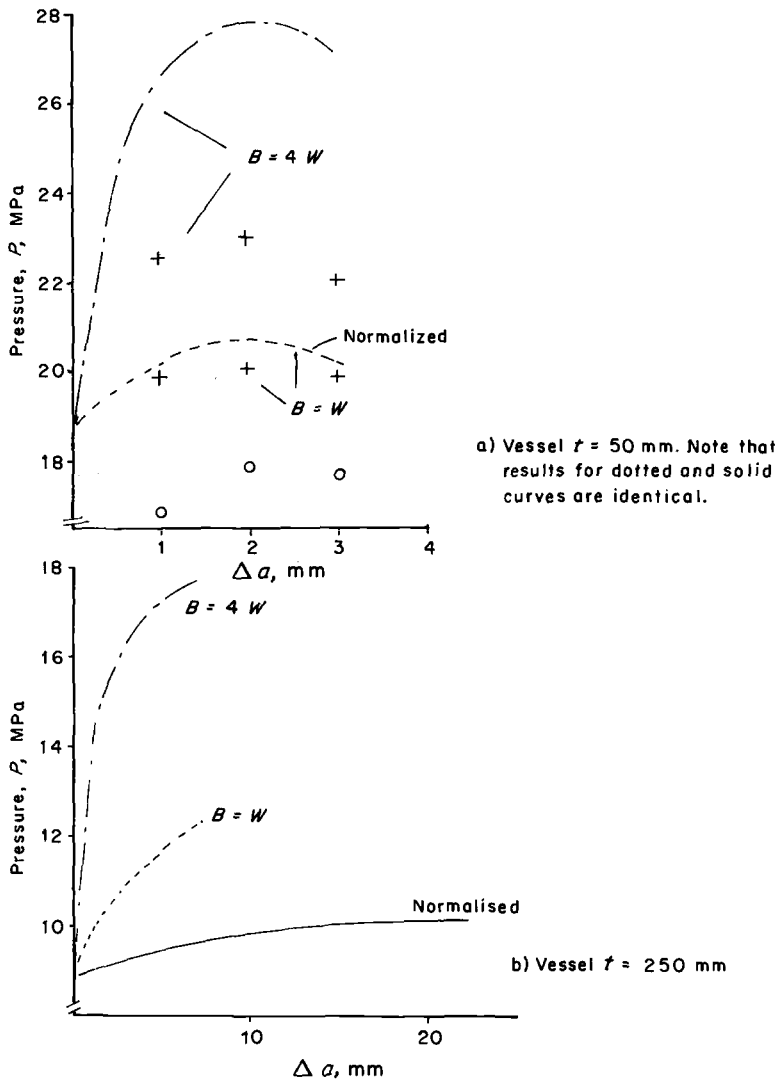


FIG. 7—Prediction of pressure vessel fracture behavior using HY130 as the base material: dotted chain line, Curve 2; dotted line, Curve 1; solid line, normalized data; +, prediction using J_1 ; o, prediction using data from Fig. 3 (side grooved).

Using any chosen definition of J (here the solid line data in Figs. 1 and 4) the choice of abscissa now arises. It must first be noted that, if J control is exceeded, then on the evidence and arguments of Refs 14 through 17 and 19 and Footnote 3, a solution can be found only if the normalizing factor, if any, appropriate to the component is the same as that for which R -curve data exist. If this were not so, the test piece and component would be governed by different variables and no further progress could be made, unless arguments such as those in Refs 17 and 19 allow transference from one geometric condition to another relevant to the case in question.

When using the normalized data the calculation procedure uses steps of the normalized abscissa, that is $\Delta a/b$, instead of just Δa , to extract J -values from the R -curve, but this must be returned to actual crack growth in the vessel by using the b value *for the vessel*. The results of applying the data in the conventional form, as a direct function of Δa , and then of using the normalized form for both sizes of vessel and for both materials are shown as graphs of pressure against crack growth in Fig. 7a and b for HY130 and Fig. 8a and b for A533B.

Discussion

Clearly for the smaller vessel with a ligament size similar to that of the test piece, the effect of normalization is minimal. For a vessel with a much larger ligament, as is the case for the vessel with $t = 250$ mm, the translation back to actual crack sizes will give a substantially larger value than results using the unnormalized data. There will be effects on the shape factor of the different values of growth implied, but at least here, that effect is rather small. The effect on the maximum pressure may well, therefore, be small (for a given choice of definition of J) provided both normalized and unnormalized R -curves rise to the same value of J , or are extrapolated thereto on the basis of the appropriate normalization.

Use of the side-grooved data for HY130 will give lower stresses and pressures for a given crack extension and lower estimates for maximum pressure, since the whole R -curve falls below the full thickness data by some 25%. This might be accepted as being within the uncertainty of the data and the most appropriate interpretation of the data since they are not, of course, from the same source references and thus from different batches of material.

A significant point of difference arises, however, between small and large vessels. For the small vessel, where the ligament of the vessel is closely similar to the ligament of the test piece, the use of normalized or unnormalized R -curves makes little difference.

However, this fact overlooks the point that the side-grooved data for HY130 do not require normalization and should, therefore, only be used for cases where no normalization is required for the structure, for example, J -controlled or ω small regimes, according to the present arguments. This apparent dilemma becomes more evident for the large vessel, where the use of normalized or unnormalized data gives results which, at least in terms of crack growth prior to maximum load, are very different, although the differences in actual value of maximum pressure are not so extreme, because the J -values are not all that different for an agreed definition of J . For this large vessel the question of whether or not to normalize when using HY130 must therefore be faced directly; if crack growth in the vessel is seen to be controlled by Δa itself then the non-side-grooved data of Fig. 1 cannot be used at all, although other data in Ref 15 for geometrically similar pieces are a function of Δa alone up to a thickness of 25 mm. Yet, thicker data necessitate reversion to a normalization regime of $\Delta a/B$. If the growth is seen as ligament controlled, then apparently the side-grooved data cannot be used, except on a lower bound argument.

The conflict arises for A533B in the reverse sense since if growth is seen to be controlled

by Δa as currently accepted, then the side-grooved test data cannot be used because they require normalization based on ligament size before they produce a unique curve. Other data in the literature that depend on Δa alone could be used, such as the geometrically similar series in Ref 24, or data such as the ω large results in Ref 27 (relating, of course, to A508 not A533B). Conversely, if the argument on control by $\Delta a/b$ is accepted, then the side-grooved data are relevant, but the other sources just mentioned are not. Note here that acceptance of the Δa only argument denies the use of (safe) lower-bound side-grooved data, unless other results exist that, contrary to Ref 25, do not need normalization. Where behavior falls within the regime of J -controlled growth the controversy is avoided, except in so far as the extent of that regime is also called into question by the arguments in Ref 19 that underpin the original phenomenological basis of Ref 14, 15, 16, and 17 and Footnote 3.

We now argue that these differences can be reconciled, even for large amounts of growth. Unfortunately, no data are known for a single material that embrace all the ranges of variables in question and, as is well known, much of the data that cover parts of the range are difficult to interpret because of limitations either in test technique or analysis or in uniformity of material. The rationalization offered is, therefore, largely heuristic at this stage.

In vessels small in relation to the toughness level, assessed at least conceptually by LEFM values of as the sizes of plastic zone, r_{mp} , or r_{ie} , introduced above, tearing will not start until the ligament is near the fully plastic state. A regime of J -controlled growth, dependent on Δa alone and with ω large, may be sufficient to govern the growth up to maximum load. Where that is near the fully plastic state, the extent of the ω large region may well exceed the value of $0.06 b$ usually associated with the so-called J -controlled regime. For vessels large in relation to the measure of toughness, growth will occur before full plasticity of the ligament. In those cases J -controlled growth is itself restricted to an amount less than the 6% usually accepted, reducing the limit to about 2% for LEFM plane strain, although the absolute amount of growth may still be significant in relation to a true initiation state. This will be followed by a regime of ω small which as shown, obeys a $\Delta a/b$ law at least in the regime immediately beyond J control. In either size, it is only if the configuration is such that shear lips can contribute to the dissipation that a further regime with ω large will exist. The key point in a given application is therefore the degree of yield in the ligament and, hence, the identification of the extent of J control and of the nature of the regime that follows it. Some, at least, of these aspects are matters more relevant to final failure than to conventional design.

Clearly many points remain to be resolved and behavior must merge gradually from one regime to another, but the present authors see these arguments as rationalizing a large number of hitherto disparate trends in the extensive literature on R -curves while opening fresh questions on the relevance and use of R -curve methods.

Recent reexamination of R -curve data for a range of materials of various levels of toughness suggests a pattern of R -curve effects running from quasi-LEFM to quasi-plastic collapse domination,⁴ highly reminiscent of that outlined by Rice et al. (see Fig. 8 of Ref 12), with the term here denoted r_{mp} being conceptually identical to their term of $0.2J_{ic}E/\sigma_y^2$, by which their abscissa was normalized. However, the discussion here and that of Ref 19 (see Appendix) extends the contained yield arguments of Ref 12 to general yield.

⁴ Wei, Y. L., Etemad, M. R., John, S., and Turner, C. E., "Some Effects of Geometry on J Resistance Curves," *Proceedings, International Conference on Fracture and Fracture Mechanics*, Fudan University, Shanghai, China, 21-24 April 1987, pp. 60-72.

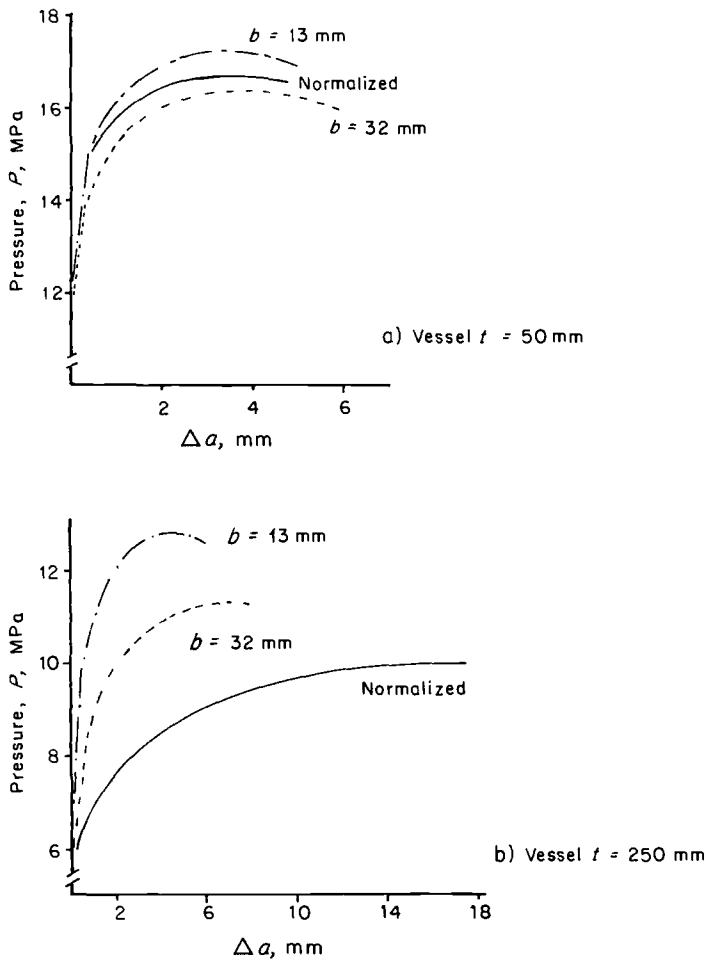


FIG. 8—Prediction of pressure vessel fracture behavior using A533B as the base material: dotted chain line, upper bound data; dotted line, lower bound data; solid line, normalized data from Fig. 4.

Conclusions

The suggestion that R -curves for a given material are not functions of Δa alone beyond J -controlled growth has been pursued for both full-thickness and side-grooved pieces. Such results as have been examined for a range of bend or compact pieces, support the argument for a normalized abscissa. A tentative suggestion is made that to eliminate the direct effect of shear lips each side-groove should equal or exceed the value of the plane-strain plastic zone at initiation, r_{ic} .

Applying this analysis to postulated case studies shows that care must be exercised beyond J control in selecting data that conform to the same geometric controls in the test piece as in the structure. In many cases it seems that the analysis would affect the amount of growth predicted rather than the value of maximum load, but there may well be combinations of circumstances where estimates of maximum load are also affected, depending on what other restrictions have been placed on the acquisition or use of particular data. Also the relevance

of plane-sided pieces that show large dissipation of work in shear lips must be carefully examined since data for side-grooved and very thick pieces, $B \gg W$, pass directly from the J -controlled ω large regime to the ω small regime.

The circumstances that control the various regimes are summarized, but data to substantiate many of the detailed arguments do not seem to be available. The authors suggest that the degree of plasticity in the remaining ligament is an important factor, influencing both the dominance and lack of dominance of a given geometric term and the extent of the J -controlled regime. The present arguments suggest a larger extent for the regime of J control with full plasticity, perhaps double the 6% currently accepted for bending-type fields, but reduction to only 2% in conditions of LEFM plane strain.

Recall that tensile-type test data have not been discussed. Although there is no reason to suppose tension test data will not normalize in the same way, the relation between tension and bending data has not been examined, and no inference is made here as to whether or not the toughnesses found under those different loading conditions can be directly related.

APPENDIX

The arguments of Ref 19 that are central to the present paper are summarized here, since they have not yet been exposed to general discussion. The main point is that the geometry dependence of R -curves must be compatible with the dominant term in the work dissipation rate from which the R -curve is derived. The regimes identified in Refs 14 through 17 and Footnote 3 that are of relevance here are the J -controlled regime and just beyond. In Ref 19 the former is shown to be Δa dependent because it is dominated by plastic hinge work. Beyond J control the dominance can be by shear lip work, in which case ω is still large and control will be by $\Delta a/c$, where $c = B$ or b or r_{mp} , or a regime of ω small may be entered, governed by flat fracture, in which control is by $\Delta a/b$, although for very small ω , $\Delta a/b$ is hardly distinguishable from Δa alone. The extent of J -controlled growth is argued to be the region of high constraint before initiation since that is the region described by the HRR J field. For bending, this extent can be estimated up to about $0.8 Q_c$ from the LEFM plane-strain plastic zone size. Beyond that load it is estimated in the reference in Footnote 3, from a rigid plastic analysis to reach about $0.11 b$, with some variation between about 8 and 15% according to the approximations accepted.

In the case of side-grooved pieces, an approximate analysis is given in Footnote 3 that suggests there will be a region of plane stress above and below the actual side grooves if the "buried" plane-strain zone exceeds the height of the side groove. From that the authors deduce that the size of a 90° groove made to eliminate the shear lip, though not necessarily to produce "full" plane strain, is the term now called r_{ie} , which is the size of the LEFM plane-strain zone taken at initiation. This simple rule seems consistent with the limited data analyzed in leaving the resultant R -curve independent of the ligament, that is, a function of Δa alone, when that size of groove is exceeded. Other restrictions are also thought to exist on the ratio of the net to gross thickness, of the form $B_{net}/B \geq 0.5$ or perhaps 0.33, in order that yield can spread from the ligament to the full thickness material. In the analysis of HY130 from Ref 25 the value of r_{ie} was found to be about 0.4 mm greater than the depth of grooving for the 12.5-mm thick pieces. The volume of material that experiences plane stress is estimated to be small and to increase the flat fracture work dissipation by only perhaps 10% or so. The data, therefore, follow the behavior of the thicker pieces that are adequately grooved quite closely.

References

- [1] Turner, C. E. in *Post-Yield Fracture Mechanics*, Vol. II, Elsevier Applied Science Publishers, London, 1985.
- [2] "Guidance on Some Methods for the Derivation of Acceptance Levels for Defects in Fusion Welded Joints," PD 6493 British Standards Institution, London, 1980.
- [3] "An Engineering Approach for Elastic-Plastic Fracture Analysis," EPRI Np1413, Project 1237-1, Electric Power Research Institute, Palo Alto, CA, 1981.
- [4] Assessment of the Integrity of Structures Containing Defects: R/H/R6," Central Electricity Generating Board, London, England, 1979.
- [5] Turner, C. E. in *Elastic-Plastic Fracture: Second Symposium, ASTM STP 803*, Vol. II, *Fracture Curves and Engineering Applications*, American Society for Testing and Materials, Philadelphia, 1983, pp. 80–102.
- [6] Turner, C. E., "Fitness for Purpose Validation of Welded Construction," Paper No. 10, Welding Institute, Cambridge, U.K., 1981.
- [7] Paris, P. C., et al. in *Elastic-Plastic Fracture, ASTM STP 668*, American Society for Testing and Materials, Philadelphia, 1979, pp. 5–36.
- [8] Turner, C. E., in *Fracture Mechanics: Eleventh Conference, ASTM STP 677*, American Society for Testing and Materials, Philadelphia, 1979, pp. 614–628.
- [9] Etemad, M. R. and Turner, C. E. in *Fracture Mechanics: Seventeenth Volume, ASTM STP 905*, American Society for Testing and Materials, Philadelphia, 1986, pp. 485–502.
- [10] Dugdale, D. S., *Journal of Mechanics and Physics of Solids*, Vol. 8, 1960, p. 100.
- [11] Bloom, J. M. in *Elastic-Plastic Fracture: Second Symposium, Vol. II, Fracture Curves and Engineering Applications, ASTM STP 803*, American Society for Testing and Materials, Philadelphia, 1983, pp. 206–238.
- [12] Rice, J. R., et al. in *Fracture Mechanics: Twelfth Conference, ASTM STP 700*, American Society for Testing and Materials, Philadelphia, 1980, pp. 189–221.
- [13] Etemad, M. R. and Turner, C. E., *International Journal of Pressure Vessels and Piping*, Vol. 21, 1985, pp. 81–88.
- [14] Etemad, M. R. and Turner, C. E. *Journal of Strain Analysis*, Vol. 20, No. 4, 1985, pp. 201–208.
- [15] Etemad, M. R., et al. "Elastic-Plastic R-Curves for Large Amounts of Crack Growth," *Fracture Mechanics: Eighteenth Symposium, ASTM STP 945*, American Society for Testing and Materials, Philadelphia, 1988.
- [16] Etemad, M. R. and Turner, C. E., *International Journal of Pressure Vessels and Piping*, Vol. 20, 1985, pp. 1–5.
- [17] Etemad, M. R. and Turner, C. E., *International Journal of Pressure Vessels and Piping*, Vol. 26, 1986, pp. 79–86.
- [18] Rice, J. R. in *Progress in Flaw Growth and Fracture Toughness, ASTM STP 536*, American Society for Testing and Materials, Philadelphia, 1973, pp. 231–245.
- [19] Turner, C. E. in *Proceedings of Size Effects in Fracture*, Institution of Mechanical Engineers, England, 1986, pp. 25–33.
- [20] Ernst, H. A. in *Elastic-Plastic Fracture: Second Symposium, Vol. I, Inelastic Crack Analysis, ASTM STP 803*, American Society for Testing and Materials, Philadelphia, 1983, pp. 191–213.
- [21] Ernst, H. A., et al. in *Fracture Mechanics: 13th Conference, ASTM STP 743*, American Society for Testing and Materials, Philadelphia, 1981, pp. 476–502.
- [22] Garwood, S. J., et al., *International Journal of Fracture Mechanics*, Vol. 11, 1975, pp. 528–530.
- [23] Shih, C. F., et al. in *Elastic-Plastic Fracture, ASTM STP 668*, American Society for Testing and Materials, Philadelphia, 1979, pp. 65–120.
- [24] Ingham, T., et al. in *Structural Mechanics in Reactor Technology*, Elsevier Applied Science, New York, 1983.
- [25] Davis, D. A., et al. in *Elastic-Plastic Fracture: Second Symposium, Vol. II, Fracture Curves and Engineering Applications, ASTM STP 803*, American Society for Testing and Materials, Philadelphia, 1983, pp. 582–610.
- [26] Andrews, W. R. and Shih, C. F. in *Elastic-Plastic Fracture, ASTM STP 668*, American Society for Testing and Materials, Philadelphia, 1979, pp. 426–451.
- [27] McCabe, D. E., et al. in *Elastic-Plastic Fracture: Second Symposium, Vol. II, Fracture Curves and Engineering Applications, ASTM STP 803*, American Society for Testing and Materials, Philadelphia, 1983, pp. 562–581.
- [28] Gibson, G. P. "Characterization of Ductile Crack Initiation and Growth in Mild Steel," Ph.D. thesis, University of London, London, UK, 1986.

- [29] Hutchinson, J. W. and Paris, P. C. in *Elastic-Plastic Fracture*, ASTM STP 668, American Society for Testing and Materials, Philadelphia, 1979, pp. 37–64.
- [30] Garwood, S. J. in *Proceedings*, International Conference on Application of Fracture Mechanics to Materials and Structures, Freiburg, West Germany, 1983, pp. 935–950.
- [31] Garwood, S. J. in *Fracture Mechanics: Twelfth Conference*, ASTM STP 700, American Society for Testing and Materials, Philadelphia, 1980, pp. 271–295.

Brian N. Leis,¹ Douglas P. Goetz,² Paul M. Scott,¹ and
C. Michael Hudson³

Fatigue Behavior of Axial and Pressure Cycled Butt and Girth Welds Containing Defects

REFERENCE: Leis, B. N., Goetz, D. P., Scott, P. M., and Hudson, C. M., “Fatigue Behavior of Axial and Pressure Cycled Butt and Girth Welds Containing Defects,” *Fracture Mechanics: Nineteenth Symposium. ASTM STP 969*, T. A. Cruse, Ed., American Society for Testing and Materials, Philadelphia, 1988, pp. 374–391.

ABSTRACT: This paper presents the results of a study directed at developing a data base for establishing fitness-for-purpose defect acceptance criteria for welds with defects. The study focused on A106 Grade B steel pipe. Data are presented for flat plate, wall segment, and vessel specimens and actual pipe sections containing either artificial or natural planar or volumetric defects. Defect acceptance criteria developed from the test data are discussed.

KEY WORDS: welds, fatigue, defects, acceptance criteria, porosity, lack of fusion, lack of penetration, cracks, A106 Grade B steel, fitness for purpose, fracture mechanics

Current criteria for the acceptance of welds are based on workmanship standards rather than criteria established in accordance with serviceability. This paper reports on a program whose purpose was to develop a rationale for accepting welds subjected to fatigue loading that contained workmanship-based code-rejectable defects on the basis of a fitness-for-purpose criterion. Much has been written on the fitness-for-purpose concept [1–7] and criteria for fracture have been developed [1,2]; however, less has been done for welds subjected to fatigue loading, particularly for welds containing naturally occurring defects. Vosikovsky [8] has studied fatigue crack growth of artificial planar defects in fitness-for-purpose analysis of axial defects in linepipes. Munse et al. [9] at the University of Illinois have looked at a variety of flaw types, including “natural” defects in steels, but have not explored the implications of their data in a specific fitness-for-purpose application. Other noteworthy studies also include the work of Lundin [10] and Booker et al. [11].

The limited available literature implies that the results may be sensitive to the material and the welding process and parameters. Accordingly, material-application-specific results have been generated to help develop a fitness-for-purpose-based defect acceptance criteria for use in piping recertification for the physical plant of the National Aeronautics and Space Administration (NASA)-Langley Research Center. Fatigue life data for A106 Grade B steel

¹ Research leader and principal engineer, respectively, Battelle Columbus Division, Columbus, OH 43201.

² Ph.D. candidate, Texas A and M University, College Station, TX 77843; formerly research engineer, Battelle Columbus Division, Columbus, OH 43201.

³ Head, Fracture Mechanics Engineering Section, NASA-Langley Research Center, Hampton, VA 23665.

in flat plate, pipe segment, vessel, and pipe run test configurations containing a variety of artificial and natural defects were generated to assess the factors controlling the fatigue life of weldments containing known defects⁴ and to form the basis for developing defect acceptance criteria. This paper summarizes the results of this study [12].

Experimental Aspects

Experimental Program

The experiments focused on girth butt welds made using a backup ring, and considered the effects of axial or pressure cycling only. All the welds were normalized to reduce possible data scatter due to variable unknown residual stresses. The parameters studied included the specimen configuration, defect type, and defect characterization. Several combinations of these parameters were tested to develop a stress-versus-life (*S-N*) curve. The stress levels were chosen so that three specimens failed between 10^4 and 10^6 cycles, while the fourth was to be at or near a fatigue endurance (or threshold for growth) stress level at 2×10^6 cycles. To the extent possible, the stress levels were to be chosen within the range considered realistic particularly in light of American National Standards Institute (ANSI) Standard B31.3. The fracture surfaces were examined in all cases.

Material

Specimens were fabricated from material from joints of 203-mm (8-in.)-nominal-diameter Schedule 40 (8.18-mm [0.322-in.]-nominal-wall-thickness) recent-vintage ASTM A106 Grade B seamless pipe fabricated from the same heat. Chemical analyses showed that the pipe material is typical of A106 Grade B pipe [12]. The remaining specimens were 76-mm (3-in.)-nominal-diameter Schedule 40 pipe segments removed from the NASA-Langley facility plant. NASA records indicate it was A106 Grade B pipe, of an early 1950s vintage. No analysis was done for the pipe removed from service.

Tensile (flattened strap) specimens were machined from both the longitudinal and transverse directions of each of the four joints of pipe in the as-received and normalized conditions (heated to 870°C (1600°F) for 30 min and air cooled). The mechanical properties for each pipe joint satisfied the requirement for ASTM A106 Grade B pipe and the microstructures were typical of A106 material, with little difference in microstructure for variations of orientation and location [12].

Welding Procedures and Natural Defects

The “artificial” weld defects were introduced into code-acceptable welds using electrical discharge machining (EDM) techniques. The welds were made using E7018 electrodes with backup rings in place. Each weld was subjected to an ultrasonic and radiograph inspection, and those passing were considered code-acceptable welds.

Approaches to simulate “natural” weld defects were qualified by trial and error to produce the desired defect. Lack of fusion (LOF), chosen as the planar defect, was achieved by

⁴ This paper does not deal with estimating or interpreting flaw sizes based on nondestructive inspection (NDI) indications. While the subsurface defects were X-ray inspected to verify their presence prior to cutting the specimens [12], no attempt was made to compare these indications with actual sizes measured after testing. As documented by Hanstock [13], Clark [14], and others [15], locating and sizing contained defects involves significant uncertainty. Reed et al. [16] have reported some success in linepipe applications.

painting a zinc-oxide mold-release compound on one side of the joint where the defect was desired. Porosity, the preferred volumetric weld defect, was introduced by intentionally reducing the gas flow rate during a gas-metal-arc (GMA) welding process used where the defect was desired. All "defective" welds were inspected both ultrasonically and radiographically, and the details were reported by Leis, et al. [12].

Specimens

The flat plate specimen was made from flattened pipe saw cut at the locations for the welds, and the edges were beveled in preparation for welding using flattened backup rings. The specimens were normalized and the final machining was done. Two sizes of artificial planar flaws were used, as shown in Fig. 1. Both were semielliptical surface flaws with an aspect ratio of depth to semi-length (a/c) of 2:3. The depth of the small flaw was 2.5 mm (0.1 in.); the depth of the large flaw was 5.1 mm (0.2 in.). Electrodes 0.254 mm (0.010 in.) thick with tapered edges were used to make sharp-tipped flaws. The artificial volumetric flaws had the same depths as the planar flaws and were semi-ellipsoidal in shape, with the shape and size identical to the planar flaw rotated on an axis perpendicular to the specimen's surface to form blind holes with curved bottoms.

Flaws were made in sound welds by cutting through the backup ring and into the weld at the midwidth of each specimen. Because the unstressed backup ring was found to "pin" the crack at the front free surface, the defect was "unpinned" by cutting the backing ring using a flat EDM electrode with a 76-mm (3-in.) radius to intersect the artificial weld defect at or just above the surface of the specimen. Care was taken to make the depth of the cut through the ring to unpin the defect just less than the thickness of the backup ring. In all cases, the depth of the weld defect was referenced to the surface of the specimen.

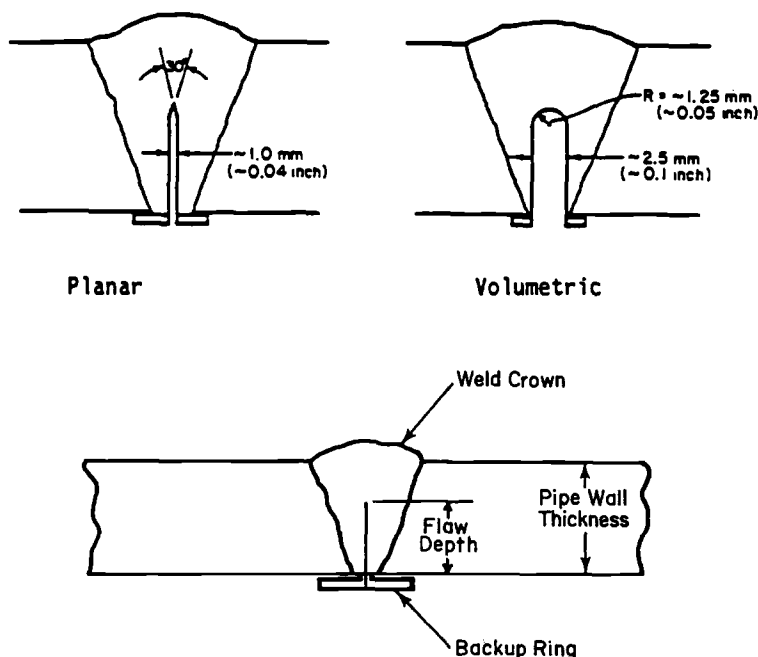


FIG. 1—Details of EDM flaws.

Wall segment specimens were made similar to the flattened plate specimens except that the pipe was not flattened. The artificial flaw design was the same as for the large planar EDM flaw used with the flat plates. The specimens with simulated weld defects had a target defect length of 30.5 mm (1.2 in.) with a target depth equal to 40% of the wall thickness.

Vessel (pipe-segment) specimens were fabricated from end-capped 203-mm (8-in.)-nominal-diameter pipe 610 mm (24 in.) long and contained a centrally located girth weld. One of the end caps was fitted with a nipple for a pressurization line. The center girth welds contained either an artificial (EDM) or a simulated weld surface defect on the inside surface. The EDM defect ran about 120° around the pipe circumference by about 4.95 mm (0.195 in.) deep (referenced to the inside surface of the pipe). For the simulated defects, the target flaw depth also was a 120° area through about 60% of the pipe wall thickness with an area equal to about 20% of the cross section. This defect depth and length were determined on the basis of linear elastic fracture mechanics (LEFM) estimates that indicated such flaws would grow through the wall thickness in reasonable lives at near-code allowable stress levels and would leak rather than rupture, based on a ligament instability analysis.

Two 76-mm (3-in.)-diameter specimens taken from the NASA-Langley Research Center physical plant were supplied with nipples and end caps already in place. Each specimen contained multiple defective welds, as detailed in Ref 12, in girth welds around tees and elbows connecting several short pipe runs.

Further detail on the specimens, defects, and welds can be found in Ref 12.

Equipment

Testing of flat plate and wall segment specimens was done in load control using commercially available closed-loop servohydraulic systems with a sinusoidal waveform at frequencies from 1 to 20 Hz. The load cell calibrations are traceable to the National Bureau of Standards (NBS). Machine alignment was checked by means of a strain-gaged alignment specimen. A reference test was made to measure bending strain distributions as a function of crack length in the pipe wall segment specimens. This strain survey data were used to correct nominal stresses used in crack growth calculations. The testing of vessels and pipe runs was done in a containment vessel in closed-loop pressure control to a sinusoidal waveform at a frequency of 1 Hz, using hydraulic oil as the pressurizing medium. The calibration of the pressure transducer was traceable to NBS. Failure was determined by either a flapper-type switch responding to an oil jet from a leak at the flaw or an increase in the depth of the oil sump in the containment vessel.

Results

Reference 12 tabulates the data presented here in *S-N* plots shown in Figs. 2 through 6. Figure 2 presents the results for flat plate specimens with planar flaws run at $R = 0.01$ only. Results of the tests run at $R = 0.01, 0.4$, and 0.6 are plotted in Fig. 3. Note that, as shown in Fig. 3*b*, the apparent effect of mean stress in Fig. 3*a* is consolidated reasonably using $S_{mx}[(3 - R)(1 - R)/2]^{1/2}$ [17] to collapse data for various stress ratios onto a single resistance curve, where S_{mx} is the maximum stress and R is the stress ratio. Figure 4 gives data from specimens with volumetric flaws in comparison with data from specimens with planar flaws. Figure 5*a* shows a summary plot of the data developed from the pipe wall segment specimens, while data for wall segments with artificial and natural flaws are compared in Fig. 5*b*.

Data developed using the pressurized specimens represent six 203-mm (8-in.)-diameter pipe segment specimens and two 76-mm (3-in.)-diameter specimens removed from service. Results for the 203-mm (8-in.)-diameter specimens were broken into two groups: artificial

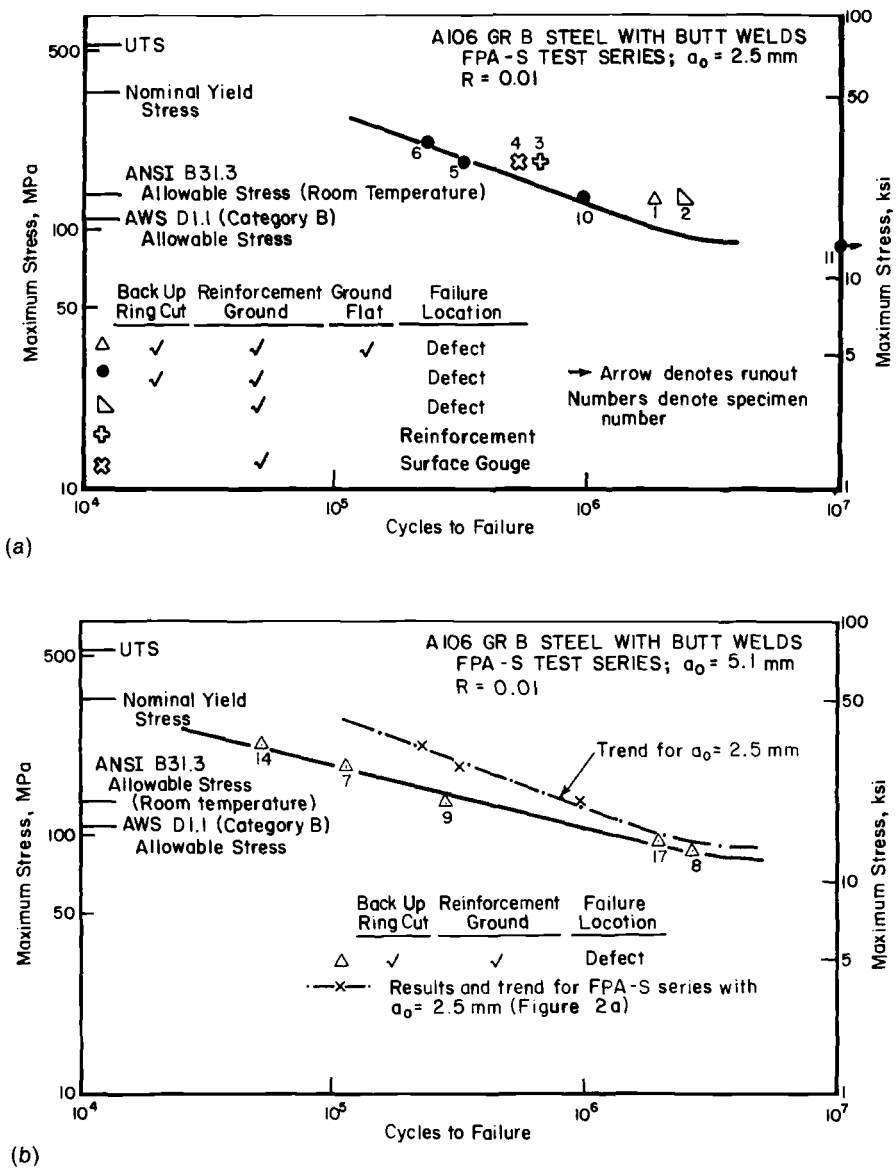


FIG. 2—Stress-life behavior of flat plate butt weld specimens with artificial planar flaws (FPA-S): (a) initial flaw size of 2.5 mm (0.1 in.); (b) initial flaw size of 5.1 mm (0.2 in.).

planar defects and artificial volumetric defects. Results for failures at the artificial flaws are plotted in Fig. 6a. Results for planar flaws in vessels tested at $R = 0.1$ are compared with the trend for planar flaws with an initial flaw depth, a_0 , equal to 2.5 mm in flat plates at $R = 0.01$ in Fig. 6b using the mean stress correlation parameter applied in Fig. 3b. Experiments on the piping runs removed from service used a maximum axial stress level of 85.9 MPa (12.5 ksi), the results of which are also plotted in Fig. 6.

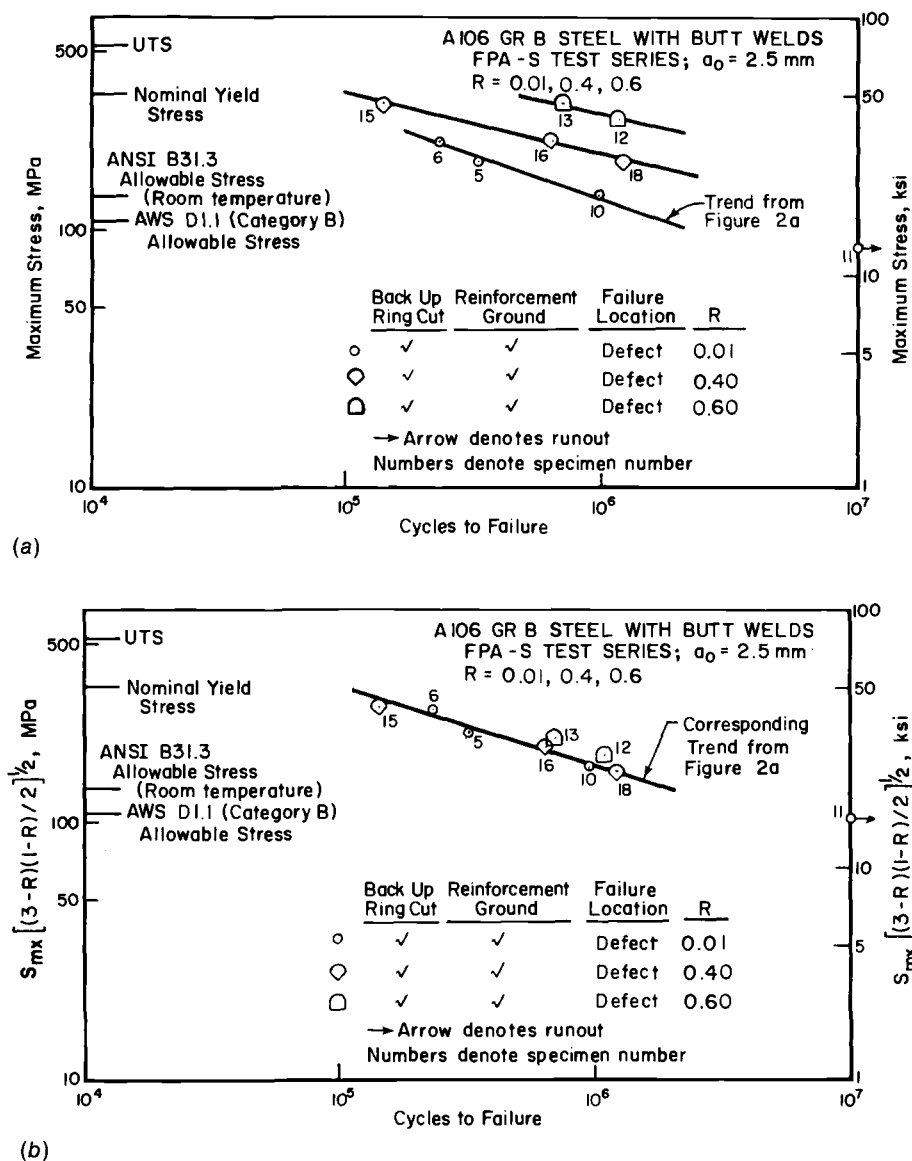


FIG. 3—Effect of mean stress life behavior of flat plate butt weld specimens with artificial planar flaws (FPA-S): (a) on maximum stress versus life coordinates; (b) consolidated data using $S_{max} [(3-R)(1-R)/2]^{1/2}$.

Discussion

Figure 2a shows that with the backup ring uncut, the fatigue life was extended up to about 1.5 times. This extended life is less than what would have been achieved if the backup ring was intact, thereby creating a buried defect (that is, if the backup ring was uncut the flaw would not be surface-connected). This was the situation for the specimen denoted by \square .

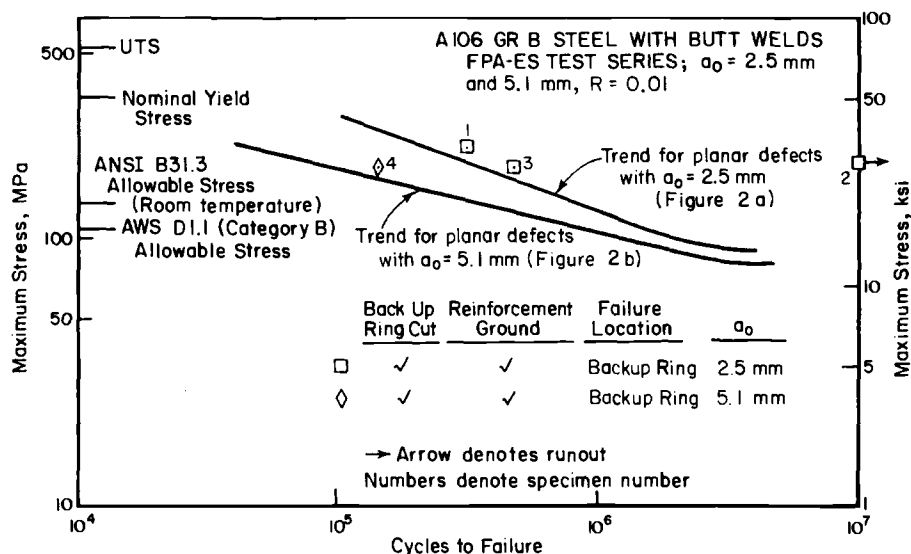


FIG. 4—Stress-life behavior for flat plate butt weld volumetric defect specimens (FPA-ES) in comparison with planar defect specimens (FPA-S).

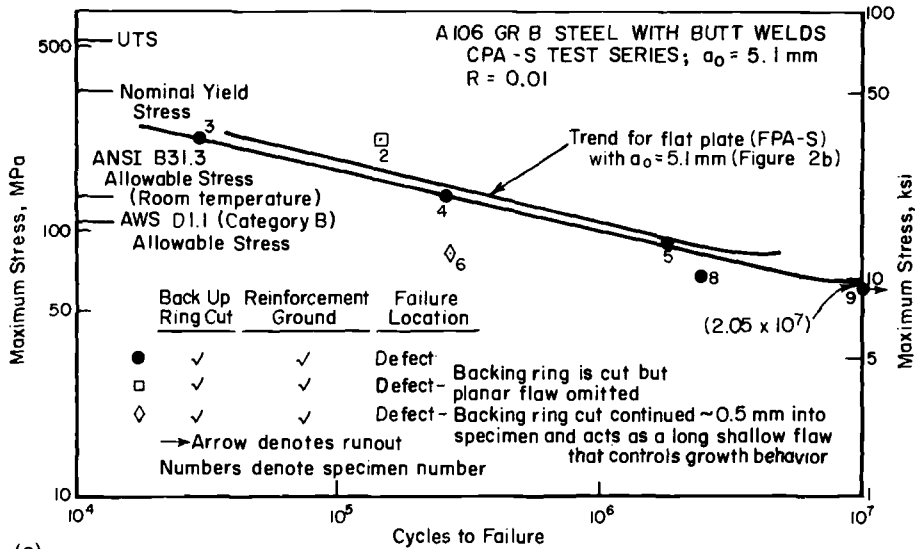
With its backup ring intact, this specimen exhibited a life 2.5 times longer than the reference trend (solid circles). The effect of imperfections in flatness can be seen by comparing the result for the ground-flat specimen, denoted Δ , with the reference trend. This effect was slight—about a factor of two extension in life.

The two specimens which failed at the weld toe, denoted + and x, are also instructive. Because the backup ring pinned the crack in these specimens, the failure location shifted to the weld toe. Cracking from the weld toe initiated and became critical before an EDM flaw, cut through almost one third of the nominal plate thickness, could deepen and become critical. At first glance, it may be thought to be remarkable that a crack could initiate and grow to failure from a code-acceptable weld toe, or from a code-acceptable gouge remaining at the toe after grinding the reinforcement, in the presence of such a large EDM defect. However, other investigators also have found that the weld toe is often a more fatigue-sensitive location than an internal weld defect [18].

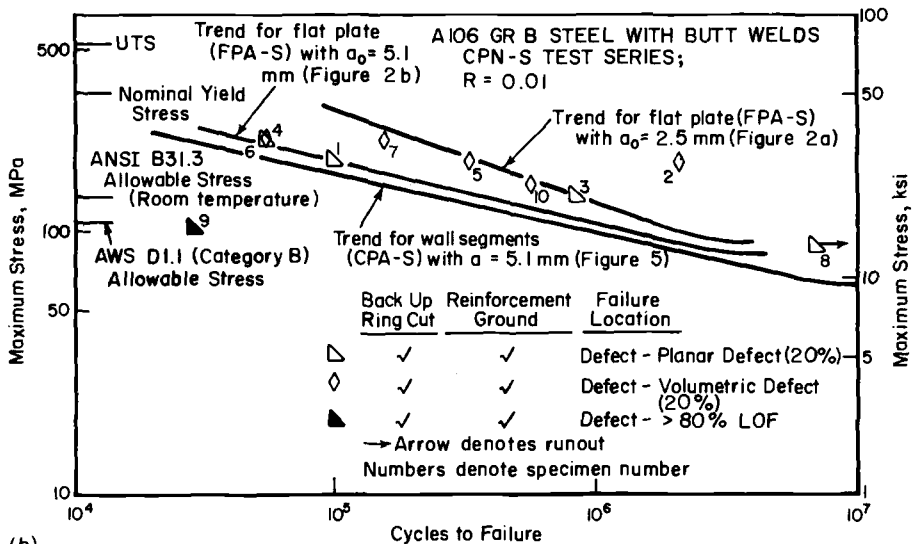
Figure 2b compares the results of tests where only the initial flaw sizes differed. At short lives the trends are quite different, the lives for the larger flaws being about 0.2 times those for the smaller flaws. But, at longer lives, the trends tend to merge.

The effect of stress ratio can be seen in the results of tests for specimens with planar EDM flaws conducted at $R = 0.4$ and 0.6, shown in Fig. 3a. However, these data should be viewed in light of their unique failure behavior which, as detailed in Ref 12, involved cracking from the backup ring as well as the EDM flaw. The fracture surfaces indicate that crack growth from the backup ring reduced the crack growth period from the EDM flaw, so that the total life was also reduced. Thus, in contrast to the earlier noted pinning of crack tips by the backup ring, which may extend the fatigue life, the backup ring may also act to shorten life by providing additional sites for multiple crack initiation.

Observe from Fig. 3a that the stress ratio appears to have a significant influence on the fatigue life. More than an order of magnitude difference developed at the extremes of $R = 0.01$ and 0.6 at high maximum stress levels. This difference increases as maximum stress decreases, similar to the trend for smooth specimens made of carbon steel whose



(a)



(b)

FIG. 5—Stress-life behavior for butt welded wall segment specimens (CPA-S): (a) results for artificial defects with $a_0 = 5.1$ mm; (b) results for natural defects with $a_0 \sim 40\%$ by area.

fatigue resistance is dominated by crack initiation. When the results of Fig. 3a are replotted on stress range versus life coordinates, the data tend to collapse but remain banded with the stress ratio. The maximum difference in life reduces to about a factor of 2.7. However, the trend is reversed from the usual pattern in that these data trends diverge as stress increases, whereas such trends usually converge to nearly twice the ultimate stress at short lives for specimens whose life is dominated by initiation. As was noted earlier, the results of Fig. 3a can be consolidated into a single tight scatter band when plotted, as in Fig. 3b,

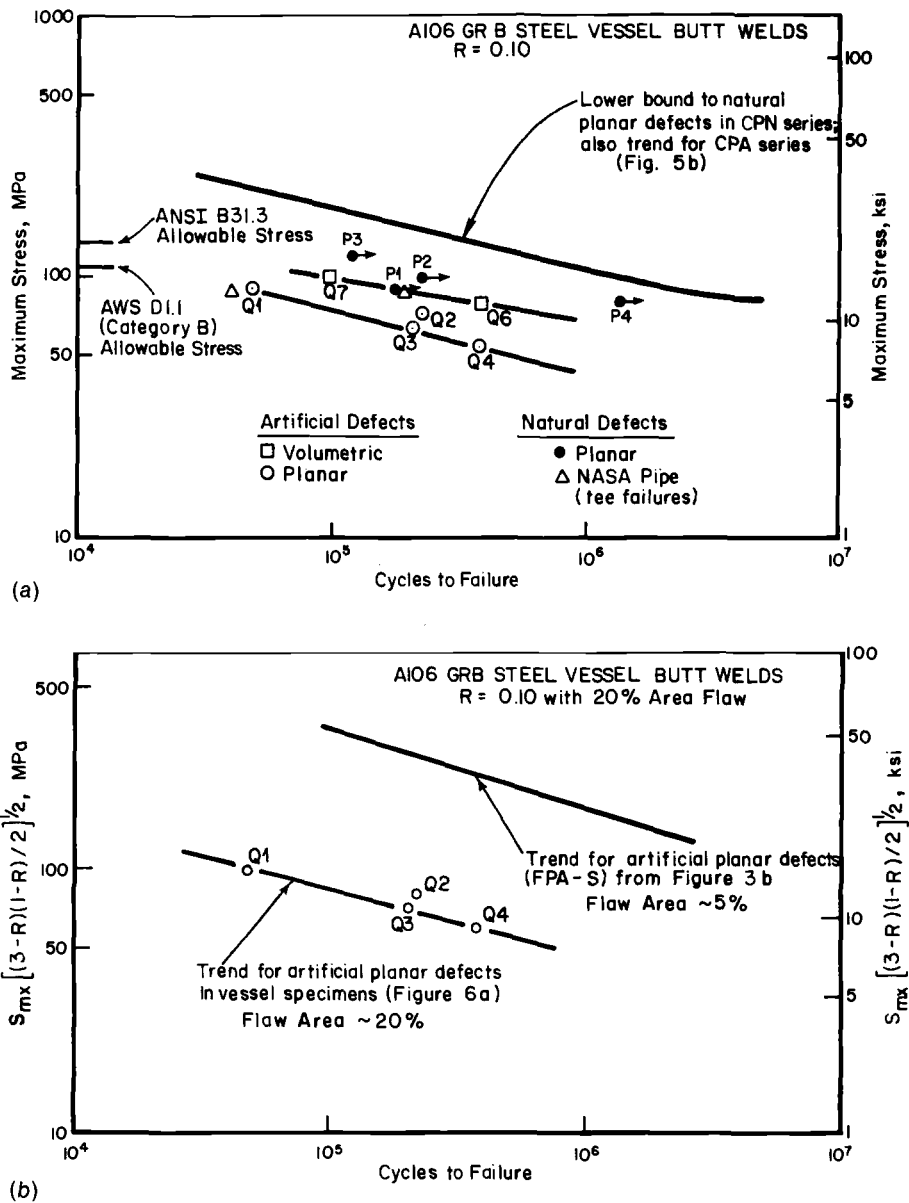


FIG 6—Stress-life behavior for butt welded vessel tests leading to failure at the desired defect: (a) stress-life behavior for planar and volumetric defects; (b) comparison of planar defects for vessel and flat plate specimens.

using a parameter [17] that has been shown to account for the effect of mean stress on crack initiation (or total life dominated by initiation) [19].

Note that the backup ring also played a significant role in the failure of the specimens with volumetric EDM flaws. The stress-life data presented in Fig. 4, which show that these specimens had lives longer than specimens tested at the same stress and flaws, actually represent cracks starting at the backup ring (similar to the results for $R = 0.4$ and 0.6) or

at the intersection of the cut in the backup ring and the blind hole. Thus, none of the failures shown in Fig. 4 simulates weld porosity.

Figure 5 presents the results developed for the wall segment specimens, including artificial (EDM) planar defects and simulated natural planar and volumetric defects. The target depth of the simulated natural defects was less than that for the artificial defect, but the length was significantly greater. The target defect areas for the case of the simulated natural defects were about 30% greater than those for the EDM defects.

Results developed for artificial defects show trends similar to those for the flat plate specimens, as is evident in Fig. 5a for specimens with $a_0 = 5.1$ mm. Thus, there is little difference between flat plate and curved specimens when similar test cross sections are used. The subtle difference in data trends is easily rationalized by bending in the curved test specimens [12].

Results for the simulated natural defects, shown in Fig. 5b, show increased scatter in comparison with the EDM data, but the trend of longer lives for volumetric defects than for planar defects is clear. For the data developed, the difference in lives between volumetric and planar defects is less than an order of magnitude, a difference somewhat less than expected.

The fact that the natural defects lie at lives longer than the artificial defects is significant. It means that, even though the natural defect areas are larger, they are less effective crack starters than the EDM defects in the absence of residual stress effects. Thus, artificial defects can be used to develop lower bound estimates of the behavior of actual defects. Note that, as shown in Ref 12, three data points are well off the trend for simulated defects because the target defect sizes were not achieved.

Figure 6 presents the results of vessel tests for welds with artificial and natural defects. The target defect is about 20% of the nominal axial cross section, in comparison with about 13% for the flat plate and wall segment specimens with the larger defects. This target size was easily controlled for the artificial (EDM) defects. However, for simulated weld defects only partial porosity of LOF develops: on average only about one third of the target level was achieved. Furthermore, the simulated porosity and LOF lie on weld beads or beveled material, and thus were not on the plane of maximum principal stress.

Examination of Fig. 6a shows that volumetric artificial defects survived from four to eight times longer than planar artificial defects of similar size. This difference, which was less than anticipated, is controlled by the relative difference in sharpness between the planar and volumetric EDM defects. As was shown earlier, the volumetric defect was really just a planar defect with a blunt tip, so that the difference in lives for this comparison may be much less than would occur for true planar and volumetric defects.

Direct comparison of the trend for either artificial or natural planar defects in curved segments and vessel tests is not possible since the absolute defect area and aspect ratio⁵ needed to produce comparable lives are very different. But, it is clear from comparing the results for wall segments ($R = 0.01$) shown as the trend line in Fig. 6a with the data for the vessels ($R = 0.1$) that defect size will be a dominant consideration in developing acceptance criteria. Correcting for the small difference in stress ratio, as was done in Fig. 3b, does not alter this fact, as is evident in Fig. 6b.

Fracture Mechanics Analysis of Fatigue Resistance

The fitness for purpose can be assessed in terms of plots of stress and life survived, such as have been shown in Figs. 2 through 6. However, the literature associates fitness for

⁵ The relative defect area is about a factor of four larger in the vessel than in the flat plate with $a_0 = 2.5$ mm (trend curve in Fig. 13b). The corresponding relative aspect ratios differ by about a factor of 14.

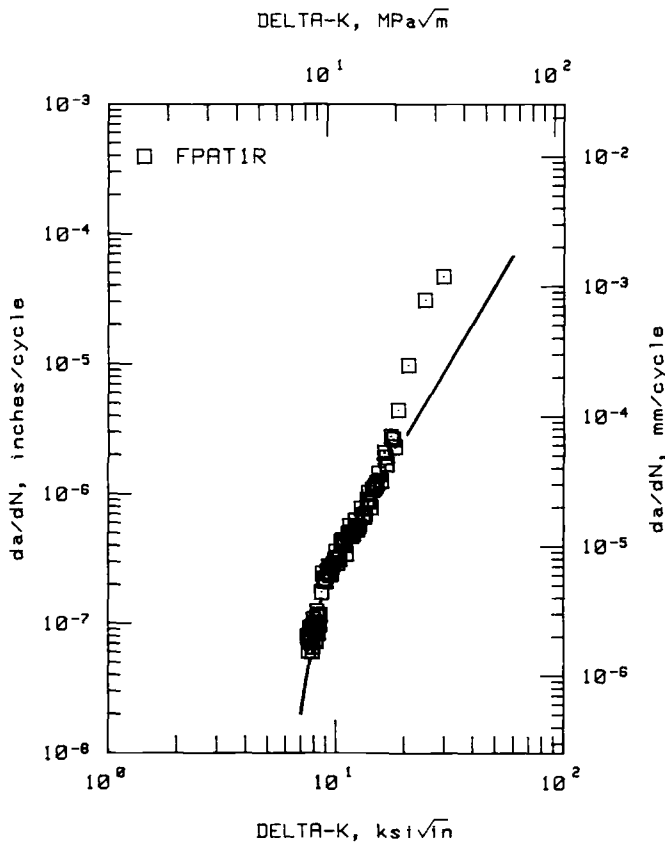


FIG 7—Fatigue crack growth rate behavior of A106 Grade B steel.

purpose with consideration of how integrity is limited by the defect through fracture mechanics analysis [1–7]. Except in cases where significant ductility precedes failure, linear elastic fracture mechanics (LEFM) forms the basis for such integrity analyses. Integrity analysis of the preflawed specimens—that is, predicting the fatigue resistance behavior, assuming the life is controlled by crack growth for the data reported in Figs. 2 through 6—requires (1) a measure of the crack growth behavior of the weld metal and (2) a measure of the crack driving force in the specimen that permits direct comparison with the materials' cracking behavior.

The crack growth behavior of the weld metal has been obtained by tracking the crack growth process of a through-wall (TW) crack using a center-cracked specimen [12]. The resulting $da/dN - \Delta K$ behavior for $R = 0.01$ is presented in Fig. 7, along with a bilinear best fit which, as shown in Ref 12, represents closely the raw $a-N$ behavior. The power law regime at rates greater than 3×10^{-6} mm/cycle matches identically the behavior developed for A106 Grade B base metal reported in the literature [20,21] and is consistent with Rolfe and Barsom [22], who state that growth in the weld metal occurs at rates equal to or less than that in the base metal.

At rates less than 3×10^{-6} mm/cycle the data for the weld metal break from the trend at higher rates, developing at a power-law slope of about 10 versus a slope of about 3 for

higher growth rates. This break from the trend at higher rates occurs at about $\Delta K = 10 \text{ MPa } \sqrt{\text{m}}$, whereas the threshold for this and similar steels is about $3 \text{ MPa } \sqrt{\text{m}}$. The reason for the lower early growth rates for the weld metal in comparison with the literature trends is traced in Ref 12 to a start-up transient.

The start-up transient period—from the initial ΔK in the test up to the long-crack growth rate trend—represents the transition from some initial defect at a given load level to a crack whose wake and crack tip are similar to that represented by the long-crack trend developed according to standards such as the ASTM Test for Constant-Load-Amplitude Fatigue Crack Growth Rates Above 10^{-6} m/Cycle (E 647-86). The absence of such transients in the literature data is a consequence of requirements in standards such as ASTM Test E 647-86 that excise early data because they depend on the specimen geometry and test conditions. However, start-up transients are real and occur at the start of the cracking process for the part-through-wall (PTW) flawed specimens and piping data reported in Figs. 2 through 6. For this reason, the prediction of crack growth life assumes that the behavior presented in Fig. 7 reasonably represents the start-up transient for the specimens tested under similar flaw-and-load (ΔK) histories. Further discussion of start-up transients can be found in Ref 12.

Predicting the crack growth life for each flawed specimen involves integrating along the $da/dN - \Delta K$ curve in Fig. 7 for the nominal ΔK history imposed. As outlined in Ref 12, the stress-intensity factor for the surface-flawed specimens was determined from the work of Newman and Raju [23]. This K solution does not account for any stress concentration due to the backup ring. Flat plate K results were adapted to curved tension specimens by using the results of the strain gage survey to modify far-field stress as a function of crack length. Initial flaw sizes were determined from postmortem measurements of the flaws. Given the sensitivity of the predicted growth period to the initial flaw size and geometry, predictions have been made for only the specimens with EDM flaws.

Crack growth predictions were made at the deepest point of the flaw and at the surface, with the aspect ratio updated accordingly. After the crack depth became equal to the thickness, the crack was treated as a through-wall crack with a semi-length equal to the current semi-crack length. The crack growth process was continued until the net-section stress reached the ultimate strength of the base metal.

Results of the predictions made are detailed in Ref 12 and summarized here. Predictions have been made using the $da/dN - \Delta K$ trend shown in Fig. 7 as well as using a similar trend without the lower-growth-rate transient, which acts somewhat like a threshold. This means that, for initial values of ΔK above the knee in Fig. 7, predictions did not show any dependence on the start-up transient. However, as initial ΔK values fell below the knee, differences in predictions using these two representations of growth rate increased. Almost all predictions for $a_o = 5.1 \text{ mm}$ involved initial values of ΔK above this knee, whereas predictions for only the higher stresses for $a_o = 2.5 \text{ mm}$ lay above the knee.

Predicted lives for the flat plate with a surface flaw based on crack growth represent only 11 to 35% of the total life for this rather simple geometry and well-defined flaw size and shape.⁶ The greatest discrepancy exists for the largest flaw. At the lower stresses for the smallest initial flaw size, growth through the start-up transient in Fig. 7 dominates the total

⁶ Experience in generating through-wall (TW) and part-through-wall (PTW) crack-growth data indicates that TW data tend to overpredict growth rates of PTW cracks, perhaps because the increased constraint along the longer crack front in the PTW crack reduces the rate in comparison with TW behavior. Nevertheless, integrity analysis makes the best use of available data, which usually comes from the less complicated TW flaw, such as that on which these predictions and this discussion are based.

life. Predictions assuming no threshold or a threshold representing the base metal (that is, $\Delta K_{th} = 3 \text{ MPa } \sqrt{\text{m}}$) all produce faster rates in this low ΔK regime and so predict even shorter lives and therefore develop greater discrepancies between observed and predicted lives. Errors well in excess of a factor of 10 on life developed when, as in most practical situations where the stresses are low and flaw sizes are small, uncertainty as to how to represent the start-up transient was met by the use of a long-crack threshold or no threshold at all.

Results for the curved-segment specimens showed trends in predictions similar to those for the flat plate specimens. The predicted lives in these cases ranged from 5 to 46% of the observed life and showed similar trends in long-life predictions depending on how the lower growth rate behavior was represented. As with the flat-plate specimens, predictions could be enhanced by making appropriate changes in the $da/dN - \Delta K$ behavior—particularly in the low-growth-rate regime. However, this is tantamount to “calibrating” the prediction process to achieve the desired result—a luxury not afforded the engineer making practical fitness-for-purpose analyses and a practice that reduces the prediction process to a curve-fitting correlation procedure. More importantly, use of the adjustments was discouraged since the changes needed to achieve consistent predictions lead to nonunique values of the adjusted parameters.

Figure 8 summarizes the absolute error for the range of predictions made on coordinates of stress and error in life (for finite lives). As discussed in Ref 12, various “adjustments” were considered to alleviate this error, but none were implemented because a unique fix could not be found for the range of stresses (lives) examined. Reed [24] has suggested by way of conjecture that predictions could be enhanced by an adjustment to the $da/dN - \Delta K$ trend based on literature data for a 70-ksi yield steel [25] (A106 Grade B is a 35-ksi yield steel). While improvements in predicted life can be achieved in this way, such predictions

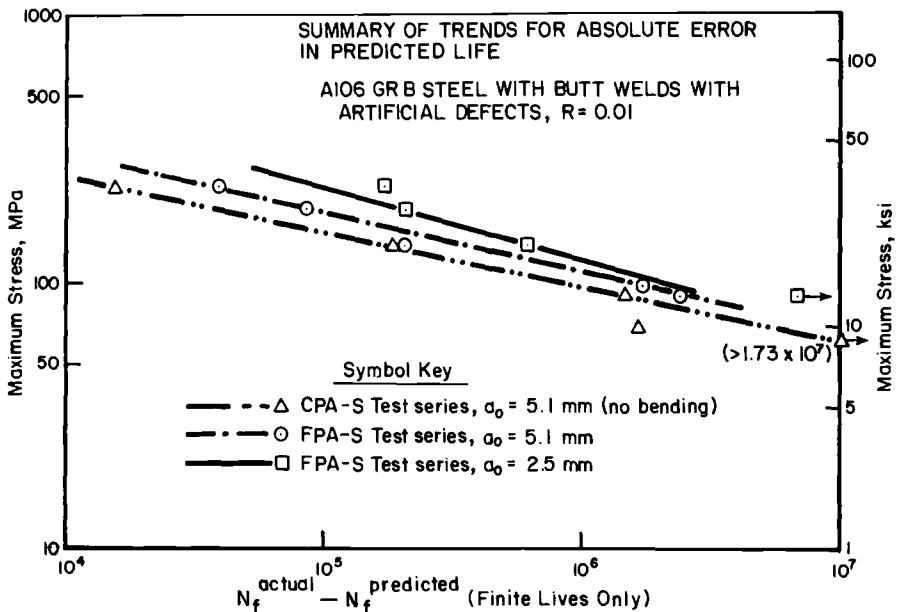


FIG. 8—Absolute error in LEFM predictions of fatigue resistance based on flaw growth for flat plate and wall segment specimens.

still show that the error made depends on the applied stress and difficulties remain in dealing with apparently nonpropagating flaws. More importantly, while various classes of steel may show similar trends in $da/dN - \Delta K$ behavior at finite lives controlled by fatigue crack growth, the literature shows a marked dependence of the threshold and toughness on the microstructure (strength) [26] for lower-strength steels. For this reason the practice of using a particular $da/dN - \Delta K$ because it suits the purpose may be justified in some situations. But its use is not justified for situations that dominate many practical problems: longer lives associated with lower stresses and smaller flaw sizes (lower growth rates at lower ΔK levels), where life is apparently dominated by growth through the near-threshold (start-up transient) domain. Further research is needed to sort out how best to deal with predictions for this class of problem, particularly the start-up transient.

Because the start-up transient can be viewed as a threshold on a case-by-case basis, the start-up transient could influence the predicted life by the same extent as a threshold. Sensitivity studies, such as that by Leis and Mayfield [21], show that small changes in threshold value can have order of magnitude effects on the predicted life for stress-intensity histories near the threshold. By analogy, the start-up effect could explain rather large differences in the predicted and observed life. Reference 21 also shows that changes in initial flaw size can cause large effects on the predicted life. For the flaws under discussion, the initial size has been accurately measured. Thus, small random errors in measuring the initial flaw size are not considered to be a cause of the consistent discrepancies in Fig. 8. However, this sensitivity to the initial defect geometry means that the earlier noted uncertainty related to interpreting NDI indications and defect sizing [13–16] will propagate through practical applications of fitness-for-purpose analysis to produce a scatter band of predicted lives. This may necessitate using a probabilistic analysis in place of the deterministic approach used herein.

Two additional factors can affect differences between predicted and observed fatigue life: the backup ring and the weld reinforcement. The backup rings were cut in these tests. Consequently, they would be expected to have little effect on fatigue life until the cracks were quite large. Similarly, the weld reinforcement is expected to have little effect since it is not large enough to significantly decrease the nominal stress. A definitive answer concerning the effect of the reinforcement cannot be given based on this work. Nor can conclusions be drawn as to if and how LEFM life prediction should be adjusted to account for the effect of reinforcement for growth in flaws in the weld defect deposit. However, others [27] have shown the influence of the reinforcement is critical to crack initiation at weld toes, but apparently do not make adjustments to the local K -field for its influence on crack growth.

Development of Defect Acceptance Criteria

The ANSI and American Society of Mechanical Engineers (ASME) piping code designated B31.3 [28] relates the allowable stress for sound welds to the specified minimum yield stress. For a sound weld (joint factor = 1), at room temperature, the B31.3 code lists an allowable stress of 137.8 MPa (20 ksi). If the cyclic stresses are considered to be displacement controlled (specifically temperature induced), the B31.3 code admits an allowable stress range of 206.7 MPa (30 ksi) at 7×10^3 cycles that reduces in steps to and holds constant at 103.3 MPa (15 ksi) at and above 10^5 cycles. The American Welding Society (AWS) D1.1 [29] code lists allowable stresses for fatigue for nonredundant structures without regard to the steel. The girth pipe welds are butt welds that fit into Category B of the AWS system of weld categories for bridge members. For this category the allowable stress is characterized by a power law at lives less than 8×10^5 cycles, and as a constant equal to 110.2 MPa (16 ksi) at longer

lives. In contrast, if the pipe weld is considered a tubular structure, as in Section 10 of Code D1.1, the girth weld falls within Category C for as-welded butt splices with complete penetration. For this case, the allowable stress is given as a trilinear line without an endurance limit, with a fatigue strength equal to about 68.9 MPa (10 ksi) at 10^8 cycles.

The AWS code for sound welds in bridge members bounds safely all flat plate and wall segment specimen data for lives less than 10^6 cycles, but beyond 10^6 cycles the continued reduction of the fatigue limit due to the flaw eventually makes the code allowable for sound welds nonconservative. The B31.3 code allowable value of 137.8 MPa is overly conservative at short lives. However, at short lives, general allowables are not governed by fatigue, so this conservatism is anticipated. At lives in excess of about 3×10^5 cycles, the B31.3 code for sound welds becomes nonconservative—again, because of the effect of the defect. When the B31.3 allowable is modified by treating the cyclic stress as displacement controlled, the reduction in the allowable stress tracks the observed trends up to 10^5 cycles. However, data for the flaws studied do fall below this allowable beyond 10^6 cycles.

The American Society of Mechanical Engineers (ASME) Boiler and Pressure Vessel (BPV) Code, Section III [30] and the AWS code include provisions that define a sound weld which reflect workmanship standards. Codes stipulate that indications exceeding this workmanship allowable must be repaired—or demonstrated safe in service. To this end, defect acceptance criteria for code-rejectable indications have been developed [12] and are summarized here.

The data developed provide the basis for acceptance criteria for the specific configurations and defect types and sizes investigated. Criteria based on the data developed, however, do not provide for scatter in properties nor do they cover a wide range of flaw sizes. For this reason, a factor of safety such as the 2 on stress or 20 on life, whichever is greater, used in the design curves for the ASME BPV code, should be used. But because (1) the predicted life is very sensitive to the flaw size and aspect ratio, and (2) the uncertainty in these flaw parameters varies greatly case by case, no factor of safety is applied here. In practice, a factor of safety should be assessed for these parameters case by case and the lower bound result should be applied. Finally, the failure criterion depends on the section width and thickness. The acceptance criteria reflect results for the section sizes and nominal thickness investigated so that judgment should be exercised in adding or subtracting life accordingly.

Figure 9 presents defect acceptance criteria including the 2 and 20 factor of safety for axial loading of flat plate butt welds. Reference 12 presents similar plots for butt welds under axial loading in curved segments and pressurized vessels (pipes), respectively. In all cases the acceptance criteria lie well below current code allowables for sound welds, except for B31.3 at very short lives.

An alternative approach in developing design criteria is to modify the current code allowables for sound welds by a factor that depends on the type of inspection and the non-destructive inspection (NDI) indication. Of the various code allowables noted above, the AWS D1.1 Section 10 allowable (tubular structures) best tracks the data trends developed for flawed specimens. A defect acceptance criterion could be developed by modifying this allowable stress by a factor that depends on the flaw size and shape and a factor of safety that reflects the uncertainty in the NDI indication and interpretation. Fracture mechanics, empirically calibrated based on actual data to avoid the earlier-discussed prediction problems, could be used in a correlative manner to interpolate between specific test cases, but care must be taken to develop an adequate data base for empirical calibration of factors like the start-up transient.

If, as implied within the AWS D1.1 criteria for sound welds, the behavior of a defective weld in a given category behaves similarly over a range of steels, defect acceptance criteria based on modifications of code rules for sound welds could be applied to other steels.

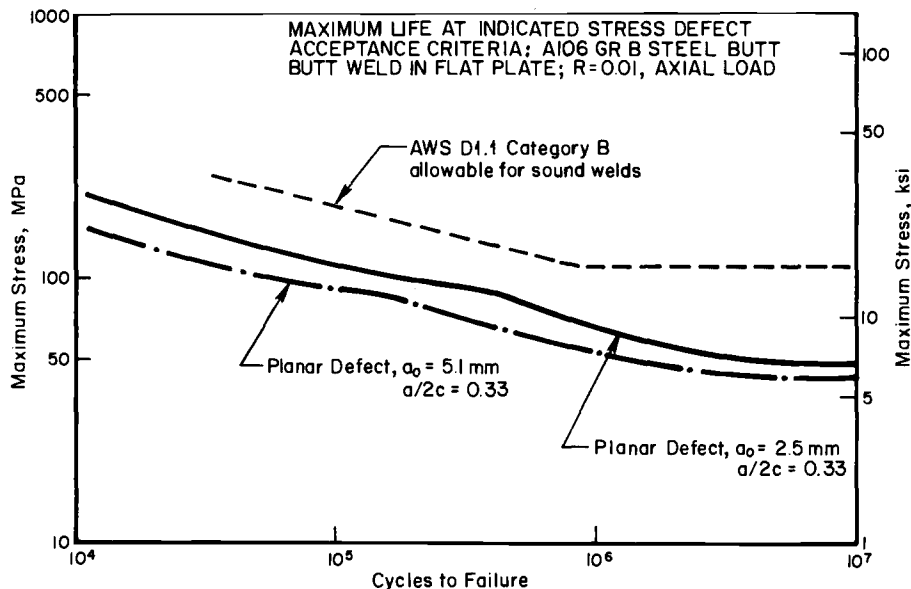


FIG. 9—Defect acceptance criteria for butt welds in A106 Grade B steel.

However, recognizing that the start-up transient will depend on the loading, the steel, and the flaw and specimen geometry, care should be exercised in such extrapolation. Particular care should be taken for applications to steels with very different chemistries and strength levels.

Summary and Conclusions

This study was directed at developing a fitness-for-purpose defect acceptance criteria for welds with defect indications. The study focused on A106 Grade B steel pipe. Data for flat plate, wall segment, and vessel specimens containing artificial or natural planar or volumetric defects were developed as the basis for assessing defect acceptance criteria.

A number of conclusions have been drawn and observations noted throughout this paper. These conclusions and observations must be taken in light of the specimens, flaws, and test techniques used in this study. Two aspects make the data developed particularly unique. First, the influence of the defect shape and size over a range of specimen geometries were examined in specimens normalized prior to testing. Second, the effect of secondary bending stresses was not considered. Significant conclusions follow:

1. There is an apparent start-up transient associated with the early growth of a defect. The duration and significance of this transient appears to depend on the stress level, defect type (natural versus artificial and planar versus volumetric), and defect geometry (size and probably aspect ratio).
2. Flat plate and wall segment specimens show similar fatigue resistance for otherwise identical flaw geometries and stress histories.
3. Defect acceptance criteria should be based on experiments using a material, test specimen, and defect configuration similar to the in-service application. Defect acceptance criteria may be developed by modifying current code allowable stresses as a function of defect

type and inspection method, using fracture mechanics analysis as an interpolative tool to correlate experimental results.

4. Rather long and deep planar defects were not as deleterious as was a slight code acceptable undercut at the toe of the weld reinforcement for both flat plate and wall segment specimens. Much has to be done to understand why the start-up transient is shorter for such surface discontinuities than for planar defects.

References

- [1] *Proceedings*, Conference on Tolerance of Flaws in Pressurized Components, Institute of Mechanical Engineers, London, UK, May 1978.
- [2] *Proceedings*, Third International Symposium on Criteria for Preventing Service Failures in Welded Structures, Japanese Welding Society, Tokyo, Japan, 1978.
- [3] *Proceedings*, First National Conference on Fitness for Purpose in Shipbuilding, Boulder, CO, October 1980, L. W. Sandor, Ed., U.S. Department of Commerce, Maritime Administration, Washington, DC.
- [4] *Proceedings*, International Conference on Welding Research in the 80's, Osaka Welding Institute, Osaka, Japan, October 1980.
- [5] *Proceedings*, International Conference on Fitness for Purpose Validation of Welded Construction, The Welding Institute, London, UK, November 1981.
- [6] *Proceedings*, Conference on Pipeline Welding and Inspection, American Welding Society, Houston, TX, September 1982.
- [7] *Proceedings*, International Conference on Fitness for Purpose in Welding Construction, American Welding Society, Atlanta, GA, May 1982.
- [8] Vosikovsky, O., "Allowable Defect Sizes in a Sour Crude Oil Pipeline for Corrosion Fatigue Conditions," *International Journal of Pressure Vessels and Piping*, Vol. 13, 1983, pp. 197-226.
- [9] Bowman, M. D. and Munse, W. H., "The Effect of Discontinuities on the Fatigue Behavior of Transverse Butt Welds in Steel," Report UILU-ENG-81-2006, Civil Engineering Department, University of Illinois, Urbana, IL, April 1981.
- [10] Lundin, C. D., "The Significance of Weld Discontinuities—A Review of Current Literature," *Welding Research Council Bulletin*, No. 222, December 1976.
- [11] Booker, M. K., Booker, B. L. P., Meier, H. B., and Hueschkel, J., "Fatigue of Weldments in Nuclear Pressure Vessels and Piping," NUREG/CR-1351, ORNL/NUREG-64, Oak Ridge National Laboratory, Oak Ridge, TN, February 1980.
- [12] Leis, B. N., Goetz, D. P., and Scott, P. M., "The Influence of Defects on the Fatigue Resistance of Butt and Girth Welds in A106B Steel," NASA CR 178114, National Aeronautics and Space Administration, Washington, DC, July 1986.
- [13] Hanstock, R. F., "Inspection in Pressure Vessel Engineering Technology," R. W. Nichols, Ed., Applied Science, London, 1971.
- [14] Clark, W. G., Jr., "Some Problems in the Application of Fracture Mechanics," in *Fracture Mechanics: Thirteenth Conference*, ASTM STP 743, R. Roberts, Ed., American Society for Testing and Materials, Philadelphia, 1981, pp. 269-287.
- [15] Harris, D. O., Lim, E. Y., and Dedhai, D. D., "Probability of Pipe Fracture in the Primary Coolant Loop of a PWR," *Probability Fracture Mechanics Analysis*, Report NUREG/CR 2189, Vol. 5, U.S. Nuclear Regulatory Commission, Washington, DC, 1981.
- [16] Reed, R. P., McHenry, H. I., and Kasen, M. B., "Fracture Mechanics Evaluation of Flaws in Pipeline Girth Welds," *Welding Research Council Bulletin*, No. 245, 1979.
- [17] Leis, B. N., "An Energy Based Fatigue and Creep-Fatigue Damage Parameter," *Journal of Pressure Vessel Technology*, Vol. 99, No. 4, 1977, pp. 524-533.
- [18] Yung, Y.-Y. and Lawrence, F. V., "Analytical and Graphical Aids for the Fatigue Design of Weldments," *Proceedings*, Conference on Fitness for Purpose in Welded Construction, Philadelphia, PA, 14-16 May 1985.
- [19] Leis, B. N. and Forte, T. P., "Fatigue Damage Analysis Under Variable Amplitude Cycling," *Random Fatigue Life Prediction*, ASME PVP Vol. 72, American Society of Mechanical Engineers, New York, 1983, pp. 89-105.
- [20] Mayfield, M. E., Forte, T. P., Rodabaugh, E. C., Leis, B. N., and Eiber, R. J., "Cold Leg Integrity Evaluation," NUREG/CR-1319, Final Report, Battelle Columbus Laboratories, Columbus, OH, January 1980.

- [21] Leis, B. N. and Mayfield, M. E., "Influence of Initial Defect Distribution on the Life of the Cold Leg Piping System," *Mechanics of Nondestructive Testing*, Plenum Press, New York, 1980, pp. 325-342.
- [22] Rolfe, S. T. and Barsom, J. M., *Fracture and Fatigue Control in Structures: Applications of Fracture Mechanics*, Prentice-Hall, Inc., Englewood Cliffs, NJ, 1977.
- [23] Newman, J. C. and Raju, I. S., "An Empirical Stress-Intensity Factor Equation for the Surface Crack," *Engineering Fracture Mechanics*, Vol. 15, No. 1-2, 1981, pp. 185-192.
- [24] Reed, J. N., consultant on pressure vessels and piping, Brookline, MA, discussion of NASA CR-178114 and NASA TM-89052, personal communication, April 1987.
- [25] Erdogan, F. and Ezzat, H., "Fracture of Pipelines and Cylinders Containing a Circumferential Crack," *Welding Research Council Bulletin*, No. 288, 1983.
- [26] Gerberich, W. W. and Moody, N. R., "A Review of Fatigue Fracture Topology Effects on Threshold and Growth Mechanisms," *Fatigue Mechanisms, ASTM STP 675*, American Society for Testing and Materials, Philadelphia, 1979, pp. 292-341.
- [27] Lawrence, F. V., Jr., Mattos, R. J., Higashida, Y., and Burk, J. D., "Estimating the Fatigue Crack Initiation Life of Welds," *Fatigue Testing of Weldments, ASTM STP 648*, American Society for Testing and Materials, Philadelphia, 1978, pp. 134-158.
- [28] Code for Chemical Plant and Petroleum Refinery Piping, ANSI B31.3 1980 ed., American Society of Mechanical Engineers, New York, 1980.
- [29] Structural Welding Code, AWS D1.1-80, 1980 ed., American Welding Society, Miami, FL, 1980.
- [30] Boiler and Pressure Vessel Code, Section III, Division 1, Nuclear Power Plant Components, 1980 ed., American Society of Mechanical Engineers, New York, 1980.

Effect of Temperature and Strain Rate on Upper Shelf Fracture Behavior of A533B Class 1 Pressure Vessel Steel

REFERENCE: Jung, Y. H. and Murty, K. L., "Effect of Temperature and Strain Rate on Upper Shelf Fracture Behavior of A533B Class 1 Pressure Vessel Steel," *Fracture Mechanics: Nineteenth Symposium, ASTM STP 969*, T. A. Cruse, Ed., American Society for Testing and Materials, Philadelphia, 1988, pp. 392–401.

ABSTRACT: The effect of interstitial impurities on the upper shelf fracture characteristics of A533B Class 1 steel was examined using single specimen unloading compliance J -integral tests. Three-point bend tests were performed on fatigue precracked side-grooved Charpy-size specimens using a specially designed compression jig that minimized misalignments usually encountered in direct compression tests. Experimental results obtained as a function of the test temperature and strain rate revealed the effect of dynamic strain aging (DSA) as a drop in the critical crack initiation fracture toughness, J_q . As predicted from DSA models, the minimum in J_q shifted to higher temperatures at higher test speeds (strain rates). The kinetics of the toughness minima agreed with the diffusion of carbon or nitrogen, or both in steels. The effect of neutron irradiation was noted to result in a shift of the J -integral minimum to higher temperatures, resulting in an *apparent* increase in toughness at lower temperatures following neutron radiation exposure. The usual radiation embrittlement was noted at higher temperatures where DSA was absent.

KEY WORDS: fracture, pressure vessel steels, Charpy, fracture toughness, interstitials, radiation, embrittlement, dynamic strain aging, fracture mechanics

The decreased upper shelf energy accompanied by an increased ductile-to-brittle transition temperature (DBTT) following neutron irradiation is known as radiation embrittlement. The detrimental effects of extrinsic impurities such as copper, phosphorus, and so forth, on the toughness and notch ductility of irradiated nuclear reactor pressure vessel (RPV) steels have been well recognized, resulting in an imposition of limits on impurity levels to minimize this neutron radiation embrittlement in modern vessel materials [1]. Although the understanding of the fundamental damage mechanisms is controversial, the current phenomenological treatment seems to be successful in alleviating or reducing the rate of embrittlement. Recently, the effects of interstitial impurities at high temperatures on fracture behavior due to dynamic strain aging (DSA) were considered [1–4]. Concern arose as to the impurity-dislocation interactions which lead to brittleness, resulting in a further decrease in the upper shelf toughness following irradiation. These effects should be of primary importance since DSA occurs at service temperatures in the intermediate-strength RPV steels. Earlier experimental work on smooth bar tensile tests on low-carbon mild steels [5,6] and RPV steels [1,7] clearly revealed dips in ductility, indicating a possible drop in fracture toughness at

¹ Graduate student and professor, respectively, North Carolina State University, Raleigh, NC 27695–7909.

these temperatures and applied strain rates. The major objective of the present study was to characterize the effect of DSA on the upper shelf fracture toughness. To this end, an experimental system was developed to evaluate J -integral fracture toughness using a single specimen unloading compliance method. It was thus possible to determine the fracture toughness as a function of the test temperature and applied loading rate. This paper describes the experimental setup and results obtained on a typical nuclear pressure vessel steel. A limited amount of data was obtained on the irradiated material, and the trends seem to follow the earlier predictions made from tensile tests on irradiated mild steel [1,8]. It is important to recognize that while there have been many investigations on the effects of DSA on the mechanical properties of steels [1,9], no systematic studies were made on fracture characteristics. In addition, most of the experimental work on radiation effects has been on the evaluation of Charpy energy of ferritic steels [10], and the effects of dislocation-interstitial interactions are masked at the high loading rates associated with this type of test.

Experimental Procedure

Material, Specimen Preparation, and Irradiation Details

The material used was A533B Class 1 pressure vessel steel [Heavy Section Steel Technology (HSST) Plate 04] with a chemical composition as shown in Table 1. The plate was austenitized at 1145 K for 1.44×10^4 s, tempered at 936 K for 1.44×10^4 s and air-cooled to ambient temperature, then stress relieved at 894 K for 7.2×10^4 s, furnace cooled to 589 K and air cooled to ambient temperature. The as-received block (330 by 406 by 64 mm) was taken at $\frac{1}{4}$ thickness of the plate. The resulting mechanical properties are given in Table 2. Precracked Charpy-size J -test specimens were fabricated so that the crack plane was located parallel to the rolling direction of the plate [Fig. 1]. A sharpened high-speed milling saw was used to produce the standard V-notch of a root radius 0.08 mm or less according to the ASTM Method of Testing Single-Arm Balances (E 319-85). During the precracking stage, stress intensity in the final 5% of the precrack was estimated to be

$$\frac{K_f}{E} = 0.043\text{mm}$$

where K_f is the maximum stress intensity factor for fatigue precracking and E is the Young's modulus. Moreover, 15% side-grooving (7.5% on each side) of the Charpy V-notch profile was imposed on precracked J -test specimens to improve the straightness of the crack front.

A limited number of these Charpy-size J -test specimens were irradiated in the Pulstar experimental reactor at North Carolina State University to a nominal fast neutron ($E_n > 1$ MeV) dose of 5×10^{17} neutrons/cm². The measured irradiation temperature was 383 ± 5 K. The irradiation dose was estimated from the measured activity of a nickel wire monitor

TABLE 1—Chemical composition (in percent by weight) of A533B Class 1 steel (HSST plate 04).^a

C	Mn	P	S	Cu	Ni	Mo	Si	V	Al
0.25	1.38	0.01	0.017	0.13	0.61	0.49	0.24	0.04	0.025

^a Heat treatment:

austenitized at 1145 K for 1.44×10^4 s,
tempered at 936 K for 1.44×10^4 s, and air cooled to ambient temperature,
stress relieved at 894 K for 7.2×10^4 s, and
furnace cooled to 589 K followed by air cooling to ambient temperature.

TABLE 2—Mechanical properties of A533B Class 1 steel.

Temperature, K	Yield Strength, MPa	Tensile Strength, MPa	Total Elongation, %	Charpy Energy, J
75	455	593	18	66
473	428	585	17	...
623	389	567	19	...

inserted into a cadmium-covered sample holder. Nickel wires were used to follow the nickel-cobalt activation reaction, $\text{Ni}(n,p)\text{Co}$.

Test Setup

All tests were conducted under stroke control mode on a closed-loop hydraulic testing machine, Instron Model 1350, with 9-kN load cell. Temperatures were controlled using a three-zone control furnace, ATS Model 2961. A tension-compression jig was designed with an automatic notch aligning three-point bend fixture. A linear variable differential transformer (LVDT) of $\pm 2.5\text{-mm}$ full range was directly attached to the loading pin to increase the accuracy of the unloading compliance measurement and to effectively reduce the effect of machine compliance. A schematic of the J -test rig is given in Fig. 2. All of the load versus

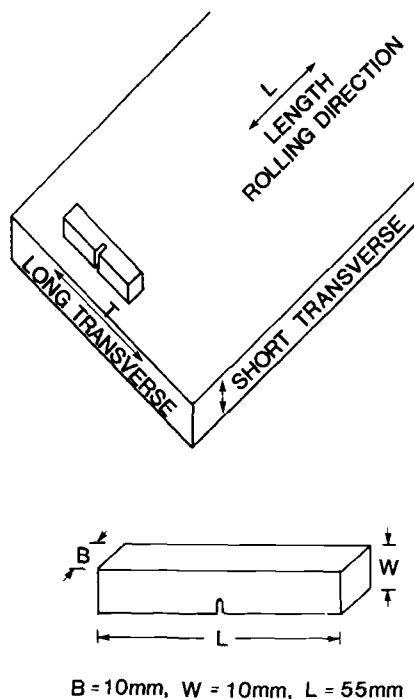


FIG. 1—Design of fracture specimens depicting orientation with respect to the plate.

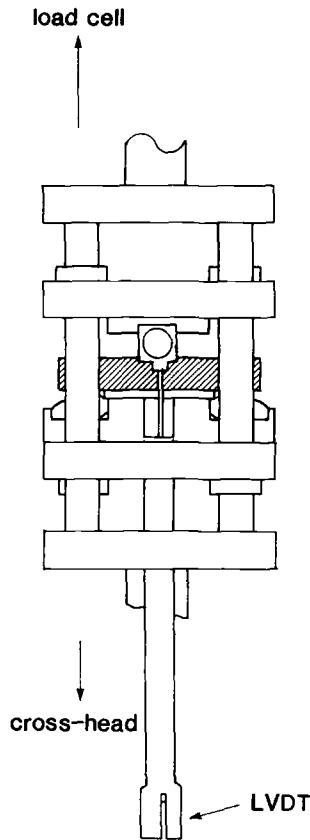


FIG. 2—Three-point bend test rig.

load-line displacement data were monitored using an on-line Apple-II microcomputer. To increase the resolution of the unloading compliance measurement, a variable amplifier (Datronics Model 3163) was connected to an LVDT conditioner (Datronics Model 3130). The present tension-compression jig, in conjunction with universal joints at the top and bottom, significantly reduced the misalignment problems encountered in the usual direct compression type three-point bend tests.

The single specimen unloading compliance *J*-tests on the unirradiated and irradiated Charpy-size specimens were performed using a specially developed test system and computer programs. Prior to each *J*-test, specimen alignment and system reliability were checked by repeated partial unloading compliance measurements applying the load well below the elastic limit. After stabilizing the prescribed test temperature, about 20 unloading steps were used to measure the dynamic crack extension. The load versus displacement signal during each partial unloading step was amplified by a factor of 20. Digital data were saved on a diskette for permanent storage. Posttest data analysis was performed on a VAX-11/750 minicomputer and graphic facility. The tested specimens were heat tinted and fractured at liquid nitrogen temperature. The final crack lengths were measured from the brittle crack fronts using the seven point averaging method.

The value of the J -integral up to each partial unloading point was calculated using

$$J_i = \frac{2A_i}{B_n(W - a_0)} \quad (1)$$

where A_i is the area under load versus the load-line displacement curve up to each partial unloading step, B_n the net thickness of the side-grooved specimen, W the width, and a the initial crack length. The plane strain elastic compliance function [11] was employed to obtain the crack extension from measured unloading compliance

$$\begin{aligned} C(a/w) = 0.24 \left(\frac{s}{w} \right) \left[1.04 + 3.28 \left(\frac{w}{s} \right) (1 + \nu^2) \right] + 2(1 - \nu^2) \left(\frac{a}{w} \right) \left(\frac{s}{w} \right) \left[4.21 \left(\frac{a}{w} \right) \right. \\ - 8.89 \left(\frac{a}{w} \right)^2 + 36.9 \left(\frac{a}{w} \right)^3 - 83.6 \left(\frac{a}{w} \right)^4 + 174.3 \left(\frac{a}{w} \right)^5 - 284.8 \left(\frac{a}{w} \right)^6 \\ \left. + 387.6 \left(\frac{a}{w} \right)^7 - 322.8 \left(\frac{a}{w} \right)^8 + 149.8 \left(\frac{a}{w} \right)^9 \right] \quad (2) \end{aligned}$$

where s/w is the span-to-width ratio ($= 4.0$) and ν is Poisson ratio.

Specimen compliance was obtained by subtracting extraneous compliance from the measured total value. In the present experimental configuration, the extraneous component comprised elastic displacement in the test fixture, supporting roller indentation on the specimen, wrapping effect (multiple-point contact) on the loading pin, and friction effects at contact areas. To characterize the extraneous displacement, a series of blunt notch specimens with different notch lengths were tested. The functional form of the extraneous displacement, V_{ex} , was evaluated from Ref 11

$$V_{ex} = \frac{P}{C_1} + \frac{V}{C_2} \quad (3)$$

where P is the applied load, V the load-line displacement at each partial unloading step, and C_1 , C_2 the experimentally determined constants.

Using the crack extension, a , from the corrected compliance and resulting J -integral, the crack growth resistance (J - R) curve was constructed on the graphics facility. For the interpretation of the crack growth resistance curve, the slope of the blunting line was assumed to be proportional to four times the flow stress. The exclusion line was determined from the J -controlled crack growth criterion for precracked Charpy specimens [12]

$$\Delta a > 0.06(W - a_0) \quad (4)$$

For the employed nominal initial crack length of 5 mm, the exclusion limit was determined to be a 0.3-mm crack extension. The data points between the blunting and exclusion lines were regarded as effective data points for J -controlled crack growth of precracked Charpy-size specimens. The crack initiation fracture toughness J_q was determined to be the value of the J -integral at the intersection point of the blunting line and the linearly regressed tearing line through the effective data points. A typical J - R curve is shown in Fig. 3.

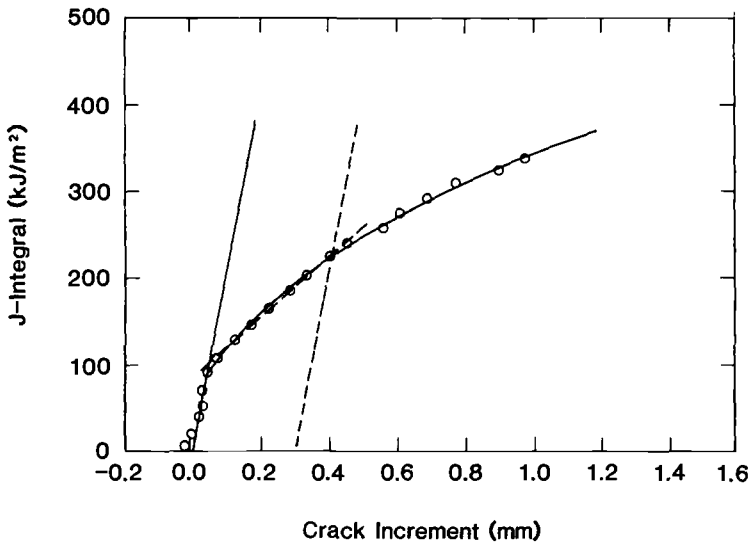


FIG. 3—Crack resistance curve obtained at 573 K at a loading-rate of 0.15 mm/min.

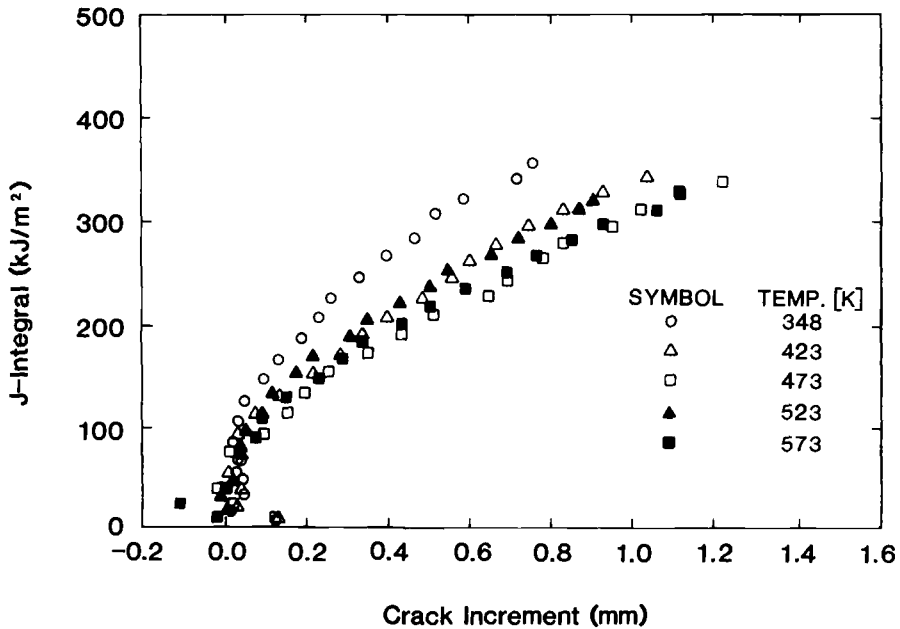


FIG. 4—Crack resistance curves (J versus Δa) at various test temperatures.

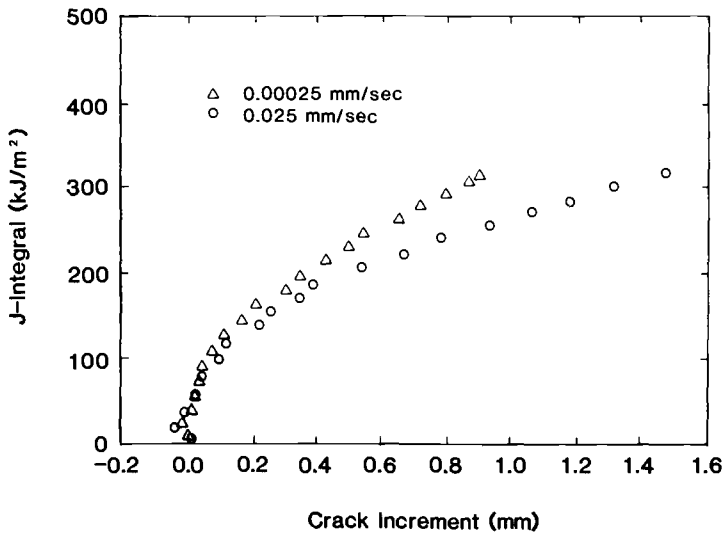


FIG. 5—Effect of loading rate on crack resistance curve at 573 K.

Results and Discussion

As described earlier, single specimen unloading compliance J -integral tests were performed using precracked Charpy size specimens loaded in a three-point bend mode. Figure 4 shows the J -integral versus crack extension Δa at different test temperatures at the nominal

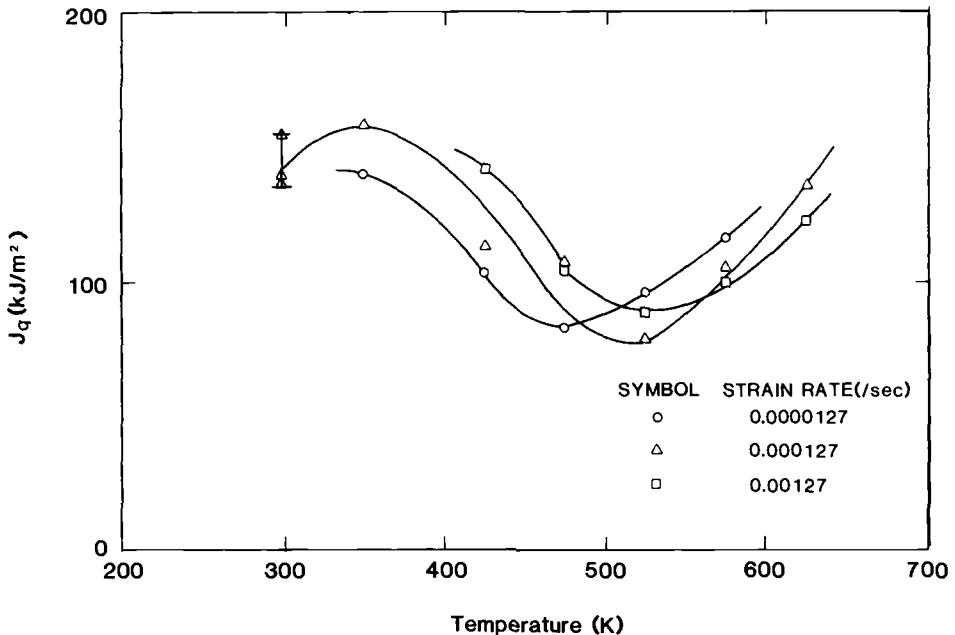


FIG. 6—Effect of test temperature and strain-rate on crack initiation fracture toughness J_q .

test speed of 2.5×10^{-4} mm/s. All the tests were run to a fixed total load-line displacement of about 2 mm. Considering the minor effects of the specimens' geometric deviations, the effect of temperature on the resistance curve is apparent. It is clearly noted that as temperature increases from ambient the resistance curve exhibited lower J -integral values until a critical temperature is reached (473 K in Fig. 4) and then higher J values resulted with increased temperature. The loading rate effect on crack resistance at a fixed test temperature is depicted in Fig. 5; however, the effect of strain rate is different for temperatures below the critical temperature at which the J values attained a minimum. Although the J -integral cannot have any stringent significance in crack growth after crack initiation on the basis of elastic-plastic fracture mechanics, the above observations constitute sufficient evidence of the effects of loading rate and temperature on the upper shelf fracture behavior of nuclear grade pressure vessel steels such as A533B Class 1. The resulting variation of crack initiation fracture toughness (J_q) with temperature and loading rate is depicted in Fig. 6. It is clear from these results that the temperature at which the J_q minimum occurs increases with applied loading rate. These results are similar to the earlier data on energy to fracture reported by Murty [1] obtained using subsize Charpy specimens. Tensile properties of these steels also revealed similar trends, implying that the drop in J_q at elevated temperatures is also due to the interaction of the interstitial impurities with dislocations at the crack front.

Regardless of the size differences between subsize Charpy slow bend and precracked Charpy-size J -test specimens, the role of critical strain prevailing in upper shelf ductile fracture behavior is expected to be the same and thus the kinetics of deformation and fracture would be identical. Evidence for this is obtained through a composite Arrhenius plot of \ln (strain rate) versus $1/T$, where the strain rates were evaluated as loading rates normalized to the length of the bending arm [13], and T is the critical temperature in degrees K at which toughness minima were noted in the subsize and Charpy size specimens. It is clear

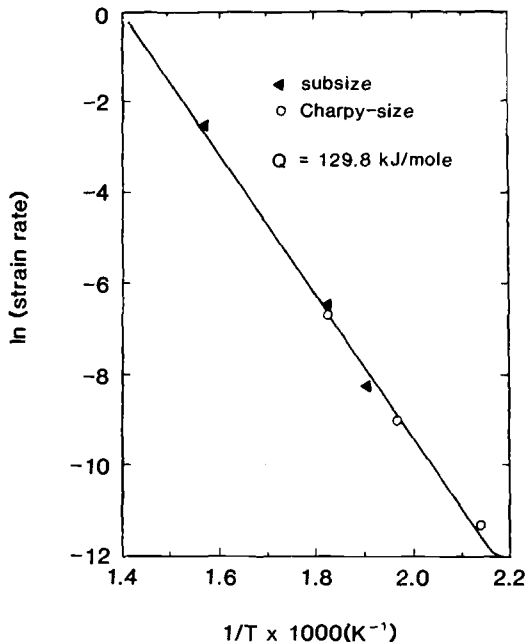


FIG. 7—Arrhenius plot of strain rate versus critical temperature for fracture energy minima.

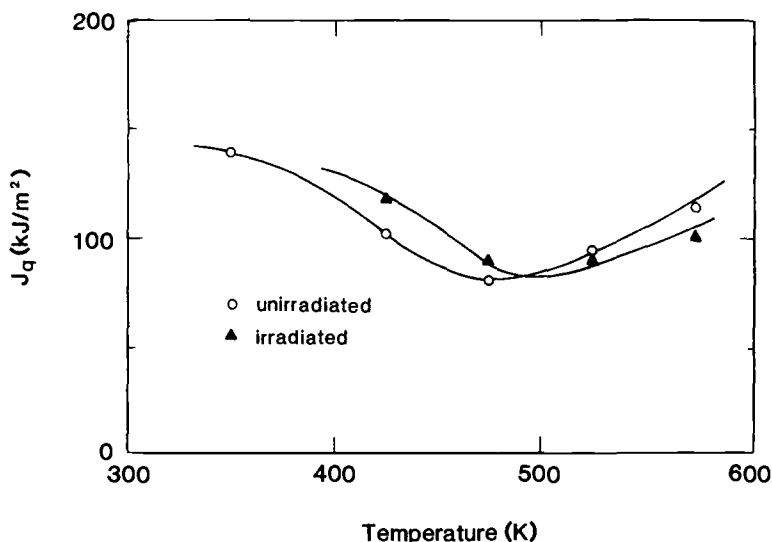


FIG. 8—Effect of neutron irradiation on temperature dependence of crack initiation fracture toughness.

from Fig. 7 that the slow bend and J_q results follow the same straight line with a slope corresponding to an activation energy of 129.8 kJ/mole, which is intermediate between the activation energies for the appearance and the disappearance of serrations. This energy value corresponds to the maximum serration height in tensile tests [9] and thus the fracture energy minima in three-point bend and J tests are regarded as arising from the interaction of the interstitial impurities with dislocations in a well developed plastic zone at the crack front. The higher activation energy of 129.8 kJ/mole is believed to be due to the addition of the binding energy of carbon and nitrogen with manganese and vanadium to the diffusion energy for carbon and nitrogen in iron.

Effect of Neutron Irradiation

A limited number of fracture tests were made on irradiated A533B steel. The effect of neutron irradiation on the fracture toughness is depicted in Fig. 8, where J_q is plotted versus the test temperature. It is clear that the energy minimum is shifted to higher temperatures following irradiation. In addition, the suppression of DSA following irradiation resulted in slightly increased J values at temperatures below the critical value. This is similar to the synergistic effect of neutron irradiation and DSA noted in tensile test data for low-carbon mild steel [8]. At temperatures above the energy minimum, irradiated material exhibited lower toughness values, indicative of the radiation embrittlement expected in these steels. Further testing is under way to characterize the effect of strain rate on the fracture behavior of the irradiated steels.

Conclusions

J -integral tests on precracked Charpy specimens of A533 Grade B Class 1 steel, performed under three-point loading as a function of the test temperature and loading rate, clearly

exhibited the effect of DSA on the fracture toughness in the upper shelf regime. Synergistic effects of neutron irradiation and DSA resulted in an apparent improvement of fracture characteristics at some temperatures and strain rates where DSA is suppressed following neutron irradiation. Present results clearly revealed that DSA causes a distinct reduction of the upper shelf energy in addition to radiation embrittlement. These effects, however, are functions of both the test temperature and loading rate.

Acknowledgments

We wish to acknowledge the financial support of the Carolina Power and Light Company and Virginia Electric and Power Company.

References

- [1] Murty, K. L., *Journal of Metals*, Oct. 1985, pp. 34-39.
- [2] Chakravarty, J. K., Wadekar, S. L., Sinha, T. K., and Asundi, M. K., "Dynamic Strain Aging of A203D Nuclear Structural Steel," *Journal of Nuclear Materials*, Vol. 119, 1983, p. 51.
- [3] Little, E. A., "Strain Aging and Neutron Scattering Studies in Irradiated PWR Pressure Vessel Steel," Twelfth International Symposium on Materials, American Society for Testing and Materials, Philadelphia, 1984.
- [4] Ostensson, B., "The Fracture Toughness of Pressure Vessel Steel at Elevated Temperatures," in *Reliability Problems of Reactor Pressure Components*, International Atomic Energy Agency, Vol. 1, 1981, p. 303.
- [5] Murty, K. L., "Synergistic Effects of Dynamic Strain Aging and Neutron Irradiation on Strength and Ductility of Mild Steel," *Proceedings, Sixth International Conference on Fracture*, Pergamon Press, New York, Vol. 3, 1984.
- [6] Murty, K. L., "Interaction of Interstitial Impurities with Radiation-Induced Defects Leading to Improved Elevated Temperature Mechanical Properties of Mild Steel," *Nuclear Technology*, Vol. 67, 1984, p. 124.
- [7] Jung, Y. H., "Effect of Dynamic Strain Aging on Fracture Characteristics of A533B-C11 Nuclear Pressure Vessel Steel," Ph.D. thesis, North Carolina State University, Raleigh, NC, 1986.
- [8] Murty, K. L., "Is Neutron Radiation Exposure Always Detrimental To Metals (Steels)?," *Nature*, Vol. 308, 1984, p. 51.
- [9] Keh, A. S., Nakada, Y., and Leslie, W. C., "Dynamic Strain Aging in Iron and Steels," in *Dislocation Dynamics*, A. R. Rosenfield and G. T. Hahn, Eds. McGraw-Hill, New York, 1968.
- [10] Steele, L. E., "Review and Analysis of Reactor Vessel Surveillance Programs," *Status of USA Nuclear Reactor Pressure Vessel Surveillance for Radiation Effects*, ASTM STP 784, American Society for Testing and Materials, Philadelphia, 1983, p. 227.
- [11] Neale, B. K., "The Determination of J_0 , the Initiation Elastic-Plastic Toughness Parameter Using Pre-cracked Charpy Specimens" TPRD/B/0012/82, Central Electric Generating Board, Berkley Nuclear Laboratories, U.K., 1979.
- [12] Hutchinson, J. W. and Paris, P. C., "Stability Analysis of J -Controlled Crack Growth," *Elastic-Plastic Fracture*, ASTM STP 668, American Society for Testing and Materials, Philadelphia, 1979, pp. 37-66.
- [13] Server, W. L., *Journal of Engineering Mechanics*, Vol. 100, 1978, p. 183.

Dynamic Inelastic Fracture

Using Combined Experiments and Analysis to Generate Dynamic Critical Stress Intensity Data

REFERENCE: Swenson, D. V. and Ingraffea, A. R., "Using Combined Experiments and Analysis to Generate Dynamic Critical Stress Intensity Data," *Fracture Mechanics: Nineteenth Symposium, ASTM STP 969*, T. A. Cruse, Ed., American Society for Testing and Materials, Philadelphia, 1988, pp. 405–426.

ABSTRACT: In this paper the authors give a short description of a finite-element model of mixed-mode dynamic crack propagation. They then discuss the use of combined experiments and analysis procedures to generate critical stress-intensity data as a function of crack velocity. Because of the sensitivity of the analysis to the boundary conditions and specified crack velocity, it is difficult to generate reliable $K_{ID}(v)$ data using this approach. This is due to uncertainties in both the analysis and the measured crack position. Suggestions are made for alternate test methods to reduce some of these uncertainties.

KEY WORDS: dynamic fracture, finite element, critical stress intensity, fracture mechanics

Dynamic fracture mechanics deals with problems in which inertia must be included in the formulation. As discussed in Refs 1 and 2, a numerical approach consists of three parts: (1) an asymptotic solution to describe the fracture process at the crack tip in terms of the global solution, (2) criteria for crack propagation velocity and direction, and (3) a numerical implementation of the above concepts.

A usual assumption in analysis is that the critical dynamic stress intensity, K_{ID} , is only a function of the crack velocity, $K_{ID}(v)$, described by a single curve. This is a natural extension of linear elastic static fracture mechanics concepts, in which a single critical stress intensity is assumed to govern failure. For dynamic fracture it is reasonable to assume that the crack velocity will change the critical stress intensity because of strain rate effects and heating at the crack tip.

Whether a single $K_{ID}(v)$ curve is appropriate has been the subject of considerable discussion in the literature [3–5]. Clearly, a single curve exists for steady-state propagation. Under transient conditions the $K_{ID}(v)$ relation may become more complex and require additional state variables in the description.

One factor contributing to the controversy surrounding the uniqueness of the $K_{ID}(v)$ curve is the difficulty of obtaining unambiguous experimental data. The two general methods used are (1) experiments in which direct measurements of $K_{ID}(v)$ are made (using methods such as caustics) [6–8], and (2) experiments in which the boundary conditions and crack tip

¹ Assistant professor, Mechanical Engineering Department, Kansas State University, Manhattan, KS 66506.

² Professor, Department of Civil and Environmental Engineering, Cornell University, Ithaca, NY 14853.

position are measured. In the second method, analysis is then performed using these boundary conditions to obtain the dynamic stress intensity indirectly during propagation [9]. That the two approaches can yield conflicting results is shown in Fig. 1.

This same difficulty is illustrated in the results (Fig. 2) presented by Atluri and Nishioka [10] for a "generation" analysis of the double cantilever experiments of Kalthoff et al. [6,7]. Atluri and Nishioka state that "the computed K_I values agree very well with the experimentally measured (using an optical method) data." However, they also present a curve showing the experimentally measured fracture toughness versus crack velocity relation (Fig. 3). We have plotted the generation data from Fig. 2 on this curve. To be consistent, the two curves should be identical. That they are not illustrates the difficulty of generating $K_{ID}(v)$ data using combined experiments and analysis even for an experiment for which the crack tip position was well known.

It is the purpose of this paper to explore further some of the uncertainties that exist in a coupled experiments and analysis approach to generating $K_{ID}(v)$ data.

Finite-Element Model

The development of a finite-element model for mixed-mode dynamic crack propagation has been described in Refs 1 and 2. Briefly, linear elastodynamic fracture mechanics concepts are implemented to allow discrete cracks to propagate through the mesh in arbitrary directions. At each time step, displacement correlation is used to obtain the mixed-mode stress intensities. Given the current state at the crack tip and a relation between the critical stress intensity and crack velocity, the crack velocity for the next time step is obtained by assuming that the change in velocity is proportional to the difference between the current

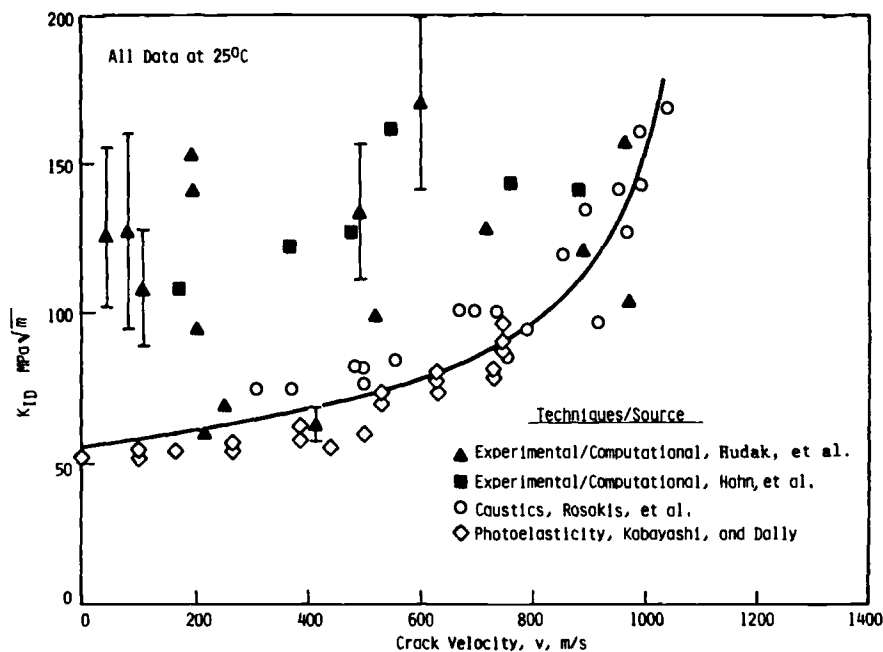


FIG. 1— $K_{ID}(v)$ for 4340 steel (after Hudak et al. [9]).

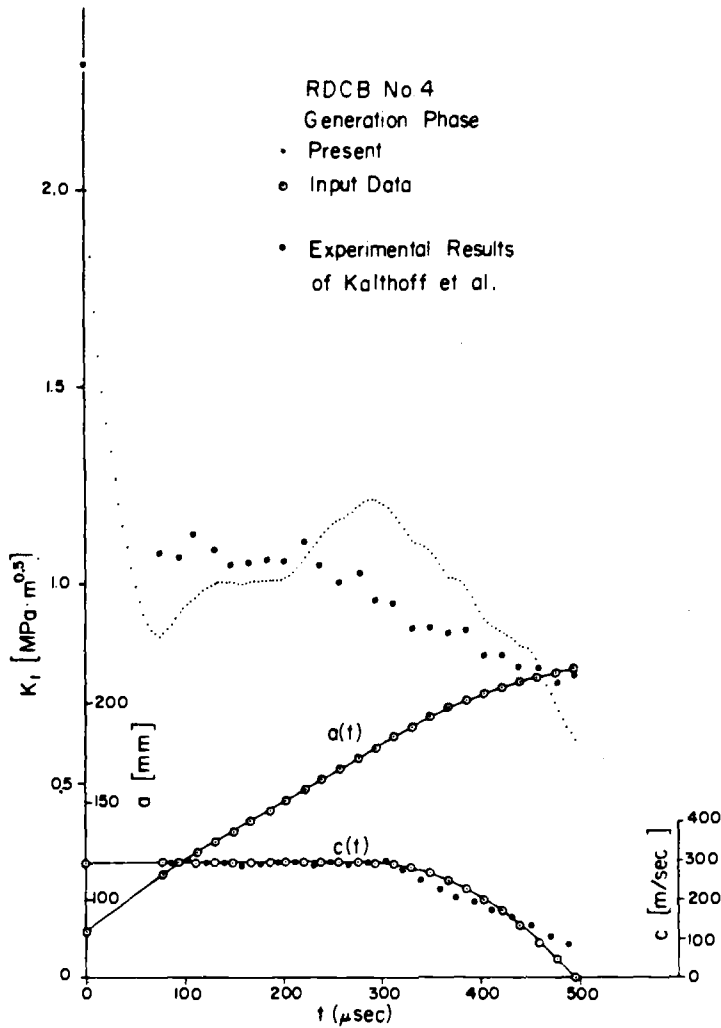


FIG. 2—Results of Generation Phase Simulation (after Atluri and Nishioka [10]).

stress intensity and the critical value. The maximum circumferential stress criterion is used to predict the crack propagation direction.

The solution scheme is implemented using explicit time integration and quadratic triangular elements. By moving the side nodes of the crack-tip elements to the quarter points, the asymptotic $r^{1/2}$ solution for displacement is included. The use of explicit time integration allows stress waves in the structure to be followed and, since the solution is implemented at the element level (global matrices are not assembled), allows remeshing without regard for element or node numbering.

At each time step, the crack tip and surrounding quarter-point nodes are moved. This gradually distorts the elements around the tip. Local remeshing is automatically performed when the crack-tip elements become excessively distorted. Both when moving the tip and when remeshing, care is taken to ensure that data are correctly transferred from the old mesh to the new mesh.

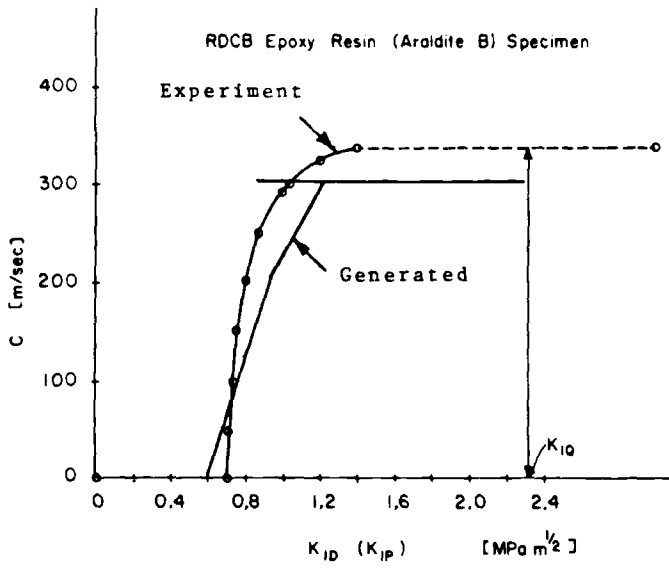


FIG. 3—Comparison of experimentally measured and generated $K_{ID}(v)$ data (after Atluri and Nishioka [10]).

Applications of the model to straight and curving crack problems are discussed in Refs 1 and 2. These include an analysis of biaxial load experiments performed by Dadkhah [11] and reported by Hawong, Kobayashi, Dadkhah, Kang, and Ramulu [12]. The correlation with experimental data is good for both the curving crack path and stress intensities during propagation.

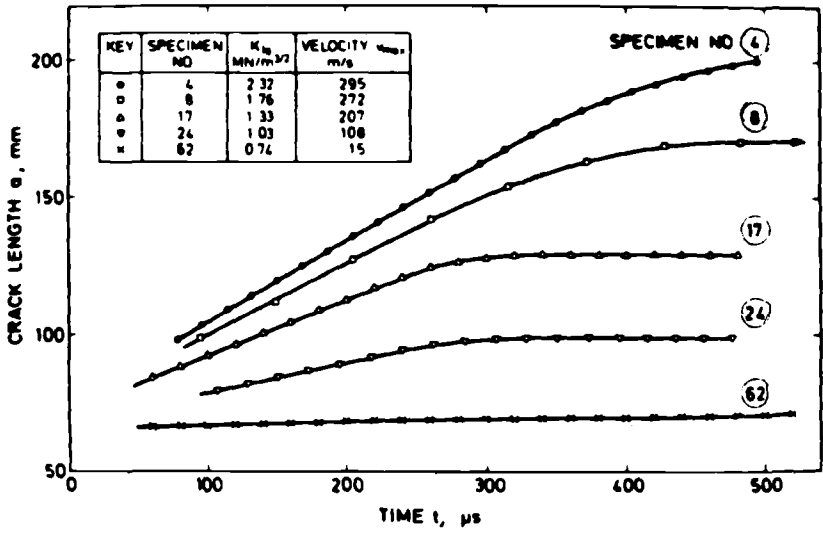


FIG. 4a—Experimental results for crack propagation and arrest: crack length history (after Kalthoff et al. [6]).

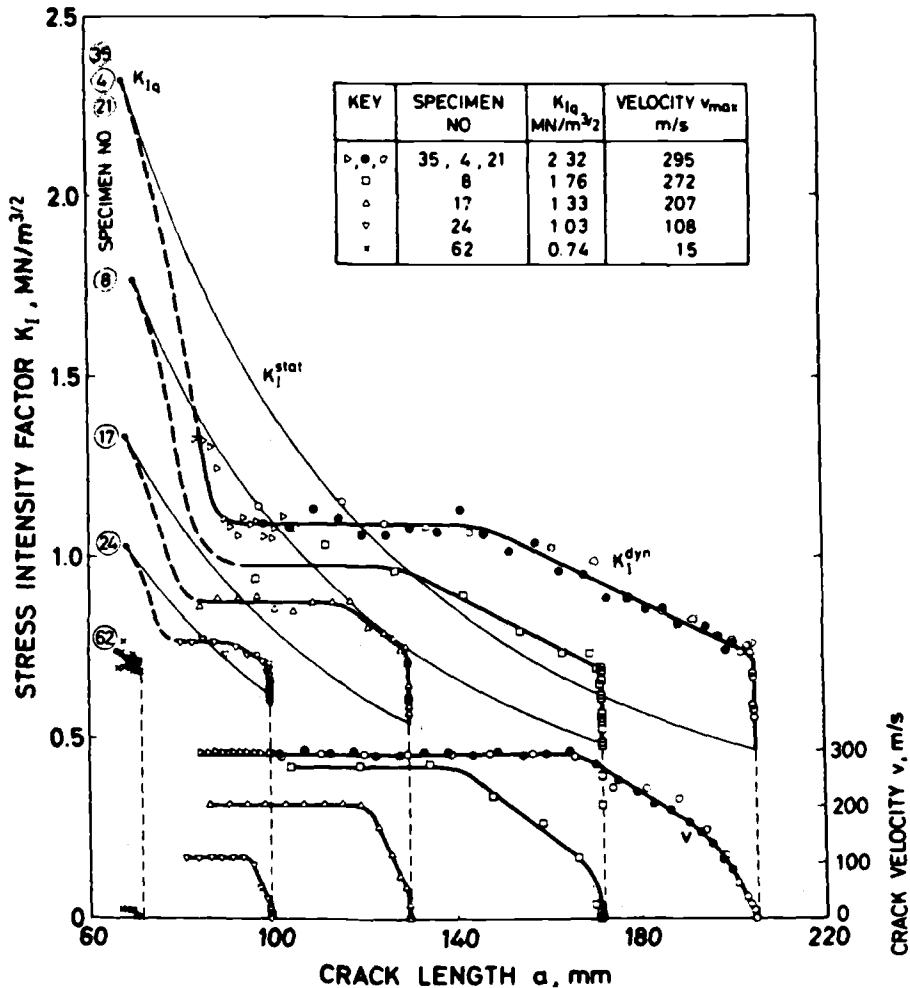


FIG. 4b—Experimental results for crack propagation and arrest: stress intensity and velocity history (after Kalthoff et al. [6]).

Crack Arrest in a Double Cantilever Beam Specimen

We will first present an analysis of the experiments performed by Kalthoff, Beinert, Winkler, and Klemm [6,7] to examine crack arrest in a double cantilever beam specimen. These experiments are the ones analyzed by Atluri and Nishioka [10] (Figs. 2 and 3). The experiments are important not only because the data are relatively clean, but also because they showed that dynamic analysis is required to model crack arrest rigorously.

The experiments were performed on double cantilever wedge specimens loaded at a slow rate. The wedge force was resisted by resting the specimen on its end, causing a compressive stress in the specimen. Shadow optical caustics were used to evaluate the stress intensity at the crack tip; thus, a single picture frame supplies the approximate crack tip position (the exact tip location is hidden by the dark shadow) and the current stress intensity. Plane stress conditions were assumed to apply during the test.

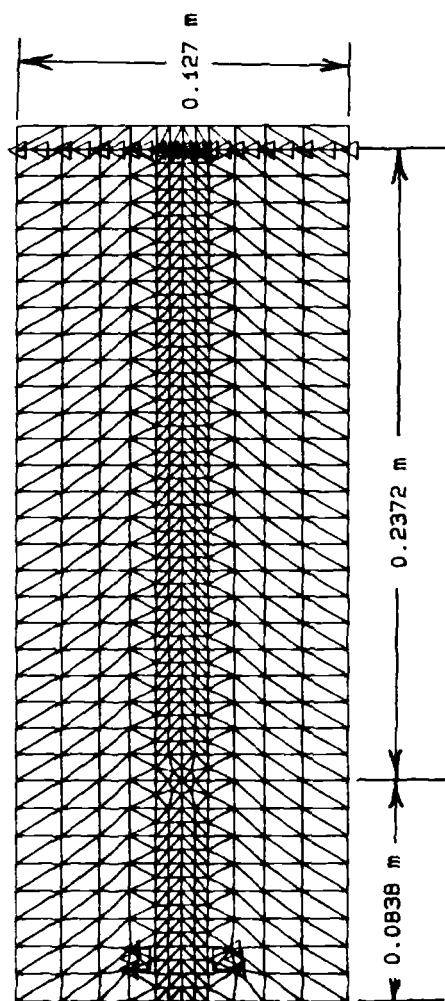
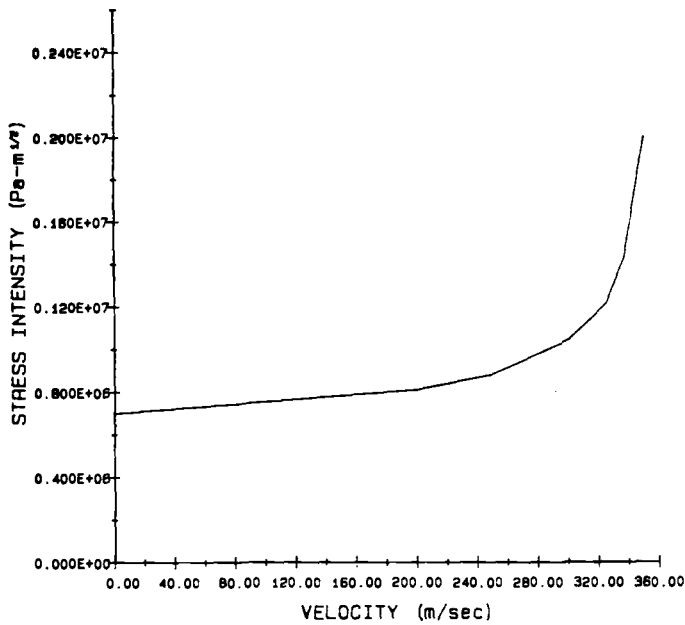
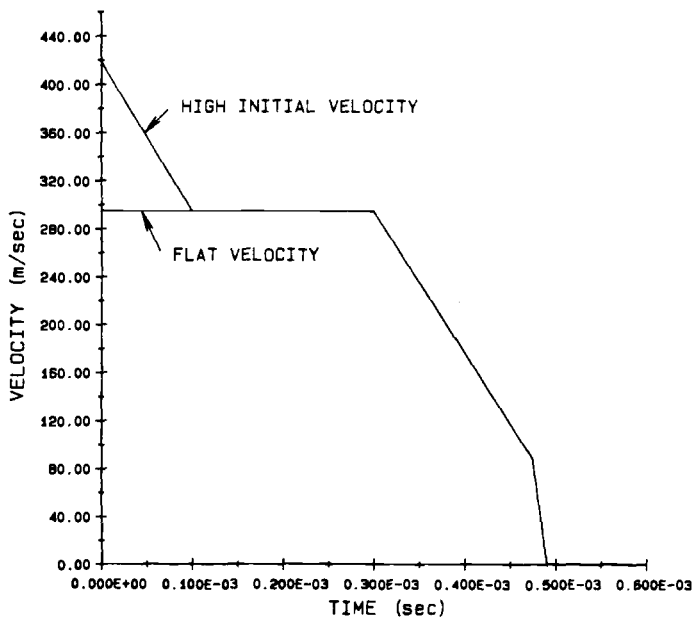


FIG. 5—Mesh used for Kalthoff experiments (triangles indicate interface elements).

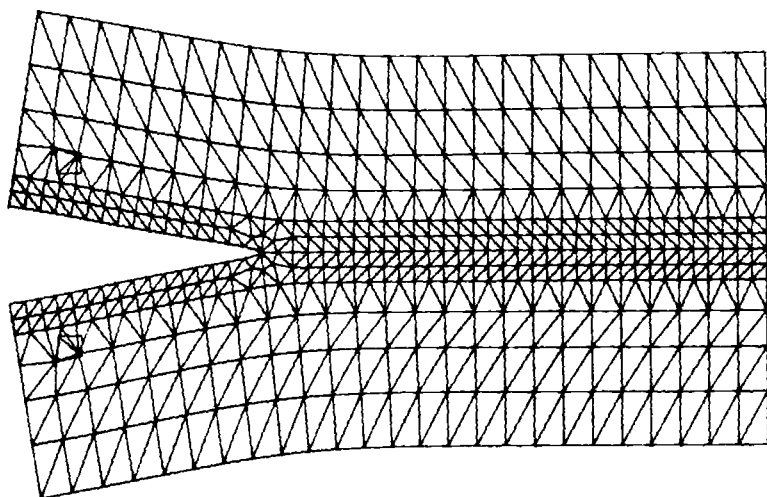


a.

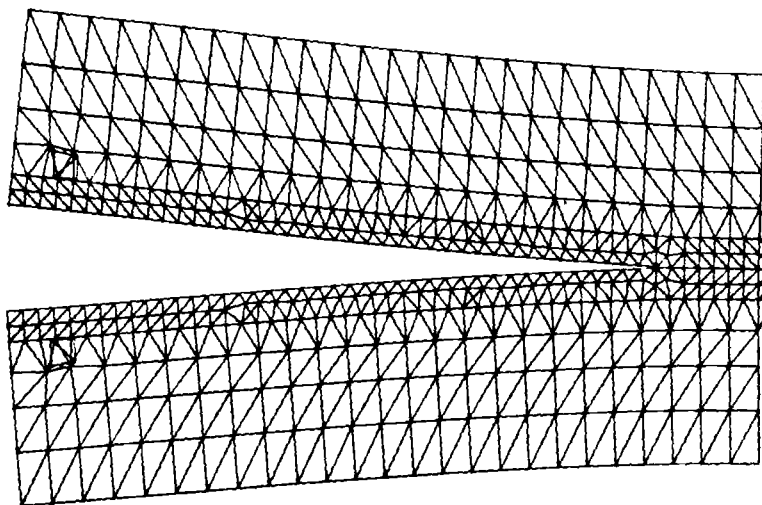


b.

FIG. 6—Input to analyses: (a) specified K_{ID} as a function of crack velocity, (b) specified crack velocity history.

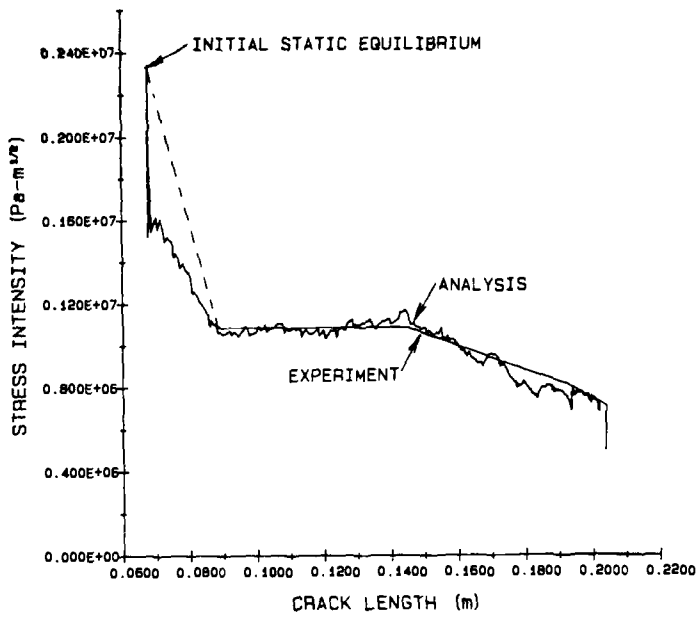


a.

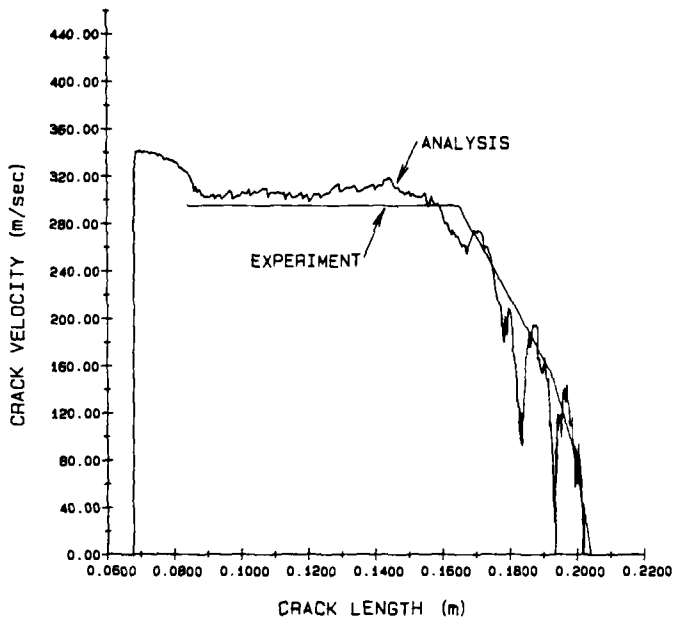


b.

FIG. 7—Displaced mesh plots with K_{ID} specified (magnification, $\times 25$): (a) displacements at initial static equilibrium (left detail), (b) after crack arrest (left detail).



a.



b.

FIG. 8—Results for analysis with specified K_{ID} : (a) stress intensity as a function of crack length, (b) crack velocity history.

The cracks were started from blunted tips of the initial notches prepared by specially modified jeweler's saws of different thicknesses. Figure 4 shows the pertinent results for four tests with different initial bluntness. We will analyze the highest loaded test, using data from Specimens 21, 4, and 35.

The mesh used for analysis is shown in Fig. 5. Interface elements model contact between the wedge and the specimen and contact between the specimen and the support plate. These elements allow the specimen to separate from the wedge and the support. The loading pins were not modeled explicitly, but were simulated by including extra mass to represent steel pins (diameter = 25 mm, assumed length = 100 mm).

The material used in the experiments was Araldite B, with a $K_{ID}(v)$ curve shown in Fig. 6a. This curve is based on Kalthoff's data (Chapter 1 of Ref 13). The elastic constants are $E = 3.66$ GPa, $\nu = 0.39$, and $\rho = 1170$ kg/m³. These give plane stress wave speeds of $c_1 = 2500$ m/s and $c_2 = 1060$ m/s.

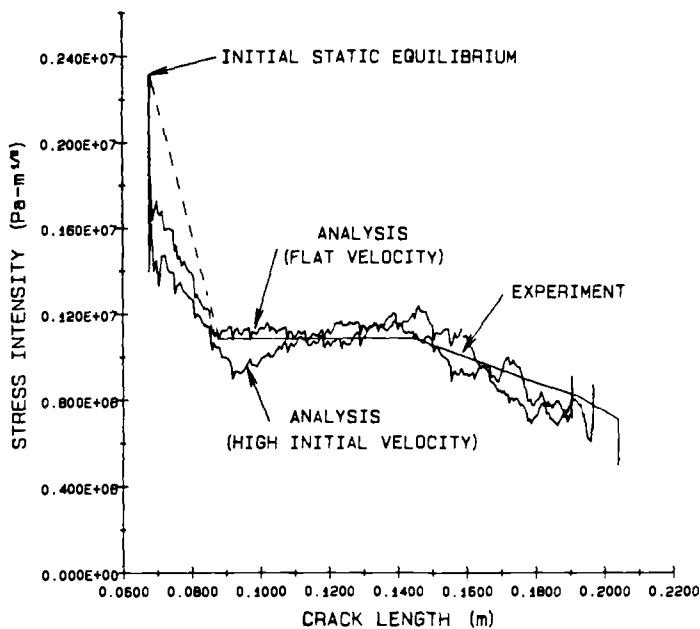
Figure 6b shows the crack velocity histories input to the model for the analyses in which the crack position was specified ("generation" studies). Two different histories were specified since no experimental data were available for crack position immediately after initiation. The uncertainty can be seen by looking at Fig. 4b, which implies a constant velocity after initiation. However, Fig. 4a shows that if a constant velocity is extrapolated back to initiation, the initial crack length is 74 mm rather than the known 67.8 mm. The conclusion is that the crack initially ran faster than the plateau velocity of 295 m/s. Other crack velocity histories could have been used; however, as will be discussed, these two histories generate $K_{ID}(v)$ curves that bound the material data.

The first results that will be discussed are those with the $K_{ID}(v)$ specified. The calculation was performed by loading the wedges and bringing the specimen to initial static equilibrium with $K_{IQ} = 2.32$ MPa m^{1/2} as measured in the experiment. The wedge displacements were then fixed and the crack was allowed to propagate. The static solution was obtained using artificial damping and dynamic relaxation. No damping was included during the dynamic solution.

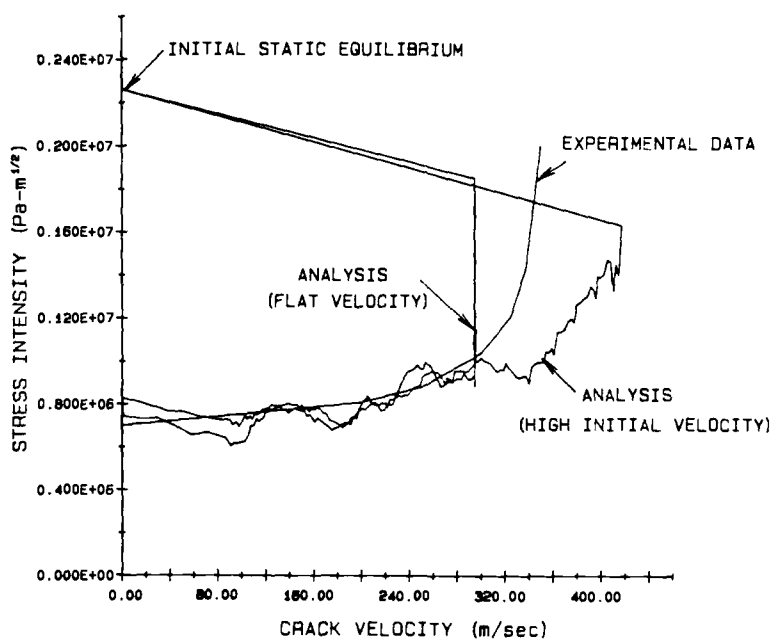
Displaced mesh plots are shown in Fig. 7. Lift-off occurred both at the wedge and at the specimen support. Figure 8 shows the calculated stress intensity as a function of crack length and crack velocity. The calculated stress intensity correlates well with the experimental data, with arrest occurring at the observed crack length. The correlation with experimentally observed crack velocity is quite good until near crack arrest, where the calculated velocity shows oscillations that are probably related to remeshing.

The results for the calculations with specified crack velocity are shown in Fig. 9. There is considerable variation in the calculated stress intensity both as a function of crack length and as a function of crack velocity. For the analysis with a flat velocity curve, the calculated stress intensities are higher than the experimentally observed values (Fig. 9b). These results are similar to Atluri and Nishioka's (Fig. 3). When the high initial velocity is input, the calculated stress intensities are lower than the observed values. These results demonstrate the difficulty of using analysis to generate material data. Even for an experiment in which the data are quite clean, relatively small differences in specified crack velocity can lead to significant differences in the calculated $K_{ID}(v)$ curve.

The sensitivity to assumed boundary conditions was further explored by changing conditions at the loading location. This included (1) fixing the loading pin location during propagation (no lift-off), and (2) including the wedge (allowing lift-off), but not the pin mass, in the calculation. The results are shown in Fig. 10. Differences in the boundary conditions change the calculated stress intensities.



a.



b.

FIG. 9—Results for analysis with specified crack velocity: (a) stress intensity as a function of crack length, (b) stress intensity as a function of crack velocity.

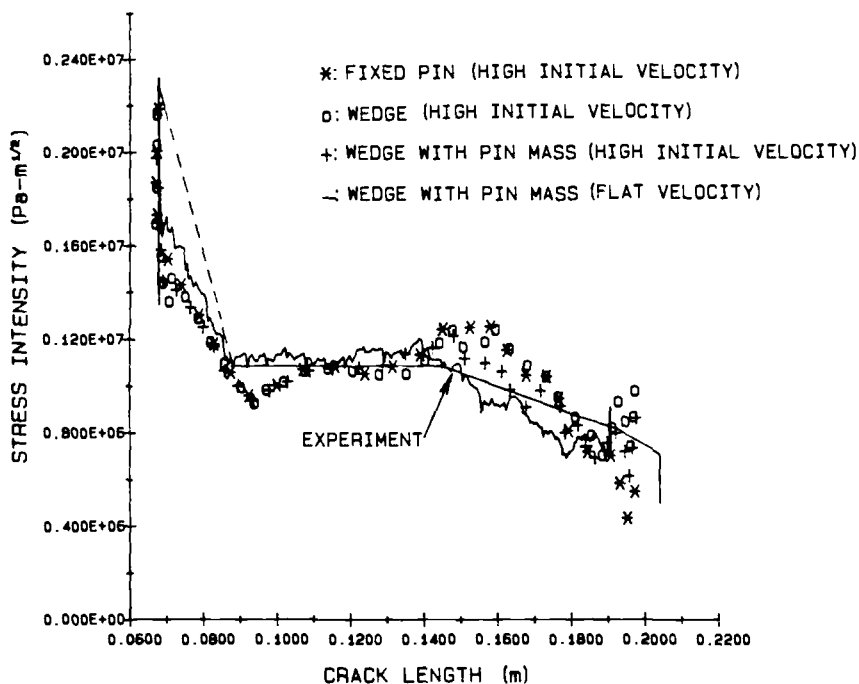


FIG. 10—Sensitivity to assumed boundary conditions analysis with specified velocity.

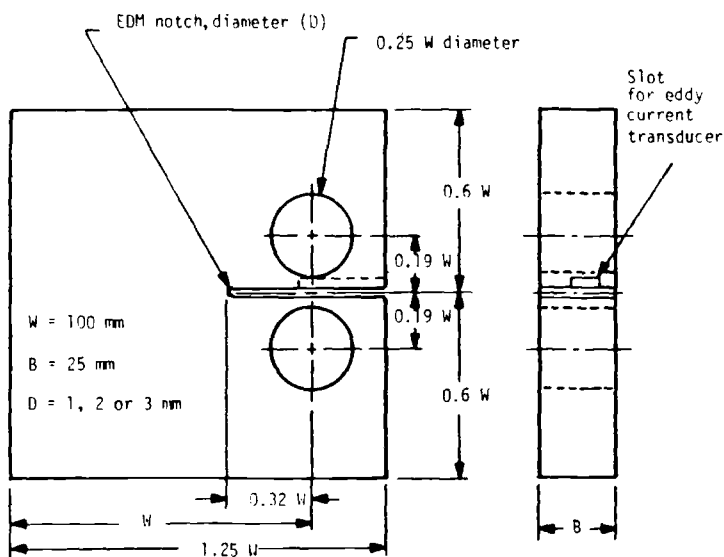
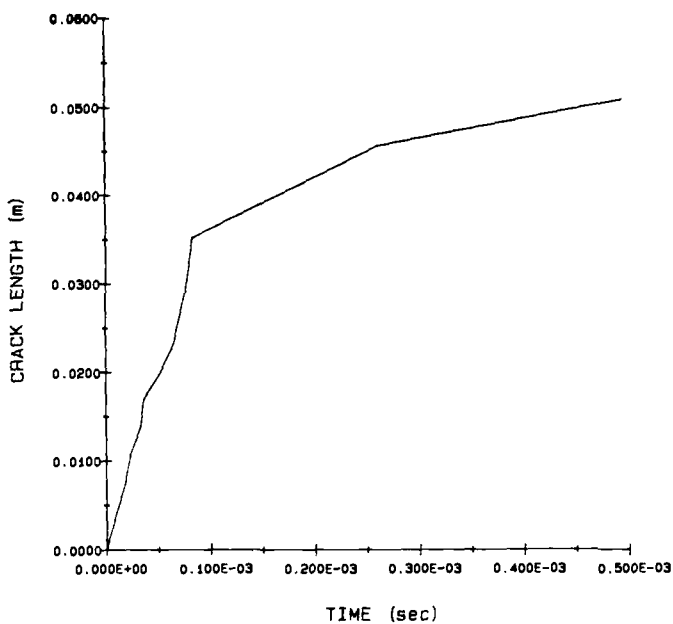
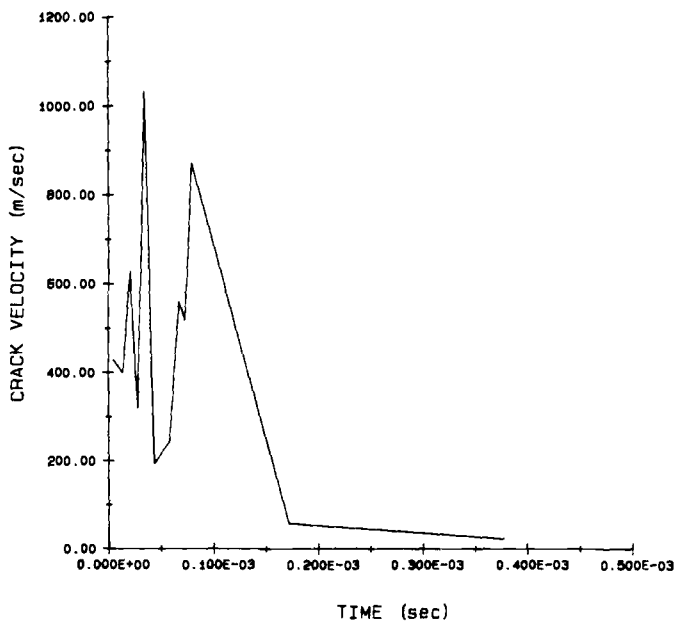


FIG. 11—Dimensions of the compact specimen (after Hudak et al. [9]).



a.



b.

FIG. 12—Crack length history: (a) crack length, (b) crack velocity (calculated from the crack length history).

Crack Arrest in a Compact Specimen

This analysis examines one specimen in a series of experiments performed on 4340 steel at Southwest Research Institute by Hudak, Dexter, FitzGerald, and Kanninen [9]. Since the stress intensity was not measured during the experiment, analysis was combined with measured crack-tip position histories and crack-opening displacements to calculate the $K_{ID}(v)$ relation.

The specimen geometry is shown in Fig. 11. The specimen was wedge loaded with the pins resting on a surface to resist the axial load without transmitting it into the specimen. Since the loading rig was relatively compliant, the pins did not remain fixed as the crack propagated. The crack opening displacement at the load line was measured using an eddy current transducer.

Crack position was measured using electrically conducting gages applied to the surface of the specimen. Crack advance is measured by the change in electrical resistance as the gages fracture. Figure 12 shows the measured crack length history and the crack velocity calculated using a simple differencing of the length history. It is not clear how much of the oscillation in calculated velocity is due to measurement error, how much is due to the difference method used to calculate velocity, and how much is true behavior. This is a critical point since the velocity must be calculated to generate a $K_{ID}(v)$ curve. How this is done directly affects the result.

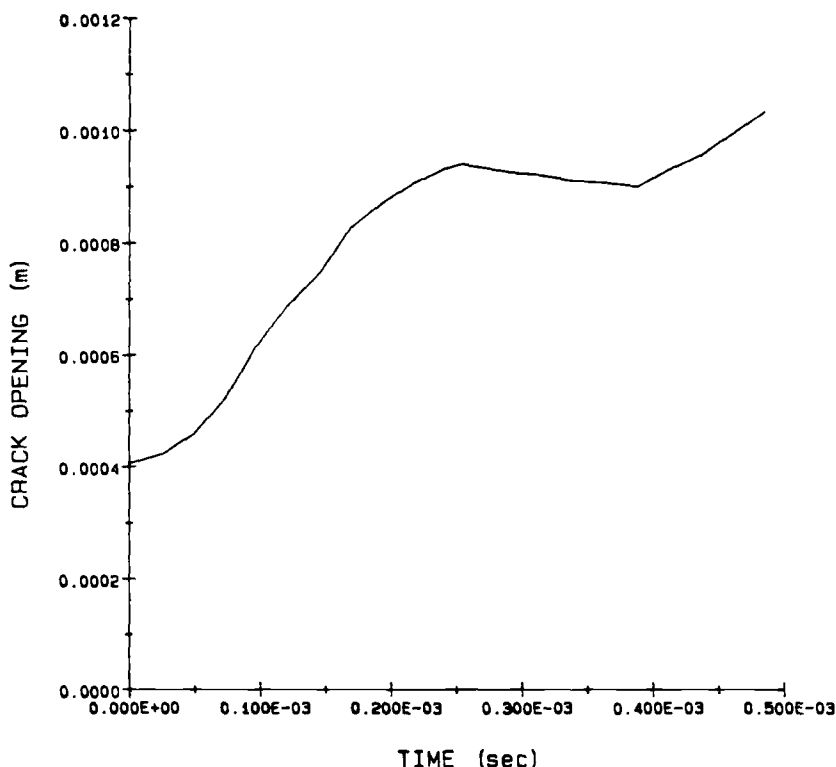


FIG. 13—Measured crack opening history.

Figure 13 shows the measured crack opening at the line load. These data are considerably smoother than the crack velocity data.

The $K_{I0}(v)$ curve calculated in the work of Hudak et al. [9] is compared with data from other sources in Fig. 1. The data of Kobayashi and Dally [14] and of Rosakis, Duffy, and Freund [8] were obtained using local measures of stress intensity during the experiment. Kobayashi and Dally used a photoelastic coating on the specimen, while Rosakis et al. used reflected caustics. The data of Hahn, Hoagland, Kanninen, Rosenfield, and Sejnoha [15] were obtained using a combined experimental and analytical technique similar to that already described for the present tests. The data obtained using local measures are consistent, while the data based on combined experiments and analysis are scattered above the local data.

In the analysis, the hole in the specimen, the loading pins, and the wedge were modeled separately. Interface elements were used to represent contact between these components. No gap was assumed between the wedge and the pins, but between the pin and the specimen a gap of 0.05 mm was assumed (based on discussion with the experimenters). The use of interface elements allows lift-off of the pins from the wedge and movement of the pins in the holes.

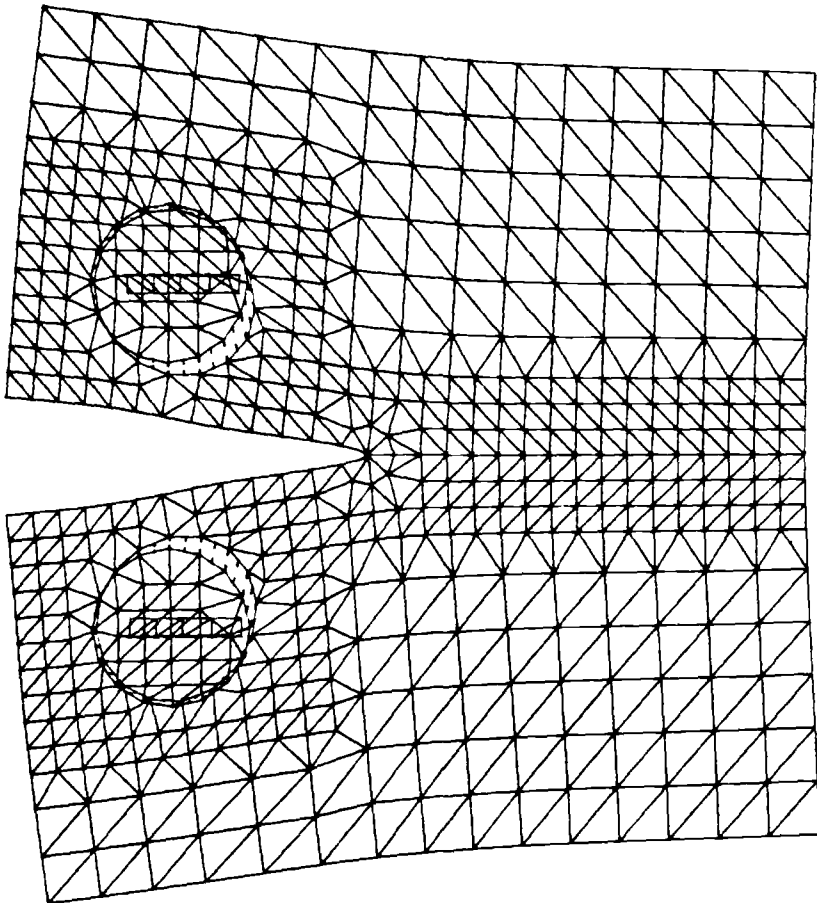


FIG. 14—Displacements at initial static equilibrium (magnification, $\times 15$).

Two calculations were performed. In the first, the $K_{ID}(v)$ curve shown in Fig. 1 was input and the crack velocity was calculated. In the second, the crack velocity (Fig. 12b) was specified, and the stress intensity was calculated. The material properties were $E = 206$ GPa, $\nu = 0.3$, and $\rho = 7833$ kg/m³, giving plane strain wave speeds of $c_1 = 5963$ m/s, $c_2 = 3187$ m/s, and $c_R = 2965$ m/s. Plane strain conditions were assumed in the analysis.

To bring the analysis to initial static equilibrium, the wedge was displaced and artificial damping applied. The displaced shape at initial static equilibrium is shown in Fig. 14. The calculated crack-opening displacement is 0.406 mm and the stress intensity is 213 MPa m^{1/2} (these compare to the measured displacement of 0.403 mm and a calculated stress intensity in Ref 9 of 193 MPa m^{1/2}). During propagation the wedge displacement was fixed.

Figure 15 shows displacements after the crack has propagated for the analysis with $K_{ID}(v)$ specified. Comparisons of crack length history, crack opening, and stress intensity are given in Figs. 16 through 18. For the analysis with $K_{ID}(v)$ specified, the crack propagates faster than experimentally measured.

The objective of the combined experiments and analysis was to generate a $K_{ID}(v)$ curve.

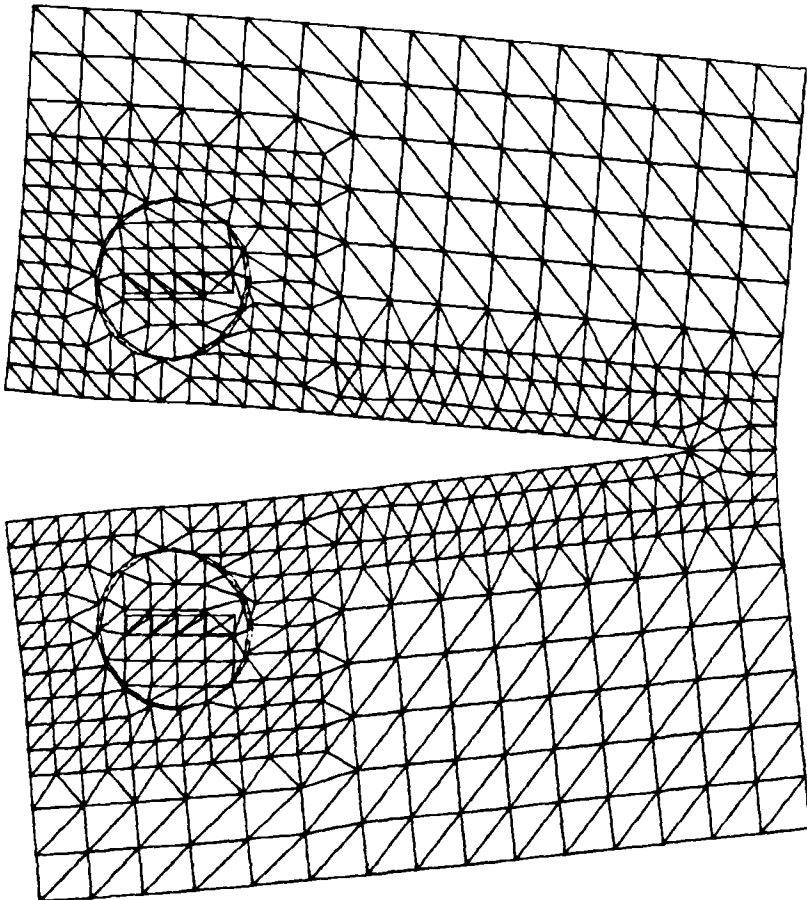


FIG. 15—Displacements after propagation (magnification, $\times 15$).

This curve, obtained from the analysis in which the crack position was specified, is shown in Fig. 19. This curve does not define a unique $K_{ID}(v)$ relation and does not correlate with data obtained by other experimenters using a local measurement of stress intensity.

There are several possible reasons for this situation:

1. The analysis could be in error.
2. The measured crack-opening displacements could be in error.
3. The measured crack position could be in error.
4. $K_{ID}(v)$ may not be a material property.
5. Some phenomenon may be occurring which is not described by the present elastic analysis.

Based on the calculations presented in Refs 1 and 2 and in the previous section of this paper, there is confidence that the analysis procedure is essentially correct. Uncertainty in modeling the boundary conditions is not sufficient to account for the differences. Since the experimenters express relatively high confidence in the measured crack-opening displacement, the most likely sources of the lack of correlation are either errors in crack position measurement or nonuniqueness of the $K_{ID}(v)$ curve.

With regard to crack position measurement, it is not clear when electrical contact is broken relative to the crack position. Presumably, the conductor breaks some time after the crack

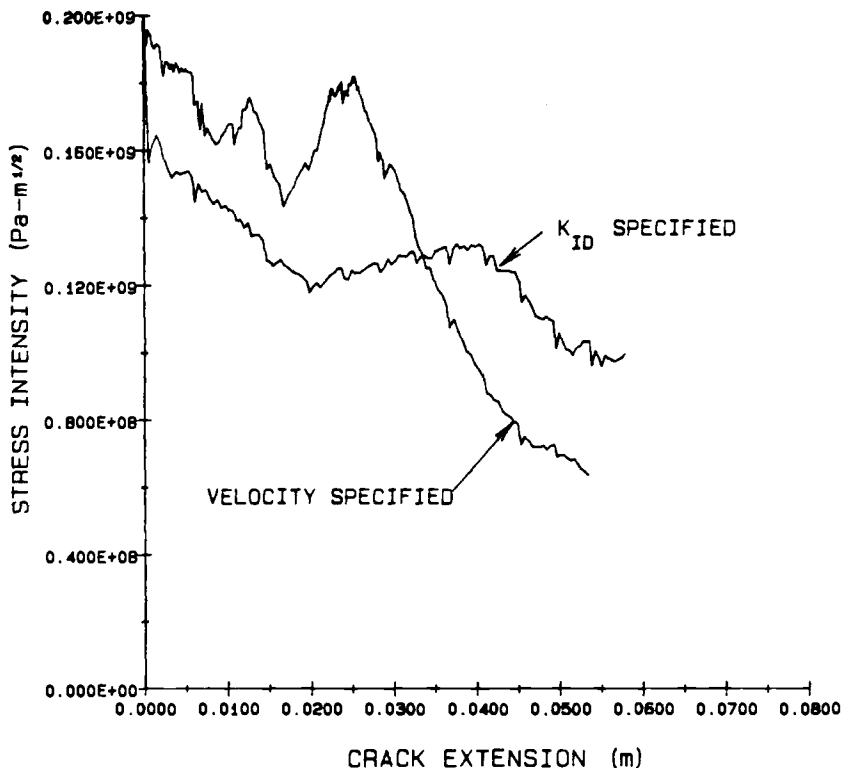


FIG. 16—Stress intensity history.

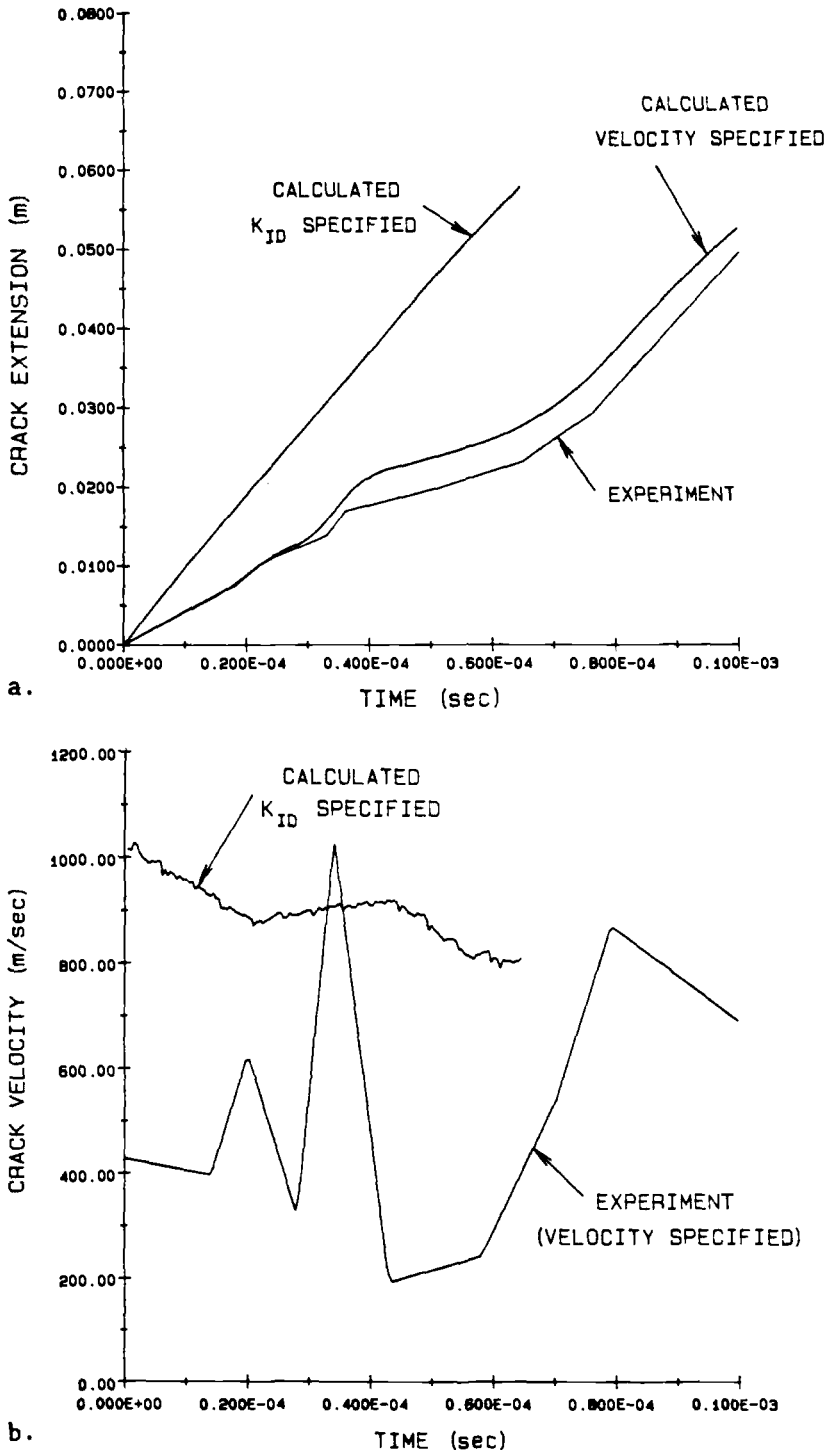


FIG. 17—Calculated crack-length history: (a) crack length, (b) crack velocity.

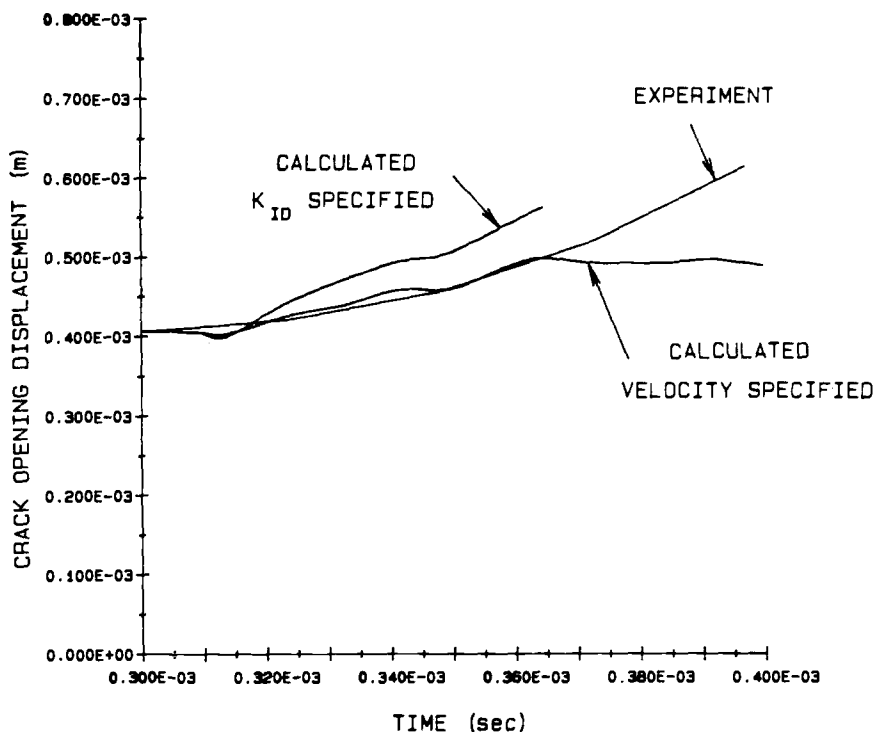


FIG. 18—Calculated crack-opening history.

tip has passed and when the crack is opening. The layer of insulation between the specimen and conductor might also delay breaking of the conductor. In light of this effect, it is interesting to note that the calculated $K_{ID}(v)$ data lies above the curve obtained using local data. This is consistent with the measured crack length being shorter than the actual crack length. That is, this effect would occur if the gage did not break until some time after the crack tip had passed. This provides an indication that the crack length data may be in error. A second difficulty is that any error in crack-tip position is exaggerated when the data are differentiated to obtain the crack velocity.

Another alternative is that $K_{ID}(v)$ cannot be described by a single curve. While this may be true for transient conditions, a single curve will exist for steady state conditions. The consistency of the data obtained locally (Fig. 1) supports a single $K_{ID}(v)$ curve (or nearly so) for this material.

Alternate Experimental Procedures

The two major sources of uncertainties in the combined experimental and analytical approach to generating $K_{ID}(v)$ data are analysis and crack-position measurement. Alternate experimental procedures could reduce some of these uncertainties.

The analytic uncertainty could be reduced by using Freund's [16] relation between the initial stress state of a cracked body and the dynamic stress intensity. This relation is

$$K = k(v)K_s(a) \quad (1)$$

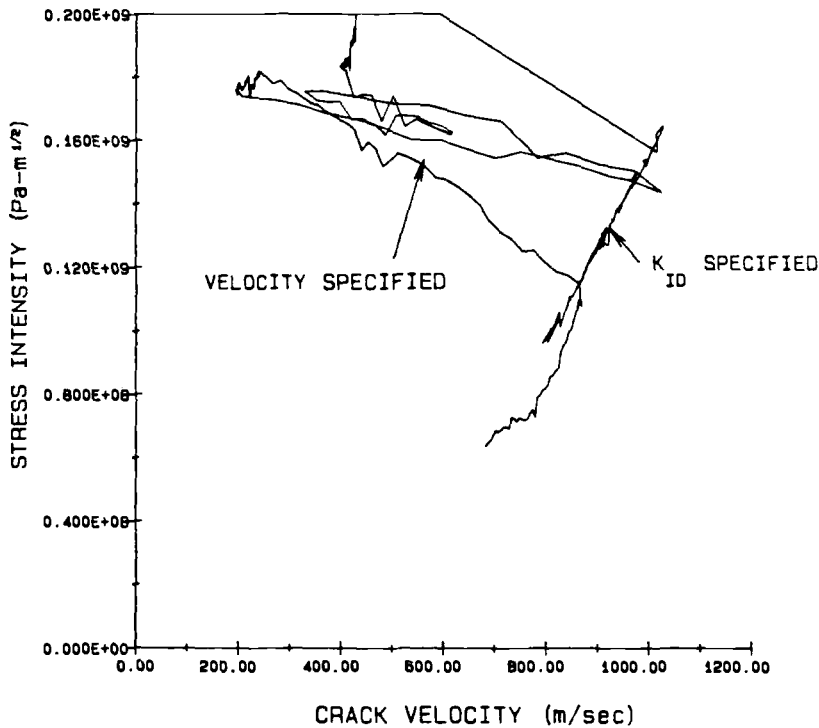


FIG. 19—Calculated stress intensity as a function of crack velocity.

where K is the dynamic stress intensity, $k(v)$ is a universal function of crack velocity and material properties, and $K_s(a)$ is the static stress intensity obtained at the current crack length, a , using the initial static stresses in the body as loads on the crack face. This relation is valid for a finite body until the arrival of reflected waves.

Using Eq 1, it is possible to obtain the current dynamic stress intensity at any time knowing the current crack velocity and position. Since there is relatively high confidence in the calculation of the initial static stress state in a specimen, the error in dynamic stress intensity would probably be reduced if calculated this way.

If a special loading fixture could be developed that would apply the displacements around a specimen corresponding to the asymptotic $r^{1/2}$ solution around the crack tip, some valuable data could be obtained. For this particular loading, $K_s(a)$ is constant and equal to the static value. This experiment would then show how rapidly the steady state condition is achieved and how rapidly a constant propagation velocity is reached.

A second (and probably larger) uncertainty is the measurement of crack position and crack velocity. If the crack position could be obtained as a continuous function, the evaluation of crack velocity would be much cleaner. Rosakis and Zehnder [4] mention several alternate methods of doing this, including radio-frequency skin effect and electrical resistance. One method not mentioned is sensing of the light emitted during propagation due to crack-tip heating. This is discussed by Weichert and Schonert [17,18], where they show that the temperatures at the tip are high enough to emit visible light during propagation. Streak photography could possibly provide a continuous record of the crack-tip position.

Conclusions

In this paper we have demonstrated some of the uncertainties that can occur when combined experiments and analysis are used to generate a $K_{ID}(v)$ curve. These uncertainties include analytic uncertainties due to boundary conditions and uncertainties due to the measured crack position data.

We have discussed the advantages of using an alternate experimental approach in which Freund's analysis is used to obtain the dynamic stress intensity and a continuous measure of crack position is obtained. With this approach, it should be possible to obtain clearer $K_{ID}(v)$ data and to begin to resolve the issue of the uniqueness of this curve.

Acknowledgments

The authors are grateful to M. Kanninen, S. Hudak, and R. Dexter of Southwest Research Institute for discussing and sharing their experimental data. This work was performed at the Department of Computer Graphics of Cornell University while the first author of this paper was an employee of Sandia National Laboratories. Partial funding was provided by National Science Foundation, grant No. 8351914. This work was supported by the U.S. Department of Energy under Contract No. DE-AC04-76DP00789.

References

- [1] Swenson, D. V., "Modeling Mixed-Mode Dynamic Crack Propagation Using Finite Elements," Ph.D. thesis, Cornell University, Ithaca, NY, January 1986.
- [2] Swenson, D. V. and Ingraffea, A. R., "Modeling Mixed-Mode Dynamic Crack Propagation Using Finite Elements: Parts 1 and 2," *Proceedings, First World Congress on Computational Mechanics*, University of Texas, Austin, TX, 22-26 Sept., 1986.
- [3] Dally, J. W., Fourny, W. L., and Irwin, G. R., "On the Uniqueness of the Stress Intensity Factor-Crack Velocity Relationship," *International Journal of Fracture*, Vol. 27, 1985, pp. 159-168.
- [4] Rosakis, A. J. and Zehnder, A. T., "On the Dynamic Fracture of Structural Metals," *International Journal of Fracture*, Vol. 27, 1985, pp. 169-186.
- [5] Dally, J. W., "Dynamic Photoelastic Studies of Fracture," *Experimental Mechanics*, October 1979, pp. 349-361.
- [6] Kalthoff, J. F., Beinert, J., and Winkler, S., "Measurements of Dynamic Stress-Intensity Factors for Fast Running and Arresting Cracks in Double-Cantilever-Beam Specimens," *Fast Fracture and Crack Arrest, ASTM STP 627*, G. T. Hahn and M. F. Kanninen, Eds., American Society for Testing and Materials, Philadelphia, 1977, pp. 161-176.
- [7] Kalthoff, J. F., Beinert, J., Winkler, S., and Klemm, W., "Experimental Analysis of Dynamic Effects in Different Crack Arrest Test Specimens," *Crack Arrest Methodology and Applications, ASTM STP 711*, G. T. Hahn and M. F. Kanninen, Eds., American Society for Testing and Materials, Philadelphia, 1980, pp. 109-127.
- [8] Rosakis, A. J., Duffy, J., and Freund, L. B., "The Determination of Dynamic Fracture Toughness of AISI 4340 Steel by the Shadow Spot Method," *Journal of the Mechanics and Physics of Solids*, Vol. 32, No. 4, 1984, pp. 443-460.
- [9] Hudak, S. J., Dexter, R. J., FitzGerald, J. H., and Kanninen, M. R., "The Influence of Specimen Boundary Conditions on the Fracture Toughness of Running Cracks," *Engineering Fracture Mechanics*, Vol. 23, No. 1, 1986, pp. 201-213.
- [10] Atluri, S. N. and Nishioka, T., "Numerical Studies in Dynamic Fracture Mechanics," *International Journal of Fracture*, Vol. 27, 1985, pp. 245-261.
- [11] Dadkhah, M. S., "Dynamic Fracture Under the Influence of Biaxial State of Stress," master's thesis, Mechanical Engineering, University of Washington, Seattle, WA, 1984.
- [12] Hawong, J. S., Kobayashi, A. S., Dadkhah, M. S., Kang, B. S. J., and Ramulu, M., "Dynamic Crack Curving and Branching Under Biaxial Loading," Office of Naval Research, Technical Report No. UWA/DME/TR-85/50, Washington, DC, 1985.

- [13] Kanninen, M. F. and Popelar, C. H., *Advanced Fracture Mechanics*, Oxford University Press, New York, 1985.
- [14] Kobayashi, T. and Dally, J. W., "Dynamic Photoelastic Determination of \dot{a} - K Relation for 4340 Alloy Steel," *Crack Arrest Methodology and Applications*, ASTM STP 711, G. T. Hahn and M. F. Kanninen, Eds., American Society for Testing and Materials, Philadelphia, 1980, pp. 189–210.
- [15] Hahn, G. T., Hoagland, R. G., Kanninen, M. F., Rosenfield, A. R., and Sejnoha, R., "Fast Fracture Resistance and Crack Arrest in Structural Steels," Report No. 55C-242, Ship Structure Committee, 1973.
- [16] Freund, L. B., "Crack Propagation in an Elastic Solid Subjected to General Loading—I. Constant Rate of Extension," *Journal of the Mechanics and Physics of Solids*, Vol. 20, 1972, pp. 129–140.
- [17] Weichert, R. and Schonert, K., "On the Temperature Rise at the Tip of a Fast Running Crack," *Journal of the Mechanics and Physics of Solids*, 1974, Vol. 22, pp. 127–133.
- [18] Weichert, R. and Schonert, K., "Heat Generation at the Tip of a Moving Crack," *Journal of the Mechanics and Physics of Solids*, 1978, Vol. 26, pp. 151–161.

George T. Hahn,¹ Pedro C. Bastias,¹ Arun M. Kumar,¹ and Carol A. Rubin¹

Analysis of Crack Arrest Under Elastic-Plastic Conditions

REFERENCE: Hahn, G. T., Bastias, P. C., Kumar, A. M., and Rubin, C. A., "Analysis of Crack Arrest Under Elastic-Plastic Conditions," *Fracture Mechanics: Nineteenth Symposium, ASTM STP 969*, T. A. Cruse, Ed., American Society for Testing and Materials, Philadelphia, 1988, pp. 427–440.

ABSTRACT: Elastic-plastic finite-element analyses of quasi-static crack propagation and arrest in a compact test specimen are described. The analyses evaluate the effect of the prior plastic deformation history of the propagation event on the shape of the J -resistance curve of the arrestor. In addition, experiments employing a special device are used to simulate fast fracture and arrest in small laboratory test specimens of ductile HY-80 steel and tough 7075 aluminum. The results show that large dynamic elevations of the J -curve are encountered during arrest. A relatively simple procedure for assessing or designing welded-in, steel crack arrestors, based on these findings is proposed.

KEY WORDS: fracture, crack arrest, J -resistance curve, HY-80 steel, 7075 aluminum, crack arrestors, crack arrest design, crack history, crack rate, dynamic J -curve, fracture mechanics

There is long-standing interest in designs that will stop a rapidly advancing crack before structural integrity is compromised [1–4]. Methods are available for determining the nil-ductility transition (NDT) temperature [3] or the arrest toughness values [5–8] of steel plates that will arrest a short crack, that is, ~ 10 mm long, emerging from a locally embrittled region. Existing toughness specifications have thus controlled the kind of "pop-in" crack that originated from an arc strike and severed the hull of the *U.S.S. Ponaganset* in 1947 [8]. However, there is no accepted and practical method for designing welded-in crack arrestors that can stop a long fracture, that is, $0.1 \text{ m} \leq a \leq 2 \text{ m}$ in large structures such as ship hulls, pressure vessels, line pipe, and so forth [9]. This remains a difficult problem because very high toughness levels— $200 \text{ MPa} \sqrt{\text{m}} \leq K_{Ia} \leq 600 \text{ MPa} \sqrt{\text{m}}$ ($200 \text{ kJ/m}^2 \leq J_{Ia} \leq 2 \text{ MJ/m}^2$)—are needed to arrest long fractures in a fully loaded structure. Figure 1 describes a practical example: a fracture initiated by a short defect in a 100-mm-wide brittle weld subjected to a constant tensile load. The adjacent steel plates probably must possess an arrest toughness, K_{Ia} , of $\approx 200 \text{ MPa} \sqrt{\text{m}}$ to stop the unstable crack from penetrating with a reasonable margin of safety.² If the plates fail to stop the fracture, a tough welded-in arrestor of the same thickness located in the path of the crack 1 m from the weld may produce arrest if it possesses

¹ Professor, graduate student, graduate student, and professor, respectively, Department of Mechanical and Materials Engineering, Vanderbilt University, Nashville, TN 37235.

² The statically evaluated K_I value for the $2a = 100$ -mm-long crack emerging from the weld zone is $K_I = 149 \text{ MPa} \sqrt{\text{m}}$. This assumes a total stress of $\sigma = 375 \text{ MPa}$ ($\sigma_{\text{applied}} = 250 \text{ MPa}$ plus $\sigma_{\text{residual}} = 125 \text{ MPa}$) and that the other dimensions are much larger than $2a$. This calls for an arrest toughness of at least $K_{Ia} = 200 \text{ MPa} \sqrt{\text{m}}$ to arrest the crack with a margin of safety.

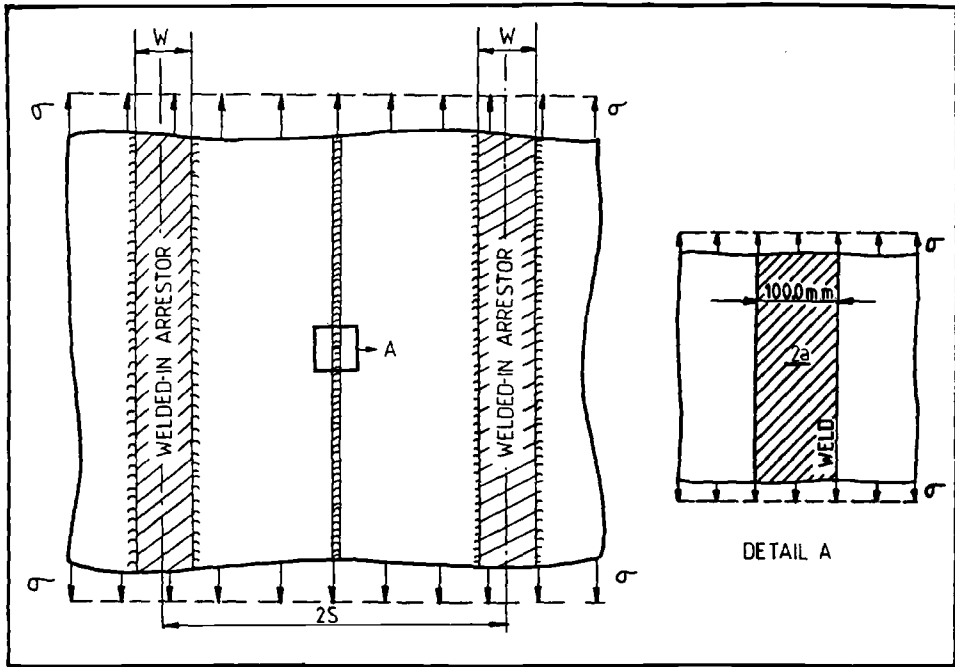


FIG. 1—Example of a practical crack arrest problem. A 100-mm-wide weld having fusion plus heat-affected zone (HAZ), with a low toughness, $K_{Ic} = 40 \text{ MPa} (\text{J}_{Ic} = 7.7 \text{ kJ/m}^2)$, contains a $2a = 4\text{-mm}$ -long crack. The crack becomes unstable when the total stress ($\sigma_{\text{applied}} = 250 \text{ MPa}$ plus $\sigma_{\text{residual}} = 250 \text{ MPa}$) reaches $\sigma = 500 \text{ MPa}$. The crack begins to extend and becomes a $2a = 100\text{-mm}$ -long rapidly propagating fracture when it emerges from the weld zone and begins to penetrate the adjacent steel plates. The questions remain: How tough do the plates have to be to assure that the crack will be arrested? How tough does a welded-in arrestor plate located in the path of the fracture $s = 1 \text{ m}$ from the weld have to be to assure arrest?

a toughness of $K_{Ia} \approx 600 \text{ MPa}$.³ Arrestors located farther from the weld would have to be proportionately thicker or tougher. Arrest requirements appropriate for fixed displacement conditions are not so severe.

The linear elastic fracture mechanics (LEFM) based toughness estimates given above are not reliable because the LEFM validity requirements are difficult to satisfy at the high K_I levels.⁴ The LEFM methods are also impractical. Arrest toughness values greater than $K_{Ia} = 150 \text{ MPa} \sqrt{\text{m}}$ are very costly to measure. The K_{Ic} values fail to account for the increase in toughness described by the R -curve, that is obtained when the ductile crack begins to penetrate the arrestor. The J -integral concept, together with the J -resistance curve, is therefore better suited for characterizing the response of relatively tough materials. With this in mind, Hahn and Dantam [10] proposed that the J_R value evaluated at $\Delta a = 1.5 \text{ mm}$, which is relatively inexpensive to determine, can serve as a measure of the crack arrest toughness

³ The statically evaluated K_I value for the $2a = 2\text{-m}$ -long crack entering a welded-in arrestor of the same thickness is $K_I = 443 \text{ MPa}$. This assumes that the weld residual stresses can now be neglected and that the other dimensions of the structure are still much larger than $2a$. An arrest toughness of at least $K_{Ia} = 600 \text{ MPa} \sqrt{\text{m}}$ is required to stop the crack with a margin of safety.

⁴ For example, to satisfy the requirement that the crack length is greater than 10 times the plastic zone extent; $a > 10 r_0 \approx 2 (K_I/\sigma_0)^2$. When $K_I = 200 \text{ MPa} \sqrt{\text{m}}$ and $\sigma_0 = 500 \text{ MPa}$, this means that $2a \geq 0.6 \text{ m}$ at arrest, which is 6 times the value involved in the preceding example.

$J_a(2) = J_R$.⁵ This measure is valid for long cracks and arrestors that display the ductile fibrous mode of fracture during the arrest process.⁶

However, the use of J -curves in arrest analyses involves the several unresolved complications illustrated in Fig. 2:

1. *Deformation History Effects*—Figure 2a, b, and c illustrates that the shape of the J -resistance curve depends on the prior plastic deformation history. The conventional J -curve (Fig. 2a), produced by ductile crack extension with a prior history of completely brittle extension, is different from the J -curve (Fig. 2b) for ductile crack extension with a prior history of ductile crack extension. The J -curve for a propagation-arrest event (in Fig. 2c)

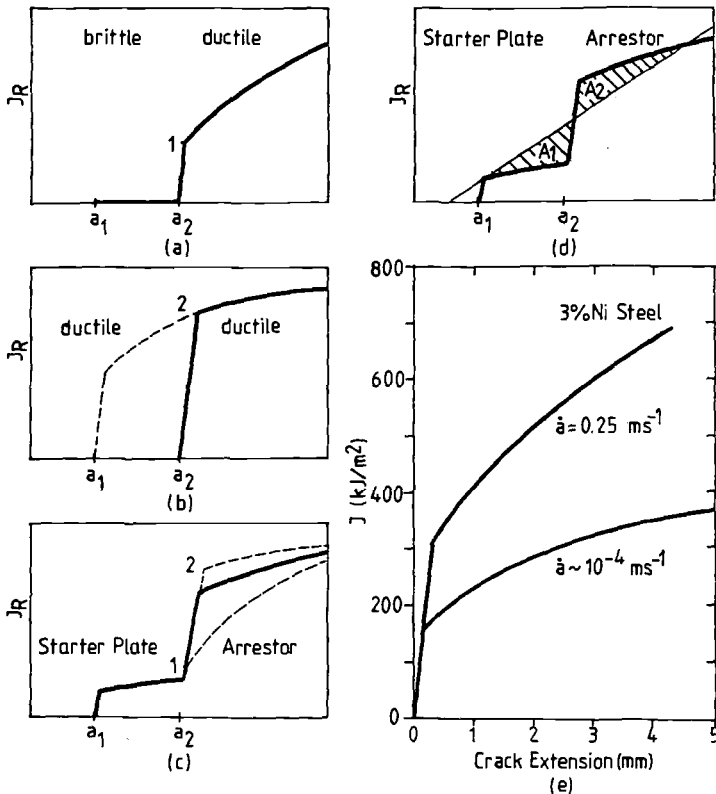


FIG. 2—Complications attending the use of J -resistance curves in the analysis of crack arrest: (a), (b), and (c) compare the shape of the J -curve for ductile crack extension from a preexisting crack of length a_2 with different prior deformation histories in the interval from a_1 to a_2 ; (d) is a schematic drawing illustrating the excess strain energy (shaded area A_1), part of which may be returned to make up the energy deficit (shaded area A_2) and permit the crack to split the arrestor; and (e) is an example of dynamic elevation of the J -curve [17,18].

⁵ Hahn and Dantam identify two measures of arrest toughness: $J_a(1) = J_{Ic}$ and $J_a(2) = J_R$ ($\Delta a = 1.5$ mm). The quantity $J_a(1)$ is appropriate when the crack extension is a small fraction of the initial crack length; $J_a(2)$ is appropriate when the extension is a large multiple of the initial length. The K_I equivalents of these two values are $K_{Ia}(1) = K_{Ic} = \sqrt{J_{Ic}E}$ and $K_{Ia}(2) = K_{IR} = \sqrt{J_R E}$.

⁶ The transition temperature of a steel arrestor must be well below the service temperature to assure that it will display high-toughness fibrous fracture under dynamic conditions rather than low-toughness cleavage.

is intermediate. This raises questions as to whether the conventional J_R curve has the right shape for a crack arrest analysis.

2. *Geometry Dependence*—The J -curve for a tough material is geometry dependent for anything but small amounts of ductile crack extension, typically no more than $0.05 \leq \Delta a/(w - a) \leq 0.1$, where w is the uncracked ligament [11]. Consequently, it is again not clear that the conventional J -curve is appropriate when arrest is preceded by large amounts of extension, as in the examples cited earlier.

3. *Kinetic Energy Release*—A part of the excess strain energy (defined by the difference between the static J driving force and J -resistance curves at instability in Fig. 2d) is converted into kinetic energy, and part of this may be returned adding to the crack driving force during arrest (see Fig. 2d) [6,12]. The kinetic energy return is difficult to evaluate without a dynamic analysis, and this complicates the task of defining the arrest condition.

4. *Dynamic Elevation of the J-Curve*—There is evidence from several sources that the J -curve for ductile crack extension, normally measured for very low rates of crack extension, that is, $\dot{a} \approx 10^{-4} \text{ ms}^{-1}$, is elevated by increasing the crack speed [13–15]. This does not fundamentally alter the ultimate crack stopping ability of the material because the crack velocity must be reduced to zero eventually to produce arrest. However, the transient elevation of the J -curve, produced by the high velocities of unstable cracks, $10^2 \text{ ms}^{-1} \leq \dot{a} \leq 10^3 \text{ ms}^{-1}$, could provide a mechanism for dissipating the returned kinetic energy.

This paper presents finite-element calculations of the effect of the prior deformation history on the shape of the J -curve. It also presents measurements of the arrest of fully brittle fractures in tough, ductile aluminum and HY-80 steel. The results show that prior history can frequently be neglected and that the J -curve retains its geometry independence when arrest is preceded by relatively brittle fracture. There are indications that the elevation of the J -curve with crack velocity can compensate for kinetic energy return. Simplified guidelines for designing crack arrestors are proposed on this basis.

Analyses and Procedures

Finite-Element Analysis

Finite-element calculations were performed to examine the effects of the deformation history—the plastic deformation produced by an advancing fracture before it reaches the arrestor—on the J -resistance curve subsequently displayed by the arrestor. To simplify the problem, quasi-static, stable crack growth and arrest were simulated in the elastic-plastic finite-element model of a 4T compact test specimen shown in Fig. 3. The model is composed of 172 quadrilateral and 8-noded elements with a total of 38 nodes forming the path of the crack. The simulations were performed with the finite-element code ABAQUS on VAX 11/780 and 11/785 machines.

The initial position of the crack tip is within the region labeled Material A, which is endowed with a relatively low toughness. Schematic resistance curves for both materials can be seen in Fig. 3. The model is subjected to a continuously increasing load-point displacement and the nodes ahead of the crack are released at the appropriate time to simulate crack extension on the symmetry plane. Details of the procedure are given elsewhere [16,18]. The crack eventually reaches the region labeled Material B after a crack extension of either $\Delta a = 6 \text{ mm}$ (shown in Fig. 3) or $\Delta a = 2 \text{ mm}$ (configuration not shown). The crack then arrests for a time, since Material B is tougher than Material A, and then continues to grow as the conditions for extension in Material B are satisfied as a result of the increasing load point displacement.

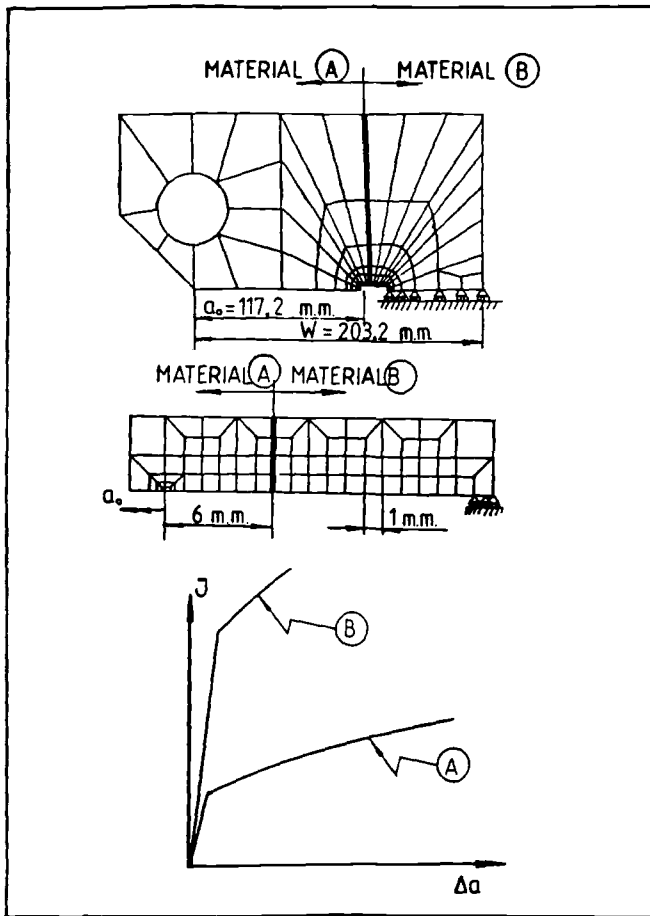


FIG. 3—Finite-element model of 4T compact test specimen.

The deformation behavior of the two materials is the same. It is given by the piecewise-linear representation of the stress-strain curve of A533B pressure vessel steel at 93°C (see Fig. 4a), and approximates power law hardening after the initial yield: $E = 198$ GPa, $\sigma_0 = 383$ MPa, and $n = 10$ [13,17]. The crack extension in Material A was controlled to proceed according to a predetermined J -resistance curve. The different J -curves employed, shown in Fig. 5, have the shapes that are displayed by low-toughness weldments. The effects of several J -curves appropriate for toughness levels in the range $50 \text{ MPa } \sqrt{\text{m}} \leq J_c \leq 120 \text{ MPa } \sqrt{\text{m}}$ were examined. Crack extension in Material B was controlled by the crack-tip opening displacement (CTOD)/resistance curve previously derived for A533B steel at 93°C [13,18]: $\text{CTOD} = 2.5332 \cdot 10^{-4} + 0.47082 \Delta a - 33.58 (\Delta a)^2$. When the extension proceeds from a preexisting (perfectly brittle) crack, the CTOD curve corresponds with a toughness of $J_{Ic} = 200 \text{ kJ/m}^2$ ($K_{Ic} = 203 \text{ MPa } \sqrt{\text{m}}$) and the conventional J -curve for ductile A533B steel shown in Fig. 4b. However, this resistance curve is viewed as a local criterion that is not influenced by the prior deformation history. Consistent with this, the CTOD curve produced an invariant crack-opening angle (COA) of 27.5° in the arrestor. The different deformation

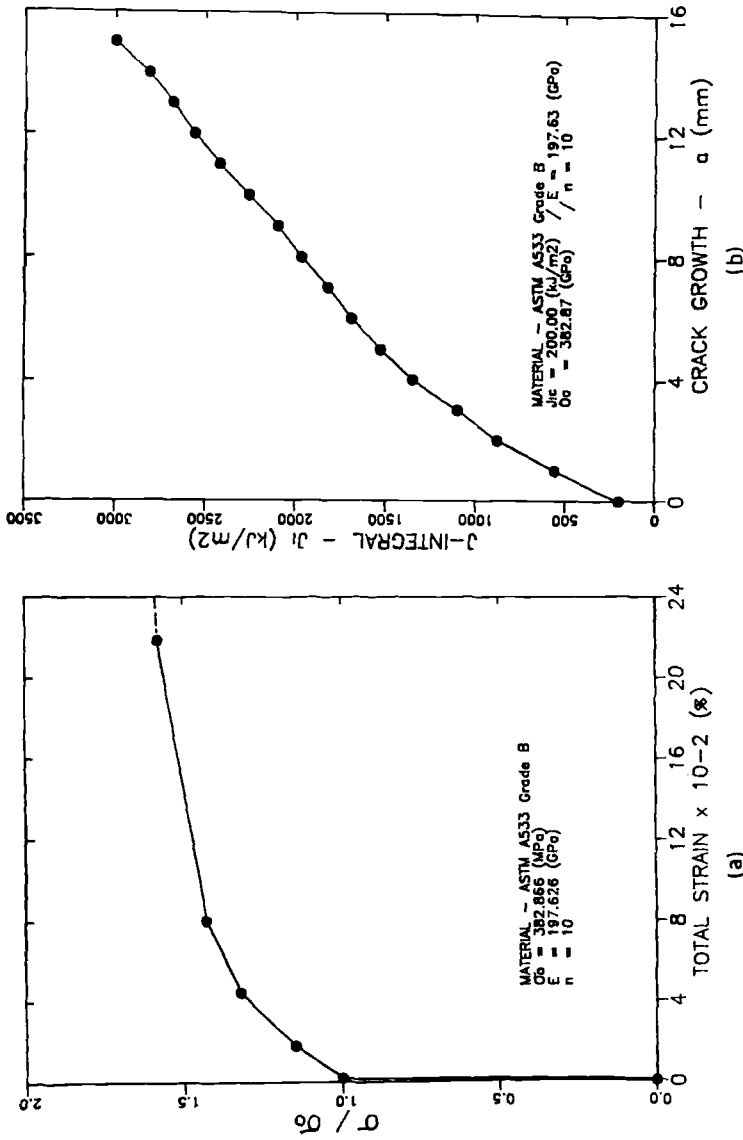


FIG. 4—Stress-strain characteristics and J-resistance curve of model materials: (a) piecewise-linear stress-strain curve of A533B pressure vessel steel employed for Material A and Material B, and (b) conventional J-resistance curve of Material B [17,18].

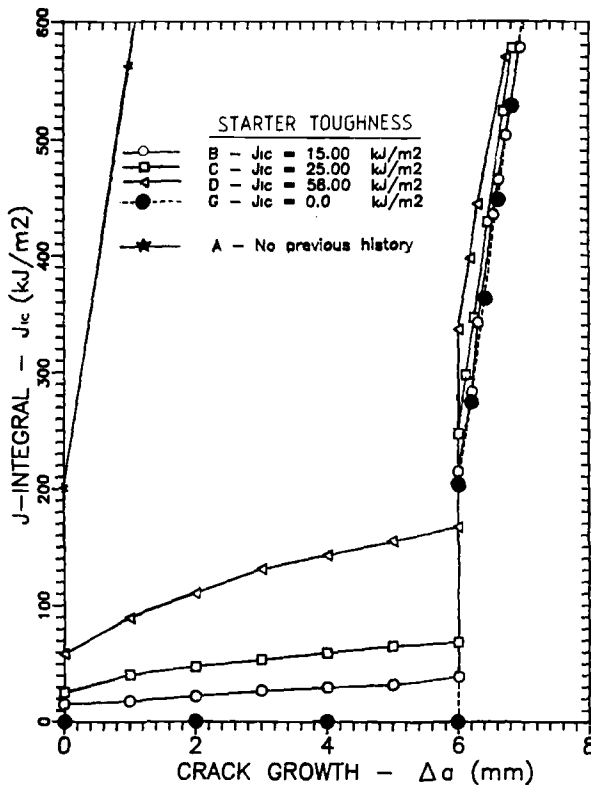


FIG. 5—Results of finite-element calculations showing the effects of the prior plastic deformation history on the shape of the J -resistance curve of the arrestor.

histories prior to arrest did affect the crack field remote from the tip and produced different $J - \Delta a$ relations for the arrestor. These J -curves were evaluated with the finite-element model as the crack penetrated into Material B.

Crack Arrest Measurements

Measurements of crack arrest in a ductile steel and aluminum alloy were carried out to evaluate the dynamic elevation of the J -curve by large crack velocities. These measurements employed a nonstandard, 152.4 by 152.4-mm (6 by 6-in.), precracked, compact-type test specimen whose measuring capacity is increased by attaching reusable, hardened steel arms. The operation of the system, referred to here as a "fast fracture device" is shown schematically in Fig. 6a and b. The test specimen and other components are described in Fig. 6c and d. To facilitate the analysis of the experiments, the variation of compliance of the system with crack length was evaluated with the aid of a finite-element model. Details of these calculations are presented elsewhere [19].

After the bolt breaks, the system behaves as if split by a zero-toughness crack which runs to the precrack and is arrested by the compact specimen; that is, there is ductile arrest with a history of completely brittle crack propagation. The displacement of the arms at the bolt and wedge at the onset of fracture were measured with standard displacement gages. These

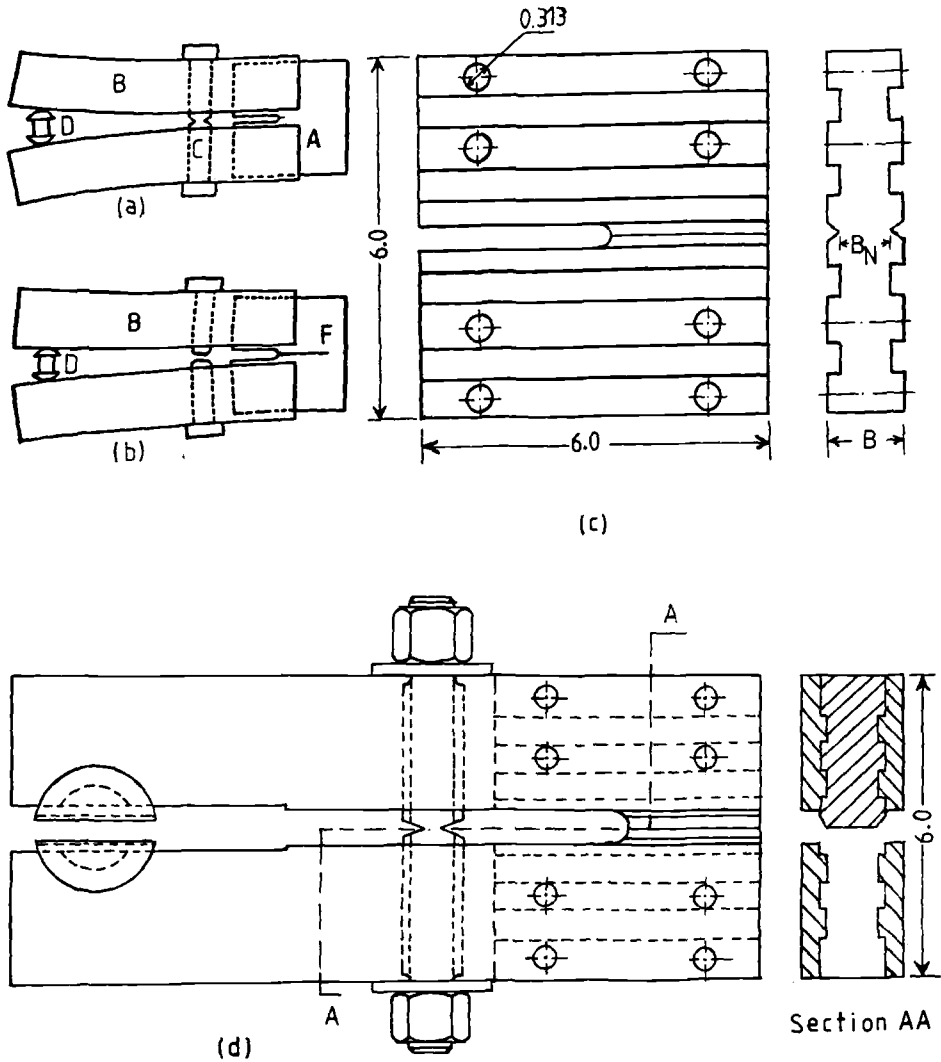


FIG. 6—Fast fracture device: (a) and (b) schematic drawing of operation, (c) test specimen, and (d) details of assembly.

displacements and the static compliance values for the system before and after arrest were used to estimate the elastic energy released during the arrest event. The average value of the propagating crack toughness, G_D , was then determined by dividing the released energy by the total fracture area, assuming that all of the released energy is consumed as fracture energy. The quantity G_D can be viewed as a measure of the elevation of the J -resistance curve as a result of crack extension and crack velocity.

Measurements were carried out on HY-80 steel and the 7075 aluminum alloy, which was solution treated at 470°C for ½ h and aged at 120°C at different time intervals to achieve a Rockwell hardness, B scale, (HRB) of 45, 78, and 92. The toughness values J_{Ic} and $J_a(2) = J_R$ are listed in Table 1.

TABLE 1—Summary of crack arrest measurements.

Material	B_N/B^a	Δa , mm	J_{Ic} , kJ/m ²	$J_a(2)$, kJ/m ²	G_D , kJ/m ²
HY-80	0.80	9	221	324	5830
7075 aluminum					
HRB 45	0.25	8.5	192	740	2680
HRB 78	0.25	50.8	52	292	670
HRB 90	0.25	>88	22	148	<490

^a B_N/B is the fraction of the specimen thickness remaining at the face grooves.

Results

Finite-Element Analyses

The results of the finite-element computations are presented in Fig. 6. These show the different J -curves which were prescribed for Material A and controlled the “start” of the relatively brittle propagation, and the corresponding calculated J -curves for Material B which served as the arrestor. The results illustrate that the J -curve for the arrestor is influenced by the deformation history and is unaffected by the deformation history when the starter toughness, that is, the J_{Ic} values for the material in which the crack starts propagating, are much lower than the arrest toughness

$$\frac{J_{Ic}(\text{starter})}{J_{Ic}(\text{arrestor})} \leq 0.1 \quad (1a)$$

or

$$\frac{K_{Ic}(\text{starter})}{K_{Ic}(\text{arrestor})} \leq 0.3 \quad (1b)$$

These results are summarized in Fig. 7, which also shows that these conclusions are relatively insensitive to the extent of propagation prior to arrest. In other words, it appears that the arrestor's response to a relatively brittle prior propagation history is the same as its response to a preexisting crack. It follows that the rules for the geometry independence of the J -curve for extension, from a preexisting (brittle) crack, will also apply. This means that the conventional J -curve for the arrestor material will describe resistance to penetration even when arrest is preceded by large crack extensions and for relatively small remaining ligaments.

Crack Arrest Measurements

The results in Table 1 show that the tough steel and aluminum alloy suffer relatively small crack penetrations prior to arrest. When the relatively large energy releases, that is, ~ 400 J, produced by the fast fracture device are combined with small penetrations and deep face grooves, large values of G_D , the fast propagating crack toughness, result. The G_D value is 18 and 3.6 times larger than $J_a(2)$ for the HY-80 steel and the tough (HRB = 45) aluminum alloy, respectively. These increases are qualitatively consistent with the measurements of Joyce [14,15] in Fig. 2e, which reveal a ~ 2 times increase in J -values for an increase in

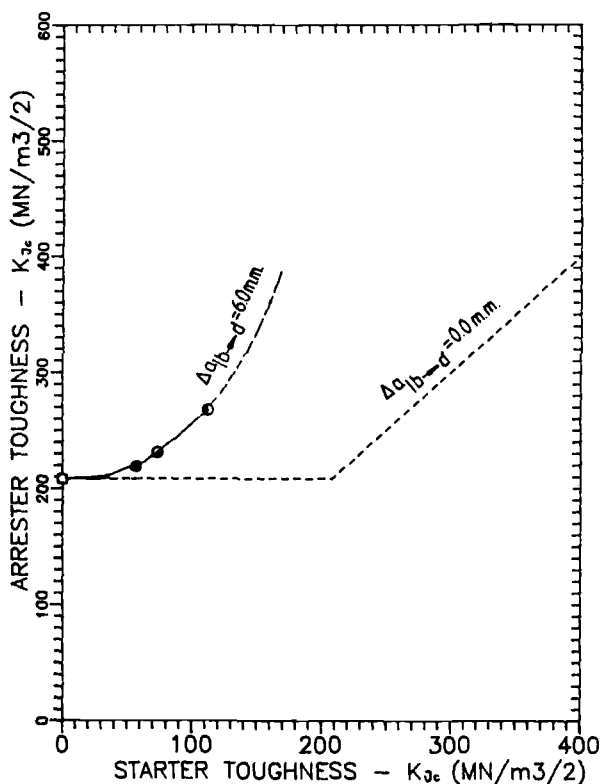


FIG. 7—Summary of finite-element calculations showing the effects of the toughness of Material A (starter toughness) on the calculated toughness of Material B (arrestor toughness) for a crack extension increment of $\Delta a = 2$ mm and $\Delta a = 6$ mm.

crack velocity from $\dot{a} \sim 10^{-4} \text{ ms}^{-1}$ to $\dot{a} \sim 0.25 \text{ ms}^{-1}$. These increases in toughness are related to the rate sensitivity of the plastic flow stress [13] and to changes in the fracture process [19].⁷

The interpretation of the present measurements involves uncertainties because other sources of energy dissipation have been neglected. However, even allowing for a factor of two error in the energy consumed by fracture, it appears that the dynamic elevation of the J -curve for arrest of fast propagating cracks by ductile steel could be ~ 10 times. Such a high transient toughness would compensate for the kinetic energy return which is not accessible to the static analysis.

Discussion

The results of this study suggest that a relatively simple J -integral based procedure may be adequate when assessing or designing tough, welded-in, steel crack arrestors for long crack extensions, that is, $\Delta a \geq 10 a_0$. The main features of such a procedure and a tentative requirement for the arrestor width are proposed here:

⁷ The fracture surfaces of the HY-80 steel and HRB 45, 7075 aluminum are ~ 5 and ~ 3 times rougher, respectively, than the surfaces produced by a slow tearing test.

1. *Crack Driving Force*—The crack driving force produced when the crack reaches the arrestor interface is evaluated in terms of J_I using a static analysis such as the one developed by Kumar, German, and Shih [20] and Kumar et al. [21]. When appropriate, an LEFM analysis can be used.

2. *Crack Arrest Toughness*—The plane-strain crack arrest toughness, $J_a(2) \equiv J_R$ ($\Delta a = 1.5$ mm), is derived from information provided by conventional techniques described in the ASTM Test for J_{Ic} , a Measure of Fracture Toughness (E 813-81) and the ASTM Recommended Practice for R -Curve Determination (E 561-81). To assure ductile, fibrous crack extension in the arrestor material, dynamic tear (DT) tests of the arrestor must show 100% fibrous fractures at temperatures from 25 to 50°C below the lowest service temperature. Effects of prior history are neglected. Plane strain conditions are assumed, since these are more easily obtained with a rapidly propagating crack, and effects of the deformation history on the J -curve of the arrestor are neglected.

3. *Arrest Criterion*—The criterion for arrest is $J_I < J_a(2)$. Complications attending kinetic energy return are neglected for steel arrestors.

4. *Arrestor Thickness*—The arrestor thickness determines the level of tensile stress and the value of J_I . Increasing the thickness will reduce J_I and improve the crack stopping capability.

5. *Arrestor Width*—The arrest criterion employed ensures that in the absence of kinetic energy return, the maximum crack penetration into the arrestor, Δa , < 1.5 mm. With kinetic energy return (that is, total crack extensions prior to arrest that are large compared with the overall dimensions of the structure), arrestor penetrations are not likely to exceed $\Delta a = 0.05a$, where $2a$ is the length of the crack arrest.⁸ To ensure that the arrestor can both survive such a penetration and contain the plastic zone of the crack to reduce the risk of weld failure, an arrestor width dimension, W , related to the plastic zone size at arrest is proposed

$$W = 0.05s + \frac{0.4 J_I E}{\sigma_0^2} \quad (2)$$

where $s \approx a$ is the spacing of the arrestors (see Fig. 1), E and σ_0 are the elastic modulus and yield strength of the arrestor, respectively, and $J_I = J_a(2)$ is as discussed in paragraphs No. 1, 2, and 3.

A similar procedure for aluminum arrestors may require an added provision for kinetic energy return since the dynamic elevation of the J -curve may be too small to accommodate it. The proposed procedure is intended to serve as a starting point for further discussion. Clearly, as a design approach, it requires careful scrutiny and should be critically tested before adoption. Values of $J_a(2)$ and corresponding estimates of the crack stopping capabilities of several steels derived from the proposed procedure are listed in Table 2.

⁸ It can be shown that a small crack propagating in a large brittle plate with negligible fracture energy dissipation will penetrate a tough arrestor a distance $\Delta a/a = 0.053$ when all of the strain energy released is returned to the crack tip provided the dynamic toughness of the arrestor is 10 times the value of $J_a(2)$ at the location of the stopped crack and LEFM conditions prevail. This penetration appears to be an upper bound for the assumed tenfold elevation of dynamic toughness, which is assumed to apply to other tough, ductile, arrestor grade steels.

TABLE 2—*Compilation of crack arrest toughness values of selected steel and an aluminum alloy for temperature producing fibrous crack extension in the arrestor.*

Material	Test Temperature, °C	σ_0 , MPa	Charpy V-Notch, J	J_{IC} , kJ/m ²	$J_a(2)$, kJ/m ²	Crack Arrest Capability, $2a$, mm ^a	Reference
HY-130	RT ^b	937	112, 116	160	258	155	22
HY-130	25	902	80	172	23
HY-130	RT	882	152	268	643	440	24
HY-80	RT	558	...	156	324	550	22
HY-80	RT	616	110	146	14
A533B(02)	149	413	176	207	523	1620	22, 25
A533B(03)	149	401	87	197	363	1190	22
A516-G70	149	303	137	156	324	1860	22
A106	RT	345	...	166	550	2420	14
7075 aluminum	RT	280	...	88	105	235	10
7075 aluminum	RT	552	...	45	45	26	10

^a Length of a centrally located crack $2a$ that can be stopped by long, nominally elastic arrestors, $\sigma = 0.5 \sigma_0$ (σ_0 is the yield stress), located on either side of the crack: $2a = 2/\pi [K_{IC}(2)/\sigma]^2$.

^b Room temperature.

Conclusions

1. Effects of the prior plastic deformation history on the shape of the J -resistance curve have been examined with a finite-element model. The calculations reveal that history effects can be neglected when the toughness ratio J_{Ic} (starter)/ J_{Ic} (arrestor) ≤ 0.1 or K_{Ic} (starter)/ K_{Ic} (arrestor) ≤ 0.3 .
2. Experiments employing a special fast-fracture device show that very large dynamic elevations of the J -resistance curve are encountered during the arrest of fast propagating cracks in tough, ductile arrestors. The measurements point to an 18-fold and 3.6-fold increase in the level of the J -curve for steel and an aluminum alloy, respectively.
3. The dynamic elevation of the J -curve for fibrous crack extension in a tough steel may be large enough to consume any kinetic energy which is returned to the crack during arrest.
4. The findings suggest that a relatively simple J -based procedure may be adequate for assessing or designing tough, welded-in steel crack arrestors.

Acknowledgments

The authors wish to acknowledge the contribution of Mengke Zhu, who participated in the design of the fast fracture device. They are grateful to Hibbitt, Karlsson, and Sorensen, Inc., for permission to use their excellent nonlinear finite-element code ABAQUS. They also wish to thank C. Thompson for her work on the manuscript. The work has been supported by the U.S. Office of Naval Research, Structural Mechanics Division, under Contract No. N00014-80C-0521. The authors wish to thank Dr. Y. Rajapakse of the Office of Naval Research for his support and assistance.

References

- [1] Williams, M. L. in *Symposium on Effect of Temperature on the Brittle Behavior of Metals with Particular Reference to Low Temperatures*, ASTM STP 158, American Society for Testing and Materials, Philadelphia, 1954, p. 11-41.
- [2] Robertson, T. S., *Journal of the Iron and Steel Institute*, Vol. 175, 1953, p. 361.
- [3] Pellini, W. S., *Principles of Structural Integrity Technology*, Office of Naval Research, Arlington, VA, 1976.
- [4] Rolfe, S. T., Rhea, D. M., and Kuzmanovic, B. O., "Fracture-Control Guidelines for Welded Steel Ship Hulls," Ship Structure Committee Report SSC-244, National Academy of Sciences, Washington, DC, 1974.
- [5] Krafft, J. M. and Irwin, G. R. in *Applied Fracture Mechanics*, ASTM STP 381, American Society for Testing and Materials, Philadelphia, 1965, p. 114-129.
- [6] Hahn, G. T., Rosenfield, A. R., Marshall, C. W., Hoagland, R. G., Gehlen, P. C., and Kanninen, M. F. in *Fracture Mechanics*, N. Perrone et al., Eds., University Press of Virginia, Charlottesville, VA, 1978, pp. 205-227.
- [7] Hoagland, R. G., Rosenfield, A. R., Gehlen, P. C., and Hahn, G. T. in *Fast Fracture and Crack Arrest*, ASTM STP 627, G. T. Hahn and M. F. Kanninen, Eds., American Society for Testing and Materials, Philadelphia, 1977, pp. 107-202.
- [8] Pellini, W. S. and Puzak, P. P., "Fracture Analysis Diagram Procedures for the Fracture-Safe Engineering Design of Steel Structures," Report 5920, U.S. Naval Research Laboratory, Washington, DC, 1963.
- [9] Kanninen, M., Mills, E., Hahn, G., Marschall, C., Broek, D., Coyle, A., Masabushi, K., and Ituga, K., "A Study of Ship Hull Crack Arrestor Systems," Ship Structure Committee Report SSC-265, National Academy of Sciences, Washington, DC, 1976.
- [10] Dantam, V. and Hahn, G. T. in *Proceedings of the U.S.-Japan Cooperative Seminar*, T. Kanazawa, et al., Eds., Toyoprint Co., Tokyo, Japan, 1981, pp. 213-220.
- [11] Hutchinson, J. W. and Paris, P. C. in *Elastic-Plastic Fracture*, ASTM STP 668, American Society for Testing and Materials, Philadelphia, 1979, p. 37-64.

- [12] Kalthoff, J. F., Beinert, J., and Winkler, S. in *Fast Fracture and Crack Arrest*, ASTM STP 627, American Society for Testing and Materials, Philadelphia, 1977, p. 161-176.
- [13] Hoff, R., "Viscoplastic Finite-Element Analysis of Rapid Fracture," Ph.D. dissertation, Vanderbilt University, Nashville, TN, 1984.
- [14] Joyce, J. A., "Static and Dynamic J - R Curve Testing of A533B Steel Using the Key Curve Analysis Technique," Report NUREG/CR-2274, Nuclear Regulatory Commission, Washington, DC, 1981.
- [15] Joyce, J. A. and Hackett, E. M., "The Application of the Key Curve and Multi-Specimen Techniques to Dynamic J - R Curve Testing of Alloy Steel," Report NUREG/CR-4579, Nuclear Regulatory Commission, Washington, DC, 1986.
- [16] Bastias, P., "Finite-Element Analysis of Crack Growth and Arrest," M.S. dissertation, Vanderbilt University, Nashville, TN, 1986.
- [17] Hoff, R., Rubin, C. A., and Hahn, G. T. in *Fracture Mechanics: Sixteenth Symposium*, ASTM STP 868, American Society for Testing and Materials, Philadelphia, 1985, p. 409-430.
- [18] Hoff, R., Rubin, C. A., and Hahn, G. T., *Engineering Fracture Mechanics*, Vol. 23, 1986, p. 105-118.
- [19] Kumar, A., "Analysis of Crack Arrest Toughness Measurement for Design of Tough Materials," M.S. dissertation, Vanderbilt University, Nashville, TN, 1985.
- [20] Kumar, V., German, M. D., and Shih, C. F., "An Engineering Approach for Elastic-Plastic Fracture Analysis," Electric Power Research Institute Report NP-1931, Electric Power Research Institute, Palo Alto, CA, 1981.
- [21] Kumar, V. German, M. D., Wilkening, W. W., Andrews, W. R., deLorenzi, H. G., and Mowbray, D. F., "Advances in Elastic-Plastic Fracture Mechanics," Electric Power Research Institute Report NP-3607, Electric Power Research Institute, Palo Alto, CA, 1984.
- [22] Gudas, J. P., Vassilaros, M. G., Joyce, J. A., Davis, D. A., and Anderson, D. R., "A Summary of Recent Investigations of Compact Specimen Geometry Effects on the J - R Curve of High-Strength Steels," Report NUREG/CR-1813, Nuclear Regulatory Commission, Washington, DC, 1980.
- [23] Joyce, J. A. and Hasson, D. F., "Characterization of Transition Temperature Behavior of HY-130 Steel by the J_{IC} -Fracture Toughness Parameter," *Engineering Fracture Mechanics*, Vol. 13, 1980, p. 417.
- [24] Hasson, D. F. and Joyce, J. A., "The Effect of a Higher Loading Rate on the J_{IC} -Fracture Toughness Transition Temperature at HY-Steels," *Journal of Engineering Materials and Technology*, Vol. 103, 1981, p. 133-141.
- [25] Wessel, E. T., "Linear Elastic Fracture Mechanics for Thick-Walled, Welded Steel Pressure Vessels, Material Property Considerations," *Practical Fracture Mechanics for Structural Steel*, P. H. M. O. Dobson, Ed., United Kingdom Atomic Energy Agency, London, UK, 1969.

Albert S. Kobayashi,¹ A. F. Emery,¹ W. J. Love,¹ Y.-H. Chao,² and O. Johansson²

Ductile Crack Bifurcation and Arrest in Pressurized Pipe

REFERENCE: Kobayashi, A. S., Emery, A. F., Love, W. J., Chao, Y.-H., and Johansson, O., "Ductile Crack Bifurcation and Arrest in Pressurized Pipe," *Fracture Mechanics: Nineteenth Symposium, ASTM STP 969*, T. A. Cruse, Ed., American Society for Testing and Materials, Philadelphia, 1988, pp. 441–465.

ABSTRACT: This paper presents selected results on ductile crack propagation, curving and branching, and crack arrest from ten dynamic pipe rupture tests. Strain gage results adjacent to the crack path showed that a Dugdale-Barenblatt strip yield zone, of the order of eight pipe diameters in length, preceded the propagating crack tip and that the maximum principal strain direction changed from the hoop to the axial direction approximately 6 to 8 pipe diameters downstream of the crack tip. This change in principal strain direction constitutes the sufficiency condition for crack curving or branching prior to crack arrest in the absence of a crack arrester. The necessary condition for crack arrest is the sudden and sufficient increase in fracture resistance due to either increased apparent fracture toughness or a pipe opening restraint in the crack path.

KEY WORDS: dynamic fracture, crack bifurcation, crack curving, ductile fracture, axial pipe rupture, fracture mechanics

When the first three authors initiated their pipe rupture studies in 1974, the objective was to study the mechanics of crack spiraling, which resulted in the arrest of a rapidly propagating axial crack in a pressurized pipe. In the ensuing 12 years, their research efforts were redirected to the mechanisms of brittle and ductile circumferential and axial crack propagation in pressurized pipes. Part of this effort resulted in a one-dimensional thermal-hydraulic depressurization code [1] and a ring model of ductile axial crack propagation [2]. While much more is to be learned of the mechanics of axial crack propagation in rupturing pipes, we have recently resurrected our initial objective of 1974, in which the spiraling crack problem of the 1960s has been replaced in the 1970s and 1980s by a crack curving and branching problem prior to crack arrest in ductile gas transmission line pipes. The crack curving and crack branching criteria [3,4], which were developed for brittle material and which were successfully used in a limited analysis of brittle pipe rupture tests [5], are unfortunately no longer applicable to the ductile pipe materials in current use.

In this paper, the authors present some preliminary experimental analysis of crack curving and branching leading to crack arrest in pressurized ductile pipes. These results are preceded by a section on additional experimental results of axial crack propagation and arrest.

¹ Professors, Department of Mechanical Engineering, University of Washington, Seattle, WA 98195.

² Graduate students, Department of Mechanical Engineering, University of Washington, Seattle, WA 98195.

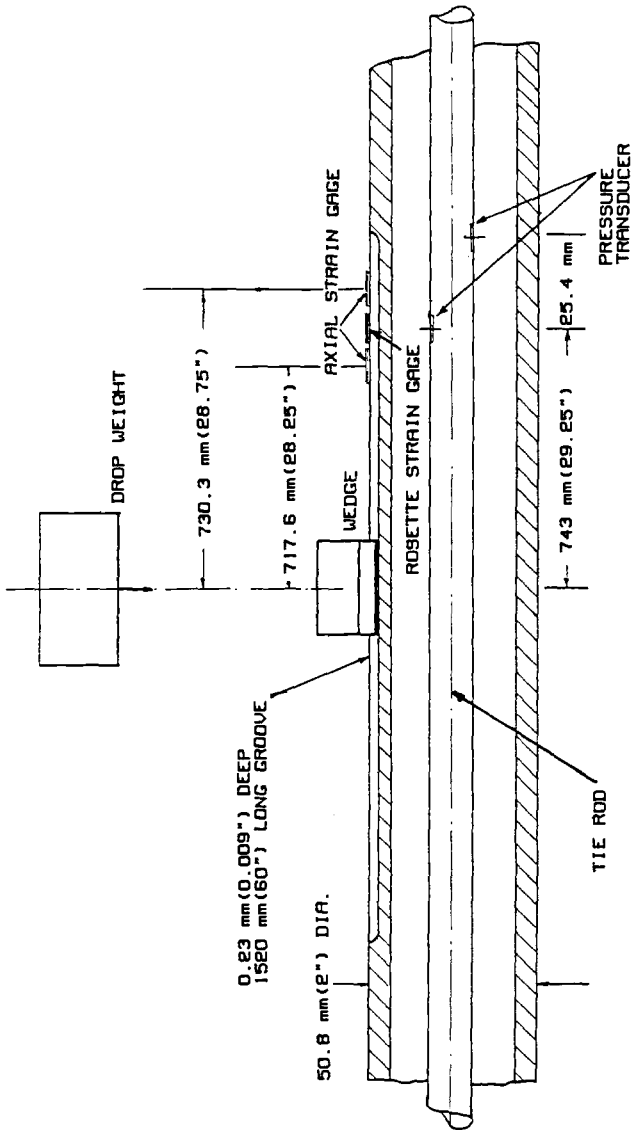


FIG. 1—Pipe burst test.

Dynamic Pipe Rupture Test Setup

Details of the experimental facility, used to measure the crack speed, crack opening shape, axial and circumferential strains, and the gas depressurization rate during burst tests of 6100-mm-length 1010 carbon steel pipes are given in Refs 6 and 7. As shown in Fig. 1, crack propagation was initiated by an electrically triggered 13.6-kg drop weight which impacted a 50.8-mm-wide flat chisel resting on the pressurized pipe. Axial crack propagation was channeled along a 1520-mm-long, 0.23 to 0.38-mm-deep, 60° vee-shaped groove on the outer surface of the pipe which was pneumatically pressurized to about 80% of its yield strength. The machined groove was necessary to initiate and maintain axial crack propagation in the thin-wall ductile pipe, which would otherwise have caused the crack to bifurcate or curve and arrest.

Two postyield strain gages, which were oriented in the axial direction along the groove, were located on both sides of a postyield strain gage rosette, as shown in Fig. 1, with the midleg of the rosette being oriented perpendicular to the groove. The axial gages were used to check the axial strains computed from the strain gage rosette readings as well as to measure the crack speed by observing the passage of the crack tip past these strain gages.

Two pressure transducers were located 25.4-mm apart in a hollow tie rod at one end of the groove as shown in Fig. 1. The average crack velocity between these two pressure transducers was determined from the transit time between the knees of the two depressurization curves [6,7].

The data recording system consists of a master and three slave units of Biomation Model 2805 transient recorders which provide eight channels of eight-bit data word. These data were transcribed onto a floppy disk through a Kaypro II eight-bit microcomputer.

Transient crack-opening profiles on the instrumented side of the pipe were recorded by a Redlake HyCam motion picture camera with a maximum framing rate of 8000 frames/s. Because of the relatively long start-up time of the Redlake camera, that is, of the order of 800 ms, the pipe rupture event was triggered through the camera.

Results

A total of ten additional pipe rupture tests were conducted since last reported [8]. These test results are summarized in Table 1. In the following, typical test results are presented and compared with numerical results where applicable.

Photographs of Crack Arrest

Figure 2 shows a sequence of high-speed photography recordings of crack bifurcation and arrest at the groove end. For this case, crack bifurcation occurred about 6.4 mm beyond the 0.38-mm-deep groove end in the ungrooved original thickness of the pipe. Figure 3 shows the postarrest photographs with crack bifurcation at one end of the two groove ends.

The sequential high-speed photographs were used to compute the crack velocities as well as to measure the crack-tip opening angles (CTOA) while the crack was travelling in the grooved and ungrooved sections of the pipe. Figure 4 shows a typical crack velocity history in the vicinity of the groove end. A precipitous drop in the crack velocity, as the crack tip entered the ungrooved section of the pipe, is followed by crack arrest. Figure 5 shows the slight variations in the crack-tip opening angles (CTOA) with variations in the crack velocities in six pipe rupture tests. Figure 6 shows the CTOA variations with crack velocities in the grooved and ungrooved sections in two pipe rupture tests. Note that the larger CTOA are associated with the lower crack velocity in the ungrooved section. The crack propagated

TABLE 1—Summary of pipe burst test results.

Test No.	Groove Depth, mm (in.)	Initial Pressure, KPa (psi)	Crack Velocity, m/s (ft/s)	Recorded Maximum Strain, %	Change in Principal Strain Direction	Crack Arresters
L30	0.38 (0.015)	6900 (1000)	251 (825)	2.6	NA ^a	none
L31	0.38 (0.015)	6900 (1000)	291 (955)	NA	NA	none
L32	0.38 (0.015)	6900 (1000)	301 (988)	2.6	8.5 D ^b	none
L33	0.38 (0.015)	6900 (1000)	232 (760)	4.0	NA	added weight
L34	0.38 (0.015)	6900 (1000)	279 (915)	4.0	NA	added weight
L35	0.23 (0.009)	7850 (1100)	219 (719)	3.5	8.0 D	added weight
L36	0.23 (0.009)	7850 (1100)	183 (601)	3.8	6.0 D	added weight
L37	0.25 (0.010)	7850 (1100)	230 (754)	2.5	6.0 D	two hose clamps
L38	0.23 (0.009)	7850 (1100)	227 (746)	6.0	8.5 D	two hose clamps
L39	0.30 (0.012)	7850 (1100)	244 (799)	6.0	6.0 D	two hose clamps

^a NA stands for not applicable.^b D denotes pipe diameter.

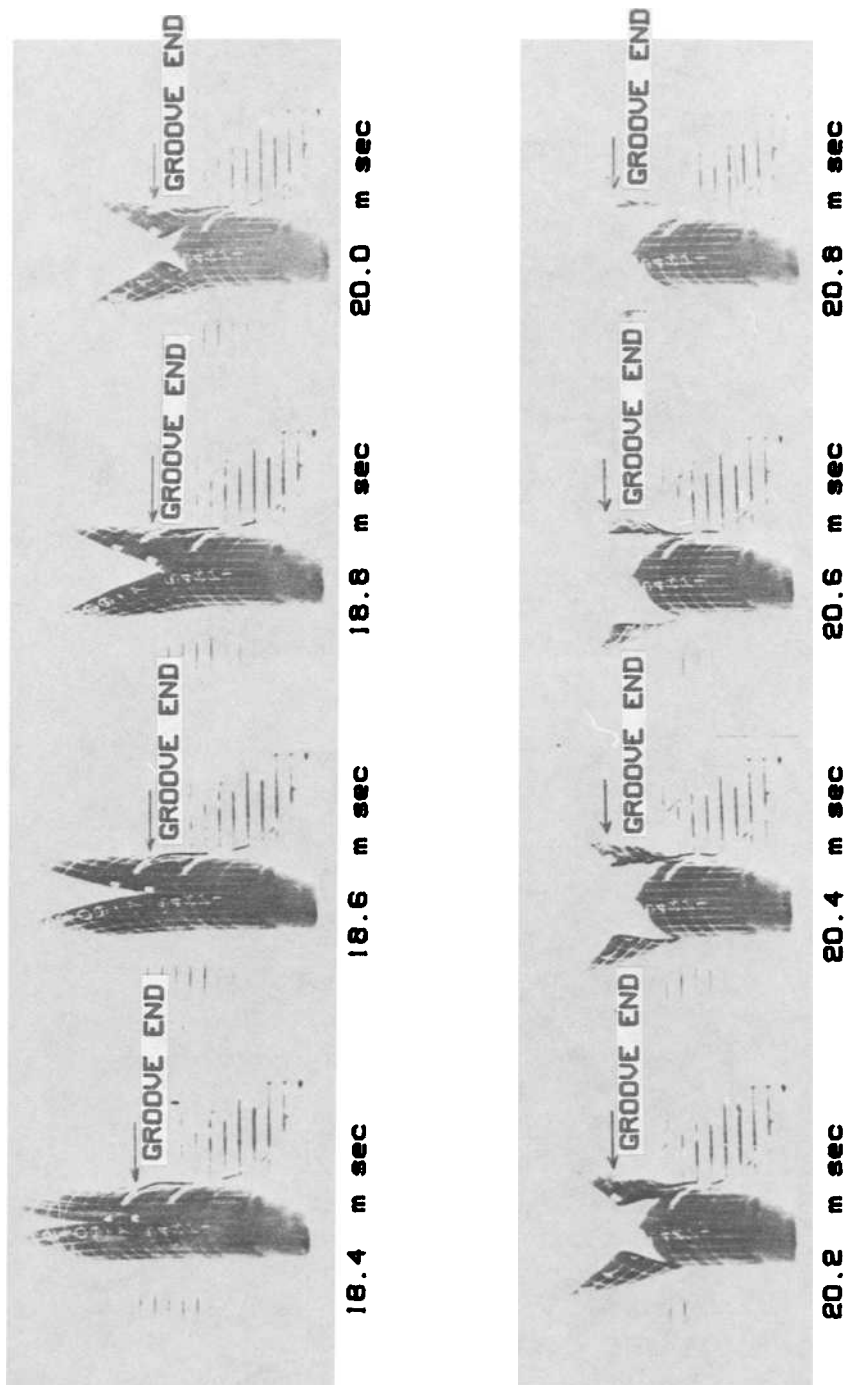


FIG. 2—Crack arrest and bifurcation at 6.35 mm downstream of the groove end. Test No. L30: groove depth 0.38 mm and pressure 6900 kPa.

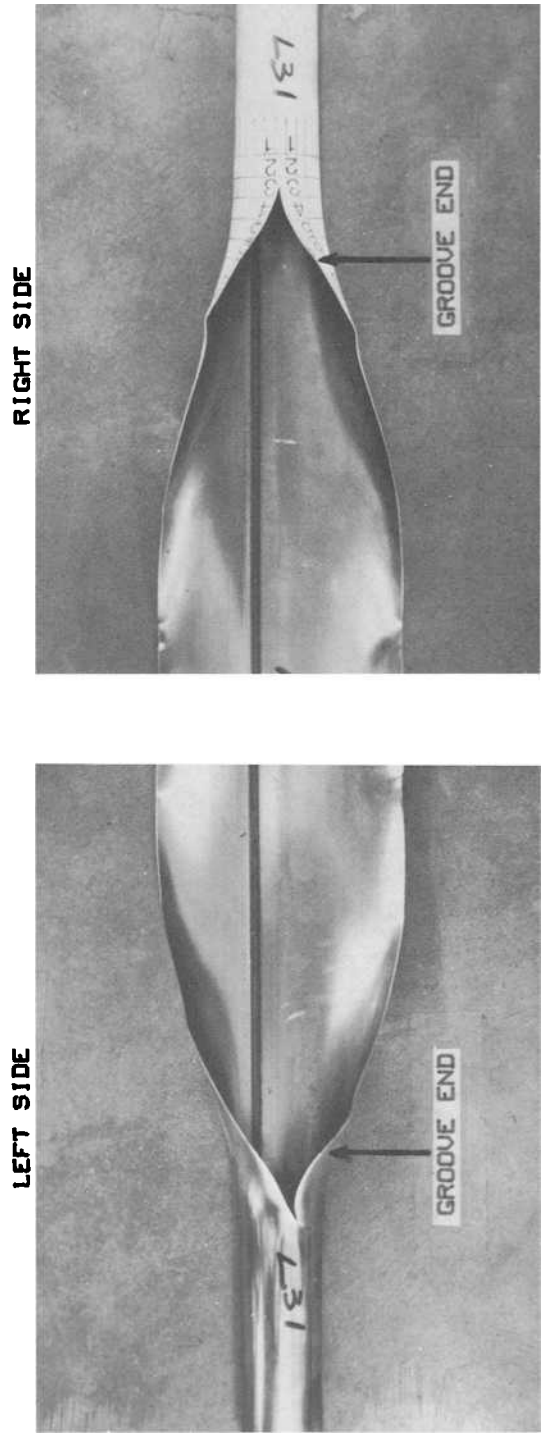


FIG. 3—Postfracture pictures at two groove ends. Test No. L30: groove depth 0.38 mm and pressure 6900 kPa.

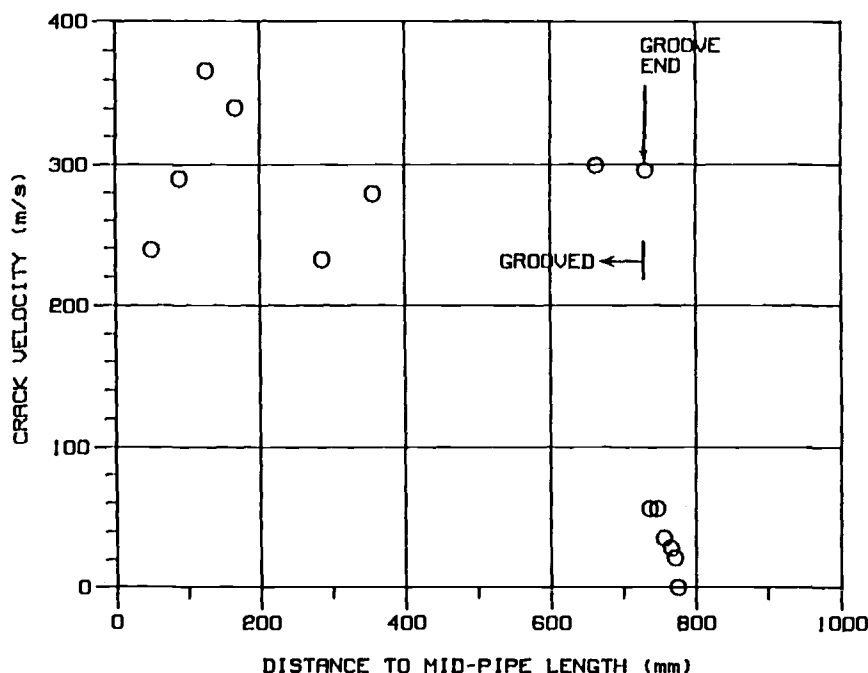


FIG. 4—Variation in crack velocity. Test No. L33: groove depth 0.38 mm and pressure 6900 kPa.

along the shallower groove of 0.23 mm at a lower crack velocity than it did along the deeper groove of 0.38 mm.

Depressurization Results

Figures 7 and 8 show two typical depressurization traces recorded at the groove end. While these traces are similar to those reported previously [6,7,8], they differ in that complete depressurization is not achieved within the recorded 5 ms period during which time the crack arrested shortly after passing over the two pressure transducers. The downstream transducer, which is closer to the arrested crack tip and which is facing the closed pipe wall opposite to the crack breach, recorded a higher pressure. The theoretical pressure traces, which are computed for a constant velocity crack using a thermal-hydraulic code [1], are also shown in Figs. 7 and 8 for comparison. As was the case in previous papers, the thermal-hydraulic code predicts within reasonable accuracy the depressurization history, including the arrival of the crack tip and the depressurization rates, for given crack velocities. Figure 9 shows a slight decrease in depressurization rate with an increase in the crack velocity.

Strain Gage Results

Figure 10 shows the strain traces of a strain gage rosette at 25.4 mm upstream of the groove and the computed maximum strain trace. Since the yield strain of this pipe material is approximately 0.0013, the perceptible strain record in Fig. 10 indicates that the yield strain is attained along the groove well in advance of the arrival of the crack tip. The passage

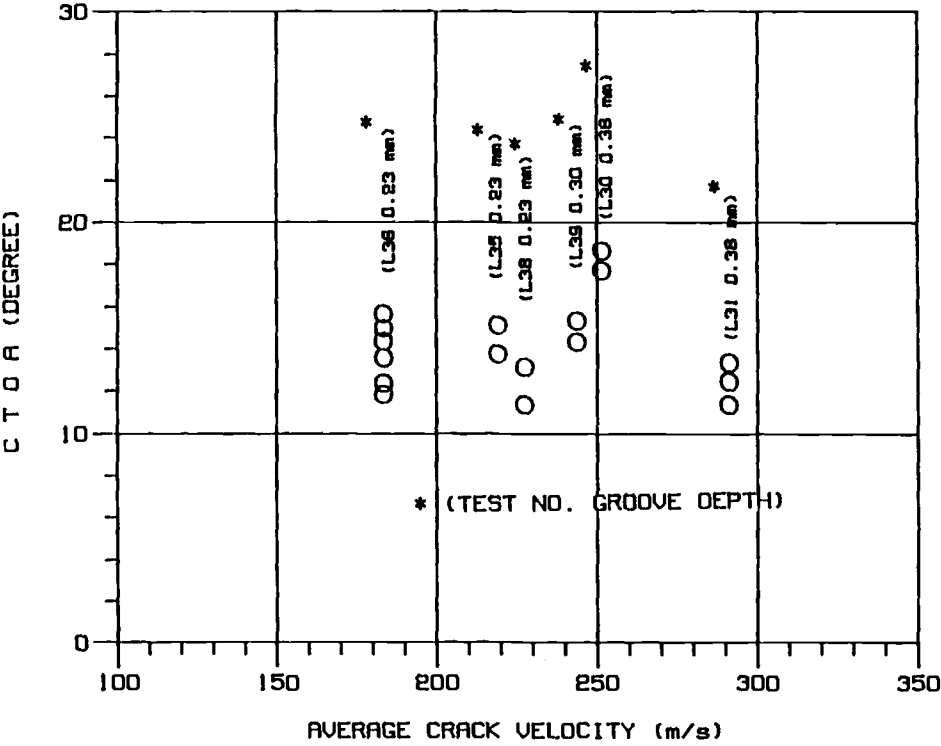


FIG. 5—CTOA variation with crack velocity.

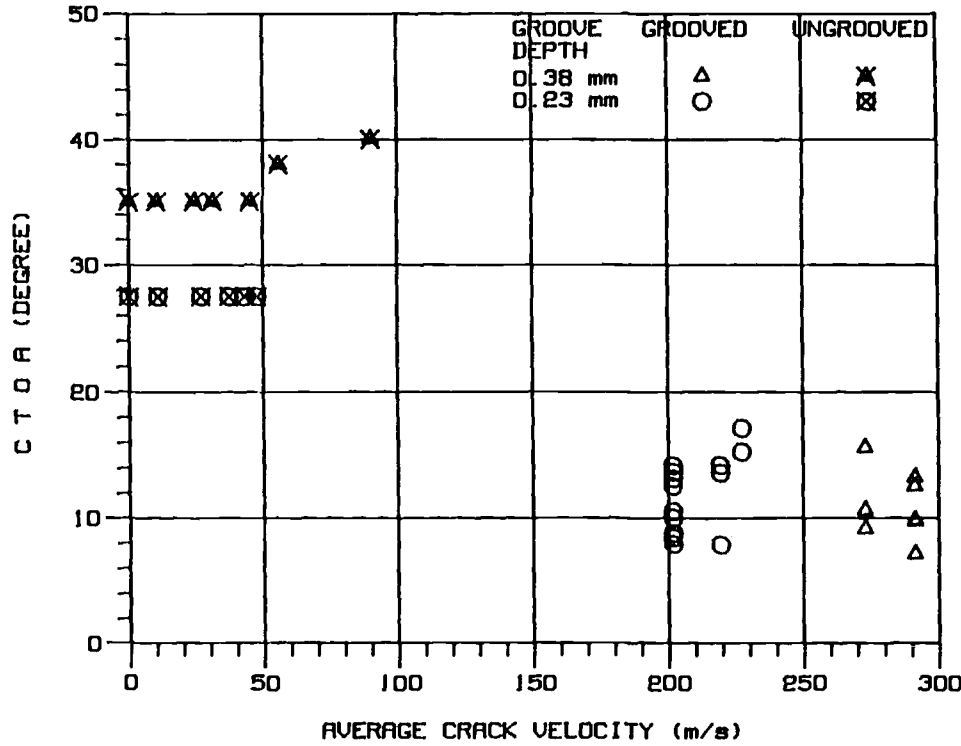


FIG. 6—CTOA variation with velocity along the groove and beyond the groove end.

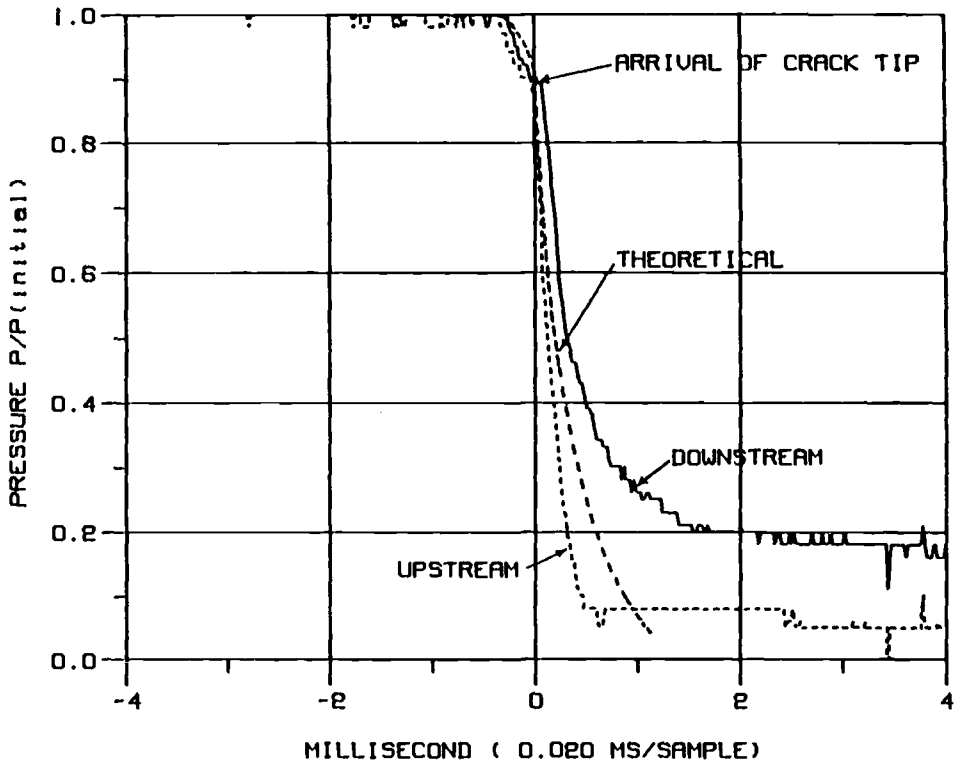


FIG. 7—Depressurization at 19 mm upstream of crack arrest and bifurcation. Test No. L32: groove depth 0.38 mm and pressure 6900 kPa.

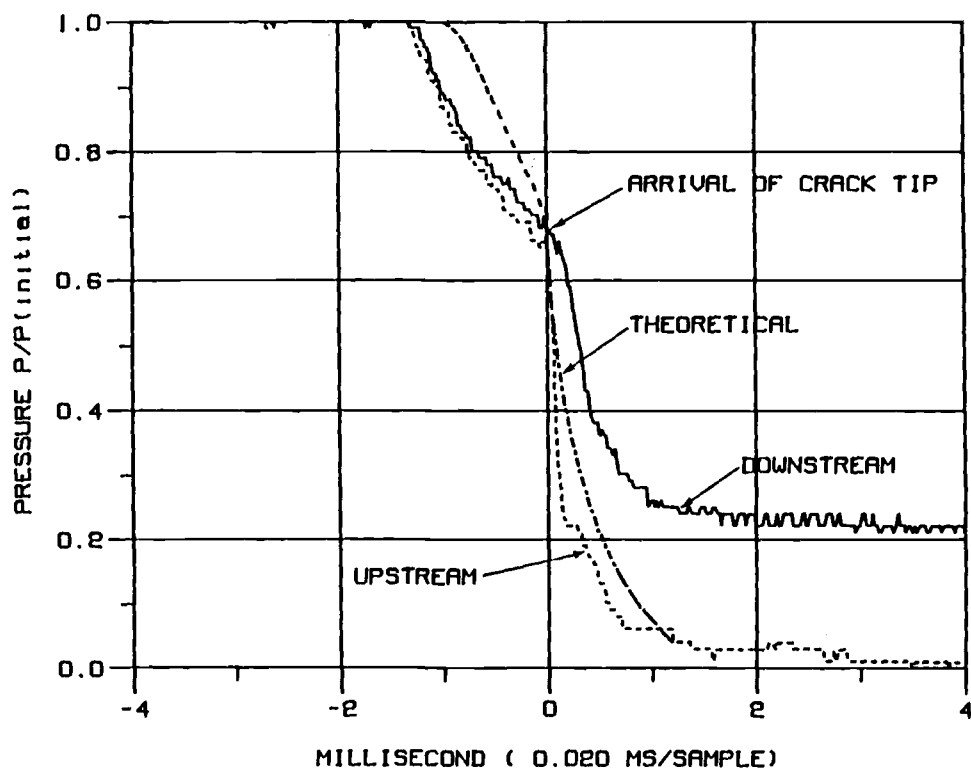


FIG. 8—Depressurization at 25.4 mm upstream of the right side groove end. Test No. L35; groove depth 0.23 mm and pressure 7850 kPa.

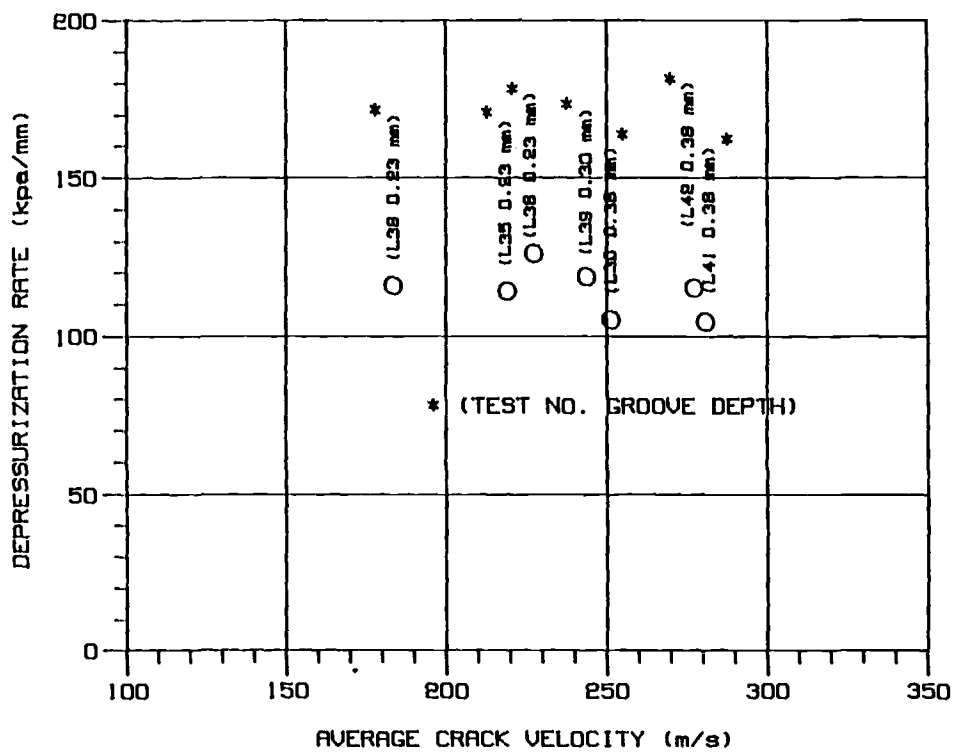


FIG. 9—Depressurization rate versus crack velocity.

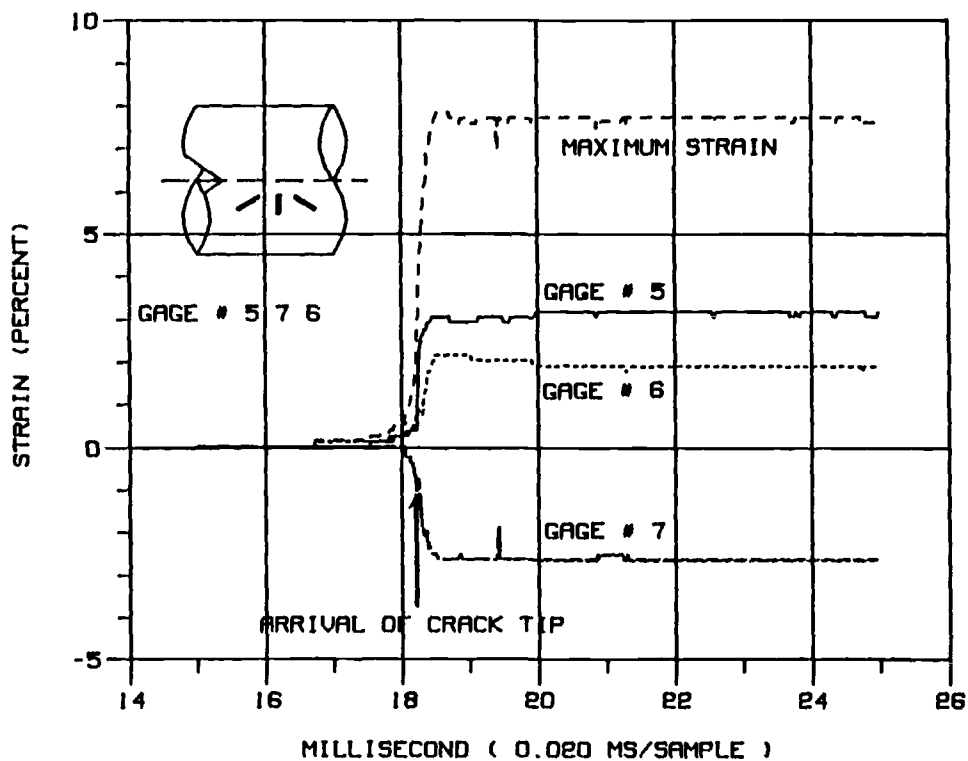


FIG. 10—Variations in strains at 19 mm upstream of crack arrest and bifurcation. Test No. L32: groove depth 0.38 mm and pressure 6900 kPa.

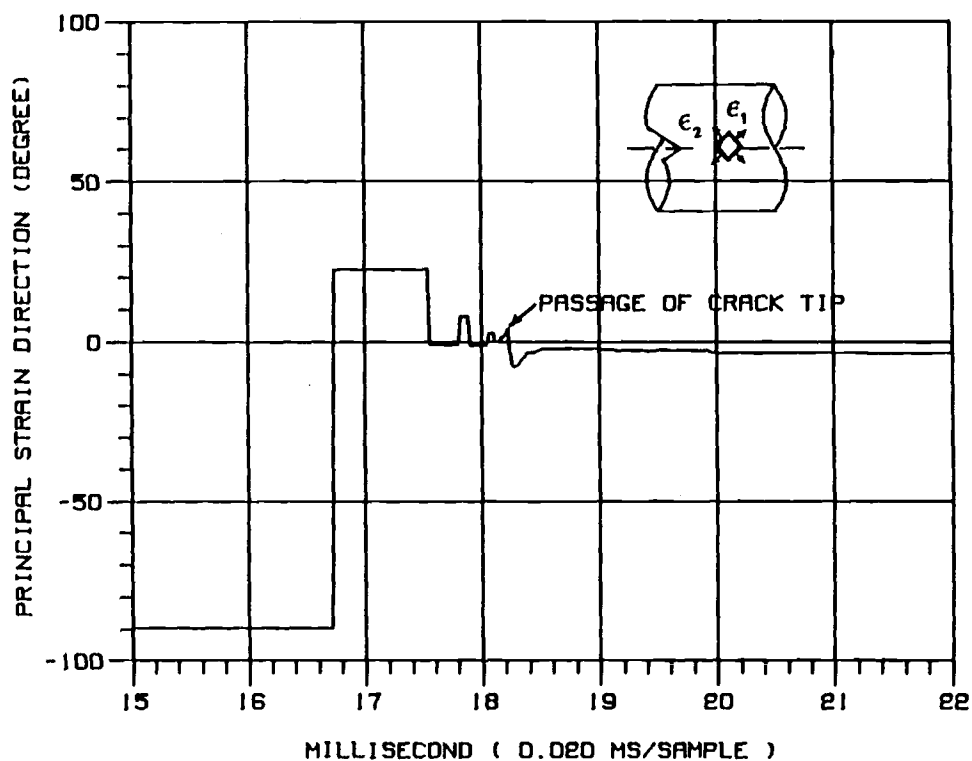
of the crack tip through the strain rosette was estimated from the recorded arrival time of the crack tip at the two pressure transducers and the associated average crack velocity. Figure 11 shows the associated change in the maximum strain direction from the hoop to the axial direction at eight and one-half pipe diameters downstream of the propagating crack tip. The abrupt fluctuations in the principal strain directions in this figure are an artifact caused by the relative insensitivity of the digital transient recording, which was programmed to record the large postyield strains, to the smaller initial elastic-plastic strains. Figures 12 and 13 show similar strain records for tests with a shallower groove. The maximum strain direction changed from the hoop to the axial direction eight pipe diameters ahead of the propagating crack tip in Test No. L35. Figure 14 shows the directional change, which occurred six pipe diameters downstream of the propagating crack tip, of the maximum strain from the hoop to the axial directions in Test No. L39. Similar strain rosette results for three other tests together with the above three are listed in Table 1. The recorded maximum strains in Table 1 are oriented in the axial direction, as shown in Figs. 10 and 12, and were attained shortly after the passage of the crack tip.

Crack Arrest Tests

The photographic records of the instrumented side of the rupturing pipe showed that the rapidly propagating crack arrests shortly after entering the ungrooved section of pipe. Figure 3 shows that such crack arrest was preceded by either crack branching or crack curving and that the sudden increase in the fracture resistance of the ungrooved section was the necessary condition for crack arrest. Although the maximum principal strain immediately ahead of the crack tip was oriented in the axial direction, as shown by Figs. 10 through 14, the reduced fracture resistance along the machined groove caused the crack to propagate axially under the minimum strain condition. When the crack tip entered the ungrooved pipe section, however, the isotropic state of fracture resistance allowed the crack tip to veer towards the hoop direction or perpendicular to the maximum principal strain direction. Countering this trend for crack rotation is the geometric constraints imposed by the two spreading crack flaps, which forces the crack tip to continue to propagate in the axial direction. The latter obviously is a function of time and thus crack bifurcation and arrest is associated with the faster cracks.

Since the outward motion of the crack flaps is induced by the kinetic energy stored in the flaps, it stands to reason that this outward motion could be reduced either by increasing the inertia of the flaps or by restricting the flap motions by imposed geometric constraints. Thus, two types of mechanical crack arresters, based on the concepts of inertia augmentation and geometric constraints, were installed near the midportion of the half-length of the pipe. One such crack arrester was modeled after that used by Shoemaker et al. [9], where sheet lead weights were attached to the pipe wall to serve as mass augmentation to the crack flaps. In Test No. L33, three masses of 23 g each, which effectively increased the wall mass density by a factor 17.6 for a pipe length of 150 mm, were added to both sides of the pipe as shown in Fig. 15. While the mass augmentation had a definite influence on the flap opening shape, as seen in Fig. 15 by the restricted breach opening where the masses were attached, the crack continued to propagate past the added weights along the 0.38-mm groove prior to being arrested in the ungrooved section. The same weights attached to a pipe with a shallow groove of 0.23 mm in depth arrested the crack in the grooved section about one-half pipe diameter beyond the added weights as shown in Fig. 16. These limited results indicate that mass augmentation only marginally arrested the propagating cracks.

Figures 17, 18, and 19 show how the crack could be arrested by pairs of pipe clamps. These pipe clamps provided a more rigid geometric constraint to the pipe flap than that



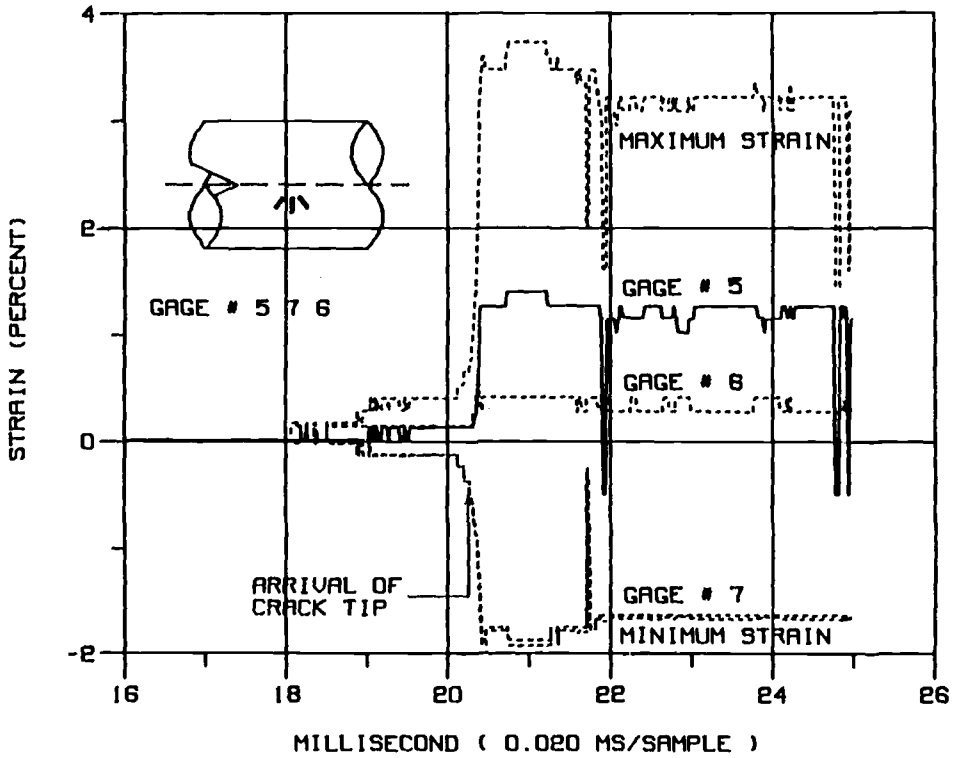


FIG. 12—Variations in strains at 25.4 mm upstream of the right side groove end. Test No. L35; groove depth 0.23 mm and pressure 7850 kPa.

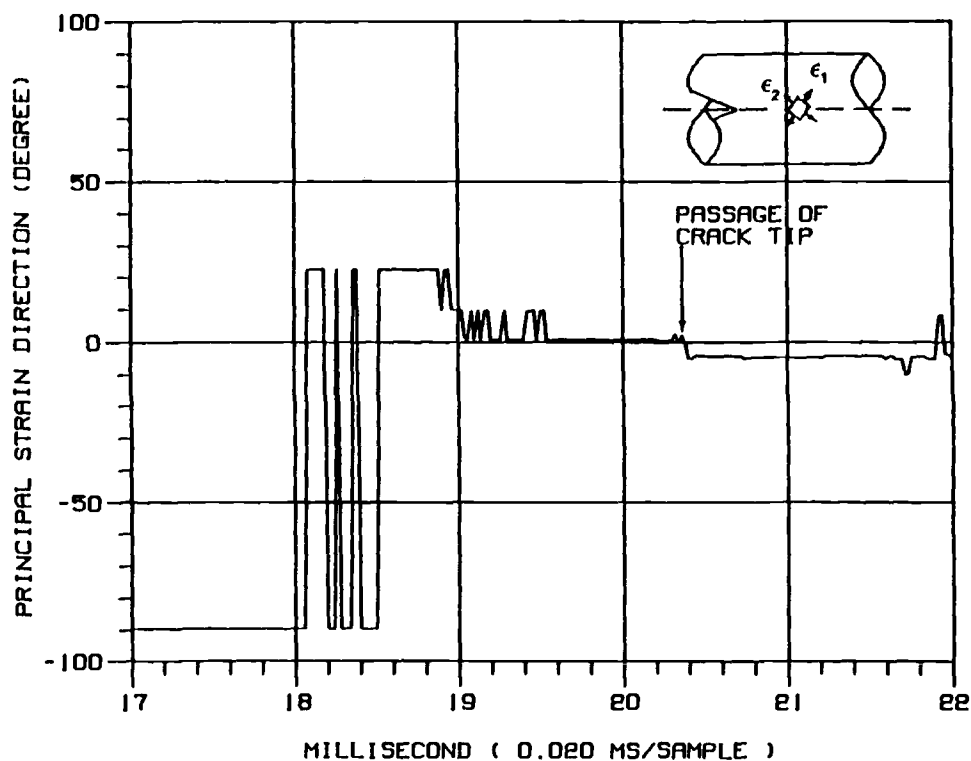


FIG. 13—Variation in principal strain direction. Test No. L35: groove depth 0.23 mm and pressure 7850 kPa.

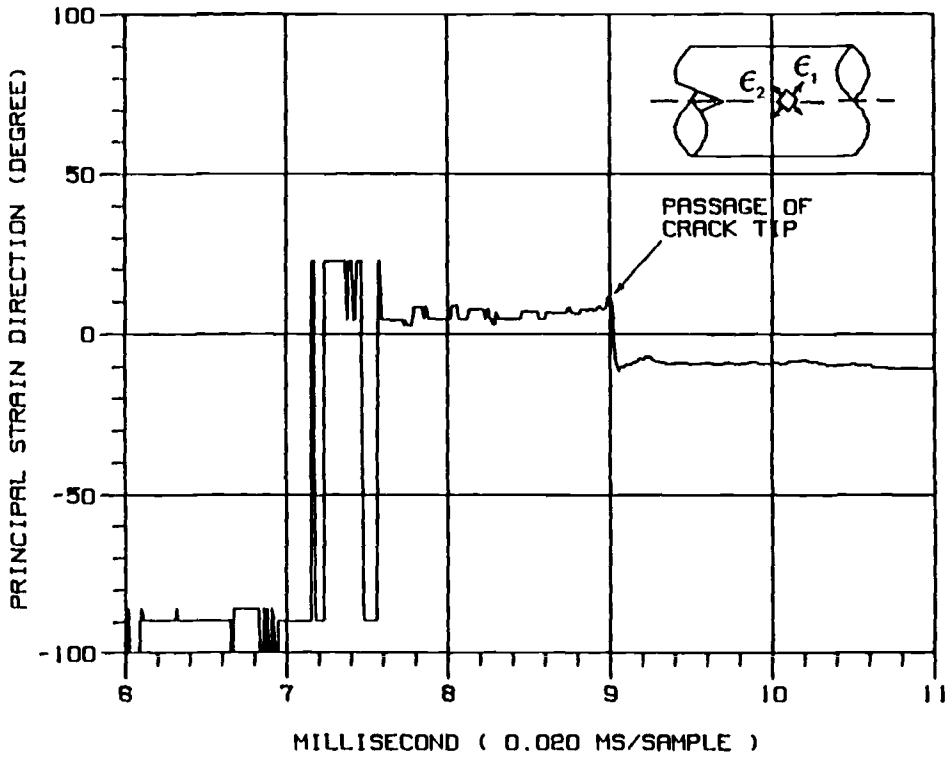


FIG. 14—Variation in principal strain direction. Test No. L39: groove depth 0.30 mm and pressure 7850 kPa.

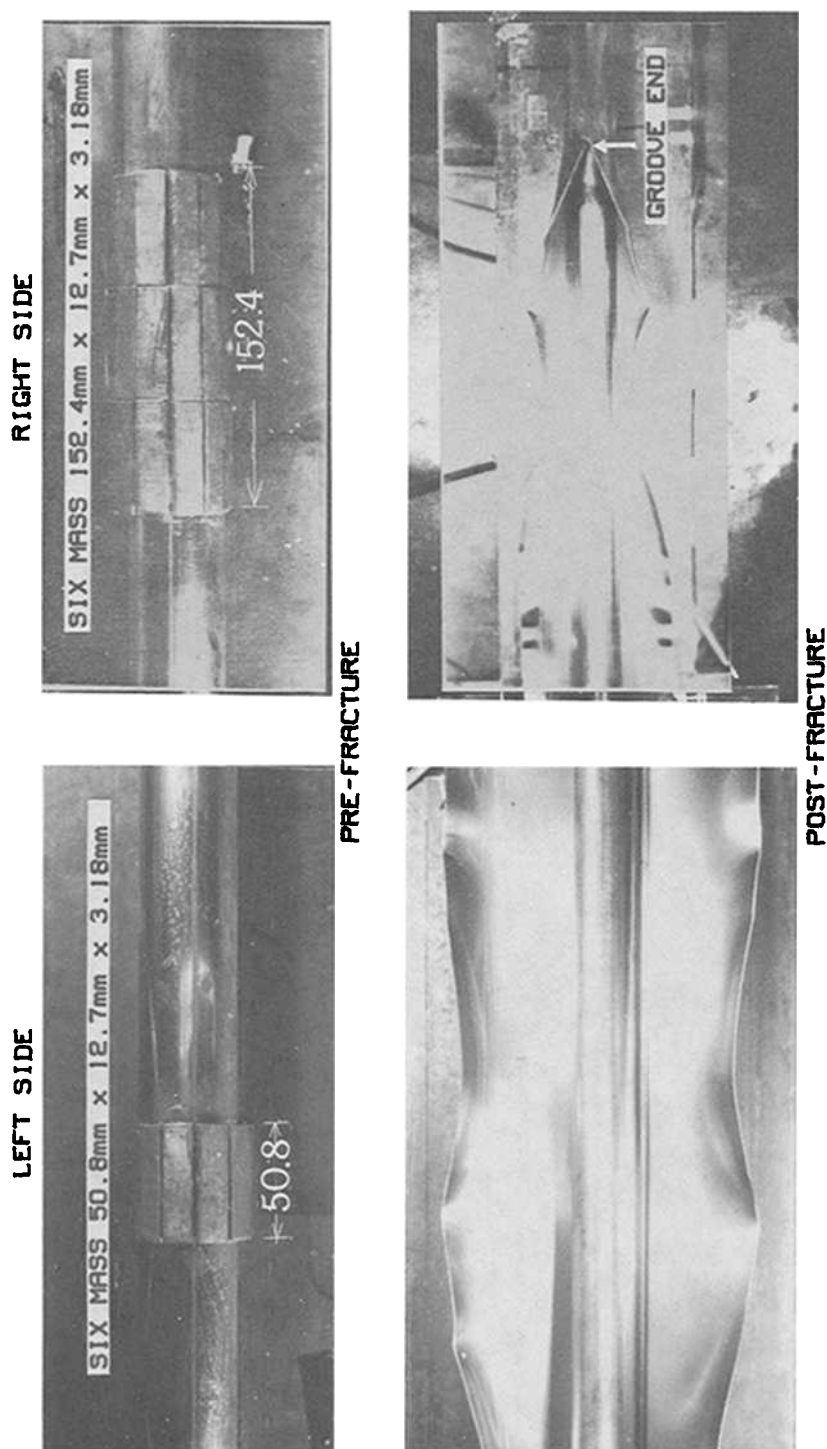


FIG. 15—Added mass as crack arrester. Test No. L33; groove depth 0.38 mm and pressure 6900 kPa.

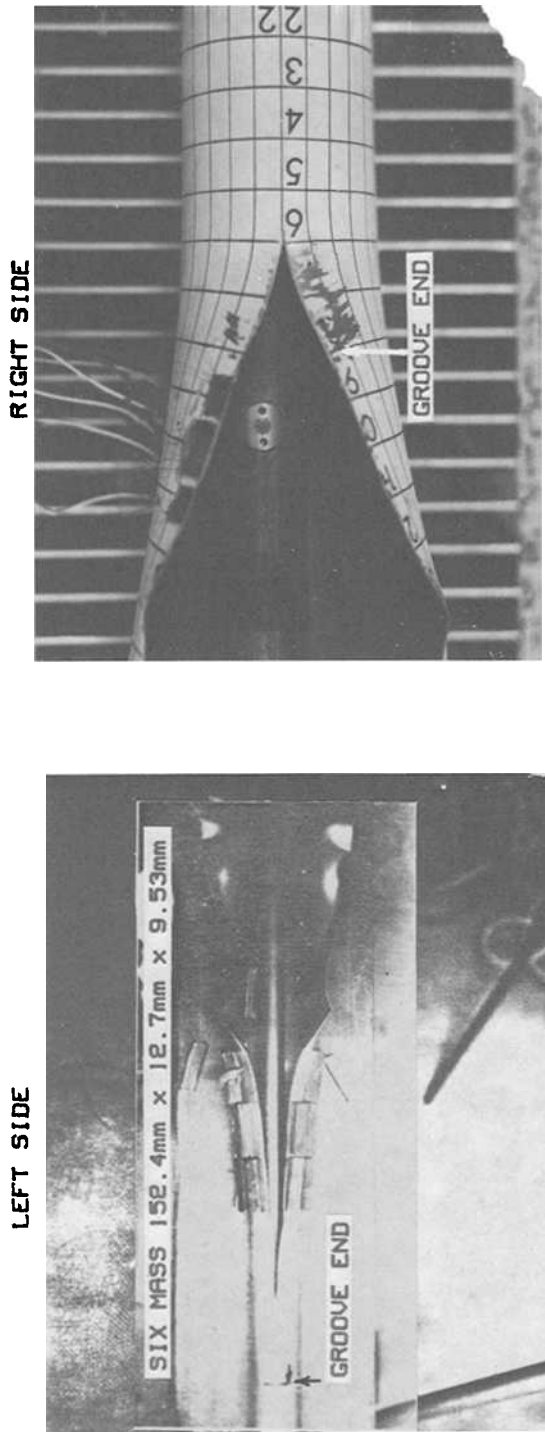


FIG. 16—Postfracture arrest pictures: added mass as arrester on the left side. Test No. L35; groove depth 0.23 mm and pressure 7850 kPa.

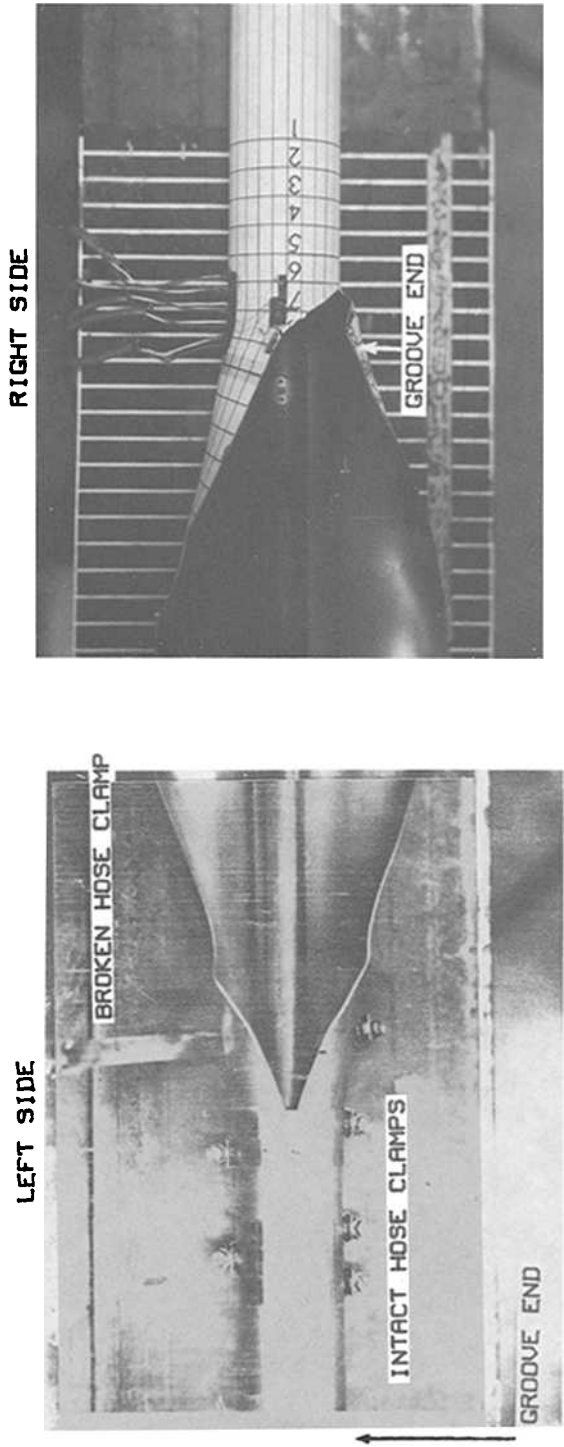


FIG. 17—Hose clamps as crack arrester on the left side. Test No. L37: groove depth 0.25 mm and pressure 7850 kPa.

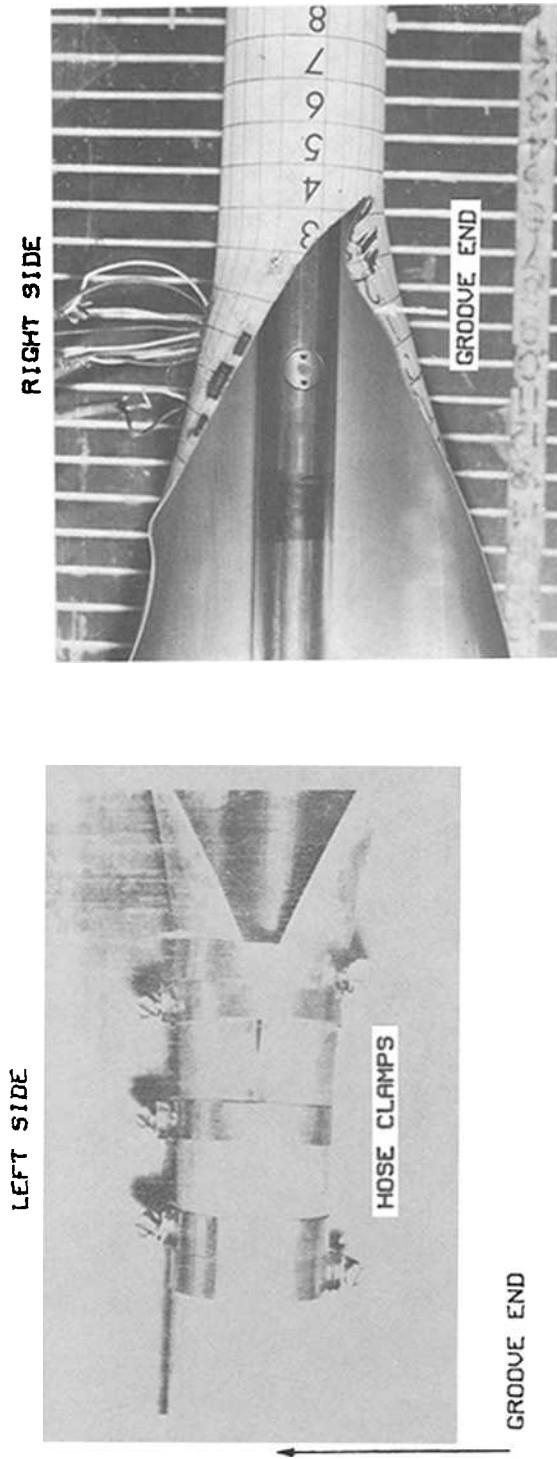


FIG. 18—Hose clamps as crack arrester on the left side. Test No. L38; groove depth 0.23 mm and pressure 7850 kPa.

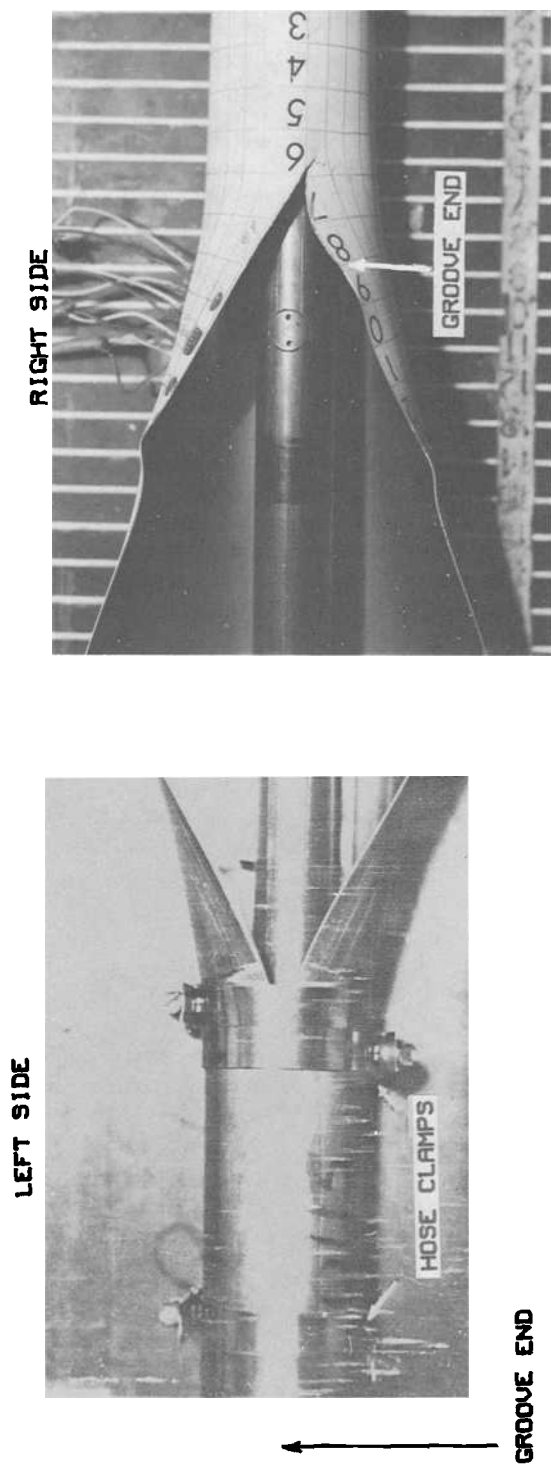


FIG. 19—Hose clamps as crack arrester on the left side. Test No. L39; groove depth 0.30 mm and pressure 7850 kPa.

imposed by the rope crack stopper [10]. Figure 17 shows that sufficient kinetic energy was absorbed by the first broken clamp so that the crack arrested at the second clamp, which was located one-half pipe diameter downstream from the first clamp. Figure 18 shows two identical clamps, which were mounted side-by-side on a pipe subjected to the same pressure, where the crack arrested slightly beyond the second clamp. Figure 19 shows that the crack arrested as it entered the second clamp. The varying stages of crack arrest in the three pipes, which were pressurized to the same initial pressure of 7580 KPa, were most likely caused by the increasing fracture resistance due to the decreasing groove depth. Thus, Test No. L 38 with the shallowest groove dissipated more energy during the fracture process and, by virtue of its lower crack velocity, had less kinetic energy to be absorbed by the clamps.

Discussion

The axial strain history is similar to those reported previously [6,7,8] and is in qualitative agreement with that reported by Urednicek [11]. The transition of the maximum principal strain direction from the circumferential to axial directions is consistent with the axial pipe fracture model of Kanninen et al. [12] with the exception that this transition occurs about 6 to 8 pipe diameters downstream of the propagating crack tip. This transition point can be considered the precursor of the spreading pipe flaps, which presumably distort the circular cross section of the pipe into an oval shape, as noted by Ives et al. [13].

Conclusions

The following conclusions, although tentative in nature, are reached as a result of the three tests.

1. The crack-tip opening angle (CTOA) of a rapidly propagating crack does not vary within the velocity range of 150 to 300 m/s. CTOA for an arresting crack propagating at a lower crack velocity is nearly double that of a rapidly propagating crack.
2. The pressure versus displacement rate slightly decreases with the increased crack velocity.
3. The maximum principal strain direction changes from the hoop to the axial directions approximately 6 to 8 pipe diameters downstream of the propagating crack tip. This change in the principal strain directions is the necessary condition for crack curving or branching prior to crack arrest.
4. Crack arrest can be accomplished by geometrically constraining the crack flap motion. Crack arrest by mass augmentation is marginal and can be accomplished only by relatively large mass augmentation.

Acknowledgment

This work was supported by the U.S. Department of Transportation, Research and Special Program Administration, Contract DTRS-5693-C-0009 under the technical direction of Dr. D. Chisholm.

References

- [1] Emery, A. F., Love, W. J., and Kobayashi, A. S., "Dynamic Finite Difference Analysis of an Axially Cracked Pressurized Pipe Undergoing Large Deformation." *Fast Fracture and Crack Arrest*, ASM STP 627, American Society for Testing and Materials, Philadelphia, 1977, pp. 95-108.

- [2] Emery, A. F., Kobayashi, A. S., and Love, W. J., "The Use of the Split Ring in Modeling Ductile Axial Crack Extension in Pipes," *Journal of Pressure Technology*, Vol. 103, No. 2, May 1981, pp. 151-154.
- [3] Sun, Y. J., Ramulu, M., Kobayashi, A. S., and Kang, B. S.-J., "Further Studies on Dynamic Crack Curving," *Developments in Theoretical and Applied Mechanics*, Vol. XI, Y. J. Chang and G. R. Karr, Eds., University of Alabama in Huntsville, Huntsville, AL, 1982, pp. 203-218.
- [4] Ramulu, M., Kobayashi, A. S., Kang, B. S.-J., and Barker, D., "Further Studies of Dynamic Crack Branching," *Experimental Mechanics*, Vol. 23, December 1983, pp. 431-437.
- [5] Ramulu, M., Kobayashi, A. S., and Kang, B. S.-J., "Dynamic Crack Curving and Branching in Pipe-Line," *Journal of Pressure Vessel Technology*, Vol. 104, No. 4, November 1982, pp. 317-322.
- [6] Kobayashi, A. S., Emery, A. F., Love, W. J., Lee, C.-H., Chao, Y.-H., and Place, B. W., "Rapidly Propagating Ductile Cracks in a 2-in. Pressurized Pipe," *Fracture, Fatigue, and Advanced Mechanics*, ASME PVP-Vol. 98-8, American Society of Mechanical Engineers, 1985, pp. 119-123.
- [7] Emery, A. F., Kobayashi, A. S., Love, W. J., Place, B. W., Lee, C.-H., and Chao, Y.-H., "An Experimental and Analytical Investigation of Axial Crack Propagation in Long Pipes," *Engineering Fracture Mechanics*, Vol. 23, No. 1, January 1986, pp. 215-226.
- [8] Kobayashi, A. S., Emery, A. F., Love, W. J., Lee, C.-H., and Chao, Y.-H., "Axial Crack Propagation in a Pressurized Pipe," *Proceedings, PVP Conference and Exhibition*, Chicago, 20-24 July 1986.
- [9] Shoemaker, A. K., McCartney, R. F., and Ives, K. D., "Mechanical Crack-Arrester Concepts for Line-Pipe Applications," *Proceedings, International Conference on Materials Engineering in the Arctic*, American Society for Metals, Metals Park, OH, 27 Sept.-1 Oct. 1976, pp. 298-305.
- [10] Bonomo, F., Bramante, M., and Spedaletti, M., "Ductile Fracture Propagation in Pipelines. Results of Instrumented Full-Scale Burst Tests on 48" and 56" Diameter Pipes for Gas Transmission," *Analytical and Experimental Fracture Mechanics*, G. C. Sih and M. Mirabik, Eds., Sijthoff and Noordhoff, Winchester, MA, 1981, pp. 567-578.
- [11] Uredniecek, M., "Control of Ductile Fracture Propagation in Large Diameter Gas Transmission Pipelines," ASME Preprint 83-WA/PVP-11, American Society of Mechanical Engineers, New York, NY, 1983.
- [12] Kanninen, M. F., Sampath, S. G. and Popelar, C., "Steady State Crack Propagation in Pressurized Pipelines Without Backfill," *Journal of Pressure Vessel Technology*, Vol. 98, 1976, pp. 56-65.
- [13] Ives, K. D., Shoemaker, A. K., and McCartney, R. F., "Pipe Deformation During a Running Shear Fracture in Line Pipe," *Journal of Engineering Materials and Technology, Transactions of the American Society of Mechanical Engineers*, October 1974, pp. 309-317.

William N. Sharpe, Jr.,¹ Zenon Waclawiw,¹ and
Andrew S. Douglas¹

Dynamic Measurement of Crack-Tip Opening Displacement

REFERENCE: Sharpe, W. N., Jr., Waclawiw, Z., and Douglas, A. S., "Dynamic Measurement of Crack-Tip Opening Displacement," *Fracture Mechanics: Nineteenth Symposium, ASTM STP 969*, T. A. Cruse, Ed., American Society for Testing and Materials, Philadelphia, 1988, pp. 466–481.

ABSTRACT: Crack opening displacements were measured at two positions very close to the tip of a crack in three-point bend specimens that were loaded explosively. Indentations were placed across the fatigue precrack at locations 100 μm and 200 μm behind the tip. These indentations, when illuminated with a laser, generate fringe patterns in space, and the motion of these fringes is proportional to the displacement between them. The fringe motion was monitored with photomultiplier tubes and an oscilloscope and converted to crack-tip opening displacement (CTOD). Explosive loading of the specimens generated stress-intensity factors increasing at a rate of $3 \times 10^6 \text{ MPa m}^{1/2}/\text{s}$.

A soft tool steel was used as a prototype material for this technique development because its material response is similar to the tough materials that are to be studied in the future. Both CTOD and crack-tip opening angle were measured in a search for an appropriate measure of resistance to dynamic fracture. Quasi-static tests were also conducted using the same measurement techniques plus a clip gage. A dynamic critical stress-intensity factor (not plane strain) was determined using a slope reduction procedure based on the static tests. The results show little change in dynamic fracture toughness for this material with increasing loading rate. The experimental techniques show promise for further dynamic studies.

KEY WORDS: crack-tip opening displacement, crack-tip opening angle, dynamic fracture toughness, tool steel, laser interferometry, explosive loading, fracture mechanics

While a number of valid techniques exist for measuring dynamic fracture toughness, the results obtained vary widely. Some show a pronounced decrease in fracture toughness with increasing rate, and some show little or no change. A decrease in the fracture toughness is potentially dangerous to structures and components that experience rapid loading, and it is necessary to study this effect more thoroughly. A simple, easy-to-use measurement technique would be of great benefit.

The objective of this work is to develop and demonstrate a new technique for measuring the crack-tip opening displacement (CTOD) very near the tip of a fatigue precrack under dynamic loading conditions. The displacements are measured with the laser-based interferometric strain/displacement gage [1] previously used for static and cyclic testing and for dynamic strain measurements. The displacements can then be used to compute the stress-intensity factor (or other measure) when the material is loaded very rapidly. If the onset of

¹ Professor, graduate student, and assistant professor, respectively, Department of Mechanical Engineering, The Johns Hopkins University, Baltimore, MD 21218.

crack propagation can be detected, then one can establish a dynamic fracture property.

The approach in the work reported here is to develop the experimental procedures for measuring the CTOD using an inexpensive and readily available material—tool steel—for prototype testing. It is tested in the soft, ductile condition, which is the most difficult to analyze because of the large-scale plasticity but is of more practical interest. Quasi-static experiments were conducted and the stress-intensity factors obtained compared with those from more traditional approaches. These same procedures were then used to determine the stress-intensity factor versus time in specimens explosively loaded at rates on the order of 3×10^6 MPa m^{1/2}/s. The experimental procedures and results of tests on the prototype material are presented in this paper.

Background

The effects of temperature and rate on the fracture toughness of structural steels were reported by Shoemaker and Rolfe [2] using three-point bend specimens impacted by a falling weight. Strains on the specimens were measured with foil gages and converted to load by assuming that the dynamic strain distribution was the same as in an equivalent quasi-static test. Loading rates corresponded to a rate-of-change of the stress-intensity factor of 2×10^5 MPa m^{1/2}/s. Another version [3] of these tests uses an instrumented loading tup. An extension of the familiar clip-gage technique in the ASTM Test for Plane-Strain Fracture Toughness of Metallic Materials (E 399-83) was evaluated in a round-robin series [4] in which high-speed closed-loop testing machines were used. The rate of loading was 1×10^4 MPa m^{1/2}/s, but “ringing” of the clip-gage signal made identification of the critical load difficult.

A completely different and clever approach was developed by Costin et al. [5] using a long rod with an annular precrack as the specimen. The specimen is loaded with an explosive charge, and stresses are measured from foil gages. Displacements are obtained with a unique optical gage across the crack, which then permits one to determine a load-displacement plot from which the dynamic fracture toughness can be obtained. Rates greater than 1×10^6 MPa m^{1/2}/s were obtained. Klepaczko [6] uses the split Hopkinson bar to measure the load and opening displacement of a wedge-shaped compact specimen with loading rates similar to other impact approaches. Giovanola [7] used a one-point bend specimen instrumented with foil gages and impacted in a Charpy impact machine to measure at rates on the order of 3×10^6 MPa m^{1/2}/s.

The optical method of caustics has been used by several investigators to measure fracture parameters under both static and dynamic conditions. A review of the significant work on both crack arrest and initiation under drop-weight loading by Kalthoff is given in Ref 8. Knauss [9,10] has used caustics to examine the dynamic fracture, including branching and three-dimensional effects, in transparent brittle materials. Rosakis [11], in examining opaque ductile materials, has found that the dynamic fracture toughness of ductile steels rises with the crack propagation velocity.

However, in all of the above investigations, measurement and analytical restrictions require that the information about the crack tip be determined from data taken on the order of the specimen thickness away from the crack tip. Thus, what is measured is an average of information travelling to and from the crack tip. A typical elastic wave velocity is 5 mm/μs which means that the information is averaged over several microseconds—an important fact when the total loading time is on the order of tens of microseconds. If the stress-intensity factor can be determined from displacements measured very close to the crack tip (that is, if linear-elastic fracture mechanics can be used), then one has in effect a “*K* gage” that does not require one to know the load history of the component. This is a tremendous advantage for dynamic testing.

Basics of the Interferometric Strain/Displacement Gage

The basic principle of the interferometric strain/displacement gage (ISDG) is actually quite simple. Two very small reflecting indentations are impressed into the surface of the specimen—one on each side of a fatigue precrack. Each indent is approximately $20\text{ }\mu\text{m}$ square, and they are placed on the order of $100\text{ }\mu\text{m}$ apart. The triangular sides of the four-sided indents are small enough that appreciable diffraction occurs when they are illuminated with visible radiation. If the radiation is coherent and monochromatic, as is the case with a laser, then the diffracted patterns interfere to form fringe patterns in space. As the two indents move relative to each other, the fringe patterns also move, and this fringe motion can be related to the displacement or strain on the specimen surface. A fringe motion of "1" corresponds to a displacement of approximately $1\text{ }\mu\text{m}$ when a helium-neon laser is used and the indents are applied with a Vicker's microhardness tester. Details of the ISDG and typical applications can be found in Ref 1, but the principle can be easily understood from the following.

A schematic of the ISDG setup is given in Fig. 1. Two fringe patterns are normally monitored because rigid body motion in a direction parallel to the line between the two indents must be averaged out. This motion is always present when the specimen is loaded in an ordinary test machine; however, the results of tests in this work show that there is little rigid body motion in that direction. One simply records the fringes as they move past an optical detector (photomultiplier tube in this case) that has an aperture narrower than the spacing between the fringes. Each "cycle" on the recorded signal indicates that one fringe has passed corresponding to a displacement of approximately $1\text{ }\mu\text{m}$. The record of

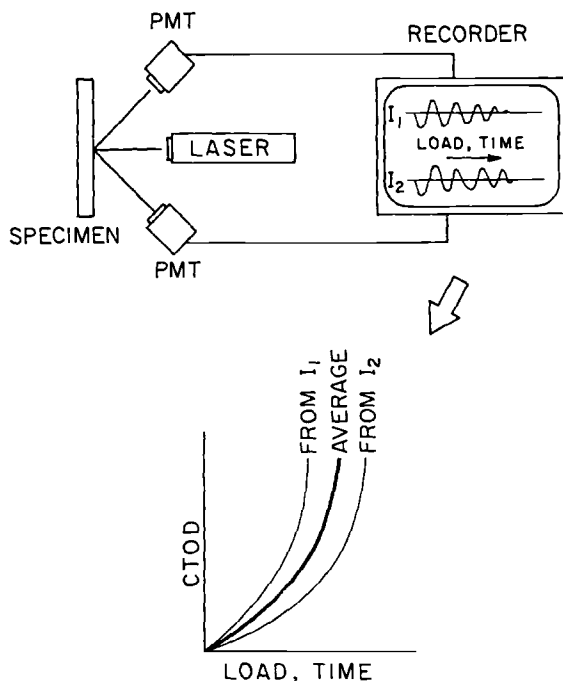


FIG. 1—Schematic of the interferometric strain/displacement gage and the data acquisition system.

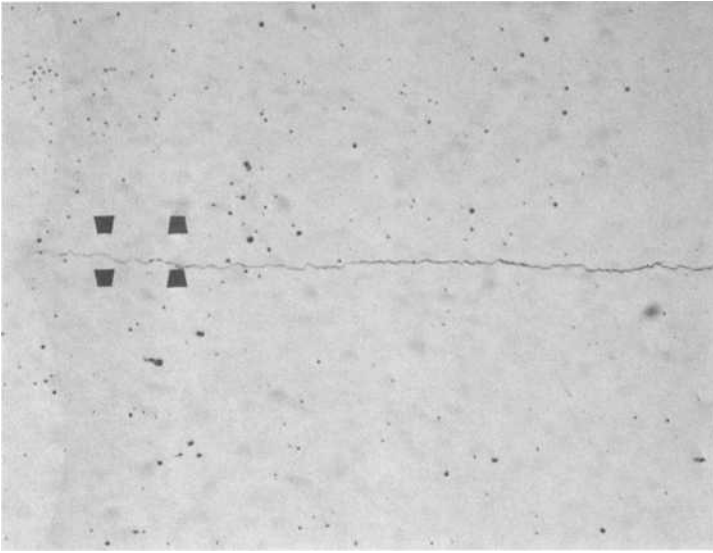


FIG. 2—Photomicrograph of two sets of indentations. The indentations are $70\text{ }\mu\text{m}$ apart. The first set is $100\text{ }\mu\text{m}$ behind the crack tip and tilted 4° up from vertical. The second set is $200\text{ }\mu\text{m}$ behind the tip and tilted 4° down.

the two fringe patterns is analyzed after the test to produce a plot of displacement versus load (in static tests) or time (in dynamic tests). The resolution of the displacement record is $0.5\text{ }\mu\text{m}$, which is quite adequate for the CTOD, which can be as large as $30\text{ }\mu\text{m}$. A more sensitive version of the ISDG using minicomputer control has been developed to measure with a resolution of $0.01\text{ }\mu\text{m}$ under quasi-static or cyclic loading [12]. The test setup is therefore simple—a laser, two photomultiplier tubes, and either a strip-chart recorder or oscilloscope.

Initially, only one set of indentations was monitored, but if two sets are used, one can record the crack-tip opening angle (CTOA). A sudden change in the CTOA might serve as an indicator of crack propagation and therefore be very useful in establishing mechanical properties. However, two sets of indents close to each other cause overlapping fringe patterns which would be unusable. This problem was solved by tilting each set of indents 4° with respect to the normal to the specimen surface. The centers of the fringe patterns are then separated by 8° , which provides ample room for positioning the photomultiplier tubes. Figure 2 is a photomicrograph of two sets of indentations astride a fatigue precrack. The spacing between the indents in each set is $70\text{ }\mu\text{m}$, and the two sets are $100\text{ }\mu\text{m}$ apart.

Material and Specimens

Society for Automotive Engineers (SAE)-01 tool steel was used for the specimens; it comes in standard sizes with a ground finish. To make a three-point bend specimen, one merely saws off a length and machines in the starter notch. The specimens were 6.35 mm thick, 12.5 mm high, and 68 mm long. Load was applied through a tup in the center of the top of the specimen, which was supported by rollers 50 mm apart. The 60° starter notch

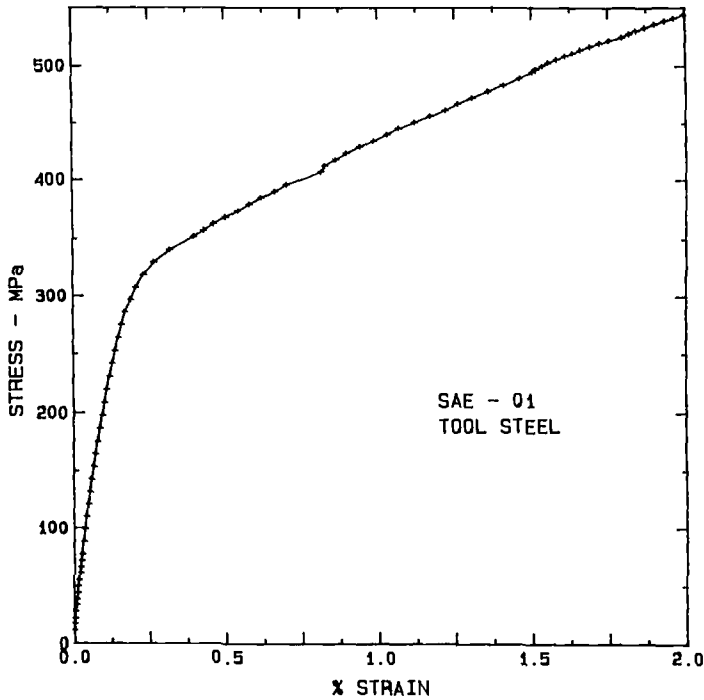


FIG. 3—Stress-strain curve for the SAE-01 tool steel used in the tests.

was machined 5 mm deep and provided with knife edges for a clip gage for the static tests.

The material as received is in a soft condition, but it can easily be hardened for more brittle behavior. However, the longer term interest here is in structural materials that exhibit considerable ductility; hence the choice of the softer material. The stress-strain curve for the test material is given in Fig. 3; the response is nearly bilinear.

Precracking leads to a curved crack front, and a typical shape of a precrack is shown in Fig. 4. This geometry was obtained by measurements after the specimen was broken and shows a 0.5-mm difference between the length at the center of the specimen and the length

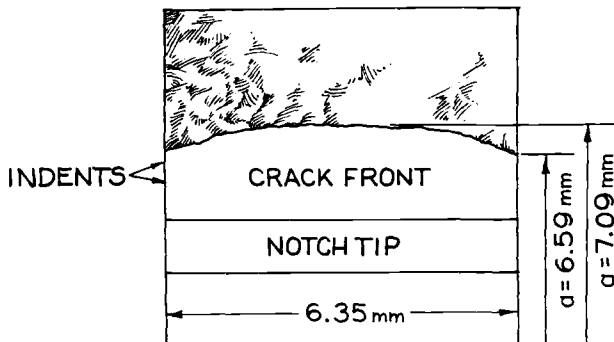


FIG. 4—Drawing of a typical shape of a fatigue precrack.

at the edges. The crack curves $500\text{ }\mu\text{m}$ and yet the indentations on the surface are $200\text{ }\mu\text{m}$ or less from the crack tip. The figure illustrates the three-dimensionality of the specimen and the difficulty of relating surface measurements so close to the tip to the bulk behavior.

Experimental Procedures

For the static tests, the specimens were mounted in an electrohydraulic test machine in a fixture with two 3.2-mm-diameter rollers spaced 50 mm apart. The center loading was applied through a rounded tup with a 4-mm radius. Four RCA 4840 photomultiplier tubes (PMTs) with an integral power supply mounted on translation stages were positioned on a table attached to the test machine. The indents were illuminated with a 15-mW helium-neon laser mounted on a tripod away from the machine. The static test was run under the control of a DEC MINC laboratory minicomputer which applied load at a rate of 20 N/s. An ASTM E-399-type clip gage was attached to the integral knife edges of the specimen; it was powered by a strain gage signal conditioner. The minicomputer sampled six analog channels—four PMTs, the load cell, and the clip gage.

A typical fringe pattern record from a static test is presented in Fig. 5. There is a short region at lower loads where the fringes do not move. This is a manifestation of the closure effect in fatigue crack growth; the crack simply does not open at the tip immediately upon application of load. The laser beam is initially positioned so that its center is over the indents. As the specimen is loaded, it moves with respect to the laser beam, which leads to a reduction in intensity—shown by decreasing amplitude of the fringe amplitude. It is necessary to carefully set the PMTs initially so that a minimum value of fringe intensity impinges on the slit covering the PMT; otherwise one would not know when the first complete fringe motion had occurred. Five hundred data points were taken during the course of the quasi-static experiment.

Figure 6 is a schematic of the dynamic setup in a blast chamber at Aberdeen Proving Grounds, Maryland. Explosive loading is applied through a detonator (a small shaped-charge explosive used to trigger larger explosives) which is approximately 6 mm in diameter by 50 mm long. The detonator is wrapped with enamelled wire which fuses together momentarily when the detonator explodes; this closes a trigger circuit to the recording oscilloscopes. The directed shock wave from the detonator passes through a short (6.3-mm-diameter by 12-mm-long) steel tup that is ground to a rounded wedge shape and is placed initially in contact with the specimen. The specimen here is also mounted on two rollers 50 mm apart.

A major problem in the development of the dynamic test procedures was shielding the recording PMTs from the flash of the explosive and from the accompanying debris. A part of the solution was the 3.2-mm-thick steel shield shown in the upper part of Fig. 6. The tup was loosely fitted into a hole in this shield and separated from the detonator by a thin (0.25-mm-thick) brass strip to prevent the flash from passing down the sides of the tup. After a test, the tup, shim, and shield were often fused together.

The plan view in Fig. 6 shows that the specimen, fixture, and detonator were located inside a blast chamber. This chamber has walls 0.7 m thick and a port that is 35 cm square. The PMTs are located in this port, and the laser along with the recording oscilloscopes placed outside the chamber. A piece of 12.5-mm-thick Plexiglas serves as a protective window into the chamber, and it is necessary to use mirrors to direct the four fringe patterns through the window onto the PMTs. Once the specimen is set up and the fringe patterns adjusted, the window is masked off with opaque tape to leave only five small apertures.

Two transient fringe pattern signals were recorded on a Nicolet oscilloscope with 20 ns per point resolution. The other two were recorded with a camera on an older Tektronix

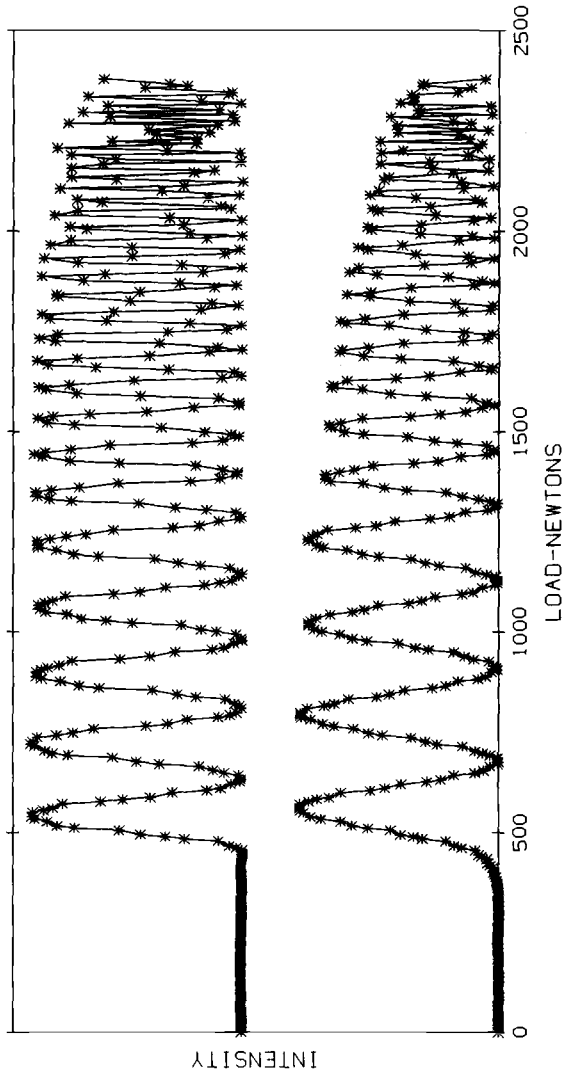


FIG. 5—Typical fringe record for a static experiment. The intensity scale is arbitrary.

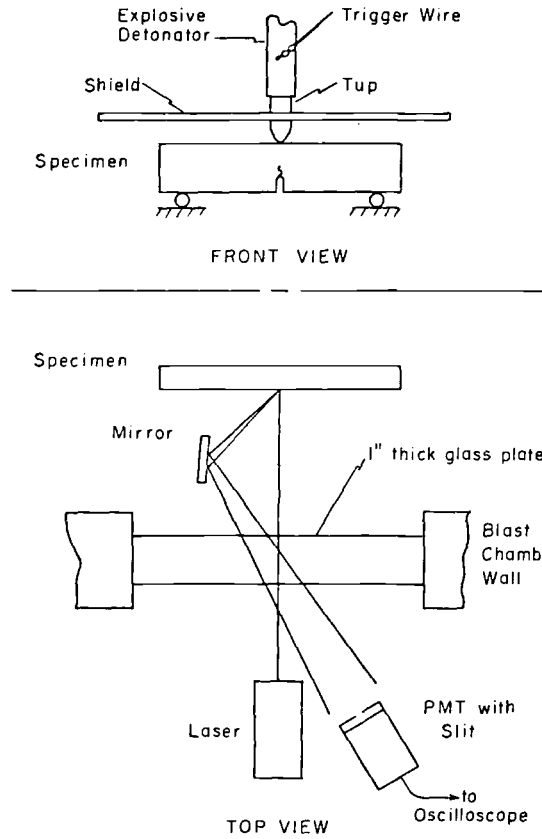


FIG. 6—Schematic of the setup for dynamic testing.

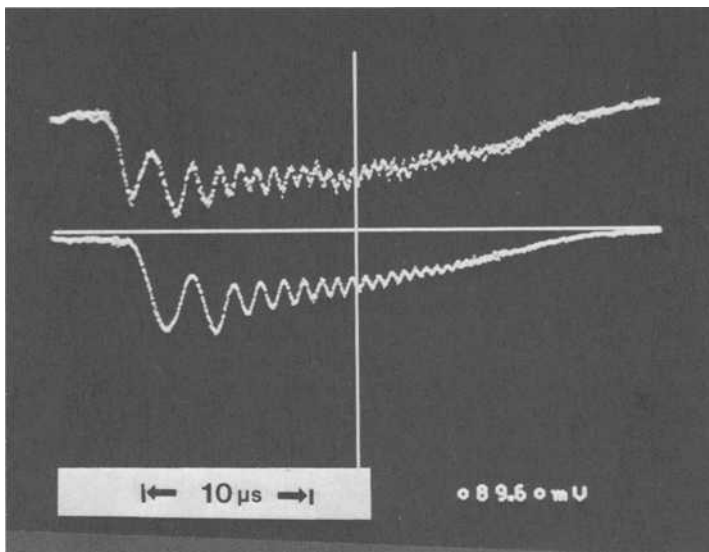


FIG. 7—Typical fringe record for a dynamic experiment. The intensity scale is arbitrary.

555 oscilloscope at 20 μs full scale. No amplifiers were used between the PMTs and the oscilloscopes, and the outputs of the PMTs were terminated with 1000 Ω resistors for high-frequency response. In some of the preliminary tests, before the flash problem was eliminated, the signals showed a rise time of $<0.1 \mu\text{s}$, so the frequency response of the recording devices is adequate for the fringe record. Following a test, the locations of the maxima and minima were read directly from the moveable cursor of the Nicolet, or with a low-power microscope and X-Y stage for the 555 photographs, and reduced to displacement-versus-time plots.

A typical dynamic fringe record for one set of indents is shown in Fig. 7; it is very similar to the static record.

Results and Discussion

Figure 8 is a plot of the displacements as computed from all four fringe patterns in a static test. The indents in this case were located 100 and 200 μm behind the tip of the precrack.

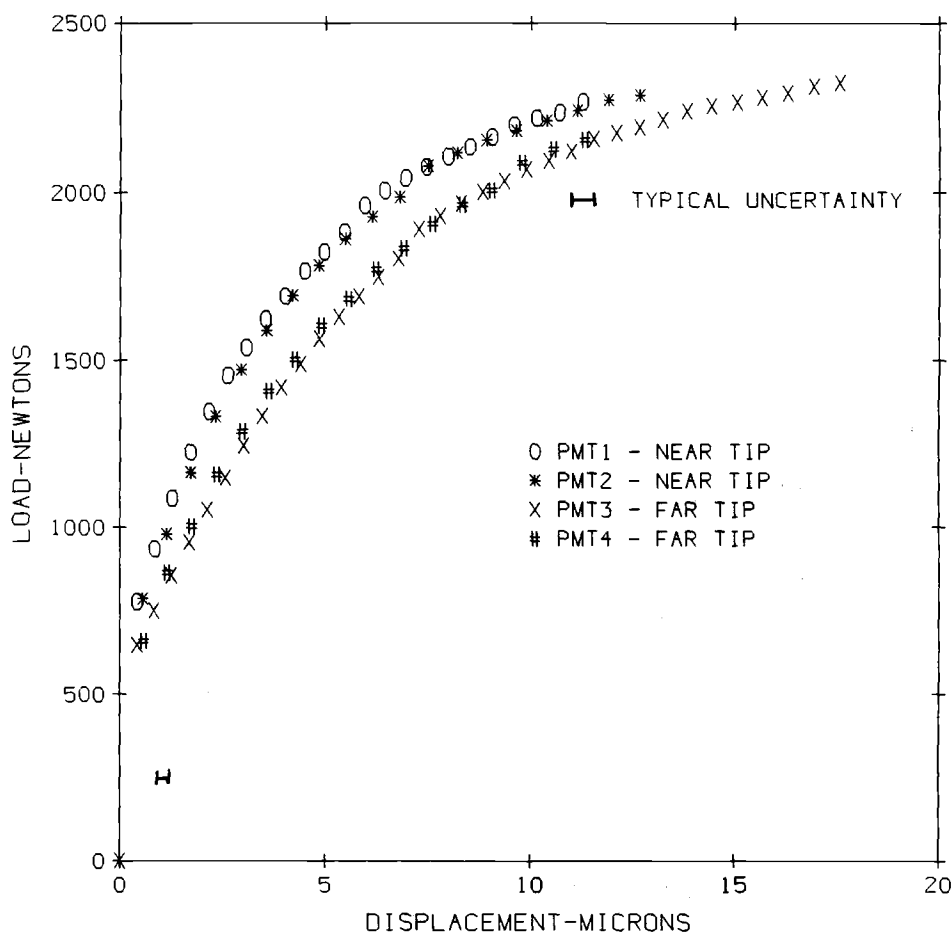


FIG. 8—Displacement records from a static experiment. Both fringe patterns are plotted for each set of indentations. Two indicators of the uncertainty in displacement are also drawn.

Both fringe records are shown for each indent to demonstrate that there is little or no rotation of the specimen during the test. A final load-displacement curve (not shown) would be obtained by averaging the two separate fringe patterns.

The full scale on the displacement is 20 μm , and it is apparent that the resolution is on the order of $\frac{1}{2}$ μm . Typical uncertainties at two values of displacement are shown by the horizontal bars; the relative uncertainty in displacement is approximately 12% at small values and 3% at larger values. The larger values are of course the ones of primary interest because that is when the precrack starts to propagate.

The closure effect, shown earlier on the fringe record, is quite evident in Fig. 8. No detectable displacement occurs until a load on the order of 500 N is reached. There is then a region of linear behavior indicating linear elastic response, followed by nonlinear behavior as the plastic zone develops at the tip of the crack. The nonlinear response comes into play earlier for the indents closest to the tip.

Note that one can compute the CTOA from the displacement records. The difference in the two displacements divided by the distance between the sets of indents gives the angle very near the tip. Such a computation has a larger relative uncertainty—on the order of 50% at the small loads and 5% at the higher loads.

The idea behind these displacement measurements is to use them to calculate a measure of the driving force at the crack tip. The approach here is to compute the stress-intensity factor (SIF) from these data, and that was done four different ways. Figure 9 shows the dimensions and locations used in these computations of the SIF. The indents furthest from the tip have a total crack-opening displacement (COD) of y_1 . Indents at X_2 with a COD y_2 are closest to the tip. Note that X_1 is the spacing between the two sets of indents.

The first approach assumes purely linear elastic behavior using the physical crack tip location as measured on the surface of the specimen when the indents were applied. The displacement at the indents furthest from the tip is then related to K by

$$y_1 = \frac{8K}{E\sqrt{2\pi}} \sqrt{X_1 + X_2} \quad (1)$$

where E is Young's modulus and plane stress has been assumed. One can then calculate K

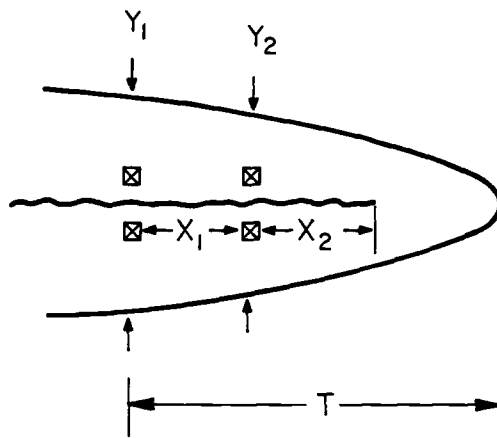


FIG. 9—The coordinate system used in computing the stress-intensity factors from the measured displacements.

from the measured y_1 and the locations of the indents relative to the tip. This approach has been used before to determine K in elastically loaded specimens [13].

Since two displacements are recorded, one can use them in a second approach to compute the location of an effective crack tip that would produce linear elastic behavior. This effective location is indicated by "T" in Fig. 9. A little algebra shows that K is given by

$$K = \frac{E\sqrt{2\pi}}{8} \sqrt{\frac{y_1^2 - y_2^2}{X_1}} \quad (2)$$

Third, the simplest inclusion of plastic response into the calculation is to use the Irwin plastic zone correction [14] and plane-stress loading. The distance from position X_1 to the corrected location of the crack tip is then the physical distance on the surface plus the size of the plastic zone. The displacement y_1 is related to the SIF by

$$y_1 = \frac{8K}{E\sqrt{2\pi}} \sqrt{X_1 + X_2 + \frac{K^2}{2\pi\sigma_{ys}^2}} \quad (3)$$

where σ_{ys} is the yield stress. Using Eq 3, one can solve for K using the measured displacement, y_1 .

The fourth and final way of computing K is to compute the displacement at the crack tip. Assume that the shape of the opening curve at positions X_1 and X_2 is part of a parabola whose origin can be calculated. The two measured displacements permit one to calculate the coefficients of the parabola and thus the displacement at any position along the crack. If the displacement at the tip of the physical crack is computed, then one can compute K ; the expressions for the CTOD (δ_i) and the relation to K are

$$\delta_i = y_1 \sqrt{\left(\frac{y_2}{y_1}\right)^2 - \frac{X_2}{X_1} \left[1 - \left(\frac{y_2}{y_1}\right)^2\right]} \quad (4.1)$$

$$K^2 = E\sigma_{ys}\delta_i \quad (4.2)$$

These four ways of extracting K from the measured displacement are compared in Fig. 10 for one static test. The stress-intensity factor computed from the linear elasticity relation (ASTM Test E 399-83) is shown by the dashed line passing through the origin. Note that all four approaches tend to be parallel at low loads to the SIF calculated from the bulk. This tends to validate the assumptions made in computing SIFs from surface displacement data near the crack tip. The load at which the crack-mouth displacement measured by the clip gage indicated initial crack propagation (again according to ASTM Test E 399-83) is denoted by P_q on the abscissa.

The two calculation schemes using purely elastic behavior show very similar responses—nonlinear from the very beginning. However, the two calculations that include plasticity, which also are similar to each other, have a linear region until the critical load, P_q , is passed. The fact that these two latter approaches show a relation which is parallel to the SIF-load relation for the bulk specimen offers hope that these surface measurements can yield sensible descriptions of specimen behavior. Again, the closure from the precracking is evident here. If one were obtaining the SIF only from the surface measurements, one would raise the computed SIF-load curve so that it extrapolated back to zero.

The conclusion here is that either the Irwin correction or the CTOD approach should be used to calculate the stress-intensity factor from the surface displacement measurements.

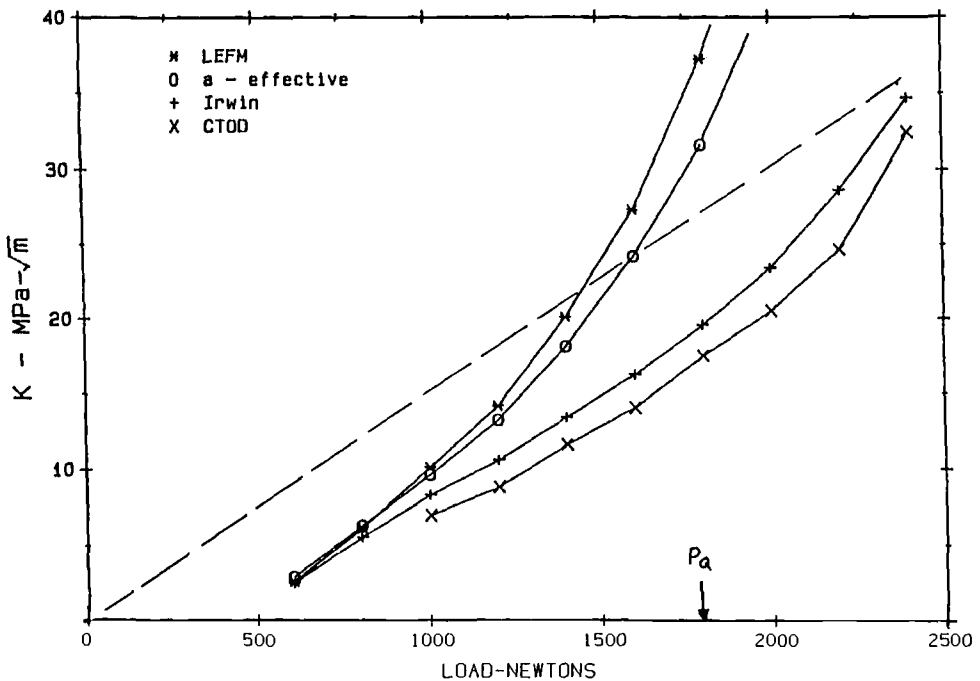


FIG. 10—A comparison of the four methods of computing the stress-intensity factors based on the surface displacements.

There is little difference between the two, and the Irwin correction is used in the following.

Figure 11 shows the measured SIF for three specimens to demonstrate the reproducibility of both the experimental and the computational approaches. The crack lengths were 6.27 mm for Test 3, 6.45 mm for Test 4, and 6.69 mm for Test 7 (the one presented in Fig. 10). The critical loads, P_q , are also denoted for each test. The plots are slightly different because of the different crack lengths, but one observes that the surface SIF corresponding to the critical load is nearly the same in all cases. Note also that the closure is slightly different for the three specimens; this is not an uncommon occurrence for specimens that were precracked in a supposedly identical fashion. The surface SIF differs from the SIF of the bulk specimen because of the closure, and it is estimated that in these specimens the bulk SIF is approximately 7 MPa m^{1/2} higher than that measured on the surface.

The CTOA as a function of load is plotted in Fig. 11; it has a high relative uncertainty (note the typical error bars) because of the small differences involved. The uncertainty associated with the determination of the SIF is also indicated by the error bars in Fig. 11 (shown on Test 7 for illustration). It is estimated that the SIF can be determined within ± 1 MPa m^{1/2} by this process.

Once the computational procedure is established for the static tests, it can be used for the dynamic tests. The assumption here is that the static equations for K apply for these stationary cracks. So, one can obtain the SIF from the surface displacement measurements without needing to know the load history, which is difficult to measure in a complicated specimen. Figure 12 shows COD from the two sets of indentations in a dynamic experiment. The delay of approximately 10 μ s before any displacement is seen is the length of time

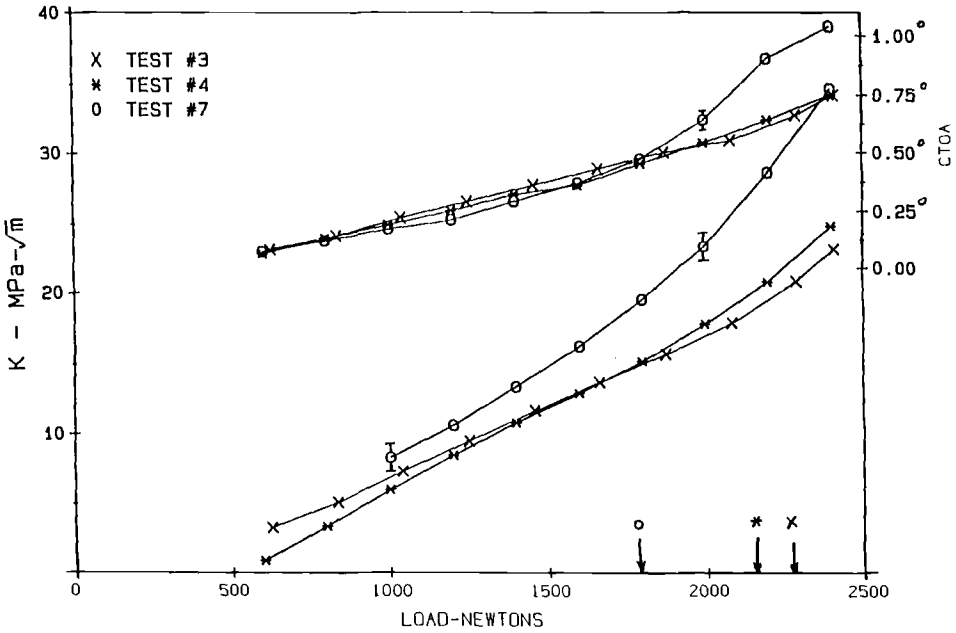


FIG. 11—Computed stress-intensity factors from three static experiments. The critical load, as determined by ASTM Test E 399-83 procedures from a clip gage, is also plotted on the abscissa for each test. The crack-tip opening angle for each test is plotted on the upper scale. Typical uncertainty bars are shown.

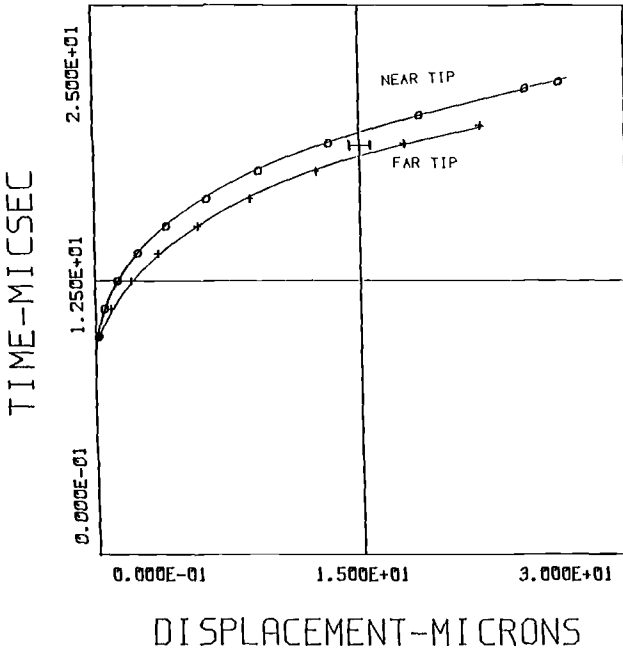


FIG. 12—Displacements from a dynamic experiment. An indicator of the uncertainty of the displacement is drawn at 15 μm .

between the trigger and the arrival of the stress wave. A typical uncertainty bar is drawn at 15 μ s, and note the similarity in shape of this result to the load-displacement record in Fig. 8. The SIFs computed from dynamic displacements in two separate experiments are presented in Fig. 13. The shift in time is not important because this came from the uncertainty in the trigger circuitry. Note that the dynamic experiment lasts only approximately 10 μ s and that the loading rate is on the order of 3×10^6 MPa m^{1/2}/s. Crack-tip opening angles are also plotted in Fig. 13.

In order to determine the fracture toughness, one must also know when the precrack starts to propagate. This is difficult to ascertain in a small specimen of a tough material. These specimens do not meet the criteria of ASTM Test E 399 for plane-strain fracture toughness testing; one is determining the P_q here. An approximate procedure that may be useful is similar to the one used in ASTM Test E 399-83 wherein deviation from initial linearity is used to establish when the crack starts to move.

In the static tests, the P_q was determined from the clip-gage data in the standard manner. The displacements at positions 200 μ m behind the tip were used, and a straight line was drawn through the initial linear portion. These indents further from the tip have a more pronounced linear region. Since the critical load was known *a priori*, the intersection of the straight line, as well as the displacement curve with the horizontal P_q line, could be determined. The ratio of the linearly extrapolated displacement to the actual displacement was not 0.95, as it was for the clip-gage data, but was 0.76, 0.79, and 0.82 (the latter value from indents 230 μ m behind the tip) for the three static tests. Since the indentations are so close to the tip, the measured plasticity has a greater effect and shows a more pronounced nonlinear displacement. The authors therefore propose that this ratio—0.78—be used to delineate crack growth in this size specimen of this material when the indents are 200 μ m behind the

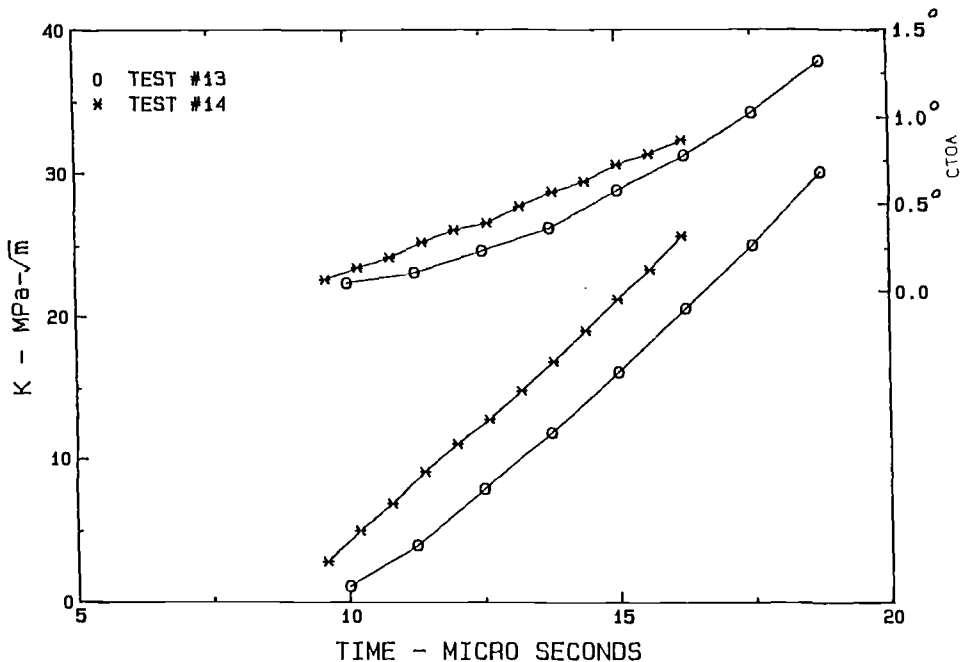


FIG. 13—Stress-intensity factors and crack-tip opening angles for two dynamic experiments.

precrack tip. We recognized that this rather arbitrary approach is not very satisfying, but it can be used to establish a material parameter in dynamic tests.

This procedure can then be used to compute the dynamic fracture toughness from the dynamic displacement data. One simply fits an initial straight line, draws a second line with a slope 0.78 smaller, and reads off the time at which this second line intersects the displacement curve. One then uses the SIF versus time curve (Fig. 13) to determine the dynamic fracture toughness. The assumption here is that the dynamic loading of the specimen is linear with time. The similarity in shape of the displacement plots and the SIF versus load or time plots support this assumption, but a separate test in which a tup was fired into an instrumented 6.35-mm diameter steel rod showed that the loading pulse is indeed linear in its rise after a short nonlinear portion. So, this procedure, which is similar to that used in static fracture toughness testing, is quite straightforward for dynamic testing, but the appropriate ratio to be used must be determined from static tests for a particular specimen size and material.

It should be noted that the appearances of the fracture surfaces, including the size of the shear lips, were quite similar for the static and the dynamic specimens. The static fracture toughnesses were 22.3, 21.8, and 21.3 MPa m^{1/2} for the three static tests; the two dynamic tests yielded values of 21.8 and 24.0 MPa m^{1/2}. As noted above, the surface SIF differs from the SIF of the bulk specimen by approximately 7 MPa m^{1/2}, and this value must be added to these surface values. All of these have an uncertainty of ± 1.0 MPa m^{1/2}. There is essentially no change in the fracture toughness over a range of rates from 3×10^{-1} MPa m^{1/2}/s to 3×10^6 MPa m^{1/2}/s for this particular ductile material.

Conclusions

The described techniques for measuring crack-tip opening displacement and crack-tip opening angle under static and dynamic loading conditions are sensitive and reproducible. Furthermore, the techniques are quite simple and use instrumentation that is usually available; only the explosive loading facility is specialized. The ability to measure so near the crack tip is particularly important in dynamic work because one does not have to estimate the loading history at the point of interest—the crack tip. While the measurements reported herein were taken at room temperature, the techniques can easily be extended to severe environmental conditions, such as high temperature, corrosive atmosphere, or the presence of nuclear radiation.

A very ductile material has been used for technique development, and the method of calculating a measure of resistance to cracking is therefore more complicated and open to question. The procedure of using the displacements at a single location and the Irwin correction for the size of the plastic zone appears to work quite well and can be used to relate the SIF on the surface to the bulk value as determined from the applied load and the specimen geometry. The phenomenon of fatigue crack closure is accentuated in these measurements so close to the crack tip, but the opening load is easily established to enable correction of the measured SIF. Once this procedure has been established in the static case, it can be used to compute the SIF under high-rate dynamic loading, which is actually the situation of interest.

The determination of fracture toughness requires identification of the onset of crack propagation, and a procedure similar to that used in ASTM Test E 399-83 has been applied to the local crack-opening displacements. This produces results that are reproducible from specimen to specimen (at least for the limited number of developmental tests). The determination of fracture toughnesses of small specimens under dynamic loading is not an easy task, and this different approach has merit. Finally, the measured local displacements have

value in their own right in that they can be used to evaluate theories and computational schemes that predict the material behavior very near the crack tip.

Acknowledgments

This work was supported by the U.S. Army Research Office under Grant No. DAAG29-85-K-0218. Partial funding of this grant was provided by Aberdeen Proving Grounds and by The David Taylor Naval Ship Research and Development Center.

References

- [1] Sharpe, W. N., Jr., *Optical Engineering*, Vol. 21, 1982, pp. 483–488.
- [2] Shoemaker, A. K. and Rolfe, S. T., *Engineering Fracture Mechanics*, Vol. 2, 1971, pp. 319–339.
- [3] Server, W. L., *Journal of Testing and Evaluation*, Vol. 6, 1978, pp. 29–34.
- [4] Shoemaker, A. K. and Seeley, R. S., *Journal of Testing and Evaluation*, Vol. 11, 1983, pp. 261–272.
- [5] Costin, L. S., Duffy, J., and Freund, L. B., *Fast Fracture and Crack Arrest*, ASTM STP 627, American Society for Testing and Materials, Philadelphia, 1977, pp. 310–318.
- [6] Klepaczko, J. R., *Journal of Engineering Materials and Technology*, Vol. 104, 1982, pp. 29–35.
- [7] Giovanola, J. H., Poulter Laboratory Technical Report 005-84, SRI International, Palo Alto, CA, 1984.
- [8] Kalthoff, J. F., *Elastic-Plastic Fracture Mechanics*, L. H. Larsson, Ed., Reidel Publishing Co., Dordrecht, The Netherlands, 1985, pp. 479–508.
- [9] Knauss, W. G. and Ravi-Chandar, K., *International Journal of Fracture*, Vol. 27, 1985, pp. 127–144.
- [10] Ravi-Chandar, K. and Knauss, W. G., *International Journal of Fracture*, Vol. 20, 1982, pp. 209–222.
- [11] Rosakis, A. J. and Zehnder, A. T., *International Journal of Fracture*, Vol. 27, 1985, pp. 169–186.
- [12] Sharpe, W. N., Jr. and Ward, M., *Journal of Engineering Materials and Technology*, Vol. 105, 1983, pp. 235–241.
- [13] Macha, D. E., Sharpe, W. N., Jr., and Grandt, A. F., *Cracks and Fracture*, ASTM STP 601, American Society for Testing and Materials, Philadelphia, 1976, pp. 490–505.
- [14] Irwin, G. R., *Handbuch der Physik VI*, Springer-Verlag, Berlin, 1958, pp. 551–590.

Dynamic Moiré Interferometry Studies of Stress Wave and Crack-Tip Diffraction Events in 1018 Steel

REFERENCE: Epstein, J. S., Deason, V. A., and Reuter, W. G., "Dynamic Moiré Interferometry Studies of Stress Wave and Crack-Tip Diffraction Events in 1018 Steel," *Fracture Mechanics: Nineteenth Symposium ASTM STP 969*, T. A. Cruse, Ed., American Society for Testing and Materials, Philadelphia, 1988, pp. 482–503.

ABSTRACT: A study of stress wave propagation around localized crack-tip regions in engineering materials is presented. The principal tool of this initial investigation is dynamic moiré interferometry, which yields full-field continuum boundary conditions of surface displacement in a real-time optical processing manner. The displacement sensitivity employed for this study is 3.3 μm ; however, the displacement sensitivity can be as high as 0.2 μm . The spatial resolution developed is less than 1 mm. After a brief review of the technique of dynamic moiré interferometry, the study of a longitudinal pulse, interacting with an artificial crack in a finite steel bar, is presented. Equations for the near-tip elastic dynamic crack displacements will be reexamined to extract localized elastic dynamic stress-intensity factors in light of the capabilities of dynamic moiré interferometry.

KEY WORDS: dynamic moiré interferometry, dynamic fracture mechanics, experimental mechanics, stress wave diffraction, fracture mechanics

Stress wave propagation in materials containing geometric discontinuities, such as cracks, involves two separate but often interacting nonlinear processes. First, the material properties locally surrounding a crack are changing as a function of time and spatial distance from the crack tip [1–3]. Second, the mechanics of stress wave propagation is also changing, not only as a function of time and distance locally in the crack region but, equally important, globally in the structure [4–10]. In reality, the materials' behavior and the mechanics phenomena are inseparable.

This paper presents an approach to understanding the basic phenomenological physics of such very complicated materials and mechanics problems. As stated, neither materials nor mechanics can be ignored or treated separately; both must be observed together to reveal the true nature of the process.

Two phenomenological observations can be made of the net mechanics/materials interaction phenomena occurring at a crack tip under dynamic loading: the local crack-tip material displacement and the thermodynamic response or temperature of the region surrounding the crack tip. Both represent the state of the material surrounding the crack tip due to

¹ Engineering specialist and principal engineer, respectively, Materials Science Div., Idaho National Engineering Laboratory, P. O. Box 1625, Idaho Falls, ID, 83415.

² Senior scientist, Sensors and Diagnostics Div., Idaho National Engineering Laboratory, P. O. Box 1625, Idaho Falls, ID 83415.

mechanics/materials interactions. Recently, dynamic moiré interferometry has been developed to measure localized crack-tip displacement fields [11]. A dynamic infrared system has been developed to measure local point temperatures of a material [12]. Both techniques hold great promise for understanding the materials/mechanics interaction effects under dynamic loading.

This paper first discusses the applied optics of dynamic moiré interferometry and then its application to the local phenomenon of diffraction at the crack tip of a longitudinal pulse. The near-field equations for dynamic elastic cracks are then reexamined in light of dynamic moiré interferometry. Finally, the paper discusses future applications of dynamic moiré interferometry.

The Applied Optics of Dynamic Moiré Interferometry

This section deals first with moiré phenomena in a classical sense and then discusses static and dynamic moiré interferometry.

Classical Moiré Methods

Classical moiré methods, both static and dynamic, have been employed for a number of years in experimental mechanics [13]. In fact, Kobayashi [14] first employed classical moiré methods to study the dynamic displacement fields of propagating cracks in magnesium plates more than 20 years ago. The term moiré refers to a phenomenon in optics that occurs when two repetitious patterns are superimposed and deformed in relation to each other (Fig. 1), forming a series of black and white bands termed "moiré fringes." Typically one pattern, or grating, is deformed (active grating) while the other pattern is undeformed (reference grating). The term "frequency" refers to the number of lines per inch (l/in.) or lines per millimetre (l/mm) of the grating. "Mechanical" or "amplitude" moiré, so called because the fringes are formed from the mechanical crossing of the two grating lines [15], is limited by the frequency of the reference grating employed. To make the moiré effect scientifically useful, the reference grating frequency must be 400 to 4000 l/mm (10 000 to 100 000 l/in.). During the last six years, moiré interferometry has been developed from a theoretical state [16] to one of great usefulness [17].

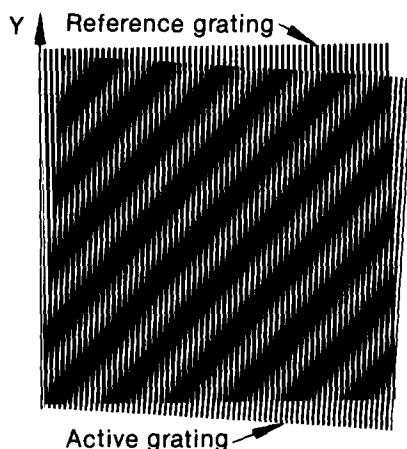


FIG. 1—The moiré phenomenon.

Static Moiré Interferometry

Moiré interferometry produces displacement fringes by light diffraction and wave-front interference rather than mechanical grating crossing effects. In fact, the high-frequency gratings employed for moiré interferometry are referred to as diffraction gratings. Recently, the feasibility of producing effective grating frequencies, f , of 4000 l/mm was shown by Post, Deason, Weissman, and Epstein.³ Such high frequencies yield microstructural displacement detail in extremely low compliance materials, such as ceramics. Moiré interferometry was first applied to static cracks in photoelastic materials by Nicoletto et al. [18]. Smith [19] also developed static stress-intensity factor (SIF) extraction algorithms, taking into account the three-dimensional free surface/crack front intersection problem [20]. A comprehensive article on moiré interferometry by Post has been published [17] and should be consulted for a detailed explanation of applications of moiré interferometry.

In brief, moiré interferometry relies on symmetric two-beam interference with diffraction gratings replicated on a specimen surface. Figure 2 shows that when two beams impinge on a diffraction grating at symmetric angles relative to the grating, their resulting diffraction orders reflect off the diffraction grating according to the grating equation

$$\sin \theta = m\lambda F_s + \sin \phi \quad (1)$$

where

- θ = the angle of diffraction,
- m = the diffraction order,
- F_s = the diffraction grating frequency,
- ϕ = the angle of incidence of the beams, and
- λ = the frequency of light employed.

If the grating is replicated onto a deforming specimen surface, as shown in Fig. 3, as the specimen surface deforms, each of the impinging beam's reflected diffraction angles will also change. In the case of two symmetric beams whose angle produces diffraction orders of -1 and $+1$ reflecting from the grating at right angles [17], when the grating deforms due to specimen deformation, the -1 and $+1$ orders will emerge with a relative angle to one another. This relative angle between the orders forms a two-beam interference pattern that is due to the in-plane deformation of the replicated diffraction grating or specimen surface, which are theoretically equivalent. The two-beam diffraction order interference pattern that results produces fringes that are lines of constant in-plane displacement whose quantitative interpretation is given by the following simple equation

$$U = \frac{N}{F} \quad (2)$$

where

- U = the constant in-plane displacement in the direction perpendicular to the grating lines of a diffraction grating,
- N = the assigned fringe order, and
- F = twice the diffraction grating frequency, for the case outlined.

Figure 4 is a schematic of a typical two-beam interferometer and deformed specimen with

³ Private correspondence, June–July, 1985.

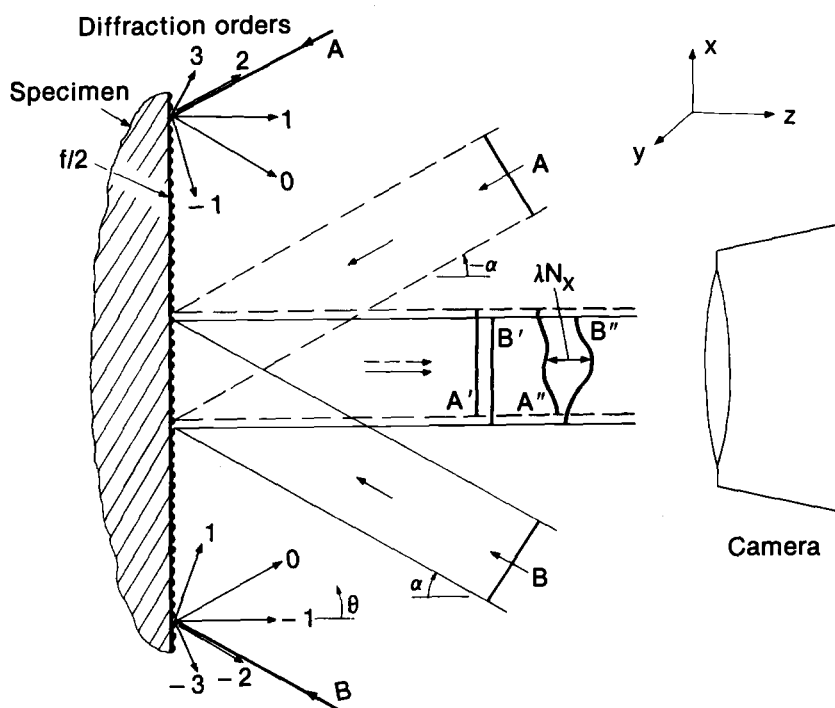


FIG. 2—Two-beam interferometry with a reflective-phase diffraction grating.

a diffraction grating. Figure 5 shows a static crack-tip moiré interferometry y displacement field in steel.

Dynamic Moiré Interferometry

With the basic concepts of moiré interferometry in hand, the extension to the dynamic case is theoretically straightforward. The continuous laser source in the static case is simply replaced with a pulsed laser source. The pulse must be fast enough to freeze the stress wave motion in the material effectively. For this study a pulsed laser system with a 20×10^{-9} -s pulse width (20 ns) was employed. This pulse width is fast enough to freeze the stress wave motion effectively in metals (5 km/s). The limit of spatial resolution, however, becomes a factor with dynamic moiré interferometry. This limit is very simply calculated by the formula: limit of spatial resolution (LSR) = wave speed \times pulse width. For a pulse width of 20 ns and a typical wave speed of 5 km/s, the spatial detail resolution becomes 0.1 mm. Other factors, such as the grating itself affecting the wave phenomena, are considered negligible. Figure 6 shows a schematic of a typical pulsed moiré interferometry system.

While theoretically, the concept of dynamic moiré interferometry is simple and elegant, the actual use can become tedious. Fortunately, over the past year at the Idaho National Engineering Laboratory (INEL) most of these problems have been solved or are under consideration. In brief, the problems encountered include the following:

(a) a system alignment using a continuous laser whose frequency is different than the pulsed laser's,

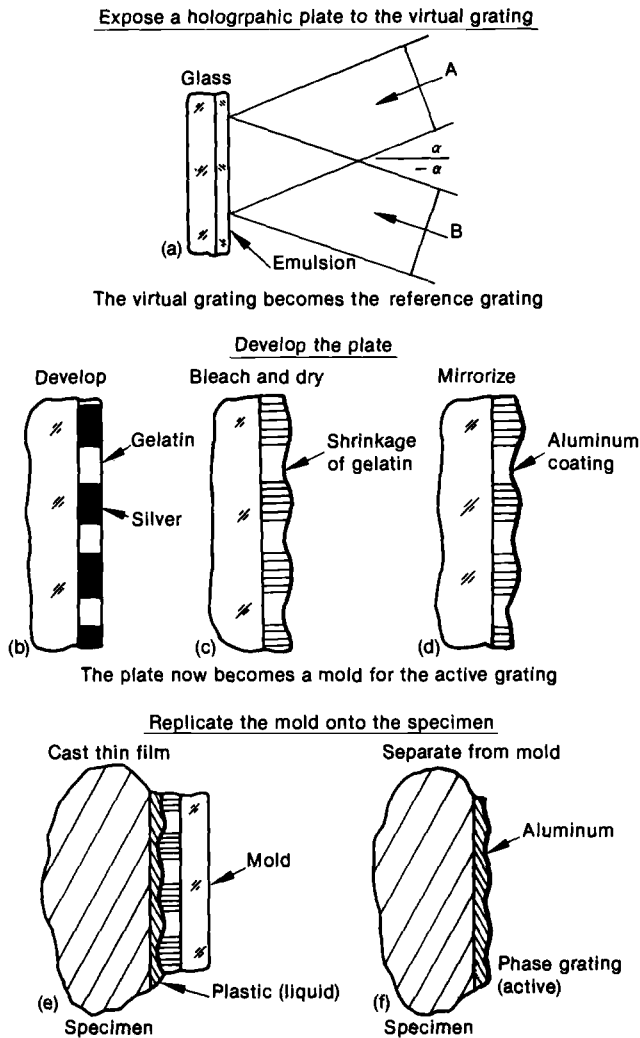


FIG. 3—The replication of a diffraction grating.

(b) system triggering and sequencing of the events taking place in the specimen, and
(c) the limited (single or double) pulsing mode of most interferometric-grade ruby laser systems.

These items will be addressed briefly.

Alignment—To make any real-time correction to the moiré pattern requires the use of a continuous laser source in alignment with the same optics train that the pulsed laser source employs. However, the alignment of an optical system using a continuous laser whose frequency (632.8 nm) differs from the pulsed ruby laser frequency (694.3 nm) is a major problem. Typically, the moiré field is “nulled” out before an impact event or the null pattern is superimposed upon a high-frequency “carrier” pattern [17] that is a constant addition to

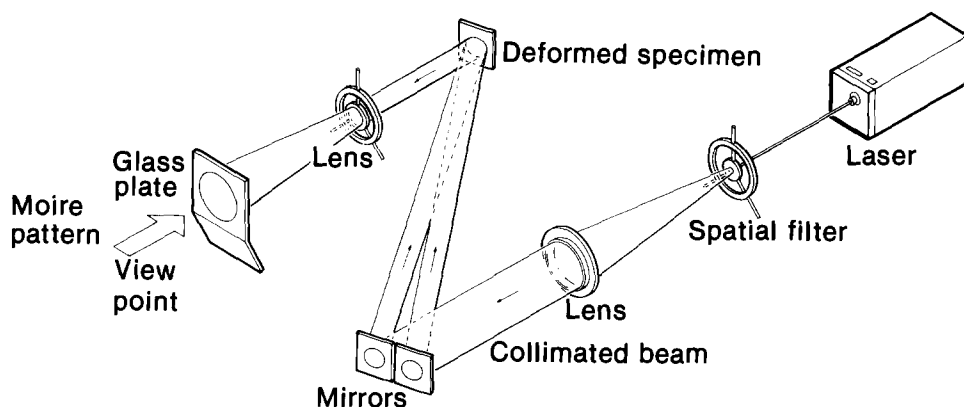


FIG. 4—A typical two-beam interferometer.

both loaded and unloaded patterns. This constant high-frequency carrier pattern containing the before-impact moiré pattern is later subtracted from the impacted pattern via Fourier filtering [22]. Since the gratings are fabricated according to the frequency of light employed, the grating fabricated by the pulsed laser is good in alignment only for the pulsed laser frequency. Typically, the mismatch in frequencies between the pulsed and continuous laser is too great to be corrected either optically or mathematically. Likewise, a continuous laser grating is suited for alignment by the continuous laser frequency and not the pulsed ruby laser frequency.

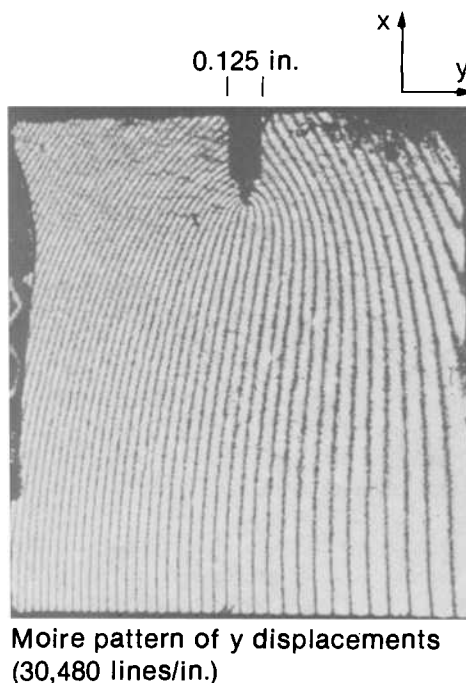


FIG. 5—Moiré interferometry displacement field in the opening mode of a crack.

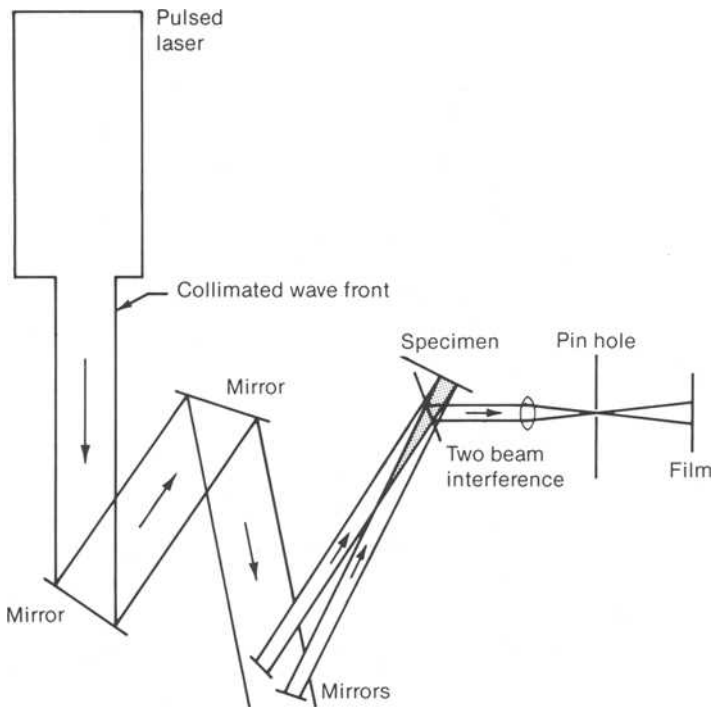
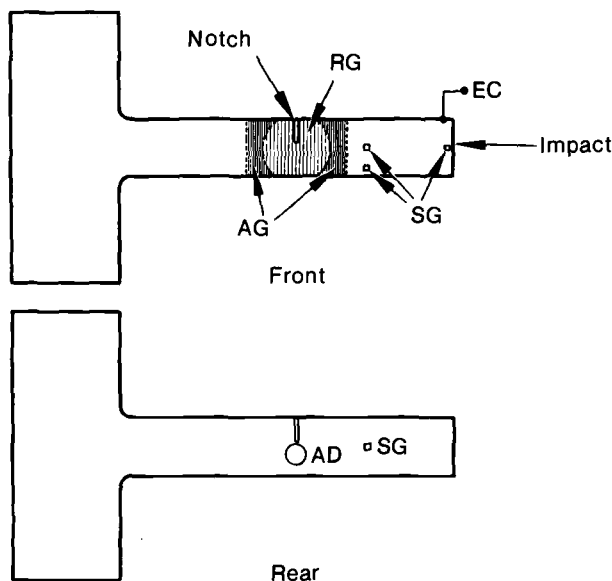


FIG. 6—Dynamic pulsed moiré interferometer.

As a result, the gratings employed for the dynamic moiré system contain *dual* gratings. These are gratings with both the pulsed ruby laser frequency and alignment frequency superimposed on one grating. Figure 7 schematically shows a steel beam specimen with the ruby laser grating on the area of interest, the crack, and the alignment grating bordering the ruby grating region. In this manner, any real-time adjustments made by the continuous laser to the alignment portion of the grating will be identically made on the pulsed ruby grating. An alternative to the dual grating system is the achromatic system [23]. Achromatic systems are self-compensating for any frequency arriving to a specimen grating. The INEL has developed such a working system; however, the study in this paper employs a dual grating system.

System Triggering and Sequencing of Events—System triggering and sequencing of events are actually two problems. First, ruby laser systems have inherent delays due to the optical pumping of the ruby rods before lasing can occur. This pumping process generally takes 1000 μ s. The rods will typically stay energetic for 1 to 2 ms, during which time the ruby rod may fire twice for two separate pulses. As can be seen, a "window" typical of dynamic studies develops.

This window effect is inherently tied to the characteristics of the laser system. The initial charging of the rod is accomplished before impact. Figure 8 shows a timing and layout schematic for the beam specimen of Fig. 7. A longitudinal pulse is delivered to the cantilever beam by a heavy mechanical impactor. When the impactor is released, but before impact, it breaks a laser beam. This beam, in turn, triggers a photoelectric gate to begin charging the ruby rods. The system clock does not begin until contact is made between the hammer and specimen tup, which in turn triggers an electrical make or break switch. When the wave



AG: Alignment grating for $\lambda = 632.8$ nm

RG: Ruby grating for $\lambda = 694.2$ nm

AD: Acoustic detector

EC: Electrical circuit to detect impact

Material: 4340 steel

FIG. 7—A cantilever beam specimen with a dual-frequency grating, acoustic detector (AD), and strain gages (SG).

travel time is known (from piezoelectric sensors), the laser firing can then be dialed in the clock so that the wave interactions with the specimen can be observed. The timing system developed for the laser consists of a single 20-MHz clock and four countdown registers providing four individual delays. There are also two inputs which can sense the presence or absence of electrical continuity and two inputs which sense optical continuity (making or breaking of a laser beam). Currently, the timing system has a resolution of $0.2 \mu\text{s}$ for positioning the observation window. Figure 9 shows the clock system.

The observation window for the sequence of stress wave events is positioned by the use of either or both shear and longitudinal acoustic wave sensors on the spatial region of observation (Fig. 7). Typical output of the piezoelectric sensors is shown in Fig. 10. This output tells the arrival of the longitudinal or shear wave and the subsequent reflections that occur, such as later structural resonance. Chronological time histories of wave travel are used to set the timing system window for observation with dynamic moiré interferometry. This time history of wave travel will be discussed in more detail in the section on results.

Laser Pulsing Mode—During the work reported here, the laser rods, at best, yielded two pulses per impact event. This was considered excellent at the time; however, as will be discussed, improvements to 109 000 pulses/s have been achieved. Because the laser for this work pulsed twice per impact event, the first pulse was set to occur during hammer release but before impact. The second pulse occurred according to the time settings of the clock system. A carrier fringe pattern was dialed into the moiré system. The net result was that

- A. Ruby/HeNe collimating lens
- B. Ruby/HeNe laser beam
- C. Beam forming mirrors
- D. Beam splitter
- E. Specimen
- F. HeNe alignment grating
- G. Ruby diffraction grating
- H. Moire imaging lens
- I. Spatial filter
- J. Camera
- K. Moire fringe pattern
- L. Hammer pivot
- M. Hammer
- N. Pin to break timing laser beam
- O. Tup
- P. Timing laser beam
- Q. Circuit to detect hammer contact

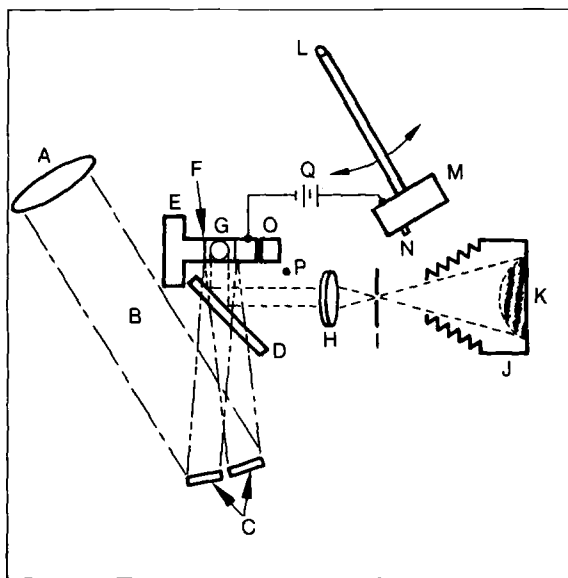


FIG. 8—Timing and impact system layout for the study of the cantilever beam shown in Fig. 7.

both before-impact and impact moiré patterns were superimposed onto one negative (Kodak No. 4143 high-speed infrared film). Because a finer and constant carrier pattern, plus the zero load state pattern, existed between both moiré patterns, the net effect after Fourier filtering of the carrier pattern on the exposed film was the true net displacement field at the time window selected. Figure 11 shows the Fourier filtering optical design. Figure 12 shows the carrier-patterned double exposure and the Fourier filtered information from this exposure.

The single to double pulsing of the ruby laser systems is currently being increased to pulsing rates of up to 109 000 pulses/s. It should be noted that many other laser systems, such as cavity dumped and chemical lasers, can achieve kiloHertz pulsing rates. However, in these alternative systems the intensity of light is very low (in microjoules), the TEM 00

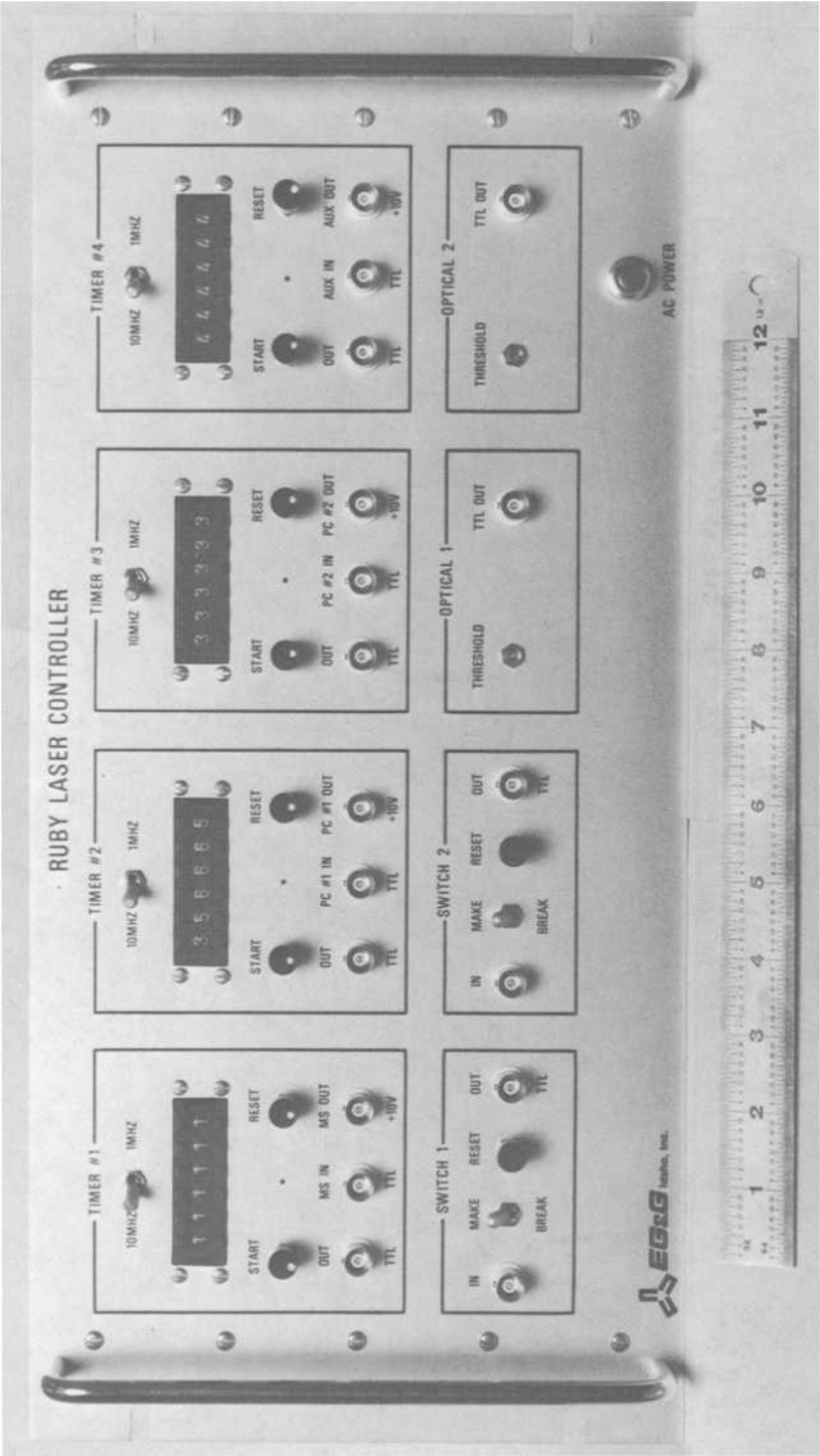


FIG. 9—The timing system for the ruby pulsed laser.

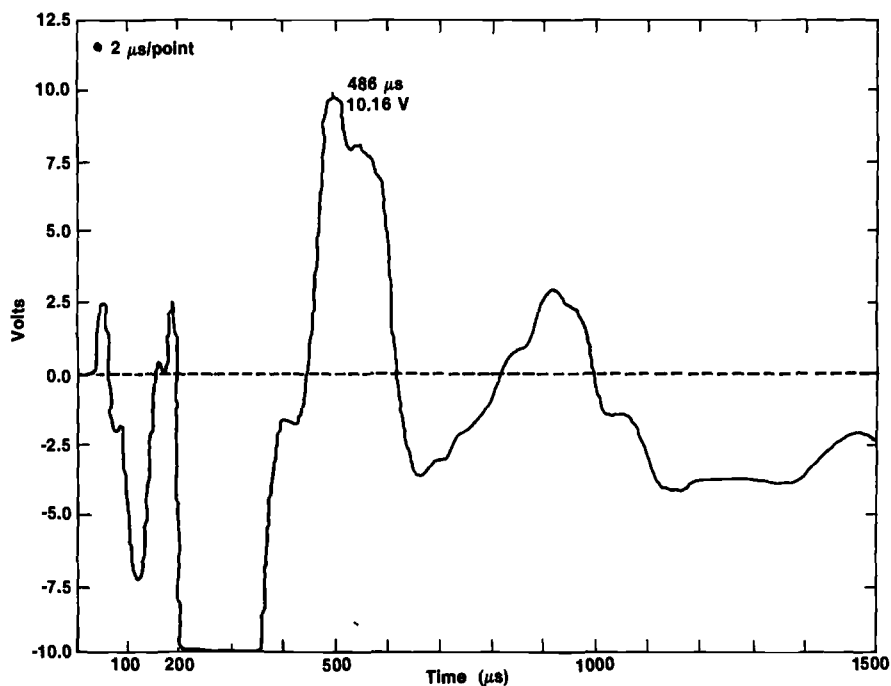


FIG. 10—Longitudinal wave history for the cantilever beam specimen (Fig. 9) struck end-on.

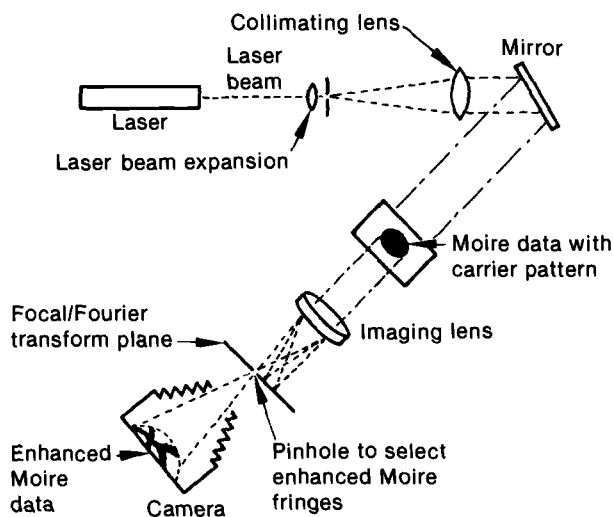
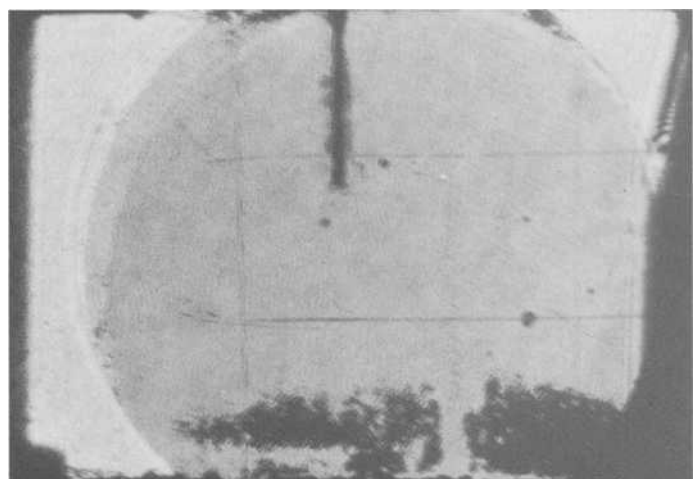
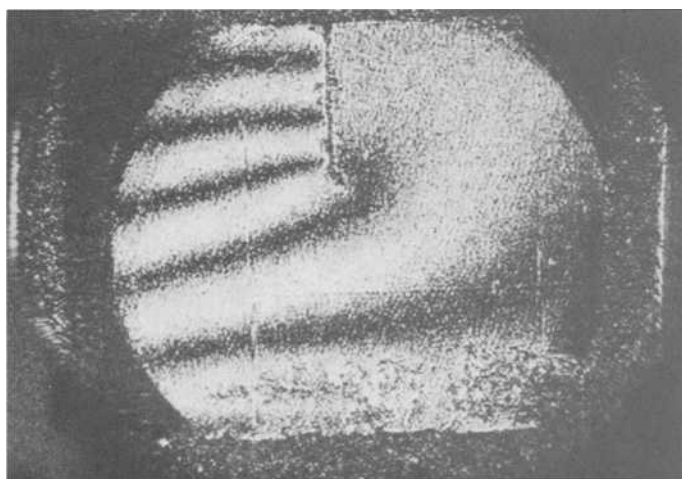


FIG. 11—Fourier filtering system.



Before

289 μ s

After

284 μ s

FIG. 12—Moiré pattern before and after Fourier filtering: (before) negative with high-frequency carrier pattern plus the displacement information; (after) Fourier filtered moiré pattern (284 μ s).

transverse intensity mode is not maintained, or the coherence length is very low compared with the 7 m of the ruby laser system. Electrooptic high-speed framing cameras may be employed with low light intensity or even continuous lasers. However, the image is transferred to the film by means of a fiber-optic bundle and intensified by a microchannel plate intensifier. The fiber-optic bundle lowers spatial resolution. The plate intensifier lowers the range of contrast typical of gray scales naturally occurring in interference patterns.

There are currently two ways to multiple pulse a ruby rod system; both rely on the principle

of releasing the ruby rod's charged energy in multiple releases instead of one. The first method, pioneered by Rowlands [24], relies on pulsed high-voltage Pockle's cell effects to act as fast shutters for the lasing ruby rod. The method developed at INEL is based on the acoustooptic effect. A material, in this case fused silica, is excited by electromagnetic waves that generate acoustic oscillations in the crystal. The optical effect of this phenomenon is that the diffraction angle of light passing through the crystal changes, due to interaction with the resulting volume diffraction grating, from the acoustic oscillation. If this excited crystal is put as a "shutter" in the ruby oscillation cavity, the net effect is that the gain of the ruby laser, and hence its output, will vary with the acoustic amplitude applied to the silica. Fused silica was chosen because of its resistance to high-power laser damage. Figure 13 shows the net rapid pulsing effect of the acoustooptic modulator in the rod, which is an effective random rapid pulsing of 109 000 pulses/s. The word "random" is chosen because the lasing of ruby rods is a quantum mechanical effect, and thus statistical in nature. Finally, this information from the rapid pulsing is "streaked" off onto a continuous loop of film in a streak camera system (Beckman Whitley Model 152) with its imaging slit removed [24]. The result of this procedure will be a continuous record of deformation with a 10- μ s resolution.

Results

This section deals with the results of dynamic moiré interferometry for stress-wave/crack-tip interactions in Type 1018 steels. The first case to be discussed will be the initial diffraction process at a crack due to a longitudinal pulse. Second, the later time scale case of structural resonance at the crack tip due to the returning wave, which is often ignored but potentially dangerous, will be considered.

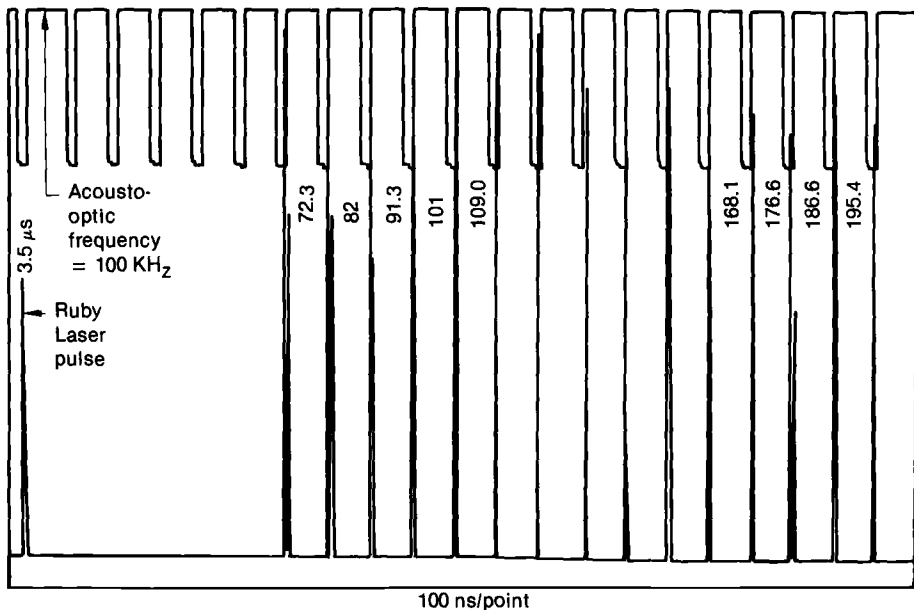


FIG. 13—Pulsing of the ruby rods with the acoustooptic modulator.

The results presented are for the simplest case of a stress-wave/crack-tip interaction: diffraction by a longitudinal or *P* wave. The theory of diffraction and wave scattering is contained in the realm of classical wave mechanics. However, the theory of the diffraction and scattering by stress concentrations, such as for a crack, is relatively new and has been developed within the last century. The more recent work is by DeHoop [25], Pao and Mao [26], Achenback [27], Achenback and Nuismer [7], and Freund [6].

A simple experiment was designed to produce the displacement fields for a stationary crack diffracting an incoming longitudinal pulse in Type 1018 steel. A cantilever beam was constructed and instrumented as shown in Fig. 7. The impact occurred at the end of the beam. The beam was initially impacted with piezoelectric sensors in the grating area to determine the wave history response of the specimen. Further, a piezoelectric driver was used to determine the longitudinal wave speed of the material up to the grating region. For the material under study, the longitudinal wave speed was determined to be 5500 m/s. Under impact, the strain gage output at the first gage in the middle of the specimen was 200 $\mu\text{mm/mm}$. This value shows that the wave itself produces stresses that are within the dynamic elastic limit of the material. To ensure that the impact at the end of the beam was indeed a longitudinal wave, the strain gages located behind the first gage (see Fig. 7) were also checked; both gages produced values of 200 $\mu\text{mm/mm}$. Further, a back-side gage was employed opposite the pair of gages to verify that out-of-plane bending was not produced. Out-of-plane bending was found to be negligible during the test. A large swinging hammer was employed to produce the end impact (Fig. 8).

Before a crack was introduced into the beam, a medium-sensitivity 300-l/mm grating was replicated on the beam midspan to confirm optically that the wave was longitudinal and verify the feasibility of the concept of dynamic moiré interferometry. Figure 14 shows the results of this preliminary test. The right hand picture is the "null" pattern existing before the wave arrived at the grating region. This pattern, as explained above, is the preexisting pattern due to an initial misalignment between the active and reference gratings. The left-hand picture in Fig. 14 shows the pattern when the front of the wave had entered the grating region. By subtracting the "null" pattern from the deformed pattern, it was found that the spatial shape of the deformation wave was a uniform longitudinal wave. The wave displacement field agreed with the strain gage data. The time window was set according to the piezoelectric transducer data at 50 μs .

Figure 15 shows the schematic representation of a longitudinal pulse encountering a crack and diffraction with the tip acting as a point source. Provided the wave is parallel to the crack, the diffraction event will produce pure Mode I loading [6]. Figure 16 is a picture of the specimen with the crack inserted. The crack is actually an artificial rectangular slit 0.2 mm in width. Smith [28] has shown that this configuration will approximate a natural crack within 10% of the SIF value. Figure 17 shows the opening crack mode displacement field sequence of the longitudinal wave encountering the crack and subsequently diffracting at the crack tip. These results confirm that a longitudinal pulse produces Mode I loading of the crack when parallel to the crack.

Discussion

Figure 10 shows that the diffraction process or initial longitudinal wave loading of the crack (50 μs) occurs with much lower piezoelectric effect or magnitude than events farther down the time history of wave travel, particularly those in the interval of 198 to 284 μs . (For Fig. 10, the negative voltage represents a tensile loading. The tensile loading shown in Fig. 10 was saturated during the time span of 198 to 360 μs .) Indeed, this surprised the authors as it was thought that the most severe loading always occurred during initial dif-

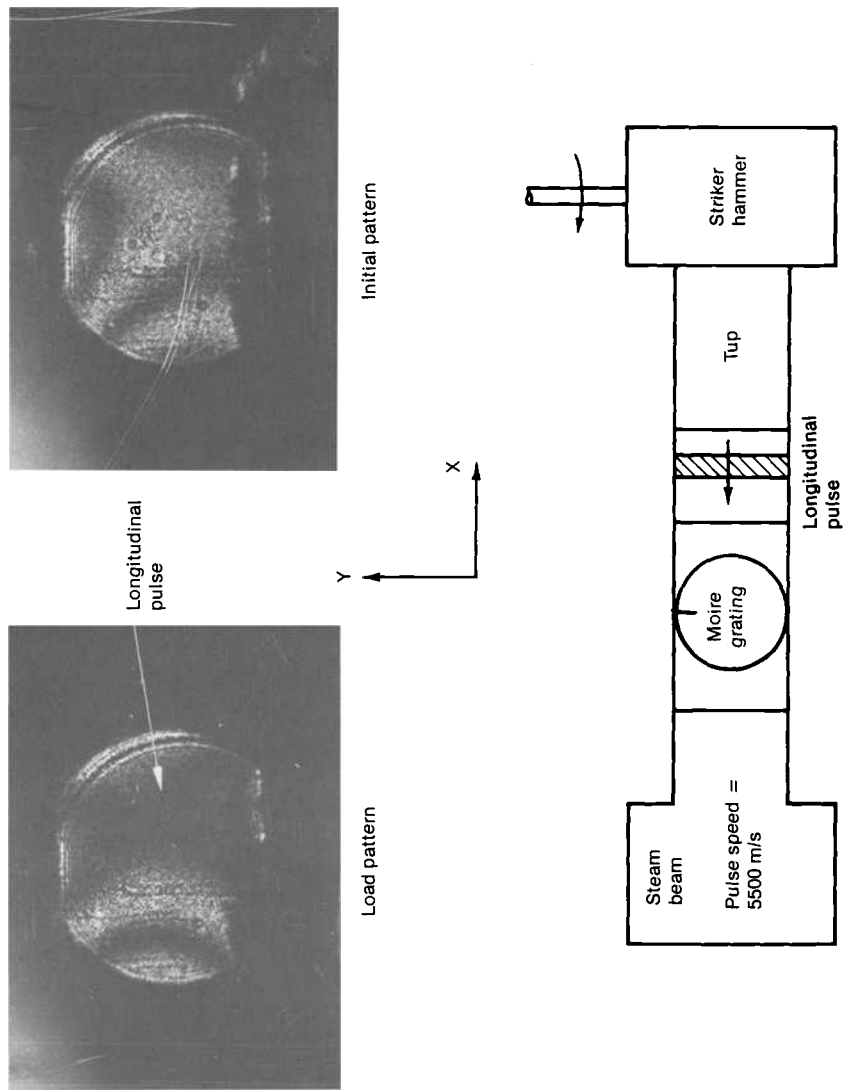


FIG. 14—Longitudinal pulse moiré pattern.

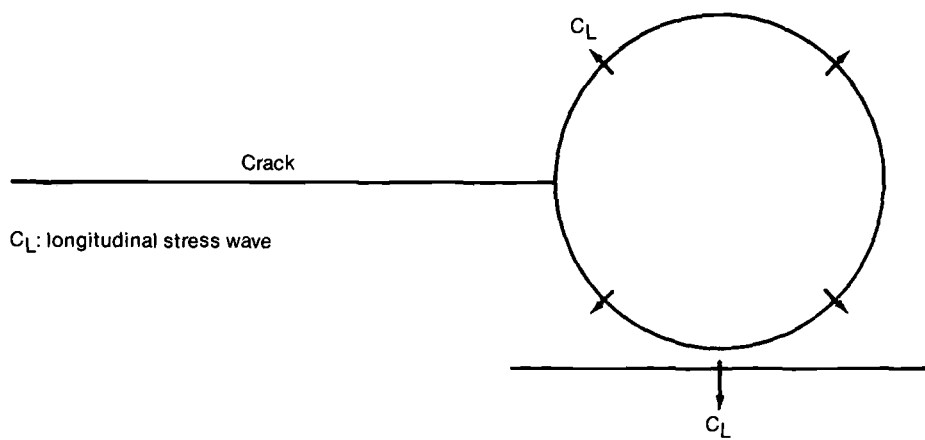


FIG. 15—Diffraction of a longitudinal pulse parallel to the crack.

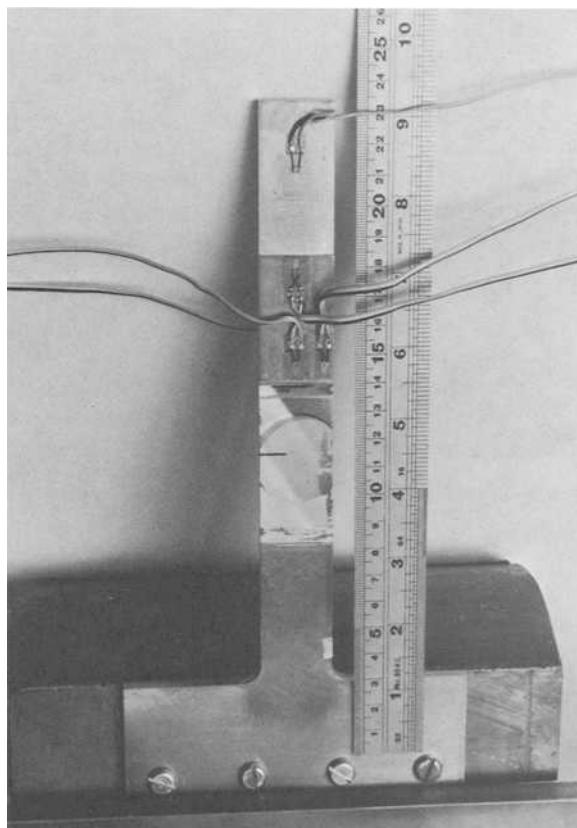


FIG. 16—Actual specimen configuration.

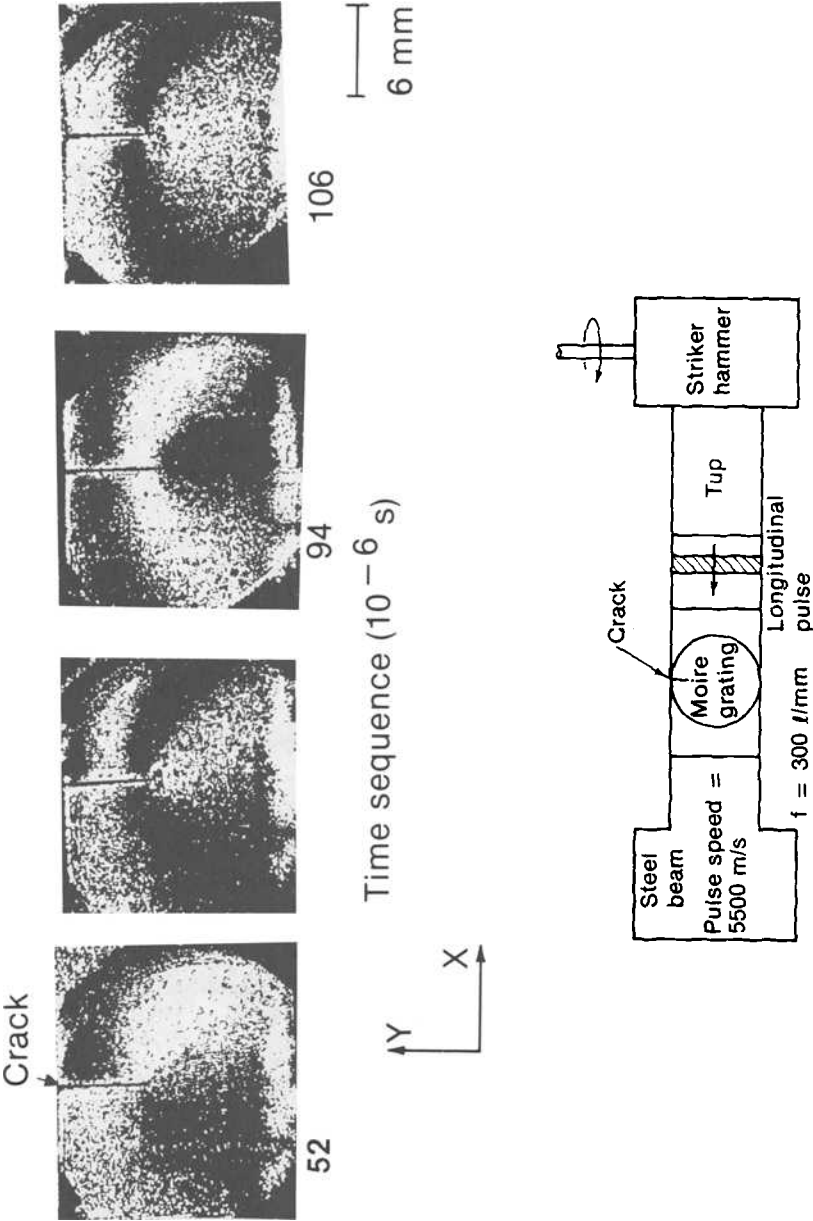


FIG. 17—Diffraction displacement field for the impacted cantilever beam.

fraction/loading of the crack. The window for observation was tuned to this interval of interest, with the results shown in Fig. 18. The fringe count in Fig. 18 shows that three times as much deformation occurs at the crack as in the initial loading or diffraction case. Further, this loading is asymmetric or mixed mode in nature. From the time history (Fig. 10) the interval of 198 to 284 μs occurs when the wave reaches the end of the clamped beam and reflects numerous times. Figure 18 shows that for the 198 to 284- μs interval, the beam is in structural resonance. This phenomenon brings out an important point that is too often ignored in the dynamic response of cracks. The structural resonance can clearly cause much more severe loading effects than the initial loading. Two regimes must be considered when evaluating the dynamic structural integrity of flawed regions: the initial and local wave dynamics and the global structural resonance of the wave interacting with the structure.

Figure 18 also shows an interesting phenomenon of resonance between the crack and the structure of the beam. It is evident in Fig. 18 that the fringe pattern for 284 μs is not only asymmetric but, from a quasi-static point of reference, incorrect. Quasi-static equilibrium dictates that the same number of fringes exist on both sides of the crack. Dynamically, however, the pattern of 284 μs is correct. The pattern of 284 μs shows that the right-hand side of the crack is a rigid body resonating in relation to the motionless left-hand side of the crack. Dynamic equilibrium in the 284- μs pattern is maintained by the sum of tractions equilibrating with the acceleration of the material.

In conclusion, from the results of this work it was found that the stress wave interaction with a crack really contains two regimes of importance. First, and most often studied, is the initial impact wave loading of a flaw, as evidenced by the displacement field of Fig. 17. After careful validation of the character of the wave (that is, that it is longitudinal), it becomes apparent that this wave indeed produces a diffraction displacement field that is Mode I in nature. Second, but often neglected in the study of stress wave propagation and cracks, is the later time history of structural resonance (Fig. 18). For structural integrity in general, this later type of loading appears to have as much serious potential for loss of integrity by flaw initiation and growth as the initial loading. The question of whether the flaw initiation is dynamic during later time resonance is open to debate. However, the authors feel that, to a large extent, crack initiation during resonance is dynamic since the structural resonance case is still dominated by stress wave propagation in the bar. In the cantilever beam case, resonance is dominated by bending waves. The results of Kalthoff [29] further bear evidence that structural resonance is indeed a dynamic event at the crack tip.

Localized Displacement Equations for a Dynamic Stress-Intensity Factor

This section derives localized dynamic stress-intensity factor K_I^D , algorithms from near-tip displacement equations. The main proposition in this derivation is that localized displacement fields of the type shown in Figs. 17 and 18 will provide the singularity dominant information.

Kobayashi [30] has noted that, provided one is close to a dynamic crack tip, a truncated stress series characterizing the dynamic crack is feasible. This observation makes practical sense in the elastic case of a propagating crack. A dynamic elastic crack may be formulated as an eigenvalue problem [31] and, as such, the stress and displacement fields are eigenfunction solutions to the eigenvalue problem. Similar to Williams' eigenvalue solution for a static crack [32], the dominant terms in the eigenvalue series for a dynamic crack reflect the nature of the fracture process. For elastic two-dimensional cracks, the leading term is the classical square root stress singularity. It is this first eigenvalue term, the stress singularity, that is the "robust" parameter of the eigenseries which dominates the solution close to the

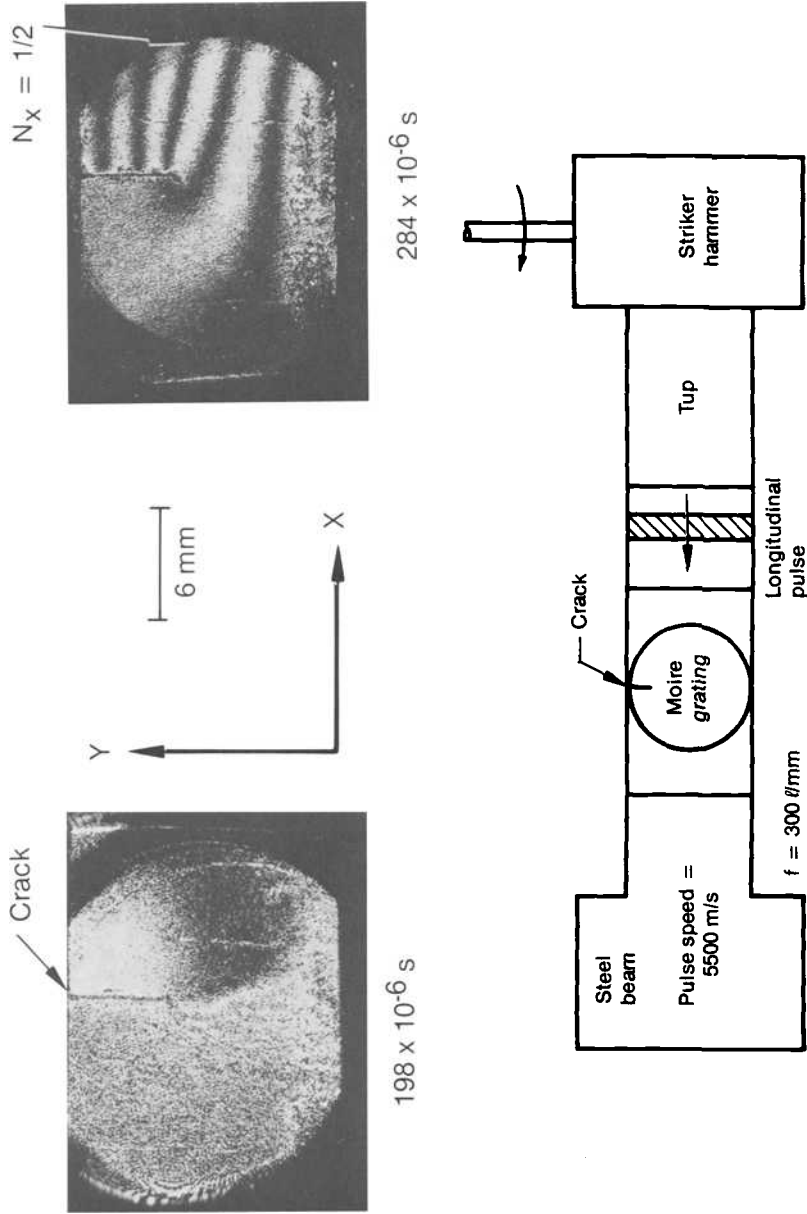


FIG. 18—Structural resonance displacement field.

crack. If data can be taken close to the crack it will naturally be indicative of the fracture process. King [33] has reported the following eigenfunctions for the displacement of a dynamic crack in steady propagation in a homogeneous linearly elastic medium

$$U_n = A_n \left(\frac{n}{2} + 1 \right) \left[r_1^{n/2} \cos \left(\frac{n\theta}{2} \right) - \frac{g(n)}{2} r_2^{n/2} \cos \left(\frac{n\theta}{2} \right) \right]$$

and

$$U_v = A_n \left(\frac{n}{2} + 1 \right) \left\{ -s_1 r_1^{n/2} \sin \left(\frac{n\theta}{2} \right) + \frac{1}{2} \left[\frac{g(n)}{s_2} \right] r_2^{n/2} \sin \left(\frac{n\theta}{2} \right) \right\}$$

where

$$g(n) = 4s_1 s_2 / (1 + s_2^2) \text{ for } n \text{ odd,}$$

$$g(n) = 1 + s_2^2 \text{ for } n \text{ even,}$$

$$r_i = (x - ct) + s_i y, \text{ and}$$

$$s_i = (1 - c^2/c_i^2)^{1/2} \text{ for } i = 1, 2,$$

where c is the crack speed, and c_1 and c_2 are the longitudinal and shear wave speeds. As King [33] has noted, $n = 0$ yields a rigid body motion, and $n = 1$ yields the familiar crack tip leading displacement power of $1/2$. As $c \rightarrow 0$, the Williams [32] static solution is found. If one considers the V displacement field, taking the first two terms (besides the $n = 0$, which yields $V = 0$)

$$V = V_1 f_1(r_i^{1/2}, \theta)_i + V_2 f_2(r_i, \theta)_i \quad i = 1, 2$$

dividing by f_1 yields

$$\frac{V}{f_1} = V_1 + V_2 \left(\frac{f_2}{f_1} \right)$$

however

$$V_1 = K_I^D$$

Thus, if one plots the displacement values divided by f_1 at a fixed θ , versus f_2/f_1 , a distance from the crack tip whose units are $r^{1/2}$, and extrapolates the data to the origin, $r \rightarrow 0$, one should obtain the dynamic stress-intensity factor K_I^D . This process has as yet not been performed on actual moiré interferometry data, so the interpretation is open to debate. Future work will test the validity of this near-field algorithm.

In conclusion, this section has laid theoretical groundwork for interpreting propagation of elastic cracks from their near-tip displacement fields. The authors define the near tip to be on the order of less than 10 mm. The assumptions involved are those for the Williams [32] static eigenvalue problem, a two-dimensional phenomena, linear elasticity, and, for the dynamic case, a steady moving crack. Such phenomena as three-dimensional free surface effects, plasticity, and acceleration of the crack have not been addressed.

Conclusions

This paper has presented the accomplishments of dynamic moiré interferometry to date. Current efforts are aimed at yielding interferograms at rates up to 100 kHz to 1 MHz. The synchronization to streak cameras is in progress. The possibility of using electrooptic image converter cameras with continuous-wave lasers has been discussed. The results for dynamic crack problems have shown promise, as discussed in this paper. The ability to resolve the local crack-tip displacement phenomena due to stress wave-materials interactions is now at hand.

The problem of local crack-tip diffraction phenomena has been studied in detail on an actual engineering material. The structural resonance occurring later in the time history of deformation has been discussed, and the potential for more severe loadings in structural resonance than in the initial loading has been highlighted. An algorithm for local elastic dynamic stress-intensity values has been developed utilizing the existence of near crack-tip displacement fields.

Future work in this program will test the validity of the developed algorithms, study local plasticity effects under dynamic loading to move towards higher loading rate regimes (the current strain rate is $10^3/\text{s}$), and study flaws in anisotropic materials under rapid loading.

Acknowledgments

The encouragement and insight of Professors Daniel Post, Albert Kobayashi, and Carlos Ruiz are greatly appreciated. The technical assistance of L. D. Reynolds and C. Shull is further acknowledged. This work was supported by the U.S. Department of Energy, Office of Energy Research, Office of Basic Engineering Sciences (Dr. O. Manley, program manager), and the Office of Naval Research, Structural Mechanics Division (Dr. Y. Ragapakse, program manager), under DOE Contract No. DE-AC07-76ID01570.

References

- [1] Rice, J. R. and Levy, N., "Local Heating by Plastic Deformation at a Crack Tip," *Physics of Strength and Plasticity*, A. Argon, Ed., MIT Press, Massachusetts Institute of Technology, Cambridge, MA, 1969, pp. 277-293.
- [2] Kanninen, M. F., Mukherjee, A. K., Rosenfield, A. R., and Hahn, G. T., "The Speed of Ductile Crack Propagation and the Dynamics of Flow in Metals," *Mechanical Behavior of Materials under Dynamic Loading*, U. S. Lindholm, Ed., Springer-Verlag, New York, 1967, pp. 96-133.
- [3] *Theoretical Foundations for Large Scale Computations for Nonlinear Material Behavior*, S. Nemat-Nasser, R. J. Asaro, and G. Hegemier, Eds., Martinus Nijhoff, Amsterdam, The Netherlands, 1984.
- [4] Freund, L. B., "Crack Propagation in an Elastic Solid Subjected to General Loading—I. Constant Rate of Extension," *Journal of the Mechanics and Physics of Solids*, Vol. 20, 1972, pp. 129-140.
- [5] Freund, L. B., "Crack Propagation in an Elastic Solid Subjected to General Loading—II. Non-Uniform Rate of Extension," *Journal of the Mechanics and Physics of Solids*, Vol. 20, 1972, pp. 141-152.
- [6] Freund, L. B., "Crack Propagation in an Elastic Solid Subjected to General Loading—III. Stress Wave Loading," *Journal of the Mechanics and Physics of Solids*, Vol. 21, 1973, pp. 47-61.
- [7] Achenbach, J. D. and Nuismer, R., "Fracture Generated by a Dilatational Wave," *International Journal of Fracture Mechanics*, Vol. 7, No. 1, 1971, pp. 77-88.
- [8] Achenbach, J. D., Keer, L. M., and Mendelson, D. A., "Elastodynamic Analysis of an Edge Crack," *Journal of Applied Mechanics*, Vol. 47, September 1980, pp. 551-556.
- [9] Simha, K. R. Y. and Fourny, W. L., "Investigation of Stress Wave Propagation Through Intersecting Bars," *Journal of Applied Mechanics*, Vol. 51, June 1984, pp. 345-353.
- [10] Doyle, J. F. and Kamle, S., "An Experimental Study of the Reflection and Transmission of Flexural Waves at a T-Joint," *Proceedings, 1985 SEM Conference on Experimental Mechanics*, Society for Experimental Mechanics, Las Vegas, NV, 1985, pp. 560-564.

- [11] Deason, V. A., Epstein, J. S., and Reuter, W. G., "A Dynamic Moiré Interferometry Technique," *Proceedings, 1985 SEM Conference on Experimental Mechanics*, Society for Experimental Mechanics, Las Vegas, NV, 1985, p. 475.
- [12] Duffy, J., "Temperature Measurements During the Formation of Shear Bands in a Structural Steel," *Mechanics of Material Behavior*, G. J. Dvorak and R. T. Shield, Eds., Elsevier Science, New York, 1984.
- [13] Durelli, A. J. and Parks, V. J., *Moiré Analysis of Shear Strain*, Prentice Hall, Englewood Cliffs, NJ, 1970.
- [14] Kobayashi, A. S., Harris, D. O., and Engstrom, W. L., "Transient Analysis in a Fracturing Magnesium Plate," *Experimental Mechanics*, October 1967, pp. 434-440.
- [15] Post, D., "Sharpening and Multiplication of Moiré Fringes," *Experimental Mechanics*, Vol. 7, No. 4, pp. 154-159.
- [16] Guild, J., *The Interference Systems of Crossed Diffraction Gratings*, Clarendon Press, Oxford, England, 1956.
- [17] Post, D., "Moiré Interferometry," *Handbook of Experimental Stress Analysis*, A. Kobayashi Ed., Prentice-Hall, Englewood Cliffs, NJ, 1986, Chapter 4.
- [18] Nicoletto, G., Post, D., and Smith, C. W., "Moiré Interferometry for High Sensitivity Measurements in Fracture Mechanics," *Proceedings, 1982 Joint Conference on Experimental Mechanics*, Society for Experimental Mechanics, Dearborn, MI, pp. 266-270.
- [19] Smith, C. W., Epstein, J. S., and Olaosebikan, O., "Boundary Layer Effects in Cracked Bodies: An Engineering Assessment," *Fracture Mechanics: Seventeenth Volume, ASTM STP 905*, American Society for Testing and Materials, Philadelphia, 1983.
- [20] Benthem, J. P., "The Quarter Infinite Crack in a Half Space: Alternative and Additional Solutions," *International Journal of Solids and Structures*, Vol. 16, 1980, pp. 119-130.
- [21] "Periodic Structures, Gratings, Moiré Patterns, and Diffraction Phenomena," *SPIE Conference Proceedings*, Vol. 240, 1980.
- [22] Goodman, J. W., *Introduction to Fourier Optics*, McGraw Hill, New York, 1968.
- [23] Leith, E. N., Swanson, G., and Leon, S., "Construction of Diffraction Optical Elements in Noncoherent Light," *SPIE Conference Proceedings*, Vol. 503, 1984, pp. 2-9.
- [24] Rowlands, R. E., Taylor, C. E., and Daniel, I. M., "A Multiple-Pulse Ruby-Laser System for Dynamic Photomechanics: Applications to Transmitted and Scattered Light Photoelasticity," *Experimental Mechanics*, September 1969, pp. 385-393.
- [25] DeHoop, A. T., "Representation Theorems for the Displacement in an Elastic Solid and Their Application to Elastodynamic Diffraction Theory," D.Sc. thesis, Technische Hogeschool, Delft, The Netherlands, 1958.
- [26] Pao, Y. H. and Mow, C. C., *Diffraction of Elastic Waves and Dynamic Stress Concentrations*, Crane, Russak, and Co., New York, 1973, pp. 573-595.
- [27] Achenbach, J. D., *Wave Propagation in Elastic Solids*, North-Holland Series in Applied Mathematics and Mechanics, Vol. 16, H. A. Lauwerier and W. T. Koiter, Eds., North-Holland, Amsterdam, 1973, pp. 380-388.
- [28] Smith, C. W., McGowan, J. J., and Jolles, M., "Effects of Artificial Cracks and Poisson's Ratio upon Photoelastic Stress-Intensity Determination," *Experimental Mechanics*, Vol. 16, No. 5, 1976, pp. 188-193.
- [29] Kalthoff, J. F., "Stress-Intensity Factor Determination by Caustics," *Proceedings, SEM 1982 Joint Conference on Experimental Mechanics*, Society for Experimental Mechanics, Honolulu, HI, 1982, pp. 1119-1126.
- [30] Kobayashi, A. S. and Mall, S., "Dynamic Fracture Toughness of Homalite-100," *Experimental Mechanics*, Vol. 18, No. 1, January 1978, pp. 11-18.
- [31] Rice, J. R., "Mathematical Analysis in the Mechanics of Fracture," Vol. 2, *Fracture*, H. Leibowitz, Ed., Academic Press, New York, 1968, Chapter 3, p. 191.
- [32] Williams, M. L., "On the Stress Distribution at the Base of a Stationary Crack," *Journal of Applied Mechanics*, Vol. 24, 1957, pp. 109-114.
- [33] King, W. W., Malluck, J. F., Abernson, J. A., and Anderson, J. M., "Application of Running Crack Eigenfunctions to Finite-Element Simulation of Crack Propagation," *Mechanics Research Communications*, Vol. 3, 1976, pp. 197-202.

Crack Arrest Theory and Applications: Part I

Determination of Dynamic Fracture Behavior in 4340 Steel Compact Crack Arrest Specimens Using Birefringent Coatings and Finite-Element Analysis

REFERENCE: Khatri, S. and Barker, D. B., “Determination of Dynamic Fracture Behavior in 4340 Steel Compact Crack Arrest Specimens Using Birefringent Coatings and Finite-Element Analysis,” *Fracture Mechanics: Nineteenth Symposium, ASTM STP 969*, T. A. Cruse, Ed., American Society for Testing and Materials, Philadelphia, 1988, pp. 507–523.

ABSTRACT: A split-birefringent coating technique, coupled with high-speed photography, was used to record the dynamic isochromatic fringe pattern associated with crack propagation and arrest in 4340 steel compact crack arrest fracture specimens. From the data contained in the isochromatic fringe patterns, the associated dynamic stress-intensity factor was calculated in two different ways. First, the dynamic stress-intensity factor was calculated from the isochromatic fringe information directly. Next, the isochromatic fringe patterns were used to obtain a crack position history which was used for input to a two-dimensional dynamic finite-element code used in the “generation mode.” These two dynamic stress-intensity factors were compared with each other and with the crack arrest toughness as calculated by the proposed ASTM method for estimating crack arrest toughness.

KEY WORDS: crack arrest, dynamic fracture, compact crack arrest (CCA) specimen, fracture mechanics

The work described in this paper is a combined numerical and experimental attempt directed towards developing a better understanding of the dynamic effects on crack propagation and arrest in a compact crack arrest (CCA) specimen. This crack-line wedge-loaded modified compact tension specimen has been widely used in crack arrest testing and is the recommended specimen in the proposed ASTM plane-strain crack arrest toughness testing procedure being formulated by a task group of ASTM Subcommittee E24.01 on Fracture Mechanics Test Methods, a subcommittee of ASTM Committee E-24 on Fracture Testing. The study reported in this paper consisted of comparing the experimentally observed fracture behavior in 4340 steel CCA specimens that had a birefringent coating mounted on one surface, with the results obtained from a two-dimensional finite-element analysis run in a “generation mode” analysis.

The numerical elastodynamic fracture analyses were performed using a two-dimensional finite-element code for stress analysis of moving cracks (SAMCR) developed at the University of Maryland. For this study, SAMCR was used in “generation mode” to model the observed fracture behavior in experiments previously conducted at the University of Maryland. These previous experiments used a split-birefringent coating technique coupled with high-speed photography to obtain the crack-tip position history for input into SAMCR. The

¹ Graduate student and associate professor, respectively, Department of Mechanical Engineering, University of Maryland, College Park, MD 20742.

high-speed photographs of the isochromatic fringe patterns in the birefringent coatings also furnished an independent means for evaluating the dynamic stress-intensity factor.

Rosakis and Zehnder [1] recently reviewed the results of various direct experimental measurements and numerical schemes in determining the dynamic stress-intensity factors in structural metals. The purpose of this paper is to add more information to the data base available for 4340 steel. Neither the technique of birefringent coatings, nor the generation mode use of a dynamic fracture code is new to the analysis of fracture in 4340 steel. Typically, the results of previous researchers have been limited to either a direct experimental measurement, with caustics or birefringent coating, or only a generation mode analysis, inputting crack position information obtained experimentally with a crack position gage and some assumption or measurement of the boundary loads or displacements. This paper presents the results from both a numerical and an experimental analysis for the dynamic stress-intensity factor during a run/arrest event in a CCA specimen.

Description of Experimental Method

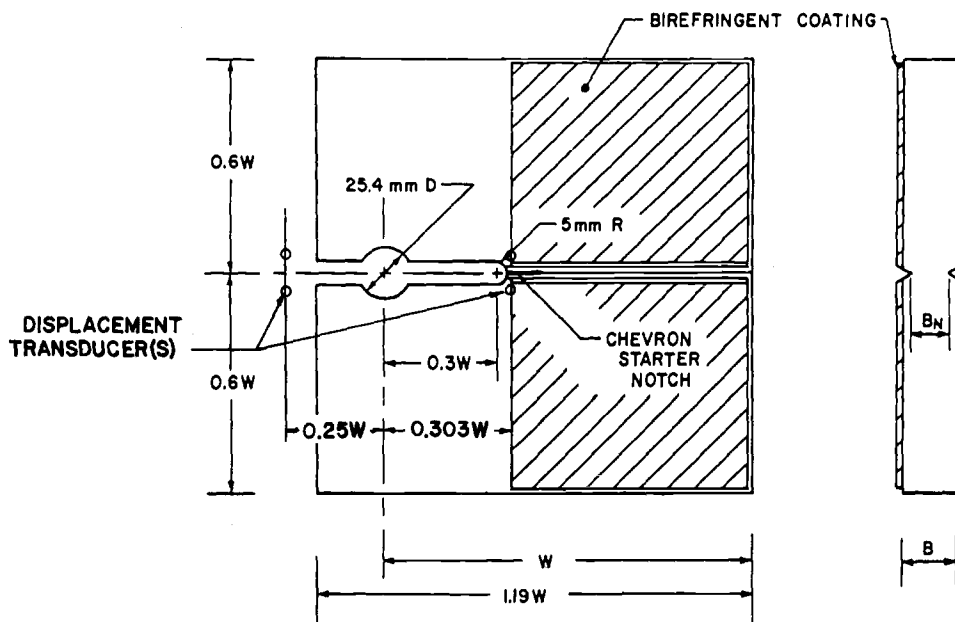
By using a split-birefringent coating technique coupled with high-speed photography, it was possible to record the dynamic isochromatic fringe patterns associated with crack propagation and arrest in 4340 steel CCA specimens. From these isochromatic fringe patterns, the crack-tip position history and the associated dynamic stress-intensity factor, K_D , could be calculated. The use of the split-birefringent coating technique alleviates the uncertainty as to whether the observed response in the coating is dominated by the fracture of the base material or by the plastic deformation and fracture of the coating itself [2].

The experiments that were used for sources of data for this paper were conducted several years ago at the University of Maryland and are described in detail in Refs 3, 4, and 5. Briefly, the CCA specimens were made from hot-rolled, annealed, aircraft-quality 4340 steel that was heat treated to varying hardness levels. Figure 1 is a schematic of the CCA specimen. The W dimension of the specimens was either 170 mm or 210 mm with a nominal thickness of 25.4 mm. Two different face groove depths were used with a B_N/B of 0.875 and 0.75. Machined chevron crack-starter notches were employed to control crack initiation. The birefringent coating mounted on one side of the specimen was nominally a 2-mm-thick polycarbonate sheet (PS-1) with a reflective backing, manufactured by Photoelastic, Inc. The coating was bonded to the steel using Hysol EA 9810 structural high-strength epoxy adhesive. The crack-opening displacement was monitored with an eddy current displacement transducer (Kaman Model KD-2300-25), mounted at a position $0.25 W$ above the load line, whose signal was recorded on a Nicolet 2090 digital oscilloscope. Some of the specimens had a second displacement transducer mounted at $0.303 W$ below the load line.

A Cordin model 330A drum camera was used with specially designed xenon flash lamps to record the dynamic isochromatics. The exposure duration was about $1.5 \mu\text{s}$ per frame. The typical run/arrest event produced 50 to 70 frames of useful data. Kodak 2495 RAR high-speed negative film, an orthochromatic film sensitive to wavelengths less than about 600 nm, used in conjunction with a Kodak No. 8 filter, provided suitably monochromatic light for recording the isochromatic fringes.

The CCA specimen was loaded in a darkened room, with the camera shutter open, by a hydraulic loading fixture schematically shown in Fig. 2. The trigger to fire the lamps occurred with the breaking of a conductive wire placed at the tip of the machined crack-starter notch. Within 15 to 20 μs of the trigger signal, the lamps developed sufficient intensity to expose the film. Figure 3 is a typical isochromatic photograph of the running crack traveling at 439 m/s.

Data processing of the photographs was performed using a digitizer tablet interfaced with



COMPACT TENSION FRACTURE SPECIMEN

$W = 210 \text{ mm}$ $B = 25.4 \text{ mm}$ $B/B_N = 8/7 \text{ or } 4/3$

FIG. 1—Schematic diagram of compact crack arrest (CCA) specimen.

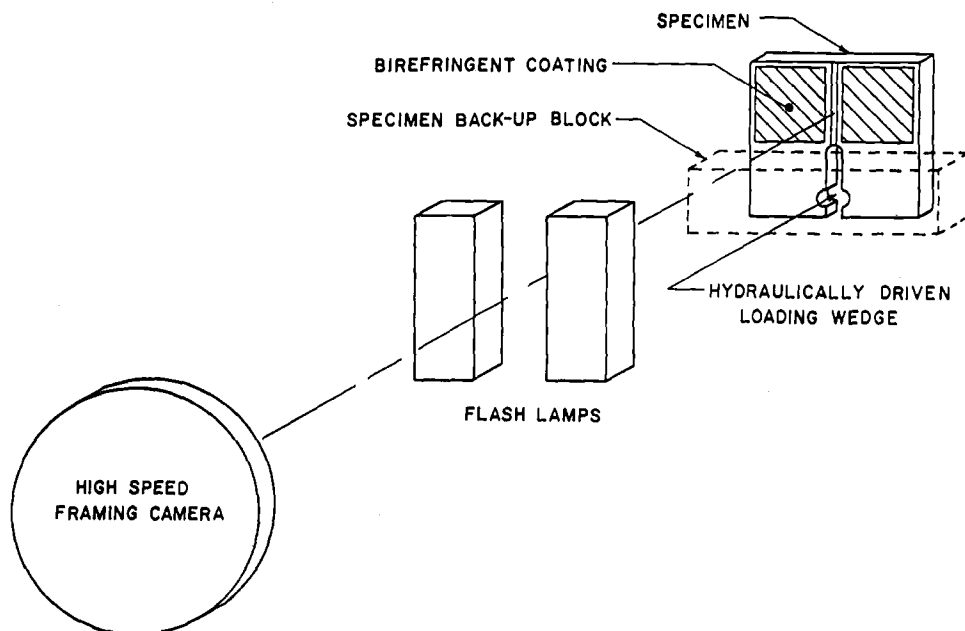


FIG. 2—Schematic of experimental loading arrangement.

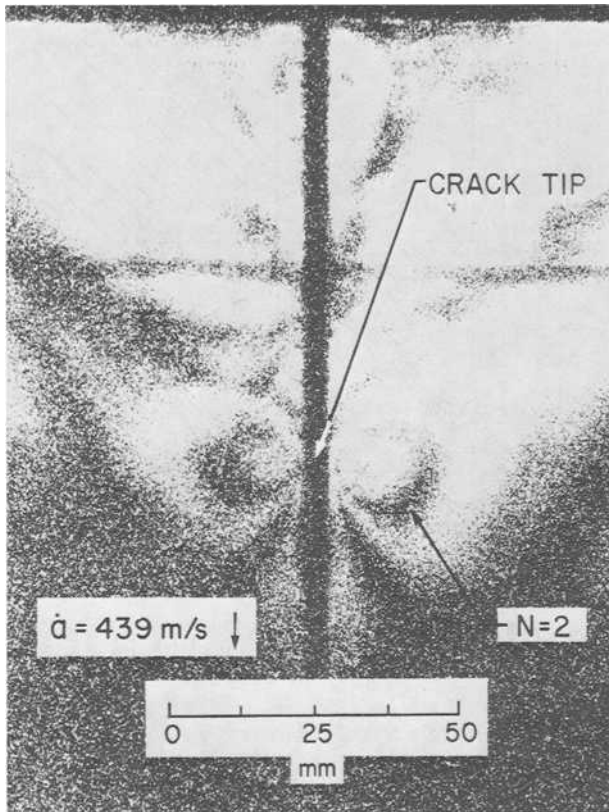


FIG. 3—Typical isochromatic photograph of running crack.

a personal computer. The crack-tip position was obtained from each frame as well as full-field isochromatic fringe data for analyzing K . The analysis of the isochromatic fringe patterns to determine K involved an overly deterministic method based on the work of Sanford [6] and is explained in detail in Ref 5. The analysis method used the first two terms in the static near-field equations. It was felt that the errors introduced by not employing the dynamic equations for the stress fields, or the higher order terms, were minimal compared with errors in resolution and accuracy in measuring the exact position of the fringe maxima. The typical scatter in K from analyzing two adjacent photographs indicated that the errors in calculating K from the isochromatics were on the order of $\pm 10\%$.

The crack-mouth opening at $0.25 W$ above the load line was continually monitored during the event. From this crack-mouth opening data and knowledge of the initial and final arrested crack length, the stress-intensity factor at initiation, K_o , and a static estimate of the stress-intensity factor at arrest, K_a , could be calculated. These calculations were done in accordance with the proposed ASTM Test for Determining the Plane-Strain Crack-Arrest Fracture Toughness K_{Ia} of Ferritic Steels (E 1221). The equation for K is

$$K = E\Delta f(x) \frac{\left(\frac{B}{B_N}\right)^{1/2}}{W^{1/2}}$$

where E is Young's modulus, Δ is either the initial crack-opening displacement or the crack-opening displacement immediately after arrest, B/B_N is the ratio of the specimen thickness to the net or notched specimen thickness, and W is the specimen in-plane size, as shown in Fig. 1. The function $f(x)$ is a function based on the nondimensional crack length, a/W , and is given in the proposed ASTM Test E 1221.

Description of the Numerical Method

SAMCR [7] is a two-dimensional, dynamic, finite-element code for the stress analysis of moving cracks developed at the University of Maryland. The code formulation is based on the conventional variational formulation of finite-element theory using the principle of virtual work. The code employs four-node isoparametric elements together with explicit time integration and a restraining nodal force model of incremental crack advance. The code can be used to provide information about the Mode I linear-elastic fracture behavior of bodies under a combination of mechanical, thermal, and pressure loadings. SAMCR operates in two modes: (1) an "application mode," in which the increment of crack extension at each time step is automatically computed based on the calculated stress-intensity factor, K , at the crack tip and the user-specified crack velocity versus the K constitutive relationship, and (2) a "generation mode," in which the states of displacement, strain, and stresses at each time step are calculated based on the user-specified crack extension history.

The finite-element mesh used to analyze the CCA specimen is shown in Fig. 4. The steel split-D pin used to apply the load to the specimen was not modeled. It was assumed that the Hertzian indentations between the pin and specimen were negligible, since both the specimen and the split-D pins were made of steel and a good fit existed between the pins and specimen. A tab on the specimen extending above the load line was modeled in order to use the experimental crack-opening displacement measured at $0.25 W$ above the load line as an input to SAMCR.

Results and Discussion

Four 4340 steel crack arrest experiments were chosen for a plane-stress generation mode analysis by SAMCR. The experimentally measured crack-opening displacement at initiation and the crack position history were used as inputs. The test results for the four analyzed experiments and the properties used for the steel are summarized in Table 1. In the table, the crack-opening displacement (COD) is measured at $0.25 W$ above the load line. The subscript o corresponds to the crack initiation and the subscript f to crack arrest. The values of K_{oc} , based on the proposed ASTM method for crack arrest fracture toughness are also shown in Table 1.

Measuring the location of the crack tip from the high-speed photographs was difficult because of the presence of the groove and the absence of birefringent material. Various least-squares curve fits were tried for the experimentally determined position versus time records, including power series, exponential, polynomial, and various combinations of these. The resulting output from SAMCR of K versus either time or the crack-tip position was relatively insensitive to the choice of the crack-tip history fitting function during the latter stages of crack propagation. It was decided that a third-order polynomial was the best function, since this function not only easily reproduced the crack-tip history but also gave the smoothest and most physically realizable crack velocity as a function of time. For some tests the crack-tip position history approximated by a second-order polynomial seemed to be adequate, but this gave a constant-velocity crack. In order to be consistent for all the experiments, a third-order polynomial function was fit to all the crack-tip position history data.

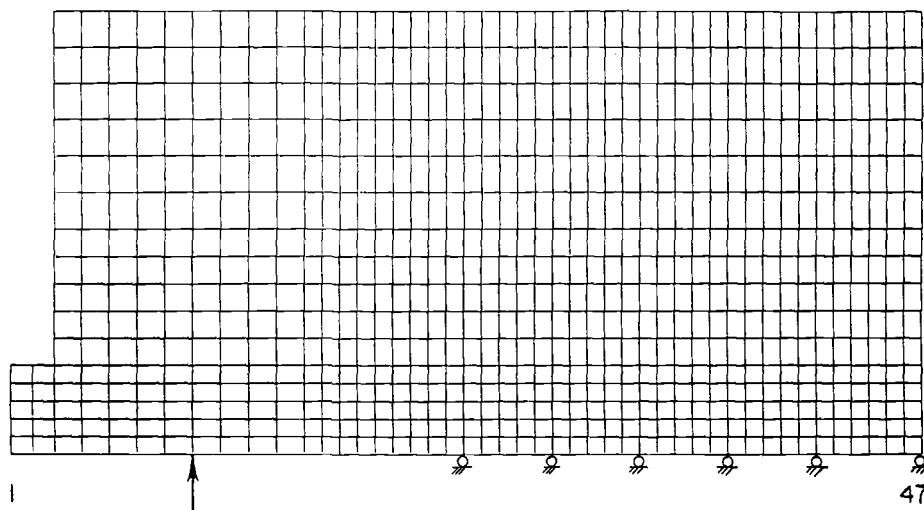


FIG. 4—Mesh in the SAMCR analysis of the CCA specimen.

A typical input crack-tip position history, as obtained from the high-speed photographs, is shown in Fig. 5. In this figure, the raw data as well as the third-order polynomial fit to the data are shown. The polynomial fit is used for the input to SAMCR. For the various experiments analyzed, it was found that the crack-tip velocity decreased from about 425 m/s (Test 413), 675 m/s (Test 415), 825 m/s (Test 362), and 450 m/s (Test 375) to zero in a period of about 250 μ s.

From SAMCR, the stress-intensity factor, K , was plotted as a function of time and crack-tip position. Figure 6 is a representative plot, showing the results for Test 413. The high-frequency oscillations in these figures are a numerical artifact and are not intended to be interpreted as real. The lower-frequency oscillations can be expected to be real and are seen to continue beyond arrest.

Influence of the Reflected Stress Waves

When the crack initiates and starts moving, the stress state surrounding the propagating crack has no knowledge of finite boundaries. The stress-intensity factor immediately after initiation drops rapidly, as seen in Fig. 6. The stress field surrounding the crack only begins

TABLE 1—Test results and material properties for 4340 steel.^a

Specimen No.	a_o/W	a_f/W	COD _o , mm	K_o , MPa m ^{1/2}
413 ^b	0.367	0.658	0.925	107.0
415 ^b	0.367	0.662	1.046	121.1
362 ^c	0.345	0.844	0.850	122.0
375 ^c	0.345	0.718	0.580	83.4

^a $E = 206.57$ GPa, Poisson's ratio = 0.3, and density = 0.007 85 Gg/m³.

^b $W = 210$ mm $B_N/B = 7/8$, $B = 25.4$ mm.

^c $W = 172$ mm, $B_N/B = 3/4$, $B = 25.4$ mm.

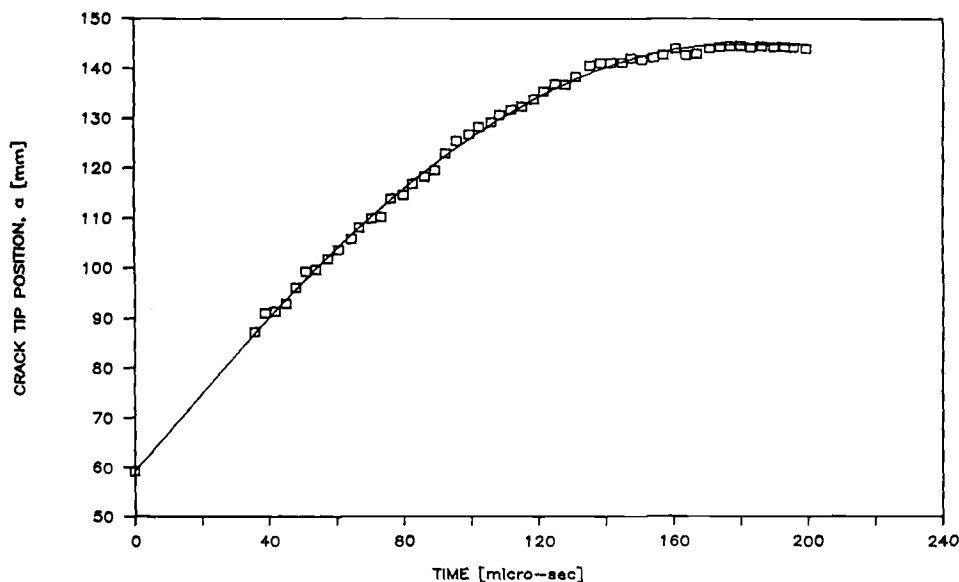


FIG. 5—Typical crack position history as obtained from the photographs and the third-order polynomial fit to the data (Test 362).

to become aware of finite boundaries when the P wave initially emitted from the crack tip and subsequently reflected from the free boundaries in front of and from the specimen sides meets the propagating crack.

This arrival time of the reflected P waves is indicated in Fig. 6. The marked time on the figure is not meant to indicate that something should happen at this particular point in time, but rather to indicate that from this point in time and later, the stress state surrounding the crack tip has some partial knowledge that the body is finite. Note that in Fig. 6 this is the period in which the stress-intensity factor starts to level out and remain relatively constant.

The next interesting point in time occurs when the reflected shear wave arrives back at the crack tip. The boundary conditions are carried by a combination of both the P wave and the shear wave. Note that the dimensions of the CCA specimen are such that the free boundaries and the load line are approximately equidistant from the crack tip. At this point in time the stress-intensity factor starts to increase. Rosakis et al. [8] have shown for a hypothetical polymer that, because of the relatively low ratio of specimen stiffness to loading mechanism stiffness, the reflected shear wave shows no measurable influence. For 4340 steel, Rosakis showed that the reflected shear wave is more significant.

The above discussion suggests that crack propagation will be very much dependent on the specimen size and geometry because of the influence of the reflected stress waves. In this finite-element analysis we assumed that the crack-tip velocity changes are smooth, but in the real world the reflected stress waves do affect the velocity of the crack with abrupt changes, thus in turn affecting the measured stress-intensity factor. The real stress-intensity factor will show more oscillations than are shown here [8].

Comparison with Photoelastic Data

The dynamic stress-intensity factors calculated by SAMCR and extracted from the experimental isochromatic fringe patterns showed an overall good agreement and are shown

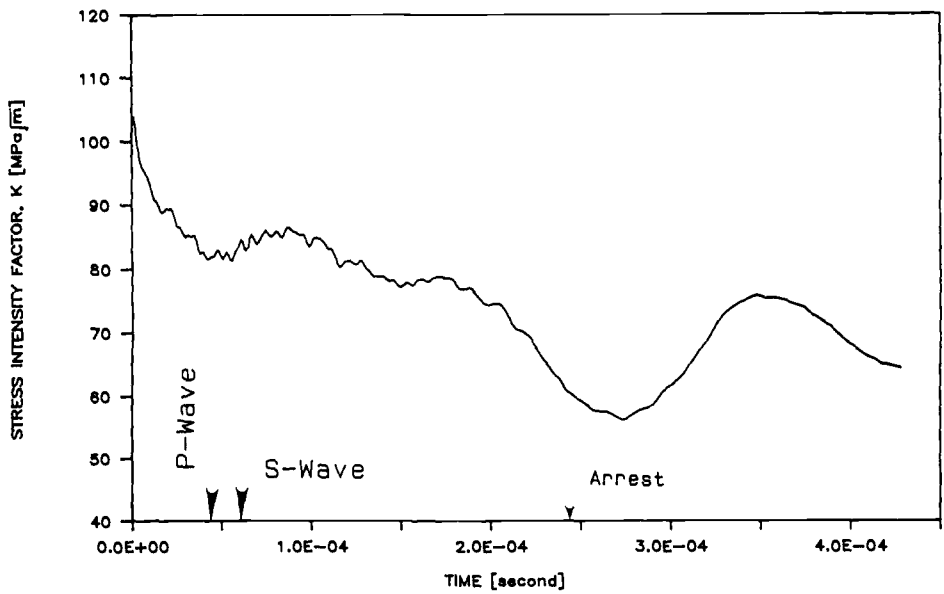


FIG. 6a—Typical calculated K from SAMCR as a function of time (Test 413).

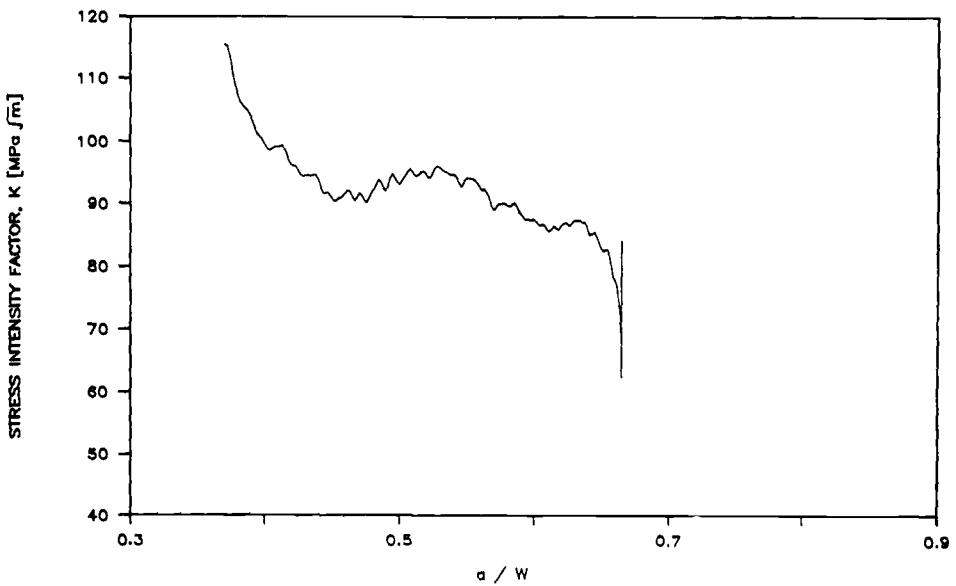


FIG. 6b— K from SAMCR as a function of position a/W (Test 413).

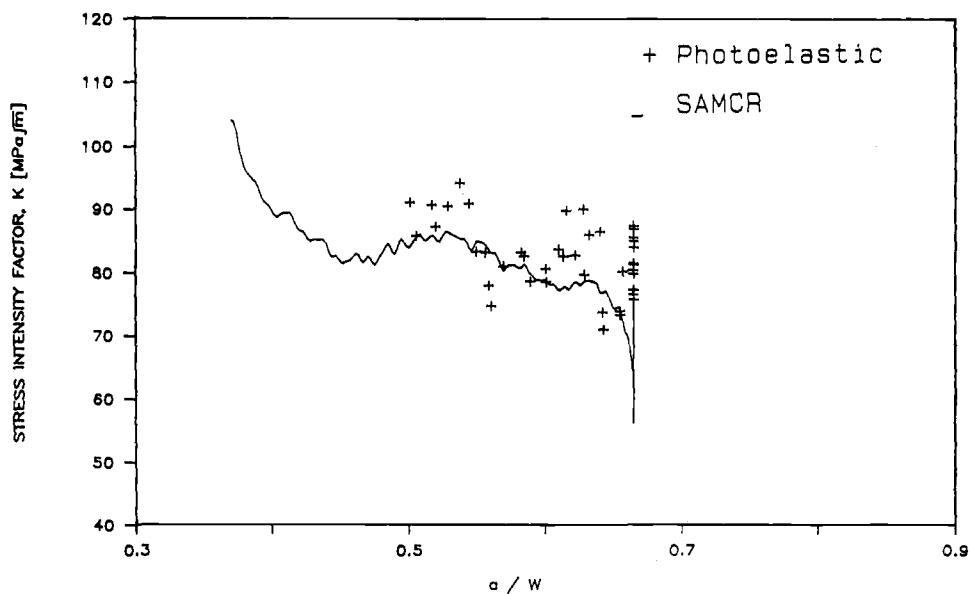


FIG. 7a—SAMCR K values compared with photoelastic results for Test 413.

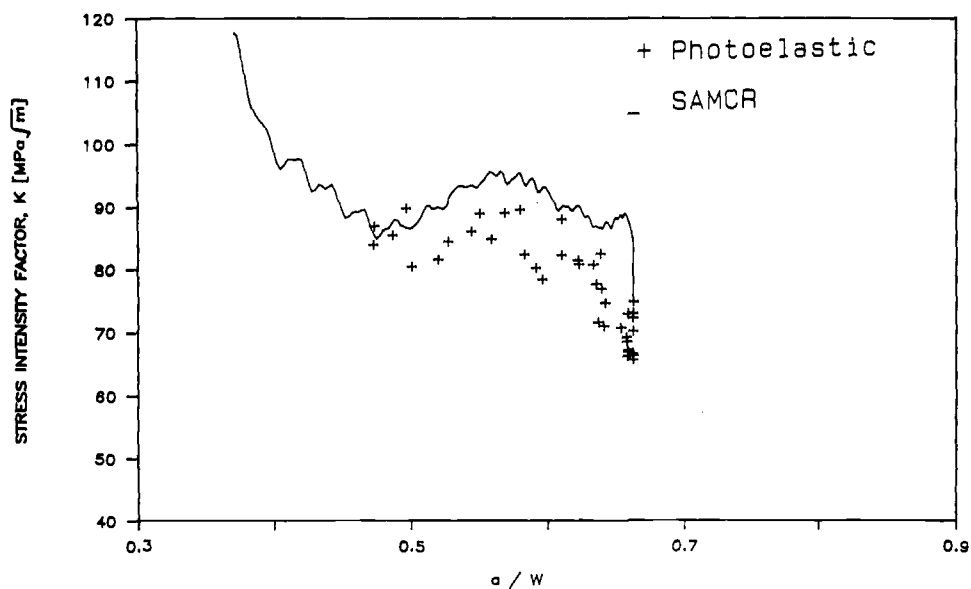


FIG. 7b—SAMCR K values compared with photoelastic results for Test 415.

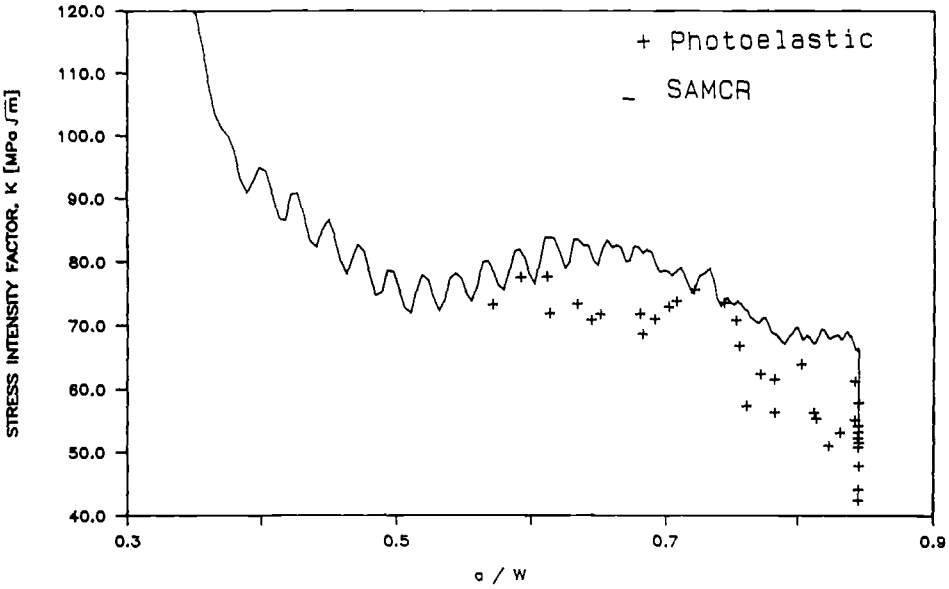


FIG. 8a—SAMCR K values compared with photoelastic results for Test 362.

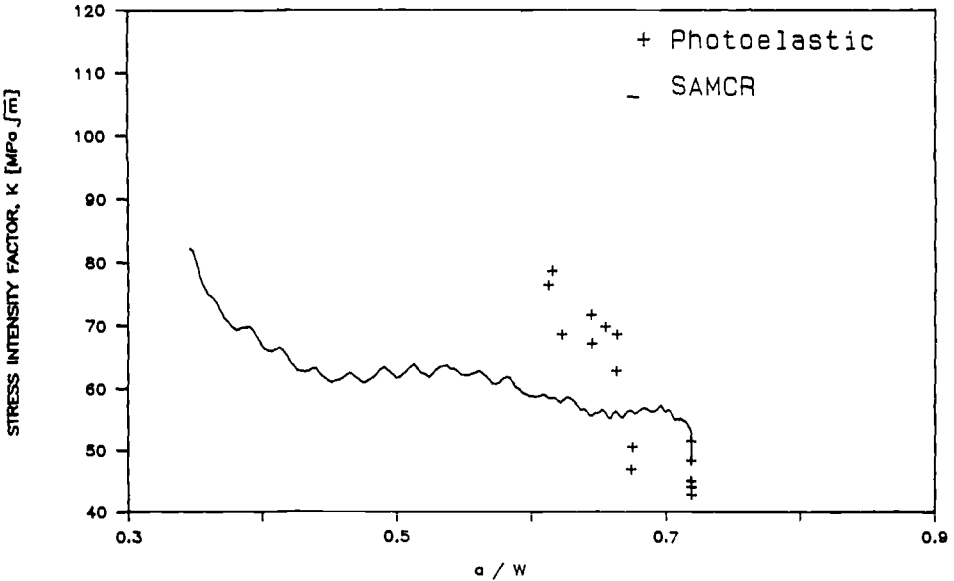


FIG. 8b—SAMCR K values compared with photoelastic results for Test 375.

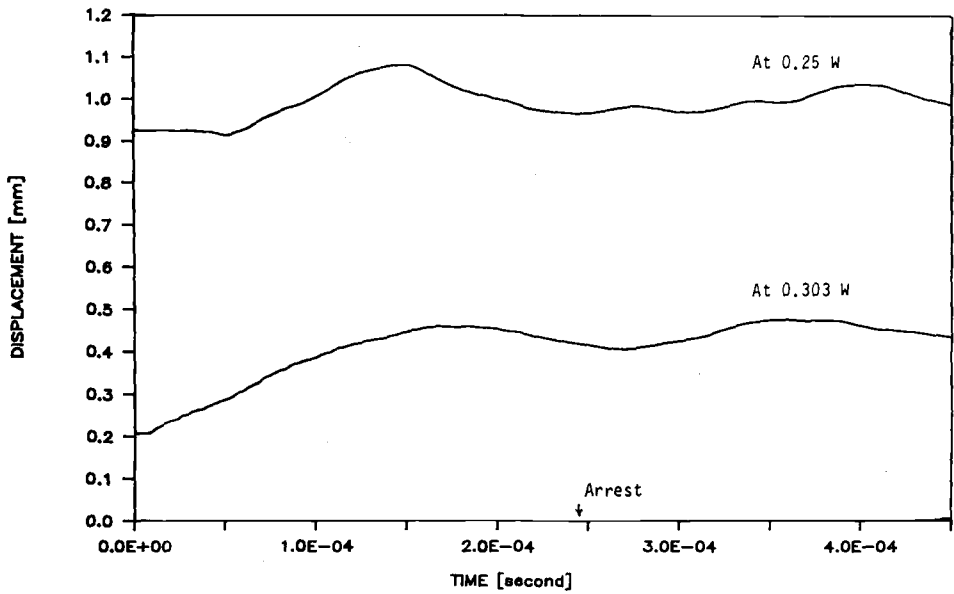


FIG. 9—Crack-opening displacement as a function of time at 0.25 W above the load line and at 0.303 W below the load line as calculated by SAMCR for Test 413.

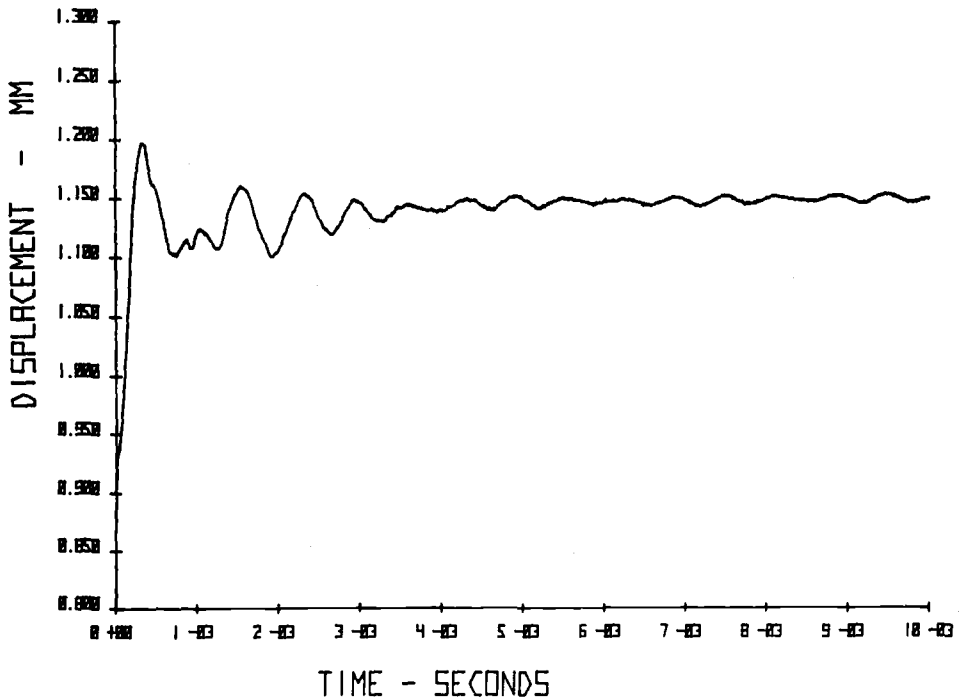


FIG. 10—Experimentally measured crack-opening displacement at 0.25 W above the load line for Test 413.

in Figs. 7 and 8. As mentioned earlier, the accuracy of the photoelastically determined K was estimated to be about $\pm 10\%$. Unfortunately, because of the finite rise time of the flash lamps, it was not possible to observe the early propagation time of the running crack. Note how the photoelastic data and the SAMCR data both show that K tends to remain almost constant during the midportion of the run event before slowly dropping at arrest. Figure 7b probably shows this agreement best since the photoelastic data have less scatter in this test. Considering the idealized elastodynamic model used in the dynamic finite-element analysis, the agreements between the experimental and numerical results are good.

Oscillations in the Crack-Opening Displacement

The SAMCR-predicted crack-opening displacement at 0.25 W above the load line starts increasing about 50 μs after the crack initiates, as can be seen in Fig. 9. It reaches a maximum approximately 150 μs after initiation before decreasing. A very similar behavior was also observed from the eddy current displacement transducers mounted on the specimens. The maximum displacement obtained by SAMCR is slightly lower than that measured in the experiment. This difference is probably due to fixing the pin displacement in the finite-element analysis. Swenson [9] found that by using gap elements it was possible to show that the CCA specimen typically lifts off the pin at the maximum crack-opening displacement.

It has been found that crack arrest occurs approximately when the crack-opening displacement at 0.303 W below the load line is at a maximum. This point in time is approximately 250 μs after initiation. After this point in time, the crack-opening displacement decreases in an oscillatory manner to some value approximately 10% larger than the initiation value, as can be seen from the experimental measurement in Fig. 10.

Comparison of K Values with Static Estimation (ASTM)

For comparison purposes the stress-intensity factor was also calculated using the proposed ASTM procedure, which employs a static fracture mechanics estimation of the dynamic stress-intensity factor at arrest. Table 2 shows the stress-intensity factor at arrest for the four tests as calculated by SAMCR, photoelastic data, and by the ASTM procedure. The ASTM proposed procedure recommends the determination of arrest toughness, K_{ar} , by using the COD value approximately 1 ms after crack arrest. In the table these are the values under ASTM COD_f. A similar calculation using the ASTM equations and the initial crack-opening displacement, COD_o, are included in the table.

A comparison between the various values must be done with caution since the SAMCR calculations are based on a fixed load line crack-opening displacement. As mentioned earlier, it is suspected that the load line displacement is in reality not fixed, but increases [9]. From the table it can be seen that the ASTM calculations using COD_o are consistently low in comparison with the other calculations. The SAMCR, photoelastic, and ASTM calculations

TABLE 2—(MPa $m^{1/2}$) at arrest calculated by various means.

Test No.	SAMCR	Photoelasticity	COD _o	ASTM COD _f
413	67.7	75.0	62.5	77.5
415	85.1	66.8	70.5	73.3
362	66.2	58.0	41.3	61.2
375	52.2	51.6	41.0	53.7

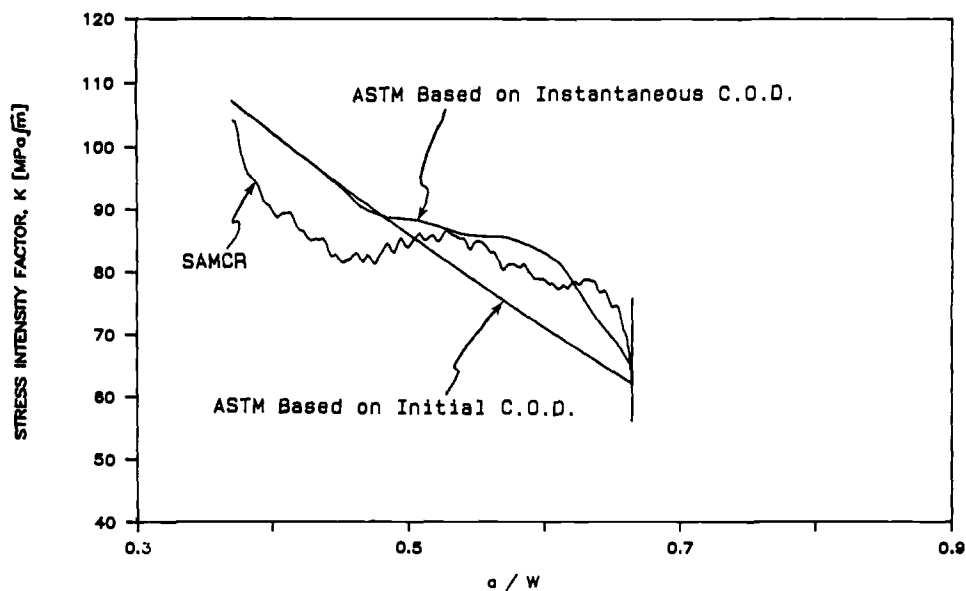


FIG. 11a—Stress-intensity factor as a function of crack length for Test 413 as calculated by SAMCR and a static equation (ASTM).

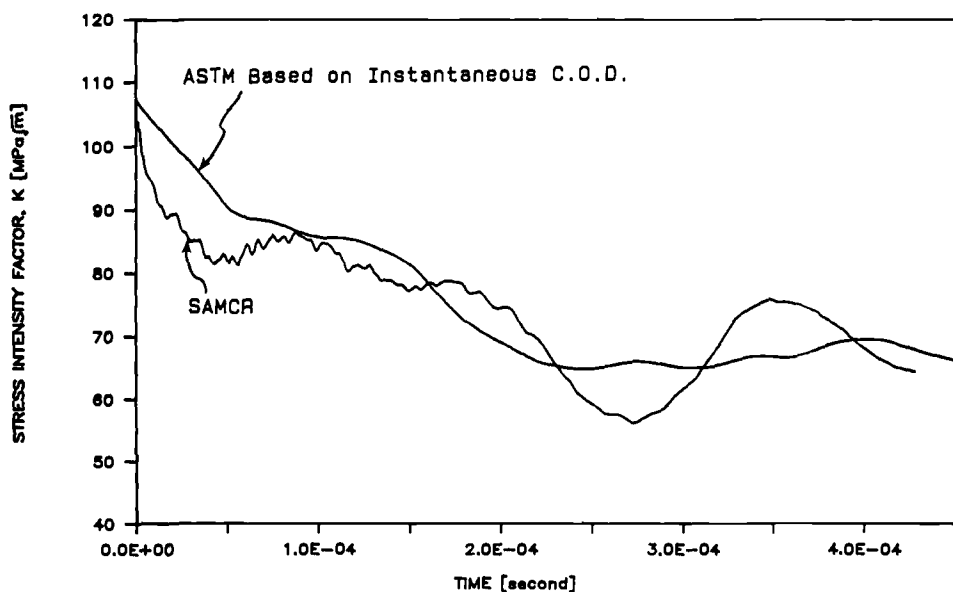


FIG. 11b—Stress-intensity factor as a function of time for Test 413 as calculated by SAMCR and a static equation (ASTM).

using COD_i are in reasonably good agreement. None that the arrest values for Tests 362 and 375 are lower than those for the other two tests. This is due to the fact that these two specimens were subjected to a slightly different heat treatment. These specimens had a Rockwell C-scale hardness (R_c) of 50, where the other two specimens had an R_c of 46. This result is consistent with the results of Irwin et al. [5].

During the SAMCR run, the displacement of the node at 0.25 W above the load line was saved at each time step. Later this value was used to statically estimate, by using the ASTM proposed procedure, the stress-intensity factor as the crack ran. Admittedly the ASTM static estimation procedure is *not* intended to predict the dynamic stress-intensity factor during crack propagation, but Fig. 11 is informative. Figure 11a is a plot of the SAMCR K and the K from a static estimate using the SAMCR instantaneous COD at 0.25 W as a function of time. In Fig. 11b, the SAMCR dynamic stress-intensity factor and an ASTM static estimate of the stress-intensity factor, based on the experimentally measured initial COD and the SAMCR instantaneous COD, is plotted as a function of crack-tip position for Test 413.

At crack initiation the stress distribution is essentially static, but when the crack initiates and grows, the phenomenon is no longer static and cannot be described by static equations. It can be seen in Fig. 11, in the initial part of the run/arrest event, that the dynamic effects are large and the static calculations do not describe the specimen behavior. During the latter part of the event, prior to arrest, dynamic effects are seen to be modest in this specimen and the actual behavior is adequately described by static calculation. At arrest, the static estimate using the initiation COD value underestimates the dynamic stress-intensity factor.

K Versus Crack Velocity Relation

Whether or not the dynamic stress-intensity factor, K_D , can be considered a unique function of crack velocity is a question of considerable discussion and seems to depend on

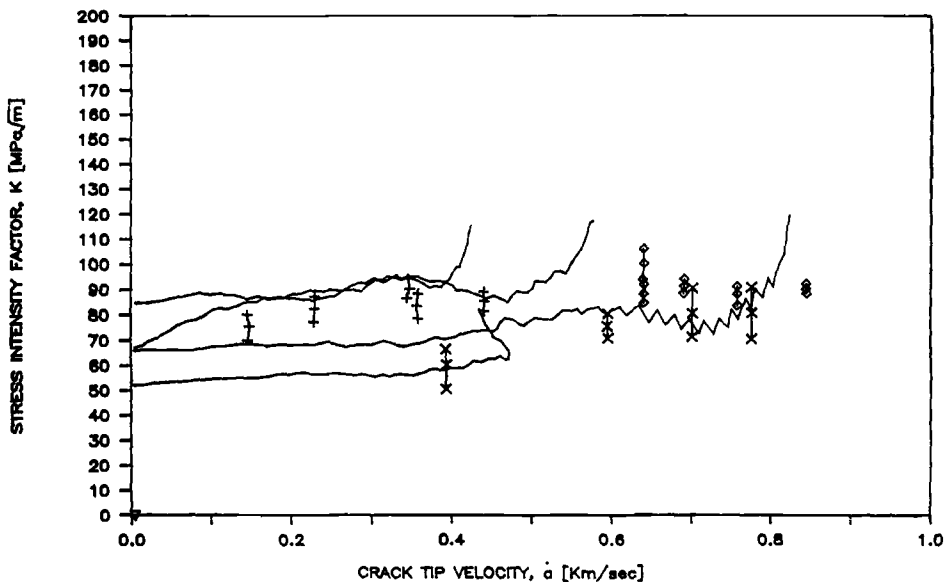


FIG. 12—Stress-intensity factor as a function of crack velocity as calculated by SAMCR and as determined from the birefringent coatings.

the material considered [1]. For 4340 steel, there does appear to be a unique curve. The photoelastic and the finite-element analysis results for the four 4340 tests considered here are plotted in Fig. 12. Also in this figure are all of the photoelastic results for 4340 steel of similar hardness that were conducted at the University of Maryland [3-5]. These results include cracks that arrested as well as higher velocity cracks that did not arrest within the specimen. To keep the plot uncrowded, the photoelastic results for each test are plotted with a mean K at different velocities.

In the figure, the high-velocity portion of each SAMCR result, where the curve goes vertical and K becomes almost independent of velocity, is questionable. This high-velocity region occurs during the very early portion of the run/arrest event, before the flash lamps had reached enough intensity to expose the film. The crack velocity in this region was obtained by an extrapolation of the fitted third-order polynomial back to initiation. This extrapolated crack-tip position history was used as input to SAMCR for the early portion of the event and thus is suspect. The curves in the later portion of the event appear more horizontal and were calculated from data that had not been extrapolated.

The additional photoelastic data for some specimens that had high-velocity cracks and that did not arrest are included to show the more general trend of the K versus velocity curve in Fig. 12. It is clear that these results are in good agreement with the results obtained with caustics [10] but seem to be higher than those obtained by Hahn et al. [11] and Hudak et al. [12], as shown in Fig. 13. Unfortunately, it is difficult to draw conclusions from this comparison unless the exact heat treatment of the various steels the investigators used is known. Irwin et al. [5] showed that there appeared to be unique curves for various heat treatments of 4340 steel.

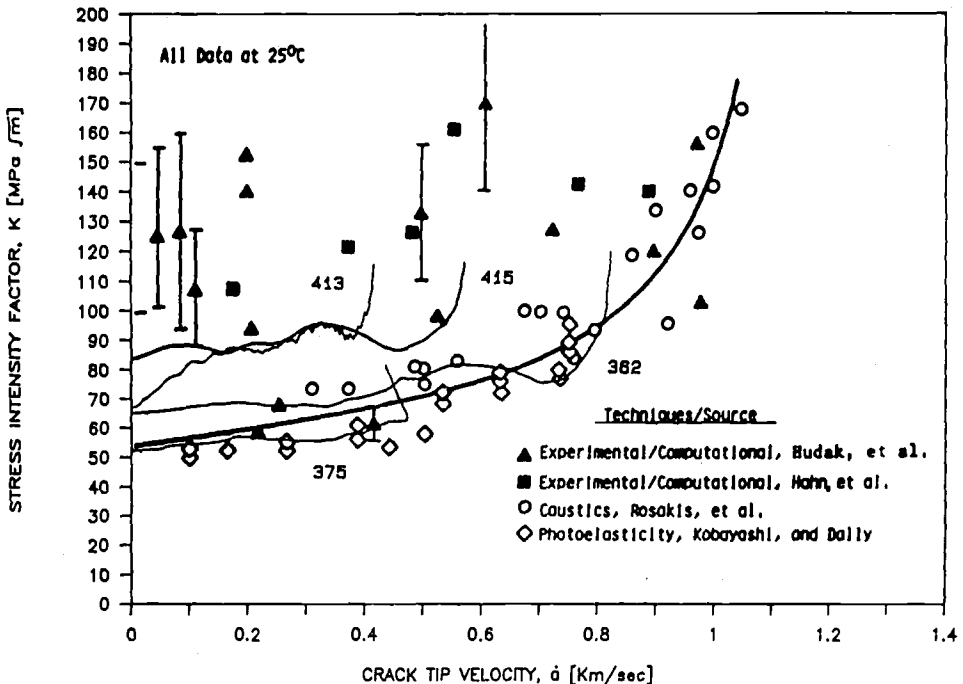


FIG. 13—Stress-intensity factor as a function of crack velocity for 4340 steel from various investigators (after Hudak et al.).

Conclusions

The work described in this paper is a combined numerical and experimental attempt directed towards developing a better understanding of the dynamic effects on crack propagation and arrest in a compact crack arrest specimen. A split-birefringent coating technique, coupled with high-speed photography, was used to record the dynamic isochromatic fringe pattern associated with crack propagation and arrest in 4340 steel compact crack arrest fracture specimens. From the data contained in the isochromatic fringe patterns, the associated dynamic stress-intensity factor was calculated two different ways. First, the dynamic stress-intensity factor was calculated from the isochromatic fringe information directly. Next, the isochromatic fringe patterns were used to obtain a crack position history that was used for input to a two-dimensional dynamic finite-element code used in the generation mode.

The results of the dynamic finite-element analysis and the photoelastic analysis suggest that crack propagation will be very much dependent on specimen size and geometry because of the influence of the reflected stress waves from the specimen boundaries. For the first part of a run/arrest event in a CCA specimen, the dynamic stress-intensity factor decreases much more rapidly than a quasi-static analysis would predict. In the latter part of the run/arrest event, the static analysis adequately describes the dynamic stress-intensity factor. The proposed ASTM procedure for determining the plane-strain fracture toughness, K_{Ic} , through a static estimate appears to be valid for the CCA specimen.

Acknowledgments

The experimental work reported in this paper was made possible by support from Oak Ridge National Laboratory (ORNL) and the U.S. Nuclear Regulatory Commission through ORNL Subcontract No. ORNL/Sub-7778 to the University of Maryland. Financial support received from the Computer Science Center of the University of Maryland for the dynamic computations is gratefully acknowledged.

References

- [1] Rosakis, A. J. and Zehnder, A. T., "On the Dynamic Fracture of Structural Metals," *International Journal of Fracture*, Vol. 27, No. 3-4, 1985, pp. 169-186.
- [2] Der, V. K., Barker, D. B., and Holloway, D. C., "A Split-Birefringent Coating Technique to Determine Dynamic Stress-Intensity Factors," *Mechanics Research Communications*, Vol. 5, No. 6, 1978, pp. 313-318.
- [3] Kobayashi, T. and Dally, J. W., "Dynamic Photoelastic Determination of the a - K Relation for 4340 Steel," *Crack Arrest Methodology and Applications*, ASTM STP 711, American Society for Testing and Materials, Philadelphia, 1980, pp. 189-210.
- [4] Irwin, G. R., Kobayashi, T., Fournery, W. L., Metcalf, J. T., and Dally, J. W., "Photoelastic Studies of Crack Propagation and Arrest in Polymers and 4340 Steel," U. S. NRC Report NUREG/CR-0542, University of Maryland, College Park, MD, November 1978.
- [5] Irwin, G. R., Barker, D. B., Sanford, R. J., Fournery, W. L., Metcalf, J. T., Shukla, A., and Chona, R., "Photoelastic Studies of Damping, Crack Propagation, and Crack Arrest in Polymers and 4340 Steel," U. S. NRC Report NUREG/CR-1455, University of Maryland, College Park, MD, May 1980.
- [6] Sanford, R. J., "Application of the Least Squares Method to Photoelastic Analysis," *Experimental Mechanics*, Vol. 20, No. 6, June 1980, pp. 192-197.
- [7] Schwartz, C. W., Chona, R., Fournery, W. L., and Irwin, G. R., "SAMCR: A Two-Dimensional Dynamic Finite-Element Code for the Stress Analysis of Moving Cracks," U. S. NRC Report NUREG/CR-3891, University of Maryland, College Park, MD, November 1984.
- [8] Rosakis, A. J., Duffy, J., and Freund, L. B., "Dynamic Crack Growth Criteria in Structural Metals," NSF Workshop on Dynamic Fracture, California Institute of Technology, Pasadena, CA, February 1983, pp. 100-118.

- [9] Swenson, D. V. "Modeling Mixed-Mode Dynamic Crack Propagation Using Finite Elements," Ph.D. dissertation, Cornell University, Ithaca, NY, 1985.
- [10] Rosakis, A. J., Duffy, J., and Freund, L. B., *Journal of the Mechanics and Physics of Solids*, No. 32, 1984, pp. 443-460.
- [11] Hahn, G. T., Hoagland, R. G., Kanninen, M. F., and Rosenfield, A. R., *Dynamic Crack Propagation*, G. C. Shi, Ed., Nordhoff, Leyden, The Netherlands, 1973, pp. 649-662.
- [12] Hudak, S. J., Dexter, R. J., FitzGerald, J. H., and Kanninen, M. F., "The Influence of Specimen Boundary Conditions on the Fracture Toughness of Running Cracks," *Dynamic Fracture Mechanics*, The Albert S. Kobayashi Anniversary Volume, M. F. Kanninen and S. N. Atluri, Eds., Pergamon Press, New York, pp. 201-213.

Approximate Methods for Analysis of Dynamic Crack Growth and Arrest

REFERENCE: Nilsson, F., "Approximate Methods for Analysis of Dynamic Crack Growth and Arrest," *Fracture Mechanics: Nineteenth Symposium, ASTM STP 969*, T. A. Cruse, Ed., American Society for Testing and Materials, Philadelphia, 1988, pp. 524–531.

ABSTRACT: Approximate methods that are less time-consuming than finite-element method (FEM) analysis are needed for dynamic crack propagation and arrest calculations. In this context the one-dimensional wave propagation models, where the cracked section is modeled by a flexibility matrix, may be a reasonable alternative. Such models are compared with fully dynamic two-dimensional FEM calculations of experimentally observed crack growth histories in an edge-cracked rectangular sheet. A fairly good agreement is obtained; the discrepancies could mainly be ascribed to differences in the end conditions. The author concludes that spring models are worth further examination in order to make them a practical tool for engineering design analysis.

KEY WORDS: crack arrest, line spring model, wave propagation, fracture mechanics

Due to the development of numerical methods it is now possible to analyze accurately an elastodynamic, two-dimensional problem for a rapidly growing and possibly arresting crack. Conversely, if the conditions for linear behavior are satisfied, the growth and a possible arrest can be predicted. The preferred method in research calculations is almost exclusively the finite-element method (FEM), which today is a reliable tool for elastodynamic analysis. However, in engineering calculations, a quasi-static approach is mostly favored. The main reason for this is that, for engineering purposes, a full elastodynamic treatment is often too expensive and cumbersome to perform. This is especially true in three-dimensional applications, where still very few research investigations have been made.

It is therefore of interest to know to what extent quasi-static methods can be used and this question has received some attention [1]. In Ref 1 it was found that quasi-static methods could be used for the type of problem considered. However, the uncertainty of the possible unconservatism still remains. It would be helpful if bounds could be constructed for the length of the arrested crack. It is in some cases possible to find an upper bound by energy considerations; however, this bound may often be so large that it is of limited interest.

There does seem to exist a need for intermediate methods, where the main characteristics of the dynamics of the problem are retained. In such cases one-dimensional wave propagation models may be of use. Several articles have been published on the use of beam theory for the analysis of dynamic crack growth in double cantilever beam specimens. However, in design, one is more interested in cases in which the crack traverses a beamlike or platelike structure. Freund and Herrmann [2] and later Adeli, Herrmann, and Freund [3] used one-dimensional theory for bending and axial wave propagation for the analysis of bending and tensile fracture of long beams. The cracked section was represented by a flexibility matrix

¹ Professor, Department of Technology, Uppsala University, Uppsala S75121, Sweden.

connecting displacement and rotation to axial force and bending moment in the same way as in the line-spring model [4]. No comparisons with other methods of solution were made in Refs 2 or 3 and, to the present author's knowledge, this has not been done elsewhere. It is one of the objectives of the present paper to compare the one-dimensional model with finite-element calculations of experimentally observed crack propagation and arrest histories. For this, the experiments performed and analyzed by Brickstad and Nilsson [5] and Brickstad [6] are chosen.

Basic Assumptions

In the following, a Mode I fracturing body under linearly elastic plane-stress conditions will be considered. Nonlinear deformation effects and damping are assumed to be negligible. The fracture criterion is assumed to be of the following type

$$\begin{aligned} K_I &= K_{pc}(\dot{a}, a) & \dot{a} > 0 \\ K_I &< K_{pc}(0, a) & \dot{a} = 0 \end{aligned} \quad (1)$$

Here K_I is the dynamic stress-intensity factor, and K_{pc} is the crack propagation toughness, which is dependent on the propagation velocity, \dot{a} , and may also depend explicitly on the crack position, a , because of material inhomogeneities or temperature differences.

The energy release rate, G , is related to K_I by the well-known relation

$$\begin{aligned} G &= \frac{1 + \nu}{E} \frac{\beta_1^2(\beta_2^2 - 1)}{(1 + \beta_2^2)^2 - 4\beta_1\beta_2} K_I^2 \\ \beta_i^2 &= 1 - \left(\frac{\dot{a}}{c_i} \right)^2 \quad i = 1, 2 \end{aligned} \quad (2)$$

where E is Young's modulus, ν is Poisson's ratio, and c_1 and c_2 are the propagation velocities of irrotational and equivoluminal waves, respectively.

According to the one-dimensional wave propagation model, we represent the body as a beam capable of axial and bending wave motion (Fig. 1). The motion of a section is determined by the axial displacement, u ; the transverse displacement, v ; and the rotation, ϕ . Assuming the axial wave propagation to be governed by the elementary theory and the bending behavior by the Timoshenko beam theory, the following set of equations results.

$$\begin{aligned} Eu_{xx} &= \rho \ddot{u} \\ \mu \kappa (v_{xx} - \phi_x) &= \rho \ddot{v} \\ EI\phi_{xx} + \mu \kappa A(v_x - \phi) &= \rho I \ddot{\phi} \end{aligned} \quad (3)$$

where μ is the shear modulus, A the area, and I the surface moment of inertia of the section.

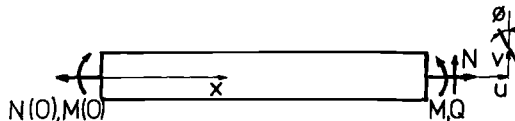


FIG. 1—Definition of generalized displacements and forces for the beam model.

In this study the shear coefficient κ was chosen to be 0.8. The value of κ for dynamic situations has been subject to some debate in the literature. In the present study the results were, however, not sensitive to different choices of κ since bending wave propagation plays a minor role for the studied configuration. The sectional generalized forces; normal force, N ; shear force, Q ; and bending moment, M , are given in terms of u , v , and ϕ by

$$\begin{aligned} N &= EAu_x \\ Q &= \kappa\mu A(v_x - \phi) \\ M &= EI\phi_x \end{aligned} \quad (4)$$

The boundary conditions at $x = +b$ are given in terms of the forces and the displacements as appropriate for the particular problem under consideration. In the cracked section $x = 0$ the boundary conditions are of the form

$$\begin{aligned} u(0) &= N(0)\alpha_{11}(a) + M(0)\alpha_{12}(a) \\ \phi(0) &= N(0)\alpha_{12}(a) + M(0)\alpha_{22}(a) \\ Q(0) &= 0 \end{aligned} \quad (5)$$

Here α_{ij} are flexibility coefficients dependent on the crack length, a . Because of symmetry the right part of the structure needs only to be considered.

The equation for the effect balance for the cracked region is written in the following form, where h is the specimen thickness

$$\frac{1}{2} G\dot{a}h = N(0)\dot{u}(0) + M(0)\dot{\phi}(0) - \frac{d}{dt} \left[\frac{1}{2} (\alpha_{11}N(0)^2 + 2\alpha_{12}N(0)M(0) + \alpha_{22}M(0)^2) \right] \quad (6)$$

Performing the differentiation and using Eq 5 leads to

$$G = N(0)^2 \frac{d\alpha_{11}}{da} + 2M(0)N(0) \frac{d\alpha_{12}}{da} + M(0)^2 \frac{d\alpha_{22}}{da} \quad (7)$$

$$\begin{aligned} w &= .406 \text{ m} \\ b &= .800 \text{ m} \\ l &= .327 \text{ m} \end{aligned}$$

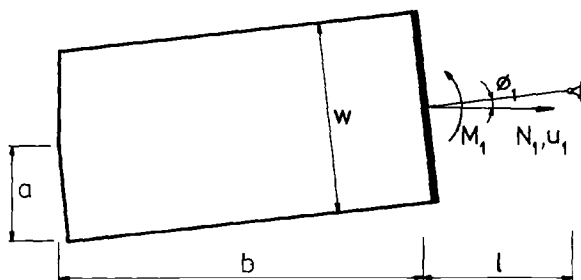


FIG. 2—Idealized geometry for the specimen used in Refs 5 and 6.

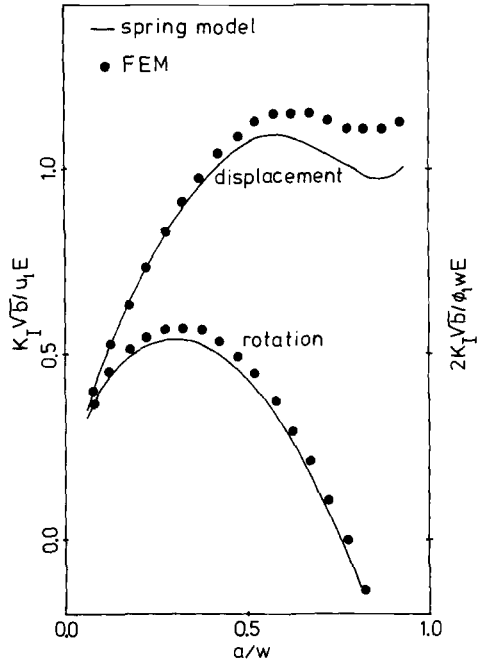


FIG. 3—Comparison of static K_I for displacement controlled conditions.

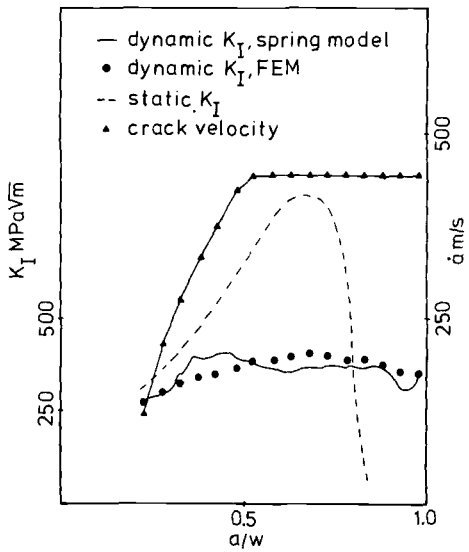


FIG. 4—Results for K_I ; prescribed forces with initial membrane stress of $1.98 \times 10^{-3} E$.

In the static case the stress-intensity factor can be written as Eq 8. Here the functions g_1 and g_2 are taken from an appropriate static solution

$$K_I = Ng_1 + Mg_2 \quad (8)$$

Utilizing the Irwin relation for the static energy release rate, Eq 9 is obtained.

$$G = \frac{1}{E} (Ng_1 + Mg_2)^2 \quad (9)$$

Identification of terms from Eq 7 and Eq 9 gives the following expression for the flexibility coefficients.

$$\alpha_{ij} = \frac{h}{E} \int_0^a g_i g_j da \quad (10)$$

If the so-defined α_{ij} are used in the dynamic analysis, one finds from Eq 6 that the energy release rate, even in this case, is given by Eq 9. The stress-intensity factor, K_I , is then obtained from Eq 2.

The solution of Eq 3 with the associated boundary conditions is accomplished by straightforward numerical integration. A finite difference approximation is made for the spatial derivatives and the time integration is performed by the central difference explicit method.

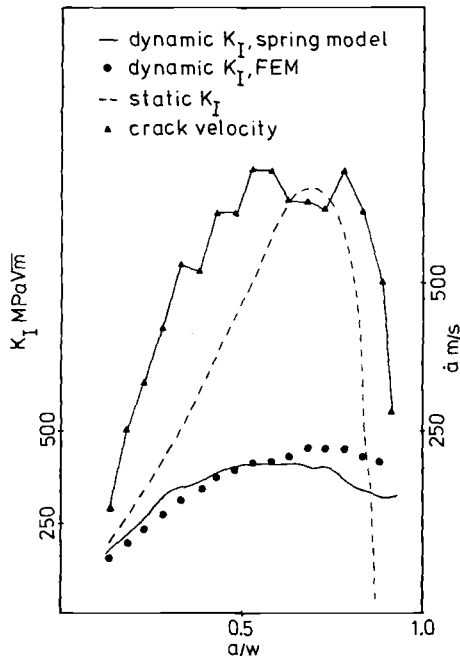


FIG. 5—Results for K_I ; prescribed forces with initial membrane stress of $3.06 \times 10^{-3} E$.

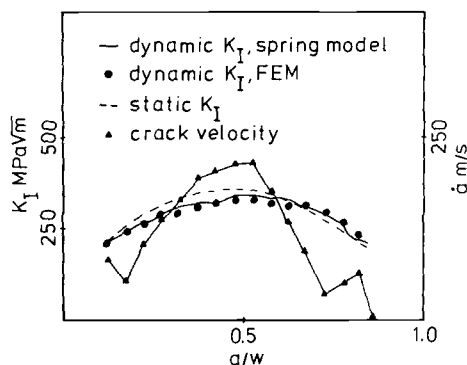


FIG. 6—Results for K_I : prescribed displacement for initial u_1 of $1.32 \times 10^{-3} b$ and ϕ_1 of $-2.20 \times 10^{-3} b/w$.

Comparison Problem and Static Considerations

The geometry considered here was used in Refs 5 and 6 for combined experimental and numerical investigations of crack propagation and arrest behavior. Half of the specimen is sketched in Fig. 2. The right boundary of the rectangular plate is constrained against the transverse strain. It moves rigidly with the translation in the axial direction, u_1 , and the rotation, ϕ_1 , around the joint. In Ref 5 the boundary conditions were given in terms of the axial force, N_1 , and the bending moment, M_1 , both as functions of time, whereas in Ref 6, u_1 and ϕ_1 were prescribed and nearly constant with small variations occurring during the process.

For the one-dimensional spring model N_1 and M_1 , respectively, u_1 and ϕ_1 are taken as boundary conditions. It is not possible to take into account the condition of zero transverse strain in the one-dimensional model and this causes a discrepancy which will be evident in subsequent discussion. In order to evaluate the flexibility coefficients, the functions g_1 and g_2 are needed. As in other spring model studies, these are chosen from the solution to the problem of an edge-cracked long strip under tension and bending, so that for this problem Eq 11 applies. The solution by Benthem and Koiter [7] was used.

$$K_I = \frac{(\pi a)^{1/2}}{(1 - \xi)^{3/2}} \frac{N}{wh} \kappa_1(\xi) (1 + 2\xi) + \frac{6M}{w^2} \kappa_2(\xi) = Ng_1 + Mg_2 \quad (11)$$

where $\xi = a/w$; h = the plate thickness; and κ_1 and κ_2 = dimensionless functions given in Ref 7. It turned out to be very important to use an accurate solution for g_1 and g_2 , since the matrix defined by Eq 8 is highly ill-conditioned. A fairly small error in the functions can make the matrix singular at some point and thus prohibit its use in the boundary conditions (Eq 5). The solution used here is believed to have an accuracy of at least within 1% and, furthermore, is exact for $\xi \rightarrow 0$ and $\xi \rightarrow 1$. The matrix coefficients were then obtained by numerical integration.

As an example, the static stress-intensity factor for the considered geometry was determined for conditions of prescribed displacement. The results are shown in Fig. 3, together with numerical results obtained in Ref 6. The value K_I has been normalized with respect to $u_1 E b^{-1/2}$ and $1/2 \phi_1 w E b^{-1/2}$. The correspondence is good for small ξ values, while for larger crack lengths a discrepancy of up to about 9% occurs, which is the effect of the constraint mentioned above. This end condition cannot be accounted for by the present

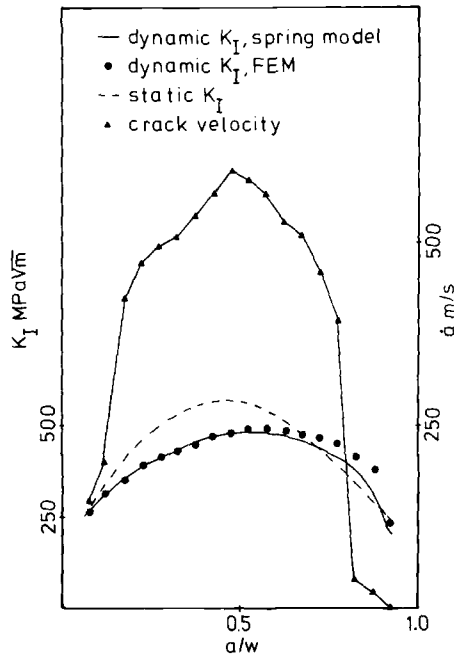


FIG. 7—Results for K_I : prescribed displacements with initial u_i of $2.12 \times 10^{-3} b$ and ϕ_i of $-3.34 \times 10^{-3} b/w$.

model and is to be kept in mind when evaluating the dynamic results. Similar discrepancies also occur for the case of prescribed forces.

Results and Discussion

The different cases in Refs 5 and 6 were reanalyzed by the spring model. Thus, the same boundary conditions in terms of N_1 and M_1 or δ_1 and ϕ_1 as in Refs 5 and 6 were applied, together with the crack propagation histories. Two examples for prescribed forces from Ref 6 are shown in Figs. 4 and 5 and Figs. 6 and 7, respectively. These examples are typical of the behavior in all cases. In the figures are shown the dynamic K_I for the spring model (solid line), the static K_I for the spring model (broken line), the values of dynamic K_I from the FEM calculations in Refs 5 and 6 (circles), and the crack velocity (triangles).

Note, first, that the general behavior of the spring model is qualitatively consistent with the FEM results. There is a tendency for K to be higher for short crack lengths for the spring model, while the reverse is true for long crack lengths. The effect for short crack lengths is possibly due to the fact that no transverse wave propagation effects are considered. Thus, the effect of the back surface sets in earlier in the spring model than in the two-dimensional model. At least part of the difference at larger crack lengths can be ascribed to the differences in the static solutions. In one case (Fig. 5) the difference is larger than can be explained by the static difference. One possible explanation is that the one-dimensional model permits faster wave propagation than the two-dimensional model. The unloading effects, due to a rapidly decreasing end force and an increasing moment tending to close the crack, are felt earlier in the cracked region for the spring model.

In the cases of prescribed forces (Figs. 4 and 5) there is a big difference between the

static and the dynamic K_I values even though the crack velocities are fairly moderate. This effect is much less pronounced in the cases for prescribed displacements even though the velocities are of comparable magnitude. In the author's opinion the present results are quite encouraging, considering that the geometry is not particularly beamlike, the length being only two times the width. Improvements are possible. A more accurate model for the axial wave motion such as the Mindlin-Herrmann model could be used. This would of course increase the computational effort somewhat, but the computer times in the present work were almost negligible in comparison with those for a two-dimensional FEM calculation.

It is also possible to account, in a crude way, for transverse wave propagation in the cracked section by using delay times for the increase of the flexibility coefficients. Some numerical experiments were performed and, while it was possible to improve the results in individual cases by choosing suitable delay times, no common method for setting these has been obtained.

Conclusions

The spring model gives results that are qualitatively in agreement with two-dimensional analysis. In the cases considered the main difference could be ascribed to the difference in the end conditions that existed.

The author believes that the spring model can be a practical tool for engineering analyses of crack-arrest events in situations in which the transverse dimension of the structure is much smaller than the other dimensions and the crack velocity is not too large. The maximum velocities encountered in this investigation may indicate the upper limits. Before employing the model more numerical testing is needed, especially for three-dimensional problems, where the spring model has its greatest advantage. The computer costs for at least one-dimensional models of two-dimensional problems are insignificant. Of course this may not necessarily be true for two-dimensional line-spring models of three-dimensional problems.

Acknowledgments

The author is greatly indebted to Dr. Björn Brickstad for allowing access to his primary data and for valuable discussions during the work. This work is part of a larger project supported by the Swedish Board of Technical Development (STU). The author wants to acknowledge this support.

References

- [1] Brickstad, B. and Nilsson, F., *Engineering Fracture Mechanics*, Vol. 23, No. 1, 1986, pp. 61–70.
- [2] Freund, L. B. and Herrmann, G., *Journal of Applied Mechanics*, Vol. 43, 1976, pp. 112–116.
- [3] Adeli, H., Herrmann, G., and Freund, L. B., *Journal of Applied Mechanics*, Vol. 44, 1977, pp. 647–651.
- [4] Rice, J. R. and Levy, N., *Journal of Applied Mechanics*, Vol. 39, 1972, pp. 185–194.
- [5] Brickstad, B. and Nilsson, F., *International Journal of Fracture*, Vol. 16, No. 1, 1980, pp. 71–84.
- [6] Brickstad, B., *International Journal of Fracture*, Vol. 21, 1983, pp. 177–191.
- [7] Benthem, J. P. and Koiter, W. T. in *Methods of Analysis to Crack Problems*, G. C. Sih, Ed., Noordhoff, Leyden, The Netherlands, 1973, Chapter 3, pp. 159–162.

Some Aspects of Performing Dynamic Measurements and Analyses on the Compact Crack Arrest Specimen for A533-B Steel

REFERENCE: Brickstad, B. and Dahlberg, L., "Some Aspects of Performing Dynamic Measurements and Analyses on the Compact Crack Arrest Specimen for A533-B Steel," *Fracture Mechanics: Nineteenth Symposium, ASTM STP 969*, T. A. Cruse, Ed., American Society for Testing and Materials, Philadelphia, 1988, pp. 532–546.

ABSTRACT: The four countries of Sweden, Norway, Finland, and Denmark are participating in a joint project which includes performing instrumented crack arrest experiments on A533-B steel. The primary aim of this study is to determine the dynamic fracture properties during propagation and arrest. Dynamic finite-element methods calculations were used to analyze earlier reported experiments on the transverse wedge-loaded compact crack arrest (CCA) specimen, in order to obtain guidance for future experiments regarding measuring technique, material characterization, and the crack-tip model. The computations indicate that the dynamic effects on the stress-intensity factor are small for the CCA specimen. It is also shown that proper determination of the displacement controlled boundary conditions can be made by measuring displacements at the load line. Computations were also made with the material treated as elastic-viscoplastic. It was found that nonlinear material behavior is likely to be important for A533-B steel at least at room temperature and higher temperatures.

KEY WORDS: crack arrest experiments, compact crack arrest specimen, A533-B steel, dynamic finite-element solutions, dynamic stress-intensity factor, load-line displacement, viscoplastic material behavior fracture mechanics

During recent years the dynamic fracture properties of the commonly used reactor steel A533-B, Class 1 have been the object of intense study. Among the large-scale projects in progress in this field are the pressurized thermal shock experiments at Oak Ridge National Laboratory (ORNL), [1], the U.S. Nuclear Regulatory Commission/Heavy Section Steel Technology (NRC/HSST) wide-plate crack arrest program at the National Bureau of Standards (NBS) [2], and the Electric Power Research Institute/Combustion Engineering (EPRI/CE) crack arrest program at Combustion Engineering [3]. Apart from obtaining information on the crack propagation phase, these tests are aimed at providing crack arrest data at temperatures near the Charpy upper shelf. This is usually achieved by using a suitable combination of specimen geometry and loading setup that causes an increasing stress-intensity factor (K_I) with crack length. A crack arrest is then obtained by applying a temperature gradient along the crack plane and thereby causing an even steeper toughness gradient.

¹ Research engineer and research manager, respectively, The Swedish Plant Inspectorate, Box 49306, S-100 28 Stockholm, Sweden.

Currently, plans are being made for a joint Scandinavian crack arrest project which has certain parallels with the projects in Refs 1 through 3. The participants are the Swedish Plant Inspectorate in Stockholm, Sweden; the Technical Research Center in Helsinki, Finland; the Institute of Technology in Trondheim, Norway; and the Risø Laboratory in Roskilde, Denmark. The test material that will be used is A533 Grade B, Class 1 steel which stems from some of the cracked halves of the first wide-plate test at NBS [2]. These plates have been sent to the Nordic countries especially for this project. Successively smaller specimens are going to be manufactured from the wide plates. The specimen geometry that we plan to use is the compact crack arrest (CCA) specimen, which is identical to the one used in the ASTM round robin crack arrest testing program [4]. One reason for this choice of specimen type is that all the participating countries have experience from earlier crack arrest tests on this geometry. The primary aim of this study is to obtain information on the dynamic fracture properties of reactor steel during propagation and arrest. With use of the CCA specimen and the conventional transverse wedge loading technique, the propagating crack will experience a decreasing K field, which somewhat limits the level of crack arrest toughness values that can be reached with this geometry. For higher temperatures, experience from the ASTM K_{Ia} round robin [4] has often shown strongly curved crack fronts, which make surface measuring techniques of determining the time-dependent crack front position less reliable. Therefore, an important experimental task within this project is to develop methods to measure the crack-front position in the interior of the crack plane.

It is evident from Refs 1 through 3 that performing dynamically instrumented crack-arrest experiments is an elaborate task, both experimentally and in the way the tests should be analyzed and interpreted. Therefore, a series of earlier reported crack arrest experiments on the CCA specimen [5] is dynamically analyzed in this prestudy to investigate the requirements necessary for using the techniques of measuring the time-dependent boundary conditions and crack-front position.

Basic Assumptions

Consider a Mode I propagating crack in a two-dimensional body. Under linear elastic fracture mechanics (LEFM) conditions the following growth criterion is assumed

$$K_I^d = K_{pc}(\dot{a}, T) \quad (1)$$

where K_I^d is the elastodynamic stress-intensity factor and K_{pc} is a material function depending on crack-tip velocity, \dot{a} , and temperature, T , at the position of the tip. The crack will come to a momentary stop if Eq 2 is fulfilled

$$K_I^d < K_{pc}(\dot{a} = 0, T) = K_{Ia}(T) \quad (2)$$

where K_{Ia} is the crack-arrest toughness and is of primary interest in determining the arrest capability of a material. Since K_I^d depends on the entire history and not only on the instantaneous conditions, a fully dynamic analysis must, in general, be performed.

In a quasi-static treatment K_I^d is replaced by K_I^s , the statically calculated stress-intensity factor, which only depends on the momentary conditions. This treatment is adopted in Ref 4.

It is, however, important to realize that for many ductile materials, it is unlikely that the basic assumptions of LEFM are valid. An important step toward a better understanding of crack growth in nonlinear materials has been the inclusion of rate effects in the plastic deformation process. Rate effects can be expected to be important because of the very high strain rates that exist in the vicinity of a running crack tip. A number of recent investigations,

both theoretical and experimental, have adopted rate-dependent models for the running crack problem, for example, Douglas [6], Aboudi and Achenbach [7], Lo [8], Brickstad [9], Freund and Hutchinson [10], Freund et al. [11], and Kanninen et al. [12]. In the investigation discussed here the authors have chosen to use the special case of Perzyna's [13] viscoplastic material model, which is described in the Appendix. It is thus appropriate to consider the energy balance for a plane body of a unit thickness containing a Mode I propagating crack. Interest is focused on the difference between, on one hand, the energy input to the body and, on the other hand, the strain energy, the kinetic energy, and the viscoplastic dissipated energy. The net change in energy is associated with crack growth, that is, it is consumed in advancing the crack. This quantity, per unit area of crack extension, represents the energy flow to the crack-tip region and is denoted by γ .

The fracture criterion adopted here may be given the following form in an isothermal case

$$\begin{aligned} \gamma &= \gamma_f(\dot{a}) & \dot{a} > 0 \\ \gamma &< \gamma_f(\dot{a} = 0) & \dot{a} = 0 \end{aligned} \quad (3)$$

where γ_f is the specific fracture energy and is regarded as a characteristic function of the material. In dynamic LEFM, dissipated energy is not considered and the resulting energy flow is then equivalent to the well-known energy release rate G , which in turn is completely equivalent to a fracture criterion based on K_I . It is not self-evident what type of criterion is most suitable to use in a nonlinear case. Other criteria have been suggested, for example, those based on critical values of the crack-opening displacement, the crack-tip opening angle, or the plastic strain.

An attractive feature with the viscoplastic material model used in this study is that, for the exponent $n < 3$ in the flow rate function (see Appendix), the near-tip field is of the elastic type (Hui and Riedel [14], McCartney [15], Lo [8], and Brickstad [9]). This may justify the definition of a near-tip stress-intensity factor, K_I^{tip} , which may control the fracture process within the region of asymptotic elastic dominance. In general, K_I^{tip} will be less than the remote stress-intensity factor defined under LEFM conditions in Eq 1, since for that case plastic dissipated energy is not considered.

Evaluation Procedure

A side view of the CCA specimen is shown in Fig. 1. It is generally understood that, in order to obtain dynamic fracture toughness properties from a crack arrest experiment, accurate measurements are needed of the time-dependent crack length, which is equivalent to the crack velocity, and of the, in general, time-dependent boundary conditions. In the CCA specimen with the transverse wedge loading technique, the displacement is controlled in the pin hole (see Fig. 1). Thus, it is desirable to measure the displacement v in the hole during a test. It should, however, be observed that the only geometrical constraint imposed on the specimen during a test is that the specimen is not allowed to move back into the split pin. It is assumed here that, because of the short duration of the test, the wedge will not be capable of significantly increasing the displacement during the crack growth event. It may, of course, lose contact during some part of the event, but such behavior will be determined by the subsequent dynamic analysis. Thus, if it is possible to obtain accurate information on the crack velocity, it is sufficient to measure the displacement v when the crack growth starts. In the subsequent evaluation the constraint condition $v \geq v(t = 0)$ is then imposed. A main difficulty, however, lies in measuring the crack velocity with sufficient

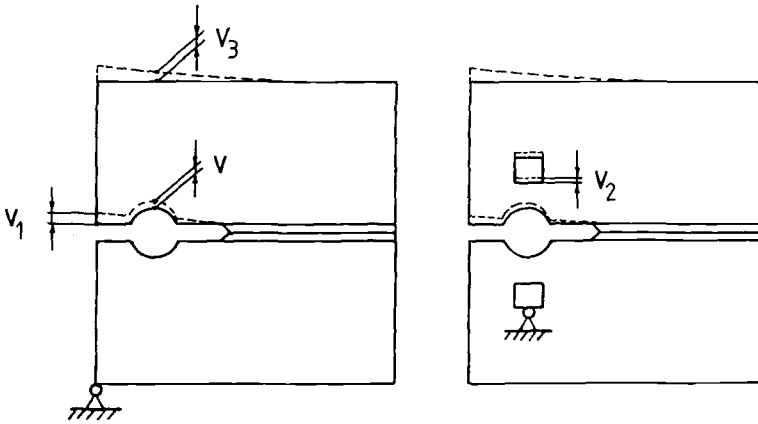


FIG. 1—Side view of the compact crack arrest specimen with indicated positions for possible displacement measurements.

accuracy. In order to have more control of the process it may still be desirable to measure the displacement at some position on the specimen during the crack growth event: for example, v_1 , v_2 , or v_3 in Fig. 1. This measurement can be compared to the displacement at the same position obtained from the dynamic analysis. If there is a significant difference and the measured displacement is reliable, something in the input to the numerical analysis is inaccurate, probably the crack velocity.

A series of earlier reported crack arrest experiments by Rahka [5] on the CCA specimen (A533B-steel) at room temperature is used here for studying the dynamic behavior during a test. He did not record the crack velocity but measured the displacement v_1 (see Fig. 1) as a function of time, which may serve as a check on the numerical computations in this

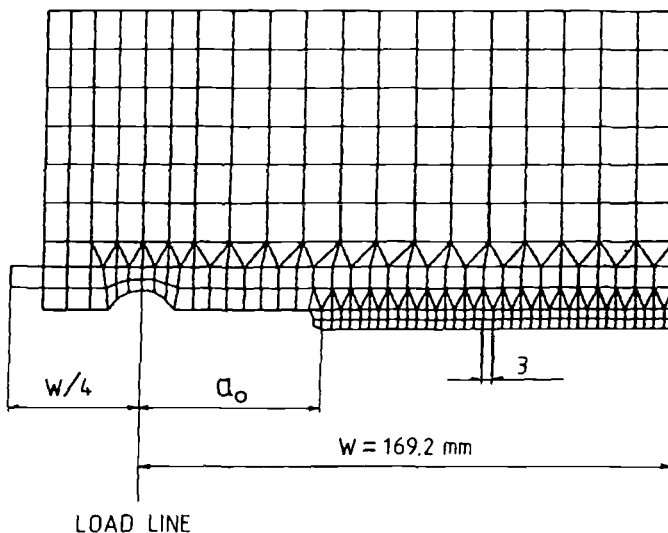


FIG. 2—FEM mesh for evaluating a crack arrest experiment.

study. The two-dimensional finite-element method (FEM) mesh for modeling the specimens used in Ref 5 is shown in Fig. 2. It consists of 354 quadrilateral and triangular elements, giving a total of 690 degrees of freedom. The single element at the front side of the specimen corresponds to the clamps at which the displacement v_1 was measured in Ref 5. A crack-arrest experiment is numerically reproduced in the following way:

The displacement v is increased until the displacement v_1 coincides with the reported value in Ref 5 at initiation of crack growth. Any effect from friction, indentation, machine compliance or unsymmetric loading possibly introduced by the loading arrangements are ignored here. After crack growth has initiated, the constraint condition $v \geq v(t = 0)$ is imposed. The propagating crack is simulated by the well-established gradual-node relaxation technique introduced by Rydholm et al. [16], in which a closing force, F_c , behind the crack tip is gradually relaxed to zero as the crack propagates through an element length, d . For elastodynamic applications, the dynamic energy release rate, G (energy flow), is then obtained by calculating the work performed by F_c and dividing it by the crack plane area of the element. By utilizing the well-known relation in Eq 4, the stress-intensity factor K_I^d is obtained

$$G = \frac{K_I^2}{E} \cdot f(\dot{a}) \quad (4)$$

Here f is a universal function given by Nilsson [17]. The usual correction of $\sqrt{B/B_N}$ was used on K_I to take account for the influence of side grooves in a plane model. Here B is the unnotched thickness and B_N is the thickness of the side-grooved crack plane. Since the crack velocity was not recorded in Ref 5, the computations were run in the "application mode"; that is, the crack propagation toughness $K_{pc}(\dot{a}, T)$ was prescribed. The crack velocity was then predicted so that the growth criterion in Eq 1 was satisfied, or the crack arrest was predicted corresponding to the relation in Eq 2. The dynamic fracture properties used are based on small-specimen data as utilized for the HSST wide-plate crack-arrest program [2] and are given by the following expressions

$$K_{pc} = K_{la} + A \cdot \dot{a}^2 \quad (5)$$

$$K_{la} = 49.96 + 16.878 \cdot \exp [0.02874(T - RT_{NDT})] \quad (6)$$

$$A = \begin{cases} [329.7 + 16.25(T - RT_{NDT})] \cdot 10^{-6} & T - RT_{NDT} > -13.9^\circ\text{C} \\ [121.7 + 1.296(T - RT_{NDT})] \cdot 10^{-6} & T - RT_{NDT} \leq -13.9^\circ\text{C} \end{cases} \quad (7)$$

where RT_{NDT} is the reference nil-ductility transition temperature; the units for K_{pc} , A , \dot{a} , and T are in $\text{MPa} \sqrt{\text{m}}$, $\text{MPa} \cdot \text{s}^2 \cdot \text{m}^{-3/2}$, m/s , and $^\circ\text{C}$, respectively. The experimental data to support the relations in Eqs 5 through 7 are very limited and it is one of the main purposes of the Scandinavian crack-arrest project to obtain more K_{pc} data. To obtain some idea of the role of rate-dependent plasticity, evaluations are performed using Perzyna's viscoplastic material model. The energy flow, γ , to the crack-tip region is calculated by the same technique as in the elastodynamic case and converted to some measure of the near-tip stress-intensity factor by Eq 4, with G replaced by γ . More information on the dynamic FEM program that has been developed for the running crack problem, can be found in papers by Brickstad and Nilsson [18] and Brickstad [9].

The following material properties have been used in the analysis:

Young's modulus	$E = 2.05 \cdot 10^5 \text{ MPa}$
Poisson's ratio	$\nu = 0.3$
Density	$\rho = 7850 \text{ kg/m}^3$

Results and Discussion

Calculation of Stress—Intensity Factors

Of the experiments published in Ref 5, several were analyzed but only one was singled out to be reported here. All experiments showed, however, the same general behavior. The following values were recorded:

Initial crack length	$a_o = 58.5 \text{ mm}$
Arrest length	$a_f = 106.9 \text{ mm}$
Displacement at initiation	$V_1 = 1.13 \text{ mm}$
Displacement after arrest	$V_1 = 1.18 \text{ mm}$

The crack lengths are measured from the load line, and the displacement v_1 is measured a distance $w/4$ behind the load line, according to Fig. 2. In the numerical analysis the displacement at the hole boundary, v , was given the constraint condition $v \geq v(t=0)$ during the whole crack event. The value $v(t=0)$ corresponds to $v_1 = 1.13 \text{ mm}$, which was the value measured at initiation of crack growth. The static stress-intensity factor K_I^s for this experiment is shown in Fig. 3. The value K_I^s is shown as a function of crack advance, $\Delta a = a - a_o$; K_I^s was determined by calculating the strain energy release rate for an incremental crack advance in the FEM mesh in Fig. 2. This method usually underestimates K_I , but only by a few percentage points with this relatively refined mesh.

Also shown in Fig. 3 is K_I^s calculated by the proposed ASTM formula [4]

$$K_I = \frac{E}{\sqrt{w}} \cdot \sqrt{\frac{B}{B_N}} \cdot v_1 \cdot f_1 \left(\frac{a}{w} \right) \quad (8)$$

where f_1 is a compliance function given in Ref 4; v_1 was taken from the quasi-static FEM calculations.

As expected, the numerical global plane strain K_I^s solution exceeds the numerical solution for global plane stress. Locally, at the crack tip, plane strain is assumed in both cases. The value for K_I^s calculated from Eq 8 lies below these solutions, but agrees quite well with the global plane stress solution, which is the most relevant one. For shorter crack advances the agreement is good, but for longer cracks the deviation approaches 10%, which may raise some doubts as to the accuracy of Eq 8.

We now turn to evaluation of the dynamic stress-intensity factor for the experiment, assuming K_{pc} to be known according to Eqs 5 through 7 with $K_{Ia} = 120 \text{ MPa} \sqrt{\text{m}}$. This value of K_{Ia} is the value of K_I^s given by the numerical plane strain solution at arrest (see

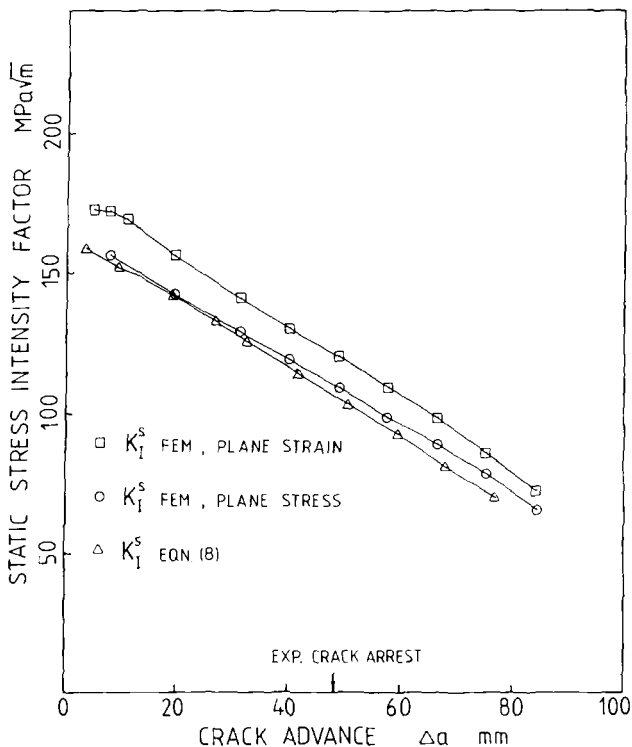


FIG. 3—Comparison of static stress-intensity factors as functions of crack advance.

Fig. 3). In the following, a state of global plane strain has been assumed arbitrarily. Figure 4 shows K_I^d and the corresponding predicted crack velocity as a function of crack advance. Two different velocity dependences in the $K_{pc}(\dot{a}, T)$ relation were used in order to find out the sensitivity of the results for the CCA specimen from the prescribed toughness properties. The notation “strong \dot{a} -dependence” in Fig. 4 represents Eqs 5 through 7, and for “weak \dot{a} -dependence” the coefficient A , in Eqs 5 and 7, was reduced by a factor of five. From Fig. 4, and also supported by evaluations of other experiments in Ref 5, the following tendencies can be seen:

Dynamic effects on K_I seem to be small here, at least apart from the initial phase. The exact shape of the velocity dependence of K_{pc} does not seem to be very important for the prediction of the point of crack arrest. It was found that after some amount of crack growth both the K_I^d solutions agree well with the quasi-static result, giving very similar values at arrest. The difference is that for the case with a weak velocity dependence, a higher velocity is predicted.

The variation of the predicted velocity with crack advance may also offer some guidance as to what resolution is necessary for the crack length versus time measurements in future instrumented tests. Clearly, the element spacing of 3 mm along the crack plane should provide a sufficient resolution.

Kalthoff et al. [19] found increasing dynamic influence on K_I at crack arrest for increasing crack jump length in experiments on double cantilever beam (DCB) specimens. The same behavior could perhaps be expected here. Therefore, the experiments were reevaluated with successively smaller postulated K_{Ia} values, which gave longer crack jumps. The result

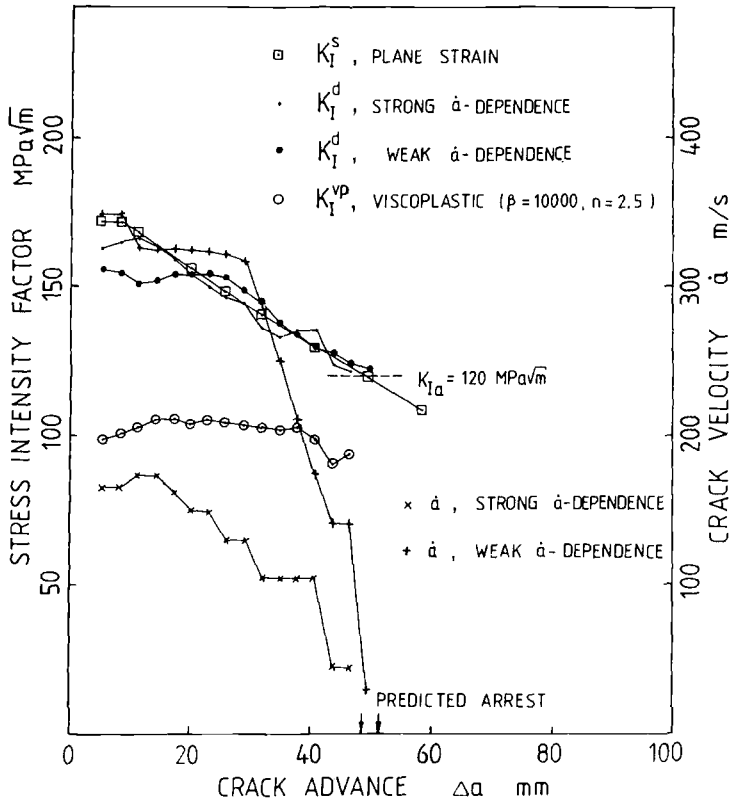


FIG. 4— K_I^s , K_I^d , K_I^{vp} , and \dot{a} as functions of crack advance for an experiment assuming $K_{Ia} = 120 \text{ MPa}\sqrt{\text{m}}$.

for the predicted K_I^d is shown in Fig. 5, where the influence from the two different \dot{a} -dependences in the K_{pc} relation described above is also shown. As can be seen, the different K_I^d values are gathered around the quasi-static K_I^s curve. A slight increase in difference between the quasi-static and dynamic solutions can, however, be observed for longer crack jumps; yet, the dynamic effects on K_I seem to be small for the transverse wedge-loaded CCA specimen. In *this* respect the proposed quasi-static method of calculating K_{Ia} in the ASTM round robin Tests [4] seems to be justified. Of course one may question how far-reaching the conclusions are that can be made based on these "application-mode" evaluations. But if the principal form (quadratic) of the velocity dependence in the K_{pc} relation is valid, and experiments hitherto have shown that this is a reasonable assumption, one should be able to cover real experimental behavior by varying both K_{Ia} and A in Eq 5.

Viscoplastic Evaluations

Information is very scarce on the rate-dependent material properties of A533-B steel. Hudak et al. [20] performed an investigation which provides some information on the effect of strain rate and temperature on the yield stress. When using their data for room temperature to determine the fluidity parameter, β , and the exponent, n , in the Perzyna model, the

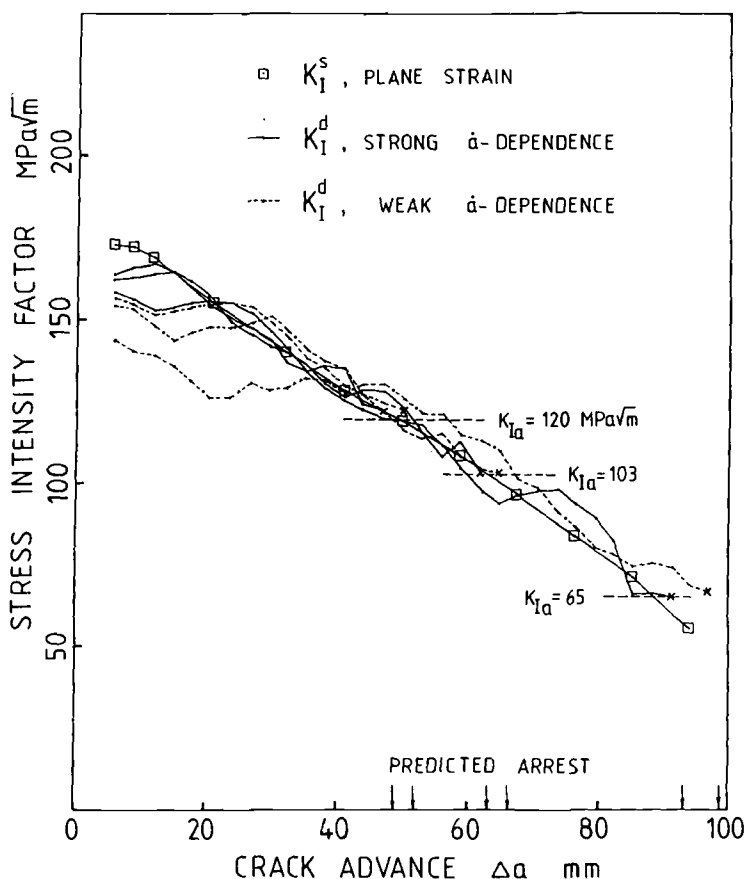


FIG. 5—Comparison of K_I^d and K_I^s as functions of crack advance for different toughness properties.

following result can be established

$$\beta = 10\,000\text{ s}^{-1}$$

$$n = 2.5$$

This corresponds to a doubling of the uniaxial yield stress for a viscoplastic strain rate equal to β . The quasi-static yield stress used was $\sigma_0 = 440$ MPa and the tangent hardening modulus $E_T = E/75$. The time-step used for these calculations was $\Delta t = 0.06\text{ }\mu\text{s}$, which is about a factor of seven smaller than that used for the elastodynamic evaluations.

The above set of parameters gives a relation of yield stress versus strain rate that agrees within 10% with the experimental results in Ref 20. However, one must still consider this as a first rough estimate of the true dynamic behavior of the material. The investigation in Ref 20 presented only one level of strain rate above 1 s^{-1} , which is the region that should be of most importance for the running crack problem. In Fig. 4 the stress-intensity factor K_I^p is shown, evaluated viscoplastically with the above set of viscoplastic parameters. This evaluation is made in the "generation mode" with prescribed crack velocities from the

"application mode" elastodynamic analysis (strong \dot{a} dependence) shown in the same figure. As can be seen, K_I^{vp} is considerably smaller, even at crack arrest, than the elastic solution. The difference is mainly consumed in dissipative processes. The numerically observed strain-rate values are of the order of 300 s^{-1} in the near crack-tip region. The active plastic zone size, immediately in front of the propagating crack tip, varied from 9 mm initially, to 4 mm prior to crack arrest. It should be observed here that the reported values of the strain rate in the vicinity of the crack tip will also depend on the element mesh density. Figure 6 shows the corresponding result when assuming $K_{Ia} = 65 \text{ MPa } \sqrt{\text{m}}$ in the elastodynamic case, thus producing a longer crack jump. In this case both the linear elastic and viscoplastic solution of K_I are at the same corresponding level as in Fig. 4 for the same amount of crack advance. However, as the stress-intensity factor decreases, corresponding to a more brittle behavior, the viscoplastic K_I^{vp} in Fig. 6 approaches the linear elastic solution.

If the result in Fig. 6 is to reflect a "generation mode" evaluation from a real experimental situation, the critical values of K_I may be meaningful to plot versus crack velocity, as in Fig. 7. Here it is clearly seen that the introduction of viscoplasticity causes a less pronounced velocity dependence, which is consistent with the investigations in Refs 9 and 21.

The preceding results for the viscoplastic evaluations are only aimed at identifying possible tendencies and for determining the importance of including rate-dependent plasticity in our future crack arrest tests. Several problems have to be solved in order to validate these trends.

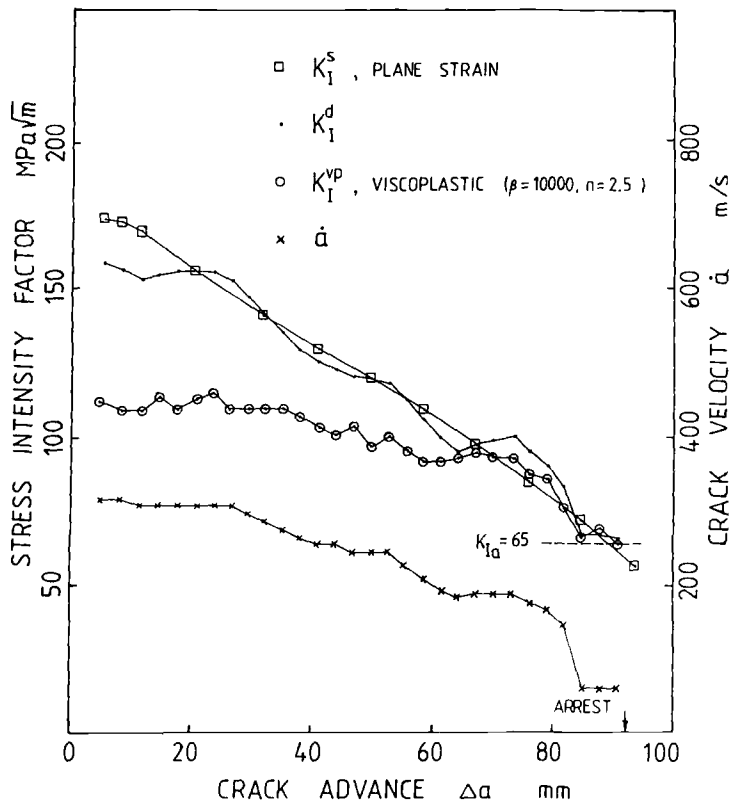


FIG. 6— K_I^S , K_I^d , K_I^{vp} , and \dot{a} as functions of crack advance for an experiment assuming $K_{Ia} = 65 \text{ MPa } \sqrt{\text{m}}$.

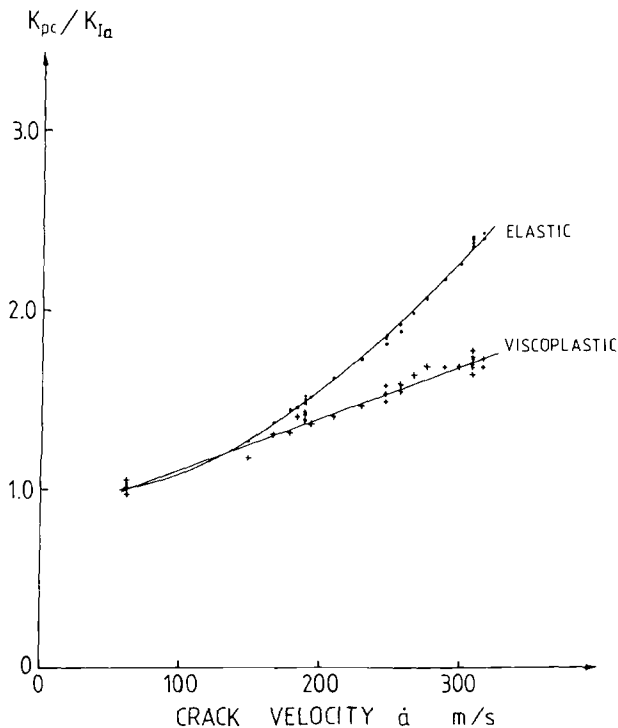


FIG. 7—Normalized values of critical K_I versus crack velocity for elastic and viscoplastic material behavior.

First, we do not yet know particularly well the viscoplastic properties of the A533-B steel, especially at the extremely high strain rates that are expected in the vicinity of a fast running crack tip. Second, one should apply a viscoplastic model in analysis of experiments where the actual crack length versus time is measured. Third, we have used the method of gradual node relaxation to simulate the growing crack and to calculate the energy flow to the crack-tip region. This method has only been verified for elastodynamic applications and further studies should be made of mesh size dependence. Different crack-tip models and other fracture criteria should also be studied. One step in this direction may be the introduction of the Akin singular finite element [22], for which the order of crack-tip singularity may be input controlled. Thesken and Gudmunson [23] successfully used this element for stationary cracks in elastic structures subjected to dynamic loads. A natural extension of this work is to develop a moving Akin singular crack-tip element in a viscoplastic body. Despite the above comments, we feel that the tendency is clear; nonelastic material behavior can be expected to be important for the A533-B steel at least at or above room temperature.

Calculation of Specimen Displacements

Figure 8 shows the computed displacements at different positions of the specimen for the experiment earlier described. The computation was run in "application mode" with the assumption of global plane strain K_{pc} according to Eqs 5 through 7 and $K_{Ia} = 120 \text{ MPa}\sqrt{\text{m}}$. The displacement v_1 as a function of time is computed both dynamically and quasi-statically. It is clearly seen that v_1 increases during crack growth, although the displacement

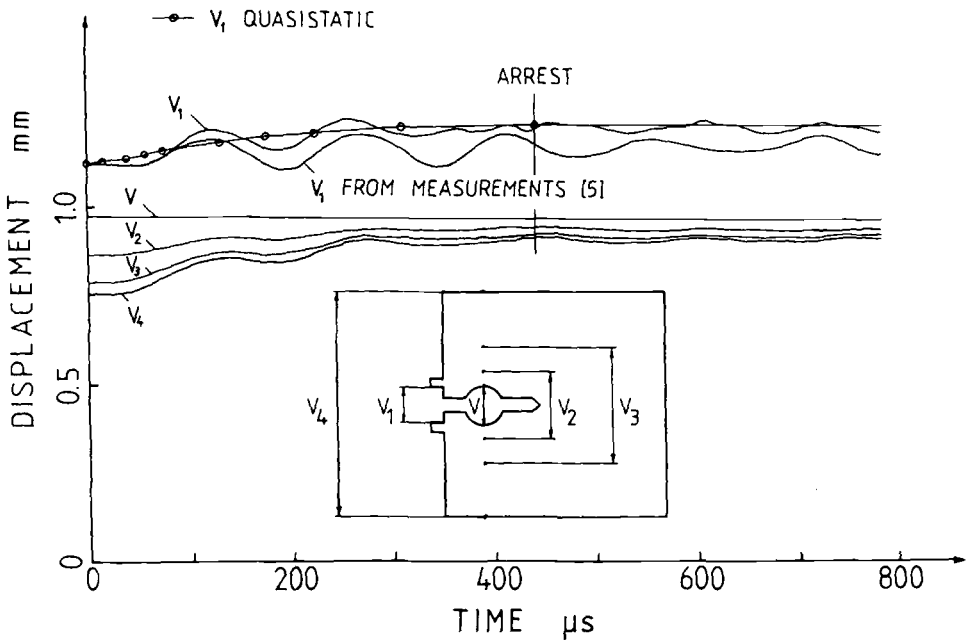


FIG. 8—Evaluated displacements versus time for an experiment assuming $K_{Ia} = 120 \text{ MPa} \sqrt{\text{m}}$. The included figure of specimen geometry indicates the positions at which the displacements are evaluated.

v at the hole boundary remains constant. That v_1 is greater at arrest than at initiation is also generally observed in the ASTM round robin tests [4]. This is explained by the compressive stresses at the load line which relax as the crack grows. This deformation wipes out other effects during crack growth which tend to give a contrary deformation. It is also observed that the computed dynamic displacements v_1 are oscillating around the quasi-static curve, and for these evaluations they almost coincide at the predicted time of arrest. This may not always be the case. As is shown below, the specimen can very well lose contact with the split pin during the crack growth event, thus giving a larger instantaneous displacement than the static displacement evaluated before or after crack growth. Also shown in Fig. 8 is the experimentally measured v_1 reported in Ref 5. It is shown that both the frequency of the computed vibrations and the general magnitude of v_1 agree well with the measurements. This offers some confidence in the computations.

The rest of the curves shown in Fig. 8 represent the displacements at various positions of the load line. Here it is also clearly shown that the load line is subjected to a compression which is decreased during crack growth. In this case the analysis predicts constant displacement v all the time. The imposed constraint condition $v \geq v(t = 0)$ does, however, allow a loss of contact, which also has been observed by Gates [24]. This is illustrated in Fig. 9, where $K_{Ia} = 65 \text{ MPa} \sqrt{\text{m}}$ has been assumed, resulting in a longer crack jump. It is interesting to note in this case, that during the time intervals when the specimen loses contact with the split pin, that is, $v > v(t = 0)$, all the load-line displacements coincide. This observation offers guidance as to how proper instrumentation of the transverse wedge-loaded CCA specimen should be done in order to measure the displacement controlled boundary conditions. First, the displacement v at initiation ($t = 0$) is determined. Up to this point static conditions prevail. During crack growth and arrest, the displacement V_{LL} at some position

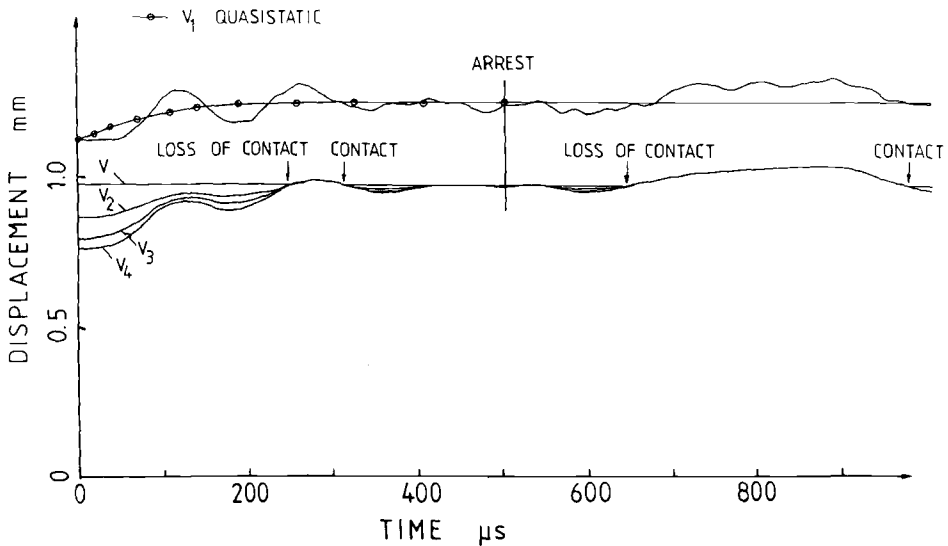


FIG. 9—Evaluated displacements versus time for an experiment assuming $K_{Ia} = 65 \text{ MPa} \sqrt{m}$.

along the load line is measured. If V_{LL} is less than $v(t = 0)$ the specimen should be in contact with the split pin and thus $v = v(t = 0)$. If V_{LL} is greater than $v(t = 0)$ the load-line displacement V_{LL} can be used directly, that is, $v = V_{LL}$. An evaluation of K_{Ia} according to the proposed ASTM procedure [4], in which the displacement is evaluated sometime after crack arrest, can thus be erroneous if the specimen loses contact with the split pin at the occurrence of crack arrest. Using V_{LL} in the evaluation as described above probably gives a better estimate in such a case.

Conclusions

The following conclusions and recommendations can be of value when performing instrumented crack arrest experiments on the transverse loaded CCA specimen for A533-B steel.

1. The dynamic effects on K_I seem to be small.
2. An evaluation of K_{Ia} according to the proposed ASTM procedure [4] is probably erroneous if the specimen loses contact with the split pin at the occurrence of crack arrest. This is a possibility that cannot *a priori* be excluded. The analyses have shown that the contact can be lost during a crack event. However, the instantaneous displacement v at the hole can be measured during loss of contact at any point on the load line. Using the instantaneous displacement instead of the displacement sometime after crack arrest, according to Ref 4 probably gives a better estimate in such a case.
3. Measurement of the displacement at any point on the load line during the experiment can also be used to verify the accuracy of subsequent dynamic analysis.
4. Intervals of 3 mm along the crack plane should provide a sufficient resolution for accurate measurements of crack length versus time.
5. Nonlinear material behavior is likely to be important for A533-B steel at least at room temperature and higher temperatures.

Acknowledgments

This paper was prepared as part of a project on crack arrest studies supported by the Nordic Liaison Committee for Atomic Energy and the Swedish Nuclear Power Inspectorate. We want to express our gratitude for this support.

APPENDIX

Elastic Viscoplastic Material

Perzyna [13] suggested the following equations for describing rate-dependent plasticity. The total strain rate is broken down into an elastic and inelastic component

$$\dot{\epsilon}_{ij} = \dot{\epsilon}_{ij}^e + \dot{\epsilon}_{ij}^{vp} \quad (9)$$

A yield condition which governs the initiation of viscoplastic flow is introduced as

$$f(\sigma_{ij}, \epsilon_{ij}^{vp}) - f_o = 0 \quad (10)$$

where f_o is the uniaxial yield stress. For strain hardening materials f_o may also be a function of some hardening parameter. The viscous effects are introduced by the following flow rule.

$$\dot{\epsilon}_{ij}^{vp} = \begin{cases} \beta \phi(f) \frac{\delta f}{\delta \sigma_{ij}} & f > f_o \\ 0 & f \leq f_o \end{cases} \quad (11)$$

where β is a fluidity parameter. A form of the flow rate function ϕ often suggested is

$$\phi(f) = \left(\frac{f - f_o}{f_o} \right)^n \quad (12)$$

with this choice of ϕ the main viscoplastic parameters to be determined by experiments are β and n .

References

- [1] Bryan, R. H., Bass, B. R., Merkle, J. G., Pugh, C. E., Robinson, G. C., and Whitman, G. D., *Engineering Fracture Mechanics*, Vol. 23, No. 1, 1986, pp. 81-97.
- [2] Pugh, C. E., "Program Objectives and Organization for the NRC/HSST-Program," paper presented at the Second Review Meeting on EPRI and NRC-Crack-Arrest Programs, National Bureau of Standards, Gaithersburg, MD, April 1986.
- [3] Ayres, D. J., Fabi, R. J., Peck, D. A., and Schoneberg, R. Y., "Tests and Analyses of Crack Arrest in Reactor Vessel Materials in an Increasing Stress-Intensity Field and Increasing Material Toughness," paper presented at the Second Review Meeting on EPRI and NRC Crack-Arrest Program, National Bureau of Standards, Gaithersburg, MD, April 1986.
- [4] Proposed ASTM Test Method for Crack Arrest Fracture Toughness of Ferritic Materials, American Society for Testing and Materials, Philadelphia, June 1984.
- [5] Rahka, K., "Vibrations in Compact Specimens During Crack Arrest Testing," *Journal of Testing and Evaluation*, Vol. 8, No. 6, 1980, pp. 318-323.
- [6] Douglas, A. S., "Dynamic Fracture Toughness of Ductile Materials in Antiplane Shear," Brown University, Providence, RI, June 1982.

- [7] Aboudi, J. and Achenbach, J. D., *International Journal of Fracture*, Vol. 21, 1983, p. 133-147.
- [8] Lo, K. K., *Journal of the Mechanics and Physics of Solids*, Vol. 31, 1983, pp. 287-305.
- [9] Brickstad, B., *Journal of the Mechanics and Physics of Solids*, Vol. 31, 1983, pp. 307-327.
- [10] Freund, L. B. and Hutchinson, J. W., *Journal of the Mechanics and Physics of Solids*, Vol. 33, 1985, pp. 169-191.
- [11] Freund, L. B., Hutchinson, J. W., and Lam, P. S., *Engineering Fracture Mechanics*, Vol. 23, No. 1, 1986, pp. 119-129.
- [12] Kanninen, M. F., Reed, K. W., Hudak, S. J., Jr., Dexter, R. J., Cardinal, J. W., Polch, E. Z., Chun, K. S., Achenbach, J. D., and Popelar, C. H., "Development of a Viscoplastic-Dynamic Fracture Mechanics Analysis Model," paper presented at the Second Review Meeting on EPRI and NRC Crack-Arrest Programs, National Bureau of Standards, Gaithersburg, MD, April 1986.
- [13] Perzyna, P., *Advances in Applied Mechanics*, Vol. 9, 1966, p. 243.
- [14] Hui, C. Y. and Riedel, H., *International Journal of Fracture*, Vol. 17, 1981, p. 409.
- [15] McCartney, L. N., *International Journal of Fracture*, Vol. 19, 1982, pp. 99-113.
- [16] Rydholm, G., Fredriksson, B., and Nilsson, F., *Numerical Methods in Fracture Mechanics*, Swansea, U.K., 1978, p. 660.
- [17] Nilsson, F., *Journal of Elasticity*, Vol. 4, 1975, pp. 73-75.
- [18] Brickstad, B. and Nilsson, F., *Numerical Methods in Fracture Mechanics*, Swansea, U.K., 1980, p. 473.
- [19] Kalthoff, J. F., Beinert, J., Winkler, S., and Klemm, W. in *Crack Arrest Methodology and Applications*, ASTM STP 711, American Society for Testing and Materials, Philadelphia, 1983, pp. 109-127.
- [20] Hudak, Jr., S. J., Dexter, R. J., and Chan, K. S., "Test Materials and Properties for the NRC/HSST Program," paper presented at the Second Review Meeting on EPRI and NRC Crack-Arrest Programs, National Bureau of Standards, Gaithersburg, MD, April 1986.
- [21] Ahmad, J., Barnes, C. R., and Papaspyropoulos, V., "A Viscoplastic Dynamic Fracture Mechanics Approach to Crack Arrest in Welded Tubular Joints," Batelle-Columbus Laboratories, Columbus, OH, February 1986.
- [22] Akin, J. E., *International Journal of Numerical Methods Engineering*, Vol. 10, 1976, pp. 1249-1259.
- [23] Thesken, J. C. and Gudmundson, P., "Application of the Akin Singular Element to Dynamic Fracture Mechanics," Department of Strength of Materials and Solid Mechanics, The Royal Institute of Technology, Stockholm, Sweden, 1985.
- [24] Gates, R. S., *International Journal of Pressure Vessels and Piping*, Vol. 17, 1984, pp. 105-123.

A Cooperative Study for the Evaluation of Crack Arrest Toughness of RPV Materials in Japan

REFERENCE: Sakai, Y., Yagawa, G., and Ando, Y., "A Cooperative Study for the Evaluation of Crack Arrest Toughness of RPV Materials in Japan," *Fracture Mechanics: Nineteenth Symposium, ASTM STP 969*, T. A. Cruse, Ed., American Society for Testing and Materials, Philadelphia, 1988, pp. 547–568.

ABSTRACT: Results are presented from an investigation of crack arrest toughness K_a , on ASTM A533B Class 1 and A508 Class 3 steels using ASTM-proposed specimens and ESSO specimens. The results show that the values of K_a , measured in accordance with the ASTM test method, increased with an increase in test temperature, and that the size requirements in the method were appropriate to obtain valid values of plane-strain crack arrest toughness K_{Ia} . It was also found that the ASTM and ESSO tests lead to about the same crack arrest toughness values when applied to large specimens of the same size. The lower bound of K_{Ia} data was significantly under that of K_{Ic} data on the test materials, though both bounds were well over the American Society of Mechanical Engineers (ASME) K_{IR} curve.

KEY WORDS: crack arrest toughness, A533B steel, A508 steel, ASTM-proposed compact crack arrest test, ESSO test, fracture mechanics

Nomenclature

- a Crack length
- a_a Crack length at arrest
- a_0 Crack length at initiation
- K_a Value of K calculated on the basis of crack length and displacement shortly after arrest
- K_{Ia} Plane-strain crack arrest toughness
- K_{Ca} Crack arrest toughness obtained by ESSO test
- K_{Ic} Plane-strain fracture toughness
- K_{IR} American Society of Mechanical Engineers (ASME) reference toughness curve
- K_Q Stress-intensity factor at initiation
- NDT Nil-ductility transition temperature [ASTM Method for Conducting Drop-Weight Test to Determine Nil-Ductility Transition Temperature of Ferritic Steels (E 208-84a)]
- RT_{NDT} Reference nil-ductility transition temperature
- σ_{YS} 0.2% yield strength in a tension test
- σ_{Yd} Dynamic yield strength

¹ Research Associate, Yokohama National University, Yokohama 240, Japan.

² Professor of Nuclear Engineering, University of Tokyo, Tokyo 113, Japan.

³ Professor Emeritus, University of Tokyo, Japan Engineering and Inspection Corp., Tokyo, Japan.

- E Young's modulus
- B Specimen thickness
- B_N Thickness of specimen across plane of face grooves
- W Distance from load line to back end of specimen
- N Slot width
- Δ Displacement measured at the specimen edge

A method for measuring crack arrest toughness values has been of great interest in the field of nuclear pressure vessel technology. In the case of a postulated loss-of-coolant accident in a reactor vessel, it is a primary safety requirement that a crack must stop before penetration of the vessel wall.

ASTM Subcommittee E24.01 on Fracture Mechanics Test Methods, a subcommittee of ASTM Committee E-24 on Fracture Testing, proposed a test method [1] for crack arrest fracture toughness of ferritic materials. The test is made using the transverse wedge-opening loading to cause a run-arrest segment of crack extension in a compact specimen, and the stress-intensity factor observed in the static condition after arrest is evaluated as a value of the crack arrest toughness K_{Ia} of the material. This method is considered promising; however, several points are not yet fully clarified:

1. There is a question of whether crack arrest toughness obtained in accordance with the proposed method is dependent on the initiation toughness or crack jump length [2]. Furthermore, it is not known whether the size limitations in the method are appropriate to obtain valid plane-strain crack arrest toughness K_{Ia} .
2. An approach to establishing relationships among the crack arrest toughness K_{Ia} , static fracture toughness K_{Ic} [evaluated from the ASTM Test for Plane-Strain Fracture Toughness of Metallic Materials (E 399-83)], and dynamic fracture toughness K_{Id} (evaluated from Annex 7 of ASTM Test E 399-83) is needed to systematize the application of linear fracture mechanics to the ongoing safety assessment of practical engineering structures.
3. The dynamic effects on crack arrest toughness K_{Ia} should be evaluated quantitatively; otherwise, at least, the fundamental question of whether the static K_{Ia} concept is reasonably more conservative for structural integrity than the dynamic analysis developed recently [3,4] should be clarified.

The Japan Welding Research Institute organized an investigation to evaluate the crack arrest capabilities of typical ferritic reactor vessel steels produced in Japan, including the evaluation of static and dynamic fracture toughness values of the steels. The results of the static and dynamic fracture toughness tests are presented in detail elsewhere [5].

A substantial number of ASTM-proposed specimens and their variations were examined by twelve different participating laboratories to expedite the development of a standard method for crack arrest toughness evaluation. The ESSO test, which is the most popular method to ensure structural integrity for long fracture, was also applied, and the data obtained were compared with data from the ASTM specimens.

Test Materials

In this study, six heats of ASTM A533 Grade B Class 1 steel and twelve heats of ASTM A508 Class 3 steel were tested in the as-received condition. The chemical compositions for each steel including the mean values and standard deviations of each element, at a quarter-thickness location, are listed in Table 1. All of these chemical compositions fully met ASTM specification requirements. The results of tensile testing at room temperature are given in Table 2. The Charpy V-notch impact test and the drop-weight nil-ductility transition tem-

TABLE 1—Chemical compositions of A533B and A508 steels ($1/4$ thickness, bottom), in weight percent.

Steel	C	Si	Mn	P	S	Ni	Cr	Cu	Mo	Al
A533B Class 1										
Mean	0.13	0.26	1.43	0.006	0.004	0.66	0.15	0.02	0.55	0.022
σ^a	0.01	0.03	0.05	0.001	0.001	0.02	0.03	0.02	0.02	0.008
ASTM specification	0.25 to max	0.15 to 0.30	1.15 to 1.50	0.035 to max	0.04 to max	0.40 to 0.70	0.45 to 0.60	...
A508 Class 3										
Mean	0.20	0.26	1.38	0.004	0.005	0.72	0.11	0.03	0.49	0.021
σ^a	0.02	0.04	0.11	0.002	0.003	0.11	0.09	0.05	0.05	0.01
ASTM specification	0.15 to 0.25	0.15 to 0.40	1.20 to 1.50	0.025 to max	0.025 to max	0.40 to 1.00	0.25 to max	...	0.45 to 0.60	...

^a σ = standard deviation.

TABLE 2—Mean values and standard deviations of tensile, Charpy impact, and drop-weight properties for A533B and A508 steels (1/4 thickness, T-direction, bottom).

Steel	Yield Strength, ^a MPa	Tensile Strength, ^a MPa	νE_{shelf} , J	T_{NDT} , °C	RT_{NDT} , °C
A533B Class 1					
Mean	486	623	224	−30	−30
σ^b	17	21	18	5	5
ASTM specification	≥345	552 to 689
A508 Class 3					
Mean	458	604	203	−30	−30
σ^b	24	23	21	5	5
ASTM specification	≥345	551 to 724

^a At room temperature.
^b σ = standard deviation.

perature (NDT) test were also conducted for each of the materials. The test results (transition temperatures and upper-shelf energy levels) are summarized in Table 2. The results of these fundamental tests are given in detail elsewhere [6].

Test Procedure

The configuration of a typical ASTM proposed specimen is shown in Fig. 1. The thickness, *B*, was 50.8 mm and the specimen width, *W*, was 169.3 mm. For the purpose of initiating cleavage fracture easily, a brittle bead (Murex-Hardex N) was weld-deposited at the bottom of a notch and a fine notch with 2-mm depth was machined on the surface of the bead. This specimen type was used in the ASTM cooperative test [7] and was also adopted in this study;

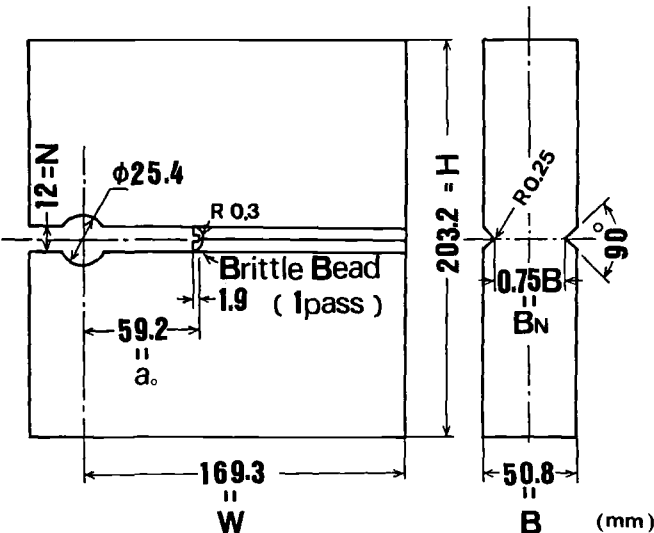


FIG. 1—Specimen geometry (standard type).

TABLE 3—Typical sizes for each specimen type, in millimetres.

Specimen Type	a_0	B	B_N	H	N	W
Standard type	59.2	50.8	38.1	203.2	12.7	169.3
Type A	35.6	30.0	18.0	122.0	12.0	101.6
Type B	59.2	25.4	19.1	203.2	12.7	169.3
Type C	94.4	50.8	38.1	320.0	12.7	266.7
Type D	280.0	100.0	75.0	960.0	40.0	800.0

hence, we called it a standard type of ASTM specimen. For discussing geometric effects, several modified types (Types A through D), for which the typical sizes were shown in Table 3, were used. Prior to testing, about half of these specimens were compressed with 500 kN to examine the effects of preloading.

The tests, using ASTM-recommended specimens (standard type and Types A through D), were performed at temperatures ranging from -100°C to room temperature, in accordance with the proposed ASTM test procedure, by the twelve different laboratories shown in Table 4. Crack-mouth opening displacements were measured at $0.25 W$ from the load line with the noncontact eddy current type of displacement gages, and the cross-head motion was stopped at the first audible evidence of crack extension. After heat tinting, a specimen was broken into two pieces and the crack length was measured on the heat-tinted fracture surfaces at the $\frac{1}{4}$ thickness, $\frac{1}{2}$ thickness, and $\frac{3}{4}$ thickness locations. The average of these three measurements defines the arrested crack length, a_a .

ESSO specimens were used to examine the effect of different test methods. ESSO specimen designs and sizes are given in Fig. 2. ESSO tests were performed at various nominal stresses on plates with a temperature gradient distributed in the direction perpendicular to the nominal stress. As shown in Fig. 3, a specimen was cooled by liquid nitrogen at the crack initiation site and was warmed by a gas burner at the end of the specimen to cause a temperature slope from about -150 to 100°C . At the same time, the specimen was tensioned by 8000-ton testing equipment. An impact energy of about $1.5 \times 10^4 J$ was loaded at the initiation site by shooting a wedge using a compressed air gun. After the initiation of a brittle crack on an undercooled spot, the crack started to propagate. Crack propagation stopped at a certain place, corresponding to the crack arrest temperature of the specific plate. After crack arrest, the specimen was broken into two pieces and the arrested crack length was measured.

TABLE 4—Participants in this study.

Ishikawajima-Harima Heavy Industries Co., Ltd.
Japan Casting and Forging Corp.
Japan Steel Works, Ltd.
Kawasaki Steel Corp., Ltd.
Kobe Steel, Ltd.
Mitsubishi Heavy Industries
Nippon Kokan
Nippon Steel Corp.
Ship Research Inst.
Sumitomo Metal Industries, Ltd.
University of Tokyo
Yokohama National University

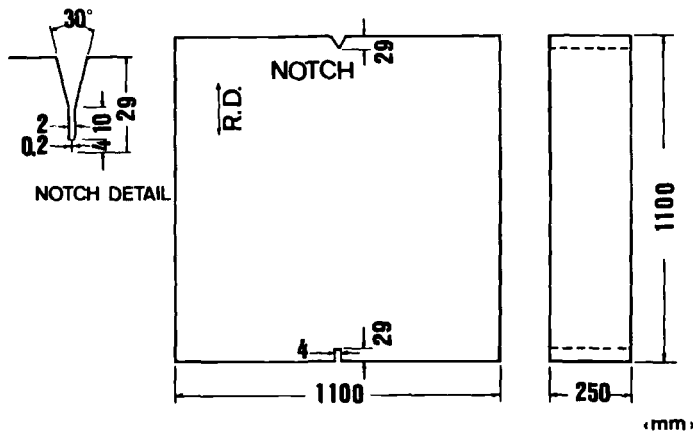


FIG. 2—ESSO specimen geometry.

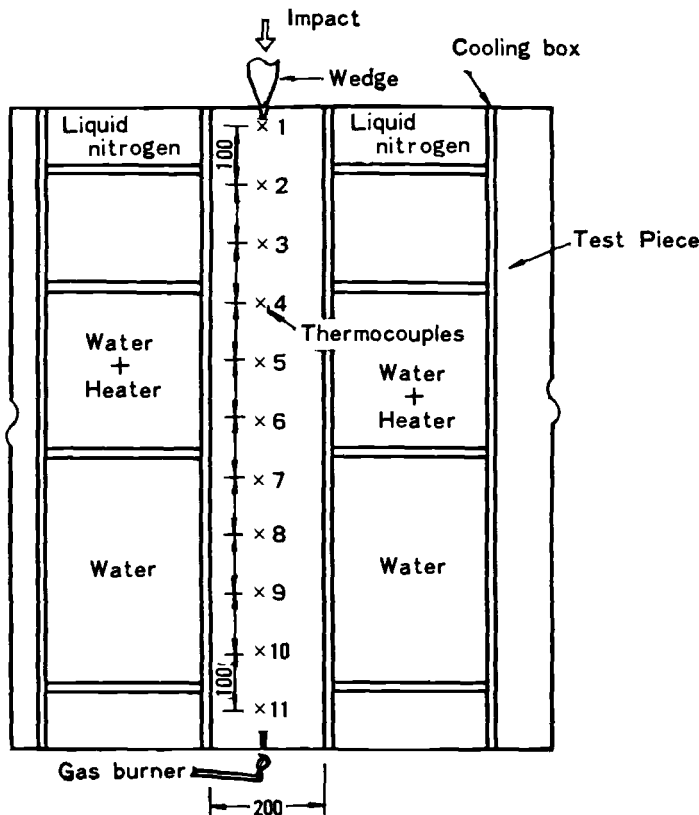


FIG. 3—A schematic illustration of testing conditions for an ESSO specimen.

Analysis

ASTM Proposed Method

Crack arrest toughness K_a and crack initiation toughness K_Q were calculated using the following equation

$$K = Y \Delta E \frac{1}{\sqrt{W}} \frac{B}{B_N} \quad (1)$$

where

$$Y = \frac{2.2434(1.7164 - 0.9X + X^2)}{9.85 - 0.17X + 11.0X^2} \sqrt{(1 - X)}$$

and where

$$X = \frac{a}{W}$$

A task group of ASTM Subcommittee E24.01 proposed the criteria shown in Table 5 in order to obtain a linear-elastic plane-strain crack arrest toughness K_{Ia} from the value of K_a calculated using the above equation. In this study, K_a was denoted as K_{Ia} when K_a was completely satisfied with each item of Table 5.

ESSO Test

Crack arrest toughness K_{Ca} was calculated using the following equation [8]

$$K_{Ca} = f(a_a) \sigma_g \sqrt{(\pi a_a)} \quad (2)$$

where

$$f(a_a) = \sqrt{\left(\frac{2W}{\pi a_a} \tan \frac{\pi a_a}{2W} \right)}$$

and where σ_g is the gross stress over the cross section.

Results

Dependence of Crack Arrest Toughness on Temperature

A substantial number of crack arrest toughness values were collected on ASTM A533B Class 1 and A508 Class 3 steels using ASTM-proposed specimens. Figure 4 shows K_a and

TABLE 5—Summary of criteria used to insure that K_a is a linear elastic, plane-strain value (from Ref 1).

Specimen Type	Feature	Criterion
A	unbroken ligament	$W - a_a > 0.15W$
B	unbroken ligament	$W - a_a > 1.25 (K_a/\sigma_{Yd})^2$
C	thickness	$B > 1.0 (K_a/\sigma_{Yd})^2$
D	crack-jump length	$a_a - a_0 > 2N$
E	crack-jump length	$a_a - a_0 > (K_0/\sigma_{YS})^2/2\pi$

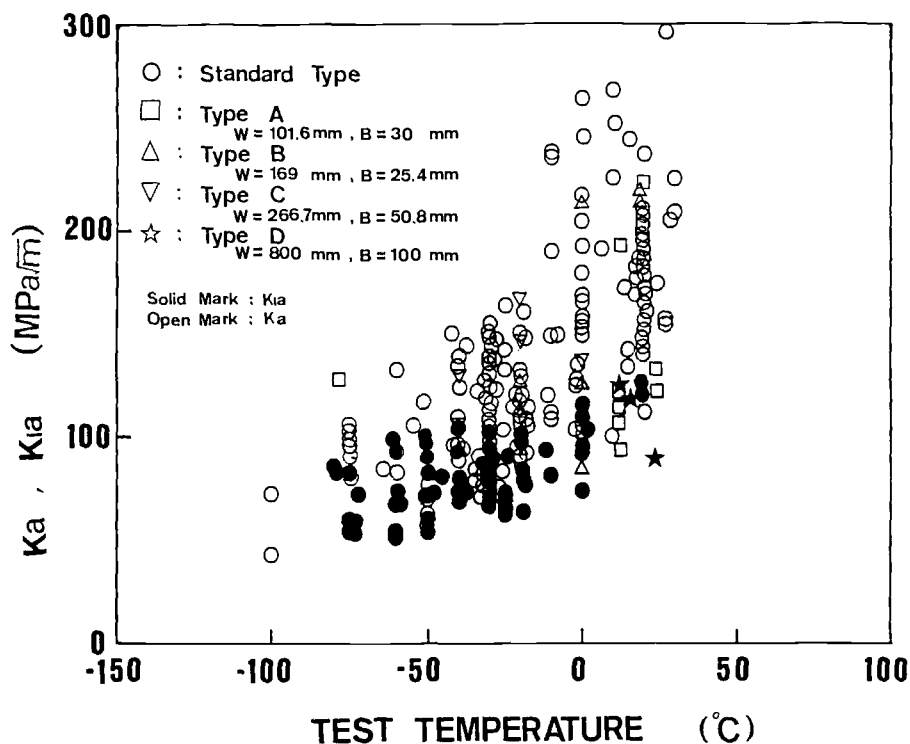


FIG. 4—Dependence of K_a and K_{Ia} on temperature for all heats of test materials.

K_{Ia} plotted against the test temperature for all heats of the test materials. As expected, increasing temperature continually increased the crack arrest toughness. A troublesome feature of the data shown in Fig. 4 is the degree of variability of K_a , which is mainly caused by (a) heat-to-heat variability, (b) variability arising from the difference in specimen geometries, and (c) variability reflected in the metallurgical and mechanical inhomogeneity of a material.

Table 6 shows the mean values and standard deviations of K_a and K_{Ia} data at RT_{NDT} and

TABLE 6a—Mean and standard deviation of crack arrest toughness values (K_a and K_{Ia}) for each heat at typical test temperatures for A533B Class 1 steel, in $MPa \sqrt{m}$.

Temperature	Heat Code						Average
	1A ^a	2A	3A	4A	5A ^a	6A	
RT_{NDT}							
Mean	...	110.1	109.2	104.5	...	98.2	105.5
σ^b	...	23.2	14.5	18.9	...	11.0	16.9
Room temperature							
Mean	...	173.4	182.5	165.4	...	169.5	172.7
σ^b	...	28.6	29.7	28.4	...	29.8	29.1

^a These materials were used for the ESSO test.

^b σ = standard deviation.

TABLE 6b—Mean and standard deviation of crack arrest toughness values (K_{Ia} and K_{IIa}) for each heat at typical test temperatures for A508 Class 3 steel, in MPa \sqrt{m} .

Temperature	Heat Code												
	1B	2B ^a	3B	4B	5B	6B	7B	8B	9B	10B	11B	12B	Average
RT _{NDT}													
Mean	111.2	...	76.3	97.4	70.3	98.8	108.1	105.2	103.2	97.4	98.2	97.8	96.7
σ^b	21.3	...	12.1	17.5	11.3	12.2	20.8	10.5	18.6	19.2	15.5	16.7	16.0
Room temperature													
Mean	185.4	...	126.1	156.2	129.7	175.3	181.1	165.3	175.4	173.1	163.1
σ^b	35.3	...	31.8	29.8	30.5	28.6	27.9	30.3	31.2	28.0	30.4

^a These materials were used for the ESSO test.

^b σ = standard deviation.

room temperature for each heat, in the case of the standard specimens. For A533B steel the mean value at RT_{NDT} was $105.5 \text{ MPa } \sqrt{\text{m}}$ with a standard deviation of $16.9 \text{ MPa } \sqrt{\text{m}}$, while for A508 steel, the mean at RT_{NDT} was $96.7 \text{ MPa } \sqrt{\text{m}}$ with a standard deviation of $16.0 \text{ MPa } \sqrt{\text{m}}$. Thus, the evaluated difference between the two steels was satisfactorily small. Assuming the data from Heats 3B and 5B are eliminated, the maximum difference among the mean values of all heats at RT_{NDT} was $13.8 \text{ MPa } \sqrt{\text{m}}$, which is smaller than the average of the standard deviations of the two steels. Therefore, it can be said that heat-to-heat variability was small within the heats, excluding Heats 3B and 5B, at RT_{NDT} . In addition, the mean values of Heats 3B and 5B at the temperature range from RT_{NDT} of -15°C to RT_{NDT} of $+15^\circ\text{C}$ were 88.1 and $87.6 \text{ MPa } \sqrt{\text{m}}$, respectively. Considering these facts, heat-to-heat variability, as well as the variability from the difference of the steels, was sufficiently small in the tested materials.

At room temperature, the means of the crack arrest toughness values for A533B and A508 steels were 172.7 and $163.1 \text{ MPa } \sqrt{\text{m}}$, respectively. From Table 6, the variation in mean values of various heats at room temperature is large in comparison with the results at RT_{NDT} . The standard deviations for A533B and A508 steels at room temperature were 29.1 and $30.4 \text{ MPa } \sqrt{\text{m}}$, respectively, which were about two times larger than those at RT_{NDT} .

This spread in values at the higher temperature region was probably because (as will be discussed later in the section concerning thickness effects), when using compact specimens, the linear-elastic concept of the ASTM method was inappropriate because of the inherent high toughness of the present materials, as is proved in Refs 5 and 6. Further, the lack of mechanical constraint, so that the plastic zone size ahead of an arrested crack tip grew larger relative to the specimen size, also contributed to the large variation in the data. In Fig. 4, the data from large specimens (Type D) show less variation than those from compact specimens, and the former data are distributed at or near the lower bound of the latter.

Dependence of K_{Ia} on Temperature

In Fig. 4, the closed symbols are valid plane-strain crack arrest toughness K_{Ia} values in accordance with ASTM size requirements. Valid K_{Ia} could be obtained by standard type, Type C, and Type D specimens; when using Type A and B specimens, none of the data satisfied the size requirement (C) in Table 5. Table 7 shows the maximum, minimum, and mean K_{Ia} values with standard deviations at typical test temperatures for standard specimens of both the A533B and A508 steels. As shown in Table 7 and Fig. 4, one can see that K_{Ia} values increased as the temperature increased, though the rate of increase was not as large in comparison with the K_a data; further, the lower bound of K_{Ia} was in good agreement

TABLE 7—Maximum K_{Ia} , minimum K_{Ia} , mean K_{Ia} , and standard deviations at typical test temperatures for the A533B and A508 materials tested, in $\text{MPa } \sqrt{\text{m}}$.

	Test Temperature, $^\circ\text{C}$				
	-70	-50	-30	0	Room Temperature
K_{Ia} (max)	82.1	98.3	104.2	108.7	132.8
K_{Ia} (min)	59.5	61.7	72.3	81.5	89.1
K_{Ia} (mean)	66.7	72.0	85.3	94.0	119.3
σ^a	10.8	11.8	12.2	13.8	14.1

^a σ = standard deviation.

with that of K_a data above -80°C . Two K_a data at -100°C , in Fig. 4, were relatively low, however, these values did not satisfy the criterion (B) in Table 5. It is also noted from Fig. 4 that the K_{Ia} values show less variation over the entire temperature range.

Dependence of K_a and K_{Ia} on K_Q

In the ASTM method there is a question of whether crack arrest toughness is independent of crack initiation toughness K_Q , or whether there is a significant relationship between them. Substantially, K_{Ia} should be independent of K_Q ; however, there is a possibility that K_{Ia} increases or decreases as K_Q increases because of dynamic effects, which are neglected in the proposed K_{Ia} concept. If strong dependence of K_{Ia} on K_Q is observed, the test method should be considered less promising.

Figures 5 and 6 show K_a and K_{Ia} measured on both steels plotted against K_Q at RT_{NDT} and room temperature, respectively. In Figure 5 there is a small upward trend of K_a with K_Q , however, the data show valid K_{Ia} values to be nearly independent of K_Q . The mean value of K_{Ia} was $85.3 \text{ MPa } \sqrt{\text{m}}$ with a standard deviation of $12.2 \text{ MPa } \sqrt{\text{m}}$, and the least squares linear fit to the data gives the following relation

$$K_{Ia} = 75.1 + 0.075K_Q \pm 12.2 \text{ MPa } \sqrt{\text{m}} \text{ at } RT_{NDT}$$

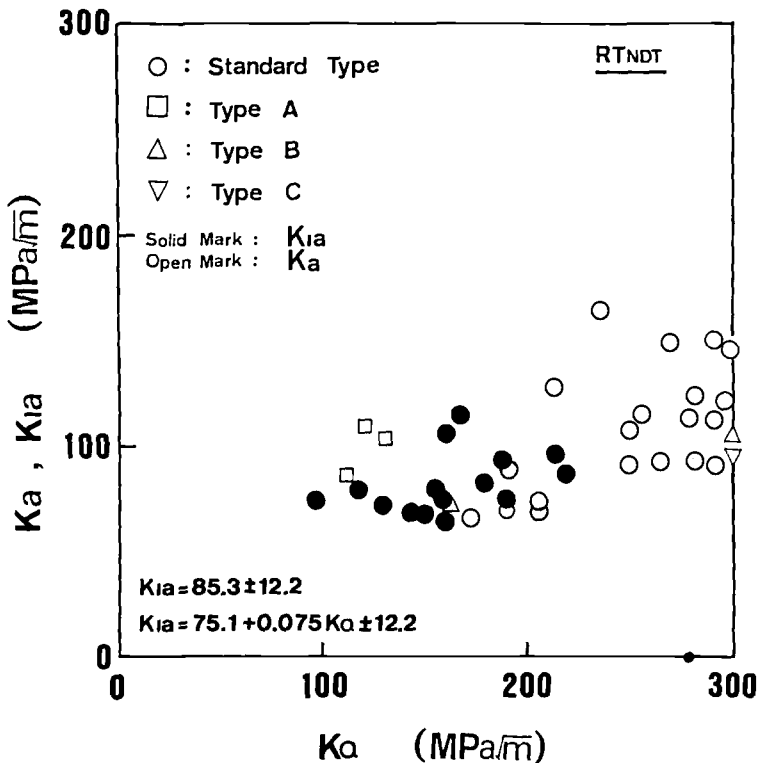


FIG. 5—Dependence of K_a and K_{Ia} on K_Q at RT_{NDT} for both steels.

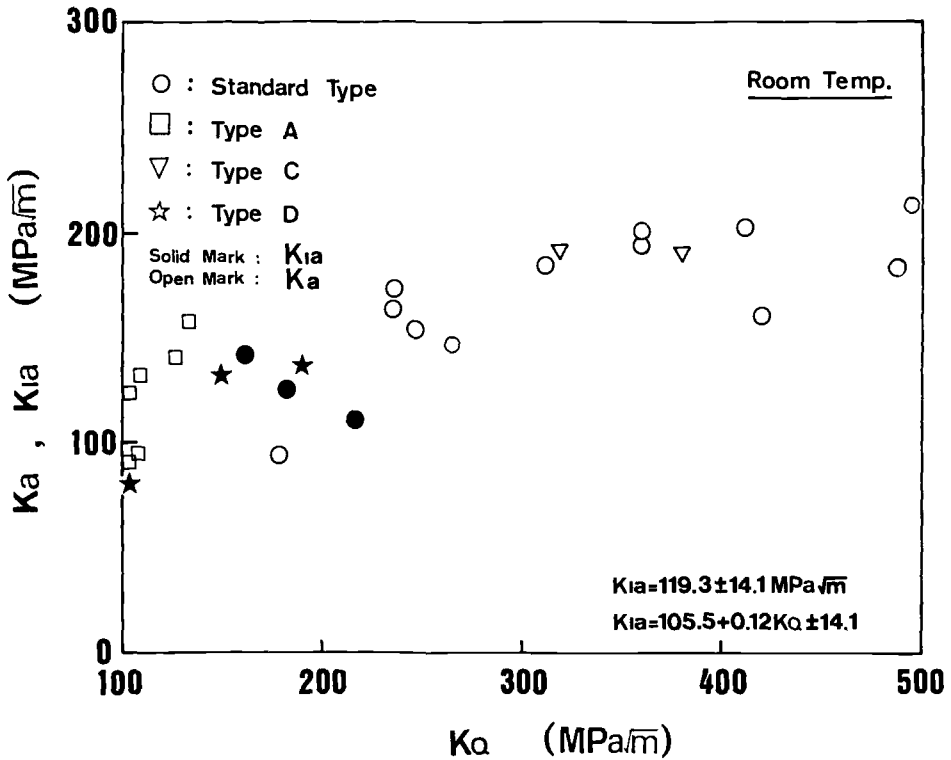


FIG. 6—Dependence of K_a and K_{Ia} on K_Q at room temperature for both steels.

The ASTM cooperative test reported the following relations [7]

$$K_{Ia} = 85.1 \pm 12.5 \quad \text{MPa} \sqrt{\text{m}} \text{ at } 0^\circ\text{C}$$

$$K_{Ia} = 87.1 - 0.115K_Q \pm 12.5 \quad \text{MPa} \sqrt{\text{m}} \text{ at } 0^\circ\text{C}$$

From these results it is clear that the mean K_{Ia} and standard deviation of both materials at RT_{NDT} correspond well with those of the ASTM data at 0°C , and that the estimation of K_{Ia} from K_Q , using the above equations, gives about the same value within the K_Q range from 100 to 220 $\text{MPa} \sqrt{\text{m}}$.

At room temperature, K_a is strongly dependent on K_Q , as shown in Fig. 6. Least squares linear fit to the data gives a positive slope, $K_a/K_Q = 0.25$. However, the dependence of K_{Ia} on K_Q was rather small in comparison with that of K_a on K_Q . The mean K_{Ia} was 119.3 $\text{MPa} \sqrt{\text{m}}$ with a standard deviation of 14.1 $\text{MPa} \sqrt{\text{m}}$, and the least squares linear fit to the data gives the following relation

$$K_{Ia} = 105.5 + 0.12K_Q \pm 14.1 \quad \text{MPa} \sqrt{\text{m}} \text{ at room temperature}$$

The ASTM cooperative study test also reported the following relations

$$K_{Ia} = 107.5 \pm 13.6 \quad \text{MPa} \sqrt{\text{m}} \text{ at room temperature}$$

$$K_{Ia} = 93.5 + 0.076K_Q \pm 13.4 \quad \text{MPa} \sqrt{\text{m}} \text{ at room temperature}$$

Comparing the present data with the ASTM data at room temperature, one can also note that the mean K_{Ia} and the standard deviations for both test programs were shown to be in good agreement with each other, though the number of K_{Ia} data of the present investigation was too small to make a precise quantitative consideration on the K_{Ia} level at room temperature.

Dependence of K_a and K_{Ia} on Crack Jump Length

Figures 7 and 8 show K_a and K_{Ia} for both steels plotted against a_a/W at RT_{NDT} and room temperature, respectively. In Fig. 7, there is a downward trend in K_{Ia} or K_a with a_a/W for standard specimen data; the expected relation illustrated by the curve is shown to be of benefit in describing the dependence of K_{Ia} on the crack jump length ratio a_a/W . The curve was defined by Eq 1 using the K_Q value of $250 \text{ MPa}\sqrt{\text{m}}$ with its a/W ratio of 0.35, assuming that the stress-intensity factor K decreased according to the factor Y in Eq 1.

On the contrary, in Fig. 8, a systematic dependence of K_{Ia} on a_a/W was not observed. However, there was a downward trend in K_a with a_a/W within the standard specimen data. Obviously, from these figures, a_a/W ratios were distributed widely and showed a dependence on specimen geometries. The ratios of the smallest specimens (Type A) indicated that the cracks propagated relatively small distances ($a_a/W = 0.4$ to 0.5), or quite a large distance ($a_a/W = 0.95$), prior to arrest. For a Type A specimen with a steep stress gradient along the small ligament, a brittle crack was likely to penetrate through the remaining width. Conversely, for a small specimen, since the welding defects and the residual stress in a

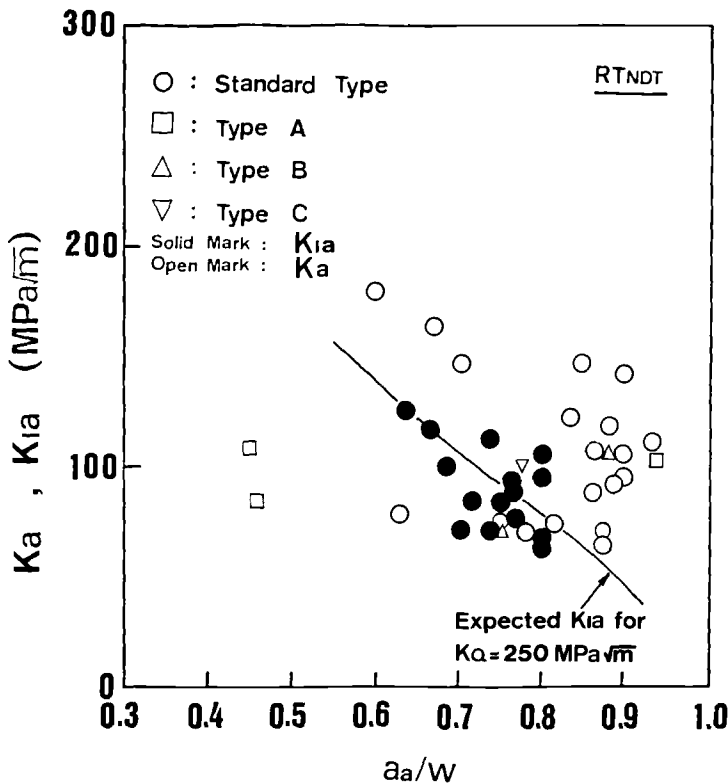


FIG. 7—Dependence of K_a and K_{Ia} on a_a/W at RT_{NDT} for both steels.

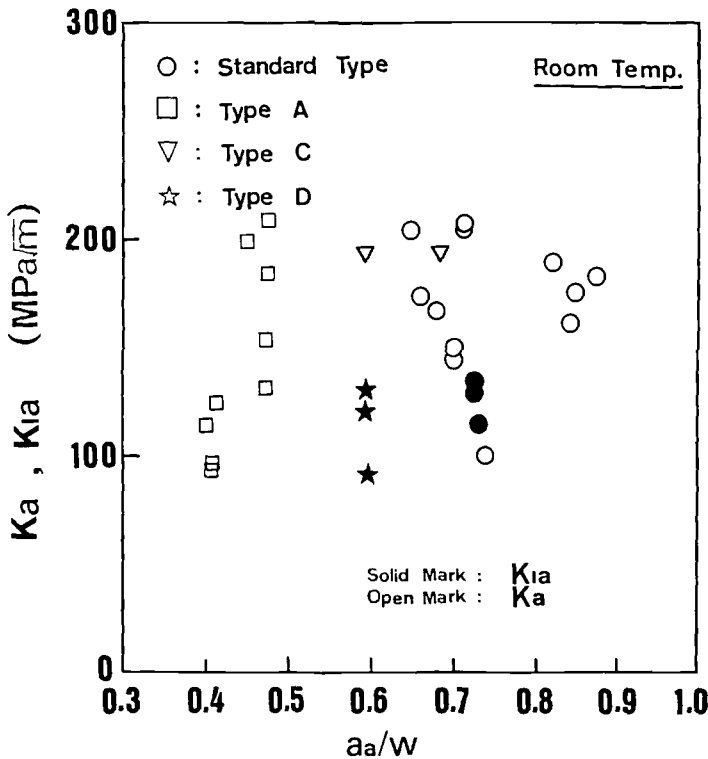


FIG. 8—Dependence of K_a and K_{Ia} on a_a/W at room temperature for both steels.

brittle bead were probably more effective in initiating a crack under a low-stress condition than for a large specimen, there was also the tendency for a crack to propagate only a small distance, like a kind of pop-in; this was overwhelmingly observed both at RT_{NDT} and room temperature in the case of Type A specimens.

In Fig. 8, the mean a_a/W for standard specimens, Type C, and Type D specimens were 0.71, 0.65, and 0.59, respectively. The scatter of a_a/W decreased as W increased and was almost negligible when using the largest specimens. Really, the variation of the ratio for Type D specimens was sufficiently small, though K_{Ia} varied to some extent. For K_a and K_{Ia} data, the mean a_a/W was 0.81 with a standard deviation of 0.16 at RT_{NDT} , while at room temperature, the mean was 0.71 with a standard deviation of 0.08 for the standard specimens. Thus, as temperature increased, the average crack jump length decreased, which proved increasing toughness (that is crack arrest capability) of the tested materials with temperature.

K_{Ca} Data Using the ESSO Test

Results for crack arrest toughness K_{Ca} are shown in Fig. 9. Figure 9 shows the dependence of K_{Ca} on temperature as obtained from tests on ESSO specimens at a load level that ranged from 1370 to 6250 ton force. The lowest value was obtained for $K_{Ca} = 35.8 \text{ MPa } \sqrt{\text{m}}$ at -125°C with an applied load of 1370 ton force, while a maximum value of $K_{Ca} = 385.3 \text{ MPa } \sqrt{\text{m}}$ was achieved at 63°C with an applied load of 6250 ton force. In Fig. 9, K_{Ca} is apparently dependent on temperature, and small increases in temperature above room

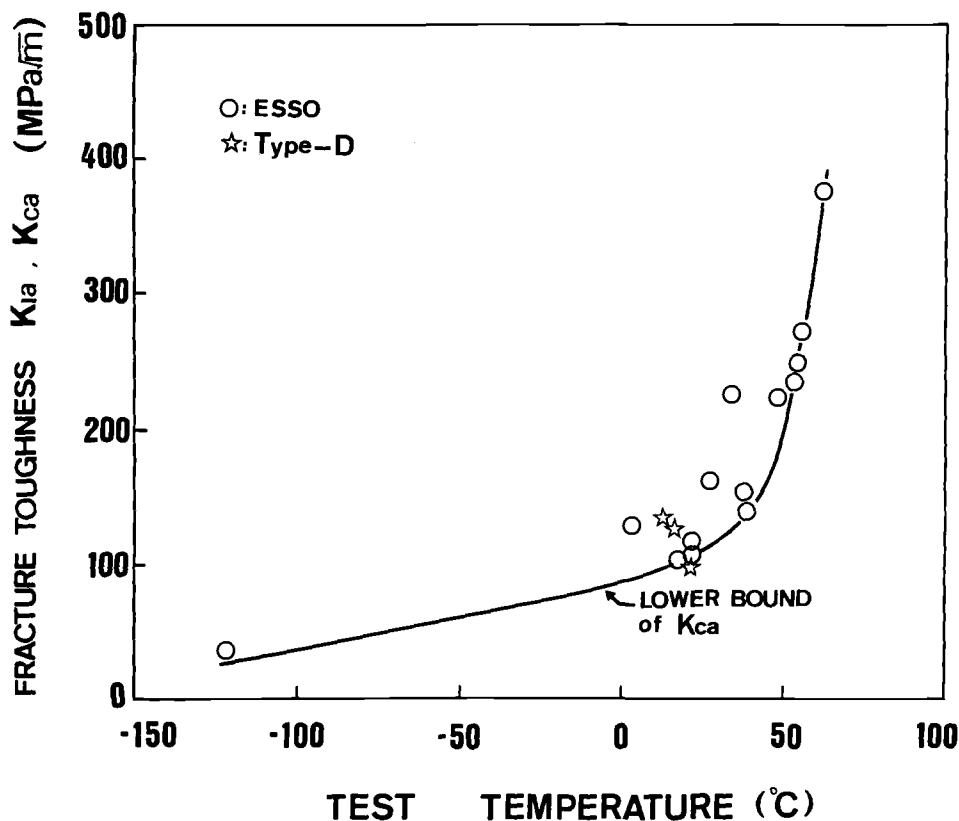


FIG. 9—Dependence of K_{Ca} and K_{Ia} from Type D specimens on temperature.

temperature resulted in very sharp increases in crack arrest toughness K_{Ca} . These results correspond closely with the results from the ASTM K_{Ia} test shown in Fig. 4. In Fig. 9, K_{Ia} data of Type D specimens are also plotted, and a very good agreement was found between the ESSO specimen data and Type D specimen data at room temperature. This implies that, although the experimental methods and analyses were different, ASTM and ESSO tests lead to about the same crack arrest toughness values when applied to large specimens of the same size.

Effects of Thickness on Crack Arrest Toughness

The effects of thickness on crack arrest toughness at room temperature is presented in Fig. 10. In the figure, K_{Ca} values obtained by ESSO specimens are also plotted. With the aid of K_{Ca} data, it is apparent that crack arrest toughness first drops and then becomes constant with increasing thickness. Assuming that a plane-strain condition was achieved at 100-mm thickness, the mean arrest toughness value was 113.3 MPa \sqrt{m} with a standard deviation of 15.3 MPa \sqrt{m} . The mean value is slightly smaller than the mean K_{Ia} (119.3 MPa \sqrt{m}) in Table 7, which was evaluated in accordance with the ASTM thickness requirement. At room temperature, the dynamic yield strength σ_{Yd} was estimated as 677 MPa following the ASTM proposed method, where σ_{Yd} is assumed to be 205 MPa greater than the static yield strength σ_{YS} .

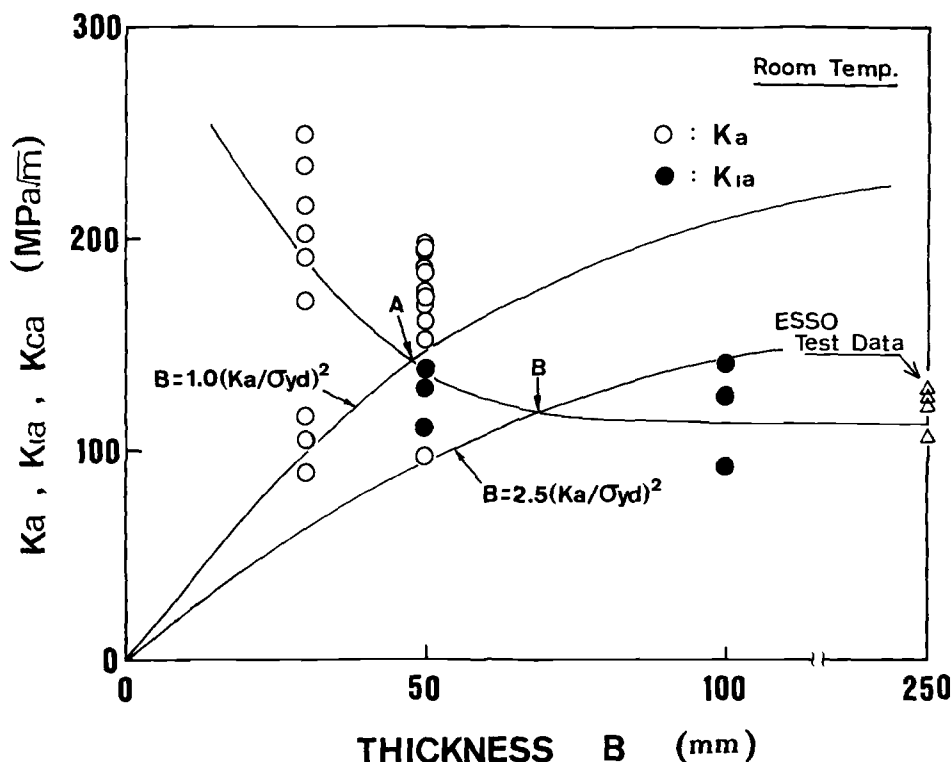


FIG. 10—Dependence of crack arrest toughness (K_a , K_{Ia} , and K_{Ca}) on specimen thickness at room temperature.

In the figure, two thickness criteria ($B = 1.0(K_a/\sigma_{yd})^2$ and $B = 2.5(K_a/\sigma_{yd})^2$) were depicted as K versus B relations. The results show that if the criterion $B \geq 2.5(K_a/\sigma_{yd})^2$ is applied to the present data, three values of Type D specimens are denoted as plane-strain crack arrest toughness K_{Ia} , and none of the data from compact specimens (standard and Type A) meet the criterion. Applying the ASTM proposed criterion, $B \geq 1.0(K_a/\sigma_{yd})^2$, three values of standard specimens as well as three values of Type D specimens are denoted as plane-strain crack arrest toughness K_{Ia} , where the lowest K_a value at 50-mm thickness could not satisfy Criterion B in Table 5. The upper bounds of K_{Ia} for the standard type and Type D specimens were almost equal; however, the lower bound of the former was somewhat higher than the latter. Moreover, there is great scatter in the data from compact specimens in comparison with the data from large specimens (Type D and ESSO specimens).

These results mean that, as is the case for the static fracture toughness test, increasing thickness effectively inhibited the plastic zone development at the crack tip of an arrest specimen. Referring to the average line and the crossing points A and B in Fig. 10, one can see that the plane-strain condition is maintained above the thickness corresponding to Point B; then, $B \geq 2.5(K_a/\sigma_{yd})^2$ is an adequate thickness requirement. On the other hand, assuming that the plane-strain condition is achieved approximately at the thickness indicated by Point A, the criterion $B \geq 1.0(K_a/\sigma_{yd})^2$ can be used to determine valid K_{Ia} values. Apparently, the former requirement is more restrictive and conservative than the latter. However, note that the difference between the mean K_{Ia} associated with each requirement

was not so large; that is, the ASTM-proposed requirement of $B \geq 1.0(K_a/\sigma_{Yd})^2$ can overestimate the mean K_{Ia} obtained in accordance with $B \geq 2.5(K_a/\sigma_{Yd})^2$ only 5%. Moreover, taking into account that the weights of a Type D and an ESSO specimen were about 700 and 2300 kg, respectively, which imposed many difficulties on performing each test procedure, therefore, it may be said that the requirement $B \geq 1.0(K_a/\sigma_{Yd})^2$ can be used as a thickness limitation to yield satisfactory results for evaluation of valid K_{Ia} values.

Comparing K_{Ia} with K_{Ic}

Figure 11 shows K_{Ia} , K_{Ca} , and K_{Ic} plotted against $T - RT_{NDT}$. Plane-strain fracture toughness K_{Ic} values were obtained in accordance with ASTM Test E 399-83 using 4TCT and 10TCT specimens instead of the present materials [5]. In the figure, the lower bound of K_{Ia} data was significantly lower than that of K_{Ic} data, though both bounds were well over the ASME K_{IR} curve and the temperature shift from the transition curve of K_{Ic} to that of K_{Ia} was about 50°C. At $T - RT_{NDT} = 0^\circ\text{C}$, the lowest K_{Ia} value was about half of the lowest K_{Ic} value, and the rate of decrease of toughness from static to arrest increased with temperature.

Crack Velocity Measurements

Crack velocities were measured using ladder gages on the surfaces of standard type and ESSO specimens. A thin uniform layer of insulator was coated on a specimen surface and

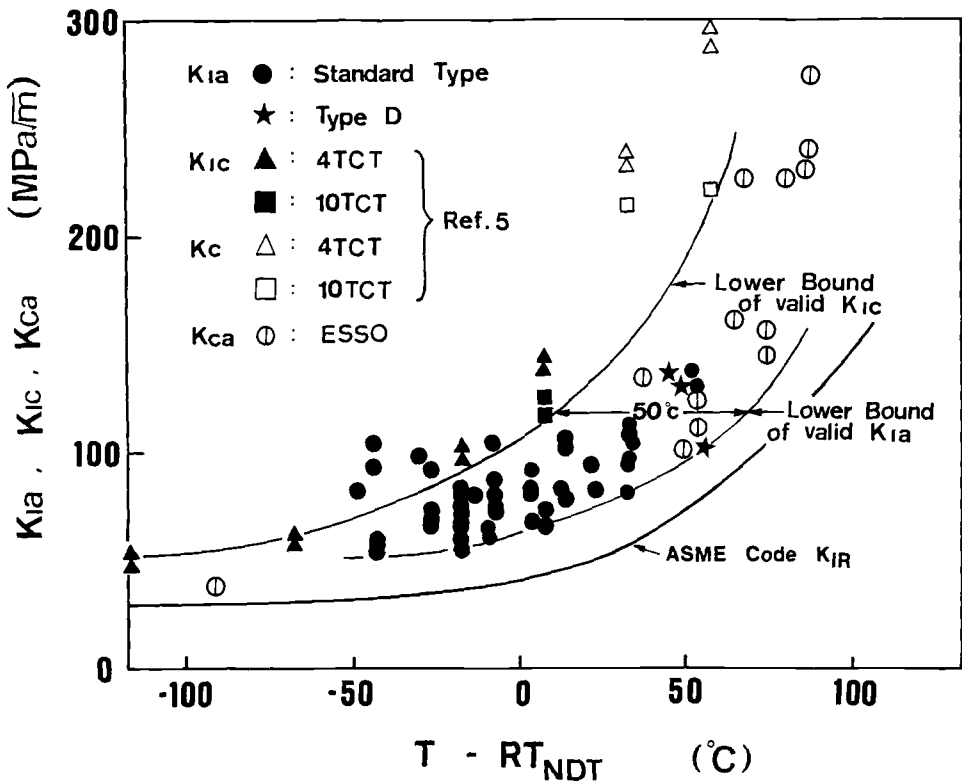


FIG. 11— K_{Ia} , K_{Ic} , and K_{Ca} versus $T - RT_{NDT}$.

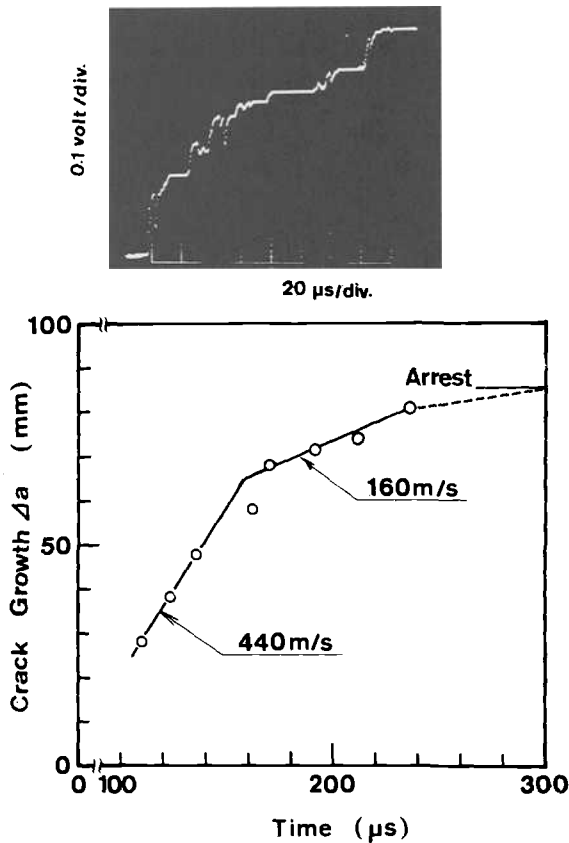


FIG. 12—A typical output of crack velocity measurement and the relation between crack length and elapsed time for a standard specimen at RT_{NDT} .

a ladder gage was made by conductive silver paint on the insulating layer. Figure 12 shows a typical result of a crack velocity measurement in the vicinity of the RT_{NDT} temperature. It is apparent from the figure that, shortly after initiation, the crack accelerated abruptly to reach a high velocity and then decelerated to a low velocity during the latter half of the crack growth. For the fast part of the propagation, the velocity was within the range of 400 to 500 m/s, while for the slow part of the propagation, the velocity was within the range of 100 to 200 m/s and presumably became less than 10 or 20 m/s just prior to arrest.

Figure 13 depicts the result of a crack velocity measurement for an ESSO specimen, showing clearly the deceleration process of a running crack. For the fast part of the jump, the velocity was approximately 1000 m/s and less than 500 m/s at the last stage of the jump. Reflected by the large amount of elastic energy stored in a specimen, the crack velocity observed in an ESSO specimen was, in general, significantly larger than that observed in a standard specimen. From these results, it may be said that the dynamic effect in a standard specimen was relatively low in comparison with that in a large specimen, so that there will possibly be a difference between the crack arrest toughness evaluated by different size specimens. However, the magnitude of the difference was not clear in this investigation.

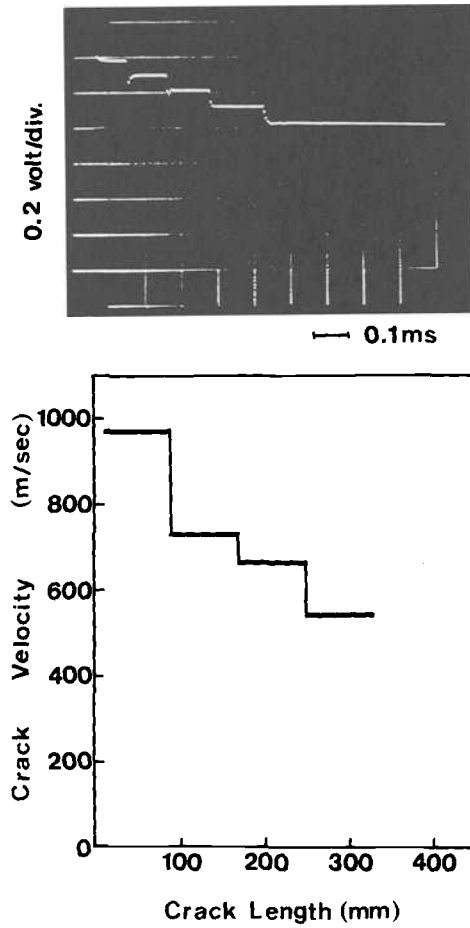


FIG. 13—A typical output of crack velocity measurement and the relation between crack velocity and crack length for an ESSO specimen.

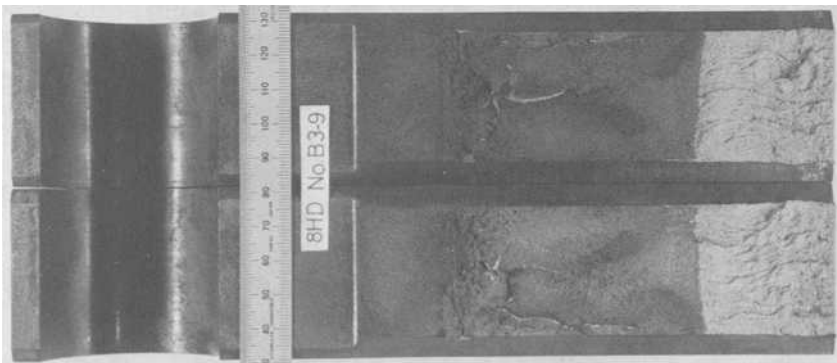


FIG. 14—Fracture surface appearance of a standard specimen tested at room temperature.

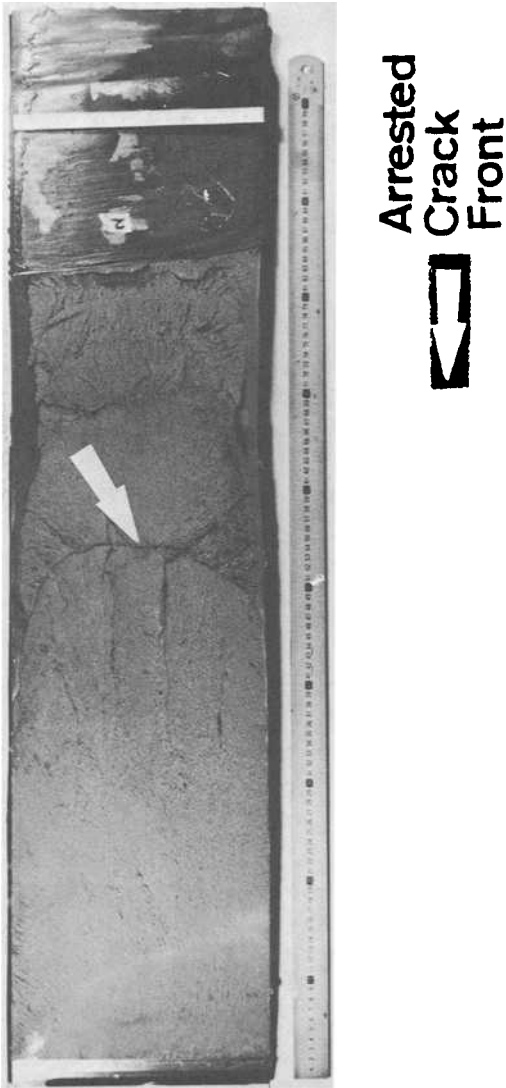


FIG. 15—Fracture surface appearance of an ESSO specimen tested with a tensile load of 5000 ton force.

Fracture Surface Appearance

Figure 14 shows the fracture surface appearance of a standard specimen tested at room temperature. The fracture surface shows the ductile area interspersed with cleavage near the initial notch and unbroken ligaments at the middle of the crack jump length. The crack front irregularity and tunneling were not observed due to the mechanical constraints introduced by side grooves. Figure 15 shows the fracture surface appearance of an ESSO specimen tested with a tensile load of 5000 ton force. A brittle crack started at the left side of the specimen and was arrested approximately at the center of the specimen length, as illustrated by an arrow in Fig. 15, where the temperature was about 6°C. In general, the fracture surfaces of ESSO specimens appeared much smoother than the surfaces of standard specimens tested at the RT_{NDT} or above, and unbroken ligaments were not observed in all cases. However, the crack front was commonly rather round, and tunneling and small shear lips along the edge of the fracture surface were observed in the case of an ESSO specimen.

Conclusions

The results of this investigation showed that the K_{Ia} concept proposed by ASTM could be successfully applied to the characterization of crack arrest toughness of ferritic materials produced in Japan. The principal conclusions can be summed up as follows:

1. The plane-strain crack arrest toughness K_{Ia} measured in accordance with the ASTM-proposed method was shown to be essentially independent of initiation toughness K_Q at RT_{NDT} and room temperature.
2. The variation of crack jump length was effectively reduced at room temperature as specimen thickness increased. The crack arrest toughness decreased as crack jump length increased, depending on the nature of Eq 1.
3. The crack arrest toughness decreased as thickness increased and became constant for thicknesses greater than 50 mm, at room temperature. The ASTM thickness requirement was shown to give a reasonable estimate of plane-strain crack arrest toughness K_{Ia} .
4. The lower bound of K_{Ia} data was significantly under the lower bound of K_{Ic} of the materials tested, though both bounds were well over the ASME K_{IR} curve.

References

- [1] Forney, W. L., et al., "Appendix: Crack Arrest Fracture Toughness of Ferritic Materials," *Metals Handbook*, 9th Ed., Vol. 8, 1985, p. 288.
- [2] Crosley, P. B. and Ripling, E. J., "Significance of Crack Arrest Toughness (K_{Ia}) Testing," *Crack Arrest Methodology and Applications*, ASTM STP 711, American Society for Testing and Materials, Philadelphia, 1980, p. 321.
- [3] Gates, R. S., "Results of a Dynamic Analysis of Crack Propagation and Arrest Data in the Modified Compact Tension Geometry," *International Journal of Pressure Vessels and Piping*, Vol. 17, No. 2, 1984, p. 105.
- [4] Beinert, J. and Kalthoff, J. F., "The Development of a Crack Arrest Test Specimen with Reduced Dynamic Effects," *Application of Fracture Mechanics to Materials and Structures*, Martinus Nijhoff Publishers, Amsterdam, The Netherlands, 1984, p. 493.
- [5] Sakai, Y., et al., "Properties of Heavy Section Steel Plates and Forgings for Nuclear Vessels Produced in Japan—Part 2. Fracture Toughness," *International Journal of Pressure Vessels and Piping*, Vol. 22, No. 2, 1986, p. 79.

- [6] Sakai, Y., et al., "Properties of Heavy Section Steel Plates and Forgings for Nuclear Vessels Produced in Japan—Part 1. General Properties," *International Journal of Pressure Vessels and Piping*, Vol. 22, No. 1, 1986, p. 57.
- [7] Crosley, P. B., et al., "Cooperative Test Program on Crack Arrest Toughness Measurements," NUREG/CR-3261, Nuclear Regulatory Commission, Washington, DC, April 1983.
- [8] Tada, H., Paris, P., and Irwin, G., *The Stress Analysis of Cracks Handbook*, Del Reserch Corp., Hellertown, PA, 1973.

D. B. Barker,¹ R. Chona,² W. R. Corwin,³ W. L. Fournery,¹
G. R. Irwin,¹ C. W. Marschall,⁴ A. R. Rosenfield,⁴ and
E. T. Wessel⁵

A Method for Determining the Crack Arrest Fracture Toughness of Ferritic Materials

REFERENCE: Barker, D. B., Chona, R., Corwin, W. R., Fournery, W. L., Irwin, G. R., Marschall, C. W., Rosenfield, A. R., and Wessel, E. T., "A Method for Determining the Crack Arrest Fracture Toughness of Ferritic Materials," *Fracture Mechanics: Nineteenth Symposium, ASTM STP 969*, T. A. Cruse, Ed., American Society for Testing and Materials, Philadelphia, 1988, pp. 569–593.

ABSTRACT: This paper summarizes the results from a round robin test program that was conducted from 1983 through 1985 to evaluate a proposed ASTM standard test method for determining the crack arrest fracture toughness of ferritic materials. The round robin attracted a total of 27 participants from the United States, Canada, Europe, and Japan, each of whom agreed to test three specimens of A514 bridge steel, three specimens of A588 bridge steel, and six specimens of A533 Grade B, Class 1 reactor pressure vessel steel. Twenty-one participants had completed their testing and forwarded test results when this paper was written, which provided a data base consisting of 54 test results for each of the bridge steels at -30°C , 70 test results for the reactor steel at 10°C , and 65 test results for the reactor steel at 25°C . This paper summarizes the test procedure followed in the round robin, discusses the results obtained, and provides the rationale for the modifications to the test method that were recommended in light of the experience gained from this test program. The test procedure has since been revised and is now proposed as the ASTM Test for Determining the Plane-Strain Crack-Arrest Fracture Toughness, K_{Ia} , of Ferritic Steels (E 1221).

KEY WORDS: crack arrest, crack-arrest fracture toughness, fracture toughness testing, standard test method development, K_{Ia} measurement, fracture mechanics, ASTM Standard E 1221

No recognized standard test method currently exists for determining arrest toughness—the ability of a material to bring to rest a fast-running crack. However, it is well established that, in structures containing gradients in either toughness or stress, a crack may initiate in a region of low toughness or high stress, or both, and arrest in another region of higher toughness or lower stress. The establishment of such a test method is thus clearly of interest, particularly to individuals concerned with the safety of large steel structures such as nuclear reactor pressure vessels and highway bridges.

The subject has, therefore, been examined over the past several years by a task group of ASTM Subcommittee E 24.01 on Fracture Mechanics Test Methods, a subcommittee of

¹ Associate professor and professors, respectively, Department of Mechanical Engineering, University of Maryland, College Park, MD 20742.

² Assistant professor, Department of Mechanical Engineering, Texas A & M University, College Station, TX 77843.

³ Manager, Heavy Section Steel Technology Program, Oak Ridge National Laboratory, Martin Marietta Energy Systems, Oak Ridge, TN 37831.

⁴ Senior scientist and research leader, respectively, Physical Metallurgy Section, Battelle Columbus Division, Columbus, OH 43201.

⁵ Consultant, Haines City, FL 33844.

ASTM Committee E-24 on Fracture Testing, and preparation of a proposed test procedure for crack arrest toughness was completed in 1983. A round robin program on crack arrest testing, whose purpose was to evaluate the proposed test method, has recently been completed.

This paper briefly describes the historical developments that led to the proposed test method, gives a description of the test procedure followed in the round robin program, discusses the results from the round robin, and provides the rationale for the modifications to the test procedure suggested by the experience gained from this testing program.

Historical Background

The quantity that needs to be measured is K_{IA} , the value of stress intensity that exists at the tip of a fast-running crack at the instant that crack arrest occurs. The subscript "I" denotes that the arrest toughness is being evaluated under conditions in which the degree of plane stress is small enough to have negligible influence on the test results. Consequently, in this and subsequent sections of this paper, the "I" has been omitted, except where it is clear that the results being discussed pertain to predominantly plane strain conditions.

For steels at temperatures close to and below the drop-weight nil-ductility temperature (NDT), determined according to the ASTM Method for Conducting Drop-Weight Test to Determine Nil-Ductility Transition Temperature of Ferritic Steels (E 208-85), results have indicated that values of K_{Ic} obtained from tests conducted with rapid loading times, following Annex A-7 of the ASTM Test for Plane-Strain Fracture Toughness of Metallic Materials (E 399-83), provide close estimates of K_{IA} . The loading time, t , required to obtain useful estimates of K_{IA} by $K_{Ic}(t)$ varies from 5 ms at NDT to several minutes at temperatures far below NDT. At temperatures above NDT, techniques for obtaining K_{IA} in this fashion are difficult to implement and require additional study and development before they can be used with confidence.

For temperatures at and above NDT, a variety of experimental procedures that provide a run/arrest segment of rapid fracturing have been developed over the past two decades and used to obtain estimates of K_{IA} . Most of these methods have used a calculation procedure which assumes that K_{IA} does not differ significantly from the value of K at a short time (1 or 2 ms) after crack arrest. The resulting estimate of K_{IA} has generally been termed K_{Ia} , the K value calculated by a static analysis from measurements made shortly after crack arrest.

Early work by Ripling and Crosley [1,2] and Battelle Columbus Laboratories [3] used pin-loaded and wedge-loaded, rectangular and contoured, double-cantilever-beam (DCB) specimens. However, concern arose that dynamic effects would be enhanced by the highly compliant specimen arms of the DCB specimen and would tend to produce larger differences between K_{IA} and K_{Ia} . Development work in crack arrest toughness testing subsequent to 1975 therefore utilized transverse wedge-loaded specimens of the more nearly square "compact" type. The primary considerations of importance were felt to be the following:

- (a) the need for a K_{Ia} measurement method in which differences between K_{Ia} and K_{IA} were negligible and
- (b) the need for a dynamic calculation procedure that could be applied to run/arrest events in large experiments and actual structures.

Progress towards a better understanding of run/arrest cleavage fracturing was assisted, after 1974, by the coordination of research activities supported mainly by the U.S. Nuclear Regulatory Commission and the Electric Power Research Institute, and by the formation of an ASTM task group on K_{Ia} measurements within ASTM Committee E-24 on Fracture Testing.

Several developments of importance to crack arrest testing took place in the late 1970s. A large Cooperative Test Program using a test method employing compact specimens was conducted during 1977 to 1979 with 29 participating laboratories, of which a substantial number were outside the United States, chiefly in Europe and Japan [4]. At the same time, static analysis K_{Ia} values, obtained from a test method similar to that of the Cooperative Test Program, were used to assist in the planning of large-cylinder thermal shock fracture experiments at Oak Ridge National Laboratory (ORNL). Dynamic analyses of the ORNL thermal shock experiment (TSE) and pressurized thermal shock experiment (PTSE) cylinders were made which indicated that, for crack jumps of moderate size, the dynamic influences would be relatively small [5]. Static analysis computations of the K at crack arrest for the TSE and PTSE tests were therefore expected to provide close estimates of the dynamic K_{Ia} value. Comparisons of crack arrest K_{Ia} values from the large cylinder tests with those obtained using static analysis small-specimen tests showed good agreement [6,7,8], and both sets of results agreed with the Cooperative Test Program data also.

The information reviewed above indicated that values of K_{Ia} from relatively simple laboratory experiments could provide useful estimates of the actual K_{Ia} pertaining to run/arrest events in large structures. The experiences and methods of the Cooperative Test Program were therefore examined further by ASTM Task Group E24.01.06 over the period 1980 to 1983, and a draft document was produced which described a proposed test procedure for determining the crack arrest fracture toughness. This test procedure was followed in the round robin program being discussed here and may be found in Ref 9.

Description of the Test Procedure

Test Specimen Geometry and Loading Arrangement

The specimen geometry used in the round robin is shown in Fig. 1 and consists of a crack-line wedge-loaded compact-type specimen with side grooves to help maintain a planar crack path. (This geometry is sometimes referred to as a compact crack arrest (CCA) specimen.) Since it is desirable to minimize the introduction of additional energy into the specimen during the run/arrest event, the loading system must have a low compliance compared with the test specimen. The test is therefore conducted by forcing a wedge into a split-pin assembly with a taper matching that of the wedge, as shown in Fig. 2. This applies an opening force across the crack-starter notch in the specimen, causing a run/arrest segment of crack extension. This loading arrangement does not permit easy measurement of the opening loads applied to the specimen. Consequently, crack mouth opening displacements are used, in conjunction with measurements of crack size and compliance calibrations, to calculate stress intensity factors.

The specimen is laid flat on a base block which contains heating and cooling coils for maintaining the temperature of the specimen at the desired value. A layer of lubricant is recommended for use between the base block and the specimen. The authors also suggest that a lubricant be used between the wedge and split pins and the split pins and the specimen loading hole. The load on the wedge and the crack mouth opening displacement (measured with a clip gage mounted at one-quarter width from the load line) are recorded during the test.

Rapid Fracture Initiation

A major difficulty in using a test procedure such as that described above is control of rapid crack initiation. It is necessary to have the run/arrest segment propagate past the region surrounding the starter notch in which large plastic deformations may have occurred

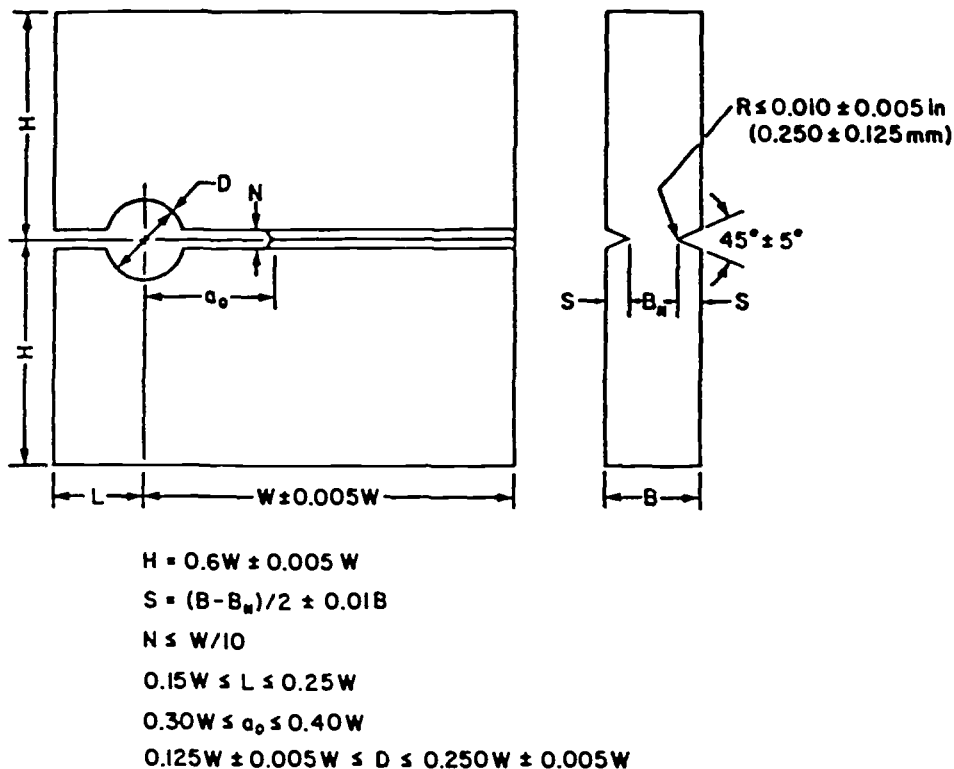


FIG. 1—The geometry and dimensions of the crack-line wedge-loaded compact specimen used for crack arrest testing (CCA specimen).

during loading. It is also necessary that crack arrest occur a sufficient distance away from the back edge of the specimen, so that the remaining net ligament provides adequate elastic enclosure of the arrested crack plastic zone. This requires a certain degree of control on the stress intensity level at initiation so that the crack propagates far enough into the specimen but does not propagate too far.

The preferred method for controlling initiation is to use a relatively blunt notch with a brittle weld bead deposited across the root of the notch to act as a crack starter. This or any other alternative method determined to be suitable can be used. The main requirement for a successful test is that a segment of rapid crack propagation of satisfactory length occur. Experience has shown that when testing low-strength and medium-strength steels, the notched brittle weld generally provides good results [9] at temperatures below the fracture appearance transition temperature (FATT) from V-notch Charpy tests.

Loading Procedure

The test procedure followed in the round robin differed in one important respect from that used previously and in the earlier Cooperative Test Program [4], in that a cyclic loading technique was introduced. In this technique, load is applied to the wedge until a rapid crack initiates, or until the crack mouth opening displacement (measured by the clip gage) reaches a predetermined value. If a rapid fracture has not initiated prior to the recommended maximum displacement being reached, the specimen is unloaded to zero load by completely

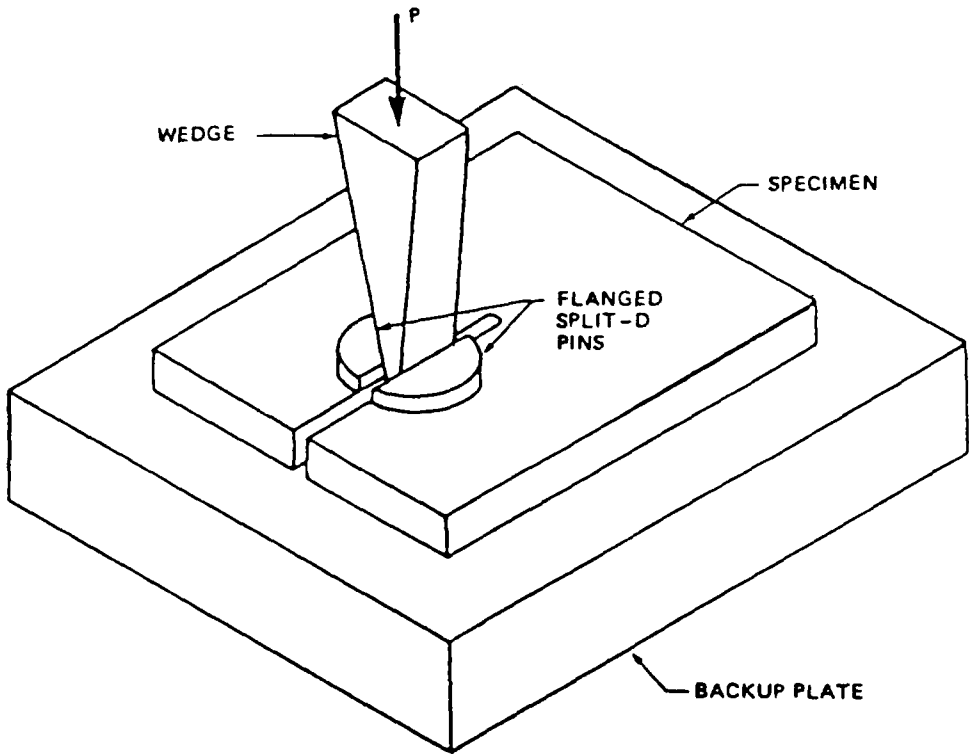


FIG. 2—Schematic of the arrangement of the specimen, base block, and wedge and split-pin assembly.

extracting the wedge. The specimen is then reloaded in the same manner as before, and load application is once again terminated, either by initiation of a rapid crack or when the opening displacement reaches a specified value. Successively higher values of the recommended maximum opening displacement are allowed on each loading cycle, until a rapid crack initiates or until the test is discontinued.

This test method infers the load applied to the specimen from measurements of the crack opening displacement and linear-elastic compliance calibrations. Components of the measured opening displacement which do not have their origin in the compliance-governed, elastic loading of the specimen can occur. These components, which can lead to overestimation of the load actually applied to the specimen, have their origin primarily in (a) the seating of the load train and clip gage, and local cracking in the brittle weld bead, and (b) the development of the plastic zone near the root of the starter notch. The purpose of the cyclic loading technique is to identify and estimate the magnitude of these contributions by applying load to the specimen in an incremental manner and keeping track of the displacement offset, if any, that results at the end of a given loading cycle when the specimen is completely unloaded.

Determination of the Arrest Toughness, K_a

As discussed above, a segment of unstable crack extension must occur for K_a to be measured. The occurrence of unstable crack extension will normally be apparent to the operator, both audibly and as an abrupt load drop on the test record. (A load drop of the

order of 50 to 60% in the brittle weld CCA specimen has been found to indicate that a sufficient length of unstable fracturing has occurred.) After the desired run/arrest event has occurred, load is removed from the wedge and the position of the arrested crack front is marked, usually by heat tinting. After marking of the crack front, the specimen is broken completely in two and the arrested crack length, a_a , is determined. The average of three measurements defines a_a . These are made on the heat-tinted fracture surface at the center (midthickness) of the specimen, and midway between the center and the bottom of the side groove on each side.

The stress-intensity factor associated with the arrest of a fast-running crack in the specimen material is then calculated from measurements of the arrested crack length and the crack opening displacement a few milliseconds after crack arrest. This estimate of K_A , the stress intensity at arrest, is termed K_a and is obtained by combining the measurements of the arrested crack length and the crack mouth opening displacements with a static compliance calibration for the specimen geometry being used.

The arrest toughness, K_a , is calculated from

$$K_a = \frac{E d_a f(x) \sqrt{\frac{B}{B_N}}}{\sqrt{W}} \quad (1)$$

where

$$f(x) = \frac{2.24(1.72 - 0.9x + x^2) \sqrt{1 - x}}{(9.85 - 0.17x + 11x^2)} \quad (2)$$

E is the Young's modulus of the specimen material; d_a is an adjusted crack opening displacement corresponding to crack arrest; x is the normalized arrested crack length, a_a/W ;

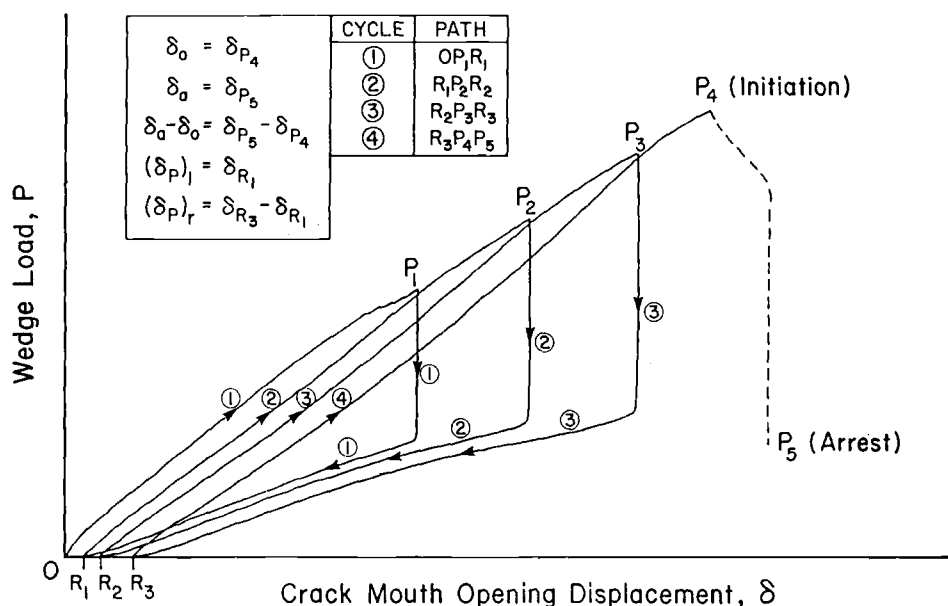


FIG. 3—Wedge load versus crack mouth opening displacement record for a specimen tested using cyclic loading for which a brittle fracture initiated on the fourth loading cycle.

B is the specimen thickness; B_N is the net specimen thickness at the crack plane; and W is the specimen width.

The expression for $f(x)$ used here was obtained by an experimental compliance calibration procedure followed by a curve-fitting process, the details of which can be found in Ref 10. A nominal stress intensity for the initial loading at the starter notch, K_0 , can also be calculated from Eq 1, with d_a replaced by d_0 and $x = a_0/W$, where d_0 is an adjusted crack opening displacement corresponding to the initiation of a rapid fracture and a_0 is the length of the starter notch.

For the specimens tested in the round robin, the quantities d_a and d_0 were taken to be the displacements corresponding to crack arrest and crack initiation, respectively, using the last loading cycle only. Figure 3 shows a typical load-displacement record for a specimen tested using cyclic loading that displayed rapid fracturing on the fourth loading cycle. For this example, the displacements d_a and d_0 used in Eq 1 would correspond to the displacement quantities $(\delta_{P_5} - \delta_{R_3})$ and $(\delta_{P_4} - \delta_{R_3})$, respectively. (It should be noted that the test record shown in Fig. 3 was obtained using a procedure developed in response to comments from the round robin participants and differs from a round robin test record in some of its details, as discussed below.)

Validity Requirements

The testing procedure used in the round robin relies on a linear elastic static analysis to infer K_a from a compliance calibration and measurements of the crack mouth opening displacement at a short time after arrest of a fast-running crack. Certain restrictions must therefore be placed on the arrested crack length.

Two restrictions that are a direct consequence of the linear elastic assumption are (1) that the rapid crack propagate at least one plane-stress plastic zone radius past the starter notch and (2) that the net ligament remaining after arrest be large enough to provide adequate enclosure of the plastic zone at arrest by an essentially elastic stress field. These restrictions translate into the requirements that $(a_a - a_0) \geq (K_0/\sigma_{YS})^2/2\pi$ and $(W - a_a) \geq 1.25(K_a/\sigma_{Yd})^2$. In addition, if the test result is to be considered representative of the plane-strain crack-arrest fracture toughness, and termed K_{Ia} , certain minimum thickness requirement must also be satisfied. The present requirement is that the thickness, B , must equal or exceed $1.0(K_a/\sigma_{Yd})^2$.

Use is made in this expression of σ_{Yd} , a formal dynamic yield strength estimate for appropriate loading times at the test temperature. For structural steels, it is assumed in this test method that σ_{Yd} is 205 MPa (30 ksi) greater than the yield strength, σ_{YS} , as measured by the ASTM Methods of Tension Testing of Metallic Materials (E 8-85). However, the strain rates associated with yielding near the tip of a fast-running crack and the abrupt nature of crack arrest give rise to loading rates that may approach 10^{-8} s (1×10^{-6} m \div 100 m/s). This suggests that the true elevation of σ_{Yd} over σ_{YS} should be much greater, and the value used here is therefore thought to underestimate the actual effective resistance to plastic flow at crack arrest substantially [11]. This explains, in part, the choice of the premultipliers 1.25 and 1.0 in place of the value of 2.5 that is usually associated with ASTM Test E 399-83. Experimental justification for these choices can also be found in Ref 12.

Results from the Round Robin Program

Program Participation and Materials Tested

A total of 27 laboratories had indicated that they would participate in the round robin program and four sets of three specimens each were to be tested by each participant. These consisted of three specimens of A588 bridge steel, three specimens of A514 bridge steel, and six specimens of A533 Grade B, Class 1 reactor steel (hereinafter denoted A533B).

The bridge steels were both tested at -30°C . The reactor steel was tested at 10°C and 25°C , three specimens being tested at each temperature. The bridge steels were tested in an L-T orientation and the reactor steel in an L-S orientation. The test temperatures specified were selected so as to give a good probability of getting a successful test while simultaneously providing information on the upper bounds of the test temperatures and K_a values, for which the method would give good results.

Twenty-one laboratories completed their testing and forwarded test results by 1 Nov. 1985, which was established as a final cutoff date for receipt of test results. The resulting data base consists of test results from 54 specimens of each of the A514 and A588 steels, 70 specimens of A533B steel tested at 10°C , and 65 specimens of A533B steel tested at 25°C .

Twenty participants used the brittle-weld technique to produce the starter notch and one participant used machined notches. Of those using brittle welds, one large group used a Hardex-N welding electrode while another group used Foxdur-500. Both electrodes gave similar results insofar as successful rapid fracture initiation was concerned [9].

Test Results

For the steels tested in the round robin, the validity requirements associated with the use of a linear elastic static analysis roughly result in the restriction that $0.60 \leq a_i/W \leq 0.85$. All results presented in this and subsequent parts of this paper satisfy this requirement.

Two of the data sets, for the A514 bridge steel and the A533B reactor steel tested at 25°C , showed substantially larger scatter than the data for the A588 bridge steel and the A533B specimens tested at 10°C . Closer examination of the test results showed that some of the specimens in these two data sets displayed nonideal fracture surface features to a significant degree. These included tunneling, large unbroken ligaments, and cracks that had failed to follow the plane of the side grooves.

The test report forms forwarded by the participants were then examined to identify, without prejudice, those specimens for which the fracture surface features would indicate that the test result would give a nontypical value for K_a . The data for the A588 and A533B tests at 10°C were not affected by this exercise. However, the number of acceptable tests for the A514 steel and the A533B steel at 25°C was reduced somewhat.

Figures 4 through 7 show the final results obtained for K_a as a function of the K_0 at initiation for the four sets of steels tested in the round robin program. The same results for K_a are repeated in Figs. 8 through 11, but are now shown as functions of the arrested crack length, a_a/W . A scatter band corresponding to the mean K_a value plus or minus one standard deviation has been marked on all figures for easy reference.

It is readily apparent from these results, that there is no dependence of K_a on the K_0 at initiation. There is, however, a tendency towards calculating a lower K_a value for longer arrested crack lengths for a given steel. Both of these observations are similar to those made for the data acquired in the Cooperative Testing Program [4] using the Materials Research Laboratory (MRL)-type specimen, which was similar to the CCA specimen used in this test method. Table 1 summarizes the data for K_a for the four sets of steels tested in the round robin program.

Discussion of Results from the Round Robin Program

A brief discussion of the results from the round robin test program has been provided here. A more comprehensive and detailed discussion is given in Ref 9, and the interested reader is referred to that document for more detailed information.

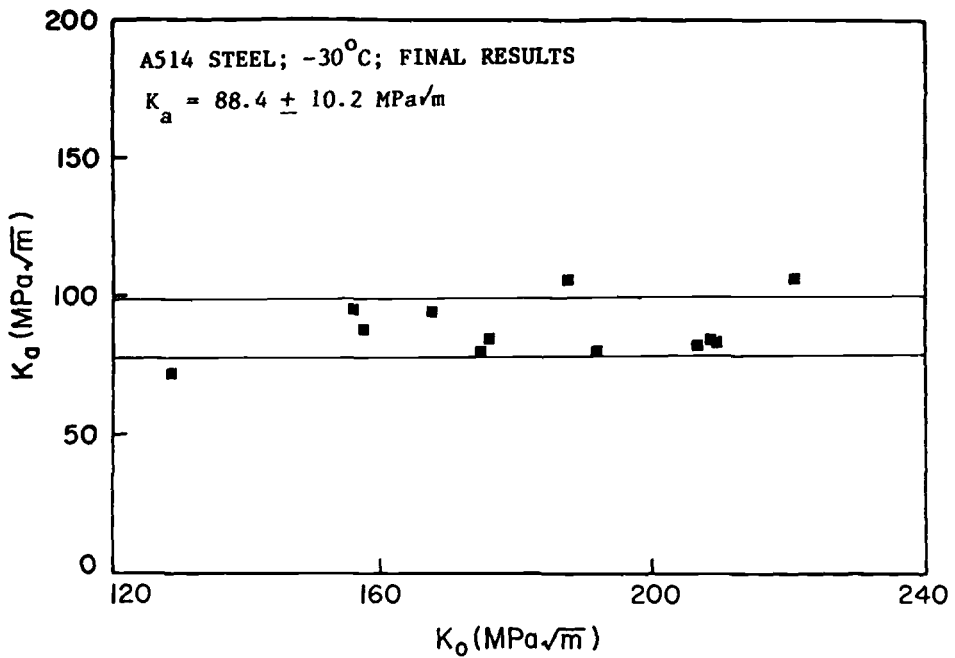


FIG. 4—Final results from the round robin program for A514 steel tested at -30°C showing K_a as a function of the K_o at initiation.

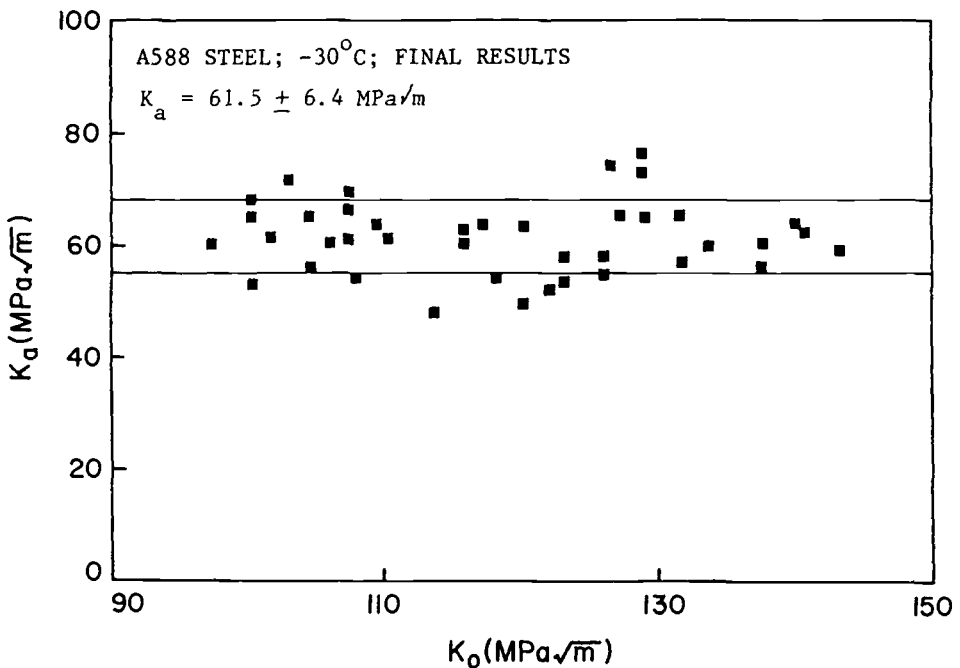


FIG. 5—Final results from the round robin program for A588 steel tested at -30°C showing K_a as a function of the K_o at initiation.

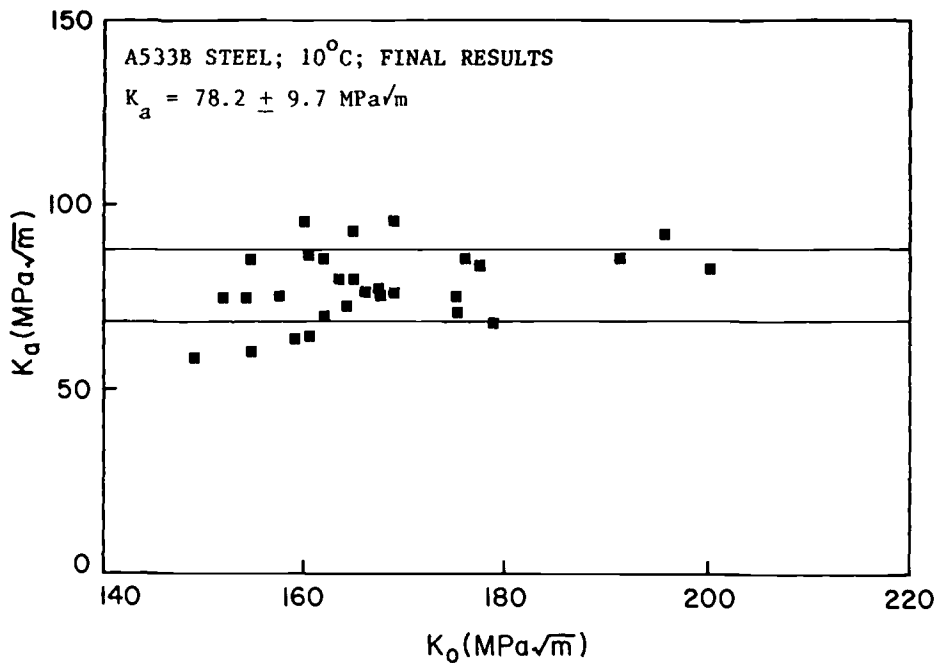


FIG. 6—Final results from the round robin program for A533B steel tested at 10°C showing K_a as a function of the K_o at initiation.

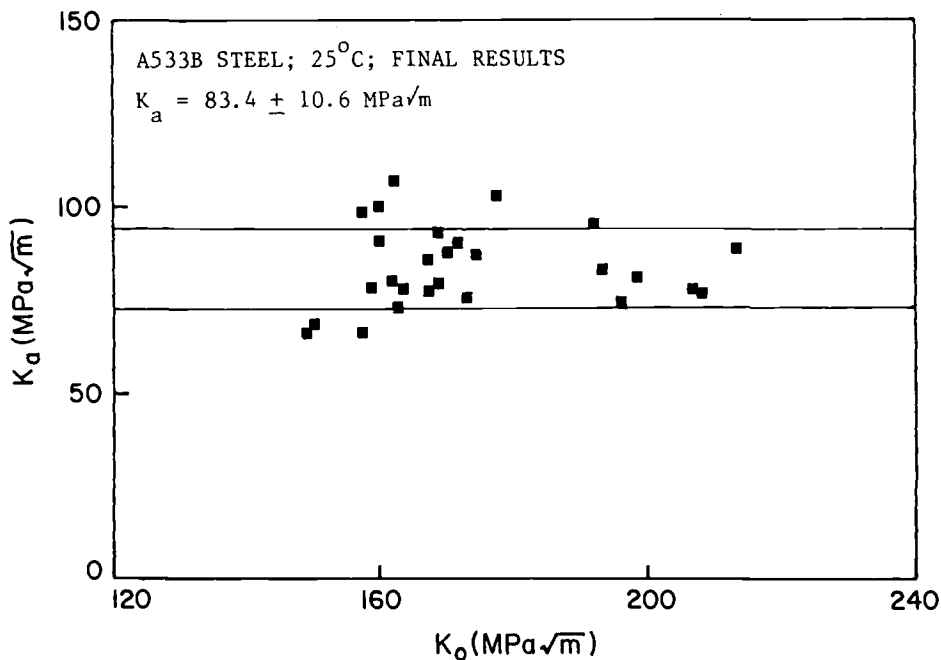


FIG. 7—Final results from the round robin program for A533B steel tested at 25°C showing K_a as a function of the K_o at initiation.

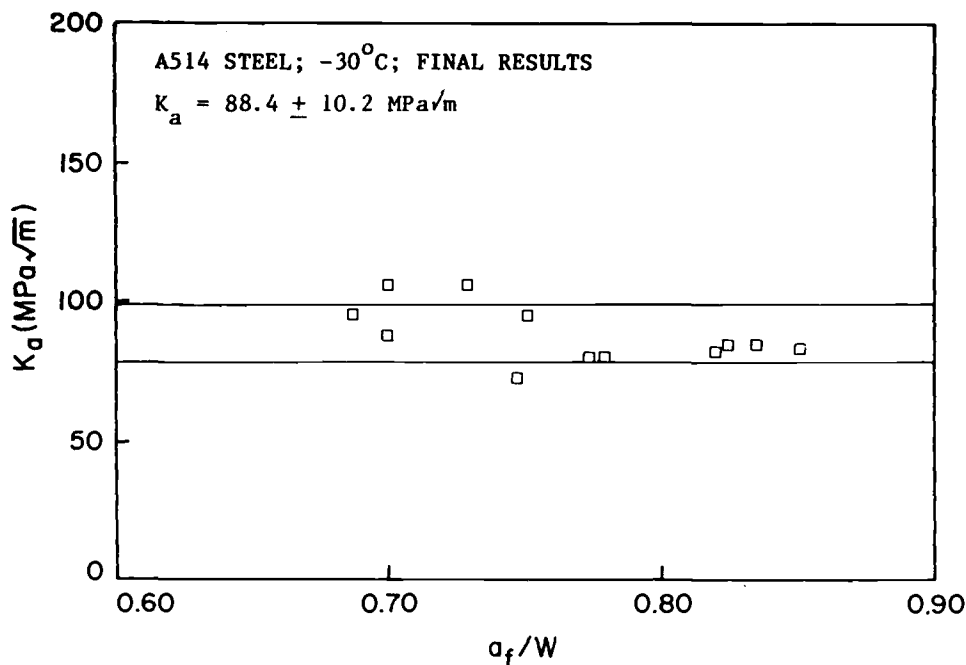


FIG. 8—Final results from the round robin program for A514 steel tested at -30°C showing K_a as a function of arrested crack length.

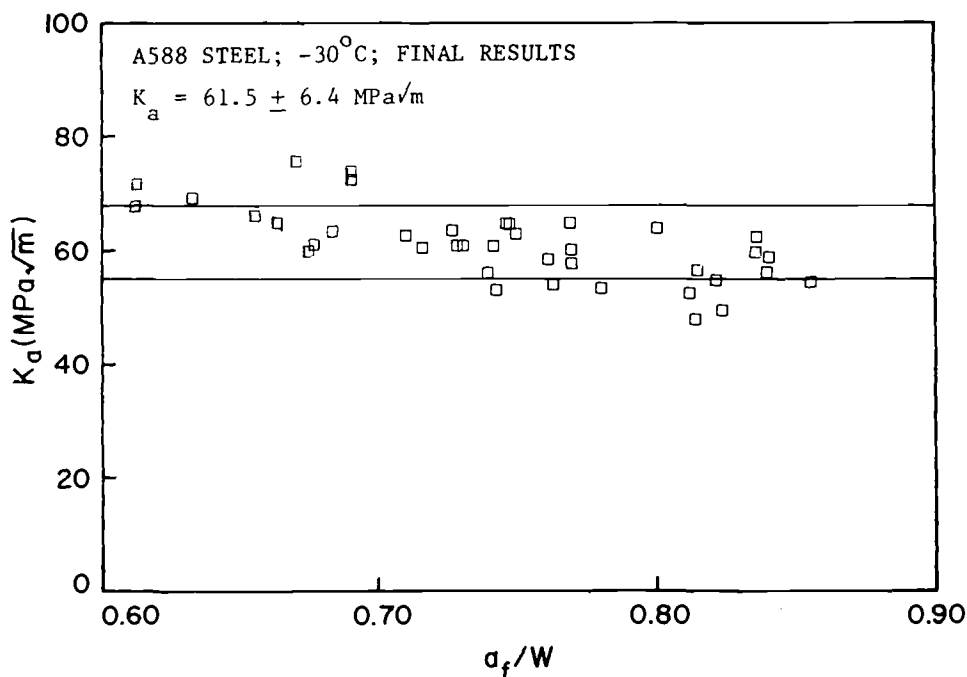


FIG. 9—Final results from the round robin program for A588 steel tested at -30°C showing K_a as a function of arrested crack length.

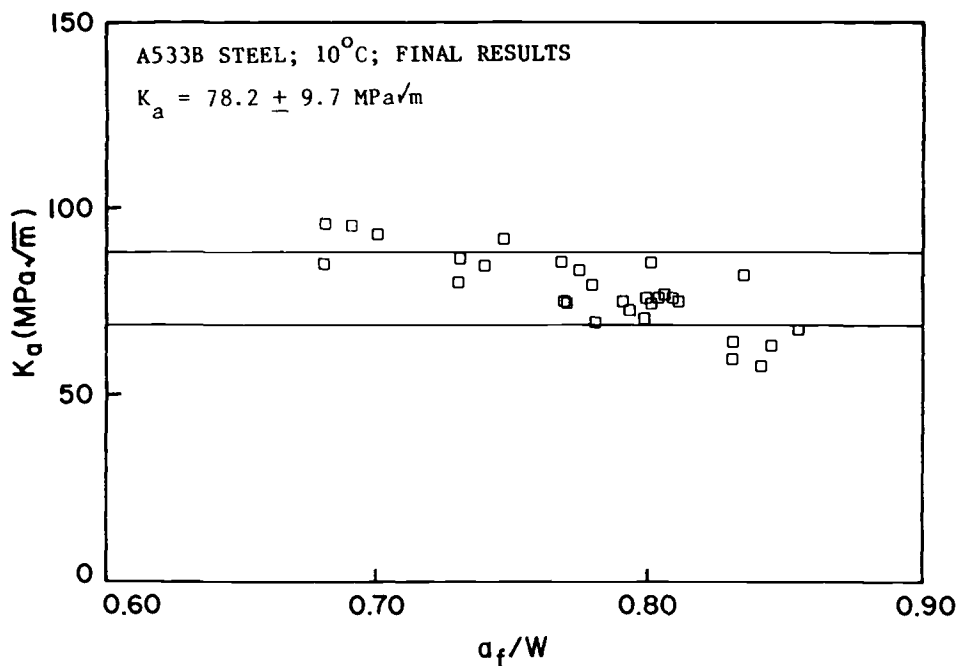


FIG. 10—Final results from the round robin program for A533B steel tested at 10°C showing K_a as a function of arrested crack length.

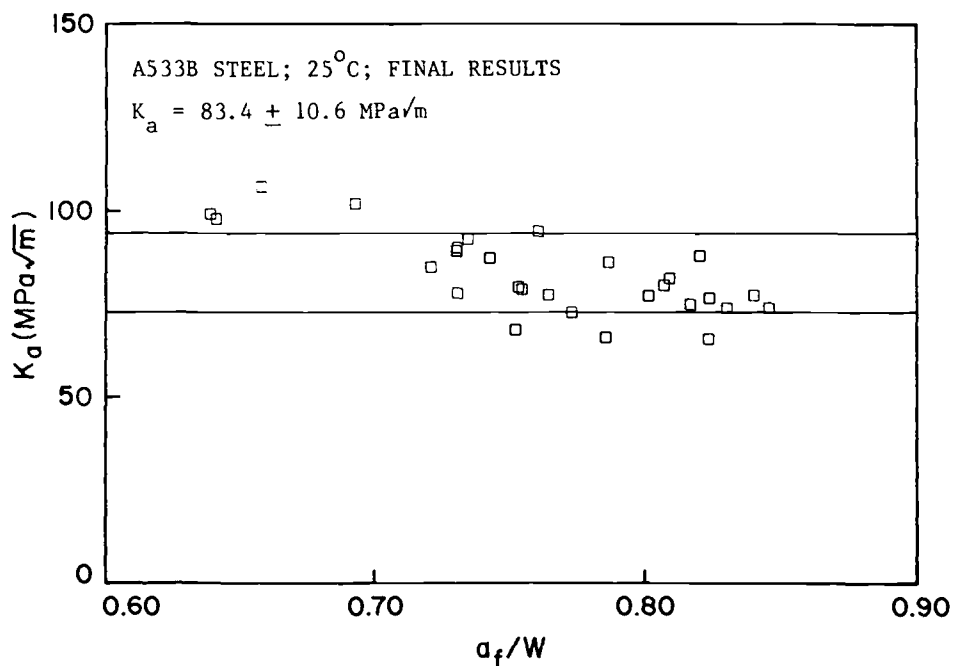


FIG. 11—Final results from the round robin program for A533B steel tested at 25°C showing K_a as a function of arrested crack length.

TABLE 1—Results for K_{IC} for each of the four sets of steels tested in the round robin.^a

	Material and Temperature			
	A514, -30°C ^b	A588, -30°C ^c	A533B, 10°C ^d	A533B, 25°C ^c
INITIAL RESULTS				
Total tests, No.	54	54	70	65
Failures to initiate, No.	4	0	10	9
Failures to arrest, No.	21	0	13	4
Valid tests, No.	18	40	30	38
Mean K_{IC} , MPa \sqrt{m}	102.0	61.5	78.2	91.2
Standard deviation				
MPa \sqrt{m}	21.0	6.4	9.7	16.6
%	(20%)	(10%)	(12%)	(18%)
FINAL RESULTS AFTER EXAMINATION OF FRACTURE SURFACES				
Valid tests, No.	12	40	30	28
Mean K_{IC} , MPa \sqrt{m}	88.4	61.5	78.2	83.4
Standard deviation				
MPa \sqrt{m}	10.2	6.4	9.7	10.6
%	(12%)	(10%)	(12%)	(13%)

^a A total of 21 laboratories reported test results from the program.

^b Specimens were cut from 2-in.-thick rolled plate and tested at full thickness in an L-T orientation; $\sigma_{YS} = 890$ MPa; $RT_{NDT} = -12^\circ\text{C}$; $NDT = -50^\circ\text{C}$.

^c Specimens were cut from 2-in.-thick rolled plate and tested at full thickness in an L-T orientation; $\sigma_{YS} = 330$ MPa; $RT_{NDT} = -9^\circ\text{C}$; $NDT = -10^\circ\text{C}$.

^d Specimens of 2-in. thickness were cut from 10-in.-thick rolled plate and tested in an L-S orientation; $\sigma_{YS} = 480$ MPa; $RT_{NDT} = -2^\circ\text{C}$; $NDT = -12^\circ\text{C}$.

Problems Encountered in Conducting a Successful Test

Most structural steels display some degree of inhomogeneity and the results from the round robin were examined to see if the location of a particular specimen relative to the parent plate would influence the probability of obtaining a successful test insofar as initiating and arresting a rapid fracture was concerned. No such influence was detected.

Another possible origin of the testing problems encountered was felt to be the biasing of the results that could occur due to systematic differences in test method implementation at different testing facilities. An examination of the data did reveal that certain systematic problems existed, primarily with regard to specimen preparation procedures. The revised test procedure will therefore contain enhanced guidelines on specimen preparation, particularly with regard to starter notch preparation.

Influence of Specimen Location on the Measured K_{IC} Value

An examination of the test results with regard to dependence of the measured K_{IC} value on specimen location relative to the parent plate was also performed. No clear indications were apparent of the likelihood of getting either a high or a low K_{IC} value based on the location of the specimen in the parent plate.

Comparison of Results from the Round Robin Test Program with the Cooperative Test Program

The Cooperative Test Program employed two different specimen designs and tested AISI 1018 and A533B steels. The specimen design used in the round robin was the same as that

of the MRL specimen in the Cooperative Test Program. However, the crack plane orientation and testing temperatures for the reactor steel specimens in the Cooperative Test Program were different from those of the round robin. Detailed quantitative comparisons between the round robin and the Cooperative Test Program results were therefore confined to the Cooperative Test Program MRL specimens of A533B tested at 0°C [temperature, T , less the reference nil-ductility transition temperature (RT_{NDT}) equals 20°C ($T - RT_{NDT} = 20^\circ\text{C}$)] and the round robin results for A533B tested at 10°C ($T - RT_{NDT} = 12^\circ\text{C}$). Qualitative comparisons of trends in K_a with K_o and a_i/W and of the degree of scatter in the results were, however, still possible.

One other important difference between the two programs was the manner in which K_a was calculated. In the Cooperative Test Program, the specimens were loaded to fracture in a single loading cycle, and K_o and K_a were calculated using the total opening displacements measured prior to initiation and shortly after arrest. In the round robin test procedure, the loading procedure generally required cyclic loading and the calculation of K_o and K_a was performed using the opening displacements at initiation and after arrest pertaining only to the cycle on which a brittle fracture initiated. It was therefore necessary to recalculate the round robin results for the A533B specimens tested at 10°C using the total crack opening displacement. The resulting K values for the tests conducted in the round robin are referred to in this section as K_o^* and K_a^* .

Figure 12 shows K_a from the Cooperative Test Program for the MRL specimens tested at 0°C, plotted as a function of K_o . The degree of scatter is indicated by the two horizontal lines corresponding to the mean K_a of 88.5 MPa $\sqrt{\text{m}}$ plus or minus a standard deviation of 9.9 MPa $\sqrt{\text{m}}$, or 11.2% of the mean value. A similar plot of K_a^* as a function of K_o^* for all of the round robin specimens of A533B steel tested at 10°C is shown in Fig. 13. In this instance the average K_a^* is 85.6 MPa $\sqrt{\text{m}}$, with a standard deviation of 10.6 MPa $\sqrt{\text{m}}$, or 12.4% of the mean value. A comparison of the two sets of data was also performed for the data as functions of the arrested crack length, a_i/W . The results are shown in Figs. 14 and 15, and once again show good agreement and similar trends.

It is clear from this comparison that, when the results from the two programs are placed on a common basis, they show good agreement not only in terms of the lack of dependence of K_a on K_o , but also in terms of the numerical values of K_a . The degree of scatter in the K_a values is also similar. The general conclusion of a K_a essentially independent of K_o also holds for the other steels tested in the round robin. The degree of scatter in the results was, of course, a function of the steel being tested, as evidenced by Table 1. A similar observation was made for the Cooperative Test Program results, for which the standard deviation of K_a ranged from 11 to 15%, depending on the particular steel and test temperature being considered. The tendency towards lower values of K_a and K_a^* for longer arrested crack lengths can also be seen for both sets of data. The reasons for this tendency are discussed in some detail in the following section.

Observed Trends of K_a with a_i/W

As discussed previously, and as evidenced in Figs. 4 through 7, the K_a values measured in the round robin were found to be essentially independent of the K level at initiation, K_o . However, Figs. 8 through 11 showed that there was a decreasing trend in K_a with an increase in the arrested crack length, a_i/W . The reasons for the decreasing trend in K_a with a_i/W merit further discussion.

The K_a value that is determined from any test performed using this test procedure is a function of both the opening displacement, δ , and the crack length at arrest, a_i/W . Consider now a situation in which a series of tests is performed using specimens of the same material,

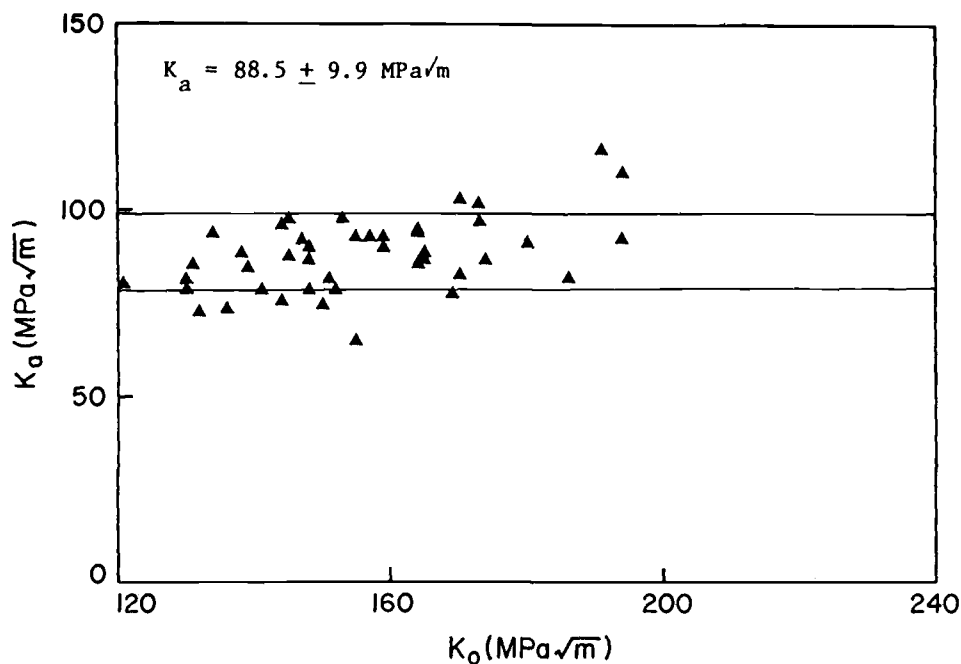


FIG. 12—Results from the Cooperative Test Program for A533B steel tested at 0°C showing K_a as a function of the K_0 at initiation.

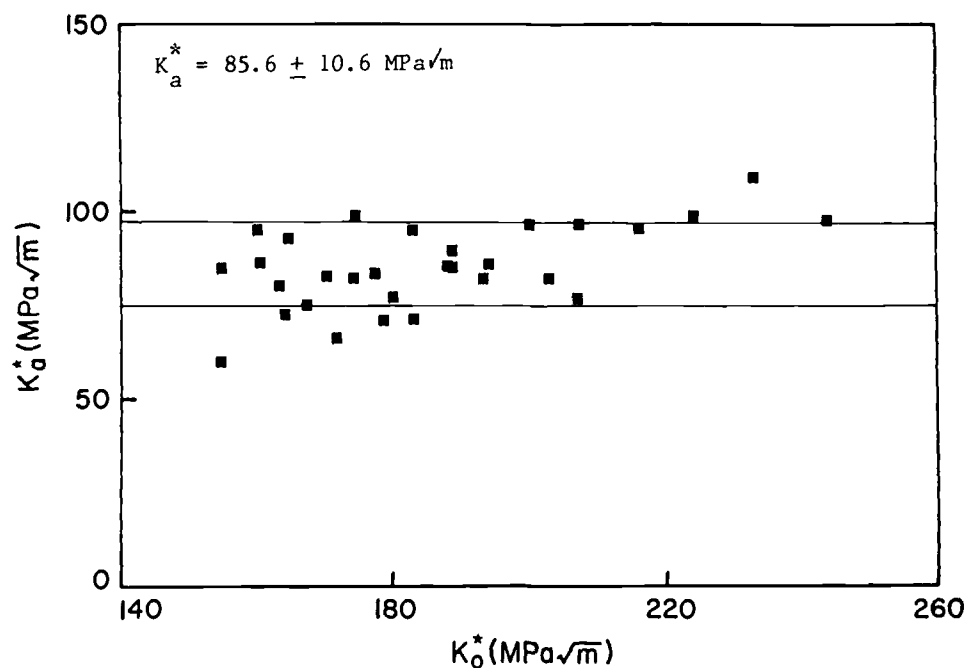


FIG. 13—Results from the round robin program for A533B steel tested at 10°C showing K_a^* as a function of the K_0^* at initiation.

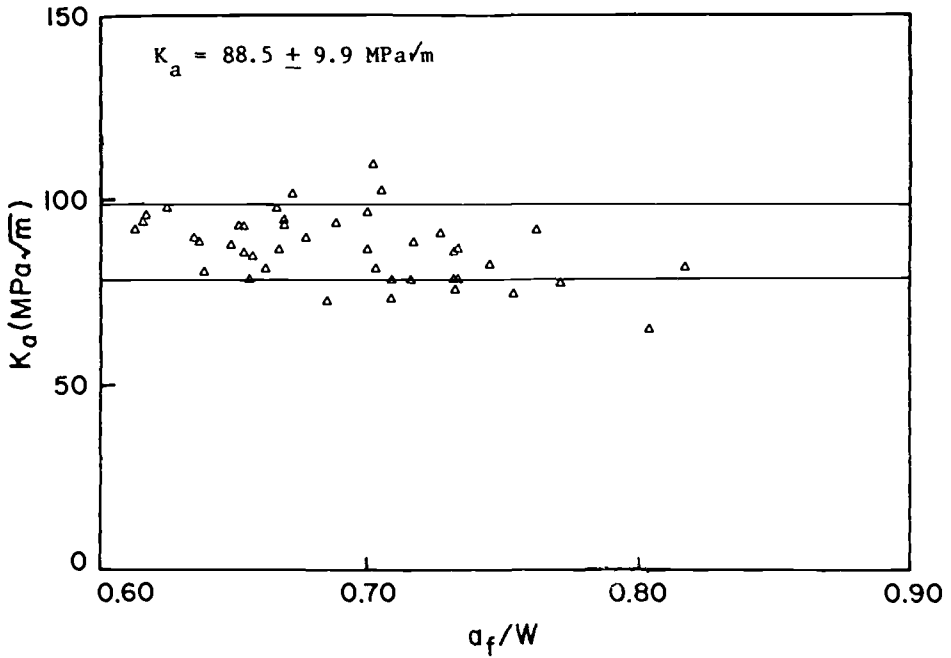


FIG. 14—Results from the Cooperative Test Program for A533B steel tested at 0°C showing K_a as a function of arrested crack length.

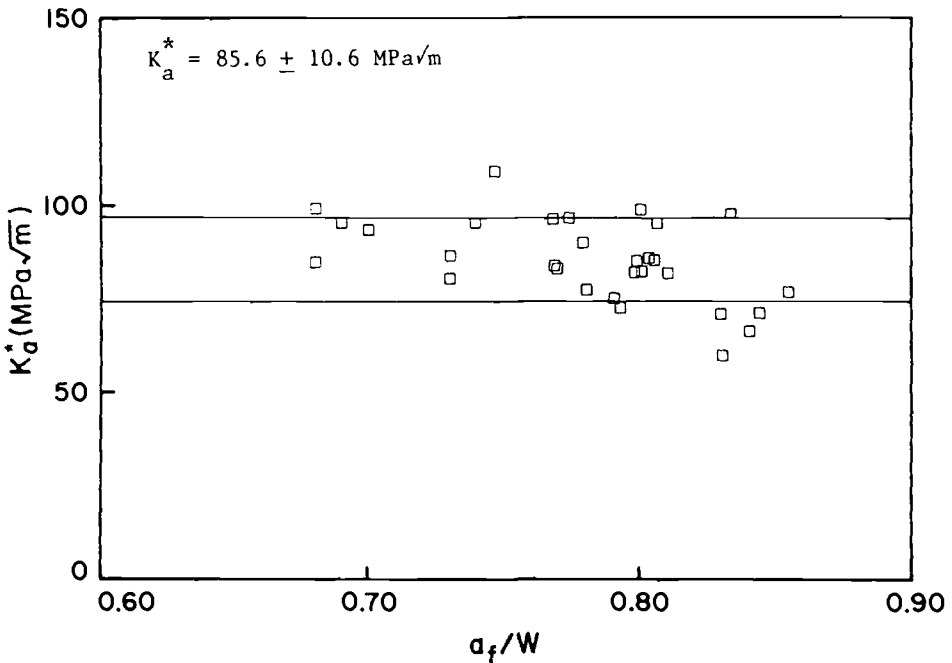


FIG. 15—Results from the round robin program for A533B steel tested at 10°C showing K_a^* as a function of arrested crack length.

with the assumption that the crack opening at initiation, δ_0 , does not change during the run/arrest event, that is, $\delta_0 = \delta_a$. If the material being tested is a perfect one, with no variability in K_a , and a rapid fracture occurs in all the specimens at the same crack opening displacement, then the test results will correspond to a single data point, which lies on the intersection of the line $K_a = \text{constant}$ and the function $K(a_f/W)$ corresponding to $\delta = \delta_0 = \delta_a = \text{constant}$ for all the tests. This is illustrated in Fig. 16a.

If one now takes a first step away from this idealization, and allows the material to have some variability in K_a , the results from a series of tests all performed with the same δ value would lie along the function $K(a_f/W)$, as illustrated in Fig. 16b. Lower values of K_a would correspond to longer arrested crack lengths and vice versa. An alternative way of approaching reality would be to consider the series of tests as having initiation take place at values of opening displacement bounded by the limits, δ_{\min} and δ_{\max} , but with no variability in the material property (K_a) being measured. (Variations in δ could occur as a result of the specimen preparation procedures followed and also because of variations in K_c .) The data points that would be obtained under this scenario would then lie along the line $K_a = \text{constant}$, bounded by the two curves for $K(a_f/W)$ corresponding to $\delta = \delta_{\min}$ and $\delta = \delta_{\max}$. In this case, a lower δ would give a shorter arrested crack length for the same K_a . This is illustrated in Fig. 16c.

The actual testing situation that is encountered displays a range of opening displacements, δ_{\min} to δ_{\max} , as well as a range of K_a values spanning $(K_a)_{\min}$ to $(K_a)_{\max}$. The resulting bounds on the region within which all the test results *must* fall are then defined by the lines $K_a = (K_a)_{\min}$ and $K_a = (K_a)_{\max}$ and the curves for $K(a_f/W)$ corresponding to δ_{\min} and δ_{\max} ,

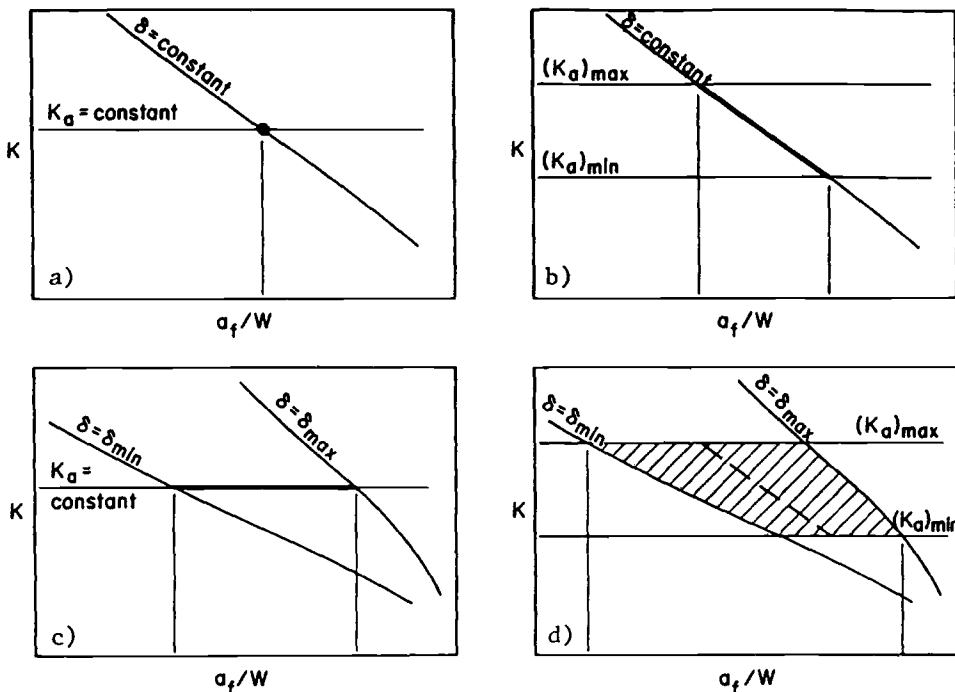


FIG. 16—Schematic illustration of the results for K_a as a function of arrested crack length that follow from the use of a static compliance calibration under ideal and real conditions.

as illustrated in Fig. 16d. It is also clear that the test results would not be uniformly distributed over the shaded region shown but would have a tendency to cluster around a curve corresponding to the mean value of δ .

Obviously, Fig. 16d most closely represents the behavior of a real material for which a large number of crack arrest tests have been performed, such as in a round robin testing situation. Consequently, whether or not one would clearly see a downward trend in K_a with a_a/W would depend on the degree of variability in K_a and on the degree of variability that was encountered in δ . This is shown in Figs. 17a through 17d, which schematically illustrate the perceptions corresponding to small and large variations in K_a coupled with small and large variations in δ .

Figures 18 and 19 repeat the results presented earlier in Figs. 9 and 10 for the A588 and A533B specimens at 10°C, respectively. The discussion detailed above has been illustrated in these figures by the addition of the curves corresponding to the mean δ_a plus or minus one standard deviation. The conclusion that can be drawn is that a downward trend in K_a with a_a/W will always be present when K_a is calculated from a static analysis based on compliance calibrations. The degree of such a trend and the perception of it is, however, a function of the variability in the material property being measured and of the range of crack opening displacements for a series of tests.

Dynamic Effects in Crack Arrest Testing

While the information reviewed above and in preceding sections of this paper indicates that values of K_a from relatively simple laboratory experiments can provide useful estimates

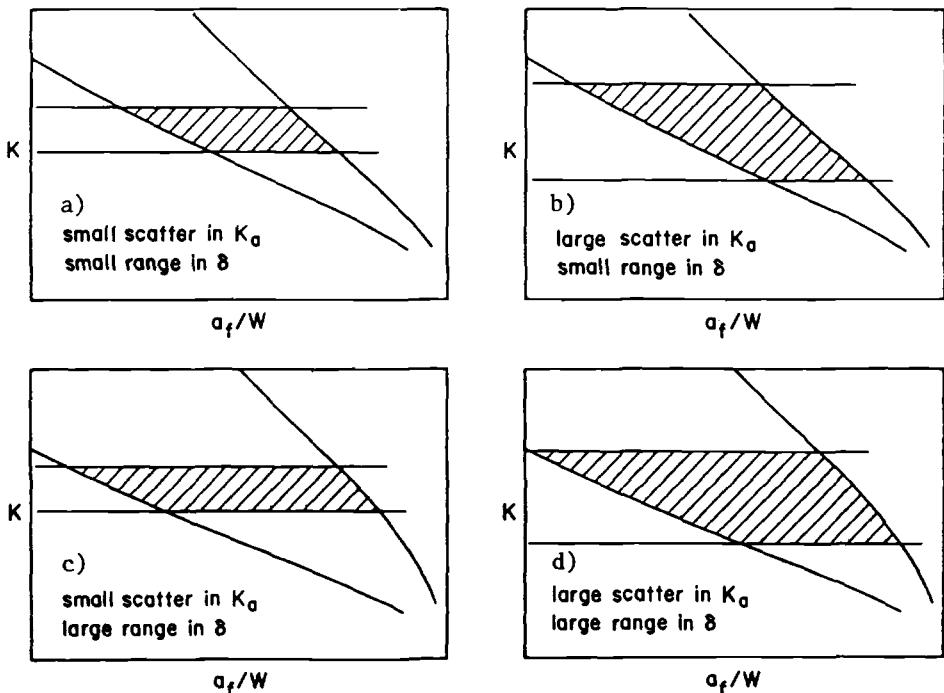


FIG. 17—Schematic illustration of the perceived trends in K_a as a function of arrested crack length that result when using a static compliance calibration for materials that have small or large scatter in K_a and small or large scatter in δ .

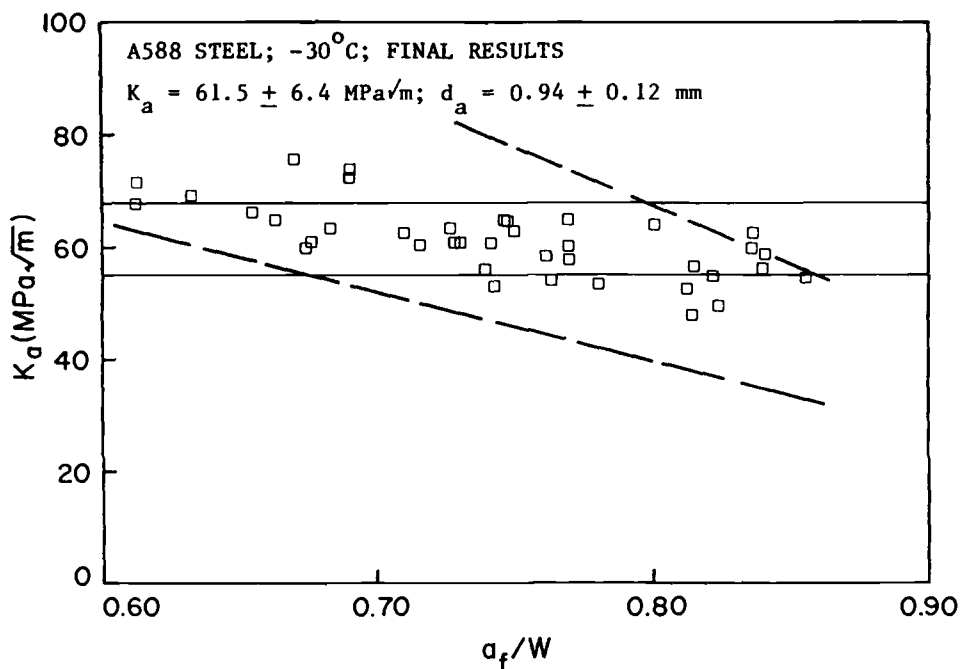


FIG. 18—Illustration of the concepts shown in Fig. 17 for the round robin results for A588 steel tested at -30°C .

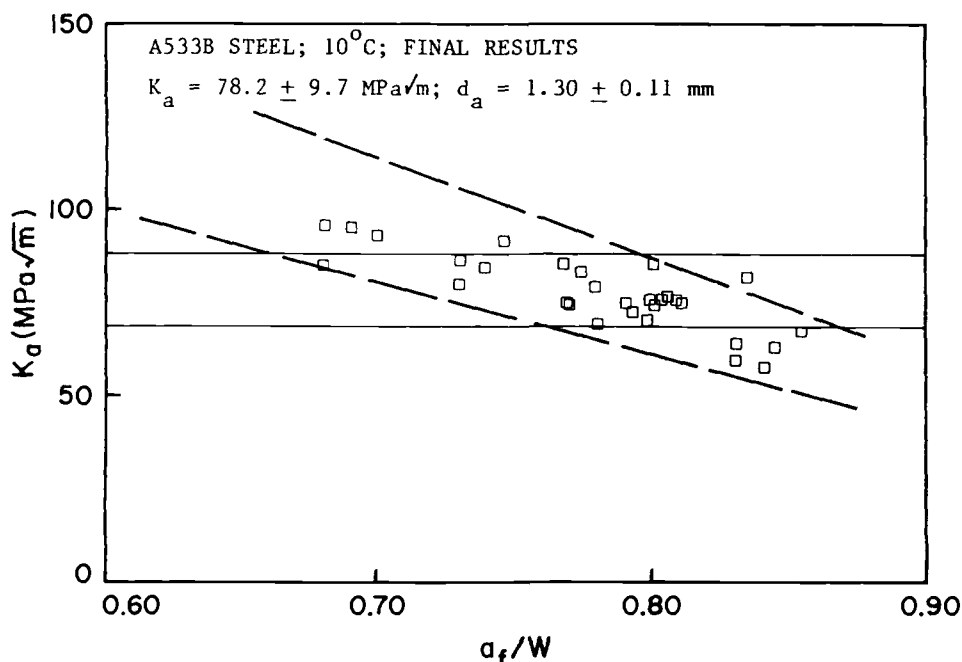


FIG. 19—Illustration of the concepts shown in Fig. 17 for the round robin results for A533B steel tested at 10°C .

of the actual K_A pertaining to run/arrest events, it is useful to bear in mind that dynamic effects can affect the results. The available evidence suggests that the degree of success that can be achieved in measuring K_A from small specimen tests depends considerably upon the specimen geometry and size and upon the manner of load application.

The crack-line wedge-loaded (CLWL) compact specimen with displacement-controlled wedge loading was purposely selected for its inherently low-compliance loading train so that a minimal amount of energy would be added to the specimen during a run/arrest event. As a first approximation, it can therefore be assumed that, during the run/arrest event, the specimen is subjected to a "fixed-grip," constant crack opening condition at the load line.

In reality, additional energy or driving force will become available from a partial release of the elastic Hertzian contact indentations that occur between the specimen and the split pin and between the split pin and the wedge. Secondly, rotation of the specimen arms about the loading pin can occur as the crack propagates into the specimen. This can, in turn, cause a breaking free from a previously frozen contact position and result in a new equilibrium position being established. These phenomena would result in a quick opening displacement that would appear as an increase in the crack opening displacement measured after arrest over that recorded at the onset of unstable crack growth. The modeling of these behaviors is complicated by nonperfect lubrication between the split pin and the wedge and between the split pin and the specimen. This quick-opening displacement of the specimen is obviously a dynamic effect that could potentially assist in driving the propagating crack further into the specimen, provided that it occurs in a timely fashion. Thus, there is a distinct possibility of the running crack being influenced by the dynamic behavior of the finite-size specimen being used. However, the relative time duration of the run/arrest event and the development of the quick opening are such that much of the effect would be felt after crack arrest had occurred for crack jumps of moderate size [9].

The size of the specimen being used is also of importance in determining the degree to which the running crack is subject to dynamic influences. When a rapid fracture first initiates, the moving crack tip does not know that it is propagating in a finite rather than an infinite medium. Only after a stress wave released at the starter notch has traversed the distance to the specimen boundary and returned to the crack tip does the crack sense the finite size of the body in which it is propagating. Consequently, the elapsed time of the run/arrest event can be considered to be composed of an infinite body phase and a finite body phase. The relative duration of the latter phase, in which the moving crack tip is subject to dynamic effects, is clearly a function of the size of the specimen being used. Evidence that the CLWL compact specimen is not dramatically influenced by dynamic effects is available from experiments that have been conducted using multiple-flash photographs of the caustic pattern at the tip of a running crack [13].

Given the presently available information, it is a plausible conclusion that the value of K at crack arrest can be estimated using small specimen tests, without the need for dynamic analysis computations. However, a major area of further research with regard to dynamic effects in crack arrest testing clearly remains. If the test results are to be evaluated using a relatively simple static analysis, care must be exercised with regard to the choice of the specimen geometry, specimen size, and manner of load application. In addition, the preceding discussion suggests that it would be desirable to place some restrictions on the crack jump length to exclude tests results for which dynamic effects could become significant. This restriction has been achieved in the proposed test method by placing an upper bound of $a_0/W \leq 0.85$ for a valid test result.

General progress with dynamic fracture research will be assisted if it is recognized that the development of evaluation methods for crack arrest toughness and the study of fast fracturing with the aid of dynamic analysis computations are mutually supportive topics with

somewhat different goals. For crack arrest toughness evaluations, emphasis on simplicity and minimum cost is obviously desirable. A simple small-specimen laboratory test cannot provide adequate boundary condition information for input to extensive dynamic computations without greatly increasing the complexity of the test and the associated instrumentation. However, the use of dynamic computations in developing and validating a test method is both necessary and desirable.

Influence of Alternative Loading Configurations

Several of the participants had agreed to test an additional set of six specimens of the A533B steel. These specimens were to be tested with a loading configuration in which the split pin would not have any flanges that could bear down on the specimen. Consequently, there would be no clamping forces exerted in the vicinity of the loading hole during the run/arrest event. This method of loading was of interest because experience has shown that it permits valid test results to be obtained at higher test temperatures than can be achieved with the configuration shown in Fig. 2 [14]. The K_a values obtained with this type of “inverted-pin” or “no-flange” loading system were distributed throughout the data set, with no apparent tendency to cluster at either the high or the low end of the range of K_a values. The use of this type of loading is being permitted in the revised test procedure when results are desired at higher test temperatures.

Recommended Modifications to the Round Robin Test Procedure

An examination of the results obtained from the round robin clearly indicated that modifications to the test procedure are called for in several areas. These modifications are either simplifying in nature or clarifications to the existing method. Their incorporation into the test procedure does not therefore suggest the need for another round robin to be conducted prior to submission of the procedure as a proposed standard test method for consideration by ASTM. The recommended modifications are discussed in the following section, together with the rationale for the recommendations.

Modified Cyclic Loading and K Calculation Procedures

As discussed previously, a scheme for sequential load/unload cycling was a part of the test procedure followed in the round robin, but was placed in an annex to the main body of the proposed ASTM test method. Although it was originally intended that cyclic loading would be required mainly when testing subsized specimens machined from the broken halves of the full-sized specimens, it was found that cycling was in fact required for the majority of the full-sized specimens. The technique, as it was spelled out in the test procedure, called for monotonic loading up to some “limiting” crack opening displacement, followed by unloading to zero load if a rapid fracture had not initiated. The resulting offset in crack opening displacement was to be recorded before starting a second loading cycle in which the displacement limit was to be about 5% greater than that permitted on the first cycle. This process was to be repeated until a rapid crack initiated.

The sequential loading procedure outlined above was found to be time-consuming and resulted in a large number of cycles prior to crack initiation in many of the specimens. The test results also showed that the first unloading cycle accounted for most of the zero-load displacement offset and that the 5% increment was perhaps overly restrictive. The requirement that the maximum allowable displacement on a given cycle must be calculated from

the previous cycle also tended to slow down the test, since this normally meant stopping the test, performing the calculation, and then resuming testing.

A related issue was the cracking of the weld bead frequently observed on the first loading cycle, prior to reaching the specified limit. This, combined with the changes in displacement related to seating of the load train, meant that the displacement offset recorded at the end of the first load/unload cycle actually included contributions from load-train seating and weld-bead cracking, as well as contributions due to local yielding ahead of the starter notch.

The extensive use of cycling for the specimens tested in the round robin argues for inclusion of cycling as a part of the test procedure rather than as an annex to the proposed ASTM test method. This is the first modification recommended in this area. Furthermore, the authors propose modifying the cyclic loading technique used in the round robin as follows.

The first loading cycle should be limited to

$$[(\delta_o)_1]_{\max} = \frac{0.69\sigma_{ys}W\sqrt{\frac{B_N}{B}}}{Ef\left(\frac{a_o}{W}\right)} \quad (3)$$

where σ_{ys} is the static yield strength of the specimen material, and the other terms are as defined for Eq 1. This limit is about 80% of the limit specified in the original test procedure and should keep the first loading cycle elastic in a global sense. The influence of load-train and clip-gage seating, as well as the change of compliance due to weld-bead cracking, can then be eliminated, with some degree of conservatism, by excluding the zero-load displacement offset recorded at the end of the first loading cycle from the displacement used to calculate K_a .

The recommended maximum opening displacement on the second and subsequent cycles is then calculated from

$$[(\delta_o)_n]_{\max} = [1.0 + 0.25(n - 1)] \left[\frac{0.69\sigma_{ys}W\sqrt{\frac{B_N}{B}}}{Ef\left(\frac{a_o}{W}\right)} \right] \quad (4)$$

where n is the number of cycles and the other terms are the same as in Eq 3. This method requires that only two calculations be made, both prior to testing, consisting of the first (or seating) cycle limit and the subsequent increment. This requirement should result in a cyclic loading procedure that is simpler to implement and should require fewer loading cycles. At the same time, these modifications should help to separate components of the opening displacement associated with seating and weld bead cracking more clearly from those associated with local yielding around the root of the starter notch prior to initiation of a rapid fracture.

The influence of the latter could be eliminated entirely by excluding all of the zero-load offset in opening displacement recorded prior to the start of the loading cycle during which the run/arrest event occurs. However, there is evidence to suggest that such a step may be overly conservative. Model tests have shown that, when the plastic zone is well enclosed by the elastic stress field in the specimen, nearly all of the offset in the zero-load displacement is recovered if the plastic zone is severed by a saw cut or by a brittle crack [15]. The degree to which this component of the strain energy stored in the specimen is recovered in time to

influence the run/arrest behavior of the rapid crack is unclear at the present time. It is therefore recommended that the K -calculation procedure of this method avoid the extremes of excluding all or none of the zero-load displacement offsets that accumulate in the second and subsequent loading cycles and that it exclude one-half of these effects when calculating K_a .

Referring back to Fig. 3, which showed a typical load-displacement record from a cyclic loading test, the quantities d_o and d_a required to calculate K_o and K_a would be calculated for that particular example as

$$d_o = \delta_{P_4} - \delta_{R_3} \quad (5)$$

and

$$d_a = \delta_{P_4} - \delta_{R_1} - 0.5[\delta_{R_3} - \delta_{R_1}] + 0.5[\delta_{P_5} - \delta_{P_4}] \quad (6)$$

The last term in Eq 6 represents one half of the quick-opening displacement that frequently accompanies the run/arrest event. The use of the factor of 0.5 for this contribution has once again been selected to account for a dynamic contribution whose exact magnitude is unclear at the present time (see the preceding discussion on dynamic effects).

A limited number of tests have been conducted using specimens remaining from the round robin and following the modified cyclic loading and K -calculation procedures outlined above. The results showed good agreement with the main body of the round robin data [9].

Determination of the Arrested Crack Length

The test procedure calls for the arrested crack front to be marked by heat tinting, following which the specimen is chilled and broken open. The arrested crack length is then determined by taking the average of three measurements at various locations on the fracture surface. Some discussion has taken place as to whether three measurement locations are adequate or whether five (or even more) would give better results.

An examination of the round robin test results indicates that the number of measurement locations used is of less importance than the interpretation of the fracture surface features. It is therefore recommended that a two-step process be followed. First, the fracture surface should be examined to determine if it displays irregularities sufficient to warrant exclusion of the test result. If this check does not exclude the result on the grounds of likelihood of a nontypical K_a value, the arrested crack length should then be determined using the three measurement locations identified previously, with the measurements being taken as visual averages across a strip of width $B_N/4$, centered at each measurement location.

Implementation of both of these steps in the crack length determination process calls for a certain degree of judgement and experience on the part of the individual performing the test. For this reason, the proposed standard has been revised to include examples of non-typical fracture surface features and sample crack length determinations for adequate guidance to the inexperienced user.

Enhanced Guidelines on Specimen Preparation Procedures

The specimen preparation guidelines provided in the test procedure were felt to require some clarification, particularly in the area of brittle-weld preparation techniques for the starter notch. An expanded appendix on this subject is being added to the test procedure that was followed in the round robin. In addition, the use of a machined notch as a rec-

ommended option is being deleted. The limited experience from the round robin in this area suggests that machined notches may not function reliably for low-strength to medium-strength steels tested at temperatures above the reference nil-ductility transition temperature (RT_{NDT}).

Summary

Results have been presented from a round robin program that was conducted to evaluate a proposed ASTM test method for crack arrest fracture toughness of ferritic materials, which uses a crack-line wedge-loaded laboratory-sized compact specimen to determine K_{Ia} . The results demonstrate that the test procedure can provide repeatable results for the quantity being measured. The results from the round robin and those obtained previously with similar test procedures show good agreement with the available data from large-scale testing, indicating that the arrest toughness determined by the use of the proposed test method can be used successfully to determine whether or not a fast-running crack will arrest in a structure.

The experience gained from the round robin and the comments received from the participants have indicated several areas in which modifications to the test procedure are called for. The recommended modifications have been discussed, together with the rationale for the recommendations made. The modifications recommended are mainly simplifying in nature or in the form of clarifications to the existing document. It is therefore felt that another round robin is not called for, since it would only provide results similar to those already obtained. The test procedure followed in the round robin has since been revised along the lines suggested in this paper and is now proposed as the ASTM Test for Determining the Plane-Strain Crack-Arrest Fracture Toughness, K_{Ia} , of Ferritic Steels (E 1221).

Acknowledgments

The support received from the U.S. Nuclear Regulatory Commission and Oak Ridge National Laboratory has contributed in large part to the successful development of the test method described here. Support from the Electric Power Research Institute and the Federal Highway Administration is also gratefully acknowledged. The success of the round robin and the writing of this paper would not have been possible without the efforts of all the laboratories and individuals who participated in the program.

References

- [1] Crosley, P. B. and Ripling, E. J., "Crack Arrest Toughness of Pressure Vessel Steels," *Journal of Nuclear Engineering Design*, Vol. 17, 1971, pp. 32-45.
- [2] Crosley, P. B. and Ripling, E. J., "Plane Strain Crack Arrest Characterization of Steels," *Journal of Pressure Vessel Technology*, November, 1975.
- [3] Hoagland, R. G., Rosenfield, A. R., Gehlen, P. C., and Hahn, G. T., "A Crack Arrest Measuring Procedure for K_{Im} , K_{Id} and K_{Ia} Properties," *Fast Fracture and Crack Arrest, ASTM STP 627*, G. T. Hahn and M. F. Kanninen, Eds., American Society for Testing and Materials, Philadelphia, 1977, pp. 177-202.
- [4] Crosley, P. B., Fourney, W. L., Hahn, G. T., Hoagland, R. G., Irwin, G. R., and Ripling, E. J., "Final Report on Cooperative Test Program on Crack Arrest Toughness Measurements," NUREG/CR-3261, University of Maryland, College Park, MD, April 1983.
- [5] Cheverton, R. D., Gehlen, P. C., Hahn, G. T., and Iskander, S. K., "Application of Crack Arrest Theory to a Thermal Shock Experiment," *Crack Arrest Methodology and Applications, ASTM STP 711*, G. T. Hahn and M. F. Kanninen, Eds., American Society for Testing and Materials, Philadelphia, 1980, pp. 392-421.
- [6] Cheverton, R. D., Ball, D. G., Bolt, S. E., Iskander, S. K., and Nanstad, R. K., "Pressure Vessel Fracture Studies Pertaining to the PWR Thermal Shock Issue: Experiments TSE-5, TSE-5A, and

- TSE-6," NUREG/CR-4249 (ORNL-6163), Oak Ridge National Laboratory, Oak Ridge, TN, June 1985.
- [7] Bryan, R. H., Bass, B. R., Bolt, S. E., Bryson, J. W., Edmonds, D. P., McCulloch, R. W., Merkle, J. G., Nanstad, R. K., Robinson, G. C., Thoms, K. R., and Whitman, G. D., "Pressurized-Thermal-Shock Test of 6-in.-Thick Pressure Vessels. PTSE-1: Investigation of Warm Pre-stressing and Upper-Shelf Arrest," NUREG/CR-4106 (ORNL-6135), Oak Ridge National Laboratory, Oak Ridge, TN, April 1985.
 - [8] Rosenfield, A. R., "Validation of Compact-Specimen Crack-Arrest Data," *Journal of Engineering Materials Technology*, Vol. 106, 1984, pp. 207-208.
 - [9] Barker, D. B., Chona, R., Fourney, W. L., and Irwin, G. R., "A Report on the Round Robin Program Conducted to Evaluate the Proposed ASTM Standard Test Method for Determining the Plain-Strain Crack-Arrest Fracture Toughness, K_{Ia} , of Ferritic Materials," NUREG/CR-4996 (ORNL/Sub/79-7778/4), University of Maryland, College Park, MD, January 1988.
 - [10] Crosley, P. B. and Ripling, E. J., "Development of a Standard Test for Measuring K_{Ia} With a Modified Compact Specimen," NUREG/CR-2294 (ORNL/Sub-81/7755/1), Materials Research Laboratory, Glenwood, IL, August 1981.
 - [11] Freund, L. B., Hutchinson, J. W., and Lam, P. S., "Analysis of High-Strain-Rate Elastic-Plastic Crack Growth," *Engineering Fracture Mechanics*, Vol. 23, No. 1, 1986, pp. 119-129.
 - [12] Rosenfield, A. R., Mincer, P. N., Marschall, C. W., and Markworth, A. J., "Recent Advances in Crack-Arrest Technology," *Fracture Mechanics: Fifteenth Symposium, ASTM STP 833*, R. J. Sanford, Ed., American Society for Testing and Materials, Philadelphia, 1984, pp. 149-164.
 - [13] Kalthoff, J. F., Beinert, J., Winkler, S., and Klemm, W., "Experimental Analysis of Dynamic Effects in Different Crack Arrest Test Specimens," *Crack Arrest Methodology and Applications, ASTM STP 711*, G. T. Hahn and M. F. Kanninen, Eds., American Society for Testing and Materials, Philadelphia, 1980, pp. 109-127.
 - [14] Rosenfield, A. R., Mincer, P. N., and Marschall, C. W., "High-Temperature Crack-Arrest Toughness Measurements Using Compact Specimens," *Fracture Mechanics: Eighteenth Symposium, ASTM STP 945*, D. T. Read and R. P. Reed, Eds., American Society for Testing and Materials, Philadelphia, 1987, pp. 73-85.
 - [15] Chona, R., Fourney, W. L., Link, R. E., and Sanford, R. J., "The Recoverability of Plastic Zone Energy in Crack Arrest," *Proceedings, 1985 SEM Spring Conference on Experimental Mechanics*, Society for Experimental Mechanics, Las Vegas, NV, June 1985, pp. 13-19.

**Crack Arrest Theory and Applications:
Part I—Analysis**

Experimental Evaluation of an Equation Applicable for Surface Cracks Under Tensile or Bending Loads

REFERENCE: Reuter, W. G. and Epstein, J. S., "Experimental Evaluation of an Equation Applicable for Surface Cracks Under Tensile or Bending Loads," *Fracture Mechanics: Nineteenth Symposium, ASTM STP 969*, T. A. Cruse, Ed., American Society for Testing and Materials, Philadelphia, 1988, pp. 597-619.

ABSTRACT: If a structural material behaves in a linear elastic manner, it is generally assumed that plane-strain fracture toughness (K_{Ic}) may be used with applicable solutions to predict conditions for catastrophic fracture. There have been a few instances where the adequacy of this approach has been verified, but these evaluations were conducted for specific applications. This paper evaluates an approach using specimens containing surface cracks, with substantial variations in crack size and shape, and loaded by either tension or bending. Test results are used to compare the critical stress-intensity factor (K_{crit}) with K_{Ic} . Moiré interferometry is used to obtain K_I at the free surface for comparison with the calculated result.

KEY WORDS: linear elastic fracture mechanics, surface cracks, tensile or bending loads, plane-strain fracture toughness, moiré interferometry, fracture mechanics

Nomenclature

- a Crack depth
- $a/2c$ Aspect ratio
- c One-half the crack length
- C_1 Eigencoefficient
- E Young's modulus
- EL Elongation
- f Reference grating frequency
- f_w Finite-width correction
- $f(\phi)$ Angular function for Eq 3
- $f(\theta)$ Orthogonal eigenfunction spanning the two-dimensional space
- g Term in Eq 3
- H Correction term in Eq 1
- K_{ap} Value of K_I at a location away from the crack tip
- K_I Applied stress-intensity factor
- K_{Ic} Plane-strain fracture toughness
- K_{crit} Maximum K_I for surface-cracked specimens
- LEFM Linear elastic fracture mechanics
- M Front and back face correction
- N Assigned fringe order
- P Load

¹ Principal investigator and engineering specialist, respectively, Idaho National Engineering Laboratory, EG&G Idaho, Inc., P.O. Box 1625, Idaho Falls, ID 83415.

- RA Reduction of area
- SEN Single-edge notch specimen
- SENB Single-edge notch bend specimen
- SENT Single-edge notch tensile specimen
- SC Surface-cracked specimen
- Q Surface-crack shape and (sometimes) plastic zone correction term
- r Distances from crack tip
- r_y Plastic zone size
- t Thickness
- U_x Displacement in x direction
- W Specimen width
- λ_u Displacement eigenvalues
- σ Applied stress
- σ_{ys} Yield stress
- σ_{ut} Ultimate tensile strength
- σ_t Applied tensile stress
- σ_b Applied bending stress
- ϕ' Parameter angle of ellipse, degree
- ν Poisson's ratio

For a material behaving in a linear elastic manner, one of the considerations in predicting structural lifetime, and a requirement in evaluating the effect of a defect on the integrity of a structure, is linear elastic fracture mechanics (LEFM). To properly use LEFM it is necessary to measure the plane-strain fracture toughness (K_{Ic}) using procedures described in the ASTM Test for Plane-Strain Fracture Toughness of Metallic Materials (E 399-83). Considerable effort has been expended to verify these analytical solutions and to develop experimental procedures for measuring K_{Ic} using specimens containing through-thickness cracks.

For the partial penetrating defects (embedded and surface cracks) of concern to structural integrity, the evaluation process compares K_{Ic} with K_{crit} calculated using an equation of the following type [1]

$$K_I = (\sigma_t + H\sigma_b) \sqrt{\frac{\pi a}{Q}} M \quad (1)$$

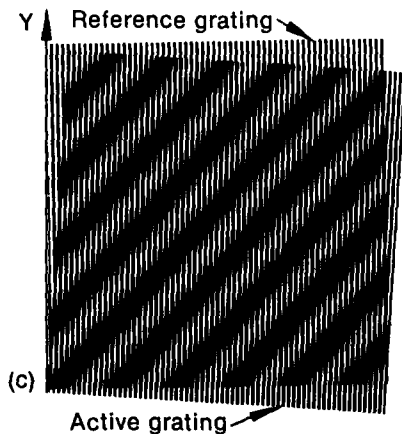


FIG. 1—An amplitude moiré pattern.

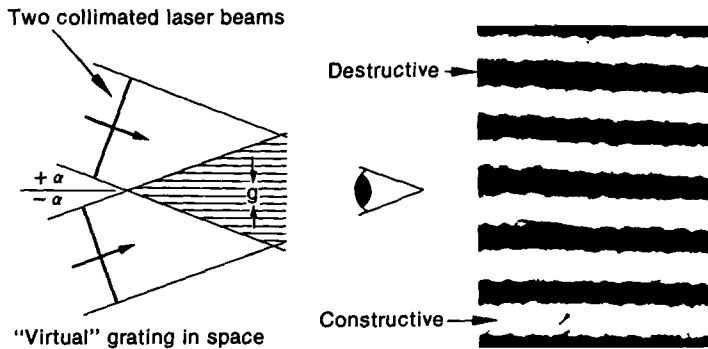


FIG. 2—The exposed pattern of two-beam interference.

where

K_I = applied stress-intensity factor, $K_I = K_{crit}$ at failure,

σ_t = tensile stress,

σ_b = bending stress,

Q = flaw shape and (sometimes) plastic zone correction term,

$Q = 1 + 1.464 (a/c)^{1.65}$ (no plastic zone correction),

a = crack depth,

$2c$ = crack length, and

$M = [M_1 + M_2(a/t)^2 + M_3(a/t)^4]f\phi gfw$.

(2)

(3)

See Ref 1 for how to obtain the parameters in Eq 3 and the H term in Eq 1.

Other solutions have been developed for estimating K_I ; an evaluation of many of these solutions [2] suggests that Eqs 1 through 3 provide one of the more accurate solutions. The only effective way to identify the most appropriate solution or solutions is to compare predictions with experimental results. This paper compares the use of K_{Ic} and Ref 1 to calculate K_{crit} . Moiré interferometry was used to verify the accuracy of the K_I calculation at the free surface.

This research program, funded by the U.S. Department of Energy Office of Basic Sciences (DOE-BES) for the past several years at the Idaho National Engineering Laboratory (INEL), is primarily focused on investigating the behavior of surface cracks in elastic-plastic and plastic conditions, but it has been necessary to verify the adequacy of solutions presently being used for LEFM conditions. The approach used compares calculated values of K_{crit} (maximum value of K_I obtained from tests of surface-cracked specimens) with K_{Ic} (obtained

TABLE 1—Nominal surface-crack specimen configuration.

Specimen Identification No.	Thickness, mm	Width, mm	Crack Depth, mm	Crack Length, mm	$a/2c$
1 through 5	5.1	50.8	0.38	50.8	0.01
B-5 and B-6	5.1	50.8	0.51	25.4	0.02
6 through 9	5.1	50.8	3.80	25.4	0.15
B-7 and B-9	5.1	63.5	3.81	35.1	0.11
B-10 and B-11	5.1	50.8	3.68	8.1	0.45
10 through 14	5.1	63.5	3.30	33.0	0.10
15 through 16	5.1	63.5	3.30	6.6	0.50
B-12 through B-14	5.1	44.4	0.89	1.78	0.50

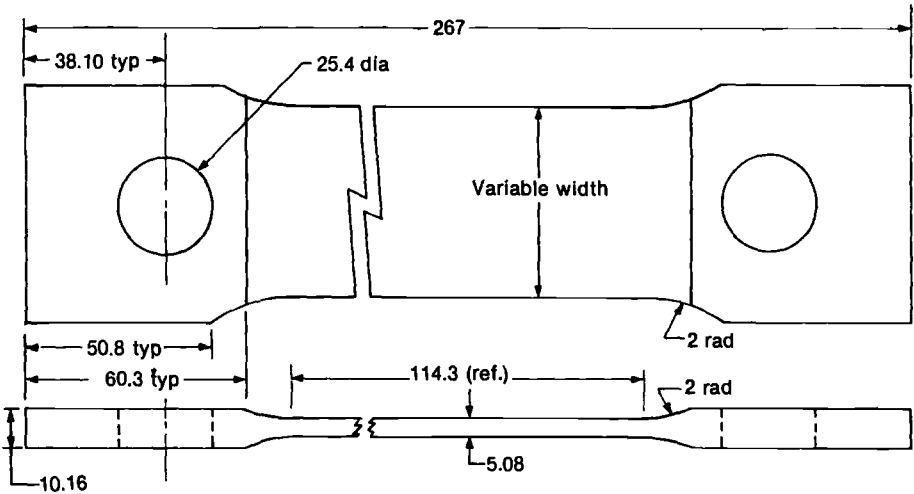
TABLE 2a—Mechanical properties—tension results.

Specimen Identification No.	Diameter, mm	Elongation, %	Reduction of Area, %	σ_{ys} , MPa	σ_{ut} , MPa
1	4.06	2.6	9.0	. . .	1552
2	4.04	2.6	7.8	1499	1550
3	4.06	2.6	9.0	1425	1507
4	4.04	2.6	7.8	1446	1509
5	4.06	2.6	9.0	1425	1493
6	4.04	2.6	7.8	1463	1516
Average		2.6	8.4	1452	1521

TABLE 2b—Mechanical properties—SENB results.

Specimen Identification No.	Thickness, mm	Width, mm	Crack Depth, mm	P_{max} , kN	K_{Ic}^a , MPa m ^{1/2}
1	10.01	9.78	4.62	4.05	41.9
2	10.01	9.75	4.52	4.00	39.8
Average					40.8
3 (second test series)	10.01	9.8	. . .	3.73	41.4

^a Satisfied the validity requirement in ASTM Test E 399-83.



- Notes:
- 1. Surface flaw size and shape to be specified.
 - 2. Surface flaw to be centered in reduced section.

FIG. 3—Surface-cracked specimen configuration.

by ASTM Test E 399-83). The experimental results were obtained using surface-cracked (SC) specimens since they best simulate a structural component containing a "natural" defect. Moiré interferometry was used to determine K_I and K_{crit} experimentally at the crack-front/free-surface region. A brief description of moiré interferometry is provided here, a more complete explanation is given by Epstein [3].

The moiré effect is observed when two repetitious patterns deform relative to each other (see Fig. 1). The fringe pattern, which results when the active or specimen grating deforms, is called a moiré pattern. The fringes are lines of constant in-plane displacement whose direction is perpendicular to the fixed or stationary reference grating. The fringe formation method shown in Fig. 1 is termed mechanical moiré because the fringes are formed by the mechanical crossing of the lines. Moiré interferometry extends the technique to a full field in-plane displacement measurement with micrometre displacement and submillimetre spatial resolution by using gratings produced by the constructive and destructive interference of two coherent light beams impinging upon a recording medium. As Fig. 2 shows, the interference effect of the two coherent intersecting beams produces a pattern similar to the

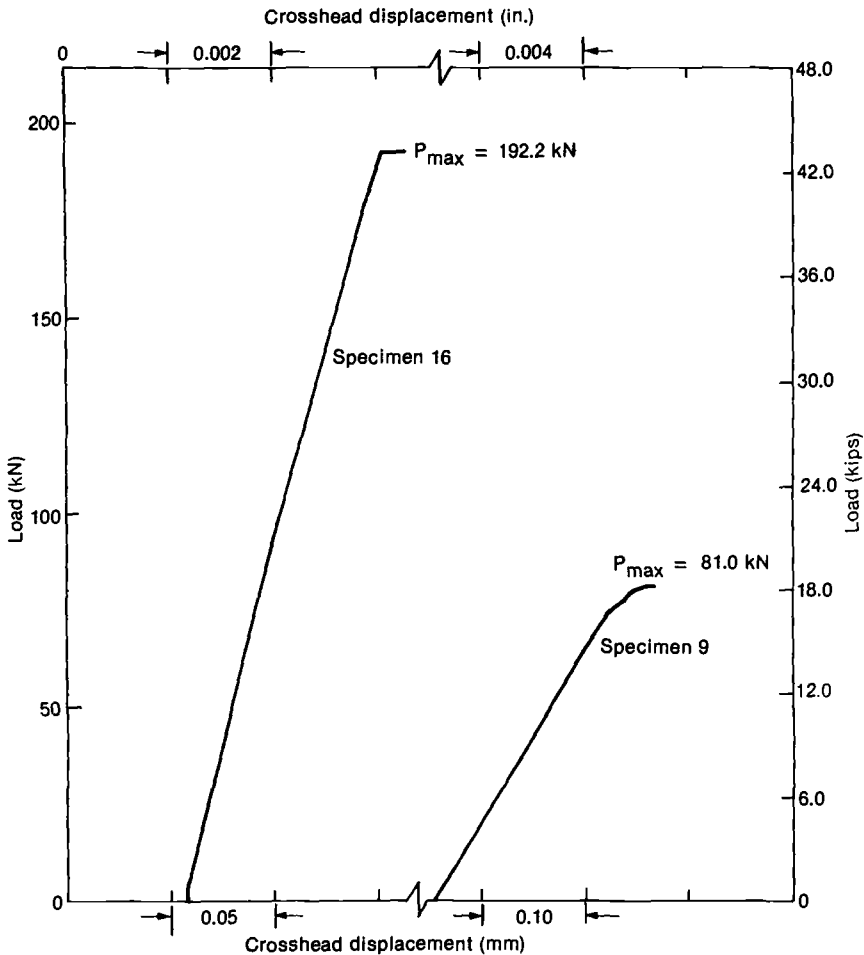


FIG. 4—Representative load-displacement plots for two specimens tested in tension.

TABLE 3—Surface-crack specimen dimensions and applicable stress.

Specimen Identification No.	Thickness, mm	Width, mm	Crack Depth, mm ^a			Crack Length, 2c, mm	Stress, MPa			
			Maximum	Realistic	Average		Deviation	Secant	Maximum	Initiation (Acoustic Emission)
TENSION TEST										
1	5.11	50.85	0.69	0.53	0.25	50.85	a	a	834.9	e
2	5.11	50.83	0.94	0.66	0.51	50.83	a	a	801.1	e
3	5.11	50.85	0.89	0.71	0.48	50.85	a	a	969.4	e
5	4.98	50.77	0.76	0.64	0.46	50.77	a	a	801.1 ^b	e
6	5.16	50.83	4.47	27.99	249.8	283.6	285.7	e
7	5.11	50.80	4.45	27.48	276.0	295.3	295.3	e
9	5.13	50.83	4.42	27.51	262.2	296.7	312.6	e
10	5.05	63.53	4.72	34.49	e	e	245.0	e
11	5.08	63.50	4.75	35.43	e	e	235.3	e
14	5.13	63.50	4.83	33.91	e	e	272.6	e
15	5.11	63.50	3.56	8.13	422.3	d	542.3 ^b	e
16	5.11	63.53	3.84	8.20	460.2	592.7	592.7	e
B-7	5.16	63.50	3.86	34.85	e	e	242.2	f
BEND TEST										
4	5.11	50.85	0.94	0.76	0.64	50.83	e	e	946.7 ^e	e
5	4.98	50.77	0.76	0.64	0.46	50.77	e	e	1097.1 ^e	e

8	5.11	50.85	4.11	26.77	708.6	^d	717.6 ^g	^e
12	5.05	63.50	4.78	34.93	612.7	^d	652.0 ^g	^e
15	5.11	63.50	3.56	8.13	1229.6	^d	1262.7 ^g	^e
B-2	5.16	50.83	0.38	0.28	0.20	50.80	^c	^c	1499.4 ^h	1413.8
B-3	5.13	50.80	0.43	0.30	0.20	50.80	^c	^c	1495.2 ^h	^f
B-5	5.16	50.83	0.64	0.48	0.38	29.67	^c	^c	1028.1 ^h	999.1
B-6	5.16	50.80	0.64	0.56	0.51	25.25	^c	^c	1118.5 ⁱ	1107.4
B-8	5.16	63.50	3.84	35.36	512.0 ^d	^d	534.1 ⁱ	494.0
B-9	5.13	63.55	3.81	35.10	585.8	576.2	587.9 ^h	578.9
B-10	5.08	50.80	3.71	8.26	983.2	^d	1024.0 ^h	992.2
B-11	5.18	50.83	3.56	7.95	945.3	^d	1004.0 ⁱ	855.3
B-12	5.16	44.40	0.86	1.83	^c	^c	1571.1 ^j	1511.1 ^j
B-13	5.16	44.48	0.89	2.03	^c	^c	1511.1 ^h	1504.2 ^j

^a Load-displacement plot is inadequate to obtain results.

^b Test specimen failed at pin hole; the remaining specimen was tested to failure in bending.

^c No deviation from linearity.

^d Specimen failed before secant offset was reached.

^e Acoustic emission techniques were not used.

^f Acoustic emission record was not useful.

^g Span = 50.80 mm.

^h Span = 115.57 mm.

ⁱ Span = 77.98 mm.

^j σ_{ys} = 1452 MPa.

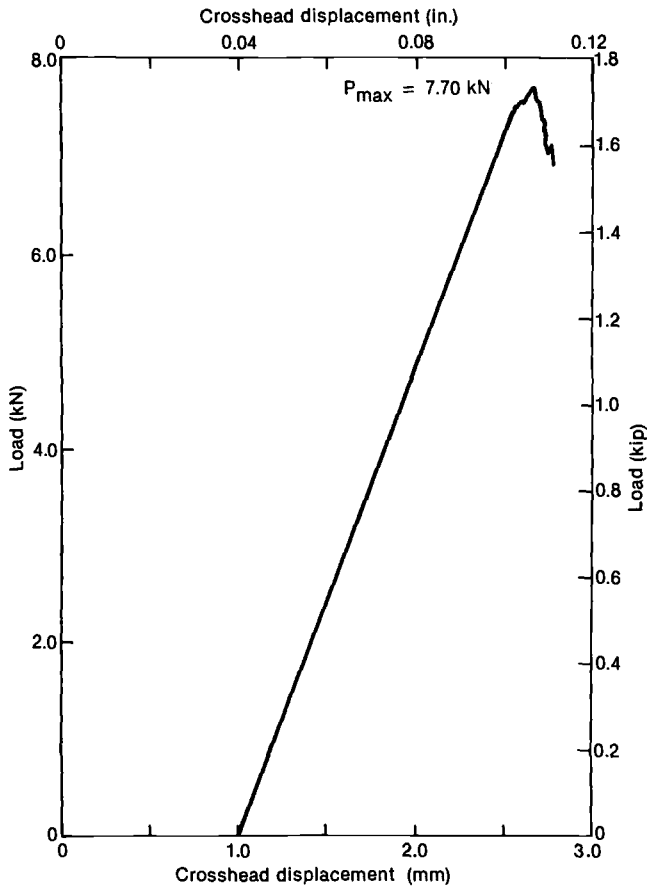


FIG. 5a—Bend test results for Specimen B-8—load-displacement plot.

grating pattern shown in Fig. 1. These diffraction gratings can have a frequency of up to half the wavelength of the light employed, thus implying a displacement resolution of, for example, approximately $0.2 \mu\text{m}$ using blue-green light. The validity of interpreting this interferometric pattern in the same way as a mechanical moiré pattern is found in Livnat and Post [4].

Testing and Results

Approach for Comparing K_{Ic} and K_{crit}

The material used in this investigation was Ti-15-3, a metastable beta alloy with a chemical composition in weight percent of 0.023 carbon, 0.15 iron, 0.014 nitrogen, 3.0 aluminum, 14.9 vanadium, 3.0 chromium, 0.012 hydrogen, 3.1 tin, 0.13 oxygen, and the balance titanium. The plate was supplied in the solution-annealed (1060 K) condition in which the microstructure is generally (depending on the thickness and cooling rate) a single beta phase. This phase is metastable and will precipitate an alpha phase during the aging cycle. The test material was aged at 714 K for 16 h to obtain a high-strength, low-toughness material. This

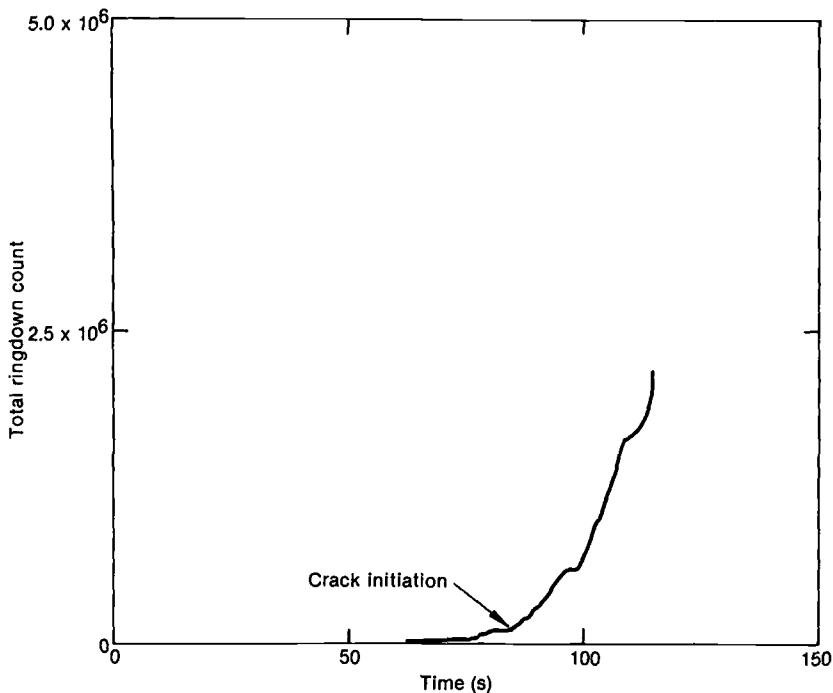


FIG. 5b—Bend test results for Specimen B-8—acoustic emission versus time.

combination was desired so that testing of the SC specimens would be conducted in the elastic region and the plastic zone size would be small.

Tensile and fracture toughness [single-edge notch bend (SENB) and SC] specimens were tested at 295 K; the specimen configurations and test results are summarized in Tables 1 and 2. The SENB specimens, (9.8 mm wide by 10.0 mm thick by 51 mm long) were tested as per ASTM Test E 399-83. The surface-cracked specimens, of the configuration shown in Fig. 3, were tested monotonically to failure. The actual specimen and precrack dimensions are provided in Table 3. All the test specimens were oriented with the specimen length parallel to the transverse rolling direction. The SENB specimens were oriented with the crack penetrating the plate thickness (T-S). The surface cracked specimens all had the cracks penetrating the plate thickness (T-S), but the crack would tend to grow in the T-L direction for an aspect ratio ($a/2c$) of 0.5. The surface-cracked specimen configurations are summarized in Table 1; it is apparent that a substantial variation existed in both crack depth and $a/2c$.

Figure 4 shows examples of the load-displacement plot for two specimens tested in tension. Some of the specimens behaved in a totally elastic manner while others exhibited plastic deformation and subcritical crack growth. The second test series (Specimens B-1 to B-14) was tested for verification purposes and to obtain data not generated by the first series (Specimens 1 to 16). Acoustic emission techniques were used in the second series to detect the load corresponding to crack growth initiation. An example of the load-displacement plots and the corresponding acoustic emission/time plots are presented in Figs. 5 and 6 for this test series. The acoustic emission plots identify the time corresponding to initiation of subcritical crack growth. The time is then used with the chart speed and crosshead speed

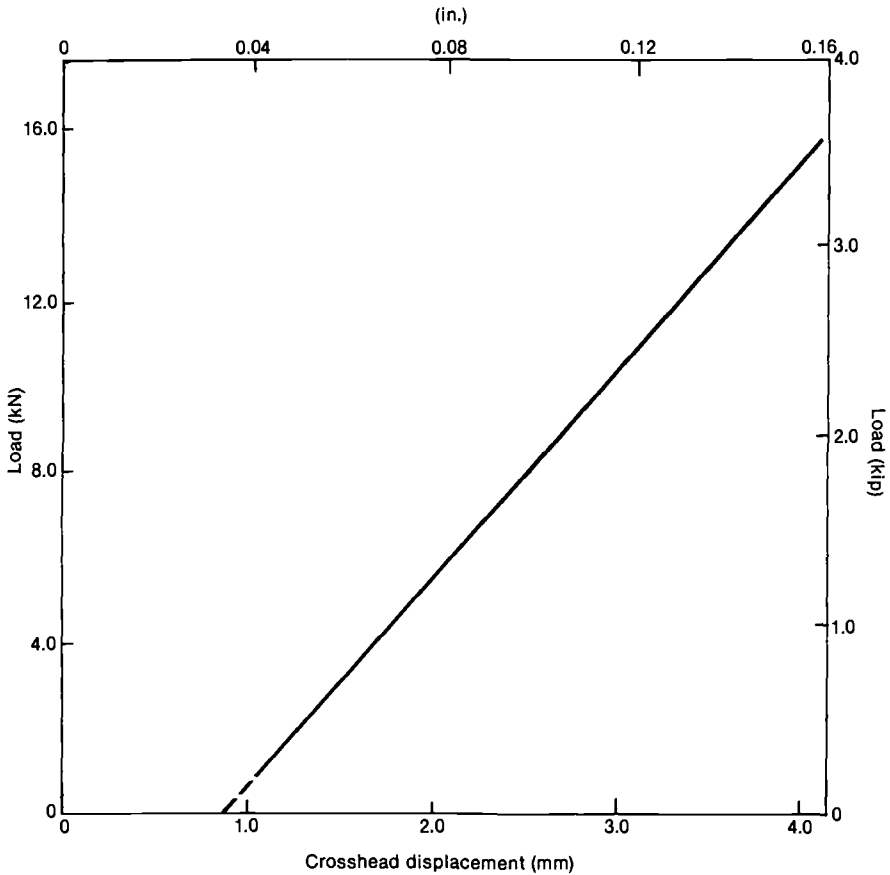


FIG. 6a—Bend test results for Specimen B-12—load-displacement plot (chart speed at 25.4 mm/min).

to identify the load corresponding to initiation of subcritical crack growth (see Figs. 6a and 6b). The results of the tensile and bend tests of surface-cracked specimens are given in Table 3.

Experimental Evaluation of K_{crit}

For this study 2400 l/mm (lines/mm) crossed gratings were applied directly ahead of the crack tip of the specimens identified in Table 4. This permitted observation in both the x and y directions of the crack-tip displacement (Fig. 7). A schematic of the moiré interferometer is shown in Fig. 8. Real-time imaging is essential; therefore, the moiré images were recorded in video format. Since the video camera frames at 30 Hz, stable crack growth was easily recorded. The video images of interest were selected from the tape and then digitized directly on a PDP 11/34 Eyecom II system. In addition, a photographic still camera was used with Kodak 2475 high-speed film and a 1/250 shutter speed to provide a clear, permanent record of the moiré pattern at selected loads. Data reduction algorithms can then be applied to selected digitized images. Figure 9 shows a crack growth sequence in the titanium; the fringes represent net displacement in the x direction of 1/2400 mm.

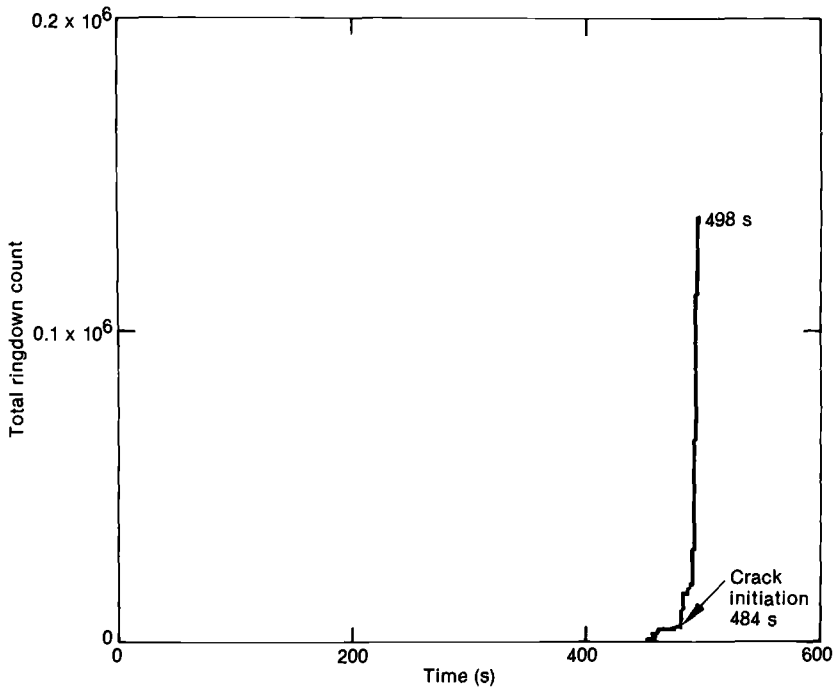


FIG. 6b—Bend test results for Specimen B-12—acoustic emission versus time.

The test data consisted of load versus time and real-time video recording of the moiré pattern versus time. The data generated by moiré interferometry were analyzed as described below. The Williams eigenfunction displacement field [5] for a crack oriented as shown in Fig. 7 is given by

$$U_x = C_1(r)^{\lambda_u^1} f_1(\theta) + \sum_{k=2}^{\infty} C_k(r)^{\lambda_u^k} f_k(\theta) \quad (4)$$

where

C_1 = the eigencoeficients,
 $f_1(\theta)$ = the orthogonal eigenfunctions spanning the two-dimensional space, and
 λ_u^1 = the eigenvalues.

For classical two-dimensional linear elastic fracture mechanics, the inverse square root stress singularity exists in the stress and thus

$$\begin{aligned} \lambda_u^1 &= \frac{1}{2} \\ \lambda_u^k &= \frac{k}{2} \end{aligned} \quad (5)$$

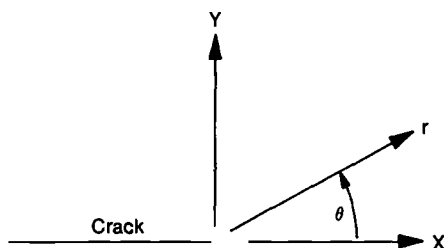


FIG. 7—The crack-tip coordinate system.

Further, if data are taken close to the crack tip so that the stress singularity dominates, then Eq 4 may be truncated to the two-parameter equation [6]

$$U_x = C_1 r^{1/2} f_1(\theta) + C_2 f_2(\theta) r \quad (6)$$

or further

$$U_x = \frac{K_I}{\mu} \left(\frac{r}{2\pi} \right)^{1/2} \cos \frac{\theta}{2} \left[\frac{1}{2} (\Phi + 1) - \sin^2 \frac{\theta}{2} \right] + \frac{(1 - \Phi)(\Phi - 1)}{8\mu} \bar{\sigma} r \cos \theta \quad (7)$$

where

$C_1 = K_I$, the Irwin [7] stress-intensity factor,

$$\mu = \frac{E}{1 - \nu},$$

$\bar{\sigma}$ = the remote far field stress under theoretical biaxial loading,

$\Phi = 3 - 4\nu$, plane strain,

$\Phi = \frac{3 - \nu}{1 + \nu}$, plane stress,

E = Young's modulus, 10.35×10^4 MPa,

ν = Poisson's ratio (0.33),

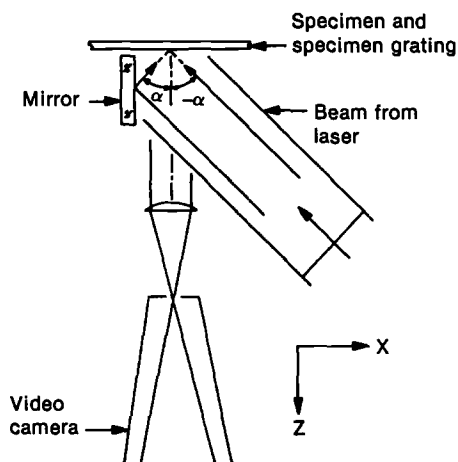


FIG. 8—Schematic of the moiré interferometer.

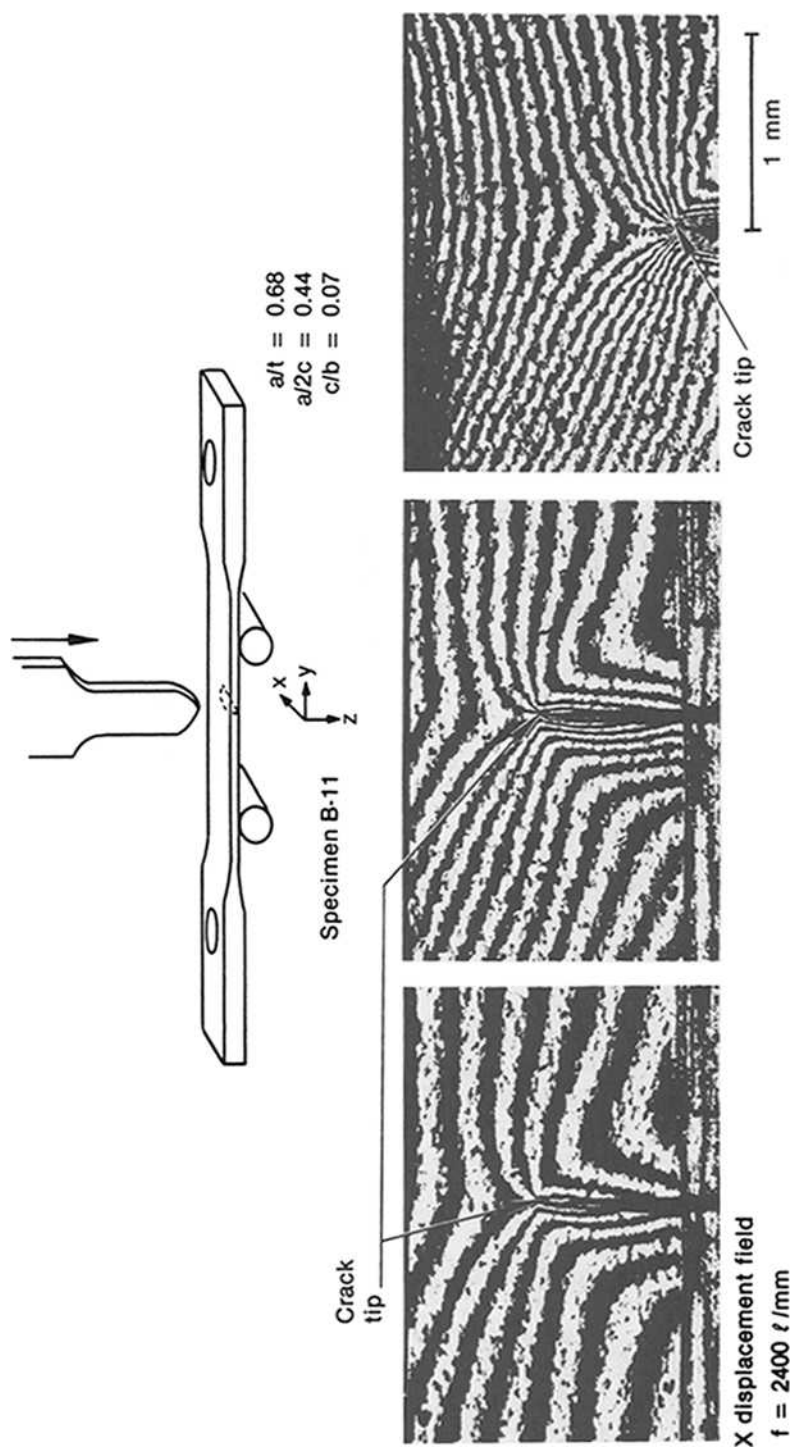


FIG. 9—Sequential moiré displacement fields of crack growth.

$$U_x = N/f,$$

N = the assigned fringe order relative to a known zero, and

f = the reference grating frequency (lines/mm or lines/in.)

Dividing Eq 7 by $r^{1/2}$ yields

$$K_{ap} = \frac{U_x C_x(\Phi)}{r^{1/2}} = K_I + U_x^*(\Phi) r^{1/2} \quad (8)$$

where

K_{ap} = value of K_I at a location away from the crack tip,

$$C_x(\Phi) = \frac{2\pi E}{3 - \nu}, \text{ plane stress,}$$

$$C_x(\Phi) = \frac{2\pi E}{(3 - 4\nu)(1 + \nu)}, \text{ plane strain, and}$$

U_x = the collection of terms on the far field nonsingular stress

Plotting K_{ap} versus $r^{1/2}$ for data in the crack-tip region and extrapolating to the origin yields K_I . It is important to realize that first a classical singularity is assumed. Log-log plots for crack displacement fields in aluminum alloy 2024-T6 ($\nu = 0.33$) yield a displacement singularity in the leading exponent of r between 0.40 and 0.45 [8], in close agreement with Benthem [9]; the singularity coefficient used is 0.5. Further, a two-parameter technique such as Eq 5 is used only with localized crack tip data; moiré interferometry provides such data. For situations where the r exponent varies greatly from the classical $1/2$, as in high Poisson's ratio materials, one should refer to Smith et al. [10] for appropriate crack-tip algorithms. Moiré patterns associated with the initial load and at intermediate time steps up to initiation of crack growth were analyzed to determine K_I .

Discussion

The following is separated into two subsections: experimental verification of K_{crit} and a comparison of K_{Ic} with K_{crit} .

Verification of K_{crit}

Moiré interferometry was used to determine K_I and K_{crit} experimentally at the intersection of the crack and the free surface. Table 4 shows the results. These results show relatively good agreement with K_I calculations based on Ref 1 and with K_{Ic} from ASTM Test E 399-83. It should be noted that an x displacement field was used in the bend test experiments of the SC specimen. Typically the data are taken at a line 90° to the crack tip. Thus, the rate of change of the x field is taken in the y direction, or

$$\frac{\partial U_x}{\partial Y} = 2W_{xy} + \frac{\partial U_x}{\partial x} \quad (9)$$

Equation 9 implies that measurements of the x displacement field at 90° will be extremely sensitive to in-plane rigid body rotations. This rotational effect can be compensated for with the K extraction algorithms of Kobayashi² or noting that the cracked geometry is one of

² Kobayashi, A., University of Washington, Seattle, WA, personal communication, March 1986.

TABLE 4— K_I determined by moiré interferometry versus theory.

Specimen Identification	Moiré K_I /Theory K_I Ratio
Three-point bending ^a Precracked Charpy ($K_I = K_{Ic}$, failure)	0.90
Tensile loading ^b ($K_I = K_{Ic}$, failure) Specimen B-7	1.02
Bending ^b (at A/E initiation) Specimen B-8	0.91
Specimen B-11	1.03

^a Theory: ASTM Test E 399-83.^b Theory: Ref 1.

minimal rotation, unlike a bending geometry, which encounters large crack-tip rigid body rotation. In general, the y displacement field should be used 90° to the crack tip. Even though the y displacement fields were not used, the agreement between K_I (moiré) and K_I (Ref 1) in Table 4 shows the adequacy of the approach based on x displacement fields. The SC specimens tested in bending were based on x displacement fields and the SC specimen tested under tensile loading was based on y displacement.

Comparison Between K_{Ic} and K_{crit}

The fracture toughness (K_{Ic}) of the titanium-base alloy is nominally 41 MPa m^{1/2}. The calculated values of K_{crit} using Eq 1 provide the basis for the ratio K_{crit}/K_{Ic} given in Table 5. These calculations are based on the stress corresponding to:

- (a) the load where deviation from linearity occurs on the load-displacement plot,
- (b) the intersection of the secant offset with the load-displacement plot,
- (c) the maximum load,

and on the acoustic emission results which identified the stress for crack growth initiation. The ratio of K_{crit}/K_{Ic} in Table 5, where K_{crit} is based on acoustic emission results, shows good agreement with the lowest of deviation, secant, or maximum for Specimens B-8 through B-13. Based on this observation, the K_{crit} value corresponding to the lowest deviation, secant, or maximum is used to identify crack initiation for all specimens tested. This assumption was made because acoustic emission was not used on many of the specimens and the authors desired a relatively consistent event associated with crack growth initiation.

For Specimens 1 through 5 and B-2 through B-6, where a long, shallow fatigue precrack was generated, it was difficult to establish the critical crack depth (a) (see Fig. 10). The maximum and average crack depths given in Table 3 are self-explanatory, but the realistic values are subjective since they are based on an approximate average over a critical length (nominally 1 cm). The ratio K_{crit}/K_{Ic} in Table 5 ranged from a minimum of 0.68, based on an average crack length, to a maximum of 1.61, based on a maximum crack length, for specimens containing long shallow cracks. Of the nine specimens (excluding No. 5 tested in tension) there are three (Nos. 1, 2, and B-5) where K_{crit}/K_{Ic} was less than 1.0. Since the ratio K_{crit}/K_{Ic} was greater than 1.0 for 18 other tests, it is expected that the same is true for the long shallow crack. Therefore, the realistic or maximum crack depths will provide a

TABLE 5—Comparison between K_{crit} and K_{IC}

Specimen Identification No.	K_{crit}/K_{Ic} Ratio		Initiation (Acoustic Emission)	Location ^c of K_{crit} , degrees	cF^2 , mm
	Deviation ^a	Maximum ^b			
TENSION TESTING					
1	...	1.17, 1.01, 0.68	...	90	0.79, 0.61, 0.30
2	...	1.36, 1.10, 0.94	...	90	1.04, 0.74, 0.58
3	...	1.61, 1.41, 1.12	...	90	0.99, 0.81, 0.56
5	...	1.23, 1.10, 0.91	...	90	0.86, 0.71, 0.53
6	1.11	1.27	...	90	4.06
7	1.20	1.29	...	90	3.99
9	1.13	1.35	...	90	4.06
10	...	1.24	...	90	4.85
11	1.14	1.20	...	90	4.85
14	...	1.36	...	90	4.88
15	>1.04	>1.34	...	0	2.67
16	1.16	1.50	...	0	2.97
B-7	...	1.11	...	90	5.10

BEND TESTING

4	...	1.29, 1.18, 1.09	...	90	1.04, 0.86, 0.71
5	...	1.39, 1.29, 1.12	...	90	0.86, 0.71, 0.53
8	1.55	1.58	...	0	2.34
12	1.51	1.62	...	0	2.69
15	2.13	2.18	...	0	2.69
B-2	...	1.49, 1.30, 1.12	1.40, 1.22, 1.05	90	0.46, 0.33, 0.25
B-3	...	1.58, 1.35, 1.13	...	90	0.51, 0.36, 0.25
B-5	...	1.18, 1.05, 0.96	1.15, 1.03, 0.93	90	0.76, 0.58, 0.46
B-6	...	1.30, 1.24, 1.18	1.29, 1.23, 1.18	90	0.79, 0.69, 0.64
B-8	1.04	1.09	1.00	0	1.85
B-9	1.19	1.20	1.18	0	1.85
B-10	1.69	1.76	1.70	0	2.69
B-11	1.60	1.70	1.44	0	2.52
B-12	...	1.32	>1.33 ^d	0	0.48
B-13	...	1.42	>1.36 ^d	0	0.48

^a Five percent secant offset.^b For specimens containing a long shallow crack, the first, second, and third terms refer to maximum, realistic, and average crack depth, respectively.^c Free surface at $\phi' = 0^\circ$; maximum crack depth at $\phi' = 90^\circ$.^d Used stress = σ_{ys} since $\sigma_{nat} > \sigma_{ys}$.

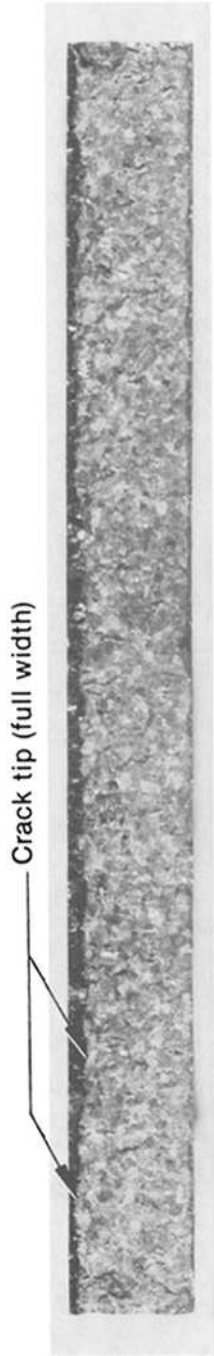


FIG. 10—Cross-section showing surface crack configuration.

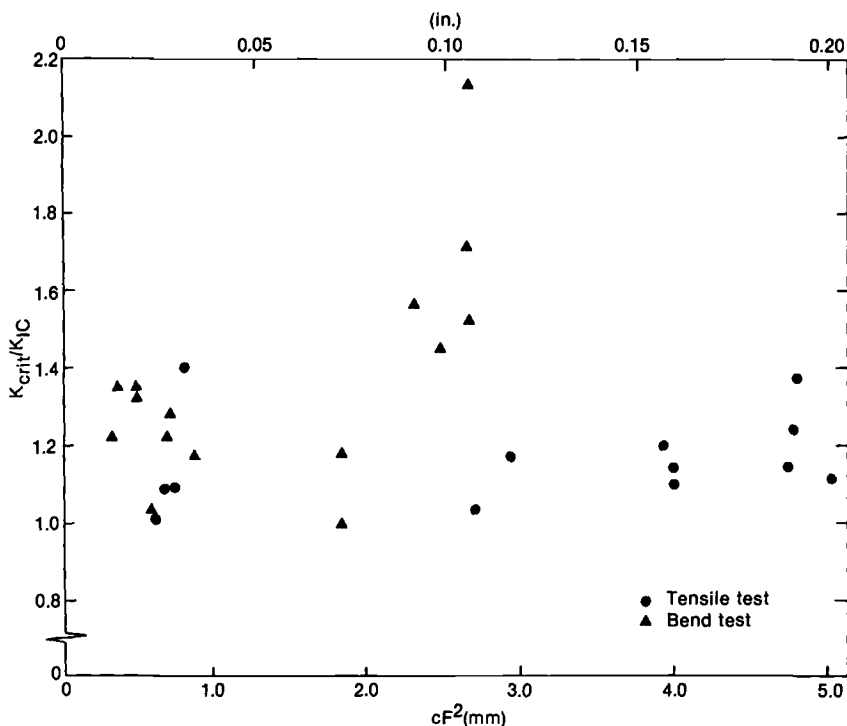


FIG. 11—Plot of K_{crit}/K_{Ic} versus crack severity (cF^2).

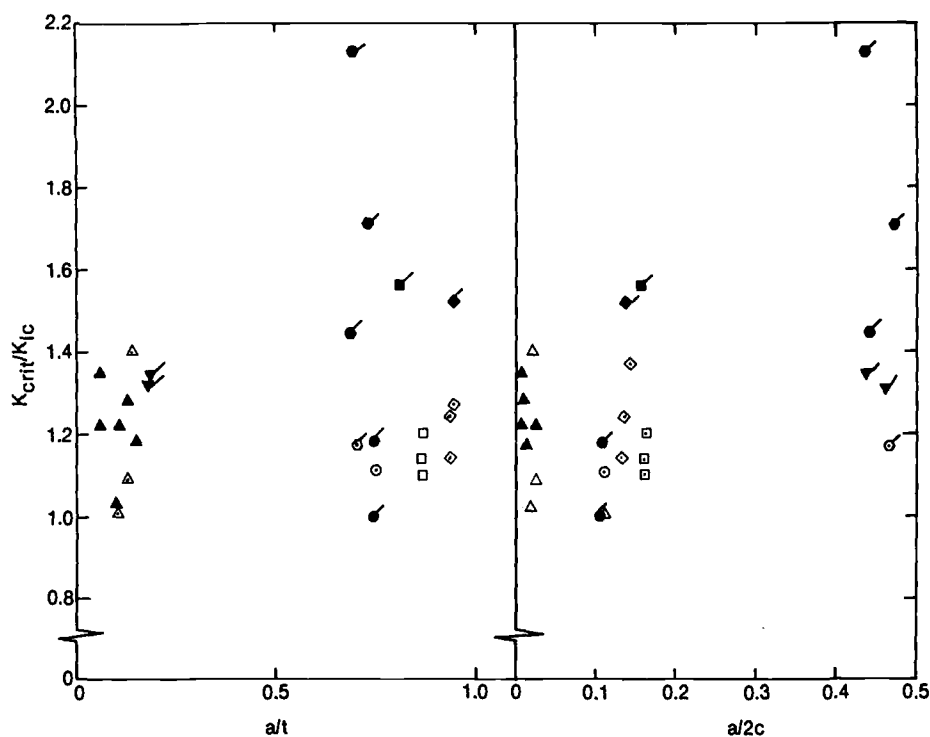
better basis for evaluating K_{crit}/K_{Ic} . The former is used since it results in a lower value of K_{crit} .

The ratios K_{crit}/K_{Ic} are plotted versus cF^2 in Fig. 11 for 28 tests. The parameter cF^2 is used to quantify the severity of a surface crack and was originally proposed by Newman [11] and later verified by statistical analysis [12] and comparisons made with other parameters [13]. The value F is related to the geometry correction term M in Eq 1 by

$$F = M \sqrt{\frac{a}{cQ}} \frac{1 - \pi ac}{Wt} \quad (10)$$

A statistical analysis was conducted in Ref 12 of a ductile Type 304 stainless steel to identify the critical parameters for initiation of crack growth of a surface flaw loaded in tension. A dimensional and statistical analysis showed a good relationship between the critical parameters and cF^2 . The evaluation of cF^2 was extended in Ref 13 where comparisons were made between a ratio of stress and a/t , $a/2c$, and cF^2 . Trends were observed for both a/t and $a/2c$, but it was not possible to predict how the two parameters interacted with each other. Plots using cF^2 showed a trend suggesting interaction between a/t and $a/2c$. Therefore, it was concluded in Ref 13 that cF^2 provided a useful tool to quantify the severity of surface cracks.

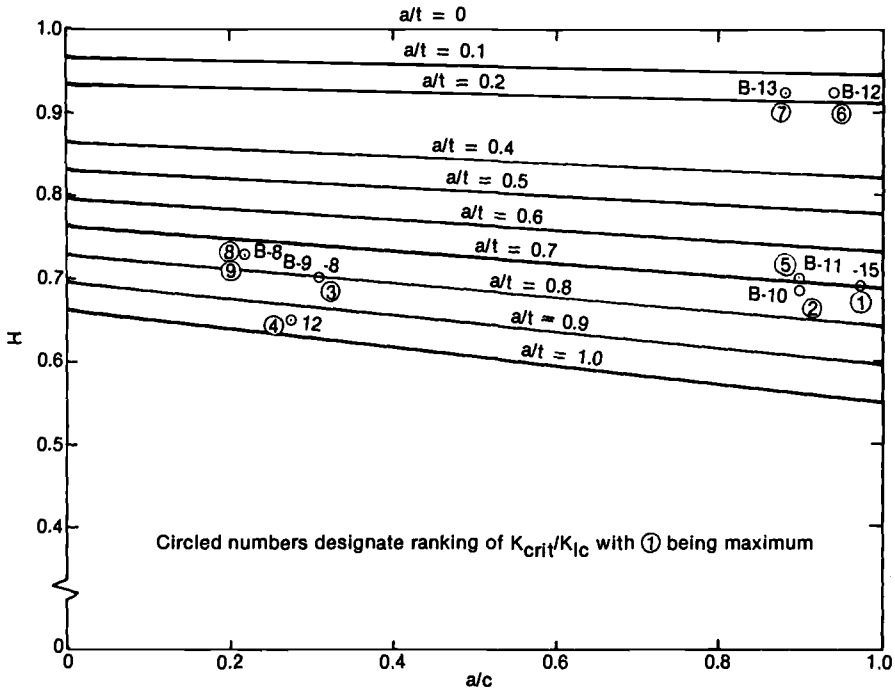
It is obvious, in Fig. 11 that Specimens 8, 12, 15, B-10, and B-11 all had K_{crit}/K_{Ic} substantially greater than the others. These specimens were all tested in bending and each exhibited a deviation from linearity before reaching maximum stress. All five specimens had

FIG. 12—Plot of K_{crit}/K_{Ic} versus a/t and $a/2c$.

$a/t > 0.7$, but $a/2c$ was either 0.14 or 0.44. These data are also plotted versus a/t and $a/2c$ in Fig. 12; it is apparent that the deeper, more semicircular shaped cracks will generally have more conservatism when tested in bending than in tension. In Fig. 12, symbols with a tail represent specimens where K_{crit} occurred at the free surface. It is apparent that K_{crit} occurred at the free surface for all specimens where K_{crit}/K_{Ic} was greater than 1.4, which suggests that the loss of constraint at the free surface requires that K_{crit} be greater than K_{Ic} before crack initiation occurs. This was not totally true, since two other specimens had K_{crit} occurring at the free surface and K_{crit}/K_{Ic} ranged from 1.0 to 1.2.

The H term in Eq 1 is identified [1] as being developed by curve fit and engineering judgment; therefore, it was examined to see if it might provide an explanation for the conservatism observed in Specimens 8, 12, 15, B-10, and B-11. The H term for each of the bend test specimens where K_{crit} occurred at the free surface ($\phi' = 0^\circ$) is plotted as a function of a/c and a/t in Fig. 13. The circled numbers designate the ranking of the specimens as a function of K_{crit}/K_{Ic} and there is no apparent correlation between the location of the specimen in Fig. 13 and the ranking. Reference 1 notes that the accuracy of Eq 1 has not been established for $a/t > 0.8$. Table 6 shows that $a/t = 0.80$ and 0.95 for two tests (specimen 8 and 12) and these happened to have $K_{crit}/K_{Ic} = 1.55$ and 1.51 , respectively. But, replicate specimens tested in tension (Nos. 6, 7, 9, 10, 11, and 14) show K_{crit}/K_{Ic} ranging from 1.11 to 1.36, which suggests it is not the tensile component that is causing the increase in conservatism.

The H term, for bending in Eq 1, is a function of a/c and a/t , and Fig. 11 from Ref 1


 FIG. 13—Specimen location in relation to H term.

shows this relationship. For $a/c = 0.3$ and a/t ranging from 0.74 to 0.95, H varies only a small amount at the free surface (until $\phi' > 22^\circ$) of the specimen. Therefore, Specimens 8, 12, B8, and B9 should have similar K_{crit}/K_{Ic} values, but Table 6 shows a substantial difference, suggesting that the H term for the free-surface region is not adequate to provide an explanation for the difference in K_{crit}/K_{Ic} . Table 6 shows a substantial difference between K_{crit} at $\phi' = 0^\circ$ and K_{crit} at $\phi' = 90^\circ$ for the two sets of specimens. For $a/c = 0.9$ and a/t of nominally 0.2 or 0.7, there is a relatively small difference in H at the free surface, but H decreases much faster as $\phi' > 0^\circ$ for $a/t = 0.7$ than it does for $a/t = 0.2$. The H term is greater for Specimens B12 and B13 than it is for Specimens 15, B10, and B11, but the latter have the larger ratio of K_{crit} to K_{Ic} . Table 6 shows a substantial difference between K_{crit} at $\phi' = 0^\circ$ and K_{crit} at $\phi' = 90^\circ$ for the two sets of specimens. Figure 14 shows that a trend exists between H and cF^2 , but it is not in total agreement with the ranking of K_{crit}/K_{Ic} . The trend suggests that if H decreased faster after $cF^2 = 2.0$ mm then K_{crit}/K_{Ic} would decrease.

At this time the only rationale for identifying a specific cF^2 value is that relatively small cracks tested in bending have similar values of K_{max} at the free surface and at maximum crack depth. For the larger cracks the difference between K_{max} at the free surface and at maximum crack depth becomes more pronounced (see Table 6). This suggests that the loss of constraint at the free surface is much more meaningful for the larger cracks. This loss of constraint does not effect the calculated values of K but causes the value of K required for failure to be greater than K_{Ic} . The difference in constraint is observed only for those specimens where K_{crit} occurs at the free surface.

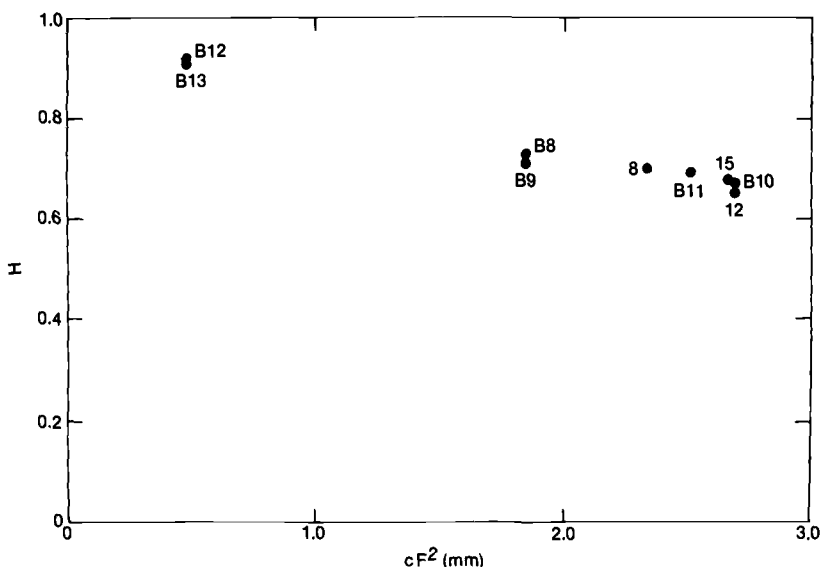
TABLE 6—Comparison of K_{max} at the free surface and at maximum depth.

Specimen Identification No.	a/t	$a/2c$	K_{max}/K_{Ic} Ratio at		Ratio of K_{max} at $\phi' = 0^\circ$ to K_{max} at $\phi' = 90^\circ$
			$\phi' = 0^\circ$	$\phi' = 90^\circ$	
8	0.80	0.15	1.55	0.35	4.4
12	0.95	0.14	1.51	0.04	37.8
15	0.70	0.44	2.13	0.18	11.8
B8	0.74	0.11	1.00	0.50	2.0
B9	0.74	0.12	1.18	0.59	2.0
B10	0.73	0.45	1.70	0.04	42.5
B11	0.69	0.45	1.44	0.14	11.3
B12	0.17	0.47	1.33	1.09	1.2
B13	0.17	0.44	1.36	1.14	1.2

Conclusions

Moiré interferometry was used on several specimens tested in tension or bending. The maximum K_I occurred at the free surface for one specimen and at maximum depth for two specimens. The experimentally determined K_I , measured at this free surface, agreed within ± 10 to 5% of the value calculated using Eq 1. This provided verification of the accuracy of Eq 1 to predict K_I at the free surface for significantly different crack configurations. It is assumed that the accuracy associated with calculating K_I around the perimeter of the surface crack is verified by these three results.

A comparison of the plot of the ratio K_{crit}/K_{Ic} versus cF^2 in Fig. 11 shows the applicability of Eq 1 for either tension or bending loads. For tensile loads, the ratio K_{crit}/K_{Ic} ranged from 1.0 to 1.4 for the 13 specimens. This amount of conservatism appears to be acceptable. For bending loads the ratio K_{crit}/K_{Ic} ranged from 1.0 to 2.1 for the 15 specimens. The conservatism

FIG. 14—Plot of H versus crack severity (cF^2).

beyond 1.4 is due to five specimens where a/t was greater than 0.7 but was insensitive to aspect ratio. The value of K_{crit} occurred at the free surface for all five specimens, which suggests that the loss of constraint of the free surface requires that K_{crit} be greater than K_{Ic} before crack initiation occurs. Even though substantial conservatism exists, the lack of nonconservatism shows the usefulness of Eq 1 for elastic conditions.

Acknowledgments

This work was supported by the U.S. Department of Energy, Office of Energy Research, Office of Basic Energy Sciences, under DOE Contract No. DE-AC07-76ID01570.

References

- [1] Newman, J. C., Jr., and Raju, I. S., "Analysis of Surface Cracks in Finite Plate Under Tension and Bending Loads," NASA Technical Paper 1578, National Aeronautics and Space Administration, Washington, DC, December 1979.
- [2] "A Critical Evaluation of Numerical Solutions to the "Benchmark" Surface Crack Problem," Benchmark Editorial Committee of the Society for Experimental Analysis, Fracture Committee, *Experimental Mechanics*, Vol. 20, N8, 1980, pp. 253-264.
- [3] Epstein, J., Deason, V. A., and Reuter, W. G., this publication, pp. 482-503.
- [4] Livnat, A. and Post, D., "The Grating Equations for Moiré Interferometry and Their Identity to Equations of Geometrical Moiré," *Experimental Mechanics*, Vol. 25, No. 2, December 1985, pp. 360-366.
- [5] Williams, M. L., "On the Stress Distribution at the Base of a Stationary Crack," *Transactions of the American Society of Mechanical Engineers*, Vol. 24, 1957, pp. 109-114.
- [6] Eftis, J., Subramonian, N., and Libowitz, H., "Crack Border Stress and Displacement Equations Revised," *Engineering Fracture Mechanics*, Vol. 9, 1977, pp. 189-210.
- [7] Irwin, G. R., "Analysis of Stresses and Strain Near the End of a Crack Traversing a Plate," *Journal of Applied Mechanics*, September 1957, pp. 361-364.
- [8] Epstein, J. S., Reuter, W. G., and Keiser, D. D., "Crack Embrittlement Displacement Fields," *Proceedings, 22nd Society for Engineering Science Conference*, Pennsylvania State University, University Park, PA, 1985.
- [9] Benthem, J. P., "The Quarter Infinite Crack in a Half Space, Alternative and Additional Solutions," *International Journal Solids and Structures*, Vol. 16, No. 4, 1980, pp. 335-348.
- [10] Smith, C. W., Epstein, J. S., and Olasobikan, O., "Experimental Boundary Layer Studies in Three-Dimensional Fracture Problems," *Advances in Aerospace Structures and Materials and Dynamics*, ASME-AO-06, November 1983, pp. 119-126.
- [11] Newman, J. C., Jr., "Fracture Analysis of Various Cracked Configurations in Sheet and Plate Materials," *Properties Related to Fracture Toughness, ASTM STP 605*, American Society for Testing and Materials, Philadelphia, 1976, pp. 104-123.
- [12] Reuter, W. G., Matthew, S. D., and Smith, F. W., "Critical Parameters for Ductile Fracture of Surface Flaws," *Engineering Fracture Mechanics*, Vol. 19, No. 1, 1984, pp. 159-179.
- [13] Reuter, W. G. and Richardson A. K., "Comparison of Fracture Toughness Measurements from Ferritic Steel Compact and Surface-Flawed Specimens," *Nuclear Engineering and Design*, Vol. 79, 1984, pp. 255-266.

A Three-Dimensional Weight Function Method

REFERENCE: Banks-Sills, L., "A Three-Dimensional Weight Function Method," *Fracture Mechanics: Nineteenth Symposium, ASTM STP 969*, T. A. Cruse, Ed., American Society for Testing and Materials, Philadelphia, 1988, pp. 620–636.

ABSTRACT: In this investigation, an exact three-dimensional weight function is developed for the elliptical crack family. Closed form expressions for the weight function of the penny-shaped and elliptical crack in an infinite body subjected to symmetric applied stresses are obtained. Several loadings are considered that lead to exact solutions which agree with those in the literature. Since crack-opening displacements for more complicated crack geometries do not appear in the literature, an approximate weight function is proposed. When applied to the geometries with known solutions, excellent agreement is obtained. When employed to determine the stress-intensity factor for a semielliptical and quarter-elliptical crack in a plate subjected to bending stresses, it produces results which are good for short cracks.

KEY WORDS: weight function, three-dimensional weight function, fracture, elliptical cracks, stress-intensity factor, fracture mechanics

Recently, the problem of determining stress-intensity factors for three-dimensional crack geometries has been receiving more attention. As an application, knowledge of the K variation along the crack front may permit more accurate fatigue crack growth analyses of these geometries [1]. A useful technique which has been developed and widely employed for two-dimensional crack geometries is that of the Bueckner-Rice weight function method [2,3]. In the present study, this method is extended to treat Mode I deformation of the elliptical crack family.

Some work has already appeared in the literature concerning three-dimensional weight functions. In 1972, Rice [3] simplified the two-dimensional weight function introduced by Bueckner [2] and in an appendix presented some ideas for extending this method to three-dimensional problems. In 1976, Besuner [4] presented an approximate three-dimensional weight function and, with Cruse, applied it to several geometries [5,6]. In 1977, Bueckner [7] extended his approach for two-dimensional geometries [2], developing the weight functions of penny-shaped and elliptical cracks in infinite bodies. These ideas appear difficult to extend to bodies with finite boundaries. Several suggestions [8–11] for calculating three-dimensional weight functions have been presented and applied to either two-dimensional or axisymmetric problems; all of these depend upon finite-element solutions.

Before describing an extension of the weight function method to three dimensions, its meaning in two dimensions [2,3] is delineated. The method was developed for two-dimensional symmetric bodies with applied loading symmetric with respect to the crack, so that only Mode I deformation is induced. In order to apply the method, knowledge of the stress-

¹ Senior lecturer, Department of Mechanics, Materials, and Structures, Tel Aviv University, Ramat Aviv 69978, Israel.

intensity factor K_I^* and the displacement field $\underline{u}^*(x, y, a)$ for the desired geometry under any symmetric applied load is required. For most cases, it is only necessary to know $\underline{u}^*(x, 0, a)$ for $0 \leq x \leq a$, that is, the displacement field on the crack face itself. In this latter case, the concept of superposition is employed to transfer the applied tractions, for the problem to which a solution is sought, to the crack faces. Then, the unknown stress-intensity factor K_I is given by

$$K_I = \frac{H}{2K_I^*} \int_{\text{crack faces}} \underline{T} \cdot \frac{\partial \underline{u}^*(x, 0, a)}{\partial a} dx \quad (1)$$

where $H = E$ for generalized plane stress or $E/(1 - \nu^2)$ for plane strain; E is Young's modulus; ν is Poisson's ratio; and \underline{T} are the tractions on the crack faces for the problem to be solved. It is assumed here that there are no body forces. This method has been applied to various two-dimensional problems [12,13]. It has also been extended and applied to two-dimensional mixed-mode problems [14,15].

In this investigation, an exact three-dimensional weight function is developed for the elliptical crack family, where applied loads are "elliptically" symmetric. As a means of comparison, several problems for which exact solutions exist are considered. For more complicated geometries, for which there are no exact solutions and the crack-opening displacement is not known for any applied load, an approximate method is proposed. It is applied to the geometries with known solutions and yields excellent agreement. In addition, it is employed to determine the stress-intensity factor for a semielliptical and quarter-elliptical crack in a plate subjected to bending stresses and is shown to produce results which are good for short cracks.

Weight Function Method in Three Dimensions

In this section, the two-dimensional weight function method is extended to treat crack geometries of the elliptical family, which include penny-shaped, elliptical, semielliptical, and quarter-elliptical cracks in infinite and finite bodies which experience Mode I deformation. The general crack geometry considered is shown in Fig. 1.

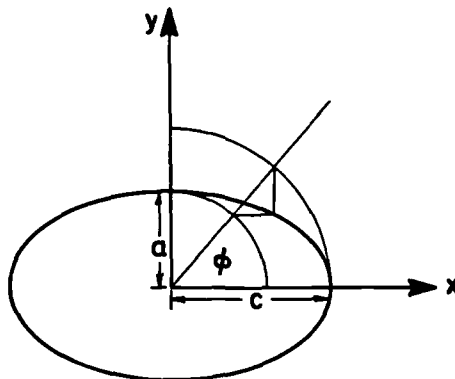


FIG. 1—Elliptical crack geometry.

Consider a local definition of Griffith's energy G for an elliptical crack

$$G(\xi) = \frac{K_I^2(\xi)}{H} \quad (2)$$

where K_I is the stress-intensity factor, H is a combination of material parameters defined previously, and ξ represents a point on the crack edge. We define unit stress-intensity factors

$$k_I^{(i)}(\xi) = \frac{K_I^{(i)}(\xi)}{P_i} \quad (3)$$

where P_i is a point force which induces only Mode I deformation. For N such applied forces, the Mode I stress-intensity factor is given by

$$K_I(\xi) = \sum_{i=1}^N K_I^{(i)}(\xi) = \sum_{i=1}^N k_I^{(i)}(\xi) P_i \quad (4)$$

Note that all stress-intensity factors implicitly depend upon the position of the applied force P_i . Substituting Eq 4 into Eq 2 leads to

$$G(\xi) = \frac{1}{H} \sum_{i=1}^N \sum_{j=1}^N k_I^{(i)}(\xi) k_I^{(j)}(\xi) P_i P_j \quad (5)$$

On the other hand

$$G(\xi) = \left. \frac{\partial U}{\partial A} \right|_P = \left. \frac{1}{L} \frac{\partial U}{\partial \ell(\xi)} \right|_P$$

where U is the internal energy, A is the crack area, L is the crack perimeter, and $d\ell(\xi)$ represents a virtual crack extension at the position ξ along the crack edge, so that

$$G = \frac{1}{2L} \sum_{i=1}^N \sum_{j=1}^N \frac{\partial C_{ij}(\xi)}{\partial \ell(\xi)} P_i P_j \quad (6)$$

where C_{ij} is the compliance; that is, $u_i^{(j)}(\xi) = C_{ij}(\xi) P_j$ (no summation). For clarification, the crack excursion dA may be thought of as consisting of the amplitude of a crack extension $d\ell$ at a point ξ along the crack front weighted so that its integral is equal to the crack perimeter L multiplied by $d\ell(\xi)$. Since P_i and P_j are arbitrary, it may be deduced from Eqs 5 and 6 that

$$k_I^{(i)}(\xi) = \frac{H}{2L k_I^{(i)}(\xi)} \frac{\partial C_{ij}(\xi)}{\partial \ell(\xi)} \quad (7)$$

For a particular load case m , where the full solution is known

$$k_I^{(m)}(\xi) = \frac{K_I^{(m)}(\xi)}{P_m}$$

so that from Eqs 4 and 7

$$K_I(\xi) = \frac{H}{2LK_I^{(m)}(\xi)} \sum_{i=1}^N \frac{\partial C_{im}(\xi)}{\partial \ell(\xi)} P_m P_i$$

or

$$K_I(\xi) = \frac{H}{2LK_I^{(m)}(\xi)} \sum_{i=1}^N \frac{\partial u_i^{(m)}(\xi)}{\partial \ell(\xi)} P_i \quad (8)$$

If instead of point forces, stresses are applied, a similar derivation leads to

$$K_I(\xi) = \int_A \sigma(x, y) h(x, y, \xi) dA \quad (9a)$$

where the weight function h is given by

$$h(x, y, \xi) = \frac{E}{(1 - \nu^2)LK_I^*(\xi)} \frac{\partial w^*(x, y, \xi)}{\partial \ell(\xi)} \quad (9b)$$

In Eqs 9a and 9b, $K_I(\xi)$ is the unknown stress-intensity factor; $\sigma(x, y)$ is the stress applied to the crack face; A is the crack area; H has been replaced by $E/(1 - \nu^2)$, since plane strain conditions are assumed along the crack front; $K_I^*(\xi)$ and $w^*(x, y, \xi)$ are the known stress-intensity factor and crack-opening displacement for the same geometry subjected to a different load; ξ is a point on the crack edge; and $d\ell(\xi)$ is a virtual crack extension.

At this point, the investigation is limited to studying the elliptical crack family. Considering a virtual crack extension $d\ell(\xi)$ for this case, one possible representation of the derivative in Eq 9 may be written as

$$\frac{\partial}{\partial \ell(\xi)} = \left[\left(\frac{\partial}{\partial a} \right)_q \sin^2 \phi + \left(\frac{\partial}{\partial c} \right)_q \cos^2 \phi \right]^{1/2} \quad (10)$$

where a and c are the minor and major axes of the ellipse, respectively, ϕ is an angular coordinate (see Fig. 1), and $q = a/c$; that is, the ellipse aspect ratio is held fixed for a virtual crack extension along the minor and major axes of the ellipse. This representation limits the generality of the development to symmetric-type loadings; that is, for the penny-shaped crack, axisymmetric, and for the elliptical crack, elliptically symmetric.

Exact Solutions

To demonstrate the accuracy of the method, Eqs 9a and 9b are applied to several problems. Consider first, a penny-shaped crack in an infinite body. For the known solution with this geometry, a remote uniform applied stress $\sigma_{zz} = \sigma$ is chosen. Then

$$K_I^* = 2\sigma \sqrt{\frac{a}{\pi}} \quad (11a)$$

$$w^*(x, y, a) = \frac{4(1 - \nu^2)\sigma a}{\pi E} \left[1 - \left(\frac{x}{a} \right)^2 - \left(\frac{y}{a} \right)^2 \right]^{1/2} \quad (11b)$$

and

$$L = 2\pi a \quad (11c)$$

Eq 11b is differentiated as prescribed in Eq 10, where $a = c$ for a penny-shaped crack, so that $\partial/\partial\ell(\xi)$ becomes $\partial/\partial a$. Then, substituting Eqs 11a, b, and c into Eq 9b yields

$$h = \frac{1}{(\pi a)^{3/2}} \left[1 - \left(\frac{x}{a} \right)^2 - \left(\frac{y}{a} \right)^2 \right]^{-1/2} \quad (12)$$

This weight function produces exact results for axisymmetric applied stresses only.

Three applied loads are considered. For a point load applied to the center of the crack

$$\sigma(x, y) = P\delta(x, y) \quad (13a)$$

where δ is the Dirac delta function, integration of Eq 9a leads to

$$K_I = \frac{P}{(\pi a)^{3/2}} \quad (13b)$$

For an applied stress

$$\sigma(r) = \sigma \left(\frac{r}{a} \right)^\gamma \quad (14a)$$

where $r^2 = x^2 + y^2$ and $\gamma > -2$, integration of Eq 9a produces

$$K_I = \sigma \sqrt{a} \frac{\Gamma\left(\frac{\gamma}{2} + 1\right)}{\Gamma\left(\frac{\gamma}{2} + \frac{3}{2}\right)} \quad (14b)$$

where Γ is the gamma function. Finally, for

$$\sigma(r) = \sigma \left[1 - \left(\frac{r}{a} \right)^2 \right]^{\gamma/2} \quad (15a)$$

where $\gamma > -1$, integration of Eq 9a yields

$$K_I = \sigma \sqrt{\frac{a}{\pi}} \frac{2}{\gamma + 1} \quad (15b)$$

The solutions given in Eqs 13b, 14b, and 15b agree with those found in Ref 16. These examples, of course, are for an axisymmetric geometry.

Next, an elliptical crack in an infinite body is considered (Fig. 1). For the known solution, the elliptical crack with a remote uniform applied stress $\sigma_{zz} = \sigma$ is chosen. Then

$$K_I^* = \frac{\sigma \sqrt{\pi a} f_\phi}{E(k)} \quad (16a)$$

where

$$f_{\phi} = \left[\sin^2 \phi + \left(\frac{a}{c} \right)^2 \cos^2 \phi \right]^{1/4} \quad (16b)$$

$E(k)$ is the complete elliptical integral of the second kind, that is,

$$E(k) = \int_0^{\pi/2} [1 - k^2 \sin^2 \theta]^{1/2} d\theta$$

and

$$k^2 = 1 - \left(\frac{a}{c} \right)^2$$

The crack-opening displacement is given by

$$w^*(x, y, a, c) = \frac{2(1 - \nu^2)}{E} \frac{\sigma a}{E(k)} \left[1 - \left(\frac{x}{c} \right)^2 - \left(\frac{y}{a} \right)^2 \right]^{1/2} \quad (16c)$$

and the perimeter of the ellipse is

$$L = 4cE(k) \quad (16d)$$

Differentiation of Eq 16c according to Eq 10 and substitution of this result together with Eqs 16a and 16d into Eq 9b yields the weight function for an embedded elliptical crack under elliptically symmetric loadings as

$$h = \frac{f_{\phi}}{2c\sqrt{\pi a E(k)}} \left[1 - \left(\frac{x}{c} \right)^2 - \left(\frac{y}{a} \right)^2 \right]^{-1/2} \quad (17)$$

For this geometry, two applied stress fields are considered: a point load at the center of the ellipse and a quadratic stress applied to the crack face. For the point load, $\sigma(x, y) = P\delta(x, y)$ integration of Eq 9a yields

$$K_I = \frac{Pf_{\phi}}{2c\sqrt{\pi a E(k)}} \quad (18a)$$

To the author's knowledge, a solution for this loading does not exist in the literature, but when $a = c$, that is, a penny-shaped crack, Eq 18a coincides with Eq 13b. For an applied quadratic stress

$$\sigma(x, y) = \sigma \left[\left(\frac{x}{c} \right)^2 + \left(\frac{y}{a} \right)^2 \right] \quad (18b)$$

integration of Eq 9a leads to

$$K_I = \frac{2}{3} \frac{\sigma \sqrt{\pi a} f_{\phi}}{E(k)} \quad (18c)$$

This solution does not agree with the one given in Ref 17. If the one in Ref 17 is reduced for the case when $a = c$, that is, a penny-shaped crack, that solution does not agree with Eq 14b, which is also found in Ref 16, when $\gamma = 2$. However, Eq 18c is in agreement with Eq 14b and hence Ref 16, which does lead to some confidence. It would of course be more satisfying if there were complete agreement. Unfortunately, there do not appear to be any other available solutions in the literature for comparison. In both cases examined, the applied stress is elliptically symmetric.

Approximate Weight Function

To pursue this method for studying both the semielliptical and quarter-elliptical crack in a plate, knowledge of both the stress-intensity factor and crack-opening displacement for these geometries and any Mode I load case is required. Unfortunately, only stress-intensity factors for this geometry are available. Hence, an approximate method is sought. In Ref 18, for two-dimensional problems, Petroski and Achenbach developed an approximate weight function from the stress-intensity factor alone. Following Ref 18, an approximate weight function is determined for three-dimensional geometries. Clearly, a suitable approximate crack-opening displacement must be chosen. To this end, the displacement is expanded about the crack edge as

$$w^*(r, a, c) = \frac{1 - v^2}{\sqrt{2}E} \frac{\sigma a}{E(k)} \left[4F\left(\frac{a}{t}, \frac{a}{c}, \phi\right)(1 - r)^{1/2} + G\left(\frac{a}{t}, \frac{a}{c}, \phi\right)(1 - r)^{3/2} \right] \quad (19)$$

where $r^2 = (x/c)^2 + (y/a)^2$ and the functions F and G are to be determined. This is an asymptotic expansion for the crack-opening displacement for r near 1. The function F is determined by expanding Eq 16c for r near unity, and G is determined from satisfaction of

$$\int_0^\xi [K_I^*(\xi)]^2 L d\ell(\xi) = \frac{E}{1 - v^2} \int_A \sigma(r, \theta) w^*(r, a, c) dA \quad (20)$$

Once an explicit expression for $w^*(r, a, c)$ is obtained, the same procedure described in the previous section is carried out to determine the weight function h .

To check the accuracy of the approximate weight function, several examples with known crack-opening displacements and solutions are examined. Employing Eqs 19 and 20, the geometries previously considered—namely, a penny-shaped and an elliptical crack in an infinite body with several different loadings—are reconsidered. For the point force applied at the crack center, the approximate stress-intensity factor for the penny-shaped crack is given by

$$K_I = \frac{P}{(\pi a)^{3/2}} \frac{\sqrt{2}}{4} (4F + G) \quad (21a)$$

where

$$F = 1 \quad (21b)$$

and

$$G = \frac{7}{6} (5\sqrt{2} - 8) \quad (21c)$$

and for the embedded elliptical crack

$$K_I = \frac{Pf_\phi}{c\sqrt{\pi a}E(k)} \frac{\sqrt{2}}{8} (4F + G) \quad (21d)$$

Both are within 3.1% of the exact solutions, given in Eqs 13*b* and 18*a*, respectively. For the penny-shaped crack and the applied stress given in Eq 14*a*, the approximate stress-intensity factor is found to be

$$K_I = \sigma\sqrt{a} \frac{\gamma + 3}{\sqrt{2}} \frac{\Gamma(\gamma + 2)}{\Gamma(\gamma + 3.5)} \left[2F + \frac{3G}{2(2\gamma + 7)} \right] \quad (22)$$

where F and G are given in Eqs 21*b* and 21*c*, respectively. Comparison with the exact solution in Eq 14*b* for $\gamma = 1$ and 2 yields differences of 0.16 and 0.21%, respectively. For the penny-shaped crack and the applied stress given in Eq 15*a* with $\gamma = 2$, the error is 0.42%. Finally, for the embedded elliptical crack, with the applied stress given in Eq 18*b*, the difference between the stress-intensity factor obtained from the approximate weight function and the exact one given in Eq 18*c* is 0.21%. This last example is carried out in detail in Appendix I.

Next, a semielliptical crack in a finite thickness plate in bending (Fig. 2, *a* and *c*) is considered. Here, the crack-opening displacement is not known. For this geometry, with remote uniform stress applied perpendicular to the crack face, an analytical expression for

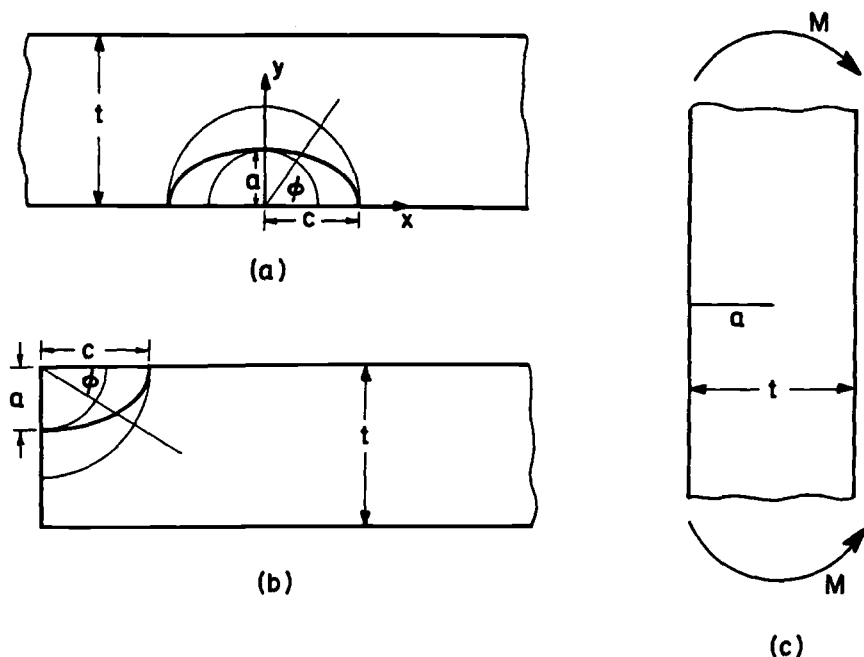


FIG. 2—(a) Semielliptical crack in a plate of thickness t , (b) quarter-elliptical crack in a plate of thickness t , (c) both loaded in bending ($\sigma_B = Mt/2I$).

K_I is taken from Ref 19 and given in Eq 36. This expression was determined from previously obtained finite-element results [20]. Employing Eqs 19 and 20, an approximate expression for the crack-opening displacement is obtained. Differentiation according to Eq 10 and substitution into Eqs 9a and 9b, together with expressions for the tensile stress-intensity factor (Eq 36) and crack perimeter, yield an integral for the unknown stress-intensity factor. With the stress distribution

$$\sigma(x, y) = 2\sigma_b \left(\frac{1}{2} - \frac{y}{t} \right) \quad (23)$$

where σ_b is the maximum bending stress, results are obtained for the stress-intensity factor. This applied stress is not elliptically symmetric. Details and an explicit expression for K_I are given in Appendix II. In Tables 1a, 1b, and 1c and Fig. 3, comparisons are made to an analytical expression determined from finite-element results [21]. (It should be noted that the expressions taken from Refs 19 and 21 are generally within 5% of the finite-element

TABLE 1a—Comparison of calculated K_I with that from Ref 21 for a semielliptical crack loaded in bending for $a/t = 0.0$ and $a/c = 0.4$.

$2\phi/\pi$	K_I	K_I [21]	Percent Difference
0.0	0.76	0.76	0
0.2	0.80	0.80	0
0.4	0.91	0.91	0
0.6	1.01	1.01	0
0.8	1.07	1.07	0
1.0	1.09	1.09	0

TABLE 1b—Comparison of calculated K_I with that from Ref 21 for a semielliptical crack loaded in bending for $a/t = 0.1$ and $a/c = 1.0$.

$2\phi/\pi$	K_I	K_I [21]	Percent Difference
0.0	1.04	1.10	5.5
0.2	0.99	1.02	2.9
0.4	0.96	0.96	0.0
0.6	0.94	0.93	-1.1
0.8	0.94	0.91	-3.3
1.0	0.94	0.90	-4.4

TABLE 1c—Comparison of calculated K_I with that from Ref 21 for a semielliptical crack loaded in bending for $a/t = 0.2$ and $a/c = 0.6$.

$2\phi/\pi$	K_I	K_I [21]	Percent Difference
0.0	0.77	0.87	11.5
0.2	0.75	0.80	6.3
0.4	0.79	0.79	0.0
0.6	0.83	0.80	-3.8
0.8	0.87	0.81	-7.4
1.0	0.88	0.82	-7.3

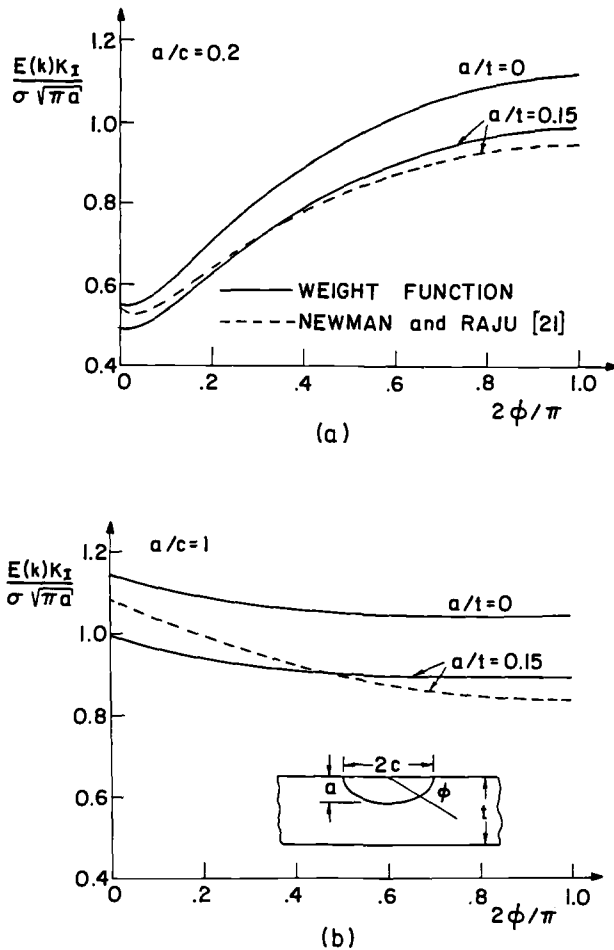


FIG. 3—Comparison of the nondimensional stress-intensity factor for a semielliptical crack loaded in bending as obtained by the weight function and Ref 21: (a) $a/c = 0.2$, (b) $a/c = 1$.

results). It may be observed that for $a/t = 0$ and all ratios of a/c , there is exact agreement between the stress-intensity factor determined here and the expression given in Ref 21. This result is not surprising since for this geometry (that is, a semielliptical crack in a half-space), the results for tension and bending are identical; hence, the formulation appears valid. As a/t increases, the results become poorer. In fact, for $a/t = 0.4$, differences as large as 30% were found. The deterioration of the results may be explained by considering that as the crack becomes longer, the bending effects become more important and the stress is less and less elliptically symmetric. Thus, it is apparent that the method is best for short cracks. Figure 3 illustrates results for $a/t = 0$ and 0.15, for two values of a/c ; the largest error is 9.2%. In Table 1c, results are presented for $a/t = 0.2$; here the largest error is 11.5%.

Finally, a quarter-elliptical crack in a finite thickness plate with the applied bending stress given in Eq 23 is examined (Fig. 2, *b* and *c*). Determination of the approximate weight function is accomplished with the stress-intensity factor for the same geometry with a remotely applied tensile stress perpendicular to the crack which is given in Eq 41 and taken

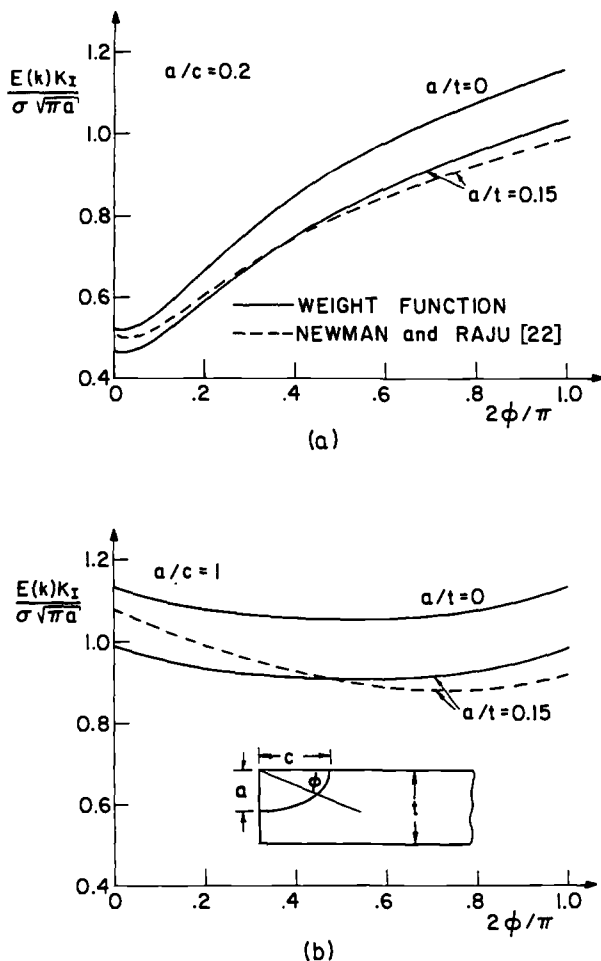


FIG. 4—Comparison of the nondimensional stress-intensity factor for a quarter-elliptical crack loaded in bending as obtained by the weight function and Ref 22: (a) $a/c = 0.2$, (b) $a/c = 1$.

from Ref 19. Manipulations similar to the ones carried out for the semielliptical crack in a plate lead to expressions for the stress-intensity factor in bending. Results are compared with expressions presented in Ref 22. It is again observed that acceptable results are obtained only for short cracks. For $a/t = 0.4$, the error grows to 25%. Results are presented in Fig. 4 for several values of a/c and a/t , with a/t remaining small. In addition, values of K_I are exhibited in Tables 2a, 2b, and 2c for different geometries. The same remarks made for the semielliptical crack can again be made here. Hence, it may be observed that the approximate method is useful, but applicable to short cracks only.

Conclusions

A three-dimensional weight function for the elliptical crack family has been presented. Closed form expressions for the weight function of the penny-shaped and elliptical crack in

TABLE 2a—Comparison of calculated K_I with that from Ref 22 for a quarter-elliptical crack loaded in bending for $a/t = 0.05$ and $a/c = 1.0$.

$2\phi/\pi$	K_I	K_I [22]	Percent Difference
0.0	1.08	1.11	2.7
0.2	1.03	1.04	1.0
0.4	1.01	1.01	0.0
0.6	1.01	1.00	-1.0
0.8	1.03	1.01	-2.0
1.0	1.08	1.06	-1.9

TABLE 2b—Comparison of calculated K_I with that from Ref 22 for a quarter-elliptical crack loaded in bending for $a/t = 0.1$ and $a/c = 0.6$.

$2\phi/\pi$	K_I	K_I [22]	Percent Difference
0.0	0.81	0.86	5.8
0.2	0.80	0.82	2.4
0.4	0.85	0.85	0.0
0.6	0.91	0.90	-1.1
0.8	0.98	0.95	-3.2
1.0	1.04	1.01	-3.0

TABLE 2c—Comparison of calculated K_I with that from Ref 22 for a quarter-elliptical crack loaded in bending for $a/t = 0.2$ and $a/c = 0.2$.

$2\phi/\pi$	K_I	K_I [22]	Percent Difference
0.0	0.45	0.52	13.5
0.2	0.57	0.60	5.0
0.4	0.72	0.72	0.0
0.6	0.84	0.81	-3.7
0.8	0.93	0.88	-5.7
1.0	1.00	0.95	-5.0

an infinite body subjected to axisymmetric and elliptically symmetric applied stresses, respectively, were obtained. Several loadings were considered, leading to exact solutions which agree with those in the literature. Since crack-opening displacements for more complicated crack geometries do not appear in the literature, an approximate weight function was proposed. This weight function was applied to the same problems for which there are known solutions which have been observed to yield excellent agreement. In addition, results with less than 14% error were obtained for short semielliptical and quarter-elliptical cracks in finite thickness plates subjected to bending.

Acknowledgment

The author is grateful to Prof. James R. Rice for his helpful comments.

APPENDIX I

Approximate Weight Function Method

For a given geometry and loading where only the stress-intensity factor is known (that is, the crack-opening displacement is not known), an approximate three-dimensional weight function can be determined by means of Eqs 19 and 20. The details of implementing these two equations for an elliptical crack embedded in an infinite body (Fig. 1) are described.

The stress-intensity factor is sought for a stress

$$\sigma(x, y) = \sigma \left[\left(\frac{x}{c} \right)^2 + \left(\frac{y}{a} \right)^2 \right] \quad (24)$$

applied perpendicular to the crack faces. The stress-intensity factor for that geometry with a constant remote applied stress is employed as the known solution. Of course, the crack-opening displacement is also known; this geometry is being employed for demonstration and comparative purposes only. The stress-intensity factor is given in Eq 16a and repeated here

$$K_I^* = \frac{\sigma \sqrt{\pi a} f_\phi}{E(k)} \quad (25)$$

where

$$f_\phi = \left[\sin^2 \phi + \left(\frac{a}{c} \right)^2 \cos^2 \phi \right]^{1/4}$$

The crack-opening displacement is approximated with the unknown functions $F(a/c, \phi)$ and $G(a/c, \phi)$ in Eq 19 as

$$w^*(r, a, c) = \frac{\sigma a}{\sqrt{2} H E(k)} \left[4 F\left(\frac{a}{c}, \phi\right) (1 - r)^{1/2} + G\left(\frac{a}{c}, \phi\right) (1 - r)^{3/2} \right] \quad (26)$$

For any crack of the elliptical crack family, the crack-opening displacement near the crack edge may be written as

$$w^* = \frac{2\sqrt{2} K_I^*}{H f_\phi} \sqrt{\frac{a}{\pi}} \sqrt{1 - r} \quad (27)$$

For r near unity, the second term in Eq 26 may be neglected. Substitution of Eq 25 into Eq 27 and comparison of this result with Eq 26 yields

$$F\left(\frac{a}{c}, \phi\right) = 1 \quad (28)$$

To determine $G(a/c, \phi)$, Eq 20 is employed; namely

$$\int_0^\xi [K_I^*(\xi)]^2 L d\ell(\xi) = H \int_A \sigma(r, \theta) w^*(r, a, c) dA \quad (29)$$

To evaluate the left side of Eq 29, a virtual crack extension is considered so that the crack expands in a self-similar manner; that is, it extends in its own plane with the ratio of the major and minor axes remaining constant. Thus

$$d\ell(\xi) = \frac{da}{f_\phi^2} \quad (30)$$

or

$$d\ell(\xi) = \frac{a}{c} \frac{dc}{f_\phi^2} \quad (31)$$

Substitution of Eq 25 and Eq 30 into the left side of Eq 29 with $L = 4cE(k)$, yields

$$\frac{4\pi\sigma^2 a^2 c}{3E(k)} \quad (32)$$

To evaluate the right side of Eq 29 and determine $G(a/c, \phi)$, Eq 26 is employed with $dA = acrd\theta$. Integration yields

$$\frac{4\sqrt{2}\pi\sigma^2 a^2 c}{5E(k)} \left[\frac{4}{3} + \frac{G}{7} \right] \quad (33)$$

Equating Eq 32 and Eq 33

$$G = \frac{7}{6} [5\sqrt{2} - 8] \quad (34)$$

To determine the stress-intensity factor for the applied quadratic stress given in Eq 24 and noting that $r^2 = (x/c)^2 + (y/a)^2$, Eqs 9 and 10 are employed, with K_1^* and w^* given in Eqs 25 and 26, respectively. The weight function is found to be

$$h(r, a, c) = \frac{\sqrt{2}f_\phi}{8E(k)c\sqrt{\pi a}} \left[4\sqrt{1-r} + \frac{2r}{\sqrt{1-r}} + G(1-r)^{3/2} + \frac{3}{2} Gr\sqrt{1-r} \right]$$

and the stress-intensity factor is

$$K_1 = \frac{\sigma\sqrt{\pi a}f_\phi}{E(k)} \frac{8\sqrt{2}}{63} \left[4 + \frac{3}{11} G \right] \quad (35)$$

The numerical coefficient in Eq 35 is 0.665 25, whereas, the numerical coefficient from the exact solution given in Eq 18c is 2/3, a difference of 0.21%.

APPENDIX II

Stress-Intensity Factors for Cracks in Bending

Determination of the stress-intensity factor for a semielliptical crack in a finite thickness plate in bending by means of the approximate formulation presented in Eqs 19 and 20 is outlined.

As the known stress-intensity factor K_I^* , the solution for a remotely applied constant stress σ , perpendicular to the crack face, is chosen. From Ref 19

$$K_I^* = \frac{\sigma\sqrt{\pi a}}{E(k)} \beta_s \left(\frac{a}{c}, \frac{a}{t}, \phi \right) \quad (36)$$

where

$$\left. \begin{aligned} \beta_s \left(\frac{a}{c}, \frac{a}{t}, \phi \right) &= \left[M_1 + M_2 \left(\frac{a}{t} \right)^2 + M_3 \left(\frac{a}{t} \right)^4 \right] g f_\phi \\ M_1 &= 1.13 - 0.09 \frac{a}{c} \\ M_2 &= -0.54 + \frac{0.89}{0.2 + \frac{a}{c}} \\ M_3 &= 0.5 - \frac{1}{0.65 + \frac{a}{c}} + 14 \left(1 - \frac{a}{c} \right)^{24} \\ g &= 1 + \left[0.1 + 0.35 \left(\frac{a}{c} \right)^2 \right] (1 - \sin \phi)^2 \end{aligned} \right\} \quad (37)$$

and f_ϕ is given in Eq 16b. These equations were fit through finite-element results [20] and are defined for $0 \leq a/c \leq 1$, $a/t \leq 1$, and $0 \leq \phi \leq \pi/2$.

In order to determine K_I for the bending stress given in Eq 23, the functions F and G of Eq 26 must be obtained. Substitution of Eq 36 into Eq 27 and comparison with Eq 26 for r near unity yields

$$F \left(\frac{a}{c}, \frac{a}{t}, \phi \right) = \left[M_1 + M_2 \left(\frac{a}{t} \right)^2 + M_3 \left(\frac{a}{t} \right)^4 \right] g \quad (38)$$

To obtain G , the expression for F , together with Eq 26, is substituted into the right side of Eq 29. Then, the integral is calculated, leading to an expression containing G . On the other hand, $L = 2cE(k)$ and Eq 36 are substituted into the left side of Eq 29, which is integrated. The solution for G leads to

$$G = 7 \left[\frac{5Q}{\sqrt{2}} - \frac{4F}{3} \right] \quad (39)$$

where

$$Q = \frac{d_0}{3} + \frac{d_2}{5} \left(\frac{a}{t} \right)^2 + \frac{d_4}{7} \left(\frac{a}{t} \right)^4 + \cdots + \frac{d_{12}}{15} \left(\frac{a}{t} \right)^{12}$$

$$d_0 = m_s^2 M_1^2$$

$$d_2 = 2m_s M_1 (m_s M_2 + m_6 M_1)$$

$$d_4 = m_5^2(2M_1M_3 + M_2^2) + 4m_5m_6M_1M_2 + m_6^2M_1^2$$

$$d_6 = 2m_5^2M_2M_3 + 2m_5m_6(2M_1M_3 + M_2^2) + 2m_6^2M_1M_2$$

$$d_8 = m_5^2M_3^2 + 4m_5m_6M_2M_3 + m_6^2(2M_1M_3 + M_2^2)$$

$$d_{10} = 2m_6M_3(m_5M_3 + m_6M_2)$$

$$d_{12} = m_6^2M_3^2$$

$$m_5 = 1 + 0.1(1 - \sin \phi)^2$$

$$m_6 = 0.35(1 - \sin \phi)^2$$

and M_1 , M_2 , and M_3 are given in Eq 37. The asymptotic crack-opening displacement w^* in Eq 26 is now known. Next w^* is differentiated according to Eq 10, substituted into Eq 9b to obtain the weight function, and Eq 9a is integrated with the stress from Eq 23. These manipulations lead to an expression for the stress-intensity factor as

$$K_I = \frac{\sigma_b \sqrt{\pi a} f_\phi}{FE(k)} \frac{2\sqrt{2}}{5\pi} \left\{ \frac{4}{3} (F + \tilde{F}) \left[\frac{\pi}{2} - \frac{8}{7} \left(\frac{a}{t} \right) \right] + \frac{8}{3} F \left[\frac{\pi}{2} - \frac{12}{7} \left(\frac{a}{t} \right) \right] \right. \\ \left. + \frac{1}{7} (G + \tilde{G}) \left[\frac{\pi}{2} - \frac{8}{9} \left(\frac{a}{t} \right) \right] + \frac{2}{7} G \left[\frac{\pi}{2} - \frac{4}{3} \left(\frac{a}{t} \right) \right] \right\} \quad (40)$$

where

$$\tilde{F} = 2 \left(\frac{a}{t} \right)^2 \left\{ g \left[M_2 + 2M_3 \left(\frac{a}{t} \right)^2 \right] + m_6 \left[M_1 + M_2 \left(\frac{a}{t} \right)^2 + M_3 \left(\frac{a}{t} \right)^2 \right] \right\}$$

$$\tilde{G} = 7 \left[\frac{5}{\sqrt{2}} \tilde{Q} - \frac{4}{3} \tilde{F} \right]$$

and

$$\tilde{Q} = \left(\frac{a}{t} \right)^2 \left[\frac{2d_2}{5} + \frac{4d_4}{7} \left(\frac{a}{t} \right)^2 + \frac{6d_6}{9} \left(\frac{a}{t} \right)^4 + \cdots + \frac{12d_{12}}{15} \left(\frac{a}{t} \right)^{10} \right]$$

In the same manner, the stress-intensity factor for a quarter-elliptical crack in a plate which is subjected to an applied bending stress may be found. The stress-intensity factor chosen as the known solution is for a remotely applied constant stress and is given as [19]

$$K_I^* = \frac{\sigma \sqrt{\pi a}}{E(k)} \beta_c \left(\frac{a}{c}, \frac{a}{t}, \phi \right) \quad (41)$$

where

$$\beta_c \left(\frac{a}{c}, \frac{a}{t}, \phi \right) = \left[M_1 + M_2 \left(\frac{a}{t} \right)^2 + M_3 \left(\frac{a}{t} \right)^4 \right] g_1 g_2 f_\phi$$

$$M_1 = 1.08 - 0.03 \frac{a}{c}$$

$$M_2 = -0.44 + \frac{1.06}{0.3 + \frac{a}{c}}$$

$$M_3 = -0.5 + 0.25 \frac{a}{c} + 14.8 \left(1 - \frac{a}{c} \right)^{15}$$

$$g_1 = 1 + \left[0.08 + 0.4 \left(\frac{a}{c} \right)^2 \right] (1 - \sin \phi)^3$$

$$g_2 = 1 + \left[0.08 + 0.15 \left(\frac{a}{c} \right)^2 \right] (1 - \cos \phi)^3$$

and f_ϕ is given in Eq 16b. These equations were fit through finite-element results and are defined for $0 \leq a/c \leq 1$, $a/t \leq 1$, and $0 \leq \phi \leq \pi/2$.

References

- [1] "Fatigue Growth of Corner Cracks at Holes," ASTM Round Robin, ASTM Task Group E24:06:01. Pittsburgh, PA, November 1983.
- [2] Bueckner, H. F., *Zuschrift für Angewandth Mathematic and Mechanik*, Vol. 50, 1970, pp. 529–546.
- [3] Rice, J. R., *International Journal of Solids and Structures*, Vol. 8, 1972, pp. 751–758.
- [4] Besuner, P. M. in *Mechanics of Crack Growth*, ASTM STP 590, American Society for Testing and Materials, Philadelphia, 1976, pp. 403–419.
- [5] Cruse, T. A. and Besuner, P. M., *Journal of Aircraft*, Vol. 12, 1975, pp. 369–375.
- [6] Besuner, P. M., *Nuclear Engineering and Design*, Vol. 43, 1977, pp. 115–154.
- [7] Bueckner, H. F. in *Fracture Mechanics and Technology*, Sijthoff and Noordhoff, Amsterdam, The Netherlands, Vol. II, 1977, pp. 1069–1090.
- [8] Labbens, R. C., Heliot, J., and Pellissier-Tanon, A. in *Cracks and Fracture*, ASTM STP 601, American Society for Testing and Materials, Philadelphia, 1976, pp. 448–470.
- [9] Vanderglas, M. L., *International Journal of Fracture*, Vol. 14, 1978, pp. R291–R294.
- [10] Parks, D. M. and Kamenetsky, E. H., *International Journal for Numerical Methods in Engineering*, Vol. 14, 1979, pp. 1693–1706.
- [11] Vanderglas, M. L. in *Numerical Methods in Fracture Mechanics*, D. R. J. Owen and A. R. Luxmoore, Eds., Pineridge Press, London, United Kingdom, 1980, pp. 51–66.
- [12] Grandt, A. F., Jr., *International Journal of Fracture*, Vol. 11, 1975, pp. 283–294.
- [13] Grandt, A. F., Jr., *International Journal of Fracture*, Vol. 14, 1978, pp. 221–229.
- [14] Bortman, Y. and Banks-Sills, L., *Journal of Applied Mechanics*, Vol. 50, 1983, pp. 907–909; *Errata*, Vol. 51, 1984, p. 711.
- [15] Banks-Sills, L. and Bortman, Y., *International Journal of Fracture*, Vol. 30, 1986, pp. 181–201.
- [16] Tada, H., Paris, P., and Irwin, G. R., *The Stress Analysis of Cracks Handbook*, Section 24, Del Research Corp., St. Louis, MO, 1973.
- [17] Kassir, M. K. and Sih, G. C. in *Mechanics of Fracture 2: Three-Dimensional Crack Problems*, Noordhoff International Publishing, Amsterdam, The Netherlands, 1975, pp. 74–117.
- [18] Petroski, H. J. and Achenbach, J. P., *Engineering Fracture Mechanics*, Vol. 10, 1978, pp. 257–266.
- [19] Newman, J. C., Jr., and Raju, I. S. in *Fracture Mechanics: Fourteenth Symposium—Vol. I: Theory and Analysis*, ASTM STP 791, American Society for Testing and Materials, Philadelphia, 1983, pp. 238–265.
- [20] Raju, I. S. and Newman, J. C., Jr., *Engineering Fracture Mechanics*, Vol. 11, 1979, pp. 817–829.
- [21] Newman, J. C., Jr., and Raju, I. S., *Engineering Fracture Mechanics*, Vol. 15, 1981, pp. 185–192.
- [22] Newman, J. C., Jr., and Raju, I. S., "Stress-Intensity Factor Equations for Cracks in Three-Dimensional Finite Bodies Subjected to Tension and Bending Loads," NASA-TM 85793, National Aeronautics and Space Administration, Washington, DC, 1984.

R. H. Van Stone,¹ M. S. Gilbert,¹ O. C. Gooden,¹ and J. H. Laflen¹

Constraint-Loss Model for the Growth of Surface Fatigue Cracks

REFERENCE: Van Stone, R. H., Gilbert, M. S., Gooden, O. C., and Laflen, J. H., "Constraint-Loss Model for the Growth of Surface Fatigue Cracks," *Fracture Mechanics: Nineteenth Symposium, ASTM STP 969*, T. A. Cruse, Ed., American Society for Testing and Materials, Philadelphia, 1988, pp. 637–656.

ABSTRACT: As surface flaws grow in high-strength nickel-base superalloys, the growth along the free surface (dc/dN) can be much slower than growth in the depth direction (da/dN), even after accounting for variations in K along the crack front. This behavior reduces the crack aspect ratio (c/a) and can result in the formation of stable shear lips at the free surface during fatigue crack growth. Trantina et al. recently performed elastic-plastic finite-element analyses of surface cracks which showed that as the applied stress approached the elastic limit, a relatively large region of constraint loss was observed where the crack front intersects the free surface. This concept was used to develop a constraint-loss modification to the Newman-Raju K solution for the surface flaw problem. This model has been applied to physically small surface crack growth in the advanced nickel-base superalloy René 95. The predicted results match the dc/dN data, which are slower than and not parallel to the corresponding da/dN - K data. This model has been combined with a dual-Walker exponent approach to model nonzero stress (R) ratios. This methodology has been used to predict the residual lives of surface flaws growing in both uniform and nonuniform stress fields within a factor of two of the experimentally observed lives. This model has also been successfully applied to small surface flaws and can predict the lives of cracks with depths (a) as small as 65 μm (0.0025 in.).

KEY WORDS: life prediction, surface flaws, nickel-base superalloys, fatigue crack growth, small cracks, fracture mechanics

The prediction of surface flaw growth under cyclic loading conditions is among the more challenging problems in linear elastic fracture mechanics (LEFM). This problem has been aided in recent years by the development of improved stress-intensity solutions such as that proposed by Newman and Raju [1]. This development has greatly assisted this problem, but investigations of nickel-base superalloys [2,3] have shown that the growth in the depth direction is faster than the crack growth along the surface, resulting in changes in crack aspect ratio as the crack grows. This feature must be modeled in order to make accurate crack growth predictions. This paper will describe the development of such a model for René 95, a high-strength γ - γ' nickel-base superalloy, and its comparison with experimental data.

¹ Senior engineer, engineer, specialist, and manager, respectively, Materials Life and Methods, GE Aircraft Engines, Cincinnati, OH 45215.

Background

The crack growth and K solutions of surface flaws is complicated by the change in stress intensity around the periphery of the crack. For the remainder of this paper, the crack depth will be referred to as a and the surface length will be $2c$. The K solution is a function of both a and c . This results in different crack growth rates in both the depth (da/dN) and along the free surface (dc/dN). This variation does not cause difficulties unless the appropriate crack growth rates cannot be described by the values of K at the depth (K_a) and surface positions (K_c). Yau [2] showed that even when considering the local stress-intensity factors, dc/dN was slower than da/dN in Alloy 718. In the intermediate range of crack growth rates (Region II), the slopes of the da/dN and dc/dN curves were the same, but the value of K_c had to be reduced by 12% so that the da/dN and dc/dN curves coincided.

The situation for other alloys is even more complicated. Figure 1a shows the crack growth rates measured in hot isostatic pressing (HIP)-compacted René 95 surface-flawed specimens at room temperature [3]. These results are for five specimens tested at three different maximum stress levels ranging from 689 to 1034 MPa (100 to 150 ksi) with a stress ratio (R = minimum stress/maximum stress) of zero. Figure 1a shows that Region II da/dN and dc/dN curves are not parallel, but diverge with increasing levels of K . Figure 1b shows the variation in crack aspect ratio (c/a) as a function of crack depth for these five specimens.

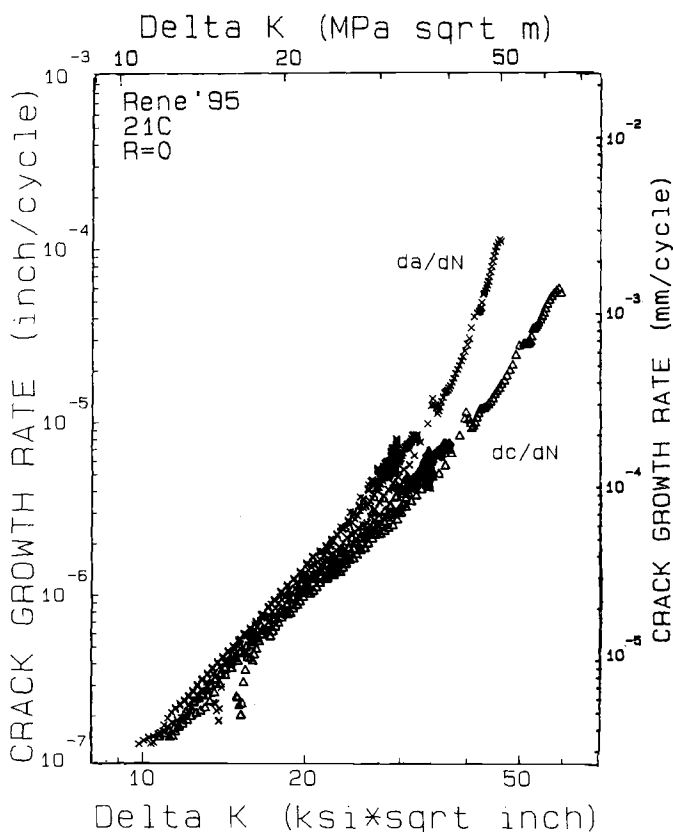


FIG. 1a—The crack growth rates of HIP-compacted René 95 at room temperature.

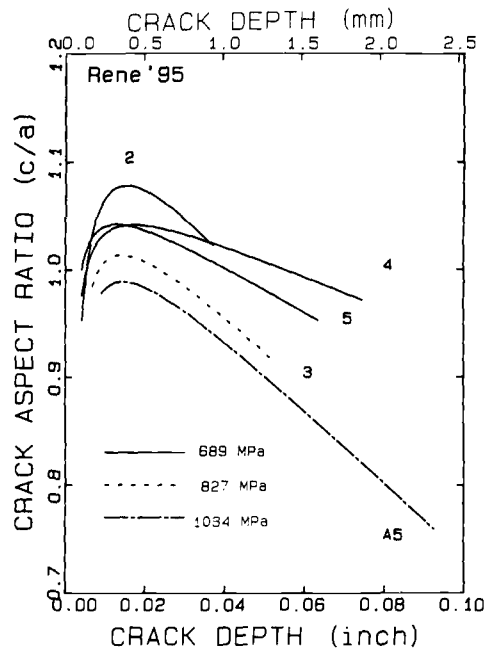


FIG. 1b—The variation in aspect ratio with crack length corresponding to the crack growth rates of HIP-compacted René 95 at room temperature.

The aspect ratio diminishes with increasing crack depth and is sensitive to the applied stress level. Along with the variations in aspect ratio, shear lips can form along the surface of specimens. Figure 2 shows a photograph of a broken crack growth specimen of extruded plus isothermally forged René 95. This specimen was tested at 399°C (750°F) with a maximum stress of 827 MPa (120 ksi) and a stress ratio (R) of 0.05. The large shear lips form during the growth of the fatigue crack. The methods developed in this investigation do not model the complex Mode II and III features of the shear lips, but attempt to model the fracture mechanics field parameters that cause the change in the aspect ratio.

It is well accepted that shear lips which form along the specimen surfaces during monotonic toughness testing are related to a loss of constraint. Andrews and Shih [4] showed that the stress-intensity factor in compact (through-crack) specimens is lower at the specimen surface than at its midplane. This was caused by more extensive yielding at the surface than at interior locations. This phenomenon is generally described by the term constraint-loss, indicating loss of plane strain constraint. It is generally accepted that surface flaw geometries experience less constraint-loss than the corresponding situation in a through-crack geometry. Trantina and co-workers [5,6] performed a three-dimensional finite-element analysis of a small, semicircular surface flaw. The finite-element analysis was performed to model monotonic loading to several levels of remote strain. The stress-intensity factor was determined at several positions along the crack front by calculating the value of the path-independent J integral and converting it to K , using the assumptions of small-scale yielding. Some of their results are reproduced in Fig. 3. Figure 3a shows the geometry factor

$$F = \frac{\pi K}{2\sigma\sqrt{\pi a}} \quad (1)$$

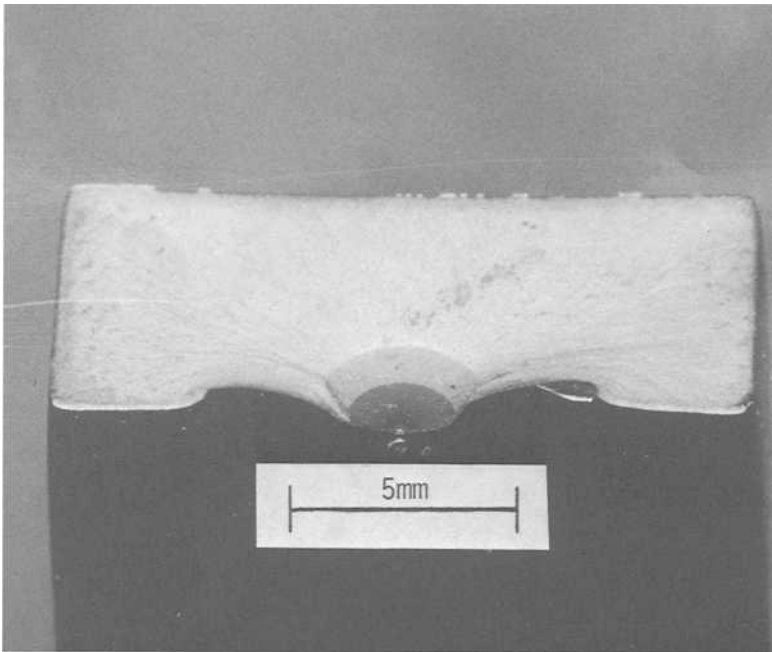


FIG. 2—*Photograph of a surface flaw test specimen of extruded and isothermally forged René 95 tested at 399°C (750°F) showing stable cyclic shear lips.*

as a function of the position around the crack. The zero degree position corresponds to the specimen surface. This figure shows that increasing strain increases K at the symmetry line (90°), but initially reduces it at the specimen surface.

The results in Fig. 3a were normalized with respect to the K at the symmetry line and replotted in Fig. 3b. This figure shows that increasing strain causes reductions of K at the surface relative to that at the symmetry line. The situations modeled by Trantina et al. [5,6] included plastic strains greater than those usually seen in most engineering applications. The point of greatest interest is the constraint loss between the elastic and $0.71 \epsilon_o$ case. For these two cases, the K at the symmetry line increased by approximately 5%, while the K at the surface diminished by approximately 6%. As shown in Fig. 3b, this resultant swing in relative K is approximately 11%. Trantina and de Lorenzi [6] used the results shown in Fig. 3b to model the change in crack shape under cyclic loading. Figure 3c shows that for an initially semicircular crack, the elastic-plastic analysis shows a tucking-in of the crack near the surface. This was not observed for the elastic analysis. Cracks of this shape are frequently observed in testing of René 95. For a crack of this shape, it is assumed that the proper value of c is the maximum length of the crack parallel to the free surface and not the shorter length on the specimen surface. This change in shape accompanies the change in aspect ratio shown in Fig. 1b. These results suggest that the change in crack shape, and possibly the shear lip formation, is caused by loss of constraint at the specimen surface.

Fracture Mechanics Model

Based on the analysis of Trantina et al. [5,6] and the observed behavior of René 95, a constraint-loss model was developed. It was designed to modify the Newman-Raju [1]

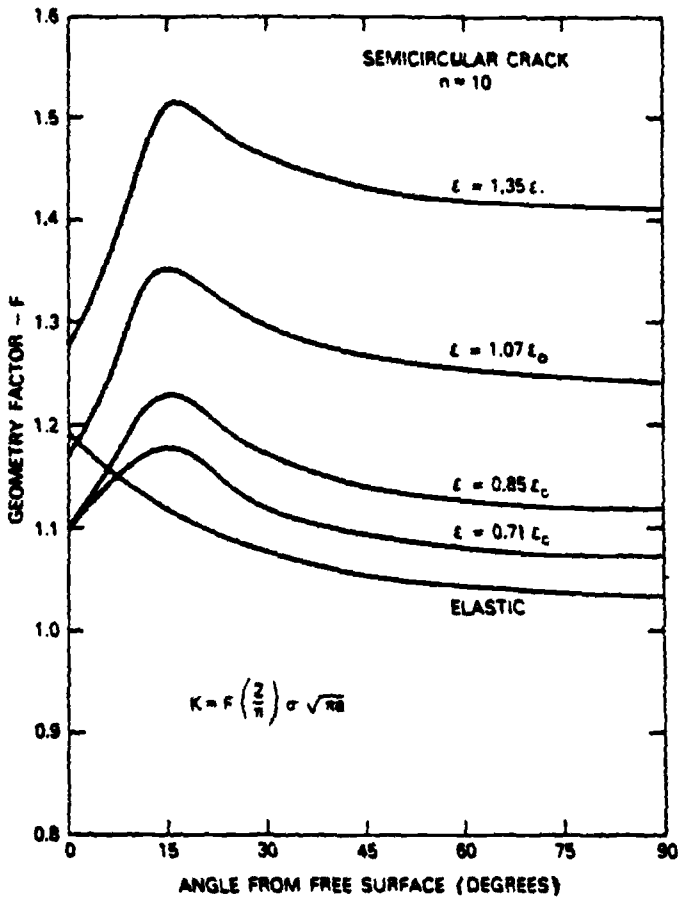


FIG. 3—Results of elastic-plastic finite-element analysis of a surface flaw: (a) showing the variation of K around the crack perimeter.

solution at the surface. It was assumed that the loss in K at the surface was proportional to the plastic zone size at the surface

$$\frac{K}{K_{el}} = \beta - A r_p \quad (2)$$

where

- K = actual K at the surface,
- K_{el} = K at surface as calculated by the elastic solution [1],
- r_p = plastic zone size at surface, and
- A, β = positive-valued constants.

The value of β should be close to unity. There may be some deviation in β from unity because of the inaccuracies of the Newman-Raju K solution at the surface. Newman [7] noted the potential errors associated with a high sensitivity of the surface K to finite-element

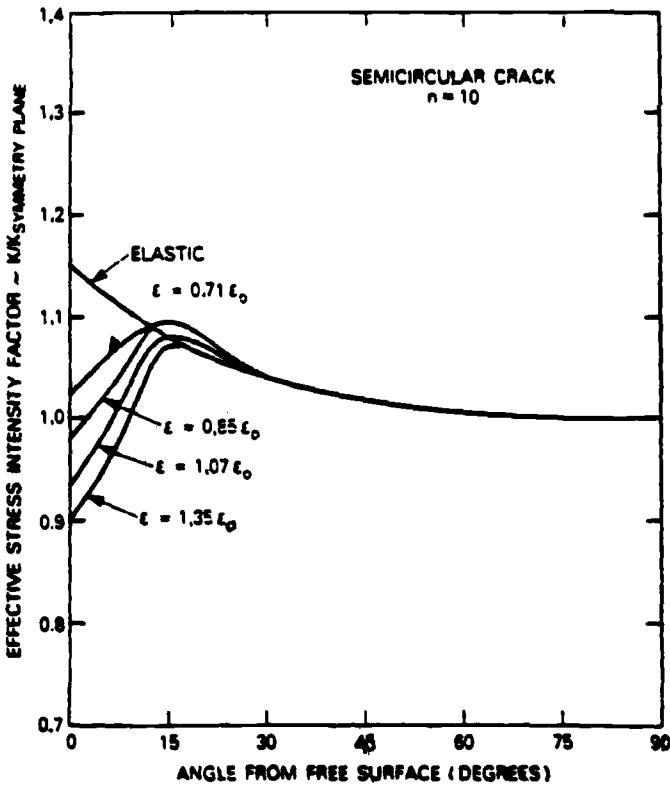


FIG. 3—Continued: (b) showing the variation of K at the surface normalized relative to K at the symmetry plane.

mesh size. The plastic zone size can be defined in a general fashion as

$$r_p = B \left(\frac{K}{\sigma_y} \right)^2 \quad (3)$$

where σ_y = yield strength and B = a constant. Substitution of Eq 3 into Eq 2 yields

$$\frac{K}{K_{el}} = \beta - AB \left(\frac{K}{\sigma_y} \right)^2 \quad (4)$$

This relationship is rather difficult to deal with, especially for cyclic deformation, due to the uncertainty in knowing the proper value of B and what type of yield stress (monotonic or cyclic and plane stress or plane strain) to use for σ_y . This issue was sidestepped by letting AB/σ_y^2 be the arbitrary constant α .

$$\frac{K}{K_{el}} = \beta - \alpha K^2 \quad (5)$$

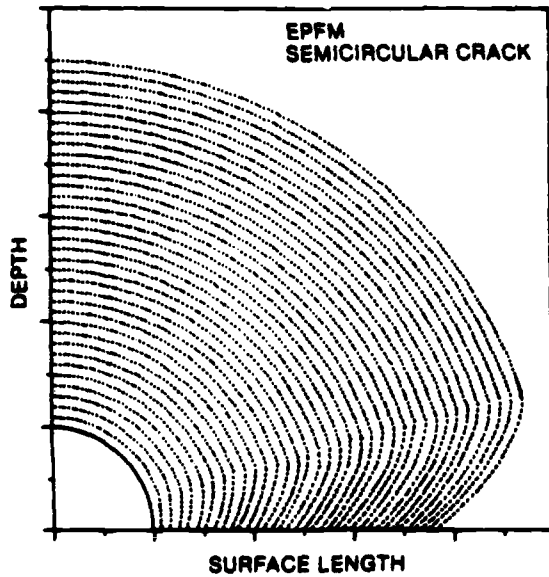


FIG. 3—Continued: (c) showing the predicted variation of the crack shape as the crack grows.

This expression can be rearranged and solved for K

$$K = \frac{\sqrt{1 + 4\alpha\beta K_{el}} - 1}{2\alpha K_{el}} \quad (6)$$

This equation can then be used to determine K from an elastic solution if α and β are known.

This constraint-loss model was employed in conjunction with a mean stress crack growth rate model. In the dual-Walker exponent mean-stress model [8], the effective K is defined as

$$K_{eff} = K_{max}(1 - R)^m \quad (7)$$

where

- K_{eff} = effective K ,
- K_{max} = maximum K ,
- R = minimum K /maximum K , and
- m = Walker exponent.

A different value of m is used for positive and negative stress ratios (m^+ and m^-). The rationale behind the dual-Walker exponent model is that the behavior for negative R -ratios is much different than for positive ones due to the relative amount of crack closure which exists. This model has been shown to work for several different nickel-base superalloys [8–10].

These models are then combined, and nonlinear optimization was performed to determine the values of the constants α , β , m^+ , and m^- . These were combined with a Knaus or

modified sigmoidal crack growth rate curve [11]. This was then programmed into a residual life computer code which was used to calculate the residual life.

Crack Growth Data and Modeling

The material used to develop and verify the constraint-loss model was extruded plus isothermally forged René 95. This is a powder metallurgy, γ - γ' alloy which was extruded and isothermally forged into a turbine disk shape. The composition and processing of this alloy are described elsewhere [12]. The crack growth data were obtained using single-edge-notched (SEN) and surface-flawed specimens frequently referred to as K_b specimens [3,11]. All specimens were tested using a d-c potential drop system based on the one developed by Gangloff [13]. The K_b specimen test method was that described by Van Stone and Richardson [3]. The crack growth rate data were analyzed using a seven-point sliding polynomial method and the Newman-Raju K solution [1] with a plasticity correction as described by Yau [2]. The SEN specimen test method was that developed by Wilcox and Henry.² The potential data were converted to crack length using the Johnson [14] potential solution. A microcomputer controlled the load to a prescribed K crack-length schedule. This type of test was used to obtain near-threshold crack growth rate data using a K -shed routine and Region II (Paris law regime) using an increasing K routine. The crack growth rates were analyzed using the seven-point sliding polynomial technique. The stress-intensity factors were determined using the Tada [15] K solution as modified by a plasticity zone correction term [2]. The details of this test method and data analysis procedure are described elsewhere [10]. Tests were performed at several elevated temperatures. The SEN specimens were heated by resistance furnaces and the K_b specimens were heated by induction. All tests were performed at a frequency of 0.33 Hz (20 cpm) in laboratory air.

The conversion of the crack growth rate data into crack growth rate curves had three steps:

1. Determination of Walker exponents (m^+ and m^-) from Region II da/dN and $(K)_a$ data.
2. Determination of the crack growth rate curve from all da/dN and $(K_{eff})_a$ data.
3. Determination of constraint-loss model values α and β from the da/dN curve (Step 2) and K_b dc/dN and $(K_{eff})_c$ data.

This process will be illustrated for crack growth rate tests performed at 399°C (750°F). This same procedure was followed for data at other test temperatures with no difficulty. SEN (threshold) tests were performed at R -ratios of 0.05 and 0.60. K_b specimen tests were performed at R -ratios of -1.0, -0.5, 0, 0.05, 0.25, 0.60, and 0.75. There were usually two K_b tests performed at each stress ratio—one at a high stress and one at a low stress. The maximum stresses in these tests ranged from 482 to 1034 MPa (70 to 150 ksi). These stresses are all below the yield strength of René 95 at this temperature.

Figure 4 shows the da/dN - K data from the SEN tests and the da/dN -(K)_a data from the K_b specimen tests at 399°C (750°F). Different symbols were used for data at each stress ratio. There does not appear to be any difference between the surface-flaw (K_b specimen) and through-crack (SEN specimen) tests. Most of the near-threshold data were obtained using SEN specimens. The Walker exponents were determined from the Region II data shown in Fig. 4, using a multilinear regression analysis of the data to the Walker relationship (Eq 7) combined with a Paris type law as described elsewhere [8]. The Walker exponents, m^+ and m^- , were then used to calculate the effective K at both the depth and surface

² Wilcox, J. R. and Henry, M. F., General Electric Corporate Research and Development, Schenectady, NY 12301, unpublished research.

locations, $(K_{\text{eff}})_a$ and $(K_{\text{eff}})_c$, respectively. Figure 5 shows the resultant da/dN and dc/dN data plotted against the appropriate value of K_{eff} . There are not very many near-threshold dc/dN data because dc/dN data cannot be obtained in the SEN through-crack specimens. These data show that the dual-Walker exponent approach [8] accurately models the influence of R on fatigue crack growth. This approach successfully worked in the near-threshold regime even though no Region I data were used to determine m^+ . Similar results have been observed for a variety of high-strength nickel-base superalloys [16]. Nonlinear optimization was used to determine the coefficients of the Knaus fatigue crack growth rate curve.

The final step in the determination of the material constants was the application of the constraint-loss constants. The goal of the constraint-loss model was to adjust $(K_{\text{eff}})_c$ so that the dc/dN data and the da/dN data populate the same curve. A least squares regression analysis was performed to determine the values of α and β in Eq 5. The values of $(K_{\text{el}})_c$ are those shown in Fig. 5b. For each data point, the $(K_{\text{el}})_c$ was determined by finding the value of $(K_{\text{el}})_a$ which corresponds to dc/dN . This process is shown schematically in Fig. 6. Figure 7 shows the resulting da/dN and dc/dN curves as a function of K_{el} . The value of $(K_{\text{el}})_c$ used in Fig. 7 was determined using a rearrangement of Eq 5

$$(K_{\text{el}})_c = \frac{(K)_c}{\beta - \alpha(K)_c^2} \quad (8)$$

The close agreement between the experimental data and the curves suggests that this constraint-loss model is a realistic way to model crack growth in René 95.

The procedure described in this section was repeated for crack growth data determined at 538 and 593°C (1000 and 1100°F). The constraint-loss model worked equally well for those conditions.

Methods Verification

The quality of a residual life estimation methodology is not solely the ability to construct accurate crack growth rate curves, but the accurate prediction of lives of both simple laboratory specimens and feature tests which simulate the geometry (stress concentration) where this methodology might be applied. A two-tiered qualification program was performed:

1. Prediction of the K_b specimen data used to establish the crack growth rate curves.
2. Prediction of residual lives for specimens where the crack grows out of a stress concentration in feature tests.

The specimen used for the feature tests was a double-edge-notched specimen whose geometry is shown in Fig. 8. Surface cracks were grown from semicircular-shaped electric-discharge-machined (EDM) notches placed at the center of one side of the machined notches. Feature tests were performed at both 399 and 593°C (750 and 1100°F). Table 1 shows the feature test matrix. The 0.2% offset yield strength of René 95 at 399 and 593°C (750 and 1100°F) is 1210 and 1175 MPa (176 and 171 ksi), respectively. The net section stresses used in the feature tests were 489 and 820 MPa (71 and 119 ksi). These stress levels are low enough to avoid net section yielding. As with the K_b and SEN tests used to determine the crack growth rates, the feature tests were cycled at a frequency of 0.33 Hz (20 cpm).

An in-house, elastic-plastic finite-element code which utilizes constant-strain triangular elements was used to analyze the double-edge-notched specimen geometry. A two-dimensional, elastic-plastic finite-element analysis was performed on this specimen using the finite-element mesh shown in Fig. 9. Elastic analysis showed that this specimen had an elastic stress concentration of 1.76. Finite-element analyses were performed at net section stresses

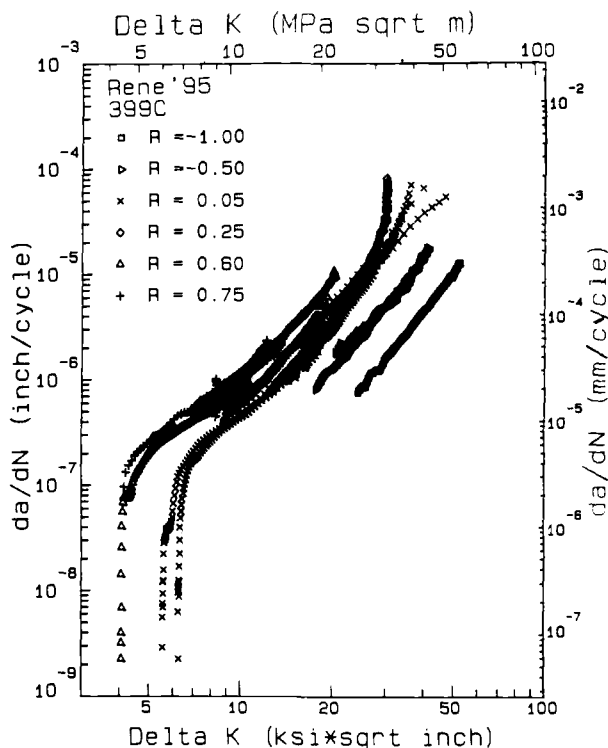


FIG. 4—The influence of R-ratio on the crack growth rates (da/dN) of René 95 at 399°C (750°F).

of 489 and 820 MPa (71 and 119 ksi) to simulate the loading of the test specimens. The resultant stress distributions were used to predict the residual lives in the feature tests. The finite-element analyses were performed using both the 399 and 593°C (750 and 1100°F) constitutive relationships for René 95.

The residual lives were predicted using an in-house computer code. The main features of this code were previously described by Yau [2]. That code utilizes the Newman-Raju [1] K solution for surface flaws and uses an influence function method [2] to calculate K values in the presence of a stress gradient. Since the work of Yau [2], that code has been modified to use the constraint-loss model described in this paper. The finite-element analyses showed that for the loadings used on these feature tests, the minimum stresses could be predicted

TABLE 1—Feature specimen test matrix.

Test Temperature	R	Maximum Net Section Stress MPa
399°C	0.00	819
	0.00	489
	0.50	819
	0.60	819
593°C	0.00	819
	0.00	489
	0.25	819
	0.50	819

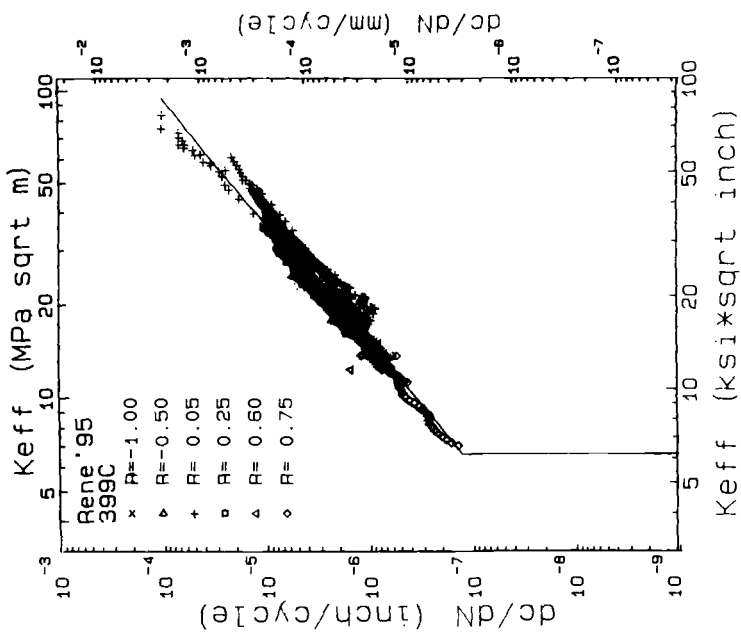


FIG. 5—Continued: (b) dc/dN with $(K_{eff})_c$.

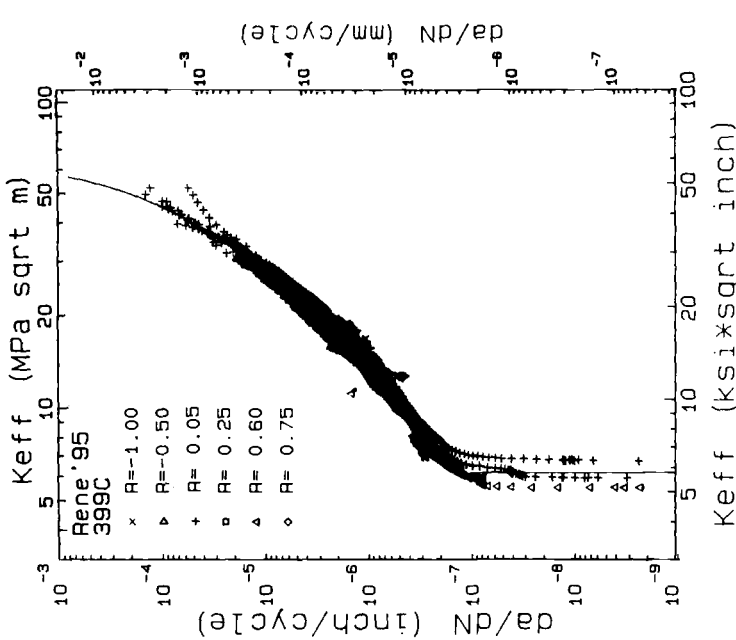


FIG. 5—Variations of 399C (750°F) Rene 95: (a) da/dN with $(K_{eff})_a$.

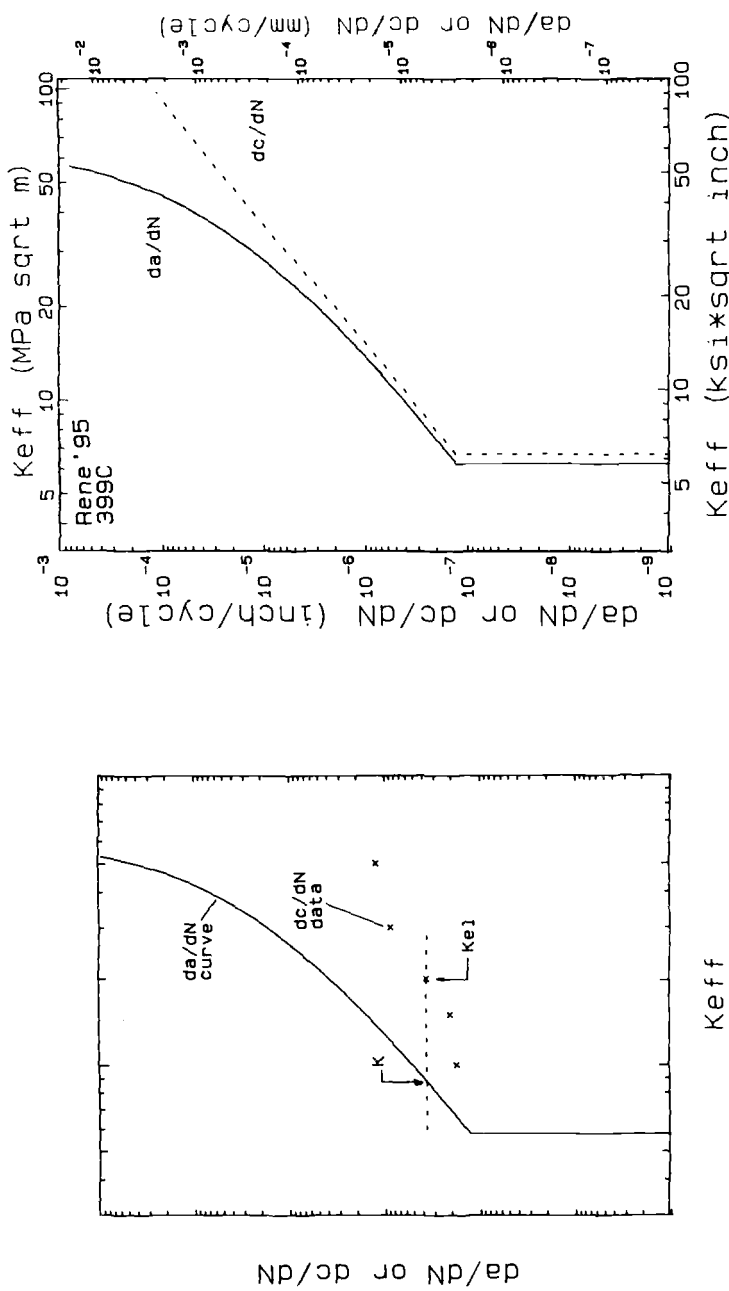


FIG. 6—Schematic diagram showing the definitions of $(K_{eff})_c$ and $(K)_c$ used in determining the constraint-loss constants.

FIG. 7—Variation of the 399°C (750°F) Rene 95 da/dN and dc/dN curves with K_{eff} .

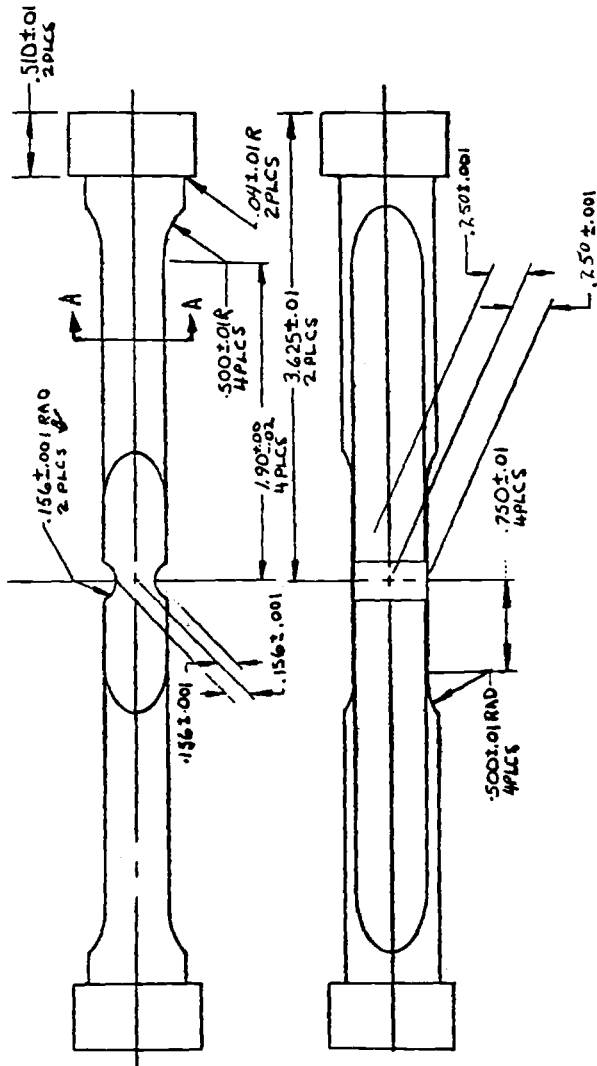


FIG. 8—Drawing of double-edge-notched feature test. The dimensions are in inches; $1 \text{ in.} = 25.4 \text{ mm.}$

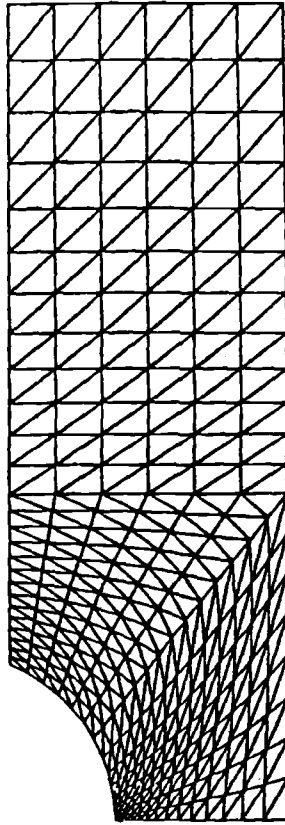


FIG. 9—Finite-element mesh used to analyze the double-edge-notched feature specimen.

quite accurately by subtracting the elastic stress distribution resulting from the load range from the stress distribution at the maximum loading condition. This is very important for the highest stress feature tests, where localized monotonic yielding occurred during initial loading, followed by elastic cycling. For this case, the value of R used in the crack growth calculations is the value calculated using the minimum and maximum values of K and not necessarily the R -ratio from the loads applied to the test specimen. It should be noted that this effect dies out as the crack front leaves the region of local plasticity at the root of the notch.

K_b Specimen Results

A total of 29 K_b specimens were tested in determining the crack growth rate curves at 399, 538, and 593°C (750, 1000, and 1100°F). The initial crack sizes used to predict the specimen life were those measured from the specimen fracture surfaces after completion of the tests. Many of the specimens were tested using the potential drop technique [3], where the tests were terminated prior to failure of the specimens. For those cases, the calculated residual lives were those calculated from the initial crack size, until the predicted crack depth equaled the final experimentally observed crack depth.

The predicted and experimentally observed residual lives of these 29 K_b specimens are

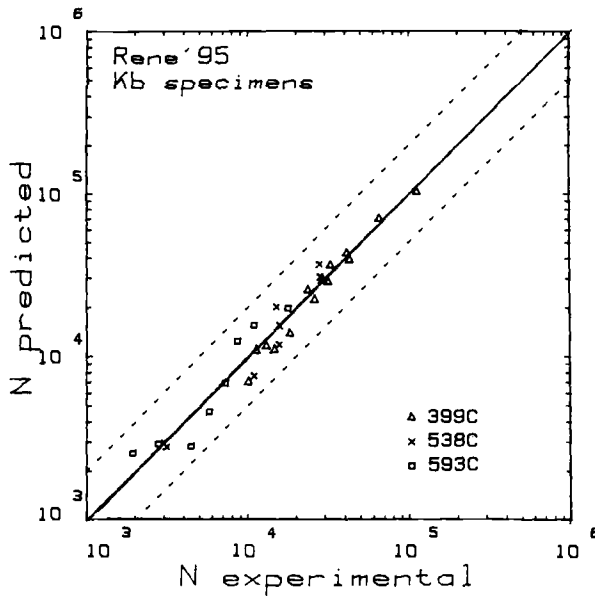


FIG. 10—Comparison of predicted and observed residual lives for 29 K_b specimens of René 95.

shown in Fig. 10. Tests at different temperatures are differentiated by different symbols. The solid line corresponds to perfect agreement between the observed and the predicted lives. The dashed lines enclose the region with less than a factor of two difference between predicted and observed lives. The ratios between the predicted and observed lives were statistically analyzed. The distribution of these lives seemed to follow a log-normal distribution. The mean of the log normal distribution was a ratio of 0.96. The ratio at the average minus three standard deviations was 0.50. The ratio at mean plus three standard deviations was 1.86. These results show that this life prediction method can accurately predict residual lives over a range of conditions.

The ratio of predicted to observed lives has been plotted as a function of maximum stress and R -ratio in Fig. 11. The dashed lines in these figures represent a factor of two in life scatter bands. Figure 11a shows very little influence of applied stress. Figure 11b shows that

TABLE 2—Ratio of predicted to observed lives for feature tests.

Test Temperature, °C	R	Maximum Net Section Stress, MPa	Experimental Cycles to Failure	Predicted Cycles to Failure	$\frac{N_{pred}}{N_{exp}}$
399	0.00	819	11 430	4 911	0.430
	0.00	489	27 790	19 435	0.699
	0.50	819	25 645	19 045	0.743
	0.60	819	39 693	28 923	0.729
593	0.00	819	1 893	1 806	0.954
	0.00	489	6 995	6 101	0.872
	0.25	819	1 907	2 122	1.113
	0.50	819	4 623	4 301	0.931

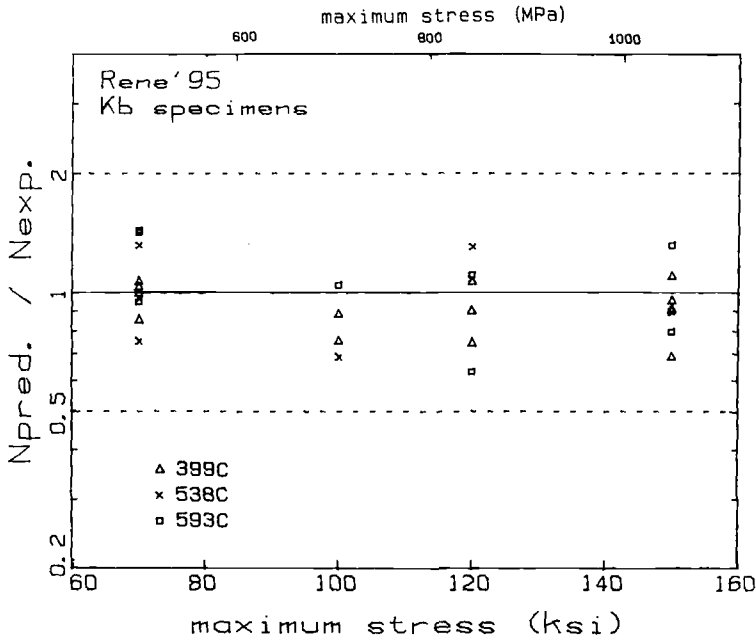


FIG. 11—Variation of ratio of predicted-to-observed lives for René 95 K_b specimens with (a) maximum stress.

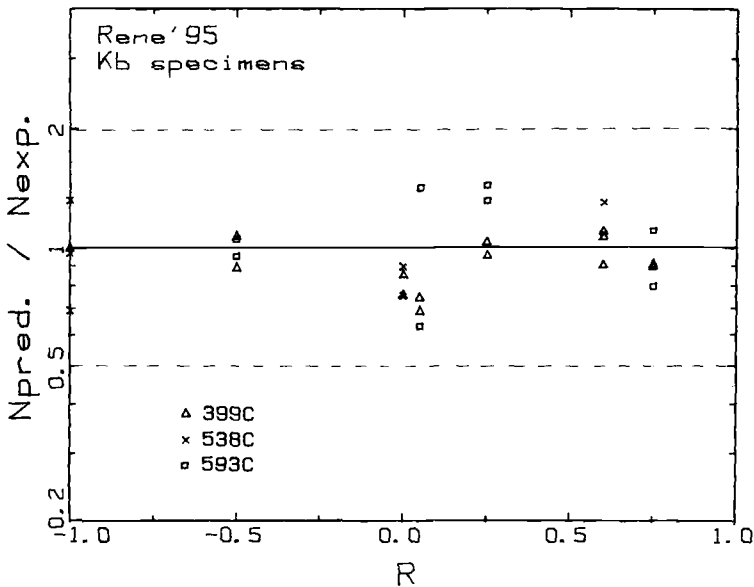


FIG. 11—Continued: (b) with R-ratio.

variations in the stress ratio (R) do not cause large variations in the ability to predict residual lives. Close examination of that figure shows that near $R = 0$, there is a slight conservatism in the predicted lives.

Feature Test Predictions

The crack lengths in the feature tests were monitored using a low-power optical microscope. Approximately 40 crack-length measurements were made during each test. These specimens were cycled until failure occurred. The EDM notch with its finite radius did not act as a sharp crack. To avoid this difficulty, the number of cycles from the start of the test until visual observation of surface cracking was observed was subtracted from the cycles to failure. The initial crack size was assumed to have the same aspect ratio as the EDM starter notch and a surface length equal to the first visual observation of cracking out of the EDM notch. Table 2 shows the ratio of the predicted-to-observed lives for the eight double-edge-notched feature tests. The residual lives of the 593°C (1100°F) tests are predicted well. The predictions of the 399°C (750°F) tests were all conservative. The high-stress, $R = 0$ test was especially conservative. The combination of high-maximum and alternating stress resulted in excessive shear-lip formation in that test. A photograph of that specimen is shown in Fig. 12. This specimen had the most tortuous, out-of-plane cracking of any specimen tested in this investigation. These results, combined with the ability to predict K_{I} specimen lives, suggest that the constraint-loss model properly models the controlling field parameters, but may not properly model the full detail of shear lips, especially in severe cases such as that shown in Fig. 12.

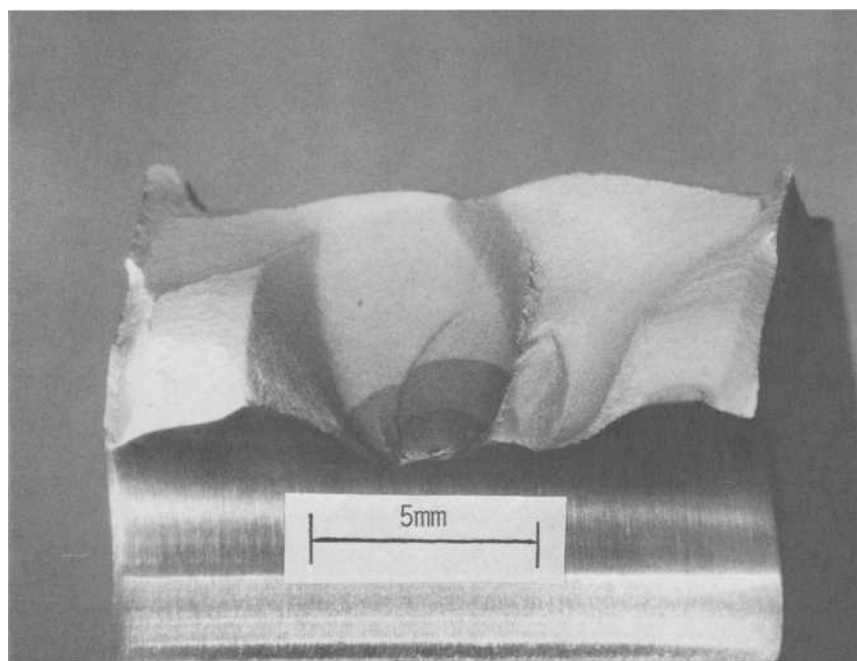


FIG. 12—Photograph of René 95 double-edge-notched feature test, tested at 399°C (750°F), with a net section stress of 820 MPa (119 ksi) and a stress ratio of 0.

These results show excellent agreement between the predicted and observed lives. When errors do occur, such as for the case of excessive shear lips, the predictions are conservative relative to the observed lives. This indicates that the constraint-loss model is an accurate method by which to predict the crack growth behavior of René 95.

Short Crack Predictions

The data reported in the previous sections were determined in specimens containing semicircular EDM notches with radii ranging from 0.10 to 0.25 mm (0.004 to 0.01 in.). The resulting precracks ranged from approximately 0.15 to 0.50 mm (0.006 to 0.020 in.). These crack sizes are in the range of interest for design conditions where the initial flaw size is based on nondestructive testing inspection limits, but the verification of its accuracy for much smaller cracks would be extremely useful in some applications. In a separate investigation,³ crack growth experiments were performed in K_{Ic} specimens of René 95 where precracks were grown from semicircular EDM notches, but the EDM notch was machined away prior to the start of the test. Thus, these tests had much smaller initial flaw sizes than those reported in previous sections of this paper. A total of nine tests were performed. The test variables included four temperatures, maximum stresses ranging from 689 to 896 MPa (100 to 130 ksi), and R -ratios ranging from -0.5 to 0.5 . These specimens were heat tinted [3] several times during each test. Residual life calculations were made from the precrack and from each heat tint on these specimens. Figure 13 shows the variation of the predicted-to-observed residual life ratio as a function of surface crack depth. The shortest crack depth was 65 μm (0.0025 in.). These data show that these crack growth data and methods can accurately predict the growth of physically small cracks in René 95.

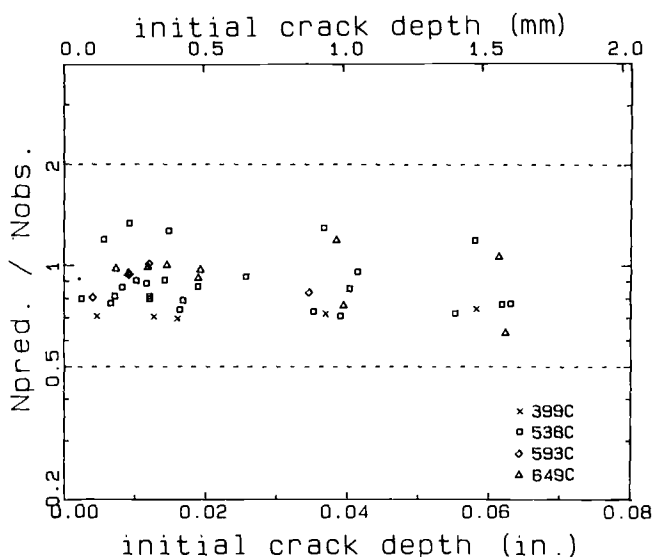


FIG. 13—Ratio of predicted-to-observed residual life for nine physically short crack growth tests on René 95.

³ Ross, W. R. and Sauby, M. E., General Electric Aircraft Engine Business Group, Cincinnati, OH 45215, unpublished research.

These results are extremely significant because the short crack tests were not used to develop the crack growth constants or methods. These data also suggest that if the crack growth of short cracks is accelerated [17], the critical K or crack length for that nonconservative situation is below that evaluated in these physically short crack experiments. The ability to model near-threshold crack growth rates as shown in Fig. 4 may significantly contribute to the ability to predict the physically short-crack data shown in Fig. 13.

Conclusions

A constraint-loss model has been developed and applied to the cyclic crack growth behavior of René 95 at elevated temperatures. This model is a modification of the Newman-Raju K solution which describes the differences in crack growth rates in the depth direction (da/dN) and along the free surface (dc/dN). The constants for this model were developed from through-crack and surface-flaw specimens. The influence of R -ratio was treated using a dual-Walker exponent approach. The combination of these two models was used to predict the growth of surface flaws in both uniformly stressed specimens and in notched specimens where the cracks grew into a stress gradient. These tests were performed over the temperature range from 399 to 593°C (750 to 1100°F) and for R -ratios ranging from -1.0 to 0.75 . The lives predicted for these specimens were within a factor of two of the experimentally measured lives. This methodology also accurately predicted the lives of specimens containing cracks with depths as small as $65\text{ }\mu\text{m}$ (0.0025 in.).

Acknowledgments

The authors would like to acknowledge the support of the U.S. Air Force which, in part, sponsored this work. They also appreciated the helpful comments and contributions of their colleagues.

References

- [1] Newman, J. C. and Raju, I. S., "Stress-Intensity Factor Equations for Cracks in a Three-Dimensional Finite Body," NASA Technical Memorandum 78805, National Aeronautics and Space Administration, Langley Research Center, Hampton, VA, 1981.
- [2] Yau, J. F., *Fracture Mechanics: Seventeenth Volume, ASTM STP 905*, American Society for Testing and Materials, Philadelphia, 1986, pp. 601-624.
- [3] Van Stone, R. H. and Richardson, T. L., *Automated Test Methods for Fracture and Fatigue Crack Growth, ASTM STP 877*, American Society for Testing and Materials, Philadelphia, 1985, pp. 148-166.
- [4] Andrews, W. R. and Shih, C. F., Elastic Plastic Fracture, *ASTM STP 668*, American Society for Testing and Materials, Philadelphia, 1979, pp. 426-450.
- [5] Trantina, G., de Lorenzi, H. G., and Wilkening, W. W., *Engineering Fracture Mechanics*, Vol. 17, 1983, pp. 925-938.
- [6] Trantina, G. and de Lorenzi, H. G., "Elastic-Plastic Fracture Mechanics Analysis of Small Cracks," *Proceedings, Army Symposium on Solid Mechanics*, 1982, Critical Problems in Systems Design, AMMRC MS 82-4, Army Materials and Mechanics Research Center, Watertown, MA, September 1982.
- [7] Newman, J. C. and Raju, I. S., "Stress-Intensity Factor Equations for Cracks in Three-Dimensional Finite Bodies," NASA TM 83200, National Aeronautics and Space Administration, Washington, DC, 1981.
- [8] Van Stone, R. H., "The Influence of Temperature and Stress Ratio on the Fatigue Crack Growth Behavior of René 95," General Electric Aircraft Engine Group Report TM 82-640, General Electric Co., Cincinnati, OH 45215, 1982.
- [9] Van Stone, R. H. and Krueger, D. D., "Investigation of Direct Aged Inconel 718 Fatigue Be-

- havior," NAVAIR Contract N00019-82-C-0373, Final Report, General Electric Aircraft Engine Business Group, General Electric Co., Cincinnati, OH 45215, December 1984.
- [10] Krueger, D. D., "Effects of Grain Size and Precipitate Size on the Fatigue Crack Growth Behavior of Alloy 718 at 428°C," M.S. thesis, University of Cincinnati, OH, 1984.
 - [11] Coles, A., Johnson, W., and Popp, H. G., *Journal of Engineering Materials and Technology*, Vol. 98, 1976, p. 305.
 - [12] Chang, D. R., Krueger, D. D., and Sprague, R. A., *Superalloys 1984*, The Metallurgical Institute of the American Institute of Mining, Metallurgical, and Petroleum Engineers, Warrendale, PA, 1984, pp. 245-273.
 - [13] Gangloff, R. P., *Fatigue of Engineering Materials and Structures*, 1982, Vol. 4, 1981, pp. 15-33.
 - [14] Johnson, H. H., *Materials Research and Standards*, Vol. 5, 1965, pp. 442-445.
 - [15] Tada, L. H., Paris, P. C., and Irwin, G. R., *The Stress Analysis of Cracks Handbook*, Del Research, St. Louis, MO, 1973.
 - [16] Van Stone, R. H. and Krueger, D. D., "Near-Threshold Crack Growth in Nickel-Base Superalloys," this publication, pp. 883-906.
 - [17] Ritchie, R. O. and Suresh, S., "Mechanics and Physics of the Growth of Small Cracks," *Proceedings*, 55th Meeting of the AGARD Structural and Materials Panel on "Behavior of Short Cracks in Airframe Components," Report No. UCB/RP/82/A100, Toronto, Canada, September 1982.

Line Spring Method of Stress-Intensity Factor Determination for Surface Cracks in Plates Under Arbitrary In-Plane Stresses

REFERENCE: Yang, C. Y., "Line Spring Method of Stress-Intensity Factor Determination for Surface Cracks in Plates Under Arbitrary In-Plane Stresses," *Fracture Mechanics: Nineteenth Symposium, ASTM STP 969*, T. A. Cruse, Ed., American Society for Testing and Materials, Philadelphia, 1988, pp. 657-668.

ABSTRACT: The elastic line spring model is updated to accept arbitrarily distributed loads acting on plates to allow determination of stress-intensity factors of surface cracks under various types of loading, such as thermal stress and residual stress. The governing integral equations are modified, owing to the inclusion of the nonlinear loads. Careful numerical treatment and computer programming can make the analysis very efficient. It has been shown that a 16-point K_I -distribution along a crack front can be obtained within 0.025 s (central processing unit) using Cray computer systems, which is at least four orders of magnitude faster than the finite-element analysis of the same problem. The outstanding computational efficiency makes the line spring model practical for many time-dependent fracture analyses in engineering applications.

Cracks with different shapes, namely, semielliptical, part-circular, and triangular cracks are investigated, and the results agree very well with the existing finite-element analysis solutions.

KEY WORDS: line spring constitutive equations, compliance function, potential energy release rate, weight function, stress-intensity factors, crack shapes, part-through cracks, thermal and residual stresses, singular integral equations, fracture mechanics

In the past few years, a great deal of work has been done to refine the line spring model since the theory was first introduced by Rice and Levy [1] and Rice [2] 14 years ago. For example, significant contributions have been made by Parks et al. [3-6] for improving the solution techniques and making the model practically applicable to the plastic regime (1981 to 1983); Erdogan [7,8] extended the model to allow new categories of crack shape, such as buried cracks and corner cracks, to be analyzed in plates and shells with finite dimensions (1982 to 1986). Development work is also taking place in the industries [9] of this country and elsewhere.

It has been demonstrated in the works cited above that the line spring model can effectively produce very useful approximate solutions for the highly complicated three-dimensional crack problems in plates and shells. The most attractive feature that the line spring model can provide comes from its outstanding computational efficiency over other numerical methods. It has been shown that the line spring method can easily save up to four orders of magnitude in computer run time as opposed to the finite-element method, for example, for a system consisting of 3500 degrees of freedom [9]. Another advantage of the line spring model is its ability to model arbitrary crack shapes freely. The major limitations of the line

¹ Senior engineer, Westinghouse Electric Corp., Nuclear Energy Systems, Pittsburgh, PA 15230.

spring model are (a) the model can only be applied to plate or shell structures, and (b) accuracy is lost when the aspect ratio of the crack (that is, the ratio of the crack length along the surface to that normal to the wall of the structure) is relatively small.

The existing line spring methodology deals mainly with cases where the structures are subjected to membrane or bending stresses, that is, linear stress distribution across the thickness of the structure. It is useful, however, to extend the line spring model to include situations where the stress across the structure wall is arbitrarily and nonlinearly distributed, for example, in the case of thermal stress or residual stress. Applications for such an updated line spring model include, for example, (1) fatigue crack growth analysis involving thermal or residual stresses or both, and (2) safety analysis for reactor vessels subjected to thermal shock loadings.

Some of the framework concerning arbitrarily distributed stress over the plate thickness in the line spring model has been given by Rice [2]. Here, a modification of the governing singular integral equations of the line spring model is made in order to take such an arbitrarily distributed stress into account. Stress-intensity factor distributions for a wide range of crack shapes subjected to stress that is expressible by a third degree polynomial equation were then generated using the updated equations; it was found that the results agree very well with those obtained by Raju and Newman [10] using the finite-element method.

The Line Spring Model

The line spring model deals with a long surface crack, or part-through crack, of any shape on the wall of plate or shell structures. The geometry of the cross section containing the crack is schematically shown in Fig. 1. The compliance over the cracked region is increased because the size of the ligament is decreased. The increased compliance results in additional displacements across the crack plane when the body is loaded, and the whole defect line, that is, the cracked section, behaves somewhat like a spring. The defect line of the structure can be considered to be composed of a series of plane-strain single-edge notched (SEN) specimens (Fig. 2), about which the mechanical characteristics are known. The compliance functions of each SEN element, which correlate the generalized loads and displacements, can be found through the well-known Irwin's [11] potential energy release concept. Such a relationship is named the line spring constitutive equation. The additional displacement, δ ,

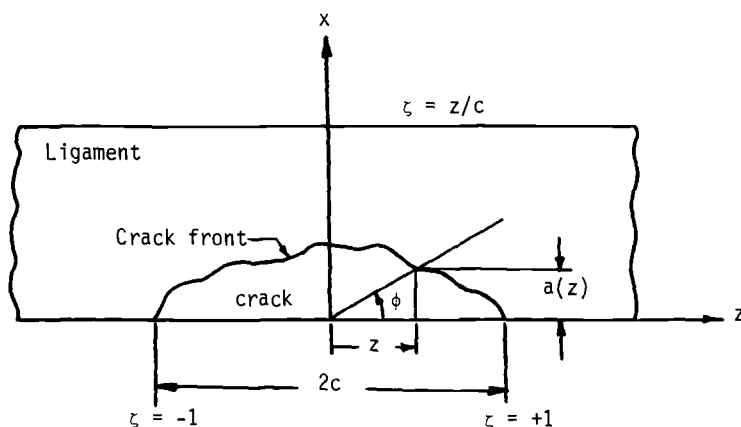


FIG. 1—Geometry of the cross section of a part-through crack shown schematically.

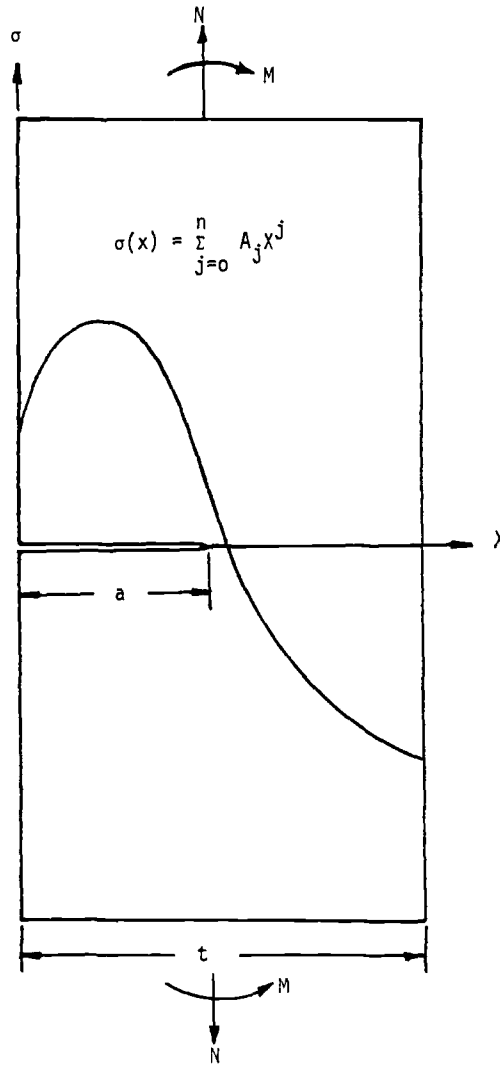


FIG. 2—Single-edge notched specimen.

and the rotation, θ , of one end of the SEN specimen relative to the other due to the presence of the crack (these are the generalized displacements mentioned above) play key roles in the line spring model. The governing line spring equations are derived from the linear elastic generalized plane stress theory for plates obeying Kirchhoff-Poisson bending theory as given below [1-3]

$$N(\zeta) + \frac{Et}{4\pi c} \int_{-1}^1 \frac{d\delta(\zeta')}{\zeta - \zeta'} = N^*(\zeta) \quad (1)$$

$$M(\zeta) + \frac{(3 + \nu)Et^3}{48\pi(1 + \nu)c} \int_{-1}^1 \frac{d\theta(\zeta')}{\zeta - \zeta'} = M^*(\zeta) \quad (2)$$

where

- E = Young's modulus,
- ν = Poisson's ratio,
- t = plate thickness,
- c = semicrack length on plate surface,
- $\zeta = z/c$ = normalized coordinate (see Fig. 1),
- N, N^∞ = local and remote, respectively, membrane force per unit length, and
- M, M^∞ = local and remote, respectively, bending moment per unit length.

Equations 1 and 2 are pairs of coupled singular integral equations correlating displacements δ, θ with the loads N, M and N^∞, M^∞ . When N and M are replaced by δ and θ using the line spring constitutive equations, which are shown explicitly in the following section of this paper, Eqs 1 and 2 reduce to a system consisting of two sets of variables, δ and θ , which can be evaluated at various points along the crack front. The line spring constitutive equations are then used to convert the results of the δ and θ back to N and M ; N and M can then be used to determine the stress-intensity factors of the representative SEN specimens of the surface crack using the following equations

$$K = \sigma_i \sqrt{\pi \xi t} F_i(\xi) \quad (3)$$

where K is the Mode I stress-intensity factor with the subscript omitted for simplicity, the index i takes on values 1 and 2 with $i = 1$ for uniform tensile load and $i = 2$ for bending load, $\xi = a/t$ = dimensionless crack depth (Fig. 2), F_i = stress-intensity factor calibration functions, $\sigma_1 = N/t$ = membrane stress, and $\sigma_2 = 6M/t^2$ = bending stress.

It should be noted that the summation convention is adopted in Eq 3 and information on the F_i functions can be found in the handbooks, for example Ref 12.

Line Spring Under Arbitrarily Distributed Stresses

The theory of the line spring model has been briefly described in the preceding section. As can be seen, only linear stresses have been considered so far. We now consider the case where the structure is subjected to a randomly distributed stress across the wall thickness of the structure. Let $p(\xi')$ be the net stress distribution excluding N and M prior to a crack being introduced to the structure as shown in Fig. 2. Then the stress-intensity factor, after a crack of depth ξ is introduced, can be expressed by

$$K = \sqrt{t} \left[\sqrt{\pi \xi} \sigma_i F_i(\xi) + \int_0^\xi p(\xi') g(\xi', \xi) d\xi' \right] \quad (4)$$

for $i = 1, 2$, where $g(\xi', \xi)$ is the influence function representing the stress-intensity factor for a crack of length ξ due to a unit load acting at point ξ' , where ξ' is less than ξ . It should be noted that the superposition principle was employed in both Eqs 3 and 4. The integral term of Eq 4 is directly taken from the weight function theory [13,14].

There are three unknowns, namely σ_1, σ_2 , and $g(\xi', \xi)$, in Eq 4 that need to be determined before the stress-intensity factor can be evaluated; σ_1 and σ_2 can be determined from the line spring governing equations, and $g(\xi', \xi)$, which is a geometric-dependent-only function, can be determined independently. The procedure for determining $g(\xi', \xi)$ is as follows:

1. Let $N = M = 0$ and $p(\xi') = \sigma_i$ = constant, which implies pure tension, for Eq 4 and

compare the results with the tension only case in Eq 3. A requirement that $g(\xi', \xi)$ has to satisfy is

$$\int_0^\xi g(\xi', \xi) d\xi' = \sqrt{\pi\xi} F_1(\xi) \quad (5)$$

2. Let $N = M = 0$ and $P(\xi') = \sigma_b(1 - 2\xi')$, which implies pure bending, for Eq 4 and compare the results with the bending only case in Eq 3. The second requirement that $g(\xi', \xi)$ has to satisfy is

$$\int_0^\xi (1 - 2\xi') g(\xi', \xi) d\xi' = \sqrt{\pi\xi} F_2(\xi) \quad (6)$$

3. Consider the weight function expression as given by Rice [13] and Bueckner [14]

$$w = \frac{E'}{2Kt} \frac{\partial u}{\partial \xi} = \frac{E'}{2Kt} \frac{\partial u}{\partial \rho} \quad (7)$$

where $E' = E/(1 - \nu^2)$ and $u = u(\xi', \xi)$ is the crack-opening displacement, and $\rho = \xi - \xi'$ is the dimensionless distance from the crack tip. For the region near the crack tip, the crack-opening displacement is given by

$$u \approx \frac{8K}{E'} \left(\frac{t\rho}{2\pi} \right)^{1/2} \quad (8)$$

Substituting Eq 8 in Eq 7 and noting that $w = w(\xi', \xi) = \sqrt{t} g(\xi', \xi)$, the third requirement that $g(\xi', \xi)$ has to satisfy, for $\xi' \rightarrow \xi$, is

$$g(\xi', \xi) \approx [0.5\pi(\xi - \xi')]^{-1/2} \quad (9)$$

4. Based on the above discussions it is clear that a functional form of $g(\xi', \xi)$ can be constructed as follows:

$$g(\xi', \xi) = (0.5\pi\rho)^{-1/2} [1 + A(\xi)\rho + B(\xi)\rho^2] \quad (10)$$

where $\rho = \xi - \xi' > 0$ and $A(\xi)$ and $B(\xi)$ are coefficients to be determined. More terms may be added if more properties of $g(\xi', \xi)$ are found.

Substituting Eq 10 in Eqs 5 and 6, two linear equations in terms of $A(\xi)$ and $B(\xi)$ are obtained which can be solved after going through some numerical operations. A complete set of $A(\xi)$ and $B(\xi)$ can be obtained for all crack lengths, such as $\xi = 0.01, 0.02, \dots, 0.95$, to cover the whole crack depth range of interest.

Since the load is divided into three parts, namely, the membrane force, the bending moment, and the distributive load, the line spring constitutive equations are modified as

$$\delta = P_{11}N + P_{12}M + P_{13}L_1 \quad (11)$$

$$\theta = P_{21}N + P_{22}M + P_{23}L_2 \quad (12)$$

where the values for P_{ij} are the compliance function and the values for L_i are associated with the distributive load.

Using Irwin's potential energy release relation [11] the compliance P_{ij} and L_1, L_2 of Eq 11 are

$$P_{11} = \left(\frac{2\pi}{E'} \right) b_{11} \quad (13)$$

$$P_{12} = P_{21} = \left(\frac{12\pi}{E't} \right) b_{12} \quad (14)$$

$$P_{22} = \left(\frac{72\pi}{E't^2} \right) b_{22} \quad (15)$$

$$P_{13} = \frac{2t}{E'} \quad (16)$$

$$P_{23} = \frac{12}{E'} \quad (17)$$

and

$$L_i = \int_0^\xi V_i(\xi', \xi) p(\xi') d\xi' \quad (18)$$

where

$$b_{ij} = \int_0^\xi \xi' F_i(\xi') F_j(\xi') d\xi' \quad (19)$$

$$V_i(\xi', \xi) = \int_{\xi'}^\xi \sqrt{\pi\xi''} F_i(\xi'') g(\xi', \xi'') d\xi'' \quad (20)$$

where the indices i and j take on values of 1 or 2. Inverting Eqs 11 and 12, the loads N and M in terms of the stiffness matrix, S_{ij} , are

$$N = S_{11}\delta + S_{12}\theta - N_p \quad (21)$$

$$M = S_{21}\delta + S_{22}\theta - M_p \quad (22)$$

where $S_{21} = S_{12}$ and $[S_{ij}] = [P_{ij}]^{-1}$ for $i, j = 1, 2$, and N_p, M_p are found to be

$$N_p = S_{11}P_{13}L_1 + S_{12}P_{23}L_2 \quad (23)$$

$$M_p = S_{21}P_{13}L_1 + S_{22}P_{23}L_2 \quad (24)$$

Expressions 21 and 22 are the modified line spring constitutive equations involving the randomly distributed stress. Substituting Eqs 21 and 22 in the original governing line spring

equations, one obtains

$$S_{11}\delta + S_{12}\theta + \frac{Et}{4\pi c} \int_{-1}^1 \frac{d\delta(\zeta')}{\zeta - \zeta'} = N^* + N_p \quad (25)$$

$$S_{21}\delta + S_{22}\theta + \frac{(3 + \nu)}{48\pi} \frac{Et^3}{(1 + \nu)c} \int_{-1}^1 \frac{d\theta(\zeta')}{\zeta - \zeta'} = M^* + M_p \quad (26)$$

Expressions 25 and 26 are the modified governing equations of the line spring model involving the randomly distributed stress. It should be noted that the quantities δ , θ , N^* , N_p , M^* , and M_p are functions of the normalized coordinate ζ which is omitted to save writing.

Equations 25 and 26 can be solved for δ and θ using the Gauss-Chebyshev integration formulas for singular integrals with the aid of the procedures recommended by Erdogan and Gupta [19]. In solving these equations it is necessary to include the condition that the additional displacements vanish at the ends of the defect line, that is, $\delta = \theta = 0$ at $\zeta =$

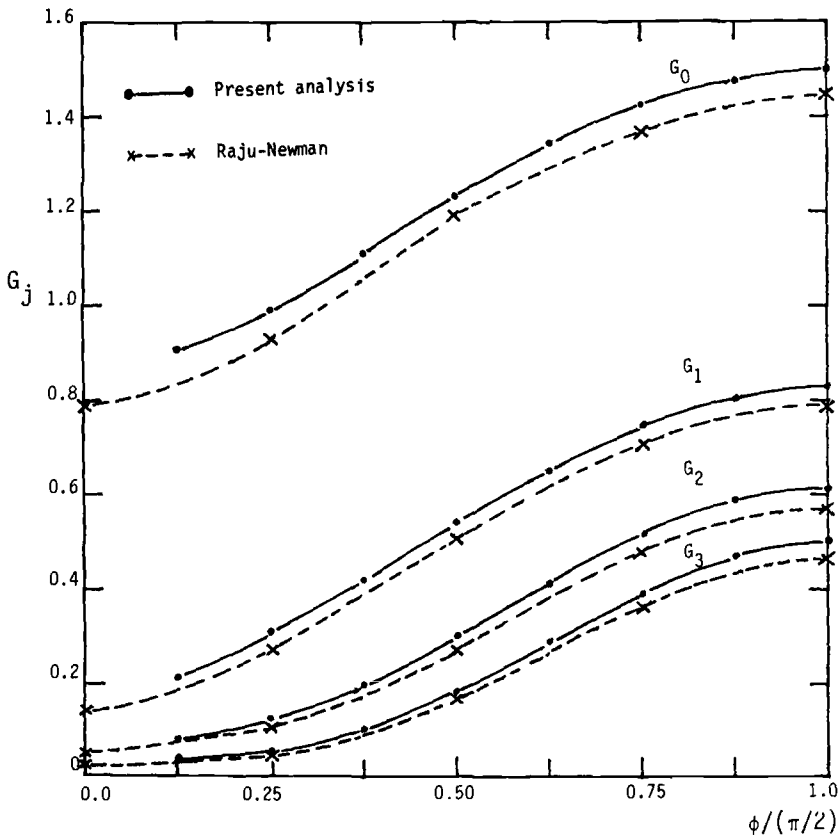


FIG. 3—Results of influence coefficients for a semielliptical crack, $a/c = 0.2$, $a/t = 0.5$.

± 1 . Equations 25 and 26 are finally reduced to a system of $2n$ linear equations for $2n$ unknowns in δ_i and θ_i , $i = 1, 2, 3, \dots, n$, where n is the number of points along the crack front to be evaluated.

It can be seen that when $p(\xi) = 0$, Eqs 25 and 26 reduce to Eqs 1 and 2. Since N_p and M_p are pure numbers for a given crack length, the solution procedures for Eqs 25 and 26 are exactly the same as that for Eqs 1 and 2. Finally, the local $N(\xi)$ and $M(\xi)$ are evaluated from Eqs 21 and 22, which are then used to determine the stress-intensity factor distribution along the crack front using Eq 4.

Analysis of Part-Through Crack Problems

Extensive studies on three-dimensional surface crack problems have been performed using the finite-element method, for example, by McGowan and Raymund [15] and by Raju and Newman [10]; the boundary integral equation method was used by Heliot et al. [16] and by Cruse et al. [17,18], just to name a few. Surface or part-through cracks are the most important, yet not the most critical, type of defect in a solid. Most of the cracks in structural components are initiated and developed from the surface and may grow to critical size under certain loading conditions.

A better understanding of the characteristics of the part-through cracks will help to prevent

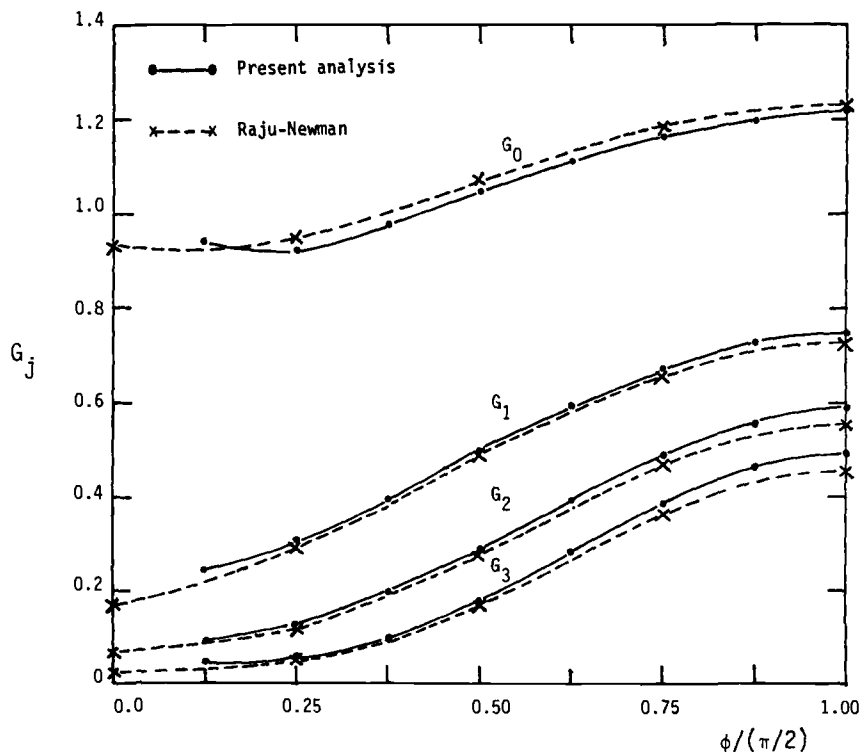


FIG. 4—Results of influence coefficients for a semielliptical crack, $a/c = 0.4$, $a/t = 0.5$.

any catastrophic losses. In many engineering applications, the shape of part-through cracks are often treated as semiellipses which will generally lead to somewhat conservative results. The line spring model can be used to estimate the margin of conservatism since any type of crack shape can be modeled and analyzed easily by the line spring model. In this section we first deal with the semielliptical cracks, with a wide range of aspect ratios and depths, and then consider some different shapes, for example, the part-circular, triangular, and rectangular cracks.

Since most of the existing solutions are associated with stress that is expressible by a polynomial, $p = A_0 + A_1\xi + A_2\xi^2 + A_3\xi^3 + \dots$, the same type of stress representation is adopted here to facilitate direct comparison. Stress-intensity factor distribution corresponding to each term (that is, uniform, linear, quadratic, and cubic) of the polynomial function can be determined separately. The total stress-intensity factor due to the combined stress, p , can be obtained using the superposition principle, as expressed by

$$K = \left(\frac{\pi a}{Q} \right)^{1/2} \sum G_j A_j \left(\frac{a}{t} \right)^j \quad (27)$$

where j is 0, 1, 2, . . . , and G_j is the influence coefficient or boundary correction factor corresponding to the j th component of stress mentioned above. Both G_j and K are functions of the aspect ratio of the crack shape, the depth of the crack, and the location at the crack front. The value Q is the square of the complete elliptic integral of the second kind and can be approximated by $Q = 1 + 1.464 (a/c)^{1.65}$. Note that $\xi = x/t$ in function $p(\xi)$.

The inverse aspect ratio, a/c , and the dimensionless crack depth, a/t , are the two parameters that will be referred to frequently in the following discussions. The crack shapes

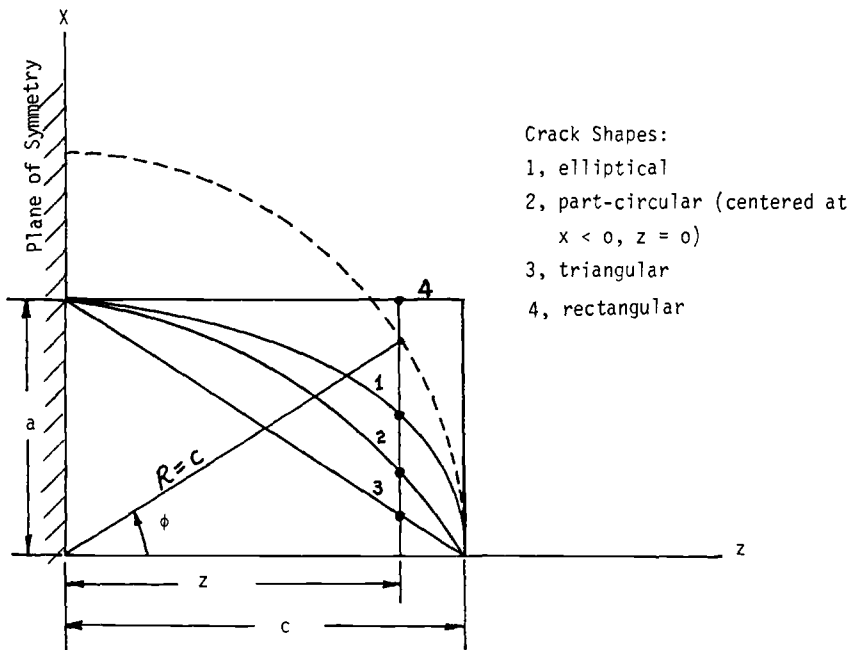


FIG. 5—Geometry of the four crack shapes studied shown schematically.

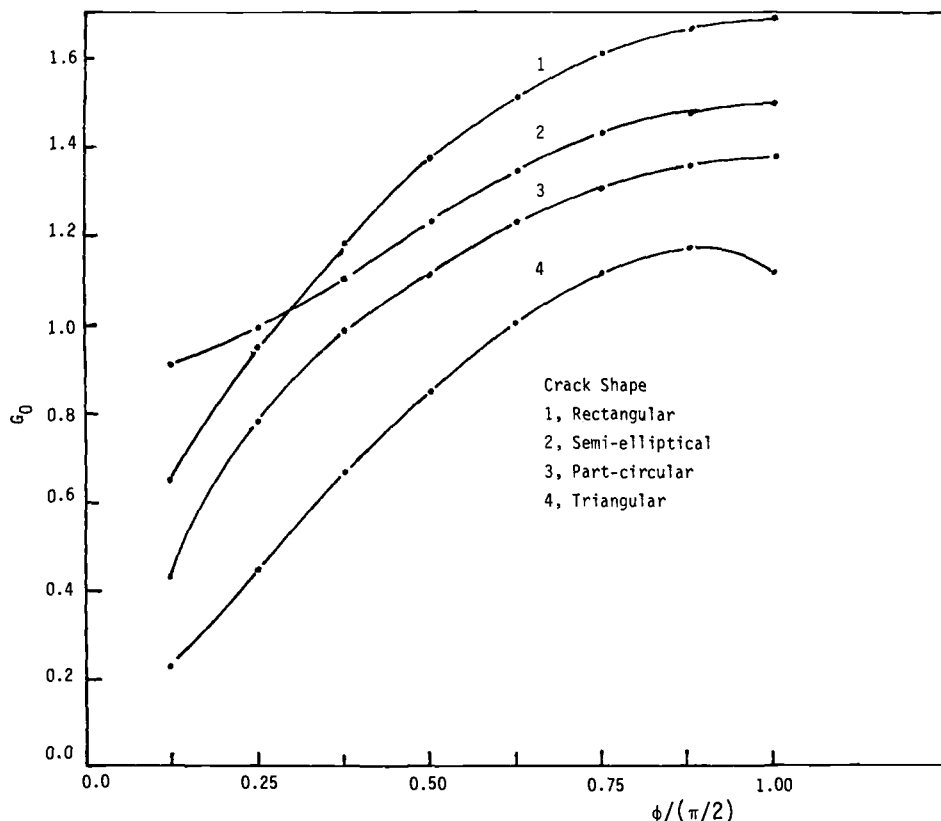


FIG. 6—Comparison of G_0 results for different crack shapes.

investigated in this report are within the ranges $a/c = 0.05$ to 0.5 and $a/t = 0.2$ to 0.8 . Some of the results of the semielliptical cracks can be directly compared with those of Raju and Newman [10].

It was found that the results obtained in the present analysis are in very good agreement with those shown in Ref 10 for most of the crack shapes studied, that is, $a/c = 0.2$ to 0.4 and $a/t = 0.2$ to 0.8 , everywhere along the whole crack front. This good correspondence is true for all stress components up to the cubic term. Results of some selected crack shapes are shown in Figs. 3 and 4, in terms of G_j .

It is interesting to notice that according to Figs. 3 and 4 the line spring results are approximately 3 to 7% higher than those of Ref 10, uniformly spread everywhere over the whole crack front for all stress components. The results produced by both methods are found to be similar graphically. The similarity as observed in these diagrams suggest that a simple numerical relationship between the two methodologies may be found for calibrating the line spring model results versus that produced by the presumably more accurate finite-element method.

It should be noted that the finite-element results mentioned here (that is, the dotted curves shown in Figs. 3 and 4) are that for a thin shell with a radius-to-thickness ratio of 10, rather than for a flat plate. Nevertheless, the difference between the plate solution and the thin

shell solution is very small, as verified by the present author using the finite-element method supported virtual crack extension method. To see how well the line spring model works when the crack is very long and shallow, a semielliptical crack with $a/c = 0.047$ and $a/t = 0.2$ was also analyzed using the virtual crack extension method [20]. This crack geometry was chosen to study the case of thermal shock loading in which the crack is most probably growing lengthwise instead of running into the wall thickness. It was found that the results obtained by the line spring method are within 95% agreement with those obtained by the virtual crack extension method for all stress components shown in the cubic stress polynomial.

A wide range of a/c and a/t for part-circular, triangular, and rectangular shaped cracks are investigated. The geometry of these cracks are schematically shown in Fig. 5. The part-circular crack is defined as the one that has a circular contour with its center located at $z = 0$ and $x < 0$. As expected, the largest stress-intensity factor is found in the rectangular crack, followed in order by the semielliptic, part-circular, and triangular cracks. Since the purpose of this paper is not to exhibit numerical data, but rather to develop a methodology, only G_0 (corresponding to the uniform tensile load) for a randomly chosen aspect ratio and crack depth (here, $a/c = 0.2$, $a/t = 0.5$) is reported as shown in Fig. 6. Based on these data, it is found that G_0 for the semielliptical crack is about 10 and 30% higher than that of the part-circular and triangular cracks, respectively. Similar results were also found for other stress components and for a wide range of a/c and a/t investigated.

Discussion and Conclusions

It has been shown that the line spring model is a powerful analytical tool that is able to effectively produce useful approximate solutions for surface crack problems in plates and shells. The existing line spring methodology deals primarily with cases where the structure is subjected to only linear stresses, namely, the membrane force or the bending moment or a combination. However, in reality, there are lots of cases where the stress over the section of the body is so complex that a linear approximation is not appropriate. Under these circumstances, an updated line spring model that takes the randomly distributed stress into account is needed. In this regard, the present paper gives the necessary analytical details, modifies the line spring governing and constitutive equations, and demonstrates their adequacy for practical applications.

The weight function theory and the superposition principle are the main tools needed in this work, although the weight function theory itself is closely related to the superposition principle. Therefore, the added terms, that is the $p(\xi)$ related quantities, do not interact with those existing in the original model. It has been verified that, if $p(\xi)$ is the only active load and if $p(\xi)$ is a linear function of ξ , the modified model will produce exactly the same results as those given by the original line spring model if the loads in both cases are equivalent.

Although a great deal of numerical operation has been added to the updated line spring model, the process time [central processing unit (CPU)] has only increased slightly as compared with what is needed in the original model. This is because the loading weight function, Eq 10, and the displacement weight function, Eq 20, are functions of geometry only. These functions need to be evaluated only once and can be stored permanently in a magnetic tape for future use. It is possible, with some careful numerical treatments, to obtain a 16-point K -distribution along a surface crack within 0.025 CPU s with a Cray computer or within 1 CPU s with a personal computer. The outstanding computational efficiency makes the line spring model practical for many time-dependent continuous analyses in engineering applications.

Acknowledgment

This work was financially supported by the Westinghouse-French Four-Party Joint Research and Development Program, PWS3.78.

References

- [1] Rice, J. R. and Levy, N., "The Part-Through Surface Crack in an Elastic-Plate," *Journal of Applied Mechanics*, Vol. 39, 1972, pp. 185-194.
- [2] Rice, J. R., "The Line-Spring Model for Surface Flaws," *The Surface Crack: Physical Problems and Computational Solutions*, J. L. Swedlow, Ed., American Society of Mechanical Engineers, New York, NY, 1972.
- [3] Parks, D. M., "The Inelastic Line-Spring: Estimates of Elastic-Plastic Fracture Mechanics Parameters for Surface-Cracked Plates and Shells," *Journal of Pressure Vessel Technology*, Vol. 103, 1981, pp. 246-254.
- [4] Parks, D. M., "Inelastic Analysis of Surface Flaws Using the Line-Spring Model," *Advances in Fracture (Fracture 1981)*, D. Francois, Ed., Vol. 5, Pergamon, Oxford, 1981, pp. 2589-2598.
- [5] Parks, D. M., Rodin, G. J., and Lockett, R. R., "The Line-Spring Model for *J*-Analysis of Surface-Cracked Plates and Shells: Calibration of the Power-Law Spring," *Elastic-Plastic Fracture: Second Symposium, ASTM STP 803*, American Society for Testing and Materials, Philadelphia, 1983.
- [6] Parks, D. M. and White, C. S., "Elastic-Plastic Line-Spring Finite Elements for Surface-Cracked Plates and Shells," *Aspects of Fracture Mechanics in Pressure Vessels and Piping*, S. S. Palusamy and S. G. Sampath, Eds., ASME PVP, Vol. 58, American Society of Mechanical Engineers, New York, 1982.
- [7] Erdogan, F. and Aksel, B., "Line Spring Model and Its Applications to Part-Through Crack Problems in Plates and Shells," this volume, pp. 125-152.
- [8] Delale, F. and Erdogan, F., "Application of the Line-Spring Model to a Cylindrical Shell Containing a Circumferential or an Axial Part-Through Crack," *Journal of Applied Mechanics*, Vol. 49, 1982, pp. 97-105.
- [9] Yang, C. Y., "Elastic-Plastic Line-Spring Method of *J*-Determination for Surface Flaws in Plates," Westinghouse Report, MT-SME-3664, Westinghouse Electric Corp., Pittsburgh, PA, 27 Dec., 1984.
- [10] Raju, I. S. and Newman, J. C., Jr., "Stress-Intensity Factor Influence Coefficients for Internal and External Surface Cracks in Cylindrical Vessels," *Aspects of Fracture Mechanics in Pressure Vessels and Piping*, ASME PVP, Vol. 58, American Society of Mechanical Engineers, New York, 1982.
- [11] Irwin, G. R., "Fracture Mechanics," *Structural Mechanics*, J. N. Goodier and J. N. Hoff, Eds., Pergamon Press, New York, 1960, p. 557.
- [12] Tada, H., Paris, P. C., and Irwin, G. R., *The Stress Analysis of Cracks Handbook*, Del Research Corp., Hellertown, PA, 1973.
- [13] Rice, J. R., "Some Remarks on Elastic Crack Tip Fields," *Internal Journal of Solids and Structures*, Vol. 8, 1972, pp. 751-758.
- [14] Bueckner, H. F., "A Novel Principle for the Computation of Stress-Intensity Factors," *Zeitschrift für angewandte Mathematik und Mechanik*, Vol. 50, 1970, pp. 526-546.
- [15] McGowan, J. J. and Raymund, M., "Stress Intensity Factor Solutions for Internal Longitudinal Semielliptical Surface Flaws in a Cylinder Under Arbitrary Loadings," *Fracture Mechanics (Eleventh Conference) ASTM STP 677*, American Society for Testing and Materials, Philadelphia, 1979, pp. 365-380.
- [16] Heliot, J., Labbens, R. C., and Pellissier-Tanon, "Semielliptical Cracks in a Cylinder Subjected to Stress Gradients," *Fracture Mechanics: Eleventh Conference ASTM STP 677*, American Society for Testing and Materials, Philadelphia, 1979, pp. 341-364.
- [17] Cruse, T. A. and Van Buren, W., "Three-Dimensional Elastic Stress Analysis of a Fracture Specimen with an Edge Crack," *Internal Journal of Fracture Mechanics*, Vol. 7, No. 1, 1971, pp. 1-15.
- [18] Cruse, T. A., "Two- and Three-Dimensional Problems of Fracture Mechanics," *Developments in Boundary Element Methods*, P. K. Banerjee and R. Butterfield, Eds., Applied Science, London, Vol. 1, 1979, pp. 97-119.
- [19] Erdogan, F. and Gupta, G. D., "On the Numerical Solution of Singular Integral Equations," *Quarterly of Applied Mathematics*, January 1972, pp. 525-534.
- [20] Yang, C. Y., "ORNL Benchmark Problems," Westinghouse Report, MT-SME-3000, Westinghouse Electric Corp., Pittsburgh, PA, 15 July 1983.

Mixed-Mode Stress-Intensity Factor Solutions for Offshore Structural Tubular Joints

REFERENCE: Rhee, H. C. and Salama, M. M., "Mixed-Mode Stress-Intensity Factor Solutions for Offshore Structural Tubular Joints," *Fracture Mechanics: Nineteenth Symposium, ASTM STP 969*, T. A. Cruse, Ed., American Society for Testing and Materials, Philadelphia, 1988, pp. 669–676.

ABSTRACT: Accurate calculations of the stress-intensity factors (K) are essential for assessment of the integrity of structural components containing crack-like defects. For the complex tubular joints used in the construction of offshore structures, accurate K solutions do not exist. Only limited results using empirically derived K values are available in the literature. This paper presents a methodology for the mixed-mode K solutions for a surface crack at the weld toe of tubular joints. Example solutions were developed for tubular X-joints under brace tension and in-plane bending using three-dimensional finite-element analyses. The complex finite-element mesh was generated using a special mesh generator. The K values were obtained from the displacement solutions of quarter-point crack-tip elements. The results demonstrate the validity of the solution scheme and contribute to the understanding of the crack-tip behavior of tubular joints.

KEY WORDS: stress-intensity factors, mixed mode, tubular joints, offshore structures, fatigue analysis, fracture mechanics

As the offshore industry moves to deeper waters and more hostile environments, accurate fatigue life predictions for complex structural tubular joints are becoming increasingly important. Since the fatigue life of tubular joints is predominantly spent in crack propagation, the availability of accurate stress-intensity factor (K) solutions is essential for fatigue calculations. Due to the complexity of the joint geometry, crack surface configuration, and loading conditions, accurate K solutions do not exist. Some empirical solutions have, however, been derived based on the manipulation of experimental fatigue crack growth data [1].

Based on field and laboratory results, it has been found that weld-toe surface flaw, which is initially straight along the tubular thickness direction, propagates following a curved path in the depth direction. It is, therefore, common that the crack surfaces of a weld-toe surface flaw are doubly warped, as is shown in Fig. 1. In addition to this crack shape complexity, a simple loading on tubular joints can result in mixed-mode behavior for a crack, further complicating the analysis.

In this paper, a finite-element procedure is used to calculate the stress-intensity factors of a weld-toe surface flaw with curved crack surfaces in a tubular joint under mixed-mode loading. The crack front asymptotic components of the displacement solutions in the quarter-point elements were converted to the appropriate stress-intensity factors using the relationships between the crack-front displacements and the stress-intensity factors. The solutions

¹ Senior engineering scientist and section director, respectively, Production Research and Development, Marine and Materials Section, Conoco Inc., Ponca City, OK 74603.

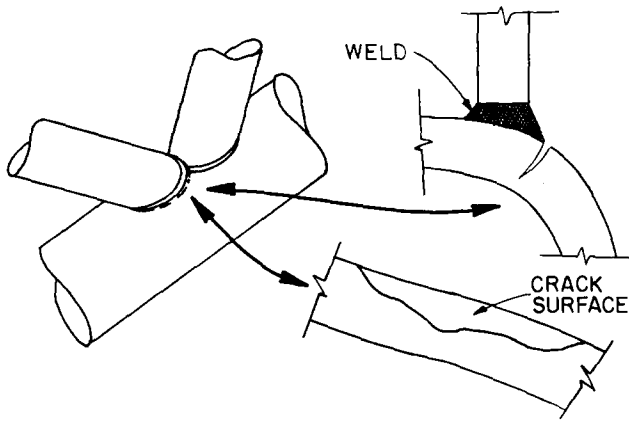


FIG. 1—Tubular joint weld-toe surface flaw.

indicate that, even for a simple tubular joint, the crack-front material behavior of a weld-toe surface flaw can be mixed-mode behavior, rather than only Mode I.

This paper presents a detailed discussion on the procedure to convert the quarter-point crack-front finite-element displacement solutions into the appropriate stress-intensity factor solutions in a general geometric situation. The fully mixed-mode solutions of a weld-toe surface flaw in an X-shaped tubular joint under brace tension and bending loads are presented along with discussions of these solutions.

Stress-Intensity Factor Evaluation from Finite-Element Displacement Solutions

For a linear elastic material, it has been found that a special isoparametric finite element—namely, the quarter-point element [2]—can accurately represent the crack-front stress singularity and asymptotic displacement behavior. Being defined in the coordinate system of a three-dimensional flaw geometry of Fig. 2, such a crack-front displacement field can be expressed by the following equations [3].

$$\begin{Bmatrix} u_n \\ u_z \\ u_t \end{Bmatrix} = \sqrt{r} B \begin{Bmatrix} K_I \\ K_{II} \\ K_{III} \end{Bmatrix} + \underline{0}(r) \quad (1)$$

where B is defined in terms of the shear modulus (G), Poisson's ratio (ν), and the crack-tip polar coordinate θ .

Once the accurate near-tip displacement solutions are obtained, the proper stress-intensity factors are calculated from Eq 1. For a three-dimensional flaw geometry, which can be modeled with elements of straight sides, the procedure has already been established [4,5]. This procedure is generalized here to treat a problem with curved crack surfaces and front. On the crack surface, $\theta = \pi$, Eq 1 will be uncoupled as

$$\underline{u}' = \begin{Bmatrix} u_n \\ u_z \\ u_t \end{Bmatrix} = \sqrt{\frac{2r}{\pi}} \frac{1}{G} \begin{Bmatrix} (1-\nu)K_{II} \\ (1-\nu)K_I \\ K_{III} \end{Bmatrix} + \underline{0}(r) \quad (2)$$

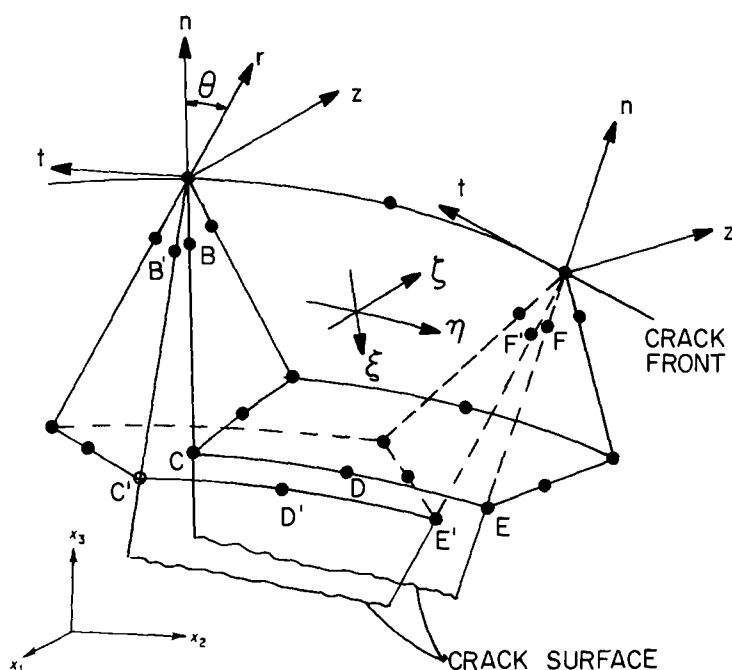


FIG. 2—Collapsed quarter-point element for curved crack.

For a collapsed 15-node, three-dimensional, isoparametric quarter-point element defined by a side on the crack surface, two sides which are normal to both the crack surface and the crack front, and three other sides (Fig. 2), it can be shown that [4]

$$\underline{u}' = \underline{a} + \sqrt{r} \underline{b} + r \underline{c} \quad (3)$$

where r is the radial coordinate defined on the n - z plane at each crack front point, and \underline{a} , \underline{b} , and \underline{c} are determined from the appropriate nodal displacements and the element geometry. The n , t , and z coordinate system in Fig. 2 is a local crack-tip body coordinate system defined consistently with that of the local crack front geometry. The stress-intensity factors, K_I , K_{II} , and K_{III} , can be obtained by identifying the proper terms with \sqrt{r} in Eqs 2 and 3.

Along a straight crack surface line on an n - z plane of an element, the displacement fields in the Cartesian coordinates, x_1 , x_2 , and x_3 , which are the global coordinates for the finite-element model (Fig. 2), are expressed as

$$u_i = u_i^0 + u_i^1 \sqrt{\frac{r}{L}} + u_i^2 \frac{r}{L} \quad (i = 1, 2, 3) \quad (4)$$

where u_i^0 , u_i^1 , and u_i^2 are functions of nodal displacements and the location on the n - z plane, and L is the radial dimension of the element on the n - z plane with a specified θ value. For a special case of an element with a straight crack front [4] and a model symmetric about the crack surface plane, the displacement coefficients with \sqrt{r} along the element side on

the crack surface are given as follows

$$u_i^1 = \begin{cases} 4u_i^F - u_i^E, & \text{at } \eta = 1.0 \\ 2u_i^B - u_i^C + 2u_i^F - u_i^E + u_i^D, & \text{at } \eta = 0.0 \\ 4u_i^B - u_i^C, & \text{at } \eta = -1.0 \end{cases} \quad (5a)$$

$$(5b)$$

$$(5c)$$

At a crack front position (with a specified nodal coordinate value of η), the relationships between displacements in the n, t, z system, \underline{u}' , and the displacements in the x_1, x_2, x_3 system, \underline{u} , can be defined by the appropriate coordinate transformation as

$$\underline{u}' = \underline{R}\underline{u} \quad (6)$$

and similarly, the relationship between b_i and u_i^1 ($i = 1, 2, 3$) as

$$\underline{b} = \frac{\underline{R}\underline{u}^1}{\sqrt{L}} \quad (7)$$

where the coordinate transformation matrix, \underline{R} , can be obtained from the crack front geometry at the point.

The stress-intensity factors can finally be obtained from Eqs 2, 3, and 7 as

$$\begin{Bmatrix} K_I \\ K_{II} \\ K_{III} \end{Bmatrix} = \frac{G}{(1 - \nu)} \sqrt{\frac{\pi}{2}} \begin{Bmatrix} b_2 \\ b_1 \\ (1 - \nu)b_3 \end{Bmatrix} \quad (8)$$

For the case of general unsymmetric structure (see Fig. 2), the stress-intensity factor solutions can be obtained by averaging those from the two elements on the crack surfaces. The average values can be obtained by using Eqs 7 and 8 and Eq 5 with u_i^j replaced by $(u_i^j - u_i^j)/2$ ($j = B, C, D, E$, and F) [4], when the two corresponding nodes on the crack surface sides of the two elements coincide.

Stress-Intensity Factor Solutions for a Weld-Toe Surface Flaw of an X-Joint

Figure 3 shows the two-plane symmetry finite-element model of the analyzed X-joint with a weld-toe surface flaw near the saddle point of the chord with the dimensions and material properties. In Fig. 3, D and d are the diameters of the chord (horizontal member) with a thickness T and the brace (vertical member) with a thickness t , respectively. The model consists of 490 three-dimensional 20-node isoparametric elements for the area near the crack and at the brace-chord intersection. Also, 509 eight-node thick-shell elements are used for the other tubular parts. The model consists of 5000 nodes. This model was developed using PRETUBE [6], which is a preprocessing program designed for the finite-element mesh development of tubular joints. This program has a built-in capability to develop a finite-element mesh for various forms of surface flaws in a tubular joint with crack-tip quarter-point singular elements.

In modeling a surface flaw, the program requires the coordinates of two points at which the curved crack front meets with the tubular surface, and the deepest flaw depth, which is located at the middle of the crack front as defined by the two surface points. These three points (two surface points and the deepest point) are then mapped into a planar semielliptical whose major and minor axes are defined by these three points. After this planar semielliptical

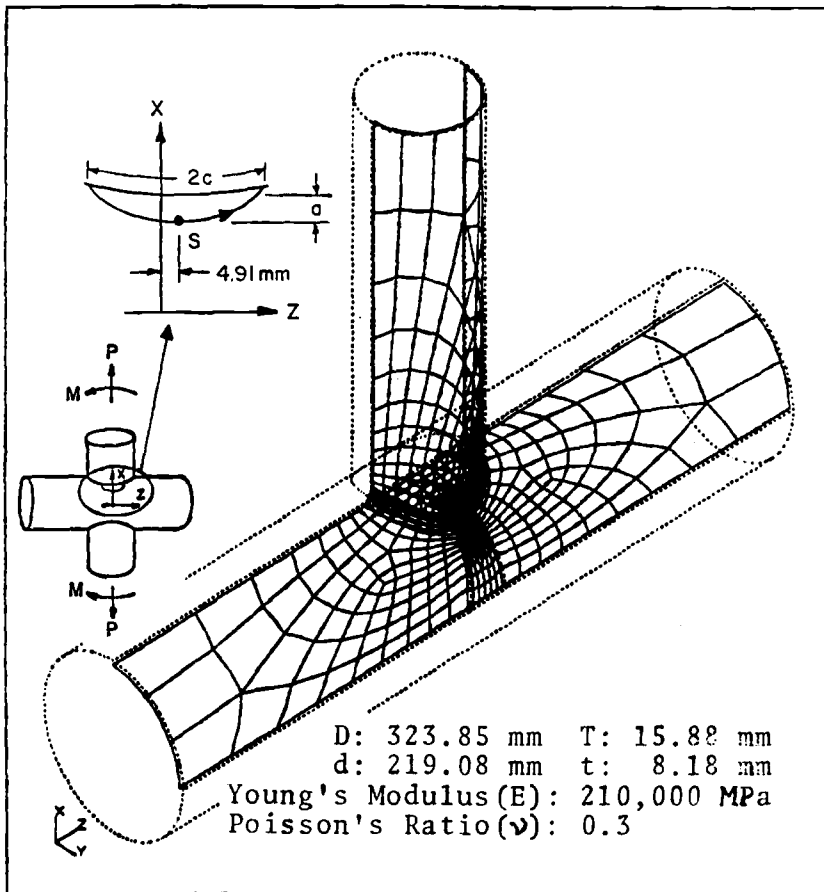


FIG. 3—Finite-element model of cracked X-joint.

flaw is defined, it is mapped back into the tube through a coordinate transformation between the rectangular coordinates of the semiellipse and the curvilinear body coordinates of the tube. The curvilinear body coordinates are defined by the path of the crack mouth on the tube surface, which is determined by the previously mentioned two surface points, and a coordinate along the thickness direction, which is normal to the crack mouth path. At present, the program can model only a straight crack surface along the depth (tube thickness) direction, and thus, a model can have a singly warped crack surface (along the crack length direction). For this reason, the present flaw may not be completely general, and the resulting stress-intensity factor solutions may represent a higher level of mixed-mode behavior than a real-world problem.

The flaw in the model is slightly offset from the structural symmetry axis (about 2% of the brace diameter). Along the crack front, ten three-dimensional, collapsed, quarter-point element clusters, each of which consists of eight elements surrounding the crack front, were modeled to represent the crack-tip singularity properly in an analysis. The dimensions of the analyzed flaw are $a = 6.9 \text{ mm}$ and $c = 13.8 \text{ mm}$.

The considered loading conditions are a brace tension and in-plane bending (Fig. 3). This model first was analyzed by TUJAP [7], a general purpose finite-element program, and

then the crack-tip asymptotic components of displacements were extracted from the quarter-point elements along the crack front and converted into the appropriate stress-intensity factors using a computer program especially developed for this purpose following the procedure of the previous section.

It took about eight central processing unit (CPU) hours on a VAX 11/780 machine for the stress analyses of the two load cases for this model. The results of the axial tension case are presented in Fig. 4. In Figs. 4 and 5, S is the crack front length coordinate measured from the deepest crack front position, and SL is the total crack front length. Since the symmetry axis of the flaw is closely aligned with that of the joint, K_I and K_{II} solutions are closely symmetric and K_{III} solutions are closely antisymmetric, as would be expected. The amplitudes of the stress-intensity factors are highest near the surface, which is consistent with the through-thickness stress distribution along the brace chord intersection, which is in a predominantly bending mode. The Mode I stress-intensity factor is dominant, since the principal direction of the applied load is perpendicular to the weld-toe contour. The results of the in-plane bending load case are shown in Fig. 5. The solution behavior is consistent with the physical behavior of the model, as in the first case. In this case, the dominant mode of crack-tip deformation is Mode III, in general. The K_{III} variation is roughly symmetric, while those of K_I and K_{II} are close to antisymmetric. For the in-plane bending case, crack surface contact and penetration were developed at a small portion of the compressed side of the crack surface, where K_I is negative, as can be seen in Fig. 5. For this region, the solution is not accurate, and it occurred because the analyses did not incorporate a multi-component contact algorithm. TUJAP does not have a capability suitable for such a contact analysis. In these plots, the data represented by the solid dots are the equivalent stress-intensity factors, K_e , which are converted from the appropriate energy release rate, G .

$$K_e^2 = K_I^2 + K_{II}^2 + \frac{K_{III}^2}{1 - \nu} \quad (9)$$

TENSION: $a=6.9$ mm; $c=13.8$ mm; $a/c=0.5$; $a/T=.44$

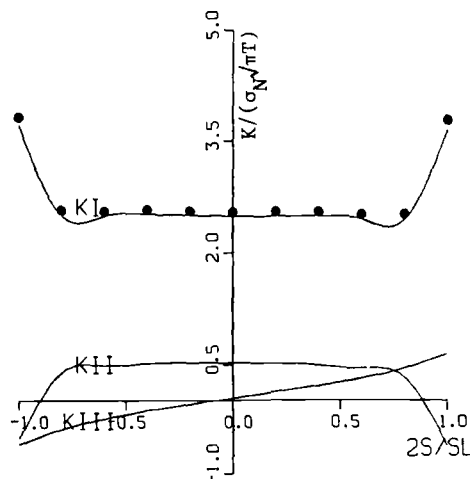


FIG. 4—Stress-intensity factors of weld-toe surface flaw (tension).

BENDING: $a=6.9$ mm; $c=13.8$ mm; $a/c=0.5$; $a/T=.44$

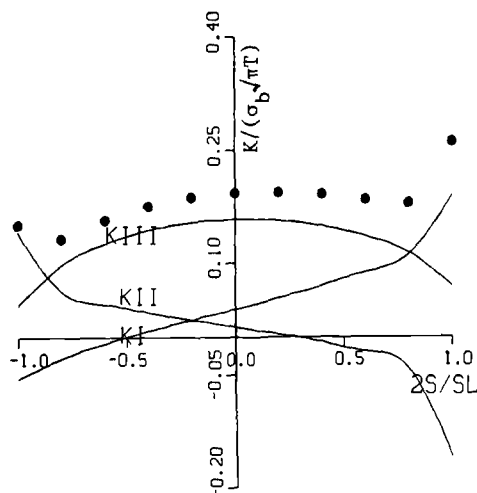


FIG. 5—Stress-intensity factors of weld-toe surface flaw (bending).

For a mixed-mode problem, any single component of the stress-intensity factors cannot represent the crack driving force properly since crack propagation is a combined result of the contributions of all three stress-intensity factors of the problem. A comparison between an equivalent stress-intensity factor, which incorporates all the existing stress-intensity factor components of a fully mixed-mode fatigue problem, and any individual component of K_I , K_{II} , and K_{III} can indicate the contribution of such an individual component to crack propagation. The validity of K_c as a fatigue crack driving force parameter has yet to be established. Further, the energy release rate expression, from which Eq 9 was derived, is valid for a two-dimensional cracked geometry.

Discussion

The stress-intensity factor solutions of mixed-mode three-dimensional problems with warped crack surfaces were developed. These solutions were not previously available because of the difficulty in modeling and the lack of an established procedure to evaluate the stress-intensity factors of a complex geometry such as the present. The solutions suggest a strong possibility of a mixed-mode crack-tip behavior for an offshore structural tubular joint weld-toe surface flaw. However, the results described in this paper should be considered as a first step to our understanding of tubular joints' fracture behavior. In these analyses, the crack was modeled as straight through the thickness direction and not curved as observed from experiments. This was necessitated by limitations in the program used to develop the finite-element model. This curvature may transform the mixed-mode solution to predominantly Mode I. This speculation is consistent with the results of some experimental data [8]. It was experimentally observed that mixed-mode fatigue crack growth behavior converged to that of Mode I by adjusting the growing direction of a crack under fatigue loading [8]. Other consideration should be given to the fact that the crack in the present model was located near the saddle point. For the in-plane bending load case, this position may not always be realistic because the hot spot for this case develops near the crown plant.

Conclusions

The significance of the results presented in this paper can be summarized as follows:

1. The present study has established that the conversion of the displacement solutions of a quarter-point crack-tip element is practical for evaluating the stress-intensity factor solutions of a three-dimensional complex mixed-mode structure with warped crack surfaces.
2. The solutions demonstrate that, even for a simple tubular joint, a mixed-mode fracture problem is possible.
3. Although the validity of the K -solutions cannot easily be verified, the physical consistency of their trends indicates their accuracy.
4. Although the CPU time required to perform this analysis on the VAX 11/780 was relatively long (about 8 h), the practicality of performing a rigorous fracture mechanics study on tubular joints has been demonstrated.
5. The results of the present analysis are important because they illustrate the potential of improving our understanding of the fracture mechanics behavior of complex tubular joint geometries.
6. For the analysis of a flaw in a tubular joint under an arbitrary load, a multicomponent contact algorithm is required to prevent the crack surfaces from penetrating each other.

Acknowledgment

The authors are grateful to the management of Conoco Inc. for permission to publish this paper.

References

- [1] Pan, R. B. and Plummer, B., "A Fracture Mechanics Approach to Nonoverlapping Tubular K -Joint Fatigue Life Prediction," OTC 2645, Offshore Technology Conference, Houston, TX, 1976.
- [2] Barsoum, R. S., "On the Use of Isoparametric Finite Elements in Linear Fracture Mechanics," *International Journal of Numerical Methods in Engineering*, Vol. 10, 1976.
- [3] Sih, G. C. and Liebowitz, H., "Mathematical Theory of Brittle Fracture," *Fracture: An Advanced Treatise*, Vol. II, Academic Press, New York, 1968.
- [4] Ingraffae, A. R. and Manu, C., "Stress-Intensity Factor Computation in Three Dimensions with Quarter-point Elements," *International Journal of Numerical Methods in Engineering*, Vol. 15, 1980.
- [5] Manu, C., "Pure Opening Mode Stress-Intensity Factor Computation for Elliptical Crack Fronts," *International Journal of Numerical Methods in Engineering*, Vol. 20, 1984, pp. 387-390.
- [6] PRETUBE, "Finite-Element Preprocessor for Tubular Joint, User's Manual," RN 83-6143, Veritec, Oslo, Norway, October 1985.
- [7] TUSTRA, "Tubular Joint Structural Analysis Module, User's Manual," The Otter Group/Sintef, Trondheim, Norway, November 1983.
- [8] Broek, D. and Rice, R. C., "Fatigue Crack Growth Properties of Rail Steels," DOT-TSC-1076, Final Report, Battelle-Columbus Laboratories, Columbus, OH, July 1977.

Crack Arrest Theory and Applications: Part II

Wide-Plate Crack-Arrest Testing: Evolution of Experimental Procedures

REFERENCE: deWit, R., Low, S. R. III, and Fields, R. J., "Wide-Plate Crack-Arrest Testing: Evolution of Experimental Procedures," *Fracture Mechanics: Nineteenth Symposium, ASTM STP 969*, T. A. Cruse, Ed., American Society for Testing and Materials, Philadelphia, 1988, pp. 679–690.

ABSTRACT: Between September 1984 and December 1985, five wide-plate crack-arrest tests on A533B quenched and tempered steel were carried out on the 26-MN tensile capacity universal testing machine at the National Bureau of Standards. Each test was different with respect to the conditions of testing, specimen configuration, and instrumentation used to monitor the dynamic response of the specimen during crack propagation and subsequent arrest. The progressive changes in test procedure discussed here represent attempts to obtain desired crack-run and crack-arrest behavior and to improve the quality of the data collected. Also, the optimization of strain gage locations and the final choice of recording instrumentation are reported in detail. Two techniques for measuring crack velocity are compared. Efforts to cause crack initiation and propagation at lower values of stress-intensity factor than were found in the first test are also discussed.

KEY WORDS: crack arrest, dynamic fracture, steel, temperature gradient, toughness, wide-plate testing, fracture mechanics

The wide-plate crack-arrest tests described were performed as part of the Heavy Section Steel Technology (HSSST) Program managed by Oak Ridge National Laboratory (ORNL) and sponsored by the Nuclear Regulatory Commission (NRC). The objectives of these tests were the following:

- (a) to provide arrest toughness data at temperatures near or above the onset of the Charpy energy upper shelf and above the limit of the American Society of Mechanical Engineers (ASME) arrest curve [1];
- (b) to provide data from which dynamic fracture models can be verified or developed; and
- (c) to evaluate techniques for dynamic measurements of relevant data, such as strain, displacement, acoustic emission, and so forth.

Background information describing the planning for these tests and the alloy to be tested is available in ORNL reports to the NRC [2,3,4]. More detailed descriptions of the tests briefly described here are also available [5,6]. A detailed description of the instrumentation has been published [7] by the present authors.

Briefly, these tests were performed by applying a tensile load to the large specimen assembly shown schematically in Fig. 1. Each test specimen was prepared from a well-

¹ Physicist, mechanical engineer, and metallurgist, respectively, Fracture and Deformation Div., Institute for Materials Science and Engineering, Gaithersburg, MD 20899.

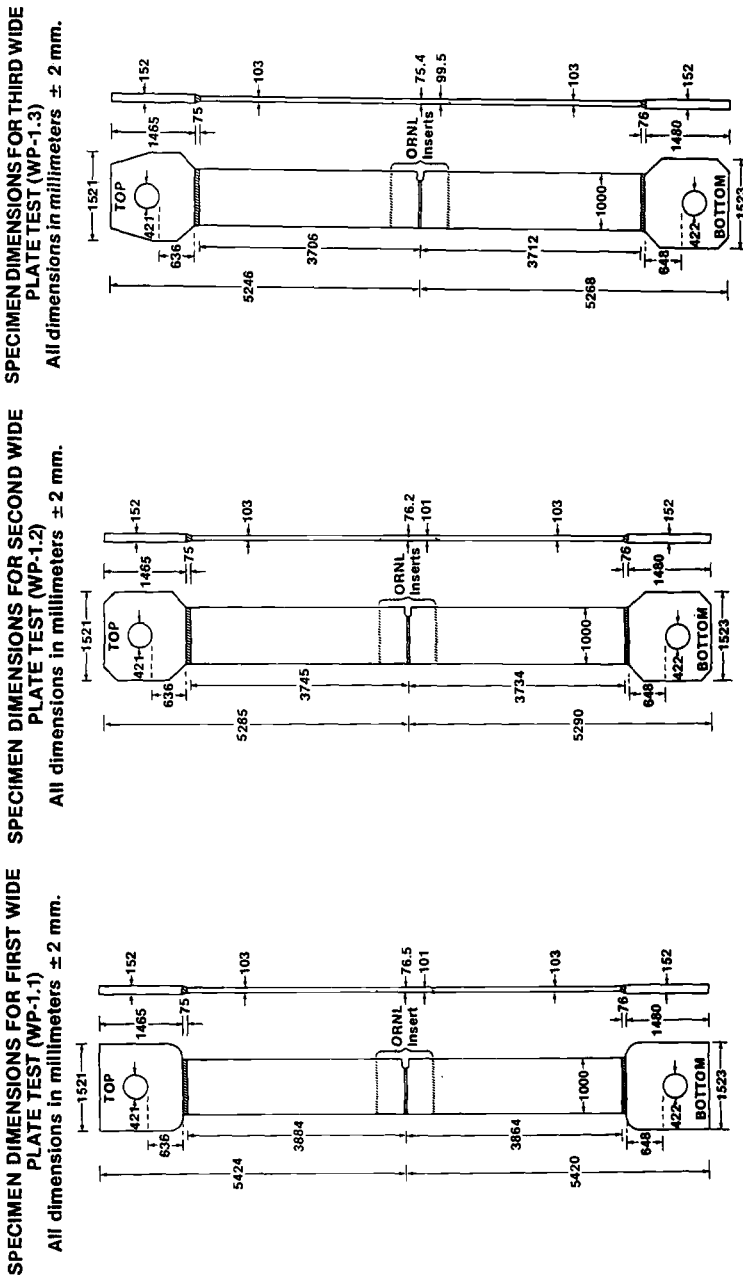


FIG. 1—Specimen configurations for the first three HSST wide-plate crack-arrest tests for A533B steel: WP-1.1.1 (left), WP-1.2 (middle), and WP-1.3 (right). The dimensions are in millimetres.

characterized plate A533B steel, contained a single-edge notch, and was centered between the two pull plates which were approximately 4 m in length. A sharp crack was placed at the root of the edge notch by ORNL through hydrogen charging of an electron-beam weld. Each face of the specimen was side grooved (12.5%) to provide a means of directing the crack and providing increased restraint of the crack front. The specimens were 1 by 1 by 0.1 m and were welded to the pull plates by the National Bureau of Standards (NBS).

The specimens were cooled on the notched edge and heated on the other edge to establish a nearly linear temperature gradient across the 1-m width. The uniaxial tensile load was applied at a constant rate until crack propagation initiated. The specimens were instrumented by NBS with about 20 strain gages and 30 thermocouples each. In addition, crack-opening displacement (COD) gages and timing stripes were used. The outputs of the various instruments were recorded throughout the development of the temperature gradient, the loading up, and the fracture event.

In order to obtain unambiguous crack-run and crack-arrest data, the effects of reflected stress waves must be minimized. Stress waves complicate and obscure the data, as well as interact with the propagating crack and cloud the conclusions that could be drawn from these tests. In order to obtain a crack run-arrest event without significant reflected waves, the pull tabs for the specimen were made relatively long in comparison with the half-length of a standard geometry crack-arrest specimen [8], which would be of the order of 0.2 m. It was concluded that a specimen 10 m in length would accomplish this objective.

The test conditions were defined by ORNL through detailed finite-element analyses [9] and are intended to initiate the crack at a temperature near or below the reference nil-ductility transition temperature (RT_{NDT}). A relatively long crack propagation (at least 150 mm) is desired to give opportunities to measure the dynamic event in great detail. Finally, stable arrest, stable tearing, unstable tearing, and tensile instability were all included in the analyses.

The thickness of the specimen was mainly determined by the desire to approach plane strain conditions at the crack tip and by the maximum load required for initiation. A thickness of 0.1 m was chosen as a reasonable dimension consistent with restraints imposed by the capacity of the testing machine. In order to enhance plane strain conditions further and to guide the crack, a groove was cut across each surface of the specimen so that the thickness along the crack path would actually be 0.075 m.

Once the desired specimen configuration was chosen, the instrumentation was planned and the layout of the strain gages was determined. Rows of strain gages were located at 0.065 m, 0.35 m, and 2 m from the crack plane. These gages would follow the dynamic strain response of the specimen to a crack run-arrest event. There would be enough strain gages present along the 0.065 m location to follow the crack position as a function of time. In addition, a ladder gage (that is, electrical continuity gages or timing stripes) placed across the crack path would be used to follow the crack position during the event. All these gages would be monitored dynamically during the event by triggering banks of transient, digital oscilloscopes. All the bridges and amplifiers were built so that the high-frequency response of the gages would not be distorted. This maximum frequency was initially chosen as 2 MHz.

Finally, in order to assure a crack jump that would yield a high crack-arrest toughness value, a technique of elevating the applied stress-intensity factor at initiation (K_I) above K_{Ic} was needed. The technique chosen involved warm prestressing the crack by first applying a load while the specimen was at a relatively high, uniform temperature. This loading was to give a K_I value equal to about 90% of the target K_I value and was followed by establishment of the temperature gradient. Thus, the specimen could be loaded to the target K_I value which exceeded K_{Ic} at the colder temperature. (The actual initiation loads have been higher

than anticipated so that the warm prestressing technique was used only with the first test, Test WP-1.1.)

This paper describes briefly how these plans were carried out. Emphasis is placed on evolutionary changes from the planned procedures that became necessary to make the measurements and obtain the desired data.

Specimen Configuration

The specimen configuration consists of two 150-mm thick tab ends and two 100-mm thick pull steel plates which are connected to the ORNL specimen inserts. The ORNL specimen was fabricated of specially characterized, A533B quenched and tempered steel alloy [5]. The specimen arrived at NBS already face-grooved, notched, and precracked to a depth of about 200 mm. The precrack was made by hydrogen charging an electron-beam weld at the root of the notch. NBS welded the specimen to the two pull plates prior to testing.

The main changes between different specimens, evident in Fig. 1, are the shapes of the tab ends and the length of the pull plates. The changes in the tabs were carried out to eliminate a stress concentration at the tab to pull-plate weld and to allow cranes on the testing machine to move freely from the back to the front of the specimen. The length changes in the pull plates resulted from the cutting out of the tested specimens and the insertion of new ones. Generally, this results in a shortening of the pull plates. However, between WP-1.3 and WP-1.4, only the material immediately adjacent to the fracture surface was removed before welding in the ORNL insert, and this resulted in a lengthening of the specimen. In general, the tab design has proven to be sufficient to support the bearing loads at the pins without plastic distortion. The pull plates have also proved to be long enough to avoid stress-wave reflection during the run-arrest events, which have been measured to take between 1 and 2 ms. Therefore, the specimen configuration, as shown for WP-1.3, will now remain unchanged for all subsequent 100-mm thick plate tests.

One problem which has surfaced is related to the out-of-plane bending of the specimen. This bending arises from residual stresses due to welding and original warpage of the pull plates. Figure 2 shows the extent of the out-of-plane displacement as measured on the

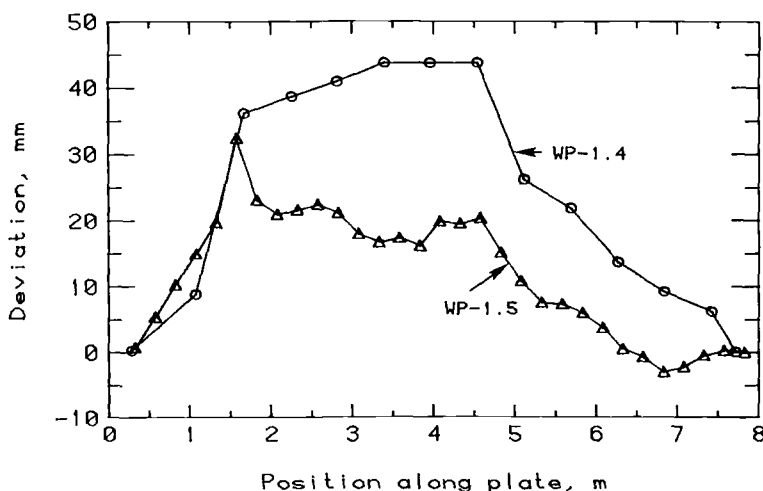


FIG. 2—Out-of-plane bowing of specimen/pull-plate assembly for unstressed specimens for Tests WP-1.4 and WP-1.5.

unstressed WP-1.4 and WP-1.5 specimens. This is an unsolved problem and necessitates strain measurements on both sides of the specimen in order to determine the real strain response during the dynamic event. New welding procedures are being employed to reduce the residual stresses. They mainly require that only a few weld passes be made on any one side before changing to the reverse side of the plate. The improvement from this welding procedure between WP-1.4 and WP-1.5 can be seen in Fig. 2. Furthermore, additional pull plates are being ordered. These are rolled thicker than desired so that finish machining can be guaranteed to achieve a flat and parallel surface over the full length of the pull plates.

Instrumentation

The strain gage layout used for the second test, WP-1.2, is shown in Fig. 3. This is similar to the layout that was planned for the first test, but due to difficulties in curing the gages, not all were applied in WP-1.1. As seen in Fig. 3, there are eight sets of 90° stacked gages

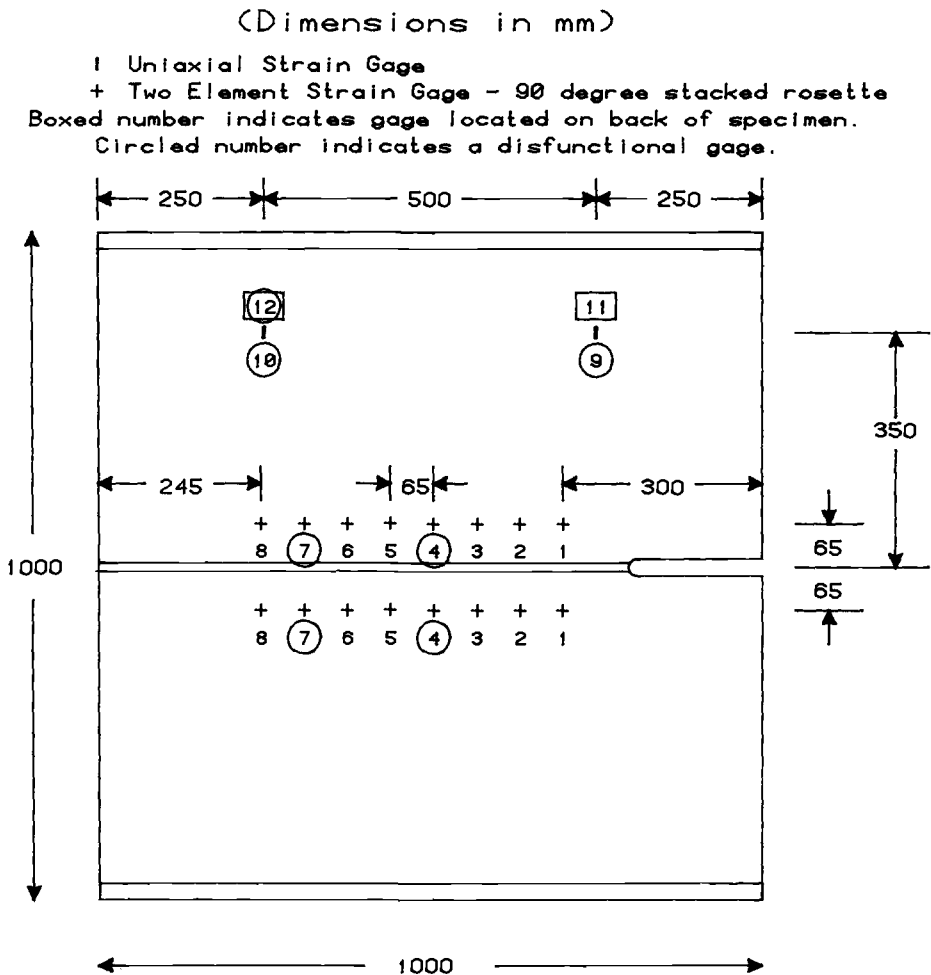


FIG. 3—Strain gage placement for Test WP-1.2.

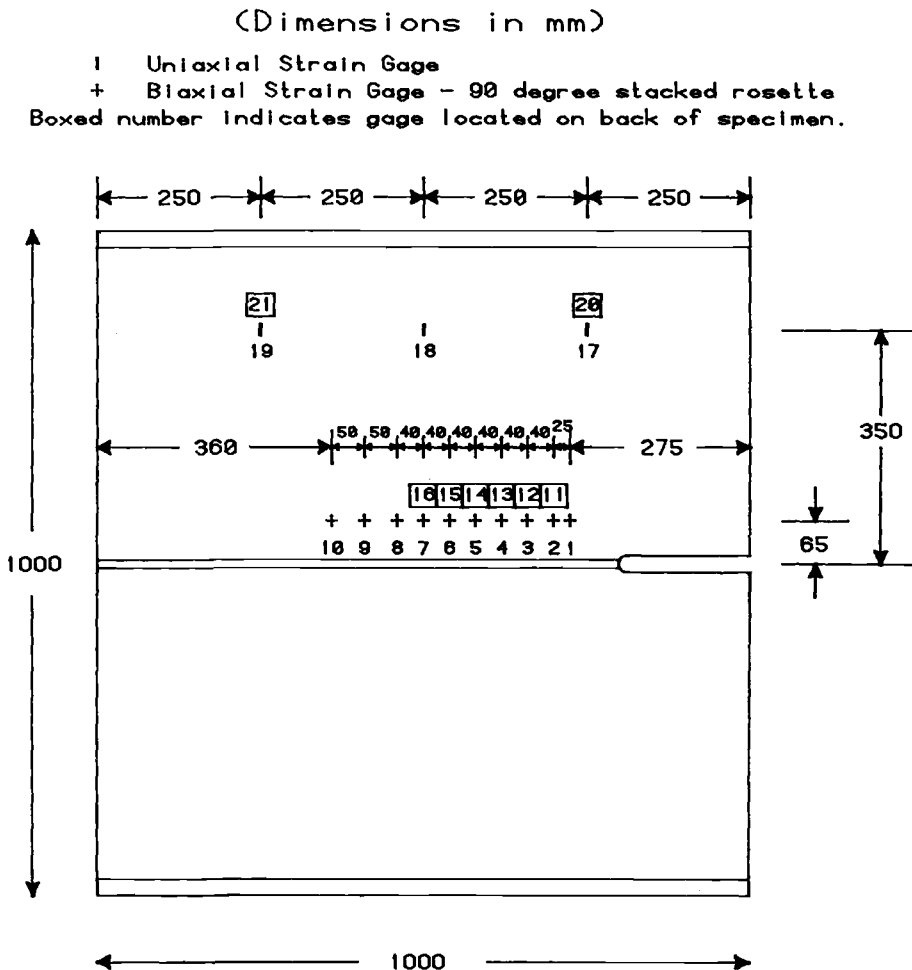


FIG. 4—Strain gage placement for Test WP-1.5.

on either side of the desired crack plane at 65 mm. Each set of gages was connected together in such a way as to nullify temperature effects and to average the strain measured on both sides of the crack plane. At 350 mm, four longitudinal gages (two on the front and two on the back) were applied. These would have been particularly useful in determining the out-of-plane bending that occurred, except that three of them failed during the test. In the far-field (that is 2 m from the crack plane), there were two 0°-45°-90° rosettes and a longitudinal gage. These defined boundary conditions for future analysis. There was also a longitudinal gage on the back to assess the extent of out-of-plane bending at this position.

Figure 4 shows the strain gage layout for WP-1.5. Note that there were ten crack-line strain gage sets on the front of the specimen and six on the back. This arrangement was chosen because the information obtained from the crack-line gages in previous tests has proved to be the most valuable and informative data collected. To maximize this information the gages were placed closer together and more have been applied. Furthermore, gages were no longer used to span the crack. These gages were eliminated because they were

found to broaden the strain pulse (by adding two peaks) as the crack went by and because the fractures have not run out of the face-groove since the first test. However, the presence of the out-of-plane bending, mentioned previously, has required that crack propagation be monitored on both sides of the plate. To this end, gages are now placed on both sides in the region where arrest is most likely to occur.

At the 350 mm position, the strain gage layout remains basically unchanged except for an additional gage located in the center. At the 2 m position, all rosettes have been replaced by a single longitudinal gage. This change was made after the earlier tests showed that the rosettes were simply confirming a uniaxial stress state at that location. Therefore, the far-field strain state at a point could be determined from the measurement of a single strain gage.

It had originally been planned to use a ladder (or velocity) gage for confirmatory measurement of crack position. Such gaging was installed in Tests WP-1.1, WP-1.2, and WP-1.3, but these gages were found to be extremely time consuming and tedious to install. A comparison between crack position measured by the ladder (or velocity) gage and by the strain gages is shown in Fig. 5. There is fairly good agreement early in the experiment. However, a significant discrepancy occurs after 0.4 ms and persists thereafter. Posttest examination of the fracture surface supported the crack positions as deduced by the strain gages. After this came to light, use of the ladder gages was discontinued.

Finally, one type of gage, which was not planned or used in WP-1.1, has been installed on all tests starting with test WP-1.2, namely the crack-opening displacement (COD) gage. One gage is applied to each side of the specimen near the notch tip. It has proven useful in determining the crack opening at the onset of crack propagation and at arrest. The gage uses a noncontacting eddy current probe and is nondistorting up to a frequency of 10 kHz.

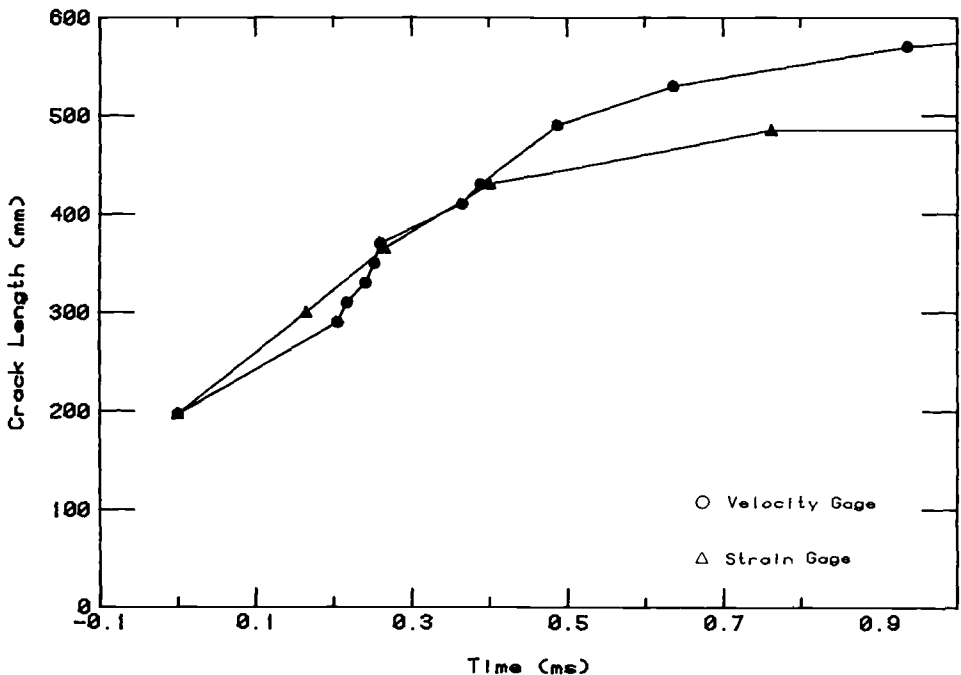


FIG. 5—Comparison of crack propagation history for Test WP-1.3 as measured by ladder (or velocity) gage and by an array of strain gages.

Data Acquisition

As described in the introduction, the authors initially planned to acquire all the data by triggering a bank of transient digital oscilloscopes at the start of crack propagation. There were many difficulties associated with this procedure. First, data were acquired as a single "snapshot" in time. This meant that to obtain absolute strain readings, the oscilloscopes had to be triggered periodically throughout the test. The data at these points in time had to be pieced together to obtain a coarse record of the total experiment and a trade-off between time window and resolution had to be chosen. The oscilloscopes could only record 4000 data points, and to obtain maximum resolution the time per point had to be as short as possible. However, such a setting meant that the total time during which data could be collected had to be very short. Should the run-arrest event last longer than expected or the trigger be somehow delayed, then valuable data would be lost. Also, using the digital oscilloscope would miss multiple run-arrest events unless the time window were set very large. Such a large window would reduce the resolution of the data to unacceptable levels.

In Test WP-1.1, the above procedure was employed, and the optimum window settings and time resolution were chosen prior to testing based on best estimates of the probable crack behavior. Oscilloscope triggering was accomplished by breaking an electrical continuity strip just ahead of the crack. In the actual event, the specimen behavior was very different from what had been expected. The triggering was delayed by several milliseconds after the crack started to run and a record of the tearing instability fracture was obtained until the time window closed. However, the cleavage run-arrest event was not captured.

In Test WP-1.2, an FM tape recorder (response: DC to 500 kHz) was used in conjunction with the transient oscilloscopes. The test apparatus is shown in Fig. 6. In this test, triggering was on time, and data records were obtained using both the tape recorder and the oscilloscopes. Posttest analysis revealed that the resolution was as good on the taped record as on the oscilloscope record. Furthermore, a very rapid reinitiation run-arrest event took place in WP-1.2. This was captured on the tape unit, but was entirely missed by the oscilloscopes. In addition to the extra run-arrest data, the taped record provided continuous monitoring of the strain field developed during the establishment of the temperature gradient and during loading. After WP-1.2, all test data were taped continuously and transient oscilloscopes were used only to monitor gages whose response was not critical. This approach has proved extremely effective and has eliminated entirely the need of a triggering system.

Fourier analysis of the data has shown that critical features of the data can be acquired by systems capable of resolving 30 kHz. Indeed, it is often possible to reproduce the undistorted curves using frequencies up to only 10 kHz. The original aim to have undistorted data collection up to 2 MHz seems unnecessary for the present test set up.

Loading Procedure

The loading procedure used in Test WP-1.1 was as initially planned, including warm prestressing the crack (WPS) by applying a load of 10 MN at 70°C. The load was then reduced to 7 MN, and the specimen was cooled on one edge and heated on the other to obtain a gradient extending from -70°C to +200°C across the 1-m specimen width. The load on the specimen was then increased until crack propagation occurred. If the WPS procedure had resulted in the expected behavior, crack propagation would have begun at 10 MN. In fact, crack propagation began at 20 MN. This extreme overload resulted in crack branching and, immediately after arrest, reinitiation by tearing leading to complete ductile fracture of the remaining ligament.

In order to obtain a lower initiation load, the WPS procedure was eliminated in Test WP-1.2. After attaining the desired temperature gradient, the specimen was loaded until

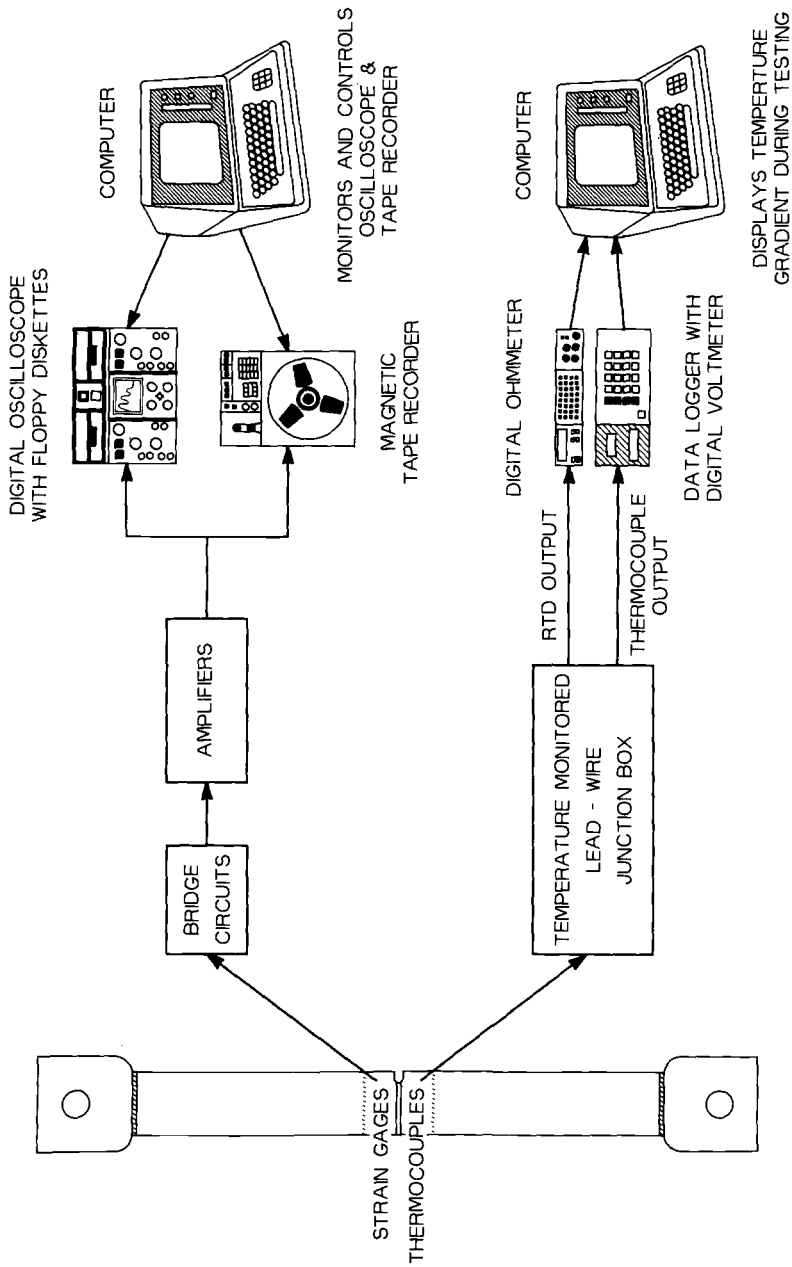


FIG. 6—Schematic of NBS data acquisition system.

crack propagation commenced at a load of 19 MN, which was still too high to achieve stable arrest. Two arrests occurred, but neither was stable. The specimen fractured in two pieces within 20 ms. For reasons which are still not clear, crack propagation initiated when the applied stress-intensity factor, K_I , was about 2.9 times the calculated K_{Ic} . This overload caused the observed ductile reinitiations.

As in WP-1.2, no WPS was used in WP-1.3. Furthermore, the stress intensification at the crack tip was increased by employing a chevron notch as shown in Fig. 7. In this test, crack initiation occurred at 11.3 MN. The arrest which occurred was nearly stable as ductile fracture took place almost 2 s after the arrest.

In WP-1.4, again, WPS was not employed and a chevron notch was used. In addition, a small, hydraulic pillow jack was placed in the notch. After attaining the desired gradient, a tensile load of 8 MN was applied. The jack was then activated. When the pressure in the jack reached 63.4 MPa, crack propagation initiated. A completely stable arrest occurred at 7.9 MN, and the load was held there for more than a minute. After demonstrating a stable crack arrest, the load was increased. At 9.7 MN an additional run-arrest event occurred. This arrest caused the load to drop to 7.6 MN. After 30 s at this load, the crack became unstable (presumably because of time-dependent plastic effects) and complete fracture to zero load took place. Note that many of the interesting features of this test would not have been documented using transient oscilloscopes and triggering systems. However, since the entire event was taped, a complete record was obtained.

Conclusion

In the planning stages of the tests described here it was thought that difficulties would be encountered in obtaining the desired temperature gradients and in achieving sufficient overloads in order to obtain significant run-arrest events. The acquisition of data was also believed to present a challenge.

The desired temperature gradients were achieved in each test. This aspect of the tests, while difficult, was carried out using the heating and cooling systems without modification. Crack initiation requiring higher than expected loads, on the other hand, has led to some problems. These problems have basically been overcome by employing a chevron crack front to increase the stress-intensity factor for a given load.

Finally, instrumentation and a data acquisition system have been developed which provide entirely satisfactory and reliable documentation of these unique experiments. While the instrumentation is not far from that initially planned for in these tests, the data acquisition system is considerably different. The taping system is much simpler and more reliable than the approach first envisioned for the recording of these test results by banks of digital oscilloscopes.

The procedures for performing these experiments have now been worked out satisfactorily, and the tests are providing reliable results. Further series of six tests each are planned for a low-upper-shelf energy base material and a low-upper-shelf energy weld material.

Acknowledgments

The authors would like to express their gratitude to Milton Vagins of the Nuclear Regulatory Commission and Claud E. Pugh of Oak Ridge National Laboratory for their encouragement and support during the performance of the research described here. In addition, the authors thank Joseph Sanford and George Irwin of the University of Maryland for advice and useful suggestions, many of which are employed in the present testing program.



FIG. 7—A chevron notch configuration was used in specimens for Tests WP-1.3, WP-1.4, WP-1.5, and WP-1.6 to reduce the initiation load: A, Notch; B, Precrack; C, Side groove; D, Fracture surface; E, Fracture surface. The scale indicates the distance from the cold edge in centimetres.

References

- [1] ASME Boiler and Pressure Vessel Code, Section XI, The American Society of Mechanical Engineers, New York, NY 1983.
- [2] "Heavy Section Steel Technology Program, Five-Year Plan, FY1984-1988," NUREG/CR4275 and ORNL/TM-9654, Oak Ridge National Laboratory, Oak Ridge, TN, July 1985.
- [3] "Heavy Section Steel Technology Program, Semiannual Progress Report for April-September 1984," NUREG/CR-3744, Volume 2, and ORNL/TM-9154/V2, Oak Ridge National Laboratory, Oak Ridge, TN, December 1984.
- [4] "ORNL Characterization of Heavy Steel Technology Program Plates 01, 02, and 03," NUREG/CR-4092 and ORNL/TM-9491, Oak Ridge National Laboratory, Oak Ridge, TN, April 1985.
- [5] "Heavy Section Steel Technology Program, Semiannual Progress Report for October 1984-March 1985," NUREG/CR-4219, Volume 1, and ORNL/TM-9593/V1, Oak Ridge National Laboratory, Oak Ridge, TN, June 1985.
- [6] "Heavy Section Steel Technology Program, Semiannual Progress Report for April-September 1985," NUREG/CR-4219 Volume 2 and ORNL/TM-9593/V2, Oak Ridge National Laboratory, Oak Ridge, TN, June 1985.
- [7] Danko, G. A., Low, S. R., III, deWit, R., and Fields, R. J., "Wide-Plate Crack-Arrest Tests: Instrumentation for Dynamic Strain Measurements," *Use of New Technology to Improve Mechanical Readiness, Reliability, and Maintainability*, T. R. Shives, Ed., Cambridge University Press, New York, 1987, pp. 178-192.
- [8] Crosley, P. B., Fournery, W. L., Hahn, G. T., Hoagland, R. G., Irwin, G. R., and Ripling, E. J., "Cooperative Test Program on Crack-Arrest Toughness Measurements," NUREG/CR-3261, U.S. Nuclear Regulatory Commission, Washington, DC, 1983.
- [9] Bass, B. R., Pugh, C. E., and Stamm, H. K., "Dynamic Analyses of a Crack Run-Arrest Experiment in a Nonisothermal Plate," *Pressure Vessel Components Design and Analysis*, Vol. 4, ASME PVP 98-2, American Society of Mechanical Engineers, New York, 1985, pp. 175-184.

*B. Richard Bass,¹ Claud E. Pugh,¹ John G. Merkle,¹ Dan J. Naus,¹
and Janis Keeney-Walker¹*

Fracture Analyses of Heavy-Section Steel Technology Wide-Plate Crack-Arrest Experiments

REFERENCE: Bass, B. R., Pugh, C. E., Merkle, J. G., Naus, D. J., and Keeney-Walker, J., "Fracture Analyses of Heavy-Section Steel Technology Wide-Plate Crack-Arrest Experiments," *Fracture Mechanics: Nineteenth Symposium, ASTM STP 969*, T. A. Cruse, Ed., American Society for Testing and Materials, Philadelphia, 1988, pp. 691-723.

ABSTRACT: A series of six wide-plate crack-arrest tests was recently completed by the Heavy-Section Steel Technology program at the National Bureau of Standards, Gaithersburg, MD, using tensile-loaded specimens of A533 Grade B Class 1 steel. Crack-arrest data were obtained at temperatures in the transition range and above the onset of the Charpy upper shelf, thereby providing a basis for the development and evaluation of improved fracture-analysis methods. The 1 by 1 by 0.102-m single-edge-notched (SEN) specimens were welded to long straight pull tabs and subjected to a transverse linear temperature gradient before loading. The crack tips were sharpened by hydrogen-charging an electron-beam weld. The tests were designed to obtain crack arrest near the middle of the specimen where the temperature would produce a high-toughness level in the upper transition region of the material. The specimens were instrumented with strain gages and thermocouples. Initial static design calculations were made using textbook formulas. Additional calculations, using an assumed set of K_{ID} versus \dot{a} and T relations and an effective stress wave concept, confirmed the reasonableness of tentative design parameters. Pretest and posttest dynamic finite-element calculations were performed for each test. Computed results are compared with transient data for crack-line strains, crack speed, crack-opening displacement, arrest location, and postarrest tearing. Results from both application-mode and generation-mode dynamic analyses are presented. The arrest toughness values calculated from the test data are summarized for temperatures ranging from the transition into the Charpy upper-shelf range.

KEY WORDS: elastodynamic fracture, crack-arrest toughness, nonisothermal tensile specimens, wide plate, dynamic finite-element model, application-mode analysis, generation-mode analysis, A533B steel, fracture mechanics

Central to the studies of the Heavy-Section Steel Technology (HSST) program is understanding pressure vessel conditions that would initiate growth of an existing crack and conditions that would lead to arrest of a moving crack. Prior studies of crack arrest have utilized small specimens and focused on reducing dynamic effects of the running crack. Small specimens, however, provide limited constraint of deformation in the crack-plane region and permit only the generation of data at temperatures below those where arrest is likely to occur in some pressurized-thermal-shock (PTS) scenarios. Recently, the HSST program

¹ Head of the Engineering Mechanics Section, head of the Pressure Vessel Technology Section, and research engineers, respectively, Heavy-Section Steel Technology Program, Oak Ridge National Laboratory, P.O. Box Y, Oak Ridge, TN 37831.

has generated crack-arrest data over an expanded temperature range through tests [1–3] of several types of larger specimens. In particular, tests of wide plates [3] are allowing a significant number of data points to be generated at affordable costs. The first series of HSST wide-plate crack-arrest tests (WP-1) was recently completed at the National Bureau of Standards (NBS) [4], Gaithersburg, MD, using specimens of A533 Grade B Class 1 steel. The second series of tests (WP-2) will utilize plate material that has been specially heat treated to produce a low upper-shelf Charpy impact energy (54 to 68 J).

The tests of the WP-1 series were aimed at providing crack-arrest data at temperatures up to and above that corresponding to the onset of the Charpy upper shelf, as well as providing information on dynamic fracture (run and arrest) processes for use in evaluating improved fracture analysis methods. The tests used tensile-loaded single-edge-notched (SEN) plate specimens (1 by 1 by 0.102 m) welded to long straight pull tabs. The specimens were cooled on the notched edge and heated on the other edge to give a linear temperature gradient along the plane of crack propagation. The crack tips were sharpened by an electron-beam welding and hydrogen-charging technique [5]. Upon initiating propagation of the crack in cleavage, arrest was intended to occur near the middle of the specimen where the temperature would produce a high toughness level in the upper transition region of the material. The specimens were instrumented with strain gages and thermocouples to provide strain and temperature data as functions of position and time.

At the time these experiments were being designed, no in-house capability existed for performing detailed numerical dynamic fracture mechanics calculations. Nevertheless, it was considered necessary to include net section eccentricity, stress wave effects, the toughness versus crack speed and temperature relations, and the possibility of tensile and tearing instability in the design calculations. Initial static calculations were made for initiation and arrest, using textbook formulas for single-edge-notched and center-cracked plate (CCP) specimens. These results were used to select the most promising combination of geometry, temperature distribution, and load. This combination of test conditions was then used as input to a more detailed method of analysis that employed an effective stress wave concept. Then, by using an assumed set of K_{ID} versus \dot{a} and T relations for the material, the position of the crack tip as a function of time was estimated. The results confirmed the reasonableness of the tentative design parameters as well as illustrated the basic nature of the dynamic and crack speed effects to be expected.

Crack propagation and arrest behavior has historically been interpreted and analyzed in terms of static fracture mechanics concepts, neglecting stress wave effects and the toughness versus crack speed relations. However, the events are inherently dynamic, so that the analysis methods should consider the inertial and strain-rate effects that are known to be present. Accordingly, the HSST program has been working on integrated efforts to develop elastodynamic fracture analysis finite-element programs and viscoplastic analysis methods [6–7]. Dynamic finite-element fracture analyses have been completed for the actual test conditions present in the WP-1 series. In this paper, computed results are compared with data for crack-line strain-time response, crack-propagation speed, crack-opening displacement, arrest location, and postarrest tearing. Results from both application-mode and generation-mode dynamic analyses are presented. In addition, the paper includes a summary of the arrest toughness calculations compiled from the test data at temperatures ranging from transition to Charpy upper-shelf values for the wide-plate material.

Background

Large single-edge and center-cracked, tensile-loaded, wide plates are among the oldest types of fracture mechanics specimens (see Chapter 2 in Ref 8). In fact, their use predates

the discovery of the linear elastic crack-tip stress-intensity factor. In 1952, Irwin and Kies [9] showed that the elastic strain energy release rate for a center-cracked tensile specimen with fixed ends depends significantly on the length of the specimen. Then, soon after the advent of linear elastic fracture mechanics, Irwin [10] proposed a method for analyzing dynamic photoelastic data for a tensile-loaded SEN specimen by means of the static formula for a periodic array of through cracks in an infinite plate commonly applied to a center-cracked tensile specimen

$$K_I = \sigma \sqrt{\pi a} \sqrt{\frac{\tan \frac{\pi a}{2W}}{\frac{\pi a}{2W}}} \quad (1)$$

where K_I is the stress-intensity factor, σ the tensile stress, a the crack depth, and W the width of the SEN specimen. Incorporated in the analysis method were the assumptions of a fixed load-point displacement and an effective specimen length that increases with time.

Recently, considerable testing of wide-plate specimens has been done in Japan [11–16]. Some of these specimens are called double-tension specimens [14] because they use a notched tensile-loaded tab attached to the edge of the specimen as an auxiliary crack starting device. In most of these references, the experimental data were analyzed by calculating the stress-intensity factor from Eq 1, or from the static formula for an SEN specimen, with multiplying factors being applied for the effects of load drop and crack speed. The latter effect was usually estimated by means of the approximation suggested by Freund [17,18]

$$K_{\text{dyn}} = K_{\text{static}} \sqrt{1 - \frac{\dot{a}}{C_R}} \quad (2)$$

where \dot{a} is the crack speed and C_R is the Raleigh wave speed. In Ref 16, an empirical expression was developed for the dependence of dynamic toughness on crack speed and temperature.

For the HSST wide-plate tests, the authors decided to follow common practice and use long pull plates so that shear waves could not originate from and return to the crack plane during a run-arrest event. The initial specimen design calculations were performed with static stress-intensity factor formulas. Since the crack speed, \dot{a} , is zero at crack arrest, no crack speed correction was necessary for estimating crack-arrest conditions. Since most wide-plate specimens tested previously by others have had very shallow starter notches, and some also have had blunt back edge notches, initial in-plane bending was negligible and Eq 1 was appropriate. However, in the HSST tests, it was planned to use an initial a_1/W value of 0.2. Thus some in-plane bending would exist at initiation, and after some trial calculations, the authors decided to use the standard SEN formula [19]

$$K_I = Y_{r1} \sigma \sqrt{a_1} \sqrt{\frac{B}{B_n}} \quad (3)$$

for crack initiation, where the subscripts on Y stand for the load and the first crack depth, B and B_n are the gross and net section thicknesses, respectively, and the factor

$\sqrt{B/B_n}$ accounts for the effect of side grooving. At crack arrest, K_{I1} was estimated from a modified form of Eq 3

$$K_{I1} = Y_{p1} \sigma \sqrt{a_2} \sqrt{\frac{B}{B_n}} \quad (4)$$

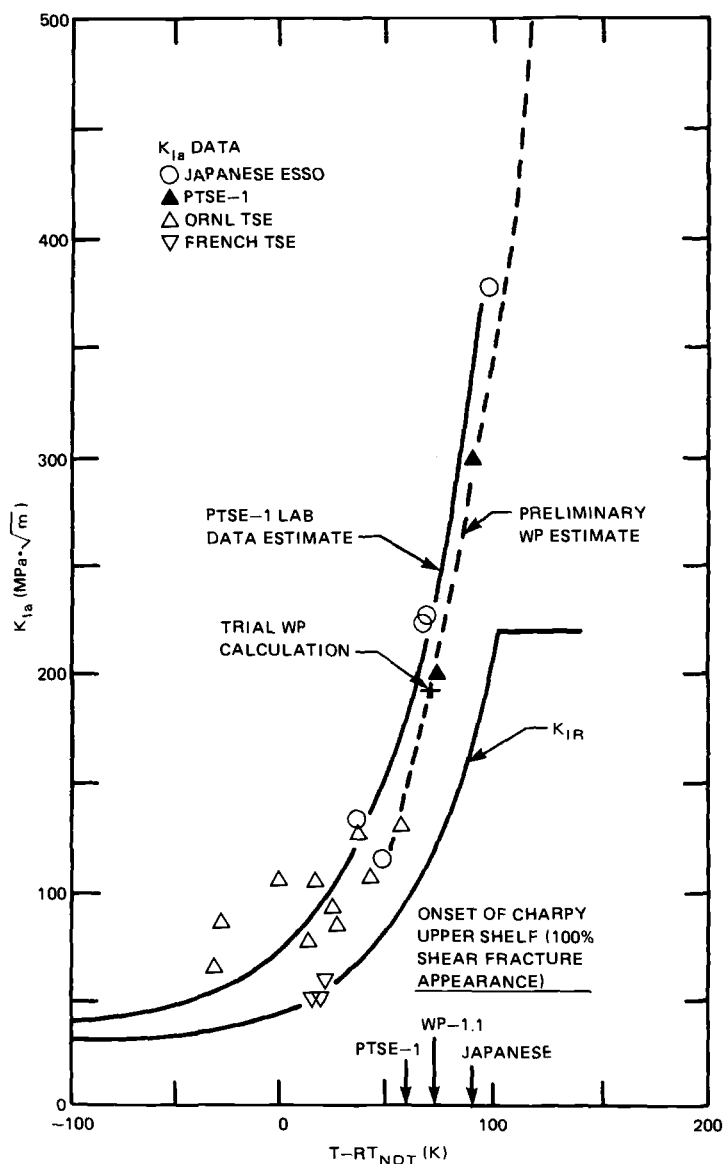


FIG. 1—Large-section crack-arrest toughness versus temperature data and preliminary estimate for wide-plate specimen design.

TABLE 1—Wide-plate specimen design conditions selected for evaluation.

Arrest conditions
$a_2/W = 0.45$
$K_{Ia} = 192 \text{ MPa } \sqrt{\text{m}}$
$T_2 = 39.4^\circ\text{C}$
Applied stress
$\sigma = 102.7 \text{ MPa}$
Initiation conditions
$a_1/W = 0.2$
$K_I = 128 \text{ MPa } \sqrt{\text{m}}$
$T_1 = -28.9^\circ\text{C}$
Edge temperatures
$T_{\min} = -83.6^\circ\text{C}$
$T_{\max} = 189.8^\circ\text{C}$
Shear wave speed
$c_2 = 3182 \text{ m/s}$
Remaining ligament stress
$\sigma_l = 248.2 \text{ MPa}$

in which the value of Y was the same as for initiation, but the value of a_2 was the arrest-crack depth. The intent of Eq 4 was to consider initial in-plane bending, but to assume no additional bending and no load drop during the run-arrest event.

A preliminary estimate of the relation between the crack-arrest toughness and temperature for the first series of wide-plate tests was made by considering the available large-section test data. Figure 1 shows data from Japanese ESSO tests [11], the first HSST pressurized-thermal-shock test (PTSE-1) [2], a series of HSST thermal-shock tests [1], a French thermal-shock test [20], and curves representing a fit to laboratory specimen data for the PTSE-1 material [2] and the American Society of Mechanical Engineers (ASME) Section XI K_{IR} curve. The dashed line in Fig. 1 is the K_{Ia} versus temperature relation used for the initial HSST wide-plate design calculations.² The reference nil-ductility transition temperature (RT_{NDT}) for the WP-1 material was estimated to be -28.9°C .

The test section dimensions were selected to be 1 by 1 by 0.102 m, with 25% side grooving to produce a crack plane thickness of 7.62 cm. The intention was to produce crack arrest at a K_{Ia} value approaching $220 \text{ MPa } \sqrt{\text{m}}$ near the middle of the plate, with an average remaining ligament stress after crack arrest less than the yield stress. It was also considered necessary to have the initial crack-tip temperature at or below the RT_{NDT} in order to initiate cleavage fracture in the elastic range under static loading. Initial design calculations were therefore performed by selecting the initial crack-tip temperature, the crack-arrest depth, and the value of K_{Ia} at arrest. From these values, the temperature at the point of crack arrest, the edge temperatures (based on a linear variation of temperature across the plate), the applied stress, and the value of K_I at initiation were determined. It was evident that some means of elevating the static initiation toughness above the plane strain value would be required in order to achieve the desired stress level. It later turned out that inherent geometrical effects not yet fully understood provided a more than sufficient elevation of the static initiation fracture toughness.

After performing parametric static design calculations, the set of conditions listed in Table 1 was selected for further evaluation, to include the estimated effects of stress waves and

² Bryson, J. W., unpublished calculations, Oak Ridge National Laboratory, Oak Ridge, TN, November 1983.

crack speed. The arrest toughness and temperature conditions used in the static analysis are indicated in Fig. 1. The applied analytical method is a composite of several other approaches. As in the static design analysis, the specimen was treated as a single-edge-notched (SEN) specimen. However, the rotations occurring in the specimen were treated in a more quantitative manner. Following a suggestion from Irwin [10], it was assumed, because of stress waves propagating from the crack plane, that the effective length of the specimen increases with time. Furthermore, at the effective ends of the specimen, it was assumed that the load and the rotation angle remain constant during crack propagation. Modifying an approach suggested by Sanders and Romualdi [21], it was assumed that the effective height of the specimen could be estimated by calculating an effective specimen area as the area lying within an effective circular stress wave front expanding from the original crack tip. The effective specimen height was taken to be the effective specimen area divided by the specimen width. By making trial calculations for three SEN specimens of Homalite 100 tested at the University of Maryland [22], it was determined that a reasonable estimate of the effective stress wave speed is 30% of the shear wave speed. The results of the Homalite 100 calculations are shown in Fig. 2. The calculations were made for cracks running at a speed of one-third the shear wave speed, at an a/W of 0.6, in specimens with three different initial crack depths. Also shown in Fig. 2 are curves for the SEN and CCP formulas and the elastodynamic

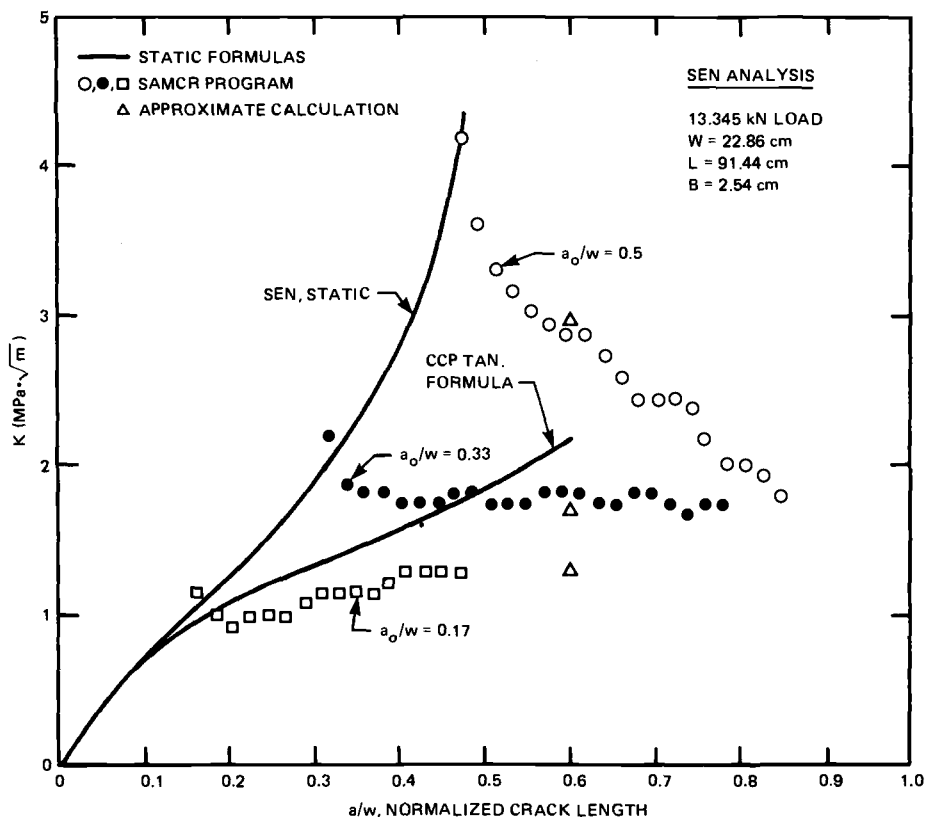


FIG. 2—Static, dynamic, and approximate dynamic analysis results for three Homalite 100 SEN specimens tested at the University of Maryland.

calculations for the three specimens made at the University of Maryland with the SAMCR computer code [22]. It can be seen that the approximate calculations are in good agreement with the SAMCR calculations, whereas the opposite is true for the CCP formula of Eq 1.

In order to make calculations for the wide-plate design, it was necessary to have a relationship between dynamic toughness, crack speed, and temperature. Such a relationship was developed empirically by Kanninen et al. [23], using the data for Japanese double-tension specimen SP-8 reported in Ref 14. A value of the nil-ductility transition temperature (NDT) was not reported for the test material in Ref 14. However, an estimate was made by using Kanninen's empirical relation between K_{Ia} and temperature for the test material. Assuming that the value of K_{Ia} at NDT is the same as that for HSST Plate 02 at its NDT of -17.8°C (about $65.9 \text{ MPa } \sqrt{\text{m}}$ [24]), it was estimated that the NDT for the double-tension test material was -6.1°C . On that basis, a dynamic fracture toughness relation was developed having the form

$$K_{ID} = K_{Ia} + A(T) \dot{a}^2 \quad (5)$$

where

$$A(T) = [121.71 + 1.296(T - RT_{NDT})] \times 10^{-6} \quad (6)$$

or

$$A(T) = [329.7 + 16.25(T - RT_{NDT})] \times 10^{-6} \quad (7)$$

if $(T - RT_{NDT})$ is less or greater than -13.9°C , respectively. Units for K_{ID} , \dot{a} , and T are $\text{MPa } \sqrt{\text{m}}$, m/s , and $^{\circ}\text{C}$, respectively. It was assumed that the equation for K_{Ia} can be chosen independently. For this analysis, the equation of a hyperbola [25] that agrees very closely with the dashed curve in Fig. 1

$$K_{Ia} = \frac{7249.3}{109.44 - (T - RT_{NDT})} \quad (8)$$

was used to estimate K_{Ia} .

The calculations were performed incrementally with respect to a/W . First, the radius of the effective stress wave and the corresponding effective specimen height at the beginning of the current incremental crack extension were determined. From the calculated compliances with and without a crack and the assumed boundary conditions, the effective end bending moment and the value of K_I were calculated at the end of the current increment of crack extension. From the known temperature distribution, the end point crack-arrest toughness and crack speed, and the average crack speed for the current crack-extension increment were determined. Then the current time increment and the total elapsed time were calculated. The calculations were continued until K_I became equal to K_{Ia} and the crack speed decreased to zero. The results for the proposed design conditions listed in Table 1 are shown in Fig. 3.

As shown in Fig. 3, the crack begins running at a speed slightly over 400 m/s , but decelerates rapidly because rotational displacements in the uncracked section are delayed by inertia. At first K_I decreases with increasing crack depth, but as the uncracked section begins to rotate, K_I begins to increase with increasing crack depth. The crack speed reaches a local minimum, increases slightly, and then decreases to zero as crack arrest is approached. The duration of the crack run/arrest event was estimated to be about 1.9 ms . While the crack is running, the value of K_I remains close to that calculated by the tangent formula, Eq 1, until a/W exceeds 0.35 . At arrest, the value of K_I was 40% greater than predicted

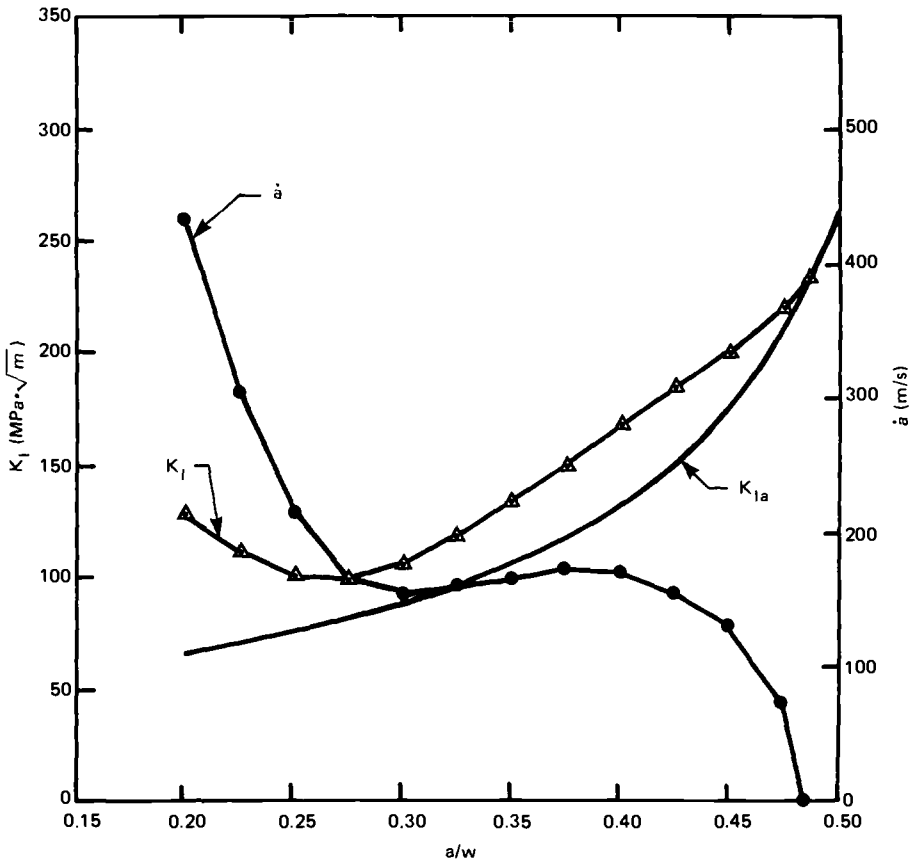


FIG. 3—Approximate dynamic analysis results for a 1 by 1 by 0.102 m wide-plate crack-arrest specimen, based on the tentative testing conditions given in Table 1.

by Eq 1, thus implying that crack-arrest toughness calculations by Eq 1 will be conservative. Crack arrest was predicted to occur near the middle of the plate, thus confirming the reasonableness of the assumed testing conditions.

Specimen Geometry, Material Properties, and Instrumentation

The overall wide-plate specimen design is illustrated in Fig. 4 to be a 1 by 1 by 0.102-m plate with a single-edge notch that gives an initial crack-depth-to-plate-width ratio (a/W) of 0.2. The total notch depth of 19.69 cm is composed of a 2.54-cm-wide gap that is machined to a depth of 18.42 cm plus an electron-beam weld-generated crack with a depth of 1.27 cm at the end of the gap. Each side of the specimen is side grooved to a depth equal to 12.5% of the plate thickness, and the grooves have a 0.25-mm root radius. The initial crack is perpendicular to the rolling direction. The specimen is welded to the pull-plate assembly which is made up of welded sections, as shown in Fig. 4. The specimen and pull-plates are 10.2 cm thick, except for the pull-tabs near the pull-pins, which are 15.24-cm thick. For test specimens WP-1.3 through WP-1.6, the crack front was cut into a chevron configuration (Fig. 5) to reduce the tensile load required to achieve crack initiation.

The initial series of wide-plate crack-arrest specimens was taken from the central portion

of 18.73-cm-thick HSST Plate 13A of A533 Grade B, Class 1 steel in a quenched and tempered condition. The properties of this plate include Young's modulus (E) = 206.9 GPa, Poisson's ratio (ν) = 0.3, thermal expansion coefficient (α) = $11 \times 10^{-6}/^{\circ}\text{C}$, and density (ρ) = 7850 kg/m³. Temperature-dependent multilinear representations of stress-strain curves for this material are described in Ref 26.

Temperature-dependent fracture-toughness relations for initiation and arrest, based on small-specimen data, are given as follows

$$K_{Ic} = 51.276 + 51.897e^{0.036(T - RT_{NDT})} \quad (9)$$

$$K_{Ia} = 49.957 + 16.878e^{0.028738(T - RT_{NDT})} \quad (10)$$

Units for K and T are in MPa $\sqrt{\text{m}}$ and $^{\circ}\text{C}$, respectively. Drop-weight and Charpy test data indicate that $RT_{NDT} = -23^{\circ}\text{C}$. The small-specimen K_{Ia} data for this material were obtained

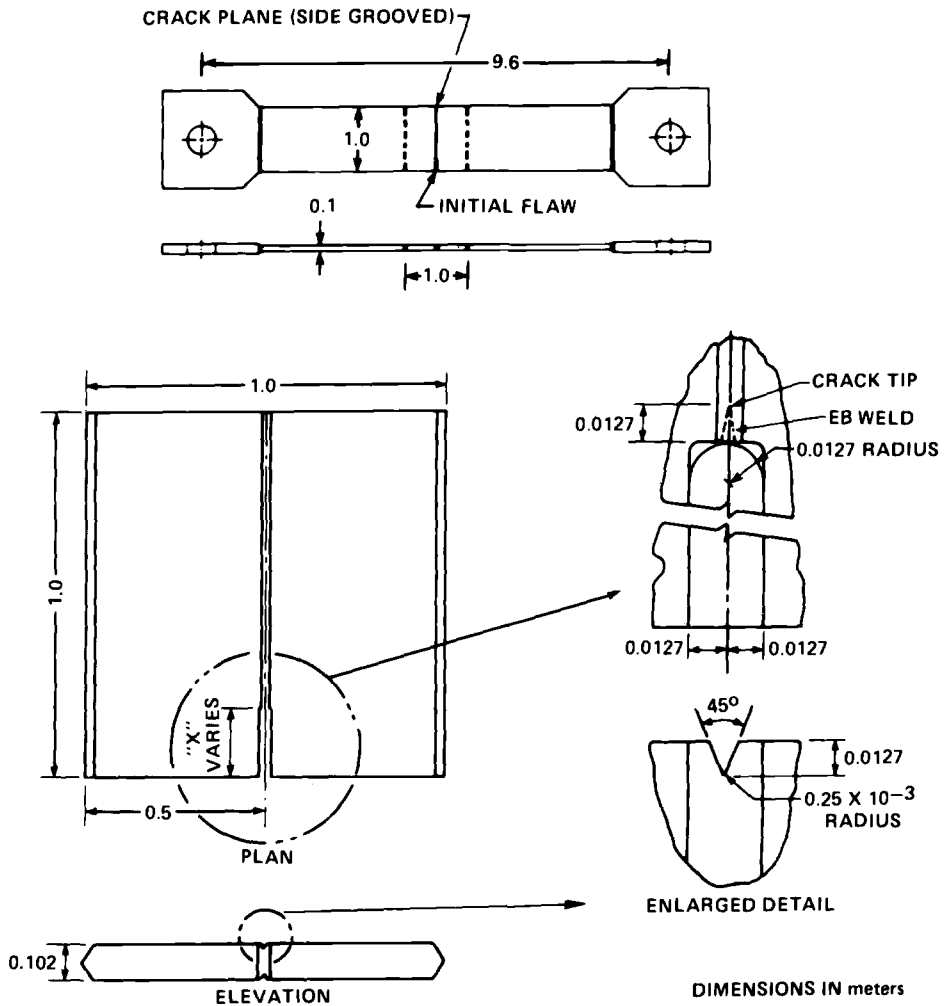


FIG. 4—Schematic of HSST wide-plate crack-arrest specimen.

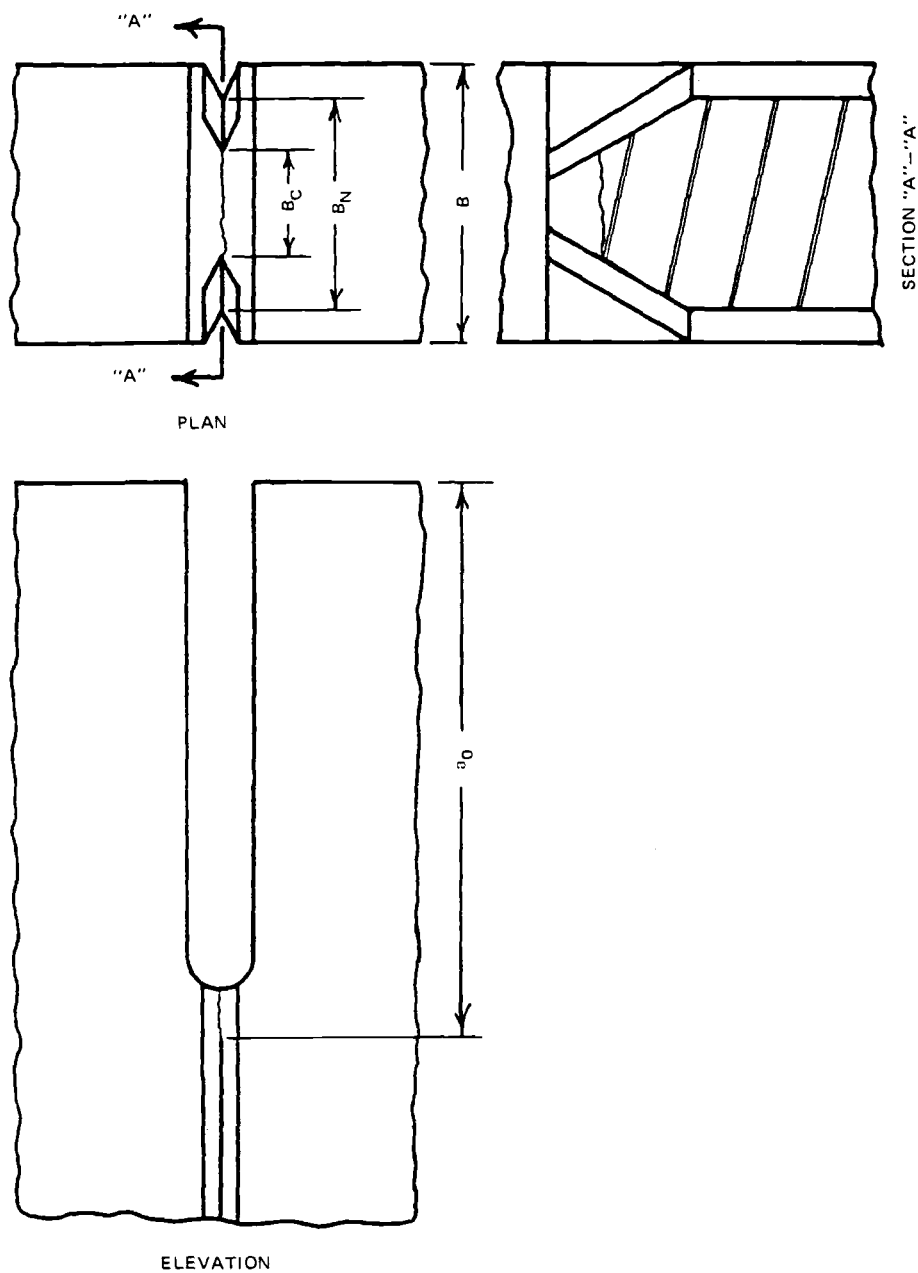


FIG. 5—Schematic of chevron configuration of crack front.

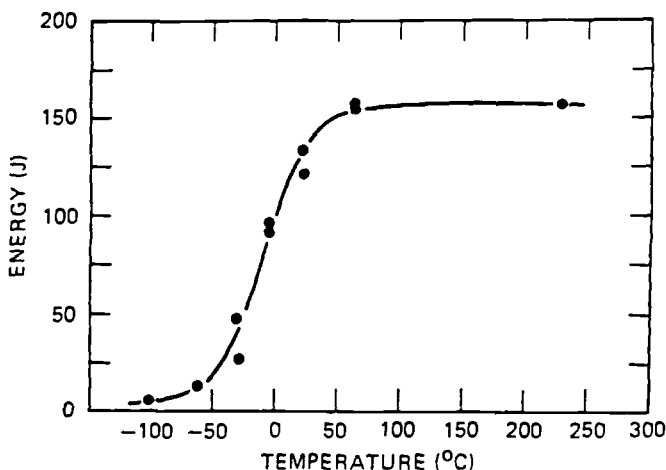


FIG. 6—Charpy V-notch data for HSST Plate 13A of A533 Grade B, Class 1 steel. (Specimens taken from middle thickness of original plate.)

by Battelle-Columbus Laboratory [27], and all other data were obtained by Oak Ridge National Laboratory (ORNL) [28]. Charpy V-notch results are given in Fig. 6 for specimens taken from the middle of Plate 13A.

To record pertinent data during the test, the wide-plate specimens were instrumented with three types of devices: (1) thermocouples, (2) strain gages, and (3) crack-opening-displacement (COD) gages. Locations of thermocouples and strain gages for the sixth specimen in the series, WP-1.6, are shown in Figs. 7 and 8, respectively. The thermocouple output was recorded during the test to ensure that the prescribed thermal conditions were met. Strain gage measurements during the test served to provide dynamic strain-field measurements for determination of crack velocity and to provide far-field strain measurements for determination of loading boundary conditions. Finally, correlation of the COD gage readings with pretest and posttest calculations gives an additional check on the loading boundary conditions.

Summary of Wide-Plate Crack-Arrest Tests WP-1.1 Through WP-1.6

A summary of the general test conditions for the six tests conducted in the WP-1 series is presented in Table 2. Although cleavage initiation was experienced at very high loads (>18 MN) in the first two tests (WP-1.1 and WP-1.2), both specimens exhibited arrest, if only for a fraction of a second, prior to tearing instability. In fact, Specimen WP-1.2 actually exhibited two such microarrest periods. Initiation loads for WP-1.3 and WP-1.4 were reduced (<12 MN) by cutting the crack front into a chevron configuration and lowering the crack-tip temperature in relation to Test WP-1.2. In Test WP-1.3, an arrest period of 2 s was experienced. A completely stable arrest occurred in Test WP-1.4. A second cleavage initiation run/arrest event was produced in WP-1.4 by an increase in load. Two short-duration cleavage initiation run/arrest events were also produced in Tests WP-1.5 and WP-1.6. Transverse temperature profiles at the approximate time of the crack initiation/arrest events are summarized in Fig. 9.

Crack-arrest toughness values have been determined by static and dynamic analyses, as

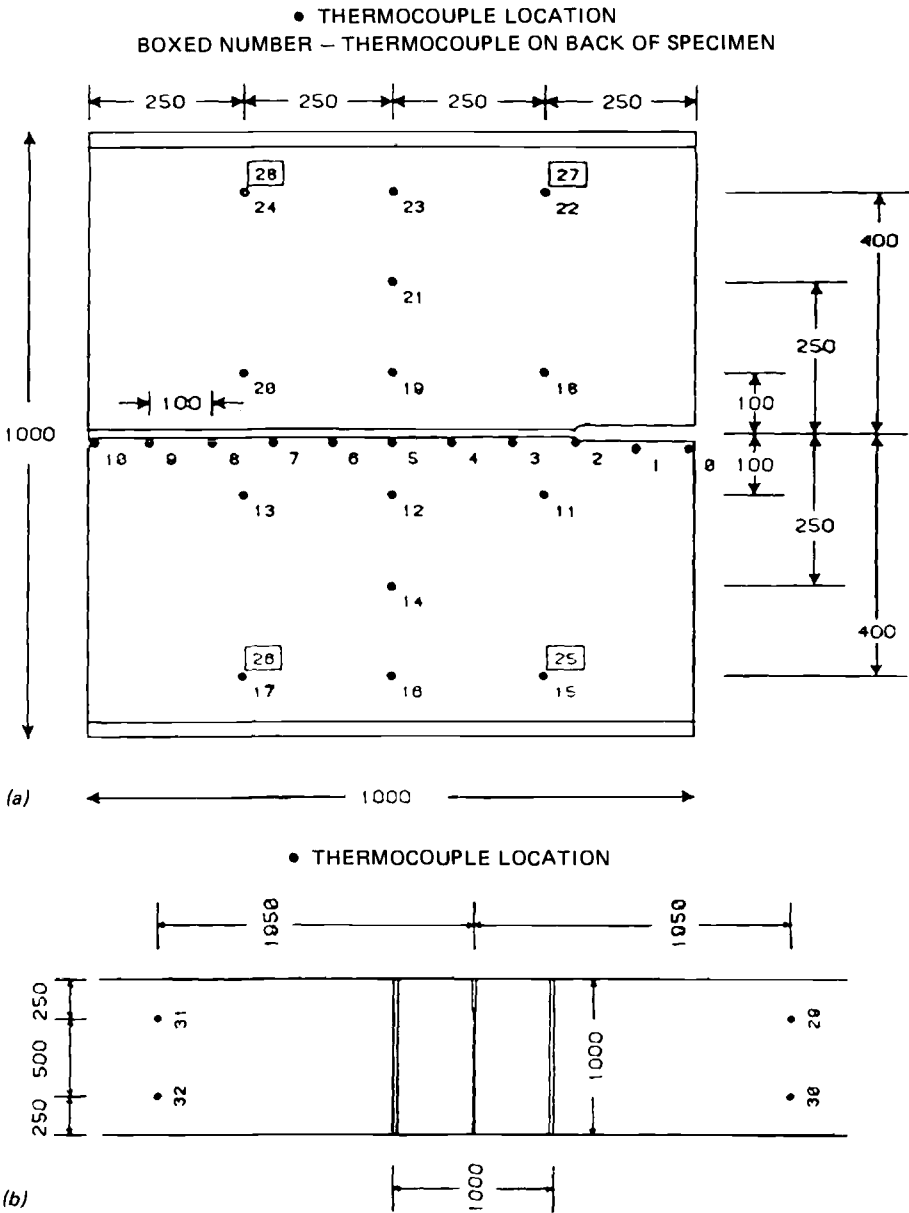


FIG. 7—Thermocouple locations: Test WP-1.6.

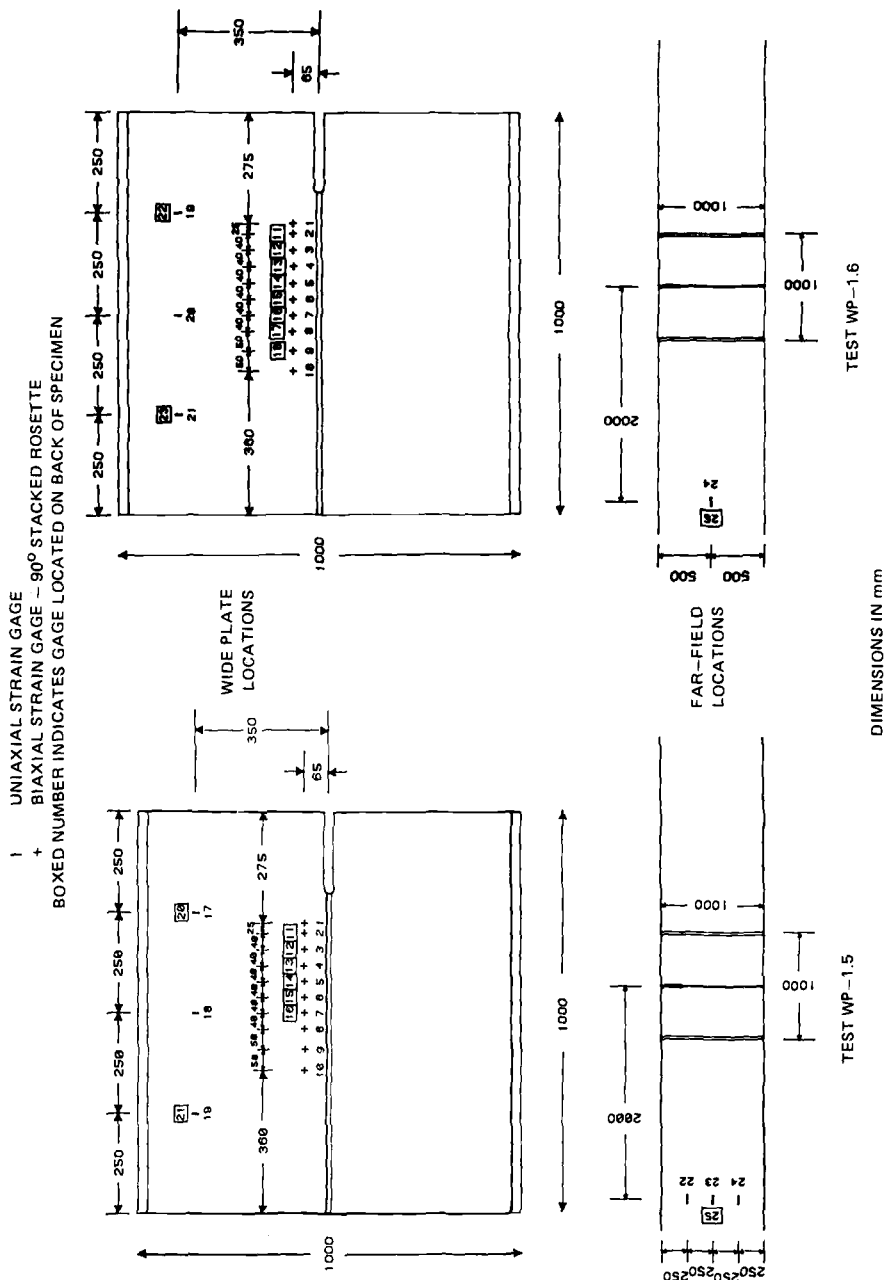


FIG. 8—Strain gage locations: Test WP-1.6.

TABLE 2—Summary of conditions employed in the first series of HSST wide-plate crack-arrest Tests WP-1 for A533 Grade B Class 1 steel.

Test No.	Crack Location, cm	Crack Temperature, °C	Initiation Load, MN	Arrest Location, ^a cm	Arrest Temperature, °C	Arrest $T - RT_{NDT}$, °C
WP-1.1 ^b	20	−60	20.1	50.2	51	74
WP-1.2A	20	−33	18.9	55.5	62	85
WP-1.2B	55.5	62	18.9	64.5	92	115
WP-1.3	20 ^c	−51	11.25	48.5	54	77
WP-1.4A	20.7 ^{c,d}	−63	7.95	44.1	29	52
WP-1.4B	44.1	29	9.72	52.7	60	83
WP-1.5A	20 ^c	−30	11.03	52.1	56	79
WP-1.5B	52.1	56	11.03	58.0	72	95
WP-1.6A	20 ^c	−19	14.50	49.3	54	77
WP-1.6B	49.3	54	14.50	59.3	80	103

^a Arrest location at the front face of the plate. Although the crack front was nonplanar, this location was selected to be consistent with the posttest analysis, which utilized results from the front face strain gages.

^b Specimen was warm prestressed by loading to 10 MN at 70°C. Specimen was also preloaded to 19 MN.

^c Crack front cut to chevron configuration.

^d Pillow jack utilized to apply pressure load to specimen's machined notch.

well as by handbook techniques. Some of the computed values are summarized in Table 3. The values computed from

$$K_I = \sigma \left[\pi a \sec \left(\frac{\pi a}{2W} \right) \right]^{1/2} \quad (11)$$

are plotted in Fig. 10 against the arrest temperature minus RT_{NDT} . Figure 10 also includes the K_{IR} curve from Section XI of the ASME Code, and the K_{Ia} curve that corresponds to small-specimen data for WP-1 material (Eq 10). The trend exhibited by these results is toward a rapid increase in crack-arrest toughness at temperatures near and above the onset of Charpy upper shelf temperatures ($T = 55^\circ\text{C}$ or $T - RT_{NDT} = 78^\circ\text{C}$). Values obtained in these tests extend above the limit of the ASME Code ($220 \text{ MPa } \sqrt{\text{m}}$). This trend is further substantiated in Fig. 11, which presents data from the WP-1 test series and from other large-scale tests [1,2,11,20].

Posttest Analysis of Test WP-1.6

Both static and dynamic computational techniques were employed in posttest analyses of each of the wide-plate tests in the WP-1 series [3,26]. The following sections describe results from application of these techniques to the sixth test, WP-1.6.

Posttest Three-Dimensional Static Analysis

Three-dimensional static finite-element analyses were performed on the WP-1.6 plate assembly (see Fig. 12) to ascertain the static stress-intensity factor at the time of crack initiation. These analyses were performed with the ORMGEN/ORVIRT [30,31] fracture analysis system in conjunction with the ADINA-84 [32] finite-element code installed on the

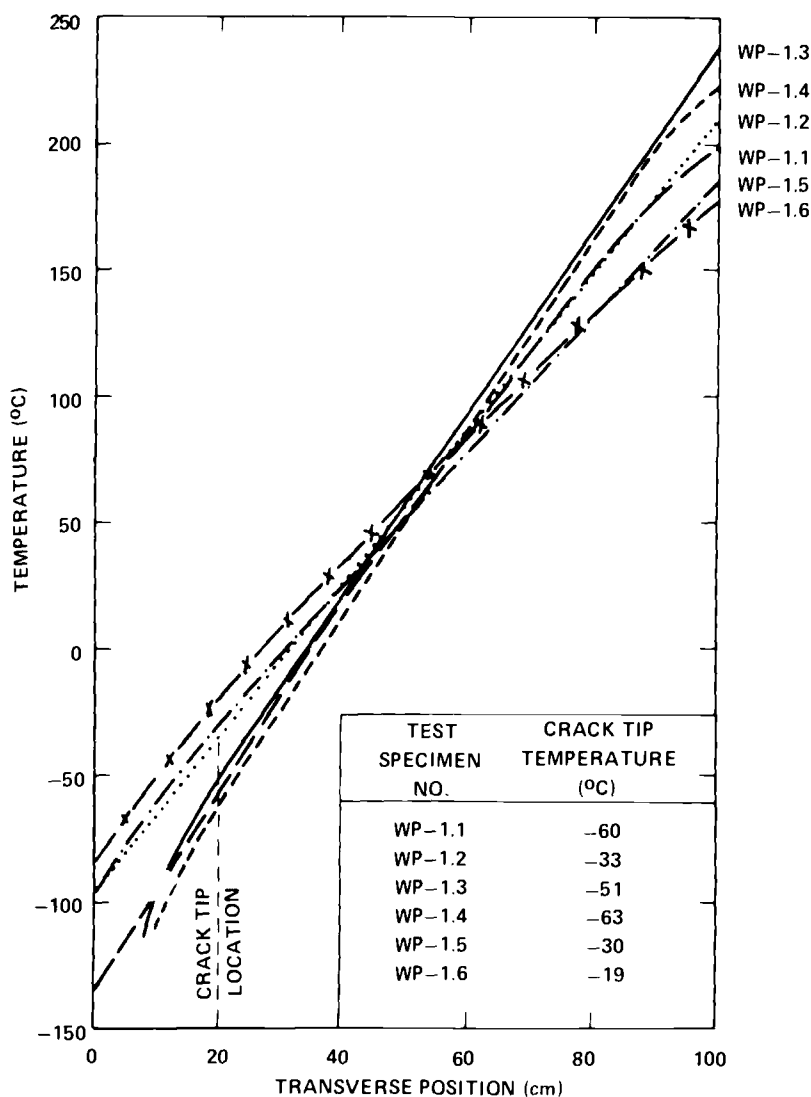


FIG. 9—Transverse temperature profiles: HSST wide-plate crack-arrest test series WP-1.

Cray X-MP supercomputer at Oak Ridge National Laboratory. The three-dimensional finite-element model incorporated a segment of the plate assembly 4.96 m in length, measured from the crack plane to the top of the load-pin hole. The crack-tip region of the model included the chevron cutout, the side grooving, and the edge notch, the dimensions of which are taken from Table 4 and Fig. 5. From symmetry conditions (neglecting out-of-plane eccentricity), one-quarter of the partial pull-plate assembly is modeled using 3751 nodes and 720 twenty-noded isoparametric elements.

The thermal deformations computed from a posttest two-dimensional analysis were superposed on the three-dimensional finite-element model to account for the in-plane thermal bending effect in the three-dimensional analyses. The boundary conditions of the two-

TABLE 3—Computed crack-arrest toughness values for HSST wide-plate tests on A533 Grade B Class 1 steel.

Test No.	Crack-Arrest Toughness Values, MPa \sqrt{m}				
	Static SEN formulas		Alternate Static Formula ^c	Dynamic Finite Element	
	Displacement Control ^a	Load Control ^b		Application Mode ^d	Generation Mode
WP-1.1	391	813	340	599	NA ^e
WP-1.2A	384	942	349	707	440
WP-1.2B	416	1489	419	NA ^e	523
WP-1.3	215	424	185	448	243
WP-1.4A	145	248	120	301	158
WP-1.4B	331	433	170	NA ^e	397
WP-1.5A	217	472	191	405	229
WP-1.5B	229	616	213	NA	300
WP-1.6A	279	565	242	501	285
WP-1.6B	306	881	290	NA ^e	NA ^e

^a From Ref 29 (pp. 2.10–2.11) while assuming $a = a_f$ and no further bending occurs due to propagation of the crack.

^b From Ref 29 (pp. 2.10–2.11) while assuming $a = a_f$ and full bending according to SEN formula when the final crack depth is used.

^c $K_I = \sigma[\pi a \sec(\pi a/2w)]^{1/2}$, with σ = far-field tensile stress, $a = a_f$ = final crack length, and w = full plate width.

^d From $K_{Ia} = 49.957 + 16.878 \cdot \exp[0.028738 \cdot (T - RT_{NDT})]$ evaluated at the temperature T of the arrested depth as computed in the analysis.

^e NA = not available.

dimensional thermoelastic analysis assumed that the heated and cooled edges of the plate were fixed at $T_{max} = 180^\circ\text{C}$ and $T_{min} = -70^\circ\text{C}$, respectively, along a 2.4-m length (centered relative to the crack plane) and that the pull-tab edges were prescribed to be $T = 20^\circ\text{C}$. The remaining surfaces of the assembly were assumed to be insulated. The in-plane thermal bending produced a load-line (through the top of the load-pin hole) eccentricity of 2.02 cm relative to the geometric center of the plate.

In the three-dimensional analysis, thermal stress effects were neglected and a uniform line-load statically equivalent to the WP-1.6 test initiation load of 14.5 MN was applied at the location corresponding to the top of the load-pin hole. The result of this analysis produced a static stress-intensity factor of $K_I = 233.8 \text{ MPa } \sqrt{m}$ at the center plane of the plate. Comparison of this computed K_I value with the static initiation value of $K_{Ic} = 111.2 \text{ MPa } \sqrt{m}$ from Eq 10 evaluated at the crack-tip temperature $T_{CT} = -19^\circ\text{C}$ and $RT_{NDT} = -23^\circ\text{C}$ yields a ratio of $K_I/K_{Ic} = 2.10$. Table 5 presents a comparison of these values with those obtained from previous tests in the WP-1 test series.

Posttest Two-Dimensional Static and Dynamic Analyses

Static and Stability Analysis—Posttest analyses of wide-plate Test WP-1.6 were carried out using computer codes based on both quasi-static and elastodynamic techniques. For the quasi-static analyses, the ORNL computer code WPSTAT [26] was used to perform both crack-arrest and crack-stability analyses. As described in Ref 26, the WPSTAT code evaluates static stress-intensity factors as a function of crack length a and temperature differential

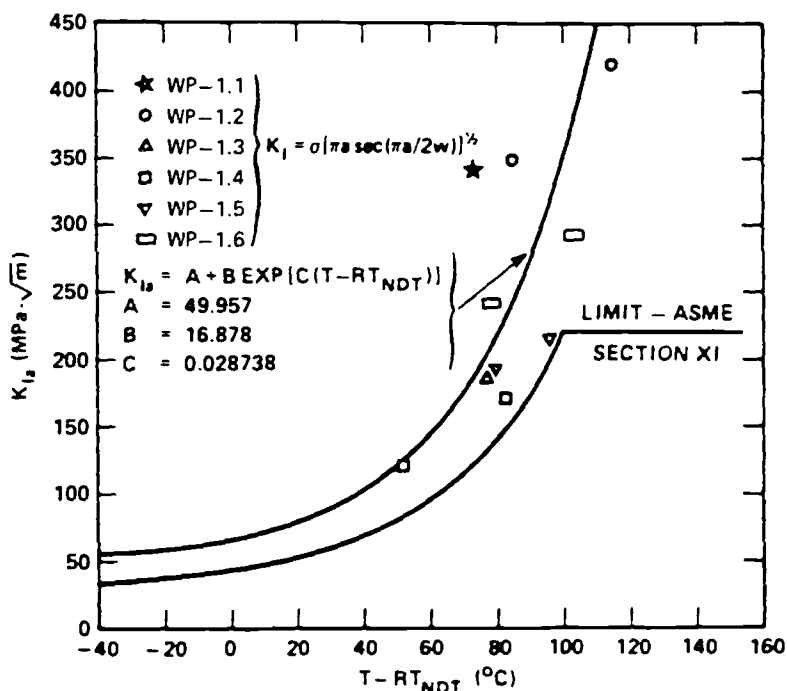


FIG. 10—Wide-plate specimen high-temperature crack-arrest data for Tests WP-1.1 through WP-1.6.

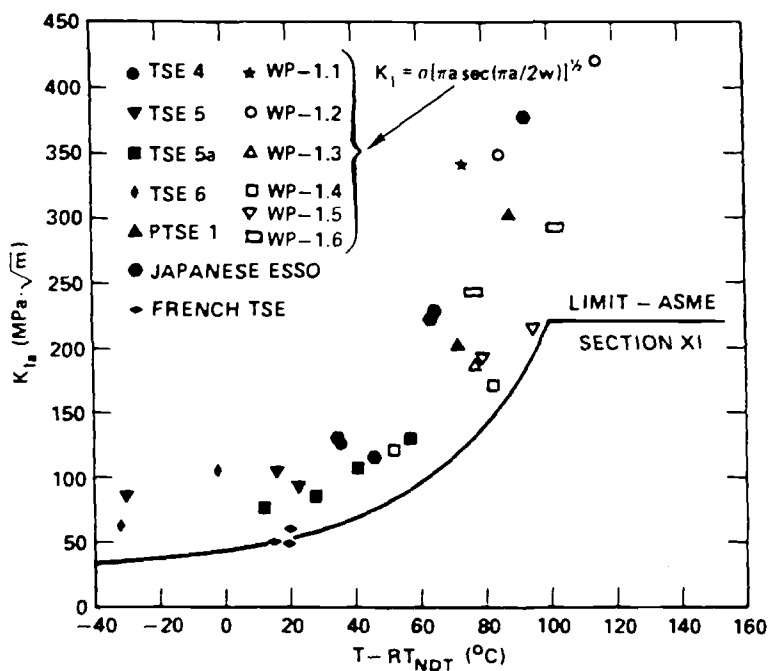


FIG. 11—Wide-plate crack-arrest data showing a consistent trend with data from other large crack-arrest specimen tests.

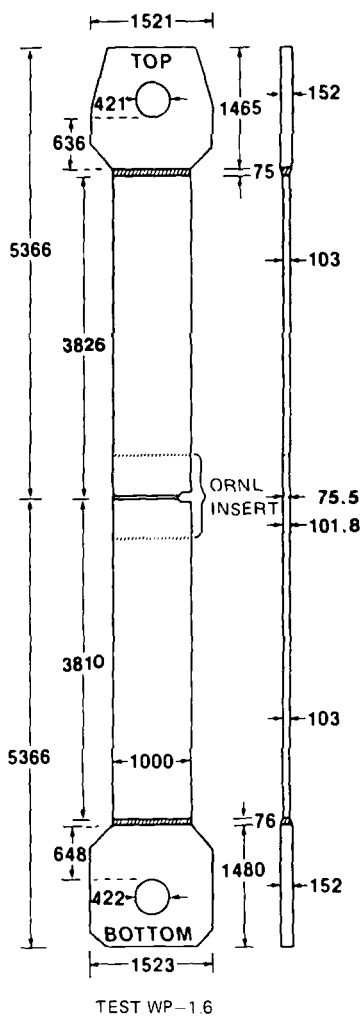


FIG. 12—Overall dimensions for HSST wide-plate crack-arrest Specimen WP-1.6.

TABLE 4—Specimen WP-1.6 dimensions.

Dimension	Symbol	Distance, mm
Initial crack length	a_0	200
Thickness	B	101.8
Notched thickness	B_N	75.5
Chevron thickness, thickness at a_0	B_C	40.0
Width	W	1000

TABLE 5—Initiation stress-intensity factor comparisons for test series WP-1.

Test Designation	Crack Tip Temperature, °C	Static Stress-Intensity Factor K_I^a , MPa $\sqrt{\text{m}}$	Crack Initiation Stress-Intensity Factor K_{Ic}^b , MPa $\sqrt{\text{m}}$	K_I/K_{Ic}
WP-1.2	−33	251.5	87.5	2.87
WP-1.3	−51	173.5	70.1	2.48
WP-1.4	−62	213.0	63.9	3.33
WP-1.5	−30	179.8	91.6	1.96
WP-1.6	−19	233.8	100.2	2.10

^a Computed from three-dimensional static analysis using ORMGEN/ADINA/ORVIRT.

^b Calculated from $K_{Ic} = 51.276 + 51.897 \exp [0.36 * (T - RT_{NDT})]$ using crack-tip temperature of initial flaw.

$\Delta T = T_{\max} - T_{\min}$ across the plate. These stress-intensity factors are computed for fixed-force conditions, $K_I^F(a, \Delta T)$, and for fixed load-pin displacement conditions, $K_I^{\text{dsp}}(a, \Delta T)$ by superposing contributions from tension and bending finite-element and handbook solutions. In addition, WPSTAT categorizes arrested crack lengths in terms of three types of instability limits that are enumerated below.

For the sixth wide-plate test, the proposed temperature profile was defined by specifying a crack-tip temperature of $T_{CT} = -20^\circ\text{C}$ at $x = 0.2$ m and a midplate temperature $T_{MP} = 55^\circ\text{C}$ at $x = 0.5$ m, implying $T_{\min} = -70^\circ\text{C}$ and $T_{\max} = 180^\circ\text{C}$. As indicated in Fig. 13, the temperature gradient actually achieved at the time of the run/arrest event deviated only slightly from the pretest objective in the region $0.2 \leq x < 0.6$. The posttest WPSTAT calculations of static stress-intensity factors $K_I^F(a, \Delta T)$ and $K_I^{\text{dsp}}(a, \Delta T)$ utilized the actual temperature profile provided in Fig. 13. For this specified temperature profile, the dependence of the arrested crack length and crack stability upon the applied initiation load F_{in} was investigated with WPSTAT, and the results are presented in Fig. 14. Figure 14 includes the statically calculated final crack length, a_{fc} , and the instability-limit crack lengths for reinitiation, $a_{rein}(F_{in})$, for tensile instability, $a_{t1}(F_{in})$, and for tearing instability, $a_{t2}(F_{in})$. The tensile instability calculation is based on the average stress in the remaining ligament equal to an ultimate tensile stress of $\sigma_u = 550$ MPa, which represents the lowest value for the temperature range of interest. For the tearing instability calculation, the material tearing resistance is assumed given in the form of a power-law J -resistance curve, $J_R = C(\Delta a)^m$, where $C = 0.3539$, $m = 0.4708$, and the units of J_R and Δa are MJ/m² and mm, respectively. In Fig. 14, the statically computed arrest length corresponding to the measured initiation load $F_{in} = 14.5$ MN is given by $a_{fc} = 0.662$ m. The computed arrest point is slightly above the a_{t1} curve, implying that tensile instability is expected for this situation. The measured initial arrest point, $a_{fm1} = 0.49$ m, is above the tearing instability curve and represents an instability condition.

In Fig. 15, the K_{Ia} function of Eq 10 was evaluated at the temperatures corresponding to the depths on the arrest crack length curve $a_f(F)$, on the incipient tearing instability curve $a_{t2}(F)$, and on the cleavage reinitiation curve $a_{rein}(F)$. The K_{Ic} function of Eq 9 was also evaluated on the curve $a_{rein}(F)$. Evaluation of the $K_{Ia}(a_f)$ curve at the initiation load $F_{in} = 14.5$ MN yielded an arrest toughness of $K_{Ia} = 598$ MPa $\sqrt{\text{m}}$ at the predicted arrest point $a_{fc} = 0.662$ m where the crack-tip temperature would be $T = 98.1^\circ\text{C}$.

The complete static and stability analyses are depicted in Fig. 16 for the initiation load of $F_{in} = 14.5$ MN. Included in the figure are curves for initiation toughness K_{Ic} , arrest toughness K_{Ia} , displacement controlled stress-intensity factor K_I^{dsp} , and force-controlled

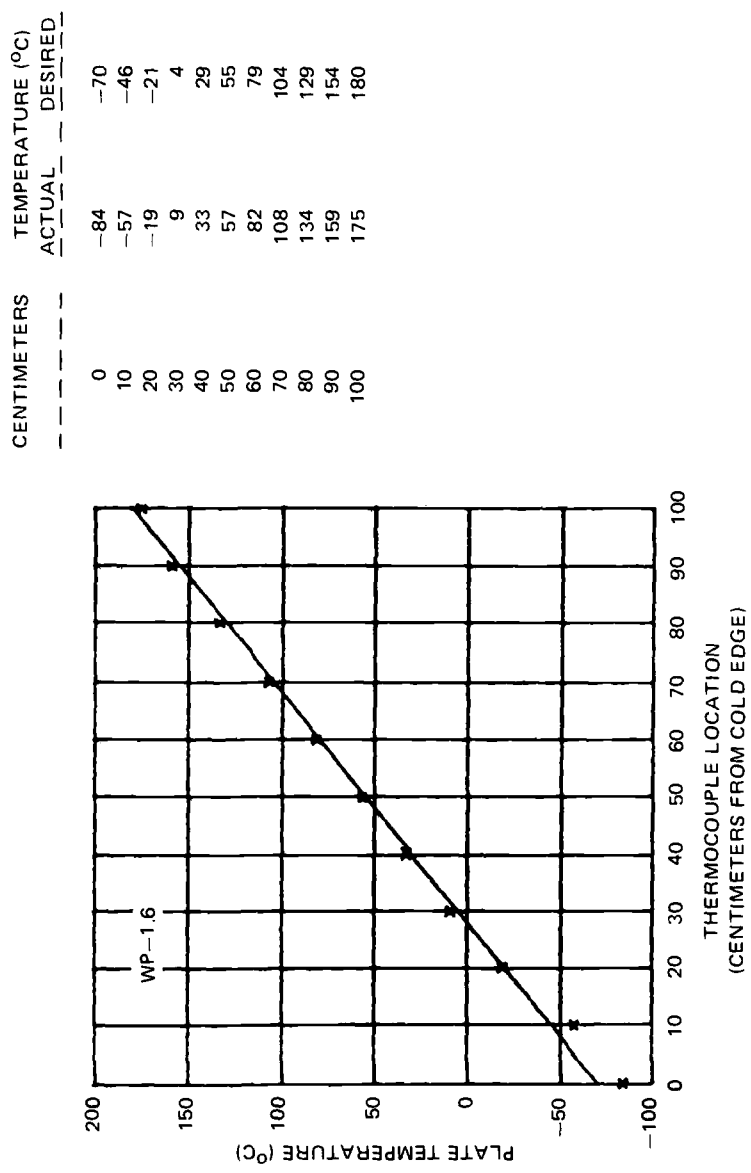


FIG. 13—Actual and target temperature distributions across the specimen width at the approximate time of specimen fracture for Test WP-1.6.

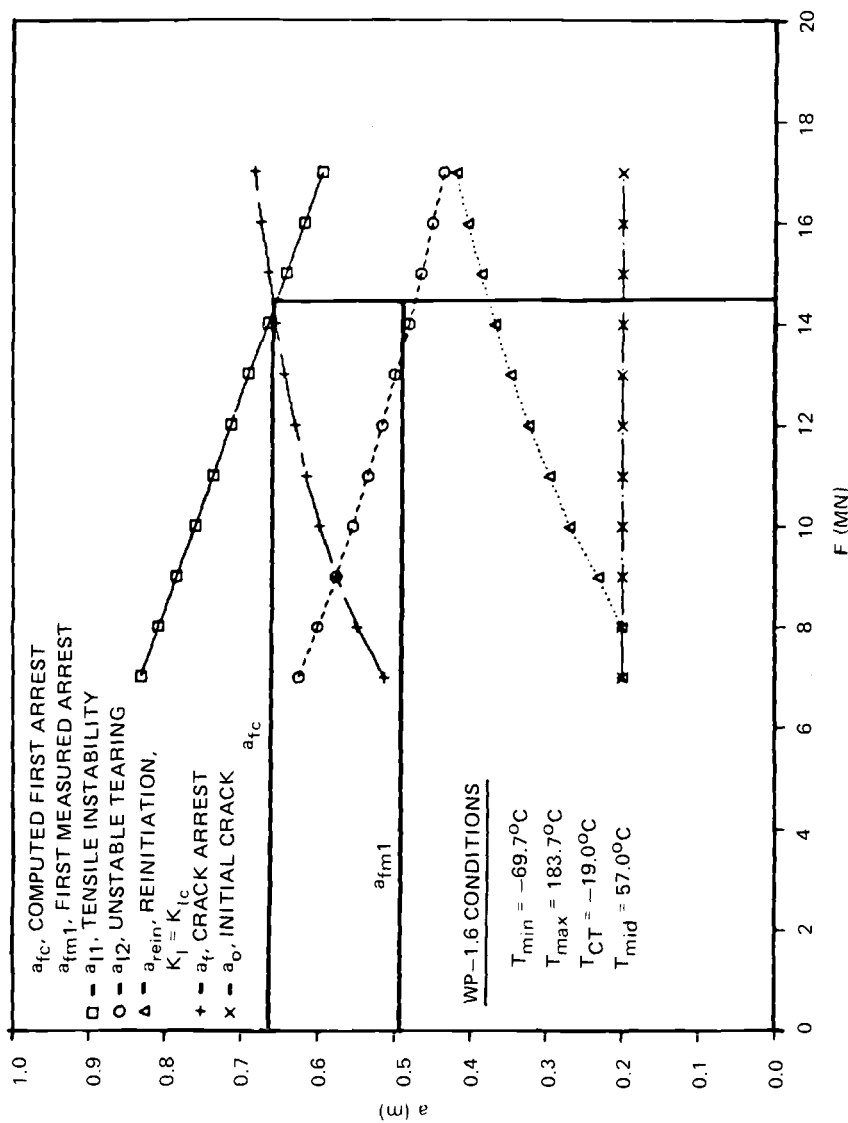


FIG. 14—Statically calculated crack lengths for Test WP-1.6.

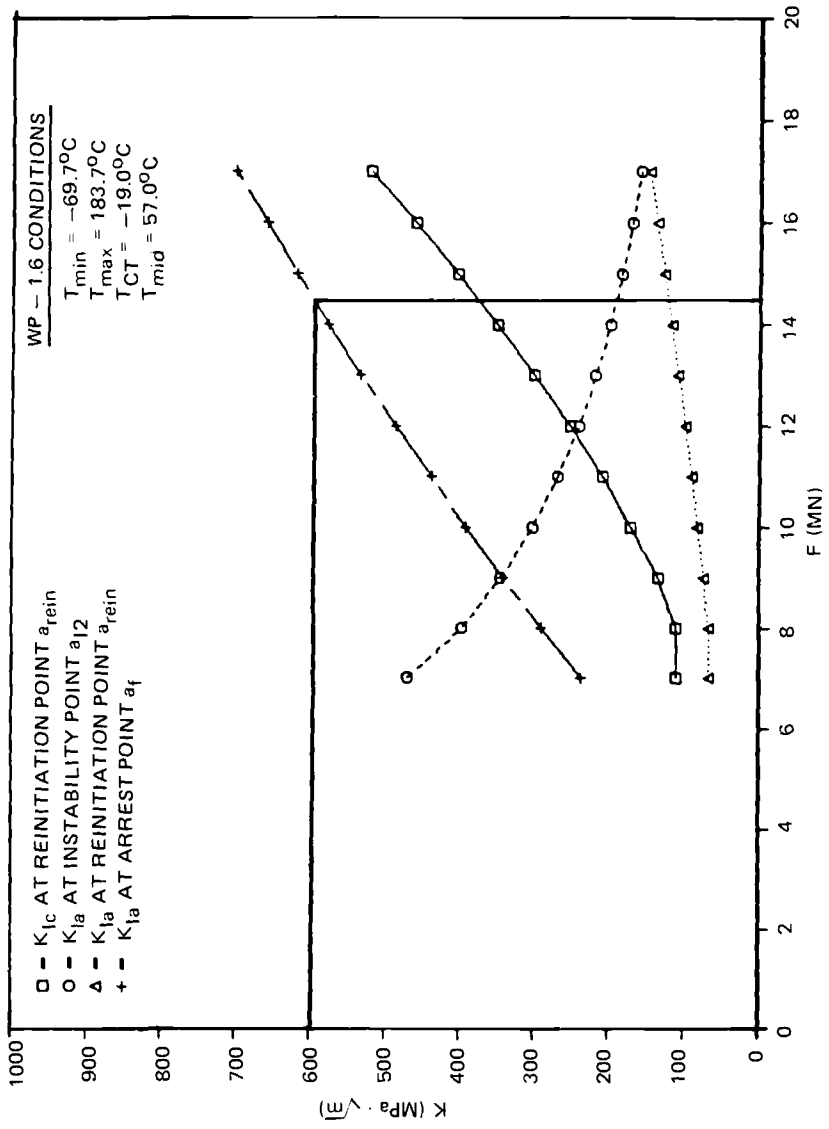


FIG. 15—Determinations of arrest toughness at the initiation load of 14.5 MN for Test WP-1.6.

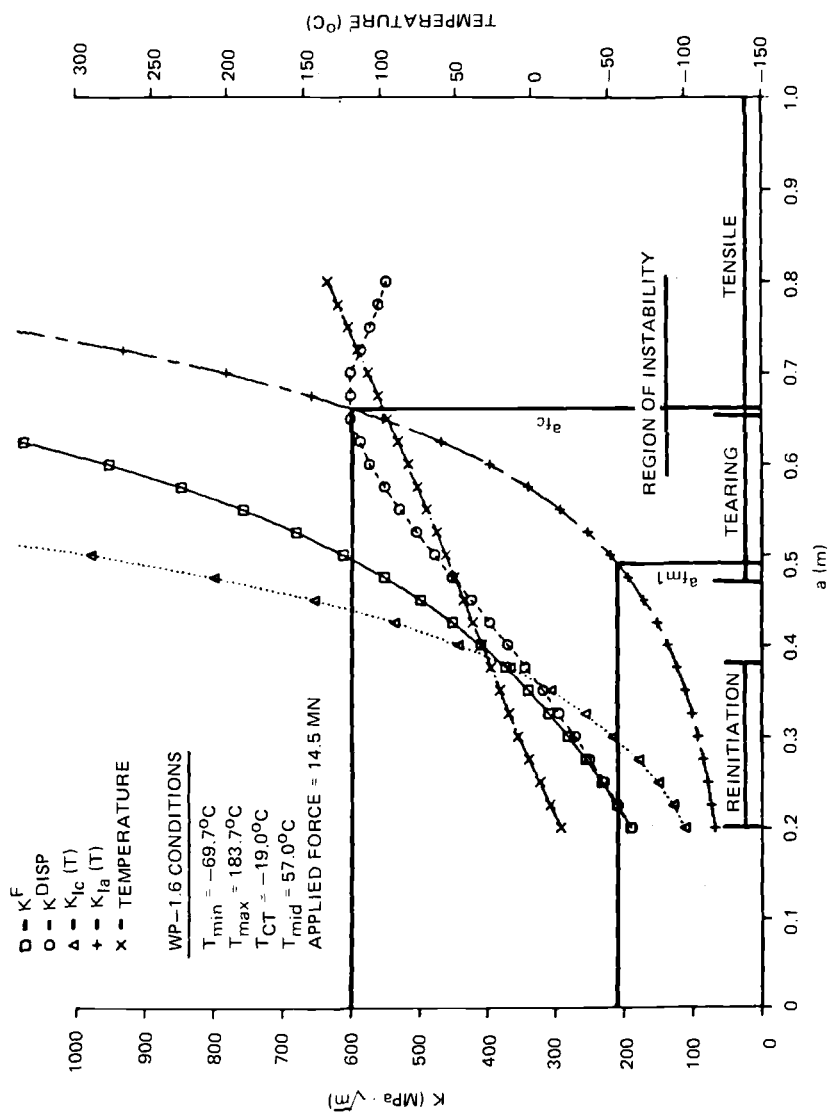


FIG. 16—Complete static and stability analyses for the initiation load of 14.5 MN for Test WP-1.6.

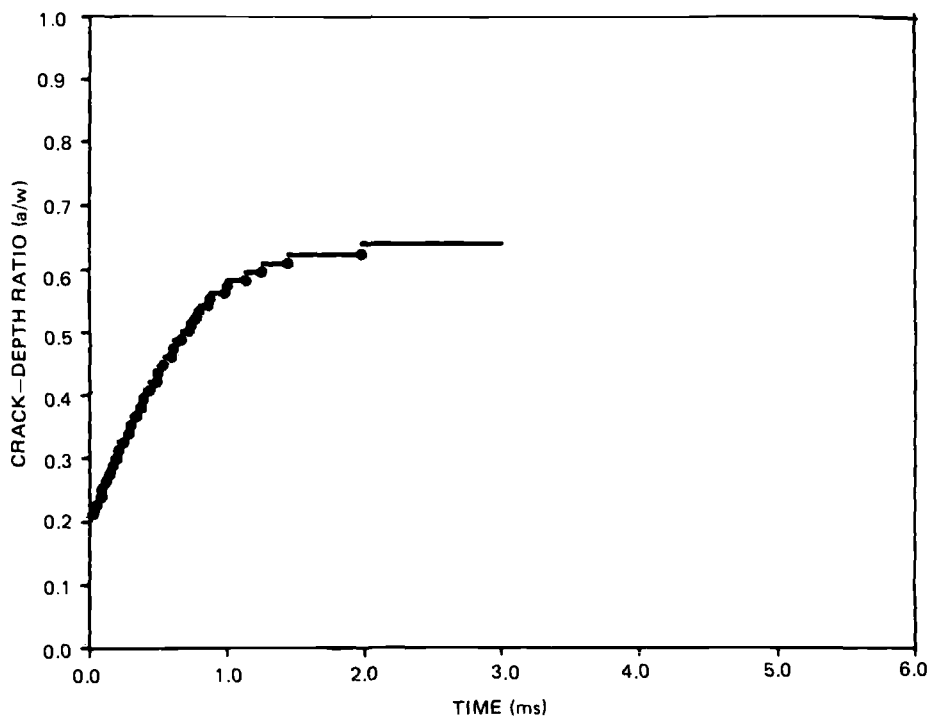


FIG. 17—Dynamic analysis crack-depth history for Test WP-1.6.

stress-intensity factor K_I^F . The regions of reinitiation, tearing, and tensile instability, and the first measured cleavage arrest point are also identified in Fig. 16.

Application-Mode Dynamic Analysis—Elastodynamic fracture analysis procedures that utilize a displacement-based finite-element formulation and the implicit Newmark-Beta scheme for the time integration have been applied to the wide-plate crack-arrest experiments. The dynamic stress-intensity factor K_I is determined in each time step from the dynamic J -integral containing the appropriate inertial and thermal terms. The crack-growth modeling technique of these codes utilizes a scheme in which crack-plane nodes, initially restrained normal to the crack plane by stiff springs, are released incrementally according to the selected analysis mode.

Elastodynamic analyses of the wide-plate test WP-1.6 were carried out with the ADINA/VPF [6] dynamic crack analysis code. The two-dimensional plane stress finite-element model of the wide-plate configuration used in the analyses consists of 794 nodes and 232 eight-noded isoparametric elements. A total of 31 spring elements are used in the crack plane to model propagation of the crack tip. Side grooves are taken into account by adjustment of the resulting stress-intensity factor calculated in each time step of the analysis. The in-plane bending of the plate assembly due to the thermal gradient across the plate was also incorporated into the analyses.

A posttest application-mode analysis of the sixth test, WP-1.6, was performed using the temperature gradient of Fig. 13 and the material properties given previously. The measured fracture load of $F_{in} = 14.50$ MN was applied at the location of the top of the load-pin hole to determine the load-point displacement $U_{LL} = 0.35281 \times 10^{-2}$ m. For the dynamic

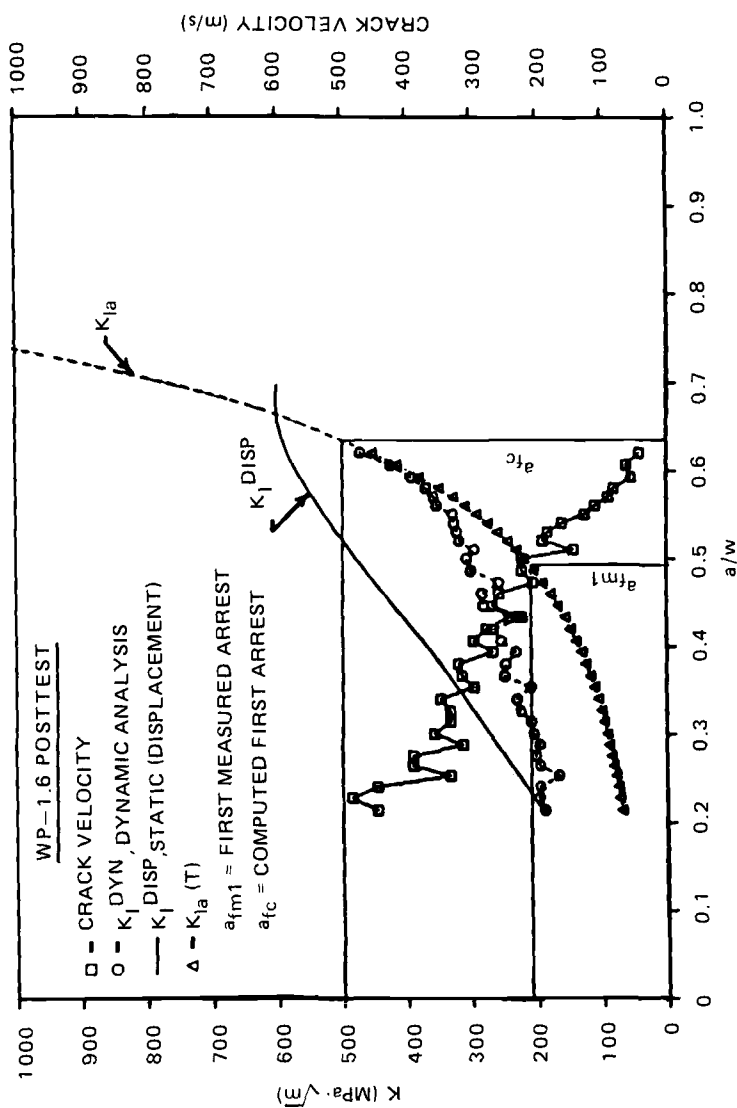


FIG. 18—Dynamic stress-intensity factor, static toughness, quasi-static displacement-controlled stress-intensity factor and crack velocity versus instantaneous crack length for Test WP-1.6.

TABLE 6—Crack position and velocity versus time from front-side strain gage measurements for wide-plate test WP-1.6.

Indicator	Position, mm	Time, ms	Velocity, ^a m/s
Initial crack	200	0	
SG1	275	0.0715	1049
SG2	300	0.1100	649
SG3	340	0.2015	437
SG4	380	0.2735	556
SG5	420	0.3720	406
SG6	460	0.4605	452
Cleavage arrest	493	0.6200	207
Slow tear	500	8.590	0.88
Cleavage reinitiation	500	8.590	...
Cleavage arrest	536	8.690	360
Slow tear	560	15.040	3.78
Cleavage reinitiation	560	15.040	...
SG9	590	15.075	875
Cleavage arrest	593	15.190	26.1
SG10	640	18.630	13.7
Remaining ligament	983	52.750	10.1

^a Velocity is the average velocity for the crack propagation between two measurement locations.

analysis, the load point was fixed at the displacement value of the initiation load and the time step was set at $\Delta t = 5 \mu\text{s}$. The calculated crack-depth history from this analysis is depicted in Fig. 17 and indicates a predicted arrest at $a_f = 0.636 \text{ m}$. Figure 18 presents the dynamic stress-intensity factor K_I^{dyn} , the static toughness K_{Ia} (from Eq 10 and Fig. 13), and the crack velocity a as a function of instantaneous crack length. The crack propagates into a rising K_I field, followed by arrest at a point where the crack-tip temperature would have been $T = 91.4^\circ\text{C}$. The arrest toughness at the arrest-point temperature is given by Eq 10 to be $K_{Ia} = 501 \text{ MPa } \sqrt{\text{m}}$. The computed arrest length exceeds the measured initial arrest length at $a_f = 0.49 \text{ m}$ with crack-tip temperature $T = 54^\circ\text{C}$ and corresponding arrest toughness $209 \text{ MPa } \sqrt{\text{m}}$ from Eq 10. The analysis results for the quasi-static displacement-controlled stress-intensity factor K_I^{dsp} are also included in Fig. 18. The application-mode

TABLE 7—Crack position and velocity versus time from back-side strain gage measurements for wide-plate Test WP-1.6.

Indicator	Position, mm	Time, ms	Velocity, ^a m/s
Initial crack	200	0	
SG12	340	0.170	823
SG13	380	0.282	357
SG14	420	0.350	588
SG15	460	0.500	267
Cleavage arrest	480	0.626	159
SG16	500	9.150	2.35
Slow tear	525	15.090	4.21
Cleavage reinitiation	525	15.090	...
Cleavage arrest	574	15.170	613
Slow tear	983	52.400	11.0

^a Velocity is the average velocity for the crack propagation between two measurement locations.

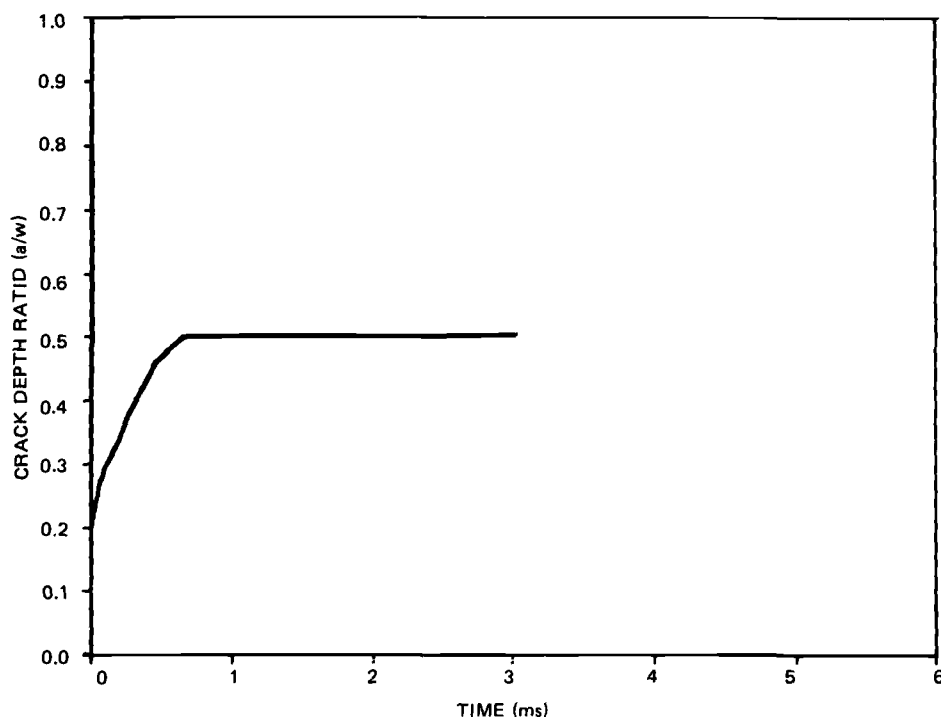


FIG. 19—Crack-depth history from front-side strain gages for Test WP-1.6.

analysis was terminated at time $t = 3$ ms, which precludes any prediction from the analysis of the reinitiation that occurred in the test at time $t = 8.6$ ms.

Generation-Mode Dynamic Analyses—From the output of the crack-line gages and from an inspection of the fracture surface, estimates of the crack position as a function of time were constructed by NBS and are given in Table 6 for the front-side strain gages and in Table 7 for the back-side strain gages. Figure 19 depicts the crack depth versus time curve from Table 6 that was used as input to ADINA/VPF for a posttest generation-mode elastodynamic analysis of Test WP-1.6. The curve in Fig. 19 incorporates the measured first crack arrest at $a_{fm1} = 0.493$ m as determined from the front-side measurements. For the dynamic analysis, the load point was again fixed at the displacement value of the initiation load and the time step was set at $\Delta t = 5 \mu\text{s}$. From these calculations, the stress-intensity factor as a function of time is given in Fig. 20. The generation-mode analysis results for the first arrest event was $a_{fm1}/W = 0.493$, $T = 54^\circ\text{C}$, and $K_{Ia} = 285 \text{ MPa } \sqrt{\text{m}}$.

The computed strain histories from selected points close to the front-side crack-line Gages 5 through 7 (Fig. 8) are depicted in Fig. 21 for the generation-mode analysis along with measured data from the gages. The sharply-defined strain peaks are associated with the fast-running crack passing under a gage point, with the peak being transformed into a more blunted curve as the crack tip slows down. The comparisons of strain histories in these figures indicates generally good agreement between measured and computed times for the occurrence of peak strain values. The transition of the strain pulse from a sharp peak in Fig. 21b to the blunted curve in Fig. 21c reflects the first arrest event between the front-side crack-line Gages 6 and 7.

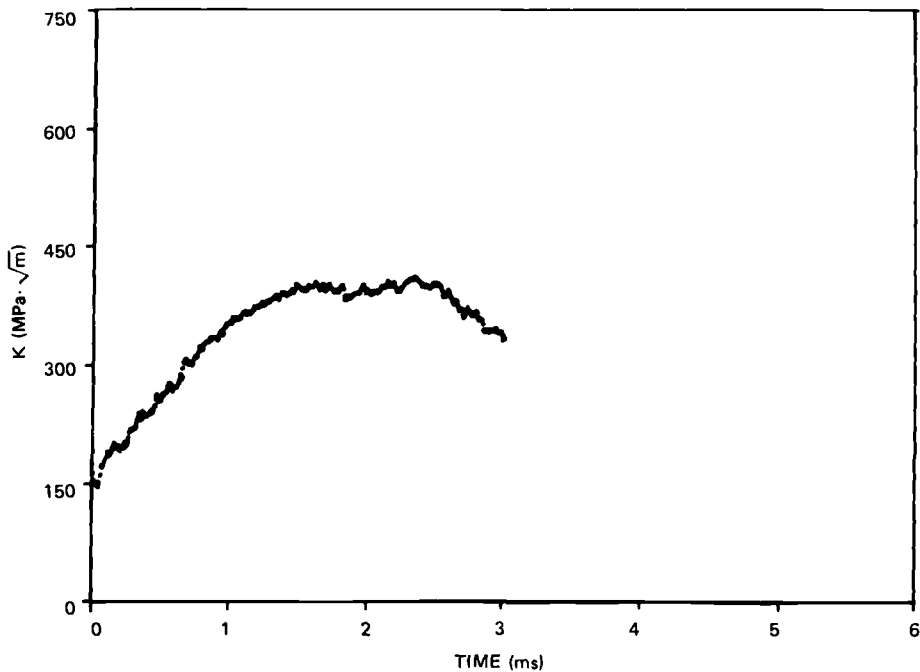


FIG. 20—Amplitude of stress-intensity factor versus time for Test WP-1.6.

In Fig. 22, the computed strain histories from the generation-mode analysis based on the crack depth versus time curve of Fig. 19 are compared with measured data from the back-side crack-line Gages 14 through 16 (Fig. 8). The transition in the shape of the strain pulse in Fig. 22 from a sharp peak to a blunted curve is consistent with the cleavage arrest indicated in Table 7 between Gages 15 and 16. These comparisons are also consistent with the observation that the crack-front propagation was fairly uniform across the plate thickness up to $a/W = 0.46$.

In Figs. 23 and 24, the COD calculated at $x = 0.15$ m from the cold edge in the generation-mode analysis is compared with measured data from the COD gages installed on the front side (F-COD) and back side (B-COD) of the plate. These comparisons suggest the possibility of a time lag in the response of the gages to the opening of the plate notch at the beginning of the run/arrest event.

Conclusions

The HSST program has an integrated effort under way to extend the range of applicability of current state-of-the-art crack-arrest practices and to develop alternatives where improvements are needed. A consistent trend is formed when the crack-arrest data now available from the three types of HSST large specimen tests are combined on a plot of K_{Ia} versus $T - RT_{NDT}$. This trend is still the case when one includes the results of thermal-shock tests from France and wide-plate (ESSO) tests from Japan. Collectively, these tests are showing that arrest can and does occur at temperatures up to and above that which corresponds to the onset of Charpy upper-shelf behavior. Further, the data suggest the existence of a limiting temperature above which a cleavage crack cannot propagate. Arrest may be followed by

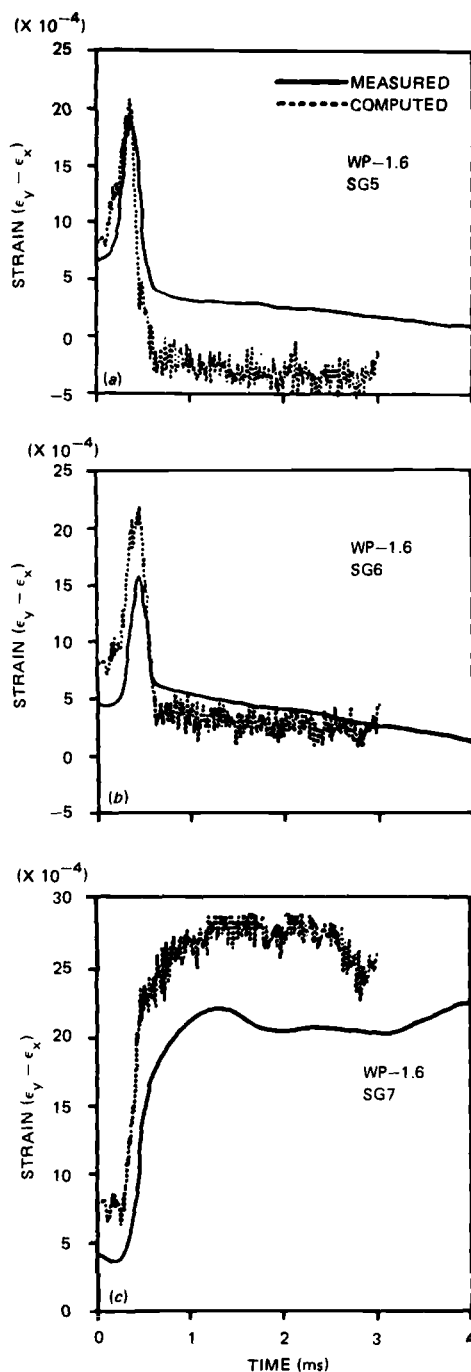


FIG. 21—Actual and computed strain histories for strain gages 5 through 7 for Test WP-1.6.

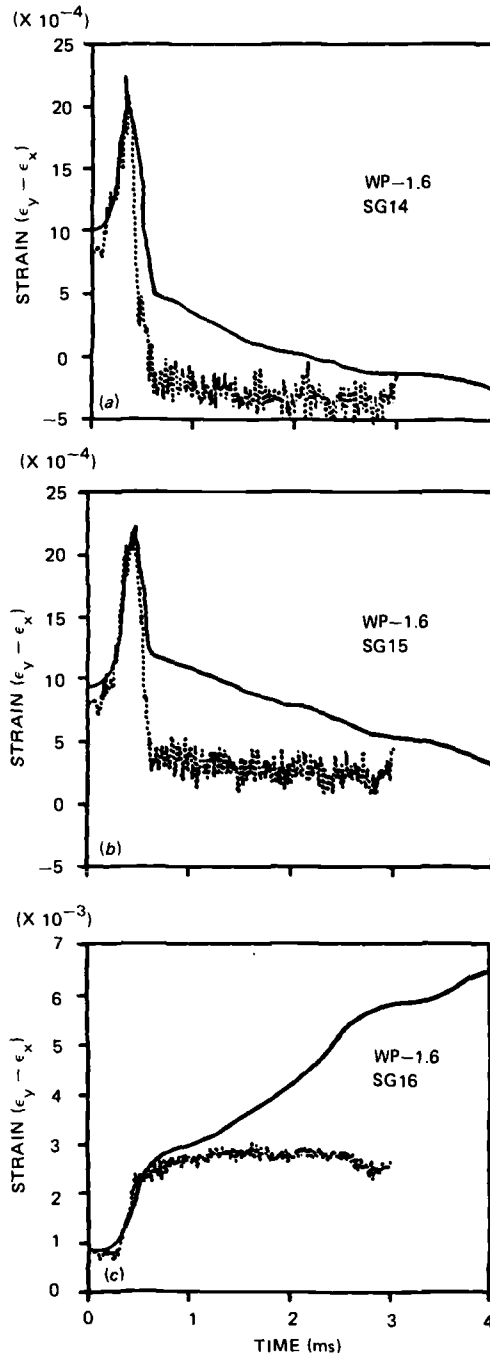


FIG. 22—Actual and computed strain histories for strain gages 14 through 16 for Test WP-1.6.

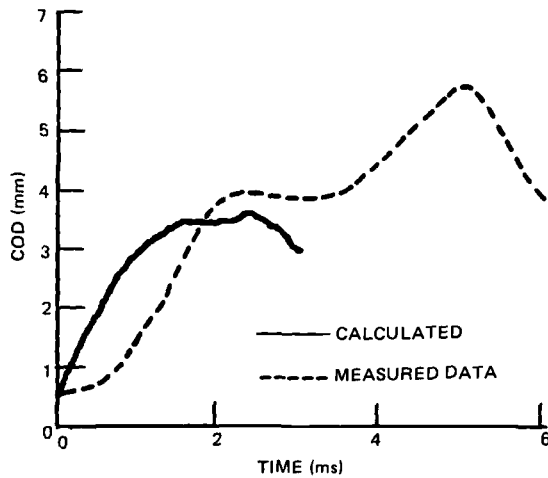


FIG. 23—Actual and computed crack-opening displacement at $a/W = 0.15$ for Test WP-1.6: front-side gage.

stable or unstable ductile crack growth, but these modes of fracture may be analyzed independent of cleavage run/arrest events. This is to say, there is no evidence of dynamic conversion from cleavage to ductile propagation. It is important to note that the data included in this study are for materials with RT_{NDT} values that differ by at least 115°C . Other materials will be examined in further test series.

The wide-plate analysis results obtained to date by the HSST program indicate that the essence of the first cleavage run/arrest event, including dynamic behavior, is being modeled. The formulation used in these analyses is based on a linear elastic fracture mechanics model which incorporates the effects of inertia. However, the presence of significant nonlinear behavior following the first cleavage arrest emphasizes the importance of including combined plastic and strain rate effects in constitutive relations to model the latter part of the exper-

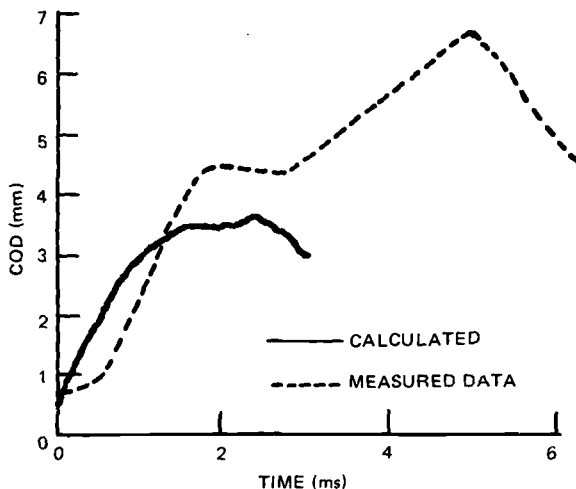


FIG. 24—Actual and computed crack-opening displacement at $a/W = 0.15$ for Test WP-1.6: back-side gage.

iments. Refinements in quantitative representation of material parameters and the inclusion of strain-rate dependence through viscoplastic modeling are currently under way in the HSST program [see Refs 6 and 7]. These improved analysis capabilities are expected to give an even more accurate basis for assessing the fracture behavior of reactor pressure vessels under PTS and other off-normal loading conditions.

Acknowledgments

The authors express recognition of the large and dedicated efforts of R. de Wit, R. J. Fields, and other staff members of the National Bureau of Standards, Gaithersburg, MD, in performing and reducing the data from the HSST wide-plate crack-arrest tests. They also gratefully acknowledge the support and guidance of the HSST technical monitor, Milton Vagins, at the U.S. Nuclear Regulatory Commission.

The submitted manuscript has been authored by a contractor of the U.S. Government under Contract No. DE-AC05-84OR21400.

References

- [1] Cheverton, R. D., et al., "Fracture Mechanics Data Deduced from Thermal-Shock and Related Experiments with LWR Pressure Vessel Material," *Journal of Pressure Vessel Technology*, Vol. 105, May 1983, pp. 102-110.
- [2] Bryan, R. H., et al., "The Heavy-Section Steel Technology Pressurized-Thermal-Shock Experiment, PTSE-1," *Engineering Fracture Mechanics*, Vol. 23, No. 1, 1986, pp. 81-97.
- [3] Pugh, C. E., "Crack Arrest Technology," Heavy-Section Steel Technology Program Semiannual Progress Report for October 1985-March 1986, NUREG/CR-4219, Vol. 1 (ORNL/TM-9593/V1), Oak Ridge National Laboratory, Oak Ridge, TN.
- [4] deWit, R., et al., "Wide-Plate Crack-Arrest Testing," Heavy-Section Steel Technology Program Semiannual Progress Report for April-September 1985, NUREG/CR-4219, Vol. 2 (ORNL/TM-9593/V2), Oak Ridge National Laboratory, Oak Ridge, TN.
- [5] Holz, P. P., "Flaw Preparations for HSST Program Vessel Fracture Mechanics Testing: Mechanical-Cyclic Pumping and Electron-Beam Weld-Hydrogen-Charge Cracking Schemes," ORNL/NUREG/TM-369, Union Carbide Corp. Nuclear Division, Oak Ridge National Laboratory, Oak Ridge, TN, May 1980.
- [6] Bass, B. R., et al., "Computational Methods Development for Dynamic Fracture Analysis," Heavy-Section Steel Technology Program Semiannual Progress Report for October 1985-March 1986, NUREG/CR-4219, Vol. 1 (ORNL/TM-9593/V1), Oak Ridge National Laboratory, Oak Ridge, TN.
- [7] Kanninen, M. F., et al., "Elastodynamic and Viscoplastic Dynamic Fracture Mechanics Analysis," Heavy-Section Steel Technology Program Semiannual Progress Report for October 1985-March 1986, NUREG/CR-4219, Vol. 1, (ORNL/TM-9593/V1), Oak Ridge National Laboratory, Oak Ridge, TN.
- [8] Hall, W. J., Kihara, H., Soete, W., and Wells, A. A., *Brittle Fracture of Welded Plate*, Prentice-Hall, Inc., Englewood Cliffs, NJ, 1967.
- [9] Irwin, G. R. and Kies, J. A., "Fracturing and Fracture Dynamics," *Welding Journal Research Supplement*, February 1952, pp. 96-s-100-s.
- [10] Irwin, G. R., "Fracture Mechanics," *Structural Mechanics*, J. N. Goodier and N. J. Hoff, Eds., Pergamon Press, New York, 1960, pp. 557-594.
- [11] *Structural Integrity of Very Thick Steel Plate for Nuclear Reactor Pressure Vessels*, JWES-AE-7806, (in Japanese), Japan Welding Council, Tokyo, Japan, 1977.
- [12] Kanazawa, T., Machida, S., and Teramoto, T., "Preliminary Approaches to Experimental and Numerical Study of Fast Crack Propagation and Crack Arrest," *Fast Fracture and Crack Arrest, ASTM STP 627*, American Society for Testing and Materials, Philadelphia, PA, 1977, pp. 39-58.
- [13] Ohashi, N., Tanaka, M., Enami, T., Ooi, H., Sekine, T., and Ando, Y., "Fracture Toughness of Heavy Section LWR Pressure Vessel Steel Plate Produced by Basic Oxygen Furnace and Ladle Refining Process," *Proceedings, Fourth International Conference on Pressure Vessel Technology*, Vol. 1, Institute of Mechanical Engineers, New York, 1980, pp. 391-396.

- [14] Kanazawa, T., Machida, S., Teramoto, T., and Yoshinari, H., "Study on Fast Fracture and Crack Arrest," *Experimental Mechanics*, Vol. 21, No. 2, February 1981, pp. 78-88.
- [15] Machida, S., Kawaguchi, Y., and Tsukamoto, M., "An Evaluation of the Crack Arrestability of 9% Ni Steel Plate to an Extremely Long Brittle Crack," *Journal of the Society of Naval Architects of Japan*, Vol. 150, 1981, translation ORNL-tr-5052, pp. 511-517.
- [16] Kanazawa, T., Machida, S., and Yajima, H., "Recent Studies on Brittle Crack Propagation and Arrest in Japan," *Fracture Mechanics Technology Applied to Material and Structure Design*, G. C. Sih, N. E. Ryan and R. Jones, Eds., Martinus Nijhoff, The Hague, The Netherlands, 1983, pp. 81-100.
- [17] Freund, L. B., "Crack Propagation in an Elastic Solid Subjected to General Loading—III. Stress Wave Loading," *Journal of the Mechanics and Physics of Solids*, Vol. 21, 1973, pp. 47-61.
- [18] Rose, L. R. F., "Recent Theoretical and Experimental Results on Fast Brittle Fracture," *International Journal of Fracture*, Vol. 12, No. 6, December 1976, pp. 799-813.
- [19] Brown, W. F. and Srawley, J. E., *Plane Strain Crack Toughness Testing of High Strength Metallic Materials*, ASTM STP 410, American Society for Testing and Materials, Philadelphia, PA, 1966.
- [20] Pellissier-Tanon, A., Sollogoub, P., and Houssin, B., "Crack Initiation and Arrest in an SA 508 Class-3 Cylinder Under Liquid Nitrogen Thermal-Shock Experiments," Paper G/F 1/8, *Transactions*, Seventh International Conference on Structural Mechanics in Reactor Technology, Vols. G and H, August 1983, pp. 137-142.
- [21] Sanders, P. H. and Romualdi, J. P., "Dynamic Considerations in Fracture Arrest by Riveted Stiffeners," *Developments in Mechanics*, J. E. Lay and L. E. Malvern, Eds., The Midwestern Mechanics Conference, Plenum Press, New York, 1961, pp. 100-111.
- [22] Fourney, W. L., et al., "Investigation of Damping and Cleavage-Fibrous Transition in Reactor-Grade Steel," HSST Program Quarterly Progress Report for July-September 1983, NUREG/CR-3344, Vol. 3 (ORNL/TM-8787/V3), Oak Ridge National Laboratory, Oak Ridge, TN.
- [23] Kanninen, M. F., et al., "Preliminary Analysis of Japanese Wide-Plate Dynamic Crack Propagation-Arrest Experiments," Battelle-Columbus Laboratories, Columbus, OH, December 1983.
- [24] Crosley, P. B. and Ripling, E. J., "Crack Arrest in an Increasing K-Field," HSSTP-TR-27, Materials Research Laboratory, Inc., Glenwood, IL, January 1973.
- [25] Merkle, J. G., "Fracture Safety Analysis Concepts for Nuclear Pressure Vessels, Considering the Effects of Irradiation," *Journal of Basic Engineering*, American Society of Mechanical Engineers, Vol. 93, No. 2, June 1971, pp. 265-273.
- [26] Bass, B. R., Pugh, C. E., and Stamm, H. K., "Dynamic Analyses of a Crack Run-Arrest Experiment in a Nonisothermal Plate," *Pressure Vessel Components Design and Analysis*, Vol. 4, ASME PVP Vol. 98-2, American Society of Mechanical Engineers, New York, 1985, pp. 175-184.
- [27] Rosenfield, A. R., et al., "Crack-Arrest Studies at Battelle Columbus," Heavy-Section Steel Technology Program Semiannual Progress Report April-September 1984, NUREG/CR-3744, Vol. 2 (ORNL/TM-9154/V2), Oak Ridge National Laboratory, Oak Ridge, TN, pp. 102-109.
- [28] Edmonds, D. P. and McGowan, J. J., "Preliminary Characterization of Wide-Plate Test Material at ORNL," Heavy-Section Steel Technology Program Semiannual Progress Report for April-September 1984, NUREG/CR-3744, Vol. 2 (ORNL/TM-9154/V2), Oak Ridge National Laboratory, Oak Ridge, TN, pp. 96-102.
- [29] Tada, R., Paris, P. C., and Irwin, G. R., *The Stress Analysis of Cracks Handbook*, Del Research Corp., Hellertown, PA, 1973.
- [30] Bass, B. R. and Bryson, J. W., *Applications of Energy Release Rate Techniques to Part-Through Cracks in Plates and Cylinders*, Vol. 1. ORMG3D: A Finite-Element Mesh Generator for 3-Dimensional Crack Geometries, NUREG/CR-2997, Vol. 1 (ORNL/TM-8527/V1), Oak Ridge National Laboratory, Oak Ridge, TN.
- [31] Bass, B. R. and Bryson, J. W., *Applications of Energy Release Rate Techniques to Part-Through Cracks in Plates and Cylinders*, Vol. 2. ORVIRT: A Finite-Element Program for Energy Release Rate Calculations for 2-D and 3-D Crack Models, NUREG/CR-2997, Vol. 2 (ORNL/TM-8527/V2), Oak Ridge National Laboratory, Oak Ridge, TN.
- [32] Bathe, K. J., "ADINA—A Finite Element Program for Automatic Dynamic Incremental Non-linear Analysis," Report AE 84-1, Massachusetts Institute of Technology, Cambridge, MA, December 1984.

David J. Ayres,¹ Raymond J. Fabi,¹ Robert Y. Schonenberg,¹ and Douglas M. Norris²

Comparison of Analysis and Experimental Data for a Unique Crack Arrest Specimen

REFERENCE: Ayres, D. J., Fabi, R. J., Schonenberg, R. Y., and Norris, D. M., "Comparison of Analysis and Experimental Data for a Unique Crack Arrest Specimen," *Fracture Mechanics: Nineteenth Symposium, ASTM STP 969*, T. A. Cruse, Ed., American Society for Testing and Materials, Philadelphia, 1988, pp. 724-751.

ABSTRACT: A new fracture test specimen has been developed to study crack extension and arrest in nuclear reactor vessel steels subjected to stress-intensity factor and toughness gradients similar to those in postulated pressurized thermal shock situations. A summary of the results of all the tests performed is presented to illustrate the range of crack arrest and crack reinitiation conditions observed. One test of this specimen with the corresponding stress analysis is described in detail. During this test the crack initiated, extended, arrested, reinitiated, extended again, and reached a final arrest. Comparison of detailed dynamic elastic-plastic finite-element analyses and dynamic strain and displacement measurements of the crack extension, arrest, and reinitiation events, combined with topographic analysis of the fracture surfaces, has led to a new understanding of the crack extension and arrest process. The results of the tests demonstrate crack arrest in a rising stress-intensity field at near-upper-shelf temperature conditions and show that the toughness required for arrest is lower than would be predicted by the analysis procedures usually employed for pressurized thermal shock evaluations.

KEY WORDS: crack arrest, dynamic finite-element analysis, dynamic fracture, crack reinitiation, crack propagation, fracture mechanics

A coordinated analytical and experimental program was conducted at Combustion Engineering (CE), Inc., under the sponsorship of the Electric Power Research Inst. (EPRI) to determine the response of precracked specimens of unirradiated reactor-vessel-grade materials subjected to conditions similar to those which might occur in pressurized water reactor (PWR) primary coolant systems during extreme cooldown/depressurization/represurization situations [1]. The specimen developed for this program is called the moment-modified compact-tension (MMCT) test specimen and is shown in Fig. 1. Separate loading devices control the stress at the crack tip (initiation zone) and in the specimen ligament (arrest zone) using a split wedge and moment arms, respectively. The specimen is chilled at the precrack end and heated on the crack-arrest end to produce an increasing toughness gradient in the material along the crack path.

The objective of the test program was to demonstrate that cracks would arrest in an increasing stress-intensity field at temperatures near the upper shelf [nil-ductility transition temperature (NDT) plus 67°C]. Seven successful crack initiation and arrest tests were performed. The crack arrest and reinitiation toughness values generated by these tests are

¹ Supervisor, principal engineer, and senior test engineer, respectively, Combustion Engineering, Inc., Windsor, CT 06095.

² Project manager, Electric Power Research Inst., Palo Alto, CA.

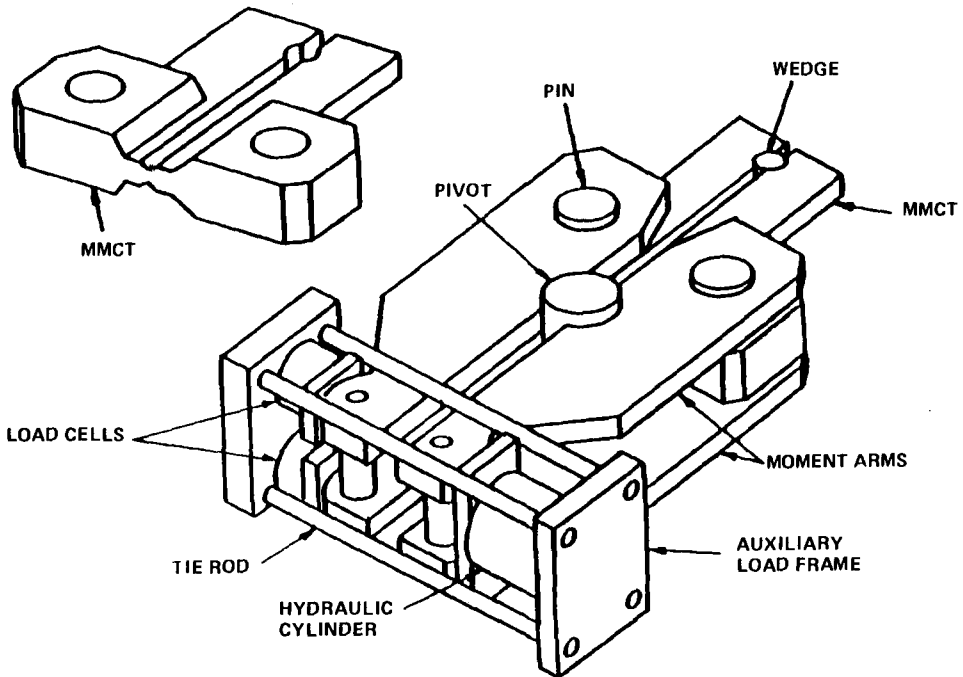


FIG. 1—MMCT test configuration.

shown in Fig. 2. The figure shows the values of K_I at crack arrest and at the maximum loading subsequent to crack arrest for seven tests (numbered 1b, 3a, 4a, 6a, 7a, 8a, 9a). The K_I at arrest is computed by a simplified static analysis, developed in this program and described in this report, which approximates the dynamic conditions at crack arrest. The K_I that was reached after crack arrest is also computed by a static analysis that represents the effect of the continued crack-tip loading due to specimen response to the presence of the extended crack.

In Tests 6a, 7a, and 9a, the crack reinitiated prior to achieving the maximum K_I shown in the figure. In Tests 1b, 3a, 4a, and 8a, the crack did not reinitiate. Therefore, the line drawn as the test reinitiation K_I line in Fig. 2 is an estimate of the division between the values which resulted in reinitiation and those which did not. Also shown for reference in Fig. 2 are the American Society of Mechanical Engineers (ASME) Section XI curves for crack initiation, K_{Ic} , and crack arrest, K_{Ia} .³ These code curves are shown to be conservative relative to the test results, but, especially for arrest, not excessively conservative.

In this paper, we describe Test 9a, in which the crack initiated, arrested, reinitiated, and rearrested. This test was instrumented with dynamic strain and crack-opening displacement gages. Dynamic finite-element calculations were performed to aid in the understanding of the crack extension process and to extract the appropriate crack-tip parameters.

Comparison of detailed dynamic elastic-plastic finite-element analyses and dynamic strain and displacement measurements of the crack extension, arrest, and reinitiation events have led to a new understanding of the crack extension and arrest process. The dynamic analysis

³ American Society of Mechanical Engineers Boiler and Pressure Vessel Code Section XI Appendix A, Figure A-4200-1, New York, 1983.

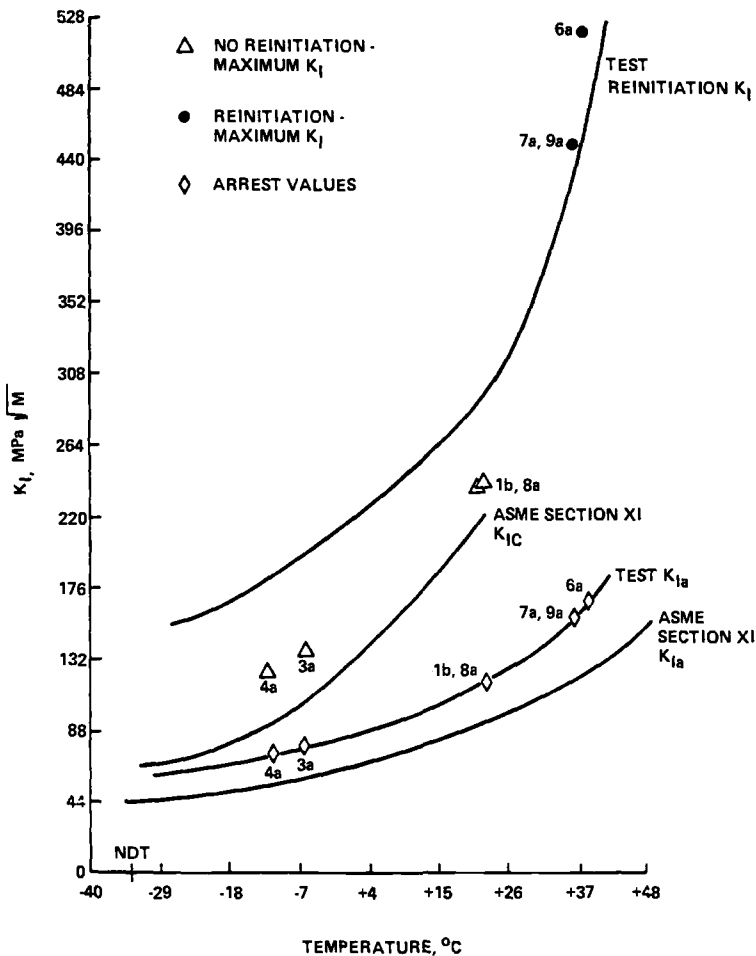


FIG. 2—Stress-intensity factors at arrest and at maximum loading after arrest for all MMCT tests.

shows that the stress-intensity factor at arrest computed by traditional static linear elastic fracture mechanics (LEFM) techniques does not relate to the instantaneous crack-tip conditions when the crack arrest occurs. The agreement between this analysis and data for both crack-opening displacement and strain indicates that the dynamic analysis does model the crack-tip condition at crack arrest.

Crack velocity data were used as input to the dynamic analysis to show that the crack moves into the specimen so fast that the bulk of the specimen does not have time to respond to the presence of the crack. The instantaneous K_I at arrest, therefore, is much lower than the K_I that would be computed from an analysis that considers the static deformed state of the cracked specimen. The results of the dynamic analysis indicate that a static analysis of this specimen properly restrained to represent inertial resistance to motion will properly model the crack-tip condition at arrest. These observations apply to any structure which moves in response to crack extension.

Following arrest, loading of the crack continues as the specimen responds to the crack

and causes the stress-intensity factor to increase to a value that does relate to the final deformed state of the cracked specimen. In Test 9a the initiation value of the crack-tip parameter was reached prior to the peak dynamic response of the specimen, and crack reinitiation and extension occurred.

Specimen Geometry and Loading Methods

The test specimen geometry and some of the associated fixtures are shown in Fig. 1. The name "moment-modified compact-tension specimen" was chosen because of the moment arms used to supply tension loads to the specimen. Most of the specimen is 50 mm thick, but the portion to which the moment arm load is applied is thickened to 100 mm. This was done to prevent yielding around the pin holes when high loads are applied. Figure 3 shows a picture of this area of the specimen. Using the moment arms, a maximum load of 3.3 MN can be applied between the loading pins. For a long crack this causes an elastic stress-intensity factor approaching $330 \text{ MPa } \sqrt{\text{m}}$. The specimen is side grooved 12.5% on each side to encourage the crack to remain centered in the specimen.

The auxiliary load frame has a hydraulic cylinder that pushes the moment arms together. The moment arms are 50 mm thick and 920 mm long. The pivot is located so that the load applied by the hydraulic cylinder is amplified at the load pins. After the proper test load conditions have been obtained, hardened gage blocks are placed between the moment arms to eliminate arm motion during crack extension to assure that no external energy is introduced into the system.

Crack initiation is achieved with a split-pin wedge that is loaded by a 222 kN MTS actuator. Figure 4 shows the specimen and the MTS actuator and load frame without the moment arms. Figure 5 shows the specimen and load frame ready for testing.

Analysis Boundary Conditions

The entire specimen and loading system is considered in the finite-element analysis model shown in Fig. 6. The model includes the specimen, the moment arms, the pin connecting the arms and specimen, the pivot about which the arms rotate, the split wedge, and even the Teflon sheet lubricant between the wedge and the specimen. Loads are applied to the moment arms until the level prescribed for each test is achieved. A block is placed between the arms, and additional load is applied to assure that the end of the arms will not move during crack extension. This fixed displacement condition is used for all static and dynamic analyses.

Similarly, the wedge is loaded by a radial displacement until crack initiation occurs. The surface of the wedge in line with the crack is prescribed in the model to be fixed at the wedge displacement at crack initiation. During crack extension, the wedge expands and can separate from the specimen in the static and dynamic analyses.

The boundary conditions in the analysis are precisely those which exist in the actual test in that displacement at the load application points is prevented during crack extension, thereby assuring that no additional energy is input to the analyzed system during crack extension. This constant energy during crack extension greatly simplifies the analysis and eliminates large errors found in many other dynamic tests.

Results of MMCT Test 9a

We conducted MMCT Test 9a on 19 June 1985. This test attempted to duplicate the double crack jumps of two previous tests using additional instrumentation to measure the dynamic

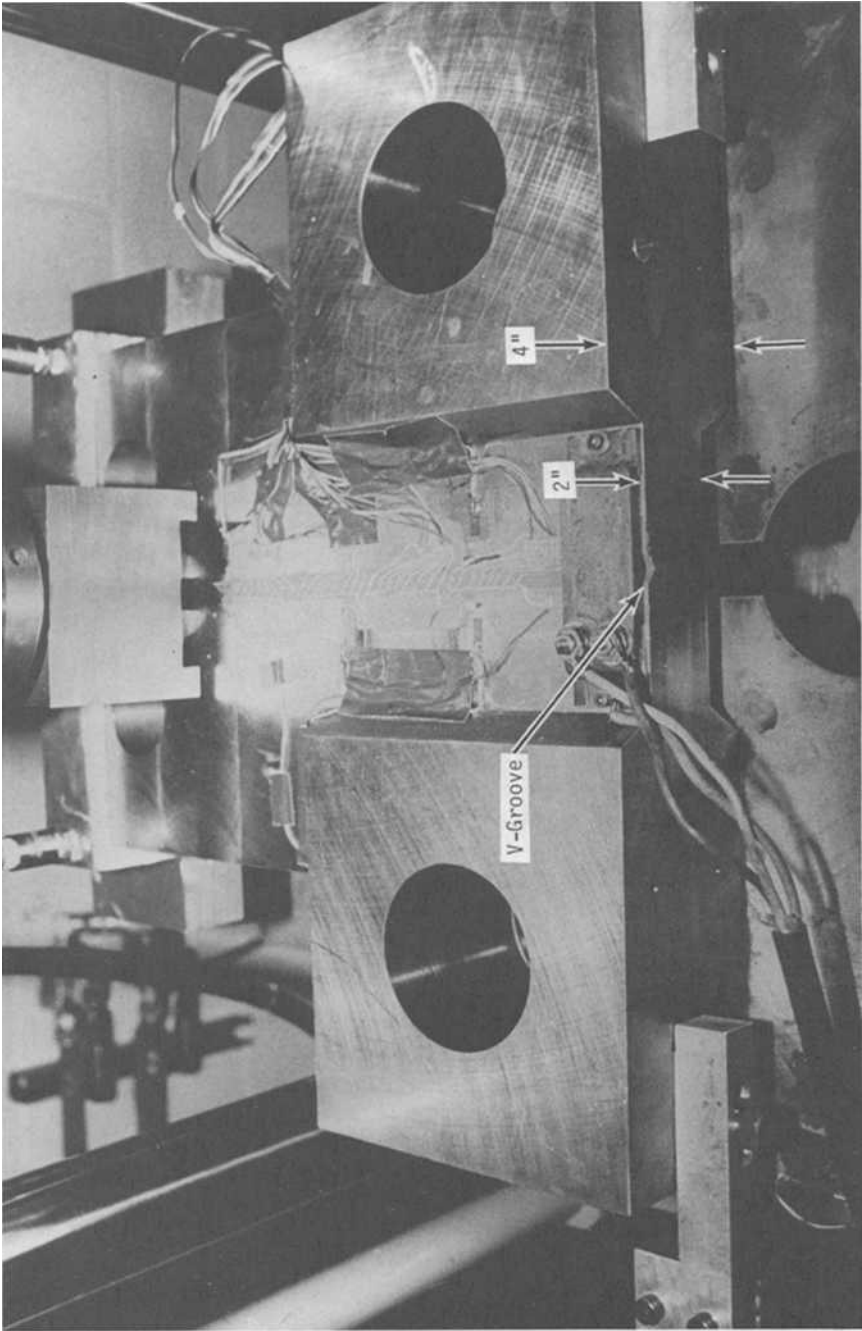


FIG. 3—Increased MMCT thickness for carrying the moment arm load.

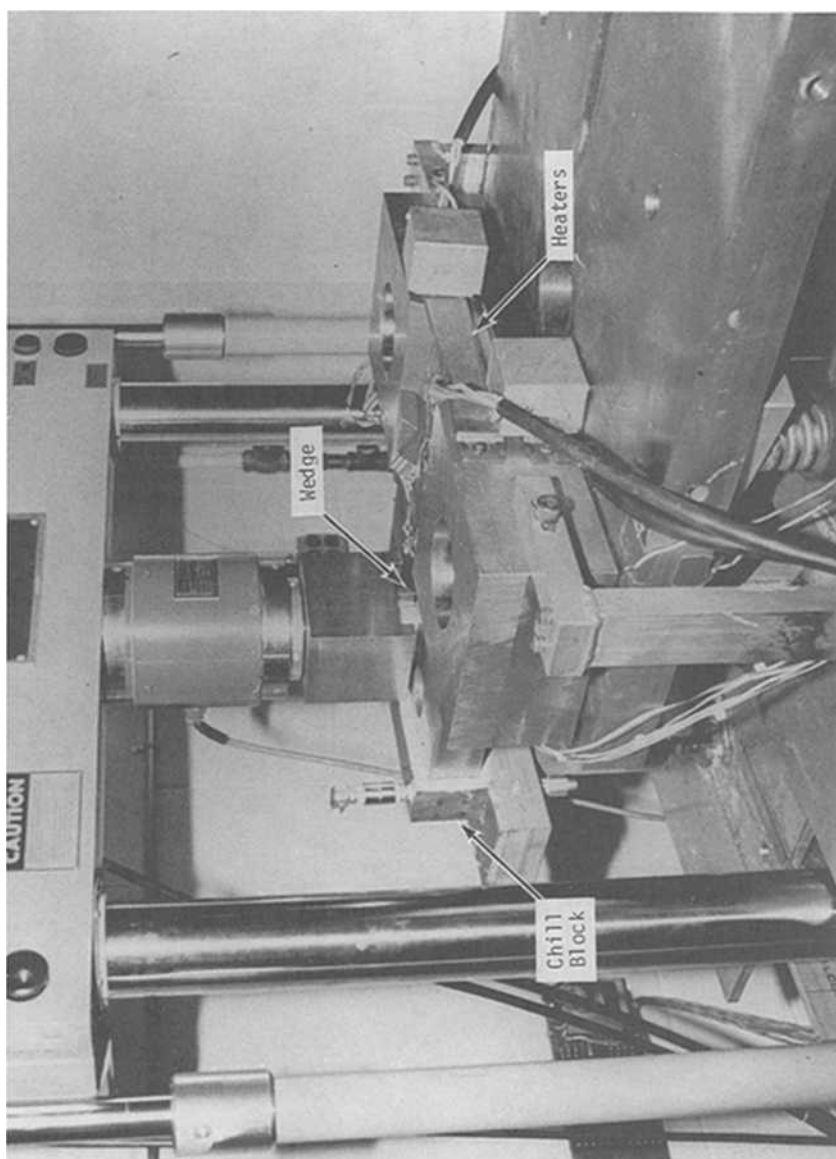


FIG. 4—Side view of an MMCT specimen.

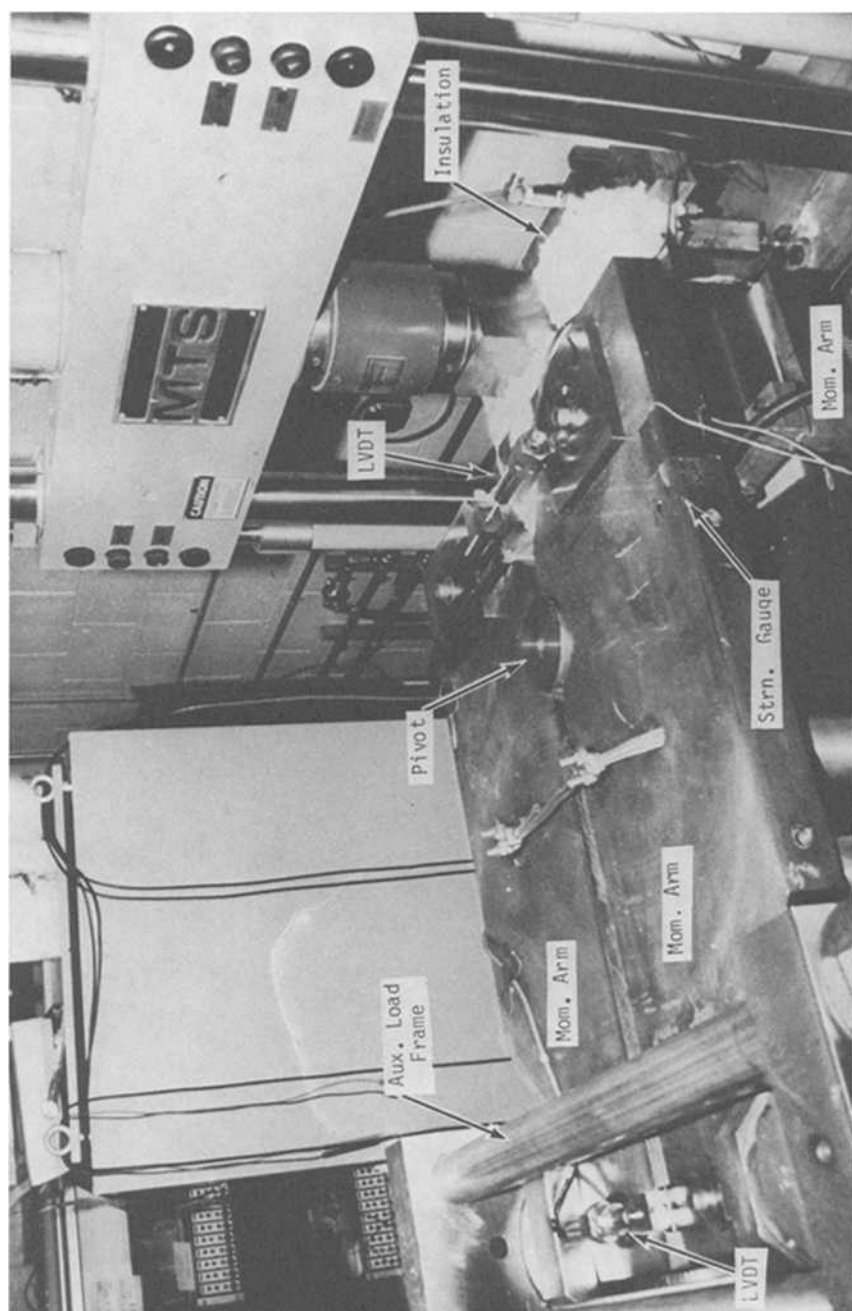


FIG. 5—Overall view of an assembled specimen.

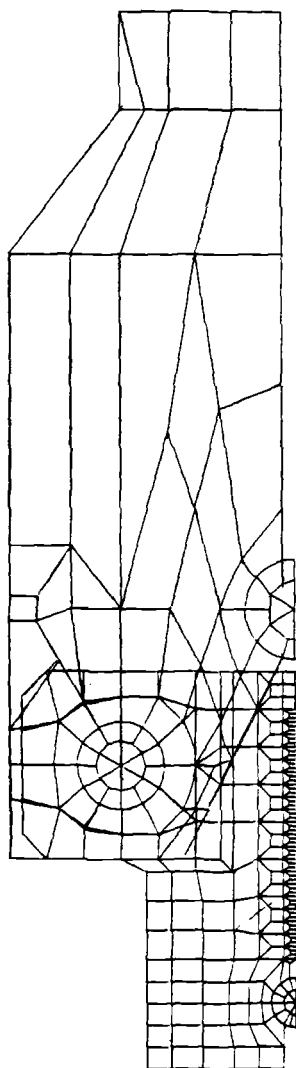


FIG. 6—Finite-element idealization of the entire MMCT setup.

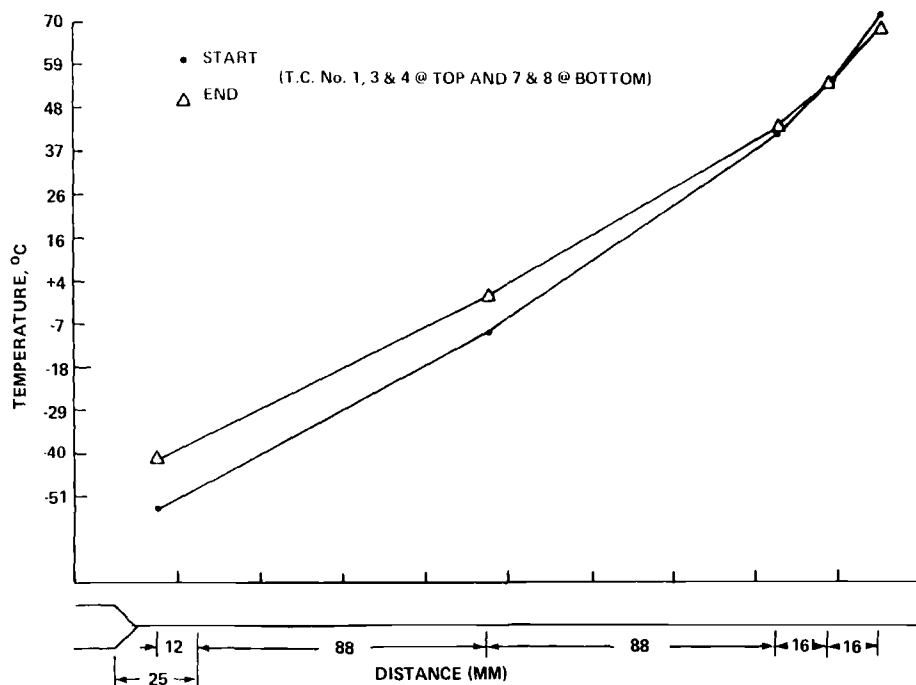


FIG. 7—Temperatures in Test 9a.

aspects of the event. The thermal gradient established for the test is shown in Fig. 7. The crack tip was at -40°C and the pin line was at 44°C at crack initiation. The thermal gradient is essentially linear, producing negligible thermal stress in the specimen. A crack was initiated by wedge insertion while applying a moment arm load of 890 kN, the maximum load that can be applied. The crack ran 180 mm and initially arrested at 38°C with a static elastically computed K_I of $297 \text{ MPa } \sqrt{\text{m}}$. A short time later a subsequent crack extension of 29 mm occurred and the crack arrested at a static elastically calculated K_I of $449 \text{ MPa } \sqrt{\text{m}}$. The specimen was photographed and dimensional changes were noted. It was then broken and examined. The loadings, initial crack extension, and subsequent reinitiation were essentially the same as those of two previous tests.

Dynamic Instrumentation—Test 9a was performed with the objective of obtaining detailed dynamic behavior data in order to understand the crack velocity and the conditions at arrest and reinitiation better. In addition to thermocouples, static strain gages, and a crack-opening clip gage used in the previous tests, three types of dynamic instrumentation were used to obtain detailed information about crack velocity and specimen response. The dynamic instrumentation included crack speed (ladder) gages, installed by C. R. Barnes of Battelle-Columbus Laboratories (BCL); four Hall effect displacement gages (HEDIG), installed by J. Giovanola of Stanford Research Institute (SRI) to measure crack-opening displacement at several locations along the crack path; and eight dynamic strain gages, installed by CE and read with instrumentation provided by R. Fields of the National Bureau of Standards (NBS) to measure strains along the crack path. The locations of the gages are shown in Figs. 8a and 8b.

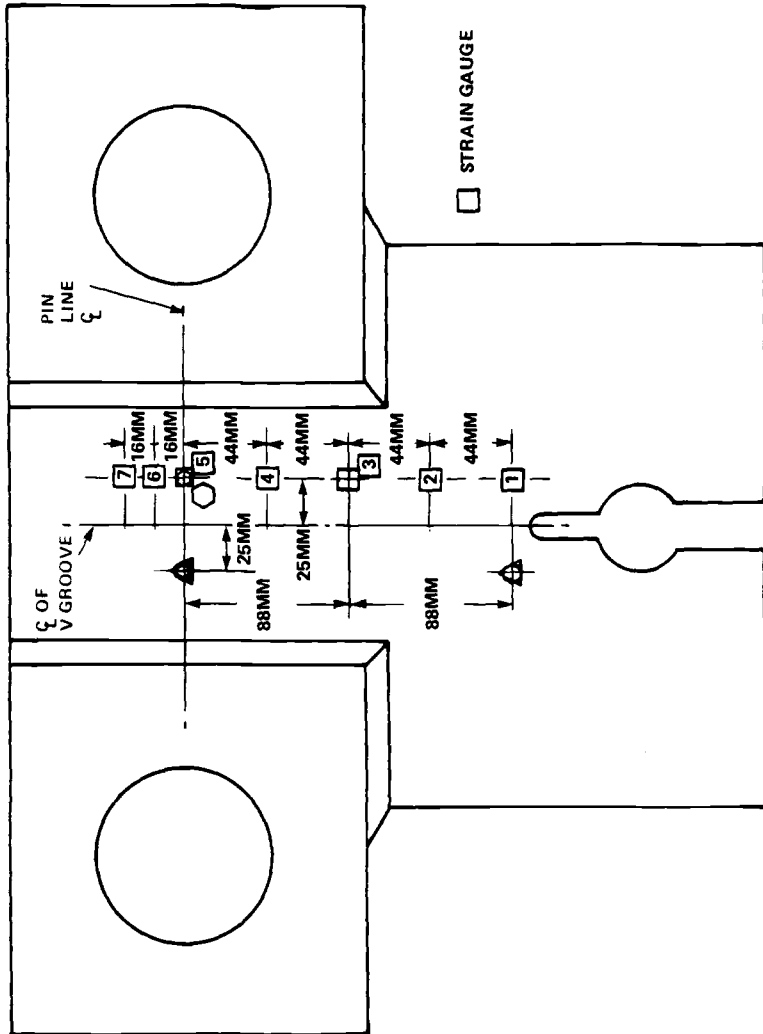


FIG. 8a—Dynamic strain gage locations in Test 9a.

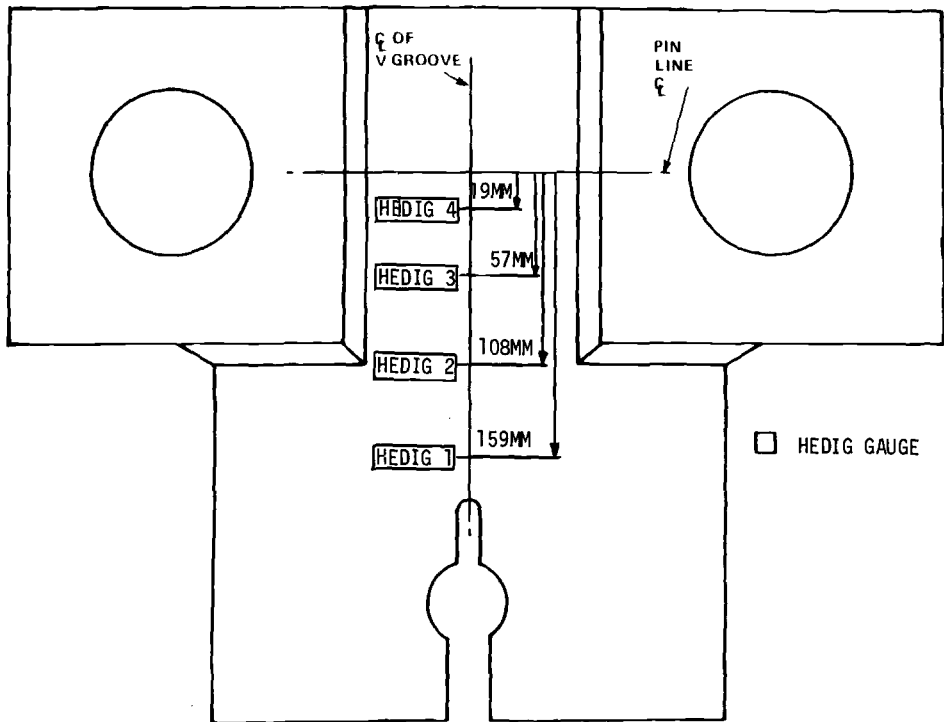


FIG. 8b—HEDIG displacement gage locations in Test 9a.

Static Observations—The relationship between K_I and the clip gage reading, determined from elastic-plastic analysis, is shown in Fig. 9. In the analysis, K_I is computed from the J -integral determined by the virtual crack extension method. Crack initiation occurred at a clip gage reading of 0.39 mm, which corresponds to a K_I of 147 MPa \sqrt{m} . After final crack arrest, the extent of crack opening is shown in Fig. 10; the fracture surfaces are shown in Figs. 11 and 12.

The conclusion that can be drawn from the static analysis relating K_I and crack depth (Fig. 13) is that the crack arrested at a K_I value of 257 MPa \sqrt{m} at NDT + 68°C. This indicates arrest at upper-shelf conditions. However, it is clear from Fig. 12 that reinitiation occurred. Therefore, these static observations do not enable an understanding of the results of this test.

Dynamic Observations—The dynamic strain gages indicated the crack velocity by increasing strain as the crack tip approached and decreasing strain as the crack tip passed by. The results of Strain Gages 1 through 4 indicated an initial high velocity and subsequent reduction as the crack proceeded into tougher material. The results of Gages 5, 6, and 7 indicate the arrest and reinitiation times.

The locations of Strain Gages 4, 5, 6, and 7 are shown with respect to the crack arrest indications in Fig. 12. Strain Gage 5, which is beyond the first arrest point, showed several different loading rates, which we interpreted to indicate the initial crack arrest and subsequent reloading of the specimen in that region. It appears that Gage 5 broke because of high strains prior to crack reinitiation. The reinitiation and arrest events are also indicated by changes in the strain rate of Gage 6.

Displacement Gages 1 and 2 show the crack-opening displacement near the crack initiation region. The time of maximum opening is a measure of the dynamic response of the cracked specimen/moment arm configuration. This response time is very long relative to the initial crack extension, and peak response occurs well after the crack reinitiation event.

Crack Velocity Determination—Reviewing the ladder gage data and the strain gage data led to the conclusion that the initial crack velocity was about 775 m/s and continued high for much of the crack length. The crack then slowed rapidly and the precise time of arrest and reinitiation were unclear. Therefore, two different crack velocity profiles were hypothesized for input to the dynamic analysis of the specimen. These velocity profiles are shown in Fig. 14 and are called the “fast crack” and the “slow crack” hypotheses. The fast crack has a specified arrest time of 0.5 ms and a reinitiation time of 1.0 ms. The slow crack has an arrest time of 1.0 ms and a reinitiation time of 1.27 ms. The final arrest time for these hypotheses were 1.09 and 1.46 ms respectively.

Dynamic Analysis of MMCT Test 9a

The primary input to the dynamic analysis was the assumption of crack-tip position versus time. The two different hypotheses of crack arrest time and the velocity approaching arrest were input to the analysis in order to compute strains and displacements so they could be compared with the experimentally measured values. Comparison of the measurements and

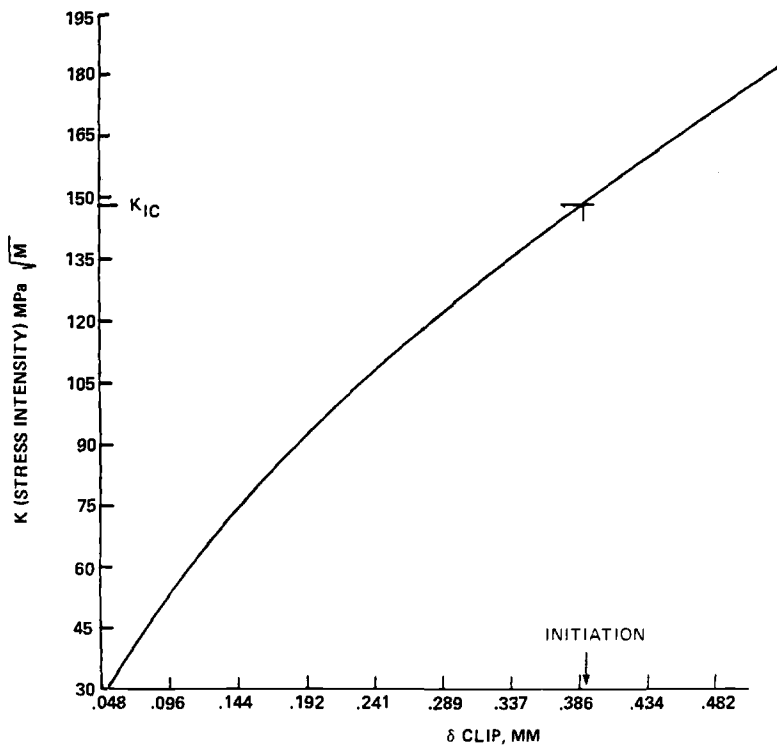


FIG. 9— K_I versus clip-gage displacement in Test 9a.

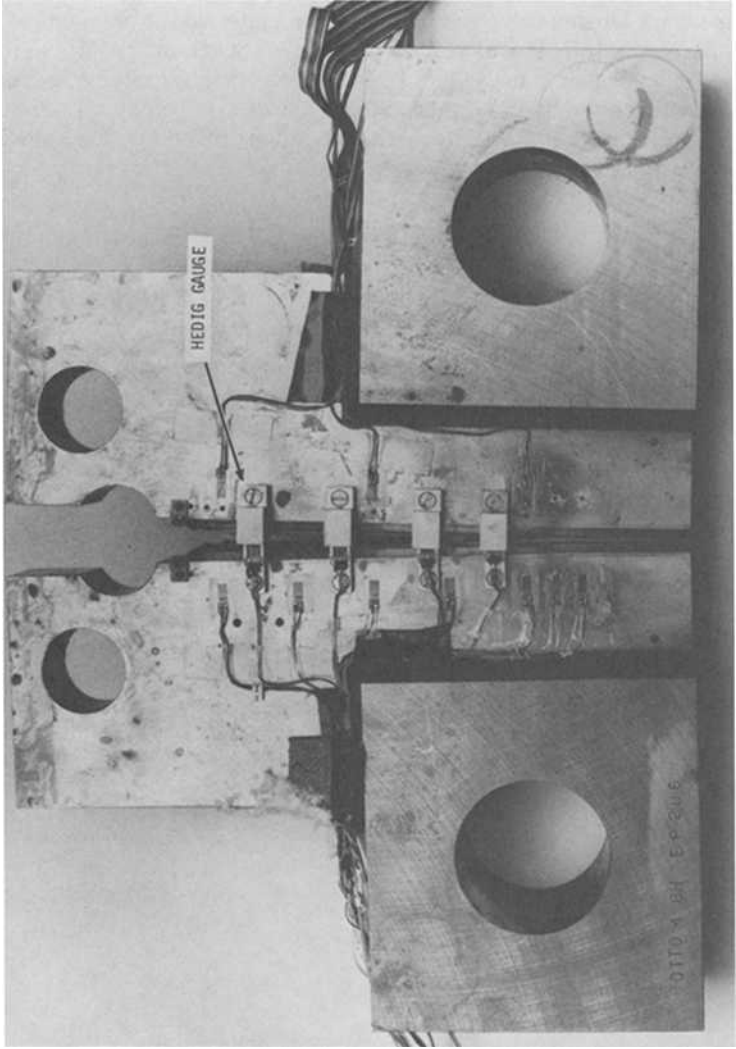


FIG. 10—Test 9a after crack extension showing the HEDIG gages and dynamic strain gages.

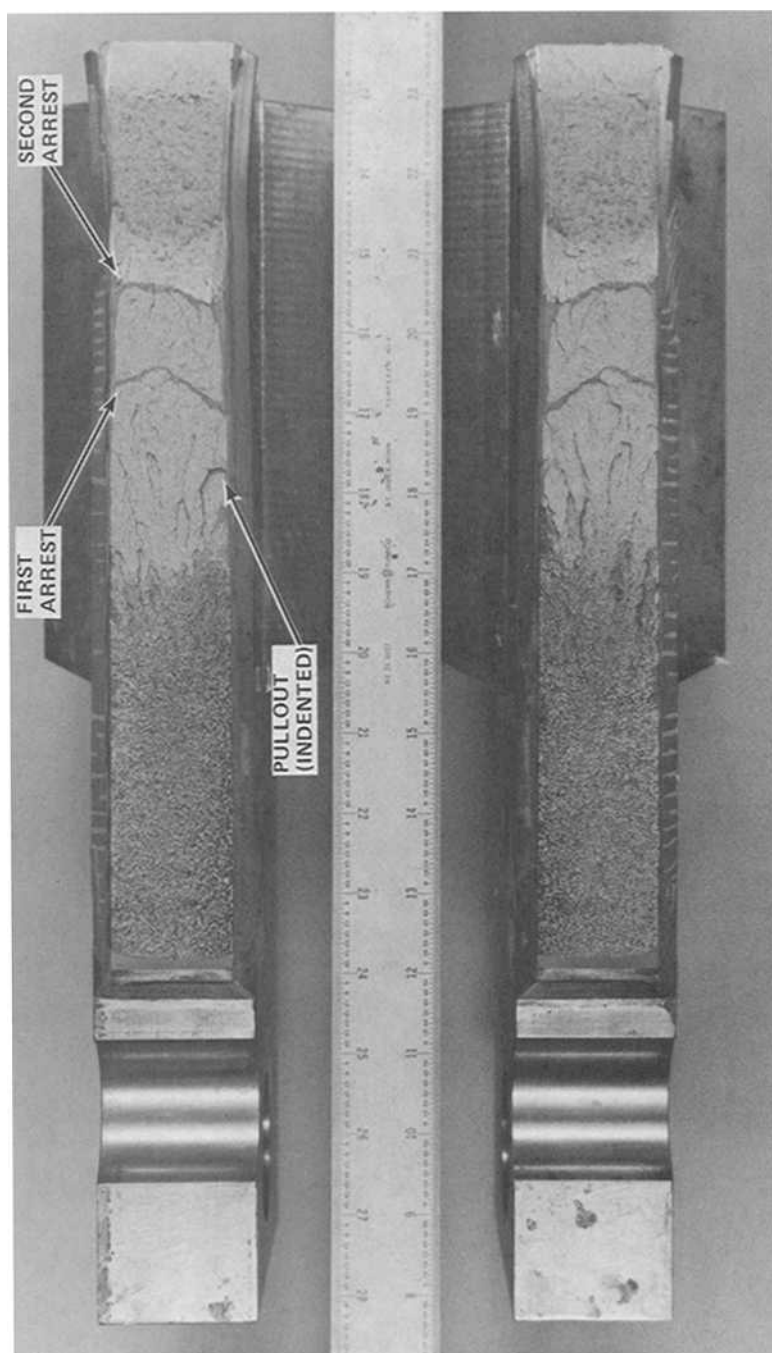


FIG. 11—Fracture surfaces in EPRI MMCT Test 9a.

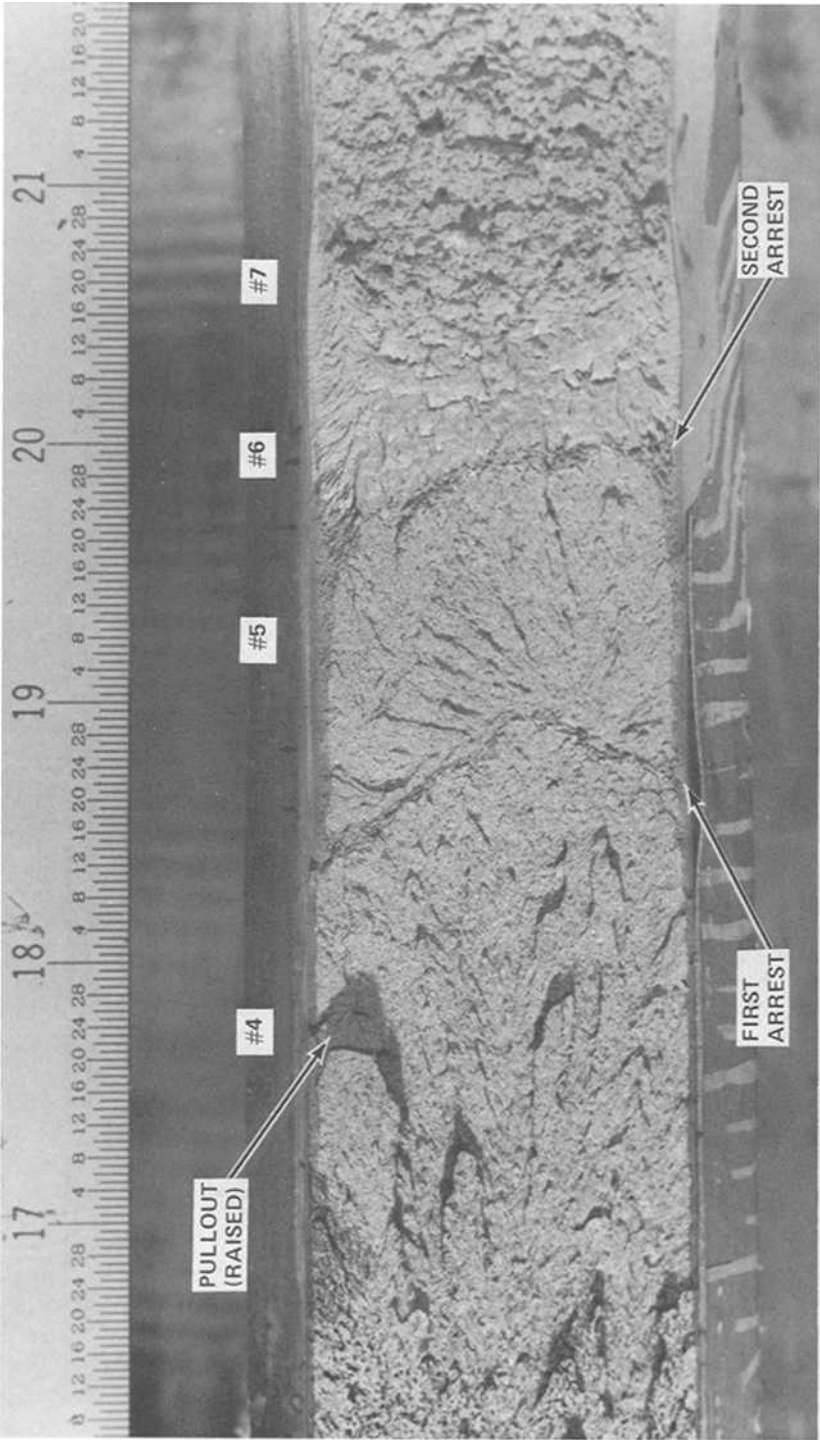
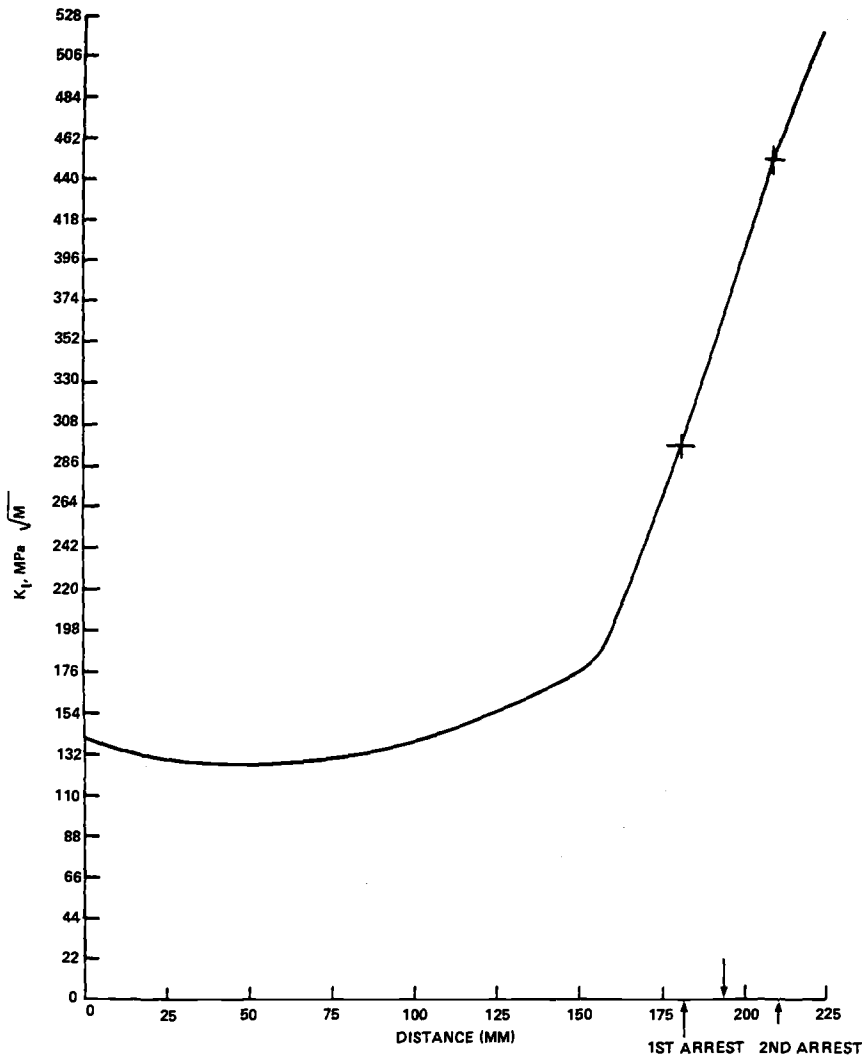


FIG. 12—Closeup of the fracture surfaces in MMCT Test 9a showing the locations of Strain Gages 4 to 7.

FIG. 13—Static elastic K_I for Test 9a.

calculated values aided in determination of the crack arrest and reinitiation times and, subsequently, in determination of the crack-tip conditions at arrest and reinitiation.

The HEDIG gages measure the crack-opening displacement after the crack has passed a gage station. It is important that the analysis match the HEDIG gages since this assures that the overall stiffness of the analytical model and loading is correct. In addition, the analysis must match the large permanent deformation left in the specimen. The plasticity and its accumulation as a function of time have an affect on the response of the specimen and can be seen in the HEDIG gage data. The specimen peak response time measured by the HEDIG gage is on the order of 2 ms.

The dynamic strain gages measure the strain at seven locations 25 mm above the crack plane. It is important that the analysis also match the strain gage response to verify the crack velocity assumption. The strain response time for these gages is on the order of 0.01

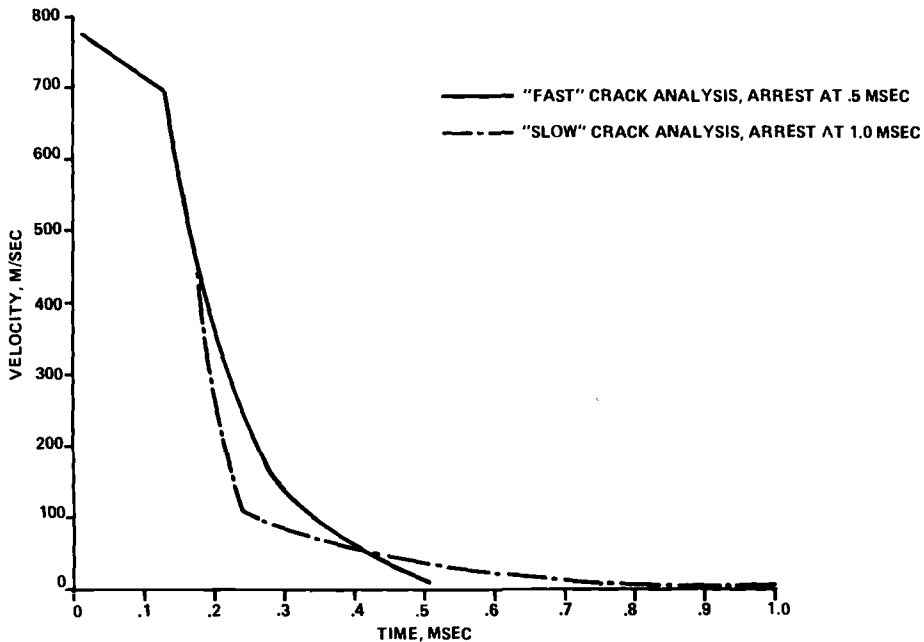


FIG. 14—Velocity versus time.

ms. Correspondence between the large strains in Gages 5, 6, and 7 at late times and the analysis results is used to discriminate between the hypothesized earlier and later arrest times.

The analytical model assumes a straight crack front through the thickness. This may be a close approximation to the conditions of the specimen early in the crack jump event. Figures 11 and 12 show the crack surfaces in the arrest area; the large deviation from a two-dimensional approximation is obvious. The crack curvature, large pull outs, and shear lips all contribute to changing the apparent stiffness of the specimen in comparison with the two-dimensional model in the arrest area, probably causing the two-dimensional model to be in error near the crack-arrest region.

Finite-Element Model

The finite-element model (see Fig. 6) is a collection of two-dimensional components connected by appropriate contact and slip conditions. The pin is modeled to be thinner than the actual pin to account for the three-dimensional effect of pin bending. The density of the pin is then adjusted to give the correct mass. The equations of motion are integrated by the Newmark-Beta operator. Time-independent constitutive equations are used. Thermal stresses are assumed to be small and are not included. The elastic-plastic properties were not varied with temperature and are based on the tests of the actual plate material.

Initial Loading

The loading prior to the crack jump is applied statically. First, the moment arm displacement is applied so that the desired force measured by the load cells on the moment arm is obtained.

The wedge load is applied as a fixed displacement to the center line of the wedge. This displacement is applied over several increments since there is yielding in the crack-tip region. The amount of wedge displacement applied in the analysis is chosen so that the displacement in the model at the clip gage location is the same as the displacement measured by the clip gage prior to crack initiation. This completes the initial loading.

The analytical model starts out in a stress state which includes some plasticity that represents the overall stress and energy state very well. Considering the moment arm, specimen, pins, pivots, and wedges as a closed system, about 91% of the energy is put into this system by the moment arm loading. The wedge loading accounts for about 9% of the total system energy.

The K_{Ic} computed from the J -integral for the loading at crack initiation of Test 9a is 147 MPa \sqrt{m} . The value of K_{Ic} from the ASME Section XI fracture toughness curves for the crack tip at the test temperature is 53 MPa \sqrt{m} , which is an indication of the conservatism of the ASME curve and the high toughness of the program material.

Crack Extension

The method of propagating the crack in the finite-element analysis uses a node release procedure. The crack is in the symmetry plane of the model. The nodes on the uncracked region of that plane are restrained to have no displacement in the direction normal to the crack plane. By removing the displacement constraints as a function of time, the crack advance is simulated as a moving boundary. To represent an amount of crack extension, the displacement constraints are removed from all nodes within that amount of extension ahead of the crack, and the corresponding nodal forces required to prevent displacement are applied. Then, over the several time increments representing the time interval required for the crack tip to reach the prescribed amount of extension, the nodal forces are linearly reduced to zero. The value of J is then computed by the virtual crack extension method at that time. The crack is then extended by the same procedure using a constant step in distance and a different time interval to represent each different crack velocity.

The J -integral formulation for static analysis is used. Since only the ring of elements closest to the crack tip are involved in the J calculation, and the displacement function of the element is static, dynamic effects within an element cannot be considered correctly. Because the volume of material is very small, the actual contribution of dynamic effects to J would also be small. It is, therefore, prudent to ignore such small quantities rather than include them with their significant error.

Ideally, small enough elements and times would allow the forces to be taken away by inertia and the small error ignored, but the procedure used allows larger crack jump steps to be made during the simulation of the entire crack jump. The analyses were continued in time until about 3 ms, well past the time of peak specimen response.

Comparison of Analysis with HEDIG Gage Results

The analysis results are compared with the data from the HEDIG gages to evaluate the correctness of the two velocity assumptions. The displacement measured by Gage 1 is compared with the analyses in Fig. 15. HEDIG Gage 1 is the closest to the initiation location and starts responding almost immediately because of the very high initial velocity. The initial slopes of the analyses and the test data are almost identical for approximately 0.4 ms. From this correspondence between analysis and data, the authors concluded that the initial part of the crack position versus time curve is very well specified in the analyses.

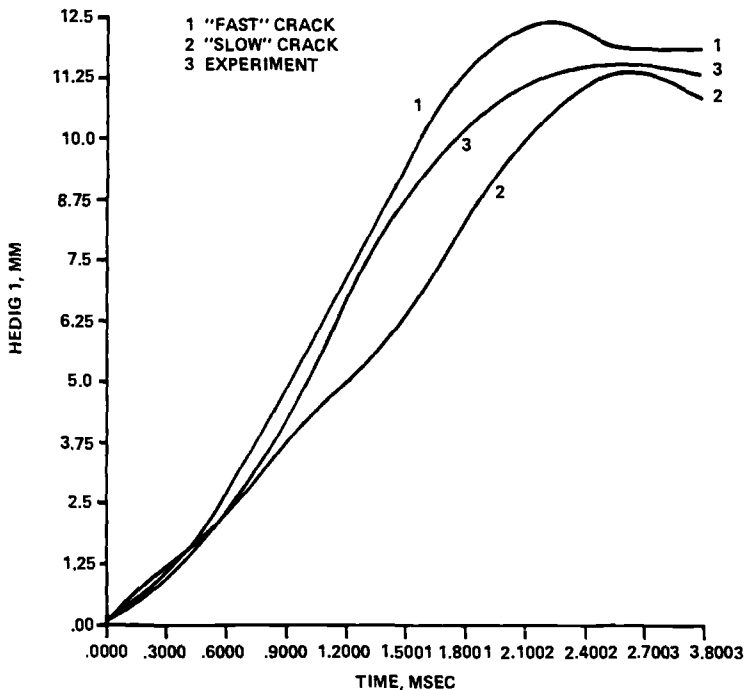


FIG. 15—HEDIG Gage No. 1 versus time.

As the crack velocity input to each analysis starts to differ, the analytical specimen response changes. For Gage 1, results of the fast crack analysis are always higher than the data, and the results of the slow crack analysis are lower. However, both analyses produce reasonable approximations to the data. This indicates that the different reinitiation times and subsequent jumps to the final crack position have little effect on the response at Gage 1. The agreement of the overall timing and very large peak displacement of the analyses and data indicates that the model correctly predicts the amount of plastic deformation.

The test data from HEDIG Gage 2 and the analysis are shown in Fig. 16. Gage 2 is slower in its response, and this is also reflected in the analysis results. The computed displacements increase initially slightly faster than the data. The long-time response shows the same comparison as Gage 1. The data fall between the analyses, with the faster crack analysis results closer to the data for most of the time.

The test data from HEDIG Gage 3 and analysis results are shown in Fig. 17. Gage 3 is closer to the first arrest point and even slower to respond than Gage 2. Again the analyses respond more at early times, but for later times bound the data, with the faster crack analysis results closer to the data for most of the time.

The test data from HEDIG Gage 4 and analyses are shown in Fig. 18. HEDIG Gage 4 is the closest to the first crack arrest location and starts responding later than all the other HEDIG gages. The analysis results start responding at the same time as the data, but again initially with a rate that is slightly higher than that for the data. For this gage the slow crack analysis results follow the data better at earlier times than the faster crack analysis results. At later times the analysis results lie equally far on either side of the data. The trend is the same as for the other gages.

Comparison of the analyses with the HEDIG gage data shows that the best agreement

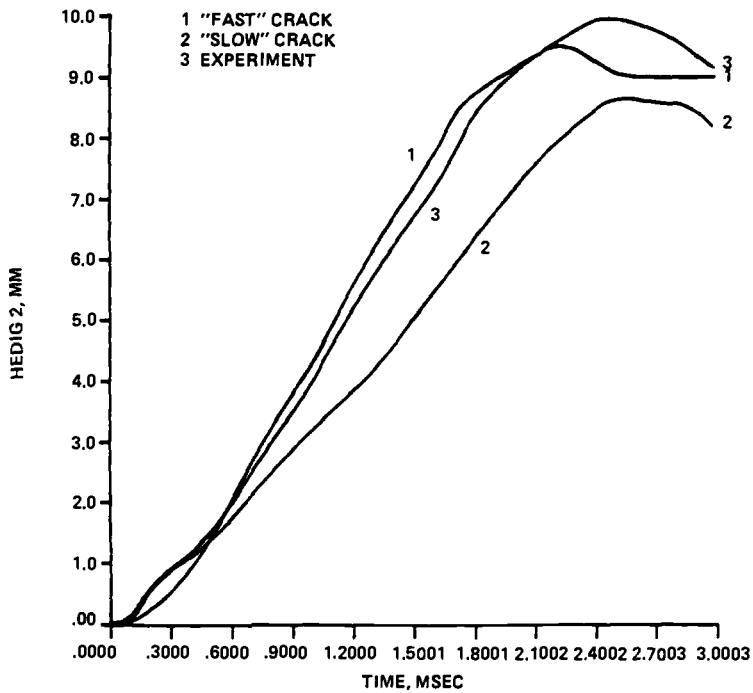


FIG. 16—HEDIG Gage No. 2 versus time.

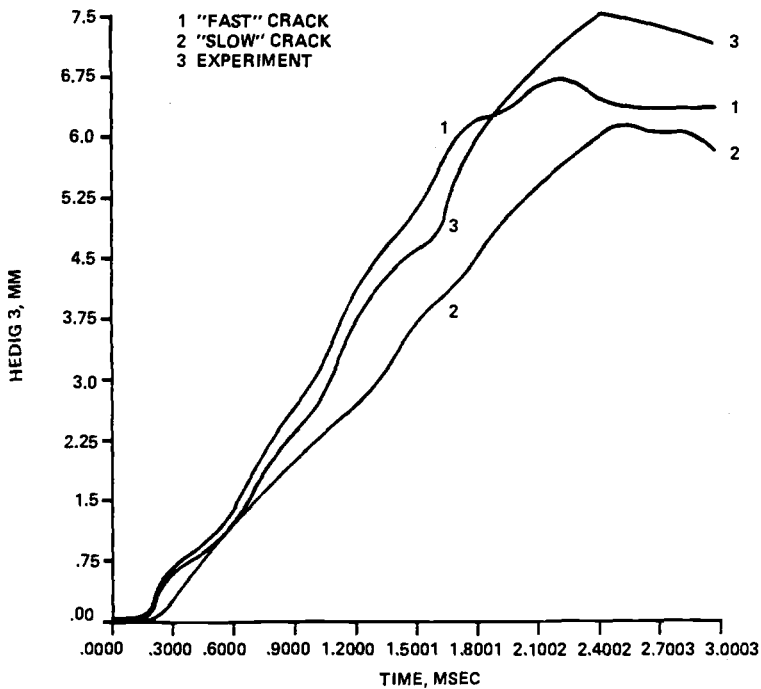


FIG. 17—HEDIG Gage No. 3 versus time.

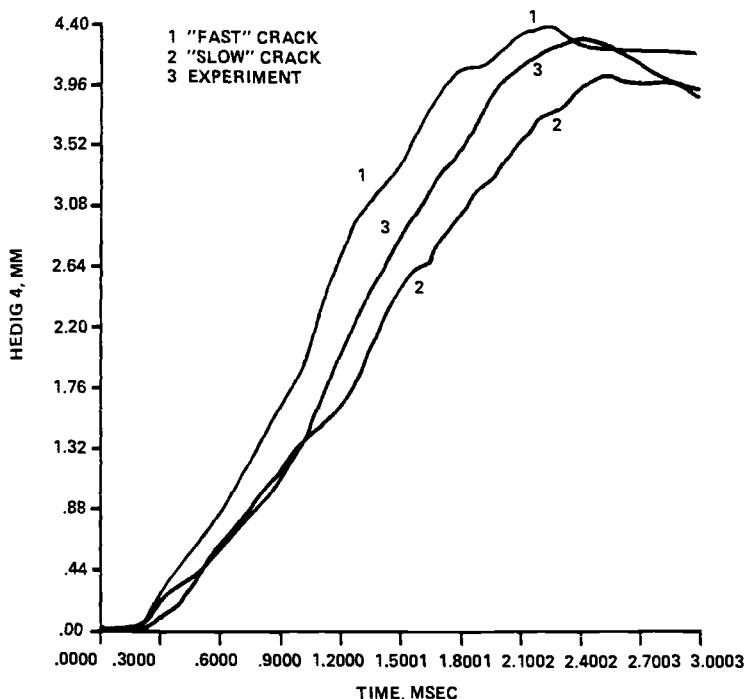


FIG. 18—HEDIG Gage No. 4 versus time.

between analysis and data is obtained with the fast crack hypothesis and the 0.5 ms first arrest time.

Comparison of Analyses with Strain Gage Results

The results of the two analyses were also compared with the strain gage data. Each of the strain gage readings was set equal to the analysis value at zero time. The subsequent response was then compared. The analysis strains are the strains at an integration point in the finite-element model closest to the corresponding strain gage.

Strain Gages 1, 2, and 3

The analysis results for Gages 1, 2, and 3 are shown in Figs. 19, 20, and 21, respectively. Since the response of these gages is over by the time the fast crack velocity and the slow crack velocity differ, these gage results cannot be used to differentiate between the velocity assumptions. The gages indicate generally good agreement between the analysis and the test results, confirming that the velocity early in the crack extension is well specified in the analysis.

Strain Gages 4, 5, 6, and 7

The strain changes reported by these gages are much larger than for Gages 1, 2, and 3. The crack front at these locations encounters the large increase in stress due to the moment arm load. The strains are large enough so that plasticity at the crack tip becomes important.

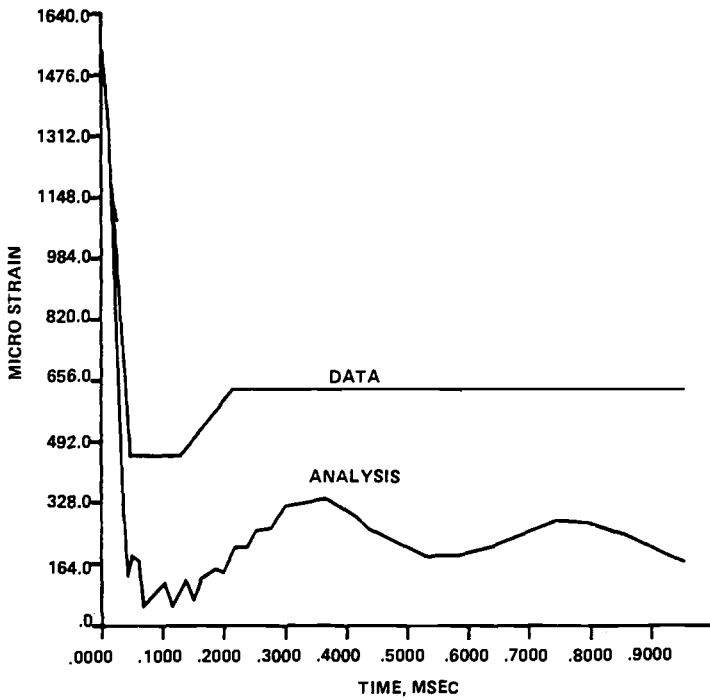


FIG. 19—Strain Gage No. 2 versus time.

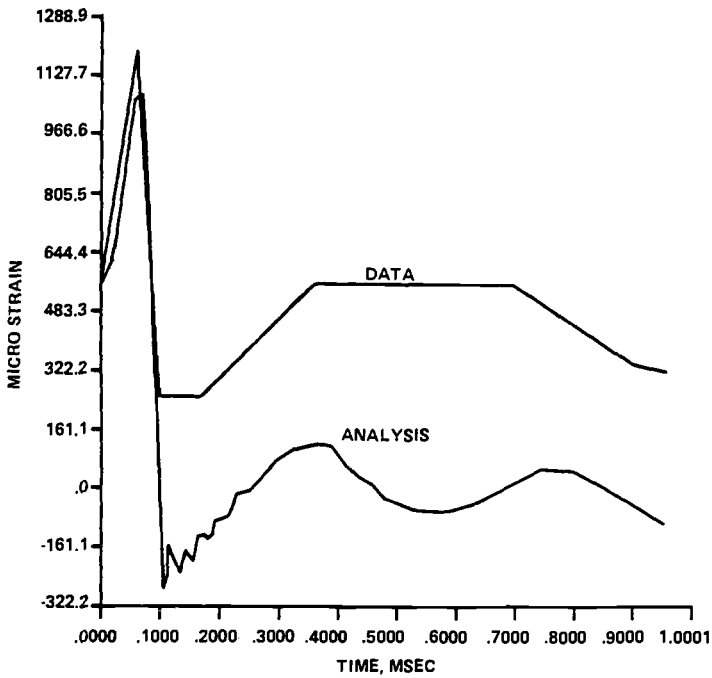


FIG. 20—Strain Gage No. 2 versus time.

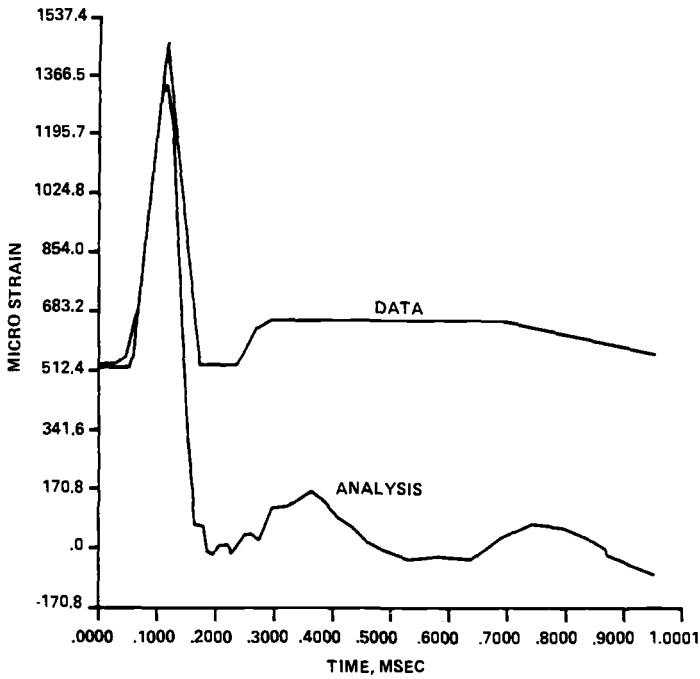


FIG. 21—Strain Gage No. 3 versus time.

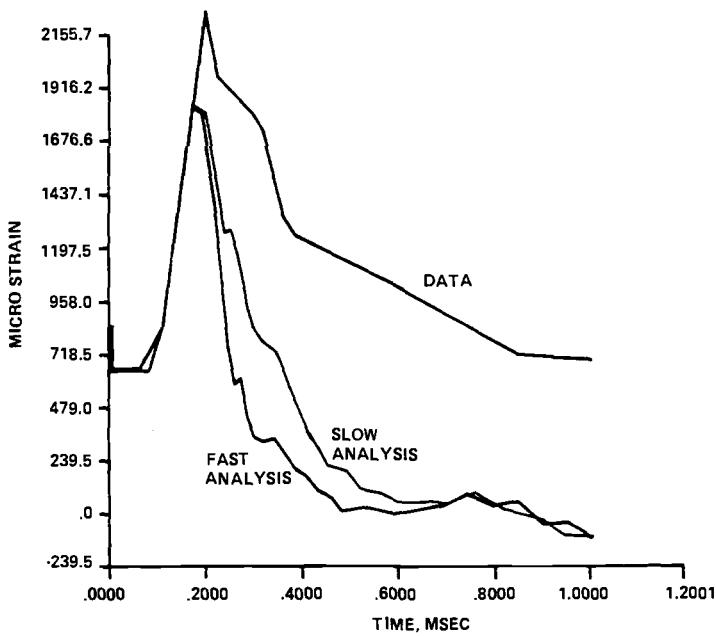


FIG. 22—Strain Gage No. 4 versus time.

It was previously shown by the HEDIG gage data and analysis results that inclusion of plasticity is necessary to describe the overall MMCT specimen response properly. Early in the crack extension, the crack propagated with what appears to be a fairly straight front. However, the three-dimensional nature of the propagation can be seen in Fig. 12 in the region from Strain Gage 4 up to first arrest. This three dimensional effect is believed to produce the delay in the strain response observed in Figs. 22 and 23 for Gages 4 and 5, respectively.

Strain Gage 6 provides important information about the first crack arrest time. The gage is ahead of the first crack arrest location and tends to be less affected by the three-dimensional nature of the crack shape. The gage is close enough to the arrest location to measure very large strains. The results of the fast and slow crack analyses and the data are shown in Fig. 24. The fast crack analysis matches the test data very well for the first 1.0 ms. The initial response happens at the correct time. This analysis has the same elastic loading slope, shows the same plateau, and has the same plastic loading slope as the test data. Beyond 1.0 ms, the analysis assumed reinitiation of the crack and the strain unloaded. The slow crack analysis does not follow the test data after 0.5 ms.

The good correspondence between the test and analysis for the fast crack case shows the analysis correctly models both the elastic and elastic-plastic response of the specimen. This gage corroborates the conclusion made from HEDIG gages and supports the arrest time of 0.5 ms. Comparison of analysis with test data also strongly suggests a reinitiation time of greater than 1.0 ms.

The comparison of the analyses and Strain Gage 7 is shown in Fig. 25. These results also support the 0.5 ms arrest time. The fast crack analysis assumed a reinitiation at 1.0 ms. The analysis after that time departs from the strain gage data. This supports the results of Gage 6 that reinitiation was at a time later than 1.0 ms, perhaps even greater than 1.4 ms.

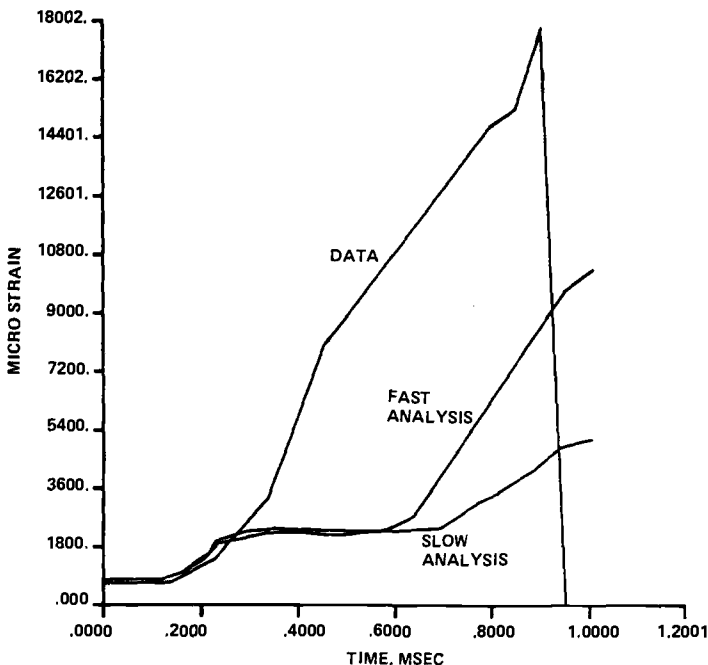


FIG. 23—Strain Gage No. 5 versus time.

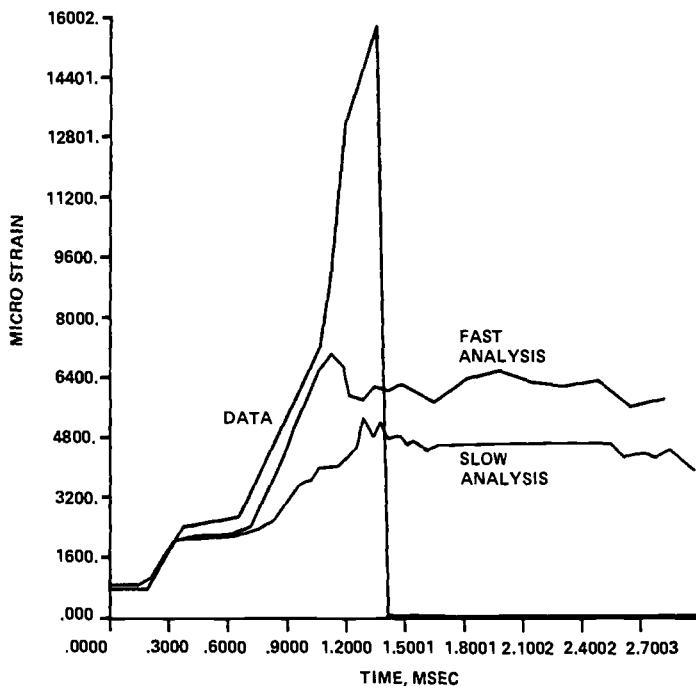


FIG. 24—Strain Gage No. 6 versus time.

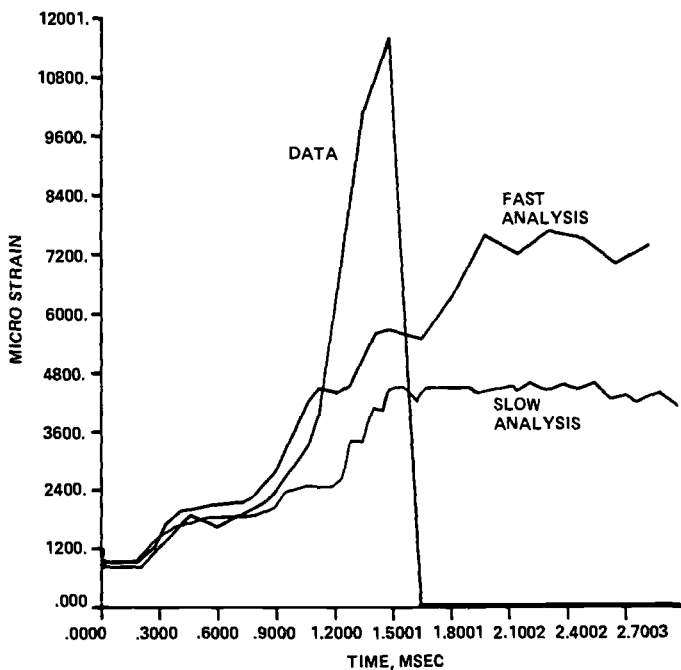


FIG. 25—Strain Gage No. 7 versus time.

Analysis, HEDIG Gage, and Strain Gage Summary

The excellent agreement between the test data and the analysis for Strain Gages 1, 2, and 3 shows that the initial conditions are well represented in the finite-element model of the test. The first portion of the crack position versus time curve is accurately provided by the experimental data. Some lack of agreement between analysis and data for Strain Gages 4 and 5 may be attributed to the limitations of the two-dimensional approximation of the finite-element model being used. Strain Gages 6 and 7 along with the HEDIG gage indicate that the fast crack analysis with an arrest time of 0.5 ms is the analysis which most closely reproduces the test results. This is closest to a major slope change at 0.455 ms on the data output of Strain Gage 5. Based on the comparison of output data from Strain Gage 5, 6, and 7 with analytical strains, the reinitiation time appears to be at or later than 1.4 ms.

K_I at Arrest

Dynamic Calculation

Once the analysis procedure was shown to represent the specimen and loading accurately as a function of time, K_I at arrest was calculated. Only the fast crack analysis will be considered, since it was judged to match the experimental data best.

At each new crack position an energy change based on Park's method of virtual crack extension was calculated as a function of time. From this, the J -integral was calculated and then the stress-intensity, K_I . The value of K_I calculated at arrest in the fast crack analysis is 143 MPa $\sqrt{\text{m}}$. A plot of K_I versus time is shown in Fig. 26.

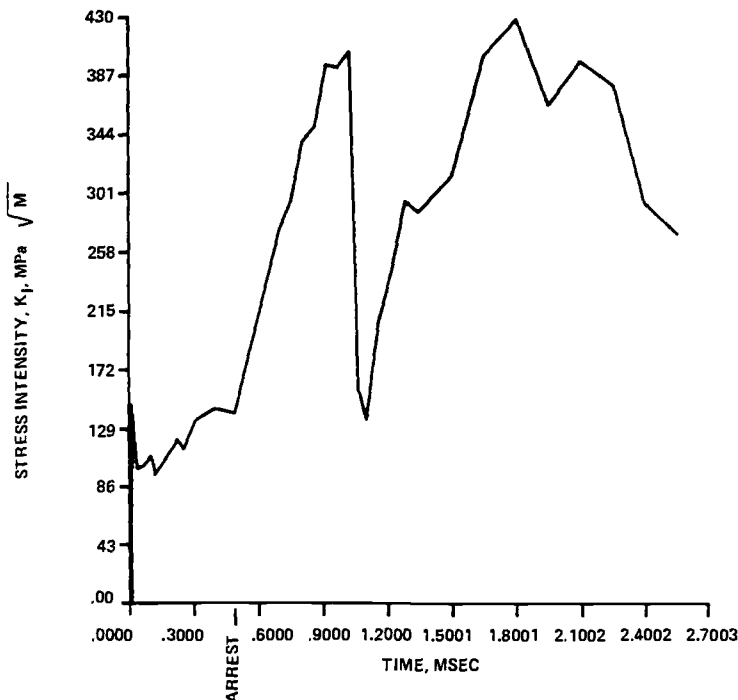


FIG. 26—Stress-intensity K_I versus time.

Subsequent to the first arrest, the crack continues loading, and K_I at the crack tip increases. The crack does reinitiate, but no compelling evidence for choosing a reinitiation time could be found in the data. A time of 1.0 ms was chosen (a) because of the great change in strain gage data readings, (b) because it was close to the time suggested by HEDIG gage and fractography analysis, and (c) because the value of K_I at this time was in the lower range of equivalent J_{Ic} values for ductile initiation. The value of K_I at 1.0 ms is about $396 \text{ MPa } \sqrt{\text{m}}$. If a later reinitiation time is chosen, as suggested by the comparison of the analysis and data for Strain Gages 6 and 7, a higher value of K_I would be calculated. However, the way in which the analysis proceeded, it appears that, for a later reinitiation time of 1.4 to 1.5 ms, the K_I would be only around $465 \text{ MPa } \sqrt{\text{m}}$ because the rate of increase was decreasing. This makes a K_I value of $396 \text{ MPa } \sqrt{\text{m}}$ a conservative lower bound for reinitiation of the crack at this temperature.

Fractographic analysis of fracture surfaces of a previous MMCT test with essentially the same loading conditions revealed that cleavage was the dominant mechanism of crack propagation up to the first crack-arrest line, even though the temperature at the arrest line was near the Charpy upper-shelf temperature. In that test, crack reinitiation and an additional 27-mm extension occurred also in the cleavage mode.

The topographic analysis of the two broken fracture surfaces provided detailed information on the microscopic fracture process. The methodology involves detailed computer modeling of the surface separation and final crack-tip stretching. This is discussed in greater detail in Ref 1, Appendix H. The crack-arrest toughness was determined from the value of the crack-tip opening displacement to be $146 \text{ MPa } \sqrt{\text{m}}$. The crack reinitiation toughness was determined as $232 \text{ MPa } \sqrt{\text{m}}$; however, a band of unbroken ligaments that formed between the first propagation area and the fractured area after reinitiation might have raised the stress-intensity factor to over $316 \text{ MPa } \sqrt{\text{m}}$. This increase in the stress intensity after crack reinitiation correlates well with the computational stress-intensity history results of Fig. 26.

Comparison of Dynamic K_I with Statically Calculated K_I

The traditional way of calculating the K_I at arrest is to apply the fixed-boundary displacements or loads statically, then calculate the value of K_I elastically. Performing this calculation for MMCT Test 9a yields a K_I at first arrest of $297 \text{ MPa } \sqrt{\text{m}}$. From the previous section, the dynamically calculated K_I at first arrest was $143 \text{ MPa } \sqrt{\text{m}}$. The corresponding value of K_{Ia} from the ASME Section XI fracture toughness curve is $123 \text{ MPa } \sqrt{\text{m}}$, and the K_{Ic} value from the Section XI curve is $308 \text{ MPa } \sqrt{\text{m}}$.

The disparity in the dynamically and statically calculated K_I means the time for the crack to run and arrest was so fast that the specimen did not have time to respond fully to the new free boundary. If an appropriate additional boundary condition is applied to the specimen to model this observation statically, then an appropriate static analysis can be performed. To model this predeformed state statically, the rotation may be constrained by fixing the back end of the specimen in the direction of crack extension. This additional condition does not affect the crack-opening displacement during the time of crack extension. This static calculation for the first arrest condition for MMCT Test 9a yields a K_I of $141 \text{ MPa } \sqrt{\text{m}}$, which is in excellent agreement with the dynamically calculated value and the topographic results.

The agreement between the dynamic computation for K_I and the predeformed static computation for K_I at crack arrest indicates that the actual value of K_I at arrest can be obtained by the predeformed static analysis. The phenomenon of the crack extending so fast that the specimen does not have time to respond significantly, clearly occurs in all structures and would be more prominent in larger structures, where the response times are

greater than in the MMCT specimen. Therefore, the method of computing K_I at arrest by a predeformed static analysis, then evaluating the effect of the subsequent deformation on the potential for reinitiation, is proposed as a general analysis procedure to be applied to all structures. Future reports by the present authors will illustrate applications of this procedure to larger specimens and realistically sized pressure vessels.

Conclusions

Our work has demonstrated that crack arrest conditions can be measured at nominally upper-shelf conditions with a new compact specimen and has provided a basic understanding of crack extension and arrest in structures. The program has also demonstrated a procedure for quantification of the parameters that govern reinitiation of an arrested crack. Detailed finite-element analyses have been shown to correlate well with dynamic test data, providing clear verification that the analysis enables the prediction of crack extension and arrest in the specimen and in structures in general. A simple elastic procedure is proposed to enable the calculation of K_I at arrest without recourse to dynamic analysis.

The application of this understanding to the reactor vessel pressurized thermal shock issue is presently under way. It is clear that previous evaluations based on static analyses over-predicted the toughness required to arrest a crack. Vessel integrity evaluations using the understanding developed in this effort, therefore, are expected to demonstrate significantly greater safety margins on crack arrest than were demonstrable with previously available methods.

Reference

- [1] Ayres, D. J., Fabi, R. J., Peck, D. A., and Schonenberg, R. Y., "Tests and Analyses of Crack Arrest in Reactor Vessel Materials in an Increasing Stress Intensity Field and Increasing Material Toughness," Research Project 2180-3, Electric Power Research Institute, Palo Alto, CA, April 1987.

Review of Pressurized-Water-Reactor-Related Thermal Shock Studies

REFERENCE: Cheverton, R. D., Iskander, S. K., and Ball, D. G., "Review of Pressurized-Water-Reactor-Related Thermal Shock Studies," *Fracture Mechanics: Nineteenth Symposium, ASTM STP 969*, T. A. Cruse, Ed., American Society for Testing and Materials, Philadelphia, 1988, pp. 752-766.

ABSTRACT: Flaw behavior trends associated with pressurized thermal shock (PTS) loading of pressurized water reactor (PWR) pressure vessels have been under investigation at Oak Ridge National Laboratory (ORNL) for approximately twelve years. During that time, eight thermal shock experiments with thick-walled steel cylinders were conducted as a part of the investigations. These experiments demonstrated, in good agreement with linear elastic fracture mechanics (LEFM), crack initiation and arrest, a series of initiation/arrest events with deep penetration of the wall, long crack jumps without significant dynamic effects at arrest, arrest in a rising stress-intensity-factor (K_I) field, extensive surface extension of an initially short and shallow flaw, and warm prestressing with $K_I \leq 0$. This information was used in the development of a fracture mechanics model that is being used extensively in the evaluation of the PTS issue.

KEY WORDS: reactor pressure vessels, thermal shock, thermal shock experiments, pressurized thermal shock, fracture mechanics, pressurized water reactors

The pressurized thermal shock (PTS) issue associated with pressurized water reactors (PWRs) has been under intensive investigation by the Nuclear Regulatory Commission (NRC), reactor vendors, and utilities since about 1974, and these efforts have recently resulted in the issuance, by the NRC, of a PTS rule [1]. As an aid in formulating the rule, the NRC sponsored the Integrated Pressurized Thermal Shock (IPTS) Program, which involved the development of appropriate probabilistic models and the subsequent calculation of the frequency of vessel failure for three specific plants [2-4]. The probabilistic fracture mechanics model was developed at the Oak Ridge National Laboratory (ORNL), and the validity of the deterministic aspects of this model was established to a large extent on the basis of a series of thermal shock experiments conducted with thick-walled steel cylinders [5-9]. (These experiments were conducted between 1975 and 1983 as a part of the NRC-sponsored Heavy-Section Steel Technology (HSST) Program [10].) This paper reviews the intent and results of the experiments with regard to development of the fracture mechanics model for the IPTS studies.

Analysis of PTS Transients

A postulated transient of particular interest in the early stages of the HSST thermal shock program was the large-break loss-of-coolant accident (LBLOCA). It is characterized by (1)

¹ Senior development specialist, Oak Ridge National Laboratory, Oak Ridge, TN 37831.

² Engineering specialist and computing specialist, respectively, Computing and Telecommunications Division, Martin Marietta Energy Systems, Inc., Oak Ridge National Laboratory, Oak Ridge, TN, 37831.

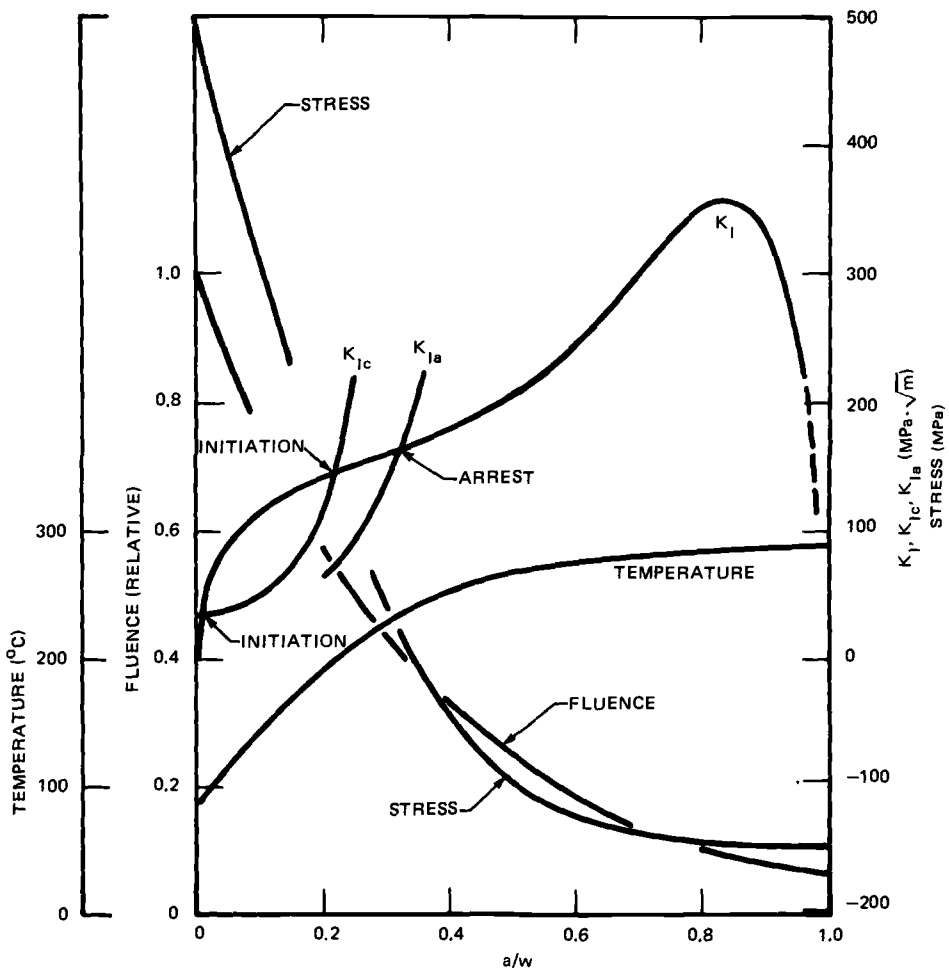


FIG. 1—Typical instantaneous temperature, stress, fluence, stress-intensity factor, and fracture-toughness distributions through the wall of a PWR vessel during LBLOCA (long axial flaw; “high” copper, nickel, and fluence; $t = 4$ min).

rapid depressurization of the primary system, (2) a severe thermal transient (the result of the depressurization and of the subsequent injection of emergency core coolant), and (3) essentially no repressurization. As a consequence of this transient, the belt-line region of the vessel is subjected to severe thermal shock, and the resultant positive gradient in temperature in the wall of the vessel contributes to positive gradients in the stress-intensity factor (K_I), the crack initiation toughness (K_{IC}), and the crack arrest toughness (K_{Ia}); this is illustrated in Fig. 1 for a case of severe radiation damage (end-of-life fluence and “high” concentrations of copper and nickel).

The set of critical crack depth curves [7] for the LBLOCA (Fig. 2)³ indicates that for a case of severe radiation damage (1) very shallow flaws can propagate; (2) propagation can consist of a series of initiation/arrest events; (3) rather long crack jumps can take place; (4)

³ In figures, a = crack depth; w = wall thickness.

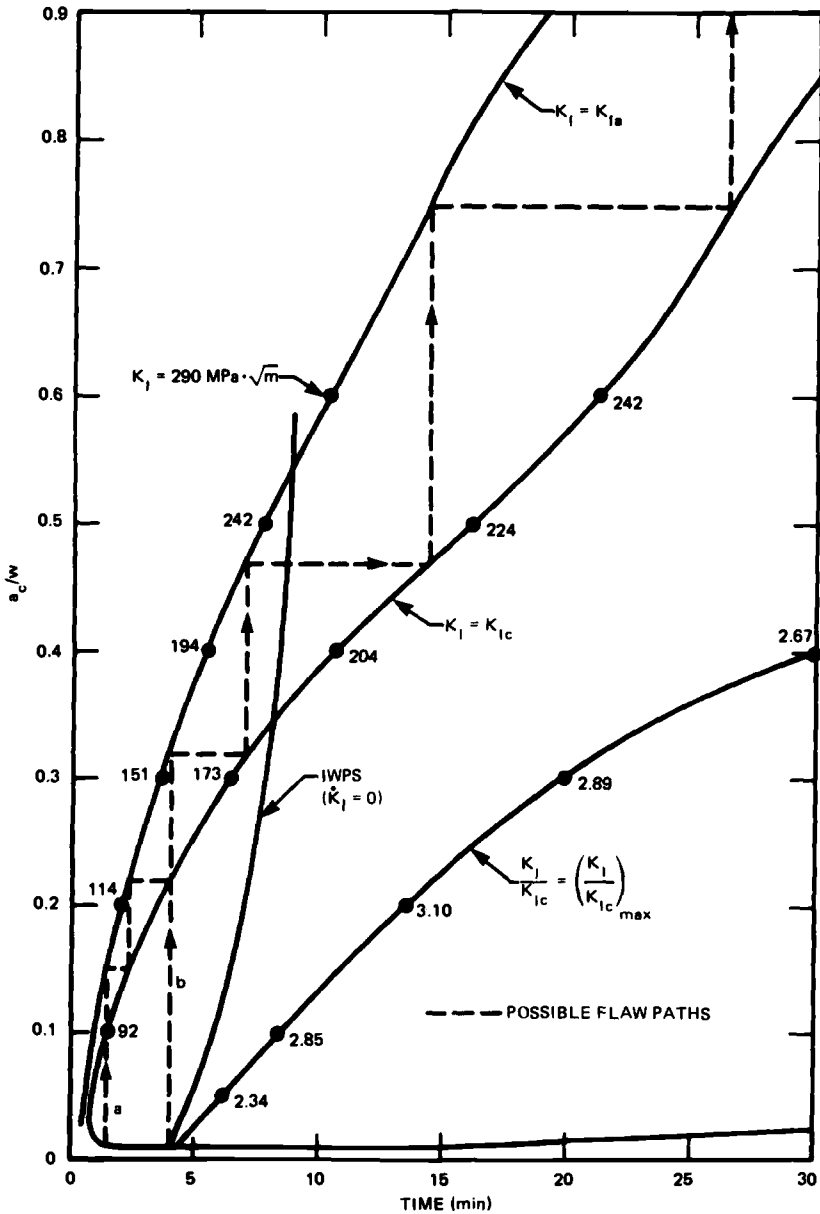
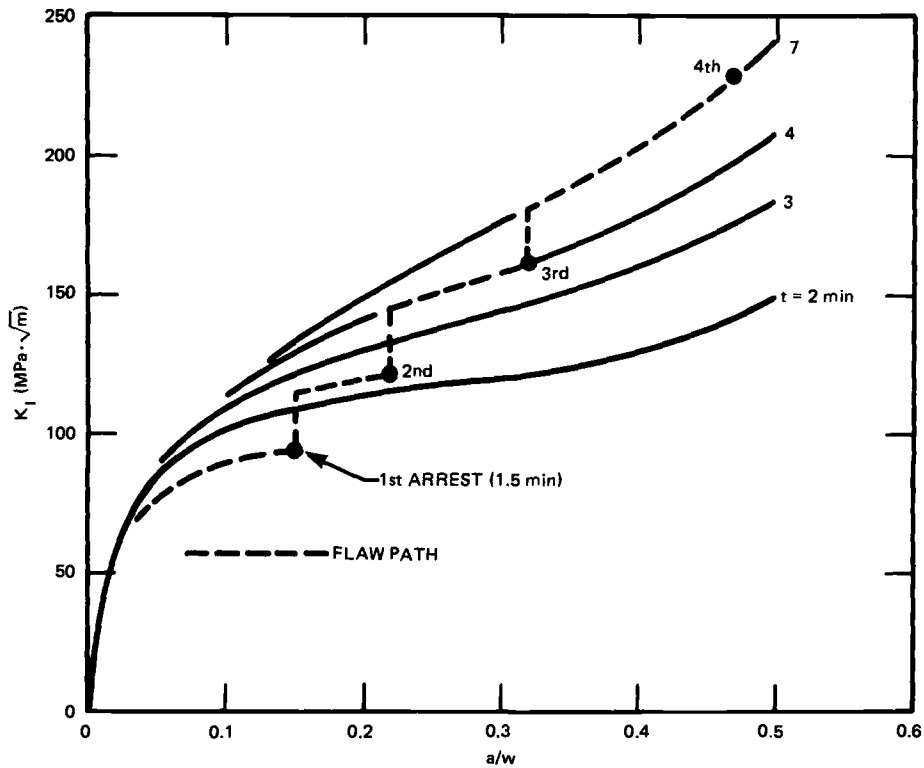


FIG. 2—Critical crack depth curves for LBLOCA.

the inability of a flaw to propagate when $\dot{K}_I \leq 0$, referred to as warm prestressing (WPS) with $\dot{K}_I \leq 0$ ⁴ [7,11], tends to limit propagation to ~60% of the wall thickness; (5) for WPS to be effective, K ratios (K_I/K_{Ic}) as large as 2.8 must be overcome; (6) even if WPS is

⁴ The condition $\dot{K}_I = 0$, $K_I = (K_I)_{\max}$ is the onset of WPS ($\dot{K}_I \leq 0$) and is referred to herein as incipient warm prestressing (IWPS) ($\dot{K}_I = 0$).

FIG. 3— K_I versus a/w for LBLOCA.

effective, a very high value of K_{Ia} is required for arrest prior to WPS; and (7) if WPS were not effective, the flaw would penetrate more than 90% of the wall but, as indicated in Fig. 1 by the abrupt drop in K_I , would not breach the wall. In addition, as shown in Fig. 3, if crack arrest takes place in the inner half of the wall during a LBLOCA, it must do so with K_I increasing with increasing crack depth.

Transients involving significant repressurization of the primary system result in higher values of and steeper gradients in K_I and introduce the possibility of crack propagation completely through the wall, as indicated in Fig. 4 for a reactor-trip transient [4].

When repressurization is initiated after the time corresponding to incipient warm prestressing (IWPS) ($\dot{K}_I = 0$), K_I may once again increase with time, but because of load-history and temperature-history conditioning of the crack tip, the fracture toughness may be elevated above K_{Ic} [11], another phenomenon referred to as warm prestressing. Loading conditions associated with both types of WPS are illustrated in Fig. 5 for a "late" repressurization PTS transient.

The above analyses were performed using linear elastic fracture mechanics (LEFM) and long (two-dimensional) axially oriented surface flaws. Similar calculations were also made for finite-length surface flaws, and the results indicated that, at least in the absence of cladding, these flaws would extend on the surface to effectively become long flaws if not limited by higher toughness regions of the vessel [12]. If the cladding were sufficiently tough, short surface flaws would not extend on the surface and thus, if short enough, presumably could not extend through the wall.

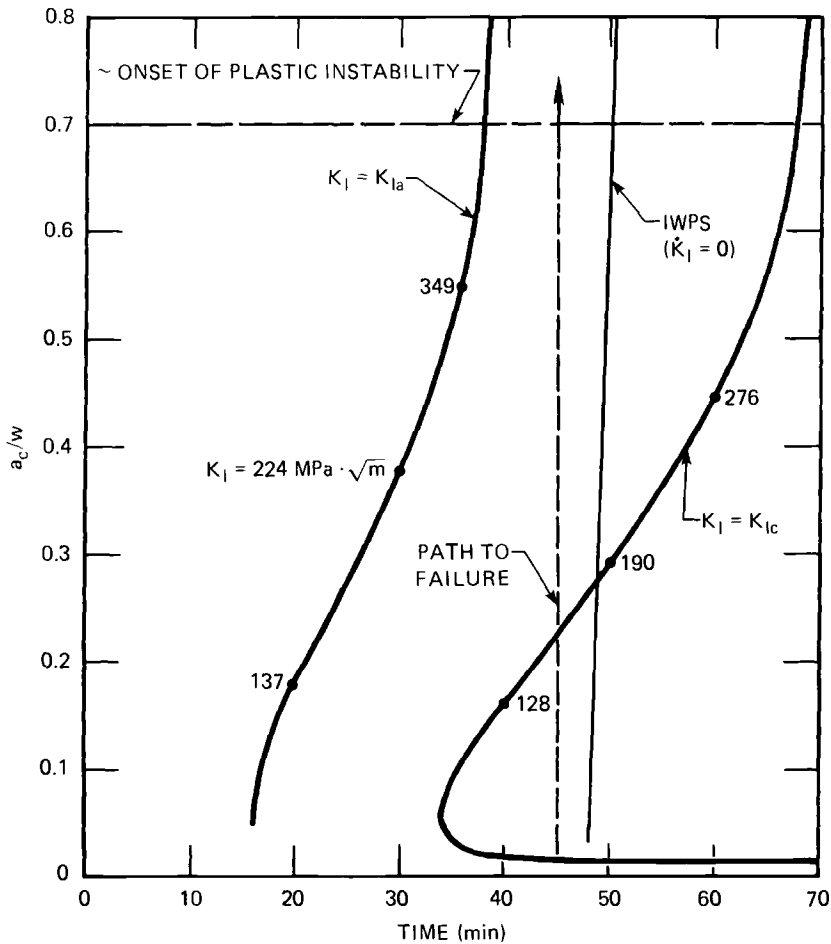


FIG. 4—Critical crack depth curves for a reactor-trip transient.

Experimental Program

The early ORNL analysis of postulated PTS transients indicated a significant potential for severe damage to the reactor pressure vessel in the event of a transient. In addition, as mentioned above, the analysis also revealed that a number of flaw behavior trends were involved that had not been adequately investigated. Thus, an experimental program was in order.

Many of the flaw behavior trends could be and were investigated in experiments involving thermal shock loading only, while a few required pressure loading in addition to thermal loading. The scope of the thermal-shock-only experiments included an investigation of all the trends associated with the LBLOCA. Thus far, eight thermal shock experiments have been conducted. As indicated by the summary of design information (Table 1), all experiments were conducted with large, thick-walled, steel cylinders, each with an intended single, axially oriented, shallow surface flaw. For Experiments TSE-2 and TSE-7 the initial intended flaw was semicircular with a radius of ~19 mm; for the other experiments the initial intended flaw extended the full length of the cylinder and was uniform in depth. All flaws were

generated by means of the electron-beam-weld process [13], which introduced the possibility of cross cracks having a surface length of ~ 6 mm (width of fusion and heat-affected zones) and a depth equal to that of the weld. Experiment TSE-5 had an unintended flaw of this type that propagated.

Test cylinders for the first four experiments had a 152-mm wall and a 533-mm outside diameter, and the material was left in the as-quenched condition. The initial temperature of the test cylinder was 288°C, and the thermal shock was applied by pumping a low-temperature mixture of alcohol and water through a narrow coolant gap adjacent to the inner surface. According to the design analysis, this combination of conditions would permit crack initiation (onset of propagation), but not extensive propagation.

To achieve multiple initiation/arrest events and deep penetration, it was necessary to use a test cylinder with a larger ratio of diameter-to-wall thickness. Thus, for the second set of four experiments the outside diameter of the test cylinder was 991 mm, and the wall thickness was either 152 mm (TSE-5, TSE-5A, and TSE-7) or 76 mm (TSE-6). A more severe thermal shock was specified for these experiments so that the test cylinder could also be used in a fully tempered condition. The shock was achieved by contacting the inner surface of the test cylinder, initially at $\sim 100^\circ\text{C}$, with liquid nitrogen. A special surface coating was used to promote nucleate boiling, which provides the necessary high heat-transfer coefficient [7].

For all of the experiments, extensive instrumentation was used to either directly or indirectly determine wall temperatures and crack depth at the time of each initiation/arrest event. This information was used for an accurate posttest calculation of critical values of K_I corresponding to these events.

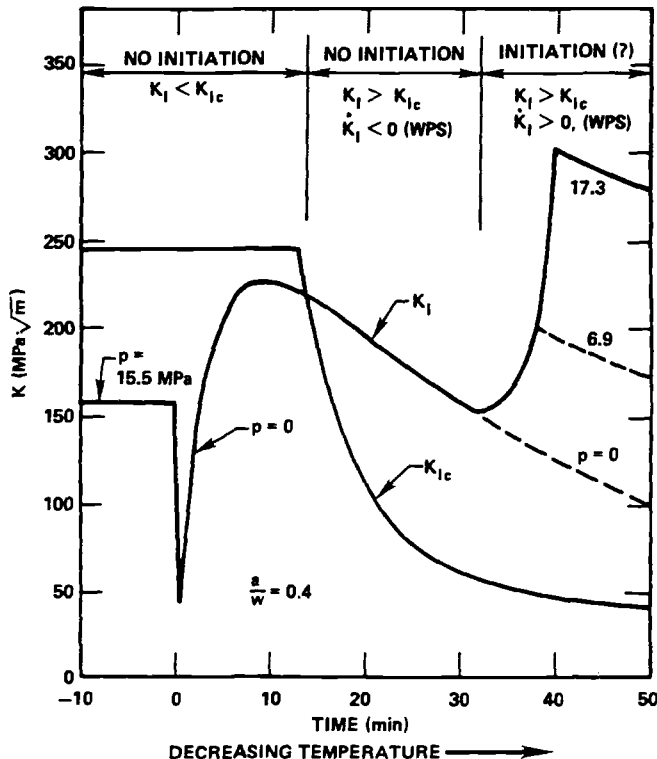


FIG. 5—Warm-prestressing phenomena associated with a PTS transient.

TABLE 1—Summary of test conditions for ORNL thermal shock experiments.

Parameter	Experiment						
	TSE-1	TSE-2	TSE-4	TSE-5	TSE-5A	TSE-6	TSE-7
Cylinder dimensions, mm							
Outside diameter	533	533	533	991	991	991	991
Wall thickness	152	152	152	152	152	76	152
Length	914	914	914	1220	1220	1220	1220
Cylinder material							
Designation				A508, Class 2 chemistry			
Tempering temperature, °C							
RT ₈₀₀ , °C	← 75	as quenched → 75	75	613	679	613	704
Flaw (initial)				66	10	66	-1
Orientation	axial	axial	axial	axial	axial	axial	axial
Length, mm	914	38	914	1220	1220	1220	37
Depth, mm	11	19	11	16	11	7.6	14
Thermal shock							
Initial temperature of cylinder, °C	288	288	288	96	96	96	96
Initial temperature of coolant, °C	4	-23	-25	-196	-196	-196	-196
Quench medium	W/A ^a	W/A ^a	W/A ^a	LN ₂ ^b	LN ₂ ^b	LN ₂ ^b	LN ₂ ^b

^a W/A = water/alcohol.^b LN₂ = liquid nitrogen.

Material Characterization Studies

An important part of the thermal shock program was the characterization of the material for each test cylinder. Tensile, Charpy, drop-weight, and fracture toughness (initiation and arrest) data were obtained as an aid in the design and posttest interpretation of the experiments. For instance, the validity of LEFM was judged on the basis of a comparison of calculated critical values of K_I , corresponding to initiation and arrest events, with valid fracture toughness data (K_{Ic} and K_{Ia}) measured in the laboratory with the relatively small "standard" specimens (henceforth referred to as laboratory specimens). For this specific purpose, K_{Ic} and K_{Ia} data from additional sources were used to supplement the rather limited amount of valid laboratory specimen data for the test cylinder material. Details of the materials studies are discussed in Refs 5 through 9.

Results of Experiments

The results of Experiments TSE-1 through TSE-7 are summarized as follows:

TSE-1—The maximum value of $K_I/K_{Ic} [(K_I/K_{Ic})_{\max}]$, which is the maximum with respect to time for the initial flaw size, was intended to be somewhat less than unity (0.7), and thus fast fracture was not expected. Unstable fracture did not occur, but the crack tip extended ~ 2 mm in a stable ductile mode as a result of the electron-beam-weld-induced residual stress and low fracture toughness at the crack tip.

TSE-2—The initial flaw was semicircular, and the value of $(K_I/K_{Ic})_{\max}$ was intended to be greater than unity and to occur close to the surface. Surface extension of the flaw was expected and perhaps radial extension, if the surface extension were sufficient. The flaw extended in surface length from 38 to 142 mm in two initiation/arrest events (one at either end). It appeared that additional surface and radial extension were prevented by warm prestressing.

TSE-3—The results for this test were not germane to this paper.

TSE-4—The value of $(K_I/K_{Ic})_{\max}$ for the "two-dimensional" flaw was intended to be greater than unity (~ 1.2). An initiation/arrest event took place with a crack jump of ~ 13 mm.

TSE-5—A series of three initiation/arrest events with deep penetration (80% of the wall) of the two-dimensional flaw occurred as expected. Two unintended events, a long crack jump and extensive propagation of an inadvertant small cross crack, indicated that dynamic effects at arrest were negligible and that an initially short crack, at least in the absence of cladding, could extend in surface length to effectively become a long flaw.

TSE-5A—A series of four initiation/arrest events with $\sim 50\%$ penetration of the wall occurred as expected. A fifth event was prevented by warm prestressing, and one of the four arrest events took place with K_I increasing with crack depth ($dK_I/da = 0.3 \text{ MPa } \sqrt{\text{m/mm}}$), as was expected. At the time of IWPS ($\dot{K}_I = 0$), the value of K_I was $152 \text{ MPa } \sqrt{\text{m}}$, and following IWPS, a maximum K ratio of 2.3 was achieved without crack initiation taking place.

TSE-6—The smaller wall thickness for this experiment (76 in comparison with 152 mm) introduced a potential for a single long crack jump to a depth greater than 90% of the wall thickness. There were actually two initiation/arrest events, the first being relatively short,

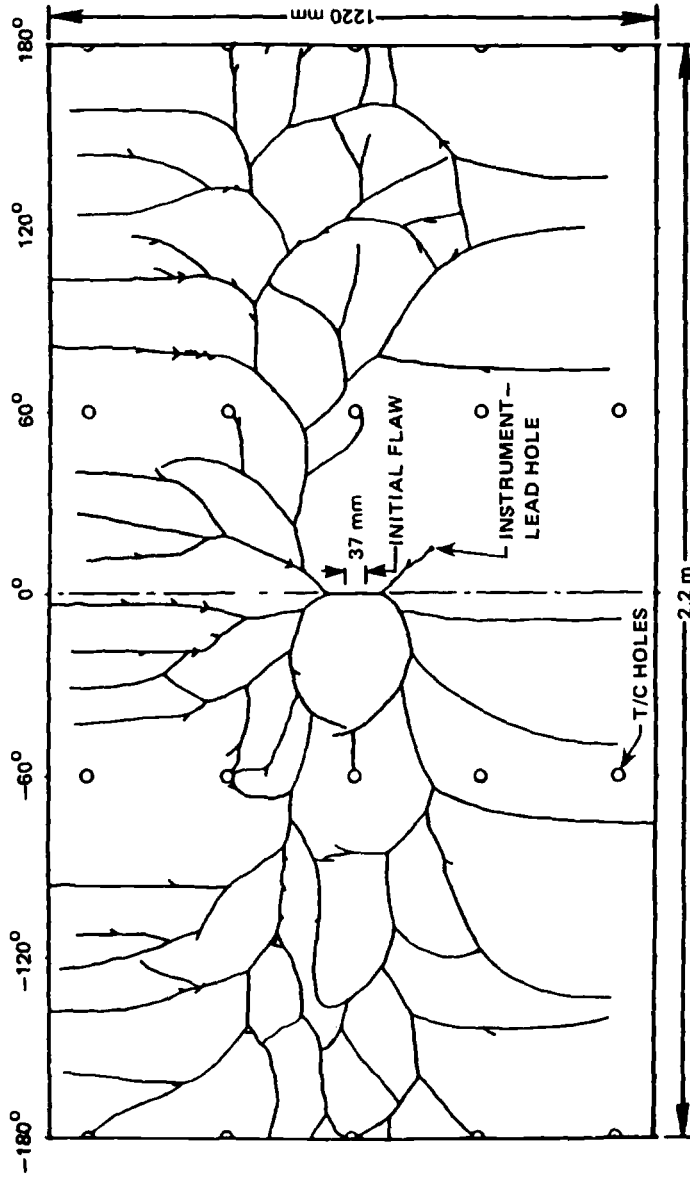


FIG. 6—Developed view of the inner surface of the Experiment TSE-7 test cylinder showing the final crack pattern.

with a total penetration of 93%. This helped to demonstrate the inability of a long flaw to penetrate the vessel wall fully under thermal-shock loading conditions only. Furthermore, once again there appeared to be negligible dynamic effects associated with arrest following a long crack jump, and the first arrest event took place with K_I increasing with crack depth ($dK_I/da = 0.8 \text{ MPa } \sqrt{\text{m/mm}}$).

TSE-7—This experiment was intended to demonstrate once again the ability of a short and shallow flaw, in the absence of cladding, to extend on the surface to effectively become a long flaw. The initial flaw was oriented axially and was essentially semielliptical in shape with a surface length of 37 mm and a depth of 14 mm. In a single event the flaw extended on the surface, bifurcating many times, to produce almost the entire cracking pattern shown in Fig. 6. Following this event, there were two more that extended the complex flaw radially to depths of $\sim 55 \text{ mm}$ in the central portion of the cylinder and to lesser depths toward the ends of the cylinder. (The second event also extended the surface length somewhat.) A fourth event was prevented by warm prestressing.

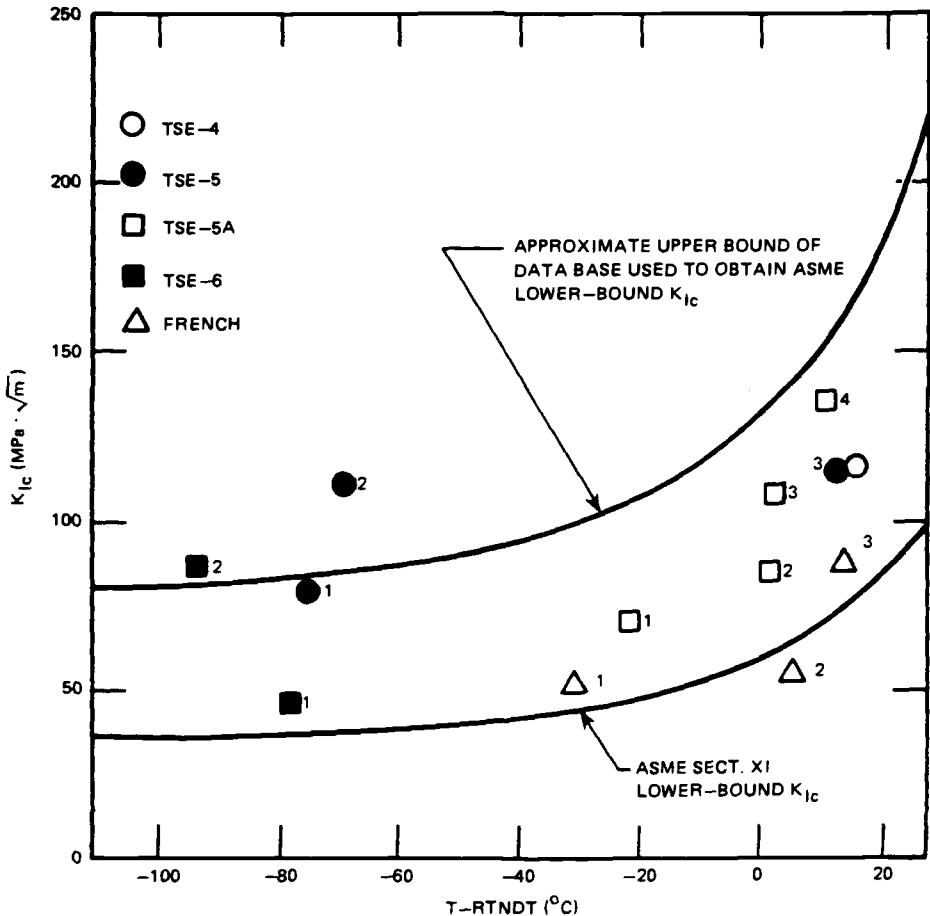


FIG. 7—Comparison of laboratory-specimen and large-specimen (test-cylinder) K_{Ic} data.

Discussion of Results

The results of the thermal shock experiments tend to establish the validity of LEFM for severe thermal shock loading conditions because in each experiment the expected general behavior of the flaw took place. However, as mentioned earlier, a more quantitative evaluation of the validity was to be performed by comparing the fracture toughness data (K_{Ic} and K_{Ia}) deduced from the experiments with valid laboratory specimen data. Critical values of K_I deduced from the thermal shock experiments and corresponding to the crack initiation and arrest events are compared with laboratory specimen data and data from a French thermal shock experiment [14] in Figs. 7 and 8. (Data from Experiments TSE-2 and TSE-7 were excluded because of the relatively large uncertainty introduced by the complex three-dimensional configuration.) It is apparent that all of the test-cylinder K_{Ic} data points, with the exception of one of the French points, are above the American Society of Mechanical Engineers (ASME) lower-bound curve and, with the exception of two points, are below an approximate upper bound of the K_{Ic} data that were used to generate the ASME lower-bound curve [15]. (The test-cylinder laboratory-specimen K_{Ic} data correspond to T minus a

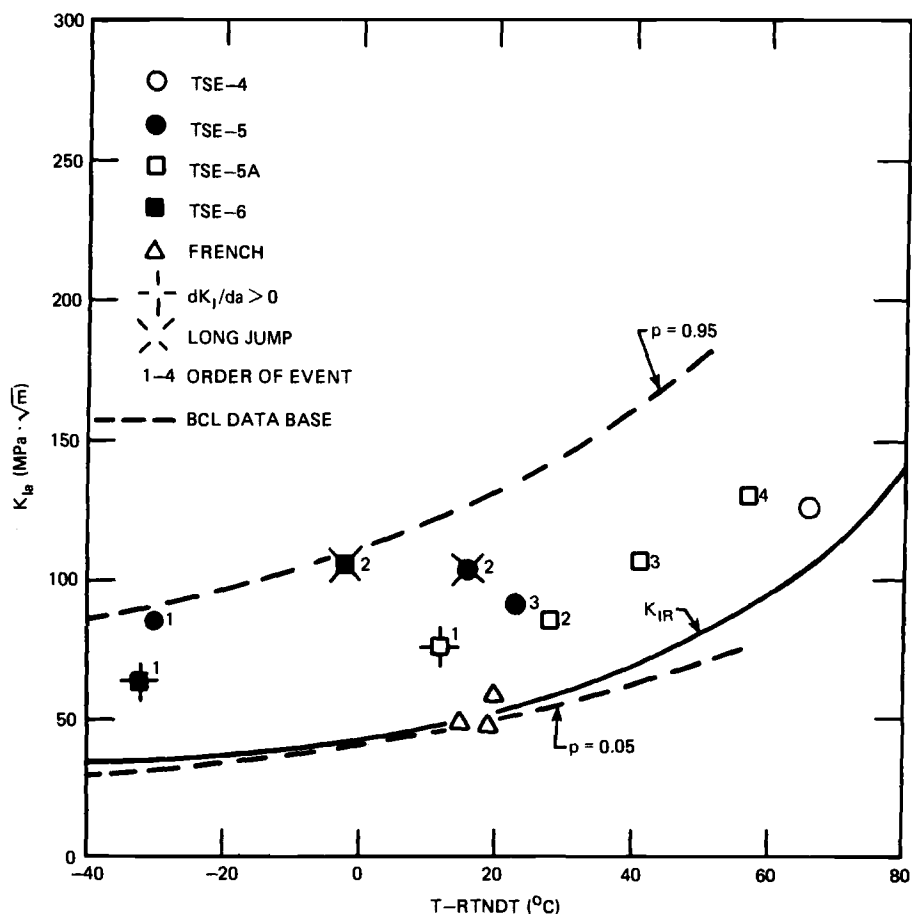


FIG. 8—Comparison of laboratory-specimen and large-specimen (test-cylinder) K_{Ia} data.

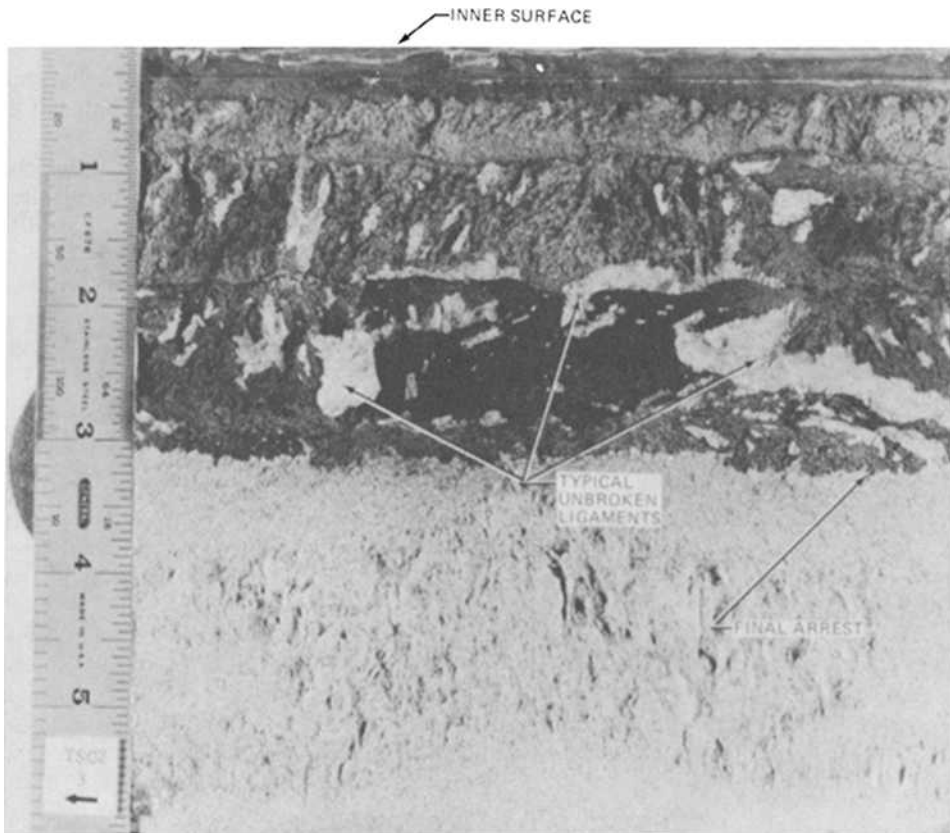


FIG. 9—Experiment TSE-5A fracture surface showing rough texture and unbroken ligaments.

reference nil-ductility transition temperature (RT_{NDT}) $\leq -65^{\circ}\text{C}$ and have essentially the same upper and lower bounds as the ASME data.)

Figure 8 includes, in addition to the ORNL and French data and the ASME K_{IR} curve, the 5th and 95th percentile curves corresponding to a Battelle-Columbus Laboratories laboratory-specimen K_{Ia} data base [16,17] which consists of 233 data points for A533 and A508 material, including 25 points obtained from the thermal shock test-cylinder characterization studies. As indicated by Fig. 8, the scatter in the laboratory specimen data is approximately $\pm 45\%$, and only a small fraction of the data points fall below the K_{IR} curve. All of the K_{Ia} values deduced from the ORNL thermal shock experiments fall within the laboratory-specimen scatter band and well above the K_{IR} curve, while the three French data points cluster about the K_{IR} curve.

A comparison of the ORNL and French data is of interest because the experiments were very similar. The test cylinders were similar in size and material and were both thermally loaded by quenching in liquid nitrogen. However, the French fracture surfaces were very flat and free of unbroken ligaments [14], while the ORNL surfaces were relatively rough and, in some cases, as shown in Fig. 9, had many unbroken ligaments. Since the restraining force of the ligaments was not accounted for in the calculation of critical values of K_I , the

existence of ligaments on the ORNL surfaces could be a reason for the generally higher indicated values of fracture toughness relative to the French values.

The two data points in Fig. 8 that correspond to arrest in a rising K_I field fall well within the scatter band of the laboratory specimen data. This indicates that the critical value of K_I for arrest in a rising K_I field is about the same as that for a falling K_I field ($dK_I/da < 0$), which is the usual condition when obtaining laboratory specimen K_{Ia} data. It should be noted, however, that the values of dK_I/da (0.3 and 0.8 MPa \sqrt{m}/mm) were somewhat less than the maximum calculated for the LBLOCA (1.8 MPa \sqrt{m}/mm for $K_I < 220$ MPa \sqrt{m}).

The large scatter in the laboratory-specimen and test-cylinder K_{Ic} and K_{Ia} data tends to preclude drawing conclusions regarding the validity of LEFM for thermal shock loading conditions. However, if one accepts the apparent fact that both very large and laboratory-sized specimens can exhibit large scatter in valid fracture toughness data, then the coincidence of the scatter bands and a lack of significant anomalies during the thermal shock experiments indicate that LEFM is valid, at least for $(T - RT_{NDT}) < 20^\circ\text{C}$ for crack initiation events and $(T - RT_{NDT}) < 60^\circ\text{C}$ for crack arrest events.

The data in Fig. 8 indicate that dynamic effects at arrest were negligible. If dynamic effects were substantial, the static analysis would tend to yield low values of K_{Ia} . As indicated by Fig. 8, the statically calculated values for the two long crack jumps (second arrest events for TSE-5 and TSE-6) are high rather than low (just below the upper bound of the laboratory specimen data).

Warm prestressing with $\dot{K}_I < 0$ may have prevented reinitiation in each of the ORNL thermal shock experiments. However, only in the case of TSE-5A was the calculated best estimate of $(K_I/K_{Ic})_{\max}$ (maximum with respect to time) for the final crack depth large enough to account for the uncertainties in the experiment and analysis. The calculated best estimate of $(K_I/K_{Ic})_{\max}$ was 2.3. With reference to Fig. 7, it can be seen that a factor of 2.3 more than accommodates the upper bound of the K_{Ic} data. Thus, warm prestressing with $\dot{K}_I < 0$ was demonstrated in a convincing manner. It is of interest to note, however, that the TSE-5A K_I value corresponding to $\dot{K}_I = 0$ (152 MPa \sqrt{m}) was somewhat less than calculated for the LBLOCA (Fig. 2) and for another severe PTS transient (Fig. 4).

Results of the thermal shock experiments conducted thus far have provided sufficient confidence in the validity of LEFM for PTS loading conditions and over a wide enough range of K_I and dK_I/da values to permit development of an LEFM model [2-4,18,19] for use as an aid in evaluating PWR vessel integrity during PTS transients [2-4]. The question of validity of WPS and arrest in a rising K_I field at K_I values larger than those achieved in the experiments was avoided by specifying a maximum value of K_{Ia} equal to 220 MPa \sqrt{m} , in which case the attainment of higher calculated values of K_I resulted in a prediction of vessel failure. Furthermore, the possibility that the cladding would restrict surface extension of initially short flaws was ignored.

Although the above fracture mechanics model was considered reasonable for the IPTS studies, additional experiments [20-24] are planned and are under way with the objective of perhaps being able to take more credit for WPS, cladding effects, and crack arrest.

Acknowledgments

The research for this paper was sponsored by the Office of Nuclear Regulatory Research, U.S. Nuclear Regulatory Commission, under Interagency Agreements 40-551-75 and 40-552-75 with the U.S. Department of Energy under Contract DE-AC05-84OR21400 with Martin Marietta Energy Systems, Inc.

References

- [1] "Fracture Toughness Requirements for Protection Against Pressurized Thermal Shock Events," *Federal Register*, Vol. 50, No. 141, July 23, 1985, Section 50.61, pp. 29937-29945.
- [2] Burns, T. J., et al., "Preliminary Development of an Integrated Approach to the Evaluation of Pressurized Thermal Shock as Applied to the Oconee Unit 1 Nuclear Power Plant," NUREG/CR-3770 (ORNL/TM-9176), Oak Ridge National Laboratory, Oak Ridge, TN, 13 April 1984.
- [3] Selby, D. L., et al., "Pressurized Thermal Shock Evaluation of the Calvert Cliffs Unit 1 Nuclear Power Plant," NUREG/CR-4022 (ORNL/TM-9408), Oak Ridge National Laboratory, Oak Ridge, TN, September 1985.
- [4] Selby, D. L., et al., "Pressurized Thermal Shock Evaluation of the H. B. Robinson Unit 2 Nuclear Power Plant," NUREG/CR-4183 (ORNL/TM-9567), Vols. 1 and 2, Oak Ridge National Laboratory, Oak Ridge, TN, September 1985.
- [5] Cheverton, R. D., "Pressure Vessel Fracture Studies Pertaining to a PWR LOCA-ECC Thermal Shock: Experiments TSE-1 and TSE-2," ORNL/NUREG/TM-31, Oak Ridge National Laboratory, Oak Ridge, TN, September 1976.
- [6] Cheverton, R. D. and Bolt, S. E., "Pressure Vessel Fracture Studies Pertaining to a PWR LOCA-ECC Thermal Shock: Experiments TSE-3 and TSE-4 and Update of TSE-1 and TSE-2 Analysis," ORNL/NUREG-22, Oak Ridge National Laboratory, Oak Ridge, TN, December 1977.
- [7] Cheverton, R. D., et al., "Pressure Vessel Fracture Studies Pertaining to the PWR Thermal-Shock Issue: Experiments TSE-5, TSE-5A, and TSE-6," NUREG/CR-4249 (ORNL-6163), Oak Ridge National Laboratory, Oak Ridge, TN, June 1985.
- [8] Cheverton, R. D., et al., "Pressure Vessel Fracture Studies Pertaining to the PWR Thermal-Shock Issue: Experiment TSE-7," NUREG/CR-4304 (ORNL-6177), Oak Ridge National Laboratory, Oak Ridge, TN, August 1985.
- [9] Cheverton, R. D., et al., "Fracture Mechanics Data Deduced from Thermal-Shock and Related Experiments with LWR Pressure Vessel Material," *Journal of Pressure Vessel Technology*, 102/ Vol. 105, May 1983.
- [10] Whitman, G. D., "Historical Summary of the Heavy-Section Steel Technology Program and Some Related Activities in Light-Water Reactor Pressure Vessel Safety Research," NUREG/CR-4489 (ORNL-6259), Oak Ridge National Laboratory, Oak Ridge, TN, March 1986.
- [11] Loss, F. J., Gray, A. A., and Hawthorne, J. R., "Significance of Warm Prestress to Crack Initiation During Thermal Shock," NRL/NUREG-8165, Naval Research Laboratory, Washington, DC, September 1977.
- [12] Cheverton, R. D. and Ball, D. G., "A Reassessment of PWR Pressure Vessel Integrity During Overcooling Accidents, Considering 3-D Flaws," *Journal of Pressure Vessel Technology*, Vol. 106/ 375, November 1984.
- [13] Holz, P. P., "Preparation of Long Axial Flaw for TSE-5A," *Heavy-Section Steel Technology Program Quarterly Progress Report July-September 1980*, NUREG/CR-1806 (ORNL/NUREG/TM-419), Oak Ridge National Laboratory, Oak Ridge, TN, December 1980, pp. 35-37.
- [14] Pellissier-Tanon, A., Sollogoub, P., and Houssin, B., "Crack Initiation and Arrest in an SA 508 Class-3 Cylinder Under Liquid Nitrogen Thermal-Shock Experiment," *Transactions, of the 7th International Conference on Structural Mechanics in Reactor Technology*, Vols. G and H, North Holland Publishing Co., Amsterdam, The Netherlands, August 1983.
- [15] *ASME Code*, Section XI, Division 1, Subsection NB-2331, American Society of Mechanical Engineers, New York, NY.
- [16] Rosenfield, A. R., "Validation of Compact-Specimen Crack-Arrest Data," *Technical Briefs, Journal of Engineering Materials and Technology*, Vol. 106, No. 2, 1984, pp. 207-208.
- [17] Rosenfield, A. R., et al., in *Heavy-Section Steel Technology Program Semiannual Progress Report October 1984-March 1985*, NUREG/CR-4219, Vol. 1 (ORNL/TM-9593/V1) Oak Ridge National Laboratory, Oak Ridge, TN, June 1985.
- [18] Cheverton, R. D. and Ball, D. G., "OCA-P, A Deterministic and Probabilistic Fracture-Mechanics Code for Application to Pressure Vessels," NUREG/CR-3618 (ORNL-5991), Oak Ridge National Laboratory, Oak Ridge, TN, May 1984.
- [19] Ball, D. G. and Cheverton, R. D., "Adaptation of OCA-P, a Probabilistic Fracture-Mechanics Code, to a Personal Computer," NUREG/CR-4468 (ORNL/CSD/TM-2333), Oak Ridge National Laboratory, Oak Ridge, TN, January 1986.
- [20] Cheverton, R. D., et al., "Thermal-Shock Technology," in *Heavy-Section Steel Technology Program Semiannual Progress Report for April-September 1985*, NUREG/CR-4219, Vol. 2 (ORNL/TM-9593/V2), Oak Ridge National Laboratory, Oak Ridge, TN, January 1986, pp. 182-192.

- [21] Bryan, R. H., et al., "Pressurized-Thermal-Shock Test of 6-in.-Thick Pressure Vessels. PTSE-1: Investigation of Warm Prestressing and Upper-Shelf Arrest," NUREG/CR-4106 (ORNL-6235), Oak Ridge National Laboratory, Oak Ridge, TN, April 1985.
- [22] Corwin, W. R., et al., "Effects of Stainless Steel Weld Overlay Cladding on the Structural Integrity of Flawed Steel Plates in Bending, Series 1," NUREG/CR-4015 (ORNL/TM-9390), Oak Ridge National Laboratory, Oak Ridge, TN, April 1985.
- [23] Corwin, W. R., et al., "Charpy Toughness and Tensile Properties of Neutron Irradiated Stainless Steel Submerged-Arc Weld Cladding Overlay," NUREG/CR-3927 (ORNL/TM-9309), Oak Ridge National Laboratory, Oak Ridge, TN, September 1984.
- [24] Bass, B. R., Pugh, C. E., and Stamm, H. K., "Dynamic Analysis of a Crack Run-Arrest Experiment in a Nonisothermal Plate," *Proceedings of the 1985 Pressure Vessel and Piping Conference*, ASME PVP-Vol. 98-2, American Society of Mechanical Engineers, pp. 175-184.

Robert H. Bryan,¹ John G. Merkle,¹ Randy K. Nanstad,² and Grover C. Robinson¹

Pressurized Thermal Shock Experiments with Thick Vessels

REFERENCE: Bryan, R. H., Merkle, J. G., Nanstad, R. K., and Robinson, G. C., "Pressurized Thermal Shock Experiments with Thick Vessels," *Fracture Mechanics: Nineteenth Symposium ASTM STP 969*, T. A. Cruse, Ed., American Society for Testing and Materials, Philadelphia, 1988, pp. 767–783.

ABSTRACT: A 148-mm-thick pressure vessel containing a long axial flaw was subjected to a combined loading of internal pressure and thermal shock. The experiment was performed to investigate the effects of loading sequence on initiation of brittle fracture and the behavior of a crack propagating into ductile regions. Two crack initiation and arrest episodes were generated, in addition to several phases of warm prestressing. Warm prestressing was shown to be effective in inhibiting initiation of cleavage fracture. A crack arrest was observed 88 K above the reference nil-ductility transition temperature (RT_{NDT}) with a stress-intensity factor of 299 MPa \sqrt{m} .

KEY WORDS: fracture mechanics, pressure vessels, nuclear vessels, pressurized thermal shock tests, combined loads, warm prestressing, brittle fracture, ductile fracture, brittle-ductile transition, crack initiation, crack arrest, steel

Background

The series of pressurized thermal shock experiments at the Oak Ridge National Laboratory (ORNL) was motivated by a concern for the behavior of flaws in nuclear reactor pressure vessels having welds or shells that were highly sensitive to embrittlement by fast neutron irradiation. The pressurized thermal shock experiment that has been completed (PTSE-1) and the one in preparation (PTSE-2) were planned to investigate fracture behavior involving complexities of combined pressure and thermal loading under states of stress that are difficult or impossible to attain in experiments on a smaller scale or with simpler modes of loading.

Previously, at ORNL twelve fracture tests of flawed 152-mm-thick steel pressure vessels were conducted under pressure loading [1–8]. The three tests performed at temperatures below the onset of the Charpy upper shelf with surface flaws in the barrel of the vessel demonstrated that the stress-intensity factor, K_I , of linear elastic fracture mechanics (LEFM) could be usefully applied to the analysis of initiation of brittle fracture in thick vessels [1,2,7]. Also, in one test of this series the occurrence of crack arrest in a negative K_I gradient at about -20°C was observed to be consistent with LEFM [7].

Eight thermal shock experiments were conducted with flawed 76 or 152-mm-thick steel cylinders [9–12]. These experiments were generally concerned with the application of LEFM to both brittle fracture initiation and arrest in thick structures. In thermal shock experiments

¹ Research specialists, Oak Ridge National Laboratory, Oak Ridge, TN 37831.

² Group leader, Metals and Ceramics Division, Oak Ridge National Laboratory, Oak Ridge, TN 37831.

crack arrest was observed in positive as well as negative K_I gradients, and the inhibiting effects of simple warm prestressing ($\dot{K}_I < 0$) in the loading history of a stationary crack were demonstrated.

In both the pressurized and the thermal shock tests, one of the principal challenges was to determine from simple test specimens the critical values of plane-strain initiation and arrest toughness, K_{Ic} and K_{Ia} , respectively, for the materials in the large test structures. In most of the structures tested, the flaws were very nearly under conditions of plane strain. In many instances, test specimens large enough for a valid determination of plane-strain fracture toughness at the relevant temperatures could not be made from representative material. Consequently, tests of small compact specimens have been used extensively for planning fracture tests of thick structures. In toughness tests of specimens too small to render valid K_{Ic} values, the specimens were observed to fracture in cleavage at widely scattered magnitudes of apparent toughness. In one flawed vessel test, which was conducted at a low transition-range temperature, the lower bound to the small-specimen toughness data for the characterization material was presumed to represent K_{Ic} for the purposes of planning the test and predicting results [7]. In this case, fracture toughness was expressed in terms of K_J defined by

$$K_J^2 = EJ_{\text{fracture}}$$

where E is Young's modulus and J is the J -integral. The predictions agreed well with the experimental results of the vessel test. Subsequent thermal shock experiments were also designed on the presumption that a lower bound to K_J data for the thermal shock characterization material would be a reasonable approximation of K_{Ic} for experimental design purposes, a presumption that appears to have been consistent with most of the experiments [11,12]. Studies of transitional fracture toughness by Landes and Shaffer [13], McCabe and Landes [14], and Iwadata [15] have also shown that J_{fracture} and K_J , which, as used here, always correspond to the onset of cleavage fracture, are usually widely scattered. These three studies [13–15], which correlated K_J and valid K_{Ic} measurements for several steels, supported the lower bound presumption and also became a basis for considering an adjustment to K_J and K_{Ic} to account for a size effect [16]. The adjustments applied in the ORNL investigations are based on an empirical equation proposed by Irwin [17]. This size-effect adjustment was an important factor in evaluating toughness measurements for pressurized thermal shock experiments.

Objectives

Fracture phenomena that were believed to be sufficiently uncertain at the inception of the program of pressurized thermal shock experiments to warrant consideration in these experiments were (1) warm prestressing, (2) crack propagation from brittle to ductile regions, (3) transitory crack stability in ductile regions, and (4) changes in the shape of propagating cracks in bimetallic zones of clad vessels. In experimental investigations it is essential that the structures tested be large enough to generate stress states representative of full-scale reactor pressure vessels. This requirement is satisfied by vessels of the type used in the intermediate vessel tests [1–8] of the Heavy-Section Steel Technology Program at ORNL. The thermal shock component of the experiment is essential to provide a fracture-toughness gradient in the vicinity of the crack that is representative of toughness gradients in reactor pressure vessels during overcooling accidents. Transient pressure loading, combined with a thermal shock, is necessary to generate the phases of fracture required to study the four phenomenological areas.

Experiment PTSE-1 was designed to investigate effects of warm prestressing on the initiation of crack propagation by cleavage and to promote rapid crack propagation into a region of the vessel that was at a temperature well above the onset of the Charpy upper shelf. Experiment PTSE-2 is being designed to investigate further warm prestressing and crack propagation from brittle to ductile regions. In the latter experiment the material in which the flaw will be embedded should have a low Charpy-impact-energy upper shelf.

Experimental Procedure

Pressurized thermal shock experiments are performed in a testing facility designed to expose a flawed vessel to coordinated loads from internal pressurization and thermal shock. The arrangement of a test vessel is shown in Fig. 1 with the vessel enclosed within a shroud, which is electrically heated to establish the desired initial temperature. A thermal shock is induced by injecting and circulating chilled coolant (water or a mixture of water and methanol) in the shroud. Coolant temperatures from -25°C to room temperature are feasible, and convective heat transfer coefficients as high as $9000 \text{ W/m}^2 \cdot \text{K}$ at the cylindrical surface of the test vessel have been attained. Pressurization is accomplished independently of the thermal shock. Pressures as high as $\sim 100 \text{ MPa}$ are attainable at useful pressurization rates.

During a transient test, the internal pressure, the temperatures at several depths in the wall of the vessel, and the crack mouth opening displacements (CMOD) of the flaw are measured. These observable factors permit the calculation of the stress, K_I , and J_I fields as

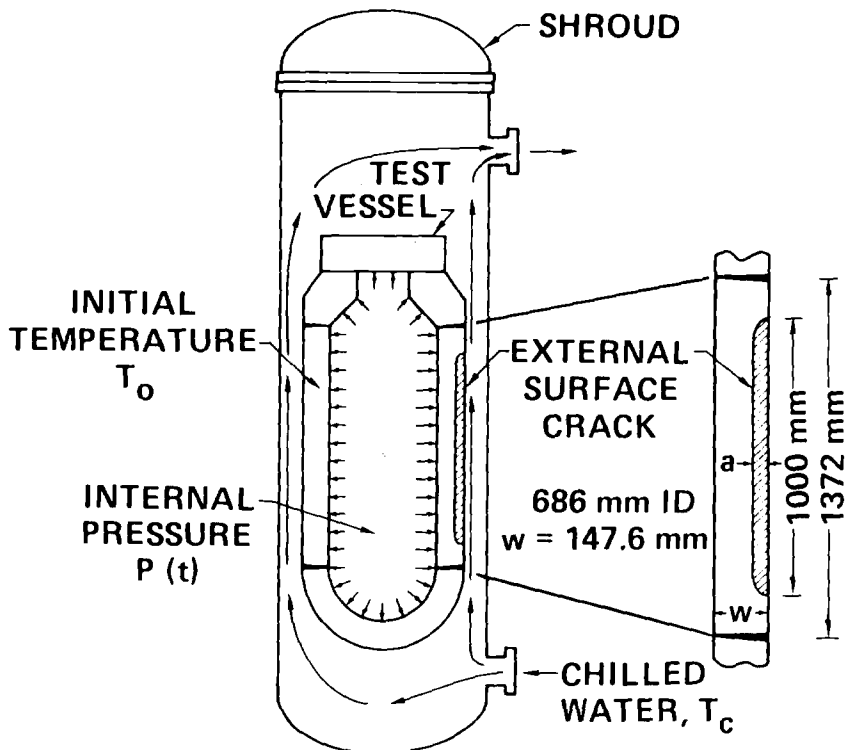


FIG. 1—Schematic drawing of a flawed test vessel in a test shroud.

a function of time for cracks of any particular size. A description of crack behavior can also be reconstructed from CMOD data and geometric information from posttest examination of the flaw. Details of the experimental procedure and apparatus are described in a topical report on Experiment PTSE-1 [18].

Experiment PTSE-1

The first experiment was performed with a vessel containing a plug of specially tempered steel, which with normal heat treatment would have met the specifications for SA-508 Class 2 steel. A 1-m-long by 12.2-mm-deep crack was implanted in the plug so that the plane of the flaw lay in a radial-axial plane of the barrel of the vessel. The material for the plug was selected to have fracture and tensile properties suitable for the objectives, namely, to investigate warm prestressing and rapid crack propagation above the onset of the Charpy upper shelf. The transients were designed on the basis of the measured material properties required to attain these objectives.

Material Characterization

The plug of material surrounding the flaw in the test vessel and the material used for characterizing the properties of the plug were cut from the same cylindrical forging, and both received the same heat treatment during vessel fabrication. Characterization of the flawed material included tension, Charpy V-notch impact, drop-weight, plane-strain fracture toughness, and J -integral tests, which were performed by the Babcock and Wilcox Co. [19]. Battelle Columbus Laboratories performed crack-arrest fracture toughness tests [20]. Temperature-dependent values of Young's modulus and the coefficient of thermal expansion were deduced from a variety of experiments discussed in Ref 18. The properties are summarized in the Appendix.

Initiation toughness data and $K_{Ic}(T)$ curves derived from the data are shown in Fig. 2. At each specimen test temperature the raw K_I values were adjusted for the effect of size (β_c adjustment [16]). The pretest curve (A) represents the exponential expression

$$K_{Ic} = a + b \exp (cT) \quad (1)$$

in which T is temperature and a , b , and c are parameters determined empirically [18]. In this case the A curve is a lower bound to β_c -adjusted K_I data from tests at temperatures for which no stable tearing preceded cleavage, that is $T \leq 75^\circ\text{C}$. The extrapolation of K_{Ic} to higher temperatures, although speculative, was necessary as a basis for designing the experiment.

The raw crack-arrest toughness values [20] were also subjected to a β_c adjustment [16,18]. The parameters of the K_{Ia} curve shown in Fig. 3 were determined by a least-squares fit of the exponential form of Eq 1 to the adjusted data with the highest and the lowest points excluded.

Fracture Analyses

Fracture analyses were performed by a combination of finite-element programs and a parametric program that efficiently accounted for ductile tearing as well as brittle fracture [18,21–23]. Initiation of brittle fracture was determined by the condition

$$K_I \geq K_{Ic} \quad (2)$$

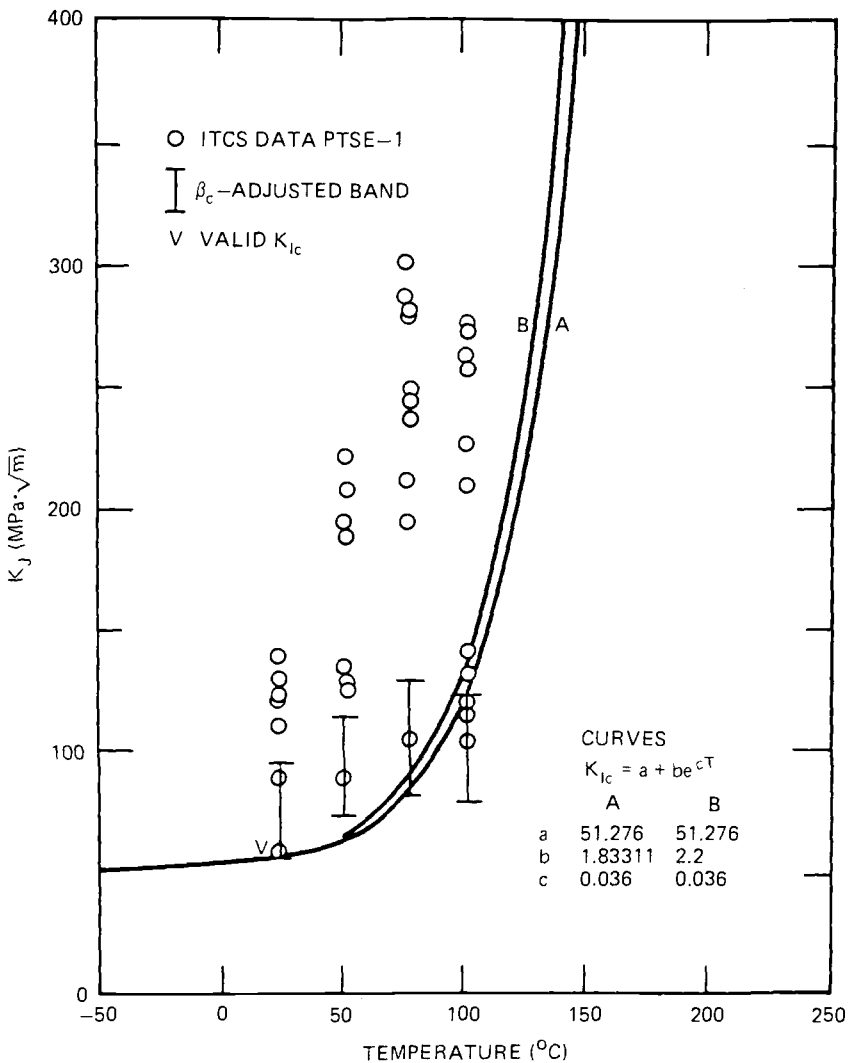


FIG. 2— K_{Ic} and K_I data for the PTSE-1 vessel. The curves represent functions used in fracture analyses.

on a suitable segment of the crack tip. A crack propagating in a brittle mode would continue to propagate in that mode as long as

$$K_I > K_{Ia} \quad (3)$$

A stationary crack was assumed to remain stationary with respect to ductile tearing when

$$J_I(a) \leq J_R(a - a') \quad (4)$$

in which a is any crack depth greater than the current depth, a' is a prior crack depth for which the crack may be considered stationary relative to other modes of fracture, and J_R is

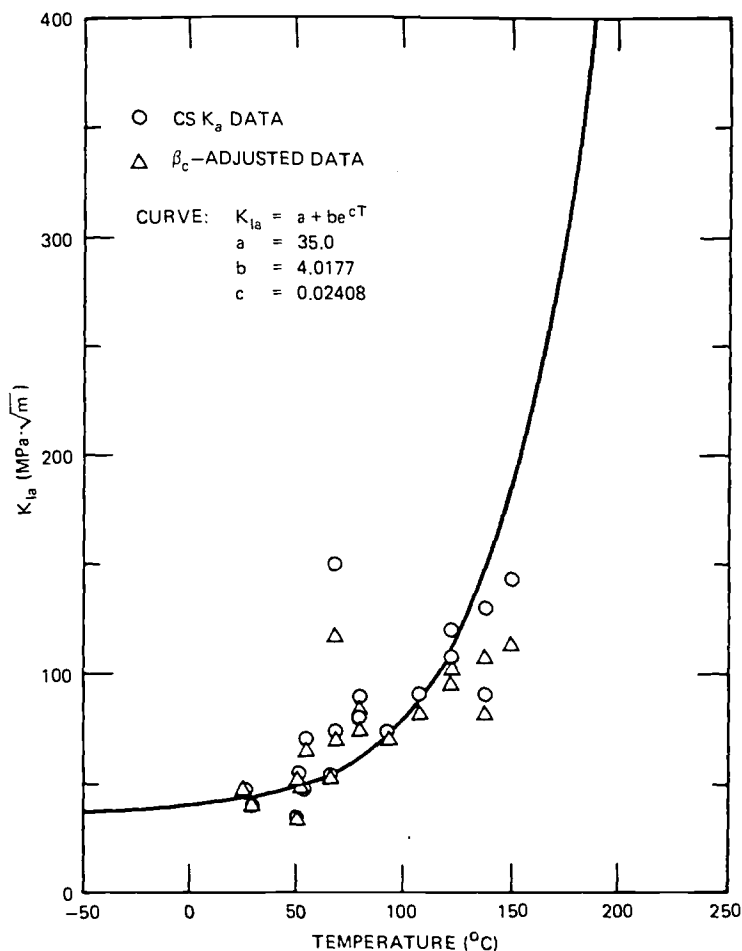


FIG. 3— K_{Ia} data for the PTSE-1 vessel. The curve represents a function used in fracture analyses.

the tearing resistance as a function of ductile crack extension, $\Delta a = a - a'$. The variables in Relationships 2, 3, and 4 were evaluated for the temperature conditions at the real or virtual crack tip.

Test Transients

Three pressurized thermal shock transients were imposed on the PTSE-1 vessel. The pressure histories are shown in Fig. 4. Each transient started with the vessel nearly isothermal with $T \approx 280$ to 290°C . Details of the transients are given in the Appendix.

Results

Events

In the first transient, PTSE-1A, the crack remained stationary. In each of the succeeding transients the crack propagated and arrested once. This behavior and the associated crack-

tip conditions are shown in Fig. 5, in which the arrows indicate the direction of advancing time. In the *A* transient the crack experienced simple warm prestressing ($\dot{K}_I < 0$) during three different periods and simple anti-warm prestressing ($\dot{K}_I > 0$) twice. In the *B* and *C* transients the crack jumped to depths of 24.4 and 41 mm, respectively. The crack arrests occurred in positive K_I gradients, namely, $dK_I/da = 0.7$ and $2.3 \text{ MPa } \sqrt{\text{m/mm}}$.

Prior to performance of the *A* transient test, Curve *A* of Fig. 2 had been used to represent $K_{Ic}(T)$ in estimates of fracture conditions. Since the noninitiation in this transient implied that the fracture toughness was greater at the time of incipient warm prestressing than the value from curve *A*, a modified relationship, represented by Curve *B*, was used in all subsequent estimates of crack initiation. Curve *B* is based on the presumption that K_I in the *A* transient is equal to K_{Ic} at precisely the time of the onset of warm prestressing. Figure 5 shows the latter K_{Ic} curve as well as the K_{Ia} curve of Fig. 3.

Transients *A* and *B* both demonstrated the strongly inhibiting effect of warm prestressing on initiation of a brittle fracture. The ratio K_I/K_{Ic} exceeded 2.0 in both transients; in the *A* transient the ratio exceeded 2.0 during a simple antiwarm prestressing phase that persisted for more than 30 s.

The temperatures, crack depths, and stress-intensity factors associated with the events shown in Fig. 5 are tabulated in the Appendix.

Characterization of Fracture

Fractographic examination of the fracture surfaces revealed that the crack extended by cleavage. Figure 6 shows a typical segment of the fracture surfaces. The initial extension was essentially pure cleavage over the first half of the extension and about 90% cleavage in the remaining area. At the time of the crack jump the temperatures across the fracture surface increased from 104°C at the tip of the initial crack to 163°C at the deepest point of the arrested crack. The surface of the second crack extension was about 85% cleavage everywhere, and temperatures across this surface were in the range of 125 to 179°C between

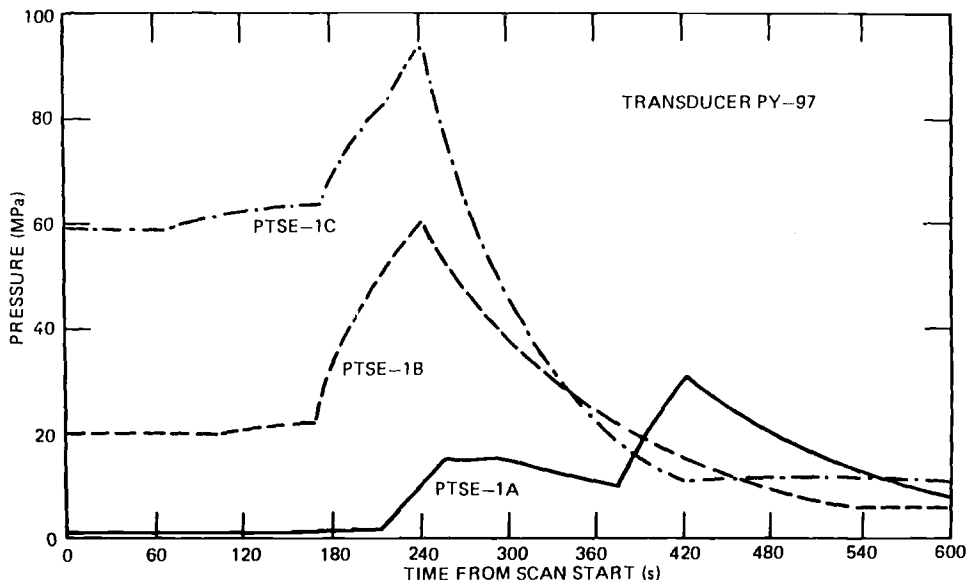


FIG. 4—Pressure versus time for the three transient phases of PTSE-1.

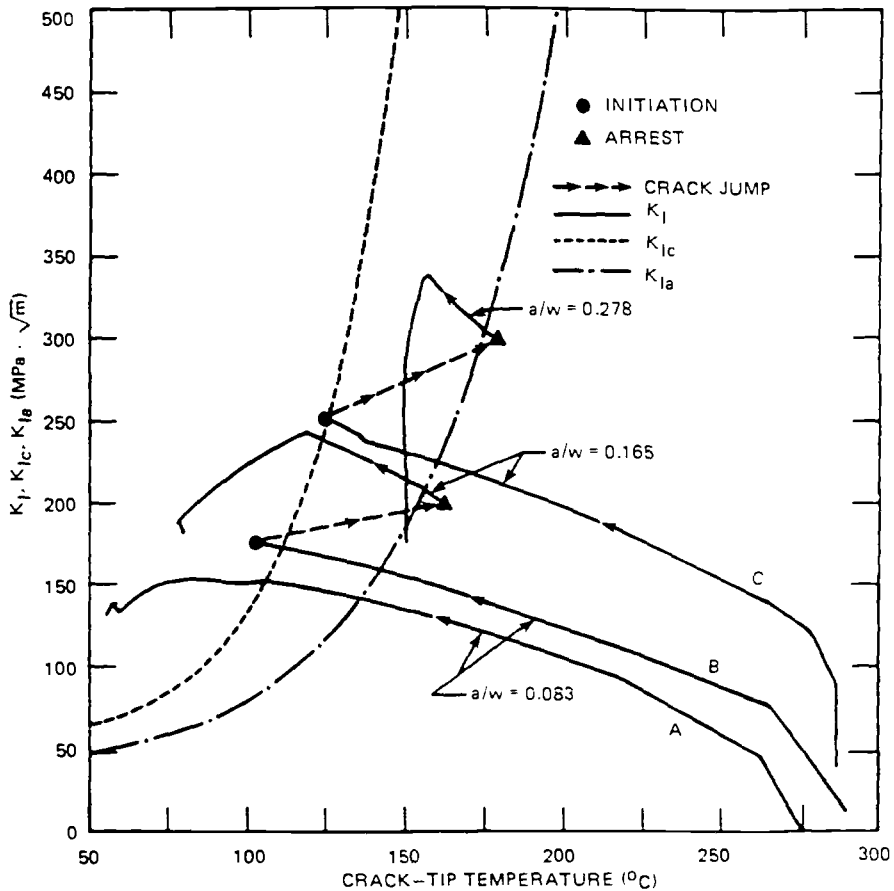


FIG. 5—Applied stress-intensity factor and toughness versus crack-tip temperature curves for PTSE-1. a = crack depth; w = wall thickness.

the deepest points of the intermediate and the final cracks. The lightest areas of the fracture surface shown in Fig. 6 are areas fractured after the test. These areas indicate that there were many unbroken ligaments.

The crack-tip contours for the initial, intermediate, and final cracks were mapped with the aid of a low-power microscope. The contours, shown in Fig. 7, indicate that the initial flaw was uniform in depth over its 1-m length and the succeeding contours were roughly semielliptical. This figure also shows that the crack extended lengthwise during the first jump to the ends of the plug of relatively low-toughness material.

One of the remarkable features of the fracture surfaces is the complete absence of macroscopic ductile tearing at the termini of the two crack extensions. Stable tearing estimates based on J_R data and the relationship from Eq 4 had indicated 2 and 11 mm of tearing up to the times of maximum loading. The absence of predicted tearing could be indicative of a fundamental incapacity of a tearing analysis based on J_R to represent a large structure accurately. It is also possible that J_R data from small specimens underestimate tearing resistance.

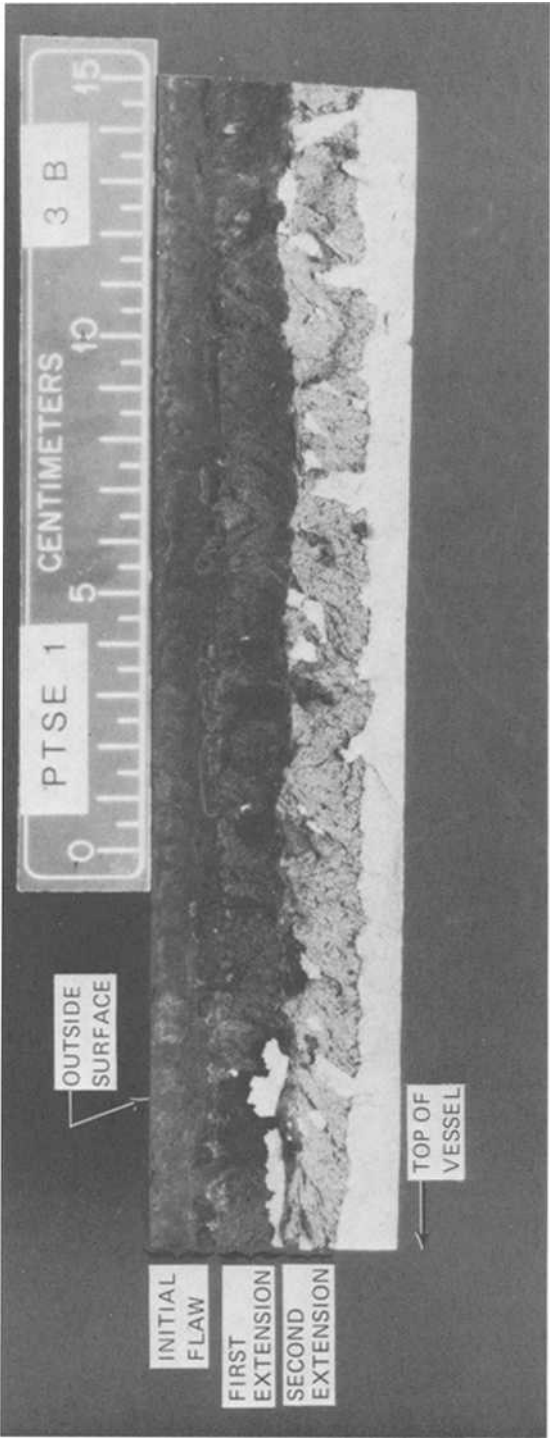


FIG. 6—Typical portion of the fracture surface from PTSE-1.

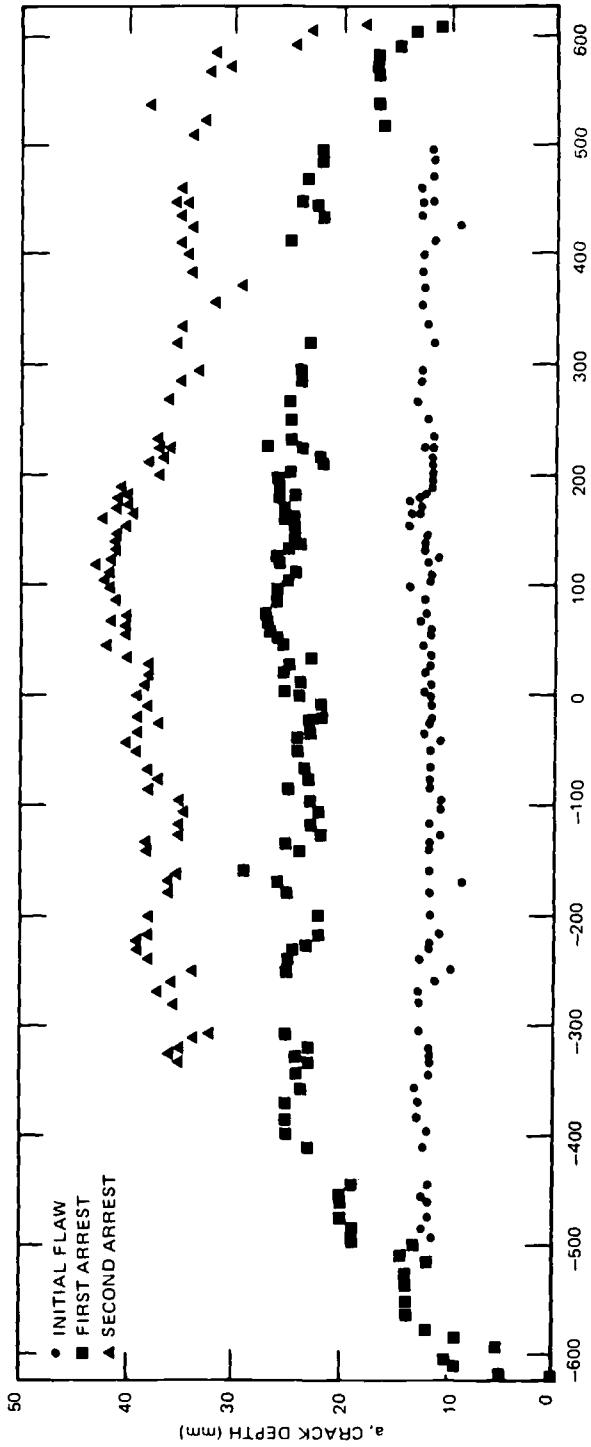


FIG. 7—Measured crack depths of the PTSE-I flaw.

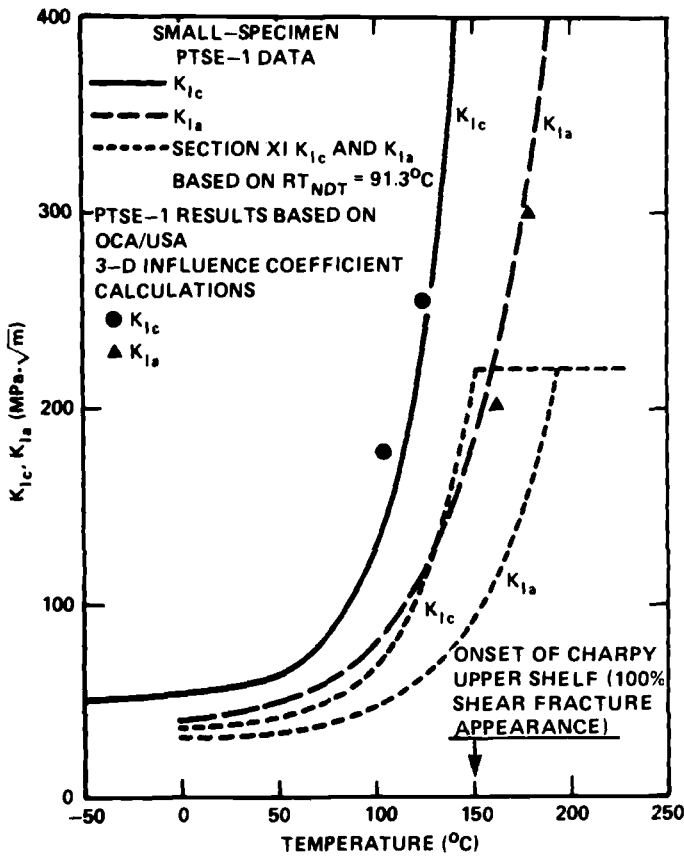


FIG. 8—Fracture-toughness values derived from PTSE-1 data compared with pretest expectations and values prescribed by Section XI of the ASME Boiler and Pressure Vessel Code.

Conclusions

Crack initiations and arrests occurring in the highly constrained PTSE-1 structure demonstrated the consistency between fracture initiation toughness inferred by LEFM from the experiment and toughness inferred from data from small fracture-toughness specimens, provided that one accounts for warm prestressing. Initiation and arrest toughness values were well in excess of the $220 \text{ MPa}\sqrt{\text{m}}$ cutoff suggested by Section XI of the American Society of Mechanical Engineers (ASME) Boiler and Pressure Vessel Code [24], as shown in Fig. 8. The inhibiting effects of warm prestressing and the complete absence of ductile tearing in this experiment suggest that further study and consideration should be given these aspects of fracture in research and in structural evaluations.

Objectives of PTSE-2

The second pressurized thermal shock experiment is designed to investigate the influence of low tearing resistance on crack propagation and growth and to extend the warm prestressing investigation clearly into the antiwarm prestressing phase. A $2\frac{1}{4}\text{Cr-1Mo}$ steel plug has been put into the test vessel. With special heat treatment the plug should have a Charpy

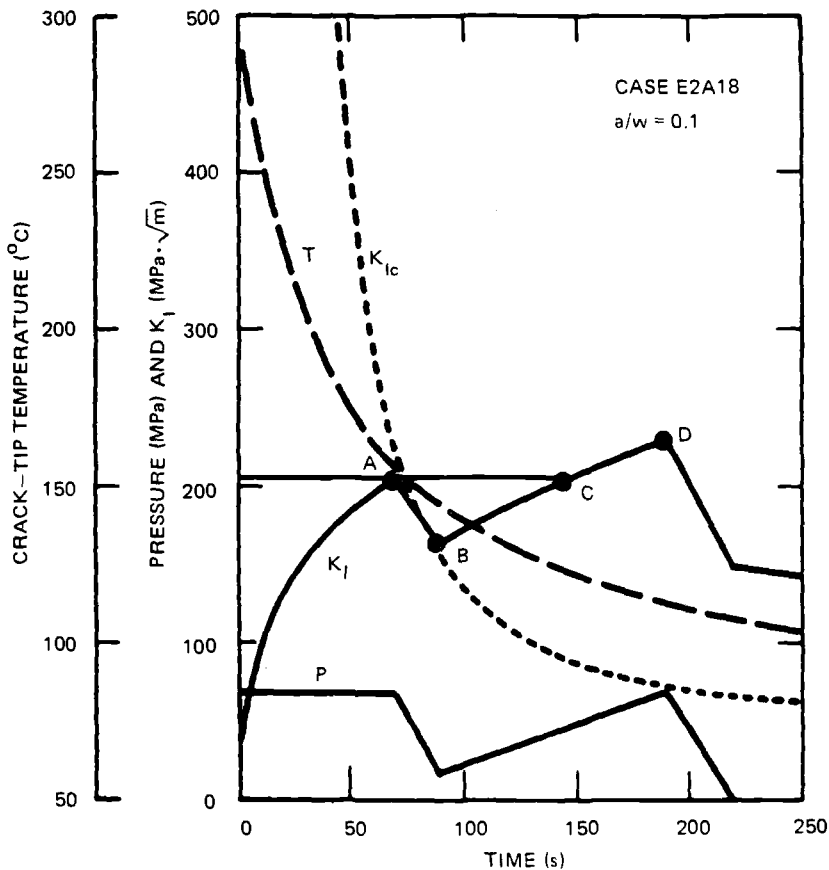


FIG. 9—Illustration of a PTSE-2 transient based on speculative material properties.

upper-shelf impact energy of less than 68 J, which is expected to imply a low tearing resistance.

This experiment will probably require two separate transients, but the major features are illustrated by a transient analyzed as a part of preliminary parameter studies (Figs. 9 and 10). The plan for the first phase of the experiment is for the flaw to be warm prestressed prior to the time that $K_I = K_{Ic}$ (between Points A and B of Fig. 9) and subsequently to experience K_I increasing with time with a magnitude exceeding (between Points C and D) the previous maximum value. The conditions during the C-D phase should initiate a brittle fracture. If initiation should occur at Point I, shown in Fig. 10, the subsequent events would be the second phase of the experiment, which is concerned with the behavior of material with low tearing resistance. The plans are to develop conditions at the time of arrest of the cleavage fracture (Point A, Fig. 10) that would produce an immediate tearing instability. Presently, the means of analyzing this transitory state are uncertain, which is one of the incentives for this experiment.

Acknowledgments

We gratefully acknowledge the contributions of H. A. Domian and others of the Babcock and Wilcox Alliance Research Center; A. R. Rosenfield and others of the Battelle Columbus

Laboratories; S. E. Bolt, J. W. Bryson, C. E. Pugh, K. R. Thoms, and G. D. Whitman of the Oak Ridge National Laboratory; B. R. Bass and D. A. Steinert of the Computing and Telecommunications Division of Martin Marietta Energy Systems; and M. Vagins of the U.S. Nuclear Regulatory Commission.

This research was sponsored by the Office of Nuclear Regulatory Research, U.S. Nuclear Regulatory Commission, under Interagency Agreements 40-551-75 and 40-552-75 with the U.S. Department of Energy under Contract DE-AC05-84OR21400 with Martin Marietta Energy Systems, Inc.

APPENDIX

PTSE-1 Material Properties

Material properties used in pretest and posttest fracture analyses of the PTSE-1 vessel are presented in Table 1 and Fig. 11. These values are regarded as the best representations

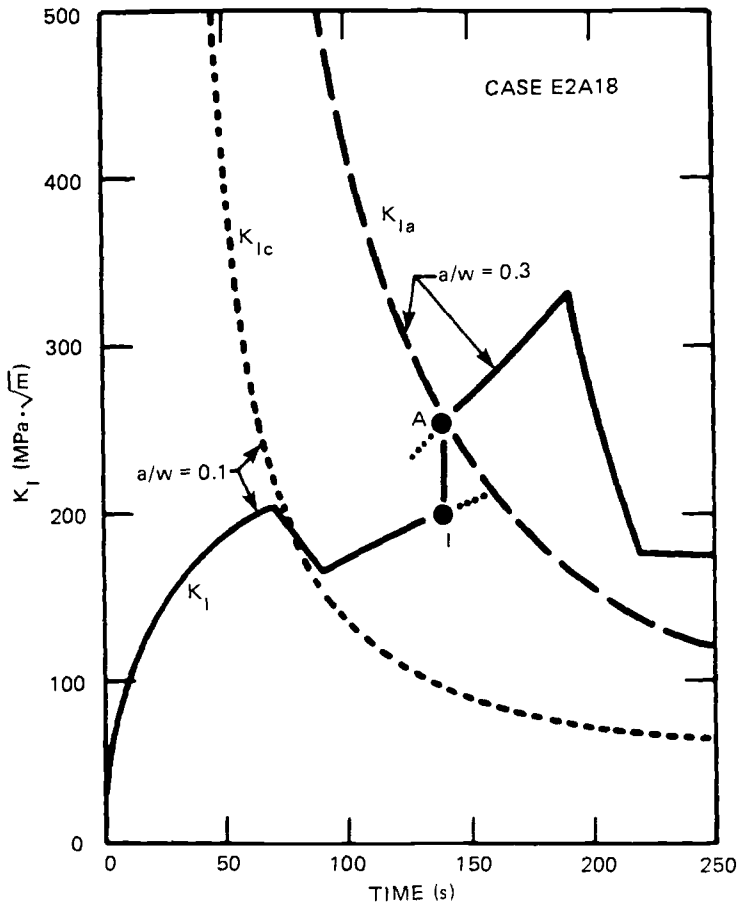


FIG. 10— K_I , K_{Ic} , and K_{Ia} versus time for an illustrative PTSE-2 transient in which it is presumed that the crack will propagate at Point I during simple antiwarm prestressing. In this case the crack arrests at Point A.

TABLE 1—Properties of PTSE-1 vessel material (A508, Class 2 steel with special tempering treatment).

Property	Value
K_{Ic}	Fig. 2
K_{Ia}	Fig. 3
J_R parameters ^a	
c	2.60
n	0.359
Onset of Charpy upper shelf, °C	150
Reference nil-ductility transition temperature, °C	91
Stress-strain ^b	Fig. 11
Young's modulus (E), GPa ^c	202.3 ^d
Coefficient of thermal expansion (α), °K ⁻¹	1.441×10^{-5} ^d
Poisson's ratio (ν) ^c	0.3
Thermal conductivity, W/m · K	41.54
Heat capacity, J/kg · K	502.4
Density, kg/m ³	7833

^a $J_R = c(\Delta a)^n$; J_R is in megajoules per square metre; Δa in metres.

^b Piecewise linear fit to the curve from stress-strain data.

^c These are properties of the A-533 Grade B Class 1 cylinder, exclusive of the plug containing the flaw.

^d These average values are based on experimental measurements of $E(T)$ and $\alpha(T)$ for the vessel material, and they give values of K_I within 1% of the values based upon the temperature-dependent properties.

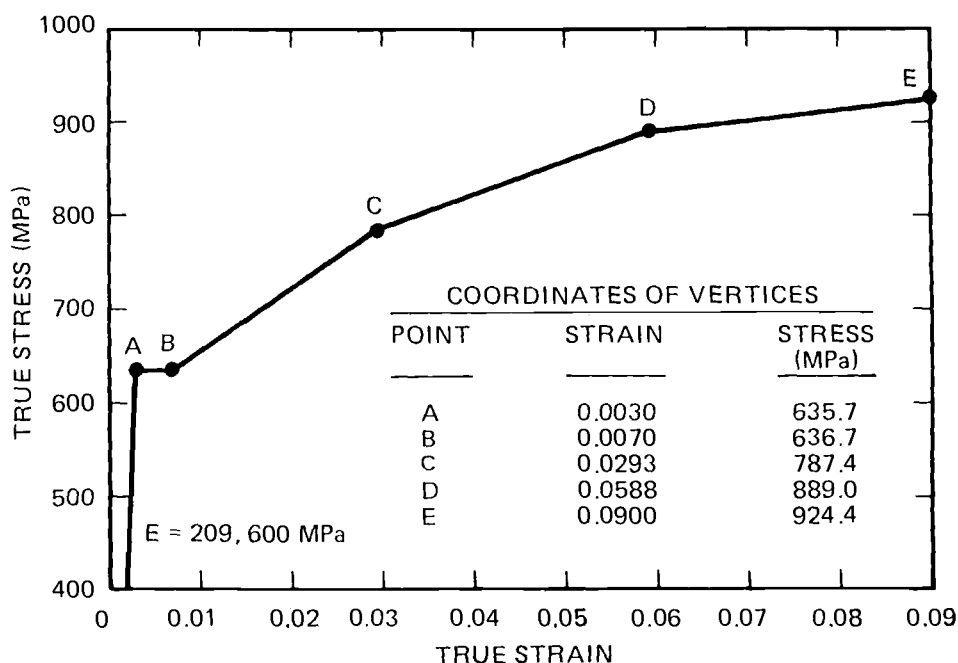


FIG. 11—Piecewise linear stress-strain relationship assumed for finite-element analysis of PTSE-1.

TABLE 2—Conditions for PTSE-1A, PTSE-1B, and PTSE-1C transients.

	Test		
	PTSE-1A	PTSE-1B	PTSE-1C
Thermal transient parameters			
Initial vessel temperature, °C	277.6	290.7	287.4
Coolant temperature [$T_c(t)$], °C	15 to 34 ^a	−22 to 0 ^a	−29 to 14 ^a
$h(t)$, W/m ² · K	8000 to 6000 ^a	5500 to 6500 ^a	4000 to 5500 ^a
Pressure transient	Fig. 4	Fig. 4	Fig. 4
Initial flaw depth			
a , mm	12.2	12.2	24.4
a/w	0.083	0.083	0.165

^a Initial and final ($t \approx 300$ s) values.

of actual properties as determined by material characterization studies that preceded the transient experiment. Many variations from these properties were studied in parametric analyses not presented here [19].

Transient Conditions

Conditions for the three transients, PTSE-1A, -1B, and -1C, are presented in Table 2. This information was obtained from the actual measurements made during the transients and, in the case of flaw depth, from posttest examination of the flaw. The thermal transient parameters presented approximately characterize the transient temperatures, which are too voluminous to include here but are reported in Ref 19.

Fracture Conditions and Events

Conditions that are related to crack behavior in the three transients are summarized in Table 3. The events identified in this table are also included in Fig. 5.

TABLE 3—Summary of fracture conditions in PTSE-1.

Experiment	Event	Time, s ^a	Crack Depth, mm	Crack-Tip Temperature, °C	K_I , MPa \sqrt{m}
PTSE-1A	1st max K_I (at $K_I \approx K_{Ic}$)	202	12.2	105	152
	2nd max K_I	260.0	12.2	78	154
	3rd max K_I	421.2	12.2	57	139
PTSE-1B	initiation	172.1	12.2	104	177
	arrest	172.1	24.4	163	201
	subsequent max K_I	240.9	24.4	118	247
PTSE-1C	initiation	195.3	24.4	125	254
	arrest	195.3	41	179	299
	subsequent max K_I	242.0	41	156	340

^a From the start of the data records. The thermal transients started at 141, 105, and 70 s from the start of the records of PTSE-1A, PTSE-1B, and PTSE-1C, respectively.

References

- [1] Derby, R. W., et al., "Test of 6-Inch-Thick Pressure Vessels, Series 1: Intermediate Test Vessels V-1 and V-2," ORNL-4895, Oak Ridge National Laboratory, Oak Ridge, TN, February 1974.
- [2] Bryan, R. H., et al., "Test of 6-Inch-Thick Pressure Vessels, Series 2: Intermediate Test Vessels V-3, V-4, and V-6," ORNL-5059, Oak Ridge National Laboratory, Oak Ridge, TN, November 1975.
- [3] Merkle, J. G., et al., "Test of 6-Inch-Thick Pressure Vessels, Series 3: Intermediate Test Vessel V-7," ORNL/NUREG-1, Oak Ridge National Laboratory, Oak Ridge, TN, August 1976.
- [4] Merkle, J. G., et al., "Test of 6-Inch-Thick Pressure Vessels, Series 4: Intermediate Test Vessels V-5 and V-9 with Inside Nozzle Corner Cracks," ORNL/NUREG-7, Oak Ridge National Laboratories, Oak Ridge, TN, August 1977.
- [5] Bryan, R. H., et al., "Test of 6-Inch-Thick Pressure Vessels, Series 3: Intermediate Test Vessel V-7A Under Sustained Loading," ORNL/NUREG-9, Oak Ridge National Laboratory, Oak Ridge, TN, February 1978.
- [6] Bryan, R. H., et al., "Test of 6-Inch-Thick Pressure Vessels, Series 3: Intermediate Test Vessel V-7B," NUREG/CR-0309 (ORNL/NUREG-38), Oak Ridge National Laboratory, Oak Ridge, TN, October 1978.
- [7] Bryan, R. H., et al., "Test of 6-Inch-Thick Pressure Vessels, Series 3: Intermediate Test Vessel V-8," NUREG/CR-0675, (ORNL/NUREG-58), Oak Ridge National Laboratory, Oak Ridge, TN, December 1979.
- [8] Bryan, R. H., et al., "Test of 6-Inch-Thick Pressure Vessels, Series 3: Intermediate Test Vessel V-8A—Tearing Behavior of Low Upper-Shelf Material," ORNL-6187, Martin Marietta Energy Systems, Inc., Oak Ridge National Laboratory, Oak Ridge, TN, May 1987.
- [9] Cheverton, R. D., "Pressure Vessel Fracture Studies Pertaining to PWR LOCA-ECC Thermal Shock: Experiments TSE-1 and TSE-2," ORNL/NUREG/TM-31, Oak Ridge National Laboratory, Oak Ridge, TN, September 1976.
- [10] Cheverton, R. D. and Bolt, S. E., "Pressure Vessel Fracture Studies Pertaining to a PWR LOCA-ECC Thermal Shock: Experiments TSE-3 and TSE-4 and Update of TSE-1 and TSE-2 Analysis," ORNL/NUREG-22, Oak Ridge National Laboratory, Oak Ridge, TN, December 1977.
- [11] Cheverton, R. D., et al., "Pressure Vessel Fracture Studies Pertaining to the PWR Thermal-Shock Issue: Experiments TSE-5, TSE-5A, and TSE-6," NUREG/CR-4249 (ORNL-6163), Martin Marietta Energy Systems, Inc., Oak Ridge National Laboratory, Oak Ridge, TN, June 1985.
- [12] Cheverton, R. D., Ball, D. G., Bolt, S. E., Iskander, S. K., and Nanstad, R. K., "Pressure Vessel Fracture Studies Pertaining to the PWR Thermal-Shock Issue: Experiment TSE-7," NUREG/CR-4304 (ORNL-6177), Oak Ridge National Laboratory, Oak Ridge, TN, August 1985.
- [13] Landes, J. D. and Shaffer, D. H. in *Fracture Mechanics: Twelfth Conference, ASTM STP 700*, American Society for Testing and Materials, 1980, pp. 368–382.
- [14] McCabe, D. E. and Landes, J. D., "The Effect of Specimen Plan View Size and Material Thickness on the Transition Temperature of A533B Steel," Research Report 80-ID3-REVEM-R2, Westinghouse Research and Development Center, Pittsburgh, PA, 17 Nov. 1980.
- [15] Iwade, T., et al. in *Elastic-Plastic Fracture: Second Symposium, ASTM STP 803*, Vol. II, American Society for Testing and Materials, Philadelphia 1983, pp. 531–561.
- [16] Merkle, J. G., "An Examination of the Size Effects and Data Scatter Observed in Small Specimen Cleavage Fracture Toughness Testing," NUREG/CR-3672 (ORNL/TM-9088), Oak Ridge National Laboratory, Oak Ridge, TN, April 1984.
- [17] Irwin, G. R., *Journal of Basic Engineering*, Vol. 82, No. 2, 1960, pp. 417–425.
- [18] Bryan, R. H., et al., "Pressurized-Thermal-Shock Test of 6-Inch-Thick Pressure Vessels, PTSE-1: Investigation of Warm Prestressing and Upper-Shelf Arrest," NUREG/CR-4106 (ORNL-6135), Oak Ridge National Laboratory, Oak Ridge, TN, April 1985.
- [19] Domian, H. A., "Vessel V-7 and V-8 Repair and Characterization of Insert Material," ORNL/Sub/82-52845/1, Babcock and Wilcox Co. Alliance, OH, May 1984.
- [20] Rosenfield, A. R., et al. in *Heavy-Section Steel Technology Program Semiannual Progress Report for October 1983–March 1984*, ORNL/TM-9154/V1, Oak Ridge National Laboratory, Oak Ridge, TN, May 1984, pp. 57–60.
- [21] Bass, B. R. and Bryson, J. W., "Applications of Energy Release Rate Techniques to Part-Through Cracks in Plates and Cylinders, Volume 1, ORGMEN-3D: A Finite Element Mesh Generator for Three-Dimensional Crack Geometries," ORNL/TM-8527/V1, Oak Ridge National Laboratory, Oak Ridge, TN, December 1982.
- [22] Bass, B. R. and Bryson, J. W., "Applications of Energy Release Rate Techniques to Part-Through Cracks in Plates and Cylinders, Volume 2. ORVIRT: A Finite Element Program for Energy

Release Rate Calculations for 2-D and 3-D Crack Models," ORNL/TM-8527/V2, Oak Ridge National Laboratory, Oak Ridge, TN, February 1983.

- [23] Bathe, K. J., "ADINA—A Finite Element Program for Automatic Dynamic Incremental Non-linear Analysis," Report 82448-1, Massachusetts Institute of Technology, Cambridge, MA, December 1978.
- [24] "Rules for In-Service Inspection of Nuclear Power Plant Components," ASME Boiler and Pressure Vessel Code, Section XI, American Society of Mechanical Engineers, New York, NY, 1983.

Crack Arrest Theory and Applications: Part II—Fatigue

Fatigue Crack Propagation Behavior and Damage Accumulation Relationships in an Aluminum Alloy

REFERENCE: O'Connor, B. P. D. and Plumtree, A., "Fatigue Crack Propagation Behavior and Damage Accumulation Relationships in an Aluminum Alloy," *Fracture Mechanics: Nineteenth Symposium, ASTM STP 969*, T. A. Cruse, Ed., American Society for Testing and Materials, Philadelphia, 1988, pp. 787-799.

ABSTRACT: Damage accumulation was studied in strain-cycled aluminum Alloy 6066-T6 cylindrical fatigue specimens. The damage was assessed by measuring the ratio of cracked to cross-sectioned areas and monitoring the apparent modulus changes after different life fractions. Both these methods were found to correlate well. Stage II fatigue crack propagation was established when the surface crack length had attained a critical value of approximately 700 μm . A linear relationship with crack depth ensued. Below this value, the crack depth was small by comparison and damage levels were below 1%. Over 60% of the fatigue life was spent in Stage I (or surface-dominated) crack growth where the cracked area was insignificant. From a practical point of view, damage was considered to begin after this life fraction and a damage mechanics model was successfully applied to the experimental results.

Damage accumulation rates were related directly to crack growth rates as a result of the relationship between damage and the cracked area. Hence, damage accumulation may be described by a Paris type of equation.

Tests at low strains involving a large amount of elasticity (elastic-to-plastic strain ratios of the order of 600) were found to maintain low damage levels over longer life fractions compared with higher strain cycled tests (with ratios of 25 and less). Damage at a given life fraction in tests with elastic-to-plastic strain ratios below approximately 25 were found to be similar. Under these conditions Miner's rule may be applied.

KEY WORDS: fatigue damage accumulation, damage mechanics, apparent modulus, cyclic strain amplitude, fracture mechanics

Damage mechanics has had considerable success in predicting the mechanical deterioration of structural materials under cyclic loading at high temperatures [1,2]. These studies have incorporated the constitutive equations for damage derived by Kachanov [3] from thermodynamic principles. Damage may be presented as a continuous variable, written in terms of stress and strain, and represented by the density of defects produced in the material on loading. For fatigue, damage is the initiation, as well as the growth of microcracks, and ultimately the complete rupture of the material. Generally, an undamaged component contains no cracks, while a fully damaged one can be defined to be either completely ruptured or partially fractured to a critical level D_c [4]. For metals the value of D_c lies in the range 0.2 to 0.8 [4].

Lemaitre and Plumtree [5] applied damage mechanics principles to quantitatively describe

¹ Research assistant, and associate dean and professor, respectively, Mechanical Engineering Dept., University of Waterloo, Waterloo, Ontario, Canada N2L 3G1.

the evolution of damage in a material subjected to cyclic straining, which may be expressed as follows

$$D = 1 - \left(1 - \frac{N}{N_f}\right)^{1/(1+p)} \quad (1)$$

where

D = damage occurring after N cycles,

N_f = number of cycles to produce a critical amount of damage, D_c , and

p = damage coefficient,

as outlined in Ref 5. On the other hand, a simple damage equation has been formulated [6] to account for the cracked area, namely

$$D = 1 - \frac{\tilde{A}}{A} \quad (2)$$

where \tilde{A} is the area of the damaged material and A is the original cross-sectional area. Damage can also be expressed in terms of the modulus of elasticity [6] as

$$D = 1 - \frac{\tilde{E}}{E} \quad (3)$$

where \tilde{E} is the apparent modulus of the damaged material and E is the modulus of the undamaged material.

The intent of the present work is to monitor the apparent modulus of elasticity and the cracked areas of specimens damaged during fatigue in order to quantify the damage, calculated from Eqs 2 and 3. Also an assessment will be made of existing damage equations, such as that derived by Plumtree and Lemaitre [7], from more fundamental relationships, namely

$$D = 1 - \left(\frac{\tilde{A}}{A}\right)^{1/2} \quad (4)$$

Experimental Materials and Procedure

Material and Properties

The alloy used in this investigation was aluminum Alloy AA6066. (The composition is in Table 1.) Bars of 50 mm diameter were machined from cast book moulds, which were then homogenized at 540°C for 8 h. These were extruded at 475°C to a 15-mm diameter. Solution heat treatment at 530°C for 1 h followed, and after water quenching, aging was performed at 175°C for 8 h (T6 temper). The cylindrical fatigue specimens were 90 mm in length with a 15-mm gage length and a nominal diameter of 5 mm. These were then polished with alumina powder to a 0.3-μm finish.

The static mechanical properties are given in Table 2.

TABLE 1—Material composition, in weight percent.

Cu	Fe	Mg	Mn	Si	Ni	Ti	Zn	Cr	V	Zr	Al
1.02	0.24	1.10	0.71	1.30	0.001	0.003	0.007	<0.005	0.007	<0.001	balance

Procedure

All the tests were conducted at room temperature on a closed-loop servohydraulic testing system under strain control using a sinusoidal waveform. A deformation rate of 0.04/s was employed for all tests. Axial strain was controlled by an extensometer with a gage length of 10 mm. Total strain amplitudes, $\Delta\epsilon/2$, between 0.20 and 2.0% were imposed. The elastic and plastic strain components at half-life are given in Table 3.

Approximately 20 hysteresis loops were recorded on an X-Y plotter at a frequency of 0.05 Hz at various intervals during the life of each specimen. The slope of the unloading curve from maximum tension gave the damaged or apparent modulus, \tilde{E} . The undamaged modulus, E , was obtained from the slope on loading after maximum compression, which was taken from the hysteresis loop recorded during the first cycle, thus allowing an assessment of damage to be made according to Eq 3.

Having recorded a hysteresis loop, the load was reduced to zero and the associated strain recorded. The extensometer was then removed and acetate replicating strips were applied over the gage length. The dried replicas were then examined through an optical stereomicroscope to locate the positions of cracks. This relatively quick examination could detect cracks of approximately 200 μm in length. After detection of these cracks the extensometer was replaced at zero load. The strain reading was set to that recorded prior to removal of the extensometer and the test was continued. The peak loads before and after this procedure corresponded exactly. After cyclic testing, examination of the dried replicas in the scanning electron microscope (SEM) allowed accurate crack length measurements to be made.

The crack profile was examined by interrupting repeated tests with strain amplitudes between 0.2 to 1.0% at various stages of the fatigue life. The cracks were opened by applying a tensile load of 150 kg and a dye was painted over the gage length. The cracked specimens were then broken using an impact machine and the crack profile was examined optically. The crack profile was very slightly curved, approximating a semiellipse with a large major-to-minor-axis ratio. This shape was found to exist over the full range of strains examined and also at damage levels of up to 50% which is used as the life criterion in this study.

For the present work, ΔJ was employed as the correlation factor for fatigue crack growth [1,8,9]. The derivation of ΔJ , corresponding to a semielliptical crack profile, is outlined in the Appendix and is expressed by

$$\Delta J = \frac{3.941}{Q} \Delta\sigma\Delta\epsilon_e a + \frac{14.115}{Q} \Delta\sigma\Delta\epsilon_p a \quad (5)$$

TABLE 2—Mechanical properties of extruded aluminum alloy 6066-T6 (longitudinal direction).

Alloy	Young's Modulus, GPa	0.2% Proof Stress, MPa	Ultimate Tensile Stress, MPa	Strain to Failure, %
6066-T6	74.1	469	492	13

TABLE 3—Elastic and plastic strain components at the half-life in tests monitored for damage.

Strain Amplitude, $\Delta\epsilon_i/2$, %	Elastic Strain Amplitude, $\Delta\epsilon_e/2$, %	Plastic Strain Amplitude, $\Delta\epsilon_p/2$, %	Elastic to Plastic Strain Ratio
0.35	0.3494	0.0006	582
0.50	0.4808	0.0192	25.0
0.75	0.612	0.138	4.4
1.00	0.606	0.394	1.5

where

$\Delta\sigma$ = cyclic stress range,

$\Delta\epsilon_e$ = elastic strain range,

$\Delta\epsilon_p$ = plastic strain range,

a = crack depth, and

Q = crack profile correction factor (see the Appendix).

Results

Cyclic Stress-Strain and Strain Life Data

Cyclic stress-strain hysteresis loops at the half-life were taken as representing the stable behavior observed during most of the fatigue life. Such loops enabled the cyclic stress-strain curve to be generated, as shown in Fig. 1, together with its fitted equation.

Superposition of the strain-life curves for the elastic and plastic components of tests with strain amplitudes, $\Delta\epsilon_i/2$, between 0.2 and 2.0% produced the strain-life relationship shown in Fig. 2.

The lowest strain amplitude used for damage analysis, $\Delta\epsilon_i/2 = 0.35\%$, lies just outside the transition region of Fig. 2 and is positioned on the elastic portion of the cyclic stress-strain curve (Fig. 1).

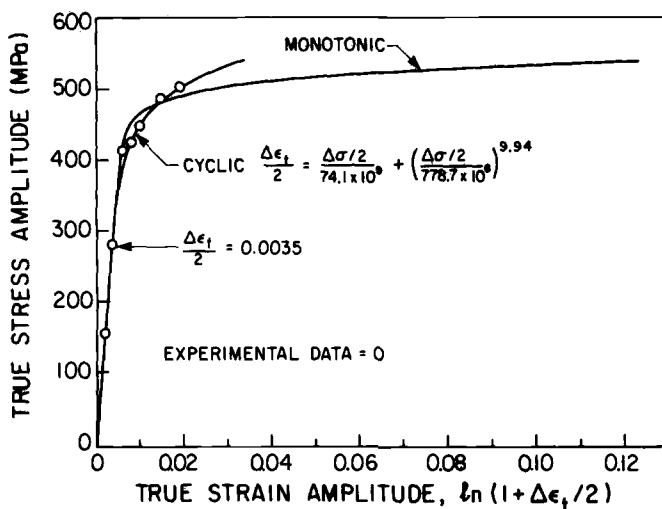


FIG. 1—Monotonic and cyclic stress-strain curves.

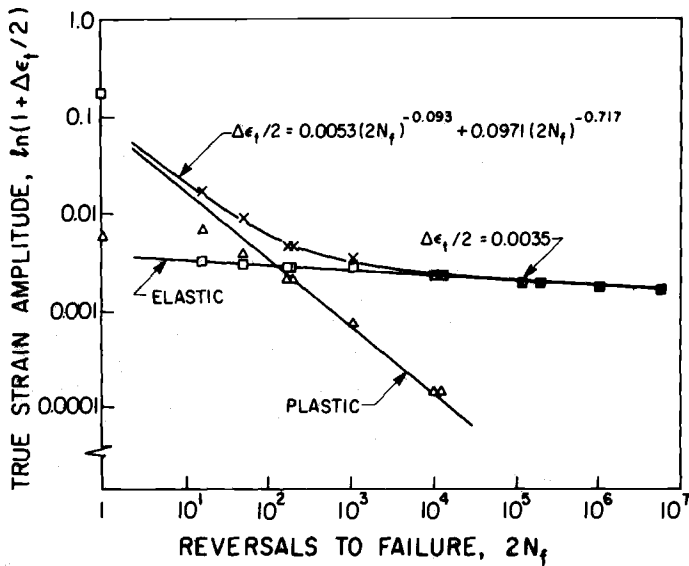


FIG. 2—Strain-life properties with the elastic and plastic components.

Damage Determined from a Cracked Area

For damage to be determined from a cracked area according to Eq 2, the crack profile must be known at all stages during the fatigue life. The linear relationship between the crack depth and surface crack length, shown in Fig. 3, indicates that the crack profile was independent of the strain level. This profile, once established, remained constant over the fatigue life. Below surface crack lengths of approximately 700 μm , the corresponding crack depths were small ($<100 \mu\text{m}$) and located at an angle to the major stress axis, indicating that propagation was dominated by shear at the free surface (Stage I crack propagation).

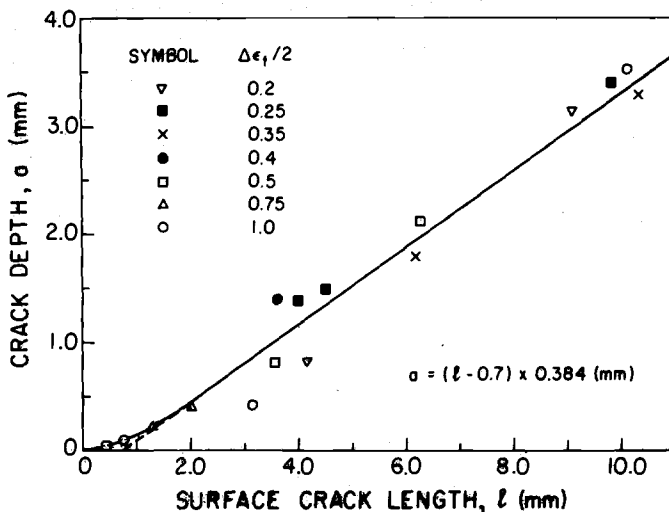


FIG. 3—Relationship between surface crack length and maximum crack depth.

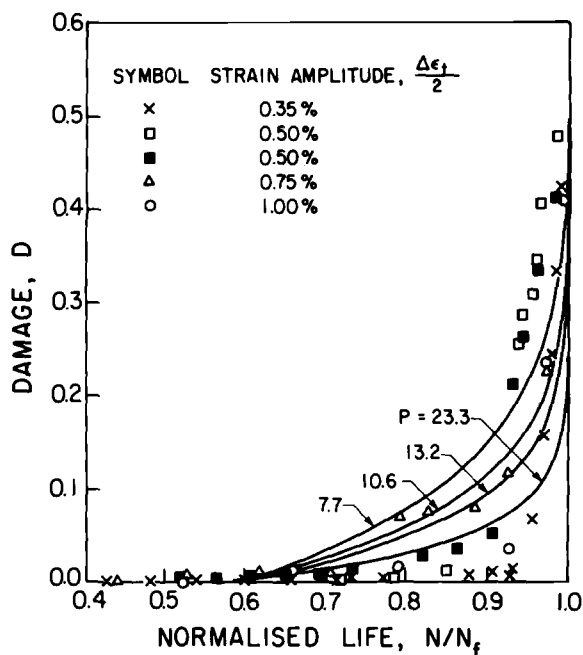


FIG. 4—Plot of damage accumulation obtained from cracked area estimates for four strain amplitudes at different life fractions (data points), with the least-squares fitted curves from Eq 6 (solid lines).

However, once a threshold or critical length was reached the crack direction changed to correspond to that for the principal stress (Stage II crack propagation).

Using the semielliptical crack shape and the depth relationships just described, the cracked area was calculated. Damage was then determined using Eq 2, and the corresponding plot of damage against normalized life, N/N_f , is shown in Fig. 4, where N_f is defined as the number of cycles required to cause 50% damage. It appears from this plot that the damage is approximately equal for all the strain levels examined up to $0.8 N_f$ and that small discernible trends of damage with strain level occur thereafter. However, low damage levels are produced over a longer life fraction at the lowest strain amplitudes, where the ratio of elastic to plastic strain is high (for example, 582 for $\Delta\epsilon_f/2 = 0.35\%$, as given in Table 3).

Surface crack lengths of about $700 \mu\text{m}$ were attained at normalized life ratios, N/N_f , of >0.6 , indicating that below this life fraction the threshold length had not been reached. Very small amounts of damage ($<1\%$) had been accumulated to that juncture. From an

TABLE 4—Damage exponents from the least-squares fitted damage equation.

Strain Amplitude, $\Delta\epsilon_f/2$, %	Damage Exponent, p (Eq 6 fitted to Fig. 4)	Damage Exponent, p (Eq 6 fitted to Fig. 6)
0.35	23.3	27.9
0.50	average = 10.5	9.1
0.75		15.5
1.00		15.5

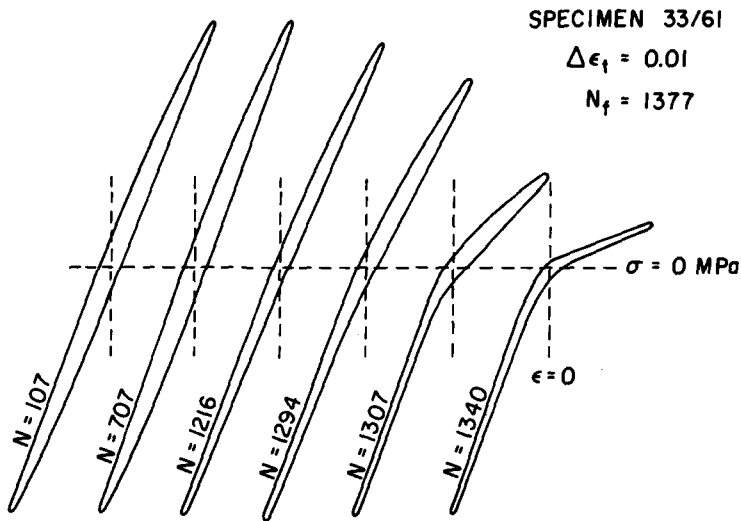


FIG. 5—Hysteresis loops recorded at different life fractions for $\Delta\epsilon_t = 1\%$.

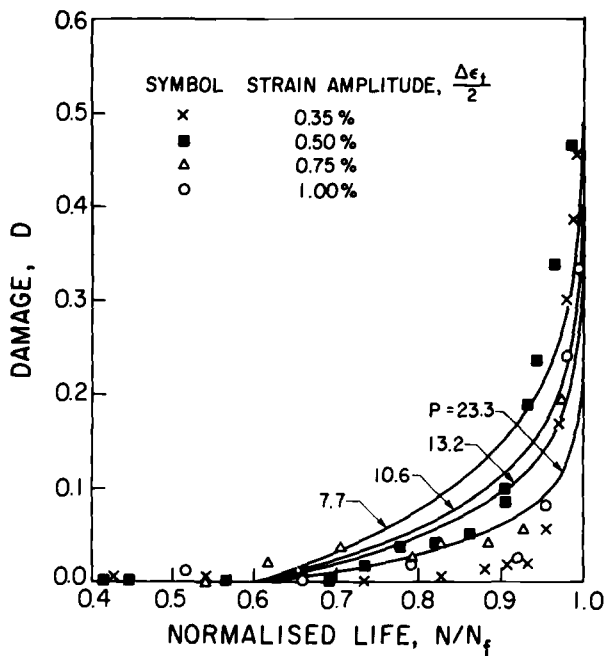


FIG. 6—Plot of damage accumulation obtained from apparent modulus changes for four strain levels (data points) superimposed on the damage curves of Fig. 4.

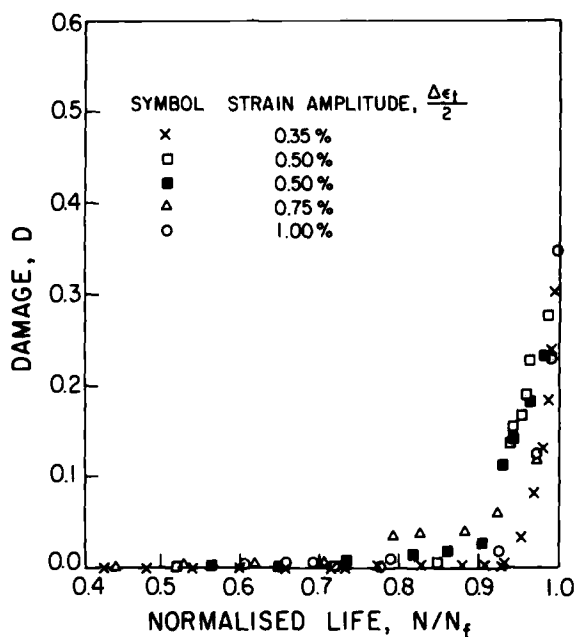


FIG. 7—Plot of damage accumulation obtained from Eq 4, at different life fractions for the strain levels examined.

analytical point of view, the damage evolution is considered to start at approximately $0.6 N_f$. Equation 1 may be modified accordingly [4], resulting in

$$D = 1 - \left(1 - \frac{N - 0.6N_f}{N_f - 0.6N_f} \right)^{1/(1+p)} \quad (6)$$

This equation was fitted to the experimental data by a least-squares fit. The damage coefficient, p , corresponding to the fitted curves is given in Table 4. The damage values over the last 10% of the life dominate the curve fitting process and hence the value of the damage coefficient, p . This is reflected in the highest p value representing the lowest strain level, which accumulates damage very late in life, as just described. In contrast, lower values of p were recorded for strains involving larger amounts of plasticity, which suggests a

TABLE 5—Comparison of damage estimates (total strain amplitude = 1.0%).

Life Fraction, N/N_f	Damage, ($1 - \bar{A}/A$) (Eq 2)	Damage, ($1 - \bar{E}/E$) (Eq 3)	Damage, [$1 - (\bar{A}/A)^{1/2}$] (Eq 4)
0.039	0.000 000	0.013	0.000 000
0.398	0.000 064	0.011	0.000 032
0.522	0.000 289	0.000	0.000 144
0.659	0.009 770	0.014	0.004 897
0.789	0.013 666	0.022	0.006 857
0.925	0.032 725	0.024	0.016 499
0.972	0.232 809	0.231	0.124 106
0.992	0.409 126	0.334	0.231 316

fundamental difference in damage evolution. Furthermore, in these cases the small variance of p suggests that damage is independent of the amount of plasticity present.

Damage Determined from Modulus Changes

Representative hysteresis loops recorded during a typical strain controlled fatigue test are shown in Fig. 5. The apparent tensile modulus decreases, indicating the presence of a crack, while the compressive modulus remains constant throughout the life. Damage, calculated from Eq 3, is plotted in Fig. 6 against normalized life. The same curves derived from Eq 6 and plotted in Fig. 4 are shown superimposed on this plot, indicating good agreement between both methods for estimating damage. Fitting Eq 6 to the experimental data given in Fig. 6 results in the same p values for strain amplitudes of 0.75 and 1.0%. Similar values were obtained using the cracked area method. See Table 4 for comparison.

Assessment of Other Damage Equations

The damage estimated from Eq 4 is shown in Fig. 7. When using this approach, however, the damage estimates were lower than those calculated from Eqs 2 and 3, and a comparison is given in Table 5. These low values may have arisen because of an oversimplified relationship between the stress intensity and the cracked area used in the derivation of Eq 4.

Discussion

The good agreement achieved by applying Eq 1 to the data derived from Eqs 2 and 3 indicates that both the apparent modulus changes and the cracked area measurements are accurate indicators of damage (see Figs. 4 and 6). Of the two, the apparent modulus changes are of greater practical significance because they can be determined more easily, whereas the cracked area method requires nondestructive techniques to find the location of the crack or cracks and to estimate their sizes. Also, the crack profile would have to be known to establish an accurate estimate of damage. Added complications, such as the presence of multiple cracks, are also overcome by the modulus method because of its direct relationship with the cracked area, irrespective of the presence of one or more cracks.

In the present investigation multiple cracking was observed early in the life and at surface crack lengths generally $<200 \mu\text{m}$ in size. Appreciable damage, however, was produced when a surface crack length exceeded about $700 \mu\text{m}$ (Fig. 3) and a dominant crack developed. Knowing that damage is directly related to the cracked area, it follows that the amount of damage is dependent on the crack depth. This relationship is shown in Fig. 8. Thus, in subsequent tests monitored by modulus changes, once damage has been found, the depth of the dominant crack can be estimated and, with this information, ΔJ can be calculated by applying Eq 5. Knowing ΔJ , the crack growth rate can be found using Fig. 9; subsequently, the component life can be estimated.

It can also be concluded from the foregoing discussion that the damage accumulation rate, dD/dN , is directly related to the crack growth rate, da/dN . This relationship is shown in Fig. 9. The damage accumulation rate follows a Paris type of equation, that is

$$\frac{dD}{dN} = C\Delta J^n \quad (7)$$

where C and n are given in Fig. 9. This equation may be integrated to give the life of the component. Thus, life predictions may be made in terms of either crack length or damage, whichever is the more convenient.

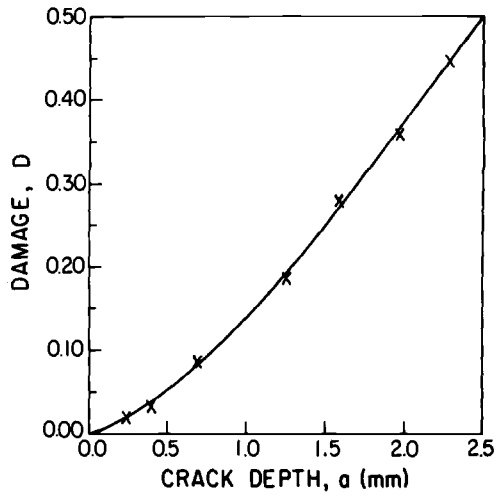


FIG. 8—Relationship between damage and maximum crack depth.

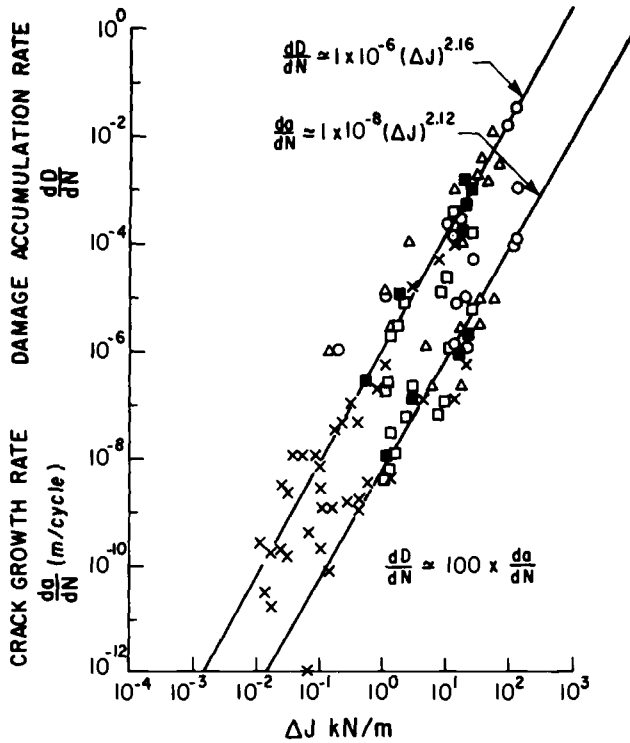


FIG. 9—Relationship between crack growth rate (da/dN), damage accumulation rate (dD/dN) and ΔJ . The symbols for the data points correspond to those in Figs. 4, 6, and 7.

Life predictions may also be made once the damage has been determined for a particular number of cycles in service, N , according to a rearranged version of Eq 6, namely

$$\frac{N}{N_f} = 0.4[1 - (1 - D)^{(1+p)}] + 0.6 \quad (8)$$

The strain level has a bearing on the value of p . For strains within the transition region of the strain life curve and with elastic to plastic strain ratios below approximately 582, damage appears to be independent of the level of plasticity. Hence, a single value of p may be used to describe damage accumulation. The average value of p at these strain levels is 10.5, as shown in Table 4. Thus, once in the transition region, the strain level may be changed and the residual life may be predicted accurately. Accordingly, Miner's rule applies.

Similar deductions may be made from Dowling's work on A533B steel [9], in which the crack length at a given life ratio was found to be independent of the strain level within the transition region of the strain-life curve. As this is also the case for the present work, it is interesting to speculate that at these higher strain levels this effect is due to the initiation of surface cracks early in the fatigue life, indicating that crack propagation is dominant. On the other hand, for low-strain fatigue, initiation becomes dominant [10] and low damage levels are maintained for longer fractions of the life. This is in accord with experimental results in which the specimen subjected to a total strain amplitude of 0.35% spent 88% of its life in Stage I crack growth with a surface crack length below about 700 μm . The corresponding value at a strain amplitude of 0.75% was 0.6 N/N_f . While this may explain why the highest p value has been obtained for the elasticity dominated test, it also suggests that damage at a given life fraction at low strains will be strain dependent since a longer initiation period is required for lower strain levels. Damage accumulation would therefore occur at correspondingly later stages, which would then lead to even higher p values than observed in this work and increasing p values with lower strains. Another possibility for the strain dependence on the damage accumulation rate (hence p value) would be the effect of crack closure, which is important under cyclic conditions dominated by elasticity.

Conclusions

1. Fatigue damage may be assessed with reasonable accuracy by measuring the cracked area or by monitoring the apparent modulus changes over the life of a component. The present work shows good correlation between the two methods.
2. Fatigue damage for a given life fraction is independent of the cyclic strain level within the transition region of the strain-life curve. Miner's rule may be applied under these conditions.
3. Damage accumulates later in the life for elasticity-dominated fatigue in comparison with fatigue within the plasticity-dominated transition region.
4. It is possible to relate damage accumulation rates to crack growth rates through crack profile relationships. The damage accumulation rate is also shown to follow a Paris-type equation.

Acknowledgments

The authors would like to express their thanks to Alcan International Ltd., Kingston, Ontario, for supplying the material used in this work. The Natural Sciences and Engineering Research Council of Canada and GKN Technology are acknowledged for financial support. Thanks are also due to Linda Lingard for assistance with the manuscript.

APPENDIX

Stress and Strain Intensity Derivation

Stress-Intensity Factor, ΔK

The stress-intensity factor for a semielliptical crack in a flat plate is given by Broek [11] as

$$\Delta K = 1.12 M_K \frac{\Delta \sigma}{2} \sqrt{\pi \frac{a}{Q}} \quad (9)$$

where

$\frac{\Delta \sigma}{2}$ = stress amplitude,

a = crack depth,

M_K = Kobayashi's correction for a free surface,

$$Q = \left[\phi^2 - 0.212 \left(\frac{\Delta \sigma}{2\sigma_y} \right)^2 \right]^{1/2},$$

σ_y = yield stress, and

$$\phi = \frac{3\pi}{8} + \frac{\pi}{8} \left(\frac{a}{c} \right)^2.$$

The term a/c is the ratio of the minor to major axis and defines the profile of the crack. As previously mentioned, the crack profile encountered was only very slightly curved. This shape could be closely approximated by assuming a minor-to-major axis ratio of 1:4.

ΔJ -Integral

The method of determining ΔJ is similar to that outlined by Dowling [9], where ΔJ was expressed as

$$\Delta J = \left[1.12 \times \frac{2}{\pi} \right] 2\pi a \left[g(n)\Delta w_e + f(n)\Delta w_p \right] \quad (10)$$

where Δw_e and Δw_p are the elastic and plastic strain energies dissipated during a fatigue cycle, and $g(n)$ and $f(n)$ are functions of the strain hardening exponent, n [12]. The first bracketed term in Eq 10 represents a correction factor for the semicircular profile observed in the work of Dowling [9].

The above equation represents the sum of the elastic and plastic strain intensities, that is

$$\Delta J = \Delta J_{\text{elastic}} + \Delta J_{\text{plastic}} \quad (11)$$

where

$$\Delta J_e = \Delta K^2/E = 2\pi a w_e, \text{ and}$$

$$\Delta J_p = 2\pi a f(n) w_p.$$

Substituting for ΔK from Eq 9 and assuming that the same geometry correction factor

applies to both components, the equation for ΔJ may be expressed as

$$\Delta J = \frac{(1.12)^2}{Q} 2\pi a(g(n)\Delta w_e + f(n)\Delta w_p) \quad (12)$$

The strain-hardening exponent, n , was determined to be equal to 0.1006, from which $f(n) = 1.97$ [12]. The Irwin plastic zone correction factor, $g(n)$, was taken as unity. Using these figures and the relations

$$\Delta w_e = \frac{\Delta \sigma^2}{2E} \quad (13)$$

$$\Delta w_p = \frac{\Delta \sigma \Delta \epsilon_p}{1 + n} \quad (14)$$

ΔJ may be expressed as

$$\Delta J = \frac{3.941}{Q} \Delta \sigma \Delta \epsilon_p a + 14.115 \frac{\Delta \sigma \Delta \epsilon_p a}{Q} \quad (15)$$

References

- [1] Douglas, M. J. and Plumtree, A. in *Fracture Mechanics: Eleventh Conference, ASTM STP 677*, C. W. Smith, Ed., American Society for Testing and Materials, Philadelphia, 1979, p. 68–84.
- [2] Lemaitre, J. and Chaboche, J. L., "A Nonlinear Model of Creep-Fatigue Damage Accumulation and Interaction," *Mechanics of Visco-plastic Media and Bodies*, J. Hult, Ed., Springer Verlag, New York, 1975, pp. 291–301.
- [3] Kachanov, L. M. "On the Time to Failure Under Creep Conditions," *Izvestia Akaddemii Nauk S.S.S.R., Otdelenie Tekhnicheskikh Nauk*, Vol. 8, 1958, pp. 26–31.
- [4] Lemaitre, J. and Chaboche, J. L., *Mecanique des Materiaux Solides*, Dunod, Paris, 1985.
- [5] Lemaitre, J. and Plumtree, A., *Journal of Engineering Materials and Technology*, Vol. 101, July 1979, pp. 284–292.
- [6] Plumtree, A. and Nilsson, J. O., "Mechanics Applied to High Temperature Fatigue Damage," *Proceedings, International Spring Meeting, French Metallurgical Society, Paris, June 1986*, pp. 396–405.
- [7] Plumtree, A. and Lemaitre, J., "Damage Mechanics Applied to High Temperature Fatigue," *Mechanical Behavior of Materials IV*, I. Carlsson and N. G. Ohlson, Eds., Pergamon Press, Oxford, NY, 1984, pp. 323–329.
- [8] Starkey, M. S. and Skelton, R. P., *Fatigue of Engineering Materials and Structures*, Vol. 5, No. 4, 1982, pp. 329–341.
- [9] Dowling, N. E. in *Cracks and Fracture: Ninth Conference, ASTM STP 601*, American Society for Testing and Materials, Philadelphia, 1976, pp. 19–32.
- [10] Manson, S. S., *Experimental Mechanics*, Vol. 5, No. 7, July 1965, pp. 193–226.
- [11] Broek, D. in *Elementary Engineering Fracture Mechanics*, Martinus Nijhoff Publishers, Boston, 1982.
- [12] Shuh, C. F. and Hutchinson, J. W. in *Engineering Materials and Technology, Transactions, American Society of Mechanical Engineers*, October 1976, pp. 289–295.

Fatigue Crack Growth at High Load Ratios in the Time-Dependent Regime

REFERENCE: Nicholas, T. and Ashbaugh, N. E., "Fatigue Crack Growth at High Load Ratios in the Time-Dependent Regime," *Fracture Mechanics: Nineteenth Symposium, ASTM STP 969*, T. A. Cruse, Ed., American Society for Testing and Materials, Philadelphia, 1988, pp. 800-817.

ABSTRACT: Experimental crack growth rates were determined in Inconel 718 middle cracked tension [M(T)] specimens at 649°C under conditions of high frequency (10 to 100 Hz) and high load ratio, R . Under these conditions, the material experiences cycle-dependent crack growth as well as time-dependent crack growth. At very high R values approaching unity, the observed growth rates are lower than those obtained under sustained load at the same mean load in the absence of the superimposed cyclic loading. Tests on compact tension [C(T)] specimens at lower frequencies were used to demonstrate the existence of three regions of behavior—cycle-dependent, mixed mode, and time-dependent.

A linear cumulative damage model was used to predict the growth rates due to combined cycle-dependent and time-dependent mechanisms. The model was developed from 427°C data for the cyclic term and sustained load crack growth data for the time-dependent term. Although the model cannot predict the synergistic effect at high R , it provides a reasonable representation of much of the data. The authors conclude that the use of low-temperature data for the cyclic term is inadequate for representing the threshold values and growth rates at low ΔK values at the higher temperature.

KEY WORDS: fatigue crack growth, elevated temperature fatigue, stress ratio, time-dependent crack growth, nickel-base superalloy, analytical models, fracture mechanics

In the application of a damage tolerance requirement to gas turbine engine components, accurate fatigue crack growth rate predictions are required. In recent years, two aspects of crack growth modeling have received considerable attention. First, time-dependent material behavior has been recognized as a contributor to crack growth at the highest use temperature of some nickel-base superalloys [1,2]. Thus, sustained load or hold-time effects in an engine spectrum have to be considered. Second, detailed mission analysis has indicated that cyclic loading can occur often at very high load ratios, R , the ratio of the minimum to the maximum load in a fatigue cycle [3]. High values of R and maximum load imply a high mean load; thus, the mean load may contribute to crack growth as well as the cyclic load. Accurate modeling of the crack growth rate, particularly at high R and high temperature, is thus demanded for accurate life predictions.

Crack growth rate modeling for turbine engine materials has been performed using a number of interpolative schemes [2,4]. These schemes, developed primarily from data on

¹ Senior scientist, Air Force Wright Aeronautical Laboratories, Wright-Patterson Air Force Base, OH 45433.

² Research scientist, University of Dayton Research Institute, Dayton, OH 45469.

materials where time-dependent behavior was minimal or nonexistent, provide procedures for interpolating among variables in the fatigue cycle which include R , frequency (f), and temperature (T). The stress-intensity range, ΔK , is used as the correlating parameter to account for differences in crack geometries. The interpolative procedures generally involve fitting a functional form of an equation to a crack growth rate curve and writing the coefficients as functions of the variables R , f , and T . This amounts to shifting, rotating, or distorting a crack growth rate curve as a function of the variables. An alternate approach, using an effective stress intensity such as that proposed by Walker [5] amounts to shifting curves along the ΔK axis as a function of R and, perhaps, of T also. In either case, it inherently assumes that crack growth rate is a smoothly varying function of R .

Recent investigations have indicated that at high values of R , crack growth rates do not behave smoothly with changes in R . In studying the influence of low-amplitude, high-frequency cycling (minor cycles) on sustained load or low-cycle fatigue crack growth (major cycles), Petrovich et al. [6] and Goodman and Brown [7], in separate investigations on Inconel 718 at 649°C, have shown that the addition of minor cycles *decreases* the crack growth rate. This effect was observed for low amplitudes of minor cycle loading and, thus, for high R values. Ashbaugh [8], in a study of threshold values in the same material, has also shown that the crack growth behavior undergoes a transition in going from low R , or primarily cyclic loading, to $R = 1.0$, or purely sustained load (no cyclic amplitude).

This investigation was undertaken, therefore, to determine the crack growth rate behavior of a material exhibiting time-dependent behavior at high values of R approaching unity. In addition, the validity of a linear summation model which accounts separately for time-dependent and cycle-dependent behavior, was assessed.

Analytical Model

Rationale

A model for the crack growth behavior would have to produce time-dependent and cycle-dependent contributions at the limits of the regime of application. The crack extensions for those contributions are associated with different growth mechanisms. It does not appear to be feasible, or reasonable, to model crack growth rate behavior with a single smooth function over the entire range of positive R values between 0 and 1. At low R , and particularly at high frequencies, the crack growth behavior is primarily cycle dependent. At the other extreme, as R approaches unity, the crack growth behavior becomes mainly time dependent. In the limit, $R = 1.0$ corresponds mathematically to purely sustained load behavior with zero cyclic amplitude.

A linear summation model is proposed which accounts separately for time-dependent and cycle-dependent contributions to crack growth. This model can, at the least, recover the actual behavior under sustained load ($R = 1.0$) as a limiting case for high R . For very high frequencies and low R , the model can also accurately represent the purely cycle-dependent crack growth behavior [4]. The linear summation model has the following form

$$\frac{da}{dN} = \left(\frac{da}{dN} \right)_{\text{cyc}} + \left(\frac{da}{dN} \right)_{\text{TD}} \quad (1)$$

where $(da/dN)_{\text{cyc}}$ represents the cyclic portion and $(da/dN)_{\text{TD}}$ the time-dependent portion.

Cycle-Dependent Term

The cyclic term in Eq 1 is obtained by curve fitting experimental data at low temperatures as a function of R . A modified sigmoidal equation (MSE) of the form

$$\left(\frac{da}{dN}\right)_{\text{cyc}} = \exp^{B'} \left(\frac{\Delta K}{\Delta K_i}\right)^P \left[\ln\left(\frac{\Delta K}{\Delta K^*}\right)\right]^Q \left[\ln\left(\frac{\Delta K_c}{\Delta K}\right)\right]^D \quad (2)$$

which has been used to represent crack growth rate data in nickel-base superalloys [2,4,9], is used to represent each curve for each value of R for which test data are available. Four parameters, da/dN_i , $(da/dN_i)'$, ΔK_i , and ΔK^* , are used to represent four geometric aspects of each da/dN versus ΔK curve. They are, respectively, the vertical location of the inflection point, the slope at the inflection point, the horizontal location of the inflection point, and the lower vertical asymptote or threshold value. Each parameter P_i , $i = 1$ to 4, is written as

$$P_i = A_i + B_i \log(1 - R) \quad (3)$$

where A_i and B_i , $i = 1$ through 4, are empirically determined constants.

The additional constants in Eq 2 are determined from the following relations [9]

$$\begin{aligned} Q &= -D = \text{constant} = 0.4 \\ \Delta K_c &= \frac{\Delta K_i^2}{\Delta K^*} \\ P &= \left(\frac{da}{dN_i}\right)' - \frac{Q}{\ln\left(\frac{\Delta K_i}{\Delta K^*}\right)} + \frac{D}{\ln\left(\frac{\Delta K_c}{\Delta K_i}\right)} \\ B' &= \ln\left(\frac{da}{dN_i}\right) - Q \ln\left[\ln\left(\frac{\Delta K_i}{\Delta K^*}\right)\right] - D \ln\left[\ln\left(\frac{\Delta K_c}{\Delta K_i}\right)\right] \end{aligned} \quad (4)$$

With the Eqs 2 through 4, the cyclic term of Eq 1 can be evaluated for any value of ΔK and R .

Time-Dependent Term

The time-dependent term is obtained by integrating the crack growth rate, da/dt , over the loading cycle. The crack growth rate is obtained as a function of K under sustained load. In a prior investigation [10], it was demonstrated that low-frequency crack growth could be predicted by integrating da/dt over the loading half of the fatigue cycle only. Using both symmetric and asymmetric triangular waveshapes and low values of R , crack growth rate was uniquely determined by the frequency of the loading portion of the cycle and was independent of the unloading frequency. Further, the numerical value of crack growth rate was accurately determined by integrating sustained-load crack growth rate data.

If this approach is adopted as R approaches unity, the model will break down because only one-half of the sustained-load crack growth rate will be recovered, since da/dt will be integrated only half of the time, that is, over half of the "cycle." It thus becomes apparent that for high R , the integration must ultimately include the entire cycle. Following this

rationale for symmetric triangular loading, the time-dependent term is proposed to have the form

$$\left(\frac{da}{dN}\right)_{TD} = (1 + \alpha) \int_{\text{half}}^{\text{loading}} \frac{da}{dt} dt \quad (5)$$

where α must be one for high R and approaches zero for low R . Since ΔK is smaller for high R than for low R at any fixed value of K_{\max} , α is chosen in the following form

$$\alpha = \begin{cases} 1, & \text{when } \Delta K \leq \Delta K_{th} \\ \exp \left[1 - \frac{\Delta K}{\Delta K_{th}} \right], & \text{when } \Delta K > \Delta K_{th} \end{cases} \quad (6)$$

where ΔK_{th} is the cyclic threshold for a given R . This functional form is arbitrary since there are no data at present to guide its evolution. It does, however, satisfy the requirements that when R approaches unity—that is, ΔK approaches zero— $\alpha = 1$ and that the integration is performed over the entire cycle. The physical reasoning behind the use of ΔK_{th} as a transition value could be that for $\Delta K \leq \Delta K_{th}$, the cyclic behavior ahead of the crack tip is essentially elastic and stress versus strain is linear on unloading as well as loading. The contribution of the unloading part of the cycle should, therefore, be approximately equivalent to that of the loading portion of the cycle.

For $\Delta K \geq \Delta K_{th}$, it is assumed that there is energy dissipation ahead of the crack tip and, further, that the stress-strain behavior will exhibit a measurable hysteresis loop. If it is further assumed that this behavior occurs under more or less fixed strain limits and that the sustained load crack growth is governed by the local stresses, then one can argue that during the loading portion of the cycle, most of the time is spent near maximum stress, while during the unloading portion, most of the time is spent at minimum stress. If this is the case, the unloading portion of the cycle will contribute significantly less to the time-dependent crack growth than the loading portion when ΔK exceeds ΔK_{th} .

Experimental Procedure

Specimens and Material

The crack growth rate data were generated from middle cracked tension [M(T)] and compact tension [C(T)] specimens of a nickel-base superalloy, Inconel 718. The composition and heat treatment of the material are given in Tables 1a and 1b. The M(T) specimens tested were machined from rolled sheet, nominally 2.4 mm thick. The width of the M(T) specimens was 50.5 mm and the total length was 216 mm. They were loaded through grips attached with pins through a triangular hole pattern at each end of the specimen. The C(T) specimens had a width, W , of 40 mm and a thickness of 10 mm. They were machined from plate material and have the standard compact geometry indicated in the ASTM Test for Constant-Load-Amplitude Fatigue Crack Growth Rates Above 10^{-8} m/Cycle (E 647-86).

Test Procedures

The data used in this investigation are a combination of data acquired from two parallel projects conducted in the authors' laboratory and data generated to resolve the objectives of this research effort. The tests for one of the two earlier projects were conducted under

TABLE 1a—Chemical composition of Inconel 718, in weight percent.

Ni	Cr	Fe	Nb + Ta	Mo	Ti	Al	Co	C	Mn	Si	Cu	Ph	S	B
50 to 55	17 to 21	balance	4.75 to 5.5	2.8 to 3.3	0.65 to 1.15	0.2 to 0.8	<1	<0.08	<0.35	<0.35	<0.30	<0.015	<0.015	<0.006

TABLE 1b—Heat treatment of Inconel 718.

Anneal at 968°C (1775°F) for 1 h then air cool to 718°C (1325°F).

Age harden at 718°C (1325°F) for 8 h and furnace cool at 55.5°C (100°F)/h to 621°C (1150°F).

Age harden at 621°C (1150°F) for a total aging time of 18 h.

Air cool to room temperature.

constant-load amplitude with M(T) specimens, and the tests for the second project were conducted under constant stress-intensity amplitude with C(T) specimens.

Most of the tests for the current effort were conducted under decreasing stress-intensity conditions on M(T) specimens. The remainder of the tests were conducted under constant-load amplitude (increasing stress intensity). In all, three different test systems were used to generate the data. Microcomputers were used to control and to acquire data on all of the test systems. The test procedures for the three different test systems are presented in the following discussion.

Load Shedding Tests at 10 Hz—To generate near-threshold fatigue crack growth rate (FCGR) data for R from 0.1 to 0.9 at 10 Hz and 649°C, tests were conducted on a computer-controlled servohydraulic test system using a sinusoidal waveform. This same test system had also been used to produce the baseline data at 427°C and the low-frequency (0.01 Hz) data at 649°C for the MSE model [11]. In that investigation, it was determined that material behavior was purely cycle-dependent at temperatures up to 427°C.

The temperature of the specimens was maintained with high-intensity lamps. The crack length was determined by a d-c electric potential technique. Optical measurements were also periodically taken of the crack lengths. Although the electric potential technique had been quite successful in determining crack lengths under constant-load and constant stress-intensity conditions, the technique did not always yield a crack growth trend consistent with optical measurements during threshold testing. The deviation in crack lengths was never large enough to create significant errors in the data to necessitate a correction in the data reduction.

The maximum load for the near-threshold tests was shed during crack extension to yield an exponentially decreasing stress-intensity factor

$$K_{\max} = K_o \exp [-0.08(a - a_o)]$$

where K_o and a_o are a reference stress-intensity factor and a reference crack length with units in millimetres. The K_o was chosen so that the FCGR data from the near-threshold tests would overlap the data obtained under constant-load amplitude. In all cases, the data were in good agreement within the overlapped region.

In many near-threshold tests, the crack length on one side of the specimen center-line would continue to grow after the crack length on the other side had stopped propagating. The uneven growth at the two crack fronts could not be attributed to misalignment of the load train since no particular side continued to grow under repeated test conditions on different specimens. Also, growth at a specific crack front was not noted when test conditions were repeated on a specimen in which the crack lengths had been "equalized" after a previous test. To equalize the crack lengths in the M(T) specimens, the load would be introduced eccentrically on the side of the specimen with the shorter crack length. After the cracks had grown to approximately the same lengths, a symmetric load distribution would be applied and each crack tip would be extended 0.25 to 0.50 mm to produce self-similar near-tip conditions for the next phase of the test.

Crack closure is postulated to have a strong influence in causing the uneven crack growth. Unfortunately, no closure measurements could be conveniently made in these tests. Subsequent tests are planned on C(T) specimens to generate data for comparison with the data from M(T) specimens.

Constant-Load Amplitude and Load Shedding Tests at 100 Hz—The FCGR tests for the various R values at 100 Hz and 649°C were conducted in a specially developed test system, described in detail in Ref 7. The test system is a combination of a pneumatic chamber and

an electromagnetic shaker which, by judicious design, can achieve high-frequency sinusoidal loading conditions under nonzero mean load. The temperature was maintained with a resistance furnace.

A microcomputer provided control of the tests. The crack lengths were determined by an a-c electric potential system. Optical measurements were also made periodically during the test. Problems during the near-threshold phase with electrical potential and uneven crack growth also occurred in these tests.

Constant Stress-Intensity Tests at Lower Frequencies—The FCGR data obtained from C(T) specimens at frequencies below 10 Hz had been produced under constant stress-intensity conditions with a microcomputer-controlled test system. Crack length was determined from compliance measurements of crack-mouth opening displacement (CMOD). The specimen was maintained at 649°C in a resistance-heated furnace while an extensometer with quartz rods, which passed through the furnace wall, was used to determine CMOD. Data obtained under these conditions, as well as additional details of the test procedure, have been previously documented in Ref 10. A triangular waveform was used for this series of tests.

Results and Discussion

A typical set of experimental data is presented in Fig. 1 for the case $R = 0.9$ at 649°C and 100 Hz. These particular data were obtained from a combination of threshold test and constant load range tests. A single line drawn through the data is used to represent each data set. The line representations are presented for subsequent data sets for the sake of clarity, with only a few exceptions.

Crack growth rate data obtained at 427°C at 10 Hz for the cyclic term in the model are represented by the lines in Fig. 2, which also represent the analytical fits for the three values of R . The interpolative model is used to match the data over the entire growth rate regime. The analytical expressions for the four parameters used in the MSE equations follow.

$$\log \Delta K^* = 1.0886 + 1.0312 \log (1 - R)$$

$$\log \frac{da}{dN_i} = -6.2244 + 0.7690 \log (1 - R)$$

$$\log \Delta K_i = 1.6299 + 0.6068 \log (1 - R)$$

$$\left(\frac{da}{dN_i} \right)' = 3.5896 + 1.9587 \log (1 - R)$$

These equations are valid for values of $R < 0.5$. For $R > 0.5$, the value calculated for $R = 0.5$ is used. This provides the best overall fit to the experimental data. The dependence on R is attributed to closure, which dominates at low values of R . In these equations, crack growth rate is in units of metres per cycle while ΔK is in $\text{MPa m}^{1/2}$.

The sustained-load crack growth data at the test temperature of 649°C are presented in Fig. 3 and represent the results of a large number of tests. None of these tests involved growth rates near threshold. The apparent threshold in the data is a result of an initial transient which has been observed in sustained load testing on this and other nickel-base superalloys [12]. The value of threshold was iterated in fitting low-frequency test data. The analytical fit, shown as a solid line, reflects the fit to the data and a best estimate of what is felt to be the true threshold for this material ($K = 19.0 \text{ MPa m}^{1/2}$) [11].

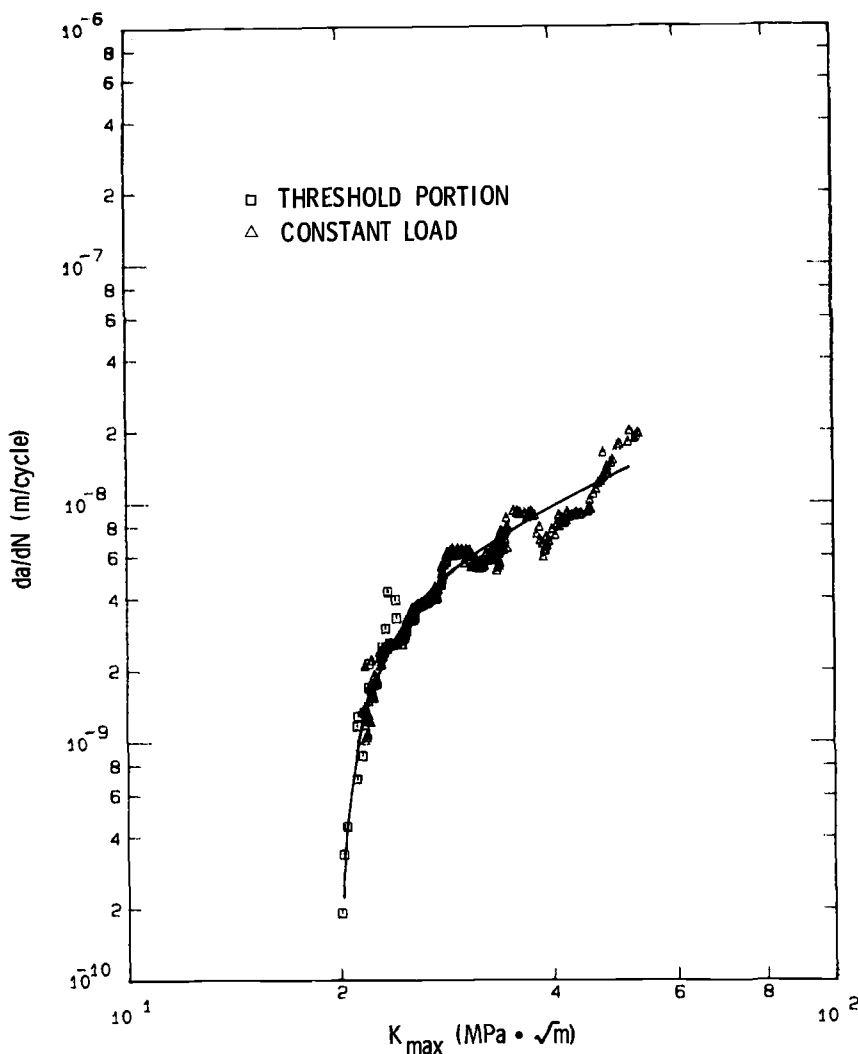


FIG. 1—Typical experimental data obtained at 649°C at $R = 0.9$ and 100 Hz. The solid line is used to represent the data set.

The linear summation model was first applied to the 649°C experimental data obtained at a frequency of 0.01 Hz. At this low frequency, the behavior is essentially time dependent and the ability to fit the data is a test of the accuracy of the time-dependent term in the model. The results, for R values of 0.1 and 0.5 are presented in Fig. 4. The solid lines, which represent the analytical predictions, are shown to fit the data quite well. The calculations were also carried out neglecting the cyclic term in the model, and no significant difference could be noted in the plot.

The experimental results for crack growth at 649°C at various values of R at frequencies of 10 and 100 Hz are summarized in Figs. 5 and 6 using single line representation. Shown also in these plots is a single line which represents both the data and the model for the

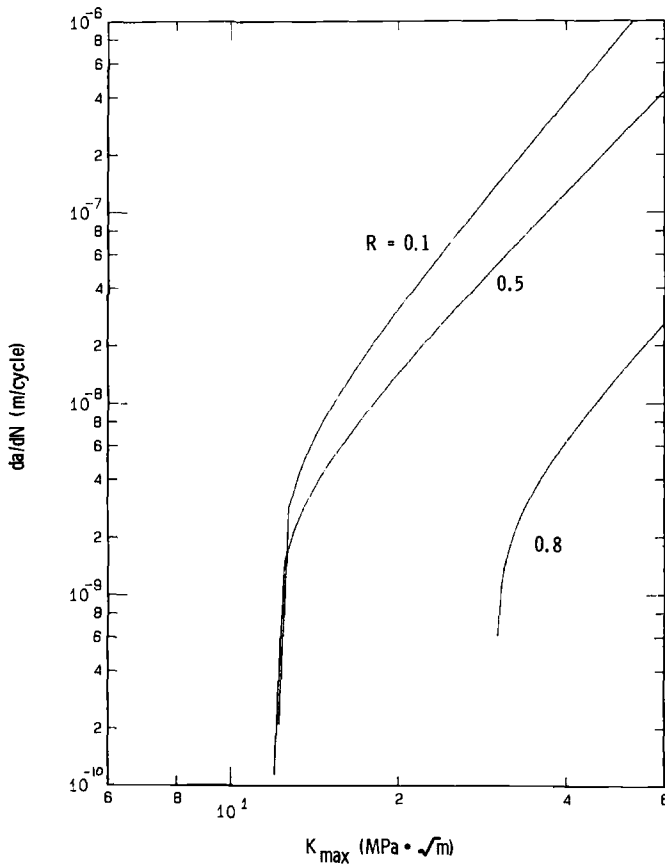


FIG. 2—Crack growth rate data at 427°C at various R for the cycle-dependent term.

limiting case of $R = 1.0$ (see Fig. 3). This corresponds to purely sustained load behavior and is converted into a growth rate per cycle by dividing da/dt by the frequency. At both 10 and 100 Hz, the data follow an orderly trend with increasing R except when going from the highest R tested (0.8 at 10 Hz, 0.9 at 100 Hz) to $R = 1.0$. In both cases, both the location of the $R = 1.0$ curve and its slope appear to be inconsistent with the remainder of the data. This is particularly noticeable in Fig. 6 for the 100 Hz data, where the trend passes through a significant inflection at any constant value of K_{\max} , particularly at higher levels of K , when going from $R = 0.8$ to 0.9 to 1.0.

Comparisons of the model predictions with the experimental data are presented in Figs. 7 and 8 for 10 and 100 Hz, respectively. The data are represented by the dashed lines, which are drawn solid in Figs. 5 and 6. The analytical predictions (Figs. 7 and 8) are shown as solid lines. Two points are quite evident from the two figures. First, the data at the highest R in each case lie below the analytical predictions. Second, the slopes of the experimental data in the Paris regime are lower than those predicted by the model for all values of R . One possible explanation is a mixed-mode effect which is not addressed in the linear summation model. The mixed-mode effect, which is discussed later, provides crack growth rates higher than those attributed to the simple addition of time-dependent and cycle-dependent contributions. The apparent mixed-mode effect appears to increase in going from higher to lower values of K .

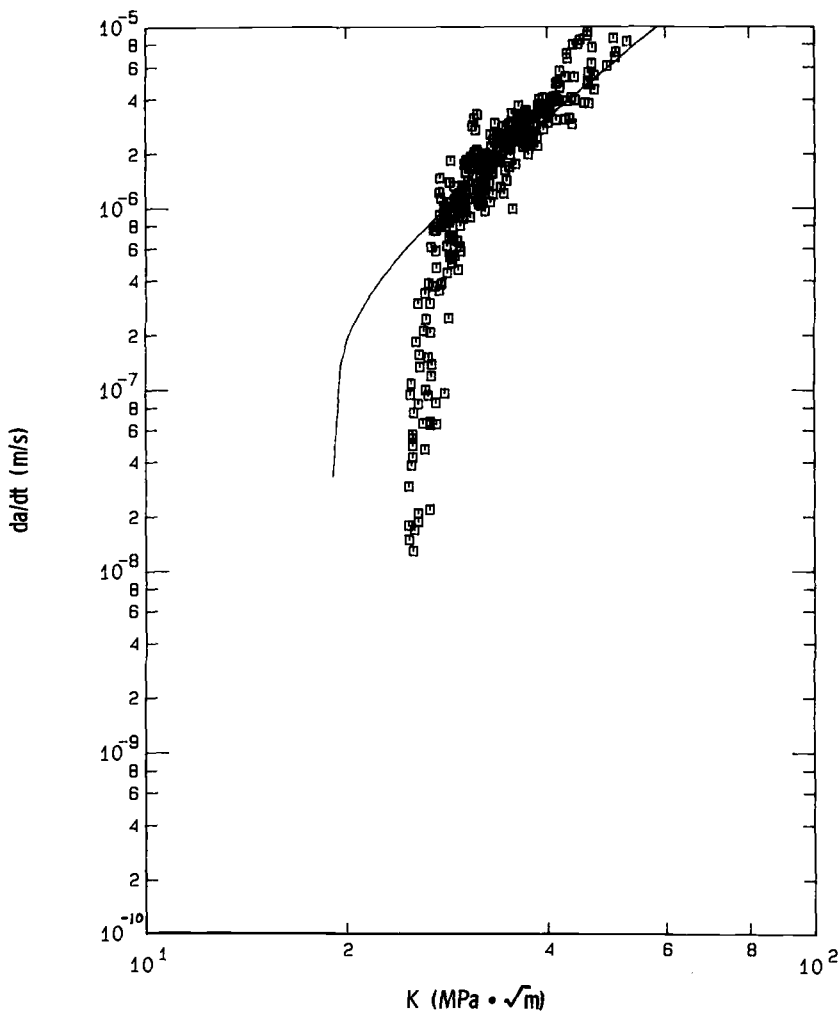


FIG. 3—Sustained-load crack growth rate data at 649°C along with the analytical fit. The threshold in the model was obtained from other data.

Another observation in Figs. 7 and 8 is the lack of correlation between the experimental and predicted values of the threshold stress intensity. The experimental threshold values lie above the analytical predictions for low values of R between 0.1 and 0.6. In addition, the threshold values for these low values of R are all below the sustained-load or purely time-dependent threshold. This indicates that the threshold values for the cycle-dependent term, which are determined from low-temperature (427°C) data, are too low.³ Thus, the cycle-dependent behavior at 649°C is not identical to the cycle-dependent behavior at 427°C.

In going to a higher temperature, it appears both that the threshold values increase and that the growth rates increase, particularly at lower ΔK values. The first effect could be due to increased closure levels due to oxides; however, no closure measurements were made in

³ Subsequent threshold tests have indicated that the thresholds at 427°C are even *lower* than those reported in this paper.

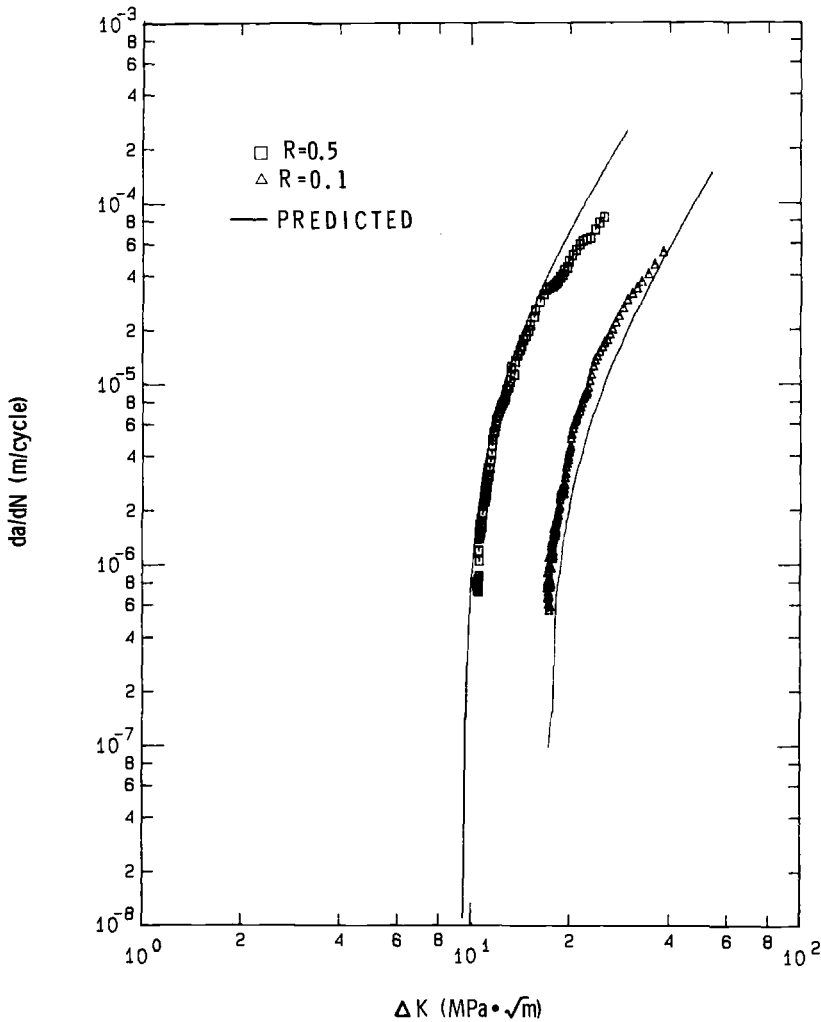


FIG. 4—Low-frequency (0.01 Hz) data at 649°C along with the linear summation model prediction.

this investigation to confirm this effect. The second effect appears to be an effect due to environmental degradation, whereby the crack growth rate increases more at lower ΔK values, where more time is available for environmental effects to occur. This latter postulate is validated by fractographic examination, which shows a purely transgranular mode at low values of ΔK at 427°C but an intergranular fracture at 649°C, even at values of R as low as 0.1 [13].

The data of Figs. 7 and 8 can be replotted as da/dt versus R for a fixed value of K_{\max} . Choosing $K_{\max} = 30$ MPa $m^{1/2}$ as a value which most of the test cases covered, the data are presented in Fig. 9 for the two frequencies, 10 and 100 Hz. The data point representing $R = 1.0$ is the sustained load crack growth rate at the value of $K = 30$ MPa $m^{1/2}$. For purely time-dependent behavior, the curves at the two frequencies would be identical since crack growth is plotted per unit of time. For purely cycle-dependent behavior, the two curves

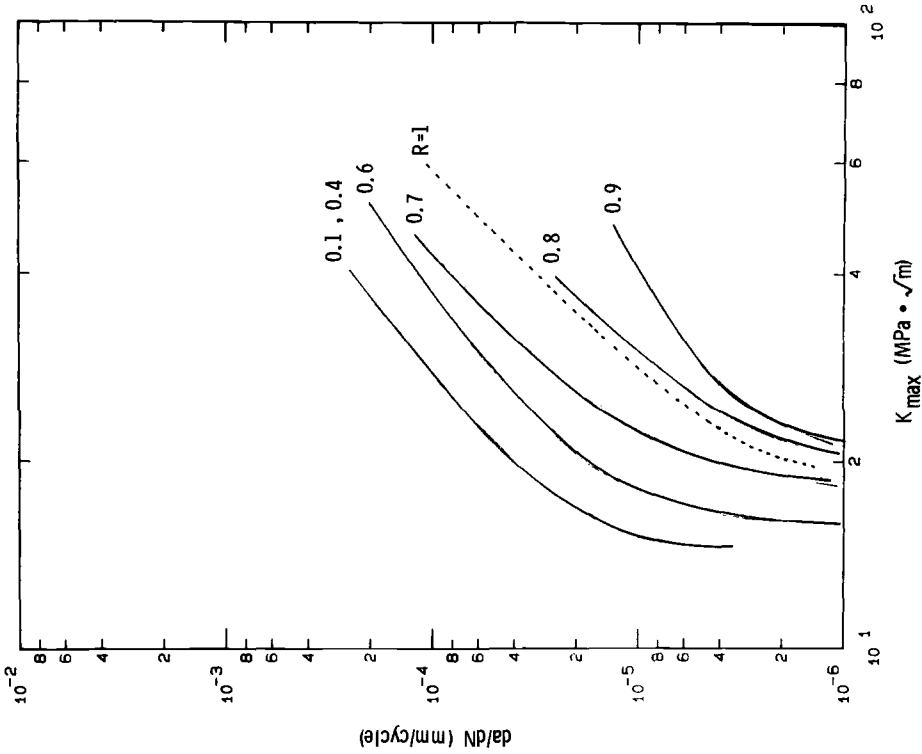


FIG. 6—Crack growth rate data at a frequency of 100 Hz.

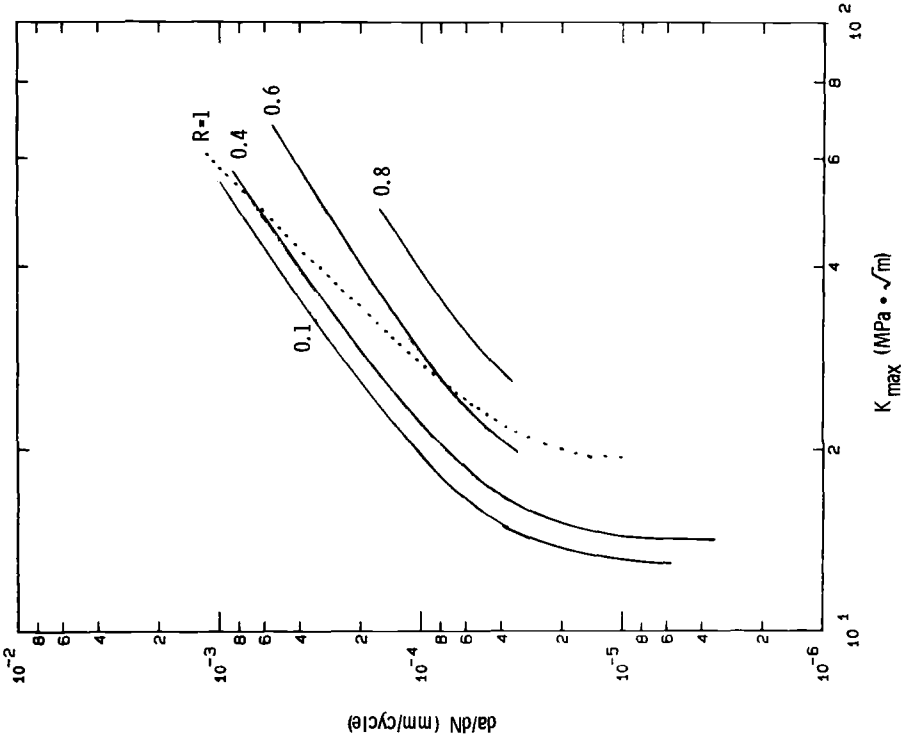


FIG. 5—Crack growth rate data at a frequency of 10 Hz.

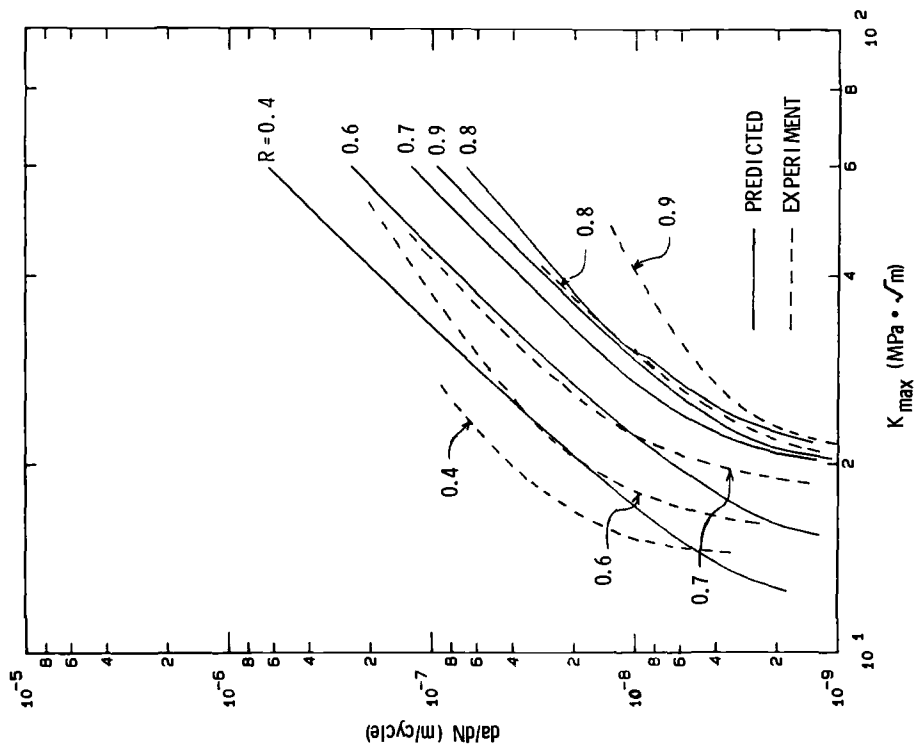


FIG. 8—Comparison of analytical predictions and experimental data at 100 Hz.

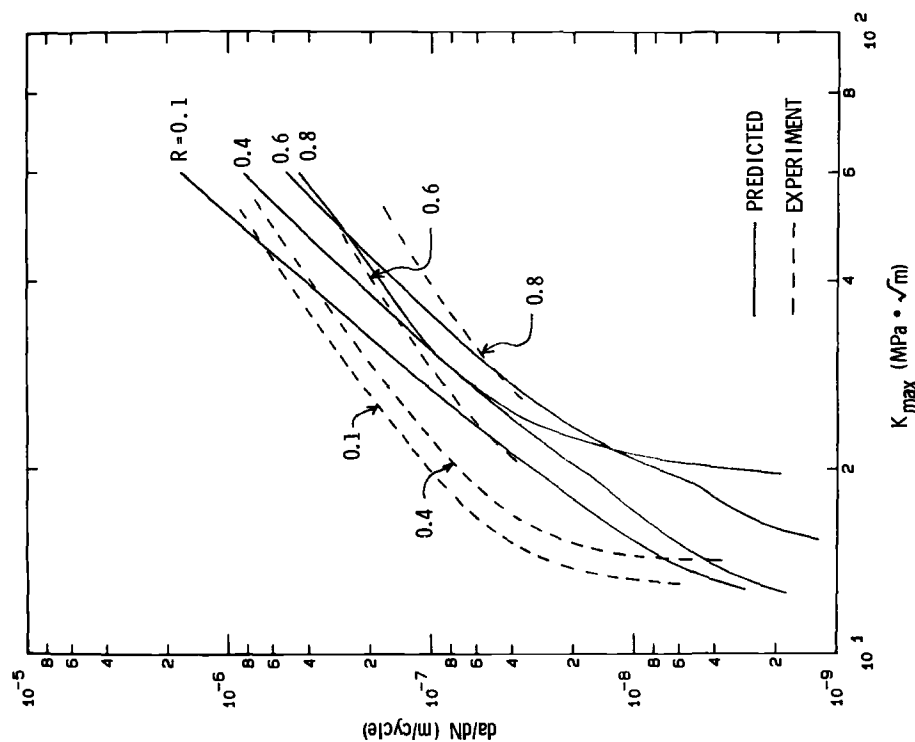


FIG. 7—Comparison of analytical predictions and experimental data at 10 Hz.

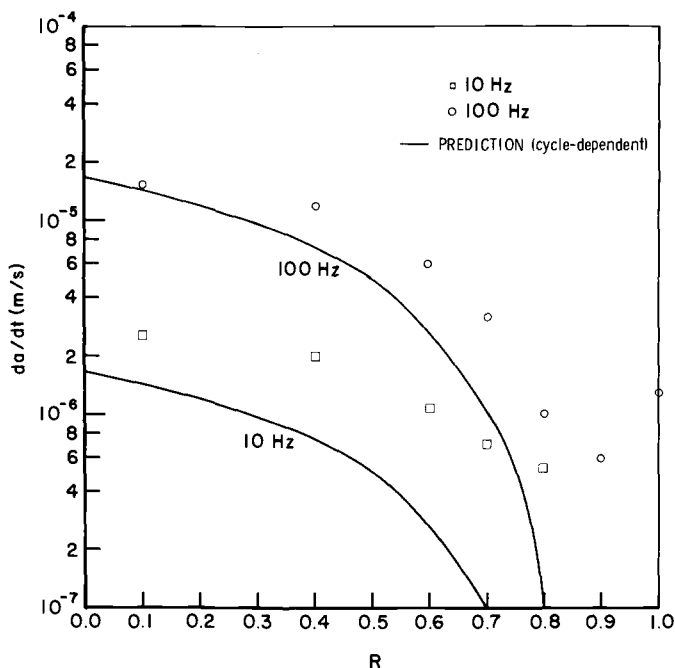


FIG. 9—Crack growth rate, da/dt , as a function of R for a fixed value of $K_{max} = 30 \text{ MPa m}^{1/2}$.

would be separated by a factor of ten. The analytical predictions for cycle-dependent behavior are shown for comparison.

For the particular value of K_{max} chosen and for low values of R , the curves are separated by approximately a factor of six. At 100 Hz, the behavior is almost purely cycle-dependent at $R = 0.1$. As R increases, the curves converge. At $R = 0.8$, for example, the curves differ by less than a factor of two and are both considerably higher than the cyclic predictions. The lack of coincidence of the curves at $R = 0.8$ ($\Delta K = 6 \text{ MPa m}^{1/2}$) indicates that a cyclic contribution is still present at 100 Hz. This is expected since the cyclic threshold was found to be $\Delta K_{th} = 4.3 \text{ MPa m}^{1/2}$ at 427°C , even though the model does not predict the correct extent of the cyclic contribution.

Both curves of Fig. 9 show the inflection point at high R going from cycling to purely sustained load. There appears to be a minimum crack growth rate at a value of R somewhere near 0.9 at 100 Hz. This suggests that if a low-amplitude cyclic load of one tenth the magnitude of a sustained load is superimposed on the sustained load, the net result will be a decrease in growth rate below that of the sustained load itself. This apparent retardation effect is consistent with the observations of Petrovich et al. [6] and Goodman and Brown [7] in the same material.

Data from a second series of tests at lower frequencies using C(T) specimens are presented in Fig. 10. These data were obtained under constant K conditions at a maximum value of $K = 40 \text{ MPa m}^{1/2}$. These data, plotted as a function of frequency, illustrate the mixed-mode behavior previously mentioned. At $R = 0.1$, at frequencies below 0.01 Hz, the data follow a line having a slope of -1 . This implies purely time-dependent behavior since decreasing frequency by a factor of ten will result in an increase in growth rate per cycle by a factor of ten.

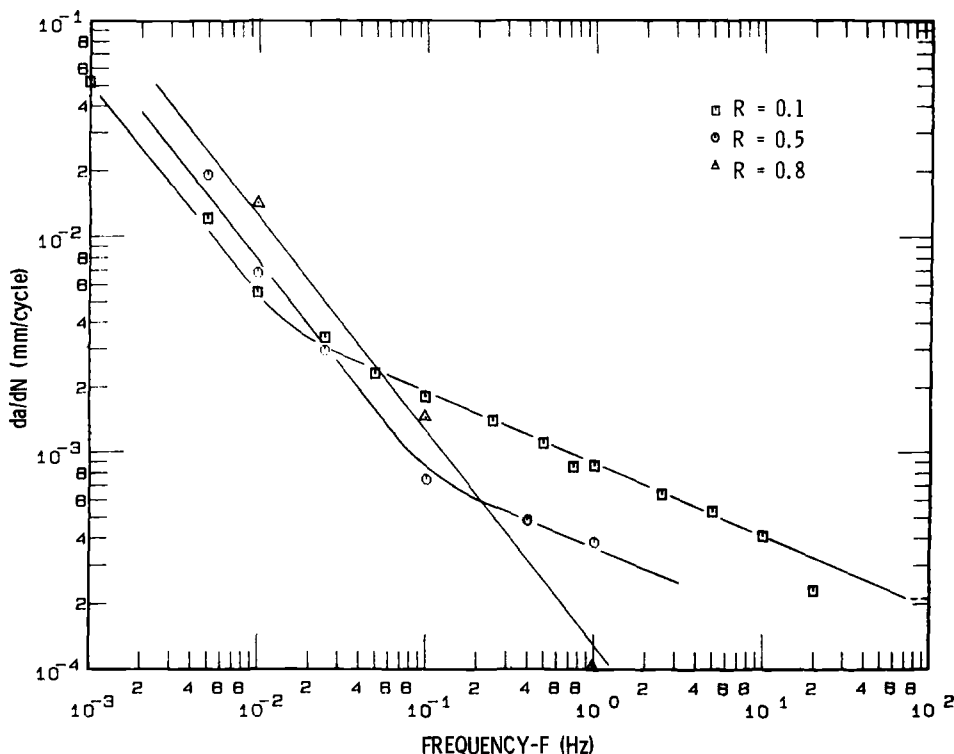


FIG. 10—Crack growth rate as a function of frequency for the C(T) specimen. $K_{max} = 40 \text{ MPa m}^{1/2}$.

At higher frequencies (see dashed line) the growth rate per cycle is expected to become constant, indicating purely cycle-dependent behavior. Between the two extremes, there is a region of mixed-mode behavior where the growth rate is higher than the sum of the two individual contributions. From the data of Fig. 10, at $R = 0.1$ and a frequency of 0.1 Hz, for example, the mixed-mode growth rate appears to be higher than either purely cycle-dependent or time-dependent behavior by over a factor of four. As R is increased, the frequency regime of mixed-mode behavior changes. At $R = 0.5$, for example, Fig. 10 shows the mixed-mode region to be above 0.1 Hz. At $R = 0.8$, the mixed-mode region is beyond the frequency range of the experimental data (1 Hz).

Using the same type of frequency plot, the data from the M(T) specimens, primarily at 10 and 100 Hz, are presented in Fig. 11. Since the material product form was different for the M(T) and C(T) specimens, different growth rates and transition frequencies are obtained. The line representing purely time-dependent behavior ($R = 1.0$) is shown for comparative purposes. The lines connecting the data points are drawn assuming that (a) all data can be represented by a combination of three lines for purely time-dependent, mixed-mode, and cycle-dependent behavior; (b) the slope of the mixed-mode line is the same as that in Fig. 10 for the C(T) data; and (c) purely cycle-dependent behavior can be determined for very high frequencies from the 427°C data at 10 Hz.

The data show quite clearly, for values of R between 0.1 and 0.6, that the behavior is a mixed-mode one in the frequency range covered (10 to 100 Hz). For $R = 0.8$, the behavior would appear to be in transition from purely time-dependent to mixed-mode behavior at

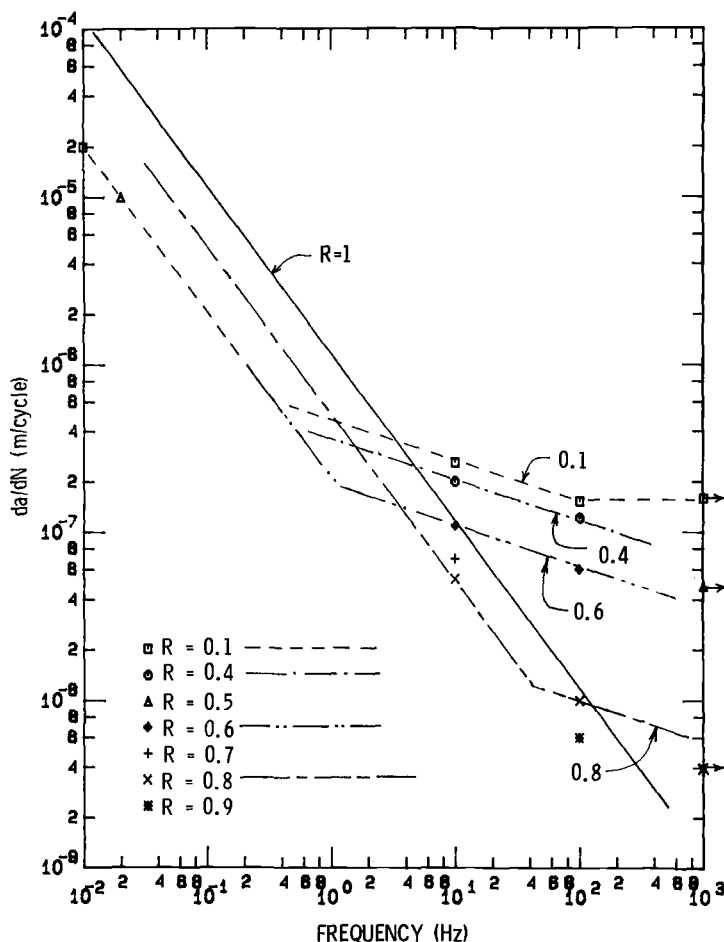


FIG. 11—Crack growth rate as a function of frequency for $M(T)$ specimens. $K_{\max} = 30 \text{ MPa m}^{1/2}$.

somewhere between 10 and 100 Hz. The data also show that at 100 Hz and $R = 0.1$, the behavior should be almost purely cycle-dependent. At $R = 0.4$ and $R = 0.6$, the behavior appears to be a mixed-mode one. Referring back to Fig. 8, the data at $R = 0.4$ and 0.6 appear above the analytical prediction at $K_{\max} = 30 \text{ MPa m}^{1/2}$. It would appear that a mixed-mode term or correction factor would be required to improve the model prediction.

Conclusions

A linear summation model which separates fatigue crack growth into cycle-dependent and time-dependent components has achieved limited success in modeling crack growth behavior at high R values and high frequencies in Inconel 718 at 649°C . Two types of interactions are observed experimentally which cannot be handled by the model. In one case, primarily for lower values of R , a mixed-mode behavior is observed, in which the observed crack growth rate is considerably higher than that predicted by the model. This is particularly true at lower values of ΔK . In the second case, for high values of R approaching

unity, the observed growth rate is lower than that predicted by the model. In this latter case, the superposition of a low-amplitude, high-frequency cyclic load on a high mean load retards the sustained load crack growth rate.

The use of low-temperature (427°C) data where behavior is exclusively cycle dependent appears to be inadequate to model the cycle-dependent behavior at a higher temperature (649°C), where time-dependent behavior or environmental effects or both are present. First, the cyclic threshold values appear to be higher at the higher temperature, which may be due to oxide-induced closure. Second, the growth rates at low values of ΔK appear to be higher, an effect attributed to environmental factors. Because of the difficulty in separating cycle-dependent from time-dependent effects at elevated temperature, particularly at high values of R , it is difficult to determine the purely cycle-dependent behavior by itself. If low-temperature data are used to establish the cycle-dependent term, the cyclic model has to be adjusted to compensate for environmental effects.

Acknowledgments

This work was supported by the U.S. Air Force under Project 2302 and was conducted at the Air Force Materials Laboratory under in-house Task 2302P1 and under Contract No. F33615-84-C-5051 with the University of Dayton Research Institute (UDRI). The authors would like to express their appreciation to Richard Goodman and David Johnson of UDRI for their invaluable assistance in the experimental phase of the program, to Dr. Tustit Weerasooriya for his comments during preparation of the paper, and to Major M. L. Heil for graciously providing data from his doctoral thesis project.

References

- [1] Nicholas, T. and Weerasooriya, T., "Hold-Time Effects in Elevated Temperature Fatigue Crack Propagation," *Fracture Mechanics: Seventeenth Volume, ASTM STP 905*, American Society for Testing and Materials, Philadelphia, 1986, pp. 155-168.
- [2] Larsen, J. M. and Nicholas, T., "Cumulative-Damage Modeling of Fatigue Crack Growth in Turbine Engine Materials," *Engineering Fracture Mechanics*, Vol. 22, 1985, pp. 713-730.
- [3] Nicholas, T., Laflen, J. H., and Van Stone, R. H., "A Damage Tolerant Design Approach to Turbine Engine Life Prediction," *Proceedings: Conference on Life Prediction for High-Temperature Gas Turbine Materials*, EPRI AP-4477, Electric Power Research Institute, Palo Alto, CA, April 1986, pp. 4-1-4-27.
- [4] Nicholas, T., Haritos, G. K., and Christoff, J. R., "Evaluation of Cumulative Damage Models for Fatigue Crack Growth in an Aircraft Engine Alloy," *Journal of Propulsion and Power*, Vol. 1, 1985, pp. 131-136.
- [5] Walker, K., "The Effect of Stress Ratio During Crack Propagation and Fatigue for 2024-T3 and 7075-T6 Aluminum," *Effects of Environmental and Complex Load History on Fatigue Life, ASTM STP 462*, American Society for Testing and Materials, Philadelphia, 1970, pp. 1-14.
- [6] Petrovich, A., Bessler, W., and Ziegler, W., "Interaction Effect of High and Low Frequency Loading on the Fatigue Crack Growth of Inconel 718," *Fracture Mechanics: Seventeenth Volume, ASTM STP 905*, American Society for Testing and Materials, Philadelphia, 1986, pp. 169-184.
- [7] Goodman, R. C. and Brown, A. M., "High Frequency Fatigue of Turbine Blade Material," AFWAL-TR-82-4151, Air Force Wright Aeronautical Laboratories, Air Force Materials Laboratory, Wright-Patterson Air Force Base, OH, October 1982.
- [8] Ashbaugh, N. E., "Time-Dependent and Cycle-Dependent Threshold Evaluation in a Nickel-Base Superalloy," *Proceedings, 18th National Symposium on Fracture Mechanics*, Boulder, CO, 24-27 June 1985.
- [9] Utah, D. A., "Crack Growth Modeling in an Advanced Powder Metallurgy Alloy," AFWAL-TR-80-4098, Air Force Wright Aeronautical Laboratories, Air Force Materials Laboratory, Wright-Patterson Air Force Base, OH, 1980.
- [10] Nicholas, T., Weerasooriya, T., and Ashbaugh, N. E., "A Model for Creep/Fatigue Interactions

- in Alloy 718," *Fracture Mechanics: Sixteenth Symposium, ASTM STP 868*, American Society for Testing and Materials, Philadelphia, 1985, pp. 167–180.
- [11] Heil, M. L., "Crack Growth in Alloy 718 Under Thermal-Mechanical Cycling," Ph.D. dissertation, Air Force Institute of Technology, Wright-Patterson Air Force Base, OH, 1986.
- [12] Ashbaugh, N. E., "Effect of Through-the-Thickness Stress Distribution Upon Crack Growth Behavior in a Nickel-Base Superalloy," *Fracture Mechanics: Fourteenth Symposium, Vol. II; Testing and Applications, ASTM STP 791*, American Society for Testing and Materials, Philadelphia, 1983, pp. II-517–II-535.
- [13] Venkataraman, S., Nicholas, T., and Ashbaugh, N. E., "Micromechanisms of Major/Minor Cycle Fatigue on Crack Growth in Inconel 718," *Fractography of Modern Engineering Materials: Composites and Metals, ASTM STP 948*, American Society for Testing and Materials, Philadelphia, 1987, pp. 383–399.

Threshold and Nonpropagation of Fatigue Cracks Under Service Loading

REFERENCE: Castro, D. E., Marci, G., and Munz, D., "Threshold and Nonpropagation of Fatigue Cracks Under Service Loading," *Fracture Mechanics: Nineteenth Symposium, ASTM STP 969*, T. A. Cruse, Ed., American Society for Testing and Materials, Philadelphia, 1988, pp. 818–829.

ABSTRACT: New testing conditions for determination of fatigue threshold and a new interpretation of this parameter make it amenable to general fatigue life design. To distinguish between the terms, the conditions for nonpropagating fatigue cracks were called the *fatigue tolerance range* and denoted as ΔK_T . The conditions for nonpropagating fatigue cracks were investigated on Inconel 617 alloy in the range of K_{\max} between 10 to 50 MPa m^{1/2} under four different types of fatigue loading conditions. It was found that ΔK_T decreases with increasing K_{\max} . Furthermore, ΔK_T decreases with increasing prior amplitude, ΔK_{pr} , up to a certain amplitude, ΔK_s , at which the effect of prior amplitudes reaches saturation. For Inconel 617 alloy, ΔK_s is between 5 and 7 MPa m^{1/2} at $K_{\max} = 10$ MPa m^{1/2} and approximately 5 MPa m^{1/2} at $K_{\max} = 35$ MPa m^{1/2}. The test result on saturation behavior at $K_{\max} = 10$ MPa m^{1/2} suggests an influence of closure on the effects of prior amplitudes. The results are explained by differing *damage states* in the near region of the crack front introduced by K_{\max} and ΔK of the prior fatigue cycles.

KEY WORDS: fatigue threshold, fatigue tolerance range, closure, spectrum loading, history effects, fatigue process zone, life prediction, fracture mechanics

Nomenclature

σ_{\max}	Maximum stress of a cycle
σ_{\min}	Minimum stress of a cycle
K_{\max}	Maximum stress-intensity factor of a cycle
K_{\min}	Minimum stress-intensity factor of a cycle
$R = \sigma_{\min}/\sigma_{\max} = K_{\min}/K_{\max}$	Load or stress ratio
$\Delta K = K_{\max} - K_{\min}$	Stress-intensity range ³
ΔK_{th}	Threshold stress-intensity range determined as the lower end of a da/dN versus ΔK curve
K_{op}	Stress-intensity factor at which a fatigue crack opens; above K_{op} the crack front experiences a tensile loading
$\Delta K_T = K_{\max} - K_{\min}$	Stress-intensity range which does not produce fatigue crack growth, but is completely in that part of the loading cycles where $K_{\min} > K_{op}$
ΔK_T	Fatigue tolerance range

¹ Graduate student, and branch head, respectively, Deutsche Forschungs- und Versuchsanstalt für Luft- und Raumfahrt (DFVLR), D 5000 Köln 90, West Germany.

² Professor, University of Karlsruhe, D 7500 Karlsruhe, West Germany.

³ In this paper, the word amplitude refers exclusively to the stress-intensity range.

- ΔK_{pr} Stress-intensity range applied immediately prior to establishing ΔK_T
- $K_{max,pr}$ Maximum stress-intensity factor applied immediately prior to establishing ΔK_T
- ΔK_S Prior stress-intensity range at which the effect of prior amplitudes reaches saturation

The parameter fatigue threshold, ΔK_{th} , as experimentally determined at present and conceptually used in design, is of limited applicability to structural life estimation under general service loading. Usually the fatigue threshold, ΔK_{th} , is measured as a lower end of a $da/dN - \Delta K$ plot, where fatigue crack propagation ceases. In these tests, ΔK is altered gradually to avoid any transition effects. Plotting these test results versus the load ratio, R , leads to the commonly known R dependence of ΔK_{th} . Schmidt and Paris [1] proposed subtracting from ΔK_{th} that part of ΔK_{th} during which the crack stays closed. Applying this proposal to the measured ΔK_{th} values means that, for all R -ratios for which $K_{min} < K_{open}$, the ΔK_{th} values have to be reduced, that is

$$\Delta K_T = \Delta K_{th} - (K_{open} - K_{min}) \quad (1)$$

For K_{min} larger than K_{op} , ΔK_{th} is equivalent to ΔK_T . Usually these tests are performed with low to intermediate R -values and, therefore, ΔK_T can only be determined if K_{op} is measured. As an example of the results (Fig. 1), ΔK_{th} is plotted versus K_{max} for a titanium alloy [2]. It is apparent that the measured threshold values can be divided into two groups. For the high K_{max} regime (B in Fig. 1), ΔK_{th} is nearly constant; however, it shows a trend toward a small decrease with increasing K_{max} . In the low K_{max} regime (A in Fig. 1), ΔK_{th} decreases relatively strongly over a small range of K_{max} . If the data points in Regime A are

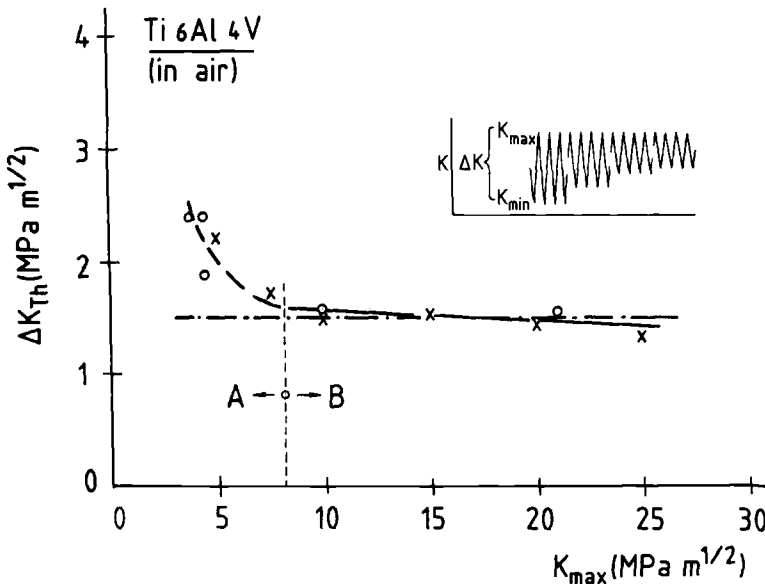


FIG. 1—Fatigue threshold measured as a function of K_{max} for Ti-6Al-4V [2].

plotted versus R -ratio, the usual ΔK_{th} versus R behavior is obtained. Since the existence of a nearly "constant" threshold range, ΔK_T (Regime B), has been proven in Refs 2, 3, and 4, the present investigation excluded the K_{max} range of Regime A, where closure was expected to interfere with measuring ΔK_T , namely $K_{max} < 10 \text{ MPa m}^{1/2}$.

It is well known that there are transient effects in the crack growth rate after sudden changes in amplitude or mean stress. These are often related to crack closure. In addition, they may also be related to changes in the threshold value. In this investigation the effect of load history on the threshold ΔK_T is determined experimentally, especially the effects associated with the prior amplitude, ΔK_{pr} .

Experimental Procedures and Material

An Inconel 617 alloy was used in the present investigation. The chemical composition and the mechanical properties of the alloy are given in Ref 5. The tests were performed on compact tension (CT) specimens with $B = 12.5 \text{ mm}$ and $W = 60 \text{ mm}$. They were machined from a plate of 18-mm thickness with the crack plane parallel to the rolling direction (T-L orientation). The tests were carried out in laboratory air at room temperature on load-controlled servohydraulic and resonance testing machines. A sinusoidally changing load with a frequency of 30 to 50 Hz on the servohydraulic and approximately 130 Hz on the resonance testing machine was applied. The fatigue crack propagation was measured by a d-c potential drop method (for details see Ref 5). Reference 5 contains the results from tests denoted Types I through IV. In order to make this paper self-explanatory, these test conditions are explained below.

The conditions for nonpropagating fatigue cracks were investigated in the range of K_{max} between 10 to 50 $\text{MPa m}^{1/2}$ under four different types of fatigue loading conditions. In all tests comprising the four types of fatigue loading, K_{max} was held constant for any fatigue cycle prior to the nonpropagation condition. The condition of nonpropagation of a fatigue crack was taken as established when the d-c potential drop method showed no indication of propagation during 2 to 3×10^6 cycles.

Type I Test

The test configuration denoted as Type I is the method for determination of ΔK_{th} at constant K_{max} , where K_{min} is increased in small steps. Thus, the amplitude prior to reaching the nonpropagation condition is only slightly different from that of the nonpropagation condition and $K_{max,pr} = K_{max}$. The detailed procedure is as follows:

At a given K_{max} , the specimen was fatigued with $\Delta K = 8 \text{ MPa m}^{1/2}$, then ΔK was decreased by raising K_{min} in steps of $1 \text{ MPa m}^{1/2}$ down to $\Delta K = 5 \text{ MPa m}^{1/2}$, from $\Delta K = 5 \text{ MPa m}^{1/2}$ to $4 \text{ MPa m}^{1/2}$ in steps of $0.5 \text{ MPa m}^{1/2}$, and below that in steps of $0.25 \text{ MPa m}^{1/2}$ (Fig. 2a). It was originally presumed and later confirmed by the tests that there is no crack growth retarding effect if the specimen has never experienced a K_{max} higher than the selected $K_{max,pr}$ of the subject test. Therefore, a load shedding procedure as presently proposed for the ASTM Test for Constant-Load-Amplitude Fatigue Crack-Growth Rates Above 10^{-8} m/Cycle (E 647-83), is not necessary for Type I tests. However, the gradual increase of K_{min} in Type I tests should be such that, before K_{min} is raised again, the plastic-zone condition must reflect the applied ΔK at the subject K_{max} . This was ensured by watching the d-c potential drop signal for stabilized crack growth rates (minimum 2×10^5 cycles with constant da/dN).

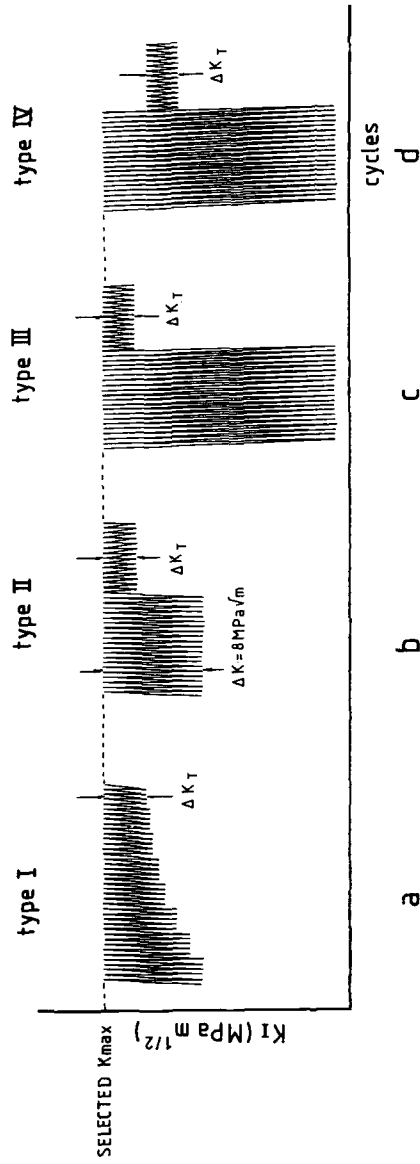


FIG. 2—Test configurations for the determination of nonpropagation conditions.

Type II Test

The amplitude prior to establishing nonpropagation conditions was chosen as $\Delta K_{pr} = 8 \text{ MPa m}^{1/2}$ for every K_{max} investigated. The $K_{max,pr}$ is equal to K_{max} . With the particular $K_{max,pr}$ and $\Delta K_{pr} = 8 \text{ MPa m}^{1/2}$, the crack propagated for approximately 0.5 mm. Then K_{min} was raised instantaneously to give a ΔK_{xi} somewhat greater than the fatigue threshold measured in Type I tests at that particular K_{max} . Usually the fatigue crack still propagated. Then the same procedure was repeated, but a somewhat smaller ΔK was applied, that is, $\Delta K_{xj} < \Delta K_{xi}$. The procedure continued till the condition for a nonpropagating fatigue crack was established (Fig. 2b).

Type III Test

The difference between Type II and Type III tests is the amount of change of K_{min} . In Type II tests the amplitude prior to establishing nonpropagation conditions is always $\Delta K_{pr} = 8 \text{ MPa m}^{1/2}$ for every K_{max} investigated, while for Type III tests the prior amplitudes, ΔK_{pr} , always had R -ratios of 0.1 (Fig. 2c). Also, $K_{max,pr}$ is equal to K_{max} .

Type IV Test





A fatigue crack is propagated at a given $K_{max,pr}$ with $R = 0.1$ for some distance. Then, K_{min} is raised and K_{max} dropped instantaneously so that the mean stress of new amplitude, ΔK_{xi} , is at 75% of the stress corresponding to $K_{max,pr}$. The ΔK_{xi} is selected to be somewhat larger than the anticipated fatigue threshold so as to show instantaneous crack propagation. The same procedure is then repeated with a smaller $\Delta K_{xj} < \Delta K_{xi}$. This procedure continued till the condition for nonpropagation was established (Fig. 2d). The amplitude prior to establishing nonpropagation ΔK_{pr} at a given $K_{max,pr}$ is identical to that of Type III tests; however, K_{max} is not equal to $K_{max,pr}$.

In Ref 5, the measured ΔK_T decreases with increasing prior amplitude, ΔK_{pr} , up to some amplitude, ΔK_s , at which saturation occurs. The assumption was made that ΔK_s is roughly $10 \text{ MPa m}^{1/2}$. In order to investigate this saturation effect, an experimental procedure similar to Type II and III tests (Fig. 2b) was adapted. Two K_{max} levels, namely 10 and $35 \text{ MPa m}^{1/2}$, were selected. Each test series started with a ΔK_{pr} approximately $0.25 \text{ MPa m}^{1/2}$ larger than ΔK_T obtained in Type I tests. With each subsequent test, ΔK_{pr} was increased by $0.25 \text{ MPa m}^{1/2}$ until ΔK_{pr} reached $6 \text{ MPa m}^{1/2}$ for the $K_{max} = 10 \text{ MPa m}^{1/2}$ series and until ΔK_{pr} reached $5 \text{ MPa m}^{1/2}$ for the $K_{max} = 35 \text{ MPa m}^{1/2}$ test series. In the subsequent tests, ΔK_{pr} was increased by $0.5 \text{ MPa m}^{1/2}$ until ΔK_{pr} reached $10 \text{ MPa m}^{1/2}$.

Results and Discussion*Previous Results*

In Table 1 the values measured for the four types of tests are given. The first column gives the K_{max} of the tests, followed by Type I, II, III, and IV test results. For each test, two numbers are given: the left side number gives the ΔK for the nonpropagation condition, while the right side number gives the lowest ΔK for which crack extension was still detected. Therefore, the upper value of ΔK_T for the nonpropagation conditions is smaller than the right side value and equal to or greater than the left side value. In Fig. 3, the trend lines of the results from the four test conditions are plotted for comparison. It can be seen that for all four test conditions ΔK_T decreases with increasing K_{max} . The influence of the prior amplitude, ΔK_{pr} , is somewhat more complex. As can be seen in Fig. 3 a difference of 0.9

TABLE 1—Stress-intensity range, ΔK , for nonpropagation (left numbers in columns) and the last measured crack propagation (right numbers in columns) for test conditions Type I through IV.

K_{\max} (MPa $m^{1/2}$)	ΔK_T (MPa $m^{1/2}$)			
	type I 	type II 	type III 	type IV 
10	3.75 - 4.01	2.49 - 2.75	2.68 - 2.85	2.70 - 2.95
15	3.40 - 3.75	2.70 - 3.01	2.08 - 2.52	2.45 - 2.69
20	2.93 - 3.25	2.48 - 2.70	2.23 - 2.49	2.01 - 2.10
25	2.88 - 2.98	1.99 - 2.19	1.99 - 2.18	1.80 - 2.01
30	3.23 - 3.48	2.31 - 2.44	2.05 - 2.15	2.23 - 2.47
35	3.26 - 3.43	2.27 - 2.59	1.99 - 2.10	2.20 - 2.48
40	2.76 - 3.01	2.12 - 2.40	1.91 - 2.07	2.00 - 2.27
45	2.74 - 2.89	1.88 - 2.29	1.78 - 2.03	1.76 - 1.90
50	2.99 - 3.22	1.76 - 1.95	1.74 - 2.01	1.21 - 1.38

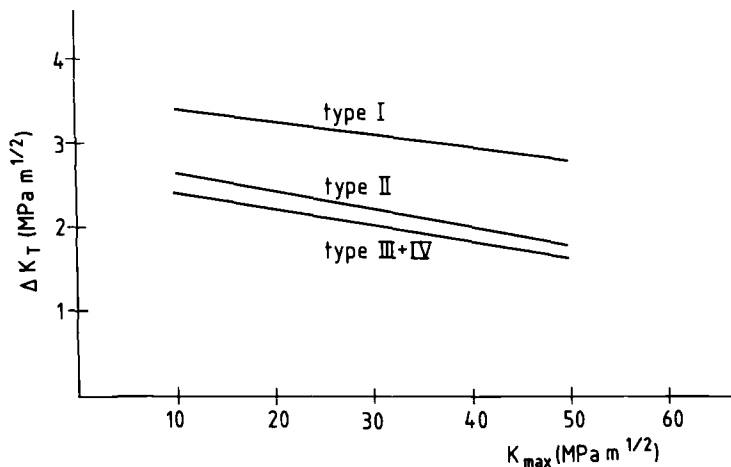


FIG. 3—Comparison of results for ΔK_T versus K_{max} from different test configurations Types I through IV.

$\text{MPa m}^{1/2}$ is found between ΔK_T obtained in Type I and that obtained in Type II tests. This represents a 30% reduction of ΔK_T , due to the larger amplitude of prior fatigue loading conditions. The difference between ΔK_T from Type I test and that from Type III tests reaches $1.1 \text{ MPa m}^{1/2}$ and corresponds to a 35% reduction of the fatigue tolerance range. Comparing the results from Type II and Type III tests, it is obvious that the difference no longer corresponds to the prior amplitude. The ΔK_T values for Type I and Type II tests reflect the respective amplitudes of cyclic loading before the condition of nonpropagation is established: that is, a small or incrementally different amplitude for Type I tests and $\Delta K_{pr} = 8 \text{ MPa m}^{1/2}$ for Type II tests. In Types III and IV tests, the amplitudes of the fatigue cycles prior to establishing nonpropagation conditions change from $\Delta K_{pr} = 9 \text{ MPa m}^{1/2}$ at $K_{max} = 10 \text{ MPa m}^{1/2}$ to $\Delta K_{pr} = 45 \text{ MPa m}^{1/2}$ at $K_{max} = 50 \text{ MPa m}^{1/2}$.

The results of Types I through IV tests are presented in Fig. 4 in a different way: ΔK_T is plotted versus ΔK_{pr} with K_{max} as a parameter. Notice that the lowest prior amplitude (from Type I results) is only incrementally larger than ΔK_T . Again the decrease of ΔK_T with increasing $K_{max,pr}$ can be seen. For constant $K_{max,pr}$, the threshold ΔK_T decreases with increasing ΔK_{pr} , suggesting a saturation value at approximately $\Delta K_s \approx 10 \text{ MPa m}^{1/2}$ according to the data plotted in Fig. 4.

Present Results

Table 2 presents the results for the test series on saturation of the ΔK_{pr} effect with K_{max} equal to 10 and $35 \text{ MPa m}^{1/2}$. The data are presented in a manner similar to that described for Table 1, except that the first column with K_{max} is now replaced by ΔK_{pr} . In Fig. 5, the measured fatigue tolerance range, ΔK_T , is plotted versus the prior amplitude, ΔK_{pr} , for the two levels of K_{max} . Here too, it can be seen that ΔK_T decreased with higher K_{max} , in agreement with Fig. 3 and Refs 2 through 4. Increasing the prior amplitude, ΔK_{pr} , decreases ΔK_T up to a saturation level, ΔK_s ; an additional increase of ΔK_{pr} has no substantial effect on ΔK_T . Taking the data presented in Fig. 5, ΔK_s is reached at $\Delta K_{pr} = 7 \text{ MPa m}^{1/2}$ for $K_{max} = 10 \text{ MPa m}^{1/2}$ and at $\Delta K_{pr} = 5 \text{ MPa m}^{1/2}$ for $K_{max} = 35 \text{ MPa m}^{1/2}$.

Nevertheless, the knee in the test series with $K_{max} = 10 \text{ MPa m}^{1/2}$ between ΔK_{pr} of 5 and $7 \text{ MPa m}^{1/2}$ suggests a different possibility. For $\Delta K_{pr} = 5 \text{ MPa m}^{1/2}$, K_{min} of the prior amplitude

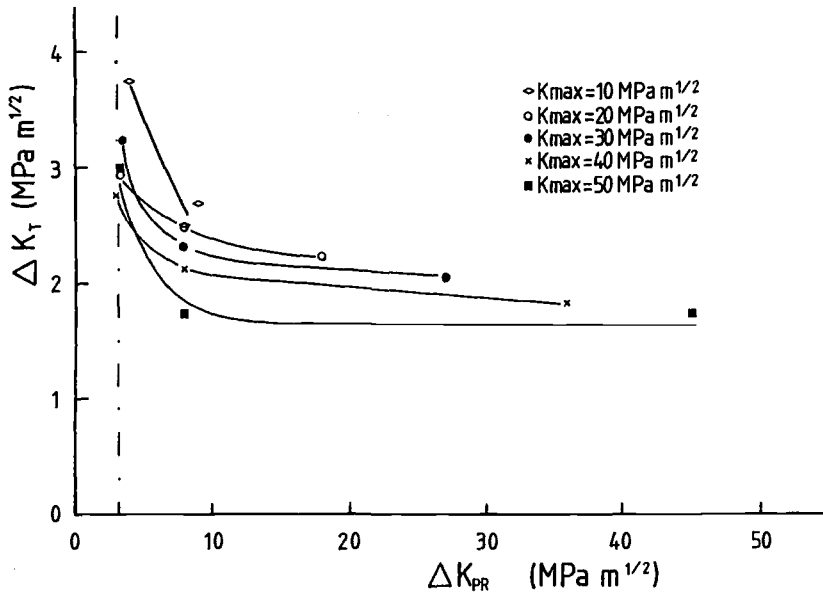


FIG. 4—Measured ΔK_T values versus prior amplitudes ΔK_{pr} from data shown in Fig. 3.

is $5 \text{ MPa m}^{1/2}$, and for $\Delta K_{pr} = 7 \text{ MPa m}^{1/2}$, K_{min} of the prior amplitude is $3 \text{ MPa m}^{1/2}$. Taking the opening level K_{op}/K_{max} as given in the available literature, it has to be expected that K_{op} lies in the range between 3 to $5 \text{ MPa m}^{1/2}$ for $K_{max} = 10 \text{ MPa m}^{1/2}$. Thus, the knee shape produced by the data points of this test series could be due to closure effects occurring during the prior amplitudes between ΔK_{pr} of 5 and $7 \text{ MPa m}^{1/2}$. It should be noted that all data points of one test series in Fig. 5 were obtained on a single CT specimen.

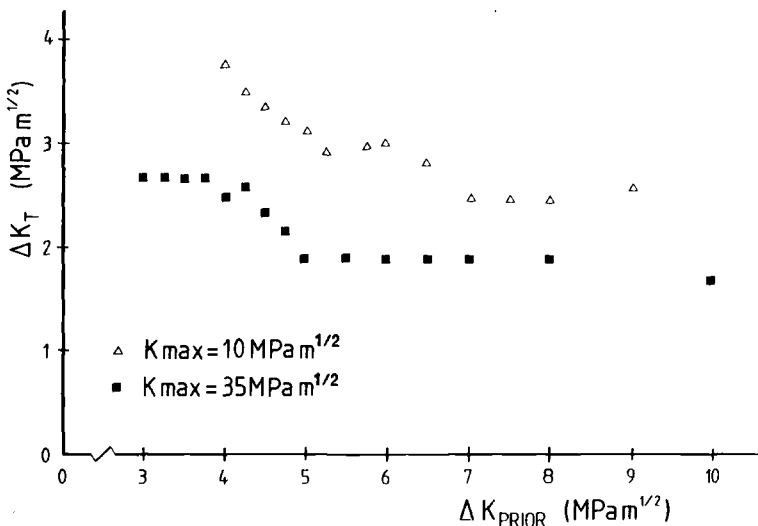


FIG. 5—Measured ΔK_T values versus prior amplitude ΔK_{pr} from test series to obtain saturation value ΔK_S .

TABLE 2—Stress-intensity range, ΔK , for nonpropagation (left-hand numbers) and last measured crack propagation (right-hand numbers) for a test series on the saturation effect of ΔK_{pr} .

ΔK_{pr} , MPa m ^{1/2}	ΔK_T , MPa m ^{1/2}	
	$K_{max} = 10 \text{ MPa m}^{1/2}$	$K_{max} = 35 \text{ MPa m}^{1/2}$
3	...	2.69 to ^a
3.25	...	2.70 to 2.95
3.50	...	2.69 to 2.94
3.75	...	2.70 to 2.95
4.00	3.73 to ^a	2.51 to 2.69
4.25	3.47 to 3.71	2.59 to 2.87
4.50	3.33 to 3.47	2.36 to 2.60
4.75	3.23 to 3.33	2.15 to 2.35
5.00	3.09 to 3.24	1.91 to 2.16
5.25	2.90 to 3.00	...
5.50	...	1.91 to 2.16
5.75	2.97 to 3.13	...
6.00	2.98 to 3.14	1.91 to 2.17
6.50	2.79 to 2.96	1.89 to 2.14
7.00	2.44 to 2.60	1.91 to 2.14
7.50	2.42 to 2.56	...
8.00	2.42 to 2.57	1.91 to 2.14
9.00	2.57 to 2.83	...
10.00	...	1.70 to 1.91
12.00	...	1.61 to 1.71
15.00	...	1.49 to 1.59

^a Not incremented smaller than $\sim 0.25 \text{ MPa m}^{1/2}$.

On the other hand, the knee in data points from the $K_{max} = 10 \text{ MPa m}^{1/2}$ test series in Fig. 5 may be due to scatter. If neighboring results from an individual test series in Table 1 are compared, a scatter of approximately $0.5 \text{ MPa m}^{1/2}$ is also found. But the data scatter in Table 1 can be associated with individual specimens and could not be reduced by repeated testing. Therefore, the observed scatter may be a natural consequence of microstructural variations in a material.

One important conclusion derived from the data presented in Figs. 3 and 4 is that the effects of the two loading parameters $K_{max,pr}$ and ΔK_{pr} are additive. This means that over the whole range of useful K_{max} values the effect of prior amplitudes, ΔK_{pr} , can be *superposed*. (Above $K_{max} \approx 50 \text{ MPa m}^{1/2}$ the Inconel 617 alloy exhibits crack extension under static load, therefore making a threshold irrelevant.) The tests run in this investigation determined the nonpropagation condition as a function of the two loading parameters $K_{max,pr}$ and ΔK_{pr} , that is to say, as a function of stress and strain level and a function of the cyclic stress and strain range. As a result of the different fatigue loading conditions, the damage in the near region of the crack front is different. The damage increases with increasing $K_{max,pr}$ and with increasing ΔK_{pr} up to saturation at ΔK_S . There is no indication that the damage caused by $K_{max,pr}$ is limited to a certain saturation. If one tries to explain the nature of the damage produced, one could cite decreasing cell size with increasing damage, persistent slip bands, or different dislocation structures in the cell walls [6–8].

The existence of nonpropagation conditions in tests like Type IV would imply a ΔK_{eff} concept which is defined differently [5] from that of Elber [9]. According to Elber

$$\Delta K_{eff} = (K_{max} - K_{op}) \propto (S_{max} - S_{op}) \quad (2)$$

If, in accordance with Elber, ΔK_{eff} correlates with crack propagation and a threshold exists under all fatigue conditions, then ΔK_{eff} has to be defined the following way: every cycle should be reduced by ΔK_T so that

for $K_{\text{op}} > K_{\text{min}}$

$$\Delta K_{\text{eff}} = (K_{\text{max}} - K_{\text{op}}) - \Delta K_T \quad (3)$$

or for $K_{\text{min}} > K_{\text{op}}$

$$\Delta K_{\text{eff}} = (K_{\text{max}} - K_{\text{min}}) - \Delta K_T \quad (4)$$

It is important to point out the testing philosophies in respect to fatigue crack propagation prediction. Determination of threshold as the lower end of the da/dN versus ΔK curve or as in Type I tests means, according to Eqs 3 and 4, that ΔK_{eff} has to be zero for a nonpropagation condition to exist. Type II and Type III tests modify this concept as to the influence of prior amplitudes.

The results from Type IV tests have further implications. Tests have been made where ΔK_T was shifted to positions between K_{op} and $K_{\text{max,pr}}$. The important point here is that the results from Type IV tests are not reflecting a particular testing situation; rather, they stand for the general condition of nonpropagation [10] anywhere between K_{op} and K_{max} . Consider such a test condition in detail (Fig. 6). It shows that when the loading condition goes from Position 1 to Position 2 and then Position 3, the cycle would have a magnitude of ΔK_T . Therefore, crack propagation would be impossible. On the other hand, if the loading condition goes from Position 1 to Position 4 and back to Position 5 (in Fig. 6)—assuming fatigue crack growth occurs only under increasing load—no fatigue crack propagation can have occurred in that part of the cycle from Position 1 to Position 2. As a consequence the authors conclude that in every fatigue cycle a stress-intensity factor excursion equal to ΔK_T has to be surpassed above K_{op} before crack growth can commence. From the general conditions for ΔK_{eff} —Eqs 3 and 4—the special conditions of nonpropagation can be derived.

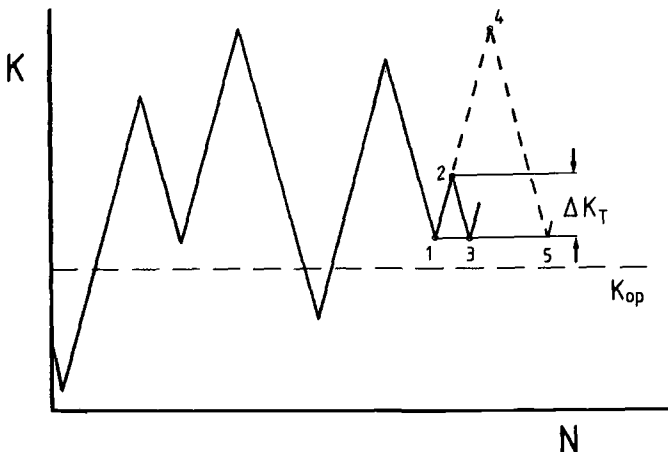


FIG. 6—Details relevant to Type IV tests.

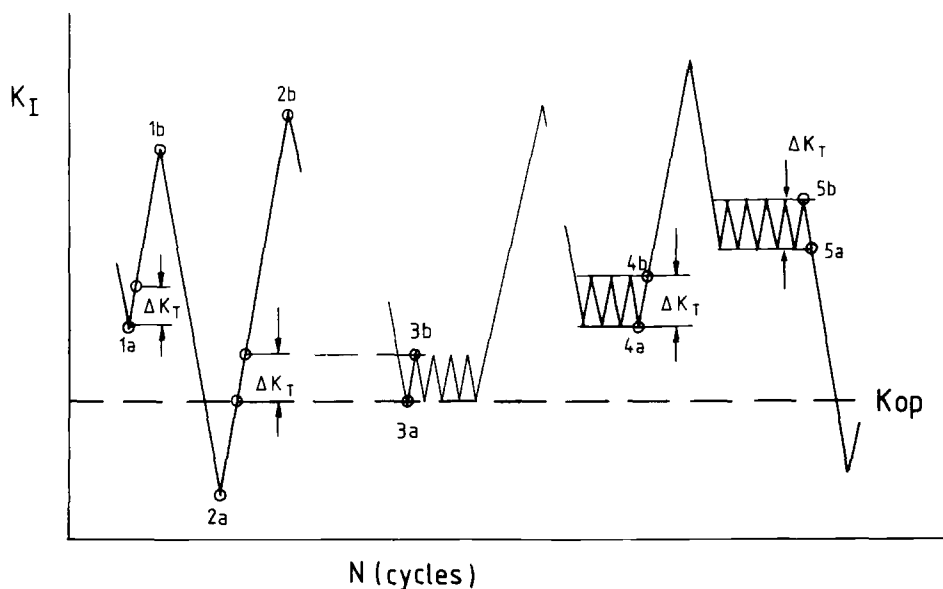


FIG. 7—Relevance of a fatigue tolerance range K_T to general fatigue loading conditions.

For $K_{op} > K_{min}$

$$\Delta K_{eff} = (K_{max} - K_{op}) - \Delta K_T = 0 \quad (5)$$

and for $K_{min} > K_{op}$

$$\Delta K_{eff} = (K_{max} - K_{min}) - \Delta K_T = 0 \quad (6)$$

Equations 5 and 6 are justified by the results obtained from Type IV tests. For service-type fatigue loading, where K_{op} may be fixed by some prior cycles, Fig. 7 shows graphically the meaning of Eqs 3 through 6. The cycles 2a, 2b and 1a, 1b in Fig. 7 correspond to Eqs 3 and 4, respectively, while cycles 3a, 3b corresponds to Eq 5. Cycles 4a, 4b and 5a, 5b represent Eq 6 graphically.

To distinguish the terms, the nonpropagation condition, ΔK_T , containing no contribution of closure and being interpreted as described above, is called the *fatigue tolerance range*.

Conclusions

1. The fatigue tolerance range, ΔK_T , decreases with increasing $K_{max,pr}$. For the Inconel 617 alloy investigated, ΔK_T decreases by approximately $1 \text{ MPa m}^{1/2}$ when $K_{max,pr}$ is increased from 10 to $50 \text{ MPa m}^{1/2}$.

2. The fatigue tolerance range, ΔK_T , decreases at a given $K_{max,pr}$ with increasing prior amplitude, ΔK_{pr} , up to a certain amplitude, ΔK_s , at which this effect saturates.

3. Determination of the prior amplitude, ΔK_s , at which saturation has occurred yielded for $K_{max,pr} = 10 \text{ MPa m}^{1/2}$, a ΔK_s between 5 and $7 \text{ MPa m}^{1/2}$, and for $K_{max,pr} = 35 \text{ MPa m}^{1/2}$, a ΔK_s of approximately $5 \text{ MPa m}^{1/2}$. The experimental data for $K_{max,pr} = 10 \text{ MPa m}^{1/2}$ suggest

a possible closure effect occurring during the prior amplitude loading with ΔK_{pr} between 5 and 7 MPa m^{1/2}. The interpretation of results presented on the saturation effect of ΔK_{pr} has to be considered preliminary, and more experimental work in this direction has to be done.

4. The experimental tests conducted and the results obtained clearly demonstrate that the fatigue tolerance range, ΔK_T , plays an important part in relation to crack propagation in every loading cycle. It is applicable to service-type loading conditions. Furthermore, Elber's ΔK_{eff} concept needs to be modified somewhat, that is

$$\Delta K_{eff} = (K_{max} - K_{op}) - \Delta K_T$$

or if $K_{min} > K_{op}$

$$\Delta K_{eff} = (K_{max} - K_{min}) - \Delta K_T$$

Acknowledgment

The authors would like to thank their colleagues at DFVLR for their helpful discussions and suggestions, particularly V. Bachmann for implementing the test conditions. Financial support of D. E. Castro by DAAD (German Academic Exchange Service) is thankfully acknowledged.

References

- [1] Schmidt, R. A. and Paris, P. C., "Threshold for Fatigue Crack Propagation and the Effects of Load Ratio and Frequency," *Progress in Flaw Growth and Fracture Toughness Testing, ASTM STP 536*, American Society for Testing and Materials, Philadelphia, 1973, pp. 79-94.
- [2] Döker, H., Bachmann, V., and Marci, G., "A Comparison of Different Methods of Determination of the Threshold for Fatigue Crack Propagation," *Fatigue Thresholds, Fundamentals, and Engineering Applications*, Engineering Materials Advisory Service, Ltd., Warley, England, 1982, pp. 45-57.
- [3] Döker, H. and Marci, G., "Threshold Range and Opening Stress-Intensity Factor in Fatigue," *International Journal of Fatigue*, Vol. 5, No. 4, October 1983, pp. 187-191.
- [4] Döker, H. and Peters, M., "Fatigue Threshold Dependence on Material, Environment and Microstructure," *Fatigue 84*, Vol. 1, Engineering Materials Advisory Service, Ltd., Warley, England, 1984, pp. 275-285.
- [5] Castro, D. E., Marci, G. and Munz, D., "A Generalized Concept of a Threshold," *Fatigue and Fracture of Engineering Materials and Structures*, Vol. 10, No. 4, 1987, pp. 305-314.
- [6] Hancock, J. R. and Grosskreuz, J. C., "Mechanisms of Fatigue Hardening in Copper Single Crystals," *Acta Metallurgica*, Vol. 17, February 1969, pp. 77-97.
- [7] Mughrabi, H., "The Cyclic Hardening and Saturation Behavior of Copper Single Crystals," *Materials Science and Engineering*, Vol. 33, 1978, pp. 207-223.
- [8] Lukáš, P., "Models for ΔK_{th} and Near-Threshold Fatigue Crack Growth," *Fatigue 84*, Vol. 1, Engineering Materials Advisory Service, Ltd., Warley, England, 1984, pp. 479-495.
- [9] Elber, W., "The Significance of Fatigue Crack Closure," *Damage Tolerance in Aircraft Structures, ASTM STP 486*, American Society for Testing and Materials, Philadelphia, 1971, pp. 230-242.
- [10] Döker, H. and Bachmann, V., "Determination of Crack: Opening Load by Use of Threshold Behavior," American Society for Testing and Materials International Symposium on Fatigue Crack Closure, 1-2 May 1986, Charleston, SC.

William A. Logsdon,¹ Peter K. Liaw,¹ and James A. Begley²

Fatigue Crack Growth Rate Properties of SA508 and SA533 Pressure Vessel Steels and Submerged-Arc Weldments in a Pressurized Water Environment

REFERENCE: Logsdon, W. A., Liaw, P. K., and Begley, J. A., "Fatigue Crack Growth Rate Properties of SA508 and SA533 Pressure Vessel Steels and Submerged-Arc Weldments in a Pressurized Water Environment," *Fracture Mechanics: Nineteenth Symposium, ASTM STP 969*, T. A. Cruse, Ed., American Society for Testing and Materials, Philadelphia, 1988, pp. 830-867.

ABSTRACT: The Stage II fatigue crack growth rate (FCGR) properties of four base materials (SA508 Class 2a; SA533 Grade A, Class 2; SA508 Class 3a; and SA533 Grade B, Class 2 steels) and two automatic submerged-arc weldments (SA508 Class 2a and SA533 Grade A, Class 2) were developed in a pressurized water environment at 288°C (550°F) and 13.8 MPa (2000 psi) at load ratios of 0.20 and 0.50. The pressurized water environment FCGR properties of these four pressure vessel steels and two submerged-arc weldments were generally conservative compared with the appropriate American Society of Mechanical Engineers (ASME) Section XI water environment reference curve. The growth rate of fatigue cracks in the four base materials, however, was considerably faster in the pressurized water environment than in a corresponding 288°C (550°F) baseline air environment. The growth rate of fatigue cracks in the two submerged-arc weldments was also accelerated in the pressurized water environment but to a lesser degree than that demonstrated by the corresponding base materials. In the air environment, fatigue striations were observed independent of the material and load ratio, while in the pressurized water environment some intergranular facets were present. The greater environmental effect on crack growth rates displayed by the base materials in comparison with the weldments was attributed to a different sulfide composition and morphology.

KEY WORDS: A508 steel, A533 steel, submerged-arc welding, weldments, pressure vessels, fatigue crack growth rate, corrosion, pressurized water, fracture mechanics

While the termination of the life of a structure or component may be based on the critical flaw size for large-scale rupture as calculated from the material's fracture toughness, it must be recognized that the total useful life of a cyclically loaded component such as a reactor pressure vessel is dependent upon the rate of growth of flaws from a subcritical size to a critical size. Therefore, an understanding of the crack growth characteristics of the required reactor pressure vessel grade materials under appropriate service conditions is essential to evaluate the useful life of a pressure vessel. Moreover, the corrosive environment fatigue crack growth rate (FCGR) data initially included in Section XI of the American Society of Mechanical Engineers (ASME) Boiler and Pressure Vessel Code relative to pressure-re-

¹ Senior engineer and fellow engineer, respectively, Metals Technologies Department, Westinghouse R&D Center, Pittsburgh, PA 15235.

² Fellow engineer, Materials Applications Department, Westinghouse R&D Center, Pittsburgh, PA 15235.

TABLE 1—Chemical compositions of four pressure vessel steels.

Material	Specimen No.	Base or Weld Material	Chemical Composition, weight %									
			C	Mn	P	S	Si	Ni	Cr	Mo	V	
SA508 Class 2a	5610	base	0.19	0.77	0.010	0.009	0.28	0.83	0.39	0.60	<.03	
SA508 Class 2a	5610	weld	0.11	0.62	0.006	0.011	0.33	0.60	<.10	0.45	<.12	
SA533 Grade A, Class 2	7160	base	0.22	1.28	0.014	0.010	0.24	0.56	...	
SA533 Grade A, Class 2	7160	weld	0.12	1.06	0.006	0.011	0.39	0.60	<.10	0.45	<.12	
SA508 Class 3a	7431	base	0.21	1.30	0.008	0.009	0.29	0.62	0.18	0.50	0.010	
SA533 Grade B, Class 2	5835	base	0.22	1.36	0.015	0.005	0.22	0.62	...	0.55	...	

TABLE 2—Heat treatments of four pressure vessel steels.

Material	Specimen No.	Heat Treatment	
SA508 Class 2a	5610	austenitize temper stress relieve	860°C (1580°F), hold 4 h, water quench 666°C (1230°F), hold 6 h, furnace cool 607°C (1125°F), hold 48 h
SA533 Grade A, Class 2	7160	austenitize temper stress relieve stress relieve	885/913°C (1625/1675°F), hold 0.5 h per 25.4 mm (1 in.) minimum, water quench 649°C (1200°F), hold 0.5 h per 25.4 mm (1 in.) minimum, water quench 593/621°C (1100/1150°F), hold 2 h, furnace cool 607°C (1125°F), hold 48 h
SA508 Class 3a	7431	austenitize temper stress relieve	871°C (1600°F), hold 6 h, water quench 666°C (1230°F), hold 6 h, air cool 607°C (1125°F), hold 48 h
SA533 Grade B, Class 2	5835	austenitize temper stress relieve stress relieve	885/913°C (1625/1675°F), hold 1 h per 25.4 mm (1 in.) minimum, water quench 641°C (1185°F), hold 1 h per 25.4 mm (1 in.) minimum, water quench 593/621°C (1100/1150°F), hold 2.75 h, furnace cool 607°C (1125°F), hold 48 h

TABLE 3—Parameters for automatic submerged-arc weldments.

Electrode size	0.40 cm (0.156 in.)
Electrode type	Mn-Mo-Ni
Flux type	Linde 0091
Current and polarity	600 d-c reverse polarity
Arc voltage	32
Travel speed	30 cm/minute (12 in./minute)
Welding position	downhand
Preheat temperature	121°C (250°F)
Interpass temperature	260°C (500°F)
Postweld heat treatment	607°C (1125°F), hold 48 h
Inspection after fabrication	magnetic particle, radiography

taining materials for vessels utilized in nuclear applications was both sparse and questionable and, in addition, directly applicable only to ferritic pressure vessel steels with minimum yield strengths of 345 MPa (50 ksi) [1].

Therefore, the authors decided that the FCGR properties of four base materials (SA508 Class 2a; SA533 Grade A, Class 2; SA508 Class 3a; and SA533 Grade B, Class 2 steels) and two automatic submerged-arc weldments (SA508 Class 2a and SA533 Grade A, Class 2) should be developed in a pressurized water environment at load ratios ($R = P_{\min}/P_{\max}$, where P_{\min} and P_{\max} are the applied minimum and maximum loads, respectively) of 0.20 and 0.50. Consequently, these FCGR tests were initiated as part of a combined French-Westinghouse four-party [Commissariat à l'Energie Atomique (CEA), Electricite de France (EdF), Framatome and Westinghouse Electric Research and Engineering for Atomic Systems, Inc. (WEREAS)] joint research and development program.

Baseline 24 and 288°C (75 and 550°F) air environment FCGR tests were also conducted on these materials [2]. The Stage I (near-threshold) FCGR properties of these pressure vessel steels were additionally generated in an air environment at 24 and 288°C (75 and 550°F) at load ratios of 0.20 and either 0.50 or 0.70 [3]. Both the base materials and the weldments were stress relieved for 48 h at 607°C (1125°F) to account for the effects of long-time stress relief heat treatments.

Materials

Fatigue crack growth rate tests were conducted on four pressure vessel steels (SA508 Class 2a; SA533 Grade A, Class 2; SA508 Class 3a; and SA533 Grade B, Class 2) and two automatic submerged-arc weldments (SA508 Class 2a and SA533 Grade A, Class 2). SA508 Class 2a and SA508 Class 3a are quenched and tempered vacuum treated carbon and alloy steels typically utilized in forgings for nuclear applications. Compared with SA508 Class 2a steel, SA508 Class 3a contains less chromium and additional manganese and is typically less susceptible to underclad cracking. SA533 Grade A, Class 2 and SA533 Grade B, Class 2 are manganese-molybdenum (Grade A) and manganese-molybdenum-nickel (Grade B) alloy plate steels typically utilized in the quenched and tempered condition for the construction of welded pressure vessels.

The chemical compositions of these four pressure vessel steels are summarized in Table 1. Each of the four base materials satisfied the chemical requirements specified by the appropriate ASTM standard specification. In addition, the restrictive chemistry requirements on both phosphorus and sulfur specified in the ASTM Specification for Quenched and Tempered Vacuum-Treated Carbon and Alloy Steel Forgings for Pressure Vessels (ASTM A508-81) were also satisfied by the SA508 Class 2a and SA508 Class 3a steels examined in

TABLE 4—Room temperature tensile properties of four pressure vessel steels.

Material	Specimen No.	Base or Weld	0.2% Yield Strength		Ultimate Strength		Uniform Elongation, %	Total Elongation, %	Reduction in Area, %
			ksi	MPa	ksi	MPa			
SA508 Class 2a	5610	base	71.3	492	90.4	623	10.1	22.4	59.8
SA508 Class 2a	5610	weld	87.2	601	97.0	669	9.9	36.8	68.2
SA533 Grade A, Class 2	7160	base	70.2	484	92.0	634	10.2	25.8	72.3
SA533 Grade A, Class 2	7160	weld	85.1	587	99.0	683	10.6	36.3	68.6
SA508 Class 3a	7431	base	81.7	563	102.9	709	8.0	18.2	55.1
SA533 Grade B, Class 2	5835	base	81.2	560	99.8	688	10.0	23.3	65.3

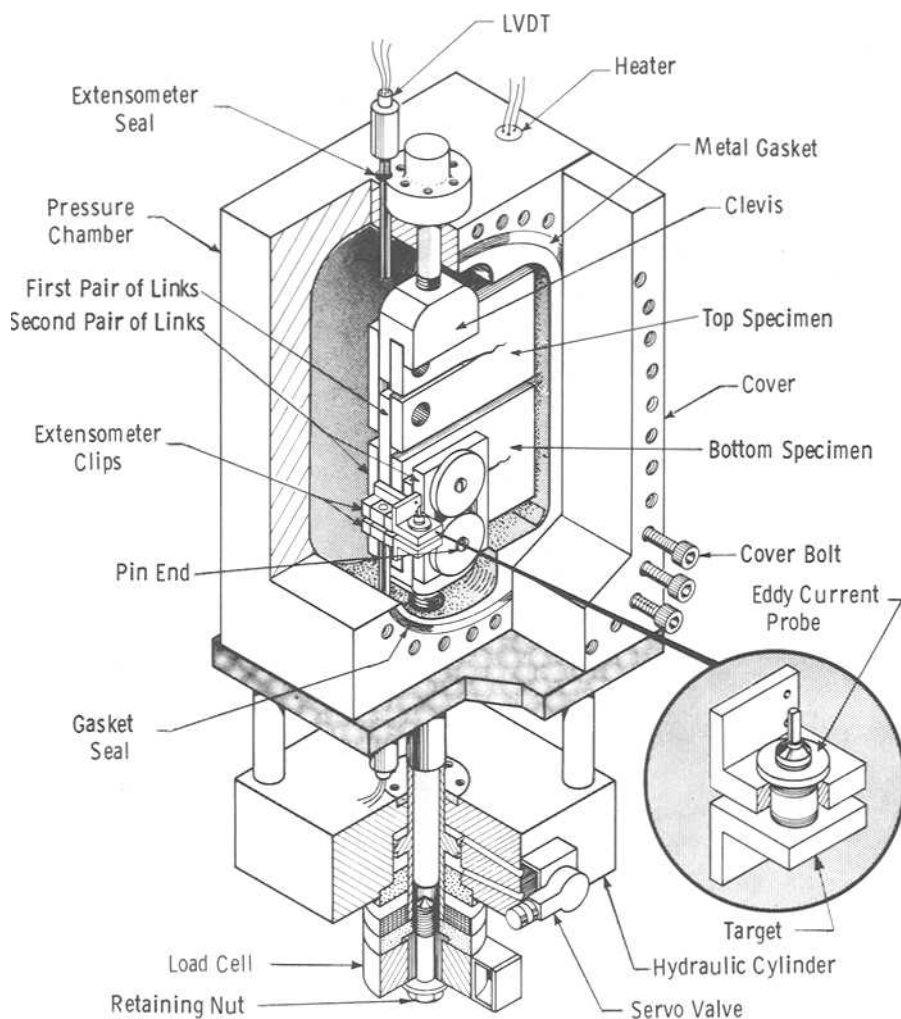


FIG. 1—Multiple specimen chamber for fatigue crack growth in a pressurized water environment.

this investigation. On the other hand, both the SA533 Grade A, Class 2 and SA533 Grade B, Class 2 plate steels failed to satisfy the restrictive chemical requirement for phosphorus specified in the ASTM Specification for Pressure Vessel Plates, Alloy Steel, Quenched and Tempered, Manganese-Molybdenum and Manganese-Molybdenum-Nickel (ASTM A 533-82).

Heat treatments relative to these four pressure vessel steels are summarized in Table 2. Note that each material was stress relieved for 48 h at 607°C (1125°F). For the automatic submerged-arc weldments, the processing parameters of which are summarized in Table 3, this stress relief took place following welding. Depending on the weldment thickness, the actual postweld stress-relief heat treatment times for typical welded nuclear pressure vessels can range from 3 to 30 h at 607°C (1125°F) according to the American Society for Mechanical

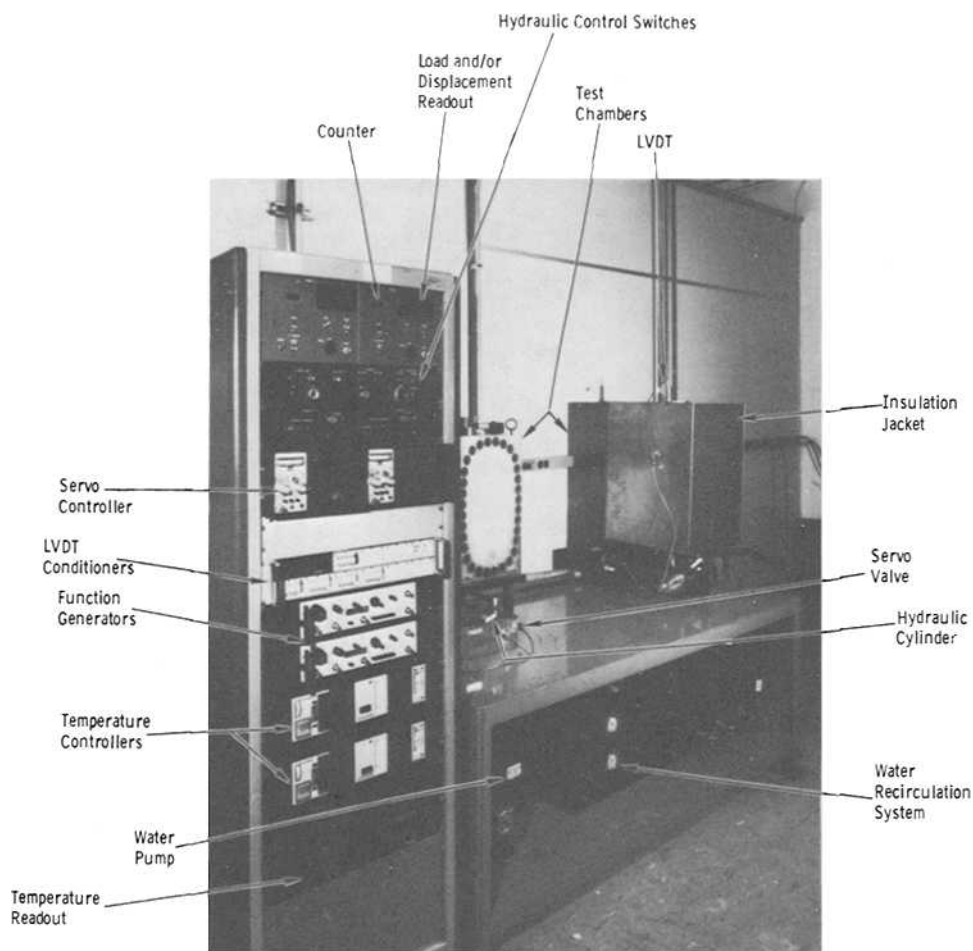


FIG. 2—Overall view of high-pressure crack growth chambers and electronic control system.

Engineers (ASME) Code Requirements [4]. Consequently, this treatment can be considered a worse-case stress-relief heat treatment for these materials [4].

The room temperature tensile properties of these four pressure vessel steels and two submerged-arc weldments are summarized in Table 4. Standard buttonhead tensile specimens, 0.91 cm (0.357 in.) diameter and 3.81 cm (1.5 in.) in gage length, were used for the base metal tests. The base metal tensile specimens were oriented so that their loading direction matched that of the compact specimens. Reduced gage length specimens, 0.64 cm (0.252 in.) in gage length, oriented transverse to the submerged-arc weld, with the center of the specimen gage length located directly in the center of the weldment, were used for the weldment tests. Care should be used when comparing base versus weld metal total elongation values since they were measured with specimens of different gage lengths. To help in this comparison, uniform elongation (deformation to the point of maximum load), a measurement independent of the specimen gage length, is also reported in Table 4.

All four base materials, as well as two submerged-arc weldments, satisfied the yield

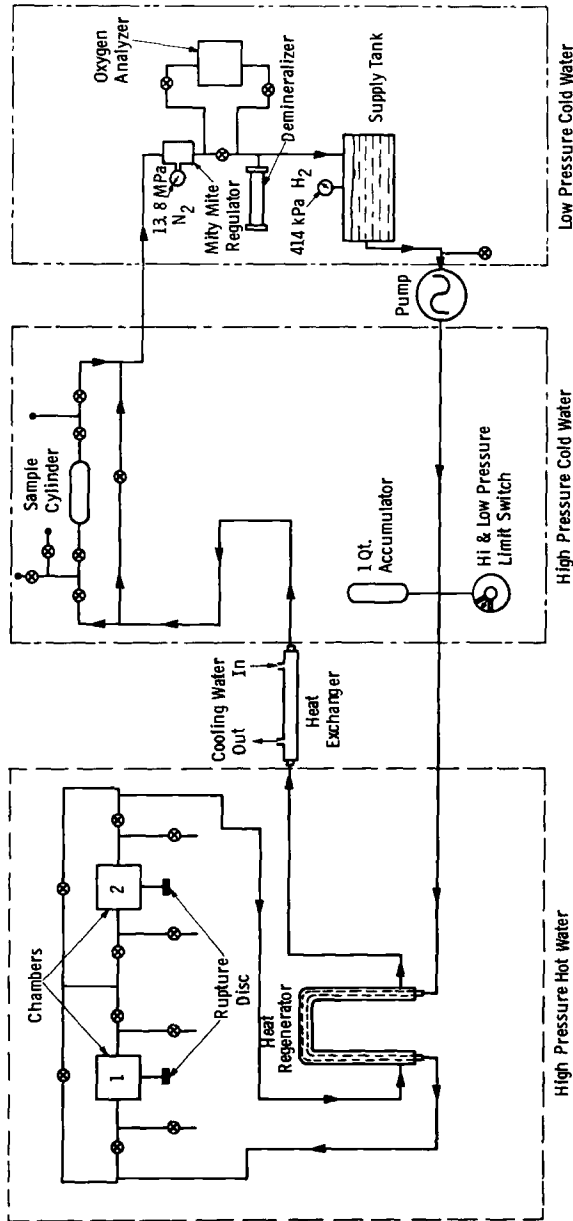


FIG. 3—Recirculating water system.

TABLE 5—*Breakdown of the pressurized water environment.*

Element	Pressurized Water
Oxygen	<5 ppb
Hydrogen	30 to 50 cm ³ /kg water (standard temperature and pressure)
Lithium hydroxide	1 ppm lithium
Chloride	<0.15 ppm
Fluoride	<0.15 ppm
pH (25°C)	5.99
Ammonia	...
Temperature	288°C (550°F)
Pressure	13.8 MPa (2000 psi) ^a
Conductivity (25°C)	9.96 μ mho/cm

^a Absolute pressure.

strength, ultimate strength, total elongation, and reduction in area requirements specified in the applicable ASTM standard specification. The yield strengths of the submerged-arc weldments proved superior to those demonstrated by the base materials.

Experimental Procedures

A detailed description of the test facility developed for automated corrosion FCGR testing in pressurized water environments was previously reported [5]. General highlights of the test facility will be described herein; those desiring greater detail are referred to Ref 5.

A schematic of the test chambers developed for conducting FCGR tests in a pressurized water environment is shown in Fig. 1. To facilitate data generation and decrease testing costs, two chambers were constructed; each chamber could accommodate two compact-type specimens. The chambers were machined from a surplus section of an A533 reactor pressure vessel and were chrome plated to improve corrosion resistance. Each chamber contained a rectangular cavity, the total volume of which was less than 4.5 L (1.2 gal). This permitted the use of a small-capacity, high-pressure pump (18.9 L/h, 5 gal/h) for water recirculation so as to maintain approximately four volume changes per hour. The small size of the cavity in each chamber also provided a minimum pressure load on the cover bolts. Cartridge heaters inserted in the chamber walls developed the required temperature.

Each chamber was mounted on top of a hydraulic cylinder that was fastened to a steel table. Note that the two chambers shared the steel table which also served as the housing for the water recirculating system (Fig. 2). For each chamber, a load cell was located at the bottom of the hydraulic cylinder.

Because the top and bottom specimens were connected by chain-type links (Fig. 1), only tension loads could be applied to the specimens. A second pair of links was placed over the two pins in each specimen to provide loading on one specimen when the other specimen was broken. The crack-opening displacement of each specimen was measured by a linear variable differential transformer (LVDT) type extensometer.

The two chambers shared a common environmental supply line. A flow diagram of the system used to pressurize the chambers is illustrated in Fig. 3. The environment was contained in a closed-loop recirculating system with the conditioned water pumped from a 37.9-L (10-gal) stainless steel storage tank. A hydrogen overpressure of 414 kPa (60 psig) was maintained in the storage tank to scavenge oxygen. A dissolved-oxygen analyzer was used to monitor the oxygen level continuously (Fig. 3). The water was pressurized with a piston-diaphragm pump and the operating pressure of 13.8 MPa (2000 psi) was controlled by a Mity Mite

regulator. The cool water pumped out of the supply tank passed through a heat regenerator that used the hot exit water from the chambers to preheat the incoming water. Details of the electronic control system and automated data acquisition equipment are included in Ref 5.

The pressurized water environment constant-load-amplitude FCGR tests were conducted at a frequency of one cycle per minute (sinusoidal waveform) on 1.3-cm (0.5-in.)-thick by 10.2-cm (4.0-in.)-wide by 12.2-cm (4.8-in.)-high compact-type specimens at load ratios of 0.20 and 0.50. The compact specimens machined from the two forgings were oriented with their notch directions parallel to the primary (longest) forging dimension. Compact specimens removed from the SA533 Grade A Class 2 and SA533 Grade B, Class 2 plate steels were machined to the T-L and L-T orientations, respectively, as per the ASTM Test for Plane-Strain Fracture Toughness of Metallic Materials (ASTM E 399-83). The weldment compact specimens were oriented with their notch directions parallel to the submerged-arc weldments. All of the specimens were precracked and tested in accordance with the ASTM Test for Constant-Load-Amplitude Fatigue Crack Growth Rates Above 10^{-8} m/Cycle (ASTM E 647-83).

Crack length was determined by the elastic compliance method. The stress-intensity factor range, ΔK , expression developed for the compact-type specimen by Saxena and Hudak was utilized in this investigation [6]. The seven-point incremental polynomial method was utilized to convert crack length, a , versus elapsed cycle, N , to crack growth rate, da/dN . Because data acquisition and analysis were automated, information on crack growth rates was instantaneously available during the test.

All da/dN versus ΔK data points that failed to satisfy the ASTM Test E 647-83 criterion established to ensure that each specimen would be predominantly elastic at all values of applied load were noted. This criterion is based on specimen dimensions and is given by

$$W - a > \frac{4}{\pi} \left(\frac{K_{\max}}{\sigma_{ys}} \right)^2$$

where W = width, a = crack length, K_{\max} is the maximum stress-intensity factor, and σ_{ys} is the material's 0.2% offset yield strength.

Details of the pressurized water environment are summarized in Table 5. Note that boric acid was not included in the pressurized water environment.

Results and Discussion

Fatigue Crack Growth Rate Tests

The FCGR properties of four pressure vessel steels (SA508 Class 2a; SA533 Grade A, Class 2; SA508 Class 3a; and SA533 Grade B, Class 2) and two automatic submerged-arc weldments (SA508 Class 2a and SA533 Grade A, Class 2) generated in a pressurized water environment are presented in Figs. 4 through 7. In each of these figures the designation PWR refers to the pressurized water environment specified in Table 5; recall that boric acid was not included in this pressurized water environment. The 288°C (550°F) air environment FCGR data, included for comparative purposes in Figs. 4 through 7, were generated with compact-type specimens of the same size as those tested in the pressurized water environment [2]. Overall, the air environment FCGR properties of these four pressure vessel steels and two submerged-arc weldments proved independent of the load ratio (0.20 or 0.70) and temperature (24 or 288°C, 75 or 550°F). Furthermore, the base and weld metal air environment FCGR properties were essentially identical.

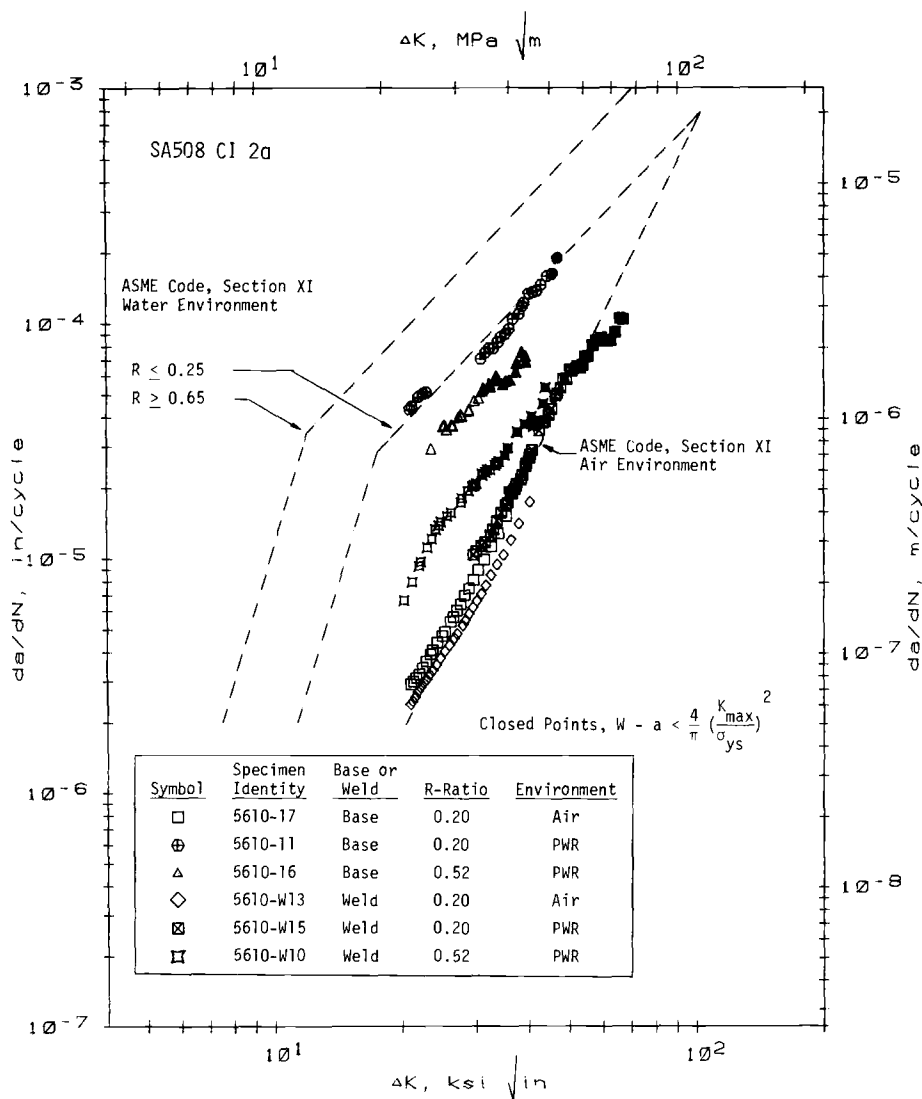


FIG. 4—Comparison of the fatigue crack growth rate properties of SA508 Class 2a base and submerged-arc weld metal.

Clearly, the growth rate of fatigue cracks was faster in the pressurized water environment than in the air environment for each of the base materials and weldments. This behavior is consistent with that reported in the literature [7-12]. Moreover, the influence of the pressurized water environment on fatigue crack propagation was more significant in the base materials than in the corresponding weldments (see Figs. 4 and 5). Furthermore, the difference in the crack propagation rates in the pressurized water versus air environment tended to decrease with increasing ΔK . Similar behavior was previously observed by other investigators [9,10,13,14]. At high ΔK levels, the fatigue crack tip moves at a fast rate and, therefore, the environments do not have adequate time to react at the crack tip, despite

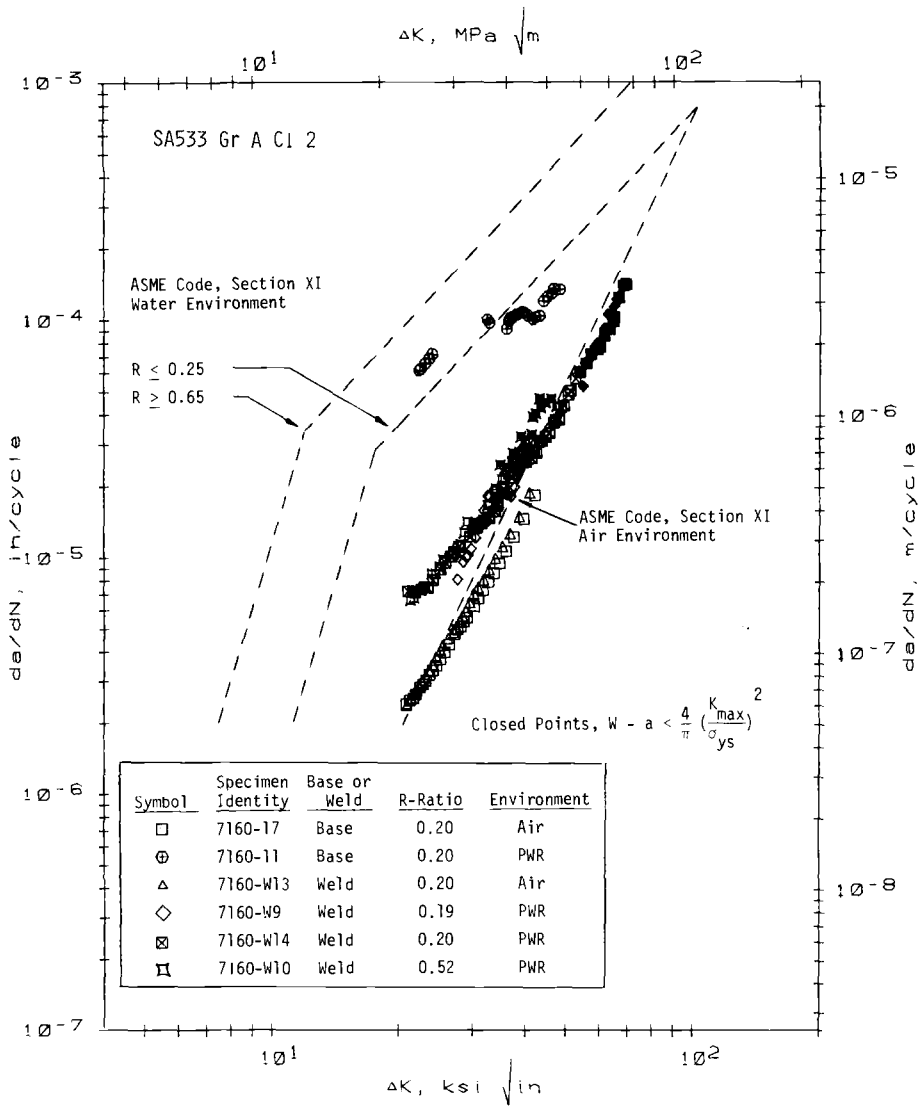


FIG. 5—Comparison of the fatigue crack growth rate properties of SA533 Grade A Class 2 base and submerged-arc weld metal.

the slow test frequency, which results in the decreasing difference between fatigue crack growth rates in the pressurized water versus air environments.

Although no influence of load ratio was observed when propagating fatigue cracks in these materials at 24 or 288°C (75 or 550°F) in an air environment [7], in the pressurized water environment increasing the load ratio from 0.20 to 0.50 typically increased the rate of crack propagation. The only exception to this behavior was demonstrated by the SA508 Class 2a base material (see Fig. 4, Specimen 5610-16). These same results were previously reported for pressure vessel steels [7,8,15,16] and stainless steels [17]. Moreover, the influence of the load ratio on fatigue crack growth rates proved more significant in the base

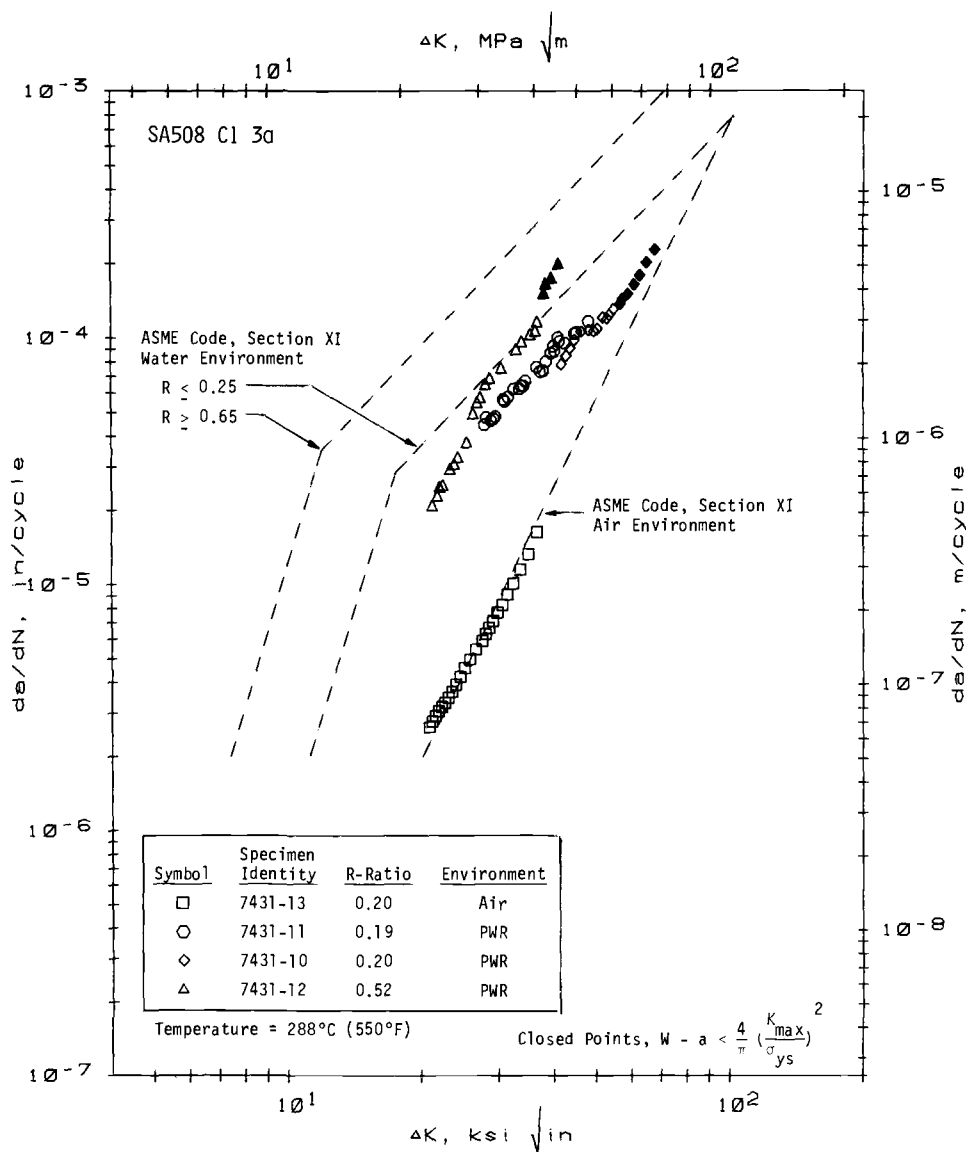


FIG. 6—The influence of environment and R-ratio on the fatigue crack growth rate properties of SA508 Class 3a steel.

materials than in the corresponding weldments. In addition, in those cases where duplicate FCGR tests were conducted in the pressurized water environment at a load ratio of 0.20 (see Figs. 5 to 7), the duplicate tests produced very consistent crack propagation rates.

The pressurized water environment FCGR properties of the four base materials and two submerged-arc weldments at a fixed load ratio are directly compared in Figs. 8 and 9. It is again clearly obvious that the growth rate of fatigue cracks in the SA508 Class 2a and SA533 Grade A, Class 2 base materials exposed to the pressurized water environment was signif-

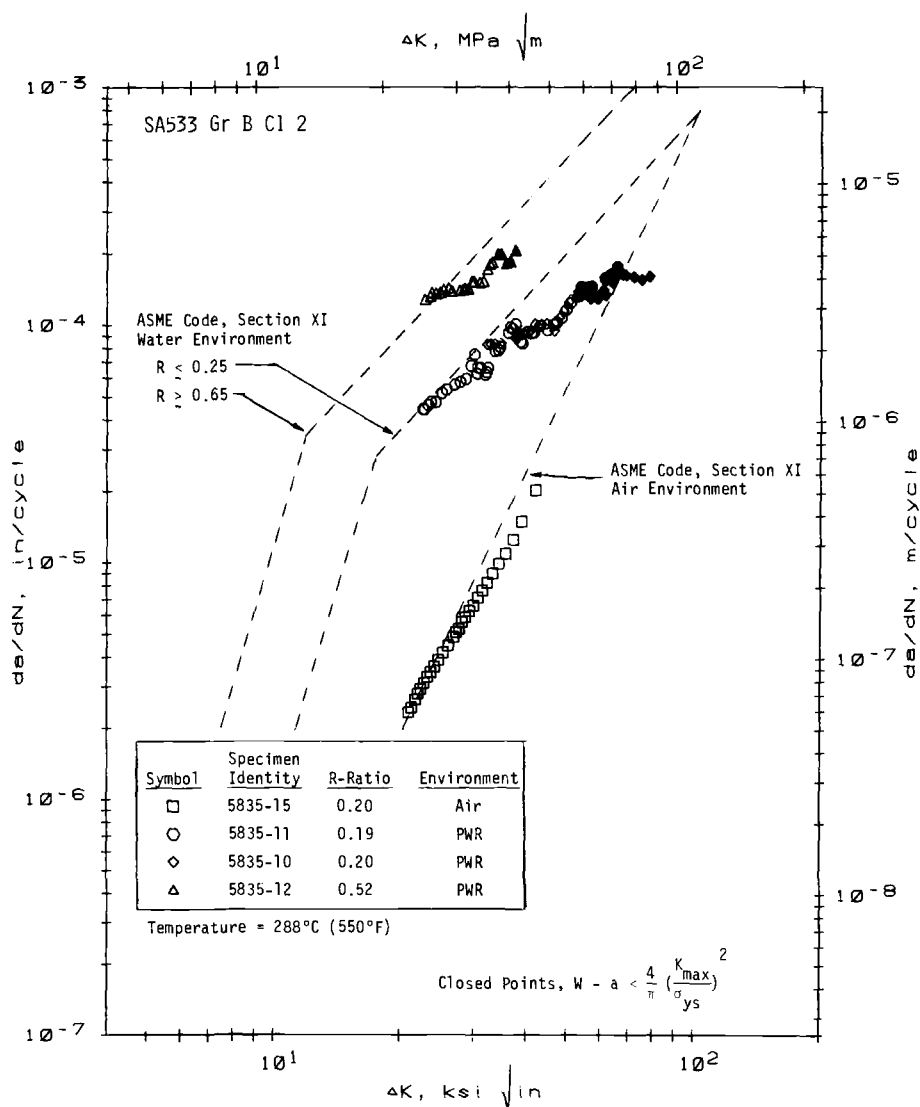


FIG. 7—The influence of environment and R-ratio on the fatigue crack growth rate properties of SA533 Grade B, Class 2 steel.

icantly faster than in the corresponding weldments. In the pressurized water environment at a load ratio of 0.20, the growth rate of fatigue cracks in the two weldments was essentially identical, while at a load ratio of 0.50, the rate of crack propagation in the SA508 Class 2a weld was slightly faster than in the SA533 Grade A, Class 2 weld. In like manner, the growth rate of fatigue cracks in the four base materials in the pressurized water environment at a load ratio of 0.20 fell within a close scatter band, while at the higher load ratio, some moderate material variability was observed; that is, the growth rate of fatigue cracks was fastest in the SA533 Grade B, Class 2 steel and slowest in the SA508 Class 2a base material.

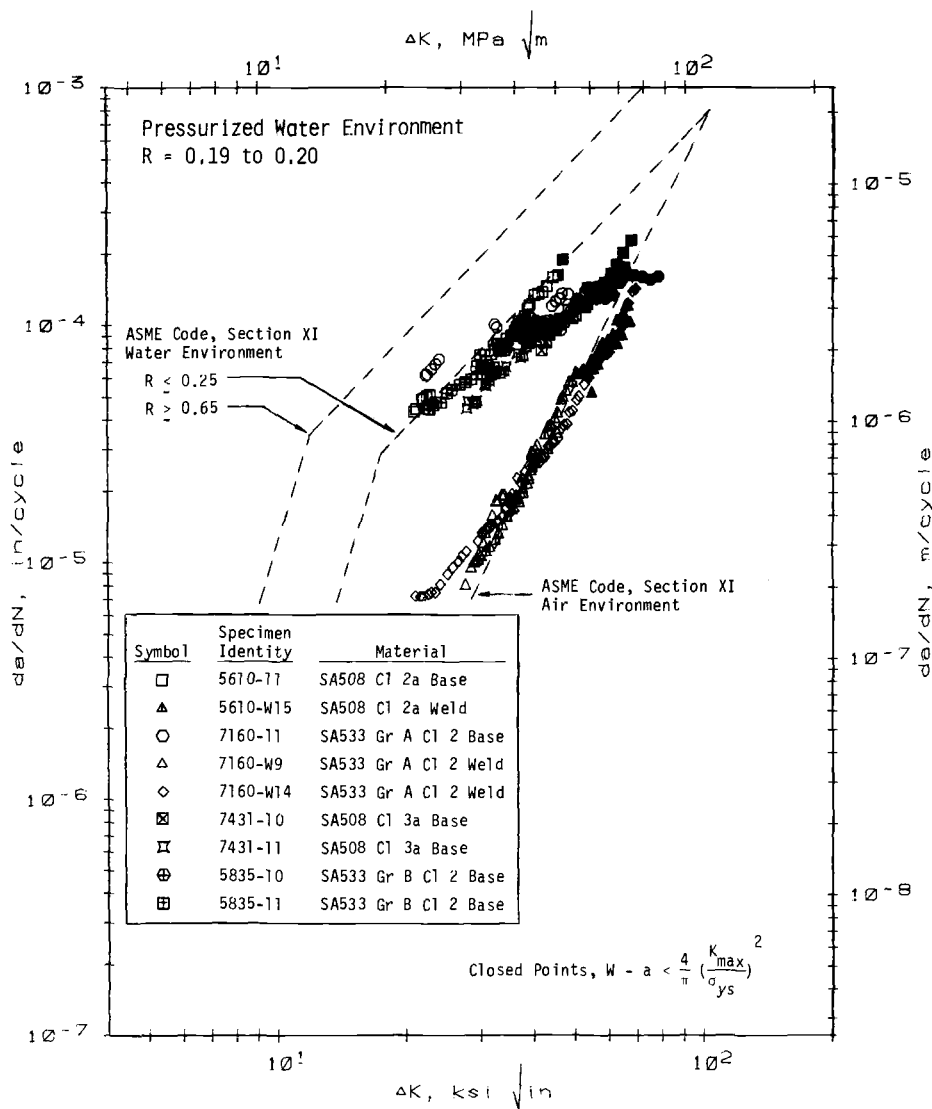


FIG. 8—Comparison of the fatigue crack growth rate properties of various pressure vessel steels subjected to a pressurized water environment at an R-ratio of 0.19 to 0.20.

Much of the literature also demonstrates little FCGR material-to-material variability in corrosive, reactor environments [15,18,19].

The growth rate of fatigue cracks in all four base materials, as well as the two submerged-arc weldments in the pressurized water environment at load ratios of 0.20 or 0.50, was generally conservative compared with the appropriate ASME Section XI water environment reference curve. Moreover, the SA508 Class 2a and SA533 Grade A, Class 2 submerged-arc weldment FCGR data fell very close to the ASME Section XI air environment reference curve even at a load ratio of 0.50.

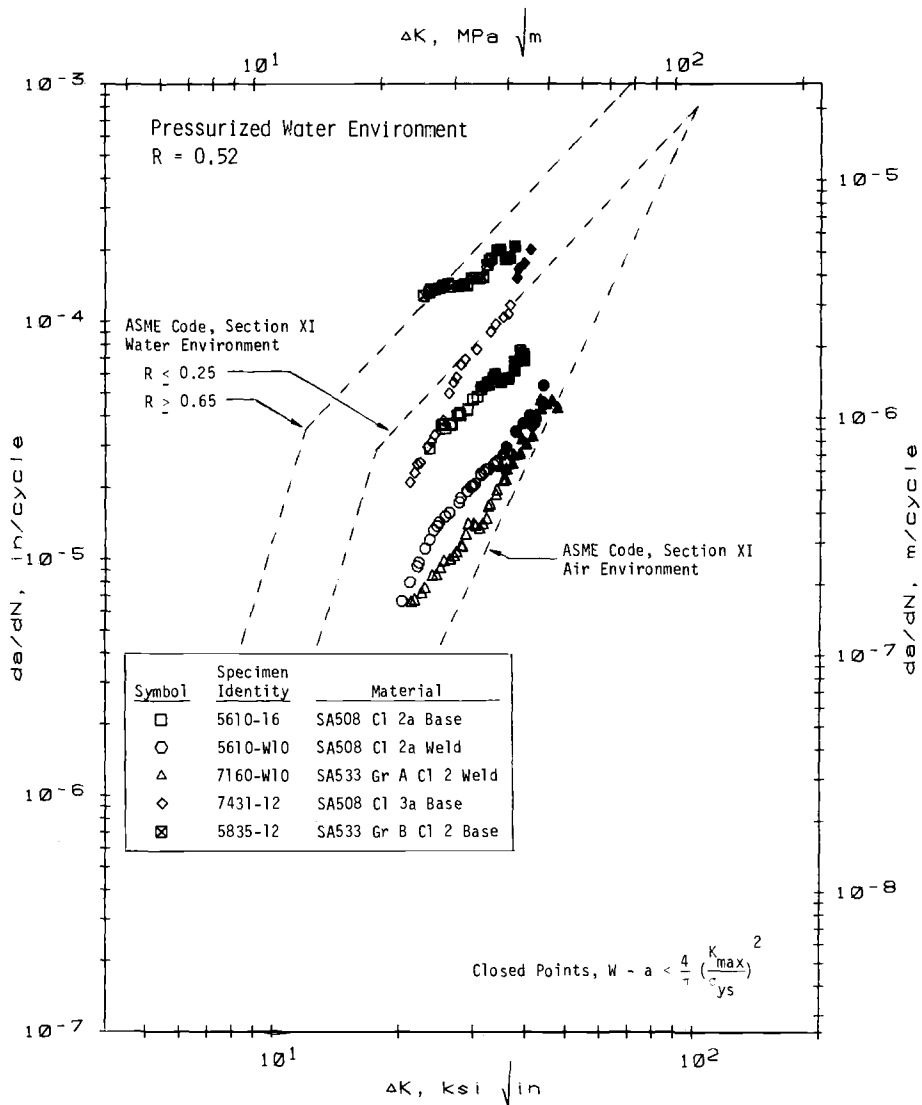


FIG. 9—Comparison of the fatigue crack growth rate properties of various pressure vessel steels subjected to a pressurized water environment at an R-ratio of 0.52.

Fracture Morphology and Mechanistic Considerations

As discussed in the previous section, the most notable feature of the FCGR data is the fact that the welds exhibited almost no environmental enhancement of growth rates while the base materials did show marked environmental effects. The chemical compositions of the base materials and welds are very similar, as are the tensile properties. One key consideration is the sulfur level, since high sulfur levels have been correlated with high environmentally enhanced growth rates [20–27]. Table 1 shows the base and weld metals to have virtually identical sulfur levels. The sulfide compositions and morphologies were char-

acterized and the fracture surfaces were examined in an attempt to explain the difference in environmentally enhanced fatigue crack growth rates.

Following the FCGR tests, the specimen fracture surfaces were carefully examined using scanning electron microscopy (SEM). Because of heavy oxide deposits present on the fracture surfaces of those specimens tested in the pressurized water environment, they were electrochemically cleaned in an Endox solution prior to SEM examinations [28].

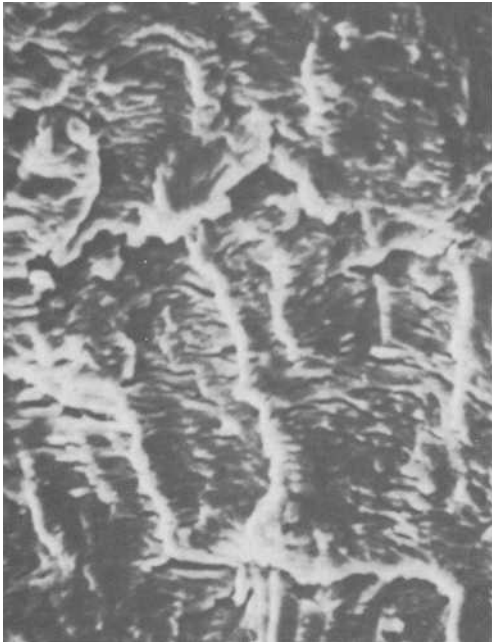
Fatigue striations were clearly observed on the fracture surfaces of each of the base material specimens tested in the 288°C (550°F) air environment. A representative air environment fracture morphology is presented in Fig. 10 for the SA508 Class 3a base material loaded at $R = 0.20$. Striations are shown at two levels of ΔK . Fatigue striations were the predominant mode of fracture at the lower ΔK level, while at the higher ΔK level, dimpled fracture was present in addition to the striations. Similar fracture morphologies were observed on the fracture surfaces of those specimens tested at $R = 0.50$. Fatigue striations were also observed on the fracture surfaces of weld metal specimens loaded in the air environment (see Fig. 11). For both the base and weld metals, secondary cracking tended to increase with increasing ΔK .

Fracture morphologies of the four base materials tested in the pressurized water environment are illustrated in Figs. 12 through 15. Fatigue striations are clearly evident. Secondary cracking is present and is more pronounced than for specimens tested in air. Fan-shaped markings occasionally cross planar facets which are covered with striations. This observation suggests some relationship between the planar facets and the underlying crystal structure. The striations on specimens tested in high-temperature water are shallow and often delineated by cracking (see Fig. 16). This, together with the fan-shaped markings, makes the term brittle striations appropriate. With the sole exception of SA508 Class 2a base material, occasional patches of intergranular cracking were also observed. The general characteristics of the fracture morphologies did not change significantly from an R -ratio of 0.20 to one of 0.50.

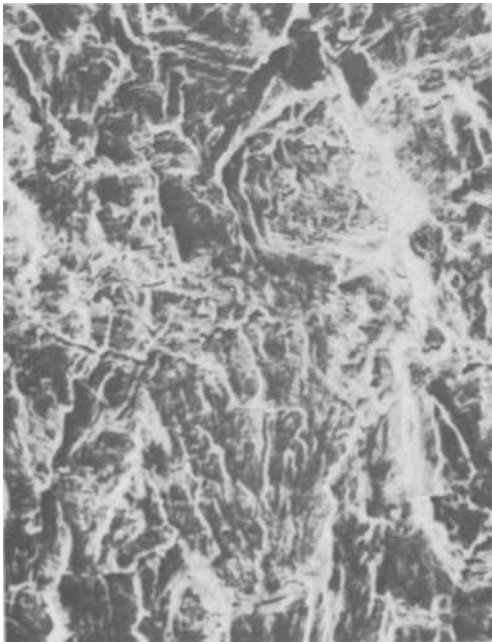
For the SA508 Class 2a and SA533 Grade A, Class 2 submerged-arc welds, featureless fractures were encountered regardless of ΔK level or R -ratio, presumably as a result of corrosive action (see Figs. 17 through 19). Fractographic appearance thus does not offer much evidence as to why the welds exhibited superior resistance to environmentally enhanced crack growth.

While the sulfur levels of the welds and the corresponding base materials are virtually identical, sulfur prints of these materials were strikingly different. The sulfur print of the base material exhibited an expected spotted appearance while that of the weld was essentially clear. Scanning electron microscopy and energy-dispersive X-ray spectroscopy (EDS) analysis of polished but unetched specimens revealed characteristic differences in both the composition and morphology of sulfur-bearing inclusions in the base and weld metals. In the base materials, sulfur is present in the form of widely dispersed manganese sulfide (MnS) inclusions with a mean diameter of about 10 μm . In contrast, Fig. 20 shows that sulfur-bearing inclusions in the welds are much smaller and more uniformly distributed. Perhaps more importantly, the sulfur content of these weld inclusions is only about 1.0% by weight with high levels of aluminum, titanium and silicon. While the sulfur content of these inclusions is low, the volume fraction is sufficient to account for a total sulfur level equal to that of the base materials.

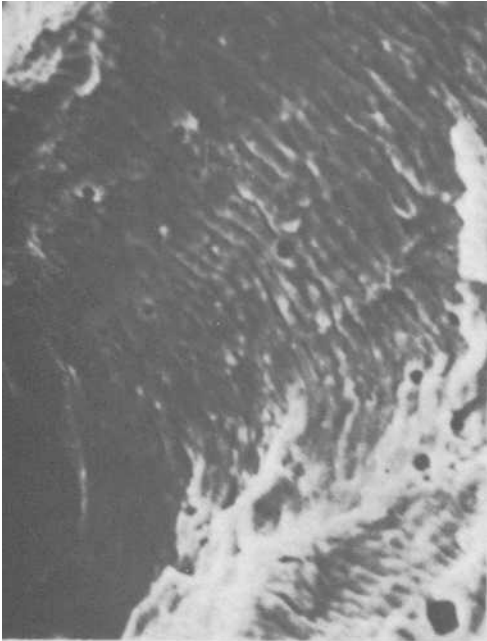
Characteristic differences in the compositions and morphologies of sulfur-bearing inclusions between the base and weld materials offer an attractive explanation of the fact that typically large environmentally enhanced fatigue crack growth rates were observed for the base materials, while almost no environmental effect was observed for the welds. Dissolution kinetics of the inclusions is expected to be affected by the huge difference in composition.



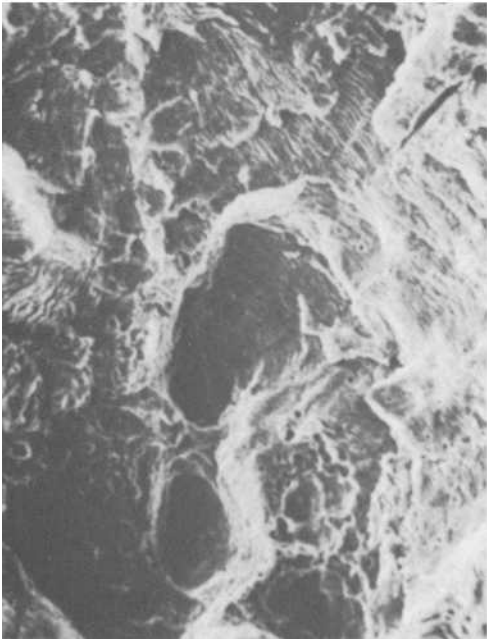
(b) $\Delta K = 20.9 \text{ ksi}\sqrt{\text{in.}}$ ($23.2 \text{ MPa}\sqrt{\text{m}}$)
|5 μm |



(a) $\Delta K = 20.9 \text{ ksi}\sqrt{\text{in.}}$ ($23.2 \text{ MPa}\sqrt{\text{m}}$)
|20 μm |

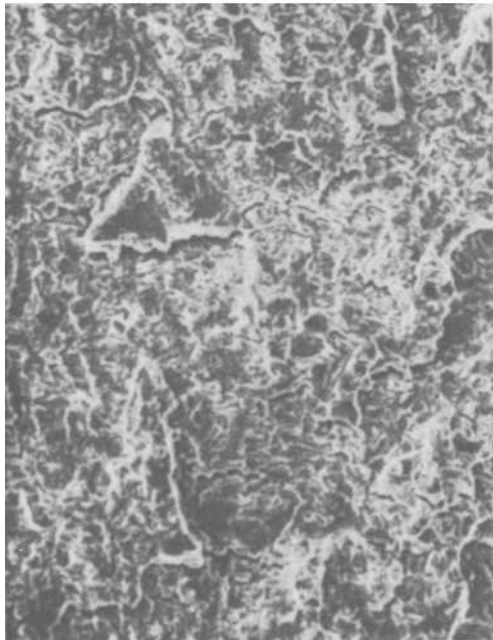


(d) $\Delta K = 49.0 \text{ ksi}\sqrt{\text{in.}}$ ($54.2 \text{ MPa}\sqrt{\text{m}}$) $5 \mu\text{m}$



(c) $\Delta K = 49.0 \text{ ksi}\sqrt{\text{in.}}$ ($54.2 \text{ MPa}\sqrt{\text{m}}$) $20 \mu\text{m}$

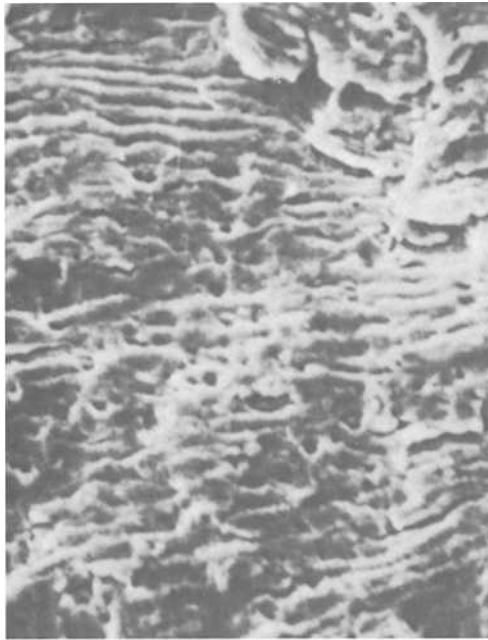
FIG. 10—Fracture morphology of SA508 Class 3a base metal (Specimen 7431-13) in an air environment at $R = 0.2$.



(a) $\Delta K = 23.9 \text{ ksi}\sqrt{\text{in.}}$ ($26.5 \text{ MPa}\sqrt{\text{m}}$) $|20\mu\text{m}|$



(b) $\Delta K = 23.9 \text{ ksi}\sqrt{\text{in.}}$ ($26.5 \text{ MPa}\sqrt{\text{m}}$) $|5\mu\text{m}|$

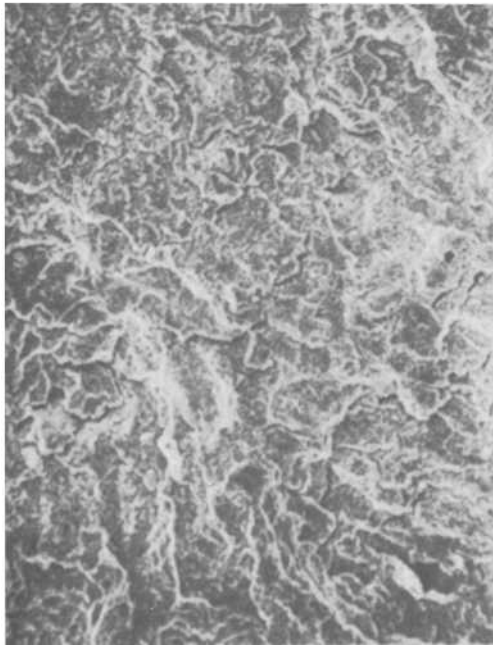


(c) $\Delta K = 83.4 \text{ ksi}\sqrt{\text{in.}}$ ($92.4 \text{ MPa}\sqrt{\text{m}}$) $|5 \mu\text{m}|$

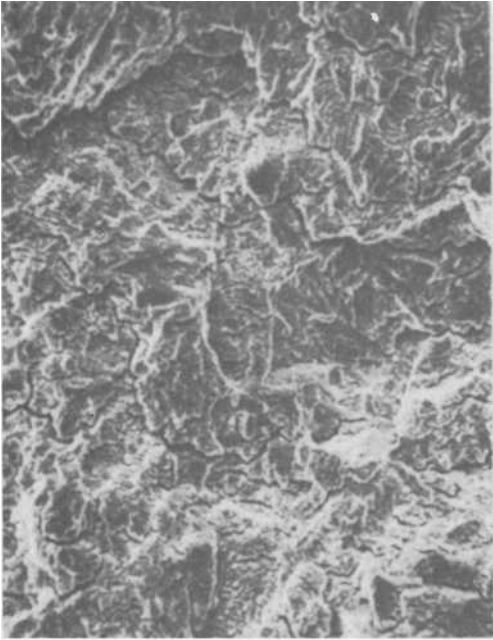


(d) $\Delta K = 83.4 \text{ ksi}\sqrt{\text{in.}}$ ($92.4 \text{ MPa}\sqrt{\text{m}}$) $|20 \mu\text{m}|$

FIG. 11—Fracture morphology of SA533 Grade A, Class 2 submerged-arc weld metal (Specimen 7160-W13) in an air environment at $R = 0.2$.



(a) $\Delta K = 20.9 \text{ ksi}\sqrt{\text{in.}}$ (23.1 MPa $\sqrt{\text{m}}$)



(b) $\Delta K = 32.7 \text{ ksi}\sqrt{\text{in.}}$ (36.2 MPa $\sqrt{\text{m}}$)

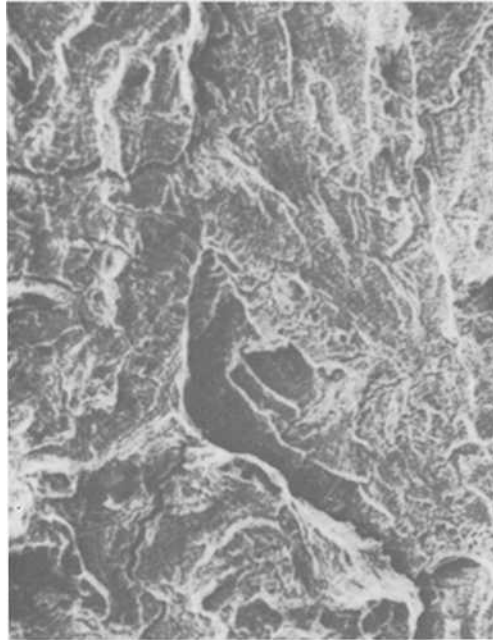


(c) $\Delta K = 39.2 \text{ ksi}\sqrt{\text{in.}}$ (43.4 MPa $\sqrt{\text{m}}$) |20 μm |
(d) $\Delta K = 55.5 \text{ ksi}\sqrt{\text{in.}}$ (61.5 MPa $\sqrt{\text{m}}$)

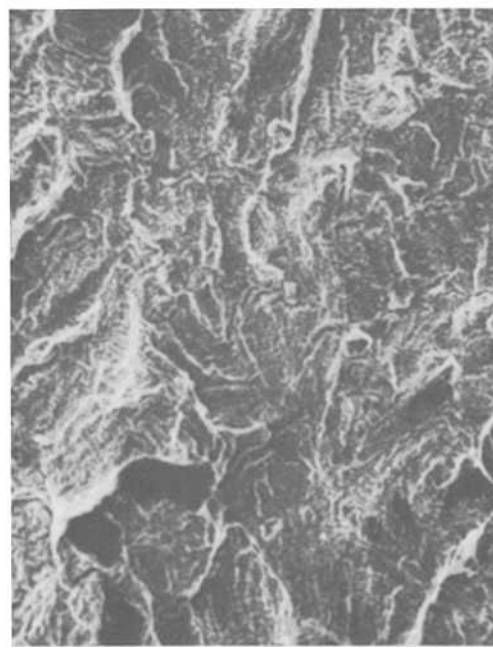


(c) $\Delta K = 39.2 \text{ ksi}\sqrt{\text{in.}}$ (43.4 MPa $\sqrt{\text{m}}$) |20 μm |
(d) $\Delta K = 55.5 \text{ ksi}\sqrt{\text{in.}}$ (61.5 MPa $\sqrt{\text{m}}$)

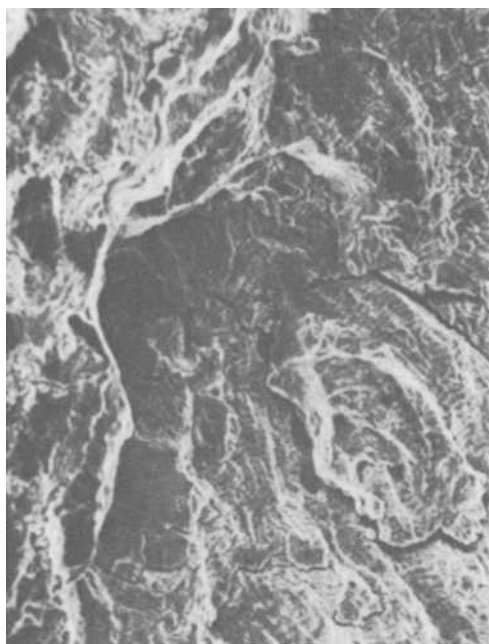
FIG. 12.—Fracture morphology of SA508 Class 2a base metal (Specimen 5610-11) in a pressurized water reactor (PWR) environment at $R = 0.2$.



(b) $\Delta K = 23.9 \text{ ksi}\sqrt{\text{in.}}$ ($26.4 \text{ MPa}\sqrt{\text{m}}$) $|20\mu\text{m}|$



(a) $\Delta K = 20.9 \text{ ksi}\sqrt{\text{in.}}$ ($23.1 \text{ MPa}\sqrt{\text{m}}$) $|20\mu\text{m}|$

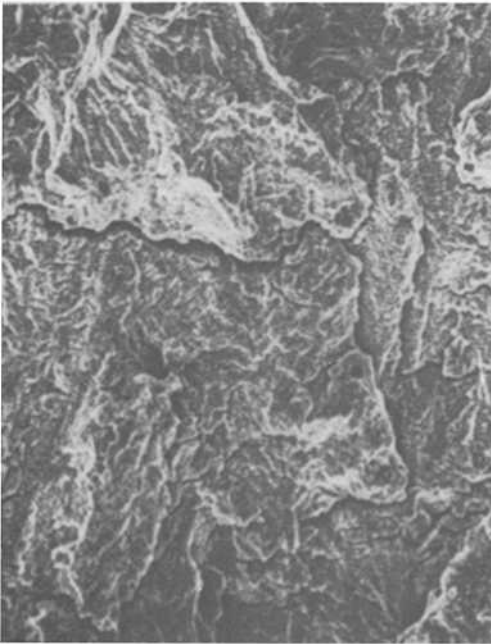


(c) $\Delta K = 32.7 \text{ ksi}\sqrt{\text{in.}}$ (36.1 MPa $\sqrt{\text{m}}$) $\left[20\mu\text{m}\right]$ (d) $\Delta K = 39.4 \text{ ksi}\sqrt{\text{in.}}$ (43.6 MPa $\sqrt{\text{m}}$) $\left[20\mu\text{m}\right]$

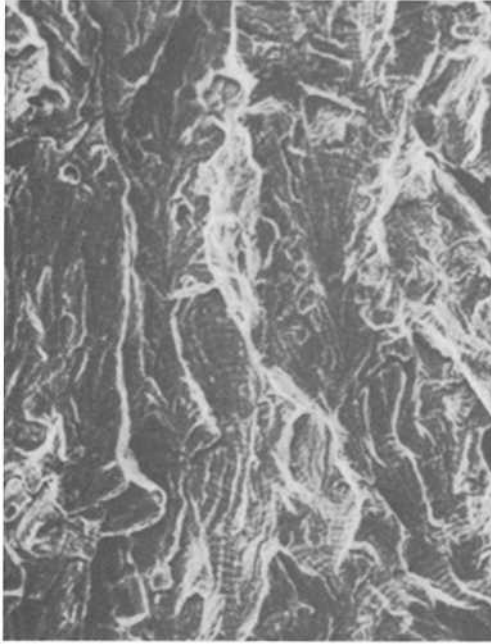


(c) $\Delta K = 32.7 \text{ ksi}\sqrt{\text{in.}}$ (36.1 MPa $\sqrt{\text{m}}$) $\left[20\mu\text{m}\right]$ (d) $\Delta K = 39.4 \text{ ksi}\sqrt{\text{in.}}$ (43.6 MPa $\sqrt{\text{m}}$) $\left[20\mu\text{m}\right]$

FIG. 13—Fracture morphology of SA533 Grade A, Class 2 base metal (Specimen 7160-11) in a PWR environment at $R = 0.2$.



(a) $\Delta K = 22.1 \text{ ksi}\sqrt{\text{in.}}$ ($24.4 \text{ MPa}\sqrt{\text{m}}$) $|20\mu\text{m}|$



(b) $\Delta K = 34.5 \text{ ksi}\sqrt{\text{in.}}$ ($38.2 \text{ MPa}\sqrt{\text{m}}$) $|20\mu\text{m}|$

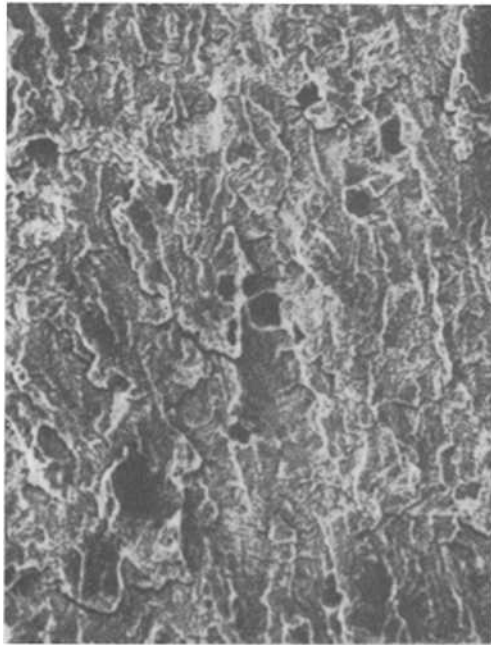


(c) $\Delta K = 41.7 \text{ ksi}\sqrt{\text{in.}}$ (46.1 MPa $\sqrt{\text{m}}$)

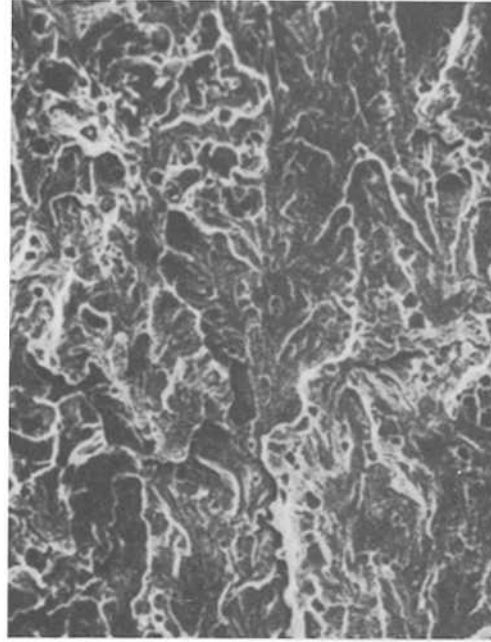


(d) $\Delta K = 54.3 \text{ ksi}\sqrt{\text{in.}}$ (60.1 MPa $\sqrt{\text{m}}$)

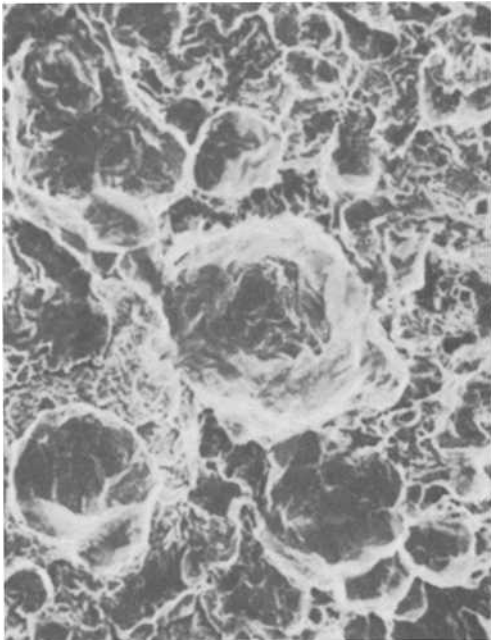
FIG. 14—Fracture morphology of SA508 Class 3a base metal (Specimen 7431-11) in a PWR environment at R = 0.2.



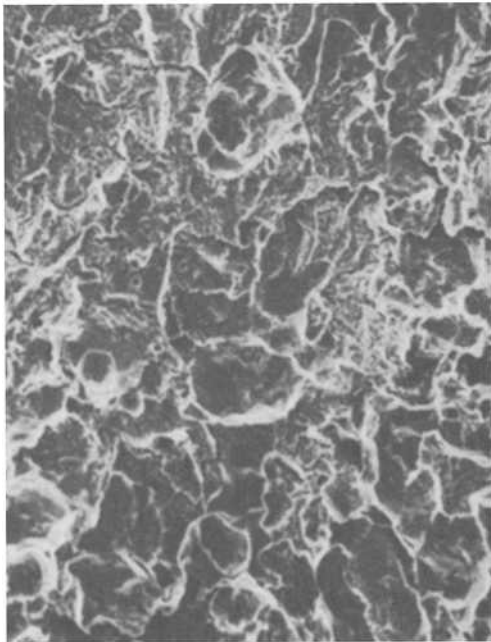
(a) $\Delta K = 22.4 \text{ ksi}\sqrt{\text{in.}}$ ($24.8 \text{ MPa}\sqrt{\text{m}}$) $|20\mu\text{m}|$



(b) $\Delta K = 34.4 \text{ ksi}\sqrt{\text{in.}}$ ($38.1 \text{ MPa}\sqrt{\text{m}}$) $|20\mu\text{m}|$

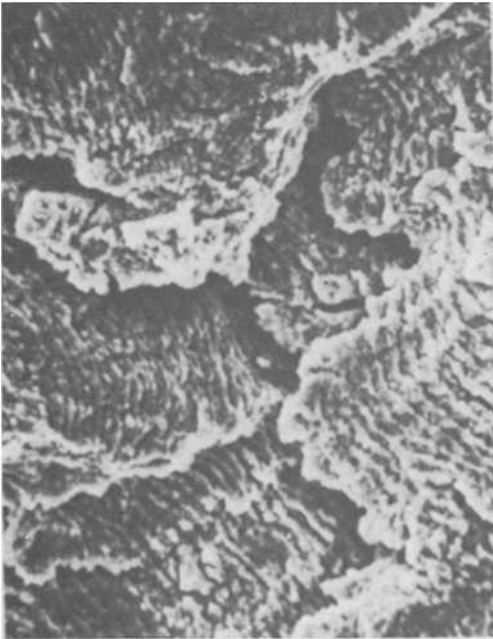


(d) $\Delta K = 65.5 \text{ ksi}\sqrt{\text{in.}}$ $(72.5 \text{ MPa}\sqrt{\text{m}})$ $|20\mu\text{m}|$



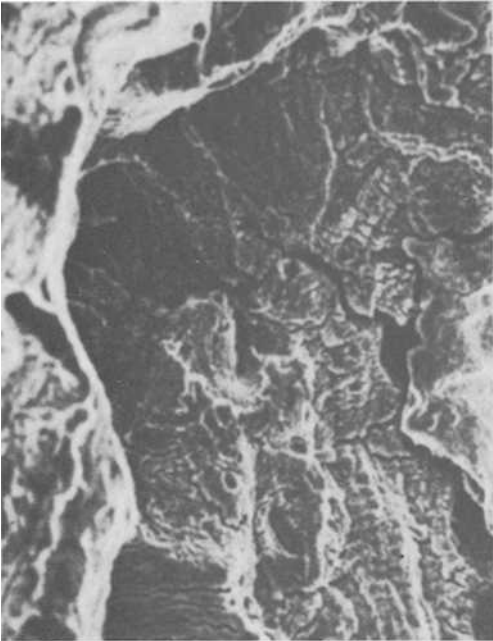
(c) $\Delta K = 41.5 \text{ ksi}\sqrt{\text{in.}}$ $(46.0 \text{ MPa}\sqrt{\text{m}})$ $|20\mu\text{m}|$

FIG. 15—Fracture morphology of SA533 Grade B, Class 2 base metal (Specimen 5835-II) in a PWR environment at $R = 0.2$.



|5 μm|

(a)



|10 μm|

(b)

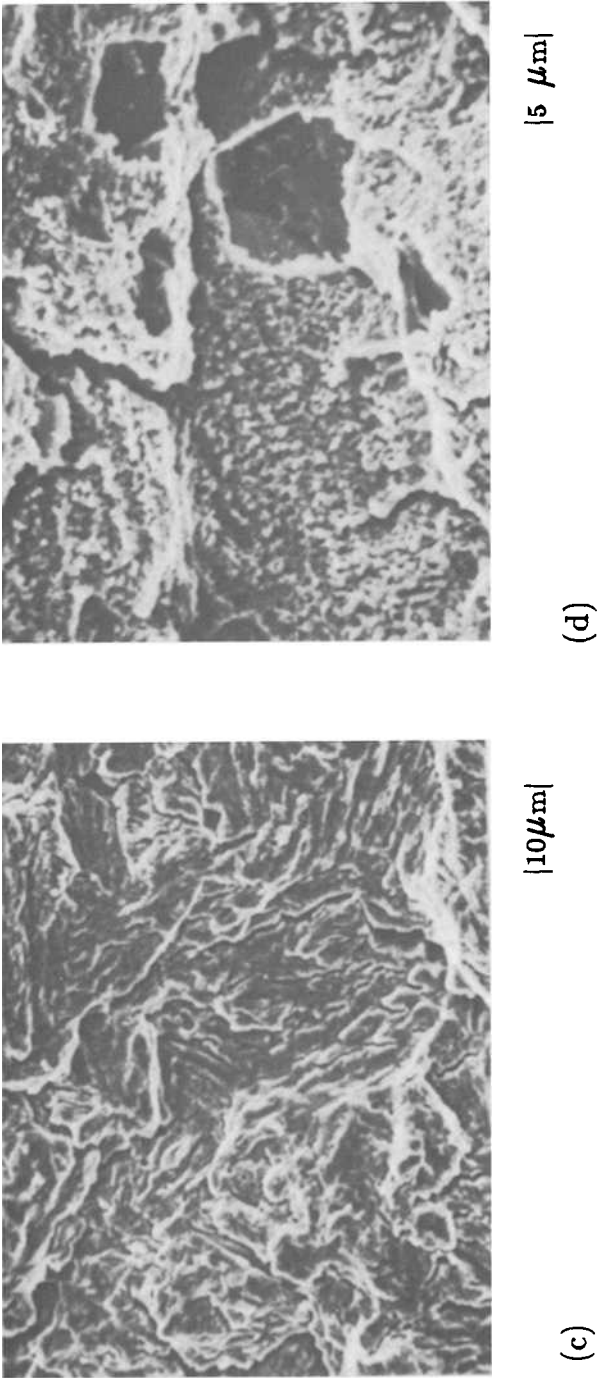
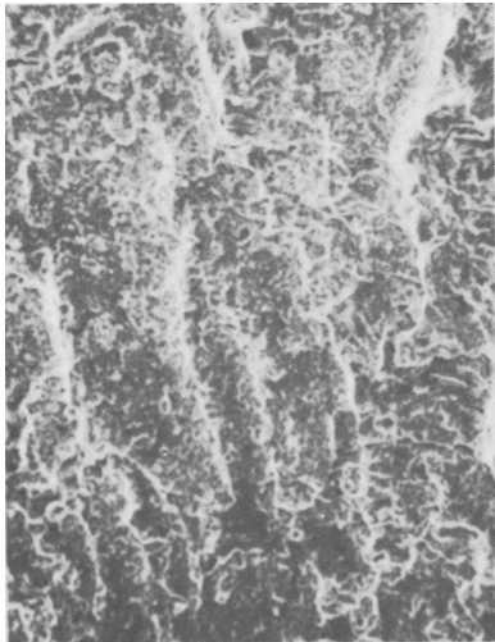
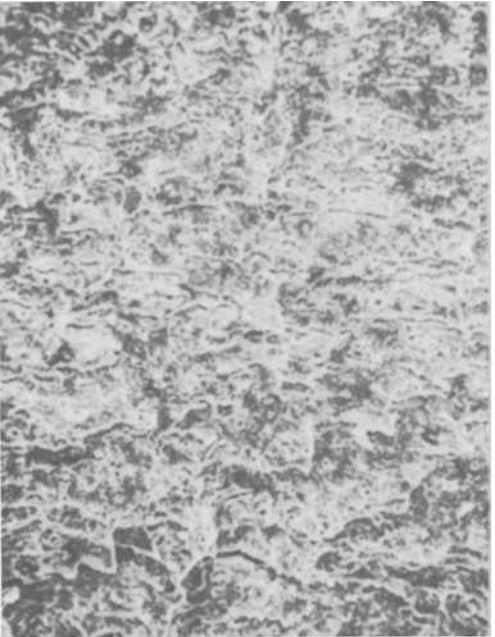


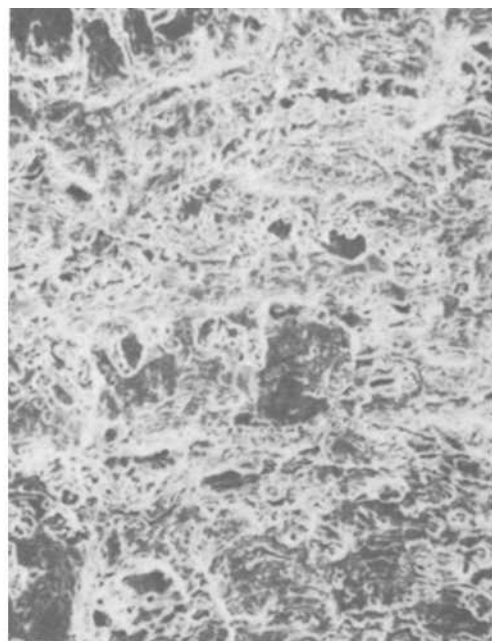
FIG. 16—Higher magnification photographs of selected figures: (a) Fig. 12c, (b) Fig. 13d, (c) Fig. 14d, and (d) Fig. 15a.



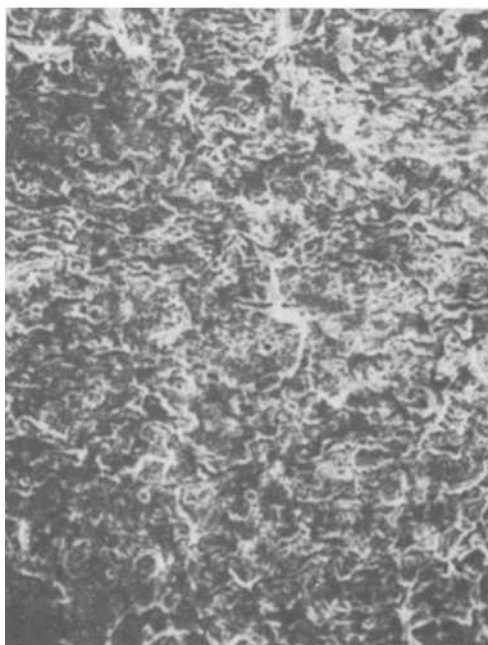
(a) $\Delta K = 27.2 \text{ ksi}\sqrt{\text{in.}}$ (30.1 MPa $\sqrt{\text{m}}$)



(b) $\Delta K = 44.1 \text{ ksi}\sqrt{\text{in.}}$ (48.8 MPa $\sqrt{\text{m}}$)

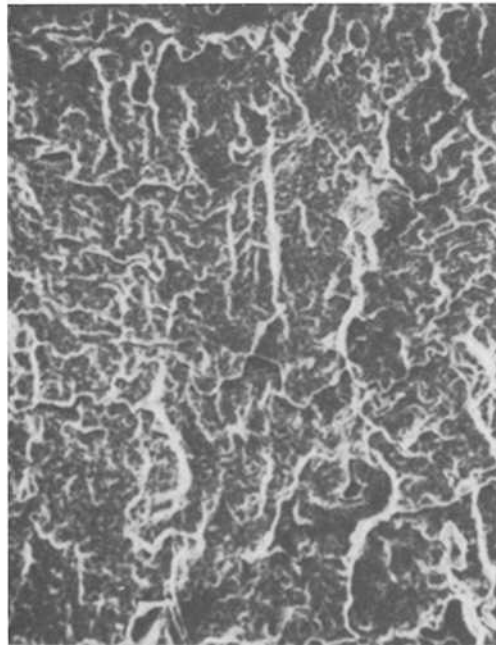

 $|20\mu\text{m}|$

(d) $\Delta K = 72.8 \text{ ksi}\sqrt{\text{in.}}$ ($80.6 \text{ MPa}\sqrt{\text{m}}$)

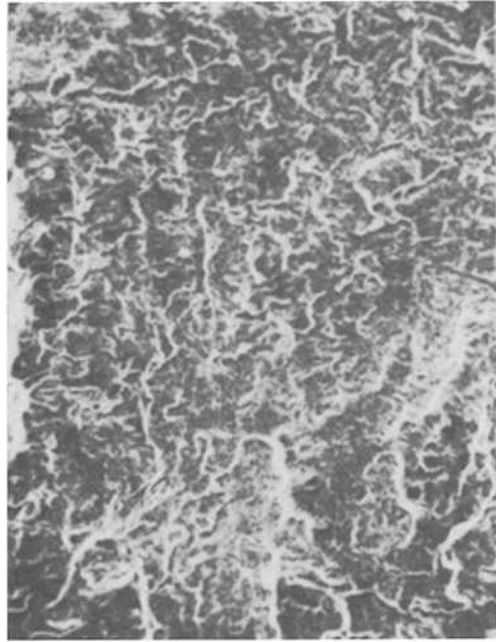

 $|20\mu\text{m}|$

(c) $\Delta K = 53.2 \text{ ksi}\sqrt{\text{in.}}$ ($58.9 \text{ MPa}\sqrt{\text{m}}$)

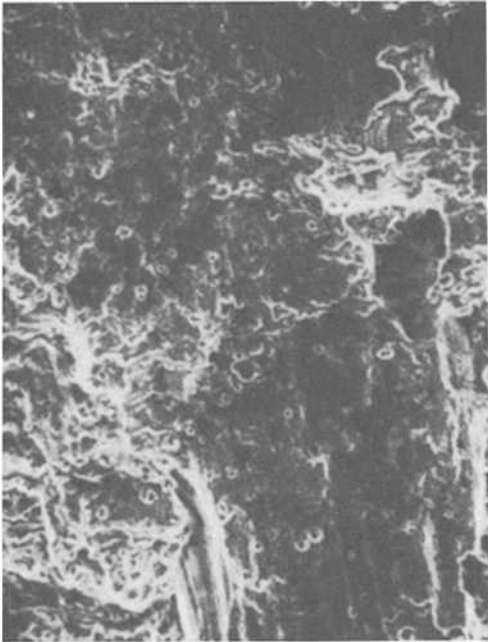
FIG. 17—Fracture morphology of SA508 Class 2a submerged-arc weld metal (Specimen 5610-W15) in a PWR environment at $R = 0.2$.



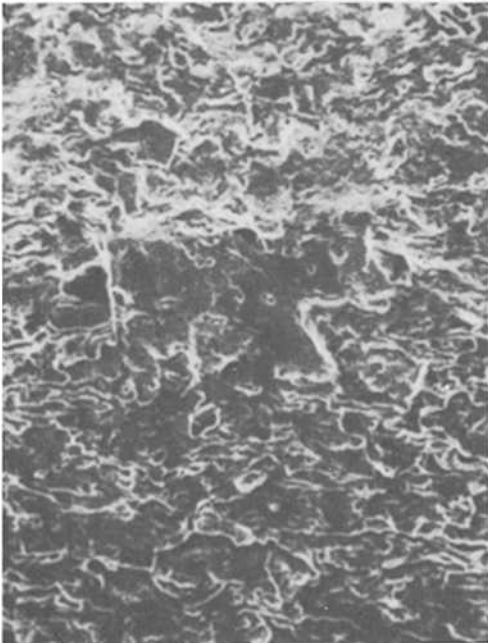
(a) $\Delta K = 21.8 \text{ ksi}\sqrt{\text{in.}}$ (24.1 MPa $\sqrt{\text{m}}$)



(b) $\Delta K = 29.0 \text{ ksi}\sqrt{\text{in.}}$ (32.1 MPa $\sqrt{\text{m}}$)

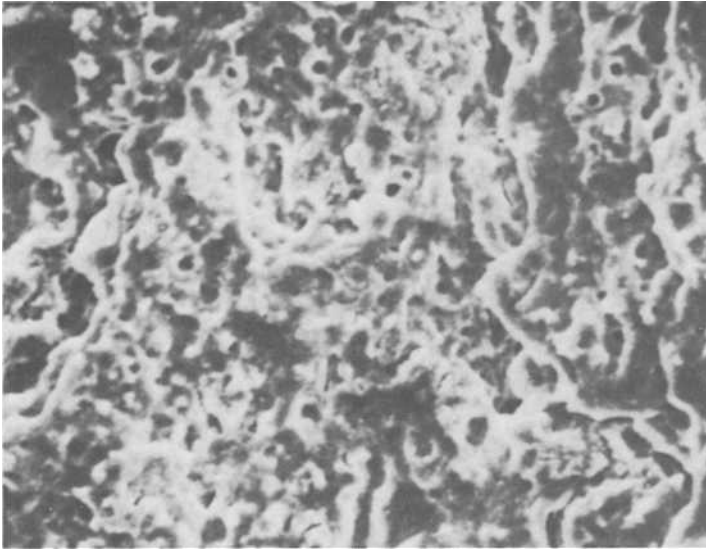


(d) $\Delta K = 78.9 \text{ ksi}\sqrt{\text{in.}}$ (87.3 MPa $\sqrt{\text{m}}$)



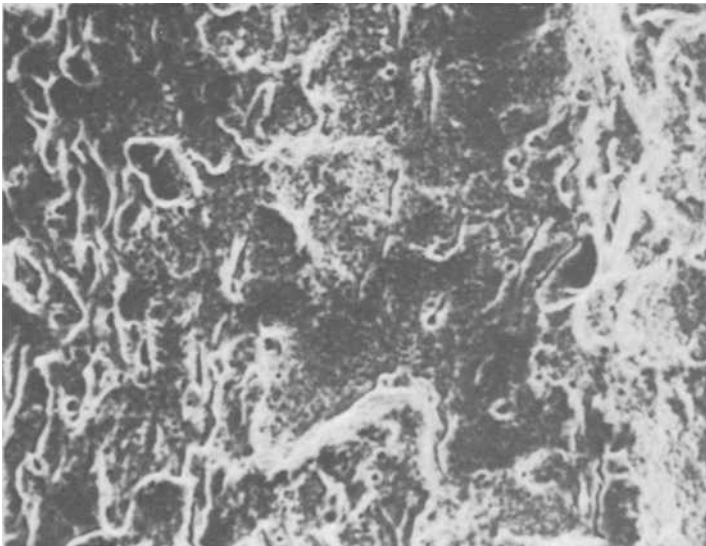
(c) $\Delta K = 50.9 \text{ ksi}\sqrt{\text{in.}}$ (56.4 MPa $\sqrt{\text{m}}$)

FIG. 18—Fracture morphology of SA533 Grade A, Class 2 submerged-arc weld metal (Specimen 7160-W14) in a PWR environment at $R = 0.2$.



(a)

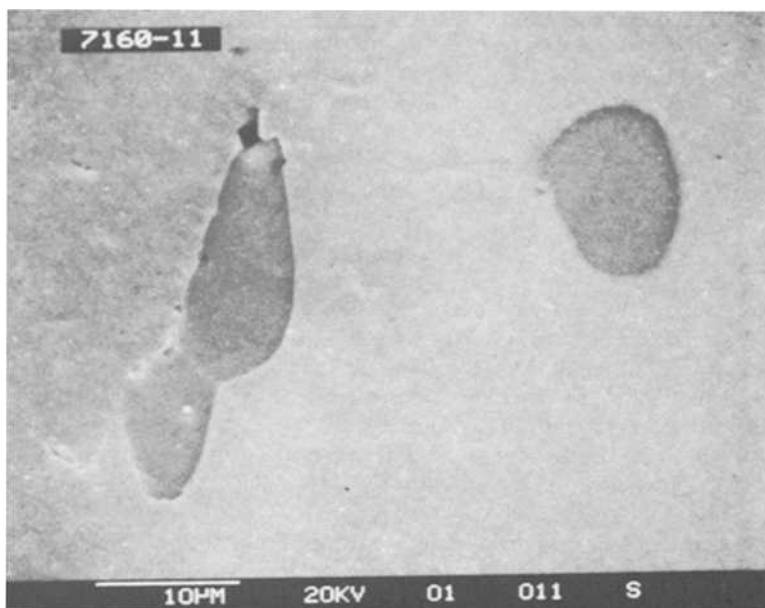
|5 μm |



(b)

|10 μm |

FIG. 19—Higher magnification photographs of selected figures: (a) Fig. 17c and (b) Fig. 18c.



(a) Base



(b) Weld

FIG. 20—Morphology of sulfide inclusions in SA533 Grade A, Class 2 base and weld metals.

The sulfur level at and near the crack tip will likewise be affected by the size and spacing of the inclusions. High dissolved sulfur levels will promote both anodic dissolution [9,29] and high levels of hydrogen [8,16,18,29-33] in the matrix. Thus, from the viewpoint of either environmentally enhanced crack growth rates, anodic dissolution, or hydrogen effects, the composition and morphology of sulfur-bearing inclusions is expected to be important. Also, from either viewpoint, the very low sulfur level of inclusions in the welds, coupled with their small size and fine dispersion, is consistent with the absence of any significant degree of environmentally enhanced fatigue crack growth rates.

Conclusions

1. The pressurized water environment FCGR properties of four pressure vessel steels (SA508 Class 2a; SA533 Grade A, Class 2; SA508 Class 3a; and SA533 Grade B, Class 2) and two submerged-arc weldments (SA508 Class 2a and SA533 Grade A, Class 2) at load ratios of 0.20 and 0.50 were generally conservative compared with the appropriate ASME Section XI water environment reference curve.
2. The growth rate of fatigue cracks was faster in the pressurized water environment than in a 288°C (550°F) air environment for each of the base materials and submerged-arc weldments.
3. The influence of the pressurized water environments on fatigue crack propagation was substantially greater in the base materials than in the corresponding welds. The dissimilarity in base and weld metal pressurized water environment FCGR properties is related to a difference in sulfide composition and morphology.

References

- [1] ASME Boiler and Pressure Vessel Code, American Society of Mechanical Engineers, New York, NY, 1974.
- [2] Logsdon, W. A. and Liaw, P. K., *Engineering Fracture Mechanics*, Vol. 22, No. 3, 1985, pp. 509-526.
- [3] Liaw, P. K. and Logsdon, W. A., *Journal of Engineering Materials and Technology*, Vol. 107, January 1985, pp. 26-33.
- [4] Logsdon, W. A., *Journal of Materials for Energy Systems*, Vol. 3, No. 4, March 1982, pp. 39-50.
- [5] Ceschini, L. J., Liaw, P. K., Rudd, G. E., and Logsdon, W. A. in *Environment-Sensitive Fracture, ASTM STP 821*, American Society for Testing and Materials, Philadelphia, 1984, pp. 426-442.
- [6] Saxena, A. and Hudak, S. J., Jr., *International Journal of Fracture*, Vol. 14, 1978, p. 453.
- [7] Scott, P. M., *Metal Science*, July 1979, pp. 396-401.
- [8] Mager, T. R., Moon, D. M., and Landes, J. D., "Fatigue Crack Growth Characteristics of A533 Grade B Class 1 Plate in an Environment of High-Temperature Primary-Grade Nuclear Reactor Water," ASME Paper 76-PVP-3, American Society of Mechanical Engineers, New York, 1976.
- [9] McMinn, A., "Corrosion Fatigue Studies on A533-B, C-Mn and Ducol W30 Pressure Vessel Steels at Ambient Temperature and Pressure in Aqueous Environments," Northern Division Report ND-R-435(s), United Kingdom Atomic Energy Authority, June 1981.
- [10] Cullen, W. H., Jr., Provenzano, V., Torronen, K. J., Watson, H. E., and Loss, F. J., "Fatigue Crack Growth of A508 Steel in High-Temperature, Pressurized Reactor Grade Water," NRL Memorandum Report 4063, National Research Laboratory, September 1979.
- [11] Gerber, T. L., Heald, J. D., and Kiss, E., "Fatigue Crack Growth in SA-508 Class 2 Steel in a High-Temperature, High-Purity Water Environment," ASME Paper 74-Mat-2, American Society of Mechanical Engineers, New York, 1974.
- [12] Prater, T. A., Catlin, W. R., and Coffin, L. F., *Journal of Engineering Materials and Technology*, Vol. 108, January 1986, pp. 2-9.
- [13] Bamford, W. H., Moon, D. M., and Ceschini, L. J., "Heavy-Section Steel Technology Quarterly Progress Report," ORNL-NUREG/TM-239, Oak Ridge National Laboratory, Oak Ridge, TN, October 1978, p. 9.

- [14] Bamford, W. H., *Journal of Engineering Materials and Technology*, Vol. 101, July 1979, pp. 182–190.
- [15] Bamford, W. H., *Proceedings*, Institution of Mechanical Engineers/Society of Environmental Engineers Joint Conference, London, 1977, pp. 51–56.
- [16] Mager, T. R., Landes, J. D., Moon, D. M., and McLaughlin, V. J., “On the Fatigue Crack Growth Characteristics of A533 Grade B Class 1 Plate in an Environment of High-Temperature Primary Grade Nuclear Reactor Water,” HSST Report No. 35, WCAP-8256, Westinghouse Electric Corporation, Pittsburgh, PA., December 1973.
- [17] Bamford, W. H., *Journal of Pressure Vessel Technology*, Vol. 101, February 1979, pp. 73–79.
- [18] Bamford, W. H. and Moon, D. M., *Corrosion* 79, National Association of Corrosion Engineers, Atlanta, GA, 1979.
- [19] Scott, P. M. and Truswell, A. E., Paper PVP 82-029, “Corrosion Fatigue Crack Growth in Reactor Pressure Vessel Steels in PWR Primary Water,” *Proceedings*, American Society of Mechanical Engineers Pressure Vessels and Piping Conference, Orlando, FL, 1982.
- [20] Slama, G. and Rabbe, P., *Proceedings*, Fifth Structural Mechanics in Reactor Technology, Postconference Seminar, Paris, France, 1981, p. 311.
- [21] Bamford, W. H., “Heavy-Section Steel Technology Report for October-December 1982,” USNRC Report NUREG/CR-2751, Vol. 4, National Research Council, Washington, DC, 1983, p. 139.
- [22] Bamford, W. H. and Ceschini, L. J., “Heavy-Section Steel Technology Report for April-June 1983,” USNRC Report NUREG/CR-3334, Vol. 2, National Research Council, Washington, DC, 1983, p. 104.
- [23] Bamford, W. H., Ceschini, L. J., and Jacko, R. J., “Heavy-Section Steel Technology Report for July-September 1983,” USNRC Report NUREG/CR-3334, Vol. 3, National Research Council, Washington, DC, 1984, p. 97.
- [24] Scott, P. M., Truswell, A. E., and Druce, S. G., *Corrosion*, Vol. 40, 1984, p. 350.
- [25] Van Der Sluys, W. A., “Corrosion Fatigue Characterization of Reactor Pressure Steels—Phase I Report,” Progress Report, EPRI Project 1325-1, Electric Power Research Institute, Palo Alto, CA, 1983.
- [26] Cullen, W. H., Kemppainen, M., Hanninen, H., and Torronen, K., “The Effects of Sulfur Chemistry and Flow Rate on Fatigue Crack Growth Rates in LWR Environments” NUREG/CR-4121, Nuclear Regulatory Commission, Washington, DC, 1985.
- [27] Van Der Sluys, W. A. and Emanuelson, R. H., *Journal of Engineering Materials and Technology*, Vol. 108, January 1986, pp. 26–30.
- [28] Yuzawich, P. M. and Hughes, C. W., *Practical Metallography*, Vol. 15, 1978, p. 184.
- [29] Vosikovsky, O., *Journal of Engineering Materials and Technology*, October 1975, p. 298.
- [30] Atkinson, J. D. and Lindley, T. C., *Proceedings*, Conference on Influence of the Environment on Fatigue, Institution of Mechanical Engineers, London, 1977.
- [31] Gallagher, J. P., *Journal of Materials*, Vol. 6, 1971, p. 941.
- [32] Barsom, J. M., *International Journal of Fracture Mechanics*, Vol. 7, 1971, p. 163.
- [33] Barsom, J. M. in *Corrosion Fatigue, Chemistry, Mechanics and Microstructure*, NACE-2, O. Devereux et al., Eds., National Association of Corrosion Engineers, Houston, TX, 1973, p. 424.

Fatigue Crack Growth in Aircraft Main Landing Gear Wheels

REFERENCE: Nagar, A., "Fatigue Crack Growth in Aircraft Main Landing Gear Wheels," *Fracture Mechanics: Nineteenth Symposium, ASTM STP 969*, T. A. Cruse, Ed., American Society for Testing and Materials, Philadelphia, 1988, pp. 868–882.

ABSTRACT: Fracture analysis of aircraft landing gear wheels under service-simulated operating loads using various fatigue crack growth characterization techniques is presented. Baseline constants for the wheel forging alloy 2014-T6 aluminum are established. The stress-intensity factors for a two-dimensional surface crack are developed using a proposed load model for the wheel's flange/bead seat radius. Crack growth predictions are performed using a modified crack growth (CRKGRO) program under spectrum load blocks. New stress-intensity factor subroutines for combined loads are added to the program library. The analytic results are compared with measured crack growth data during full-scale structural tests. Good agreement between analytic and structural test results was obtained, and a damage characteristic curve for the wheel flange is proposed. Qualitatively, fracture surface observations supported proposed crack-tip load models, state of stress, and crack growth data.

KEY WORDS: main landing gear wheel, surface crack, 2014-T6 aluminum forging alloy, stress-intensity factor, structural test, crack growth analysis, fractography, baseline constants, fracture mechanics

Nomenclature

A	Element at a bead seat cross section
K_I	Stress-intensity factor
ΔK	Stress-intensity factor range
M	Bending moment
N	Number of cycles
P	Force—cross section
Q	Flaw shape parameter, $f(a/c)$
R	Stress ratio
V	Shear force
a	Crack depth
b	Half width
c	Half crack length
C	Crack growth coefficient
m	Walker parameter
n	Crack growth exponent
t	Flange thickness
da/dN	Crack growth rate per cycle
ϕ	Parametric angle

¹ Aerospace engineer, Fatigue, Fracture, and Reliability Group, Structural Integrity Branch, AFWAL Flight Dynamics Laboratory, Wright-Patterson Air Force Base, OH 45433; formerly, senior fracture mechanics engineer, B. F. Goodrich Co., Aerospace and Defense Division, Troy, OH.

The structural and economic damage to aircraft operators due to landing gear wheel failures has been the subject of an earlier study [1]. The damage to flight control, electrical, and hydraulic systems, as well as to structures of primary aircraft systems, including explosive decompression of the pressurized cabin and resulting injuries to personnel, have been reported. Both the Federal Aviation Administration [2] and the United States Air Force [3] have emphasized the need for damage-tolerant aircraft structures. Fatigue crack growth studies on aircraft wheels conducted in the past have focused on fractographic techniques [4]. From design considerations, it is desirable to predict the life of an existing crack using linear elastic fracture mechanics (LEFM) based techniques. The work presented in this paper is an attempt to accomplish such an objective.

Analysis of past service failures [5] established that most wheel failures initiate from a corrosion pit which frequently forms at the wheel flange/bead seat radius (Fig. 1) enhancing the stresses there. These stresses cause such sites to transform into a surface crack and eventually may lead to structural failure. Fatigue crack growth analysis of such surface cracks is discussed in the following sections and includes the establishment of stress-intensity factors by proposing load models for the wheel flange and the development of baseline fatigue crack growth data and constants. The stress-intensity factor solutions and material data are applied to perform crack growth predictions using a crack growth (CRKGRO) program [6,7]. A feature of the work at hand is an analysis verification structural test conducted on a wheel with a service-induced initial crack under appropriate spectrum loads. Good agreement between analytic predictions and structural wheel test results was obtained. Observations of the fractographic surfaces supported the load models and the proposed stress-intensity factors and were, in general, in qualitative agreement with fatigue crack growth results.

Analysis

A proper fatigue crack growth analysis based on LEFM concepts requires appropriate solutions of stress-intensity factors and the development of constant amplitude cyclic stable crack growth data. A discussion of these topics and their application to crack life prediction methodology is presented in this section.

Stress-Intensity Factors

The aircraft wheel flange loads during service loading (landing and takeoff, and so forth) are transmitted from radial and transverse loads on landing gear wheel tires and associated inflation pressures. The deformations of the tire under such loads introduce distributed loads on the flanges parallel to the wheel's axial and radial directions, as shown in Fig. 2. The spectrum loads are derived from the aircraft's gross takeoff and landing weights and various maneuvers. A representative load spectrum for a wheel-tire assembly is presented in Table 1. The wheel radial loads are derived from the aircraft's gross weight, center of gravity, and nose wheel data [5]. It is generally assumed that each of the main wheels shares an equal amount of load. The transverse loads are introduced during turns. An increase in inflation pressures occurs due to increase in surface speeds and distances on runways. The load spectrum was supplied by a transport jet manufacturer and represents an average of the fleet-wide usage derived from flight data with actual recordings of take-off and landing weights. Thus, under loads given in Fig. 2, an element located at a generalized point at the cross section through the flange thickness is subjected to axial and flexural stresses. In addition, shear stresses are induced in the flange thickness due to the transverse forces acting there. Based on the state of stresses proposed above, a simplified crack-tip load model

TABLE 1—Load spectrum for a commercial jet transport aircraft.

Condition Number	Radial Load, kN (kips)	Transverse Load, kN (kips)	Angle, degrees	Inflation Pressure, kPa (psi)	Roll Distance, %
1	212.1 (47.7)	-36.7 (-8.25)	3	1558 (226)	0.62
2	164.6 (37.0)	-30 (-6.75)	3	1531 (222)	0.94
3	208.6 (46.9)	0	0	1661 (241)	21.82
4	161.7 (36.1)	0	0	1641 (238)	29.36
5	149 (33.5)	-40.5 (-9.1)	4 to 3/4	1641 (238)	0.56
6	129.9 (29.2)	-38.9 (-8.75)	5	1531 (222)	0.96
7	158.8 (35.7)	0	0	1641 (238)	17.38
8	135.7 (30.5)	0	0	1613 (234)	28.38

for the crack's circumferential and axial extension in the flange section is shown in Fig. 3. The mission stress spectrum was developed from stresses measured at the locations where cracks are observed. The axial and bending components of normal stresses may be determined from the magnitude of stresses at upper and lower flange surfaces, noting that the shear stresses vanish there. The stress spectrum is further modified by superimposing the stresses existing in the residual surface layer.

The stress-intensity factor solutions for surface cracks have been discussed in the literature [8,9]. A general expression for the stress-intensity factor for a plate of finite thickness with a surface crack (Fig. 4) is of the following form

$$K_I = \sigma \left(\frac{\pi a}{Q} \right)^{1/2} F \left(\frac{a}{c}, \frac{a}{t}, \frac{c}{b}, \phi \right) \quad (1)$$

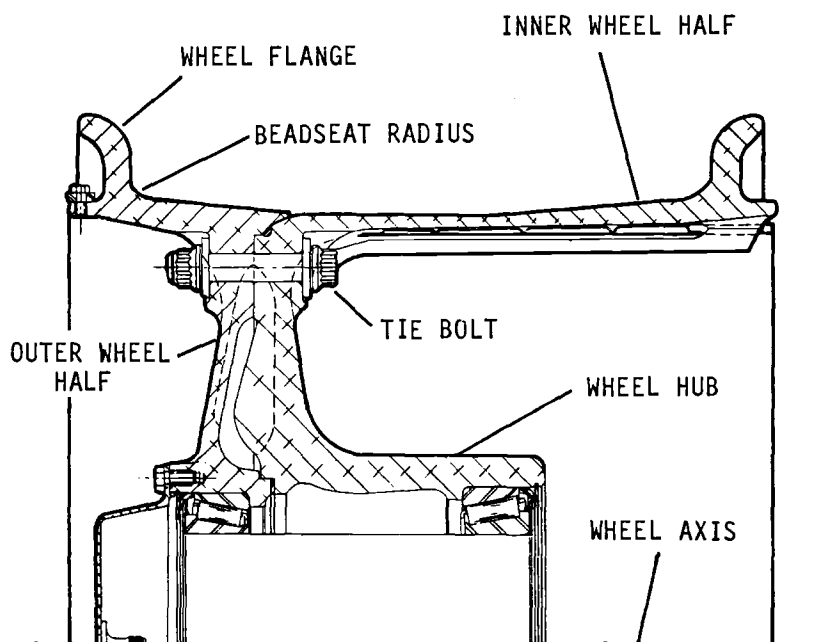


FIG. 1—Radial section of an aircraft main landing gear wheel assembly showing location of flange/bead seat radius.

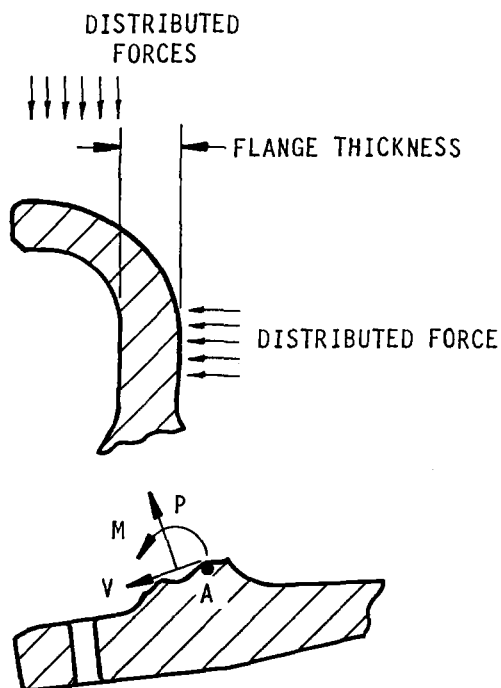


FIG. 2—An illustration of the distribution of loads on the aircraft wheel flange.

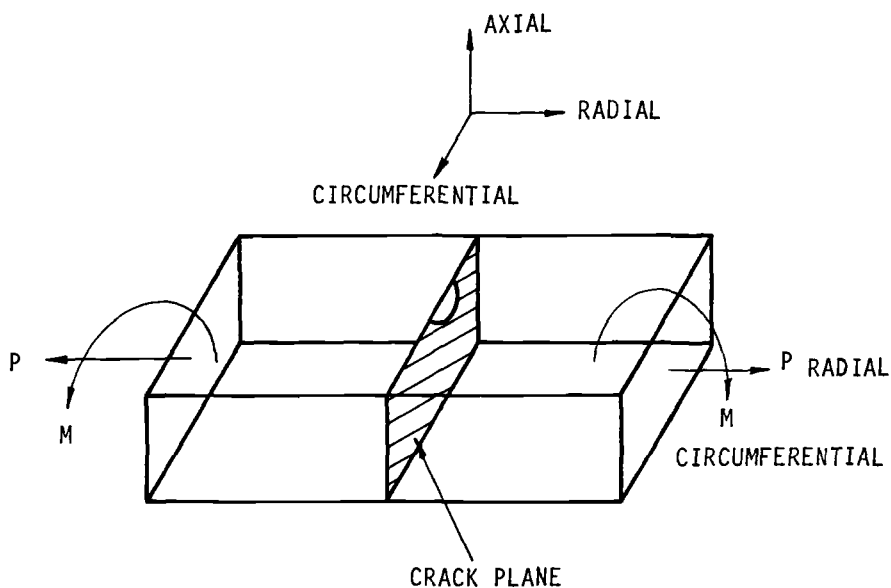


FIG. 3—Analytic crack-tip load model for an aircraft wheel flange.

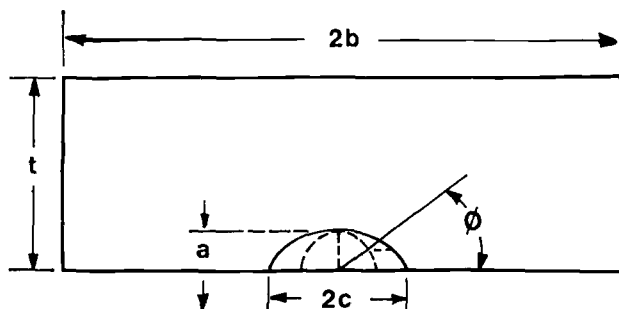


FIG. 4—A sketch of the surface crack geometry.

where Q , the surface crack shape parameter, has been discussed by Shah and Kobayashi [8]. The corrections to the stress-intensity factor solutions due to crack geometry, finite thickness and width, and the point of interest at the crack front are provided by the function F . For this problem, the stress-intensity factor was obtained by superposition, for example

$$K_I = K_I(\text{axial}) + K_I(\text{bending}) \quad (2)$$

The tension and bending components of the stress-intensity factors were calculated from Newman and Raju's solutions [10] for shallow surface cracks in three-dimensional bodies. By expressing magnitude of tensile stresses as a percent of bending stresses, it was possible to use closed form relations. An approximate value of Q for a shallow crack, also suggested in Ref 10, is

$$Q = 1 + 1.464 \left(\frac{a}{c} \right)^{1.65} \quad (3)$$

Crack shape functions and finite width and thickness corrections in Eq 1 are also given in Ref 10. The stress-intensity factors for the crack length were evaluated below the flange surface at a point in the residual surface layer where stresses changed directions.

Fatigue Crack Growth Behavior

A landing gear wheel is typically manufactured from 2014-T6 aluminum alloy using closed die forging of blocker type under 8 to 20 ton hydraulic presses, depending on the wheel's size. The final product is machined to a specified size, stress rolled, and anodized. The base line fatigue crack growth data were generated from constant-amplitude cyclic tests on compact tension specimens. The specimens were machined from the flange sections of a wheel. The specimen geometry was designed in accordance with (ASTM) Test for Constant-Load-Amplitude Fatigue Crack Growth Rates Above 10^{-8} m/Cycle (E 647-81). The thickness of the specimen was representative of an average jet transport wheel flange. The crack propagation direction in the specimens was designed to correspond to the wheel's circumferential direction, and the direction of applied stress was along the wheel's radial direction. The specimens were continuously saturated with a 3.5% saltwater solution during load cycling. The test frequency was maintained at 30 Hz. The test environmental conditions and frequencies were designed to simulate the landing gears operating environment. The load ratio during stable growth was 0.7. The crack growth rate versus stress-intensity factor range values obtained using a seven-point polynomial data analysis are plotted in Fig. 5. Various

symbols represent data points for specimens machined from different locations of the wheel flange sections. A continuous saturation of the crack tip with a 3.5% salt water solution at a frequency of 30 cycles per second had only a minor effect on crack growth rates observed in air. Similarly, interchanging the crack propagation and applied stress directions for compact specimens machined from wheel flanges did not show appreciable differences in the crack growth rates. The constant-amplitude cyclic crack growth data was represented by Walker's equation and expressed in the following form [7]

$$\frac{da}{dN} = C \left[\frac{\Delta K}{(1-R)^{1-m}} \right]^n \quad (4)$$

For this analysis, a value of 0.6 for Walker's exponent, m , was used. This value for Walker's exponent has been suggested in the literature [6,7]. It is also within the range originally proposed by Walker. Additional crack growth tests conducted at various stress ratios [12] show that this value consolidates the crack growth data well. The constants C and n were evaluated using Eq 4.

It was observed that the data fell within a linear band for the stable growth range. The lines marked upper and lower bound in Fig. 5 represent the fastest and slowest crack growth rates observed experimentally. Similarly, the mean of the data trend was used to denote average crack growth rates. The calculated values for lower, average, and upper bounds of C and n obtained using Eq 4 are presented in Table 2. The numerical accuracy of the

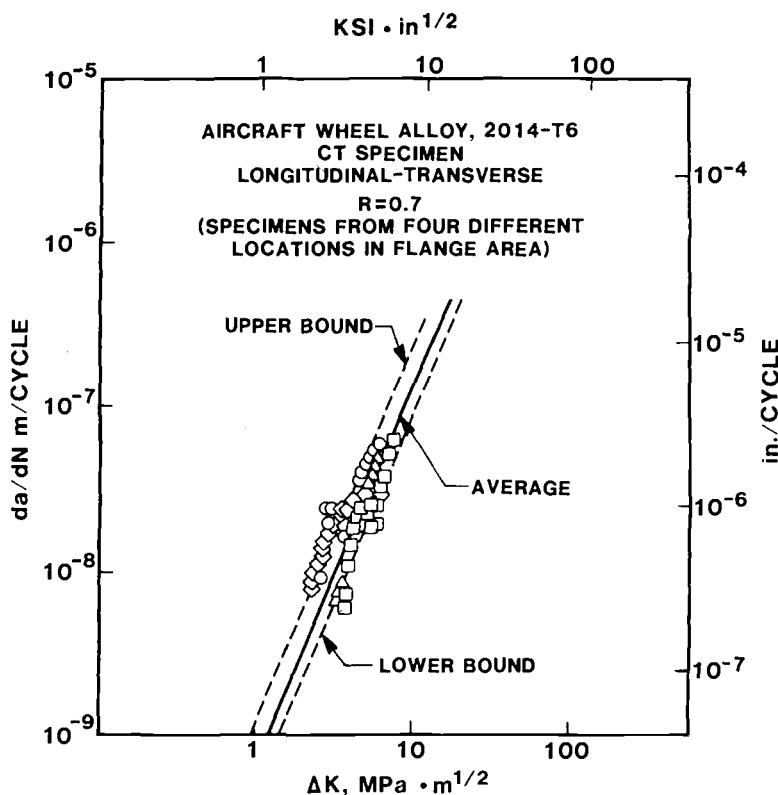


FIG. 5—A plot of da/dN versus K for aircraft wheel forging alloy, 2014-T6 aluminum.

TABLE 2—Fatigue crack growth constants for an aircraft wheel forging alloy, 2014-T6 aluminum.

	Coefficient, C	Exponent, n
Lower bound	7.21×10^{-9}	2.415
Average	9.92×10^{-9}	2.448
Upper bound	1.44×10^{-8}	2.556

constants thus calculated may be checked by substituting their values in Eq 4 and plotting da/dN as a function of ΔK .

Fatigue Life Prediction

Fatigue life predictions for an existing surface crack at the wheel flange section under spectrum loads was performed using the interactive version of the modified CRKGRO computer code. The CRKGRO program was developed by Rockwell International Corp. for the United States Air Force to design damage-tolerant aircraft structures [6]. The structural crack growth rates in the program were calculated using Walker's modified equation. The load interaction effects due to overloads on crack growth rates were incorporated using the Willenborg yield zone based retardation model in its modified form. The details of the CRKGRO program have been documented in previous studies [6,7]. A subroutine for stress-intensity factors for a plate with a surface crack subjected to combined loading using Eqs 1 and 2 was added to the program. It is realized that a realistic design of inspectable initial damage size is often a complex task and depends upon crack location, its accessibility for inspection, cracked component size, and material and reliability of equipment and the operator. For the purpose of this analysis, it was assumed that the initial crack was 0.76 mm (0.030 in.)² deep and 1.52 mm (0.060 in.) long. The use of this crack size has become a common practice in the landing gear wheel and brake industry. Its selection was based upon records of previous inspections by aircraft operators. It may be noted, however, that for the purpose of this study, the starting point for the crack size is not important. The objective of this study was to compare computer predictions of life with the life measured under the dynamometer test. An initial crack size is required by the computer program. An analytic crack growth curve from its initial size to critical length may also be used to estimate crack lengths at times of inspection when a crack may have been missed. A mission stress spectra for the wheel flange was developed and consisted of maximum and minimum stresses with the corresponding number of stress cycles. The maximum and minimum stress values were determined from experimental measurement of the stresses under spectrum loads listed in Table 1 in a roll test dynamometer. The maximum stress value used in mission stress was the value of the maximum principal stress.

The CRKGRO program uses the range pair method of cycle counting. However, the number of load cycles in this analysis was calculated from measured load-tire deformation data established previously. The number of cycles is related to the number of wheel revolutions which, in turn, depend on the roll distance. Thus, the number of cycles for each condition is proportional to the roll distance listed in Table 1. To simplify input required for analysis, the program was run in blocks of load cycles. Each block represents the roll distance per flight for a given aircraft and airport. The crack growth analysis in the program was based upon Vroman's integration scheme [7] of cumulative damage. The extension of the initial crack is calculated from maximum and minimum stresses and the number of cycles

² The original measurements were made in English units.

for the first condition by integration of the crack growth equation. If the crack extension is 1% of the initial crack size or less, the crack is advanced by the amount of the calculated crack extension, and the second condition is considered with the updated crack size as the current crack length. If the crack extension is larger than 1%, the number of cycles required to grow the crack 1% is calculated. The crack size is increased by 1% and the same condition is considered again with the remaining number of cycles in that condition. This process of integration is repeated for each condition in the block and then repeats with each updated crack length [7]. The analysis terminates when the calculated maximum stress-intensity factor approaches the value of the critical stress-intensity factor, and the corresponding number of blocks to cause failure is determined.

Analysis Verification Test

A full-scale structural test on a main-landing-gear outer-wheel half with a surface crack at the bead seat radius of the flange was conducted to verify computational crack growth analysis. The test wheel had served for ten years on a commercial jet transport and had accumulated 3835 flights prior to the last eddy current inspection. At that time, a 8.1-mm (0.320-in.)-long crack was present. Crack propagation (CPB-02) and crack detection (CD-02) gages were installed in advance of the crack tips (Fig. 6). The wheel was assembled with



FIG. 6—Crack growth in a wheel flange with crack propagation and crack detection gages.

its mating inner-wheel half and the required size and ply rating tire utilized. The entire assembly was mounted on a roll test dynamometer axle. A similar dynamometer is used for durability qualification tests of aircraft wheels for original equipment manufacturers. The wheel assembly was subjected to spectrum loads simulating average fleet-wide service usage (Table 1). The angle in degrees listed in column four of Table 1 denotes the angle by which the dynamometer test wheel must be turned to maintain the required radial-transverse load combination. The inflation pressures listed in column five for each condition were experimentally measured in an actual aircraft. For operational efficiency, the loads were applied in blocks of 160.9 km (100 miles). At the end of the tenth block, a special load spectrum with 20% higher taxi loads was applied to produce a distinctive surface mark on the propagation crack surface. The standard load spectrum was again resumed. Applied radial and transverse loads are automatically recorded in a roll test dynamometer throughout the test. Also, the roll distance is predialed and the loading automatically terminates when the prescribed distance is reached. The roll distance is a more precise measure of life than the number of flights. This distance is directly related to the number of load cycles. On the other hand, the amount of roll distance varies from flight to flight depending upon the sizes of the runways at the connecting airports. A slip ring was attached to the wheel axle so that a continuous record of instantaneous resistances of crack propagation gages can be made. The resistance changes per single strand cut were calibrated on a dogbone specimen. The actual resistance changes during the wheel test differed slightly from both the manufacturer specifications as well as the laboratory-calibrated values. It is not known why the gage resistance values differed. However, the resistance magnitude has no effect on the measured crack length. It is the step change in a resistance value which represents incremental step change in crack size. It is due to the fact that a particular gage strand when broken, changes the value of the gage resistance abruptly. The wheel was rolled at a speed of five miles per hour for the taxi loads and three miles per hour for combined radial/transverse loads simulated aircraft turns. These test speed limits have been designed to avoid overheating of the tire assembly. In an actual flight, the tire assembly cools down as the aircraft becomes airborne. The inflation pressures listed in column five of Table 1 are representative of the pressures encountered during service.

The primary objective of this test was to characterize the change in crack length as a function of roll miles under spectrum loads by measuring surface crack lengths by crack propagation/detection gages (Fig. 6). Periodic crack size inspections, light optical photographs, and interpretation of surface markings on the fracture surface were employed for verifications. The test was terminated at a preselected crack length prior to fracture.

Fracture Surface Observations

Macroscopic and microscopic observations of the fracture surfaces in several cracked and failed service wheels were made under a low-power optical microscope, a scanning electron microscope (SEM), and a transmission electron microscope (TEM). Such observations provided valuable information on crack origin, geometry of the propagating crack (aspect ratio as a function of crack size), mechanisms of fracture, critical crack length, and qualitative aspects of crack growth rates.

Light optical microscopy established that a crack at the flange/bead seat radius of the wheel nucleates in the form of an easily resolvable corrosion pit or a semicircular area of discoloration also associated with corrosion. The cracks may have single or multiple origins. The location of the crack origin may be traced from chevron markings, as shown in Fig. 7, for a representative flange crack. Other similar studies show that an initially semicircular crack develops into a semielliptical shape as it extends. The ratio of crack length ($= 2c$) to



FIG. 7—*Fracture surface of a typical wheel flange failure in service.*

its depth ($= a$) increases with the crack size and reaches as high as seven or more on an average (Fig. 7). Such fatigue crack propagation behavior supports the assumption for the crack load model (Fig. 3) that stress gradients exist at the crack front. The vicinity of the crack origin in the depth direction under SEM observation revealed areas of Stage I fatigue cracking [12]. This area appeared to have a high-cycle and low-stress brittle appearance with cleavage fractures without display of striations. Elsewhere, there were areas of striations indicating that crack propagation took place under fatigue. However, the striation spacings could not be resolved because of the high degree of scatter under spectrum loads, and the matter was taken to TEM microscopy. Replicas of fracture surfaces were prepared and examined in a transmission electron microscope. Figure 8 displays striations observed on the surface of a service-induced crack located at a depth of about 2.5 mm (0.100 in.) from the wheel flange surface. Surface observations at increased depths indicated that final fracture occurs under tensile overload, represented by dimples formed as a result of initiation, growth, and coalescence of voids. In addition to the fractographic analysis of service wheels, the fracture surface of the test wheel was studied to establish initial crack length and experimental critical crack size and to compare experimental crack growth behavior with that under service loads and CRKGRO predictions. Figure 9 shows growth bands formed at the crack surface during 1979 km (1230 miles) of rolling under the dynamometer test. Twelve full-size bands and one partial growth band ahead of the service crack were identified. The crack growth

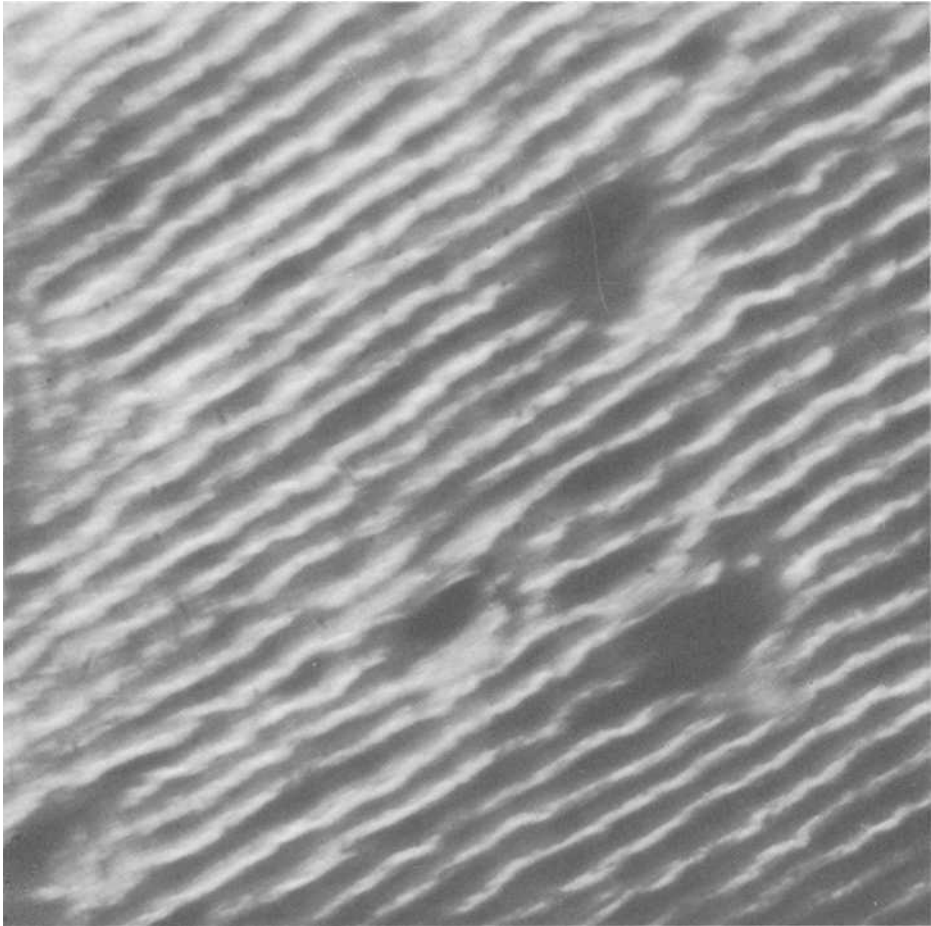


FIG. 8—A display of striations, typical on the depth of a service crack, under a transmission electron microscope at $\times 38\,000$.

band formed during the tenth block is distinguished by its relatively lighter color and larger width. It was assumed that crack growth bands were caused by individual load blocks. The growth band boundary lines indicate positions of propagating crack fronts during rising or falling portions of the applied cyclic load. The band to the right of the tenth block band was assigned to the last three blocks (two full size and one partial). Similarly, the location of the initial crack was identified by moving nine blocks to the left. It may be noted from Fig. 9 that the band boundary lines get closer and tend to disappear in the depth direction. For this reason the measurement of crack growth along the depth during each block could not be determined with high precision.

Results and Discussion

In this section, crack growth results of analytic predictions using the CRKGRO program, experimental measurements on a structural wheel test, and macroscopic/microscopic fracture

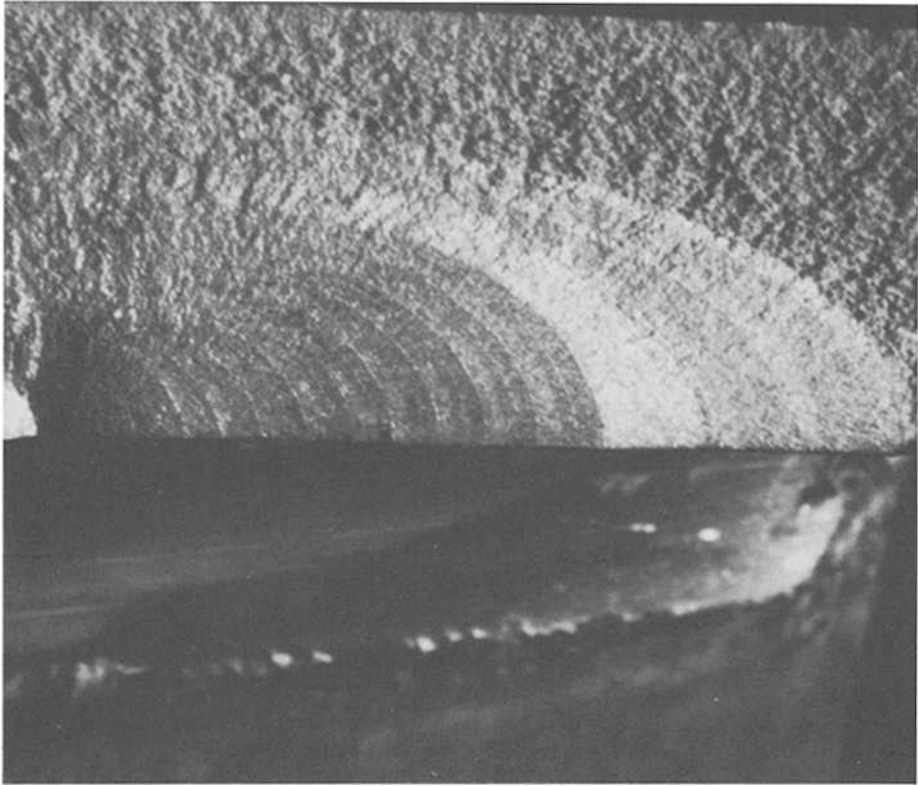


FIG. 9—Fracture surface showing crack progression bands and arrest lines under structural wheel test.

surface observations of service and test wheels are integrated to establish crack growth rates along the circumferential direction of the wheel and in the direction of the flange thickness. A corrosion pit assumes the shape of a semicircular crack during its initial growth (Figs. 7 and 9). Further extension of the crack occurs with higher growth rates in the length direction and the crack becomes a shallower and shallower semiellipse (Figs. 7 and 9). Initially, the crack grows at slight angles with the wheel's circumferential direction. This is due to the fact that the maximum principal stresses are not aligned with the wheel's radial direction. The crack growth is primarily due to fatigue, though the initial growth was observed to occur under Stage I fatigue [12], and the onset of instability was triggered by overloading.

Flange Damage Characterization Curve

The normalized crack length versus the roll distance curves based on these results are plotted in Fig. 10. The crack length was normalized with respect to the critical crack length and the number of flights are represented by fractional roll miles. From a practical point of view, it is desirable to express crack growth results as a function of the number of flights. However, landing and takeoff distances vary from flight to flight by a factor of greater than two. Aircraft operators prefer the use of roll distance over the number of cycles. The roll distance may be simply determined from flight records data. The solid line portion of the

experimental curve represents crack length measurements from records of resistances of crack propagation gages and crack detection gages. Crack length measurements were verified by visual measurements during periodic inspections by removing the wheel from the test assembly. The portion of the experimental curve joining two solid circular data points represents the crack growth which occurred during the dynamometer test. The initial lower portion of this curve includes the crack growth that occurred in service within the last inspection interval. The upper dashed curve follows the trend of the analytic crack growth predictions. These segments of the curve were predicted from correlations of analytic and experimental trends. The various data points along this curve are based on interpretations of crack progression bands formed on the surface of the test wheel (Fig. 9). It was assumed that the width of each crack growth band represented the damage that occurred during the corresponding load block. The analytic predictions for crack growth using average values of crack growth constants (Table 2) are represented by the upper curve. Similarly, predictions based on the lower bound of the constants are given by the curve just below the experimental curve (Fig. 10).

The results in Fig. 10 show that crack growth rates under dynamometer loads are lower than analytic predictions using average crack growth data and are higher than the predictions based on lower-bound data. The analytic prediction of crack growth life is 10% lower than that determined from structural test results. Low analytic life predictions may be due to the fact that the stress-intensity factor solutions proposed by Newman and Raju [10] tend to be conservative [13]. Another explanation for the low life predictions may be the slightly different value of the Walker parameter " m " for the wheel flange material. The initial crack growth trends for an analytic crack and a structural test crack almost overlap. This suggests that the analytic crack-front and the structural test crack-front encounter slightly different stress conditions after the crack has grown a certain amount. A typical service-originated crack under service loads or wheel test spectrum loads moves away from the bead seat radius toward lower stress regions of the flange. The analytic crack growth prediction was based on a mission stress spectra derived from stresses measured at the bead seat radius without the presence of a crack. It may also be noted that the analytic predictions incorporated residual stress effects on an average basis [11]. The effects of stress gradients in the length direction may be simply incorporated by measuring the stress along the direction of

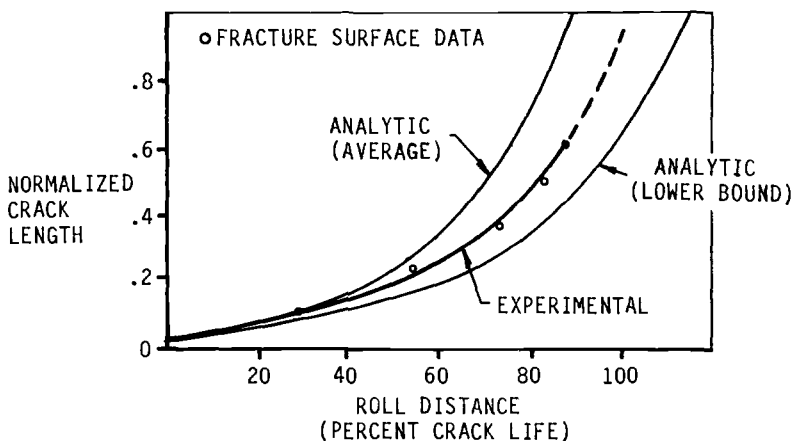


FIG. 10—Wheel flange damage characterization curves showing plots of normalized crack length versus rolling distance.

crack propagation in the flange. However, since the measured and predicted life differences were considered small, these approaches were not extensively pursued.

Crack Growth in the Depth Direction

Analytically predicted crack growth results showed that the rate of crack growth through the thickness increases until the crack reaches about half its critical size and decreases thereafter. Such crack growth behavior is expected due to the presence of stress gradients caused by flexural stresses. Although striations on crack fracture surfaces were clearly visible as shown in Fig. 8, the measurements of striation spacing under both the SEM and TEM showed a high degree of scatter. A simple average of such measurements under TEM at various points along the crack depth showed that the crack penetration rates decrease substantially (by a factor of two and one half) at a depth of approximately half the critical crack size. A similar crack growth pattern may be deduced from interpretations of the fracture surface of the wheel subjected to dynamometer loads (Fig. 9). This presented a qualitative verification of the analytic crack growth rates in a bending stress field. Although precise measurements of crack depths from Fig. 9 could not be made, an approximate plot of crack depth versus roll distance may be constructed by combining damage characterization curves (Fig. 10) with established crack aspect ratios. The aspect ratios may be calculated from the records of fracture surfaces of wheels with different crack lengths detected during inspections. However, application of such a plot in fracture control planning would require a reliable technique to measure the crack size along its depth.

Conclusions

A complex state of stress at the crack front of a growing crack located at the landing gear wheel flange bead seat radius was observed to exist. New stress-intensity factor solutions based on stress gradients and residual stresses present at the advancing crack front were added to the CRKGRO program library of stress-intensity factor subroutines. With these modifications, the analytic predictions for crack growth show good agreement with the measured crack lengths in a full-scale structural test on a cracked wheel. As a result of this work, a flange damage characteristic curve for potential application in wheel design, based on damage tolerance analysis, is proposed. Qualitative correlation of crack growth behavior based on fracture surface microscopic studies with analytic and experimental results is established. The crack growth rates along the wheel flange thickness are characterized by trends that initially increase until approximately half the thickness. Thereafter, a drop in crack growth rates is predicted and observed. More rigorous approaches to three-dimensional modeling of the flange problem, the effects of residual stress variations through the flange thickness, and experimental and fractographic verifications of crack penetration rates remain as tasks for further study.

Acknowledgments

The author gratefully acknowledges the contributions of M. A. Owen for service load spectrum development, R. P. Skow for metallurgical analysis, and E. M. Davis for conducting structural wheel tests. The fractographic analysis reported in this work was conducted at Battelle-Columbus Laboratories and S. G. Gelles Associates, Columbus, Ohio. Constant amplitude crack growth tests were performed at the University of Dayton Research Institute.

References

- [1] Wiebe, W., "A Fractographic Study of Fatigue Failure of Aircraft Wheels," NRC, NAE LR-541, National Research Council, National Aeronautical Establishment, Ottawa, Canada, 1970.
- [2] Swift, T., "Application of Damage Tolerance Technology to Type Certification," Paper No. 811062, SAE Technical Paper Series, Society of Automotive Engineers, Warrendale, PA, 1981.
- [3] Wood, H. A., "Expansion of the ASIP Process to Aircraft Subsystems—A Status Report," USAF Structural Integrity Program Conference, U.S. Air Force, Wright-Patterson Air Force Base, OH, 1985.
- [4] Wiebe, W., "Quantitative Fatigue Crack Propagation Analysis by Means of Electron Fractography," NRC, Aeronautical Report LR-450, National Research Council, Ottawa, Canada, 1966.
- [5] Durup, P. C. and Brussat, T. R., "Wheel Performance Evaluation," Phase I Report, Federal Aviation Administration Technical Center, Atlantic City, NJ, June 1985.
- [6] Chang, J. B., "Improved Methods for Predicting Spectrum Loading Effects," AFWAL-TR-81-3092, Air Force Wright Aeronautical Laboratories, Wright-Patterson Air Force Base, OH, 1981.
- [7] Chang, J. B., "Assessment of Sensitivity of Crack Growth Rate Constants to Predictive Accuracy of Part-Through Crack Fatigue Life Prediction," *Part-Through Crack Fatigue Life Prediction*, ASTM STP 687, American Society for Testing and Materials, Philadelphia, 1979.
- [8] Shah, R. C. and Kobayashi, A. S., "Stress-Intensity Factor Equations for an Elliptical Crack Approaching the Surface of a Semiinfinite Solid," *International Journal of Fracture Mechanics*, Vol. 9, No. 2, 1973.
- [9] Newman, J. C., Jr. and Raju, I. S., "Stress-Intensity Factor Equations for Cracks in Three-Dimensional Finite Bodies," *Fracture Mechanics: Fourteenth Symposium—Vol. 1*, ASTM STP 791, American Society for Testing and Materials, Philadelphia, 1983, pp. 238–245.
- [10] Newman, J. C., Jr. and Raju, I. S., "Analysis of Surface Cracks in Finite Plates Under Tension or Bending Loads," NASA TP-1578, National Aeronautics and Space Administration, Washington, DC, 1979.
- [11] Underwood, J. H. and Throop, J. F., "Surface Crack K -Estimates and Fatigue Life Calculations in Cannon Tubes," *Part-Through Crack Fatigue Life Prediction*, ASTM STP 687, American Society for Testing and Materials, Philadelphia, 1979.
- [12] Nagar, A., "Fatigue Crack Growth Methodology for Aircraft Landing Gear Wheels," Engineering Report No. ER 5453, BF Goodrich Aerospace and Defense Div., Troy, OH, 1986.
- [13] Heckel, J. B. and Rudd, J. L., "Evaluation of Analytical Solutions for Corner Cracks at Holes," *Fracture Mechanics: Sixteenth Symposium*, ASTM STP 868, American Society for Testing and Materials, Philadelphia, 1985, pp. 45–64.

Near-Threshold Crack Growth in Nickel-Base Superalloys

REFERENCE: Van Stone, R. H. and Krueger, D. D., "Near-Threshold Crack Growth in Nickel-Base Superalloys," *Fracture Mechanics: Nineteenth Symposium, ASTM STP 969*, T. A. Cruise, Ed., American Society for Testing and Materials, Philadelphia, 1988, pp. 883–906.

ABSTRACT: The influence of stress ratio on the elevated-temperature crack growth behavior of the nickel-base superalloys René 95 and Alloy 718 is discussed. The near-threshold and Region II crack growth behavior of a wide variety of microstructures for each alloy are explained using phenomenological descriptions of closure, that is, K -dependent or K -independent closure. K -dependent closure is the type of closure observed for nickel-base superalloys where increasing the R -ratio causes a uniform lateral shift of the entire fatigue crack growth curve. K -independent closure is the type commonly reported for steels and titanium alloys where increasing the R -ratio has a larger influence on near-threshold crack growth than on Region II crack growth. The existence of K -dependent closure in nickel-base superalloys results in microstructurally sensitive crack growth rates, even at high R -ratios. This permits the use of K -based crack growth prediction techniques and simplifies alloy and process development for applications having complex loading spectra.

KEY WORDS: fatigue crack growth, threshold crack growth, crack closure, nickel-base superalloys, stress ratio, microstructure, fracture mechanics

The trend in advanced engineering structures towards the use of high-strength alloys has promoted the use of fracture mechanics in both material selection and component design. As a result, it has become necessary to develop alloys that combine high strength, conventional fatigue properties, and resistance to crack growth. The high-pressure turbine disk in advanced aircraft gas turbine engines is an example of a critical component which utilizes high-strength nickel-base superalloys and is designed using fracture mechanics. The material selection and design of this application is particularly complicated because of the complex combination of thermal and stress cycling. In a recent investigation [1], several locations of a turbine disk were studied to isolate the conditions which must be considered when developing crack propagation life prediction techniques. Figure 1 shows the variation in stress ratio (R = minimum stress/maximum stress) as a function of temperature for 18 mission and location combinations in an advanced aircraft engine. These loading profiles are dominated by cycles with high R -ratios (high mean stresses). High R -ratio cycling requires that the range in stress be relatively low. In many cases, this results in a stress-intensity factor range (ΔK) which falls within or below the near-threshold crack growth regime where crack closure can have a large influence [2].

This paper will examine the crack growth behavior of several nickel-base superalloys for a variety of microstructures, stress ratios, and temperatures. These results will be discussed in terms of their impact on crack growth mechanisms, the interpretation of closure phenomena, life prediction models, and material development.

¹ Senior engineer and lead engineer, respectively, General Electric Co., Cincinnati, OH 45215.

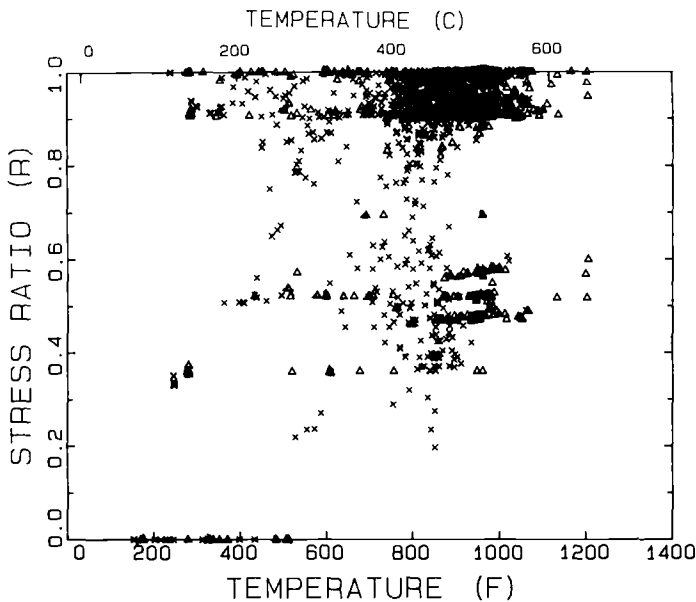


FIG. 1—Variation of R -ratio with temperature for 18 mission and temperature combinations in an aircraft engine turbine disk.

Literature Review

The concept of crack closure was first proposed by Elber [3] in the early 1970s. Since that time, this phenomenon has been used to account fully or partially for the effects of R -ratio, environment, and microstructure on fatigue crack growth rates. Crack closure occurs when the crack faces remain in contact at loads above that prescribed for the minimum K (K_{\min}). The region in the vicinity of the crack tip thus experiences a lower effective ΔK . Crack closure can be induced by plasticity in the vicinity of the crack tip, crack face corrosion and oxidation deposits, or crack face irregularity and roughness. These mechanisms have been termed plasticity-induced, oxide-induced, and roughness-induced closure, respectively [2].

In plasticity-induced closure, compressive residual stresses caused by localized yielding are left in the wake of a propagating crack. These residual stresses result in crack closure at positive applied loads and limit the range in K where the crack is fully open.

Oxide-induced closure arises from the buildup of corrosion or oxide products on crack faces which can cause premature contact at K levels greater than K_{\min} . This particular type of closure has often been used to explain the pronounced effects of environment on fatigue crack growth rates. Paris et al. [4] first proposed the existence of an oxide-induced closure mechanism to account for the observed increase in the fatigue crack growth threshold (K_{th}) for steels tested in distilled water in comparison with the threshold measured in air. Since that time, investigations for low-strength steels have shown that dry gaseous or vacuum environments provide lower ΔK_{th} data than slightly humid environments [5,6]. These observations, measurement of the crack-face oxide thickness [5,6], and the diminished environmental effects with increasing R -ratio [6,7] support the existence of an oxide-induced closure mechanism. This phenomenon has also been used to explain the occurrence of sharply defined thresholds in turbine casing steels [8] and in the nickel-base superalloy Alloy 718 [9].

Irregular or rough fracture surfaces can induce high closure loads at low R -ratios when in-plane shear or Mode II displacements wedge open the crack at discrete contact points along the crack face. This closure mechanism, like oxide-induced closure, has a greater effect in the near-threshold regime and diminishes with increasing R -ratio. Ritchie and Suresh [10] proposed that the strong Region I influence results from a combination of Mode I and Mode II displacements at low growth rates. The influence at high growth rates would be much lower because only Mode I displacements are operative at high growth rates. Their explanation was also consistent with the typical fatigue crack morphologies observed for Stage I and II growth. Roughness-induced closure has been particularly useful in explaining the effects of grain size on near-threshold fatigue crack growth rates at low R -ratios. Gray et al. [11] observed that pearlitic rail steels with a coarse-grained microstructure had higher thresholds than those with a fine-grained microstructure. The beneficial effect of grain size, however, was absent at an R -ratio of 0.70. A similar type of behavior has been observed by Allison [12] in titanium alloys.

Very few closure measurements have been made on nickel-base superalloys. Zawada and Nicholas² measured crack closure in compact specimens of René 95 having two grain sizes. The specimens were tested at 649°C (1200°F) with an R -ratio of 0.1. They showed that for both grain sizes the K at crack closure was a constant value over the entire range of ΔK . Based on oxide thickness measurements and closure measurements in smooth and side-grooved specimens, they concluded that this behavior resulted from oxide-induced closure.

Approach

This paper will discuss the results of several recent investigations on the fatigue crack growth behavior of two high-strength nickel-base superalloys, Alloy 718 and René 95. These investigations were performed to study the influence on fatigue growth rate properties of one or more of the following: processing, microstructure, test temperature, and R -ratio. Although crack closure was not directly measured, the evaluation of near-threshold (Region I) and intermediate (Region II) crack growth rates as a function of R -ratio provided some insight into the presence or absence of different types of closure. Some of the results are in sharp contrast to the observations reviewed in the previous section.

The discussion will be divided into two sections. The first section will describe the influence of temperature on the crack growth properties of a number of alloy and process combinations. Test temperature has an interesting effect on the fatigue crack growth curves of nickel-base superalloys. Figure 2 shows the crack growth rates of DA718, a high-strength processing condition of Alloy 718, at 149 and 538°C (300 and 1000°F) [13]. As the test temperature increases, ΔK_{th} increases and Region II crack growth rates become faster. This results in the crossing of the fatigue crack growth curves or the "crossover" phenomenon. The influence of stress ratio on this behavior will be discussed in detail.

The second part of this paper will discuss the influence of grain size, precipitate size, and R -ratio on the crack growth properties of Alloy 718. These results are from a systematic evaluation of grain and precipitate sizes on crack growth rates at 428°C (800°F).

At elevated temperatures, the fatigue crack growth rates of nickel-base superalloys are often subject to environmentally assisted damage, particularly for long cycle durations. All the data shown in this paper are for 0.33-Hz (20-cpm) cycling and, with one exception, were obtained at temperatures not greater than 538°C (1000°F) cycling. Under these conditions, the influence of environmentally assisted time-dependent crack growth is very small.³

² Zawada, L. P. and Nicholas, T., "The Effect of Loading History on Closure Behavior in René 95," *Fracture Mechanics: Eighteenth Symposium, ASTM STP 945*, 1988.

³ Van Stone, R. H., General Electric Aircraft Engine Business Group, Cincinnati, OH, unpublished research, 1982-1986.

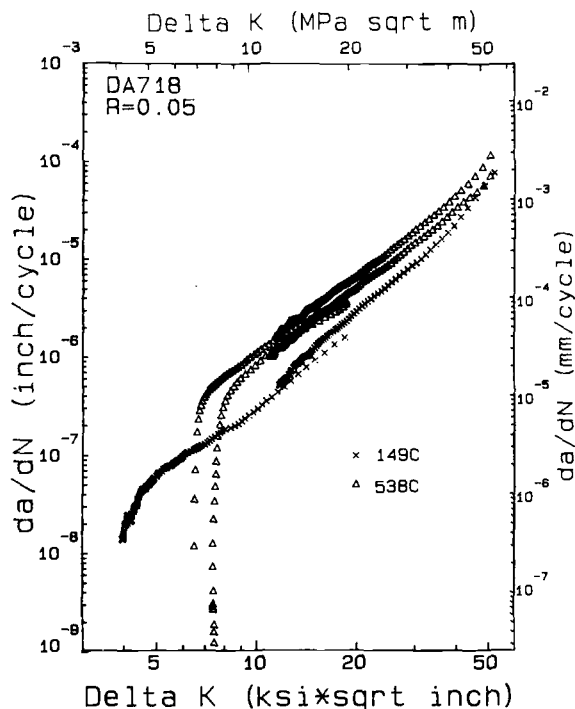


FIG. 2—The crack propagation rates of DA718 at 149 and 538°C (300 and 1000°F) with K for an R -ratio of 0.05.

Materials

The materials used for the crack growth investigations were processed from two well-known nickel-base superalloys, cast and wrought Alloy 718 and powder metallurgy (PM) René 95. These alloys are used in a wide variety of aircraft gas turbine components, including compressor and turbine disks. Although both alloys are nickel-base and age-hardenable, Alloy 718 is strengthened by the DO_{22} γ'' precipitate (Ni_3Nb), while René 95 is strengthened by the Li_2 γ' precipitate phase [$\text{Ni}_3(\text{Al}, \text{Ti}, \text{Nb})$]. The materials covered a large spectrum of processing conditions and microstructures. Table 1 [13–16] provides the processing conditions, microstructure, and typical strength level for each material studied in the crossover investigations. Table 2 lists the heat treatment, grain size, precipitate size, and strength level of the materials studied in the Alloy 718 investigation. More detailed descriptions of the materials are provided in the associated references.

Fatigue Crack Growth Test Techniques

Fatigue crack growth tests in the investigations of Alloy 718 and René 95 were performed using two specimen geometries. Most of the tests utilized a pin-loaded single-edge notch (SEN) specimen. The nominal thickness and width of the SEN specimens was 2.54 mm (0.1 in.) and 10.16 mm (0.4 in.), respectively. Electric discharge machining (EDM) was used to introduce 0.1-mm (0.004-in.) deep fatigue starter notches which traversed one edge of each SEN specimen at the center of the gage length. One of the studies [14] used a conventional buttonhead loaded low-cycle fatigue test specimen. These axisymmetric specimens had a

TABLE 1—Processing conditions, microstructure, and typical strength level for the materials used in the crossover studies.

Alloy Designation	Process	Solution Temperature, °C	Age Temperature, °C	Typical Grain Size, μm	Room Temperature, 0.2% Yield Strength, MPa	Reference
DA718	cast + forged	none	718/621	8	1357	[13]
Hot-isostatic-pressing (HIP)- compacted René 95	PM + 1121°C HIP	1121	871/649	8	1275	[14]
	PM + 1204°C HIP	1121	760	25	1199	[15]
	PM + 1121°C HIP	1121	930	8	1061	[15]

TABLE 2—Heat treatment, microstructure, and yield strength of Alloy 718 used in the grain size studies [16].

Solution Temperature, °C	Aging Treatment, °C/h	Grain Size, μm	Precipitate Size, μm	427°C (800°F), 0.2% Yield Strength, MPa
968	718/5	20	<0.02	945
	718/200	20	0.15	921
1093	718/5	250	<0.02	795
	718/200	250	0.15	881

nominal gage length of 25.4 mm (1 in.) and a nominal gage diameter of 6.4 mm (0.25 in.). Small 0.1-mm (0.004-in.)-deep semicircular fatigue-starter notches were introduced at the center of the gage length by EDM. Compared to the compact geometry, both specimens had a short-crack/high-stress geometry.

Crack growth in each investigation was monitored using a direct-current (d-c) potential drop technique. The basic technique was originally developed by Gangloff [17]. Subsequent work adapted this technique to the axisymmetric low-cycle fatigue [18] and SEN specimen⁴ geometries. Direct current is passed through the specimen, and potential monitoring probes located on both sides of the starter notch measure the change in potential as the crack grows. Potential values are converted to crack length using the Coffin-Rowe [19] solution for the axisymmetric specimen geometry (surface crack) or the Johnson [20] solution for the SEN geometry (through crack). K values were determined using the Newman-Raju [21] solution as modified by LeFort⁵ for the axisymmetric specimens or the Tada [22] solution for the SEN specimens.

Fatigue cycling was performed in air at 0.33 Hz (20 cpm). The axisymmetric specimens were cycled in load control, and the SEN specimens were cycled using load-control or K -control. A typical SEN test consisted of a load or K -controlled segment to precrack the specimen, a K -shed segment to determine Region I growth rates and K_{th} , and a K -controlled segment to determine Region II crack growth rates [23]. In the K -shed segment, K_{max} was decreased at a rate given by

$$C = \frac{1}{K_{max}} \left(\frac{dK_{max}}{da} \right) \quad (1)$$

The value of C in all cases was $-1.18/\text{mm}$ ($-30/\text{in.}$). This shed rate has been shown⁶ to be within the range where near-threshold growth rates are not affected by a variation in C for high-strength nickel-base superalloys like Alloy 718 and René 95.

The crack growth rates shown in this paper were determined using the seven-point sliding polynomial technique. In the near-threshold regime, the data were determined from rapidly decreasing crack growth rates and did not include data from crack arrest.

⁴ Wilcox, J. R. and Henry, M. F., General Electric Corporate Research and Development, Schenectady, NY, unpublished research, 1982.

⁵ Lefort, P. C., General Electric Co., Schenectady, NY, private communication to R. P. Gangloff [17], 1981.

⁶ Henry, M. F. General Electric Corporate Research and Development, Schenectady, NY, private communication, 1982.

Crossover Behavior

The fatigue crack growth crossover with temperature was first noted in nickel-base superalloys by Van Stone, Krueger, and Duvelius [18] in Alloy 718. In their investigation, Alloy 718 was studied using R -ratios near zero, and the crossover phenomenon was thought to be related to a closure mechanism, such as oxide-induced closure. A more extensive evaluation of the crack growth crossover phenomenon was subsequently performed by Van Stone and Krueger [13]. They studied the fatigue crack growth rates of DA718 at 149 and 538°C (300 and 1000°F) using R -ratios of 0.05 and 0.75. The 0.75 R -ratio was selected to minimize the influence of oxide-induced closure. If the crack growth curves exhibited the crossover behavior at an R -ratio of 0.05, but not 0.75, it would reinforce the hypothesis that this phenomenon was caused by oxide-induced closure. Their results for an R -ratio of 0.05 have been previously shown (Fig. 2). The results at an R -ratio of 0.75 are presented in Fig. 3. It is evident that the crossover occurs at both R -ratios. This strongly suggests that the crossover phenomenon is not related to oxide formation or an oxide-induced closure mechanism.

Region II fatigue crack growth data can be modeled using a combination of the Paris relationship [24]

$$da/dN = CK^n \quad (2)$$

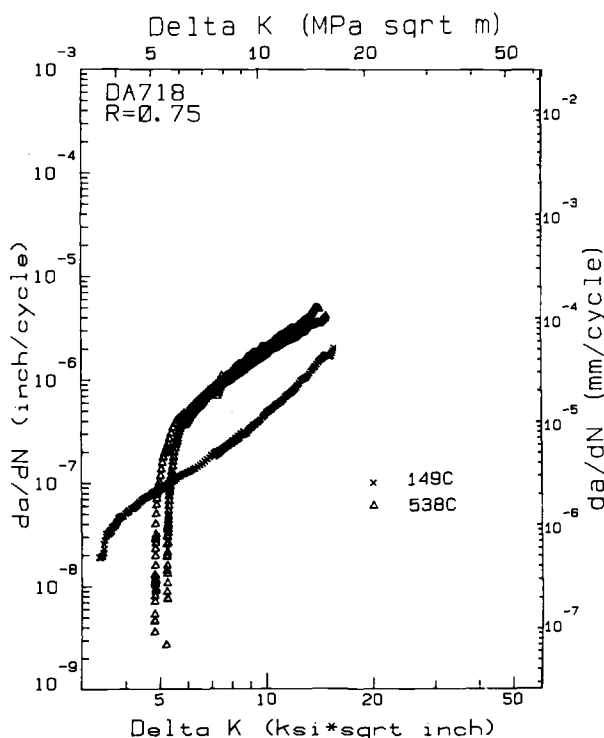


FIG. 3—The crack propagation rates of DA718 at 149 and 538°C (300 and 1000°F) with K for an R -ratio of 0.75.

where

da/dn = fatigue crack growth rate,
 K = stress-intensity factor, and
 C, n = regression constants,

and the Walker equation [25] which describes the influence of R -ratio

$$K_{\text{eff}} = K_{\text{max}} (1 - R)^m \quad (3)$$

where

K_{eff} = effective value of K ,
 K_{max} = maximum value of K in a cycle, and
 m = a regression constant.

The exponent m is frequently referred to as the Walker exponent. For positive R -ratios, the value of m varies from zero to unity and results in a variation of K_{eff} from K_{max} to ΔK , respectively. Thus, the value of m describes the relative influence of alternating and maximum K for non-zero R -ratios.

Substitution of the expression for K_{eff} from Eq 3 for K in Eq 2 results in

$$\frac{da}{dN} = CK_{\text{max}}^n (1 - R)^{mn} \quad (4)$$

This expression has successfully modeled the influence of R -ratio on the Region II crack growth rates of René 95 over a wide range of R -ratios and test temperatures [14]. The crack growth data shown in Figs. 2 and 3 were also treated in this fashion. Figure 4 (*left*) shows the 538°C (1000°F) Region II data as a function of ΔK . The Walker exponent for this set of data, 0.812, was determined using regression analysis. Figure 4 (*right*) shows the same data plotted against K_{eff} using this value of m . In the Walker model, the value of K_{eff} can be determined by multiplying ΔK by $(1 - R)^{m-1}$. Thus, when crack growth rate curves for different R -ratios are parallel using the conventional log-log representation, the Paris-Walker relationship will satisfactorily model the influence of R -ratio.

Figure 5 shows the crack growth rate data from Figs. 2 and 3 plotted as a function of K_{eff} where the Walker exponent was determined using only the Region II data. Both the near-threshold and Region II regimes of crack growth are satisfactorily modeled. This implies that the crack growth and closure mechanisms which operate in the Region II regime are the same as those that operate in the near-threshold regime.

The crossover behavior has been observed in a variety of nickel-base superalloys. Figure 6 shows fatigue crack growth rates determined for PM René 95 [14] at 21 and 538°C (70 and 1000°F). These data were obtained using the axisymmetric fatigue specimens which contained a semi-elliptical-shaped crack. The results indicate that the crossover behavior is not caused by the SEN specimen geometry and that it is not restricted to a given type of alloy.

In a separate investigation [15], PM René 95 was processed to have a large grain size or overaged precipitates. The crack growth rates were determined at 538 and 649°C (1000 and 1200°F) for an R -ratio of 0.05. Figures 7 (*left*) and 7 (*right*) show the crack growth rates for the large-grained and overaged conditions, respectively. These results illustrate that the crossover behavior is not restricted to specific types of microstructures. This behavior has also been observed in PM René 95 processed using extrusion and isothermal forging [26],

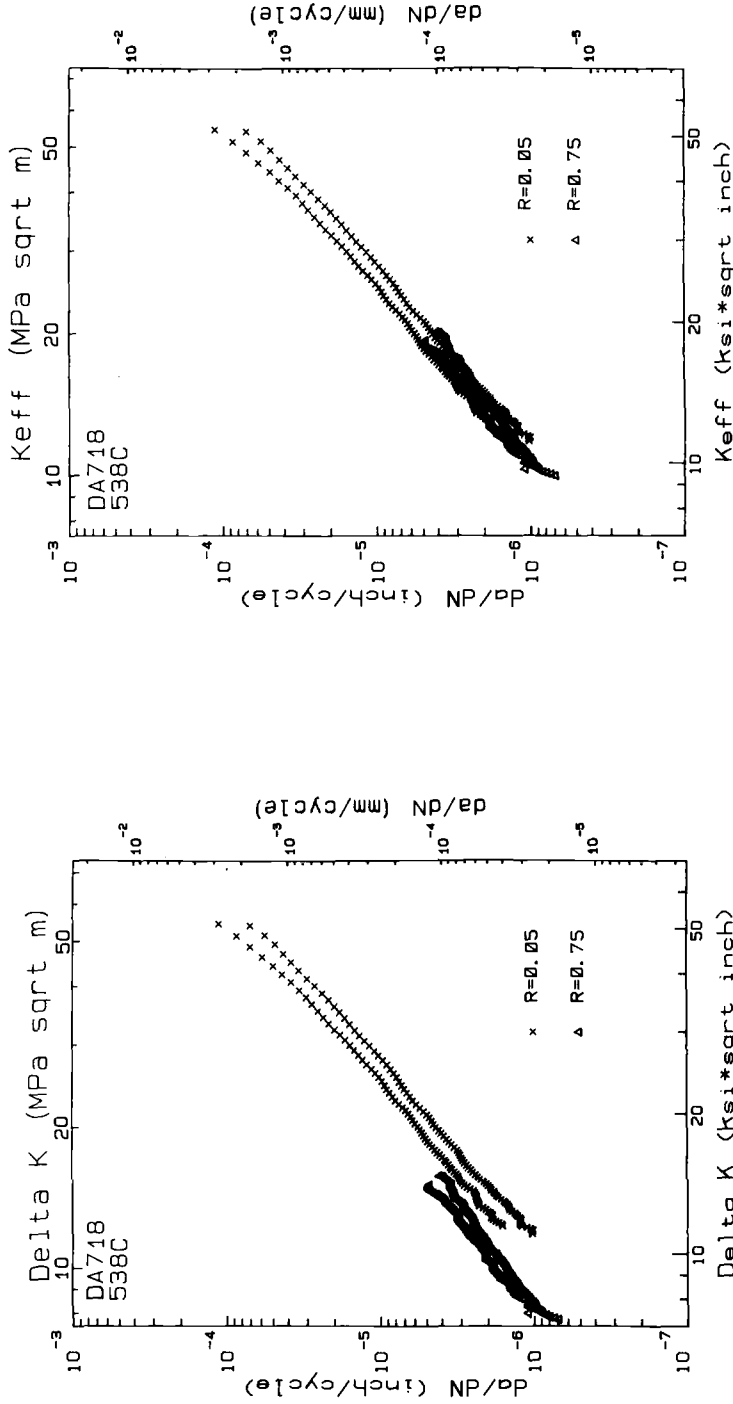


FIG. 4—The 538°C (1000°F) Region II crack growth rates of DA718 as a function of (left) K and (right) K_{eff}.

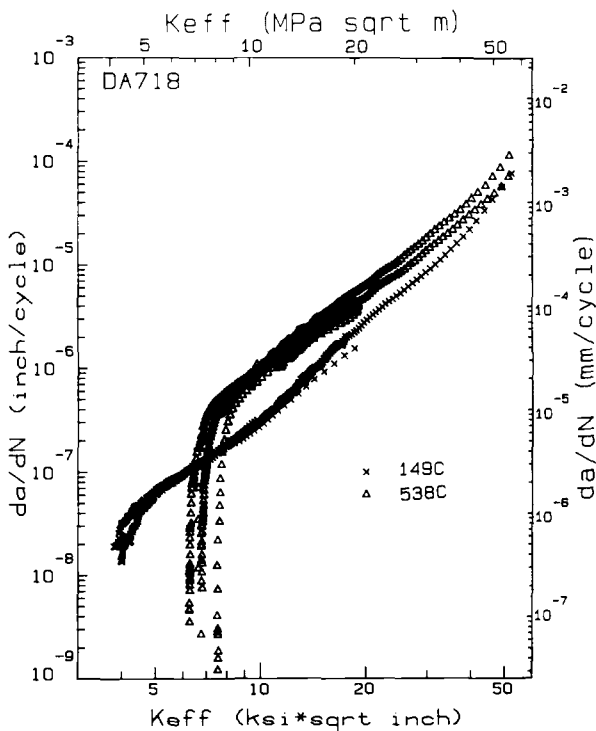


FIG. 5—The 149 and 538°C (300 and 1000°F) crack growth rates of DA718 as a function of K_{eff} .

titanium alloys [12], and titanium aluminides.³ Because this range in materials represents a wide variation of alloy types, strengthening precipitates, and microstructures, it has been suggested [13] that the crack growth crossover phenomenon is related to local crack-tip blunting by combinations of creep and cyclic plasticity rather than other proposed mechanisms, such as oxide-induced closure or variation in microscopic deformation modes with temperature.

Grain Size Effects

The influence of microstructure on the fatigue crack growth properties of Alloy 718 at 428°C (800°F) and two R -ratios was recently investigated by Krueger et al. [16]. It was shown that an increase in grain size or γ'' precipitate size reduced Region II crack growth rates. These microstructural effects were explained on the basis of deformation mode and slip reversibility. The influence of microstructure on the fatigue crack growth and deformation behavior is described in detail elsewhere [16]. The effect of R -ratio, however, is particularly pertinent to this review and will be discussed here.

Four of the microstructures evaluated by Krueger et al. [16] comprised a two-by-two matrix of grain size and precipitate size. Table 2 shows that the grain and precipitate sizes differ by about an order of magnitude. This range in microstructure is much larger than the range of microstructures evaluated in the crossover studies (Table 1).

Near-threshold and Region II growth rates were determined at R -ratios of 0.05 and 0.75 using the SEN specimen geometry and d-c potential drop technique. During the initial

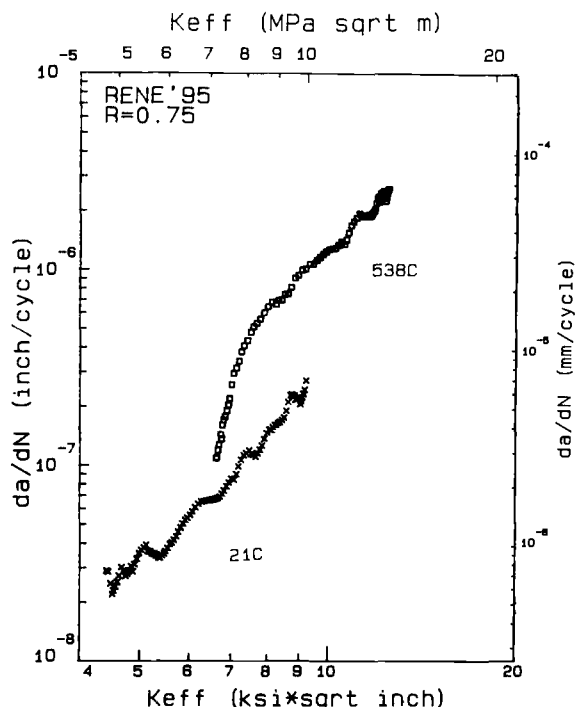


FIG. 6—The 21 and 538°C (70 and 1000°F) crack growth results of hot-isostatic-pressing (HIP)-compacted René 95 as determined in surface-flawed specimens at an R -ratio of 0.75 as a function of K_{eff} .

evaluation of test specimens with R -ratios of 0.05, it was immediately noted that grain size had a pronounced effect on fatigue crack topology. Figure 8 shows scanning electron microscope (SEM) micrographs which illustrate the typical fatigue fracture surface observed for fine and coarse-grained microstructures. The coarse-grained microstructure clearly exhibits a much more tortuous surface topology. Based on the work of Gray et al. [11] and Allison [12], this suggests that the observed grain size effect may largely be the result of the roughness-induced closure phenomenon.

Fatigue crack growth rates for the two fine-grained microstructures are shown in Fig. 9 (left and right). For both precipitate sizes, the high R -ratio caused a uniform lateral shift of the data over the entire range of ΔK . This result suggests that a wide range in precipitate size does not induce oxide- or roughness-induced closure. Analysis of the data using the modeling technique described previously showed that the Walker exponent determined for the Region II data satisfactorily collapsed both the near-threshold and Region II growth rates. The $da/dN:K_{eff}$ plots of Fig. 10 illustrate the results of this analysis. The values of m for the large and small precipitate data are 0.75 and 0.80, respectively.

Figure 11 shows that the high R -ratio tests of both coarse-grained microstructures also resulted in a uniform lateral shift of the crack growth data. The effects of R -ratio over the entire range in K were again modeled by Walker exponents determined from the Region II data (Fig. 12). The values of m for both the large-grained microstructures, independent of precipitate size, was 0.64. These findings strongly suggest that the behavior of coarse-grained Alloy 718 at near-threshold crack growth rates is not influenced by the roughness-induced closure phenomenon.

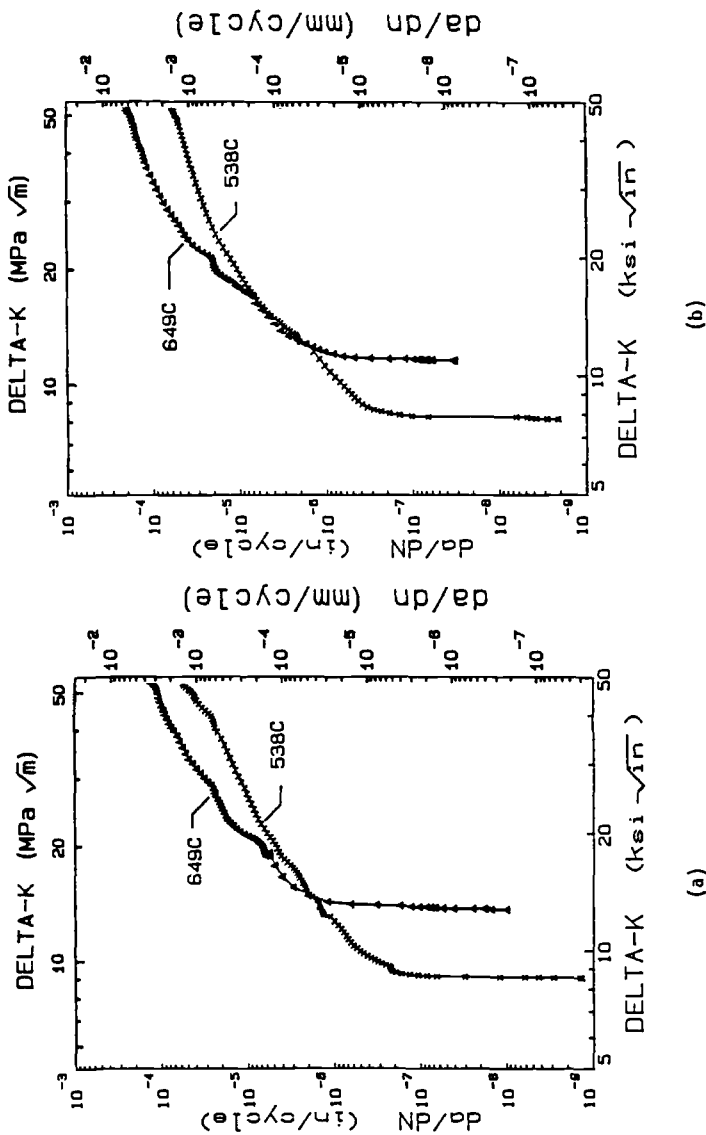


FIG. 7—Examples of the fatigue crack growth rate crossover behavior in HIP-compacted Ren95 processed to have (a) enlarged grain size and (b) enlarged τ' precipitate size.

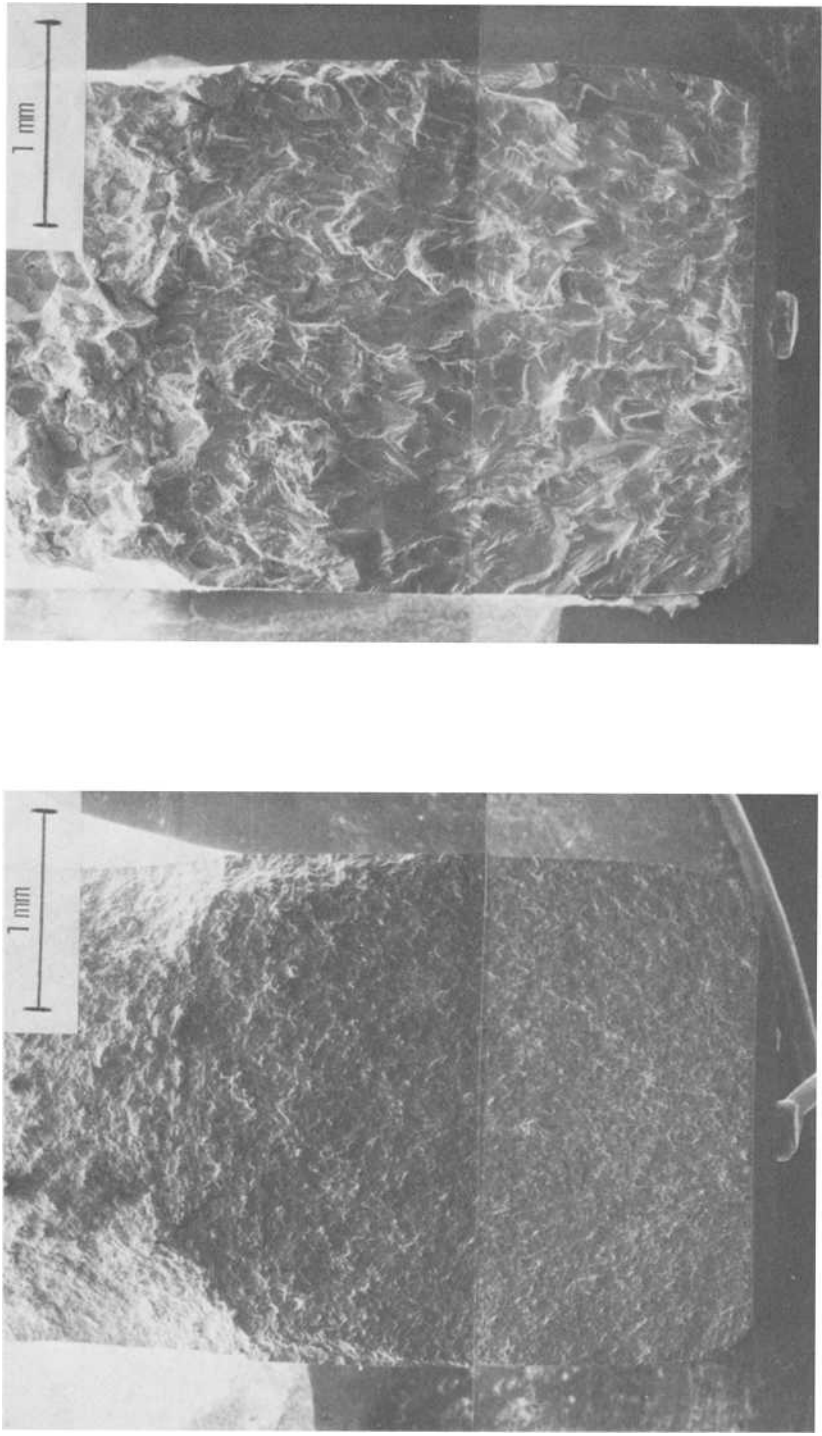


FIG. 8—SEM micrographs showing fatigue fracture surfaces of (left) fine-grained and (right) coarse-grained Alloy 718 with overaged precipitates.

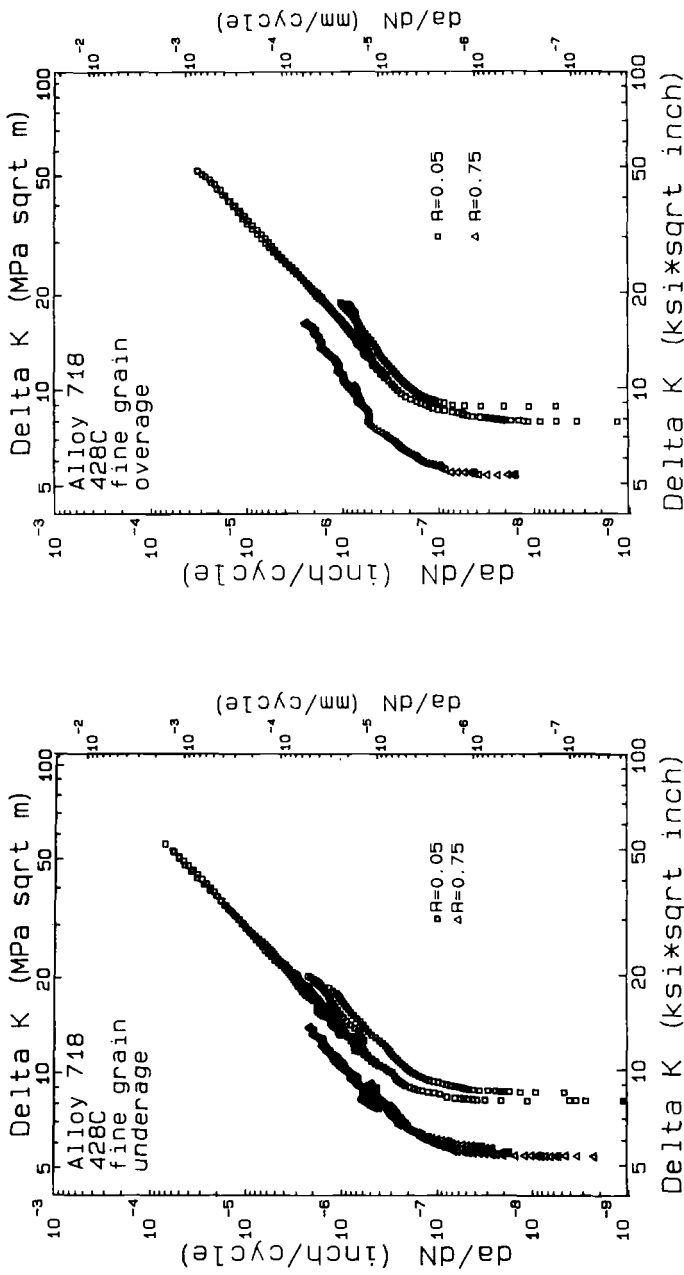


FIG. 9—Variation of 428°C (800°F) fatigue crack growth rates with K and R -ratio for fine-grained Alloy 718 with (left) small and (right) large precipitate size.

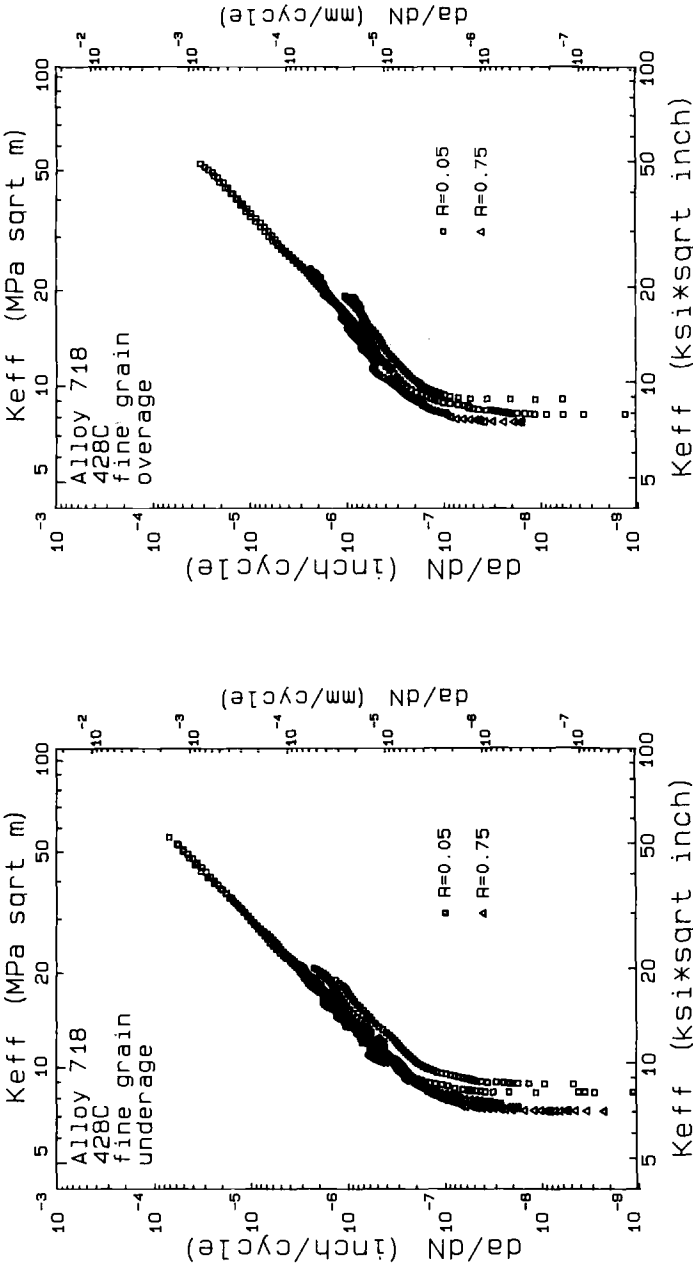


FIG. 10—Variation of 428°C (800°F) fatigue crack growth rates with K_{eff} and R-ratio for fine-grained Alloy 718 with (left) small and (right) large precipitate size.

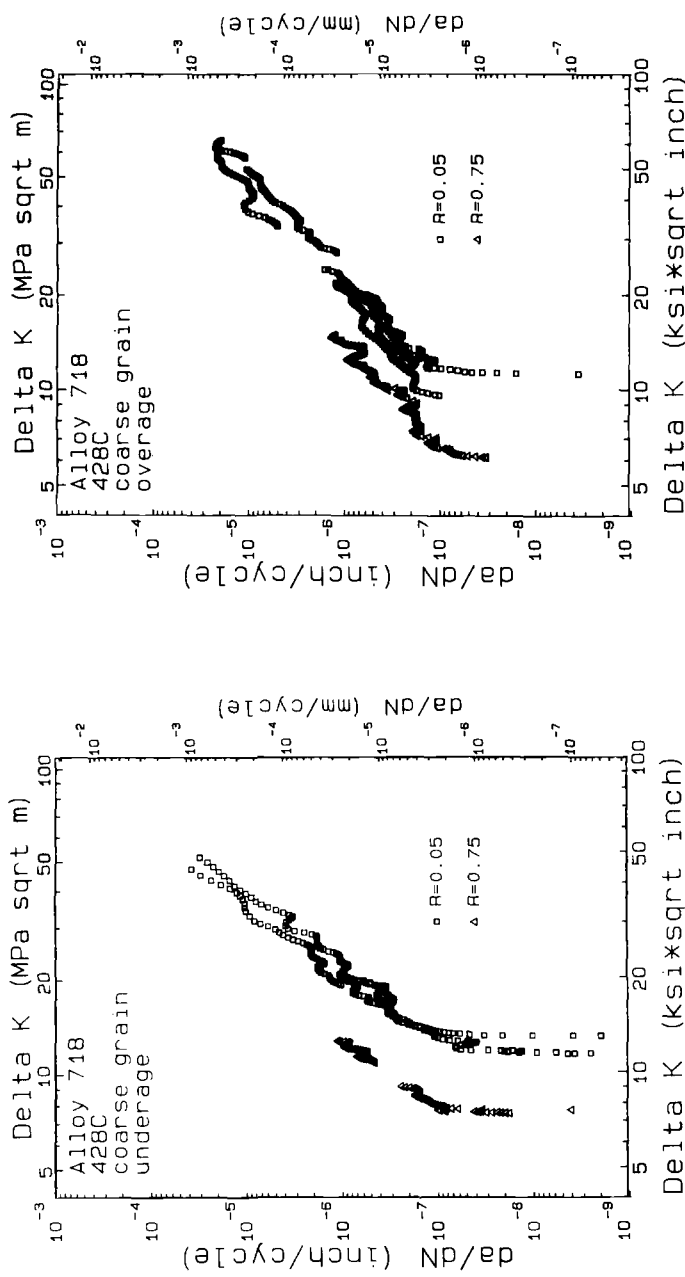


FIG. 11—Variation of 428°C (800°F) fatigue crack growth rates with K and R -ratio for coarse-grained Alloy 718 with (left) small and (right) large precipitate size.

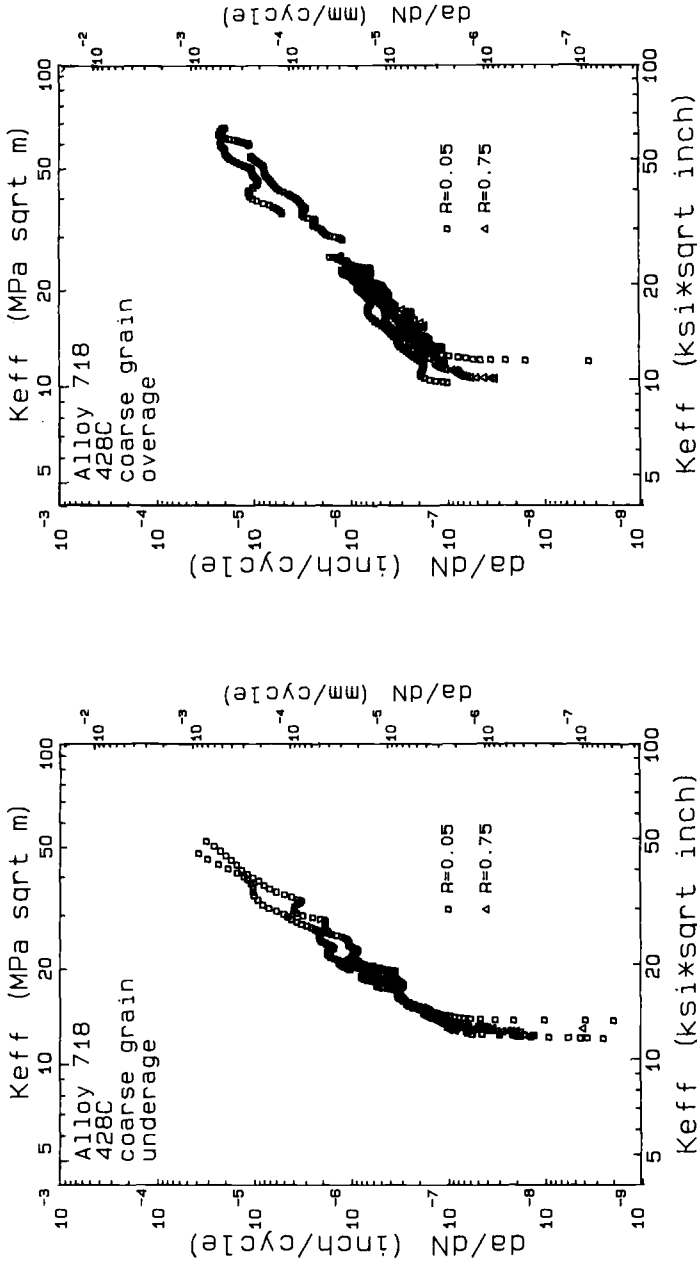


FIG. 12—Variation of 428°C (800°F) fatigue crack growth rates with K_{eff} and R-ratio for coarse-grained Alloy 718 with (left) small and (right) large precipitate size.

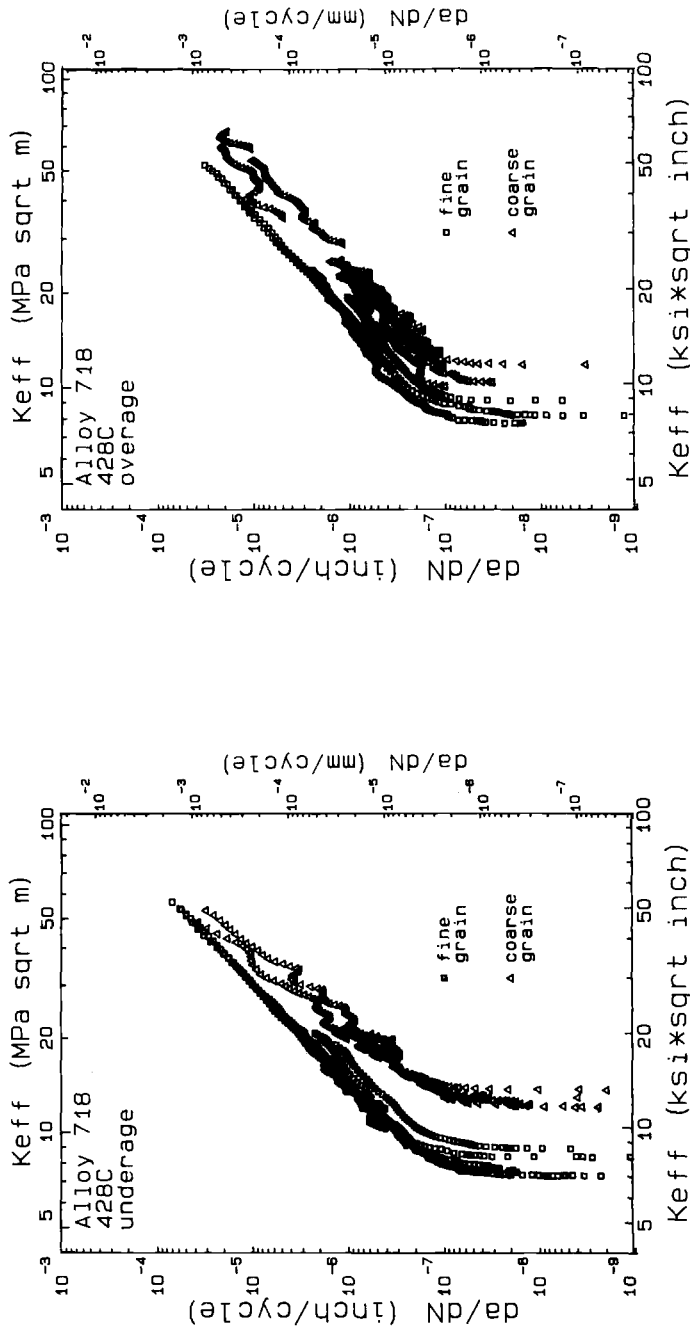


FIG. 13—Variation of 428°C (800°F) fatigue crack growth rates with K_{eff} for Alloy 718 with (left) small and (right) large precipitate size.

Unlike the previous studies on steels [11] and titanium alloys [12], the microstructural effects observed for Alloy 718 at a near-zero R -ratio were also observed at a high R -ratio [16]. This is illustrated in Fig. 13, which shows $da/dN:K_{\text{eff}}$ results for each precipitate size. For both precipitate sizes, the coarse-grained microstructures exhibit slower Region II crack growth rates. The influence of grain size is thus present at both high and low R -ratios.

Discussion

In this discussion, the types of closure will be classified using phenomenological descriptions rather than the more conventional mechanistic descriptions. This is appropriate because these investigations did not directly measure closure using techniques such as crack-mouth extensometry or back-face strain gages. The magnitude and sources of closure are thus somewhat subjective. The phenomenological classification approach categorizes closure as either K -dependent or K -independent. Examples of these two types of closure are shown schematically in Fig. 14.

For the case of K -dependent closure [Fig. 14 (left)] the value of K at closure (K_{cl}) is dependent on the applied K . Increasing R -ratio results in a similar movement of both the near-threshold and Region II crack growth rates. This type of behavior would be expected for plasticity-induced closure where the degree of closure is dependent on the size of the plastic wake zone behind the crack. The plastic zone size is clearly dependent on K [27,28] and as a result, a larger amount of closure occurs at higher values of K .

It should be noted that the type of R -ratio effects shown in Fig. 14 (left) can also be caused by traditional mean stress effects not related to the closure phenomenon. Closure effects tend to be most important in the near-threshold regime, while the mean stress or K effects are most apparent in Region II.

Figure 14 (right) illustrates the case for K -independent closure. This type of closure results

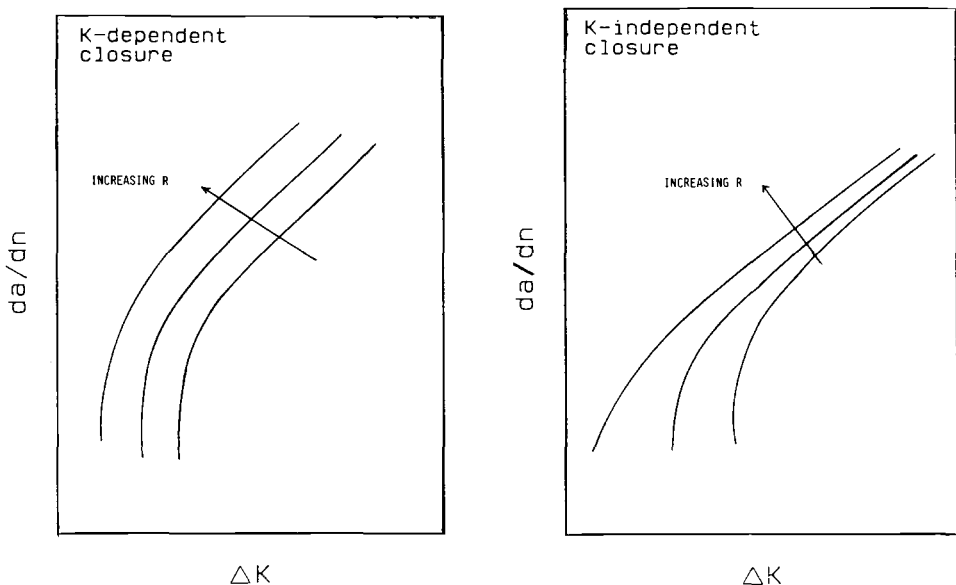


FIG. 14—Schematic figures showing the influence of R -ratio on the fatigue crack growth rates for (left) K -dependent and (right) K -independent types of closure.

in a constant value of K_{cl} for all values of ΔK . As a result, there is a larger influence of closure at low values of K and the curves deviate more at near-threshold growth rates. This behavior would be expected from roughness-induced or oxide-induced closure.

As noted in the literature review, K -independent closure has often been reported for steels and titanium alloys. This is not the case for a wide variety of nickel-base superalloys. Figures 5, 10, and 12 clearly illustrate that the Walker model accurately treats the influence of R -ratio on fatigue crack growth rates. The Walker model results in a uniform lateral shift of growth rate curves with R -ratio. Data which can be described using the Walker model in both Region I and II are not subject to K -independent closure.

To further illustrate the differences between these two types of closure, the DA718 data shown in Figs. 2 through 5 were treated assuming a K -independent type of closure. For this analysis, the value of K_{th} at an R of 0.05 was set equal to the value of K_{cl} . The value of K_{eff} was then defined as

$$K_{eff} = K_{max} - K_{cl} \quad \text{for } K_{min} < K_{cl} \quad (5)$$

and

$$K_{eff} = \Delta K \quad \text{for } K_{min} > K_{cl} \quad (6)$$

Figure 15 shows the results of this analysis where da/dN is plotted as a function of ΔK [13]. This illustrates that K -independent closure will result in nonparallel fatigue crack growth rate curves. In the Region II regime, an increase in R initially results in acceleration of crack growth rates, but additional increases in R have no influence. The increase in Region

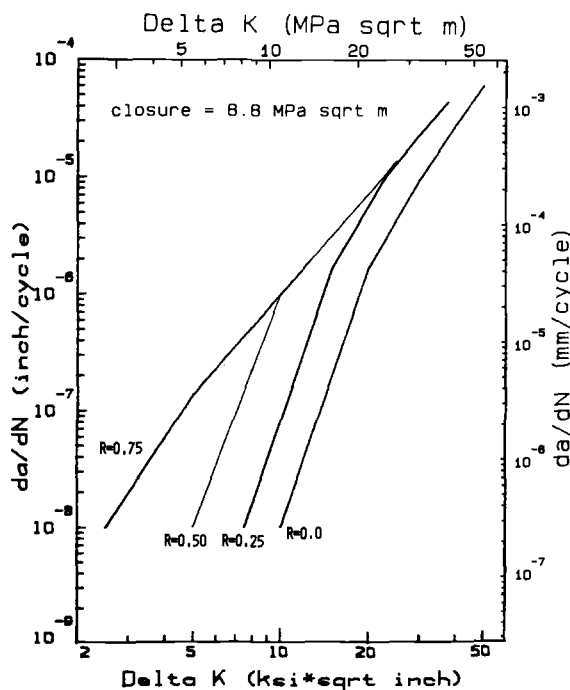


FIG. 15—Influence of R -ratio on the fatigue crack growth properties of DA718 assuming a K_{cl} of $8.8 \text{ MPa } \sqrt{\text{m}}$ ($8 \text{ ksi } \sqrt{\text{in.}}$).

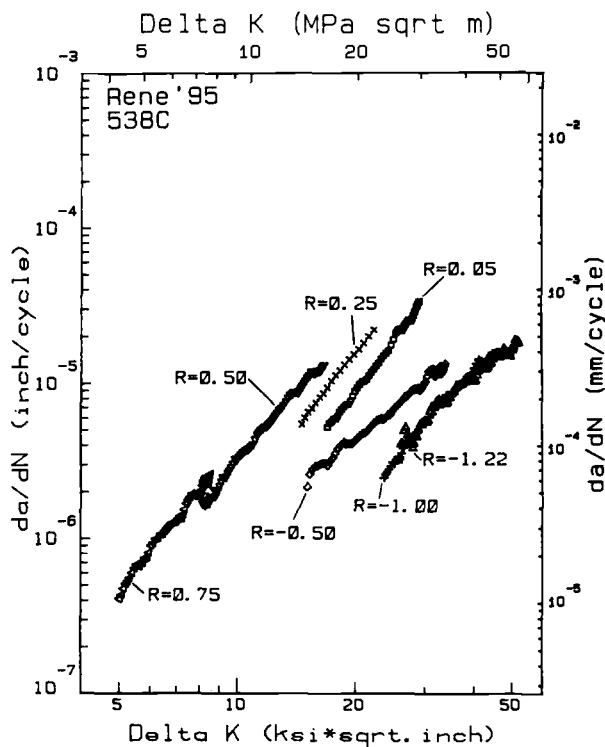


FIG. 16—The variation of Region II fatigue crack growth rates of René 95 at 538°C (1000°F) with R -ratio.

II growth rate occurs when K_{cl} is less than K_{min} and Eq 5 applies. Data in the previous figures showed crack growth data for only two values of R . Figure 16 shows PM René 95 crack growth data [14] for six R -ratios. The Region II crack growth rates increase systematically with increasing R -ratio. These results follow the behavior expected for K -dependent closure or the traditional mean stress effect.

There have been several investigations where K -independent closure has been reported for nickel-base superalloys. Zawada and Nicholas² measured crack closure in two grain sizes of René 95 at 649°C (1200°F) using compact specimens cycled with a R -ratio of 0.05. Both microstructures had a constant value of K_{cl} and it was concluded that this resulted from oxide-induced closure. In his study of Alloy 718, Yuen [9] concluded from oxide thickness measurements of a specimen with an R -ratio of 0.1 and from calculated crack-tip opening displacements that oxide-induced closure was the primary closure mechanism. His R -ratio of 0.5 crack growth rate data were parallel to the near-zero R -ratio data, even in the near-threshold regime. As noted above, this type of near-threshold data is inconsistent with an oxide-induced closure mechanism. One must be cautious when using oxide thickness measurements to confirm the presence of oxide-induced closure. The evaluation of a single R -ratio and the correlation between oxide thickness and a calculated crack-tip opening displacement do not show a cause-and-effect relationship. It should also be noted that Van Stone et al. [18] drew similar conclusions based on near-zero R -ratio data before their work on DA718 [13].

The relative shapes of the crack growth rate curves for different R -ratios can be extremely

useful in considering closure mechanisms. The analysis presented in Fig. 15 and the results shown in this paper strongly suggest that the crossover behavior is not caused by oxide-induced closure. The curve shape approach does not determine the type of closure, but can be used to determine the phenomenological closure classification.

The evaluation of the four Alloy 718 microstructures showed that, even in the presence of extremely tortuous crack paths, there was a strong influence of microstructure on crack growth rates at high R -ratios. This result is in sharp contrast with the results of Gray et al. [11] on pearlitic steels and Allison [12] on α titanium alloys. In Alloy 718, it was concluded that the variations of crack growth rates with microstructure are controlled, to a large extent, by the character of the deformation (slip) modes rather than by roughness-induced closure.

The absence of K -independent closure mechanisms for nickel-base superalloys with different strengthening precipitates, processing, and microstructures strongly suggests that this is a general behavior for this class of materials. In the absence of closure measurements, the parallel shift of crack growth data with R -ratio suggests that the dominant closure mechanisms are plasticity-induced. This type of behavior has important implications for crack growth prediction methodologies and alloy and process development programs.

The parallel shift of crack growth curves with R -ratio permits the use of life prediction methodologies based strictly on K without separate treatment for closure [26]. This simplifies the analysis of complex missions like those shown in Fig. 1, where the value of K_{eff} can be calculated knowing K_{max} and R . The situation for a closure-based methodology could be more complex because the degree of closure may be related to the compliance of the structure. If this were the case, it would become necessary to perform detailed finite-element analyses of complex, crack-containing geometries. This process could become extremely difficult for the wide number of variables which must often be considered (that is, localized plasticity, crack shape, and crack size). When using a K -based methodology, the only necessary stress analysis is that of the uncracked geometry [26,29].

The existence of K -dependent closure in nickel-base superalloys also simplifies the development of improved materials for complex loading spectra. Because this type of behavior results in similar microstructural effects at both low and high R -ratios, new materials can be adequately screened using near-zero R -ratio crack growth tests. The most improved alloys can then be evaluated more extensively at other stress ratios.

All near-threshold data reported in this paper were determined using SEN specimens. These specimens have a lower bending component and a steeper K -gradient than compact specimens. Data obtained with this type of specimen have accurately predicted the size of inclusions that can act as fatigue initiation sites [13] and the lives of surface flaws in complex geometries under complex loading conditions [26]. The difference between the results presented here on nickel-base superalloys (SEN specimens) and those reviewed for other materials (compact specimens) may, in part, result from differences between the SEN and compact specimen geometries. Both specimens are subject to problems at elevated temperatures where the oxidation of testing fixtures may prevent the free rotation of the specimen on pins. This problem would appear to be more severe for the compact geometry because of its larger bending component. These problems become more aggravated in near-threshold tests where the loads are low and the crack lengths become long as a result of load- or K -shedding procedures. More research is required to determine the influence of specimen geometry on crack closure behavior. At present, it is difficult to attribute the contrasting results described in this paper to specimen geometry effects.

Conclusions

This paper has reviewed the influence of R -ratio on the near-threshold and Region II crack growth rates of nickel-base superalloys at elevated temperature. There appear to be

marked differences between the crack growth behavior of nickel-base superalloys and that of other families of high-strength structural materials. Although the influence of microstructure on the crack propagation rates is similar, superalloys are subject to K -dependent closure, where changes in R -ratio cause uniform, lateral shifts in the fatigue crack growth curves. The other materials experience K -independent closure where there is a larger influence of R -ratio on near-threshold than on Region II crack growth rates. The existence of K -dependent closure in superalloys was shown to be independent of precipitate type, alloy processing, grain size, and precipitate size. This type of closure facilitates K -based crack growth prediction methodologies and simplifies the evaluation of crack growth properties in material development.

Acknowledgments

The authors would like to express their appreciation of the U.S. Naval Air Systems Command, the U.S. Air Force, and the General Electric Co., which sponsored this research. The authors are also indebted to M. F. Henry of General Electric Corporate Research and Development and S. D. Antolovich of Georgia Institute of Technology for their helpful comments and effort during these investigations.

References

- [1] Van Stone, R. H., "Advanced Cumulative Damage Modelling," Air Force Materials Laboratory Contract F33615-84-C5032, General Electric Aircraft Engine Group, Cincinnati, OH 45215, 1985.
- [2] Ritchie, R. O. in *Fracture Mechanics: Eighteenth Symposium*, ASTM STP 945, in press.
- [3] Elber, W., *Engineering Fracture Mechanics*, Vol. 2, 1970, pp. 37-45.
- [4] Paris, P. C., Bucci, R. J., Wessel, E. T., Clark, W. G., and Mayer, T. R., *Stress Analysis and Growth of Cracks*, ASTM STP 513, American Society for Testing and Materials, Philadelphia, 1972, pp. 141-176.
- [5] Stewart, A. T., *Engineering Fracture Mechanics*, Vol. 13, 1980, pp. 463-478.
- [6] Suresh, S., Zamiski, O. F., and Ritchie, R. O., *Metallurgical Transactions*, Vol. 12A, 1981, pp. 1435-1443.
- [7] Liaw, P. K., Leax, T. R., Williams, R. S., and Peck, M. G., *Metallurgical Transactions*, Vol. 13A, 1982, pp. 1607-1618.
- [8] Haigh, J. R., *Engineering Fracture Mechanics*, Vol. 7, 1975, pp. 271-284.
- [9] Yuen, J. L., "Near-Threshold Corrosion FCG Behavior of a Nickel-Base Superalloy in Air and Inert Environment," Ph.D. thesis, Stanford University, Stanford, CA, 1982.
- [10] Ritchie, R. O., and Suresh, S., *Metallurgical Transactions*, Vol. 13A, 1982, pp. 937-940.
- [11] Gray, G. T. III, Thompson, A. W., Williams, J. C., and Stone, D. H., *Fatigue Thresholds*, J. Backlund, A. Blom, and C. J. Beevers, Eds., EMAS Publications Ltd., Warley, U. K., 1981, pp. 345-360.
- [12] Allison, J. E., "Investigation of the Influence of Slip Character on the Fatigue Crack Growth Properties of Titanium Alloys," Ph.D. thesis, Carnegie-Mellon University, Pittsburgh, PA, 1983.
- [13] Van Stone, R. H. and Krueger, D. D., "Investigation of Direct Aged Inconel 718 Fatigue Behavior," NAVAIR Contract N00019-82-C-0373, Final Report, General Electric Aircraft Engine Business Group, Cincinnati, OH 45215, December 1984.
- [14] Van Stone, R. H., "The Influence of Temperature and Stress Ratio on the Fatigue Crack Growth Behavior of René 95," Report TM 82-640, General Electric Aircraft Engine Group, Cincinnati, OH 45215, 1982.
- [15] Krueger, D. D., Van Stone, R. H., and Henry, M. F., "Metallurgical Effects on Fatigue Behavior of Gas Turbine Disk Alloys," NAVAIR Contract N00019-82-C-0226, General Electric Aircraft Engine Group, Cincinnati, OH 45215, August 1985.
- [16] Krueger, D. D., Antolovich, S. D., and Van Stone, R. H., "Effects of Grain Size and Precipitate Size on the Fatigue Crack Growth Behavior of Alloy 718 at 428°C," *Metallurgical Transactions*, Vol. 18A, 1987, pp. 1431-1449.
- [17] Gangloff, R. P., *Fatigue Engineering Materials and Structures*, Vol. 4, 1981, pp. 15-33.
- [18] Van Stone, R. H., Krueger, D. D., and Duvelius, L. T. in *Fracture Mechanics: Fourteenth Symposium, Vol. II: Testing and Application*, ASTM STP 791, American Society of Testing and Materials, Philadelphia, 1984, pp. II-553-II-578.

- [19] Coffin, L. F. and Rowe, G. in *Automated Test Methods for Fracture and Fatigue Crack Growth*, ASTM STP 877, American Society for Testing and Materials, Philadelphia, 1985, pp. 148–166.
- [20] Johnson, H. H., *Materials Research and Standards*, Vol. 5, 1965, pp. 442–445.
- [21] Newman, J. C. and Raju, I. S., “Stress-Intensity Factor Equations for Cracks in a Three-Dimensional Finite Body,” NASA Technical Memorandum 78805, National Aeronautics and Space Administration, Langley Research Center, Hampton, VA, 1971.
- [22] Tada, L. H., Paris, P. C., and Irwin, G. R., *The Stress Analysis of Cracks Handbook*, Del Research Corp., Hellertown, PA, 1973.
- [23] Krueger, D. D., “Effects of Grain Size and Precipitate Size on the Fatigue Crack Growth Behavior of Alloy 718 at 428°C,” M. S. thesis, University of Cincinnati, Cincinnati, OH, 1984.
- [24] Paris, P. C., “Fatigue—An Interdisciplinary Approach,” *Proceedings*, Tenth Sagamore Conference, Syracuse University Press, Syracuse, NY, 1964, p. 107.
- [25] Walker, K. in *Effects of Environment and Complex Load History on Fatigue Life*, ASTM STP 462, American Society for Testing and Materials, Philadelphia, 1970, pp. 1–14.
- [26] Van Stone, R. H., Gilbert, M. S., Gooden, O. C., and Laflen, J. H., “Constraint Loss Model for the Growth of Surface Fatigue Cracks,” this publication, pp. 637–656.
- [27] Irwin, G. R., “Plastic Zone Near a Crack and Fracture Toughness,” *Proceedings*, Seventh Sagamore Ordnance Materials Research Conference, Report Number MeTE 661-611/F, Syracuse University Research Institute, August 1960, p. iv–63.
- [28] Rice, J. R. in *Fatigue Crack Propagation*, ASTM STP 415, American Society for Testing and Materials, Philadelphia, 1968, p. 247.
- [29] Nicholas, T., Laflen, J. H., and Van Stone, R. H., “A Damage Tolerant Design Approach to Turbine Life Prediction,” *Proceedings*, Minnowbrook Symposium on Life Prediction Methods,” 1986.

Effect of Frequency on Fatigue Crack Growth Rate of Inconel 718 at High Temperature

REFERENCE: Weerasooriya, T., "Effect of Frequency on Fatigue Crack Growth Rate of Inconel 718 at High Temperature," *Fracture Mechanics: Nineteenth Symposium, ASTM STP 969*, T. A. Cruse, Ed., American Society for Testing and Materials, Philadelphia, 1988, pp. 907-923.

ABSTRACT: Fatigue crack growth was studied at 650°C as a function of frequency for several ratios of minimum-to-maximum stress intensity (R) and for two values of maximum stress-intensity factor (K_{\max}), for a nickel-base superalloy, Inconel 718. All the tests were conducted under computer control at constant K_{\max} . Crack lengths were monitored at low frequencies from compliance calculations based on crack-mouth opening displacement measurements. At higher frequencies, crack length was measured using a d-c electric potential system. It was found that fatigue crack growth rate can be characterized in three distinct frequency regions. These three regions represent fully cycle-dependent, mixed, and fully time-dependent crack growth behavior, and each region can be modeled by a power law function. Observation of micromechanisms support the existence of these three different modes of crack growth.

KEY WORDS: fatigue crack growth, time-dependent growth, cyclic-dependent growth, nickel-base superalloy, crack growth rate model, frequency effects, fracture mechanics

Turbine engine disks of nickel-base superalloys are subjected to cyclic stresses and thermal transients at elevated temperatures as a result of throttle excursions and thermal gradients [1]. These operations produce loading patterns that cover a range of frequencies, amplitudes, and wave shapes. The U.S. Air Force has recently introduced damage tolerance requirements for critical structural components such as turbine disks. It is important, therefore, to be able to predict the growth rate of fatigue cracks in disk materials under the appropriate loading and temperature histories experienced in engines. This can be accomplished through a systematic study of the influence of the individual loading variables and the possible interactions among them. In the development of any model, the governing microstructural mechanisms should provide guidance.

The rates and micromechanisms of crack growth in nickel-base superalloys are, in general, a function of the maximum stress-intensity factor (K_{\max}), temperature (T), frequency (f), stress ratio (R), hold-time (t_H), and wave shape, as well as the material and microstructure. If all the variables except K_{\max} are held constant, then the crack growth rate for most nickel-base superalloys such as Inconel 718 can be correlated with the stress-intensity factor as the governing parameter [2-9]. The other variables can then be used as modifying parameters in modeling the behavior. To fully characterize fatigue crack growth rate (FCGR) as a function of one of the above variables, experiments can be conducted with other variables held constant throughout the test.

¹ Research Scientist, University of Dayton Research Institute, Dayton, OH 45469.

Modeling the FCGR behavior (growth rates and micromechanisms) reduces to determining the explicit relationships of the independent variables in the expressions

$$\frac{da}{dN} = F_1(K_{\max}, T, f, R) \quad (1)$$

$$\text{micromechanism of growth} = F_2(K_{\max}, T, f, R) \quad (2)$$

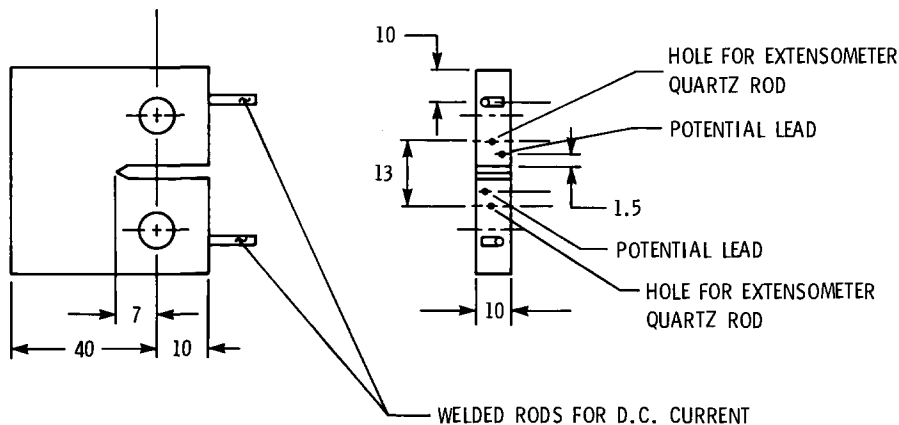
In this paper, rates and micromechanisms of fatigue crack growth were studied as a function of two independent variables, frequency and R , in Eqs 1 and 2 at $T = 650^\circ\text{C}$.

In air and vacuum, under low-cycle fatigue conditions, crack growth rate as a function of frequency has been studied in detail by Solomon [10,11]. He identified the existence of three major frequency regimes in air. Under K -controlled linear elastic fracture mechanics (LEFM) conditions [12], the present author obtained similar results for Inconel 718 at 650°C . The results from this investigation and others [6,7] show that for a given K_{\max} , FCGR decreases with increasing frequency. At higher frequencies, the growth rate approaches a constant value. It has also been observed that the crack growth mechanism changes from intergranular to transgranular with increasing frequency.

Experimental Technique

Overview

Systematic studies of fatigue crack growth as a function of test variables generally involve large numbers of constant load tests leading to scatter from specimen to specimen. In this investigation, the growth rates were obtained at two K_{\max} values for three R values in a range of five decades of frequencies using only two specimens to obtain the necessary



NOTES:

1. SPECIMENS FROM 0.5 INCH PLATE MATERIAL
2. CRACK ORIENTATION: TL
3. DIMENSIONS IN mm

FIG. 1—The CT specimen modified for d-c potential and displacement measurements.

experimental information for the investigation. To minimize possible closure effects on crack growth, relatively high stress-intensity factors, which lie in the mid-power-law region of the FCGR versus K_{\max} curves were selected. In designing the experiments, the fact that the growth rate could be correlated with a power law function of K_{\max} was taken into consideration. The power law FCGR function has been reported in the literature and has also been observed in this laboratory under various frequencies and hold-time conditions [13]. This testing approach facilitated the study of crack growth behavior over a range of five decades of frequencies.

Specimen Geometry and Material

A series of FCGR tests were conducted on Inconel 718 Nickel-base superalloy. Tests were conducted using the standard ASTM Test for Constant-Load-Amplitude Fatigue Crack Growth Rates Above 10^{-8} m/Cycle (E 647-81) on compact tension (CT) specimens having a width, W , of 40 mm and a thickness, B , of 10 mm. To make the d-c potential measurement of crack length, two Inconel 718 metal rods were welded to the CT specimen for the connection of the d-c current supply. Leads for the d-c electric potential measurements were spot-welded across the crack mouth. A diagram of the CT specimen with d-c current rods is shown in Fig. 1. Note also the location of the two holes which accepted the ends of the quartz rods attached to the extensometer used for compliance measurements.

All specimens were fabricated from the same heat of material. The chemical composition of the Inconel 718 material is shown in Table 1. The heat treatment was as follows:

- Step 1. Anneal at 968°C (1775°F) for 1 h, air cool to 718°C (1325°F).
- Step 2. Age harden at 718°C (1325°F) for 8 h, then furnace cool at 56°C/h (100°F/h) to 621°C (1150°F).
- Step 3. Age harden at 621°C (1150°F) for an additional 8 h.
- Step 4. Air cool to room temperature.

Test Conditions

All crack growth tests were conducted under constant stress-intensity conditions. Two K_{\max} values of 27.8 and 40 MPa $m^{1/2}$ were chosen to define the levels. Both these values lie

TABLE 1—Chemical composition for Inconel 718.

Element	Weight %
Ni	50–55
Fe	balance
Mo	2.8–3.3
Al	0.2–0.8
C	<0.08
Si	<0.35
P	<0.015
B	<0.006
Cr	17–21
Nb + Ta	4.75–5.5
Ti	0.65–1.15
Co	<1.0
Mn	<0.35
Cu	<0.30
S	<0.015

in the mid-power-law region of the FCGR versus K_{\max} curve. The tests were conducted over frequencies chosen from the range 0.001 to 50 Hz, at a temperature of 650°C. Three different R ratios, 0.1, 0.5, and 0.8 were used in these experiments. A triangular loading waveform was utilized in all of the tests.

Specimens were precracked at 650°C to a crack length given by ASTM Test E 647-81 ($a = 10$ mm) by applying a constant stress intensity that was less than the stress intensities used in the experiments.

Test System

An automated test system based on a microcomputer was employed in conducting these experiments. An electrohydraulic servo-controlled test station with a 25-kN load cell was used to apply loading during the course of these tests. The microcomputer was used in real time for feedback control of the test parameters and also to acquire and reduce data. The specimen was heated with a resistance furnace, and the temperature at a point on the specimen was controlled at $650 \pm 2^\circ\text{C}$. The temperature variation along the crack path was noted to be less than 10°C .

Measurement of Crack Length

Crack length was measured in the range of frequencies between 10^2 and 10^{-3} Hz, using a hybrid crack measuring system. In this system, crack lengths were measured by both compliance and d-c electric potential techniques. During testing, K_{\max} control was accomplished in different frequency ranges using one of the two techniques. Due to the inability of the extensometer to track the displacement correctly, the d-c electric potential technique was used exclusively at high frequencies ($f > 1.0$ Hz). For lower frequencies ($f \leq 1.0$ Hz), controlling crack lengths were determined by the compliance technique. For the $f \leq 1.0$ Hz case, the d-c electric potential crack length data were also collected for later evaluation of their accuracy and long-term stability under the effect of environment at very low frequencies. Acquisition of load and displacement data (compliance) from the specimen to the microcomputer was accomplished using a digital oscilloscope. Electric potential data acquisition from the test machine to the microcomputer was performed utilizing a digital voltmeter.

The crack length was estimated at periodic cycle intervals chosen by the operator. The cycle interval was chosen to give crack length increments of less than 0.025 mm. After the crack length is determined, using the stress-intensity relationship given in ASTM Test E 647-81, the new load that is necessary to keep the K_{\max} constant is determined by the computer software to within $\pm 0.1\%$. This computed load was then set up at the function generator through the IEEE 488 interface.

Compliance Method—During the test, crack length was determined indirectly from compliance measurements using displacement data obtained with a high-temperature extensometer having quartz extension rods. With these quartz rods, the extensometer was maintained at ambient temperature since it was kept outside the furnace. Displacement and load data obtained simultaneously in digital form with the oscilloscope were transferred to the computer through the IEEE 488 interface bus. A straight line was fitted to a selected set of data, chosen by a specified load window, using a least-squares error minimization procedure. Compliance obtained from the fitted straight line was converted to crack length using a

relationship obtained by Saxena and Hudak [14] given in Eq 3, where C is the compliance, E is the modulus, B is the thickness of the specimen, and $b = a/W$.

$$CEB = \left(1 + \frac{0.25}{b}\right) \left(\frac{1+b}{1-b}\right)^2 \cdot (1.61369 + 12.6778b - 14.2311b^2 - 16.6102b^3 + 35.0499b^4 - 14.4943b^5) \quad (3)$$

Electric Potential Method—Using the d-c electric potential technique, crack length was determined at higher frequencies by measuring the potential across the crack tip at a constant d-c current of 10 A. The constant current was generated by a stable power supply while the potential was measured by the voltmeter. Both the power supply and the voltmeter were attached to the computer through the IEEE 488 bus. Using these instruments and the developed software, data were acquired and test conditions were controlled. To eliminate the thermal electrometric force (EMF), the potential data were also obtained at zero current. The electric potential data were acquired a given number of times at the upper one-third of a predefined number of successive cycles. The thermal EMF adjusted average value of the potential was then converted to a crack length using an experimentally determined calibration curve.

Correction for Apparent Changes in Crack Length—It was observed that whenever f , K_{\max} , or R was changed, the crack length estimated by the compliance method changed. The change in compliance-estimated crack length occurred immediately after the change in external parameter and was not associated with any real change in crack length. Rather than continue to use the newly estimated crack length that was established after the change, a procedure was developed to ensure continuity in crack length before and after the change in loading parameter. In essence, the procedure involved modifying the apparent elastic modulus after each change in loading parameter, so that the crack length before and after the change remained the same based on Eq 3.

Test Procedure

Using a triangular waveform, tests were conducted using two different procedures. In one test series, the temperature and R were held constant while the crack was grown for periods at various frequencies. In the other test category, while the frequency and temperature were held constant, the crack was grown for periods at different R values. Frequency and R sequences were selected to make distinct markings on the fracture surface. These marks were later used in verifying the crack lengths measured by d-c potential and compliance methods. Figure 2 provides an example of a fracture surface from the tests. After fracture, each specimen was prepared for observation under optical and scanning electron microscopes to determine the mechanisms of crack growth.

Growth Rate Monitoring

At the beginning of the test, the frequency and R sequence for the specimen was input to the computer. After each growth segment of 0.75 mm, either the frequency or R was automatically changed as specified. While the test was being conducted, the crack length as a function of the number of cycles was monitored by the operator on a graphical display. Crack growth rates derived from a linear regression representation of the data over the

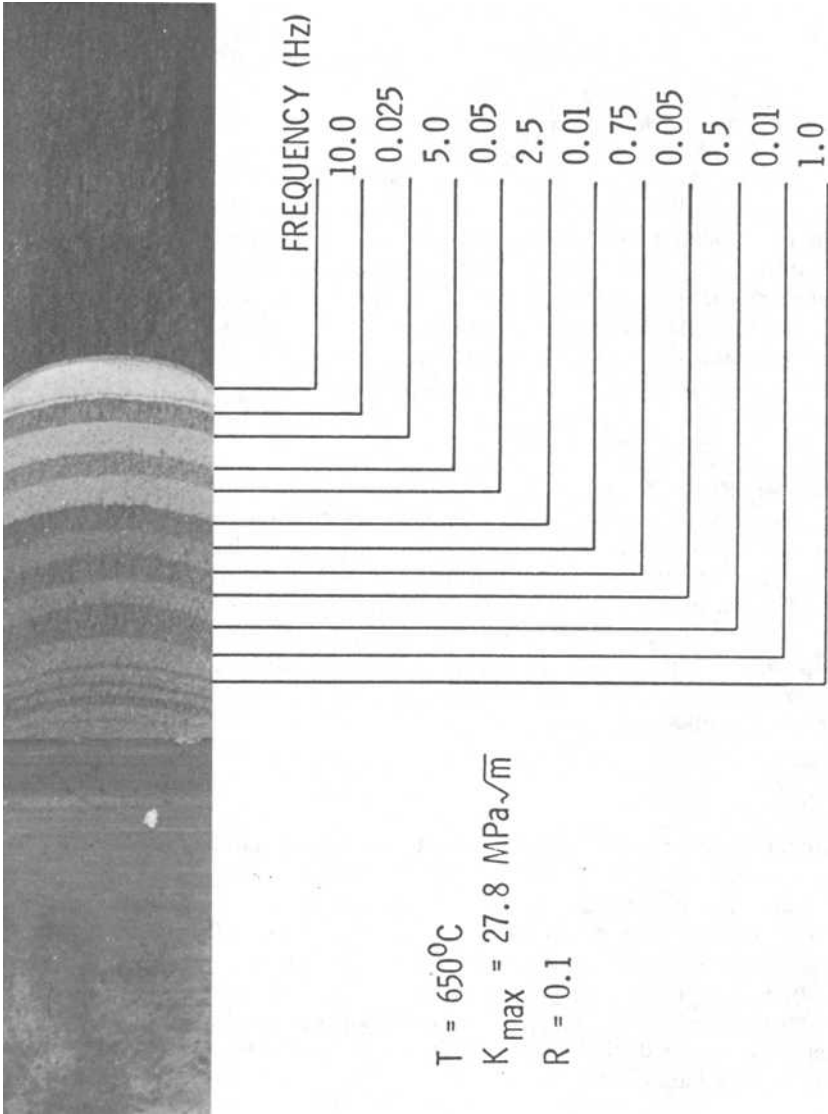


FIG. 2—Fractured specimens of Inconel 718 showing different cracking regions corresponding to test under different conditions.

region where constant growth rate was observed were also displayed. With the aid of this real-time display of data, the FCGR were obtained within crack extensions as small as 0.5 mm for given combinations of frequency, temperature, R , and K_{\max} values. The graphical display also helped the operator determine if the crack growth rate had reached a steady-state value. This sophisticated testing procedure made it possible to obtain large amounts of data within a short time with very few specimens. To check the variability of growth rate, the crack was grown at $f = 1$ Hz, $T = 650^{\circ}\text{C}$, $R = 0.1$, and $K_{\max} = 40 \text{ MPa m}^{1/2}$ at various crack lengths in the specimens. The variability of the FCGR from specimen to specimen and location to location was observed to be within a scatter band of 10% from the mean value for a given set of f , R , T , and K_{\max} [15].

Results and Discussion

Growth Rate-Frequency Plots at $R = 0.1$

Fatigue crack growth data were obtained for Inconel 718 alloy as a function of frequency at $R = 0.1$ and at a temperature of 650°C . Typical crack length versus cycle data with a fitted linear line are shown in Fig. 3 for a given test condition ($K_{\max} = 27.8 \text{ MPa m}^{1/2}$ and $f = 1$ Hz). FCGR data as a function of frequency, obtained by fitting a least-squares error linear regression line for the crack length versus cycles curves, are shown in Fig. 4 for the maximum stress-intensity factors of 27.8 and $40 \text{ MPa m}^{1/2}$ for $R = 0.1$ and $T = 650^{\circ}\text{C}$. Also in this figure, FCGR data, at 1 Hz in vacuum [16] at 650°C and at 1 and 4 Hz in air at room temperature, are given for both K_{\max} values. In Fig. 5, FCGR data for $K_{\max} = 40 \text{ MPa m}^{1/2}$ are presented using a time basis, that is da/dt is described as a function of frequency.

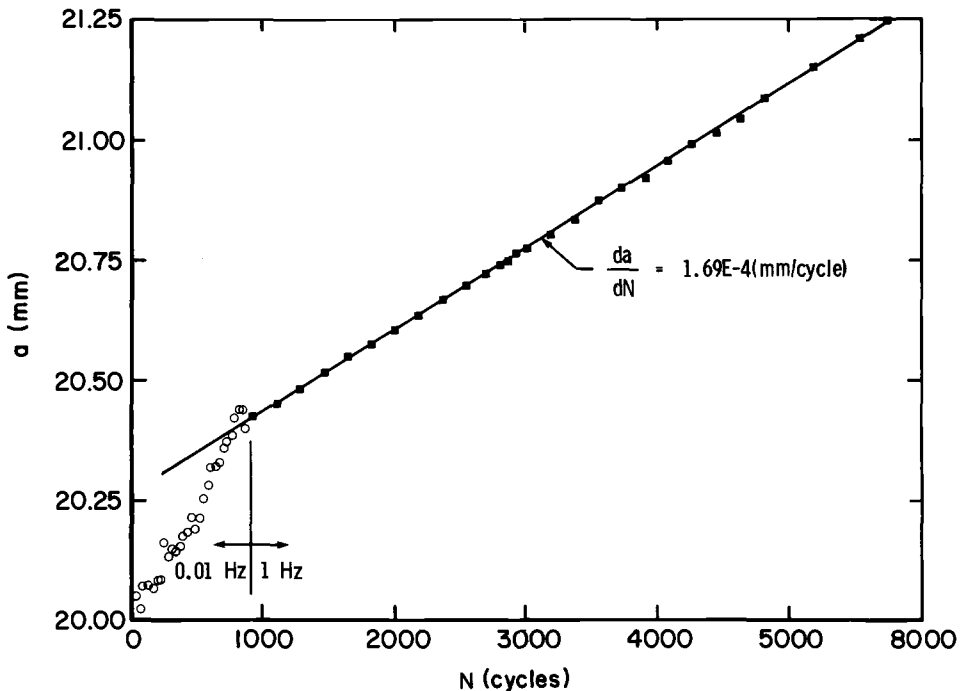


FIG. 3—Typical a versus N experimental data with the fitted linear regression line.

In Fig. 4, the da/dN versus frequency curves can be represented with three linear lines, with a continuous transition from one to the other. The curve representing $K_{\max} = 40 \text{ MPa m}^{1/2}$ is discussed in detail in the proceeding paragraphs.

Fully Time Dependent Growth—In Fig. 4, FCGR increases with decreasing frequency with a -1 slope for the portion of the curve for frequencies below 0.01 Hz . This region represents fully time-dependent behavior where cycling has no effect on the growth rate based on time. The horizontal region of the da/dt curve in Fig. 5 also illustrates the fact that the processes are fully time dependent in this frequency regime. Under these conditions, time that is required to grow the crack a specific distance is a constant, and therefore, the factors determining the growth is independent of the number of cycles elapsed during that time. The damage is believed to occur by an environmentally enhanced rather than by a classical creep process.

Environmentally Enhanced Cycle Dependent (Mixed) Growth—For frequency values between 0.01 and 10 Hz , the log-log plot of da/dN versus frequency is linear with a slope of -0.34 . In this middle frequency region, environment is affecting the cyclic damage, and fracture is due to an environmentally enhanced fatigue process (mixed-mode region).

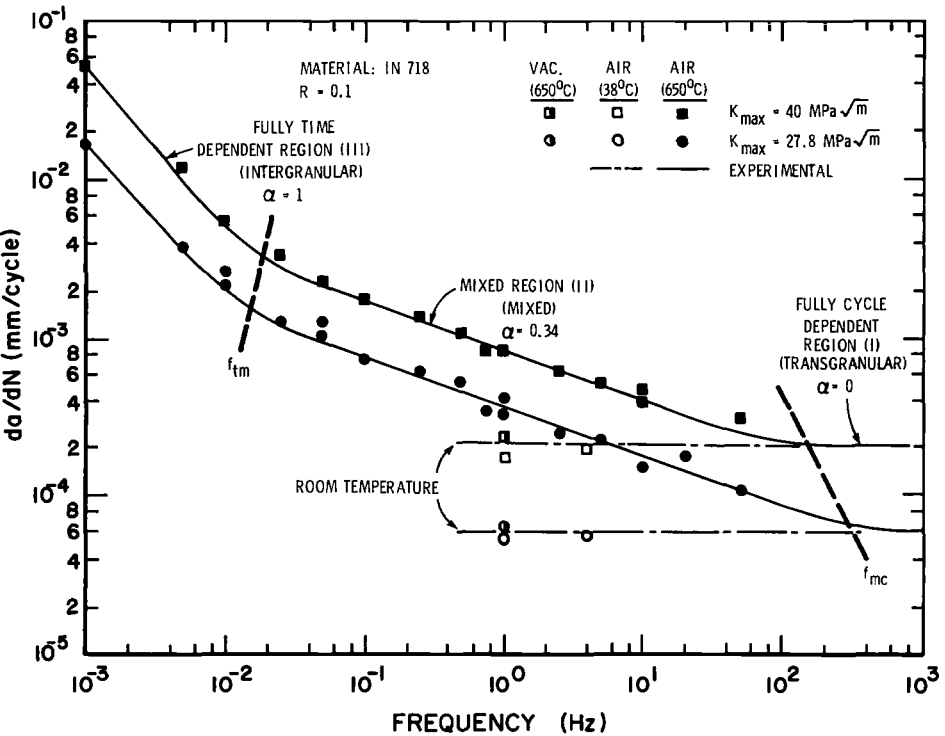


FIG. 4—Fatigue crack growth rate, (da/dN), for Inconel 718 as a function of frequency at $R = 0.1$; temperature = 650°C at two different K_{\max} values, 27.8 and $40 \text{ MPa m}^{1/2}$. Also data in vacuum at 1 Hz [17] and room temperature air data are given.

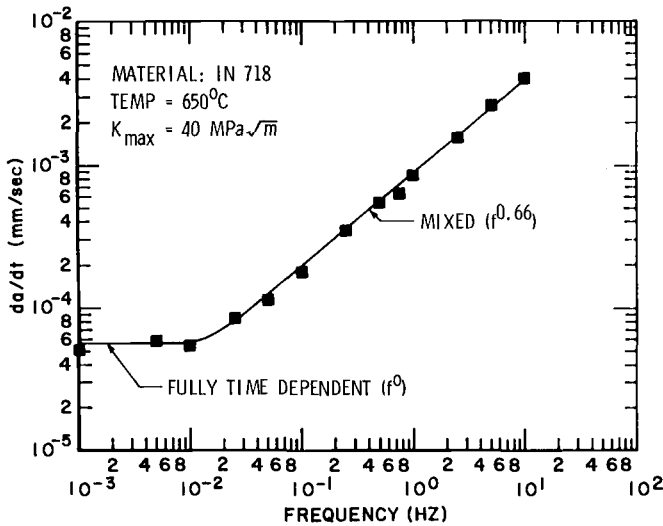


FIG. 5—Time rate of crack growth, (da/dt) , for Inconel 718 as a function of frequency at $K_{max} = 40 \text{ MPa m}^{1/2}$, $R = 0.1$, and temperature = 650°C .

Fully Cycle Dependent Growth—Although there are not many data points at frequencies greater than 10 Hz, for higher frequencies, da/dN is constant and should approach the frequency independent growth rate line at room temperature or high vacuum at 650°C . Though such a behavior was not specifically observed in air tests at 650°C , as we were unable to achieve ultrahigh frequencies for the work reported in this paper, it was observed by Tien [17] that if the frequencies were sufficiently high, the effect of oxygen on the elevated temperature fatigue behavior could be suppressed resulting in a time-independent, but fully cycle-dependent process of damage. The asymptotic nature of the growth rate at higher frequencies was also proposed by Solomon and Coffin [11]. At frequencies greater than 50 Hz, fatigue crack growth is occurring so fast that there is insufficient time for the environment to contribute to any damage at the crack tip. Hence, at very high frequencies, growth rates should approach the frequency-independent growth rates at room temperature or in high vacuum at 650°C , where there is no environmental damage. In this region, fracture at the crack tip is believed to occur under a pure cyclic plastic deformation process. In both cases, though there is no environmental damage at the crack tip due to oxidation, at room temperature, rewelding of the crack is prevented by the surface oxide film [18]. To establish the FCGR-frequency behavior independent of environmental effects at 650°C , additional work is being conducted in vacuum [19].

Effect of K_{max} on FCGR-Frequency Plots at a Given R ($R = 0.1$)

Fatigue crack growth rates as a function of frequency are shown in Fig. 4 for maximum stress-intensity factors of $27.8 \text{ MPa m}^{1/2}$ and $40 \text{ MPa m}^{1/2}$. Both of the stress-intensity values in Fig. 4 lie in the mid-power-law region of the da/dN versus K_{max} curve, as shown by Ashbaugh [9]. When K_{max} is $27.8 \text{ MPa m}^{1/2}$, we also observed the existence of the above-discussed three regions at 650°C . For the fully time-dependent region, da/dN is observed to be an inverse function of frequency, f , while for the mixed region, it is an inverse function of f^α ($\alpha = 0.34$). At very high frequencies, that is, in the fully cycle-dependent region,

growth rates should approach a constant value, the room temperature growth rate, which is independent of the frequency and hence the oxidizing environment. The slopes of the three regions of the da/dN versus frequency curves are seen to be reasonably independent of K_{\max} for a given R value of 0.1 at 650°C for the two values of K_{\max} chosen in this investigation. Also from Fig. 4, as K_{\max} increases, the transition frequency from time-dependent to mixed regime increases and transition frequency from mixed to cycle-dependent decreases.

Effect of R on Growth Rate-Frequency Plots at $K_{\max} = 40 \text{ MPa m}^{1/2}$

Tests were conducted at $K_{\max} = 40 \text{ MPa m}^{1/2}$ for values of $R = 0.1, 0.5$, and 0.8 . The purpose of these tests was to examine the effect of stress ratio on FCGR as a function of frequency. Observed FCGR data are shown in Fig. 6. Also data in vacuum [16] at 1 Hz at 650°C and in air at room temperature are presented in this figure for R values of 0.1 and 0.5. At very high frequencies, FCGR is independent of frequency and should approach the growth rate at room temperature. All FCGR-frequency data in air at 650°C were characterized as falling within one of three regions: a fully time-dependent region with a slope of -1 , a mixed region with a slope of -0.34 , and a fully cycle-dependent region with a slope of zero. As R values were increased, the transition frequencies were shifted toward higher frequencies. Therefore, all three regions of crack growth were not observed for the high R

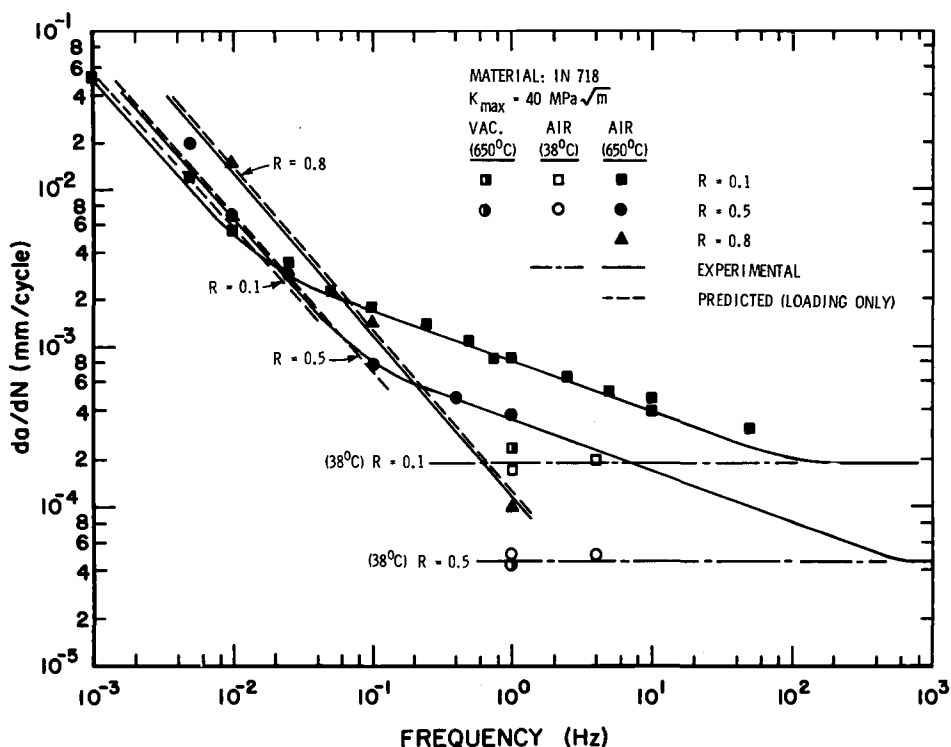


FIG. 6—Fatigue crack growth rate, (da/dN), for Inconel 718 as a function of frequency at $K_{\max} = 40 \text{ MPa m}^{1/2}$; temperature = 650°C for three different R values, 0.1, 0.5, and 0.8. Also 1 Hz vacuum data points [17] and room temperature data are given for $R = 0.1$ and 0.5.

values, since some of the transition frequencies apparently fell outside the range of tested frequencies. In this study, for $R = 0.5$, only the fully time-dependent and mixed-mode regions were observed. For $R = 0.8$, all data appeared to lie in the fully time-dependent region. For a given frequency, as R was increased, crack growth rate behavior tends to shift from a fully cycle-dependent mode to a mixed mode and, finally, to a fully time-dependent mode. This behavior was expected since, as R was increased, the crack tip tends to be at higher loads for a longer time for the same frequency, thus promoting environmentally enhanced damage at the crack tip.

Transition Frequencies

From Figs. 4 and 6, the existence of transition frequencies, from fully time-dependent to mixed fracture (f_{TM}) and from mixed to fully cyclic-dependent fracture (f_{MC}), can be observed. Using these transition frequencies, at a constant temperature, Eq 1 can be written in the form

$$\left(\frac{da}{dN}\right)_T = F_c(R, K_{\max}) \cdot f_{MC}^\alpha \cdot f_{TM}^{1-\alpha} \cdot \left(\frac{1}{f}\right) \left[1 + \left(\frac{f}{f_{TM}}\right)^2\right]^{(1-\alpha)/2} \left[1 + \left(\frac{f}{f_{MC}}\right)^2\right]^{\alpha/2} \quad (4)$$

where $F_c(R, K_{\max})$ is the fatigue crack growth rate as a function of K_{\max} and R at room temperature and high frequency, and α corresponds to the negative slope of the mixed region of the fatigue crack growth rate versus frequency curves. Fatigue crack growth maps, such as shown in Fig. 4 and given in Eq 4, can be used to indicate transition frequency boundaries and FCGR behavior of three regions of fatigue crack growth [20].

Micromechanisms of Crack Growth

Figure 7 shows typical fractographs taken from the three frequency regimes discussed above. An example of the fully cycle-dependent region is shown in Fig. 7a. As shown in Fig. 7a, crack growth is caused by the formation of striations due to cyclic plastic deformation at the crack tip. A typical fracture surface taken from the mixed-mode region is given in Fig. 7b. In this case, a mixture of transgranular and intergranular fracture was observed. Figure 7c is a typical representation of fracture in the fully time-dependent region. In this region, cracking occurred only along the grain boundaries, and the total fracture surface was covered with grain boundary facets.

In general, as frequency was decreased, fracture morphology changed from pure transgranular to a mixture of transgranular-intergranular and, finally, to a fully intergranular mode independent of R or K_{\max} . These three frequency regimes that correspond to the observed changes in the fracture morphology are approximately identical to the regimes that were detected from the changes in the slopes of the FCGR-frequency curves discussed in previous sections, for different values of R as well as K_{\max} , as shown in Figs. 4 and 6.

Mechanisms of Damage in the Fully Time-Dependent Regime

In the time-dependent region, crack growth occurred along the grain boundaries. Among the factors that could account for the time-dependent mechanisms are oxidation damage and creep-fatigue damage along the grain boundaries. Creep damage normally occurs by grain boundary cavitation and triple point cracking [21,22]. There was very little evidence of the presence of either of these mechanisms. Thus, the environment appears to dominate

INCONEL 718

4 μ

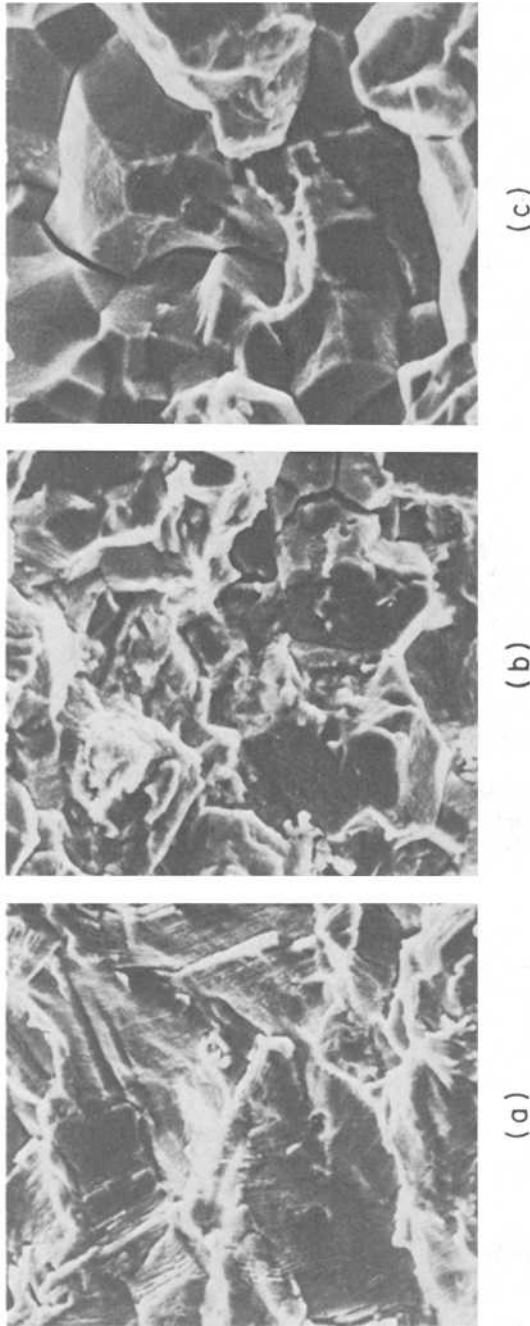


FIG. 7—Scanning electron fractographs of typical fracture surfaces for (a) cycle-dependent (10 Hz) region, (b) mixed (0.5 Hz), and (c) time-dependent (0.001 Hz). These tests were conducted at 650°C, $R = 0.1$, and $K_{max} = 40 \text{ MPa m}^{1/2}$.

the mechanism for damage under time-dependent conditions. There is evidence for this type of damage on the fracture surfaces: cracks were covered with oxides at lower frequencies. In general, oxygen can diffuse through grain boundaries faster than the bulk material at high temperatures. Environmental embrittlement of nickel-base superalloys at high temperature by oxygen penetration along the grain boundaries has been postulated in detail by Woodford and Bricknell [23]. In nickel-base superalloys, embrittlement is due to the penetration of gaseous species, primarily oxygen along the grain boundaries. Oxidation kinetics along the grain boundaries can be represented by an expression of the form

$$d = C \cdot t^n \cdot \exp\left(\frac{-Q}{RT}\right) \quad (5)$$

where d is the depth of oxygen penetration; C , n , Q , and R are constants; T is temperature; and t is time [24]. But Eq 5 may not be applicable in modeling the grain boundary oxidation kinetics because the stress effects are not represented in the expression.

Modeling the Growth Behavior

Phenomena of corrosion fatigue crack growth rate behavior (two regimes of pure cycle and pure time-dependency in these cases) have been described in terms of linear superposition by Gallagher and Wei [25] and Solomon and Coffin [11] for low-cycle fatigue crack growth in vacuum at high temperature. As Solomon [10] has seen, crack growth rate data could not be expressed with a linear superposition model when the mixed regime is appreciably large. From Figs. 4 and 6, the FCGR at 650°C for a K_{\max} in the mid-power-law region of growth rate behavior and R values up to a maximum of 0.8 can be represented by the general expression

$$\frac{da}{dN} = \text{MAX}(F_c, F_m, F_t) \quad (6)$$

where F_c , F_m , and F_t are functions of R , f , and K_{\max} , which describe the FCGR behavior in the three frequency regimes, cycle-dependent, mixed, and time-dependent, respectively. In Eq 6, the MAX function represents the maximum value of F_c , F_m , and F_t . The unified expression given in Eq 6 can be easily incorporated into a computer life prediction scheme, as almost all computer compilers have a built-in intrinsic MAX function. Derivation of the above three functional expressions is discussed below.

Prediction of Growth Rates in the Fully Time-Dependent Region—A prediction was made of the cyclic crack growth rate under fully time-dependent behavior based solely on sustained load crack growth data. For this case, by integrating the sustained load crack growth behavior during the total time period of the triangular waveform

$$\frac{da}{dN} = 2 \int_0^{1/2f} \frac{da_s}{dt} \cdot dt = 2C \int_0^{1/2f} [K(t)]^n \cdot dt \quad (7)$$

where $K(t)$ varies linearly with time for the triangular waveform and is given by

$$K(t) = R \cdot K_{\max} + 2 \cdot K_{\max} \cdot (1 - R) \cdot t \cdot f \quad (8)$$

where f is the frequency and $da/dt = C \cdot K^n$ is the sustained load crack growth behavior of the material ($n = 3$). In Eq 7, da/dN represents the crack growth in one cycle. From substituting the triangular waveform relation for $K(t)$ in Eq 7

$$\frac{da}{dN} = \frac{C \cdot K_{\max}^n}{f} \cdot \frac{1 - R^{n+1}}{(n+1)(1-R)} \quad (9)$$

For the triangular waveform in the fully time-dependent region, the crack growth rates predicted by Eq 9 were approximately two times that of the experimental data for a given frequency. Hence, for the triangular waveform in the fully time-dependent region, as shown in Fig. 6, the crack growth rate could be predicted by integrating the sustained load crack growth behavior along only the rising portion of the cycle. Dashed lines represent the predicted data from Eq 7 integrating only on the loading cycle of the waveform. This is consistent with the observations by Ashbaugh [9], who showed that under nonsymmetric waveshape loading, the observed FCGR corresponds to the FCGR of the rising portion of the cycle only. But as R increases above 0.8, the driving force, ΔK will be less than ΔK_{th} for this material. Assuming, when $R > 0.8$, that the integration should be performed on the total period of the cycle, FCGR in the fully time-dependent regime is given by the expression

$$F_f(R, K_{\max}, f) = \frac{da}{dN} = \frac{C \cdot K_{\max}^n}{f} \cdot \frac{1 - R^{n+1}}{(n+1)(1-R)} \cdot y \quad (10)$$

where $y = 0.5$ for $(1 - R)K_{\max} \geq \Delta K_{th}$ and $y = 1.0$ for $(1 - R)K_{\max} < \Delta K_{th}$. An expression of this type would satisfy the limit condition, R approaches 1, where $(da/dN) \cdot f$ should approach the sustained load crack growth rate, da/dt .

Prediction of Growth Rates in the Mixed Region—In the mixed region, FCGR was shown above to be proportional to $f^{-\alpha}$ for $R = 0.1$ and 0.5 at K_{\max} of $40 \text{ MPa m}^{1/2}$, and for $R = 0.1$ at K_{\max} of $27.8 \text{ MPa m}^{1/2}$. Using this observation, FCGR can be represented by the expression

$$F_m(R, K_{\max}, f) = \frac{da}{dN} = C_m \cdot R_m(R) \cdot \frac{K_{\max}^{n_m}}{f^\alpha} \quad (11)$$

where C_m and n_m are constants, and R_m is a function of R . If R_m is assumed to be of the Walker form [26,27]

$$R_m(R) = (1 - R)^{m_m} \quad (12)$$

then m_m could be evaluated from the data given in Fig. 6 ($m_m = 1.50$ and $n_m = 2.42$). We were unable to verify this expression from the study reported in this paper, as only two data points ($R = 0.1$ and 0.5) were available for any frequency chosen from the mixed regime. In future work, additional experiments will be conducted at other R values between 0.1 and 0.5 for more data points in this regime.

Prediction of Growth Rates in the Fully Cycle-Dependent Region—In the fully cycle-dependent or environmentally-independent regime, FCGR is independent of the frequency. Also in this regime, the FCGR approaches a value given by a room temperature experiment as discussed earlier. Figure 8 shows the FCGR as a function of $(1 - R)$ for two K_{\max} values,

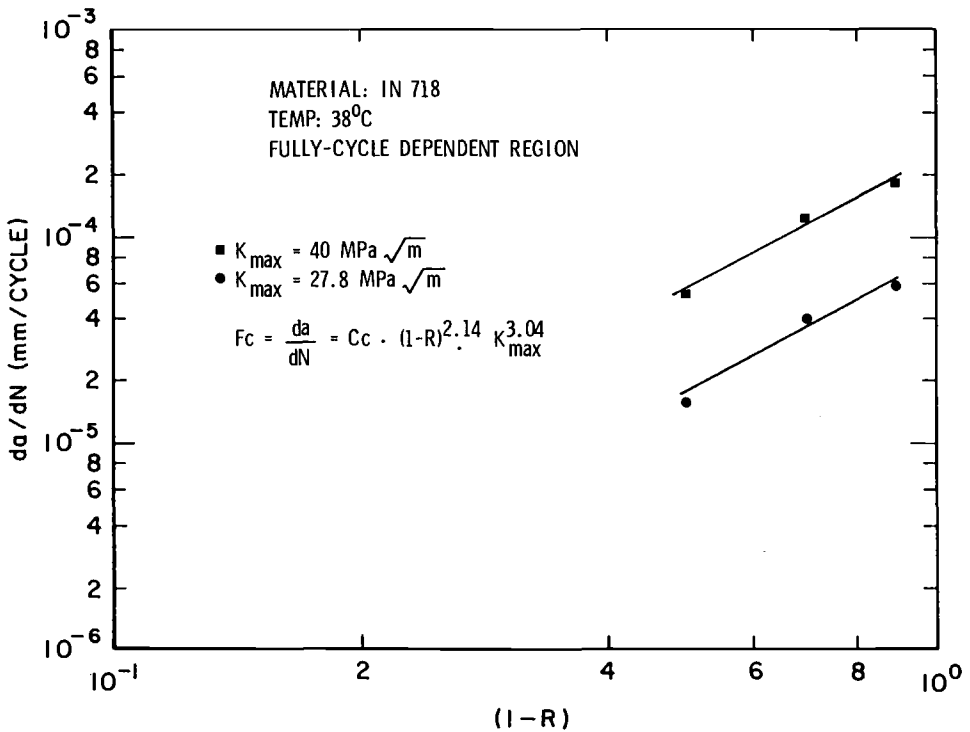


FIG. 8—FCGR for Inconel 718 at room temperature (38°C) and 1 Hz, as a function of $(1 - R)$ for $K_{\max} = 27.8$ and $40 \text{ MPa m}^{1/2}$.

27.8 and $40 \text{ MPa m}^{1/2}$ at room temperature. In this log-log plot, the variation of FCGR can be represented by straight lines for both K_{\max} values, where slopes of the two lines (m_c) are identical, and $m_c = 2.14$. In this frequency regime, FCGR can be represented by the expression

$$F_c(R, K_{\max}) = \frac{da}{dN} = C_c \cdot (1 - R)^{m_c} \cdot K_{\max}^{n_c} \quad (13)$$

where $n_c = 3.04$.

Conclusions

At high temperatures, frequency dependence of fatigue crack growth rate can be divided into three modes of damage: fully cycle-dependent, mixed, and fully time-dependent damage, irrespective of R -values, maximum stress intensity, and frequency. Three different models were derived for these frequency regimes, which can be represented with a single function to get the overall crack growth rate under any condition of R , K_{\max} (in the mid-power-law regime), and frequency as shown in Eq 6. Micromechanisms of fatigue crack growth which were obtained from extensive fracture surface analysis also indicate the existence of these three regimes of damage, thus providing a physical basis for the above modeling.

Acknowledgment

This work was supported by the Materials Laboratory at Wright-Patterson Air Force Base under AF Contract F33616-81-C-5015 and was conducted within the laboratories of the Metals and Ceramics Division of the Materials Laboratory. The author gratefully acknowledges the helpful discussions he had with Dr. T. Nicholas of AFWAL/Materials Laboratory and Dr. N. E. Ashbaugh of the University of Dayton Research Institute during the course of this work. He also appreciates the critical review of this paper by Dr. J. P. Gallagher of the University of Dayton Research Institute.

References

- [1] Larsen, J. M. and Nicholas, T., "Cumulative-Damage Modeling of Fatigue Crack Growth in Turbine Engine Materials," *Engineering Fracture Mechanics*, Vol. 22, No. 4, 1985, p. 713.
- [2] James, L. A., "Fatigue Crack Propagation Behavior of Inconel 718," HEDL Rep. TME 75-80, Hanford Engineering Development Laboratory, Westinghouse Hanford Co., Richland, WA, September 1975.
- [3] Mills, W. J. and James, L. A., "Effect of Heat-Treatment on Elevated Fatigue Crack Growth of Two Heats of Alloy 718," Paper 78-WA/PVP-3, American Society of Mechanical Engineers, New York, NY, December 1978.
- [4] Clavel, M. and Pineau, A., "Fatigue Behavior of Two Nickel-Base Alloys I: Experimental Results on Low-Cycle Fatigue, Fatigue Crack Propagation and Substructures," *Materials Science and Engineering*, Vol. 55, 1982, p. 157.
- [5] Pedron, J. P. and Pineau, A., "The Effect of Microstructure and Environment on the Crack Growth Behavior of Inconel 718 Alloy at 650°C Under Fatigue, Creep, and Combined Loading," *Materials Science and Engineering*, Vol. 56, 1982, p. 143.
- [6] Clavel, M. and Pineau, A., "Frequency and Wave-Form Effects on the Fatigue Crack Growth Behavior of Alloy 718 at 293 K and 823 K," *Metallurgical Transactions*, Vol. 9A, 1978, p. 471.
- [7] Shahinian, P. and Sadananda, K., "Creep-Fatigue-Environment Interactions on Crack Propagation in Alloy 718," *Engineering Aspects of Creep*, Vol. 2, Paper C239/80, Institute of Mechanical Engineers, London, 1980.
- [8] Nicholas, T., Weerasooriya, T., and Ashbaugh, N. E., "A Model for Creep/Fatigue Interactions in Alloy 718," *Fracture Mechanics: Sixteenth Symposium, ASTM STP 868*, M. F. Kanninen and A. T. Hopper, Eds., American Society for Testing and Materials, Philadelphia, 1985, p. 167.
- [9] Ashbaugh, N. E., "Waveshape Effects upon Crack Growth in Inconel 718," paper presented at the 15th National Symposium on Fracture Mechanics, University of Maryland, College Park, MD, July 1982.
- [10] Solomon, H. D., "Frequency Dependent Low-Cycle Fatigue Crack Propagation," *Metallurgical Transactions*, Vol. 4, 1973, p. 341.
- [11] Solomon, H. D. and Coffin, L. F., Jr., "Effect of Frequency and Environment on Fatigue Crack Growth in A286 at 1100°F," *Fatigue at Elevated Temperature, ASTM STP 520*, American Society for Testing and Materials, Philadelphia, 1973, p. 112.
- [12] Weerasooriya, T., "Effect of Frequency on Fatigue Crack Growth Rate at High Temperatures," paper presented at the 16th National Symposium on Fracture Mechanics, Columbus, OH, August 1983.
- [13] Nicholas, T. and Weerasooriya, T., "Hold-Time Effects in Elevated Temperature Fatigue Crack Propagation," *Fracture Mechanics: Seventeenth Volume, ASTM STP 905*, J. H. Underwood et al., Eds., American Society for Testing and Materials, Philadelphia, 1986, p. 155.
- [14] Saxena, A. and Hudak, S. J., Jr., "Review and Extension of Compliance Information for Common Crack Growth Specimens," *International Journal of Fracture*, Vol. 14, No. 5, 1978, p. 453.
- [15] Weerasooriya, T. and Dirkes, E. M., "Variability of Fatigue Crack Growth Rate as a Function of Temperature, Frequency, and Stress-Intensity Factor for Constant K Testing," paper presented at the American Institute of Aeronautics and Astronautics Mini-Symposium, Air Force Institute of Technology, Wright-Patterson Air Force Base, OH, March 1983.
- [16] Venkataraman, S., Nicholas, T., and Zawada, L. P., "Environmental and Closure Effects on the Fatigue Crack Growth Behavior of High Temperature Aircraft Alloys," paper presented at the American Society for Metals Symposium on Crack Propagation Under Creep and Creep-Fatigue, Orlando, FL, October 1986.

- [17] Tien, J. K., "The Influence of Ultrasonic Frequency and Temperature on the Fatigue Behavior of a Nickel-Base Superalloy," Paper No. 12, 1971 American Institute of Mining, Metallurgical, and Petroleum Engineers' Meeting, 18 Oct. 1971, Detroit, MI.
- [18] Tien, J. K. and Gamble, R. P., "The Room Temperature Fatigue Behavior of Nickel-Base Superalloy Crystals at Ultrasonic Frequency," *Metallurgical Transactions*, Vol. 2, 1971, p. 1933.
- [19] Venkataraman, S., Nicholas, T., and Weerasooriya, T., "Effect of Environment on Cycle and Time Dependent Crack Growth of In 718," paper presented at the American Society for Metals Symposium on Crack Propagation Under Creep and Creep-Fatigue, Orlando, FL, October 1986.
- [20] Weerasooriya, T., "Crack Growth Mechanism Maps for Inconel 718," paper presented at the American Society for Metals Symposium on Crack Propagation Under Creep and Creep-Fatigue, Orlando, FL, October 1986.
- [21] Raj, R. and Ashby, M. F., "Intergranular Fracture at Elevated Temperature," *Acta Metallurgica*, Vol. 21, 1975, p. 1625.
- [22] Fields, R. J., Weerasooriya, T., and Ashby, M. F., "Fracture-Mechanisms in Pure Iron, Two Austenitic Steels, and One Ferritic Steel," *Metallurgical Transactions*, Vol. 11A, 1980, p. 333.
- [23] Bricknell, R. H. and Woodford, D. A., "The Embrittlement of Nickel Following High-Temperature Air Exposure," *Metallurgical Transactions*, Vol. 12A, 1981, p. 425.
- [24] Oshida, Y. and Liu, H. W., "Grain Boundary Oxidation and an Analysis of the Effects of Preoxidation on Subsequent Fatigue Life," *Low-Cycle Fatigue, ASTM STP 942*, American Society for Testing and Materials, Philadelphia, 1987.
- [25] Gallagher, J. P. and Wei, R. P., "Crack Propagation Behavior in Steels," *Proceedings, International Conference on Corrosion Fatigue: Chemistry, Mechanics, and Microstructure*, 1972, p. 409.
- [26] Walker, K., "The Effect of Stress Ratio During Crack Propagation and Fatigue for 2024-T3 and 7075-T6 Aluminum," *Effects of Environment and Complex Load History on Fatigue Life, ASTM STP 462*, American Society for Testing and Material, Philadelphia, 1970, p. 1.
- [27] Coles, A., Johnson, R. E., and Popp, H. G., "Utility of Surface-Flawed Tensile Bars in Cyclic Life Studies," *Journal of Engineering Materials and Technology*, Vol. 98, 1976, p. 305.

Indexes

Author Index

A

Aksel, B., 125
Anderson, T. L., 291
Ando, Y., 547
Ashbaugh, N. E., 800
Ayres, D. J., 724

B

Babuška, I., 101
Ball, D. G., 752
Banks-Sills, L., 620
Barker, D. B., 507, 569
Bass, B. R., 691
Bastias, P. C., 427
Bathias, C., 318
Begley, J. A., 830
Brickstad, B., 532
Bryan, R. H., 767

C

Castro, D. E., 818
Chao, Y.-H., 441
Cheverton, R. D., 752
Chiang, F.-P., 281
Chona, R., 569
Coffin, L. F., 235
Corwin, W. R., 569
Cruse, T. A., 1, 19

D

Dahlberg, L., 532
Deason, V. A., 482
deWit, R., 679
Douglas, A. S., 466

E

Emery, A. F., 441
Epstein, J. S., 482, 597

Erdogan, F., 125
Etemad, M. R., 356

F

Fabi, R. J., 724
Fields, R. J., 679
Folias, E. S., 56
Fourney, W. L., 569

G

Garwood, S. J., 291
Gilbert, M. S., 637
Goetz, D. P., 374
Gooden, O. C., 637
Gordon, J. R., 291

H

Hahn, G. T., 427
Hudson, C. M., 374

I

Ingraffea, A. R., 405
Irwin, G. R., 569
Iskander, S. K., 752

J

Johansson, O., 441
Jung, Y. H., 392

K

Keeney-Walker, J., 691
Khatri, S., 507
Kobayashi, A. S., 441
Kordisch, H., 73
Krueger, D. D., 883
Kumar, A. M., 427

L

Laflen, J. H., 637
 Lambert, Y., 318
 Landgraf, R. W., 220
 Leis, B. N., 374
 Liaw, P. K., 830
 Logsdon, W. A., 830
 Love, W. J., 441
 Low, S. R. III, 679

M

Marci, G., 818
 Marschall, C. W., 569
 Merkle, J. G., 691, 767
 Mills, W. J., 330
 Moyer, E. T., 153
 Munz, D., 818
 Murty, K. L., 392

N

Nagar, A., 868
 Nanstad, R. K., 767
 Naus, D. J., 691
 Newman, J. C., Jr., 43
 Nicholas, T., 800
 Nilsson, F., 524
 Norris, D. M., 724

O

O'Connor, B. P. D., 787
 Orringer, O., 260

P

Plumtree, A., 787
 Pugh, C. E., 691

R

Raju, I. S., 43
 Reuter, W. G., 482, 597
 Rhee, H. C., 669
 Robinson, G. C., 767
 Rosenfield, A. R., 569
 Rubin, C. A., 427

S

Saillard, P., 318
 Sakai, Y., 547
 Salama, M. M., 669
 Schonenberg, R. Y., 724
 Scott, P. M., 374
 Sharpe, W. N., Jr., 466
 Smith, C. W., 5
 Sommer, E., 73
 Steele, R. K., 260
 Swedlow, J. L., 88
 Swenson, D. V., 405
 Szabó, B. A., 101

T

Turner, C. E., 356

V

Van Stone, R. H., 637, 883
 Vlieger, H., 169

W

Waclawiw, Z., 466
 Weerasooriya, T., 907
 Wessel, E. T., 569
 Wu, X.-P., 281

Y

Yagawa, G., 547
 Yang, C.-Y., 657

Subject Index

A

ADINA computer program, 74, 77
 Aircraft landing wheels, fatigue crack growth,
 872–874
 analysis verification, 875–876
 depth direction of, 881
 fatigue life prediction, 874–875
 flange wheel damage characterization
 curves, 879–881
 fracture surface observations, 876–878
 stress-intensity factors, 869–872
 Airworthiness regulations, stiffened-skin
 structures, 170–177
 Alloys
 22Ni-Mo-37Cr compact specimens, 74
 2024-T3 skins stiffened with 7075-T6 alloy,
 182–199
 aluminum
 2014-T6, 868
 6066-T6, 787
 7075, 433–436
 superalloys
 Inconel 718, 800, 883, 907
 René 95, 637
 Ti-15-3, 604
 Aluminum
 H-1100, three-dimensional crack-tip de-
 formation, 284–288
 weldments, *R*-curves and maximum load
 toughness, 298–310
 American Welding Society, D1.1 code, 387–
 388
 ANSI standards, B31.3: 375, 387
 Application-mode dynamic analyses, wide-
 plate crack arrest tests, 714–717
 Approximate methods, for dynamic crack
 propagation and arrest, 524
 ARREST program for residual strength, 177–
 199
 ASME Boiler and Pressure Vessel Code
 Section III, 240
 Section XI, 725, 777, 830

ASME standards, B31.3: 387

ASTM standards

A 508-81: 832
 A 533-82: 834
 B 645-84: 88
 E 8-85: 575
 E 208-84a: 547
 E 208-85: 88, 570
 E 319-85: 393
 E 399: 89
 E 399-83: 266, 273, 467, 476, 478, 480, 548,
 563, 570, 575, 598, 600, 601, 605, 610
 E 561-81: 437
 E 606-80: 228
 E 647-81: 908
 E 647-83: 820
 E 647-86: 228, 385, 803
 E 740-80(86): 43
 E 813-81: 331, 336, 337, 437
 E 1221: 507, 510, 511, 518–520, 522, 533,
 539, 543, 544, 547, 548, 569
 Automotive structure, mechanical durability
 assurance, 220

B

Bending

equation for surface cracks, 597
 surface crack growth, 38–39

Birefringent coatings, dynamic fracture be-
 havior of compact crack arrest spec-
 imens, 508–511

Boiling water reactor piping, intergranular
 stress-corrosion cracking, 235–239

BOND program for residual strength, 177–
 199

Boundary conditions, displacement-con-
 trolled, determination, 542–544

Boundary element solution technique for
 cracks (BEST/CRX), 23

Boundary integral equation

modeling of three-dimensional surface
 cracks, 21–26

Boundary integral equation—(*cont.*)
 traction, three-dimensional surface crack modeling, 26–29
 Boundary-layer effects, stress-intensity factors for corner cracks in rectangular bars, 51

British standards, BS 5447: 88

Brittle fracture, warm prestressing effects, 772–773

Brittle materials, residual strength, 212–213

C

Chemical composition, A533B Class 1 and A508 Class 3 steels, table, 549

Clean steel practice, rail economic life and, 274–275

Closure effects

K -dependent and K -independent, 901–904
 prior amplitude effects and, 825

Collapse controlled failure, critical tearing modulus and, 310–312

Compact crack arrest specimens

with birefringent coatings, dynamic fracture behavior, 507

displacement controlled boundary condition determination, 542–544

dynamic fracture properties during propagation and arrest, 532

Component analysis, mechanical durability analysis and, 226

Composition effects, fracture toughness of stainless steel welds, 341–346

Computational modeling, boundary integral equation for surface cracks, 21–29

Constraint, local, three-dimensional elastic-plastic finite-element analysis, 73–86

Contour integral method

edge-cracked panels, 117–121

extraction of stress-intensity factors, 111–113

L-shaped plane elastic bodies, 114–117

Cooperative Test Program for crack arrest, 571

round robin results and, 581–582

Corner cracks, in rectangular bars, stress-intensity factors, 43

CORPUS program for crack growth, 199–211

GARTEUR program and, 205–207

Crack arrest

compact specimens, 418–423

compact specimens with birefringent coatings, 507

double cantilever beam specimens, 409–417

dynamic fracture properties of A533-B steel, 532

under elastic-plastic conditions, 427

finite-element and line spring models, comparison, 529–531

nuclear reactor vessel steels

analysis and HEDIG gage results, 741–744

analysis and strain gage results, 744–748

stress-intensity factor at arrest, 749–751

pressurized ductile pipe, 441

thick pressure vessels, 772–776

Crack arrestors

deformation history, effect on J -resistance curves, 430–437

toughness values for steels and aluminum alloys, 438

weld-in steel, assessment and design procedure, 436–437

Crack arrest testing, dynamic effects, 586–589

Crack-arrest testing, wide-plate

dynamic finite-element fracture analyses

application-mode dynamic analysis, 714–717

generation-mode dynamic analysis, 717–718

posttest static and stability analysis, 706–714

posttest three-dimensional static analysis, 704–706

specimen geometry, material properties, and instrumentation, 698–701

test conditions, 704

Heavy Section Steel Technology Program

data acquisition, 686

dynamic finite-element fracture analyses, 691

instrumentation, 683–685

loading procedures, 686–688

objectives, 679

specimen configurations, 682–683

test conditions, 681–682

Crack arrest toughness

ASTM-proposed method, 553, 547

crack jump length and, 559–560

- ESSO test, 547, 553, 560–561
 - plane-strain
 - crack jump length and, 559–560
 - plane-strain fracture toughness and, 563
 - temperature effects, 556–557
 - round robin tests
 - arrest toughness determination, 573–575
 - loading arrangement, 571
 - loading procedure, 572–573
 - rapid fracture initiation, 571–572
 - recommended modifications, 589–592
 - results, 575–589
 - specimen geometry, 571
 - validity requirements, 575
 - stress-intensity factors at initiation and, 557–559
 - temperature effects, 553–556, 576
 - thickness effects, 561–563
 - Crack curving, in pressurized ductile pipe, 441
 - Crack extension, *R*-curves for predicting, 294–307
 - Crack front
 - free surface intersection stress behavior, boundary integral equation method, 29–33
 - straight, mixed-mode stress-intensity factor computation, 157–158
 - Crack growth, fatigue (*see* Fatigue crack growth)
 - Crack initiation
 - local crack-tip loading and constraint factor, 78–86
 - in thick pressure vessels, 772–776
 - Crack jump length, crack arrest toughness and, 559–560
 - Crack propagation
 - diagrams in damage tolerance analysis, 173
 - dynamic fracture properties, 532
 - effect of reflected stress waves, 512–513
 - finite-element and line spring models, comparison, 529–531
 - local crack tip loading and constraint factor, 78–86
 - mixed-mode dynamic, finite-element model, 406–408
 - Cracks
 - amplitude of stress singular terms, computation, 101
 - bolt hole, in rail, 270–271
 - elliptical (*see* Elliptical cracks)
 - internal, line spring model, 133–137
 - multiple, line spring model, 133–137
 - part-through in plates and shells, line spring model, 125
 - threshold and nonpropagation under service loading, 818
 - Crack-tip deformation, three-dimensional, in plastically deformed three-point bending aluminum, 281
 - Crack-tip diffraction, moiré interferometry, 494–499
 - Crack-tip opening angle, measurement from displacement record, 475
 - Crack-tip opening displacement
 - ductile fracture analyses and, 291–292
 - measurement with laser-based interferometric strain/displacement gage, 466
 - Crack velocity
 - alternate experimental procedures, 423–425
 - critical stress-intensity data generation, 405, 409–423
 - measurement techniques, comparison, 685
 - standard and ESSO specimens, 563–567
 - stress-intensity factors and, 520–521
 - Critical dynamic stress intensity, generation by combined experiments and analysis, 405, 409–423
 - Critical tearing modulus, determination, 310–312
 - CRKGRO computer program, 869, 874–875, 877, 881
 - Crossover behavior, fatigue crack growth in nickel-based superalloys, 901–904
 - Cutoff function method
 - edge-cracked panels, 117–121
 - extraction of stress-intensity factors, 113
 - L-shaped plane elastic bodies, 114–117
 - Cycle-dependent crack growth
 - Inconel 718 at high temperature, 914
 - modeling, 919
 - prediction of growth rates, 920–921
 - Cylindrical holes in plates, thickness effect on stress concentration factor, 57–64
- D**
- Damage accumulation, in aluminum alloy 6066-T6 cylindrical fatigue specimens, 787

- Damage analysis, automotive structures, 228–232
- Damage characterization curves, aircraft wheel flanges, 879–881
- Damage tolerance
 - in power generation industry, 235
 - residual strength and crack propagation diagrams, 173
 - stiffened-skin structures, 169
 - analytical verification, 176–177
 - compliance requirements, 171–174
- Data acquisition, in mechanical durability analysis, 223
- Defects
 - acceptance criteria, 387–389
 - welds, fitness-for-purpose defect acceptance criteria, 374
- Deformation history, effect on *J*-resistance curve of crack arrestors, 430–437
- Delta ferrite particles, effect on fracture toughness of stainless steel welds, 347–351
- Detail fracture, in rail, 263–270
- Displacements, displacement controlled boundary condition, 542–544
- Double-cantilever beams, wedge-loaded, for crack growth monitoring, 253–254
- Ductile fracture
 - analysis with *R*-curves and maximum load toughness, 291, 294–307
 - crack arrest in pressurized pipe, 441
 - crack-tip opening displacement and, 291–292
 - in thick pressure vessels, 774
- Ductile materials, residual strength, 214–217
- Durability, mechanical (*see* Mechanical Durability)
- Dynamic fracture, in compact crack arrest specimens with birefringent coatings, 507
- Dynamic strain aging, effects on A533B Class 1 pressure vessel steel, 392, 400–401

E

- Eisenberg model, 325–328
- Elastic-plastic fracture
 - ductile fracture analysis with single toughness value, 291
 - R*-curves and, 356

- three-dimensional crack-tip deformation, 281
- Electric Power Research Institute method, *R*-curves and maximum load prediction, 356
- Elliptical cracks
 - in bending, stress-intensity factors, 633–636
 - three-dimensional weight function method, 620, 621–626
 - approximate method, 626–630
 - exact solutions, 623–626
- Embrittlement, radiation (*see* Radiation embrittlement)
- EnJ method, *R*-curves and maximum load prediction, 356
- ESSO test for crack arrest toughness
 - calculation, 553
 - data, 560–561
- Extraction methods, stress singular terms for cracks and reentrant methods, 111–113

F

- Fatigue analysis, automotive structures, 228–232
- Fatigue behavior, defect-containing welds, 374
- Fatigue crack growth
 - aircraft landing wheels, 868
 - in aluminum alloy 6066-T6 cylindrical fatigue specimens, 787
 - CORPUS program, 199–211
 - environmentally enhanced cycle-dependent, 914, 920
 - environmental, Type 304 stainless steel
 - hydrogen water chemistry effects, 249
 - oxygen water chemistry effects, 245–249
 - frequency effects at high temperature, 907
 - micromechanisms, 917
 - at high load ratios in time-dependent regime, 800
 - in large-scale yielding, *J*-integral and, 318
 - modeling in cycle- and time-dependent regimes, 919
 - near-threshold, in nickel-based superalloys, 883
 - crossover behavior, 889–892
 - grain-size effects, 892–901

piping components, monitoring, 250–254
 in power generation industry, 235
 pressure vessels, *R*-curve data, 362–366
 pressure vessel steels and submerged-arc weldments, 830
 fracture morphology, 844–866
 tests, 838–844
R-curves and, 357–362
R ratio effect, 323, 329
 surface cracks
 in bending, 38–40
 constraint-loss model, 637
 in tension, 35–37
 Fatigue resistance, defect-containing welds, 383–387
 Fatigue threshold, effects of load history and prior amplitude, 818
 Fatigue tolerance range, effects of load history and prior amplitude, 818
 Federal Aviation Regulation 25.571: 170–174
 Finite-element methods
 crack arrest in nuclear reactor vessel steels, 724
 crack propagation and arrest
 dynamic fracture properties in compact crack arrest specimens, 432
 line spring model and, 529–531
 quasi-static, elastic-plastic analyses, 427, 430–437
 displacement solutions, conversion to stress-intensity factors, 670–672
 local crack-tip loading and constraint factor, 73–86
 mixed-mode
 dynamic crack propagation, 406–408
 stress-intensity calculations, 153
 stress analysis of moving cracks in compact crack arrest specimens, 511–521
 stress-intensity factors
 contour integral method, 111–113
 cutoff function method, 113
 three-dimensional
 corner cracks in rectangular bars, stress-intensity factors, 45–47
 surface cracks, boundary integral equation method, 23
 Fitness-for-purpose, defect acceptance criteria for welds with defects, 374, 383–384

Flaw behavior
 during large-break loss-of-coolant accidents, 756–764
 pressurized thermal shock in thick vessels, 767
 Fractography, weld fracture surface morphologies, 341, 350–353
 Fracture analyses, dynamic finite-element, of wide-plate crack arrest tests, 691
 Fracture, detail, in rails, 263–270
 Fracture mechanisms, stainless steel welds, 347–351
 Fracture resistance, rail, 272–273
 Fracture-safe engineering design, 356
 Fracture toughness
 computation from dynamic displacement data, 480
 plane-strain
 crack arrest toughness and, 563
 critical stress-intensity factor and, 604–606, 611–617
 pressure vessel A533B Class 1 steel
 dynamic strain aging, 392, 400–401
 neutron irradiation effect, 400
 testing, stainless steel welds, 330
 Free-surface effects, integrated frozen stress-moiré interferometric analysis, 5
 Frequency effects, fatigue crack growth at high temperature, 907
 Frozen stress photoelasticity, 6, 10–11

G

GARTEUR program, 205–207
 Gas-tungsten-arc welds, fracture toughness, 330
 Generation-mode dynamic analyses, wide-plate crack arrest tests, 717–718

H

Hall effect displacement gages, 732, 739, 741–744
h-extension process, 102–103
 High temperatures, frequency effect on fatigue crack growth rate, 907
 Holography, sandwich holospeckle interferometry, 282–288
 Hydrogen level in water, stress-corrosion cracking and, 249–250

I

- Inelastic fracture, dynamic, generation of critical stress intensity data, 405
- Integrated methods, frozen stress-moiré interferometric analysis, 7–9, 13–16
- Interferometric strain/displacement gage, crack-tip opening displacement measurement, 468–469, 471, 474–479
- Interferometry
 - frozen stress-moiré interferometric analysis, 7–9, 13–16
 - sandwich holospeckle, three-dimensional crack-tip deformation, 282–288
- Intergranular stress-corrosion cracking, in boiling water reactor piping, 235–238
 - laboratory monitoring, 239–240
 - modeling, 255–256
 - remedies, 239
 - smart monitors, 256–258
 - surface crack testing methods, 240–244
 - water chemistry effects, 245–250
 - wedge-loaded double-cantilever beam monitors, 253–254
- Interstitial impurities, effect on fracture of A533B Class 1 pressure vessel steel, 392

J

- J*-curves
 - J*-resistance, crack arrestors, deformation history effect, 430–437
 - three-dimensional elastic-plastic finite-element analyses, 73–86
- J*-integral
 - delta *J* determination, 798–799
 - ductile fracture analysis with, 291–293
 - fatigue crack growth in large-scale yielding and, 318
 - fracture toughness of stainless-steel welds, 336–340
 - R*-curve data beyond *J*-controlled growth, 357–362

L

- Large-break loss-of-collant accidents, 752–755, 764
- Lifetime predictions
 - automotive structures, damage analysis and, 228–232

- crack growth in nickel-based superalloys, 904
- mechanical durability in automotive structures, 220
- residual life estimation in nickel-based superalloy René 95, 645–655
- smart monitors for intergranular stress-corrosion cracking, 256–258
- surface cracks in aircraft landing wheels under service loading, 874–875
- three-dimensional effects, 73
- Linear elastic fracture mechanics
 - fatigue crack growth in aircraft landing wheels, 869–875
 - pressurized thermal shock loading of pressurized water reactor steels, 752–755
 - three-dimensional problems, integrated optical measurement method, 7–9, 13–16
 - two-dimensional technology and, 88
- Line spring model
 - coplanar multiple cracks, 137–149
 - crack propagation and arrest, finite-element methods and, 529–531
 - cracks in plates under thermal and residual stresses, 660–664
 - internal and multiple cracks, 133–137
 - limitations, 150, 657–658
 - part-through cracks, 664–667
 - part-through cracks in plates and shells, 125
 - theory, 658–660
- Load history, effect on fatigue threshold, 818
- Loading, crack tip, three-dimensional elastic-plastic finite-element analysis, 73–86
- Loads
 - bending or tensile, equation for surface cracks, 597
 - vehicle, analysis, 223–225
 - wheel, effect on rail, 275–276
- L-shaped plane elastic bodies, stress-intensity factors, 114–117

M

- Manganese silicide particles, effect on fracture toughness of stainless steel welds, 347–351

Material properties

- A533-B steel compact crack arrest specimens, 539–542
 - in mechanical durability analysis, 226–228
- Maximum load toughness, *R*-curve prediction for maximum stress and crack extension, 291
- Maximum pressure, pressure vessels, *R*-curve data, 362–368
- Mechanical durability, automotive structures component analysis, 226
 - design, 212–223
 - material properties, 226–228
 - service data, 223
 - vehicle loads analysis, 223–225
- Mesh refinement, effect on stress-intensity factors for corner cracks in rectangular bars, 51–52
- Microstructure, effect on fatigue crack growth of Alloy 718, 892–901
- Microvoid coalescence, fracture toughness of stainless steel welds and, 347–351
- Models
 - computational, boundary integral equation for surface cracks, 21–29
 - constraint-loss, for surface fatigue crack growth, 637
 - dual-Walker exponent mean-stress, 643–644
 - intergranular stress-corrosion cracking in piping, 255–256
 - linear cumulative damage, fatigue crack growth, 801–803, 807–812
 - line spring (*see* Line spring model)
 - one-dimensional, crack propagation and arrest, 525–531
- Modulus of elasticity, apparent
 - damage accumulation plot, 793
 - damage determination from changes in, 795
- Moiré interferometry, 601, 604
 - applied stress-intensity factor and critical stress-intensity factor, determination, 610–611
 - dynamic, stress wave and crack-tip diffraction events, 482
 - experimental evaluation of critical stress-intensity factor, 606–610
 - static, 484–485
 - stress-intensity factor estimates, 7–9, 13–16

Moment-modified compact-tension test specimens, 724

Monitoring

- crack growth in piping, 250–254
- laboratory, stress-corrosion cracking in welding pipe, 239–240
- smart monitors for intergranular stress-corrosion cracking, 256–258

N

- Neutron irradiation, effect on fracture toughness of pressure vessel steel, 400
- Nodal-force method, mixed-mode stress-intensity factor determination, 154–157
- Numerical methods
 - J* concept applicability to fatigue crack growth, 325–328
 - SAMCR, 507, 511–521

O

- Offshore structures, tubular joints, mixed-mode stress-intensity factors, 669
- Optical methods, integrated, three-dimensional effects measurement, 5
- Oxygen level in water, stress-corrosion cracking and, 245–249

P

- Panels, edge-cracked, stress-intensity factors, 117–121
- p*-extension, 103
- Piping
 - boiling water reactor, intergranular stress-corrosion cracking
 - laboratory monitoring, 239–240
 - modeling, 255–256
 - monitoring, 250–254
 - remedies, 239
 - smart monitors for, 256–258
 - surface crack testing methods, 240–244
 - water chemistry and, 245–250
 - pressurized, ductile crack bifurcation and arrest, 441
- PLASCOR computer program, 217
- Plates
 - cylindrical-hole weakened, thickness effect on stress concentration factor, 57–64

Plates—(cont.)

part-through cracks, line spring model, 125
under randomly distributed stress, line spring model, 660–664

wide

dynamic finite-element fracture analyses, 691
maximum stress and crack extension prediction, 294–307
R-curves and maximum load toughness, 294–310

Poison's ratio, effect on stress-intensity factors for corner cracks in rectangular bars, 52–53

Pressure vessels

fatigue crack growth in pressurized water environment, 830
initiation and maximum pressure, *R*-curve data, 362–368
upper shelf fracture behavior, 392

Pressurized thermal shock transients, analysis, 752–755

Pressurized water, fatigue crack growth in pressure vessels steels and submerged-arc weldments, 830

Pressurized water reactors

crack extension and arrest in reactor vessel steels, 724
thermal shock studies, review, 752

PRETUBE computer program, 672

PROBE computer program, 114

R

R-6 method, *R*-curves and maximum load prediction, 356

Radiation embrittlement, dynamic strain aging effect on A533B Class 1 pressure vessel steel, 392, 400–401

Rail

bolt hole cracks, 270–271
clean steel practice, 274–275
detail fractures, 263–270
fracture resistance, 272–273
residual stress, 272–273
structural integrity, 260
vertical split heads, 271–272
wheel load effects, 275–276

R-curves

in elastic-plastic fracture mechanics, 356

maximum load toughness for maximum stress and crack extension and, 291

Reentrant corners, amplitude of stress singular terms, computation, 101

Repeat inspection interval, for stiffened-skin structures, 176

Residual strength

ARREST and BOND programs, 177–199
diagrams in damage tolerance analysis, 173
unstiffened-skin materials, 212–217

Residual stress

plate surface cracks, line spring model for stress-intensity factor, 657
in rail, 272–273

R ratio

constraint-loss and dual-Walker exponent models, 643–645, 655
effects on crack growth
AISI 316 compact tension specimens, 323, 329
nickel-based superalloys, 901–904
high values, time-dependent crack growth rate, 800

Rupture, pressurized pipe, ductile propagation and arrest, 441

S

Safe inspection period, for stiffened-skin structures, 174–176

Sandwich holospeckle interferometry, three-dimensional crack-tip deformation, 282–288

Scanning electron microscopy, fracture surfaces in aircraft landing wheels, 876–878

Scattered light photoelasticity, 6, 10–11

Shells

part-through cracks, line spring model, 125
under randomly distributed stress, line spring model, 660–664

Shielded-metal-arc welds, fracture toughness, 330

Smart monitors, for intergranular stress-corrosion cracking, 256–258

Speckle photography, sandwich holospeckle interferometry, 282–288

Split heads, vertical, in rail, 271–272

Steel

1010, 443

1018, 494–499
 4340 compact specimens, 418–423, 507
 A106 Grade B, 374
 A508 Class 2
 thick vessels, 767
 thick wall cylinders, 752
 A508 Class 3, 547
 A514 bridge, 569
 A533B
 compact crack arrest specimens, 532
 R-curve data, 359–363
 wide-plate crack-arrest testing, 679
 wide plates, 298–307
 A533B Class 1, 547
 dynamic finite-element fracture analyses, 691
 reactor pressure vessel, 569
 upper shelf fracture behavior, 392
 A588 bridge, 569
 API 5LX56 wide plates, 298–307
 HY-130, *R*-curve data, 359–363
 HY-80, crack arrest analysis, 433–436
 SA333 Grade 6 carbon, 244
 SA508 Class 2a, 830
 SA508 Class 3a, 830
 SA533 B-1, 244
 SA533 Grade A, 830
 SA533 Grade B, Class 2, 830
 SAE-01 tool, 469–474
 stainless
 316 wide plates, 298–307
 AISI 316, 322–325
 Type 16-8-2 welds, 330
 Type 304, 244
 Type 308 welds, 330
 Stiffened-skin structures
 airworthiness regulations, 170–177
 damage tolerance, 169
 repeat inspection period, 176
 safe inspection period, 172, 174–175
 threshold inspection period, 176
 Strain amplitude, aluminum alloy 6066-T6
 cylindrical fatigue specimens, 790
 Strain rate, effect on upper shelf fracture
 behavior of A533B Class 1 steel, 392
 Stress analysis of moving cracks (SAMCR),
 507, 511–521
 Stress concentration factor, specimen thick-
 ness effect, 57–64

Stress fields, corner point of cylindrical-hole-
 weakened plates, 67–68
 Stress-intensity factors
 aircraft wheel flange during service load-
 ing, 869–872
 applied, moiré interferometric determi-
 nation, 610–611
 boundary-layer effect, 51
 compact crack arrest specimens, dynamic
 effects, 537–539
 computation from crack-tip opening dis-
 placement data, 475–480
 contour integral extraction method, 111–
 113
 corner cracks in rectangular bars, 46–53
 crack and hole problems and, 68–69
 critical
 experimental moiré interferometric
 evaluation, 606–610
 generation by combined experiments and
 analysis, 405, 409–423
 plane-strain fracture toughness and, 604–
 606, 611–617
 cutoff function method, 113
 dynamic
 ASTM, photoelastic data, and SAMCR
 calculations, table, 518
 calculation from isochromatic fringe
 patterns in compact crack arrest spec-
 imens, 508–511
 crack velocity and, 520–521
 localized displacement equations, 499–
 501
 edge-cracked panels, 117–121
 at initiation, crack arrest toughness and,
 557–559
 integrated frozen stress-moiré interfero-
 metric method, 7–9, 13–16
 L-shaped plane elastic bodies, 114–117
 measurement with boundary integral
 equation and finite-element methods,
 21–26
 mesh refinement effect, 51–52
 mixed-mode solutions
 offshore structural tubular joints, 669
 three-dimensional crack fronts, 153
 weld-toe surface flaw of an X-joint, 672–
 675
 moiré interferometric determination, 610–
 611

Stress-intensity factors—(*cont.*)

- moment-modified compact-tension test specimen at arrest, 749–751
- plate surface cracks under randomly distributed stress, line spring model, 657
- Poisson's ratio effect, 52–53
- prior amplitudes, effect on fatigue tolerance range, 818
- range for nonpropagation of fatigue cracks, 823, 826
- semielliptical cracks
 - in bending, 633–636
 - in a flat plate, 798

Stress, maximum, *R*-curves for predicting, 294–307

Stress waves

- propagation, dynamic moiré interferometry, 482
- reflected, effect on crack propagation, 512–513

Submerged-arc welds

- fatigue crack growth rate, 830
- fracture toughness, 330

Sulfur-bearing inclusions, in base and weld metals, 845, 866

Superalloys

- Inconel 718, 800, 883, 907
- René 95, 883

Surface cracks

- aircraft wheel flanges, analysis, 869–875
- under bending or tensile loads, equation for, 597
- in boiling water reactor piping, test methods, 240–244
- corner cracks in rectangular bars, stress-intensity factors, 43
- part-through, line spring model analysis, 664–667
- small, life predictions in nickel-based superalloy René 95, 654–655
- three-dimensional
 - boundary integral equation analysis, 19
 - traction boundary integral equation, 26–29
- X-joint weld-toe, stress-intensity factor, 672–675

Surface flaws, growth, constraint-loss model in nickel-based superalloy, 637

T

Temperature effects

- crack arrest toughness, 553–556, 576
- fracture toughness of stainless steel welds, 341–346
- nonlinear material behavior of A533-B steel, 539–542
- plane-strain crack arrest toughness, 556–557
- upper shelf fracture behavior of pressure vessel steel, 392

Temperature gradients, in wide-plate crack-arrest testing, 681, 686–688

Tensile loads, equation for surface cracks, 597

Tensile properties, pressure vessel steels at room temperature, 833

Tension, surface crack growth, 35–37

Thermal shock

- crack extension and arrest in nuclear reactor vessel steels, 724
- internal pressure loading of thick pressure vessels and, 769–777
- pressurized water reactor-related, review, 752

Thermal stress, plate surface cracks, line spring model for stress-intensity factor, 657

Thickness effects

- crack arrest toughness, 561–563
- stress concentration factor, 57–64

Three-dimensional effects

- crack-tip deformation in plastically deformed three-point bending aluminum, 281
- elastic surface crack modeling, 19
- frozen stress-moiré interferometric analysis, 7–9, 13–16
- lifetime predictions and, 73
- local crack-tip loading and constraint factor, 73–86
- mixed-mode stress-intensity factor calculation, 153
- part-through cracks in plates and shells, line spring model, 125
- specimen thickness effects on stress concentration factor, 57–64
- two-dimensional technology and, 88

Three-dimensional weight function method
(*see* Weight function method)
Threshold inspection interval, for stiffened-
skin structures, 176
Time-dependent crack growth, 802–803
Inconel 718 at high temperature, 914
micromechanisms, 917–919
modeling, 919
prediction of growth rates, 919–920
Titus system, 325–328
Traction boundary integral equation, three-
dimensional surface crack modeling,
26–29
Transmission electron microscopy, fracture
surfaces in aircraft landing wheels, 876–
878
Triaxiality of stress-strain state (*see* Con-
straint)
Tubular joints offshore structures, mixed-
mode stress-intensity factors, 669
TUIAP computer program, 673–674
Two-dimensional technology, linear elastic
fracture mechanics and, 88

V

Viscoplasticity
A533-B steel compact crack arrest speci-
mens, 539–542
equations for rate-dependent plasticity, 545

W

Warm prestressing
brittle fracture initiation and, 772–773
incipient, 754–755, 759, 764
Water chemistry, effect on intergranular
stress-corrosion cracking, 245–250

Wave propagation, one-dimensional model,
525–531
Weight function method
line spring model and, 660–661, 667
three-dimensional, for elliptical cracks, 620,
621–626
approximate method, 626–630, 632–633
exact solutions, 623–626
Welding processes, effect on fracture tough-
ness of stainless steel welds, 341–346
Weldments, submerged-arc, fatigue crack
growth, 830
Welds (*see also specific welds*)
aluminum, *R*-curves and maximum load
toughness, 298–310
with defects, fitness-for-purpose defect ac-
ceptance criteria, 374
stainless steel Types 308 and 16-8-2
chemical composition, 332
delta ferrite morphology, 339
fracture toughness, 330
tensile properties, 335
Weld toe, X-joint surface flaw, mixed-mode
stress-intensity factor, 672–675
Wheels
aircraft (*see* Aircraft landing wheels)
loads, effect on rail, 275–276
Wide-plate tests
crack arrest
application-mode dynamic analysis, 714–
717
generation-mode dynamic analysis, 717–
718
dynamic finite-element fracture analyses,
691
R-curves and maximum load toughness,
294–310

ISBN 0-8031-0972-5